This project has received funding from the European Union's Horizon 2020 research and innovation programme under grant agreement No. 700748

LIQUEFACT

Assessment and mitigation of liquefaction potential across Europe: a holistic approach to protect structures/ infrastructure for improved resilience to earthquake-induced liquefaction disasters.

H2020-DRA-2015

GA no. 700748

Deliverable D4.4

Database of calibrated numerical modelling results

Author(s):	A. Flora, E. Bilotta, V. Nappa, A. Chiaradonna, G. Fasano, S. Lirer, J. Quintero, M.D.L. Millen, A. Viana da Fonseca, C.G. Lai, G. Andreotti, A.G. Özcebe, F. Bozzoni, E. Zuccolo
Responsible Partner:	University of Napoli Federico II
Version:	2.0
Date:	27.01.2020
Distribution Level (CO, PU)	PU

This project has received funding from the European Union's Horizon 2020 research and innovation programme under grant agreement No. 700748

Document Revision History

Date	Version	Editor	Comments	Status
07 January 2019	1		First draft	Draft
27 January 2020	2		Final version	Submitted

List of Partners

Participant	Name	Country
ARU (Coordinator)	Anglia Ruskin University Higher Education Corporation	United Kingdom
UNIPV - Eucentre	Università degli Studi di Pavia	Italy
UPORTO	Universidade do Porto	Portugal
UNINA	Università degli Studi di Napoli Federico II.	Italy
TREVI	Trevi Società per Azioni	Italy
NORSAR	Stiftelsen Norsar	Norway
ULJ	Univerza v Ljubljani	Slovenia
UNICAS	Università degli Studi di Cassino e del Lazio Meridionale	Italy
SLP	SLP Specializirano Podjetje za Temeljenje Objektov, D.O.O, Ljubljana	Slovenia
ISMGEO	Istituto Sperimentale Modelli Geotecnici Società a Responsabilità Limitata	Italy
Istan-Uni	Istanbul Universitesi	Turkey

This project has received funding from the European Union's Horizon 2020 research and innovation programme under grant agreement No. 700748

CONTENTS

1 INTRODUCTION 18

1.1 ORGANIZATION, GOALS AND PURPOSE OF THIS DOCUMENT 18

1.2 THE EXPERIMENTAL EVIDENCES GAINED IN THE PROJECT 19

2 DEFINITION OF THE SEISMIC INPUT 20

2.1 BUILDING A SUBSOIL MODEL FOR PIEVE DI CENTO SITE 20

2.2 MOTIONS USED AS INPUT FOR CENTRIFUGE TESTS AND NUMERICAL ANALYSES ... 24

2.2.1 SELECTION OF THE NATURAL ROCK OUTCROP MOTIONS 24

2.2.2 PROPAGATION OF THE SCALED ROCK MOTIONS UP TO THE DEPTH OF 15 METERS 27

3 NUMERICAL ANALYSES 29

3.1 SOIL CONSTITUTIVE MODELS 29

3.1.1 FINN-BYRNE MODEL 29

3.1.2 UBC3D-PML 30

3.1.3 SANISAND 37

3.1.4 PM4SAND 40

3.1.5 PDMY02 MODEL 44

3.1.6 STRESS-DENSITY MODEL 44

3.2 NUMERICAL CODES 47

3.2.1 FLAC 2D & 3D 47

3.2.2 PLAXIS 2D 47

3.2.3 OPENSEES 47

3.3 MODELS CALIBRATION PROCEDURES 48

3.3.1 MODELS CALIBRATION FOR THE SIMULATION OF CENTRIFUGE TESTS 48

3.3.1.1 CHARACTERISTICS OF THE DRAINS ADOPTED IN THE NUMERICAL SIMULATIONS OF HD SCHEMES 58

3.3.1.2 NUMERICAL PROCEDURE ADOPTED TO SIMULATE THE EFFECT OF INDUCED PARTIAL SATURATION 59

3.3.1.3 CHARACTERISTICS OF THE STRUCTURE 60

This project has received funding from the European Union's Horizon 2020 research and innovation programme under grant agreement No. 700748

3.3.2 MODELS CALIBRATION FOR THE SIMULATION OF THE FIELD TRIALS AT THE TEST SITE 61
3.3.2.1 Finn-Byrne model 61
3.3.2.2 SANISAND model 62
3.4 LIST OF ANALYSES FOR THE CENTRIFUGE TESTS 68
3.5 LIST OF THE PARAMETRIC ANALYSES 71
3.5.1 LIST OF ANALYSES FOR THE STUDY ON THE EFFECT OF HORIZONTAL DRAINS 71
3.6 LIST OF ANALYSES FOR THE FIELD TRIAL TESTS 74
4 NUMERICAL SIMULATION OF CENTRIFUGE TESTS ON REFERENCE MODELS 75
4.1 SINGLE LAYER PROFILE IN FREE FIELD CONDITION 75
4.1.1 UBCSAND 75
4.1.1.1 ID: SF_xx_TC_UBC_31 75
4.1.2 PM4SAND 79
4.1.2.1 ID: SF_xx_TC_PM4_31 79
4.1.3 FINN-BYRNE AND PDMY02 83
4.1.3.1 ID: SF_xx_TC_FBY_31 83
4.2 SINGLE LAYER PROFILE WITH A SIMPLIFIED STRUCTURE ON TICINO SAND 89
4.2.1 UBCSAND 89
4.2.1.1 ID: SS_xx_TC_UBC_31 89
4.2.1.2 ID: SS_xx_TC_UBC_31+ 95
4.2.2 PM4SAND 101
4.2.2.1 ID: SS_xx_TC_PM4_31 101
4.2.2.2 ID: SS_xx_TC_PM4_31+ 107
4.2.3 PDMY02 113
4.2.3.1 ID: SS_xx_TC_PDM_31 113
4.3 TWO LAYERS PROFILE IN FREE FIELD CONDITION ON TICINO SAND 116
4.3.1 UBCSAND 116
4.3.1.1 ID: DF_xx_TC_UBC_31 116
4.3.2 PM4SAND 121
4.3.2.1 ID: DF_xx_TC_PM4_31 121

This project has received funding from the European Union's Horizon 2020 research and innovation programme under grant agreement No. 700748

4.4 TWO LAYERS PROFILE WITH A SIMPLIFIED STRUCTURE ON TICINO SAND.....125
4.4.1 UBCSAND 125
4.4.1.1 ID: DS_xx_TC_UBC_31+ 125
4.4.2 PM4SAND..... 131
4.4.2.1 ID: DS_xx_TC_PM4_31+ 131
4.5 FINAL REMARKS.....137
5 NUMERICAL SIMULATION OF CENTRIFUGE TESTS WITH MITIGATION TECHNIQUES. 138
5.1 HORIZONTAL DRAINS IWITH THE SINGLE LAYER PROFILE 138
5.1.1 UBCSAND 138
5.1.1.1 ID: SF_HD_TC_UBC_31 138
5.1.2 PM4SAND..... 142
5.1.2.1 ID: SF_HD_TC_PM4_31.....142
5.2 HORIZONTAL DRAINS WITH THE TWO LAYERS PROFILE 146
5.2.1 UBCSAND 146
5.2.1.1 ID: DF_HD_TC_UBC_31.....146
5.2.2 PM4SAND..... 151
5.2.2.1 ID: DF_HD_TC_PM4_31 151
5.3 HORIZONTAL DRAINS UNDERNEATH A STRUCTURE 156
5.3.1 UBCSAND 156
5.3.1.1 ID: SS_HD_TC_UBC_31+ 156
5.3.2 PM4SAND..... 162
5.3.2.1 ID: SS_HD_TC_PM4_31+.....162
5.4 INDUCED PARTIAL SATURATION ON THE HOMOGENEOUS PROFILE IN FREE FIELD CONDITIONS 168
5.4.1 PM4SAND..... 168
5.4.1.1 ID: SF_IPS_TC_PM4_31.....168
5.4.1.2 ID: SF_IPS_TC_PM4_31+.....172
5.5 FINAL REMARKS.....176
6 PARAMETRIC STUDY TO EVALUATE THE PERFORMANCE OF MITIGATION TECHNIQUES AGAINST SOIL LIQUEFACTION 177
6.1 HORIZONTAL DRAINS (HD) 177

This project has received funding from the European Union's Horizon 2020 research and innovation programme under grant agreement No. 700748

6.1.1 FEM SIMULATIONS WITH PLAXIS2D 177
6.1.1.1 ID: SF_HD_H05_s05 & ID: SF_HD_H05_s10 177
6.1.1.2 ID: SS_xx_xx_xx 183
6.1.1.3 ID: SS_HD_H05_s10 190
6.1.1.4 ID: SS_HD_H05_s05 197
6.1.1.5 ID: DF_HD_H05_s05 & ID: DF_HD_H05_s10 204
6.1.1.6 ID: DS_xx_xx_xx 209
6.1.1.7 ID: DS_HD_H05_s10 216
6.1.1.8 ID: DS_HD_H05_s05 223
6.1.1.9 ID: SF_HDU_H05_s05 230
6.1.1.10 ID: SF_HDU_H05_s10 235
6.1.1.11 ID: SF_HDU_H05_s15 240
6.1.1.12 ID: SF_HDU_H10_s05 245
6.1.1.13 ID: SF_HDU_H10_s10 250
6.1.1.14 ID: SF_HDU_H10_s15 255
6.1.1.15 ID: SF_HDU_H15_s05 260
6.1.1.16 ID: SF_HDU_H15_s10 265
6.1.1.17 ID: SF_HDU_H15_s15 270
6.1.1.18 ID: DF_HDU_H05_s05 275
6.1.1.19 ID: DF_HDU_H05_s10 280
6.1.1.20 ID: DF_HDU_H05_s15 285
6.1.1.21 ID: DF_HDU_H10_s05 290
6.1.1.22 ID: DF_HDU_H10_s10 295
6.1.1.23 ID: DF_HDU_H10_s15 300
6.1.1.24 ID: DF_HDU_H15_s05 305
6.1.1.25 ID: DF_HDU_H15_s10 310
6.1.1.26 ID: DF_HDU_H15_s15 315
6.1.1.27 ID: SS_HDU_H05_s05 320
6.1.1.28 ID: SS_HDU_H05_s10 327
6.1.1.29 ID: SS_HDU_H05_s15 334
6.1.1.30 ID: SS_HDU_H10_s05 341

This project has received funding from the European Union's Horizon 2020 research and innovation programme under grant agreement No. 700748

6.1.1.31 ID: SS_HDU_H10_s10 348
6.1.1.32 ID: SS_HDU_H10_s15 355
6.1.1.33 ID: SS_HDU_H15_s05 362
6.1.1.34 ID: SS_HDU_H15_s10 369
6.1.1.35 ID: SS_HDU_H15_s15 376
6.1.1.36 ID: SS_HDU_H05_s05 383
6.1.1.37 ID: SS_HDU_H05_s10 390
6.1.1.38 ID: SS_HDU_H05_s15 397
6.1.1.39 ID: SS_HDU_H10_s05 404
6.1.1.40 ID: SS_HDU_H10_s10 411
6.1.1.41 ID: SS_HDU_H10_s15 418
6.1.1.42 ID: SS_HDU_H15_s05 425
6.1.1.43 ID: SS_HDU_H15_s10 432
6.1.1.44 ID: SS_HDU_H15_s15 439
6.2 FINAL REMARKS 446
7 NUMERICAL ANALYSES OF FIELD TRIALS 450
7.1 DESCRIPTION OF THE FIELD TRIALS 450
7.1.1 SITE CHARACTERIZATION 450
7.1.2 MITIGATION TECHNIQUES 452
7.1.3 EXPERIMENTAL TESTING PROGRAM 452
7.2 3D NUMERICAL MODEL 454
7.3 NUMERICAL SIMULATIONS ON VIRGIN SOIL 459
7.3.1 ANALYSES USING THE FINN MODEL (VS_FIN) 459
7.3.2 ANALYSES USING THE SANISAND MODEL (VS_SAN) 462
7.4 NUMERICAL SIMULATIONS ON SOIL WITH INDUCED PARTIAL SATURATION (IPS_FIN) 465
8 PARAMETRIC STUDY TO EVALUATE STRUCTURAL PERFORMANCE AT THE TEST SITE 469
8.1 1D NONLINEAR EFFECTIVE-STRESS ANALYSIS OF THE GROUND CONDITIONS 469
8.1.1 GENERALITIES 469
8.1.2 KEY MODEL ASPECTS 469
8.1.3 GROUND MOTIONS 469

This project has received funding from the European Union's Horizon 2020 research and innovation programme under grant agreement No. 700748

8.1.4 GEOMETRICAL MODEL 469
8.1.5 BOUNDARY CONDITIONS 471
8.1.6 MATERIAL MODELS 471
8.1.7 STATIC PROPERTIES OF THE SOILS 471
8.1.8 PERMEABILITY 472
8.1.9 DYNAMIC PROPERTIES OF THE SOILS 472
8.1.9.1 LIQUEFIABLE SAND 472
8.1.9.2 NON LIQUEFIABLE SANDS 473
8.1.9.3 RAYLEIGH DAMPING PARAMETERS 474
8.1.10 RESULTS 475
8.2 2D NONLINEAR EFFECTIVE-STRESS ANALYSIS OF THE GROUND CONDITIONS 484
8.2.1 GENERALITIES 484
8.2.2 KEY MODEL FEATURES 484
8.2.3 BUILDING 485
8.2.4 RESULTS 485
8.3 FINAL CONSIDERATIONS ON 1D AND 2D ANALYSES 494
8.4 STRUCTURAL ANALYSIS: MODEL DESCRIPTION 494
8.4.1 GENERALITIES 494
8.4.2 KEY FEATURES OF THE PHYSICAL MODEL 494
8.4.3 GROUND MOTIONS 498
8.4.4 STRUCTURAL MODEL 498
8.4.4.1 BEAMS AND COLUMNS 498
8.4.4.2 BEAM-COLUMNS JOINTS 498
8.4.4.3 MASONRY INFILLS 499
8.4.5 FOUNDATION MODEL 500
8.4.5.1 INTRODUCTION 500
8.4.5.2 MATERIAL MODELS FOR SPRING AND DASHPOT ELEMENTS 501
8.4.5.3 PROCEDURE OF ANALYSIS 505
8.5 STRUCTURAL ANALYSIS: MODEL PERFORMANCE 506
8.5.1 NONLINEAR PUSHOVER ANALYSIS 506
8.5.2 RESULTS 511

This project has received funding from the European Union's Horizon 2020 research and innovation programme under grant agreement No. 700748

8.5.2.1 INTER-STOREY DRIFT 511
8.5.2.2 FOUNDATION SETTLEMENT 515
8.5.3 DISCUSSION 518
8.6 FINAL CONSIDERATIONS ON BUILDINGS PERFORMANCE 521
REFERENCES 523
APPENDIX A: VERIFICATION OF PIEVE DI CENTO SITE DURING M6.1 MAY, 20 2012 EVENT (§2) 529
A.1. INTRODUCTION 529
A.2. RESULTS CONSIDERING THE SHAKE TABLE MOTIONS AT 15 METERS 530
APPENDIX B: CONTOUR PLOTS OF ΔU FROM THE PARAMETRIC ANALYSES (§6.1) 531
B.1. FREE FIELD SINGLE LAYER 531
B.2. SINGLE LAYER WITH STRUCTURE 541
B.3. FREE FIELD TWO LAYERS 551
B.4. TWO LAYERS WITH STRUCTURE 560
APPENDIX C: 1-D model results (§8.1) 571
APPENDIX D: 2-D model results (§8.2) 589

This project has received funding from the European Union's Horizon 2020 research and innovation programme under grant agreement No. 700748

List of Figures

Figure 3.1. (a) In-situ investigation and geological section across the test-site. (b) Geological A-A' section of Po Plain (after Paolucci et al., 2015 and after Minarelli et al., 2016). Interface of QM (Marine Quaternary) is used as the discontinuity for the seismic bedrock. Orange line shows the location of the test site. 21

Figure 3.2. Shear wave velocity profile used for Pieve di Cento site. (a): in larger depth range, (b): in smaller depth range (from Chiaradonna et al., 2018b). 23

Figure 3.3. Comparison of acceleration and velocity response at 15 meters of depth in time and frequency scales with different models. 27

Figure 4.1. Evolution of the plastic shear modulus G_p as a function of the plastic component γ^p of the shear strain. 32

Figure 4.2. Volumetric soil behavior. 33

Figure 4.3. Representation of the soil densification effect in the p'-q plane. 35

Figure 4.4. Boundary surfaces in p':q space. 39

Figure 4.5. Relative state parameter index. 42

Figure 4.6. Comparison between the cyclic test on the Toyoura Sand carried out with the original S-D Model (Fortran) and the S-D Model implemented in FLAC 2D. 46

Figure 4.7. Left: Modelled and reference modulus degradation curves. Right: modelled and reference small strain moduli profiles. 49

Figure 4.8. Comparison between experimental and numerical undrained cyclic resistance curves. 51

Figure 4.9. Top left: Triaxial loading scheme, top right: reference test data, bottom left: calibrated parameters (the ones highlighted by grey have functional correlation, the rest are kept same in all calibration procedures), bottom right: quad plot in terms of deviatoric strain-number of cycles, excess pore water pressure – number of cycles, axial strain – deviatoric stress, mean effective stress – deviatoric stress. Parameters of the constitutive model are explained in the text body. 54

Figure 4.10. Comparison of simulated response with experimental response in terms of quad plot. Explanation of variables are presented in Figure 3.3 and the paragraph following. It is noted that only the highlighted parameters are changed. 55

Figure 4.11. Comparison of simulated CRR curve with respect to the one formulated by Fioravante and Giretti (2016) 56

Figure 4.12. Left: Secant shear modulus degradation curve, right: shear and bulk moduli-depth relation. Reference curves are from Fioravante (2000). 57

Figure 4.13. Horizontal drain surface with holes. 58

Figure 4.14. Pipe system to connect horizontal drains to atmosphere. 58

This project has received funding from the European Union's Horizon 2020 research and innovation programme under grant agreement No. 700748

Figure 4.15. Shear modulus degradation curves calibrated on laboratory data. 61

Figure 4.16. Comparison between simulated and experimental data for the test 13/02/2018. 63

Figure 4.17. Comparison between simulated and experimental data for the test 22/02/2018. 63

Figure 4.18. Comparison between simulated and experimental data for the test 23/02/2018. 64

Figure 4.19. Comparison between simulated and experimental data for the test 21/05/2018. 64

Figure 4.20. Comparison between simulated and experimental data for the test 07/03/2018. 65

Figure 4.21. Comparison between simulated and experimental data for the test 19/03/2018. 65

Figure 4.22. Comparison between simulated and experimental data for the test 22/03/2018. 66

Figure 4.23. Comparison between simulated and experimental cyclic resistance curve. 66

Figure 4.24. Comparison between simulated and experimental normalized shear modulus, G/G_0 and damping ratio, D curves. 67

Figure 5.1. Conceptual drawing of the numerical models. Sides shown with same colour follow the same horizontal displacement. Ground motion is applied as the scaled version of the motion simulated during the centrifuge test. Note: In FLAC model, connections of sides B-C and D-E have physical contact, whereas in OpenSees it is achieved through equalDOF constraint for the horizontal component. 84

Figure 5.2. Comparison of modelled (blue) and recorded (red) responses in terms of acceleration and pore water pressure at various locations for homogeneous profile in free-field case (PDMY02 model, considering normal kH=1.4 x 10-3 m/s in the numerical domain). Left: Acceleration responses. Right: Pore water pressure response. Note: recorded and modelled acceleration responses (acc2-acc4) are lowpass filtered with a zero-phase 3rd order Butterworth filter with the corner frequency 49 Hz order 3. 86

Figure 5.3. Comparison of modelled (blue) and recorded (red) responses in terms of acceleration and pore water pressure at various locations for homogeneous profile in free-field case (PDMY02 model, considering reduced kH=0.5 x 10-3 m/s in the numerical domain). Left: Acceleration responses. Right: Pore water pressure response. Note: recorded and modelled acceleration responses (acc2-acc4) are lowpass filtered with a zero-phase 3rd order Butterworth filter with the corner frequency 49 Hz order 3. 87

Figure 5.4. Comparison of modelled (blue) and recorded (red) responses in terms of acceleration and pore water pressure at various locations for homogeneous profile in free-

This project has received funding from the European Union's Horizon 2020 research and innovation programme under grant agreement No. 700748

field case (Finn-Byrne model, nearly undrained assumption). Left: Acceleration responses. Right: Pore water pressure response. Note: recorded and modelled acceleration responses (acc2-acc4) are lowpass filtered with a zero-phase 3rd order Butterworth filter with the corner frequency 49 Hz order 3 88

Figure 5.5. As Figure 3.7 but with structural zones and elements. 113

Figure 5.6. Comparison of modelled (blue) and recorded (red) responses in terms of acceleration and pore water pressure at various locations for homogeneous profile with structure case (PDMY02 model, considering normal kH=1.4 x 10-3 m/s in the numerical domain). Note: recorded and modelled acceleration responses (acc2-acc4) are lowpass filtered with a zero-phase 3rd order Butterworth filter with the corner frequency 49 Hz order 3. 115

Figure 7.1. single layer of liquefiable sand. 446

Figure 7.2. Double layer with liquefiable sand and upper clay. 448

Figure 8.1. (a) Location (a) and plan view (b) of the test site. 450

Figure 8.2. Representative soil profile and location of soil sampling 451

Figure 8.3. Representative soil profile and CPTU results (a), soil behaviour type index Ic (b) 452

Figure 8.4. Pictures of the S-wave vibrator and vibrating base plate (a) and main specifications of the machine. 453

Figure 8.5. Photogrammetric survey of the testing areas (a) and cross section (b). 454

Figure 8.6. Numerical model used for simulation of the field trials. 455

Figure 8.7. Initial effective vertical stress (in Pa) (a) and pore pressure (in Pa) (b) distribution. 457

Figure 8.8. Effective vertical stress state induced by the S-vibrator before the shaking in 3D view (a) and along the cross section cutting the baseplate (b). 458

Figure 8.9 Recorded acceleration time history recorded at the baseplate and applied as input at the surface of the model. 458

Figure 8.10. Plan (a) and cross section (b) of the field trial on treated soil with IPS. 465

Figure 8.11. Vertical profiles of maximum acceleration and pore pressure ratio along the baricentric axis of the soil model. 466

Figure 8.12 Time histories of velocity recorded during the field-trial compared with the simulated ones. 467

Figure 8.13. Time histories of pore water pressure recorded during the field-trials compared with the simulated ones 467

Figure 8.14. Simulated time history of vertical displacement under the baseplate compared with the experimental settlement measured after the end of the shaking on site. 468

This project has received funding from the European Union's Horizon 2020 research and innovation programme under grant agreement No. 700748

Figure 9.1. 1-D numerical model in FLAC. 470
Figure 9.2. Calibration of (v_s-τ) factor. 470
Figure 9.3. Excess pore pressure ratio in the center of the second layer, motion 3. 476
Figure 9.4. Excess pore pressure ratio in the centre of the second layer, motion 15 476
Figure 9.5. Excess pore pressure ratio 477
Figure 9.6. Excess pore pressure ratio in the second layer at the top (L2T), centre (L2C) and at the bottom (L2B), using different groundwater level, motions 2, 10 and 17 478
Figure 9.7. Response spectra of the base and surface 479
Figure 9.8. Response spectra, motion 475-2 (2), 975-3 (10) and 2475-3 (17) 480
Figure 9.9. Response spectra using three different groundwater level 481
Figure 9.10. Fourier spectra. 482
Figure 9.11 Fourier amplitude ratio for all motions. 483
Figure 9.12. Numerical model with building in FLAC. 484
Figure 9.13. Excess pore pressure ratio under the building and in free field, motion 3. 486
Figure 9.14. Excess pore pressure ratio under the building and in free field, motion 15. 487
Figure 9.15. Excess pore pressure ratio 488
Figure 9.16. Response spectra under the structure (UB: under the building; and, FF: free field)) 489
Figure 9.17. Response spectra, motion 475-2, 975-3 and 2475-3 490
Figure 9.18. Fourier spectra under the structure. 491
Figure 9.19. Fourier spectra in free field conditions. 491
Figure 9.20. Transfer function 492
Figure 9.21. Settlements in the middle of the structure (lines from FLAC analyses and dots calculated from Karamitros simplified settlement estimation method) 493
Figure 9.22: Physical model of the reference structure 497
Figure 9.23: Foundation-soil systems: (a) rigid foundation on bedrock; (b) rigid foundation on compressible soil; (c) isolated footings on compressible soil 497
Figure 9.24: Numerical model for cases (a) and (b) and detail of the beam-column joints configuration. 499
Figure 9.25: Numerical model for structure with isolated footings. 501
Figure 9.26: Model for vertical stiffness degradation. 503
Figure 9.27: Load applied in pushover analysis on fixed base and spring-damper system 507
Figure 9.28: Results of pushover analysis. 510

This project has received funding from the European Union's Horizon 2020 research and innovation programme under grant agreement No. 700748

Figure 9.29: Example of inter-storey drift for motion m3 with return period of 475 years .512
Figure 9.30. Peak inter-storey drift.....514
Figure 9.31. Residual inter-storey drift.....517
Figure 9.32. Foundation settlements of building 1 submitted to surface motion 975-m3...517
Figure 9.33: Comparison between inter-storey drifts of fixed base structures. Response to input motions against surface motions. 519
Figure 9.34: Comparison between inter-storey drifts of structures subjected to surface motions. Response of fixed base structures against spring-damper structures. 520

Figure A.1 Shear wave velocity profiles. (a) up to 230 meters, (b) up to 1 meters (from Chiaradonna et al., 2018b). 529
Figure A.2. Results of excess pore water ratio profiles (from left to right: for 475, 975, and 2475 years).....530

Figure B.1 Acceleration at base and bottom of the model, motion 1, 475-1.....571
Figure B.2. Acceleration at base and bottom of the model, motion 2, 475-2.....571
Figure B.3. Acceleration at base and bottom of the model, motion 3, 475-3.....572
Figure B.4. Acceleration at base and bottom of the model, motion 4, 475-4.....572
Figure B.5. Acceleration at base and bottom of the model, motion 5, 475-5.....573
Figure B.6. Acceleration at base and bottom of the model, motion 6, 475-6.....573
Figure B.7. Acceleration at base and bottom of the model, motion 7, 475-7.....574
Figure B.8. Acceleration at base and bottom of the model, motion 8, 975-1.....574
Figure B.9. Acceleration at base and bottom of the model, motion 9, 975-2.....575
Figure B.10. Acceleration at base and bottom of the model, motion 10, 975-3.....575
Figure B.11. Acceleration at base and bottom of the model, motion 11, 975-4.....576
Figure B.12. Acceleration at base and bottom of the model, motion 12, 975-5.....576
Figure B.13. Acceleration at base and bottom of the model, motion 13, 975-6.....577
Figure B.14. Acceleration at base and bottom of the model, motion 14, 975-7.....577
Figure B. 15. Acceleration at base and bottom of the model, motion 15, 2475-1.....578
Figure B.16. Acceleration at base and bottom of the model, motion 16, 2475-2. 578
Figure B.17. Acceleration at base and bottom of the model, motion 17, 2475-3. 579
Figure B.18. Acceleration at base and bottom of the model, motion 18, 2475-4. 579
Figure B.19. Acceleration at base and bottom of the model, motion 19, 2475-5. 580

This project has received funding from the European Union's Horizon 2020 research and innovation programme under grant agreement No. 700748

Figure B.20. Acceleration at base and bottom of the model, motion 20, 2475-6. 580
Figure B.21. Acceleration at base and bottom of the model, motion 21, 2475-7. 581
Figure B.22. Shear stress vs shear strain, motion 1, 475-1.....581
Figure B.23. Shear stress vs shear strain, motion 2, 475-2.....582
Figure B.24. Shear stress vs shear strain, motion 3, 475-3.....582
Figure B.25. Shear stress vs shear strain, motion 4, 475-4.....582
Figure B.26. Shear stress vs shear strain, motion 5, 475-5.....583
Figure B.27. Shear stress vs shear strain, motion 6, 475-6.....583
Figure B.28. Shear stress vs shear strain, motion 7, 475-7.....583
Figure B.29. Shear stress vs shear strain, motion 8, 975-1.....584
Figure B.30. Shear stress vs shear strain, motion 9, 975-2.....584
Figure B.31. Shear stress vs shear strain, motion 10, 975-3.....584
Figure B.32. Shear stress vs shear strain, motion 11, 975-4.....585
Figure B. 33. Shear stress vs shear strain, motion 12, 975-5.....585
Figure B.34. Shear stress vs shear strain, motion 13, 975-6.....585
Figure B.35. Shear stress vs shear strain, motion 14, 975-7.....586
Figure B.36. Shear stress vs shear strain, motion 15, 2475-1.....586
Figure B.37. Shear stress vs shear strain, motion 16, 2475-2.....586
Figure B.38. Shear stress vs shear strain, motion 17, 2475-3.....587
Figure B.39. Shear stress vs shear strain, motion 18, 2475-4.....587
Figure B.40. Shear stress vs shear strain, motion 19, 2475-5.....587
Figure B.41. Shear stress vs shear strain, motion 20, 2475-6.....588
Figure B.42. Shear stress vs shear strain, motion 21, 2475-7.....588

Figure C.1. Acceleration at base and bottom of the model, motion 1, 475-1.....589
Figure C.2. Acceleration at base and bottom of the model, motion 2, 475-2.....589
Figure C.3. Acceleration at base and bottom of the model, motion 3, 475-3.....590
Figure C.4. Acceleration at base and bottom of the model, motion 4, 475-4.....590
Figure C.5. Acceleration at base and bottom of the model, motion 5, 475-5.....591
Figure C.6. Acceleration at base and bottom of the model, motion 6, 475-6.....591
Figure C.7. Acceleration at base and bottom of the model, motion 7, 475-7.....592
Figure C.8. Acceleration at base and bottom of the model, motion 8, 975-1.....592

This project has received funding from the European Union's Horizon 2020 research and innovation programme under grant agreement No. 700748

Figure C.9 Acceleration at base and bottom of the model, motion 9, 975-2.....593
Figure C.10. Acceleration at base and bottom of the model, motion 10, 975-3.....593
Figure C.11. Acceleration at base and bottom of the model, motion 11, 975-4.....594
Figure C.12. Acceleration at base and bottom of the model, motion 12, 975-5.....594
Figure C.13. Acceleration at base and bottom of the model, motion 13, 975-6.....595
Figure C.14. Acceleration at base and bottom of the model, motion 14, 975-7.....595
Figure C.15. Acceleration at base and bottom of the model, motion 15, 2475-1.....596
Figure C.16. Acceleration at base and bottom of the model, motion 16, 2475-2.....596
Figure C.17. Acceleration at base and bottom of the model, motion 17, 2475-3.....597
Figure C.18. Acceleration at base and bottom of the model, motion 18, 2475-4.....597
Figure C.19. Acceleration at base and bottom of the model, motion 19, 2475-5.....598
Figure C.20. Acceleration at base and bottom of the model, motion 20, 2475-6.....598
Figure C.21. Acceleration at base and bottom of the model, motion 21, 2475-7.....599

List of Tables

Table 3.1. Geotechnical model for Pieve di Cento site.....24
Table 3.2. Details regarding selected and scaled sets of 7 natural, rock outcrop acceleration motions for return periods of 475, 975, and 2475 years. T_r: return period in years, M_w: moment magnitude, R_{ep}: epicentral distance in kilometers, SF: scale factor, Source File: filename in the parent database. 26
Table 4.1. Final parameters used in Finn-Bryne model.....48
Table 4.2. Final parameters used in UBC3D-PML model.....49
Table 4.3. PM4sand parameters.....51
Table 4.4. Final parameters used in Finn-Byrne model.....53
Table 4.5. Properties of the structural elements.....60
Table 4.6. Set of parameters of the Finn-Bryne model adopted in the simulations.....61
Table 4.7. Lists of the main features of the cyclic shear tests.....62
Table 4.8. Model parameters of SANISAND for Pieve di Cento grey silty sand.....67
Table 4.9. ID structure: 1_2_3_4_5. 70
Table 4.10. ID structure: 1_2_3_4. 71
Table 4.11. Centrifuge numerical back-analyses. 72
Table 4.12. Trial site numerical simulations. 74
Table 7.1. Series of analyses was conducted on the scheme with a single layer.....446

This project has received funding from the European Union's Horizon 2020 research and innovation programme under grant agreement No. 700748

Table 7.2. Series of analyses was conducted on the scheme with a double layer. 448
Table 8.1. Soil properties adopted in the 3D numerical model. 455
Table 8.2 Depth of the sensors from the ground level. 465
Table 9.1 Input parameters of the Mohr-Coulomb model 472
Table 9.2 Input parameters of the PM4Sand model. 473
Table 9.3. Input parameters of the hysteretic damping model 474
Table 9.4: Geometric parameters for the reference model 495
Table 9.5: Random parameters for the reference model 496
Table 9.6: Random parameters generated for the five models 496

This project has received funding from the European Union's Horizon 2020 research and innovation programme under grant agreement No. 700748

1 INTRODUCTION

1.1 ORGANIZATION, GOALS AND PURPOSE OF THIS DOCUMENT

The main objective of Work Package 4 of the LIQUEFACT project is to study and comparatively analyse some of the most advanced ground improvement technologies for the mitigation of liquefaction risk. The activities developed in this Work Package are both experimental (at different scales: laboratory, centrifuge small scale models, field trials) and numerical.

This document focuses on the results obtained with the numerical analyses, considering the case of virgin soil (no ground improvement technique), that of the use of Horizontal Drains (HD), and that related to the use of Induced Partial Saturation (IPS), with the final goal to gain evidences of the pros and cons of the two selected liquefaction risk mitigation techniques.

As a first step, in **Chapter 2** the report introduces the considerations that led to the definition of the seismic input motions at the field trial test site (Pieve di Cento, Italy). Such motions were used as inputs in the centrifuge tests carried out at ISMGEO (Task 4.2), as reported in *Deliverable D4.2* (*Report on validation of retrofitting techniques from small scale models*).

Since liquefaction is a very complex, coupled mechanism, the constitutive models to be adopted in the simulations are much more complex than the ones usually adopted for static simulations of geotechnical problems. Therefore, in **Chapter 3** the main features of the advanced constitutive models implemented in the numerical codes (FLAC 2D and 3D, PLAXIS 2D, OpenSEES) and used in the simulations are briefly summarized. In this chapter, the calibration procedures followed to simulate the different experiments (in the centrifuge or at the test site) are also introduced.

Then, in **Chapter 4** (for the virgin soil cases) and **Chapter 5** (for the cases with mitigation techniques) the results of physical centrifuge modelling reported in the previously mentioned *Deliverable D4.2* are used as benchmarks to validate numerical modelling.

A deeper insight via a parametric analysis of the effectiveness of the considered mitigation technologies is reported in **Chapter 6** for HD.

In **Chapter 7**, modelling choices and numerical simulations aiming to reproduce the results obtained at a real scale in the field trial (in which ground shaking was applied via a mega shaker placed at ground level above a deeply instrumented subsoil) are reported. The details of the experimental results obtained at the field trials test site will be presented in *Deliverable D4.1* (*Report on the comparison of soil response before and after ground treatment at the pilot site*, to be uploaded on month 36), and only some essential experimental information is briefly recalled in this chapter.

Chapter 8 reports the results of a parametric analysis carried out to show the performance of some r.c. framed structures using the stratigraphy of the field trials test site.

Appendixes at the end of this document report some details of all the numerical analyses shown in the document, as recalled in the relevant sections.

This project has received funding from the European Union's Horizon 2020 research and innovation programme under grant agreement No. 700748

The results reported in this document are the outcome of the cooperation among different research groups. In writing the document, each partner took care of a specific section. In particular, UNINA is responsible for the whole document (as leader of Work Package 4) and has written all the sections for which no alternative indication is given in the following. UNIPV-Eucentre wrote the following sections (or parts of sections): §2, §3.1.1, §3.1.5, §3.1.6, §3.2.3, part of §3.3.1, §4.1.3, §4.2.3, Appendix A. UPORTO wrote §8, Appendix C, Appendix D.

1.2 THE EXPERIMENTAL EVIDENCES GAINED IN THE PROJECT

Numerical simulations are a powerful tool to get an insight on engineering problems, like the mitigation of liquefaction risk, only if they have been calibrated on and compared with consistent experimental results. Since liquefaction is a very complex mechanism, involving the temporary and cyclic transition from the mechanical behaviour of a granular soil to that of a fluid, good experimental data are needed to guide the numerical analyses. In this project, it was chosen to gain experimental evidences on untreated and treated soils at different scales:

a) at a lab scale, on small specimens that may be considered as unit element volume tests (as described in *Deliverable D4.1*);
b) in the centrifuge, where small scale models of liquefaction boundary value problems are spun up to respect scaling laws and then shaken, thus resembling the results obtained at real scale (as described in *Deliverable D4.2*);
c) at the real scale in a liquefiable test site, generating dynamic loading at ground level via a mega shaker and registering the effects in the subsoil in terms of relevant variables (as described in *Deliverable D4.3*).

In this document, the results obtained at the lab scale have been used in the calibration of the constitutive models, while those obtained in the centrifuge and at the field trials test site are used as benchmark results, to be simulated as closely as possible with the numerical analyses thus allowing a more comprehensive numerical parametric analysis. Obviously, this procedure follows a "blind" approach when the experimental results to simulate are not known (or not considered), while when these are already available and considered, calibration and simulation can be adjusted to have the best fitting of numerical and experimental results, whith an "open eyes" approach.

This project has received funding from the European Union's Horizon 2020 research and innovation programme under grant agreement No. 700748

2 DEFINITION OF THE SEISMIC INPUT

The procedure to compute the seismic motion to use as input for the centrifuge tests as well as the numerical analysis is herein reported.

2.1 BUILDING A SUBSOIL MODEL FOR PIEVE DI CENTO SITE

The soil deposits at the testing site (Pieve di Cento, Italy) have been characterized on the basis of the outcomes from the campaign carried out in the LIQUEFACT project (e.g. boreholes, Cross-Hole tests, etc.), whose results were integrated with geological and geotechnical information retrieved from the literature and from previous investigation campaigns acquired from the technical staff of the Emilia-Romagna Region. The stratigraphy near the test site is gathered from the study of Minarelli et al. (2016), which presents the geological information supported also by deep downhole (DH) investigations along a ~35 km-long segment in the Po Plain, starting from Cento and ending in Occhiobello (Figure 2.1a) (Martelli and Romani, 2013; Paolucci et al., 2015). The closest distances from the test site to the investigation line and the nearest deep downhole investigation are in the order of 2 and 5 kilometres, respectively.

Figure 2.1b shows the geological section of interest. Detailed information on the depth of the geological interfaces was obtained from a geological section from the CARG Project (http://www.isprambiente.gov.it), which includes two deep boreholes, called as Pievedicento001 (till 1.5km) and S13 CARG (till 70m). Minarelli et al. (2016) noted that the depth of the seismic bedrock (V_s=800 m/s) is not clearly determined; therefore, in this work the bedrock depth is assumed to coincide with the top of the Marine Quaternary formation (QM), located 230 m below ground level.

This project has received funding from the European Union's Horizon 2020 research and innovation programme under grant agreement No. 700748

a)

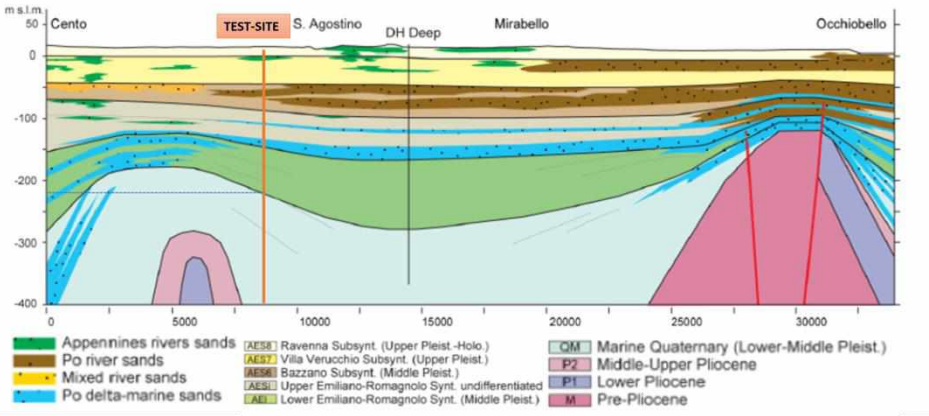

b)

Figure 2.1. (a) In-situ investigation and geological section across the test-site. (b) Geological A-A' section of Po Plain (after Paolucci et al., 2015 and after Minarelli et al., 2016). Interface of QM (Marine Quaternary) is used as the discontinuity for the seismic bedrock. Orange line shows the location of the test site.

Because of the high depth of the bedrock, a deep soil profile has been defined by using the information regarding the spatial distributions of the layers and the V_s ranges associated with different geological units, as provided by Minarelli et al. (2016). On the other hand, the available site investigation in the shallowest soil layers allowed to characterize in extreme detail the soil profile in the first 15 m under the ground level.

This project has received funding from the European Union's Horizon 2020 research and innovation programme under grant agreement No. 700748

Figure 2.1a reports the considered soil stratigraphy and the related Vs profile. The soil column consists of a sequence of silty-clay and sandy soil deposits, divided into several geological units, called subsynthems (Minarelli et al., 2016). Shear wave velocity and thickness was assigned to every subsynthem based on the DH results presented by Minarelli et al. (2016) and on the retrieved geological sections. Dynamic material curves are generated by considering Darendeli (2001) framework, in which the plasticity index is selected as 0 and 30 for 0-6 and 6-220 meters, respectively. Apart from the main influencing parameters (mean effective confining stress and plasticity index), other parameters are assigned as 1, 1, 10 for over-consolidation ratio (OCR), excitation frequency, and number of cycles (N) respectively.

Figure 2.1b focuses on the shallow stratigraphic sequence and the shear wave velocity profile as identified from a borehole and a cross-hole test carried out at the test site. The soil column consists of a sandy silt layer overlaying a silty sand layer, which is supposed to be the liquefiable layer. In the considered borehole, a thin clayey layer is identified in the silty sand deposits between 4.2 and 4.8 m depth. The same formation is in the soil profile beyond 6 m depth from the ground surface, as shown by combining the data coming from the 10 m borehole and pre-existing Cone Penetration Tests (CPT). The shear wave profile comes from the interpretation of the results of the Cross-Hole test. A linear trend has been defined in the clay layer; it has been adopted for the whole clay formation and the interbedded thin clay layer, which is not revealed by the Cross-Hole test.

Table 2.1. reports the main properties (thickness, unit weight, shear wave velocity) of the different strata of the geotechnical model.

This project has received funding from the European Union's Horizon 2020 research and innovation programme under grant agreement No. 700748

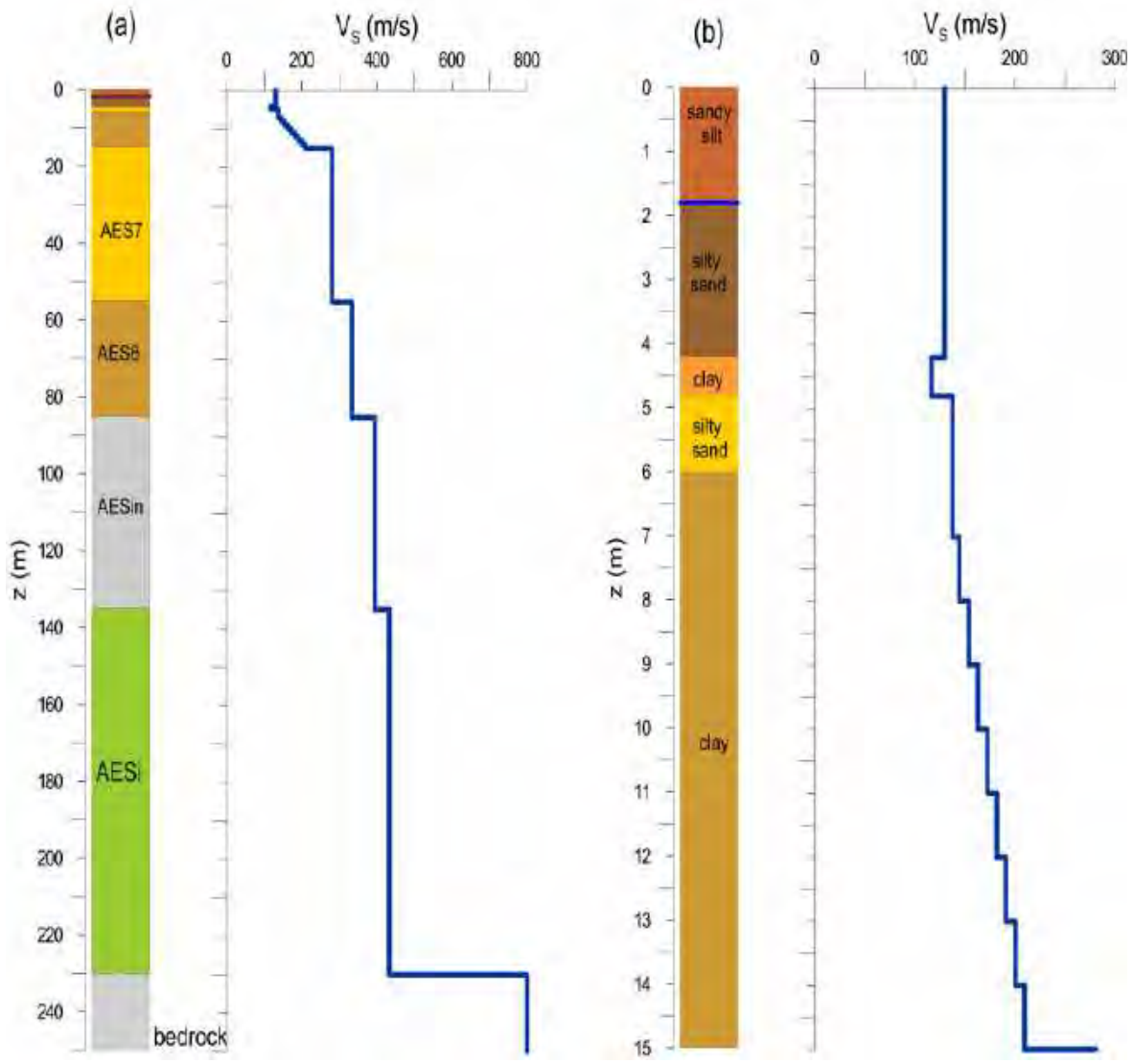

Figure 2.2. Shear wave velocity profile used for Pieve di Cento site. (a): in larger depth range, (b): in smaller depth range (from Chiaradonna et al., 2018b).

This project has received funding from the European Union's Horizon 2020 research and innovation programme under grant agreement No. 700748

Table 2.1. Geotechnical model for Pieve di Cento site.

Profile	**Soil**	**H (m)**	**γ (kN/m3)**	**V_s (m/s)**
Shallow	Sandy silt	1.8	16	130
	Silty sand	2.4	18.9	130
	Clay	0.6	18.9	117
	Silty sand	1.2	18.9	138
	Clay	9	18.9	138 ÷ 210
Deep	AES7	10	19.62	281
	AES7	10	19.62	281
	AES7	10	19.62	281
	AES7	10	19.62	281
	AES6	15	19.62	344
	AES6	15	19.62	344
	AESin	50	19.62	394
	AESi	95	19.62	434
	Halfspace	-	22	800

2.2 MOTIONS USED AS INPUT FOR CENTRIFUGE TESTS AND NUMERICAL ANALYSES

2.2.1 SELECTION OF THE NATURAL ROCK OUTCROP MOTIONS

A set of 7 natural accelerograms recorded on rock ground conditions was selected for each considered return period (i.e. 475, 975, and 2475 years). The selection was made using an updated version of the program ASCONA (Corigliano et al., 2012), which provides a set of recordings satisfying several criteria (like magnitude, distance, spectral shape, etc), with the additional requirement of compatibility with a target spectrum (in this case, the elastic acceleration response spectrum prescribed by the Italian design code for each considered hazard level), in a specified range of periods (in this case, [0.01-0.1s]). Recordings are taken from an internal database composed by accelerograms collected from accredited strong motion databases (ESM - European Strong-Motion database version 0.1, PEER NGA-West2 and Kik-net strong motion database). In order to assure compatibility with the target spectrum, recordings are scaled following the PEER scaling approach, which is given by the following equation:

This project has received funding from the European Union's Horizon 2020 research and innovation programme under grant agreement No. 700748

$$SF = \frac{\sum_i w(T_i)\ln\left(S_{a,tar}(T_i)/S_{a,rec}(T_i)\right)}{\sum_i w(T_i)} \qquad (2.1)$$

where *SF* is the scaling factor, *w* is a *weight function* defined for 261 spectral periods T_i evenly-spaced in log scale from 0.01s to 4 sec, $S_{a,rec}$ (T_i) is the elastic acceleration spectral ordinate of the recorded spectrum at T_i, $S_{a,tar}(T_i)$ is the elastic acceleration spectral ordinate of the target spectrum at T_i, and $w_i(T_i)$ is the weighting factor for T_i. In this work, w_i=0.5 is used for T= [0-0.1) s, w_i=1.0 is used for T= [0.1-1.0] *s*, and w_i= 0.1 is used for T_i= (1.0-4.0] s.

Among the sets of accelerograms satisfying the user-defined criteria and the spectrum-compatibility requirement, the set selected by ASCONA (characterized by the minimum average misfit between the mean response spectrum of the recordings and the target spectrum) has been adopted. The 21 selected accelerograms are listed in Table 2.2.

This project has received funding from the European Union's Horizon 2020 research and innovation programme under grant agreement No. 700748

Table 2.2. Details regarding selected and scaled sets of 7 natural, rock outcrop acceleration motions for return periods of 475, 975, and 2475 years. T_r: return period in years, M_w: moment magnitude, R_{ep}: epicentral distance in kilometers, SF: scale factor, Source File: filename in the parent database.

GM_ID	T_r (years)	M_w	R_{ep} (km)	SF	Source File
GM11	475	5.74	12.57	1.51	NGA RSN146_COYOTELK_G01320.AT2
GM12	475	5.90	10.10	1.79	ESM IT.ATN..HNN.D.19840507.174943.C.ACC.ASC
GM13	475	6.69	38.07	0.91	NGA RSN1091_NORTHR_VAS000.AT2
GM14	475	6.60	26.00	1.21	KiKnet 0KYH070010061330.NS2
GM15	475	6.60	62.00	1.24	KiKnet SAGH050503201053.EW2
GM16	475	5.20	11.80	2.26	ESM IT.AQP..HNN.D.20090409.005259.C.ACC.ASC
GM17	475	6.10	97.00	1.65	KiKnet MYGH041103280724.EW2
GM21	975	6.90	62.90	0.95	ESM EU.HRZ..HNE.D.19790415.061941.C.ACC.ASC
GM22	975	5.74	12.57	2.02	NGA RSN146_COYOTELK_G01320.AT2
GM23	975	5.90	10.10	2.39	ESM IT.ATN..HNN.D.19840507.174943.C.ACC.ASC
GM24	975	6.93	28.64	0.56	NGA RSN765_LOMAP_G01000.AT2
GM25	975	6.69	38.07	1.19	NGA RSN1091_NORTHR_VAS090.AT2
GM26	975	6.60	31.00	0.89	KiKnet SMNH100010061330.EW2
GM27	975	6.60	37.00	2.21	KiKnet SAGH010503201053.NS2
GM31	2475	6.90	62.90	1.33	ESM EU.HRZ..HNE.D.19790415.061941.C.ACC.ASC
GM32	2475	5.74	12.57	2.82	NGA RSN146_COYOTELK_G01320.AT2
GM33	2475	5.90	10.10	3.34	ESM IT.ATN..HNN.D.19840507.174943.C.ACC.ASC
GM34	2475	6.93	28.64	0.59	NGA RSN765_LOMAP_G01000.AT2
GM35	2475	6.69	38.07	1.66	NGA RSN1091_NORTHR_VAS090.AT2
GM36	2475	6.60	31.00	1.24	KiKnet SMNH100010061330.EW2
GM37	2475	6.60	37.00	3.09	KiKnet SAGH010503201053.NS2

This project has received funding from the European Union's Horizon 2020 research and innovation programme under grant agreement No. 700748

2.2.2 PROPAGATION OF THE SCALED ROCK MOTIONS UP TO THE DEPTH OF 15 METERS

As described in Deliverable 4.2 (Airoldi et al., 2018), the physical models used in the centrifuge were 30 cm high. Since in the centrifuge tests they were spun up at 50 g, the corresponding tested soil prototype depth is 15 m. Therefore, the definition of the total motion at 15 meters was necessary for the shaking table installed at the seismic centrifuge equipment of ISMGEO.

Given the fact that this piece of work was done at the very preliminary stage (with very little information on the tested soil), a sensitivity study has been carried out by considering three different constitutive models for the soil layers through the use of several different scaled ground motions (see Table 2.2). The adopted models are:

- Model (i): Equivalent linear model,
- Model (ii): Total stress, hysteretic model,
- Model (iii): Effective stress based loosely coupled Finn-Byrne model only for the top 6 meters. The main features of the Finn-Byrne model are discussed in §3.1.1.

The motion at 15 meters of depth was not very sensitive to the choice of the constitutive model. As an example, Figure 2.3 reports the comparison of the results obtained with the three different models at the depth of 15 m using ground motion GM23 (see Table 2.2).

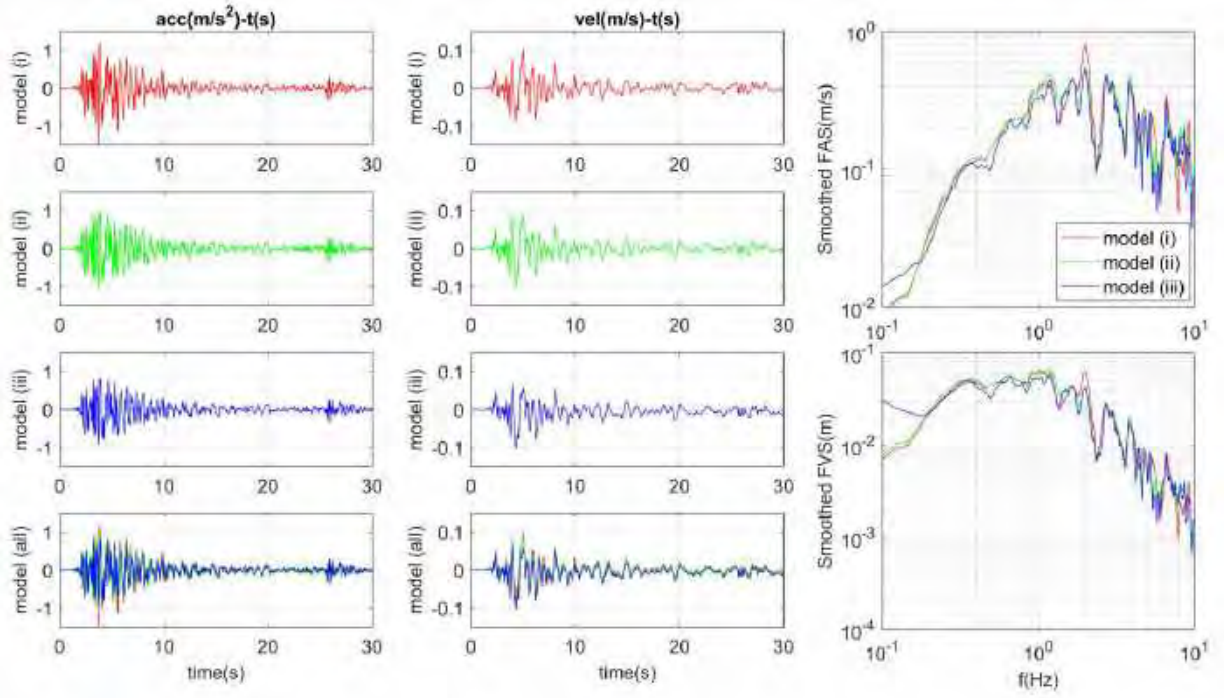

Figure 2.3. Comparison of acceleration and velocity response at 15 meters of depth in time and frequency scales with different models.

This project has received funding from the European Union's Horizon 2020 research and innovation programme under grant agreement No. 700748

Therefore, 21 ground motions have been provided by following model (ii) and scaled according to proper scaling laws, as discussed in Deliverable D4.2.

These ground motions have been also adopted as seismic input in the dynamic analyses on the shallow soil profile in effective stress condition according to a loosely coupled approach. Two different semi-empirical models were adopted to simulate the mainshock of the 2012 seismic sequence: the Finn-Byrne Model and a simplified pore water pressure model recently developed by Chiaradonna et al. (2018). Further details on this research work can be found in Appendix A.

This project has received funding from the European Union's Horizon 2020 research and innovation programme under grant agreement No. 700748

3 NUMERICAL ANALYSES

3.1 SOIL CONSTITUTIVE MODELS

3.1.1 FINN-BYRNE MODEL

The Finn-Byrne model is a two parameters incremental shear-volumetric coupling relationship for sand. The relationship is based upon experimental data and gives predictions that are in agreement with data of relative density and stress conditions (Byrne 1991).

Empirical evidence indicates that volumetric compression strains are induced by cyclic shear strain, due to a coupling between the shear and volumetric response of sand. These volumetric strains are plastic in nature rather that elastic as they are not recovers at the end of the loading cycle.

The basis of the approach is an equation linking the increment of volumetric strain per cycle of load with the shear strain occurring during that particular cycle. Under drained conditions, the increments can be simply added to give the accumulated volumetric strain with number of cycles. Under undrained conditions, the increment of volumetric strain leads to a rise in pore water pressure that is computed by imposing volume constraints together with an elastic rebound modulus.

The cyclic shear - volumetric coupling equation is:

$$\frac{\Delta\varepsilon_{vd}}{\gamma} = C_1 exp\left(-C_2 \frac{\varepsilon_{vd}}{\gamma}\right) \qquad (3.1)$$

where γ is the current shear strain, $\Delta\varepsilon_{vd}$ is the cumulative irreversible volumetric strain, $\Delta\varepsilon_{vd}$ is the irreversible volumetric strain increment and C_1 and C_2 are model parameters. The parameter C_1 controls the amount of volume change, while the parameter C_2 rules the shape of the accumulated volume change with the number of cycles. Since the shape of such volume change can be considered the same for all densities (Byrne 1991), parameter C_2 is computed as a function of C_1 for all relative densities as:

$$C_2 = 0.4/C_1 \qquad (3.2)$$

Then, eq. (3.1) involves only one parameter (C_1) to be calibrated, which depends on the density of the sand and can be assessed from cyclic loading tests or can be estimated from relative density or results of standard penetration test (SPT), based upon available data. The value of C_1 is expressed therefore as function of relative density or normalized standard penetration test as follows:

This project has received funding from the European Union's Horizon 2020 research and innovation programme under grant agreement No. 700748

$$C_1=7600(D_r)^{-2.5} \quad (3.3)$$

$$C_1=8.7(N_{1,60})^{-1.25} \quad (3.4)$$

The pore water pressure build-up for saturated undrained conditions can be computed from the volume compatibility as follows:

$$\Delta\varepsilon_v = \Delta\varepsilon_v^e + \Delta\varepsilon_v^p \quad (3.5)$$

In which $\Delta\varepsilon_v$ is the total incremental change in volumetric strain per ½ cycle, $\Delta\varepsilon_v^e$ is the elastic incremental change in volumetric strain per ½ cycle and $\Delta\varepsilon_v^p$ is the plastic incremental change in volumetric strain per ½ cycle. Since for saturated undrained conditions, $\Delta\varepsilon_v$ =0, equation (3.5) becomes:

$$\Delta\sigma'_v = -K\Delta\varepsilon_v^p \quad (3.6)$$

Where $\Delta\sigma_v'$ is the change in vertical effective stress per ½ cycle and K is the bulk modulus of the sand skeleton. If there is no change in total stress, $\Delta\sigma_v$=0, then the change in pore water pressure is $\Delta u=\Delta\sigma_v'$, hence:

$$\Delta u = K\Delta\varepsilon_v^p \quad (3.7)$$

Knowing $\Delta\varepsilon_v^p$ from equation (3.1) for any known half cycle of strain, the pore water pressure build-up per half cycle can be computed from equation (3.7).

3.1.2 UBC3D-PML

UBC3D-PML (Petalas 2012) is a constitutive model based on the UBCSand model (Puebla et al. 1997) that uses two yield surfaces of the Mohr-Coulomb type, one related to isotropic hardening and the other to kinematic hardening.

It is an elastoplastic model with non-associated plastic flow rule and is based on the Drucker-Prager's low and Rowe's stress dilatancy hypothesis. The model parameters calibration can be performed by using empirical relationships based on sand relative density (Beaty and Byrne 2011).

This model has been developed for the prediction of liquefaction in sandy soils. Its formulation is based on classical plasticity theory with a hyperbolic strain hardening rule, based on the Duncan-Chang approach with modifications. The hardening rule relates the mobilized friction angle to the plastic shear strain at a given stress. The flow rule in the model

This project has received funding from the European Union's Horizon 2020 research and innovation programme under grant agreement No. 700748

is based on the stress-dilatancy theory developed by Rowe (1962), linearized and simplified according to energy considerations. The UBC3D model uses the Mohr-Coulomb yield condition in a 3-D principal stress space. Moreover, a modified non-associated plastic potential function based on Drucker-Prager's criterion is used, in order to maintain the assumption of stress-strain coaxially in the deviatoric plane for a stress path beginning from the isotropic line (Tsegaye 2010).

A soil densification rule is added in order to predict a more realistic evolution of excess pore pressures during cyclic loading. This allows the increase of the volumetric strains with a decreasing rate during shearing.

The elastic behaviour occurring within the yield surface is governed by a non-linear law. Two parameters control this non-linear behaviour: the elastic bulk modulus K and the elastic shear modulus G. K and G are non-linear functions of the mean stress:

$$K = K_B^e P_A \left(\frac{p}{P_{ref}}\right)^{me} \qquad (3.8)$$

$$G = K_G^e P_A \left(\frac{p}{P_{ref}}\right)^{ne} \qquad (3.9)$$

where K_B^e and K_G^e are the bulk and the shear modulus, respectively, at a reference stress level. The factors ne and me are parameters that define the rate of stress dependency of stiffness. The reference stress level (pref) is commonly taken as the atmospheric pressure (PA=100 kPa). Pure elastic behaviour is predicted by the model during the unloading process. Once the stress state reaches the yield surface, plastic behaviour is predicted as long as the stress point is not going immediately back into the elastic zone. The hardening rule governs the amount of plastic strain as a result of mobilization of the shear strength ($\sin\varphi_{mob}$). The mobilized friction angle derived from the Mohr-Coulomb yield criterion is given as:

$$\sin\varphi_{mob} = \frac{\sigma_1' - \sigma_3'}{\sigma_1' + \sigma_3'} = \frac{t_{mob}}{s'} \qquad (3.10)$$

where t_{mob} is the mobilized shear stress and s is the mean effective stress.

The hyperbolic hardening rule relates the increment of the sine of the mobilized friction angle to the plastic shear strain increment as follows:

This project has received funding from the European Union's Horizon 2020 research and innovation programme under grant agreement No. 700748

$$\delta\gamma^p = \left(\frac{1}{G^*}\right)\delta \sin\varphi_{mob} \qquad (3.11)$$

$$G^* = K_G^p \left(\frac{p'}{P_A}\right)^{np} \left\{1 - \left(\frac{\sin\varphi_{mob}}{\sin\varphi_{peak}}\right) R_F\right\}^2 \qquad (3.12)$$

where K_G^p is the plastic shear modulus number; np is the plastic shear modulus exponent; φ_{mob} is the mobilized friction angle, which is defined by the stress ratio; φ_{peak} is the peak friction angle; and R_F is the failure ratio $\frac{n_f}{n_{ult}}$, ranging from 0.5 to 1.0, where n_f is the stress ratio at failure and n_{ult} is the asymptotic stress ratio from the best fit hyperbola. The evolution of the plastic shear modulus with the plastic component γ^p of the shear strain is reported in Figure 3.1.

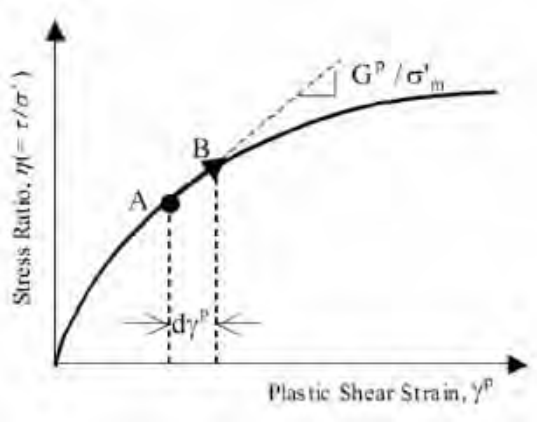

Figure 3.1. Evolution of the plastic shear modulus G_p as a function of the plastic component γ^p of the shear strain.

In the UBC3D-PLM model the flow rule of the original UBCSAND model is used, which was derived from energy considerations by Puebla et al. (1997). The flow rule used in UBCSAND is based on three observations:

1. there is a unique stress ratio, defined by the constant volume friction angle φ_{cv}, for which plastic shear strains do not cause plastic volumetric strains;

2. stress ratios which lie below $\sin\varphi_{cv}$ exhibit contractive behaviour, while stress ratios above it leads to a dilative response;

3. the amount of contraction or dilation depends on the difference between the current stress ratio and the stress ratio at $\sin\varphi_{cv}$.

This project has received funding from the European Union's Horizon 2020 research and innovation programme under grant agreement No. 700748

The variation of the plastic volumetric strain is given by:

$$d\varepsilon_v^p = sin\psi_m d\gamma^p \quad (3.13)$$

where:

$$sin\psi_m = sin\varphi_m - sin\varphi_{cv} \quad (3.14)$$

The evolution of the volumetric soil behaviour is shown in Figure 3.2.

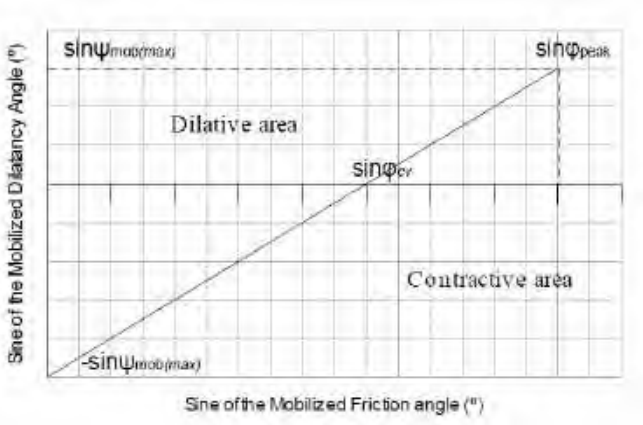

Figure 3.2. Volumetric soil behavior.

The densification rule is fully valid for symmetric loading cycles, for the case that shearing starts from the isotropic stress state. In a p' − q stress space when the mobilized friction angle is very small a half cycle is counted. The drained plastic shear modulus K_G^p becomes stiffer after the first full cycle in function of the follow equation:

$$K_G^p = K_{G,primary}^p \left(4 + \frac{n_{cross}}{2}\right) hard\ fac_{dens} \quad (3.15)$$

where n_{cross} is the number of half cycles generated from the beginning of the test, hard is a factor which is correcting the densification rule for loose soils and fac_{dens} is a multiplier which is a user input parameter to adjust the densification rule. A correction is made in the densification rule for loose sands $\left(5 \leq N_{1,60} \leq 9\right)$ according to the experimental observations and following the formulation of the UBCSAND for hard factor correlated to the SPT number and it follows the experimental observation proposed by Beaty and Byrne (2011) and reported by Naesgaard (2011):

This project has received funding from the European Union's Horizon 2020 research and innovation programme under grant agreement No. 700748

$$hard = \min\left(1, \max(0.5; 0.1N_{1,60})\right) \quad (3.16)$$

the plastic shear modulus is limited by the maximum $N_{1,60}$ for a very dense soil that is defined as 60:

$$K^p_{G,max} = K^p_G\left(\max N^2_{1,60mox}\right)0.003 + 100 \quad (3.17)$$

The new yield surfaces are schematically presented in Figure 3.3.

In Case a, primary loading occurs during the first half cycle in an arbitrary simple shear test starting from the p' axis. The initial input parameter for the plastic shear modulus K^p_G is used and both yield surfaces expand until the maximum stress state.

In Case b, elastic unloading occurs and the secondary yield surface shrinks until it reaches the isotropic axis where $\sin\varphi_{mob}$ is very small. A half cycle is counted. Since an isotropic hardening rule is used for the primary yield surface, it remains at the maximum stress state reached since the beginning of the test.

In Case c, secondary loading occurs but with an identical plastic shear modulus as used in primary loading followed by elastic unloading. A full cycle is counted. After the full cycle the densification rule is activated.

In Case d, secondary loading occurs with a plastic shear modulus 4.5 times stiffer than used in primary loading. The secondary yield surface expands until it reaches the maximum stress state of the primary yield surface. Then primary loading is predicted again until the new maximum stress state.

Finally, *in Case e*, when the primary yield surface touches the peak stress state (governed by the peak friction angle) the secondary yield surface is deactivated. After the deactivation of the secondary yield surface the primary loading surface is used again.

A new input parameter is defined at this stage in order to include the post-liquefaction behaviour of the soil. If a non-zero multiplier fac_{post} is specified, from that stage in the primary yield surface a modified plastic shear modulus will be used based on the following equation:

$$K^p_G = K^p_{G,primary}\, fac_{post} \quad (3.18)$$

By setting the fac_{post} parameter to a value lower than one, the post-liquefaction behaviour of the soil is simulated. The post-liquefaction reduction of the plastic shear modulus given by eq. (3.18) is consistent with experimental observations. If the factor equals to 1 then a plastic modulus identical to that used in primary loading is taken. Both possibilities are depicted in case e.

This project has received funding from the European Union's Horizon 2020 research and innovation programme under grant agreement No. 700748

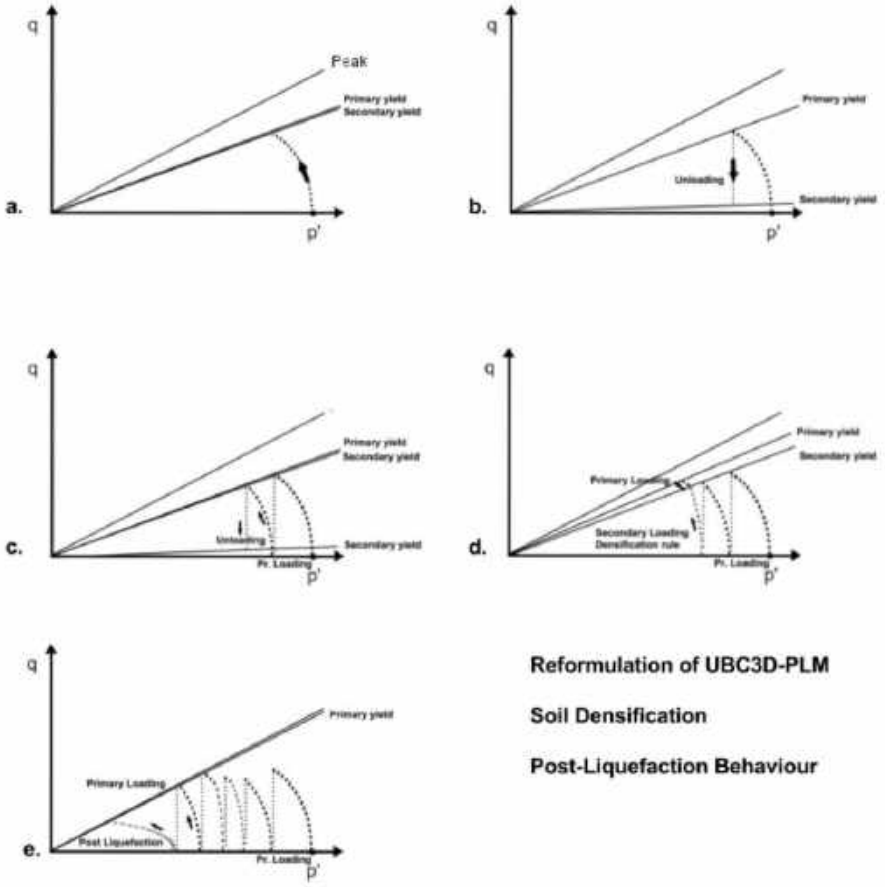

Figure 3.3. Representation of the soil densification effect in the p'-q plane.

The undrained behaviour of the soil is treated implicitly by the UBC3D- PLM constitutive model. Therefore, the increment of the pore water pressure is computed at each step of the analysis. Considering a saturated soil specimen, the increments in total stress during loading is given by the following equation:

$$dp = K_u d\varepsilon_v \qquad (3.19)$$

where K_u is the bulk modulus of the undrained soil and $d\varepsilon_v$ is the increment of total volumetric strain. The effective stress increment can be computed as follows:

This project has received funding from the European Union's Horizon 2020 research and innovation programme under grant agreement No. 700748

$$dp' = K' d\varepsilon_v \tag{3.20}$$

where K' is the bulk modulus of the soil skeleton.

The increment of the water pore pressure is computed by the following equation:

$$dp_w = \frac{K_w}{n} d\varepsilon_v \tag{3.21}$$

where K_w is the bulk modulus of the water and *n* is the soil porosity.

The relationship between the total stresses, the effective stresses and the pore pressure is assumed according to Terzaghi's theory:

$$dp = dp' + dp_w \tag{3.22}$$

$$\frac{K_w}{n} = (K_u - K') \tag{3.23}$$

The value of K_u, the bulk modulus in undrained condition, is a function of the Poisson's ratio as follow:

$$K_u = \frac{2G^e(1 + \nu_u)}{3(1 - 2\nu_u)} \tag{3.24}$$

Where G^e is the elastic shear modulus and ν_u is the Poisson's ratio in undrained condition, it is equal to 0.495 value close to the limit equal 0.5.

For the unsaturated soil the fluid bulk modulus is calculated by the following equation:

$$K_{w,unsat} = \frac{K_w^{sat} K_{air}}{S K_{air} + (1 - S) K_w^{sat}} \tag{3.25}$$

where K_w^{sat} is the bulk modulus of the saturated water and K_{air} is the bulk modulus of air equal to 1kPa. Finally, S is the degree of the saturation.

The calibration of model parameters can be performed by using empirical relationships based on sand relative density (Beaty and Byrne 2011), which are based on the SPT number $N_{1,60}$. It is possible to relate this last parameter to the relative density (RD) using the relationship (Idriss and Boulanger 2008):

This project has received funding from the European Union's Horizon 2020 research and innovation programme under grant agreement No. 700748

$$N_{1,60} = 46\,RD^2 \qquad (3.26)$$

3.1.3 SANISAND

The Dafalias & Manzari (2004) model is an elastoplastic constitutive model for granular liquefiable soils. It is a nonlinear, coupled model written in terms of effective stresses, and it is a stress-ratio controlled, critical state compatible model, which takes into account the effect of fabric changes in the multi-axial generalization. The model used in this work is a version of the family of SANISAND (Simple ANIsotropic SAND) models developed by Dafalias and coworkers. One of the merits of this model is that one set of material parameters can be applied to dramatically different stresses and densities, thus showing its ability to catch the key mechanical factors ruling on the behaviour of granular soils. The material parameters have been carefully calibrated in literature for Toyoura sand, based on the large amount of excellent experimental data available for this Japanese sand. Some material parameters can be considered as default values for most sands, thus not needing to be calibrated separately on the specific sand of interest. By so doing, the number of parameters to be calibrated is reduced.

The model has a fabric-dilatancy related term, which is a scalar in triaxial conditions and a tensor in the generalized stress space. This term models the effect of fabric changes during the dilatant phase on the subsequent contractive response upon load increment reversals, and allows a realistic simulation of the sand behaviour under undrained cyclic loading.

The plastic strain rate direction depends on a modified Lode angle in the multiaxial generalization, a feature necessary to produce realistic stress-strain simulations in non-triaxial conditions.

The fabric changes during loading with the stress ratio q/p' (where q and p' are respectively the deviatoric and spheric stress components). The increase in stress under a constant stress ratio is assumed to cause only elastic strain, as long as no crushing of grains takes place. This is consistent with the very small variation of void ratio observed for a loading path to a given stress ratio over a large range of confining stresses, at least for sands not extremely loose.

The model is based on the critical state soil mechanics principles, and expresses the slope of the so-called phase transformation line as a function of the state parameter ψ.

Softening of dense sands is modelled introducing a collapsing peak-stress ratio bounding surface, whose formulation is implemented following the original proposal of Wood and Liu (1994). The model is able to capture the features of cyclic loading, even though loading reversal simulation proved to be not extremely accurate for low confining effective stresses.

As previously said, the model is expressed in terms of effective stresses, being the principal stresses σ'_1, σ'_2 and σ'_3, while ε_1, ε_2 andε_3 are the corresponding principal strains. The triaxial

This project has received funding from the European Union's Horizon 2020 research and innovation programme under grant agreement No. 700748

variables are $q=\sigma'_1-\sigma'_3$; $p'=(1/3)\ (\sigma'_1+\sigma'_2+\sigma'_3)$, $\varepsilon_q=(2/3)(\varepsilon_1-\varepsilon_3)$, and $\varepsilon_v=\varepsilon_1+\varepsilon_2+\varepsilon_3$. The stress ratio is $\eta=q/p'$. The incremental stress-strain relations are given by:

$$d\varepsilon_q^e = \frac{dq}{3G} \qquad d\varepsilon_v^e = \frac{dp'}{K} \tag{3.27}$$

$$d\varepsilon_q^p = \frac{d\eta}{H}; \qquad d\varepsilon_v^e = d\left|d\varepsilon_q^p\right| \tag{3.28}$$

where G and K are the elastic shear and bulk incremental moduli respectively, H is the plastic hardening modulus associated with the increment in stress ratio $d\eta$, and *d* is the dilatancy.

The elastic moduli G and K introduced in the hypoelastic formulation of the reversible components of strains (eq. 3.27) are functions of p' and of the current void ratio e:

$$G = G_0 \cdot p_{at} \frac{(2.97-e)^2}{1+e} \left(\frac{p'}{p_{at}}\right)^{\frac{1}{2}}; \qquad K = \frac{2(1+\nu)}{3(1-2\nu)} G \tag{3.29}$$

where G_0 is a constant; ν is the Poisson ratio; and p_{at} is the atmospheric pressure. The degradation of the shear modulus and the increase of hysteretic damping depend on the mean effective stress p'.

Since deviatoric plasticity occurs only when $d\eta \neq 0$, a stress-ratio defined yield surface is proposed as:

$$f = |\eta - \alpha| - m = 0 \tag{3.30}$$

This equation represents geometrically a ''wedge'' in the p':q space with an opening angle of 2mp', shown by the shaded area in Figure 3.4, whose bisecting line has a slope α. When the stress ratio η is inside the wedge, only elastic strains are induced by any variation $d\eta\neq0$. When η satisfies the condition f=0 (eq. (3.30), yielding is activated, and any outwards $d\eta$ induces plastic strains. In this case the wedge moves along with η to keep the condition f=0 (meaning that α is changing), and the size of the elastic wedge (ruled by parameter m) may change as well. Kinematic and isotropic hardening are thus taking place, with a corresponding back stress ratio in the terminology of theoretical plasticity.

Under monotonic drained triaxial compression loading, η may increases up to the bounding peak stress ratio M^b, shown by a straight dashed line in Figure 3.4. As well known, M^b is a state dependent parameter. The stress-ratio related hardening modulus H depends on the ''distance'' $b = M^b - \eta$. Assuming a linear relationship, such a dependency can be written as:

$$H = h(M^b - \eta) \tag{3.31}$$

This project has received funding from the European Union's Horizon 2020 research and innovation programme under grant agreement No. 700748

where h is a function of the state variables (void ratio e, mean stress p' and stress ratio η). The relation proposed for h is:

$$h = \frac{b_0}{|\eta - \eta_{in}|}; \qquad b_0 = G_0 h_0 (1 - c_h e) \left(\frac{p'}{p_{at}}\right)^{-\frac{1}{2}} \tag{3.32}$$

h_0 and c_h are scalar parameters and η_{in} is initiation stress ratio of a loading process.

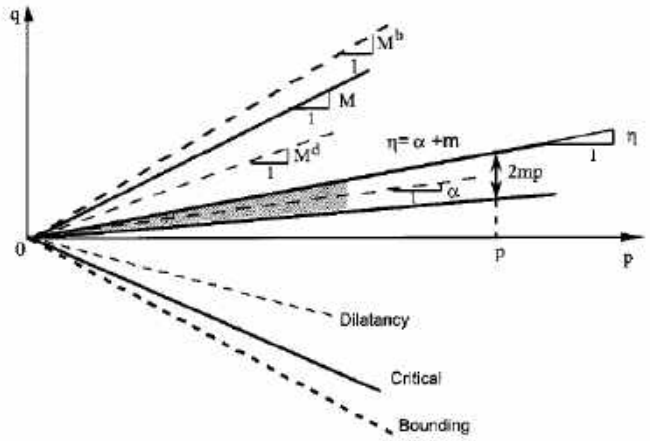

Figure 3.4. Boundary surfaces in p':q space.

The dilatancy, d, is proportional to the difference $M^d - \eta$ according to Rowe's theory, where M^d is the value of η corresponding to the phase transformation. A possible formulation of the dilatancy is:

$$d = A_d (M^d - \eta) \tag{3.33}$$

where A_d is again a state dependent parameter, whose expression will be given at the end of this section. M^b and M^d are expressed as:

$$M^b = M\ exp(-n^b \Psi); \qquad M^d = M\ exp(-n^d \Psi) \tag{3.34}$$

At failure, the void ratio tends to the critical state one, whose value is:

$$e_c = e_0 - \lambda_c \left(\frac{p'_c}{p_{at}}\right)^{\xi} \tag{3.35}$$

This project has received funding from the European Union's Horizon 2020 research and innovation programme under grant agreement No. 700748

e_0 is the critical void ratio for p'$_c$=0, while λ_c and ξ are the parameters defining the shape of the critical state curve.

Fabric changes affect the dilatant behaviour of sands and thus the tendency to build-up pore pressures during cyclic loading. A new variable z (called fabric-dilatancy variable) is therefore introduced to take this dependency into account, whose incremental variation low is:

$$dz = -c_z\langle -d\varepsilon_v^p \rangle (sz_{max} + z) \qquad (3.36)$$

where c_z, s and z_{max} are new parameters. The MacCauley brackets $\langle\cdot\rangle$ give a zero value if the argument is negative. Therefore, any positive (compressive) increment of plastic volumetric strain does not change the fabric-dilatancy variable (i.e. dz=0).

Parameter A_d introduced in eq. (3.33) depends on soil fabric, and can be written as a function of the fabric-dilatancy variable z as:

$$A_d = A_0(1 + \langle sz \rangle) \qquad (3.37)$$

Being A_0 a new soil parameter.

3.1.4 PM4SAND

The PM4SAND (version 3) model follows the basic framework of the stress-ratio controlled, critical state compatible, bounding surface plasticity model for sands presented by Dafalias and Manzari (2004), who extended the previous work by Manzari and Dafalias (1997) by adding a fabric-dilatancy related tensor quantity to account for the effect of fabric changes during loading. The fabric-dilatancy related tensor was used to macroscopically model the effect that microscopically-observed changes in sand fabric during plastic dilation have on the contractive response upon reversal of loading direction. The modifications were developed and implemented to improve the ability of the model to match existing engineering design relationships currently used to estimate liquefaction-induced ground deformations during earthquakes. These modifications are described in the manuals (version 1 in Boulanger 2010, version 2 in Boulanger and Ziotopoulou 2012, and version 3) and in the associated publications, as listed in the mentioned manuals.

The model is written in terms of effective stresses, with the conventional prime symbol dropped from the stress terms for convenience because all stresses are effective for the model. The stresses are represented by the tensor **r**, the principal effective stresses are σ_1, σ_2, and σ_3, the mean effective stress is p, the deviatoric stress tensor is s, and the deviatoric stress ratio tensor r. The current implementation was further simplified by casting the various equations and relationships in terms of the in-plane stresses only. This limits the implementation to plane-strain (2D) applications, having the further advantage in its

This project has received funding from the European Union's Horizon 2020 research and innovation programme under grant agreement No. 700748

simplified implementation to improve the computational speed. The relationships between the various stress terms can be summarized as follows:

$$\boldsymbol{\sigma} = \begin{pmatrix} \sigma_{xx} & \sigma_{xy} \\ \sigma_{xy} & \sigma_{yy} \end{pmatrix} \tag{3.38}$$

$$p = \frac{\sigma_{xx} + \sigma_{yy}}{2} \tag{3.39}$$

$$\boldsymbol{s} = \boldsymbol{\sigma} - p\boldsymbol{I} = \begin{pmatrix} s_{xx} & s_{xy} \\ s_{xy} & s_{yy} \end{pmatrix} = \begin{pmatrix} \sigma_{xx} - p & \sigma_{xy} \\ \sigma_{xy} & \sigma_{yy} - p \end{pmatrix} \tag{3.40}$$

$$\boldsymbol{r} = \frac{\boldsymbol{s}}{p} = \begin{pmatrix} r_{xx} & r_{xy} \\ r_{xy} & r_{yy} \end{pmatrix} = \begin{pmatrix} \frac{\sigma_{xx} - p}{p} & \frac{\sigma_{xy}}{p} \\ \frac{\sigma_{xy}}{p} & \frac{\sigma_{yy} - p}{p} \end{pmatrix} \tag{3.41}$$

In eq. (3.40), $\boldsymbol{I}$ is the identity matrix. The deviatoric stress and deviatoric stress ratio tensors are symmetric with $r_{xx} = -r_{yy}$ and $s_{xx} = -s_{yy}$ (meaning a zero trace).

The strains are represented by a tensor ε, expressed as the sum of the volumetric strain ε_v and of the deviatoric strain tensor e. The volumetric strain is,

$$\varepsilon_v = \varepsilon_{xx} + \varepsilon_{yy} \tag{3.42}$$

and the deviatoric strain tensor is,

$$\boldsymbol{e} = \boldsymbol{\varepsilon} - \frac{\varepsilon_v}{3}\boldsymbol{I} = \begin{pmatrix} \varepsilon_{xx} - \frac{\varepsilon_v}{3} & \varepsilon_{xy} \\ \varepsilon_{xy} & \varepsilon_{yy} - \frac{\varepsilon_v}{3} \end{pmatrix} \tag{3.43}$$

In incremental form, the deviatoric and volumetric strain terms are decomposed into an elastic and a plastic part,

$$d\boldsymbol{e} = d\boldsymbol{e}^{el} + d\boldsymbol{e}^{pl} \tag{3.44}$$

This project has received funding from the European Union's Horizon 2020 research and innovation programme under grant agreement No. 700748

$$d\varepsilon_v = d\varepsilon_v^{el} + d\varepsilon_v^{pl} \tag{3.45}$$

where:

$d\boldsymbol{e}^{el}$ = elastic deviatoric strain increment tensor

$d\boldsymbol{e}^{pl}$ = plastic deviatoric strain increment tensor

$d\varepsilon_v^{el}$ = elastic volumetric strain increment tensor

$d\varepsilon_v^{pl}$ = plastic volumetric strain increment tensor

This constitutive model follows the critical state theory and uses the relative state parameter index (ξ_R) as defined by Boulanger (2003) and shown in Figure 3.5. This relative parameter is defined by an empirical relationship for the critical state line:

$$\xi_R = D_{R,cs} - D_R \tag{3.46}$$

$$D_{R,cs} = \frac{R}{Q - \ln\left(100\frac{p}{p_A}\right)} \tag{3.47}$$

where $D_{R,cs}$ is the relative density at critical state for the current mean effective stress, instead, Q and R are two parameters that define the shape of critical curve.

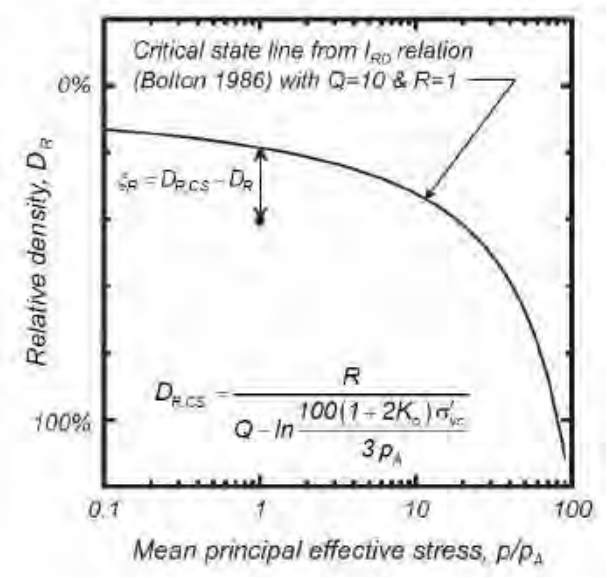

Figure 3.5. Relative state parameter index.

This project has received funding from the European Union's Horizon 2020 research and innovation programme under grant agreement No. 700748

Bounding, dilatancy and critical surfaces are incorporated in PM4SAND following the form of Dafalias and Manzari (2004).

The bounding (M^b) and dilatancy (M^d) ratios can be related to the critical stress (M) ratio:

$$M^b = M \cdot \exp\left(-n^b \xi_R\right) \tag{3.48}$$

$$M^d = M \cdot \exp\left(-n^d \xi_R\right) \tag{3.49}$$

where n^b and n^d are model parameters. The relationship for M is:

$$M = 2 \cdot \sin\left(\phi_{cv}\right) \tag{3.50}$$

where ϕ_{cv} is critical state friction angle.

As the soil is sheared toward critical state $\left(\xi_R = 0\right)$, the values of M_b and M_d will both approach the value of M. Thus, the bounding and dilatancy surfaces move together during shearing until they coincide with the critical state surface when the soil has reached critical state.

The few experimental data for loose-of-critical sands (having no peak) show that the maximum friction angles (presumably determined at the limit of strains possible within the laboratory tests) were only slightly smaller than the critical state values, such that extending the above relationships to loose-of-critical sands may tend to underestimate the peak friction angles (in this case theoretically coinciding with the critical state one). Consequently, in the present formulation the model allows n_b and n_d to be different for loose-of-critical and dense-of-critical states for the same sand.

A large portion of the post-liquefaction reconsolidation strains are due to the sedimentation effects which are not easily incorporated into either the elastic or plastic components of behaviour. For this reason, in the PM4SAND a post-shaking function was implemented. In a strongly pragmatic way, this function reduces volumetric and shear moduli, thus increasing reconsolidation strains to somehow simulate the sedimentation ones (not included in the model).

The post-shaking elastic moduli are determined by multiplying the conventional elastic moduli by a reduction factor F_{sed} as,

$$G_{post-shaking} = F_{sed} \cdot G \tag{3.51}$$

This project has received funding from the European Union's Horizon 2020 research and innovation programme under grant agreement No. 700748

$$K_{post-shaking} = F_{sed} \cdot K \qquad (3.52)$$

for more information on the F_{sed} it is possible refer to Boulanger and Ziotopoulou (2015). For the calibration of the model it is possible to refer to Luque Nuques (2017), as also recalled in the relevant parts of §3.3.

3.1.5 PDMY02 MODEL

The Pressure Dependent Multi-Yield 02 (PDMY02) model, already implemented in OpenSEES, is the updated version of the Pressure Dependent Multi-Yield (PDMY) material that is presented in Yang et al. (2003). The model is based on plasticity principles and it considers the concept of nested yield surfaces that is first proposed in the publication of Prevost (1985). In PDMY models, like Prevost (1985), nested yield surfaces serve as the plasticity-based representation of nonlinear soil response as a function of the induced shear strain. Although it is possible to define the critical state line within the model, the formulation of PDMY02 is not based on critical state soil mechanics framework, thus, different sets of parameters are needed for different states of soil.

Further information and representative values for the parameters are extensively presented in the webpage dedicated in OpenSEES:

(http://opensees.berkeley.edu/wiki/index.php/PressureDependMultiYield02_Material).

3.1.6 STRESS-DENSITY MODEL

Definition:

The Stress-Density (S-D) model developed by Cubrinovski (1993) and Cubrinovski and Ishihara (1998a and 1998b) is an advanced constitutive model for the simulation of sand liquefaction processes. It is based on the state concept and has been developed for modelling the undrained behaviour of sand under monotonic and cyclic loading.

The principal feature of this model is the influence of the initial state (considered in the e:p plane) on the plastic behaviour through the use of the state index. Unlike other more conventional sand models, in which each density is considered as an index property for a separate material, the adopted modelling concept enables an integral representation of sand behaviour over the relevant range of densities and stress states. Besides the physical relevance of the concept, its practical benefit is that a single set of material parameters can be used to model sand behaviour for any practically relevant initial void ratio and confining stress.

This project has received funding from the European Union's Horizon 2020 research and innovation programme under grant agreement No. 700748

Implementation to FLAC2D:

Currently, this model is available exclusively in the Japanese version of the FEM code Diana, which, as the majority of the FEM codes, is based on the implicit solution of the constitutive differential equations. The present contribution describes the state of progress of the activities carried out for the implementation of the S-D Model in FLAC-2D (Itasca, 2015), which is a finite difference code based on the explicit solution. The aims of the implementation of this advanced constitutive model in FLAC are essentially two. In one hand, the S-D model offers an alternative and a term of comparison with the other advanced constitutive models currently available to model the liquefaction problem. On the other hand, the implementation in FLAC gives the possibility to use the S-D Model within the explicit formulation, which well suites the highly nonlinear problems like liquefaction.

The S-D Model was originally written in Fortran by Cubrinovski (1993). The implementation of user defined models (UDM) in FLAC requires that the constitutive models must be written in C++ and compiled as a DLL file (dynamic link library). Another important aspect of the FLAC platform is that the solid body is divided by the user into a finite difference mesh composed of quadrilateral elements. Internally, FLAC subdivides each element into two overlaid sets of constant-strain triangular elements. The deviatoric stress components of each triangle are maintained independently, requiring sixteen stress components to be stored for each quadrilateral ($4\times\sigma_{xx}$, σ_{yy}, σ_{zz}, σ_{xy}). Triangles have been selected in order to avoid the hourglass problem. If one pair of triangles becomes badly distorted (e.g., if the area of one triangle becomes much smaller than the area of its companion), then the corresponding quadrilateral is not used. If both overlaid sets of triangles are badly distorted, FLAC issues an error message.

FLAC calls the constitutive model for each triangle that makes up the zone. The increment of strains is the input passed by FLAC to the constitutive model that, in turn, it passes as output the new stresses values to FLAC, which are used to compute the next increment of strains.

The phases of implementation are essentially three:

1) Definition of the implementation technique compatible with FLAC.

2) Implementation and verification of the S-D Model at the level of a single zone of the mesh composed by four triangles.

3) Implementation and verification of the S-D Model for multiple zones.

Currently, the step one has been terminated and the phase two is nearing completion. The approach designed and used for the implementation of the model (step 1) is based on the mixed language technique. A DLL compiled in C++ has been used as interface between the DLL compiled in Fortran, which contain the constitutive model, and the environment of FLAC which requires the C++ language. FLAC calls the DLL interface written in C++ that converts the variables (e.g. model parameters and increment in strains) in a format compatible with the Fortran DLL of the constitutive model that, in turn, it returns to the interface the new stresses.

This project has received funding from the European Union's Horizon 2020 research and innovation programme under grant agreement No. 700748

In the second phase, the model has been implemented in FLAC to work exclusively with a single zone of the mesh composed by four triangles. Figure 3.6. shows a first comparison between the original version of the S-D Model simulating a cyclic undrained test on the Toyoura Sand and the results of the S-D Model implemented in FLAC 2D.

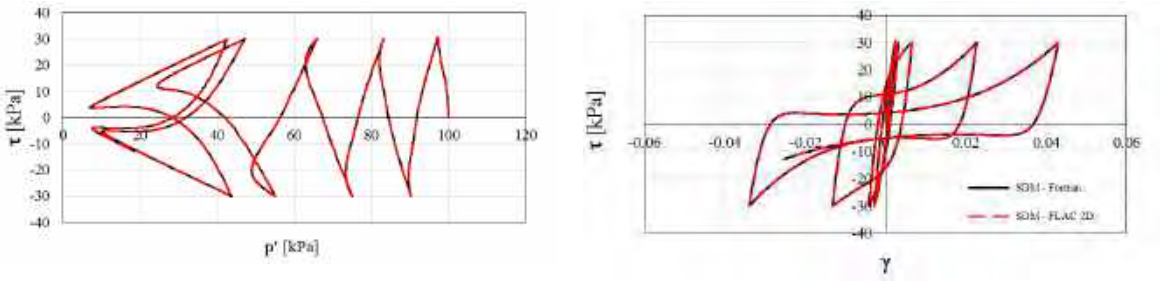

Figure 3.6. Comparison between the cyclic test on the Toyoura Sand carried out with the original S-D Model (Fortran) and the S-D Model implemented in FLAC 2D.

This project has received funding from the European Union's Horizon 2020 research and innovation programme under grant agreement No. 700748

3.2 NUMERICAL CODES

3.2.1 FLAC 2D & 3D

FLAC is an explicit finite difference program for engineering computation developed by Itasca Consulting Group Inc. This program simulates the behaviour of structures built of soil, rock or other materials that may undergo plastic flow when their yield limits are reached. Materials are represented by elements, or zones, which form a grid that is adjusted by the user to fit the shape of the object to be modelled. Each element behaves according to a prescribed linear or nonlinear stress/strain law in response to the applied forces or boundary restraints. The material can yield and flow, and the grid can deform (in large-strain mode) and move with the material that is represented (this feature is most important in liquefaction issues).

AVAILABLE SOFTWARE LICENSE:

FLAC 2D: 213-039-0067-13153

FLAC 3D: 242-039-017-22148

3.2.2 PLAXIS 2D

PLAXIS is a finite elements program. It is used for the analysis of deformation, stability and groundwater flow in geotechnical engineering. It is a part of the PLAXIS products range, a suite of finite element programs that is used worldwide for geotechnical engineering and design. PLAXIS works by matrix and it is based on equations of continuum deformation. The stress increments are obtained by integration of the stress rate.

AVAILABLE SOFTWARE LICENSE:

PLAXIS 2D: 2-1329070

3.2.3 OPENSEES

OpenSEES (Open System for Earthquake Engineering Simulation) is an object-oriented finite element software framework which is first developed by McKenna et al. (2000) at Pacific Earthquake Engineering Research Center (PEER). Its primary use is to serve as a computational platform that is apt to conduct linear/nonlinear, static/dynamic simulations of soil and structural configurations being subjected to seismic effects.

As defined in its webpage (http://opensees.berkeley.edu/OpenSees/home/about.php), OpenSEES is an open-source platform, containing a wide range of element formulations and material constitutive models for both soil and structural modelling. Further, OpenSEES includes a variety of numerical algorithms and solution methods, proposing a good set of alternatives for difficultly converging systems under high levels of nonlinearity. Finally, the platform also offers parallel computing capabilities to make the analyses possible also for numerical models having large numbers of degrees of freedoms. The version being used is 2.5.0 (Rev 6477).

This project has received funding from the European Union's Horizon 2020 research and innovation programme under grant agreement No. 700748

3.3 MODELS CALIBRATION PROCEDURES

3.3.1 MODELS CALIBRATION FOR THE SIMULATION OF CENTRIFUGE TESTS

- For Finn-Byrne model:

As previously discussed, the definition of the Finn-Byrne model is based on the relative density of the soil domain under investigation. For the case of centrifuge tests, the relative density of the profile is taken as the relative density estimated after the consolidation phase and before the dynamic excitation.

Depth-dependent shear and bulk moduli profiles are assigned according to a model that is developed for Ticino sand (Fioravante, 2000). Modulus degradation relation, on the other hand, is compared with the interpretation of Belotti et al. (1996) as well as generic curve proposed by Darendeli (2001).

In Table 3.1. the set of parameters used for the Finn-Byrne model is summarized.

Table 3.1. Final parameters used in Finn-Bryne model.

Parameter	Definition	Value
C_1	Calibration parameter	0.49
C_2	Calibration parameter	0.81
ϕ' (°)	Effective friction angle	34
K_w (kPa)	Bulk modulus of water	1.0×10^6

In Figure 3.7 (left side), modulus degradation relation adopted is compared with Darendeli (2001) and the interpretation of the data presented by Belotti et al. (1996); whereas in (right) modelled and reference (Fioravante, 2000) small strain moduli profiles are presented.

This project has received funding from the European Union's Horizon 2020 research and innovation programme under grant agreement No. 700748

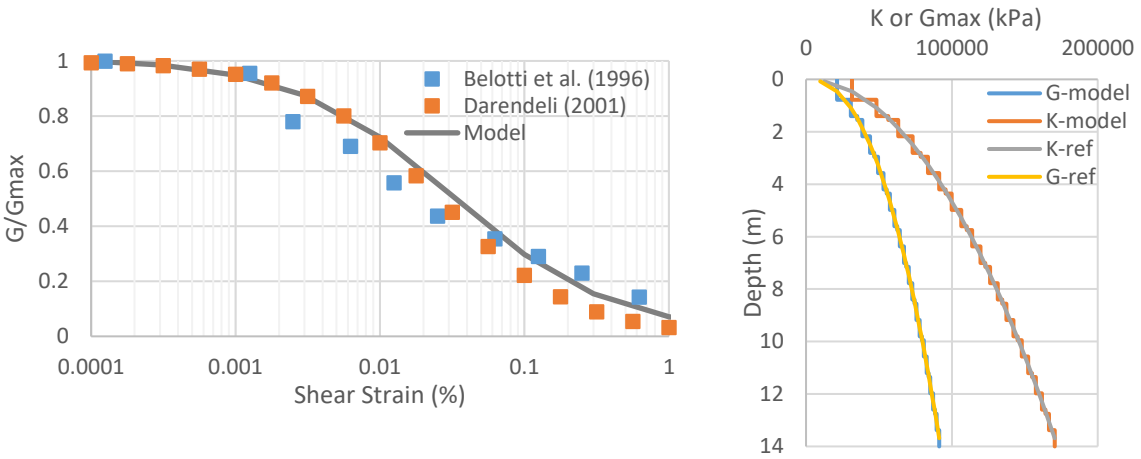

Figure 3.7. Left: Modelled and reference modulus degradation curves. Right: modelled and reference small strain moduli profiles.

- For UBC3D-PML model:

The definition of UBC3D-PML model is based on the relative density of the soil domain under investigation, which is thus the reference parameter to adopt for calibration, following the indications of Beaty and Byrne (2011). For some of the parameters, however, it is necessary to add a calibration based on the results of undrained cyclic laboratory tests. A cyclic resistance curve is taken into account for the calibration, as obtained in laboratory. For the case of centrifuge tests, the relative density of the profile is taken as the relative density estimated after the consolidation phase, just before the cyclic excitation.

For the parameter f_{dens} a cyclic resistance curve for Ticino sand (Fioravante et al., 2016) was used.

The comparison between the experimental and numerical undrained cyclic resistance results is shown in Figure 3.8. The parameters used for best fitting the experimental results are reported in Table 3.2.

Table 3.2. Final parameters used in UBC3D-PML model.

Parameter	Description	Value	Unit
$N_{1,60}$	SPT number		-
K_G^e	elastic shear modulus		-
K_B^e	elastic bulk modulus		-
K_G^p	plastic shear modulus		-
m_e	elastic stress dependency parameter	0.5	-

This project has received funding from the European Union's Horizon 2020 research and innovation programme under grant agreement No. 700748

n_e	elastic stress dependency parameter	0.5	-
n_p	plastic stress dependency parameter	0.4	-
ϕ_{cv}	critical state friction angle	33	°
ϕ_{peak}	peak state friction angle		°
R_f	failure ratio		-
ν	Poisson coefficient	0.25	-
f_{dens}	densification factor	0.5	-
f_{Epost}	post-liquefaction factor	1.0	-

Parameter f_{Epost} is set to 1 as suggests by Petalas (2012).

As before said, this procedure gives the calibration of the f_{dens} parameter.

- For PM4Sand model:

The PM4Sand constitutive model is calibrated to represent Ticino sand using the results of laboratory element tests reported in literature. PM4Sand has 22 input parameters but, as discussed in §3.1.4, only three of them are required as independent inputs: the initial relative density (D_{R0}), the shear modulus coefficient used to define the small strain shear modulus (G_0) and the contraction rate parameter used for the calibration of the undrained shear strength (h_{p0}). For this study, these three parameters were calibrated against the experimental data published for Ticino sand (Fioravante & Giretti 2016), while all the other parameters have been left with their default values, as suggested by the authors. The value of the shear modulus coefficient G_0 was determined as a function of the relative density obtained in the centrifuge tests using the follow relationship:

$$G_0 = 167 \cdot \sqrt{46 \cdot D_R^2 + 2.5} \qquad (3.53)$$

The parameter h_{p0} scales the plastic contraction rate and is the primary parameter for the calibration of undrained cyclic strength. It is calibrated using an iterative process, in which undrained single-element DSS simulations are conducted to match with a target liquefaction triggering curve by keeping the other parameters fixed.

The results of the calibration are shown Figure 3.8. The properties adopted to simulate the cyclic resistance curve are reported in Table 3.3.

This project has received funding from the European Union's Horizon 2020 research and innovation programme under grant agreement No. 700748

Table 3.3. PM4sand parameters.

Parameter	Description	Value	Unit
G_0	shear modulus coefficient	624	-
hp_0	contraction rate parameter	0.1	-
p_A	atmospheric pressure	101.3	kN/m^2
e_{max}	maximum void ratio	0.923	-
e_{min}	minimum void ratio	0.574	-
n_b	bounding surface parameter	0.5	-
n_d	dilatancy surface parameter	0.1	-
ϕ_{cv}	critical state friction angle	33	°
nu	Poisson's ratio	0.3	-
Q	critical state line parameter	8	-
R	critical state line parameter	1.2	-

For both UBC3D-PML and PM4SAND, the comparison with the experimental results used for calibration is reported in Figure 3.8.

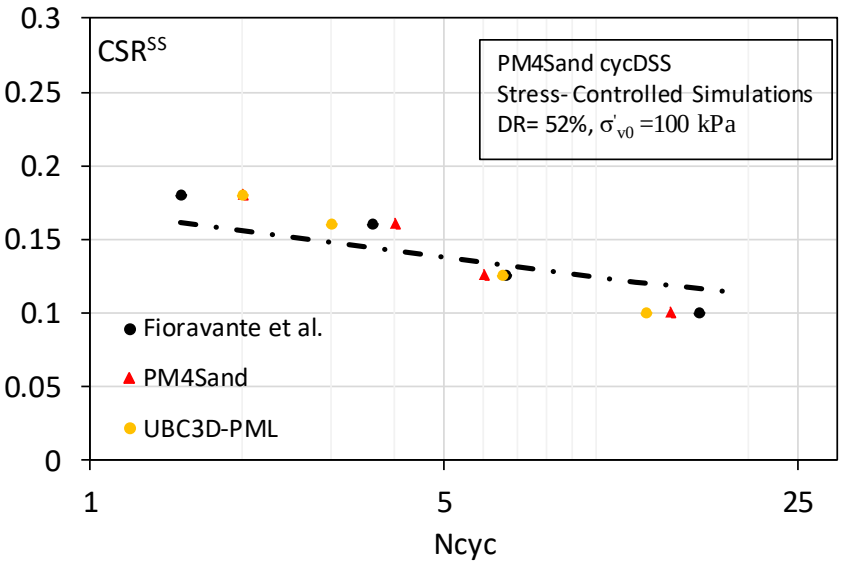

Figure 3.8. Comparison between experimental and numerical undrained cyclic resistance curves.

This project has received funding from the European Union's Horizon 2020 research and innovation programme under grant agreement No. 700748

- For PDMY02 model:

Since PDMY02 is not based on critical state theory, a general understanding is necessary to understand the simulated soil response by considering a variety of scenarios. In this study, three step calibration procedure was followed:

Calibrating the constitutive model considering a 3D brick element (brickUP), being subjected to cyclic triaxial stress path under a high CSR (= 0.21);

Repeating step (i) with a low CSR (= 0.17);

Modelling the CRR-number of cycles curve by considering the liquefaction criterion as double amplitude axial strain exceeding 5%.

For steps (i) and (ii), two similar relative density soil (~55%) consolidated under isotropic confinement pressure of 100 kPa, resulting in different state parameters ?=-0.137 and ?=-0.147. The results of these test are synthesized in Fioravante and Giretti (2016) and complete set of digital data have been provided by ISMGEO partner.

For step (iii), instead, the functional form of the CRR-model, calibrated particularly for Ticino sand by Fioravante and Giretti (2016), is used for soil layer ad mid-depth of homogeneous Ticino sand model (at 7 meters at prototype scale, with a target relative density = 48 %).

$$CRR^{TX}(N,\Psi) = \frac{3}{(1+2\cdot 0.44)} \cdot \frac{0.071(1-\Psi)^{7.8}}{N^{0.177(1-\Psi)}} \qquad (3.54)$$

where N is the number of cycles and Ψ the state parameter (=-0.134 for depth = 7 m).

As for the Finn-Byrne model, shear modulus-depth relation is assigned according to Fioravante (2000), and the modelled modulus degradation relation is compared with Belotti et al. (1996) and Darendeli (2001).

Calibrations were carried out based on 3 steps:

(a) Single element test, triaxial cyclic undrained test with CSR=0.21, ψ=-0.137, p'_0=100 kPa
(b) Single element test, triaxial cyclic undrained test with CSR=0.17, ψ=-0.147, p'_0=100 kPa
(c) Comparison of cyclic resistance curves for ψ=-0.1336, p'_0=40 kPa

The final set of calibrated parameters for y=-0.1336 is provided in Table 3.4.

This project has received funding from the European Union's Horizon 2020 research and innovation programme under grant agreement No. 700748

Table 3.4. Final parameters used in Finn-Byrne model.

Parameter	Definition	Unit	Value	Remarks (specific to this study)
G_{ref}	Reference small strain shear modulus at effective reference mean pressure	MPa	100	
K_{ref}	Reference soil bulk modulus at reference pressure	MPa	225	
p_{ref}	Reference mean pressure	kPa	100	
n	Stress-dependency coefficient	-	0.42	See Figure 3.9
γ_{max}	Maximum octahedral shear strain	-	0.1	
ϕ'	Effective friction angle	°	34	
ϕ'_{pt}	Phase transformation angle	°	27	$\phi'_{pt} \approx \phi' - (-81.05c_1+11.475)$
c_1	Parameter defining the rate of shear induced volume decrease	-	0.055	Main parameter
c_2	Parameter defining dilation history on contraction tendency	-	1	
c_3	Parameter reflecting $K\sigma$ effect	-	0.019	$c_3 \approx -1901.3(c_1)^3 + 223.96(c_1)^2 - 3.0957(c_1) + 0.0057$
d_1	Model parameter on dilative response	-	0.03	
d_2		-	0.6	
l_1	Damage parameter to define accumulated permanent shear strain as a function of dilation history	-	1	
l_2	Damage parameter to define biased accumulation of permanent shear strain as a function of load reversal history	-	0	
E	Initial void ratio	-	0.76	Final value is 0.76, however 0.745 and 0.735 is also used in replicating the small-scale tests
cs_1	Parameters defining the critical state line	-	0.923	Assigned according to Fioravante and Giretti (2016)
cs_2		-	0.046	
cs_3		-	0.5	
p_{atm}	Atmospheric pressure	kPa	98.1	
K_w	Bulk modulus of pore water		$1.1x10^6$ to $2.2x10^6$	Calibration is done with K_w=2.2e6. K_w=1.1e6 is used only for a single case where degree of saturation = 99%

This project has received funding from the European Union's Horizon 2020 research and innovation programme under grant agreement No. 700748

Calibration stage (a)

Digital data is provided by ISMGEO partner for the material is published in Fioravante and Giretti (2016). In Figure 3.9. calibration process is summarized in terms of quad-plot.

<table>
<tr>
<td> 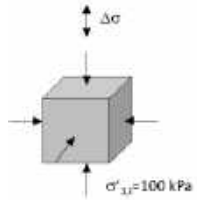
</td>
<td>Reference test in Fioravante and Giretti (2016):
TS4_13_1
e_0 (initial void ratio)=0.740, ψ (state parameter) = - 0.137,
CSR^{TX} (Cyclic resistance ratio-triaxial) = 0.21,
p_0'=100 kPa (Isotropic consolidation pressure)</td>
</tr>
<tr>
<td>G_{ref} = 100 MPa
K_{ref} = 225 MPa
p_{ref} = 100 kPa
n = 0.42
γ_{max} = 0.1
ϕ'=34°, ϕ'_{pt} = 26°
c_1 = 0.045
c_2 = 1.0, c_3 = 0.15
d_1 = 0.03
d_2 = 0.6, d3 = 0
l_1 = 1, l_2 = 0
e = 0.74
cs_1 = 0.923
cs_2 = 0.046
cs_3 = 0.500
p_{atm} = 98.1 kPa</td>
<td> 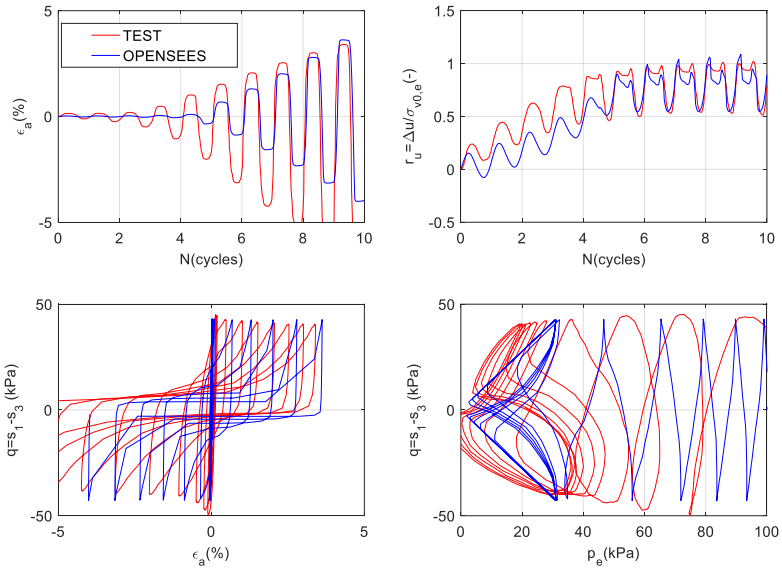
</td>
</tr>
</table>

Figure 3.9. Top left: Triaxial loading scheme, top right: reference test data, bottom left: calibrated parameters (the ones highlighted by grey have functional correlation, the rest are kept same in all calibration procedures), bottom right: quad plot in terms of deviatoric strain-number of cycles, excess pore water pressure – number of cycles, axial strain – deviatoric stress, mean effective stress – deviatoric stress. Parameters of the constitutive model are explained in the text body.

This project has received funding from the European Union's Horizon 2020 research and innovation programme under grant agreement No. 700748

Calibration stage (b)

Digital data is provided by ISMGEO partner for the material is published in Fioravante and Giretti (2016). In Figure 3.10. calibration process is summarized in terms of quad-plot. All the parameters are as defined in previous point.

<table>
<tr>
<td> 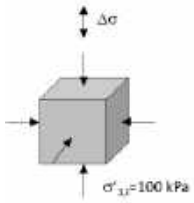
</td>
<td>Reference test in Fioravante and Giretti (2016):
TS4_13_4
e_0 (initial void ratio)=0.730, ψ (state parameter) = - 0.147,
CSR^{TX} (Cyclic resistance ratio-triaxial) = 0.17,
p_0'=100 kPa (Isotropic consolidation pressure)</td>
</tr>
<tr>
<td>G_{ref} = 100 MPa
K_{ref} = 225 MPa
p_{ref} = 100 kPa
n = 0.42
γ_{max} = 0.1
ϕ'=34°, ϕ'_{pt} = 24°
c_1 = 0.021
c_2 = 1.0, c_3 = 0.022
d_1 = 0.03
d_2 = 0.6, d3 = 0
l_1 = 1, l_2 = 0
e = 0.74
cs_1 = 0.923
cs_2 = 0.046
cs_3 = 0.500
p_{atm} = 98.1 kPa</td>
<td> 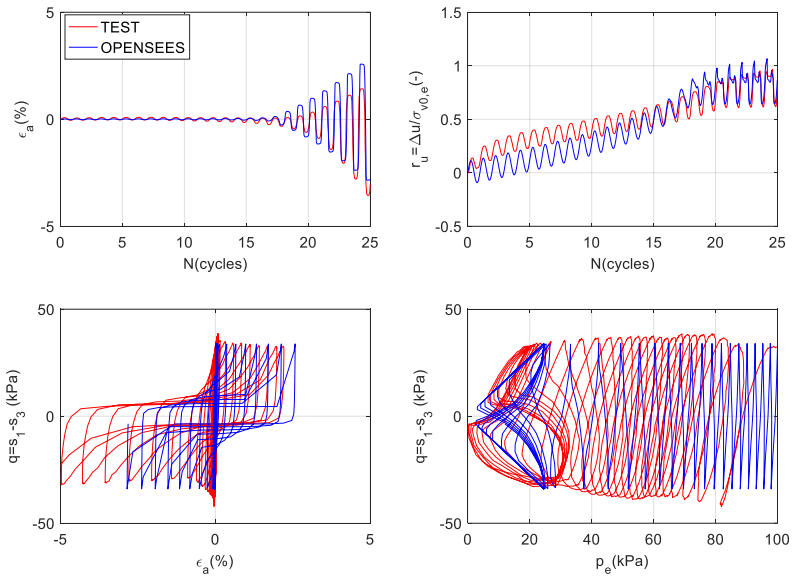
</td>
</tr>
</table>

Figure 3.10. Comparison of simulated response with experimental response in terms of quad plot. Explanation of variables are presented in Figure 3.3 and the paragraph following. It is noted that only the highlighted parameters are changed.

When one compares the responses presented in Figure 3.9 and Figure 3.10, the following points could be stated:

- Asymmetric response in the experimental curves are not captured by the numerical model,
- Numerical model develops the pore water pressure relatively with a slower rate at confining pressures away from the failure envelope, however the response turns out to be opposite once effective confining pressure gets smaller,

This project has received funding from the European Union's Horizon 2020 research and innovation programme under grant agreement No. 700748

- As expected, c_1 is a strong function of state parameter rather than solely the relative density which two models almost share the same value,
- Overall response captured by the numerical model is considered to be acceptable.

Calibration stage (c)

Given the indications captured in calibration stages (i) and (ii), now the model is calibrated for the target representative state parameter at mid-depth (=-0.1336) by making use of the CRR relation proposed by Fioravante and Giretti (2016). It is expected that state-dependent contraction parameter should be in principle larger than 0.045, as a matter of fact assigned as 0.055. Liquefaction criterion is taken as the same with respect to Fioravante and Giretti (2016), which is the differential axial strain between two consecutive cycles exceeding the value of 5%. In Figure 3.11 result of calibration is presented in terms of the comparison between the model CRR prediction with respect to the one formulated in the relevant article.

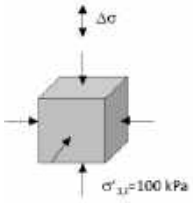

Reference CRR curve in Fioravante and Giretti (2016):

$$CRR^{TX}(N,\Psi) = \frac{3}{(1+2\cdot 0.44)} \cdot \frac{0.071(1-\Psi)^{7.8}}{N^{0.177(1-\Psi)}}$$

ψ (state parameter) = - 0.1336,
p_0'=40 kPa (Isotropic consolidation pressure at mid-depth)

G_{ref} = 100 MPa
K_{ref} = 225 MPa
p_{ref} = 100 kPa
n = 0.42
γ_{max} = 0.1
ϕ'=34°, ϕ'_{pt} = 27°
c_1 = 0.055
c_2 = 1.0, c_3 = 0.19
d_1 = 0.03
d_2 = 0.6, d3 = 0
l_1 = 1, l_2 = 0
e = 0.76
cs_1 = 0.923
cs_2 = 0.046
cs_3 = 0.500
p_{atm} = 98.1 kPa

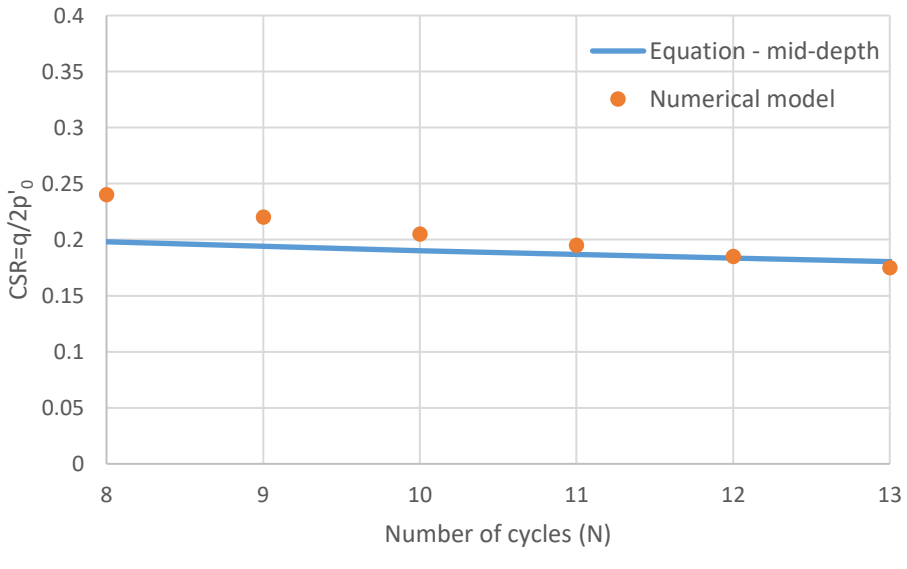

Figure 3.11. Comparison of simulated CRR curve with respect to the one formulated by Fioravante and Giretti (2016)

This project has received funding from the European Union's Horizon 2020 research and innovation programme under grant agreement No. 700748

It could be stated that there is a considerable mismatch at smaller number of cycles, where functional form of CRR shows rather flat response that could not be captured reliably by the numerical model. Yet, for the range of 8-13 cycles (which corresponds to the magnitude around 7.0), the comparison is found satisfactory.

In all the calibration steps and in the further analyses, the modulus degradation used (at 100 kPa) is as defined in Figure 3.12 (left) and the depth-dependent shear and bulk moduli considered in 2D analyses are presented. It should be noted that rather stiffer low to moderate G/Gmax curve is adopted to control better the contraction response at those strain levels, whereas it converges to Belotti et al (1996) data points for larger shear strains. Small strain shear modulus is perfectly matched with the relation proposed by Fioravante (2000), whereas K-model is preferred to be not matched since it controls the initial consolidation pressure of 2D soil zones through the definition of Poisson's ratio. Thus, more stiff volumetric response is considered with respect to reality.

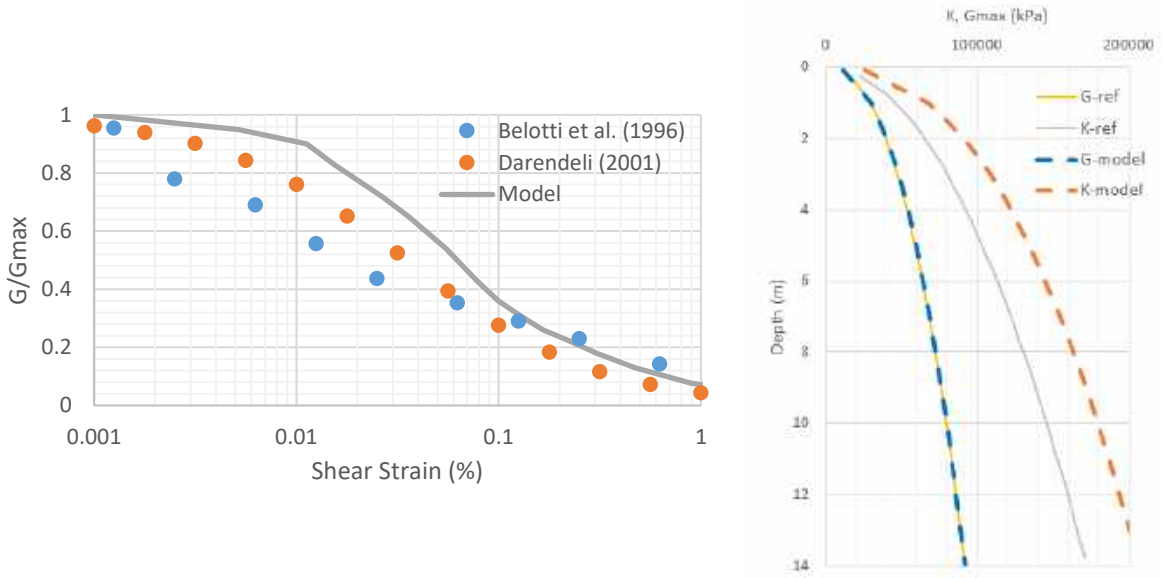

Figure 3.12. Left: Secant shear modulus degradation curve, right: shear and bulk moduli-depth relation. Reference curves are from Fioravante (2000).

This project has received funding from the European Union's Horizon 2020 research and innovation programme under grant agreement No. 700748

3.3.1.1 CHARACTERISTICS OF THE DRAINS ADOPTED IN THE NUMERICAL SIMULATIONS OF HD SCHEMES

In the centrifuge tests to realize the horizontal drains mitigation technique silicon pipes were used (Figure 3.13). Each pipe has an external diameter of 6 mm and internal diameter of 4 mm.

On pipes surface diametrically opposed holes were made, these holes have 0.5 mm diameter and 5 mm spacing.

Figure 3.13. Horizontal drain surface with holes.

Using a pipe system (Figure 3.14), each horizontal drain is connected to atmosphere, this guarantees a hydrostatic distribution of water inside the drains and thus a right function of the drains system.

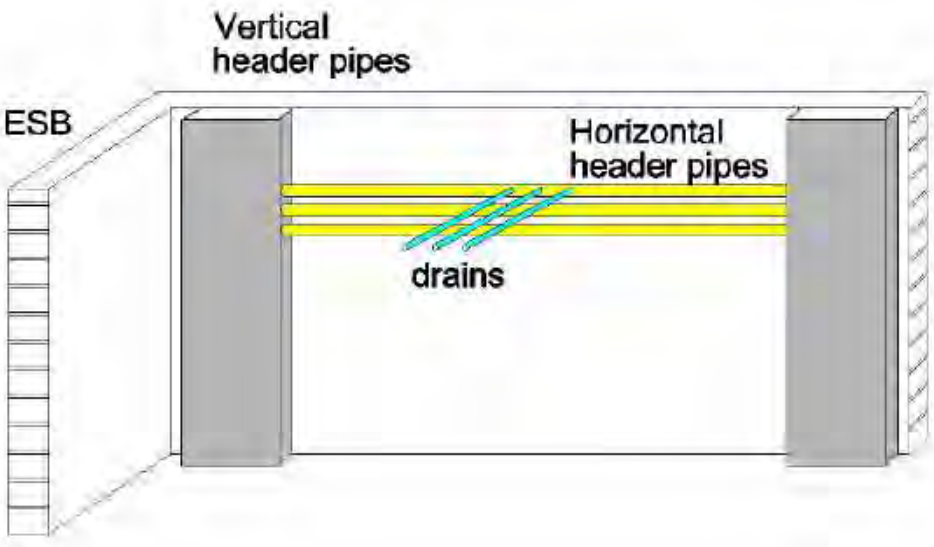

Figure 3.14. Pipe system to connect horizontal drains to atmosphere.

This project has received funding from the European Union's Horizon 2020 research and innovation programme under grant agreement No. 700748

The drains, realized in this way, have a finite value of permeability. It is not possible to modelizer the drains as a hydraulic condition in numerical back analyses of the centrifuge tests, but it is necessary to realize the drain with the really thickness and give it a finite permeability. The value of drains permeability is obtained from numerical back analyses of centrifuge tests and it is equal to $1.46 \cdot 10^{-4}$ m/s.

3.3.1.2 NUMERICAL PROCEDURE ADOPTED TO SIMULATE THE EFFECT OF INDUCED PARTIAL SATURATION

The Induced Partial Saturation technique was implemented in the centrifuge tests as a possible mitigation technique against liquefaction. In the numerical analyses the effect of this technique was directly modelled by reducing the degree of saturation (S_r), since this is a possible option with the adopted models. The Van Genuchten hydraulic water retention curve has been adopted to describe the behaviour of the unsaturated soil. The Van Genuchten function is a three parameters equation and relates the saturation to the pressure head ψ. This model requires the direct input of the residual saturation S_{res}, the saturation at p=0, S_{sat} and three fitting parameters. The bulk modulus of the water in unsaturated condition was calculated by the Plaxis software as:

$$K_w^{unsat} = \frac{K_w^{sat} \cdot K_{air}}{S \cdot K_{air} + (1 - S) \cdot K_w^{sat}} \qquad (3.55)$$

In the numerical simulations the degree of saturation was reduced from 1 (saturated conditions) to obtain the best fitting of the experimental results. A degree of saturation equal to 0.6 was found to give to best fitting of the experimental data. The suction was imposed equal to zero in the range of degrees of saturation $0.6 \leq S \leq 1$. The parameters of the water retention curve were assigned to fit this condition.

This project has received funding from the European Union's Horizon 2020 research and innovation programme under grant agreement No. 700748

3.3.1.3 CHARACTERISTICS OF THE STRUCTURE

In some centrifuge tests a simplified structure on strip foundations was added. The structure was made by two different materials: steel for the beam and the columns and aluminium for the foundations. It was characterized by a natural period of 0.3 s. In the numerical analyses, the structure was modelled using linear elastic plate elements. The damping of the building is simulated by means of Rayleigh formulation. The material properties adopted for all the structural elements are shown in Table 3.5.

Table 3.5. Properties of the structural elements.

Parameter	Description	Foundations	Beam	Columns	Unit
EA	Normal stiffness	7000000	52500000	31500000	kN/m
EI	Flexural rigidity	5833	273400	59060	$kN/m^2/m$
w	Weight	2.75	19.25	11.55	kN/m/m

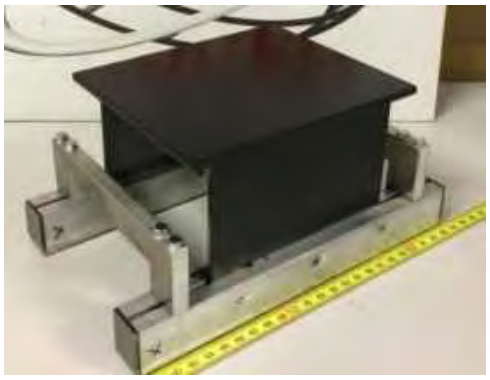

Figure 1. Structure realized for the centrifuge tests

This project has received funding from the European Union's Horizon 2020 research and innovation programme under grant agreement No. 700748

3.3.2 MODELS CALIBRATION FOR THE SIMULATION OF THE FIELD TRIALS AT THE TEST SITE

The deformability parameters of the constitutive models have been defined according to the V_s profile available for the site (see *Figure 2.2* and Table 2.1).

For the liquefiable sandy layers, 2 constitutive models were alternatively adopted: the Finn-Byrne model and the SANISAND model. The calibration procedure for both of them is reported hereafter.

3.3.2.1 Finn-Byrne model

As discussed in Section 3.1.1, the parameters of the Finn-Byrne model controlling the development of water overpressure are two: C1=7600·(Dr)-2.5, where the value of relative density D_r=35% has been defined from the interpretation of the CPTU tests executed on site (§7), and C2=0.4/C1 (Itasca, 2011). Hysteretic damping has been assigned to all layers with calibration of the shear modulus degradation curves (see Figure 3.15) according to the results of laboratory tests (Chiaradonna et al., 2018a, 2018b).

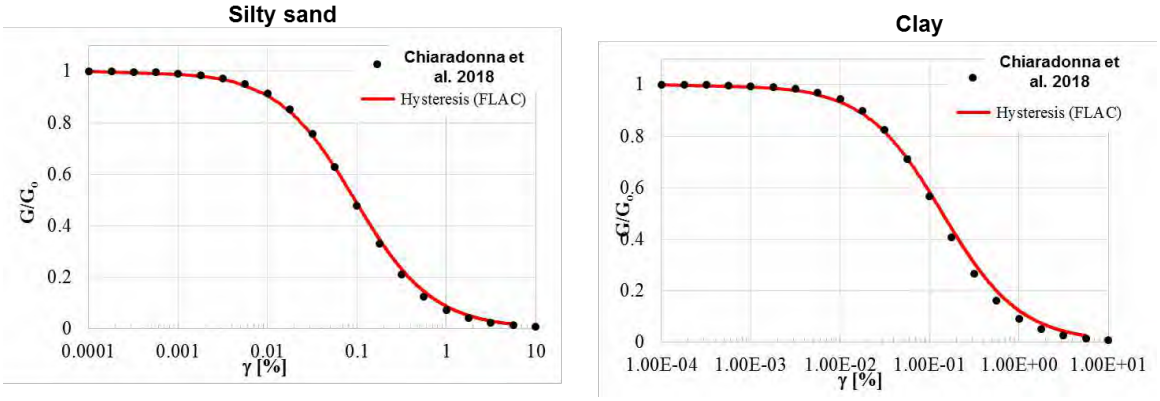

Figure 3.15. Shear modulus degradation curves calibrated on laboratory data.

Table 3.6. Set of parameters of the Finn-Bryne model adopted in the simulations.

Parameter	Definition	Value
Dr	Relative density	0.38
Cc1	Calibration parameter	0.854
C_1	Calibration parameter	0.427
C_2	Calibration parameter	0.468

This project has received funding from the European Union's Horizon 2020 research and innovation programme under grant agreement No. 700748

3.3.2.2 SANISAND model

The calibration of the SANISAND model was carried out in two steps:

(a) Single element test simulation of cyclic simple shear (CSS) undrained tests on undisturbed and reconstituted specimens of Pieve di Cento grey silty sand;
(b) Comparison between experimental and simulated cyclic resistance, CRR-N_{cyc}, curve;
(c) Comparison between experimental and simulated normalized shear modulus, G/G_0 and damping ratio, D curves obtained from cyclic torsional shear (TS) test on undisturbed sample of Pieve di Cento grey silty sand.

Table 3.7 lists the main features of the cyclic shear tests (CSS) used in the calibration process (step *a* and *b*). Figures Figure 3.16 -Figure 3.22 show the comparison between simulated and experimental test data. The comparison in terms of cyclic resistance curves and normalized shear modulus, G/G_0 and damping ratio, D curves are shown in Figure 3.23 and Figure 3.24, respectively. The final set of model parameters obtained from the calibration process is provided in Table 3.8.

Table 3.7. Lists of the main features of the cyclic shear tests.

CSS test	e	Dr (%)	CRR	N_{cyc} (r_u=0.9)	Sample
13/02/2018	-	-	0.115	67	Reconstituted
22/02/2018	0.690	43.9	0.15	7	
23/02/2018	0.696	42.5	0.13	9	
21/05/2018	-	-	0.14	8	
07/03/2018	0.668	48.9	0.12	33	GP z=5m (CH2)
19/03/2018	0.697	42.3	0.11	36	GP z=3m (CH1bis)
22/03/2018	0.631	57.2	0.12	12	GP z=3m (CH1bis)

This project has received funding from the European Union's Horizon 2020 research and innovation programme under grant agreement No. 700748

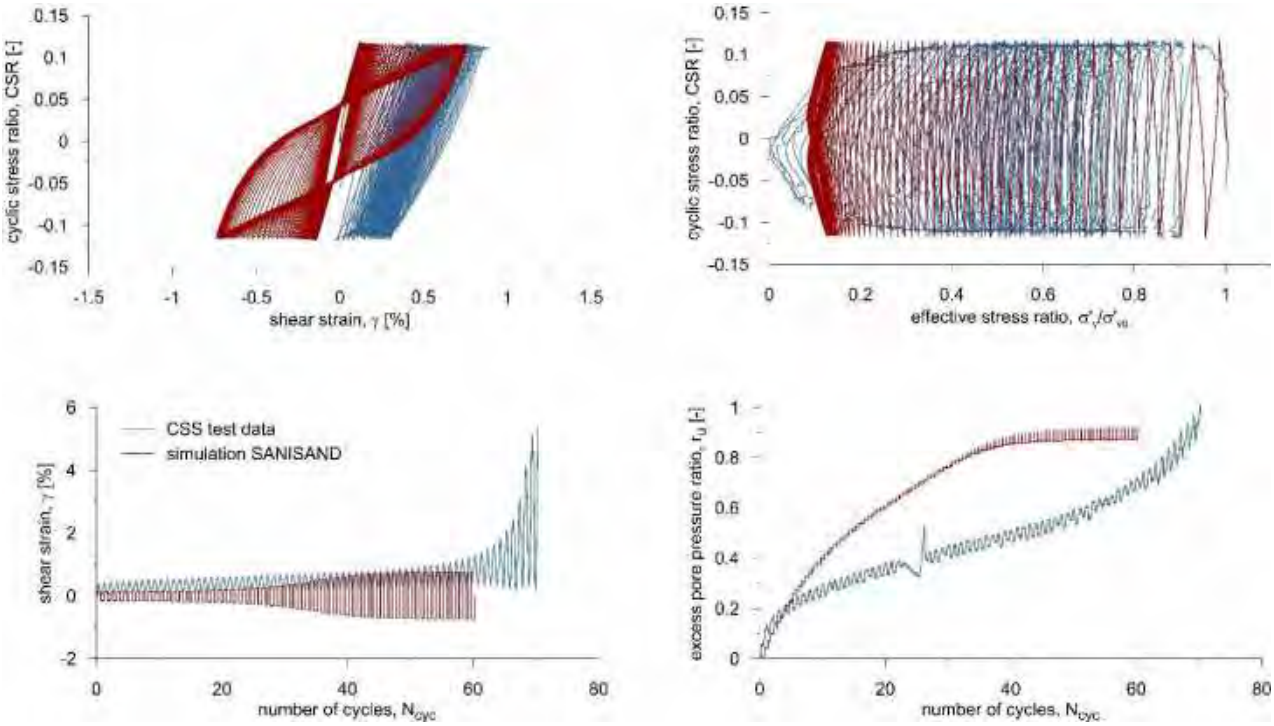

Figure 3.16. Comparison between simulated and experimental data for the test 13/02/2018.

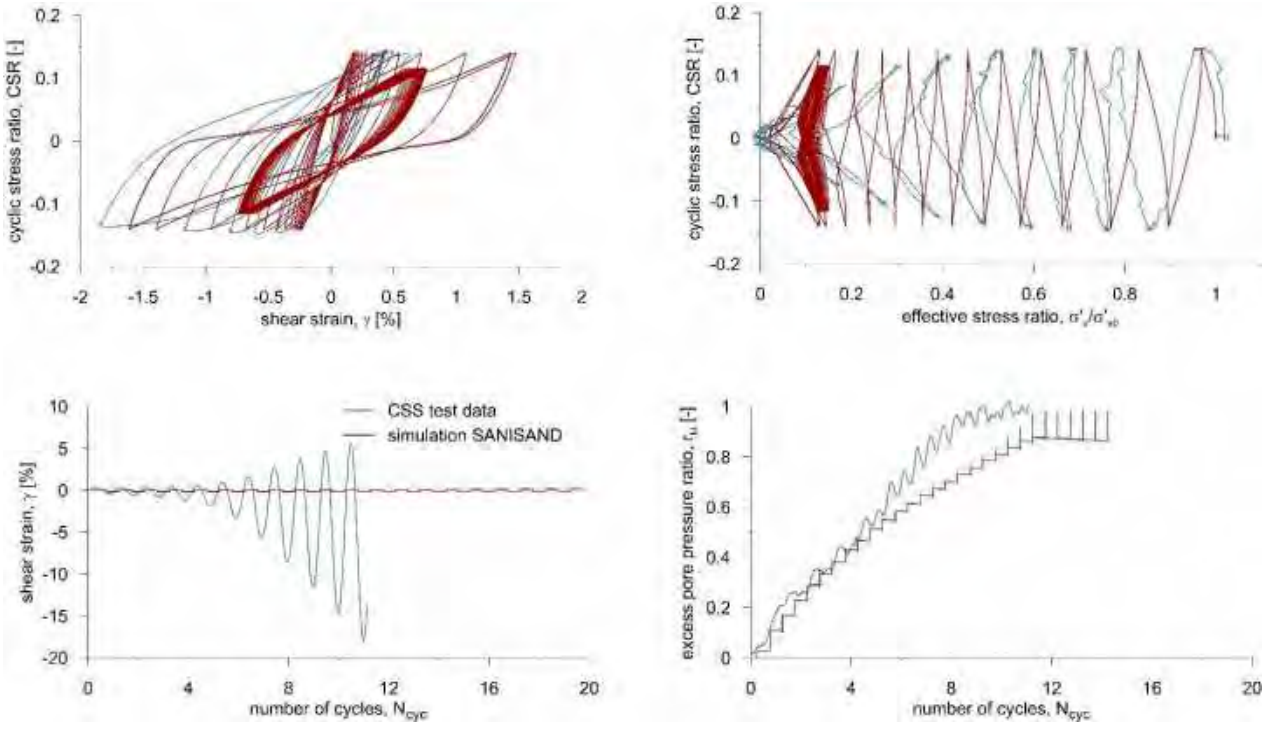

Figure 3.17. Comparison between simulated and experimental data for the test 22/02/2018.

This project has received funding from the European Union's Horizon 2020 research and innovation programme under grant agreement No. 700748

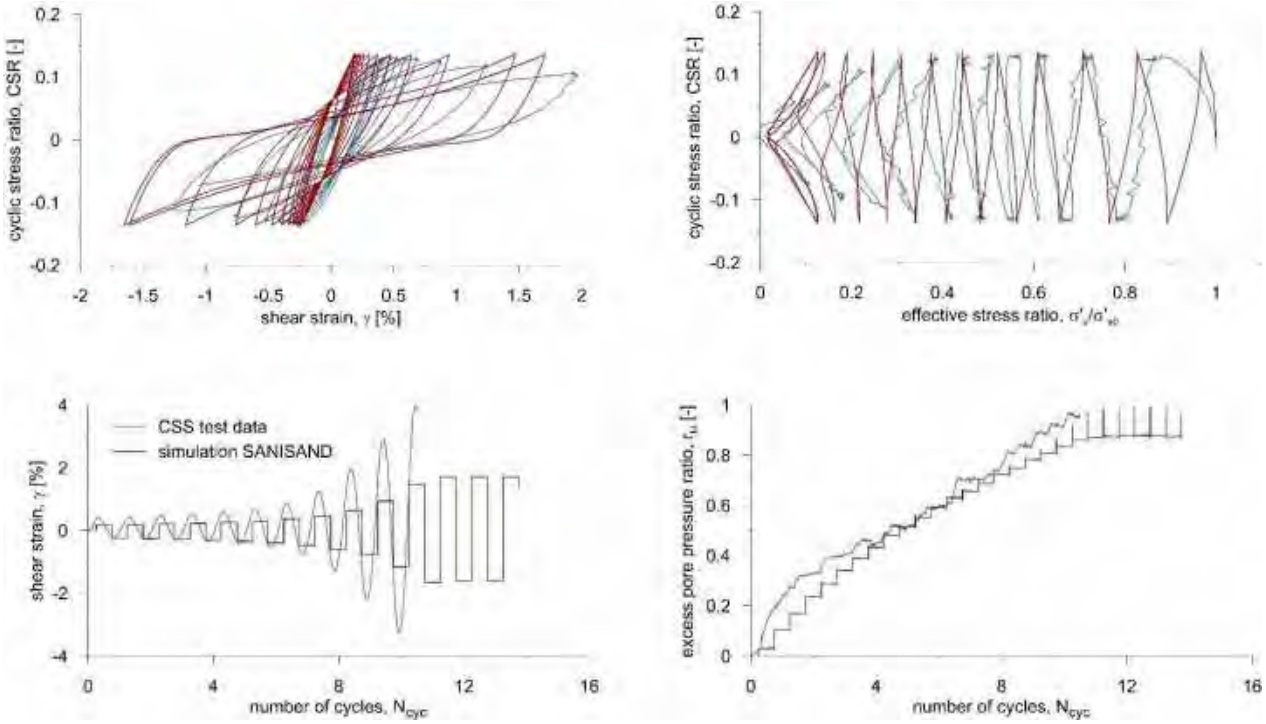

Figure 3.18. Comparison between simulated and experimental data for the test 23/02/2018.

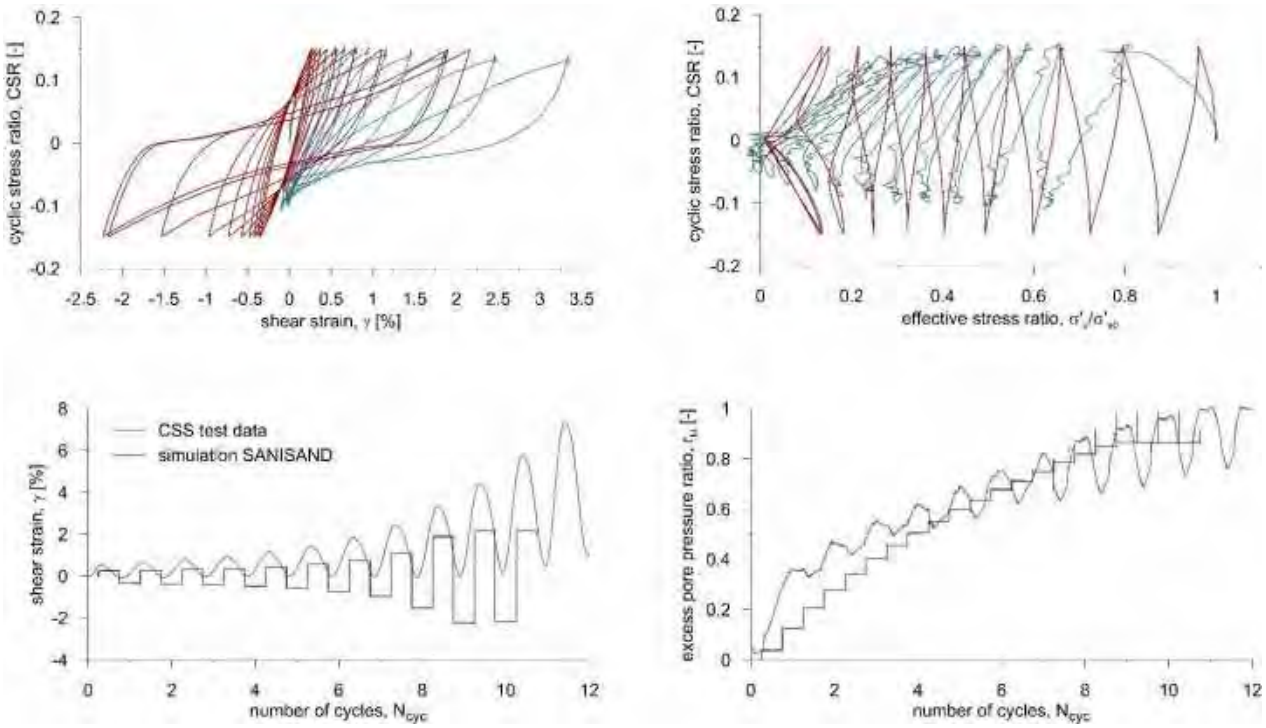

Figure 3.19. Comparison between simulated and experimental data for the test 21/05/2018.

This project has received funding from the European Union's Horizon 2020 research and innovation programme under grant agreement No. 700748

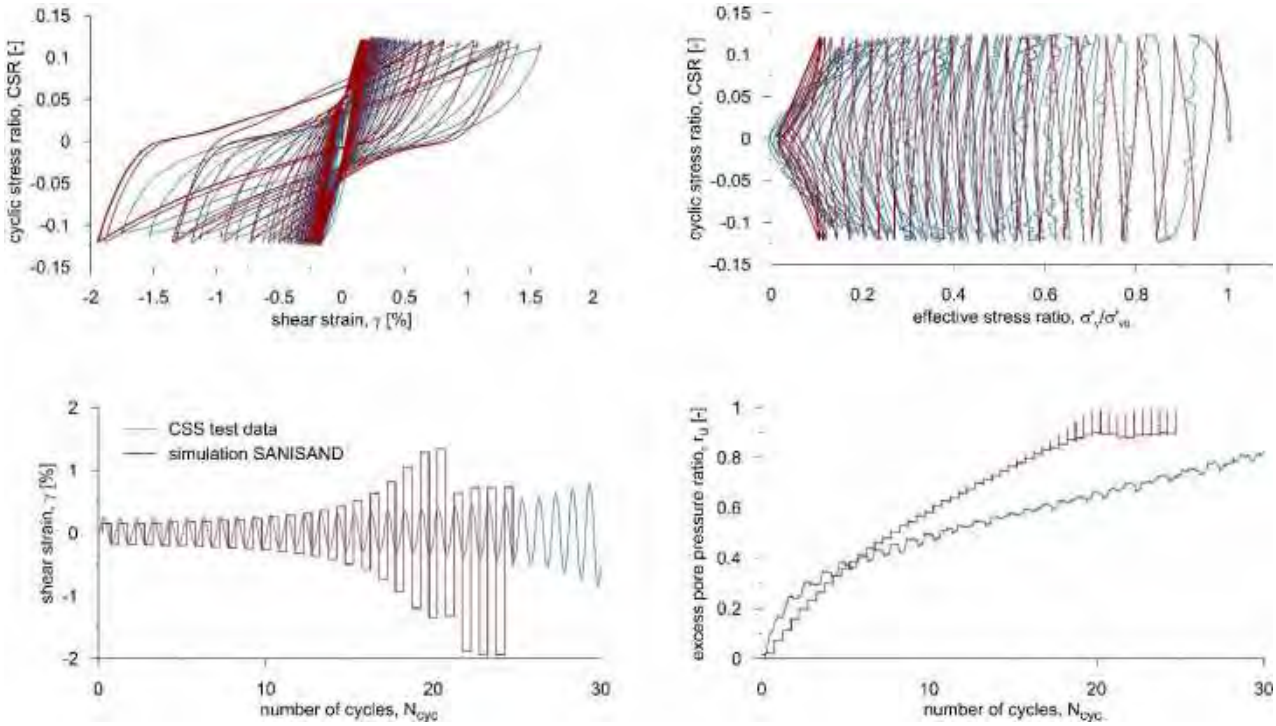

Figure 3.20. Comparison between simulated and experimental data for the test 07/03/2018.

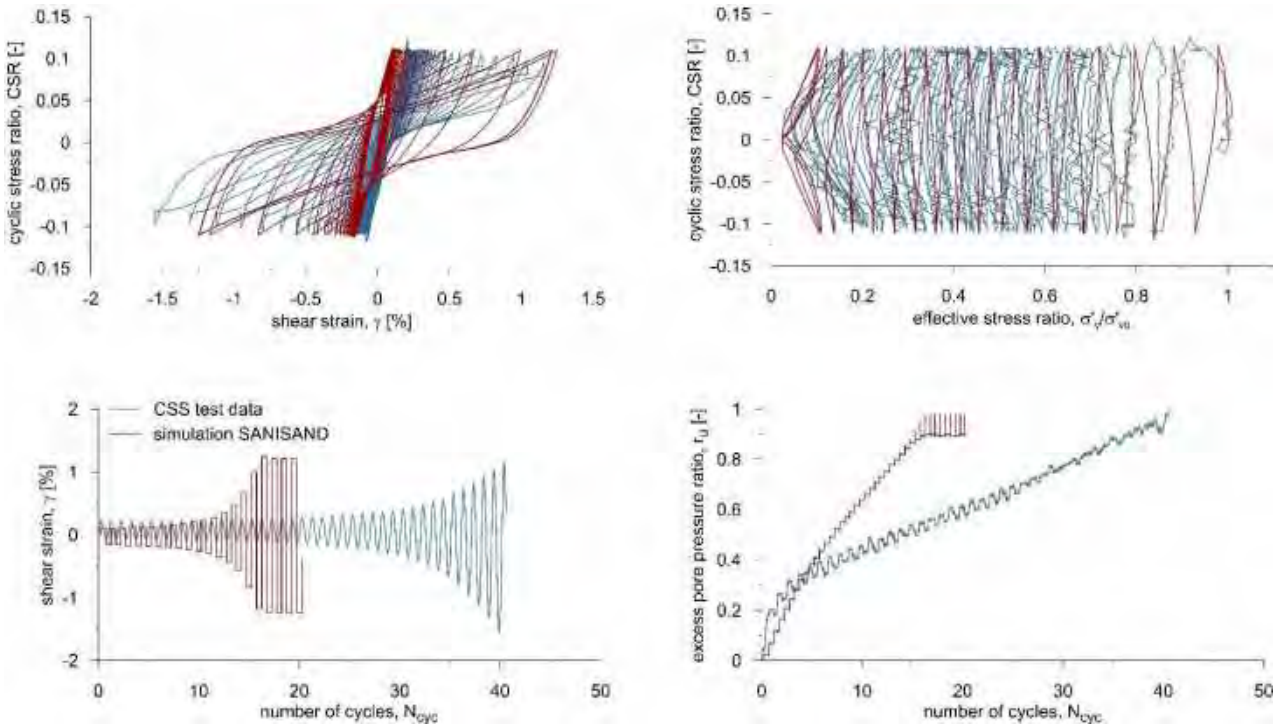

Figure 3.21. Comparison between simulated and experimental data for the test 19/03/2018.

This project has received funding from the European Union's Horizon 2020 research and innovation programme under grant agreement No. 700748

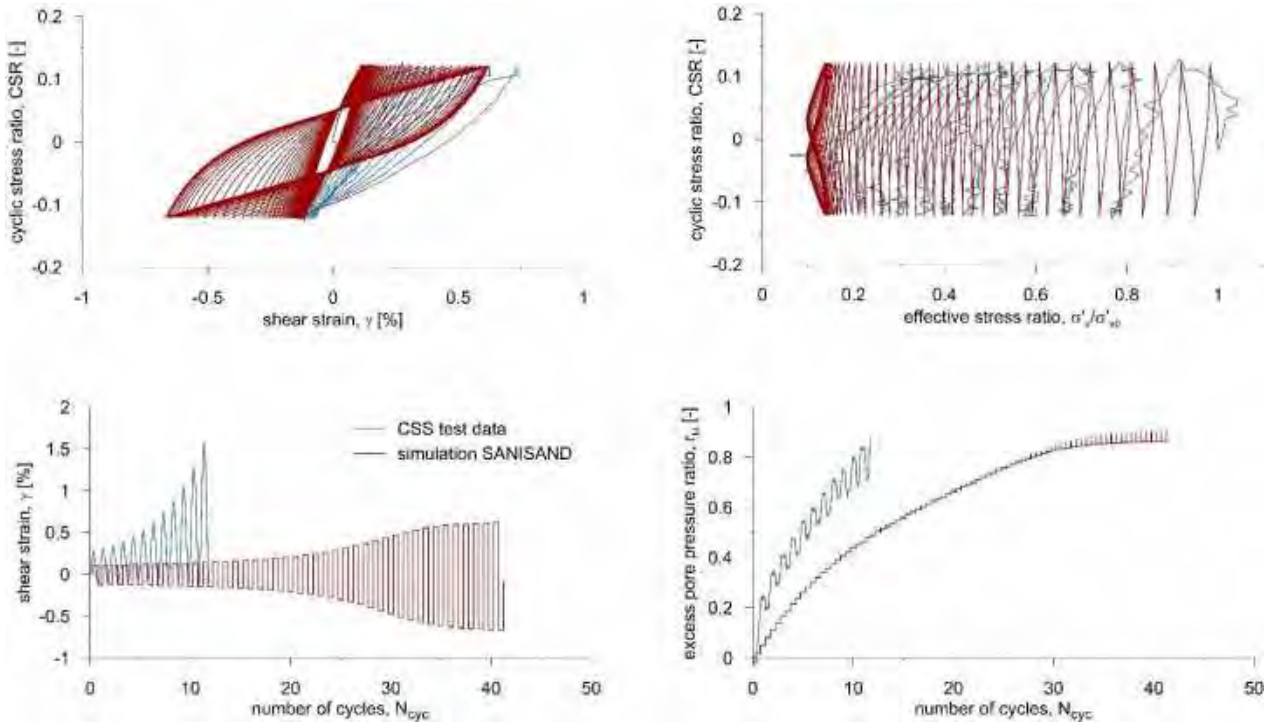

Figure 3.22. Comparison between simulated and experimental data for the test 22/03/2018.

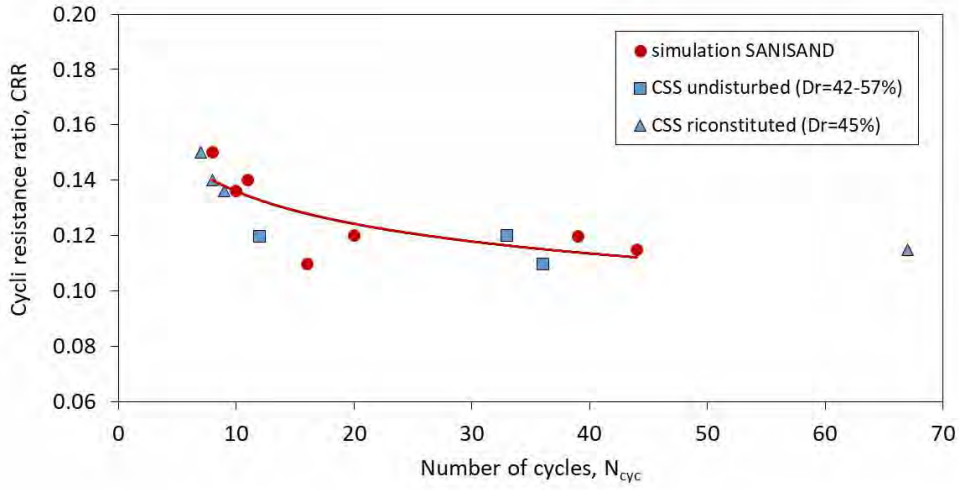

Figure 3.23. Comparison between simulated and experimental cyclic resistance curve.

This project has received funding from the European Union's Horizon 2020 research and innovation programme under grant agreement No. 700748

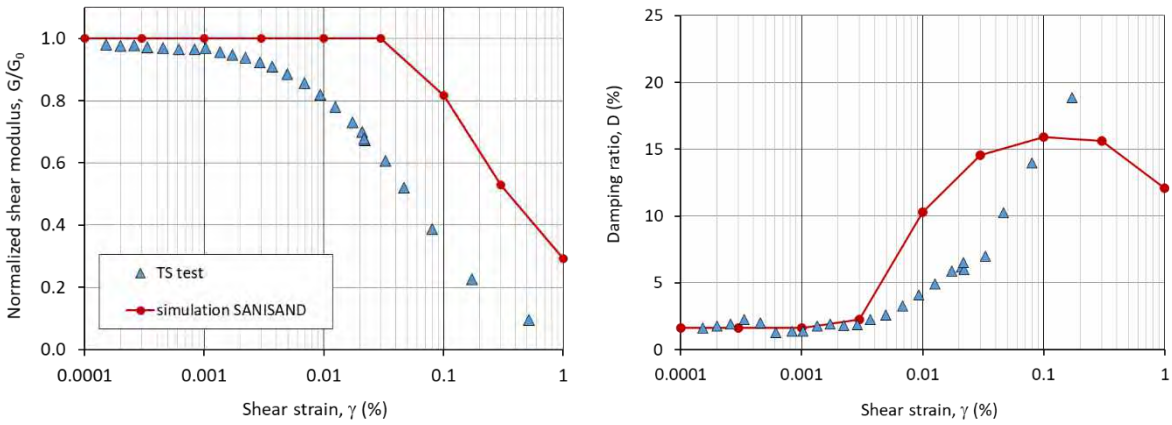

Figure 3.24. Comparison between simulated and experimental normalized shear modulus, G/G_0 and damping ratio, D curves.

Table 3.8. Model parameters of SANISAND for Pieve di Cento grey silty sand.

Constant	Variable	Value
Elasticiy	Go	40
	ν	0.3
Critical State	M	1.264
	c	1
	λc	0.018
	e0	0.817
	ξ	0.7
Yield surface	m	0.01
Plastic Modulus	h0	4.5
	ch	0.95
	nb	4.5
Dilatancy	A0	0.1
	nd	5
Fabric-dilatancy tensor	zmax	11
	cz	1000

This project has received funding from the European Union's Horizon 2020 research and innovation programme under grant agreement No. 700748

3.4 LIST OF ANALYSES FOR THE CENTRIFUGE TESTS

ID	Centrifuge test	Model	Material	Constituive model	Ground motion	Numerical code
SF_xx_TC_PM4_31	M1_S1_GM31	single layer	Ticino sand	PM4SAND	GM31	PLAXIS2D
SF_xx_TC_UBC_31				UBCSAND	GM31	PLAXIS2D
SF_xx_TC_PDM_31				PDMY02	GM31	OPENSEES
SF_xx_TC_FBY_31				Finn-Byrne	GM31	FLAC2D
SF_xx_PV_SAN_17	M1_S3_GM17	single layer	Pieve di Cento sand with fine content	SANISAND	GM17	FLAC3D
SF_xx_PV_SAN_23	M1_S3_GM23	single layer	Pieve di Cento sand with fine content	SANISAND	GM23	FLAC3D
SF_xx_PV_SAN_34	M1_S3_GM34	single layer	Pieve di Cento sand with fine content	SANISAND	GM34	FLAC3D
DF_xx_TC_PM4_31	M2_S1_GM31	double layer	Ticino sand	PM4SAND	GM31	PLAXIS2D
DF_xx_TC_UBC_31				UBCSAND	GM31	PLAXIS2D
SS_xx_TC_PM4_31	M1F_S1_GM31	single layer with structure	Ticino sand	PM4SAND	GM31	PLAXIS2D
SS_xx_TC_UBC_31				UBCSAND	GM31	PLAXIS2D
SS_xx_TC_PDM_31				PDMY02	GM31	OPENSEES
SS_xx_TC_PM4_31+	M1F_S1_GM31+	single layer with structure	Ticino sand	PM4SAND	GM31+	PLAXIS2D
SS_xx_TC_UBC_31+				UBCSAND	GM31+	PLAXIS2D
DS_xx_TC_PM4_31+	M2F_S1_GM31+	double layer with structure	Ticino sand	PM4SAND	GM31+	PLAXIS2D
DS_xx_TC_UBC_31+				UBCSAND	GM31+	PLAXIS2D
SF_HD_TC_PM4_31	M1_S1_HD1_GM31	single layer with horizontal drains	Ticino sand	PM4SAND	GM31	PLAXIS2D
SF_HD_TC_UBC_31				UBCSAND	GM31	PLAXIS2D

This project has received funding from the European Union's Horizon 2020 research and innovation programme under grant agreement No. 700748

SF_HD_TC_PM4_31	M1_S1_HD2_GM31	single layer with horizontal drains	Ticino sand	PM4SAND	GM31	PLAXIS2D
SF_HD_TC_UBC_31				UBCSAND	GM31	PLAXIS2D
DF_HD_TC_PM4_31	M2_S1_HD1_GM31	double layer with horizontal drains	Ticino sand	PM4SAND	GM31	PLAXIS2D
DF_HD_TC_UBC_31				UBCSAND	GM31	PLAXIS2D
DF_HD_TC_PM4_31	M2_S1_HD2_GM31	double layer with horizontal drains	Ticino sand	PM4SAND	GM31	PLAXIS2D
DF_HD_TC_UBC_31				UBCSAND	GM31	PLAXIS2D
SS_HD_TC_PM4_31+	M1F_S1_HD1_GM31+	single layer with structure and horizontal drains	Ticino sand	PM4SAND	GM31+	PLAXIS2D
SS_HD_TC_UBC_31+				UBCSAND	GM31+	PLAXIS2D
DS_HD_TC_PM4_31+	M2F_S1_HD1_GM31+	double layer with structure and horizontal drains	Ticino sand	PM4SAND	GM31+	PLAXIS2D
DS_HD_TC_UBC_31+				UBCSAND	GM31+	PLAXIS2D
SF_IPS_TC_PM4_31	M1_S1_IPS4_GM31	single layer with induced partial saturation	Ticino sand	PM4SAND	GM31	PLAXIS2D
SF_IPS_TC_UBC_31				UBCSAND	GM31	PLAXIS2D
SF_IPS_TC_PM4_31+	M1_S1_IPS4_GM31+	single layer with induced partial saturation	Ticino sand	PM4SAND	GM31+	PLAXIS2D
SF_IPS_TC_UBC_31+				UBCSAND	GM31+	PLAXIS2D
DF_IPS_TC_PM4_31	M2_S1_IPS4_GM31	double layer with induced partial saturation	Ticino sand	PM4SAND	GM31	PLAXIS2D
DF_IPS_TC_UBC_31				UBCSAND	GM31	PLAXIS2D
DF_IPS_TC_PM4_31+	M2_S1_IPS4_GM31+	double layer with induced partial saturation	Ticino sand	PM4SAND	GM31+	PLAXIS2D
DF_IPS_TC_UBC_31+				UBCSAND	GM31+	PLAXIS2D
SS_IPS_TC_PM4_31+	M1F_S1_IPS4_GM31+	single layer with structure and induced partial saturation	Ticino sand	PM4SAND	GM31+	PLAXIS2D
SS_IPS_TC_UBC_31+				UBCSAND	GM31+	PLAXIS2D
SS_IPS_TC_PM4_31++	M1F_S1_IPS4_GM31++	single layer with structure and induced partial saturation	Ticino sand	PM4SAND	GM31++	PLAXIS2D
SS_IPS_TC_UBC_31++				UBCSAND	GM31++	PLAXIS2D

This project has received funding from the European Union's Horizon 2020 research and innovation programme under grant agreement No. 700748

The identification name (defined as ID) proposed in the previous table and adopted in the simulations has been conceived to synthetically take into account all the relevant characteristics of the tests to be simulated. It is composed of 5 parts (1_2_3_4_5), separated by the underscore line. The first ID part (part 1) refers to subsoil stratigraphy and the possible presence of a structure at ground level; the second ID part (part 2) refers to the ground improvement technology adopted; the third ID part (part 3) refers to the type of sand constituting the liquefiable soil layer; the fourth ID part (part 4) refers to the constitutive model adopted in the analyses; the fifth and last ID part (part 5) refers to the adopted ground motion. In detail, ID logic is reported in the following table.

Table 3.9. ID structure: 1_2_3_4_5.

ID part	REFERS TO	SYMBOL	EXPLANATION
1	Stratigraphy and structure	SF	single layer (S), free-field (F)
		DF	double layer (D), free-field (F)
		SS	single layer (S) with structure (S)
		DS	double layer (D) with structure (S)
2	Kind of ground improvement technology adopted to mitigate liquefaction	xx	No use of ground improvement (virgin soil)
		HD	horizontal drains (HD)
		IPS	induced partial saturation (IPS)
3	Type of sand constituting the liquefiable layer	TC	Ticino sand
		PV	Pieve di Cento sand
4	Adopted constitutive model	PM4	PM4Sand model
		UBC	UBCSand model
		SAN	SaniSand model
		PDM	PMDY02 model
		FBY	Finn-Bryne model
5	Ground motion used in the analyses	31	Ground motion 31
		31+	Ground motion 31+
		31++	Ground motion 31++

So, for instance, analysis SF_xx_TC_PM4_31 is carried out with a single layer in free field conditions, with no ground improvement, considering Ticino sand and using PM4 to model its behaviour, shaking it at the base with the ground motion 31. The analysis SF_HD_TC_PM4_31 is carried out in the identical conditions but for the use of horizontal drains.

This project has received funding from the European Union's Horizon 2020 research and innovation programme under grant agreement No. 700748

3.5 LIST OF THE PARAMETRIC ANALYSES

3.5.1 LIST OF ANALYSES FOR THE STUDY ON THE EFFECT OF HORIZONTAL DRAINS

The ID of the parametric analyses does not show any reference to the type of sand and to the seismic input because of all them have been carried out considering the Ticino sand and using input motion GM31. The ID is therefore made of four parts (1_2_3_4) having the meaning indicated in the following table

Table 3.10. ID structure: 1_2_3_4.

ID part	REFERS TO	SYMBOL	EXPLANATION
1	Stratigraphy and structure	SF	single layer (S), free-field (F)
		DF	double layer (D), free-field (F)
		SS	single layer (S) with structure (S)
		DS	double layer (D) with structure (S)
2	Disposition of the horizontal drains	00	No drains (virgin soil)
		HD	localized horizontal drains (HD)
		HDU	Uniformally distributed horizontal drains (HUD)
3	H/D (depth of upper row of drains over drains diameter) ratio	00	No drains (virgin soil)
		h05	H/D=5
		h10	H/D=10
		h15	H/D=15
4	s/D (spacing over drains diameter) ratio	00	No drains (virgin soil)
		s05	s/D=5
		s10	s/D=10
		s15	s/D=15

This project has received funding from the European Union's Horizon 2020 research and innovation programme under grant agreement No. 700748

Table 3.11. Centrifuge numerical back-analyses.

Type	Model	d [m]	H [m]	s [m]	h/d	s/d	Results	ID (SINGLE LAYER)	ID (DOUBLE LAYER)
Simulation of the centrifuge schemes (sand, sand & clay) using the set of parameters calibrated on the centrifuge free field test (SF_xx_TC_PM4_31)	Drains	0,3	1,5	1,5	5	5	Soil acceleration time histories, soil Fourier spectra, soil response spectra, excess pore pressure, excess pore pressure ratio, soil vertical displacement	SF_HD_H05_s05	DF_HD_H05_s05
				3		10		SF_HD_H05_s10	DF_HD_H05_s10
	Structure	-	-	-	-	-	Soil acceleration time histories, soil Fourier spectra, soil response spectra, excess pore pressure, excess pore pressure ratio, soil vertical displacement, structure acceleration time histories, structure Fourier spectra, structure response spectra, Structure vertical displacement	SS_00_00_00	DS_00_00_00
	Drains and structure	0,3	1,5	1,5	5	5	Soil acceleration time histories, soil Fourier spectra, soil response spectra, excess pore pressure, excess pore pressure ratio, soil vertical displacement, structure acceleration time histories, structure Fourier spectra, structure response spectra, Structure vertical displacement	SS_HD_H05_s05	DS_HD_H05_s05
				3		10		SS_HD_H05_s10	DS_HD_H05_s10
Parametric analyses (only sand, sand &	Drains	0,3	1,5	1,5	5	5	Soil acceleration time histories, soil Fourier spectra, soil response spectra, excess pore	SF_HDU_H05_s05	DF_HDU_H05_s05
				3		10		SF_HDU_H05_s10	DF_HDU_H05_s10

This project has received funding from the European Union's Horizon 2020 research and innovation programme under grant agreement No. 700748

clay) (in the ID the label HDU means a Uniform set of Horizontal Drains, to distinguish it from the non-uniform schemes adopted in the centrifuge)				4,5		15	pressure, excess pore pressure ratio, soil vertical displacement	SF_HDU_H05_s15	DF_HDU_H05_s15
			3	1,5	10	5		SF_HDU_H10_s05	DF_HDU_H10_s05
				3		10		SF_HDU_H10_s10	DF_HDU_H10_s10
				4,5		15		SF_HDU_H10_s15	DF_HDU_H10_s15
			4,5	1,5	15	5		SF_HDU_H15_s05	DF_HDU_H15_s05
				3		10		SF_HDU_H15_s10	DF_HDU_H15_s10
				4,5		15		SF_HDU_H15_s15	DF_HDU_H15_s15
	Drains and structure	0,3	1,5	1,5	5	5	Soil acceleration time histories, soil Fourier spectra, soil response spectra, excess pore pressure, excess pore pressure ratio, soil vertical displacement, structure acceleration time histories, structure Fourier spectra, structure response spectra, Structure vertical displacement	SS_HDU_H05_s05	SS_HDU_H05_s05
				3		10		SS_HDU_H05_s10	SS_HDU_H05_s10
				4,5		15		SS_HDU_H05_s15	SS_HDU_H05_s15
			3	1,5	10	5		SS_HDU_H10_s05	SS_HDU_H10_s05
				3		10		SS_HDU_H10_s10	SS_HDU_H10_s10
				4,5		15		SS_HDU_H10_s15	SS_HDU_H10_s15
			4,5	1,5	15	5		SS_HDU_H15_s05	SS_HDU_H15_s05
				3		10		SS_HDU_H15_s10	SS_HDU_H15_s10
				4,5		15		SS_HDU_H15_s15	SS_HDU_H15_s15

d: diameter
H: depth from water table
s: spacing

This project has received funding from the European Union's Horizon 2020 research and innovation programme under grant agreement No. 700748

3.6 LIST OF ANALYSES FOR THE FIELD TRIAL TESTS

Table 3.12. Trial site numerical simulations.

ID	Field-trial test	Treatment	Constituive model for liquefiable soil	Numerical code
VS_SAN	TEST 1	NO	SANISAND	FLAC3D
VS_FIN		NO	FINN	FLAC3D
IPS_FIN	TEST 8	IPS	FINN	FLAC3D

This project has received funding from the European Union's Horizon 2020 research and innovation programme under grant agreement No. 700748

4 NUMERICAL SIMULATION OF CENTRIFUGE TESTS ON REFERENCE MODELS

4.1 SINGLE LAYER PROFILE IN FREE FIELD CONDITION

4.1.1 UBCSAND

4.1.1.1 ID: SF_xx_TC_UBC_31

The model consists of a homogenous soil profile of Ticino sand. The ground motion applied was the number 31.

ID: SF_xx_TC_UBC_31	TEST: M1_S1_GM31

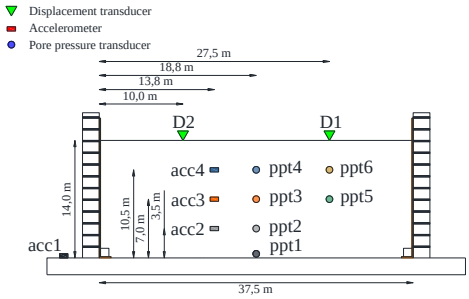

Layouts of the model reproduced in Plaxis 2D

The UBC3D-PML constitutive model is used to represent Ticino sand The properties adopted in the numerical analyses are summarized in following table.

Table with UBCSand parameters.

Parameter	Description	Value	Unit
$N_{1,60}$	SPT number	10.4	-
K_G^e	elastic shear modulus	946	-
K_B^e	elastic bulk modulus	1577	-
K_G^p	plastic shear modulus	407	-
m_e	elastic stress dependency parameter	0.5	-
n_e	elastic stress dependency parameter	0.5	-
n_p	plastic stress dependency parameter	0.4	-
ϕ_{cv}	critical state friction angle	33	°
ϕ_{peak}	peak state friction angle	34	°
R_f	failure ratio	0.77	-
ν	Poisson coefficient	0.25	-

This project has received funding from the European Union's Horizon 2020 research and innovation programme under grant agreement No. 700748

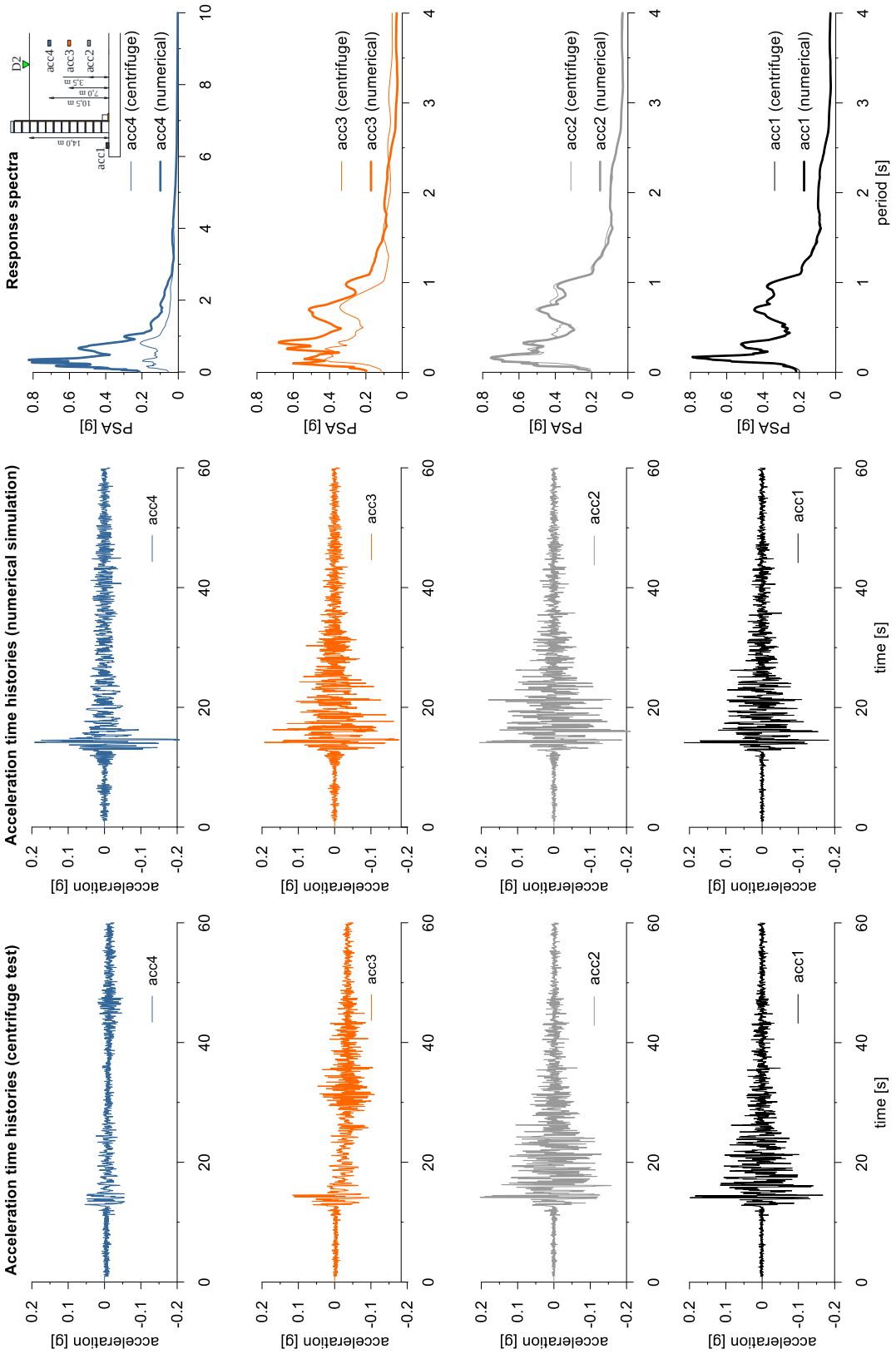

This project has received funding from the European Union's Horizon 2020 research and innovation programme under grant agreement No. 700748

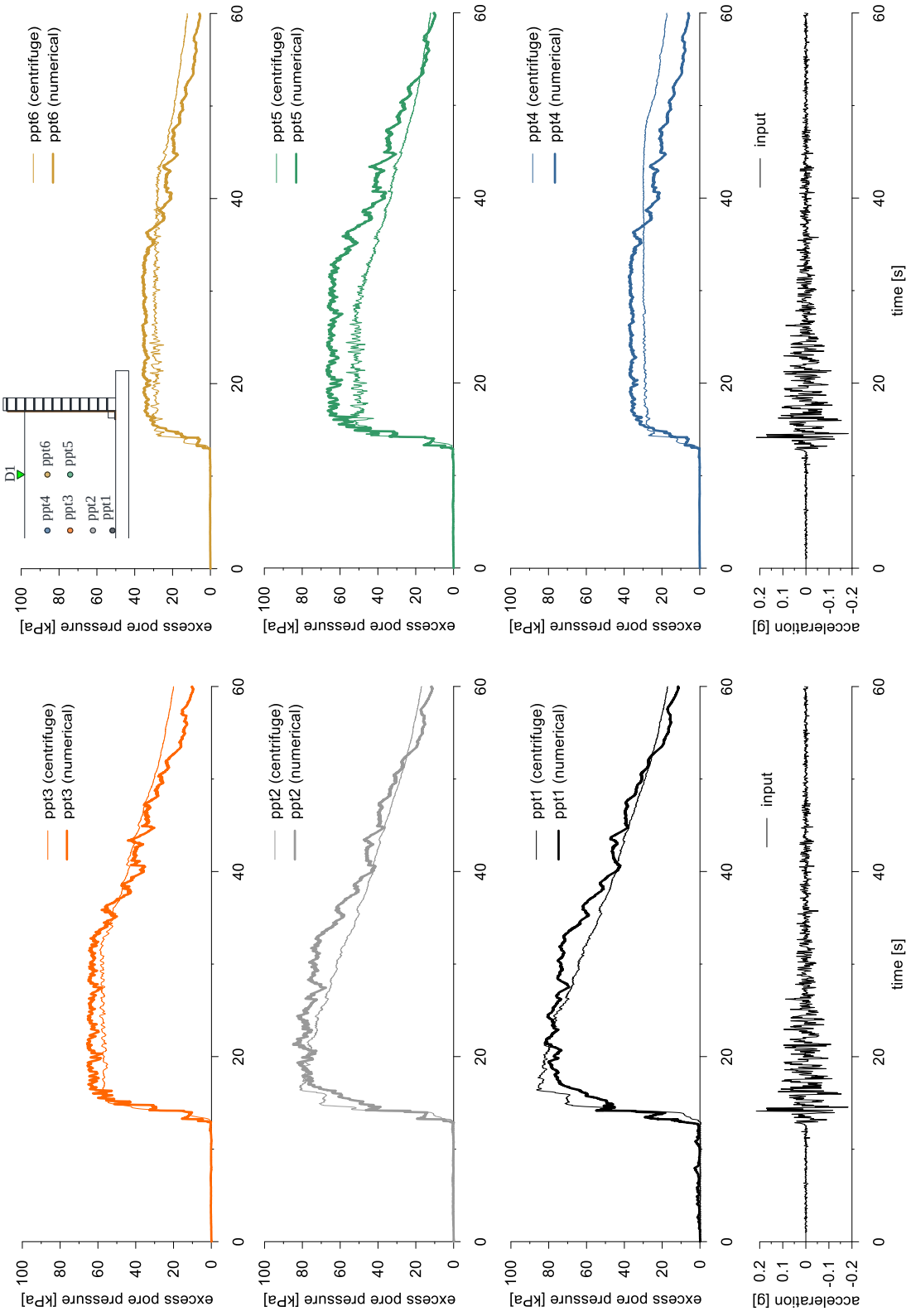

This project has received funding from the European Union's Horizon 2020 research and innovation programme under grant agreement No. 700748

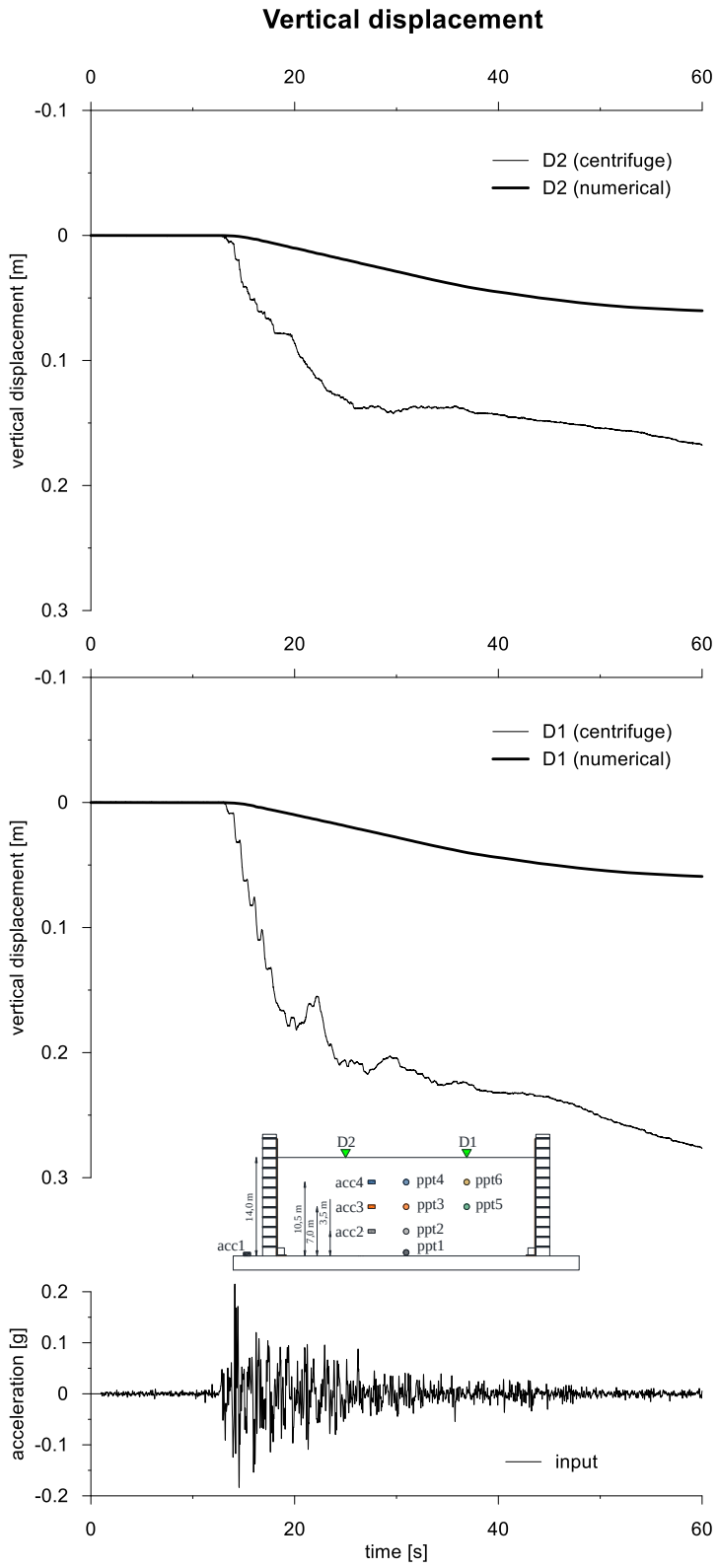

This project has received funding from the European Union's Horizon 2020 research and innovation programme under grant agreement No. 700748

4.1.2 PM4SAND

4.1.2.1 ID: SF_xx_TC_PM4_31

The model consists of a homogenous soil profile of Ticino sand. The ground motion applied was the number 31.

ID: SF_xx_TC_PM4_31	TEST: M1_S1_GM31

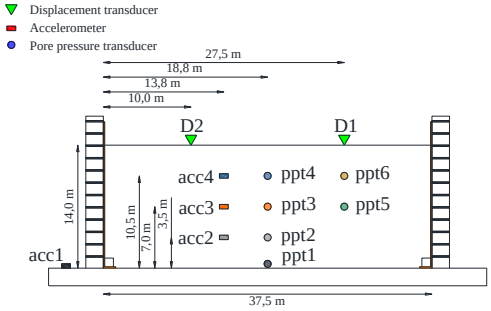

Layouts of the model reproduced in Plaxis 2D

The PM4Sand constitutive model is used to represent Ticino sand. The properties adopted in the numerical analyses are summarized in following table.

Table with PM4sand parameters

Parameter	Description	Value	Unit
D_{R0}	Initial relative density	0.47	-
G_0	shear modulus coefficient	594	-
hp_0	contraction rate parameter	0.1	-
p_A	atmospheric pressure	101.3	kN/m^2
e_{max}	maximum void ratio	0.923	-
e_{min}	minimum void ratio	0.574	-
n_b	bounding surface parameter	0.5	-
n_d	dilatancy surface parameter	0.1	-
ϕ_{cv}	critical state friction angle	33	°
nu	Poisson's ratio	0.3	-
Q	critical state line parameter	8	-
R	critical state line parameter	1.2	-

This project has received funding from the European Union's Horizon 2020 research and innovation programme under grant agreement No. 700748

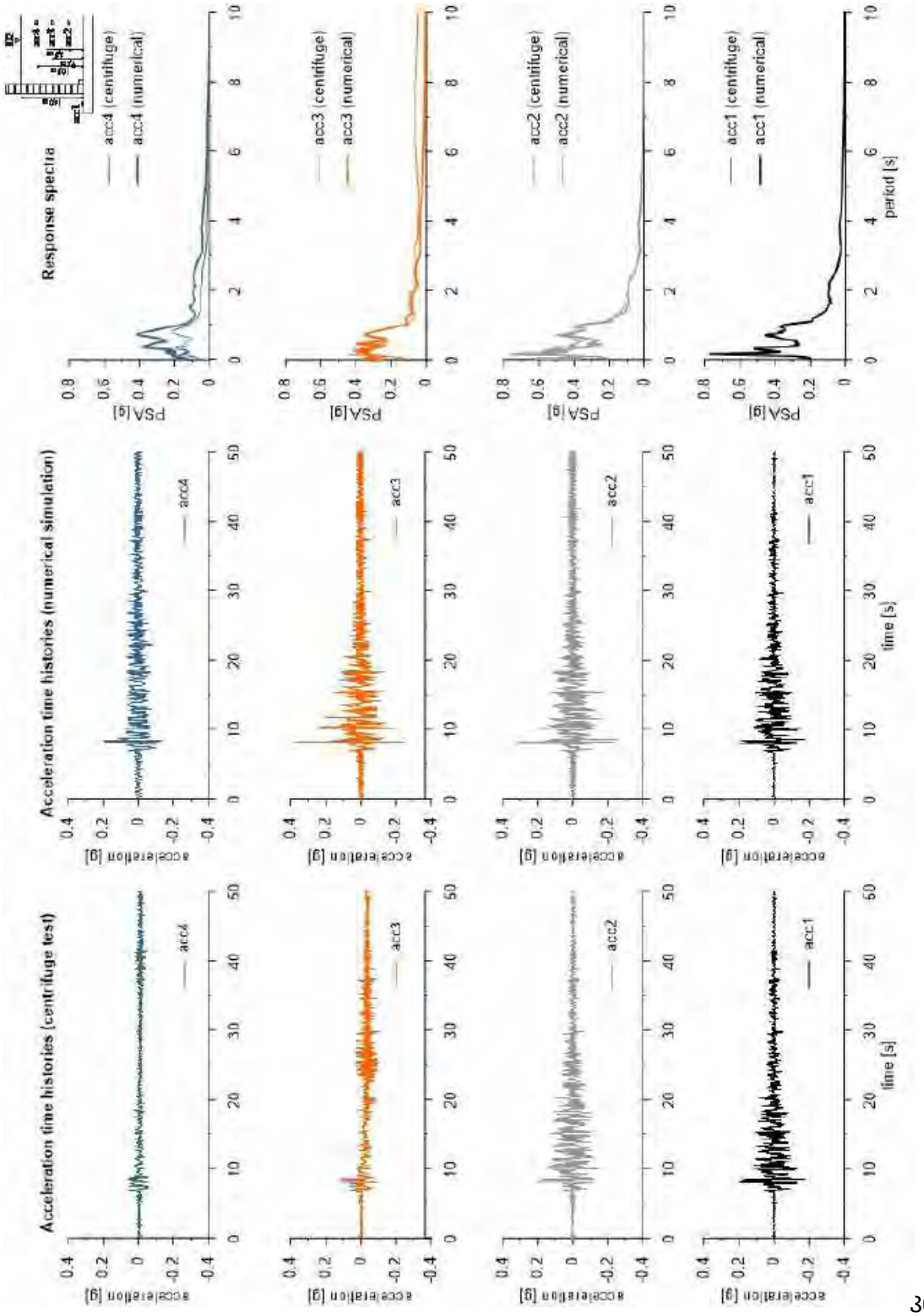

This project has received funding from the European Union's Horizon 2020 research and innovation programme under grant agreement No. 700748

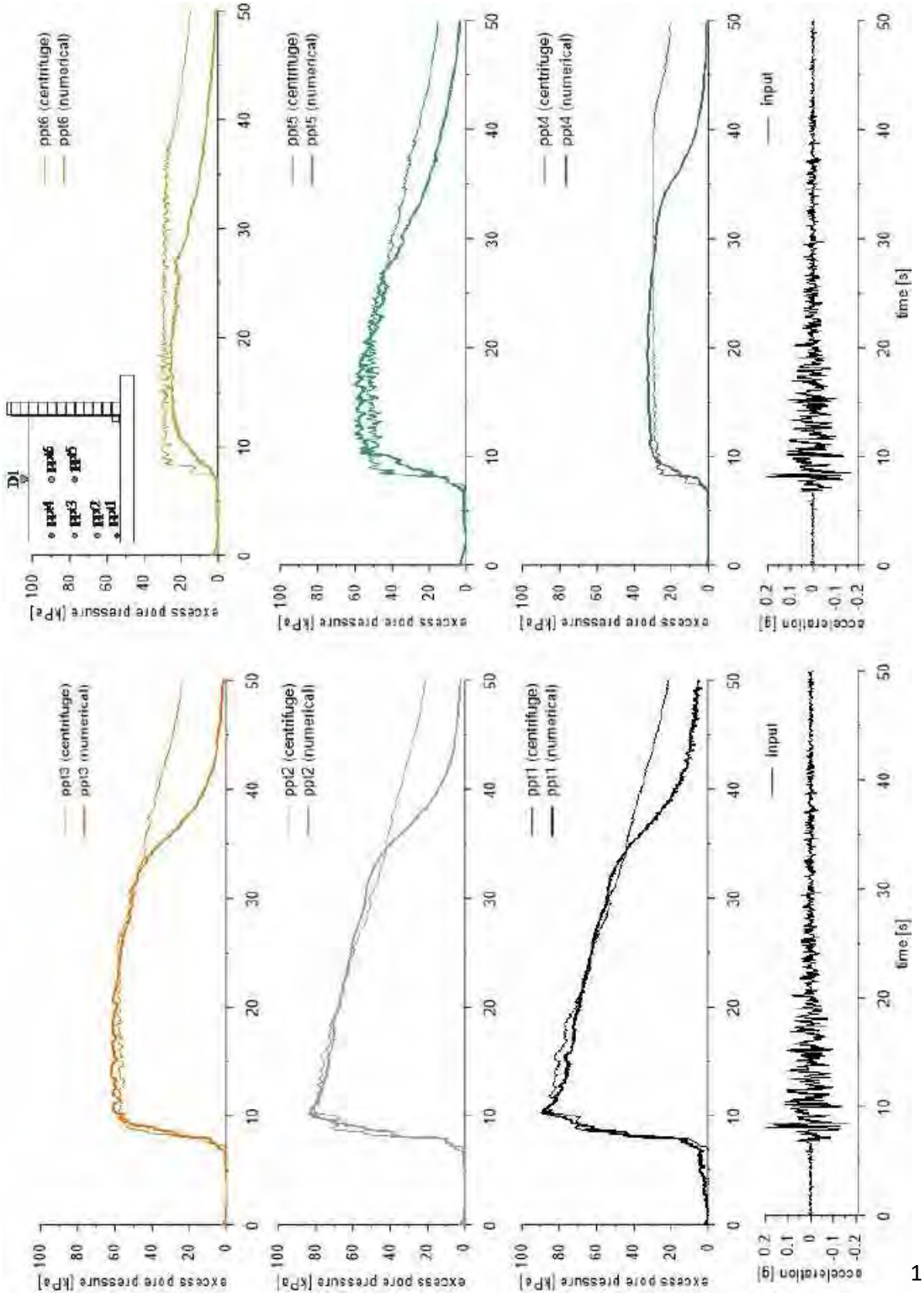

This project has received funding from the European Union's Horizon 2020 research and innovation programme under grant agreement No. 700748

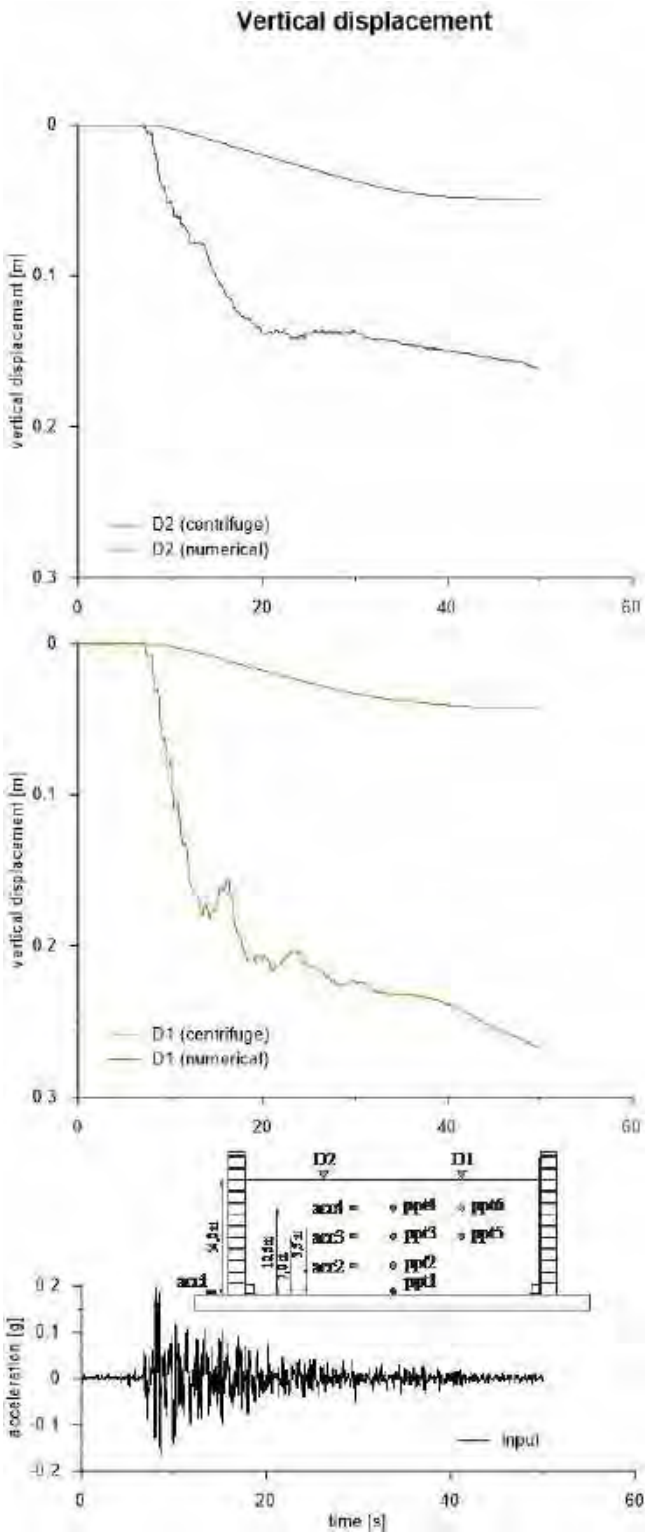

This project has received funding from the European Union's Horizon 2020 research and innovation programme under grant agreement No. 700748

4.1.3 FINN-BYRNE AND PDMY02

4.1.3.1 ID: SF_xx_TC_FBY_31

The model presented in Deliverable D4.2 (M1_S1_GM31) is modelled under plane strain assumptions in FLAC2D (Finn-Byrne model) and in OpenSees (PDMY02 model). The models are created in prototype scale, by following proper scaling factors.

- In FLAC2D model with Finn-Byrne constitutive relation, in-built coupled element formulation is used that allows the compressibility of soil skeleton as a function of induced shear strain. The observed response in centrifuge test is essentially undrained during the seismic excitation. Due to this reason, we adopted undrained analyses in FLAC models. Model parameters used are synthesized in Section 3.1. In addition to those, small amount of Rayleigh damping is also used.
- In OpenSees model with PDMY02 constitutive relation, 2D plane strain brickUP elements are used to allow partially drained response. Model parameters are summarized in Section 3.1. Given the fact that the dissipative characteristics at low strains are underestimated (due to stiffer secant shear modulus), 1% of Rayleigh damping is provided at 0.2 and 5 Hz. Hydraulic conductivity of Ticino sand is defined as 1.66 x 10^{-3} m/s at 40% relative density, we projected it to a relative density of 55% and calculated the new conductivity coefficient as 1.4 x 10^{-3} m/s according to framework of Revil and Cathles (1999). Further, due to the presence of partially saturated conditions in the physical model, a sensitivity study on soil hydraulic conductivity is carried out to find out the observed hydraulic conductivity during the centrifuge test.

Both models have soil zones in the order of 0.5 meters and contain the walls of the equivalent shear beam box, the stiffness and mass of which are represented under 2D plane strain conditions. Conceptual definition of the models is presented in Figure 4.1.

This project has received funding from the European Union's Horizon 2020 research and innovation programme under grant agreement No. 700748

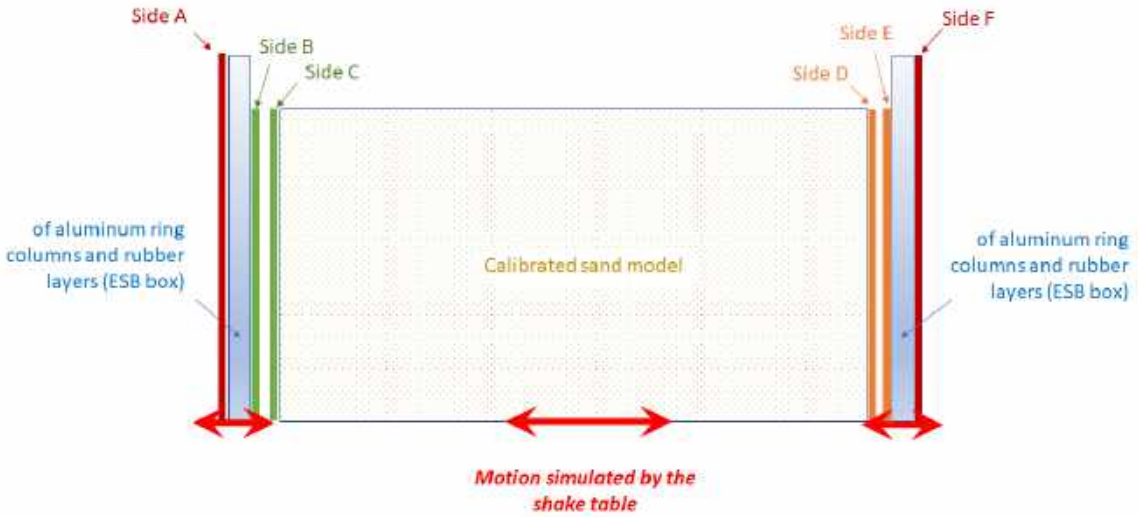

Figure 4.1. Conceptual drawing of the numerical models. Sides shown with same colour follow the same horizontal displacement. Ground motion is applied as the scaled version of the motion simulated during the centrifuge test. Note: In FLAC model, connections of sides B-C and D-E have physical contact, whereas in OpenSees it is achieved through equalDOF constraint for the horizontal component.

The results are provided in the following figures:

- Figure 4.2. PDMY02 model with k_H=1.4 x 10^{-3} m/s
- Figure 4.3. PDMY02 model with k_H=0.5 x 10^{-3} m/s
- Figure 4.4. Finn-Bryne model (undrained)

In Figure 4.2 to Figure 4.4 no comparisons of vertical displacements ad d1 and d2 are provided since it is discussed that recorded values of displacement transducers contain erroneous readings (Fioravante, 2018).

The following conclusions are drawn:

- From Figure 4.2:
  - Excess pore water pressure agreement at superficial depths (pwp4 and pwp6) seem to be the best, whereas the agreement worsens when the level of overburden increases. Consistently, in all of the pore water pressure comparisons, a faster rate of dissipation is noted in the modelled response. This is the reason why a sensitivity study on hydraulic conductivity is carried out.

  - The acceleration response on the other hand is found accurate at 10.5 meters depth (acc2), whereas the level of accuracy worsens with reducing overburden. This is because the underestimation of excess pore water pressure response throughout the profile. Since profile response of the model does not show liquefaction, it can propagate (yet with high damping) the ground motion in a broad frequency range.
- From Figure 4.3:
  - Excess pore water pressure agreement is found to be good for each comparison. Both modelled and tested profiles show the effects of cyclic mobility at deeper zones which gets significantly more severe at superficial conditions.
  - Like the case of Figure 4.2, the agreement of acceleration response is the best at 10.5 meters, for the other depths, higher frequency oscillations are still observable, yet they are comparably lower with respect to Figure 4.2.
  - Modelled response is found acceptable in overall terms.
- From Figure 4.4:
  - Excess pore water pressures are overestimated at deeper zones (pwp1, pwp2, pwp5), whereas they are underestimated at shallower zones (pwp3, pwp4, pwp6).
  - In terms of the acceleration response, still the agreement of acc2 is the best, yet it is comparably poorer in terms of high frequency content with respect to what is present in Figure 4.3. Almost for all acceleration responses model the response until 6 seconds in a reliable manner. However, after this instant the acceleration response at mid- to superficial depths are governed by the present level of excess pore water pressure, which is underestimated in Finn-Bryne model.
  - The model shows the "shielding-effect" of loosely-coupled models, as discussed in the report edited by Kavazanijian et al. (2016), that is the inability of transmit the ground motion to upper layers in a reliable manner once seismic waves pass through a layer under the effects of liquefaction.
- It should be emphasized that Finn-Byrne model is comparably simpler than PDMY02 model, thus it is rather normal to expect a less accurate numerical response. Yet, in most of the practical cases, the level of information on the sandy matrix is not nearly detailed as the current knowledge on Ticino sand and due to these reasons use of loosely-coupled models remain still practical in current day of practice.

This project has received funding from the European Union's Horizon 2020 research and innovation programme under grant agreement No. 700748

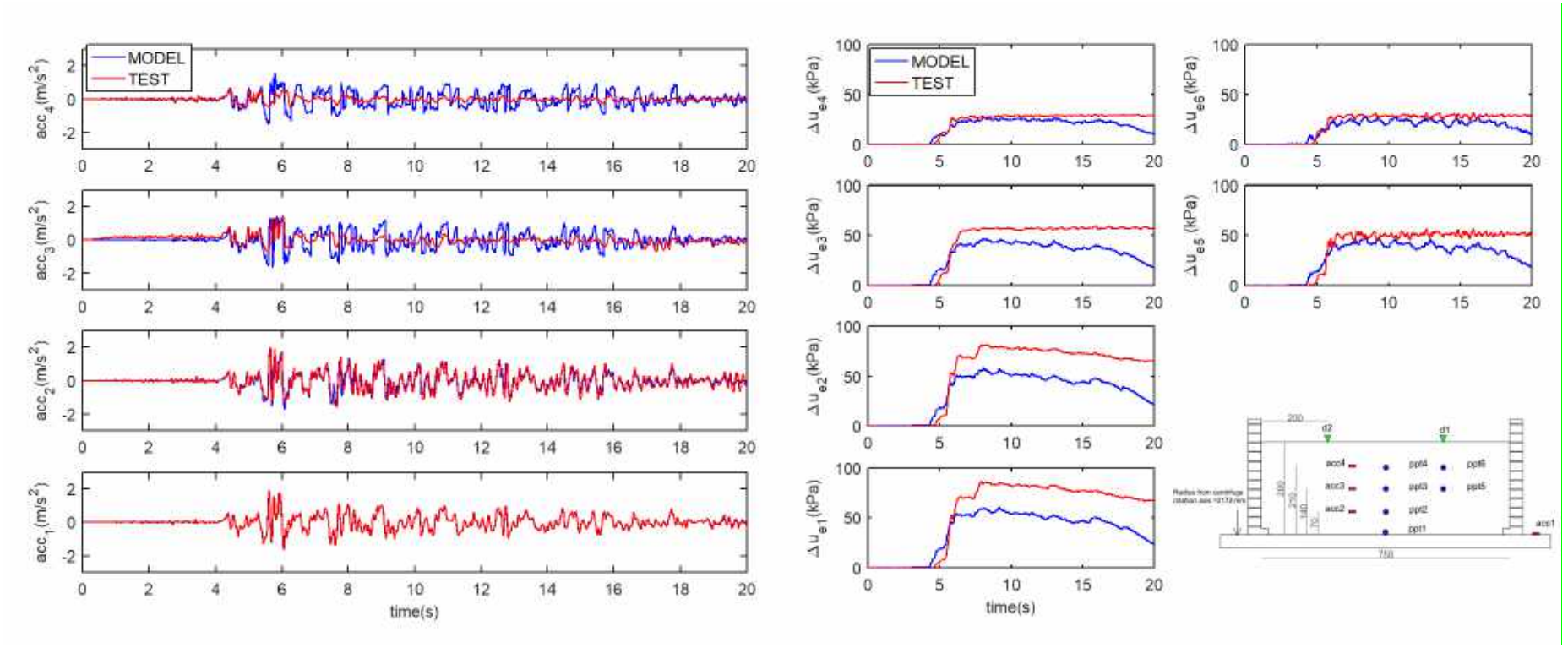

Figure 4.2. Comparison of modelled (blue) and recorded (red) responses in terms of acceleration and pore water pressure at various locations for homogeneous profile in free-field case (PDMY02 model, considering normal kH=1.4 x 10-3 m/s in the numerical domain). Left: Acceleration responses. Right: Pore water pressure response. Note: recorded and modelled acceleration responses (acc2-acc4) are lowpass filtered with a zero-phase 3rd order Butterworth filter with the corner frequency 49 Hz order 3.

This project has received funding from the European Union's Horizon 2020 research and innovation programme under grant agreement No. 700748

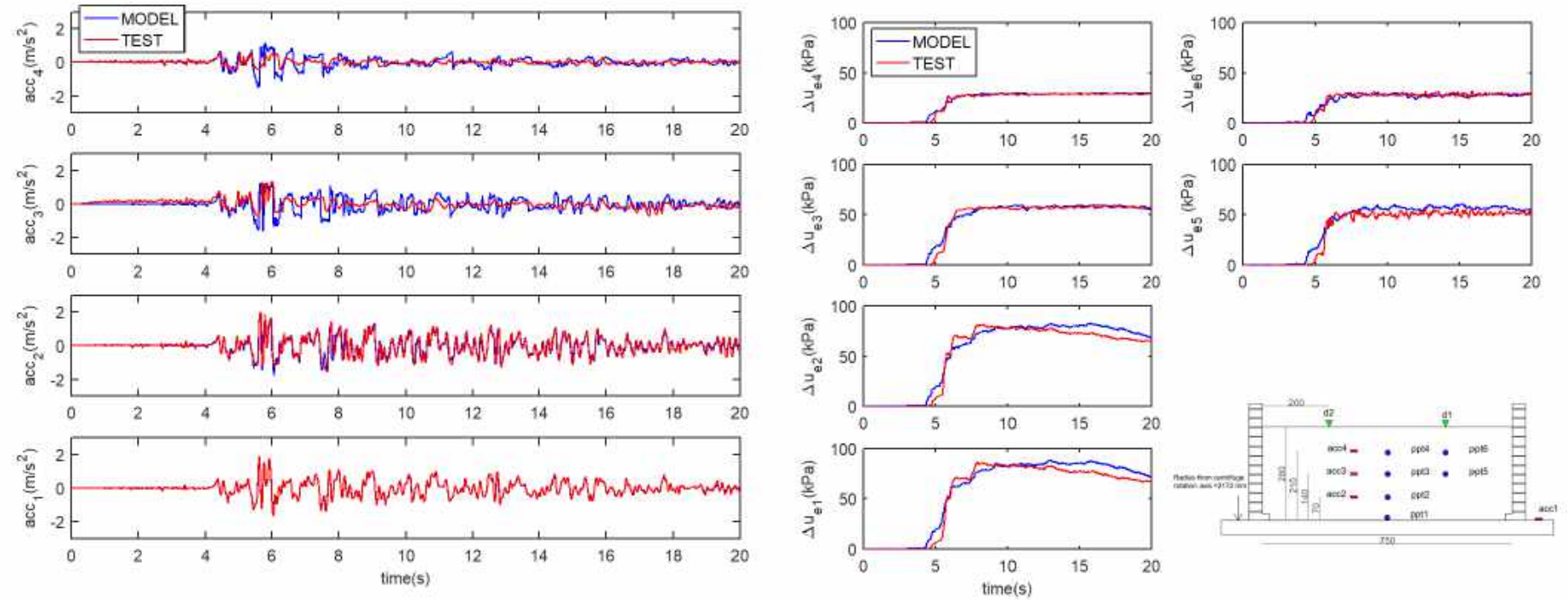

Figure 4.3. Comparison of modelled (blue) and recorded (red) responses in terms of acceleration and pore water pressure at various locations for homogeneous profile in free-field case (PDMY02 model, considering reduced kH=0.5 x 10-3 m/s in the numerical domain). Left: Acceleration responses. Right: Pore water pressure response. Note: recorded and modelled acceleration responses (acc2-acc4) are lowpass filtered with a zero-phase 3rd order Butterworth filter with the corner frequency 49 Hz.

This project has received funding from the European Union's Horizon 2020 research and innovation programme under grant agreement No. 700748

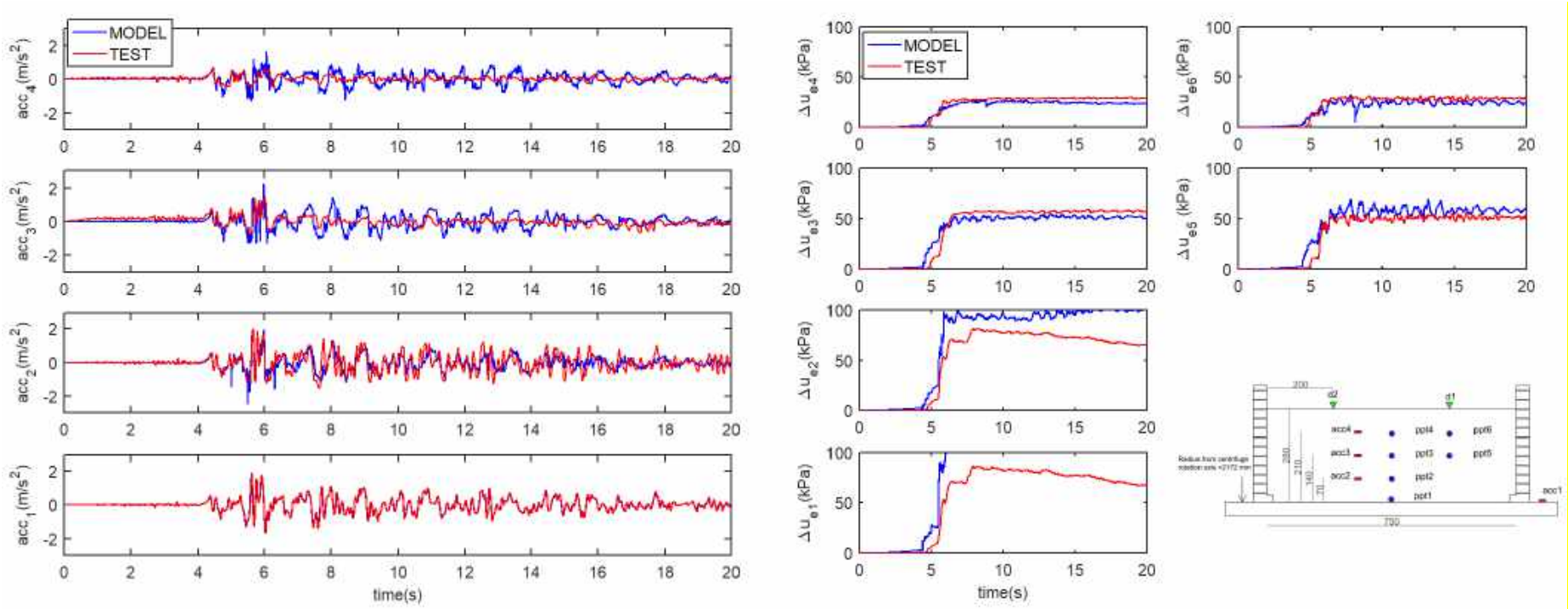

Figure 4.4. Comparison of modelled (blue) and recorded (red) responses in terms of acceleration and pore water pressure at various locations for homogeneous profile in free-field case (Finn-Byrne model, nearly undrained assumption). Left: Acceleration responses. Right: Pore water pressure response. Note: recorded and modelled acceleration responses (acc2-acc4) are lowpass filtered with a zero-phase 3rd order Butterworth filter with the corner frequency 49 Hz.

This project has received funding from the European Union's Horizon 2020 research and innovation programme under grant agreement No. 700748

4.2 SINGLE LAYER PROFILE WITH A SIMPLIFIED STRUCTURE ON TICINO SAND

4.2.1 UBCSAND

4.2.1.1 ID: SS_xx_TC_UBC_31

The model consists of a homogenous soil profile of Ticino sand with an upper structure model. The ground motion applied was the number 31.

ID: SS_xx_TC_UBC_31	TEST: M1F_S1_GM31

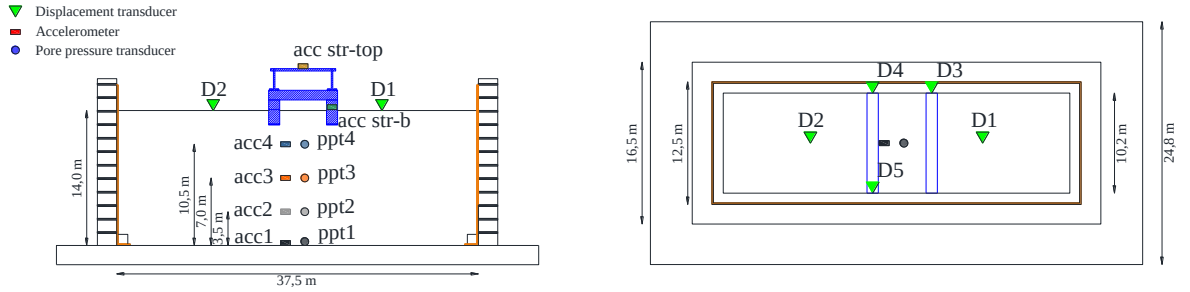

Layouts of the model reproduced in Plaxis 2D

The UBC3D-PML constitutive model is used to represent Ticino sand The properties adopted in the numerical analyses are summarized in following table.

Table with UBCSand parameters.

Parameter	Description	Value	Unit
$N_{1,60}$	SPT number	11	-
K_G^e	elastic shear modulus	966	-
K_B^e	elastic bulk modulus	751	-
K_G^p	plastic shear modulus	453	-
m_e	elastic stress dependency parameter	0.5	-
n_e	elastic stress dependency parameter	0.5	-
n_p	plastic stress dependency parameter	0.4	-
ϕ_{cv}	critical state friction angle	33	°
ϕ_{peak}	peak state friction angle	34.1	°
R_f	failure ratio	0.77	-
ν	Poisson coefficient	0.25	-

This project has received funding from the European Union's Horizon 2020 research and innovation programme under grant agreement No. 700748

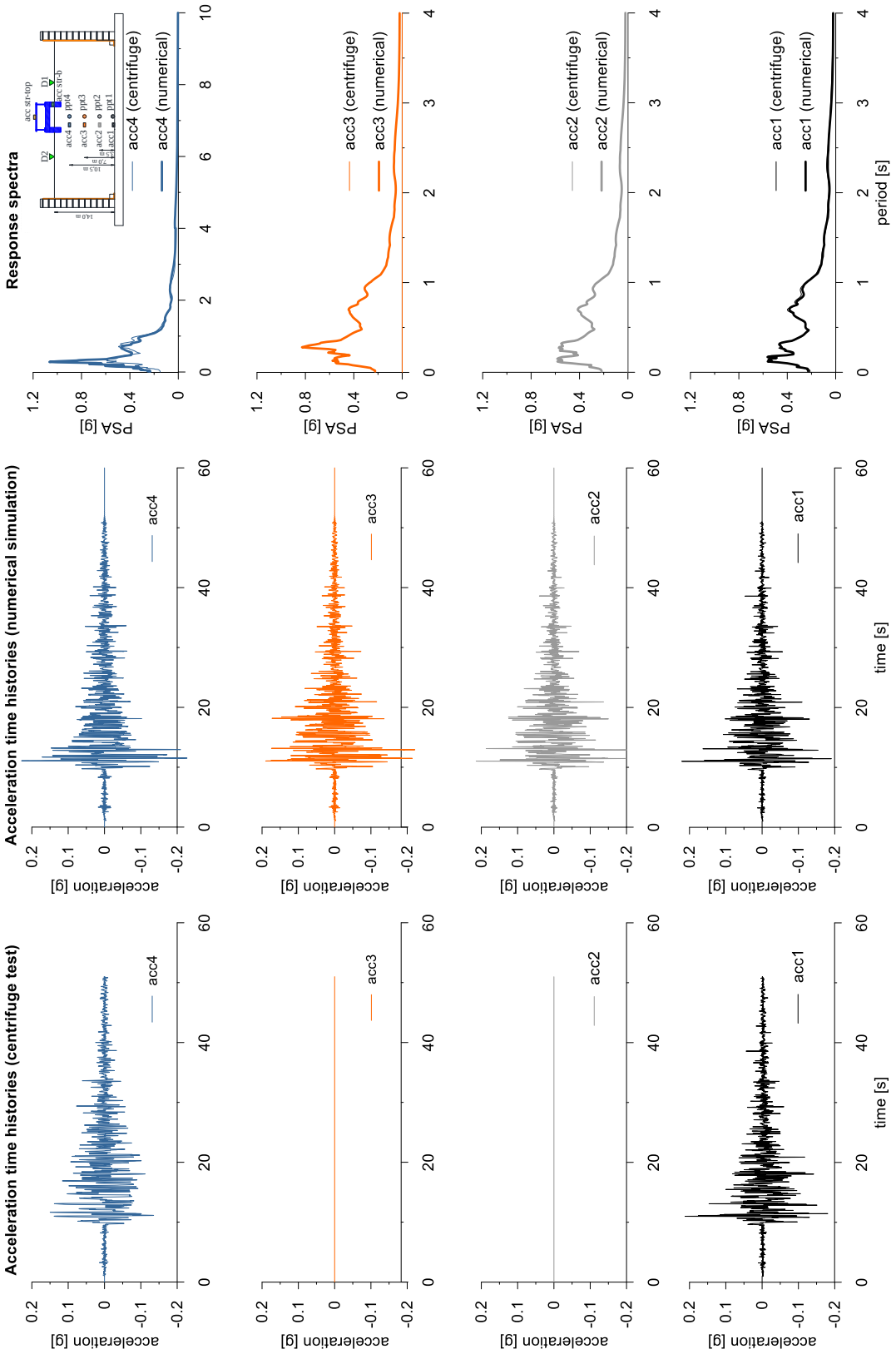

This project has received funding from the European Union's Horizon 2020 research and innovation programme under grant agreement No. 700748

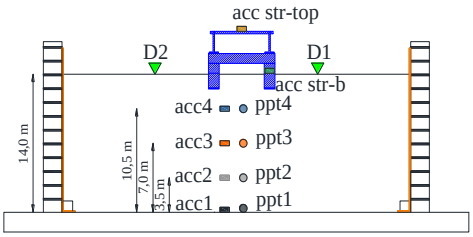

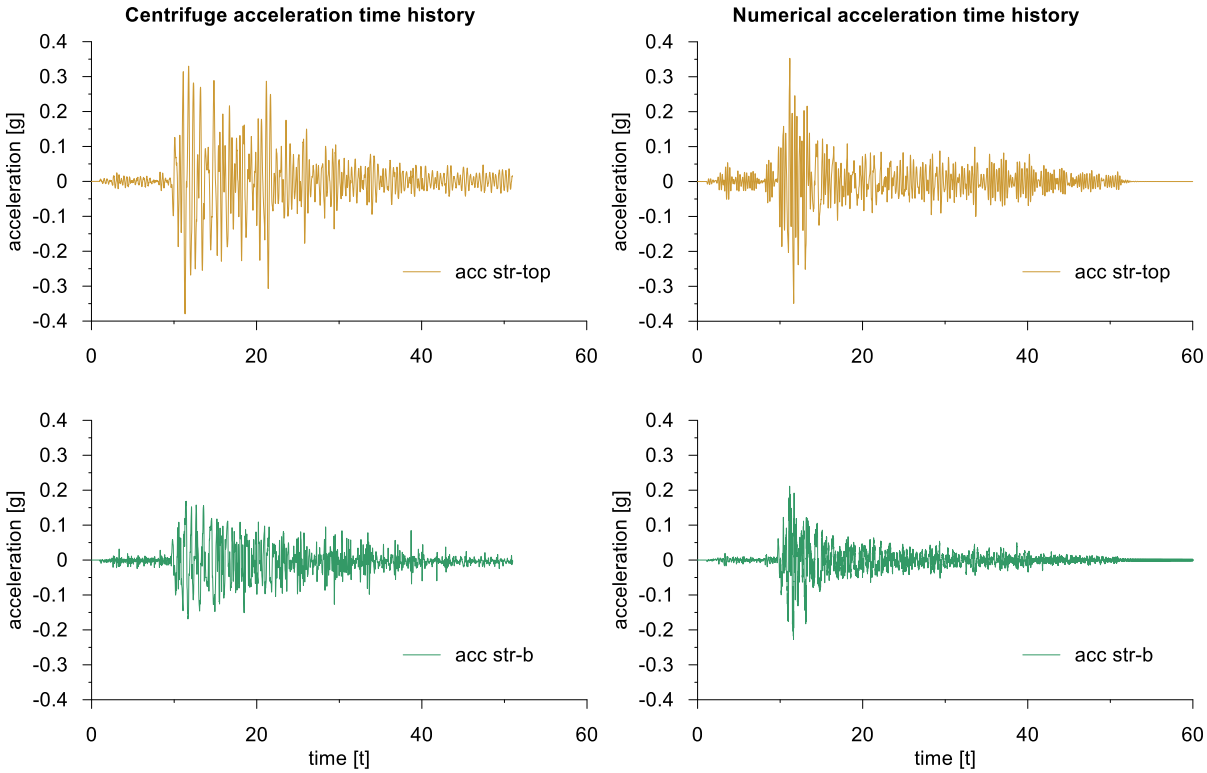

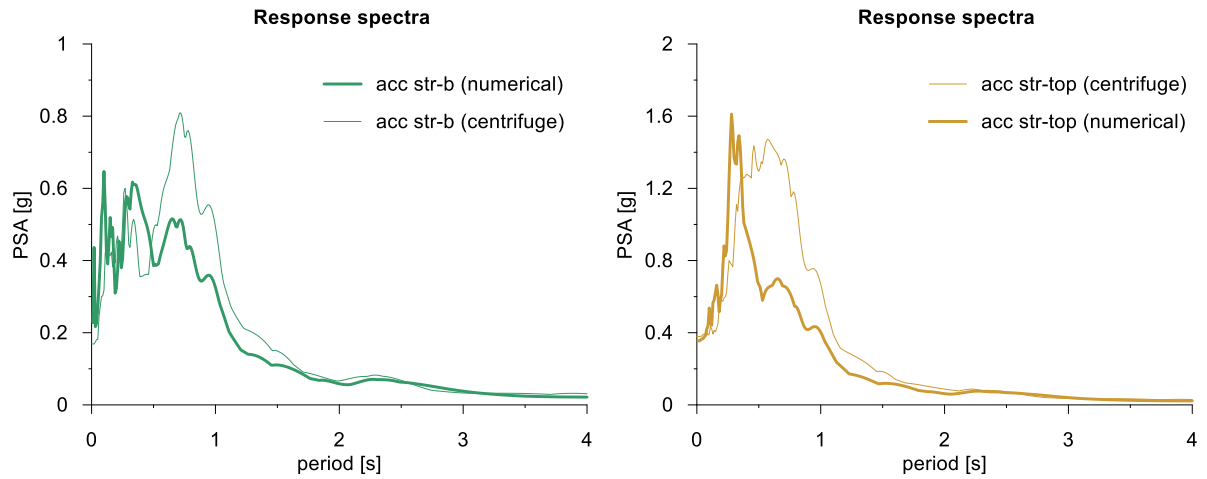

This project has received funding from the European Union's Horizon 2020 research and innovation programme under grant agreement No. 700748

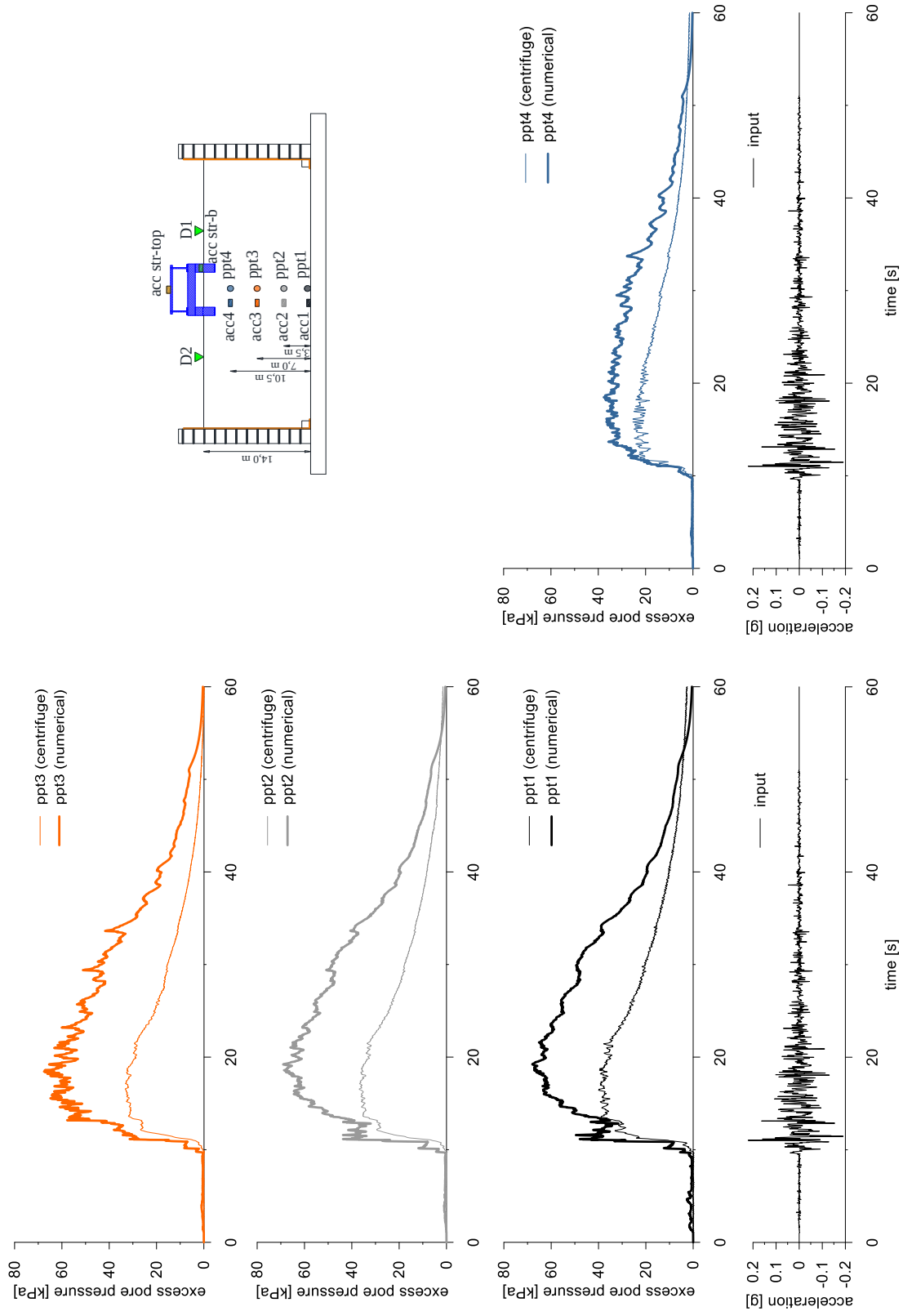

This project has received funding from the European Union's Horizon 2020 research and innovation programme under grant agreement No. 700748

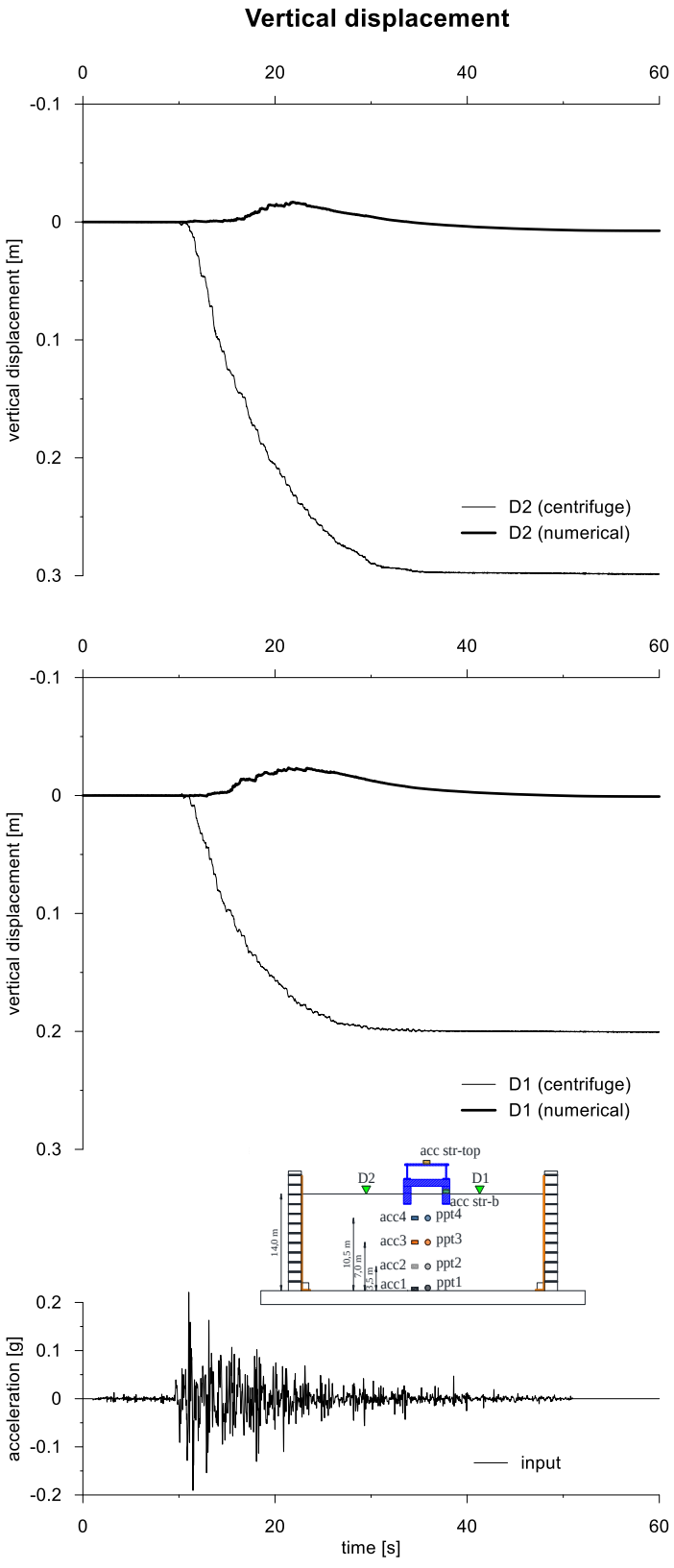

This project has received funding from the European Union's Horizon 2020 research and innovation programme under grant agreement No. 700748

Vertical displacement

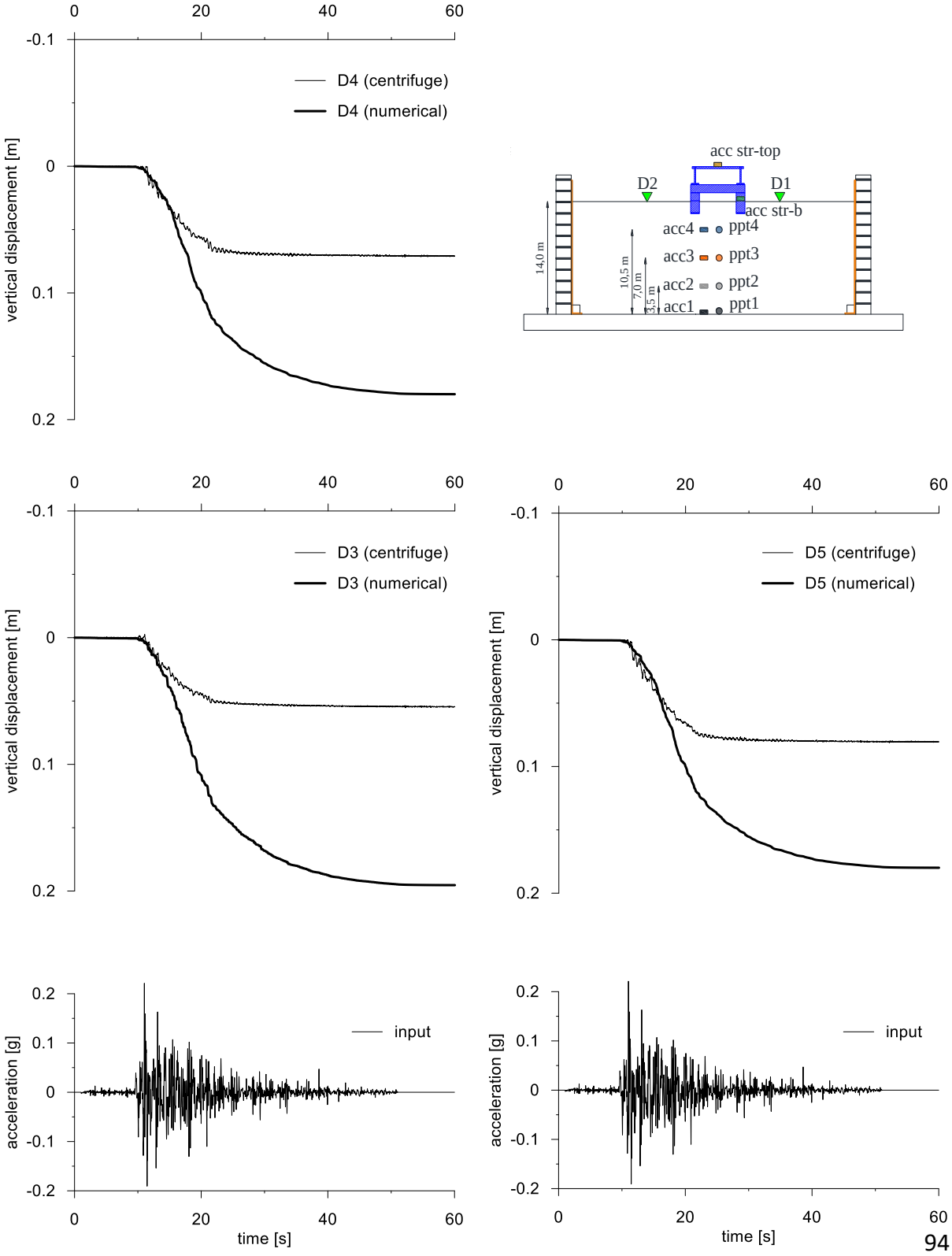

This project has received funding from the European Union's Horizon 2020 research and innovation programme under grant agreement No. 700748

4.2.1.2 ID: SS_xx_TC_UBC_31+

The model consists of a homogenous soil profile of Ticino sand with an upper structure model. The ground motion applied was the number 31+.

ID: SS_xx_TC_UBC_31+	TEST: M1F_S1_GM31+

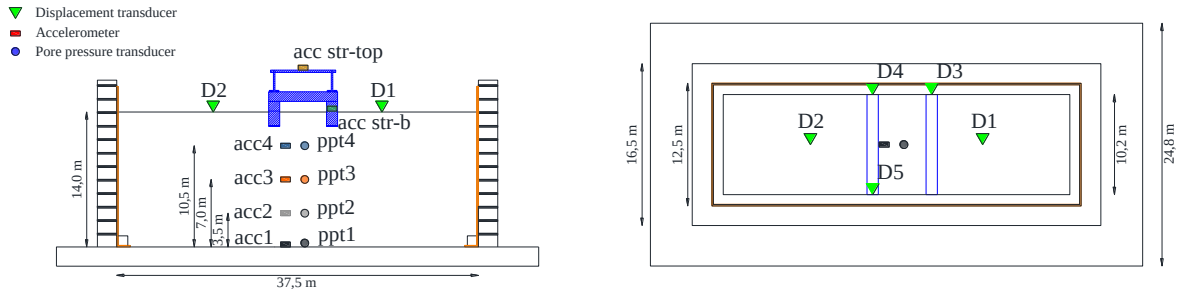

Layouts of the model reproduced in Plaxis 2D

The UBC3D-PML constitutive model is used to represent Ticino sand The properties adopted in the numerical analyses are summarized in following table.

Table with UBCSand parameters.

Parameter	Description	Value	Unit
$N_{1,60}$	SPT number	12.7	-
K_G^e	elastic shear modulus	1012	-
K_B^e	elastic bulk modulus	1687	-
K_G^p	plastic shear modulus	592	-
m_e	elastic stress dependency parameter	0.5	-
n_e	elastic stress dependency parameter	0.5	-
n_p	plastic stress dependency parameter	0.4	-
ϕ_{cv}	critical state friction angle	33	°
ϕ_{peak}	peak state friction angle	34.3	°
R_f	failure ratio	0.75	-
ν	Poisson coefficient	0.25	-

This project has received funding from the European Union's Horizon 2020 research and innovation programme under grant agreement No. 700748

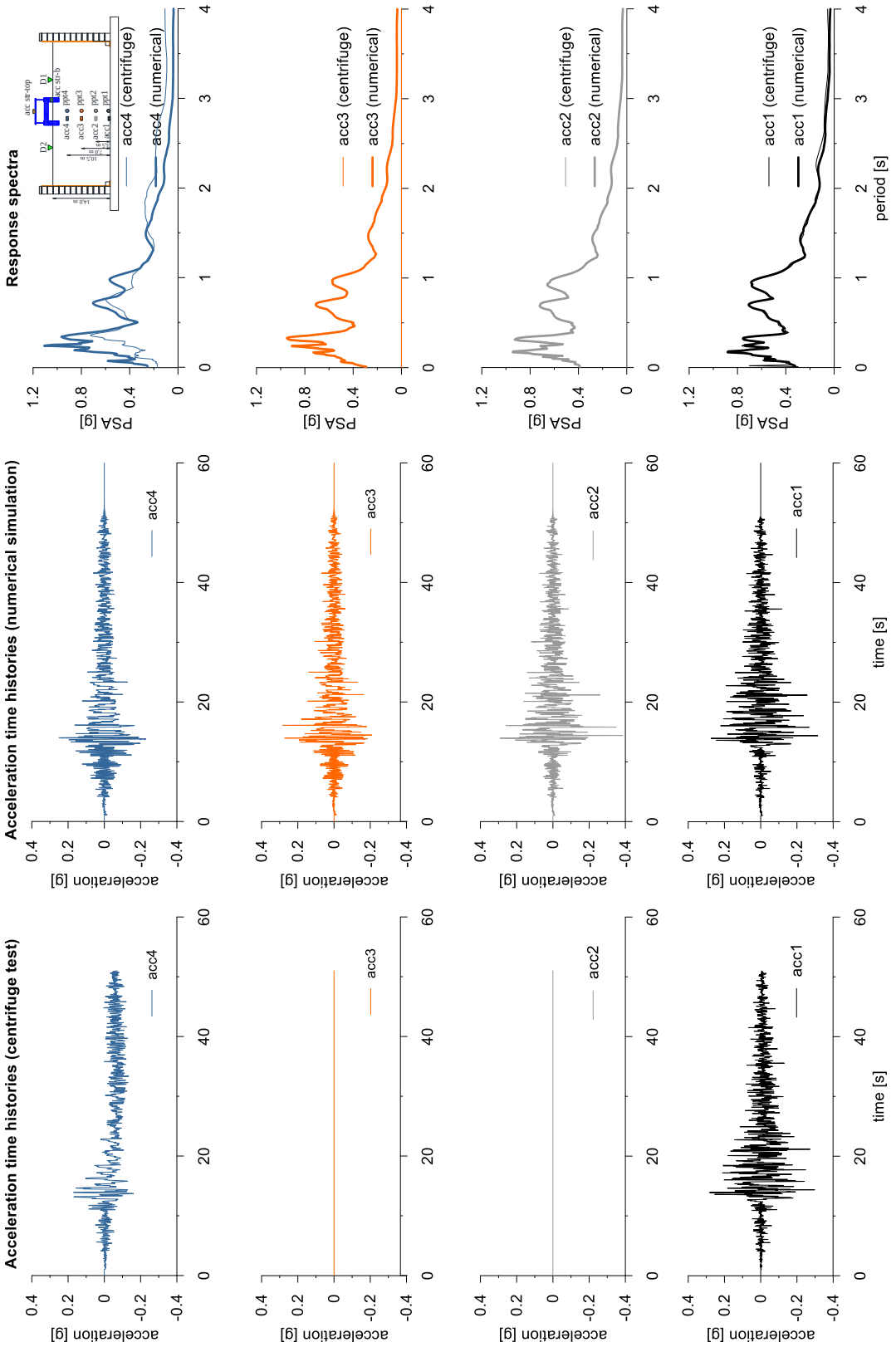

This project has received funding from the European Union's Horizon 2020 research and innovation programme under grant agreement No. 700748

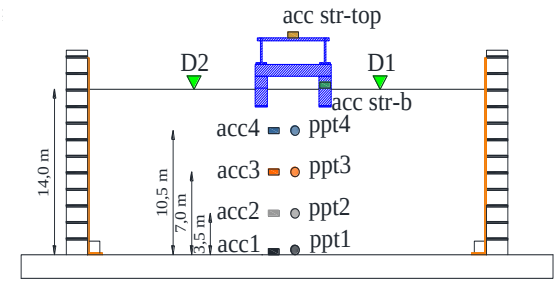

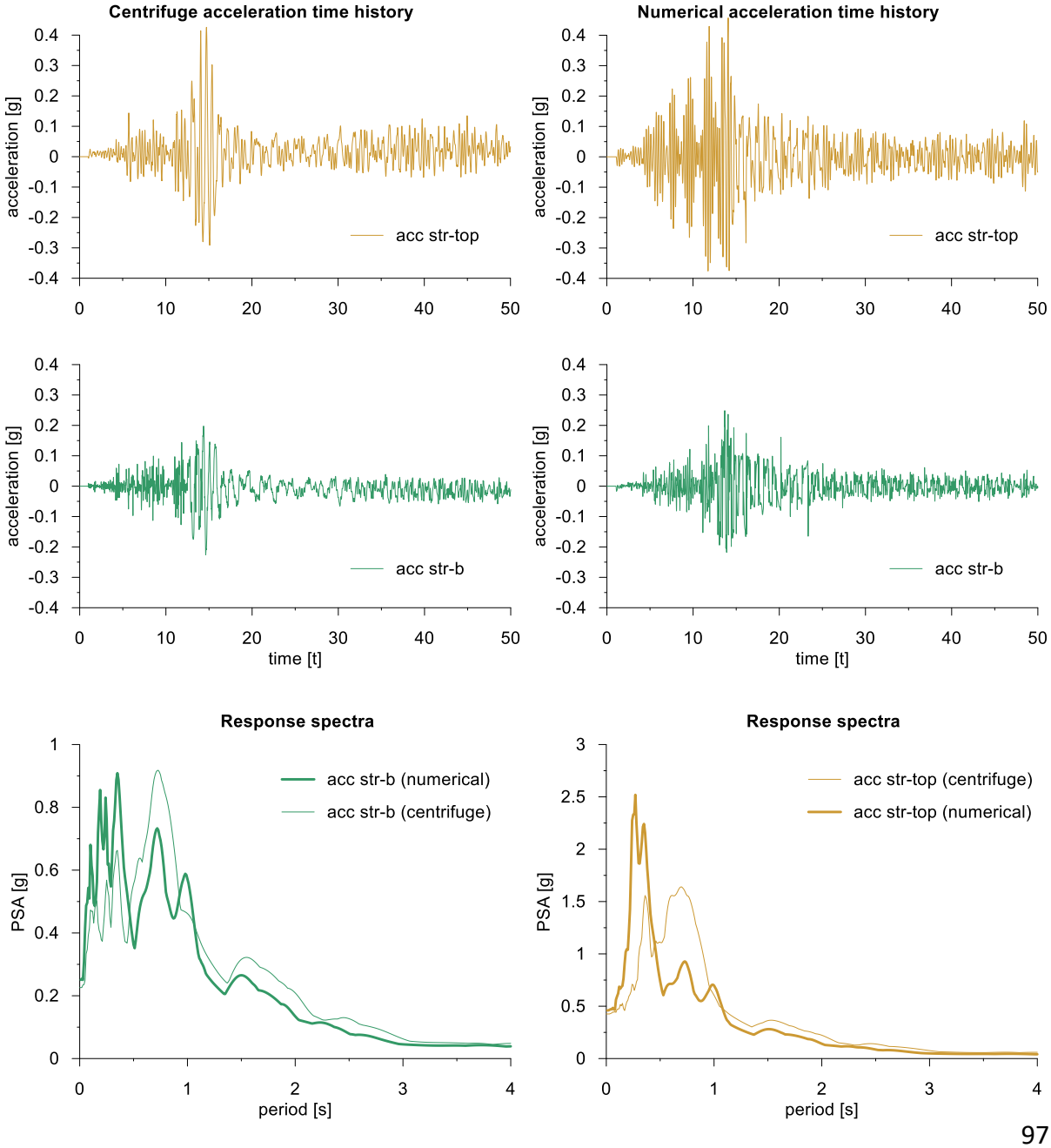

This project has received funding from the European Union's Horizon 2020 research and innovation programme under grant agreement No. 700748

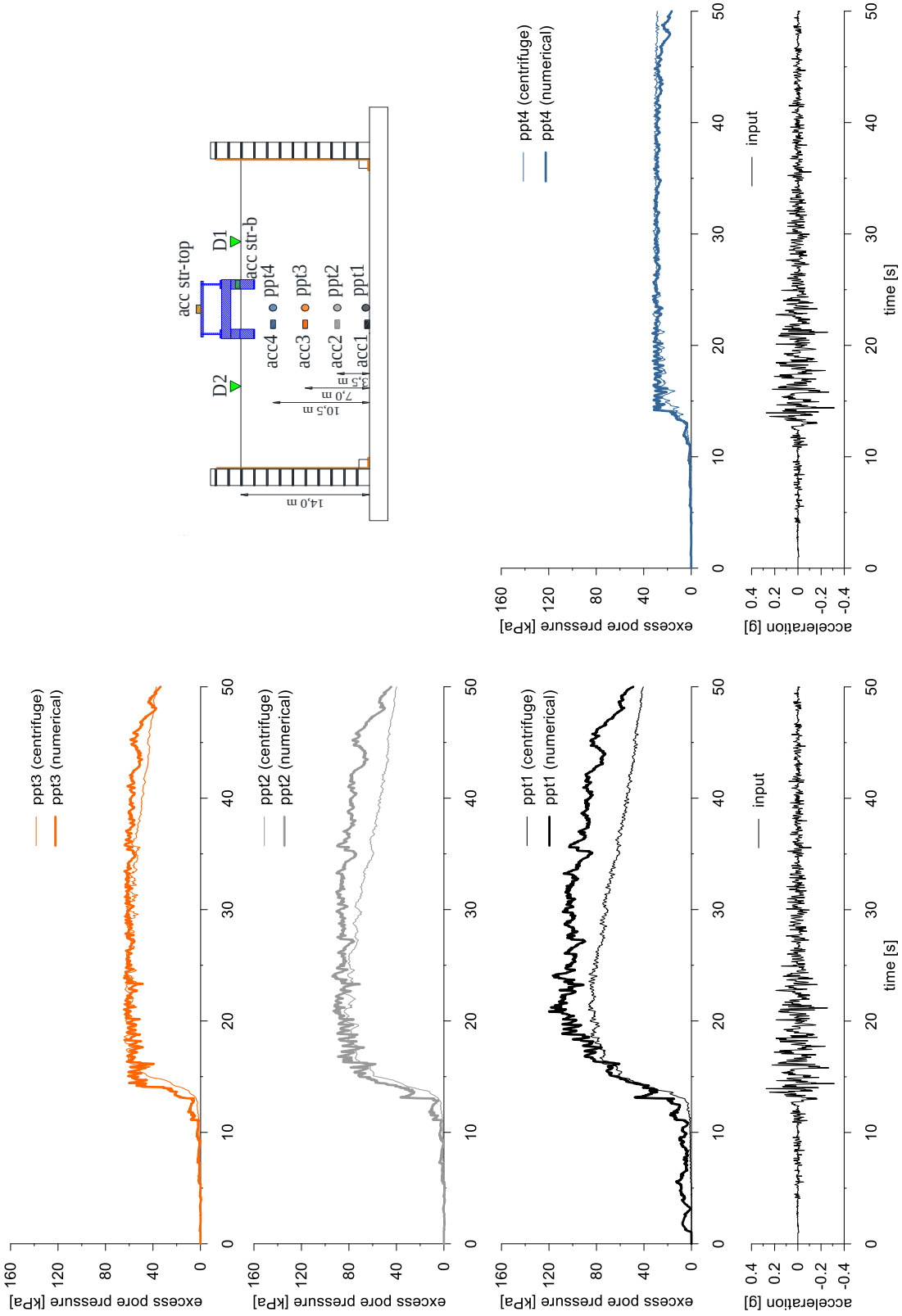

This project has received funding from the European Union's Horizon 2020 research and innovation programme under grant agreement No. 700748

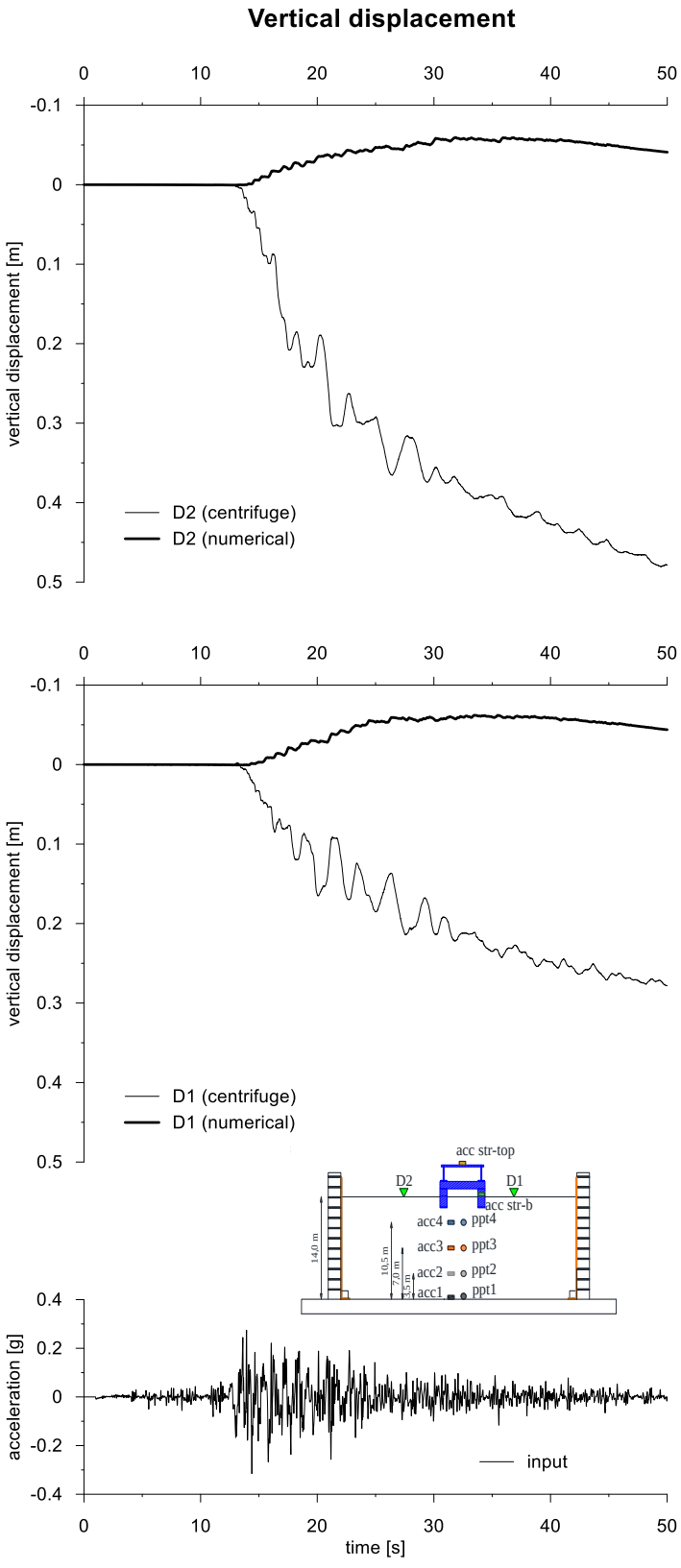

This project has received funding from the European Union's Horizon 2020 research and innovation programme under grant agreement No. 700748

Vertical displacement

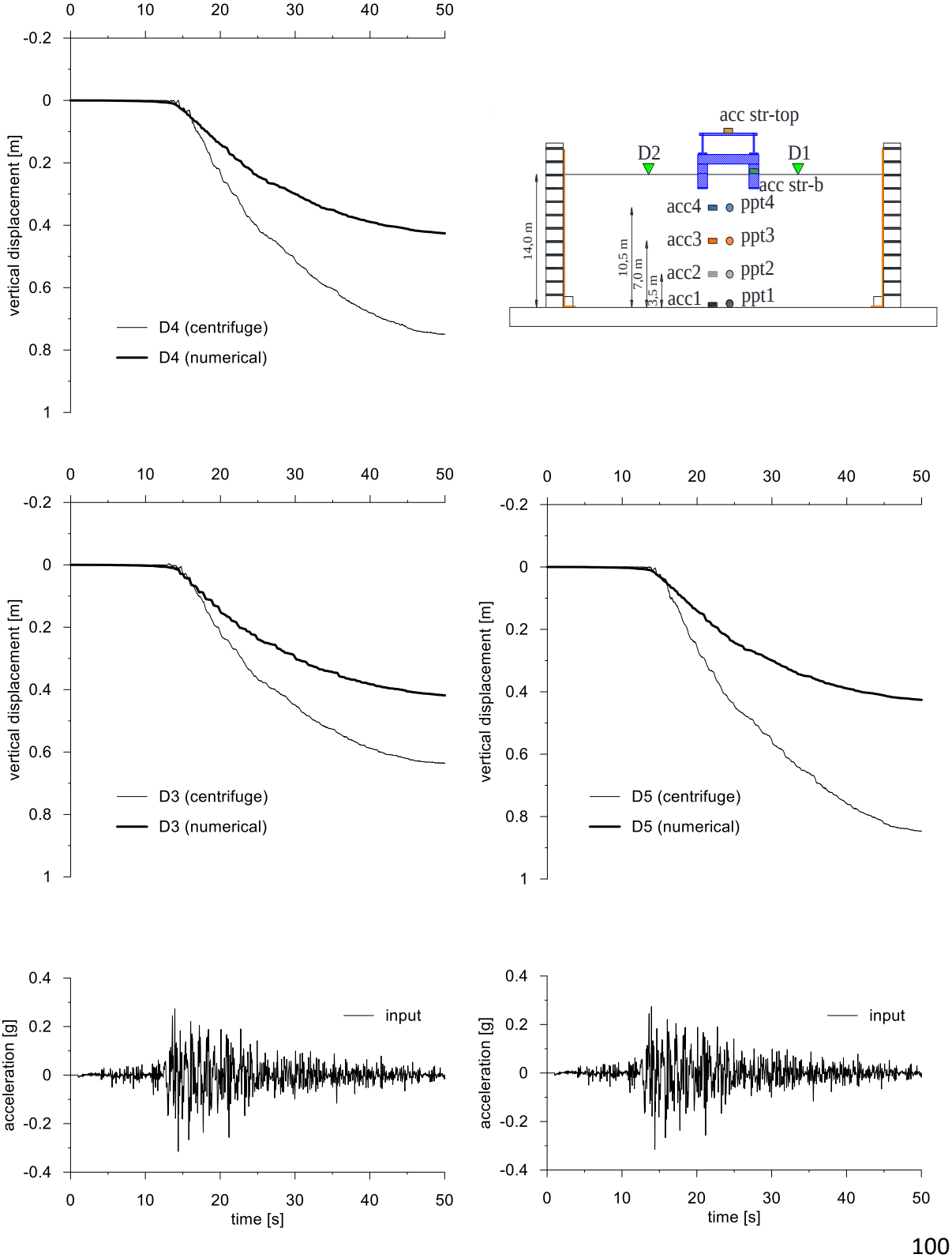

This project has received funding from the European Union's Horizon 2020 research and innovation programme under grant agreement No. 700748

4.2.2 PM4SAND

4.2.2.1 ID: SS_xx_TC_PM4_31

The model consists of a homogenous soil profile of Ticino sand with an upper structure model. The ground motion applied was the number 31.

ID: SS_xx_TC_PM4_31	TEST: M1F_S1_GM31

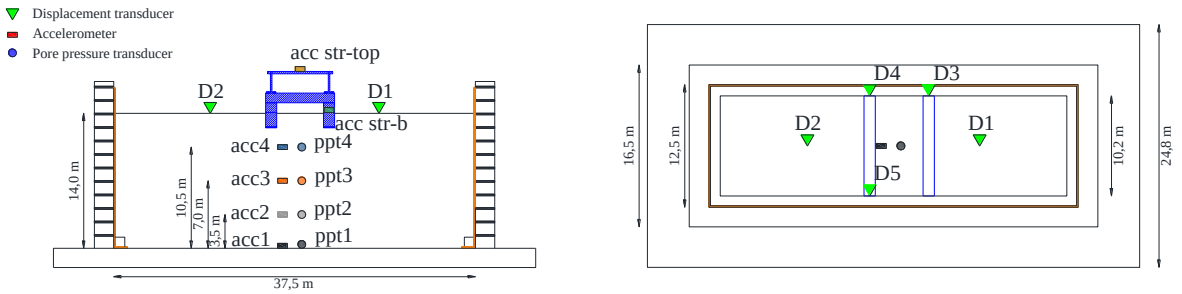

Layouts of the model reproduced in Plaxis 2D

The PM4SAND constitutive model is used to represent Ticino sand The properties adopted in the numerical analyses are summarized in following table.

Table with PM4sand parameters

Parameter	Description	Value	Unit
D_{R0}	Initial relative density	0.45	-
G_0	shear modulus coefficient	374	-
hp_0	contraction rate parameter	0.1	-
p_A	atmospheric pressure	101.3	kN/m^2
e_{max}	maximum void ratio	0.923	-
e_{min}	minimum void ratio	0.574	-
n_b	bounding surface parameter	0.5	-
n_d	dilatancy surface parameter	0.1	-
ϕ_{cv}	critical state friction angle	33	°
nu	Poisson's ratio	0.3	-
Q	critical state line parameter	8	-
R	critical state line parameter	1.2	-

This project has received funding from the European Union's Horizon 2020 research and innovation programme under grant agreement No. 700748

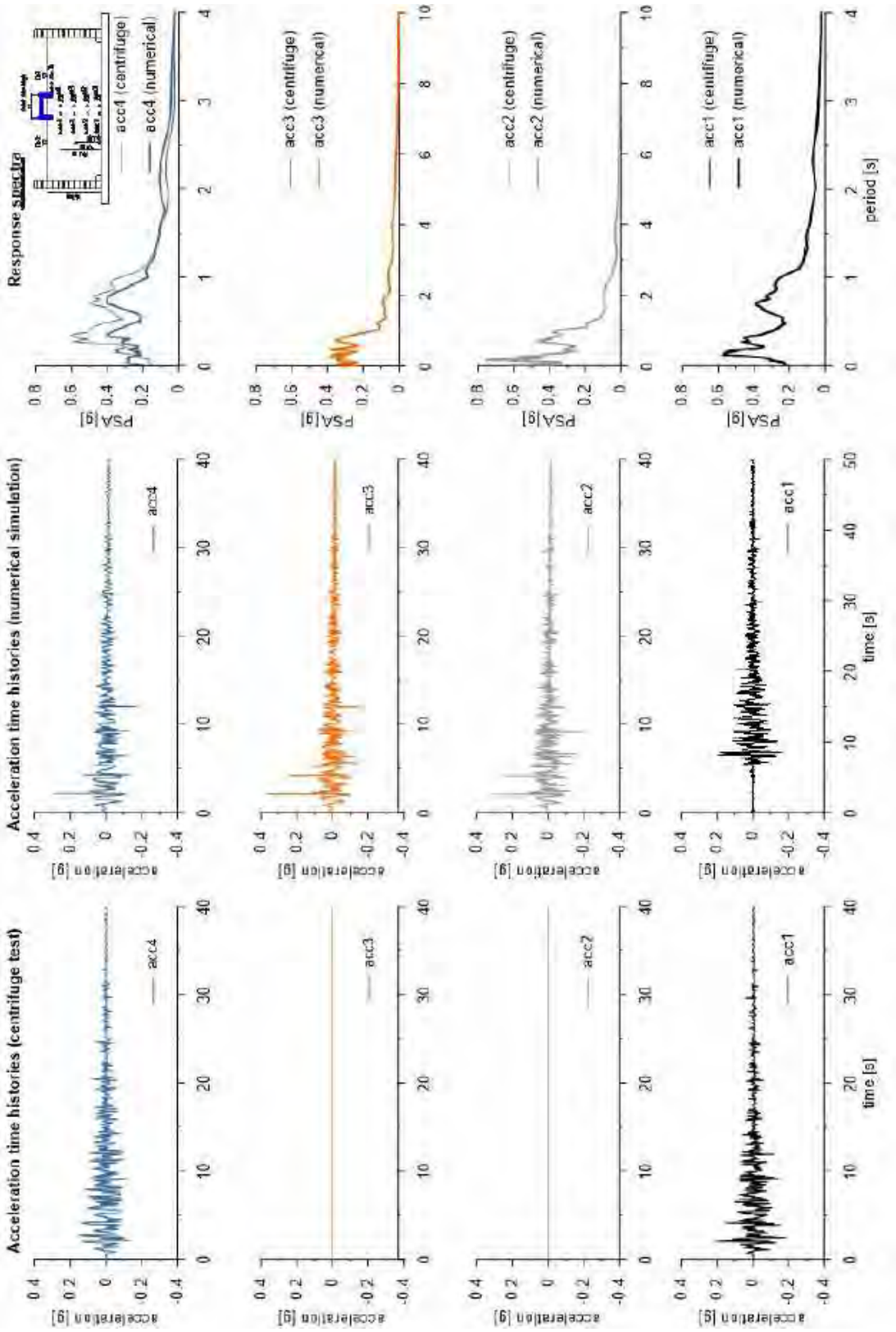

This project has received funding from the European Union's Horizon 2020 research and innovation programme under grant agreement No. 700748

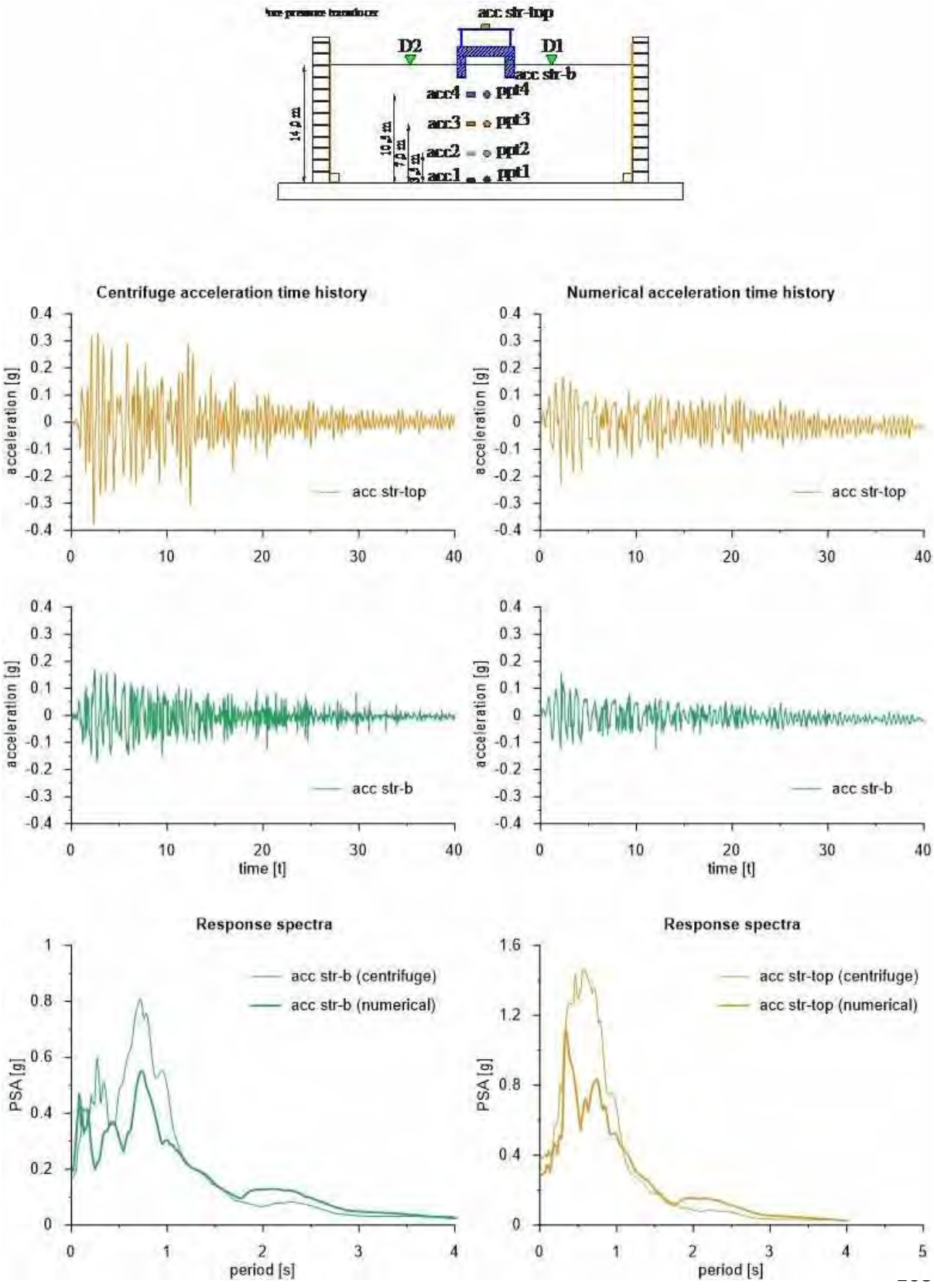

This project has received funding from the European Union's Horizon 2020 research and innovation programme under grant agreement No. 700748

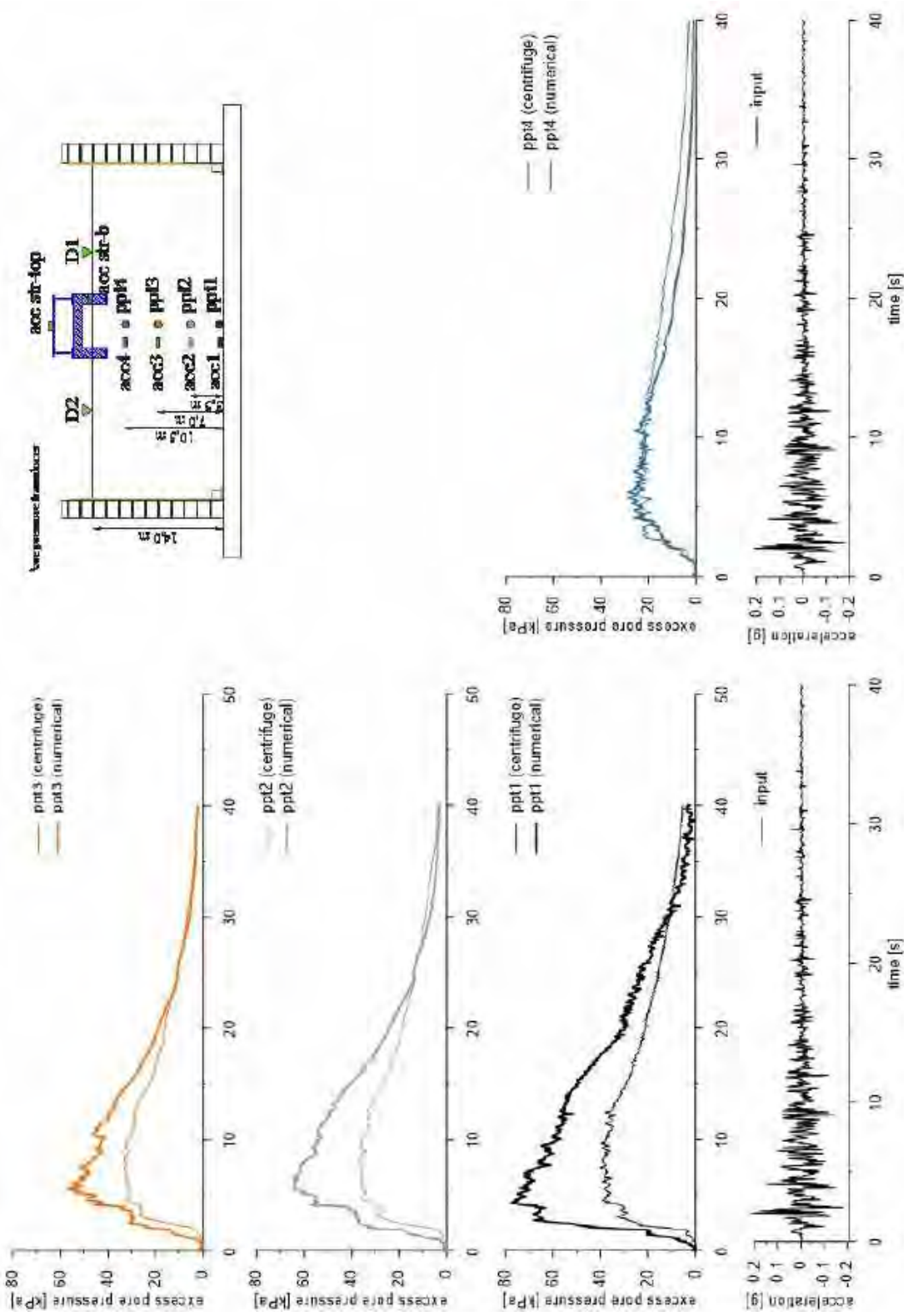

This project has received funding from the European Union's Horizon 2020 research and innovation programme under grant agreement No. 700748

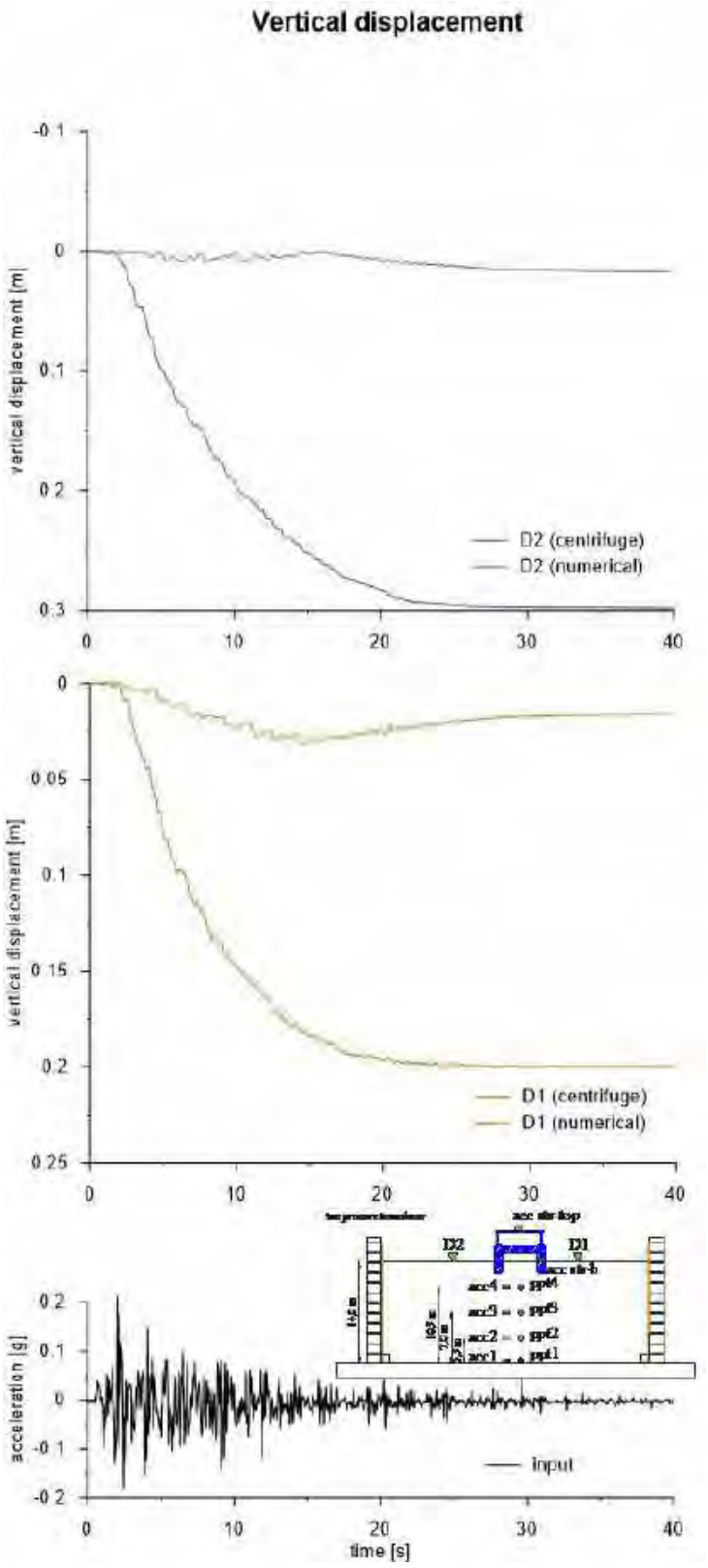

This project has received funding from the European Union's Horizon 2020 research and innovation programme under grant agreement No. 700748

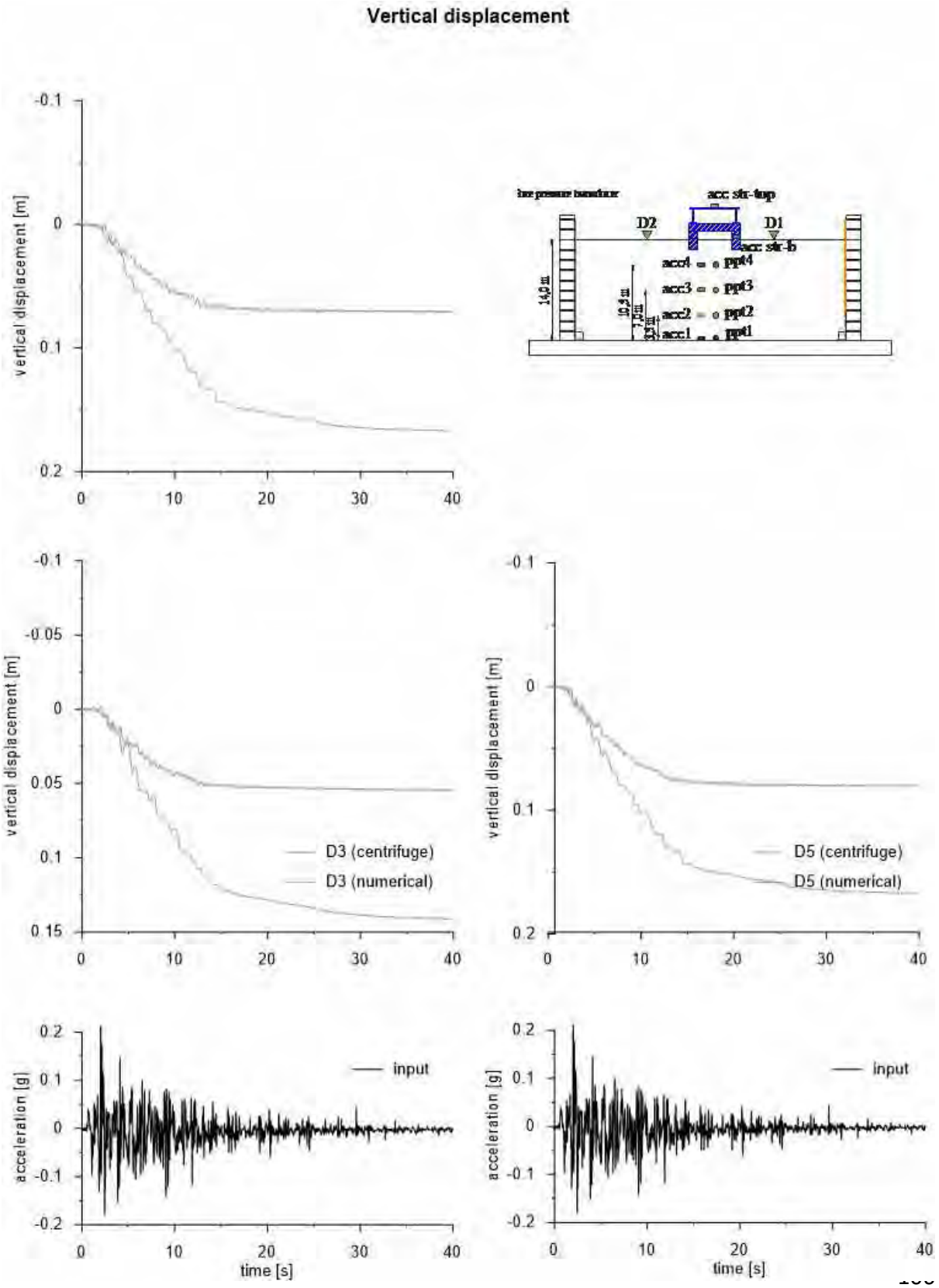

This project has received funding from the European Union's Horizon 2020 research and innovation programme under grant agreement No. 700748

4.2.2.2 ID: SS_xx_TC_PM4_31+

The model consists of a homogenous soil profile of Ticino sand with an upper structure model. The ground motion applied was the number 31+.

ID: SS_xx_TC_PM4_31+	TEST: M1F_S1_GM31+

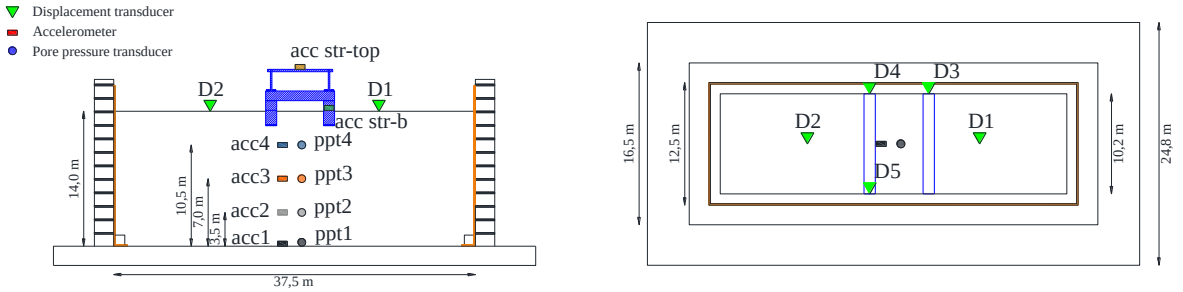

Layouts of the model reproduced in Plaxis 2D

The PM4SAND constitutive model is used to represent Ticino sand The properties adopted in the numerical analyses are summarized in Table 1.

Table with PM4sand parameters

Parameter	Description	Value	Unit
D_{R0}	Initial relative density	0.48	-
G_0	shear modulus coefficient	594	-
hp_0	contraction rate parameter	0.1	-
p_A	atmospheric pressure	101.3	kN/m^2
e_{max}	maximum void ratio	0.923	-
e_{min}	minimum void ratio	0.574	-
n_b	bounding surface parameter	0.5	-
n_d	dilatancy surface parameter	0.1	-
ϕ_{cv}	critical state friction angle	33	°
nu	Poisson's ratio	0.3	-
Q	critical state line parameter	8	-
R	critical state line parameter	1.2	-

This project has received funding from the European Union's Horizon 2020 research and innovation programme under grant agreement No. 700748

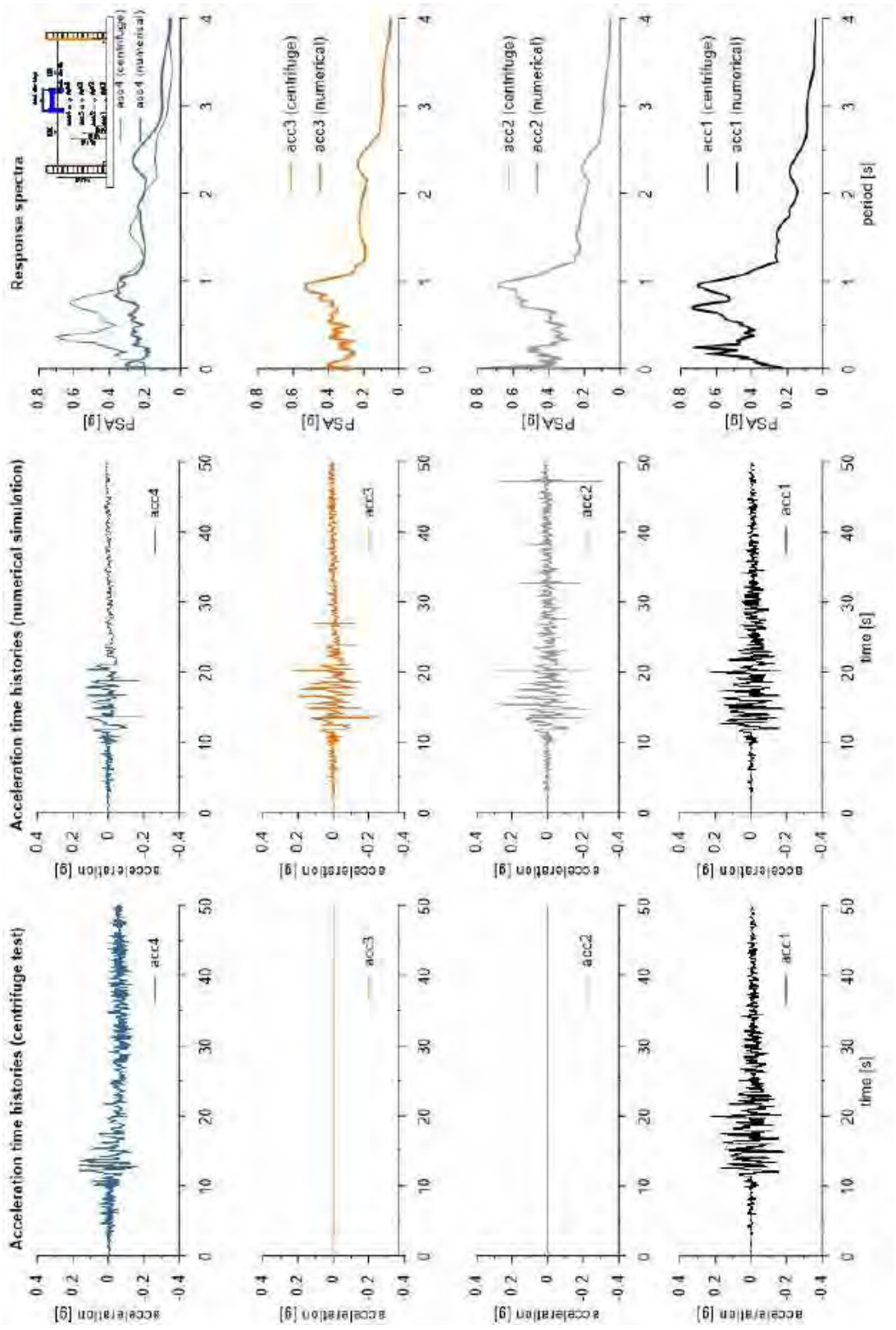

This project has received funding from the European Union's Horizon 2020 research and innovation programme under grant agreement No. 700748

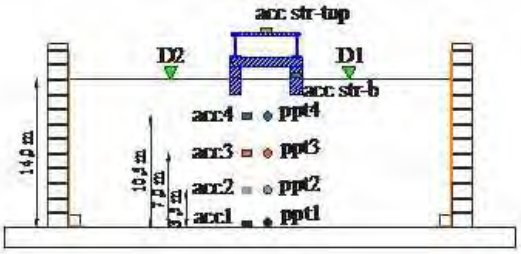

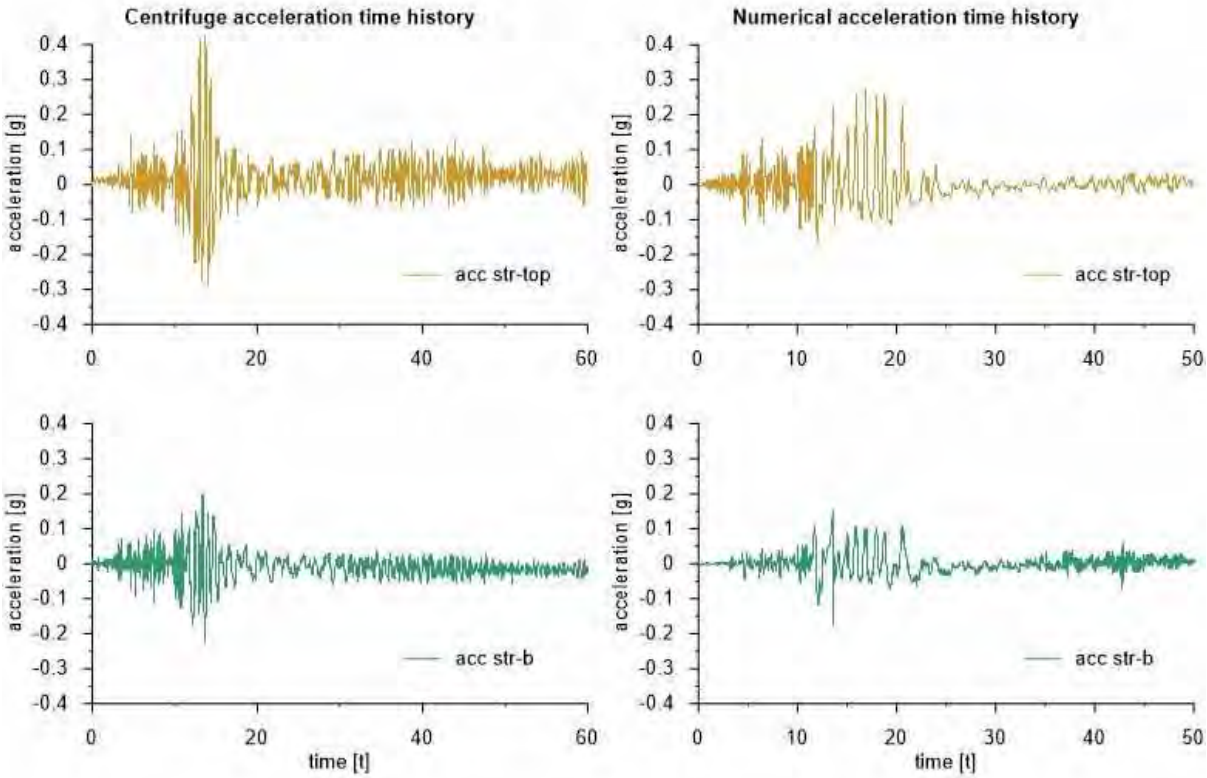

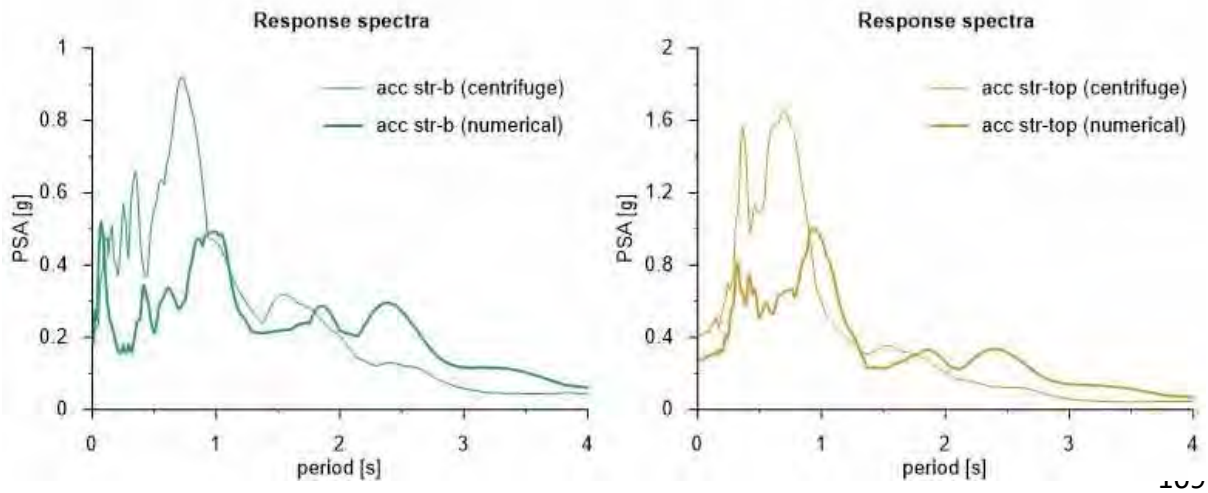

This project has received funding from the European Union's Horizon 2020 research and innovation programme under grant agreement No. 700748

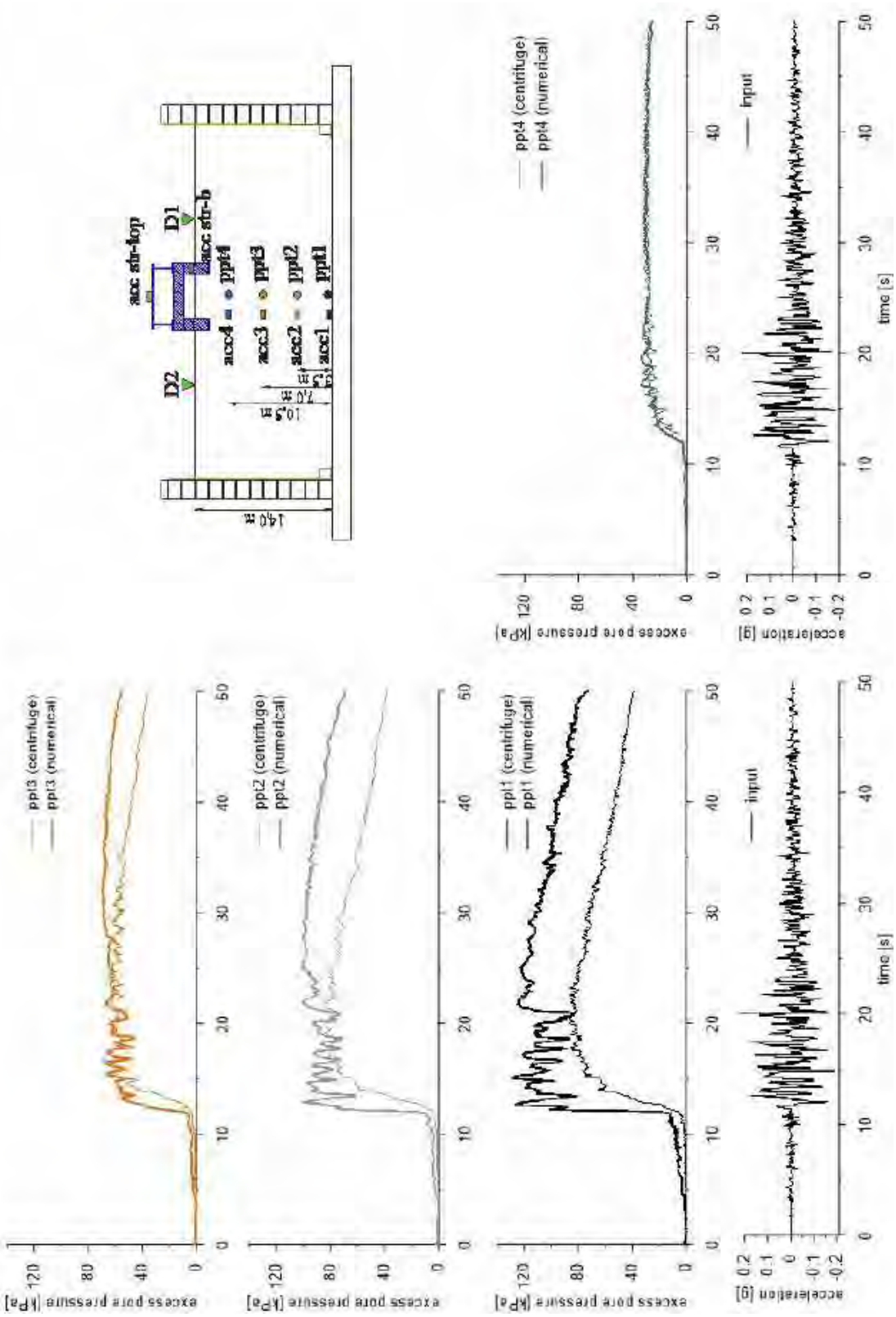

This project has received funding from the European Union's Horizon 2020 research and innovation programme under grant agreement No. 700748

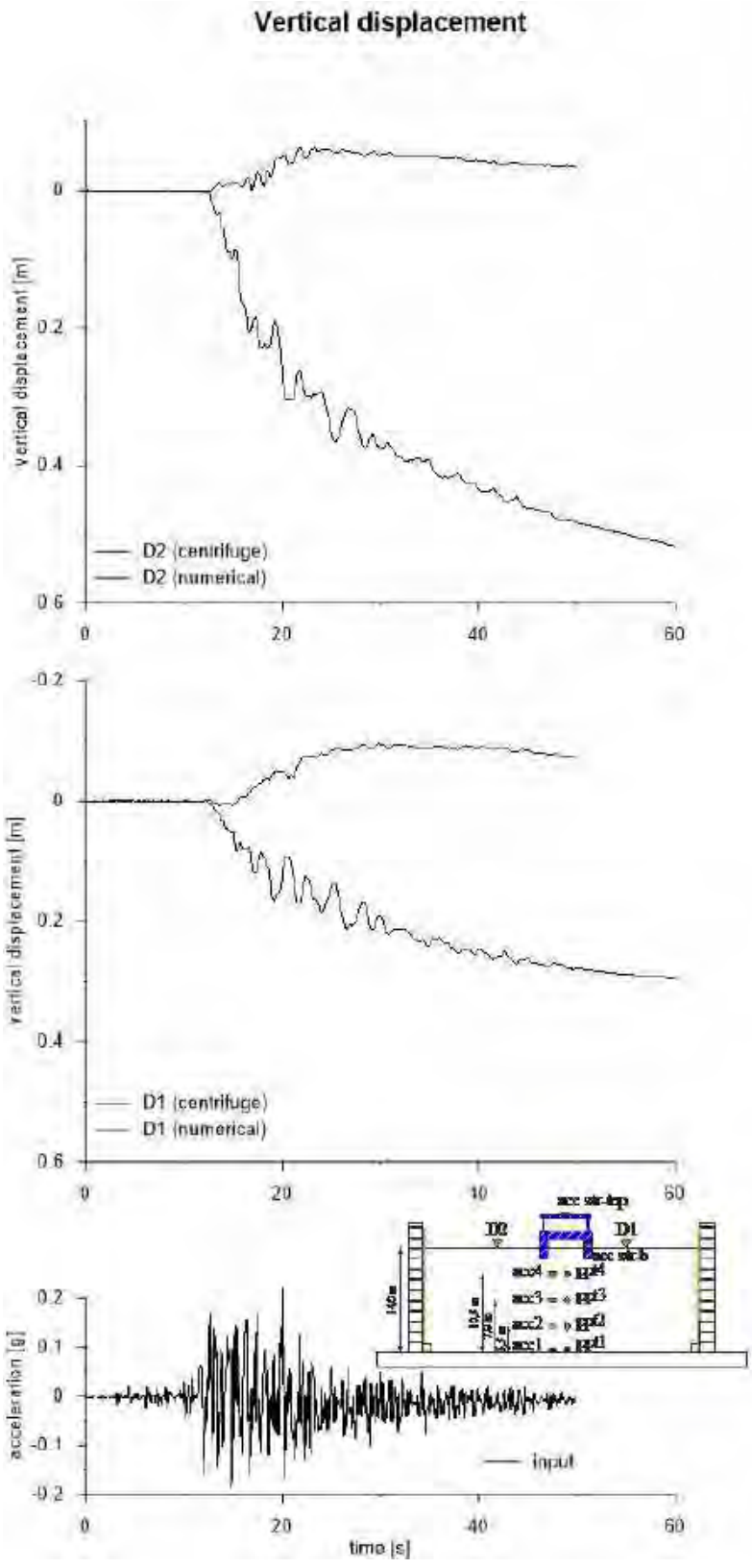

This project has received funding from the European Union's Horizon 2020 research and innovation programme under grant agreement No. 700748

Vertical displacement

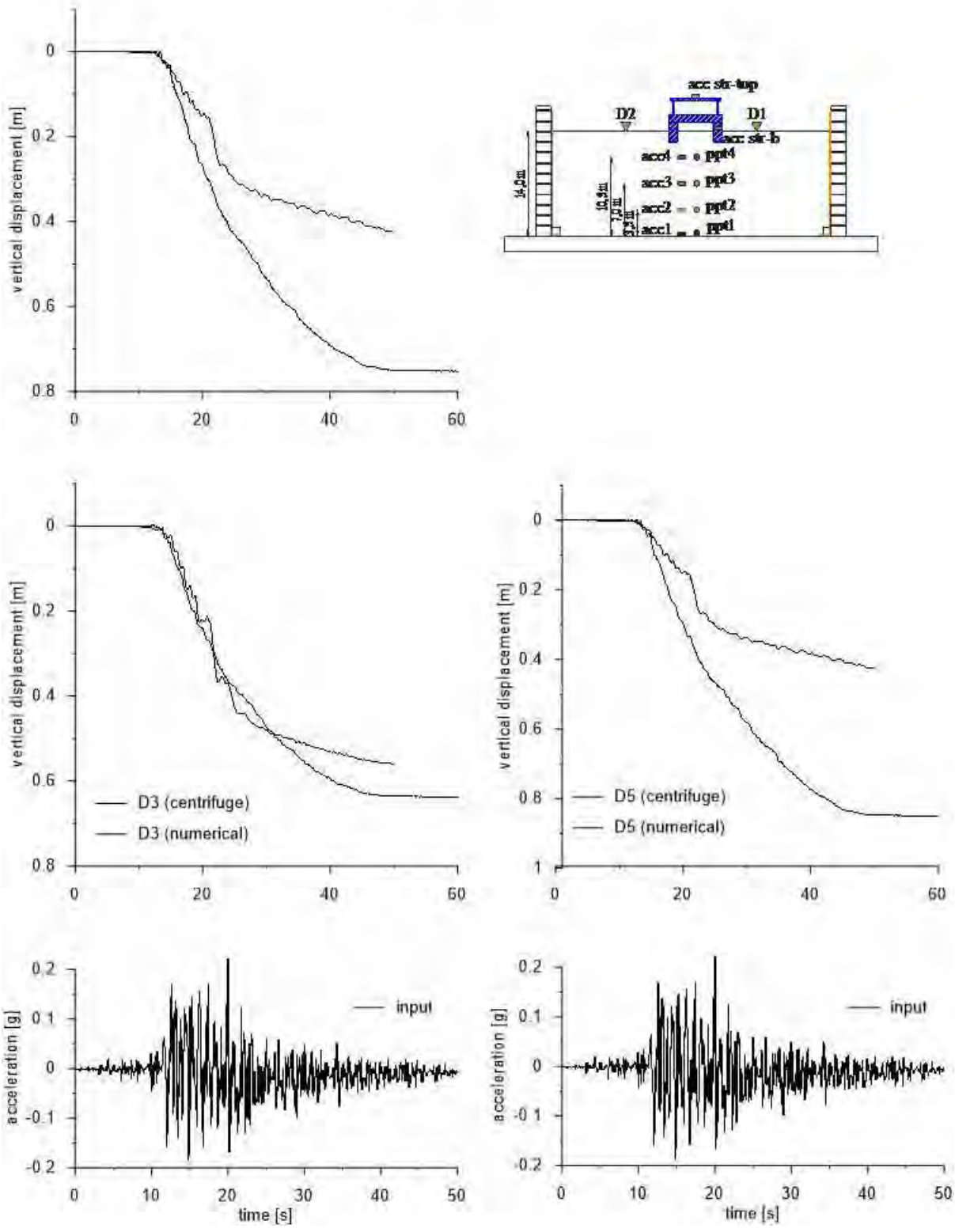

This project has received funding from the European Union's Horizon 2020 research and innovation programme under grant agreement No. 700748

4.2.3 PDMY02

4.2.3.1 ID: SS_xx_TC_PDM_31

The model presented in Deliverable D4.2 (M1F_S1_GM31) is modelled under plane strain assumptions in OpenSees (PDMY02 model). OpenSees model shares the same assumptions with 3.2, apart from the fact that k_H = 1.4 x 10-3 m/s is adopted with K_w=2.2 x 10^6 kPa. Foundation of the structural element is constructed through impermeable continuum elements on which the steel frame is mounted by using beam-column elements as shown in Figure 4.5.

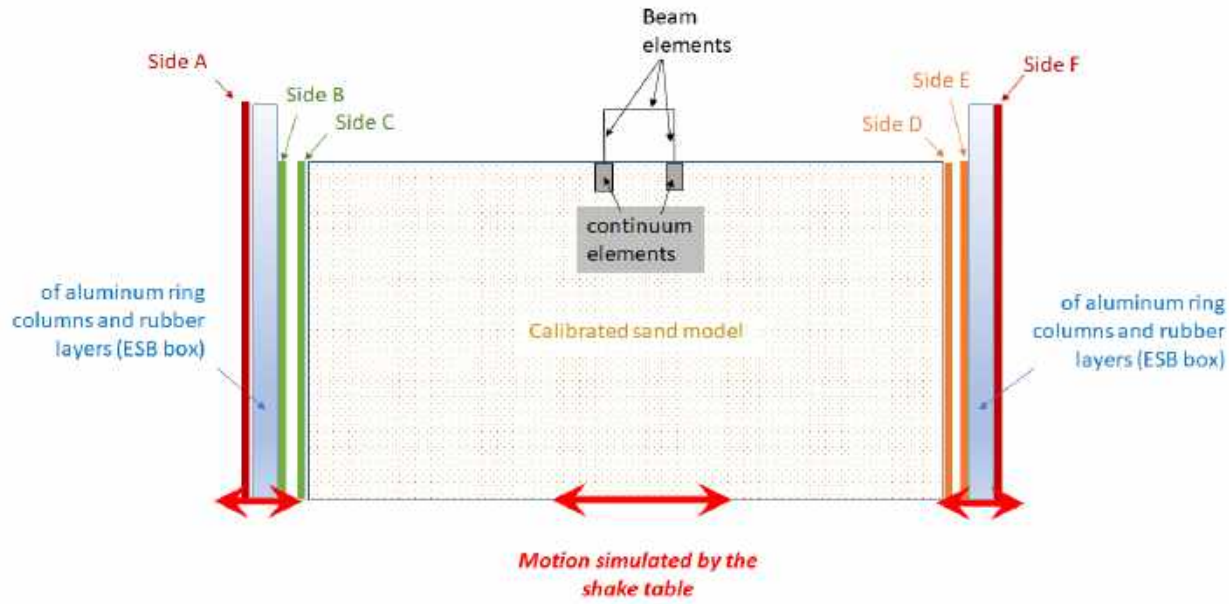

Figure 4.5. As Figure 3.7 but with structural zones and elements.

In Figure 4.6, comparison of observed and simulated responses is provided and the following conclusions could be made:

- Pore water pressure responses (generation and dissipation) are captured with a reliable agreement at all measurement locations. It is noted slightly faster rate of dissipation and faster rate of initial generation, yet those points do not seem very relevant to change significantly the overall response of the system.
- Acceleration responses of the model also agree reliably with the observed responses for both soil and structural zones, implying the fact that apart from the dynamic response of sand zones, inertial and kinematic soil structure interaction response is captured in an acceptable manner.

This project has received funding from the European Union's Horizon 2020 research and innovation programme under grant agreement No. 700748

- The comparison between the modelled and observed foundation settlements do show moderately good agreement for one support (~3.5 cm vs 5 cm) and poor agreement for the other support (~3.5 cm vs 7 cm). Given the fact that the rest of the modelled response quantities are in accordance with the observed response, it is thought that disagreement in terms of support displacement is a limitation of the calibrated constitutive model, which may be also influenced by the overly stiff bulk modulus of soil skeleton (discussed in Section 3.1).

This project has received funding from the European Union's Horizon 2020 research and innovation programme under grant agreement No. 700748

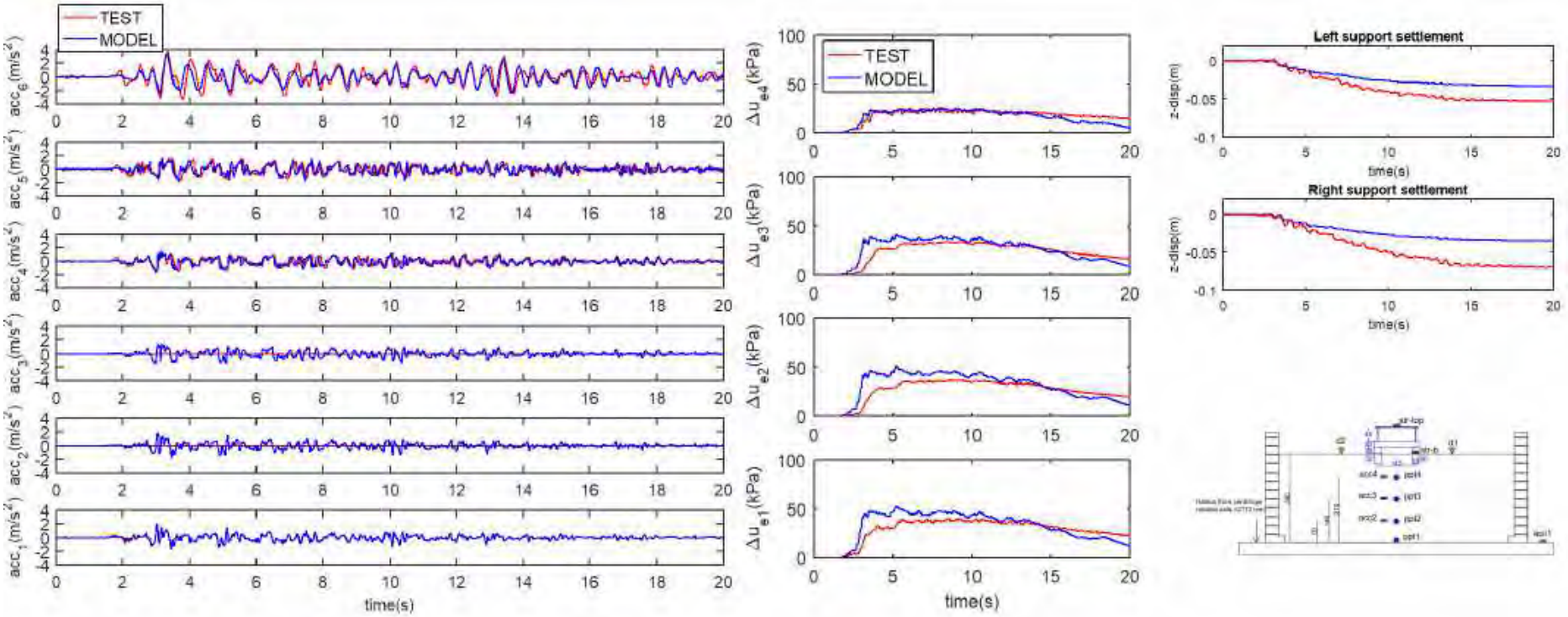

Figure 4.6. Comparison of modelled (blue) and recorded (red) responses in terms of acceleration and pore water pressure at various locations for homogeneous profile with structure case (PDMY02 model, considering normal kH=1.4 x 10-3 m/s in the numerical domain). Note: recorded and modelled acceleration responses (acc2-acc4) are lowpass filtered with a zero-phase 3rd order Butterworth filter with the corner frequency 49 Hz order 3.

This project has received funding from the European Union's Horizon 2020 research and innovation programme under grant agreement No. 700748

4.3 TWO LAYERS PROFILE IN FREE FIELD CONDITION ON TICINO SAND

4.3.1 UBCSAND

4.3.1.1 ID: DF_xx_TC_UBC_31

The model consists of a liquefiable layer of Ticino sand and an upper clay layer. The ground motion applied was the number 31.

ID: DF_xx_TC_UBC_31	TEST: M2_S1_GM31

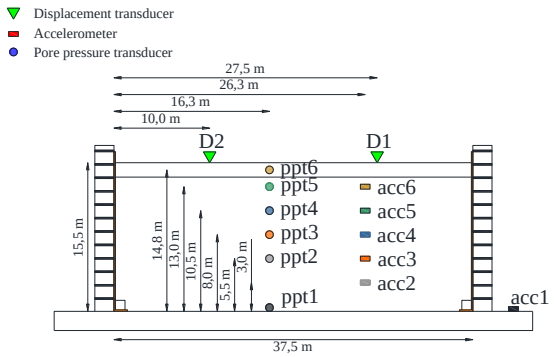

Layouts of the model reproduced in Plaxis 2D

The UBC3D-PML constitutive model is used to represent Ticino sand The properties adopted in the numerical analyses are summarized in following table.

Table with UBCSand parameters.

Parameter	Description	Value	Unit
$N_{1,60}$	SPT number	11.7	-
K_G^e	elastic shear modulus	986	-
K_B^e	elastic bulk modulus	1643	-
K_G^p	plastic shear modulus	508	-
m_e	elastic stress dependency parameter	0.5	-
n_e	elastic stress dependency parameter	0.5	-
n_p	plastic stress dependency parameter	0.4	-
ϕ_{cv}	critical state friction angle	33	°
ϕ_{peak}	peak state friction angle	34.2	°
R_f	failure ratio	0.76	-
ν	Poisson coefficient	0.25	-

This project has received funding from the European Union's Horizon 2020 research and innovation programme under grant agreement No. 700748

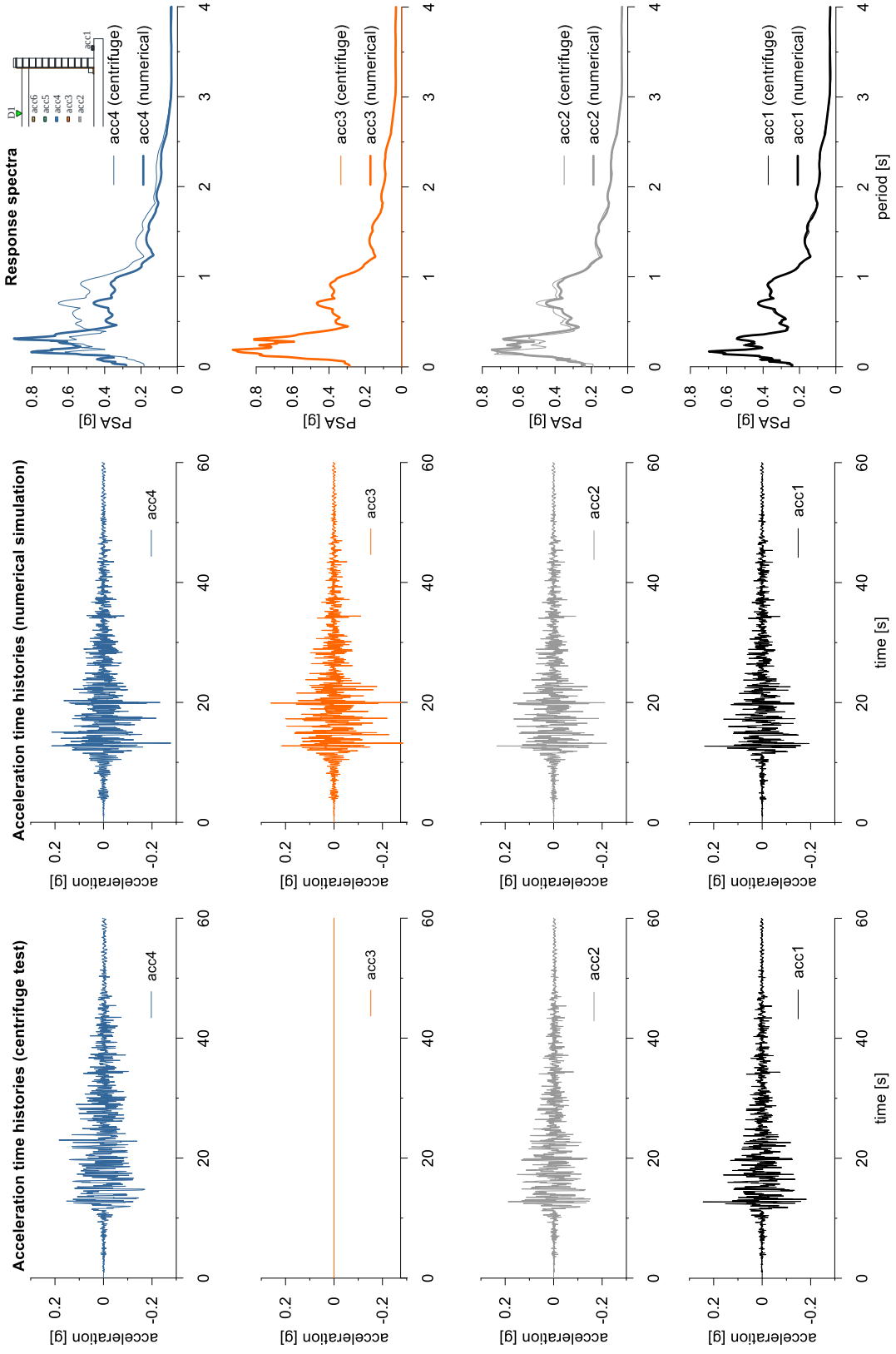

This project has received funding from the European Union's Horizon 2020 research and innovation programme under grant agreement No. 700748

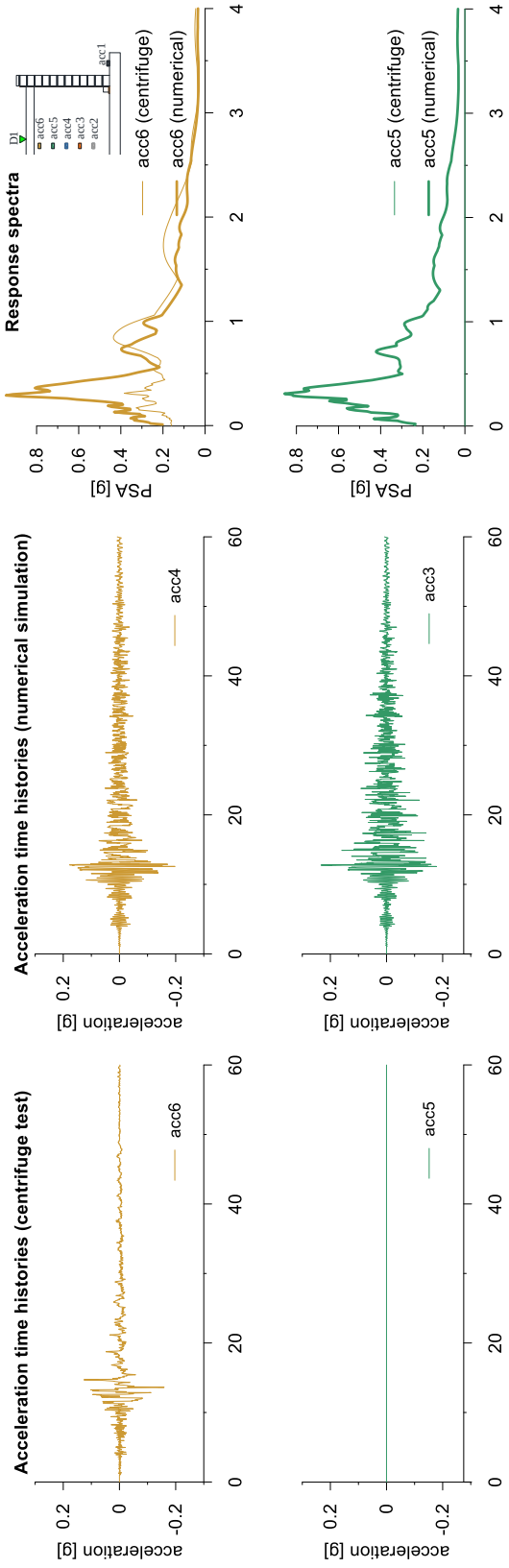

This project has received funding from the European Union's Horizon 2020 research and innovation programme under grant agreement No. 700748

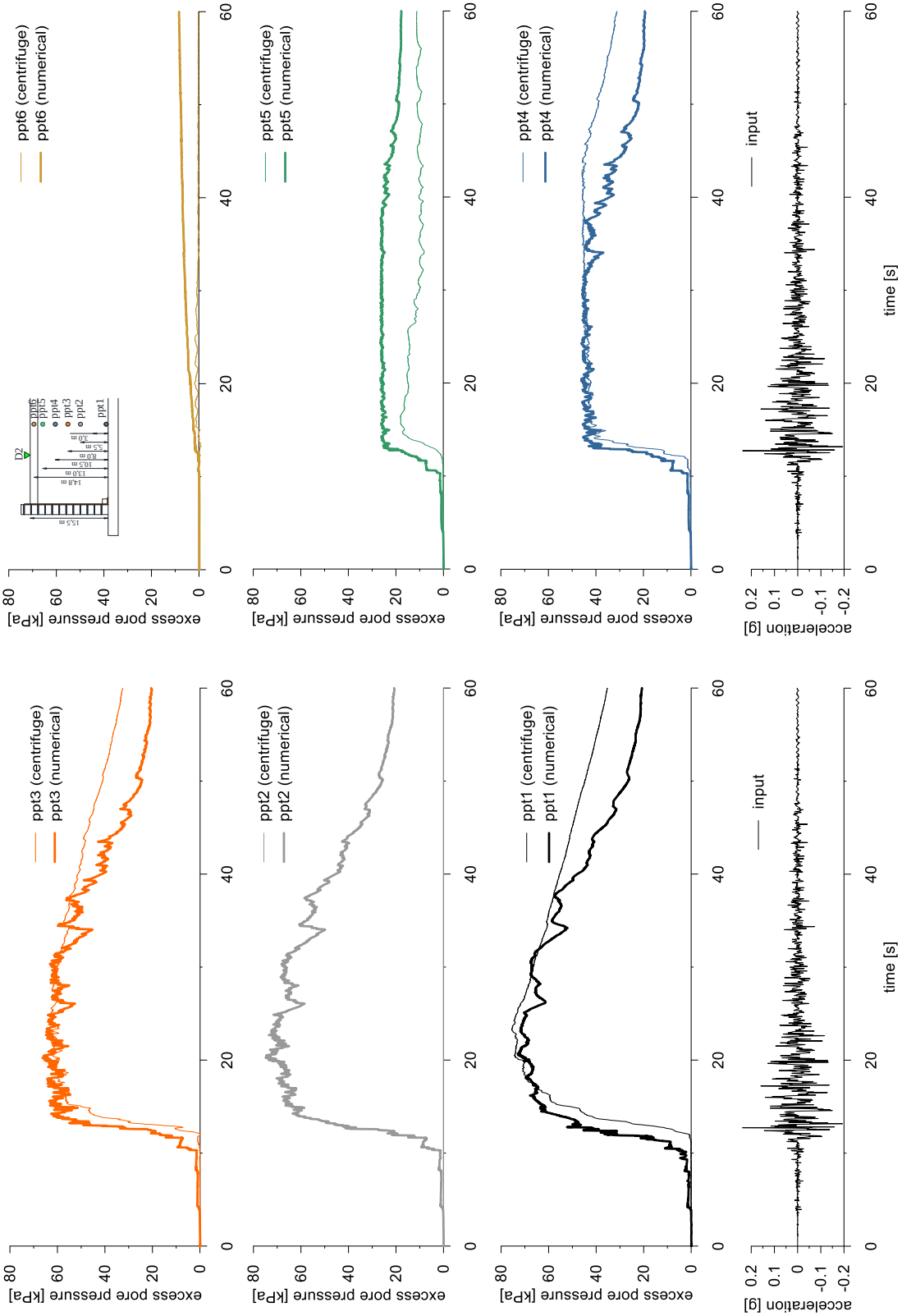

This project has received funding from the European Union's Horizon 2020 research and innovation programme under grant agreement No. 700748

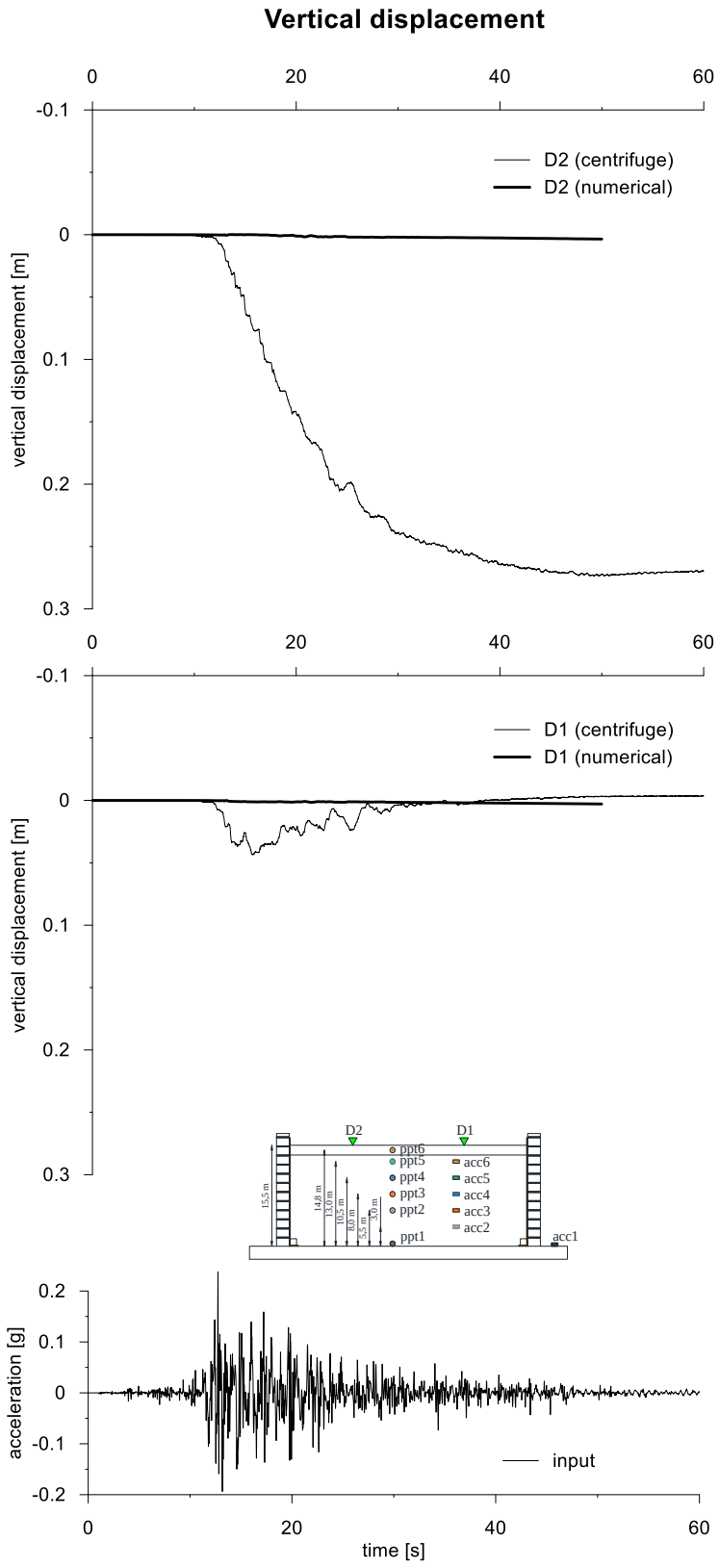

This project has received funding from the European Union's Horizon 2020 research and innovation programme under grant agreement No. 700748

4.3.2 PM4SAND

4.3.2.1 ID: DF_xx_TC_PM4_31

The model consists of a liquefiable layer of Ticino sand and an upper clay layer. The ground motion applied was the number 31.

ID: DF_xx_TC_PM4_31	TEST: M2_S1_GM31

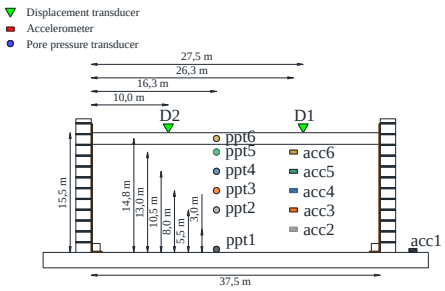

Layouts of the model reproduced in Plaxis 2D.

The PM4SAND constitutive model is used to represent Ticino sand The properties adopted in the numerical analyses are summarized in Table 1.

Table with PM4sand parameters

Parameter	Description	Value	Unit
D_{R0}	Initial relative density	0.50	-
G_0	shear modulus coefficient	624	-
hp_0	contraction rate parameter	0.1	-
p_A	atmospheric pressure	101.3	kN/m^2
e_{max}	maximum void ratio	0.923	-
e_{min}	minimum void ratio	0.574	-
n_b	bounding surface parameter	0.5	-
n_d	dilatancy surface parameter	0.1	-
ϕ_{cv}	critical state friction angle	33	°
nu	Poisson's ratio	0.3	-
Q	critical state line parameter	8	-
R	critical state line parameter	1.2	-

This project has received funding from the European Union's Horizon 2020 research and innovation programme under grant agreement No. 700748

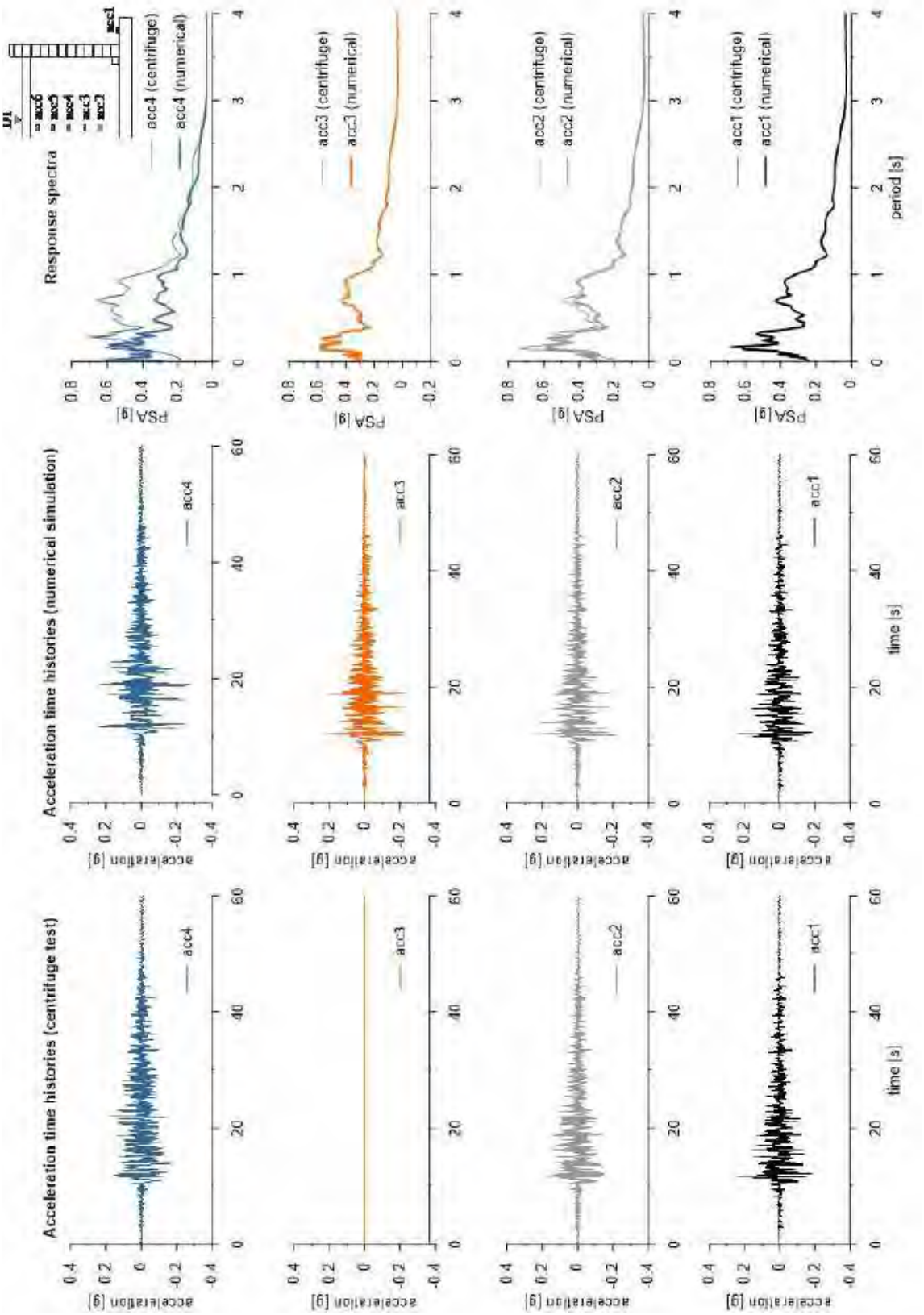

This project has received funding from the European Union's Horizon 2020 research and innovation programme under grant agreement No. 700748

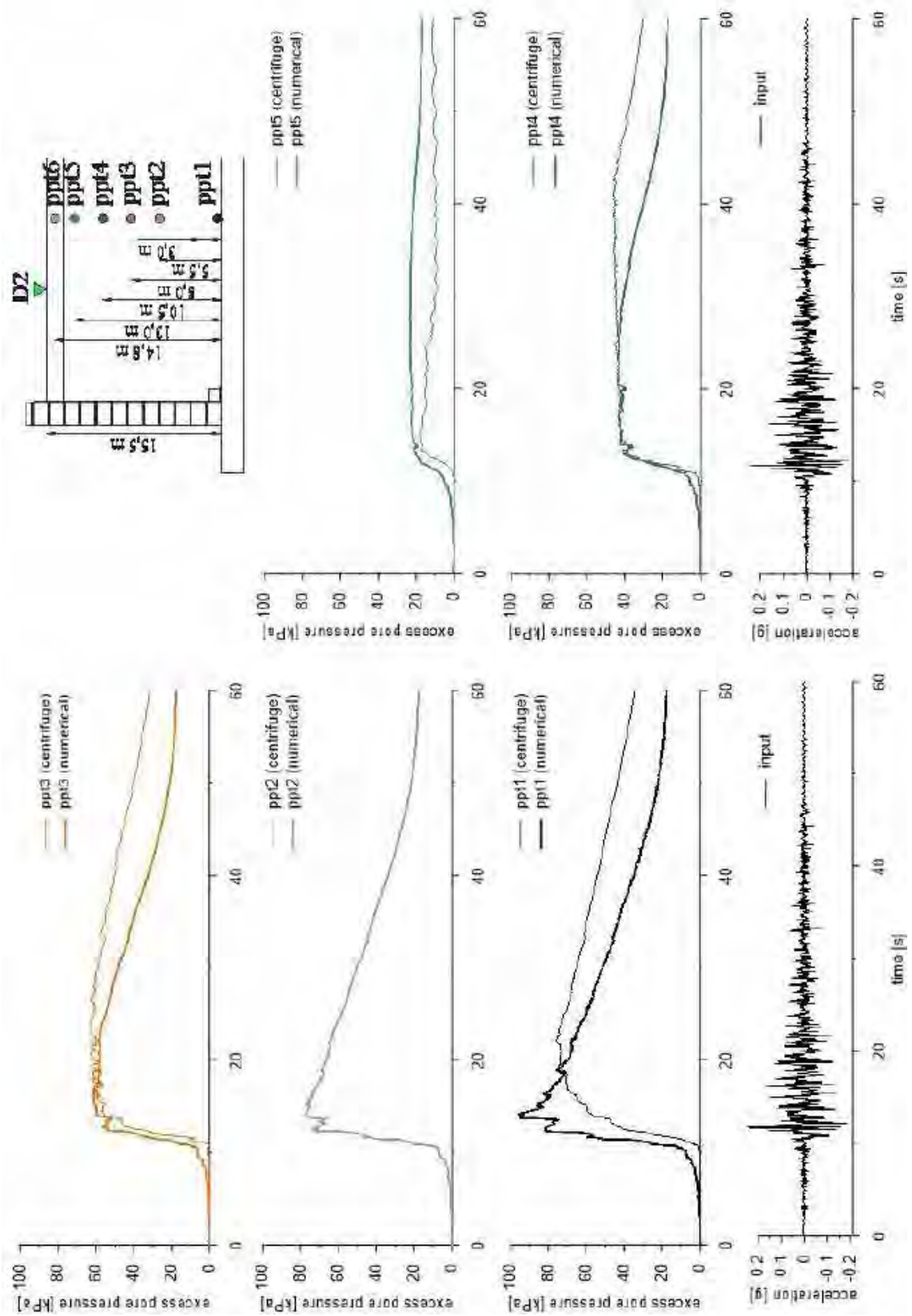

This project has received funding from the European Union's Horizon 2020 research and innovation programme under grant agreement No. 700748

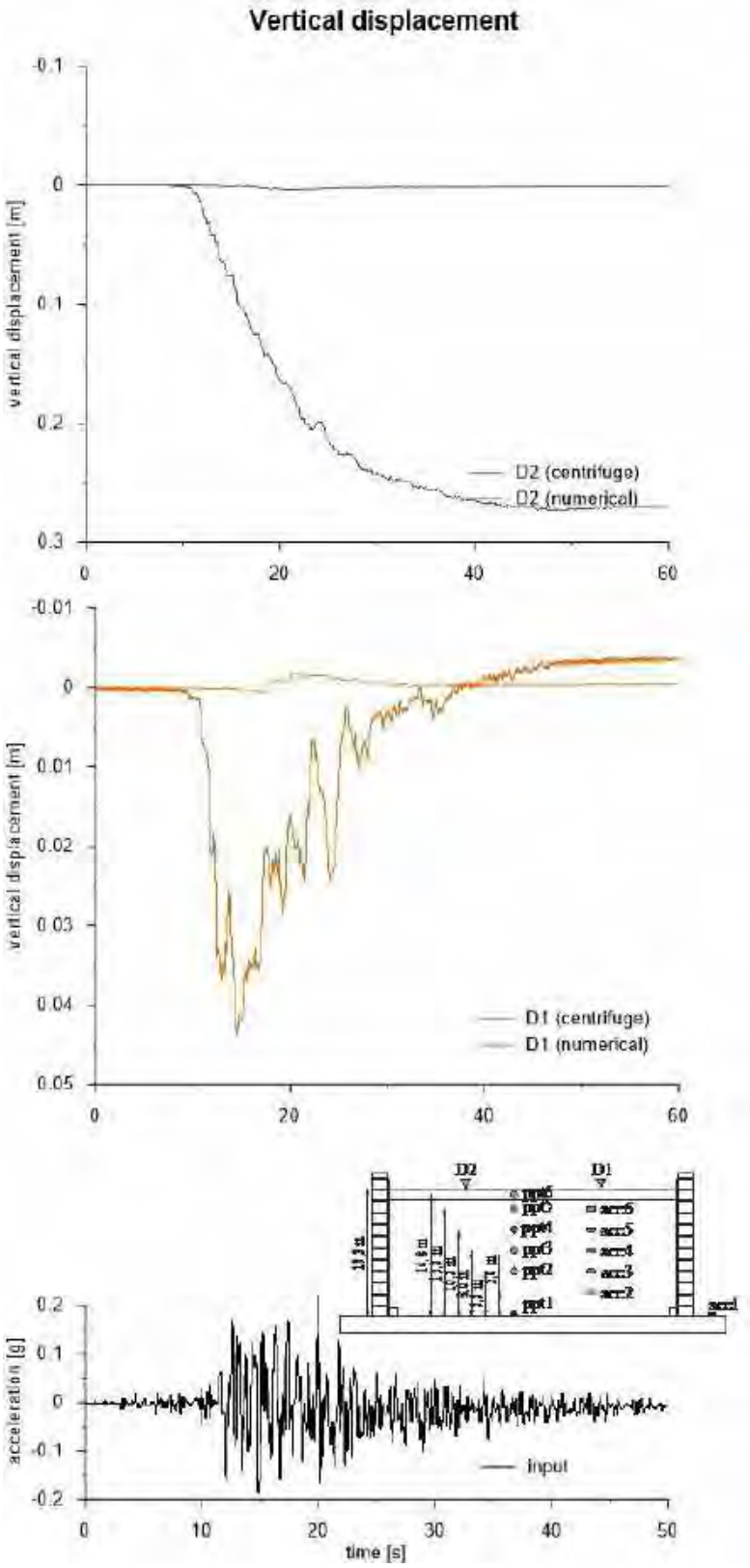

This project has received funding from the European Union's Horizon 2020 research and innovation programme under grant agreement No. 700748

4.4 TWO LAYERS PROFILE WITH A SIMPLIFIED STRUCTURE ON TICINO SAND

4.4.1 UBCSAND

4.4.1.1 ID: DS_xx_TC_UBC_31+

The model consists of a liquefiable layer of Ticino sand and an upper clay layer with a structure model. The ground motion applied was the number 31+.

ID: DS_xx_TC_UBC_31+	TEST: M2F_S1_GM31+

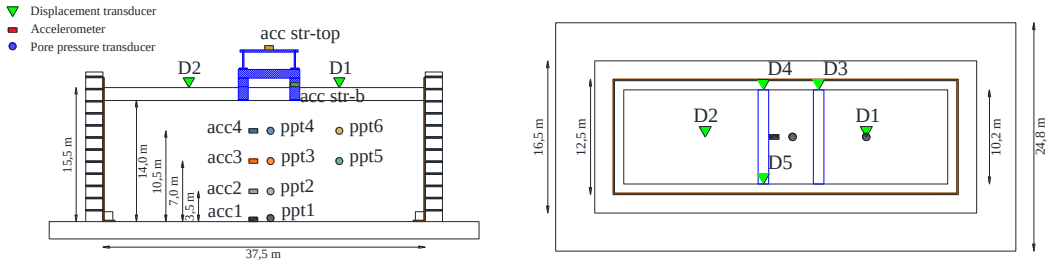

Layouts of the model reproduced in Plaxis 2D

The UBC3D-PML constitutive model is used to represent Ticino sand The properties adopted in the numerical analyses are summarized in following table.

Table with UBCSand parameters

Parameter	Description	Value	Unit
$N_{1,60}$	SPT number	12.4	-
K_G^e	elastic shear modulus	1004	-
K_B^e	elastic bulk modulus	1674	-
K_G^p	plastic shear modulus	566	-
m_e	elastic stress dependency parameter	0.5	-
n_e	elastic stress dependency parameter	0.5	-
n_p	plastic stress dependency parameter	0.4	-
ϕ_{cv}	critical state friction angle	33	°
ϕ_{peak}	peak state friction angle	34.2	°
R_f	failure ratio	0.75	-
ν	Poisson coefficient	0.25	-

This project has received funding from the European Union's Horizon 2020 research and innovation programme under grant agreement No. 700748

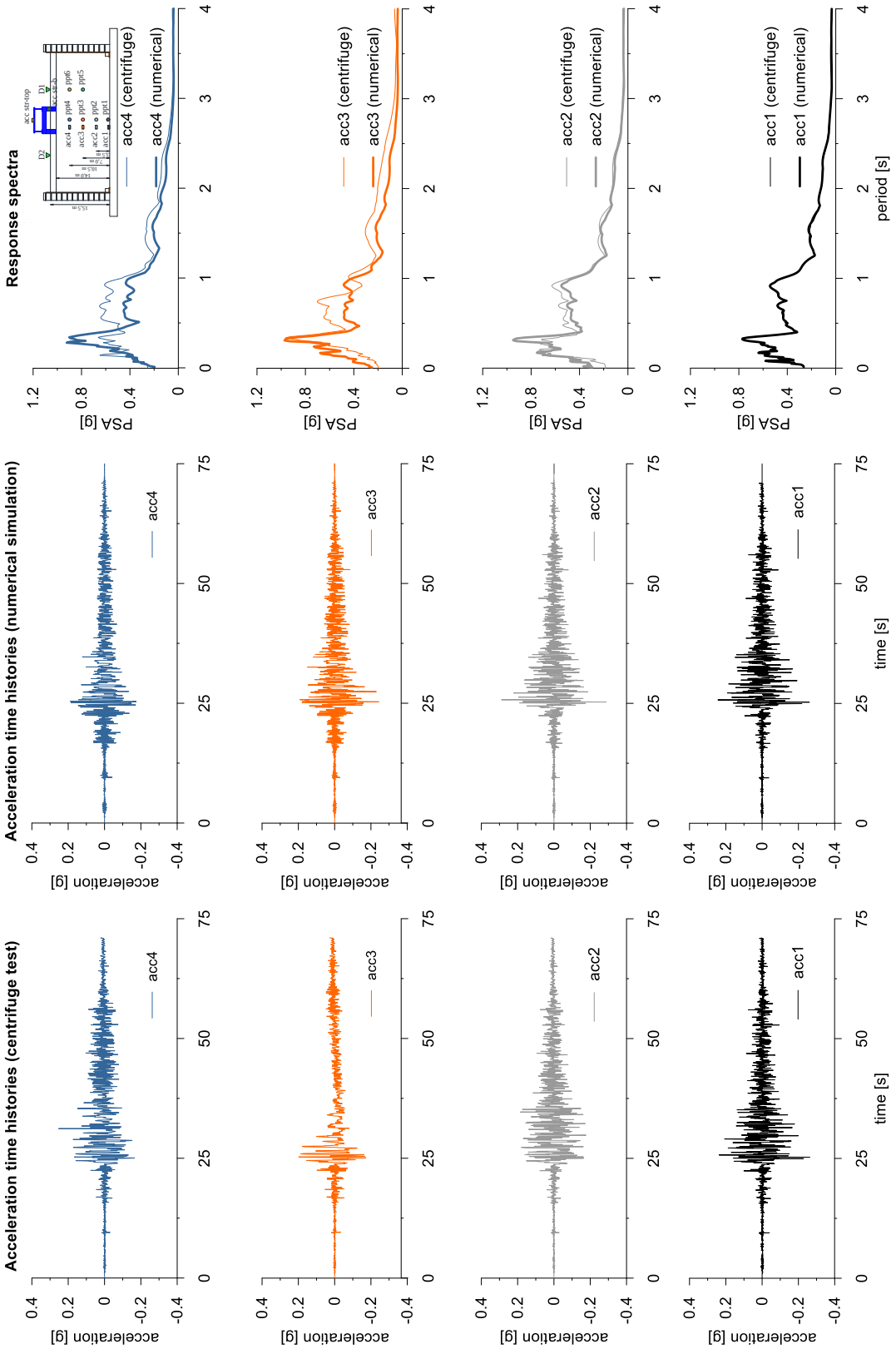

This project has received funding from the European Union's Horizon 2020 research and innovation programme under grant agreement No. 700748

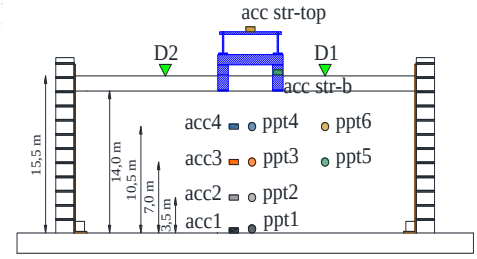

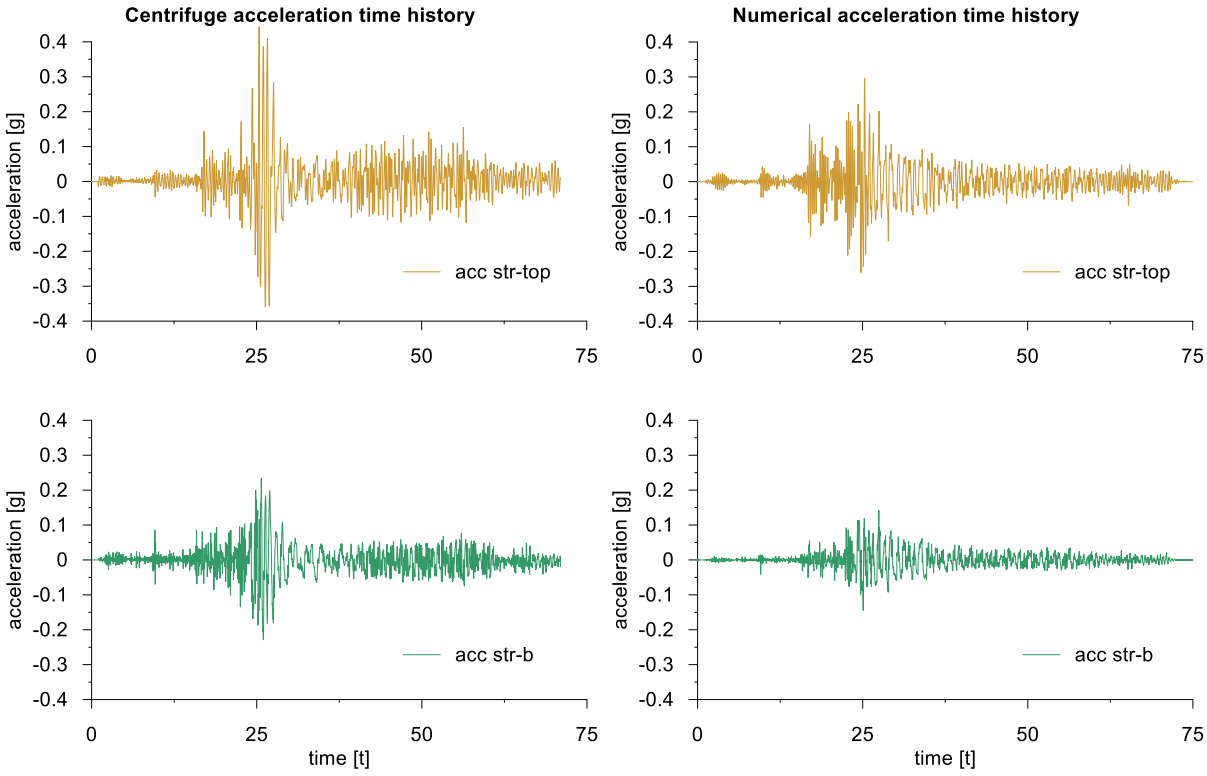

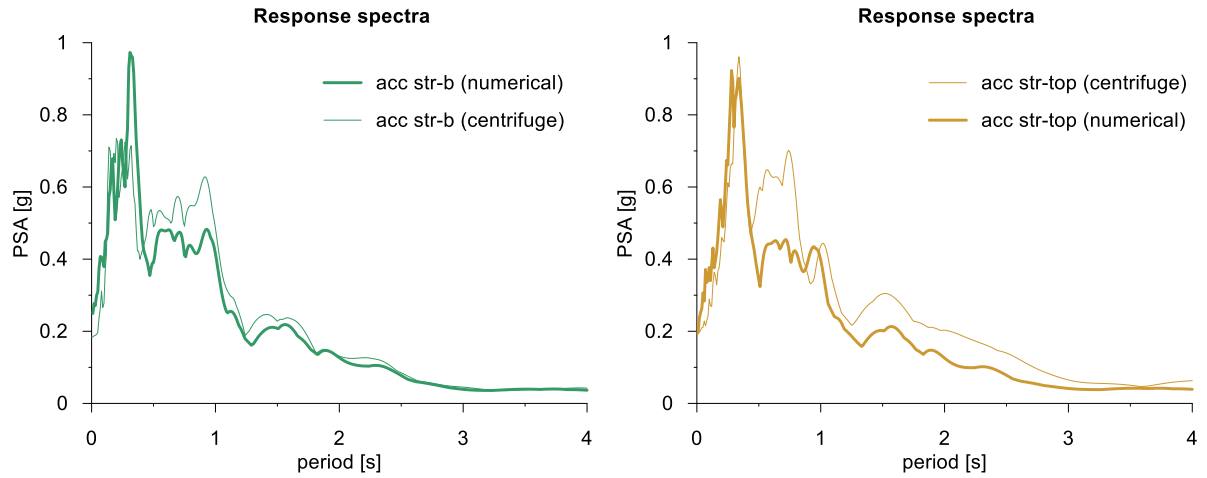

This project has received funding from the European Union's Horizon 2020 research and innovation programme under grant agreement No. 700748

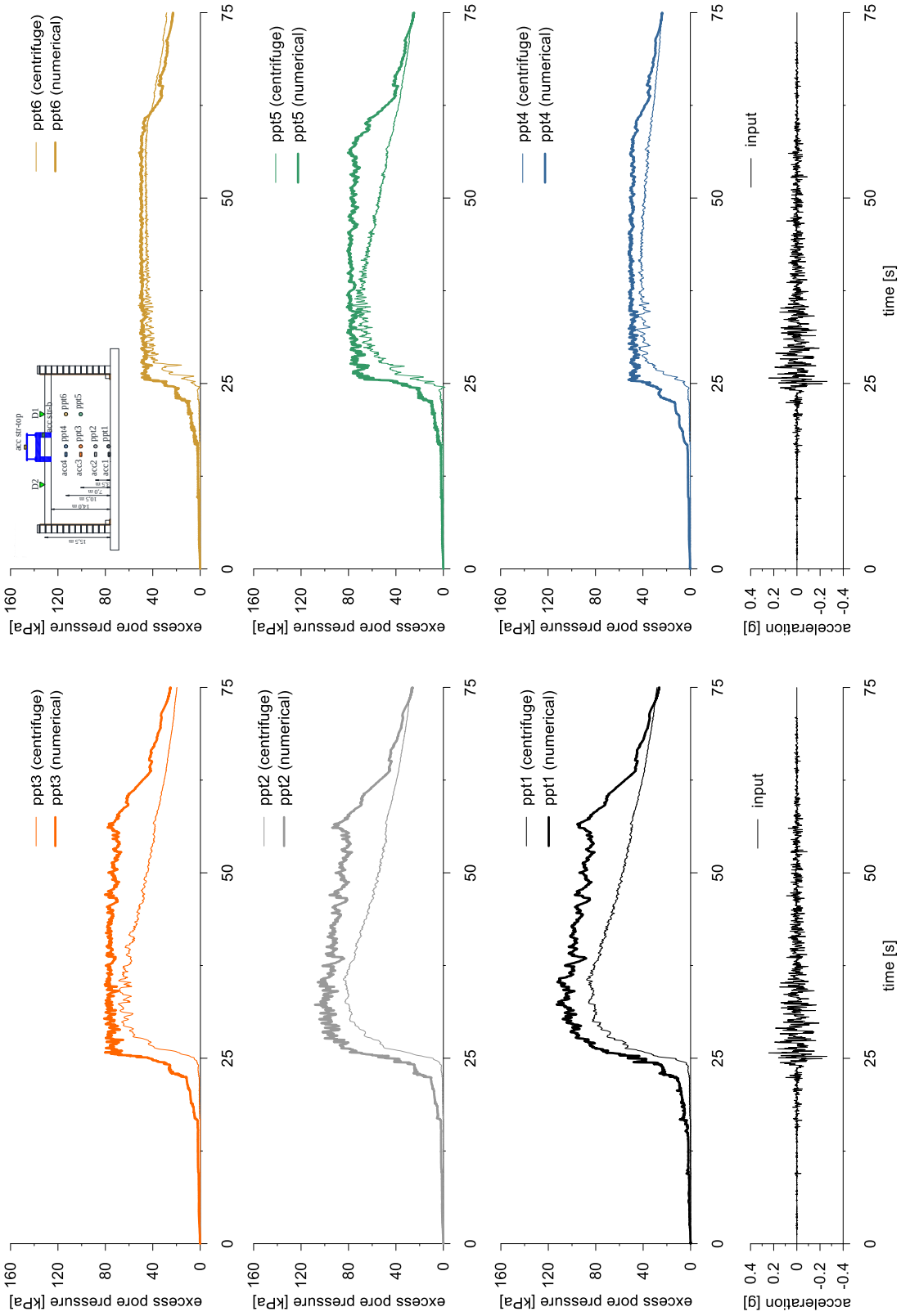

This project has received funding from the European Union's Horizon 2020 research and innovation programme under grant agreement No. 700748

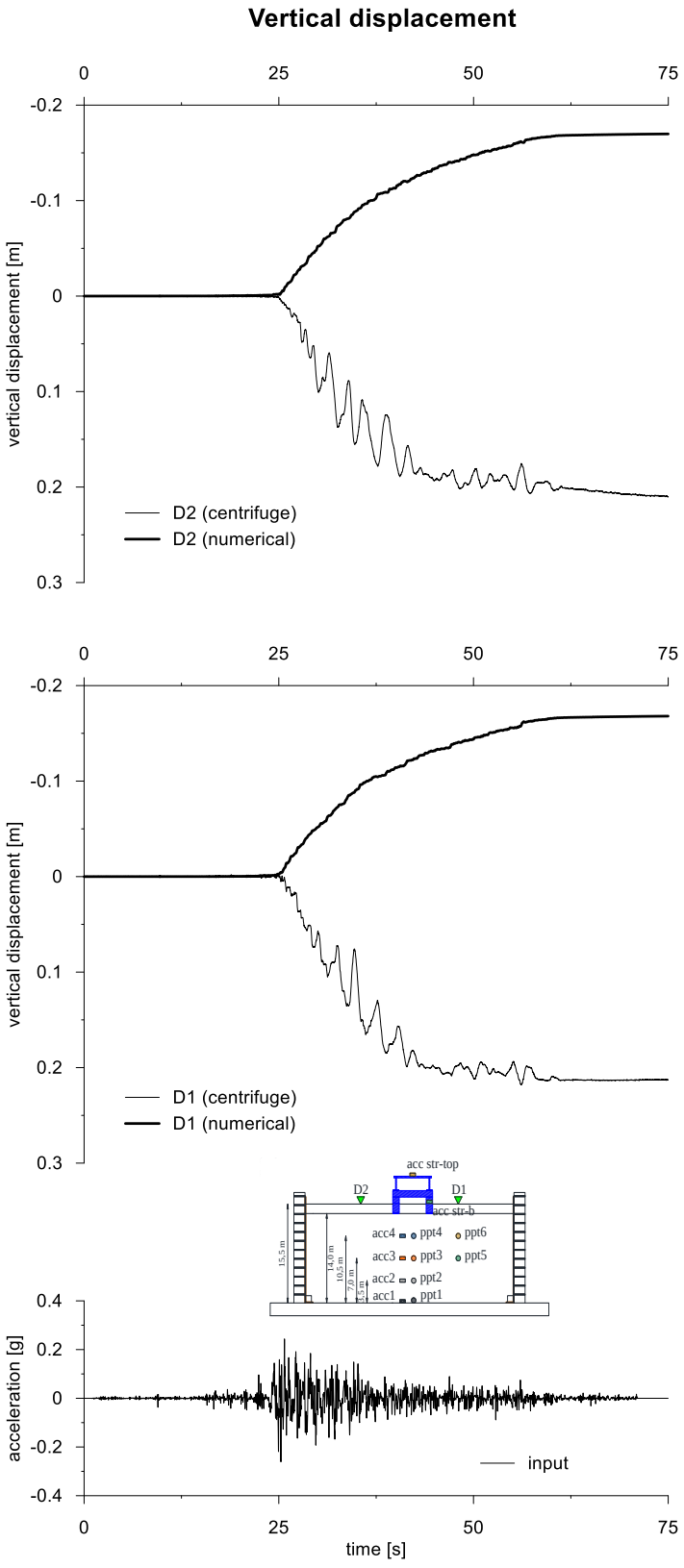

This project has received funding from the European Union's Horizon 2020 research and innovation programme under grant agreement No. 700748

Vertical displacement

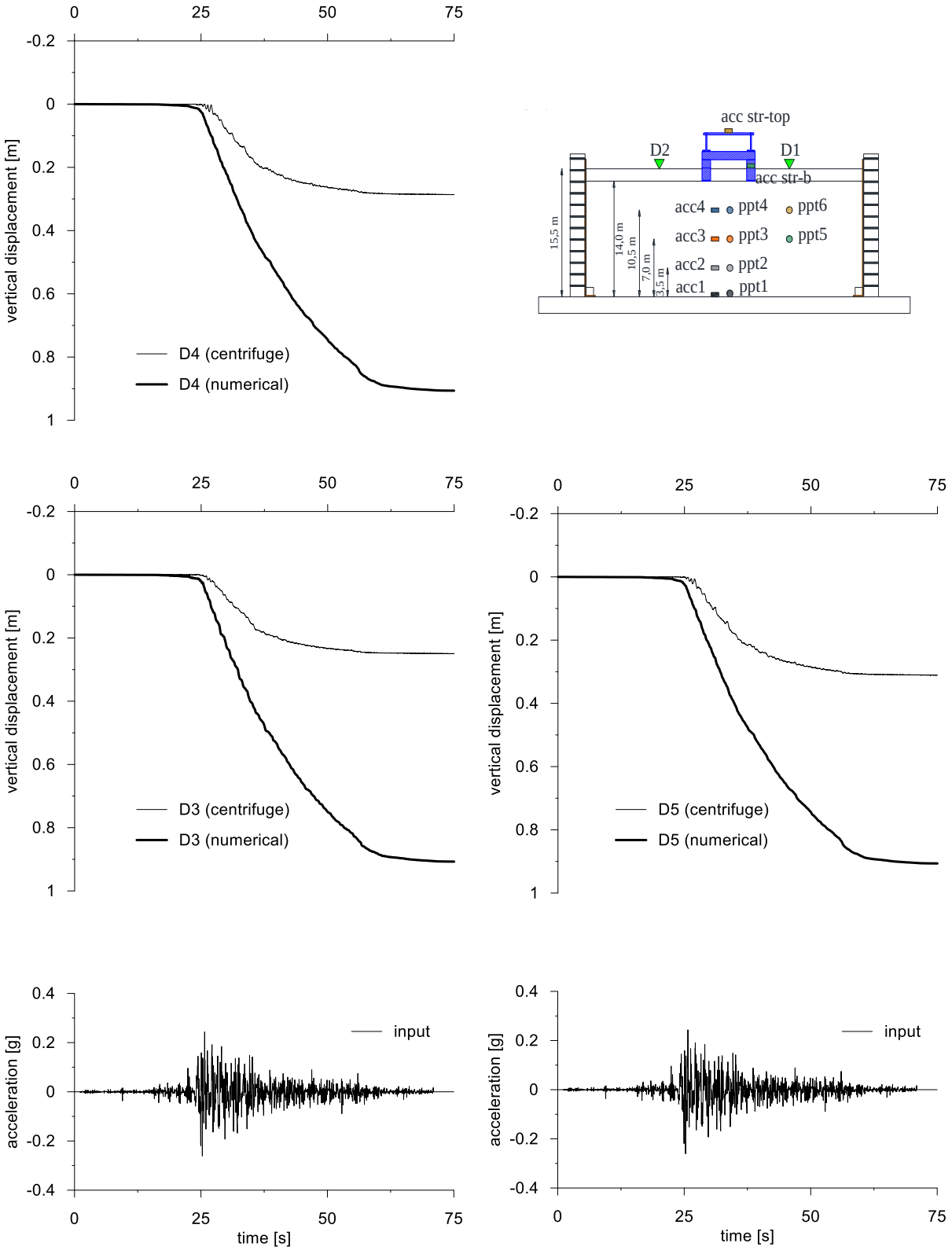

This project has received funding from the European Union's Horizon 2020 research and innovation programme under grant agreement No. 700748

4.4.2 PM4SAND

4.4.2.1 ID: DS_xx_TC_PM4_31+

The model consists of a liquefiable layer of Ticino sand and an upper clay layer with a structure model. The ground motion applied was the number 31+.

ID: DS_xx_TC_PM4_31+	TEST: M2F_S1_GM31+

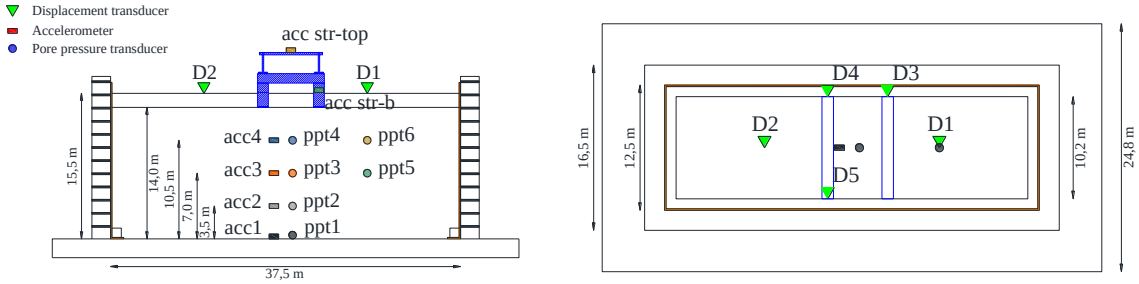

Layouts of the model reproduced in Plaxis 2D

The PM4SAND constitutive model is used to represent Ticino sand The properties adopted in the numerical analyses are summarized in following table.

Table with PM4sand parameters

Parameter	Description	Value	Unit
D_{R0}	Initial relative density	0.52	-
G_0	shear modulus coefficient	594	-
hp_0	contraction rate parameter	0.1	-
p_A	atmospheric pressure	101.3	kN/m^2
e_{max}	maximum void ratio	0.923	-
e_{min}	minimum void ratio	0.574	-
n_b	bounding surface parameter	0.5	-
n_d	dilatancy surface parameter	0.1	-
ϕ_{cv}	critical state friction angle	33	°
nu	Poisson's ratio	0.3	-
Q	critical state line parameter	8	-
R	critical state line parameter	1.2	-

This project has received funding from the European Union's Horizon 2020 research and innovation programme under grant agreement No. 700748

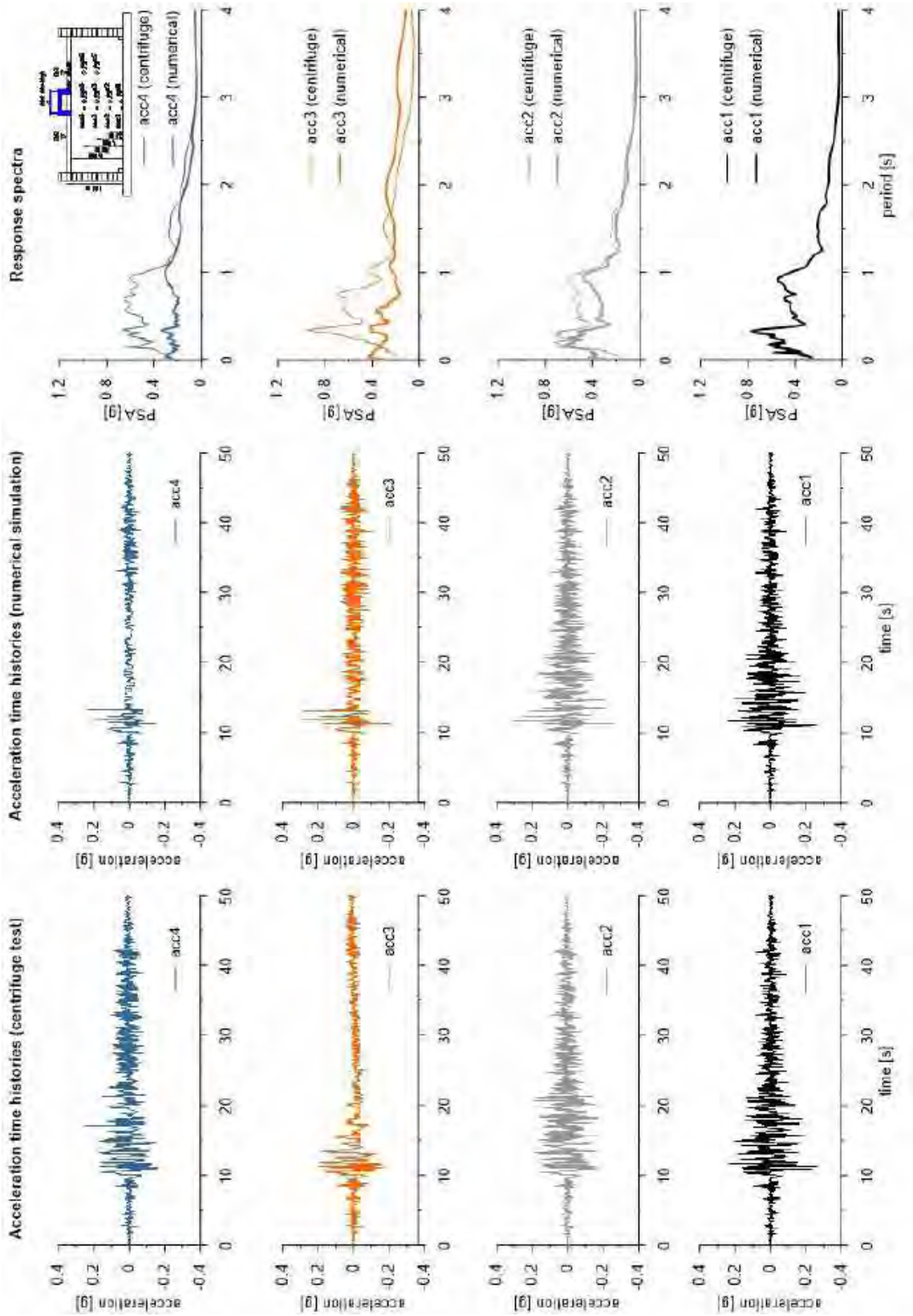

This project has received funding from the European Union's Horizon 2020 research and innovation programme under grant agreement No. 700748

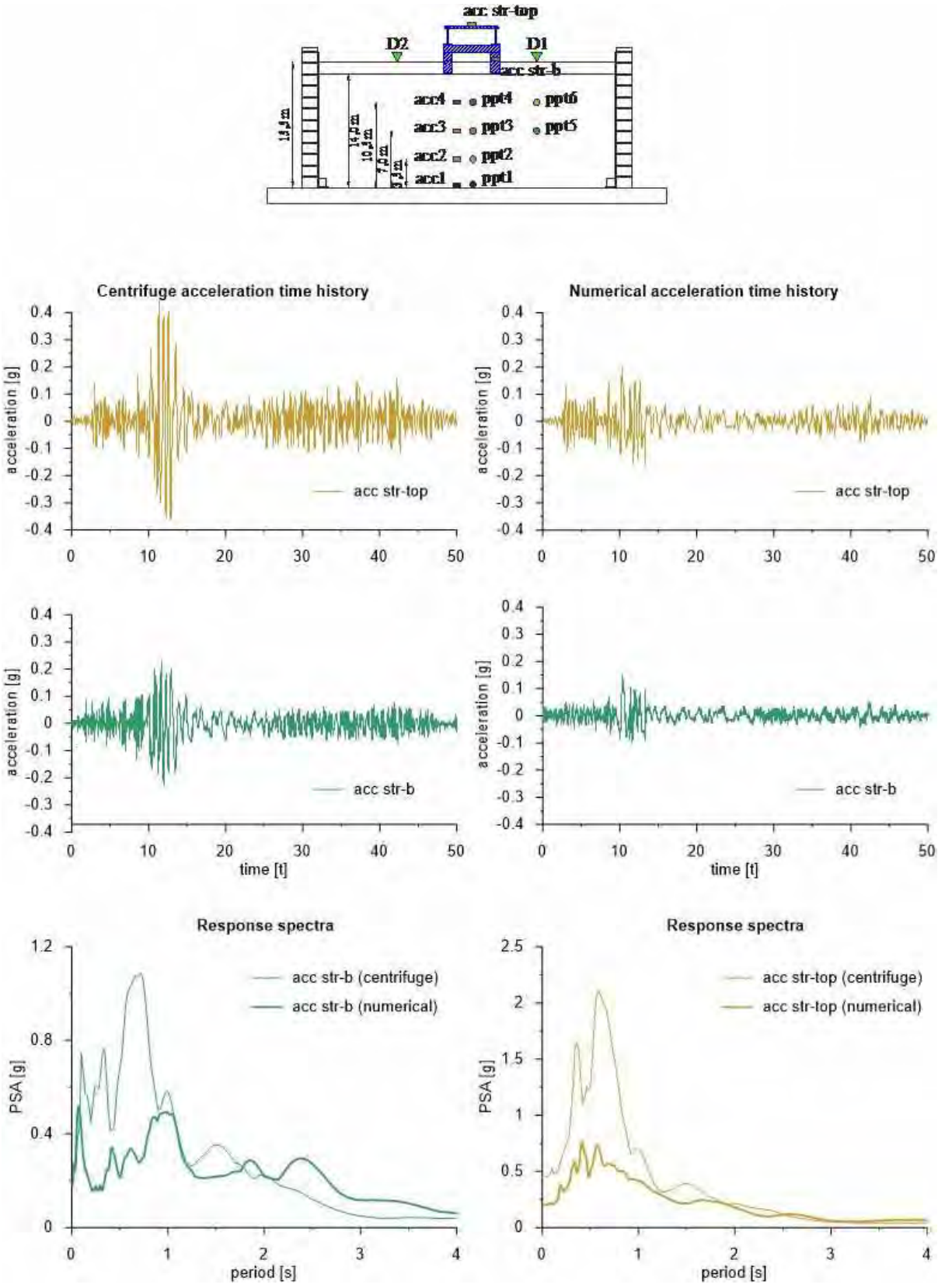

This project has received funding from the European Union's Horizon 2020 research and innovation programme under grant agreement No. 700748

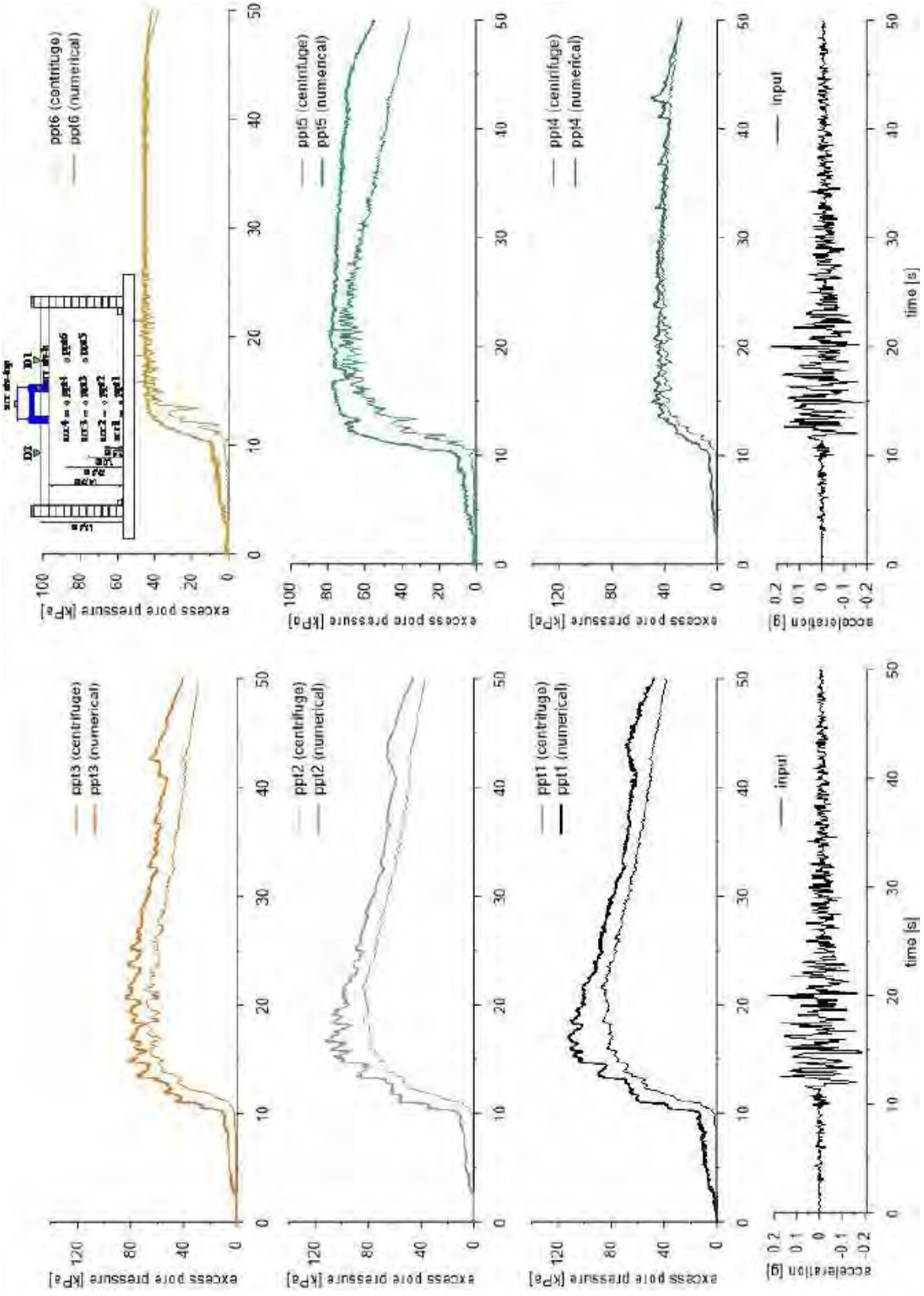

This project has received funding from the European Union's Horizon 2020 research and innovation programme under grant agreement No. 700748

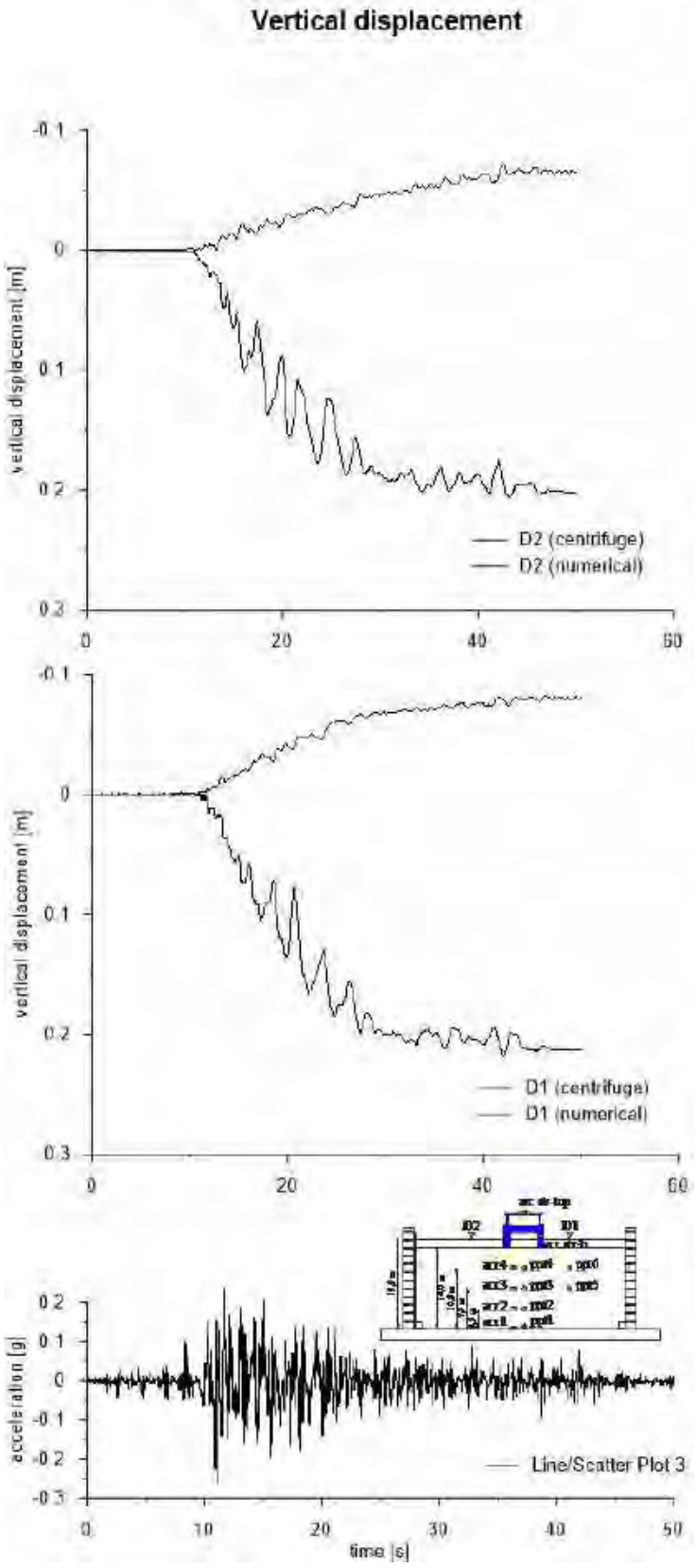

This project has received funding from the European Union's Horizon 2020 research and innovation programme under grant agreement No. 700748

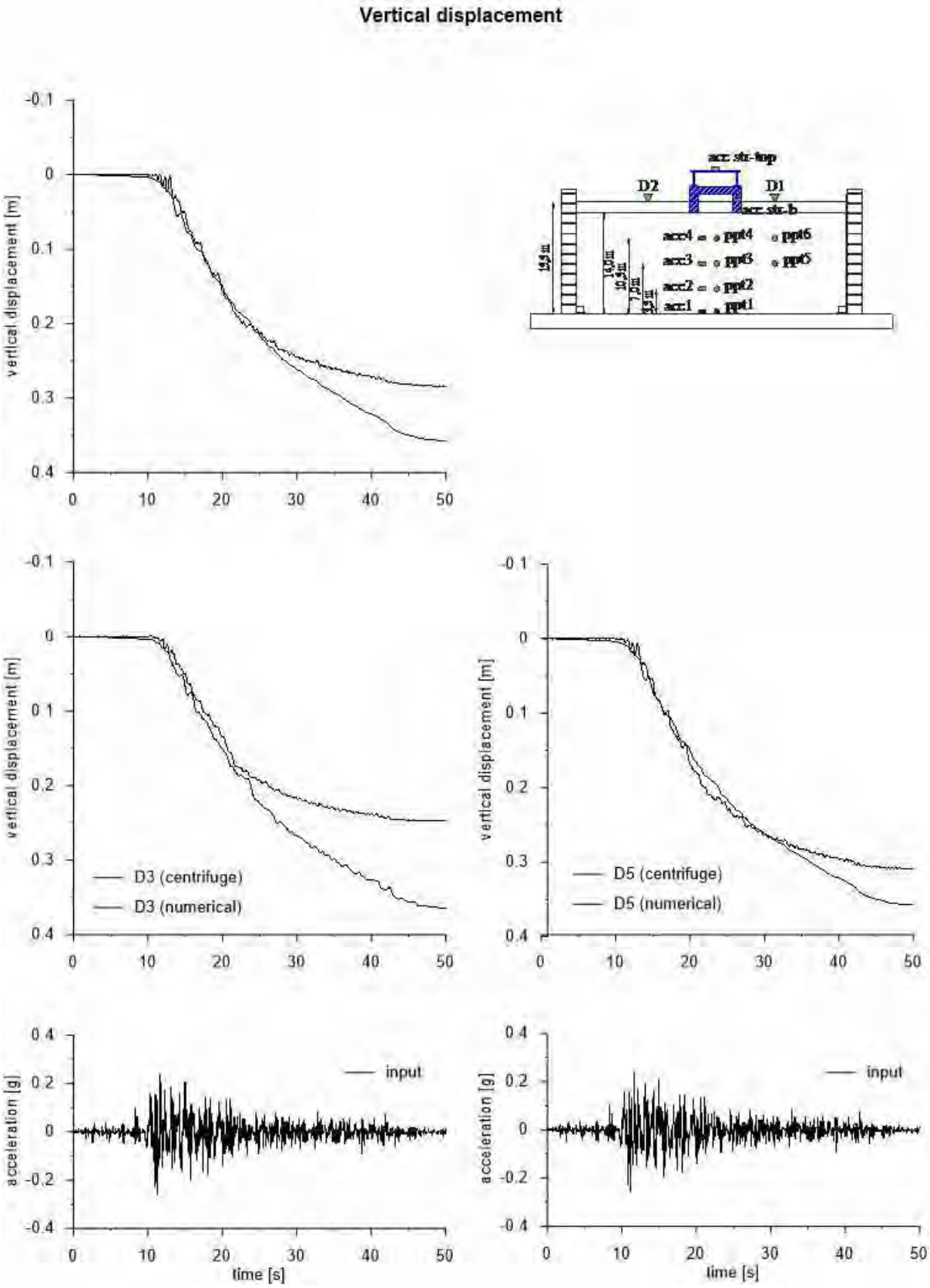

This project has received funding from the European Union's Horizon 2020 research and innovation programme under grant agreement No. 700748

4.5 FINAL REMARKS

In this section, the centrifuge tests carried out without mitigation interventions have been simulated with different models.

The four constitutive models are all able to catch the pore pressure build up along the soil profile caused by the imposed ground motion, even though the more loosely coupled one (Finn-Byrne) lacks the ability to transmit realistically the seismic action to the upper part of the subsoil profile.

On the contrary, the simulations are generally speaking unable to get realistically the vertical displacements measured at ground level. This is not surprising because, as observed in literature, the complex coupled liquefaction mechanism is very difficult to be simulated in all its aspects. As a consequence, in the calibration a choice has to be usually done, either aiming to simulate the pore pressure build up or the final measured displacements. In this case, the previous choice was adopted (§3.3.1). One of the reasons of such a choice is the experimental observation that in the centrifuge sometimes local punching of the LVDTs placed at ground level happened, resulting in an unrealistic value of the measured displacements.

In some of the simulations, it was not possible to compare the results in terms of acceleration and/or pore pressure in all the positions of the existing transducers with the experimental values because the instruments were not working in some of the tests.

This project has received funding from the European Union's Horizon 2020 research and innovation programme under grant agreement No. 700748

5 NUMERICAL SIMULATION OF CENTRIFUGE TESTS WITH MITIGATION TECHNIQUES

5.1 HORIZONTAL DRAINS IWITH THE SINGLE LAYER PROFILE

5.1.1 UBCSAND

5.1.1.1 ID: SF_HD_TC_UBC_31

The model consists of a homogenous soil profile of Ticino sand with the application of horizontal drains mitigation technique. The ground motion applied was the number 31.

ID: SF_HD_TC_UBC_31	TEST: M1_S1_HD1-2_GM31

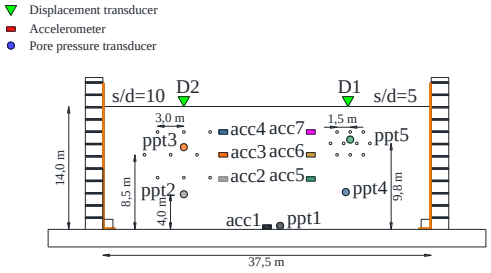

Layouts of the model reproduced in Plaxis 2D

The UBC3D-PML constitutive model is used to represent Ticino sand The properties adopted in the numerical analyses are summarized in following table.

Table with UBCSand parameters

Parameter	Description	Value	Unit
$N_{1,60}$	SPT number	13.7	-
K_G^e	elastic shear modulus	1037	-
K_B^e	elastic bulk modulus	1728	-
K_G^p	plastic shear modulus	681	-
m_e	elastic stress dependency parameter	0.5	-
n_e	elastic stress dependency parameter	0.5	-
n_p	plastic stress dependency parameter	0.4	-
ϕ_{cv}	critical state friction angle	33	°
ϕ_{peak}	peak state friction angle	34.4	°
R_f	failure ratio	0.74	-
ν	Poisson coefficient	0.25	-

This project has received funding from the European Union's Horizon 2020 research and innovation programme under grant agreement No. 700748

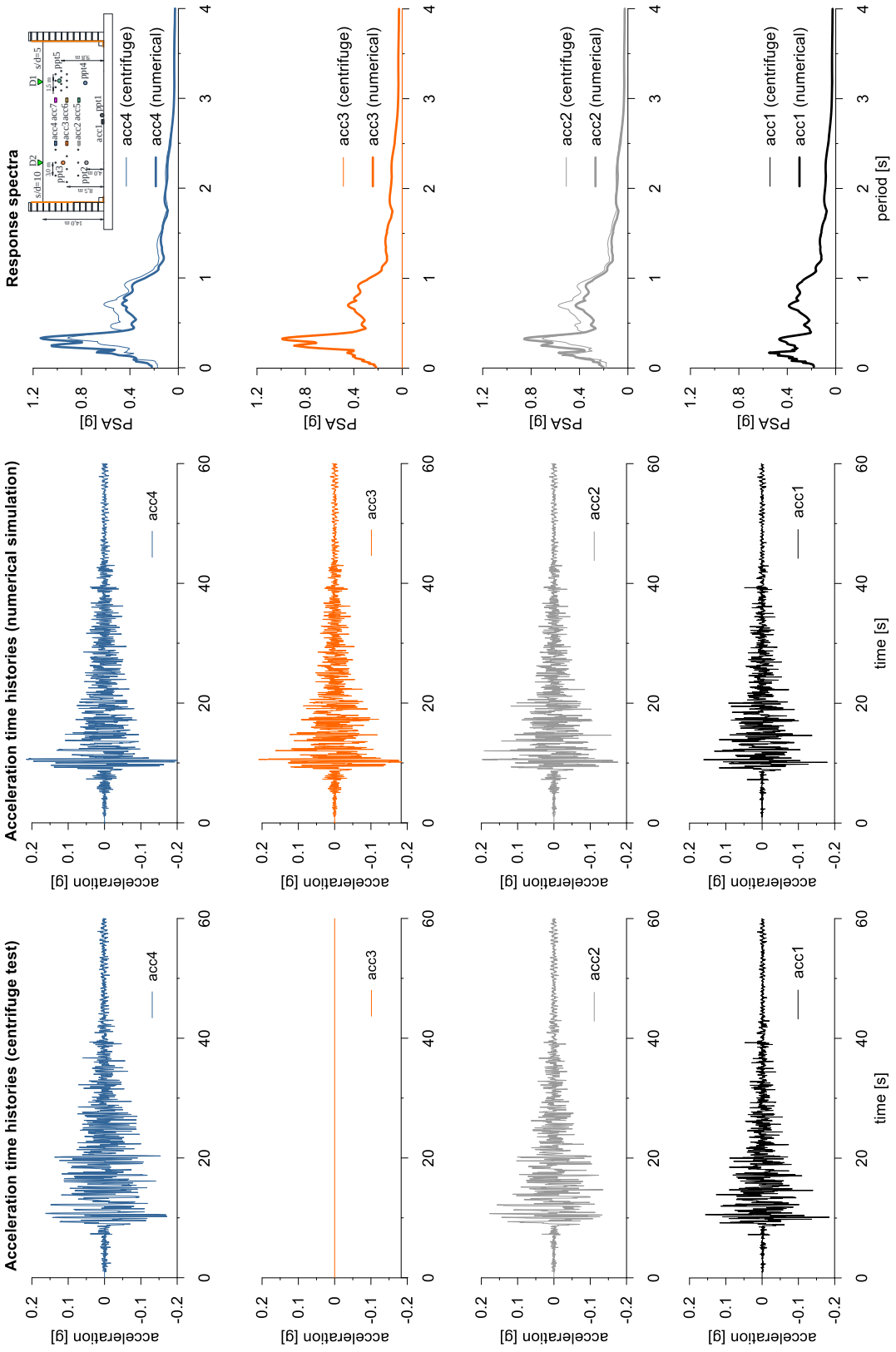

This project has received funding from the European Union's Horizon 2020 research and innovation programme under grant agreement No. 700748

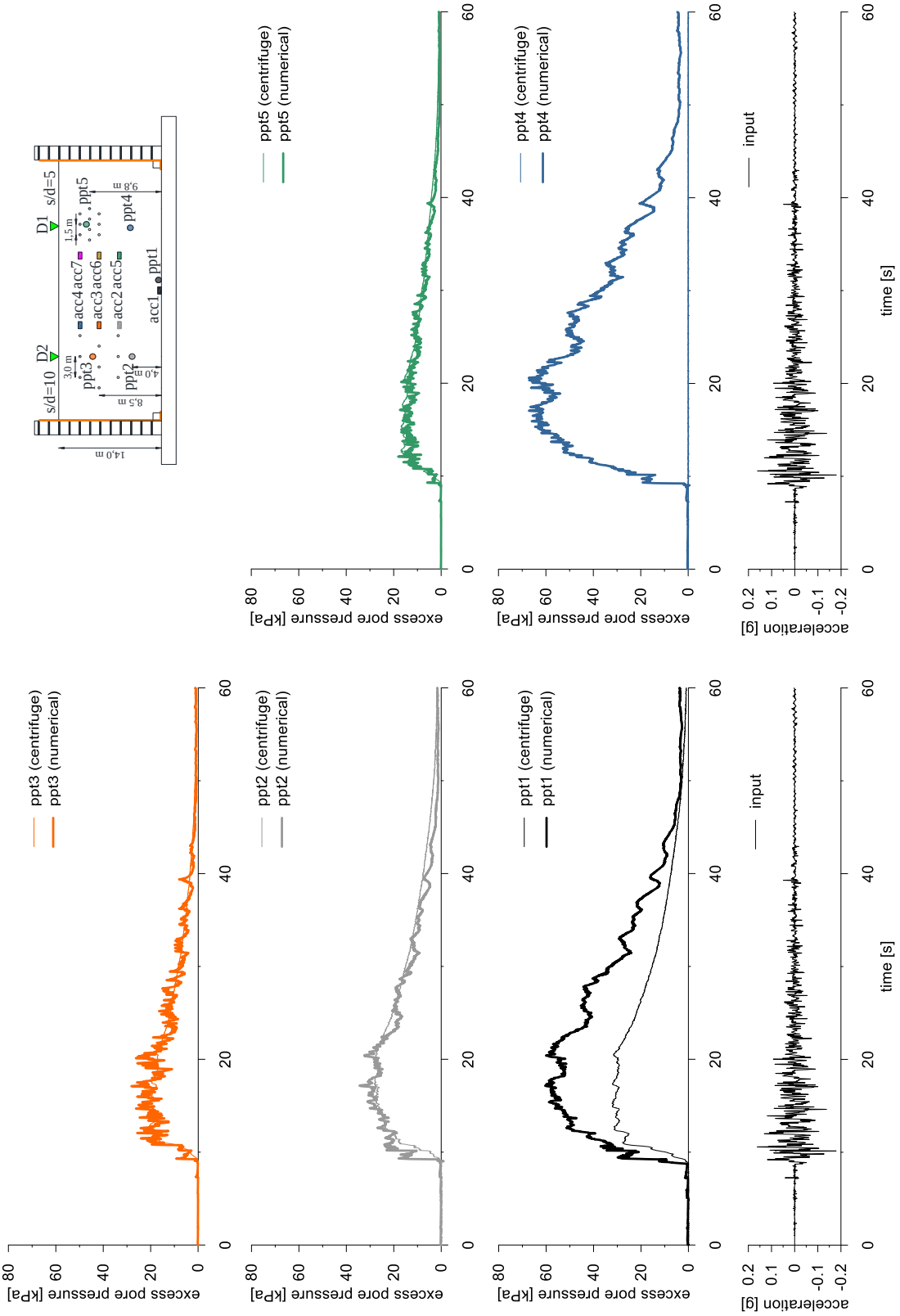

This project has received funding from the European Union's Horizon 2020 research and innovation programme under grant agreement No. 700748

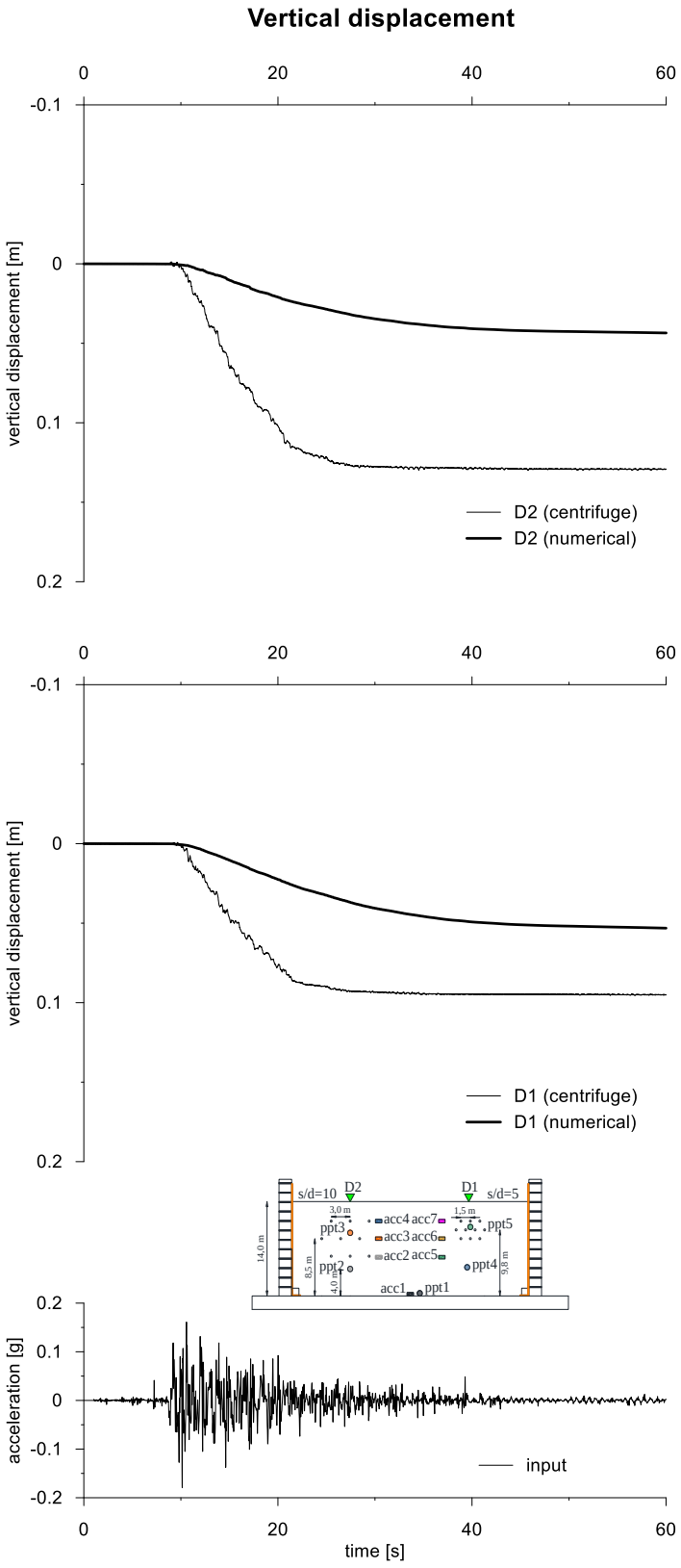

This project has received funding from the European Union's Horizon 2020 research and innovation programme under grant agreement No. 700748

5.1.2 PM4SAND

5.1.2.1 ID: SF_HD_TC_PM4_31

The model consists of a homogenous soil profile of Ticino sand with the application of horizontal drains mitigation technique. The ground motion applied was the number 31.

ID: SF_HD_TC_PM4_31	TEST: M1_S1_HD1-2_GM31

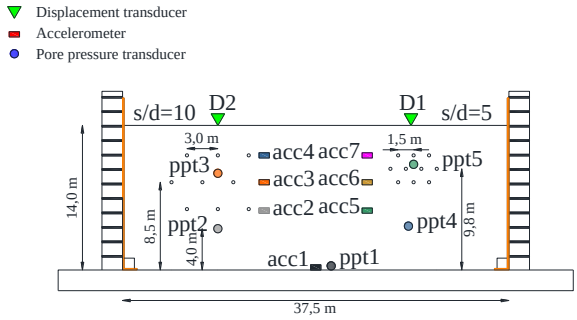

Layouts of the model reproduced in Plaxis 2D

The PM4SAND constitutive model is used to represent Ticino sand The properties adopted in the numerical analyses are summarized in Table 1.

Table with PM4Sand parameters

Parameter	Description	Value	Unit
D_{R0}	Initial relative density	0.54	-
G_0	shear modulus coefficient	594	-
hp_0	contraction rate parameter	0.1	-
p_A	atmospheric pressure	101.3	kN/m^2
e_{max}	maximum void ratio	0.923	-
e_{min}	minimum void ratio	0.574	-
n_b	bounding surface parameter	0.5	-
n_d	dilatancy surface parameter	0.1	-
ϕ_{cv}	critical state friction angle	33	°
nu	Poisson's ratio	0.3	-
Q	critical state line parameter	8	-
R	critical state line parameter	1.2	-

This project has received funding from the European Union's Horizon 2020 research and innovation programme under grant agreement No. 700748

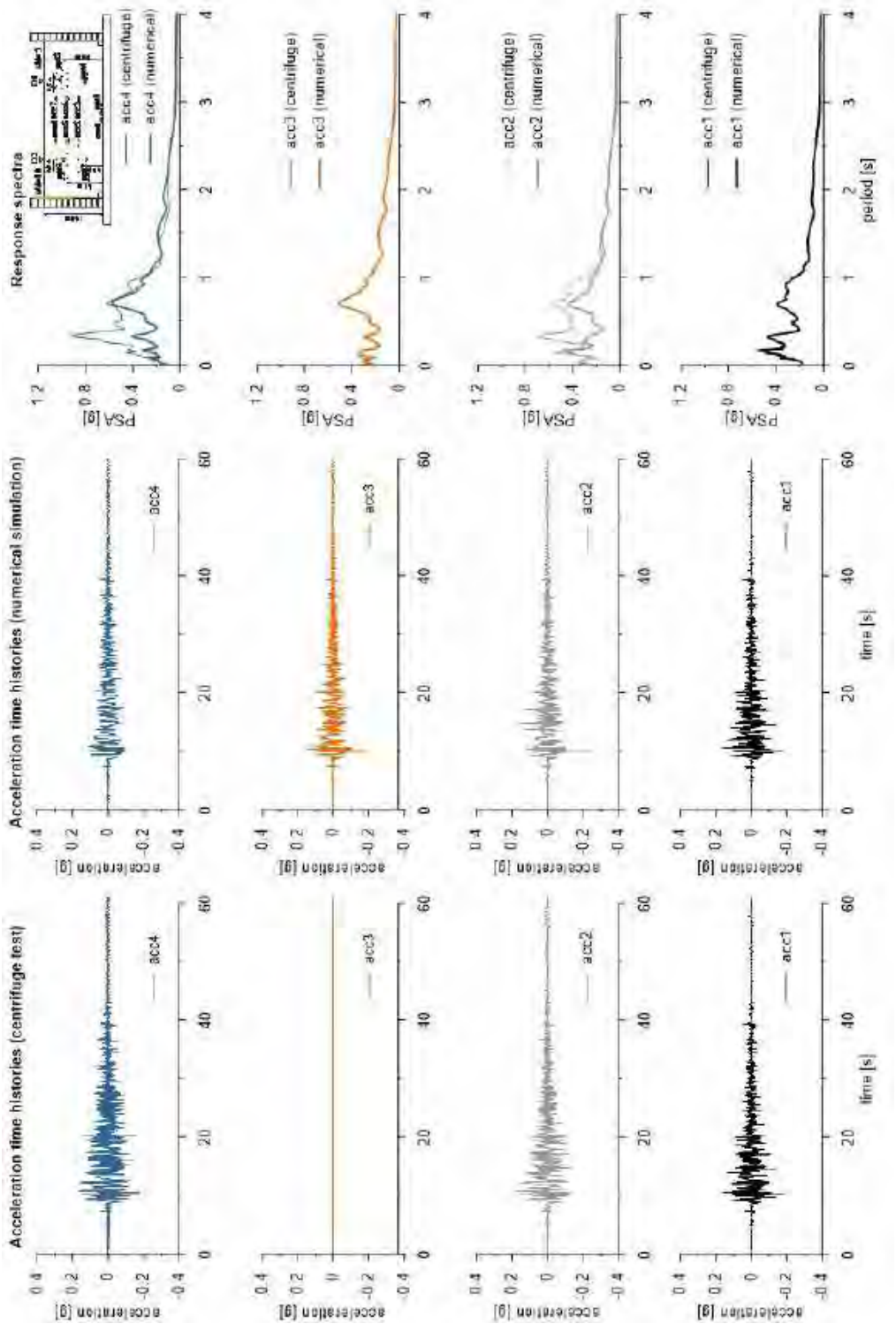

This project has received funding from the European Union's Horizon 2020 research and innovation programme under grant agreement No. 700748

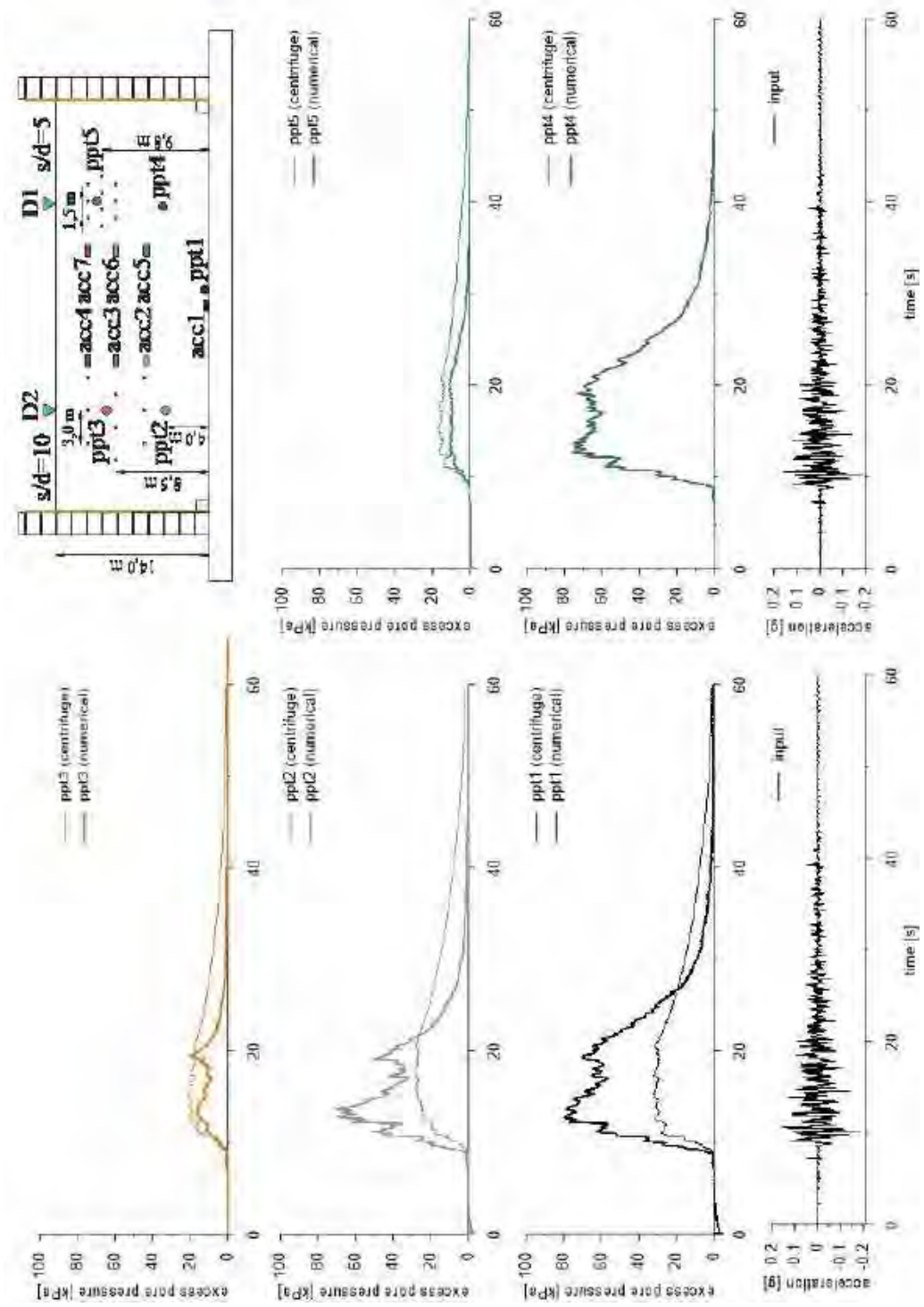

This project has received funding from the European Union's Horizon 2020 research and innovation programme under grant agreement No. 700748

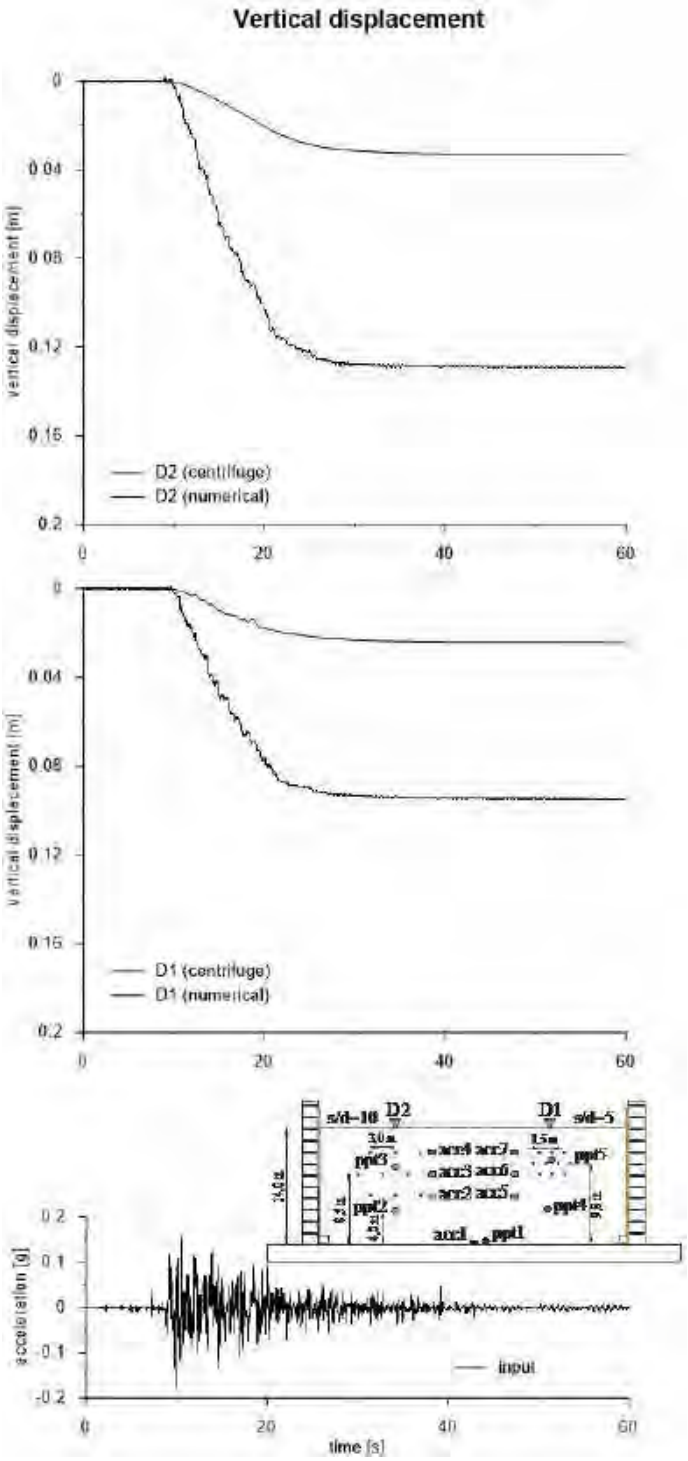

This project has received funding from the European Union's Horizon 2020 research and innovation programme under grant agreement No. 700748

5.2 HORIZONTAL DRAINS WITH THE TWO LAYERS PROFILE

5.2.1 UBCSAND

5.2.1.1 ID: DF_HD_TC_UBC_31

The model consists of a homogenous soil profile of Ticino sand and upper clay layer with the application of horizontal drains mitigation technique. The ground motion applied was the number 31.

ID: DF_HD_TC_UBC_31	TEST: M2_S1_HD1-2_GM31

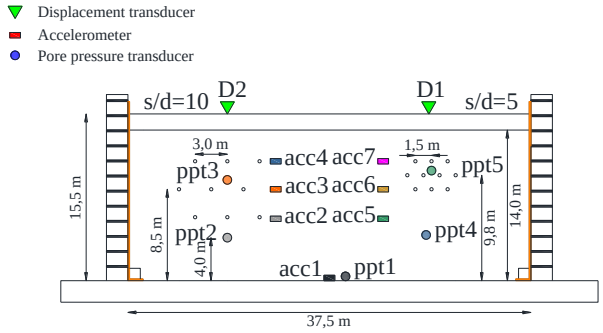

Layouts of the model reproduced in Plaxis 2D

The UBC3D-PML constitutive model is used to represent Ticino sand The properties adopted in the numerical analyses are summarized in following table.

Table with UBCSand parameters

Parameter	Description	Value	Unit
$N_{1,60}$	SPT number	12.7	-
K_G^e	elastic shear modulus	1011	-
K_B^e	elastic bulk modulus	1685	-
K_G^p	plastic shear modulus	588	-
m_e	elastic stress dependency parameter	0.5	-
n_e	elastic stress dependency parameter	0.5	-
n_p	plastic stress dependency parameter	0.4	-
ϕ_{cv}	critical state friction angle	33	°
ϕ_{peak}	peak state friction angle	34.3	°
R_f	failure ratio	0.75	-
ν	Poisson coefficient	0.25	-

This project has received funding from the European Union's Horizon 2020 research and innovation programme under grant agreement No. 700748

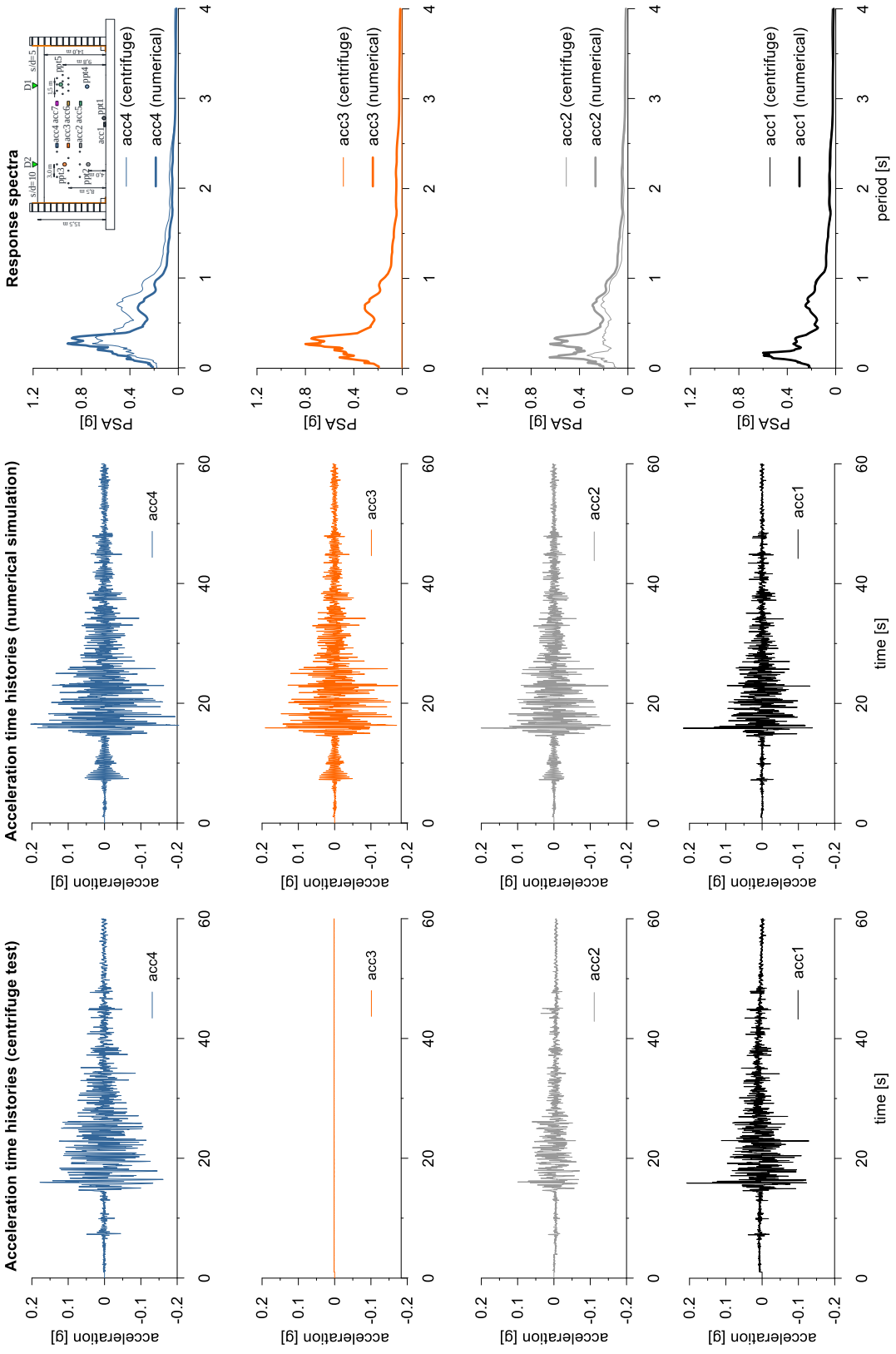

This project has received funding from the European Union's Horizon 2020 research and innovation programme under grant agreement No. 700748

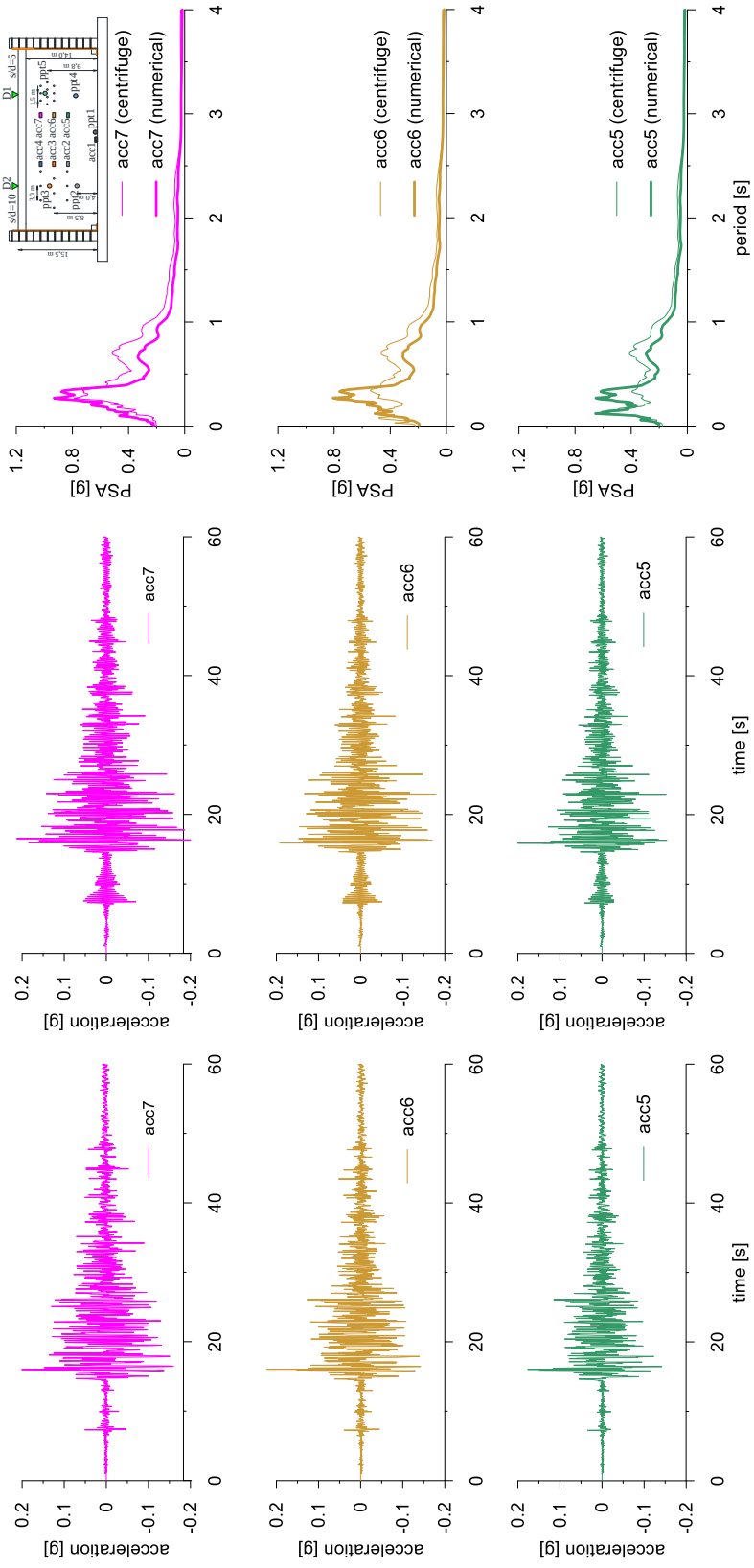

This project has received funding from the European Union's Horizon 2020 research and innovation programme under grant agreement No. 700748

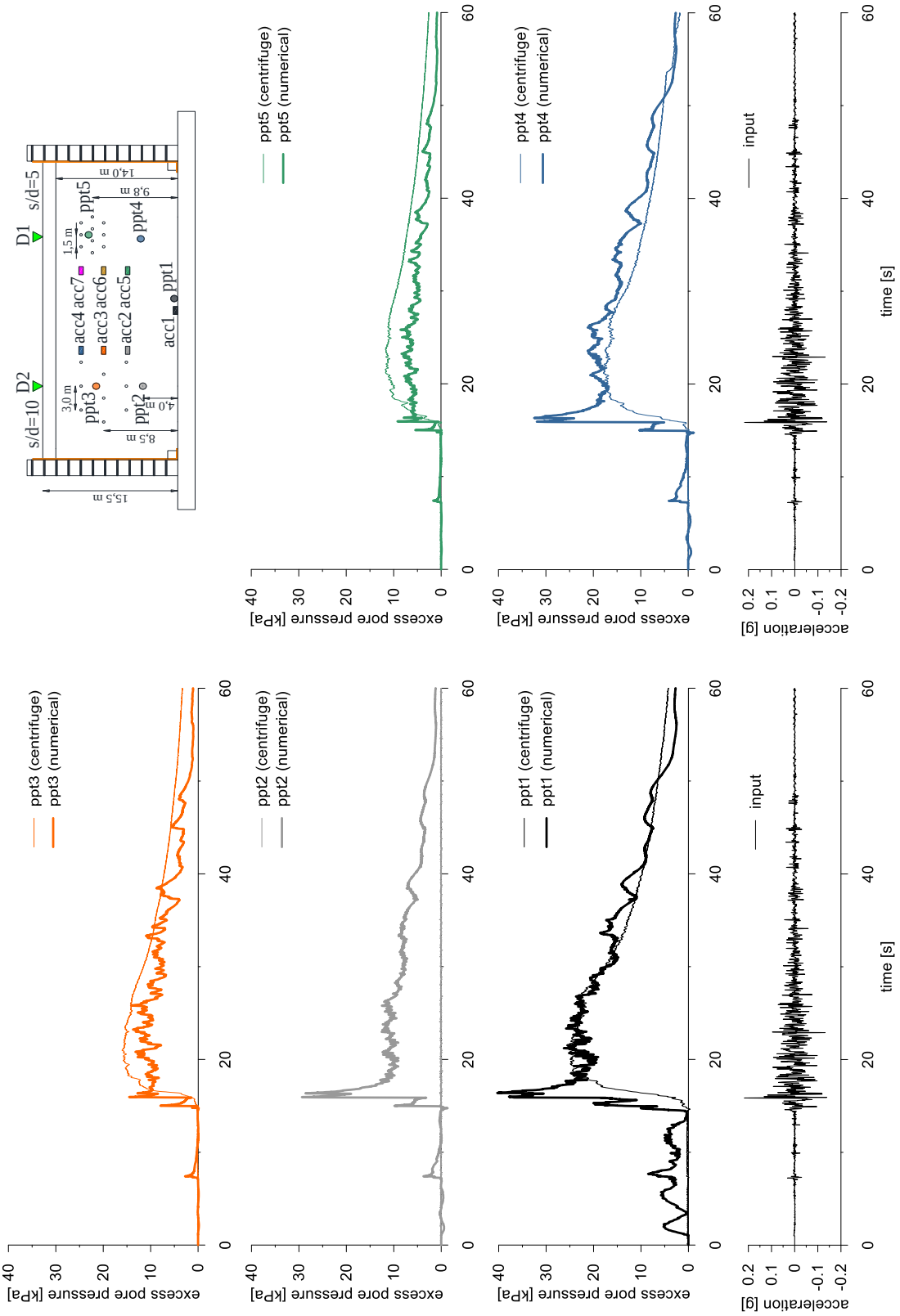

This project has received funding from the European Union's Horizon 2020 research and innovation programme under grant agreement No. 700748

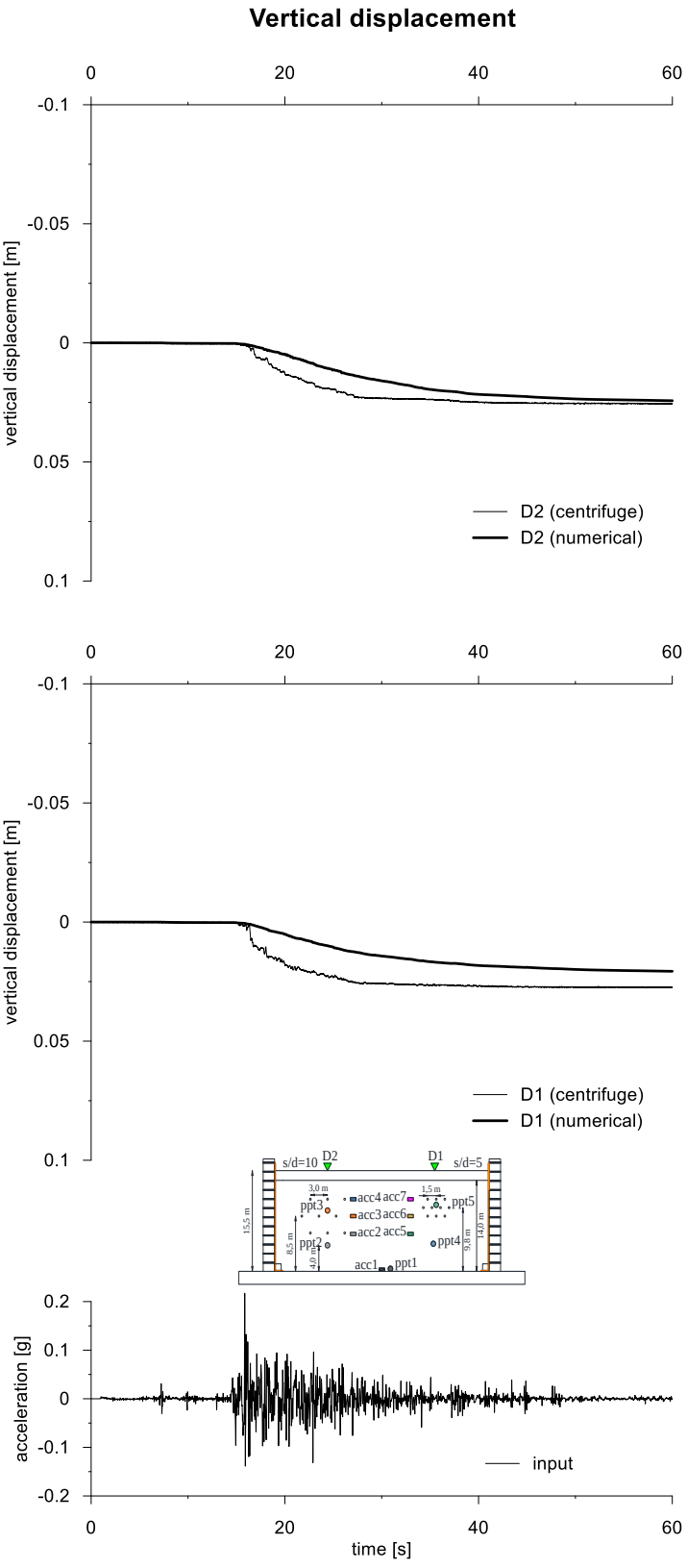

This project has received funding from the European Union's Horizon 2020 research and innovation programme under grant agreement No. 700748

5.2.2 PM4SAND

5.2.2.1 ID: DF_HD_TC_PM4_31

The model consists of a homogenous soil profile of Ticino sand and upper clay layer with the application of horizontal drains mitigation technique. The ground motion applied was the number 31.

ID: DF_HD_TC_PM4_31	TEST: M2_S1_HD1-2_GM31

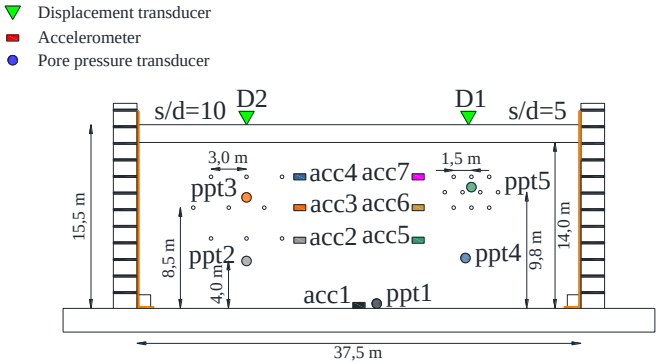

Layouts of the model reproduced in Plaxis 2D

The PM4Sand constitutive model is used to represent Ticino sand The properties adopted in the numerical analyses are summarized in following table.

Table with PM4Sand parameters

Parameter	Description	Value	Unit
D_{R0}	Initial relative density	0.52	-
G_0	shear modulus coefficient	650	-
hp_0	contraction rate parameter	0.1	-
p_A	atmospheric pressure	101.3	kN/m^2
e_{max}	maximum void ratio	0.923	-
e_{min}	minimum void ratio	0.574	-
n_b	bounding surface parameter	0.5	-
n_d	dilatancy surface parameter	0.1	-
ϕ_{cv}	critical state friction angle	33	°
nu	Poisson's ratio	0.3	-
Q	critical state line parameter	8	-
R	critical state line parameter	1.2	-

This project has received funding from the European Union's Horizon 2020 research and innovation programme under grant agreement No. 700748

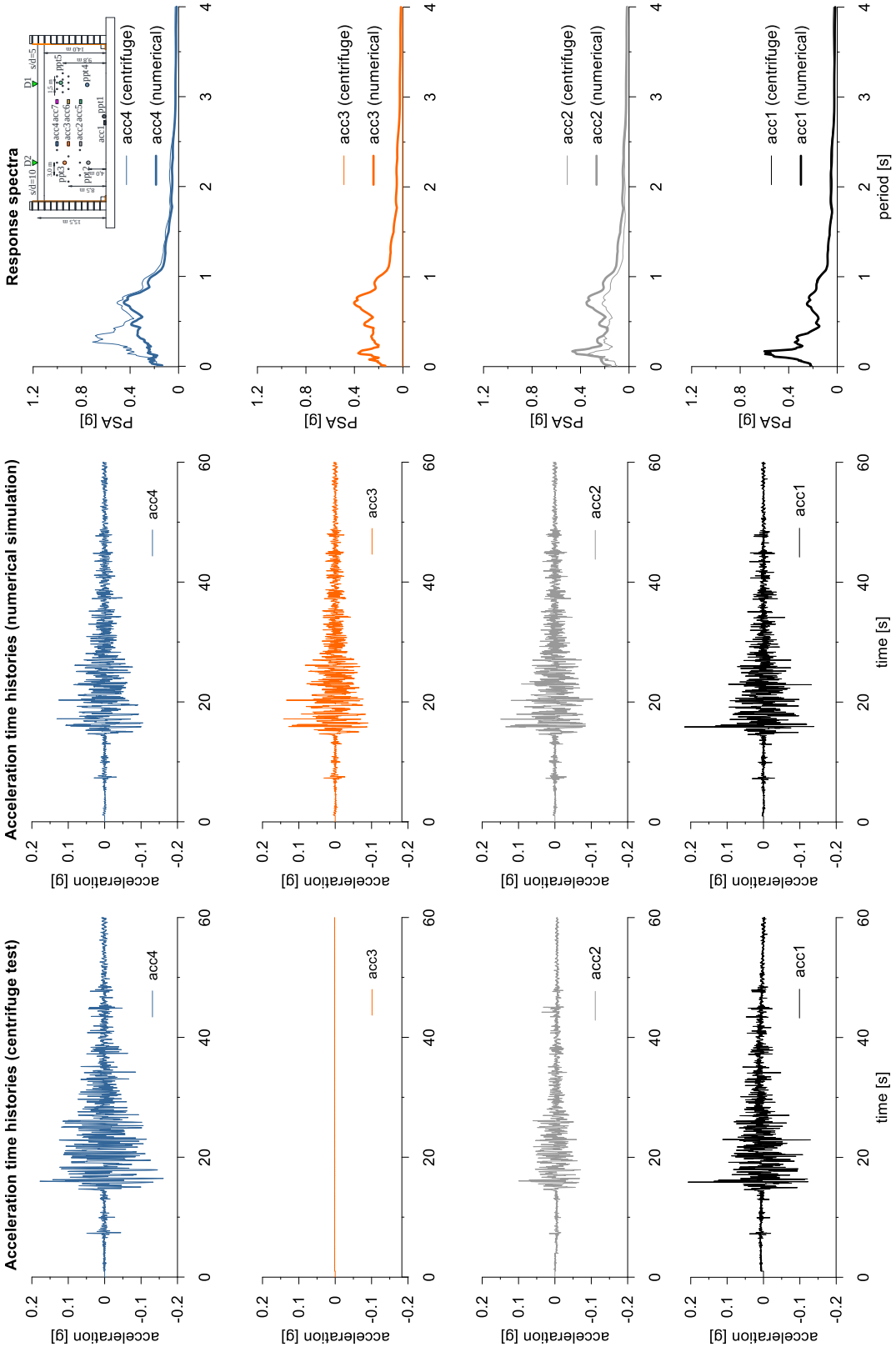

This project has received funding from the European Union's Horizon 2020 research and innovation programme under grant agreement No. 700748

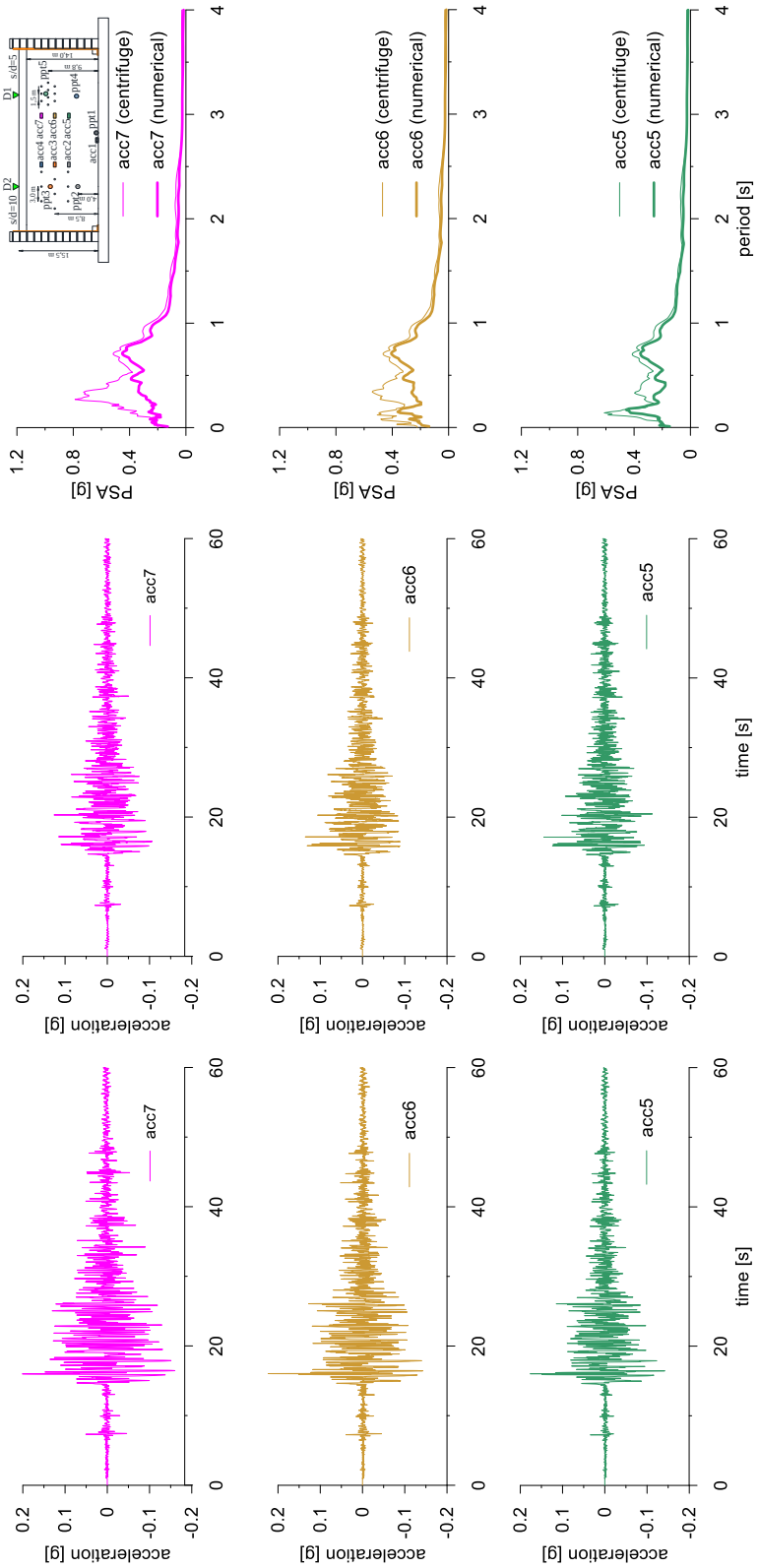

This project has received funding from the European Union's Horizon 2020 research and innovation programme under grant agreement No. 700748

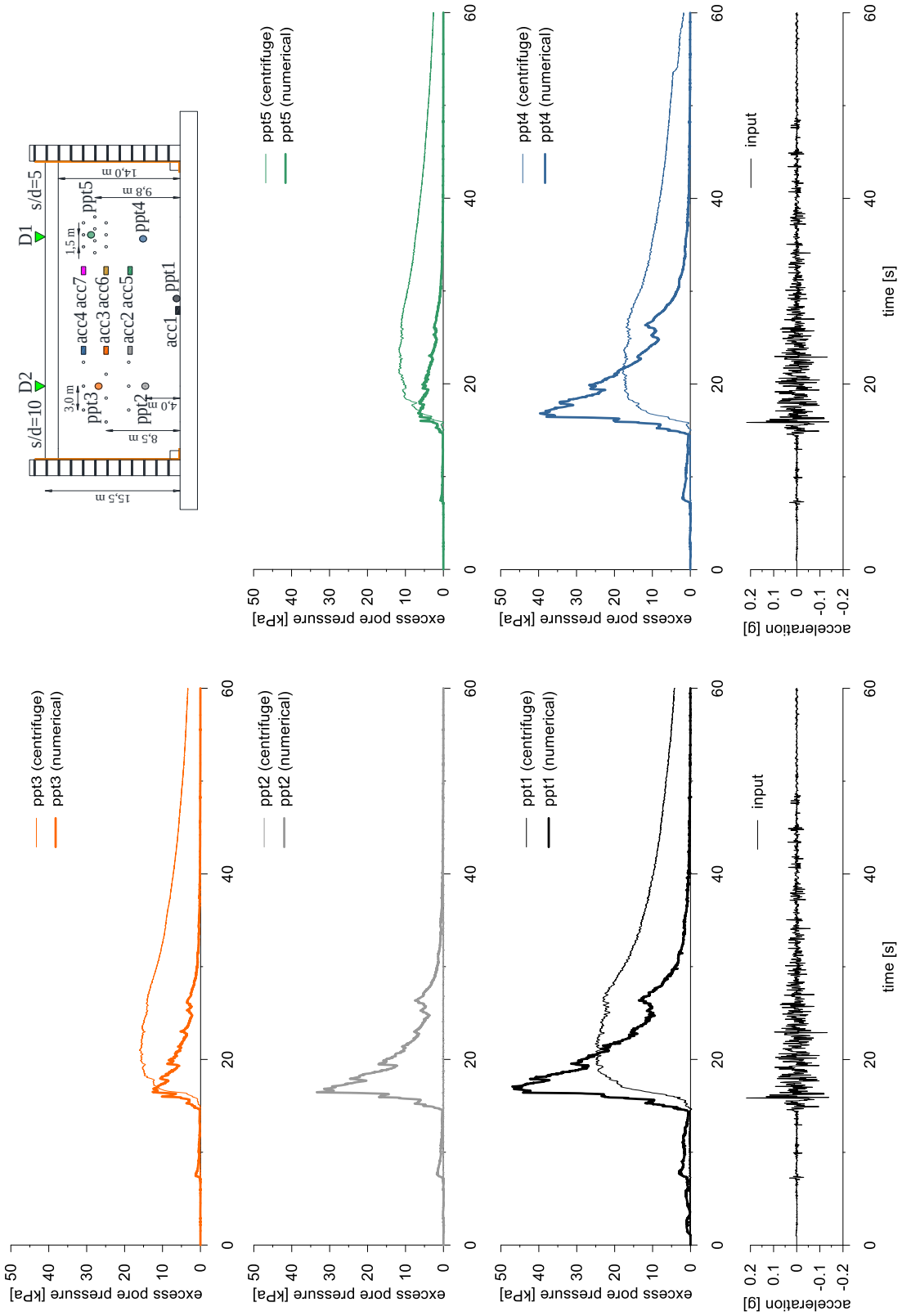

This project has received funding from the European Union's Horizon 2020 research and innovation programme under grant agreement No. 700748

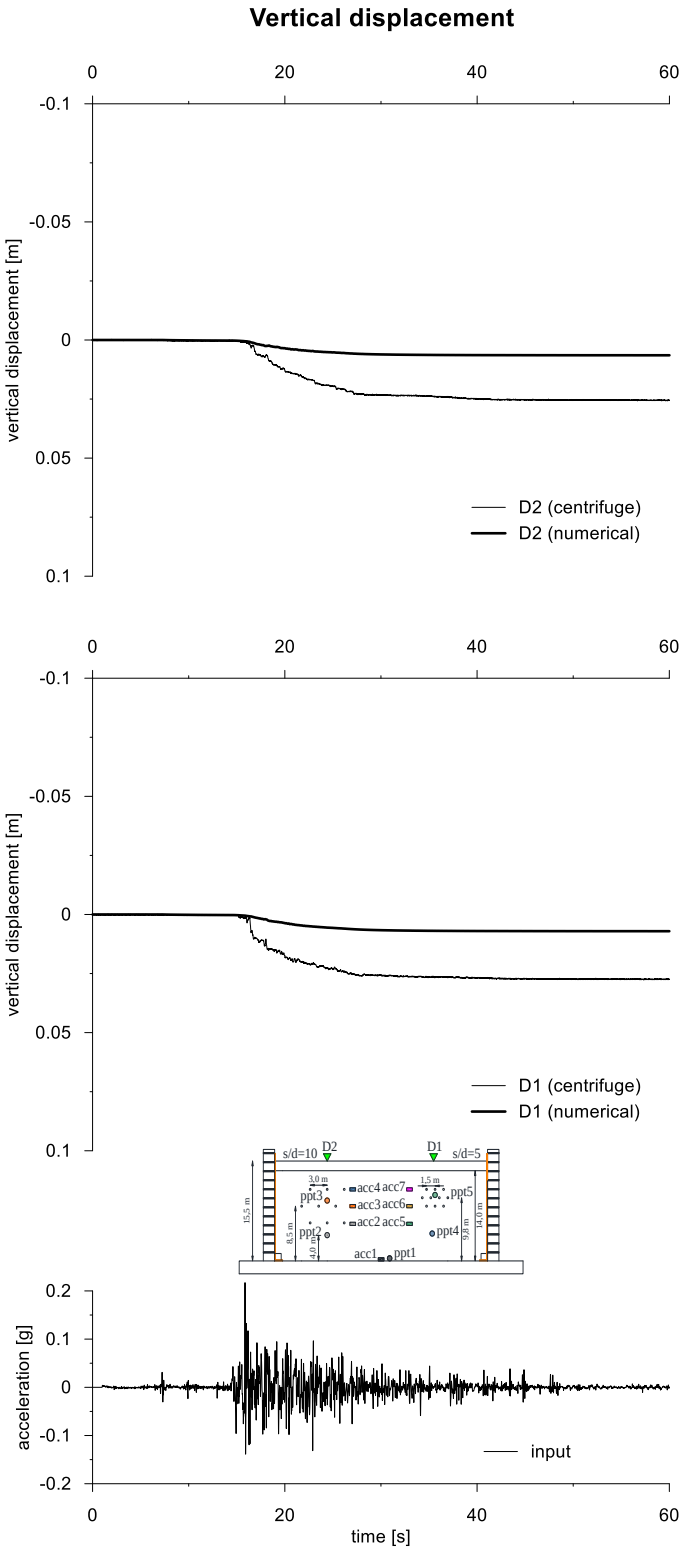

This project has received funding from the European Union's Horizon 2020 research and innovation programme under grant agreement No. 700748

5.3 HORIZONTAL DRAINS UNDERNEATH A STRUCTURE

5.3.1 UBCSAND

5.3.1.1 ID: SS_HD_TC_UBC_31+

The model consists of a liquefiable layer of Ticino sand with a structure model and horizontal drains technique. The ground motion applied was the number 31+.

ID: SS_HD_TC_UBC_31+	TEST: M1F_S1_HD1_GM31+

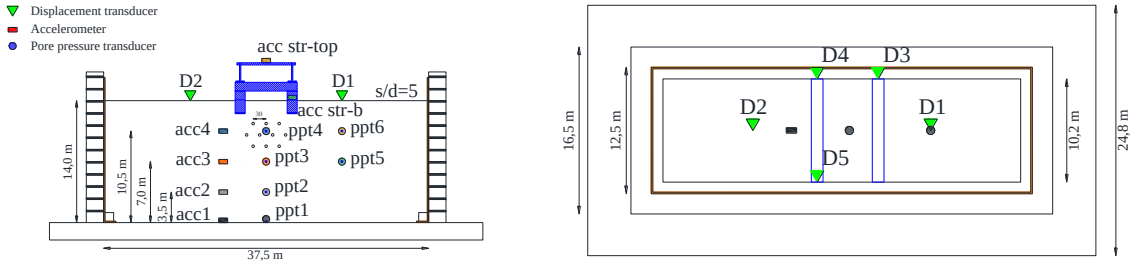

Layouts of the model reproduced in Plaxis 2D

The UBC3D-PML constitutive model is used to represent Ticino sand. The properties adopted in the numerical analyses are summarized in Table 1.

Table with UBCSand parameters

Parameter	Description	Value	Unit
$N_{1,60}$	SPT number	12.1	-
K_G^e	elastic shear modulus	994	-
K_B^e	elastic bulk modulus	1657	-
K_G^p	plastic shear modulus	534	-
m_e	elastic stress dependency parameter	0.5	-
n_e	elastic stress dependency parameter	0.5	-
n_p	plastic stress dependency parameter	0.4	-
ϕ_{cv}	critical state friction angle	33	°
ϕ_{peak}	peak state friction angle	34.2	°
R_f	failure ratio	0.76	-
ν	Poisson coefficient	0.25	-

This project has received funding from the European Union's Horizon 2020 research and innovation programme under grant agreement No. 700748

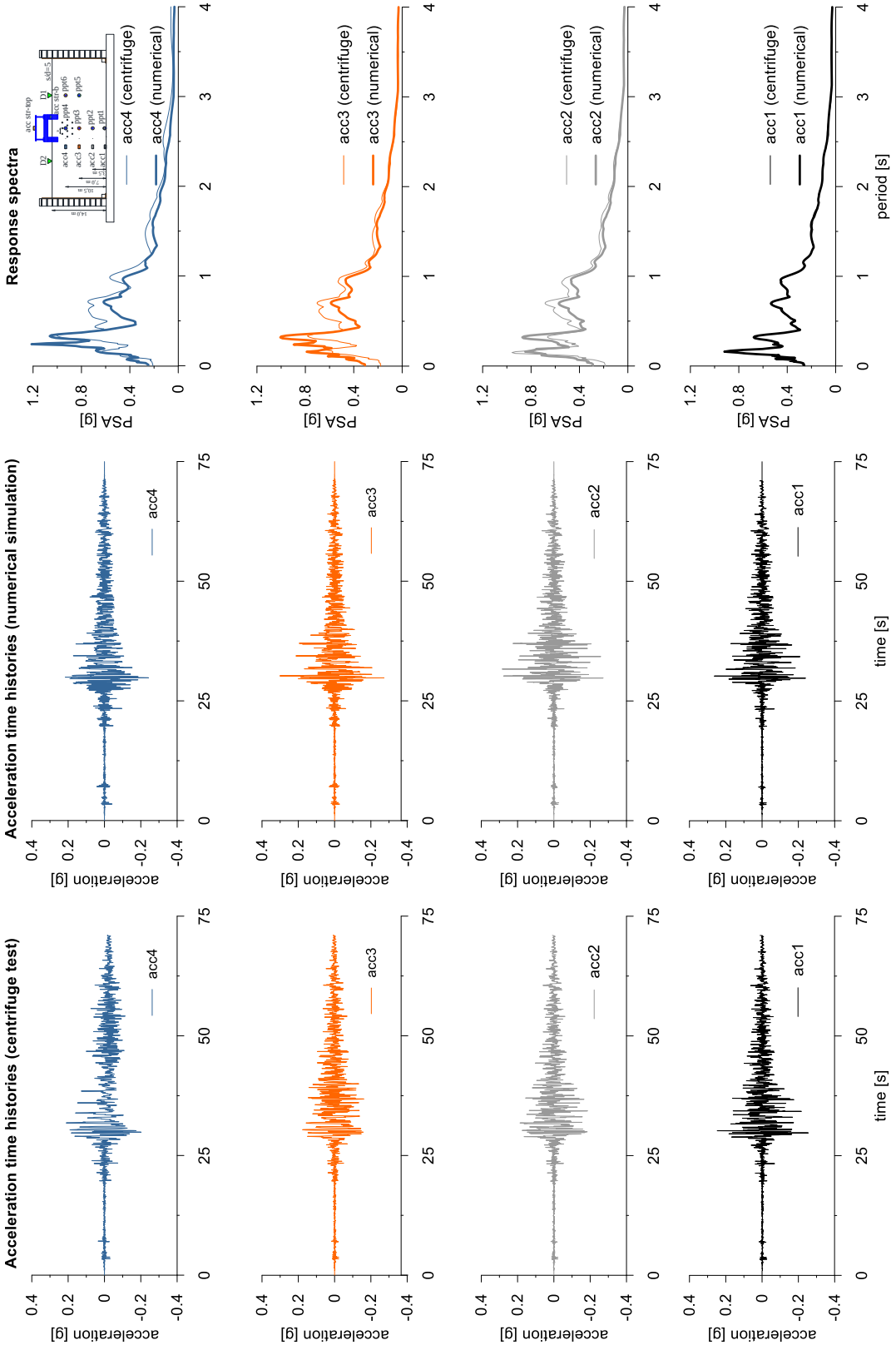

This project has received funding from the European Union's Horizon 2020 research and innovation programme under grant agreement No. 700748

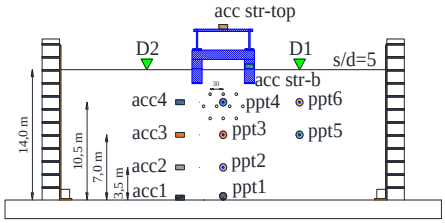

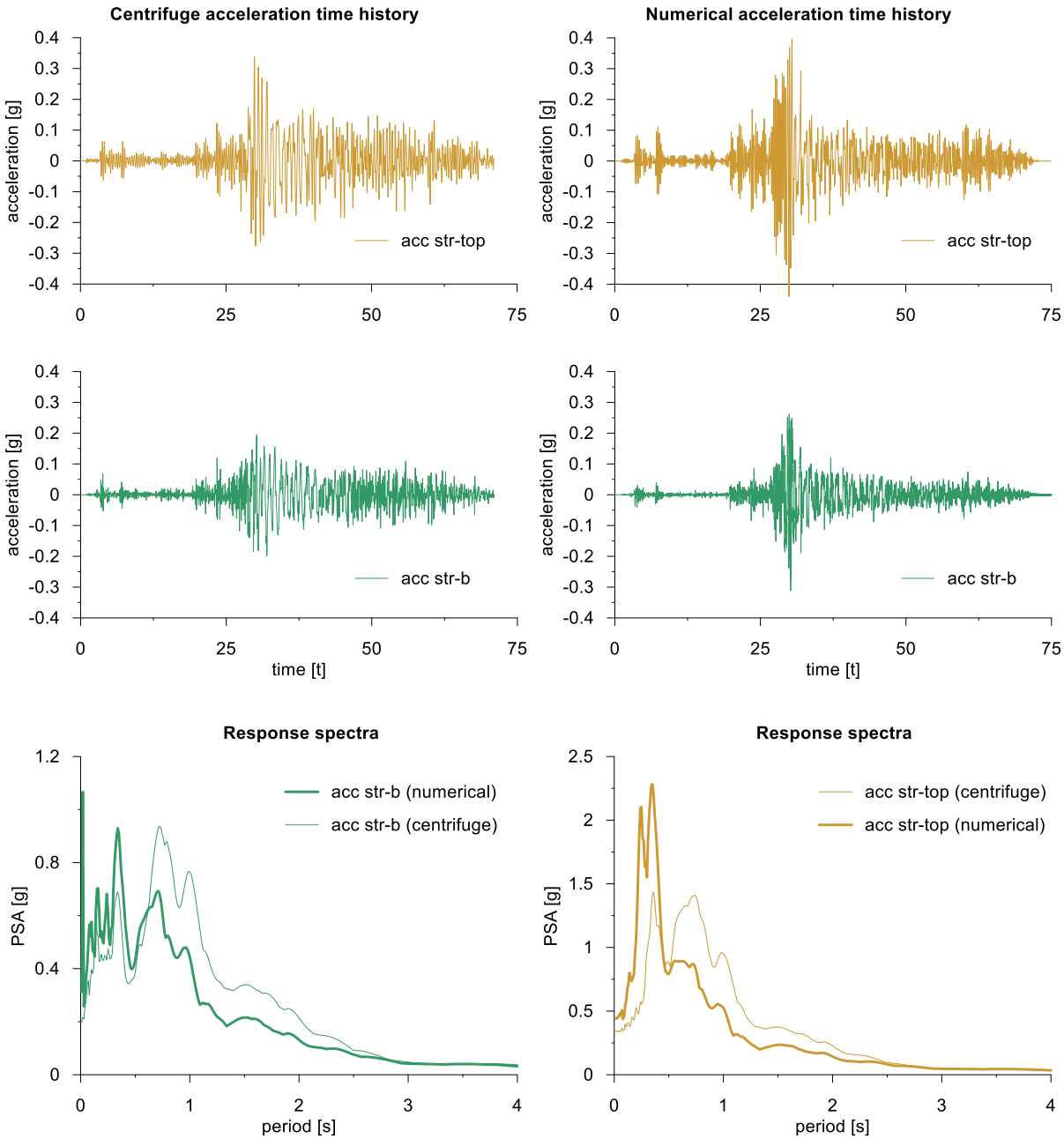

This project has received funding from the European Union's Horizon 2020 research and innovation programme under grant agreement No. 700748

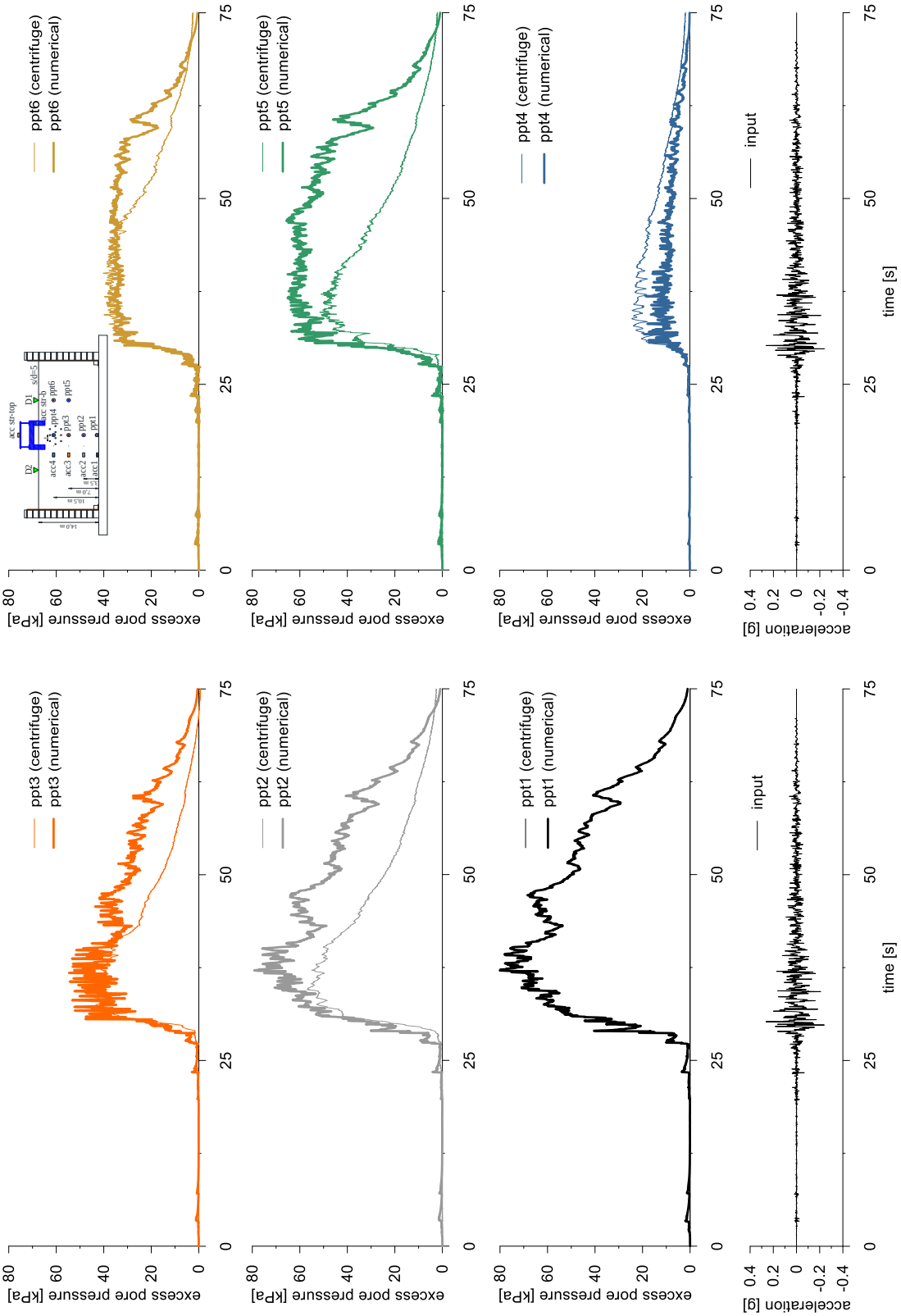

This project has received funding from the European Union's Horizon 2020 research and innovation programme under grant agreement No. 700748

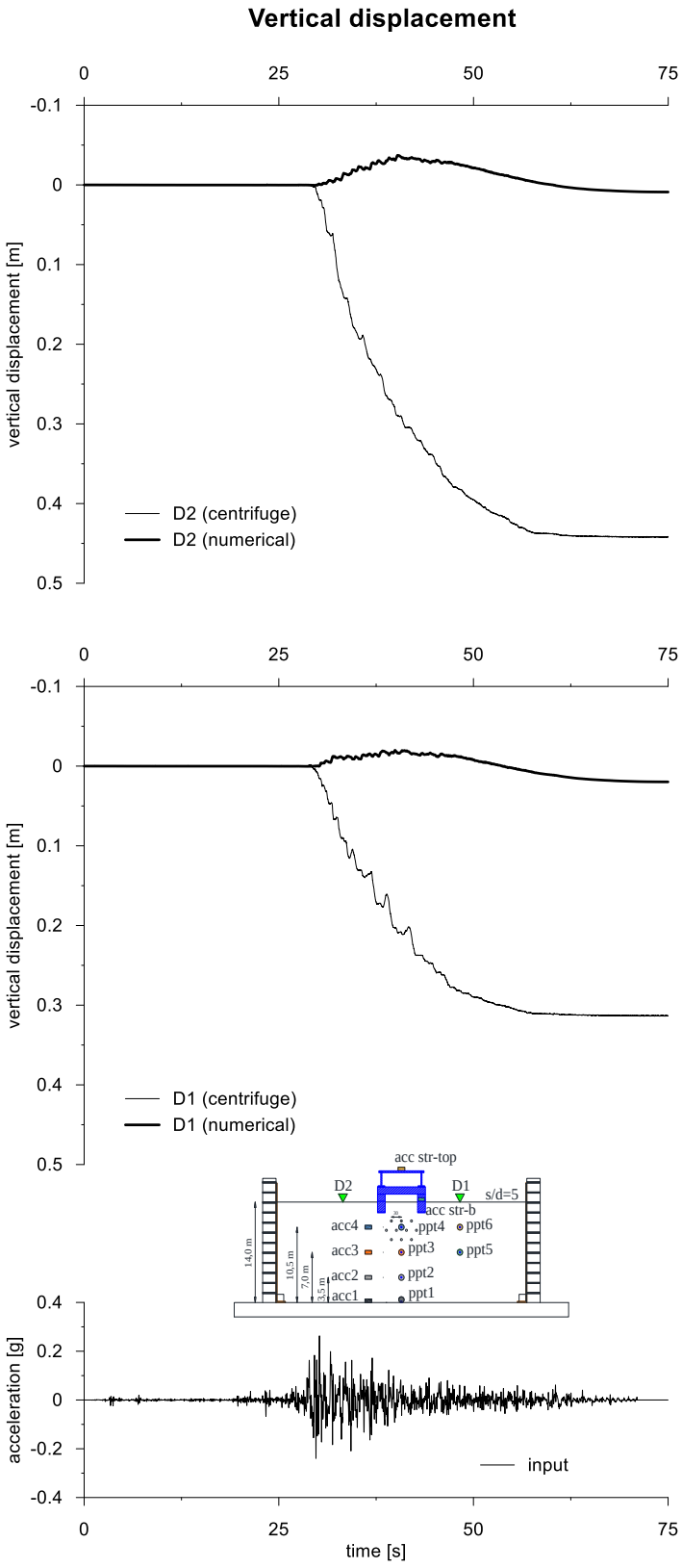

This project has received funding from the European Union's Horizon 2020 research and innovation programme under grant agreement No. 700748

Vertical displacement

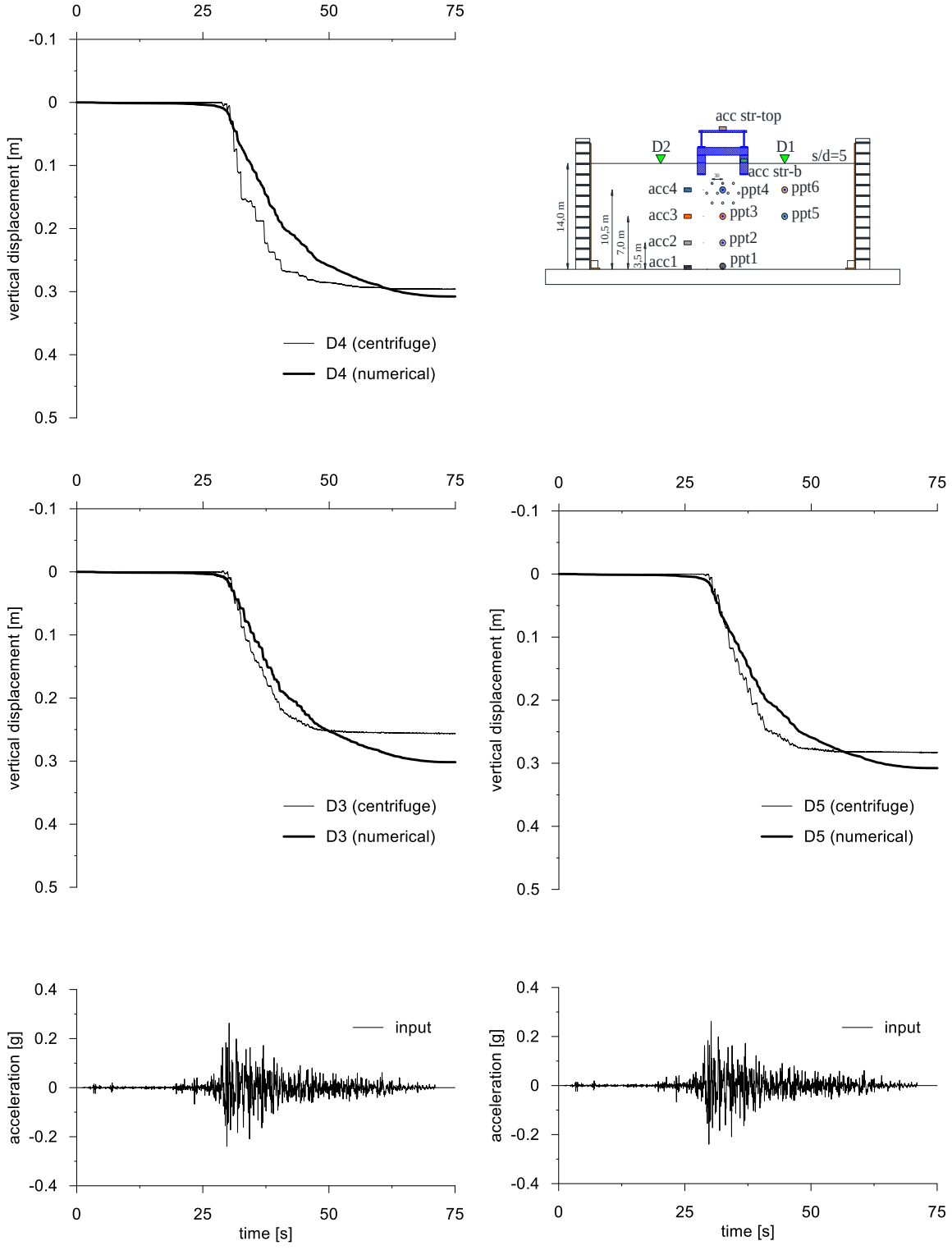

This project has received funding from the European Union's Horizon 2020 research and innovation programme under grant agreement No. 700748

5.3.2 PM4SAND

5.3.2.1 ID: SS_HD_TC_PM4_31+

The model consists of a liquefiable layer of Ticino sand with a structure model and horizontal drains technique. The ground motion applied was the number 31+.

ID: SS_HD_TC_PM4_31+	TEST: M1F_S1_HD1_GM31+

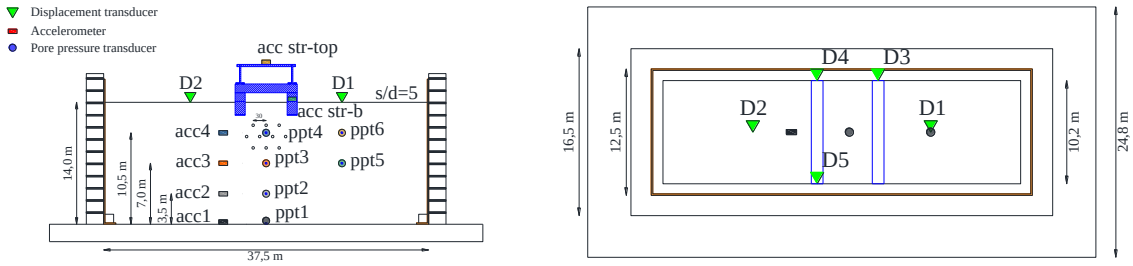

Layouts of the model reproduced in Plaxis 2D

The PM4SAND constitutive model is used to represent Ticino sand. The properties adopted in the numerical analyses are summarized in Table 1.

Table with PM4Sand parameters

Parameter	Description	Value	Unit
D_{R0}	Initial relative density	0.52	-
G_0	shear modulus coefficient	594	-
hp_0	contraction rate parameter	0.1	-
p_A	atmospheric pressure	101.3	kN/m^2
e_{max}	maximum void ratio	0.923	-
e_{min}	minimum void ratio	0.574	-
n_b	bounding surface parameter	0.5	-
n_d	dilatancy surface parameter	0.1	-
ϕ_{cv}	critical state friction angle	33	°
nu	Poisson's ratio	0.3	-
Q	critical state line parameter	8	-
R	critical state line parameter	1.2	-

This project has received funding from the European Union's Horizon 2020 research and innovation programme under grant agreement No. 700748

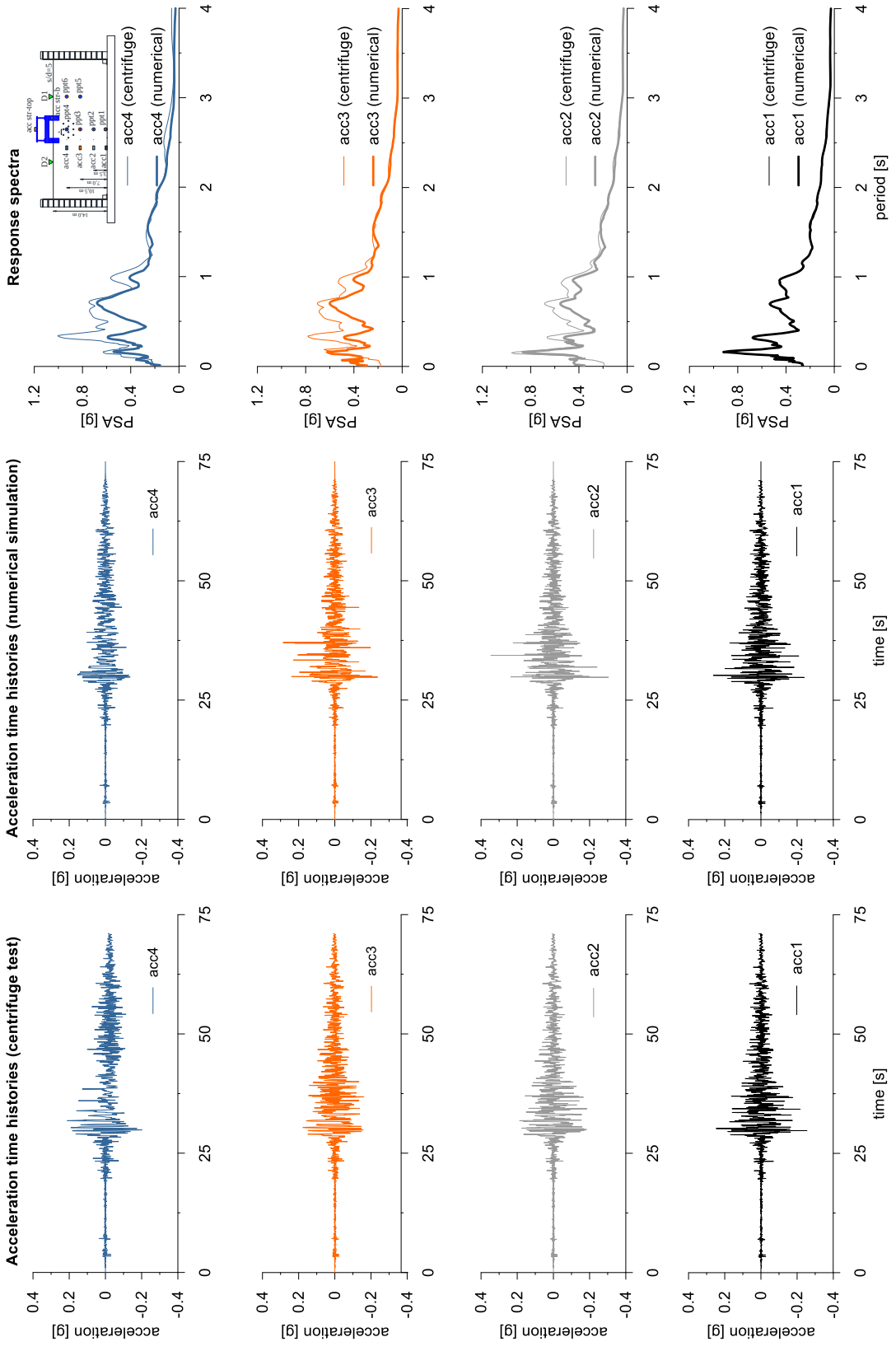

This project has received funding from the European Union's Horizon 2020 research and innovation programme under grant agreement No. 700748

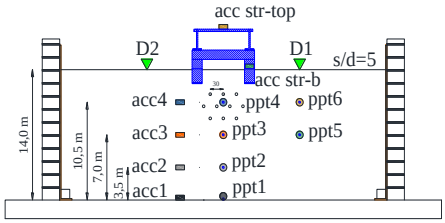

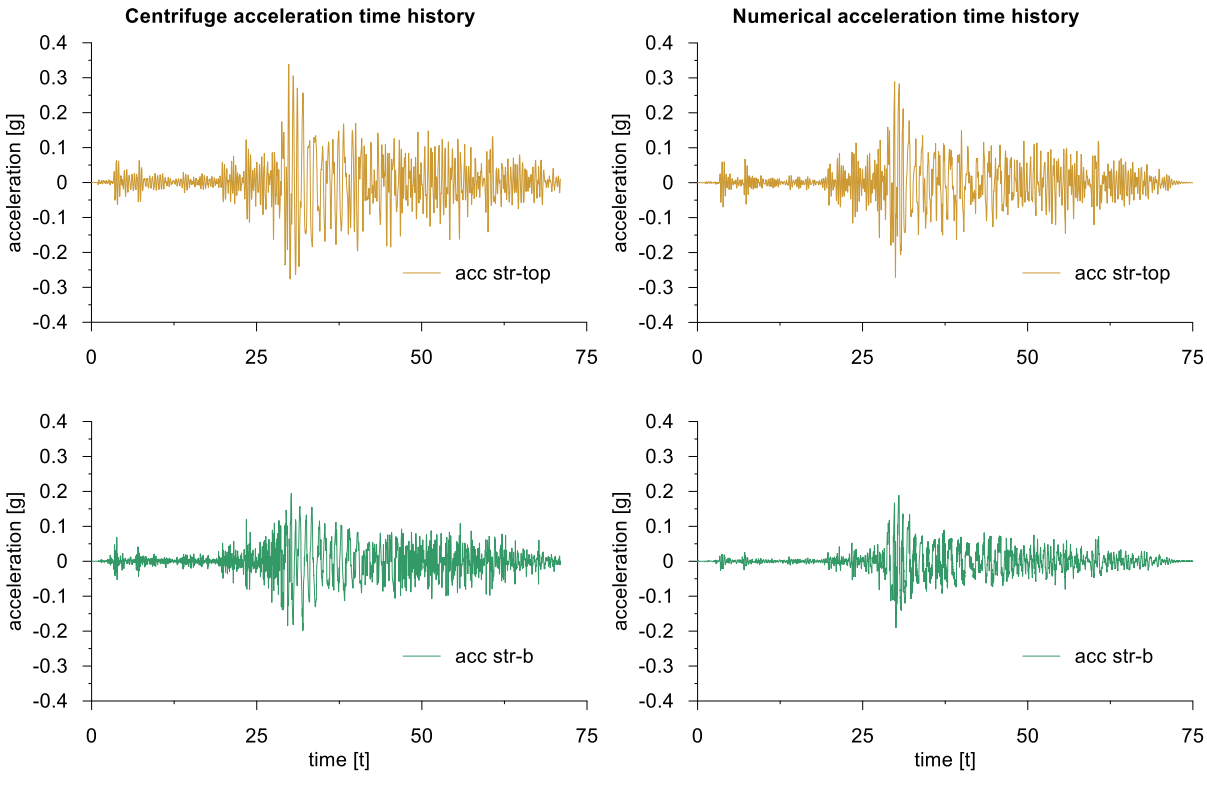

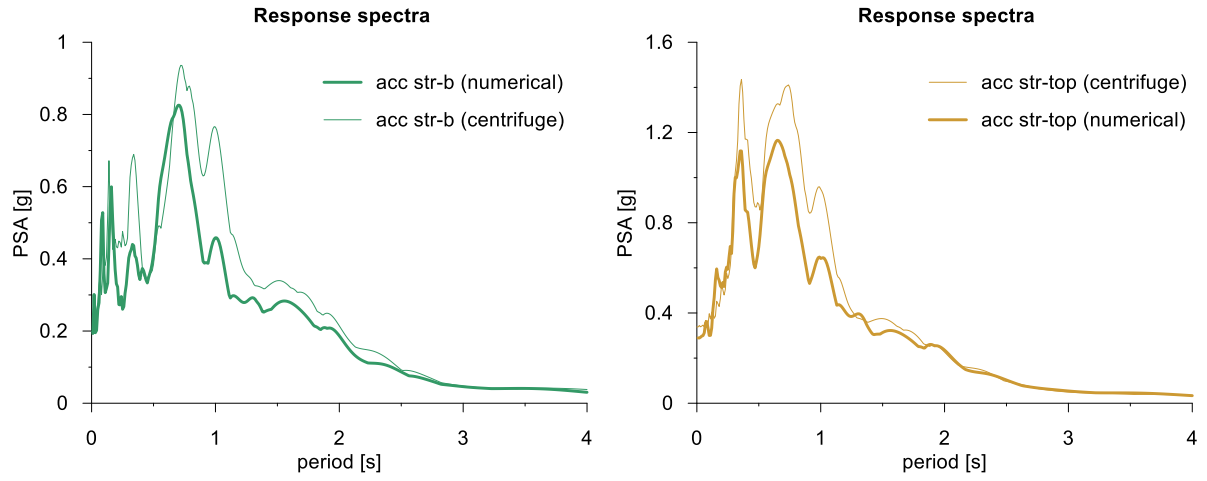

This project has received funding from the European Union's Horizon 2020 research and innovation programme under grant agreement No. 700748

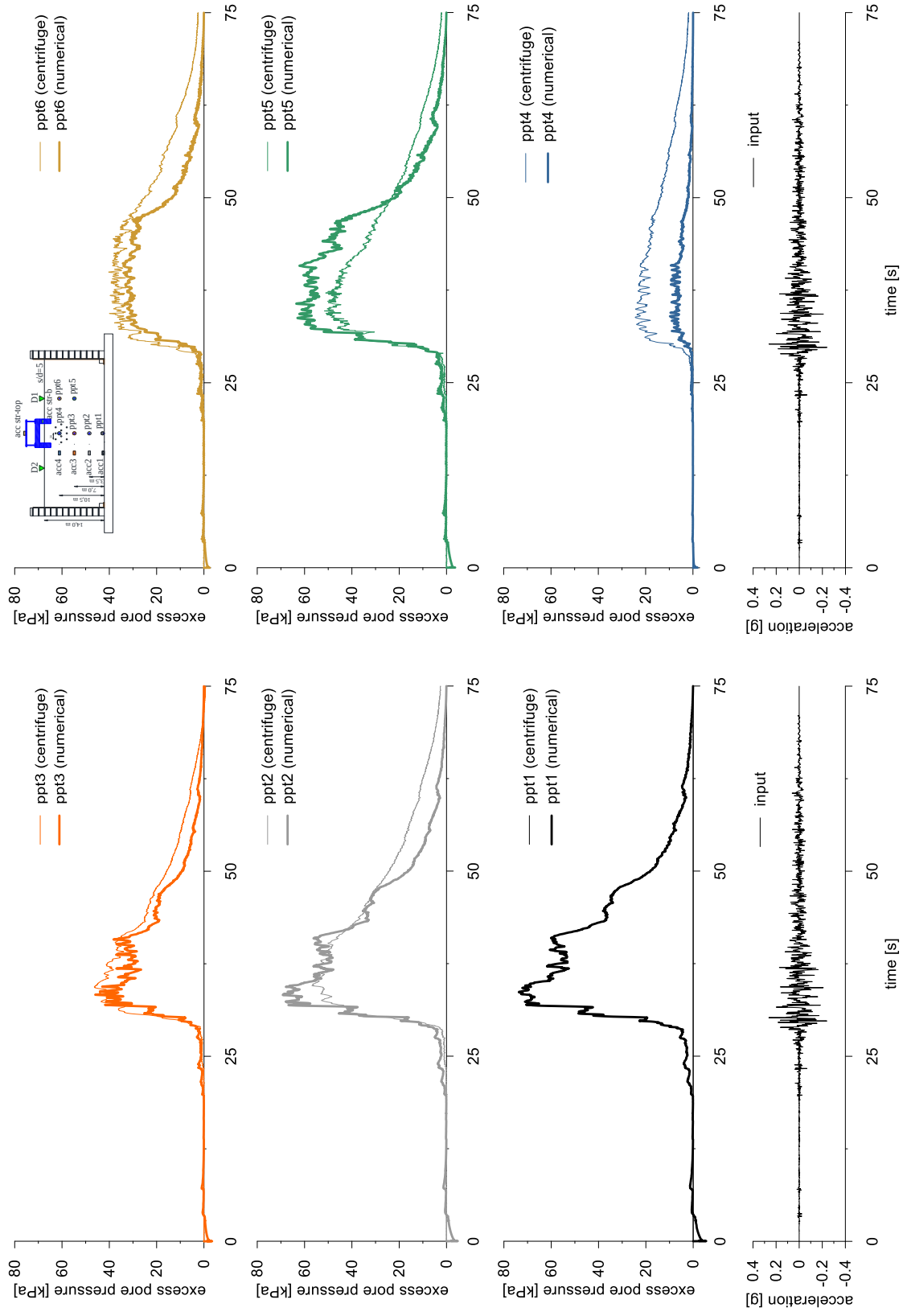

This project has received funding from the European Union's Horizon 2020 research and innovation programme under grant agreement No. 700748

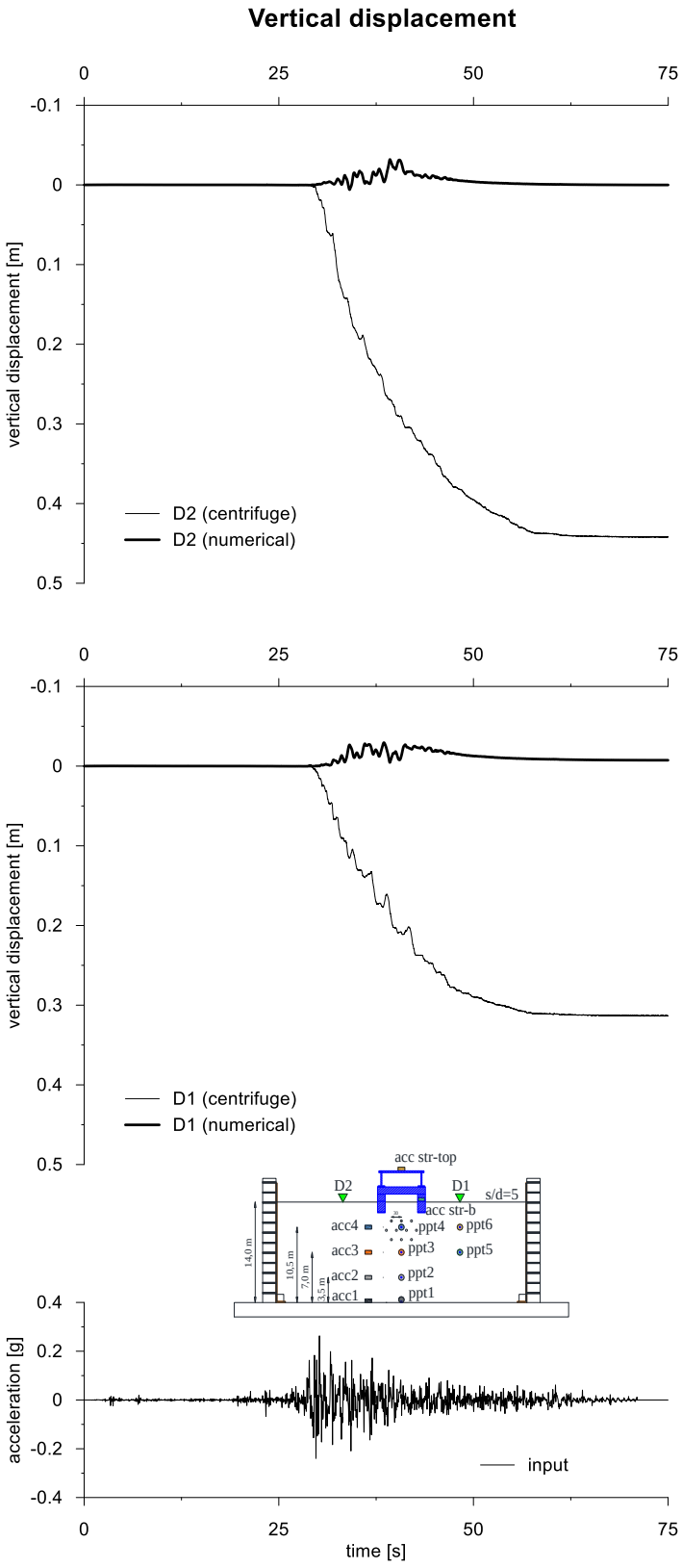

This project has received funding from the European Union's Horizon 2020 research and innovation programme under grant agreement No. 700748

Vertical displacement

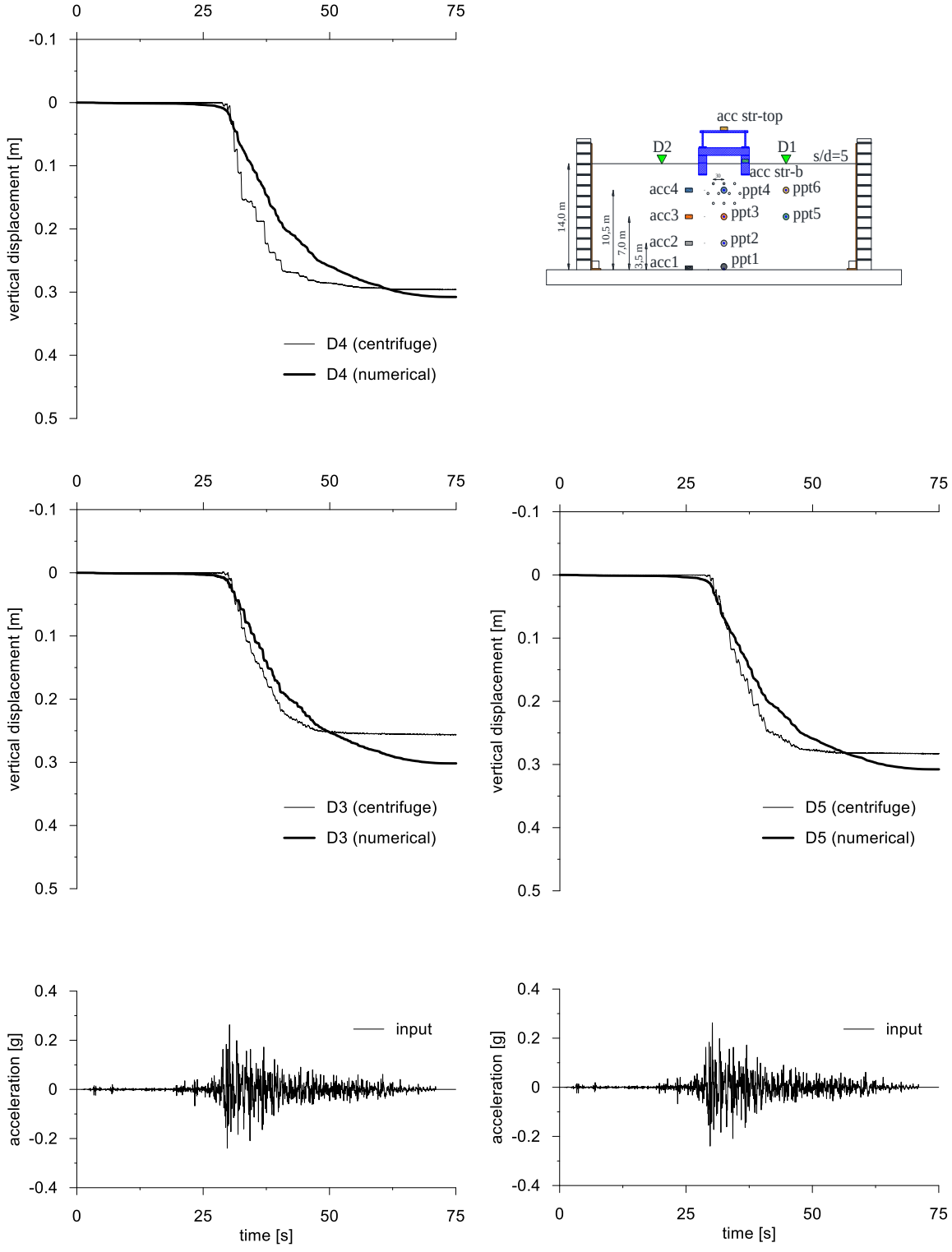

This project has received funding from the European Union's Horizon 2020 research and innovation programme under grant agreement No. 700748

5.4 INDUCED PARTIAL SATURATION ON THE HOMOGENEOUS PROFILE IN FREE FIELD CONDITIONS

5.4.1 PM4SAND

5.4.1.1 ID: SF_IPS_TC_PM4_31

The model consists of a homogenous soil profile of Ticino sand with application of induced partial saturation technique. The ground motion applied was the number 31.

ID: SF_IPS_TC_PM4_31	TEST: M1_S1_IPS4_GM31

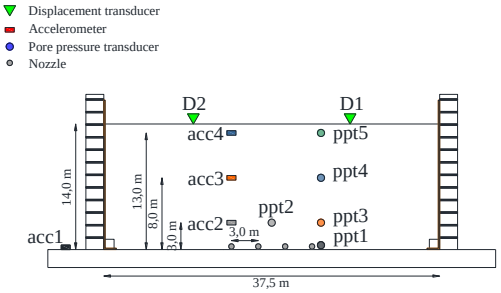

Layouts of the model reproduced in Plaxis 2D

The PM4SAND constitutive model is used to represent Ticino sand The properties adopted in the numerical analyses are summarized in Table 1.

Table with PM4Sand parameters

Parameter	Description	Value	Unit
D_{R0}	Initial relative density	0.52	-
G_0	shear modulus coefficient	594	-
hp_0	contraction rate parameter	0.1	-
p_A	atmospheric pressure	101.3	kN/m^2
e_{max}	maximum void ratio	0.923	-
e_{min}	minimum void ratio	0.574	-
n_b	bounding surface parameter	0.5	-
n_d	dilatancy surface parameter	0.1	-
ϕ_{cv}	critical state friction angle	33	°
nu	Poisson's ratio	0.3	-
Q	critical state line parameter	8	-
R	critical state line parameter	1.2	-

This project has received funding from the European Union's Horizon 2020 research and innovation programme under grant agreement No. 700748

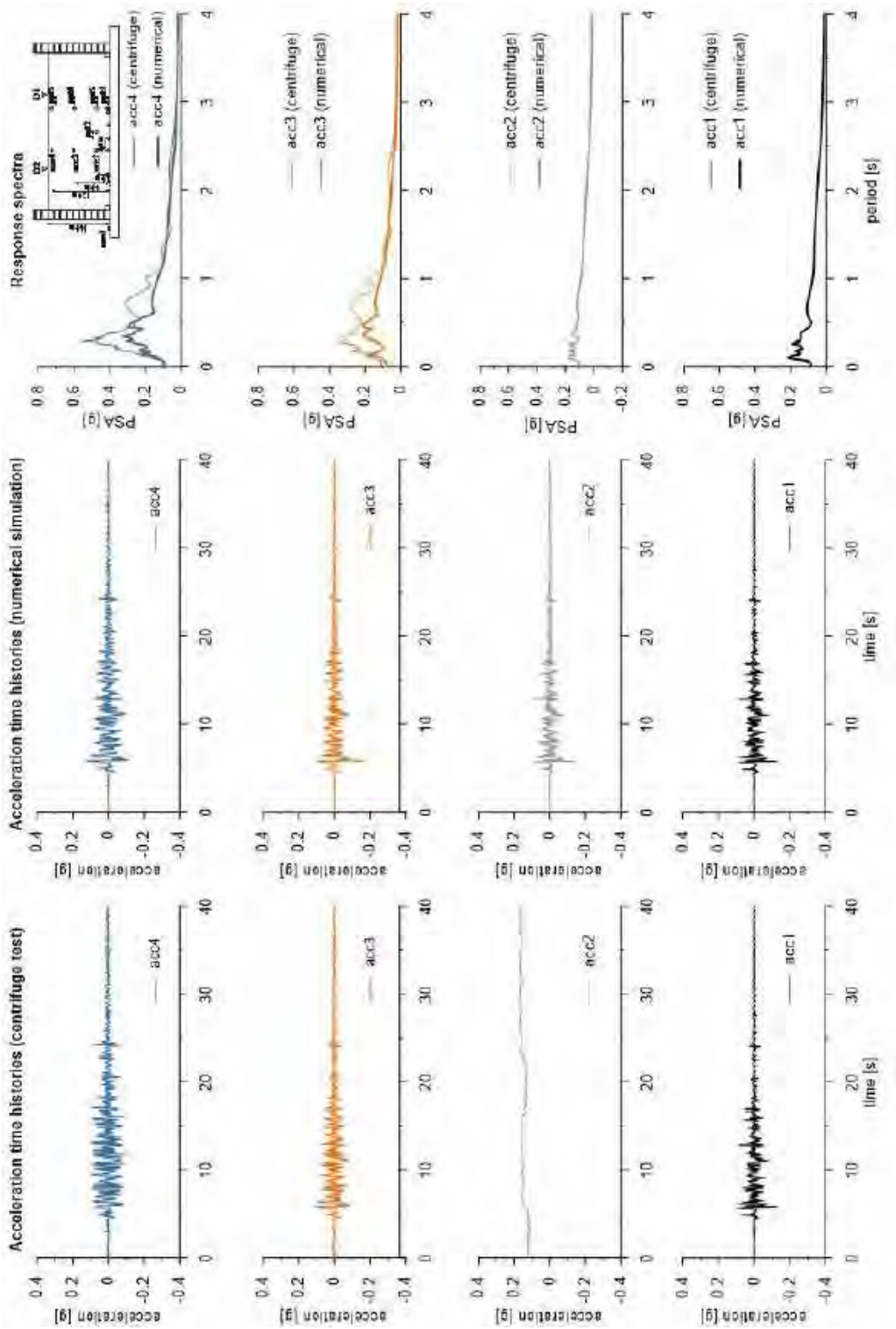

This project has received funding from the European Union's Horizon 2020 research and innovation programme under grant agreement No. 700748

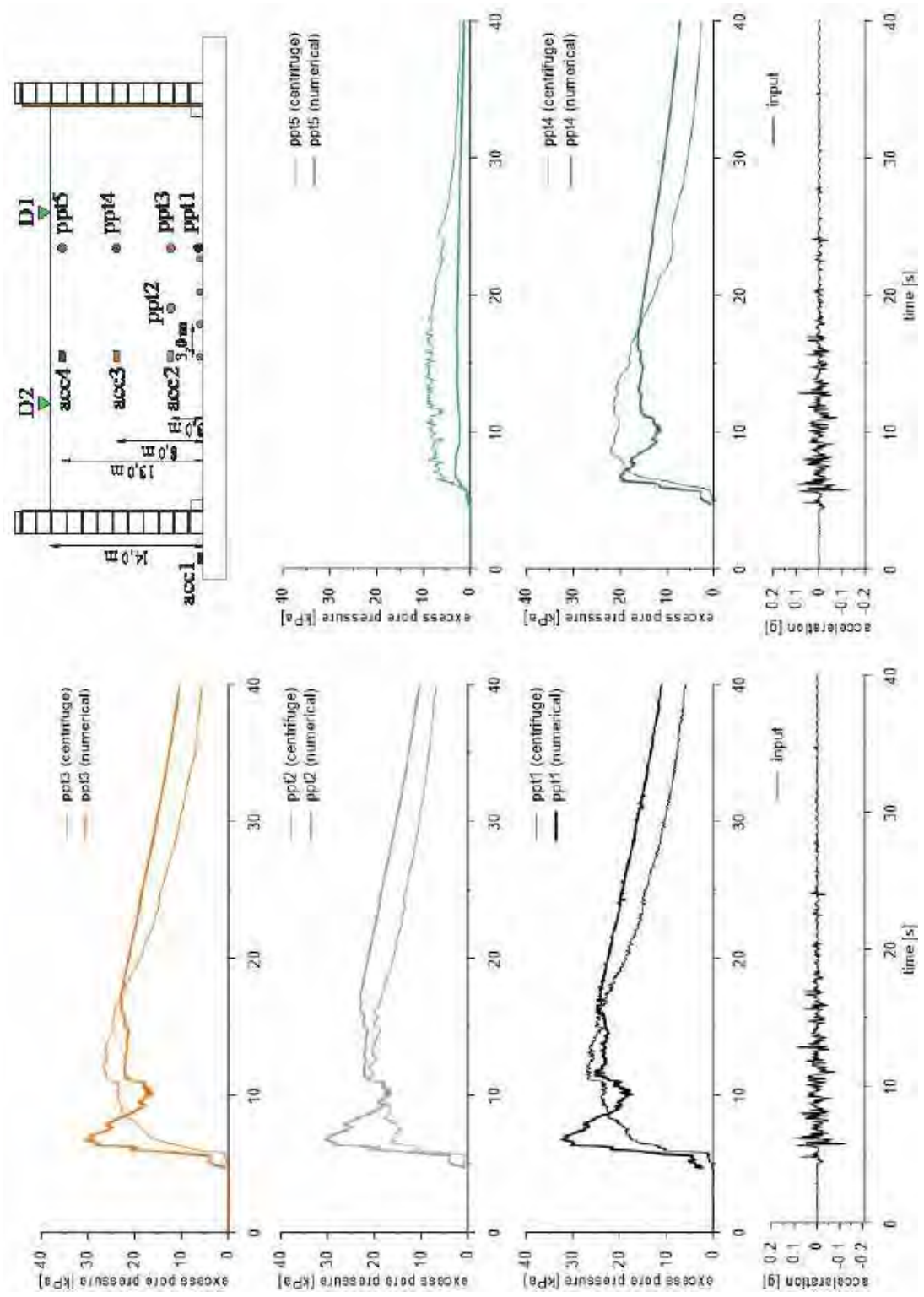

This project has received funding from the European Union's Horizon 2020 research and innovation programme under grant agreement No. 700748

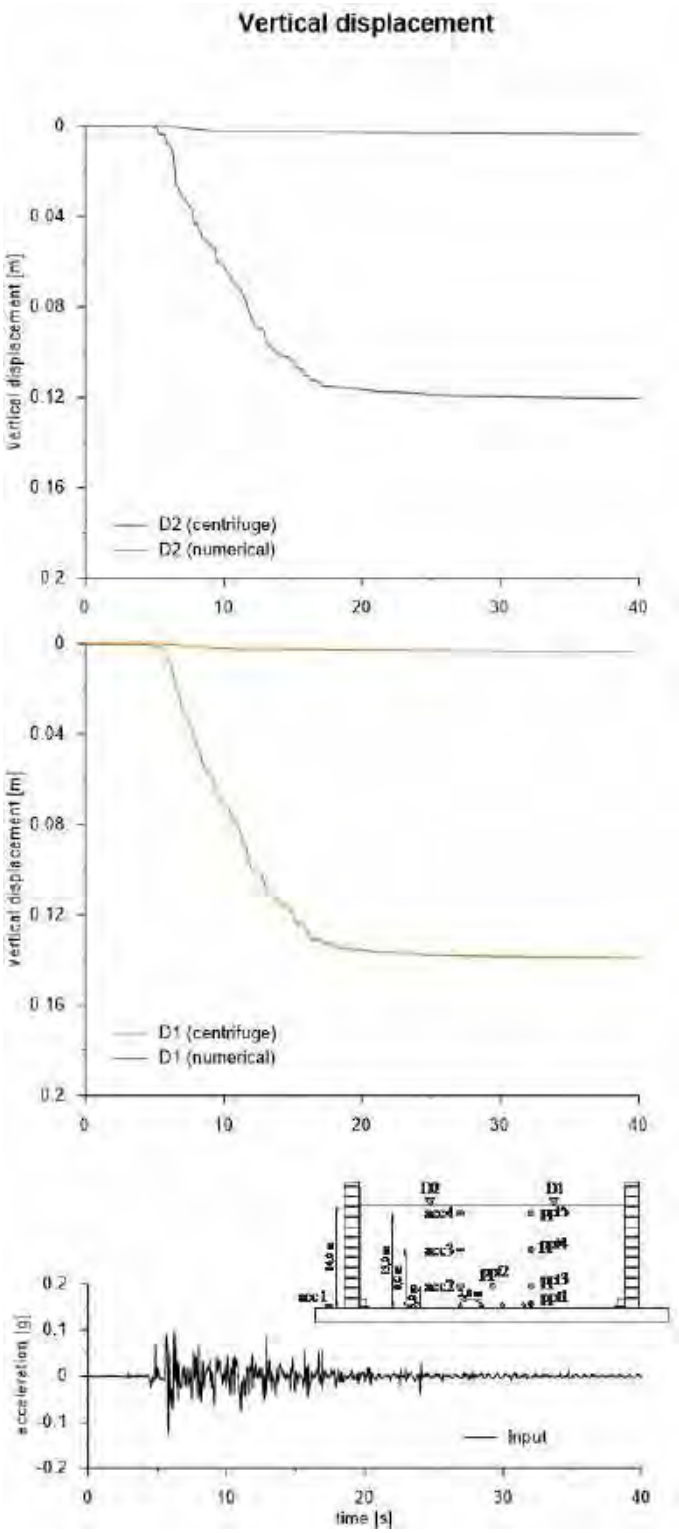

This project has received funding from the European Union's Horizon 2020 research and innovation programme under grant agreement No. 700748

5.4.1.2 ID: SF_IPS_TC_PM4_31+

The model consists of a homogenous soil profile of Ticino sand with application of induced partial saturation technique. The ground motion applied was the number 31.

ID: SF_IPS_TC_PM4_31+	TEST: M1_S1_IPS4_GM31+

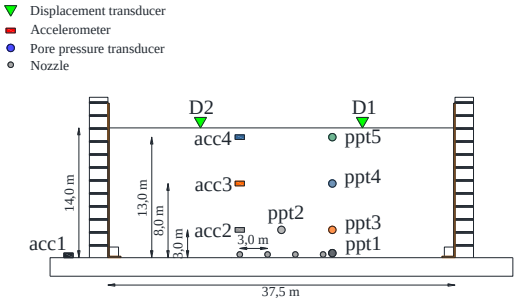

Layouts of the model reproduced in Plaxis 2D.

The PM4SAND constitutive model is used to represent Ticino sand The properties adopted in the numerical analyses are summarized in Table 1.

Table with PM4Sand parameters

Parameter	Description	Value	Unit
D_{R0}	Initial relative density	0.57	-
G_0	shear modulus coefficient	697	-
hp_0	contraction rate parameter	0.1	-
p_A	atmospheric pressure	101.3	kN/m^2
e_{max}	maximum void ratio	0.923	-
e_{min}	minimum void ratio	0.574	-
n_b	bounding surface parameter	0.5	-
n_d	dilatancy surface parameter	0.1	-
ϕ_{cv}	critical state friction angle	33	°
nu	Poisson's ratio	0.3	-
Q	critical state line parameter	8	-
R	critical state line parameter	1.2	-

This project has received funding from the European Union's Horizon 2020 research and innovation programme under grant agreement No. 700748

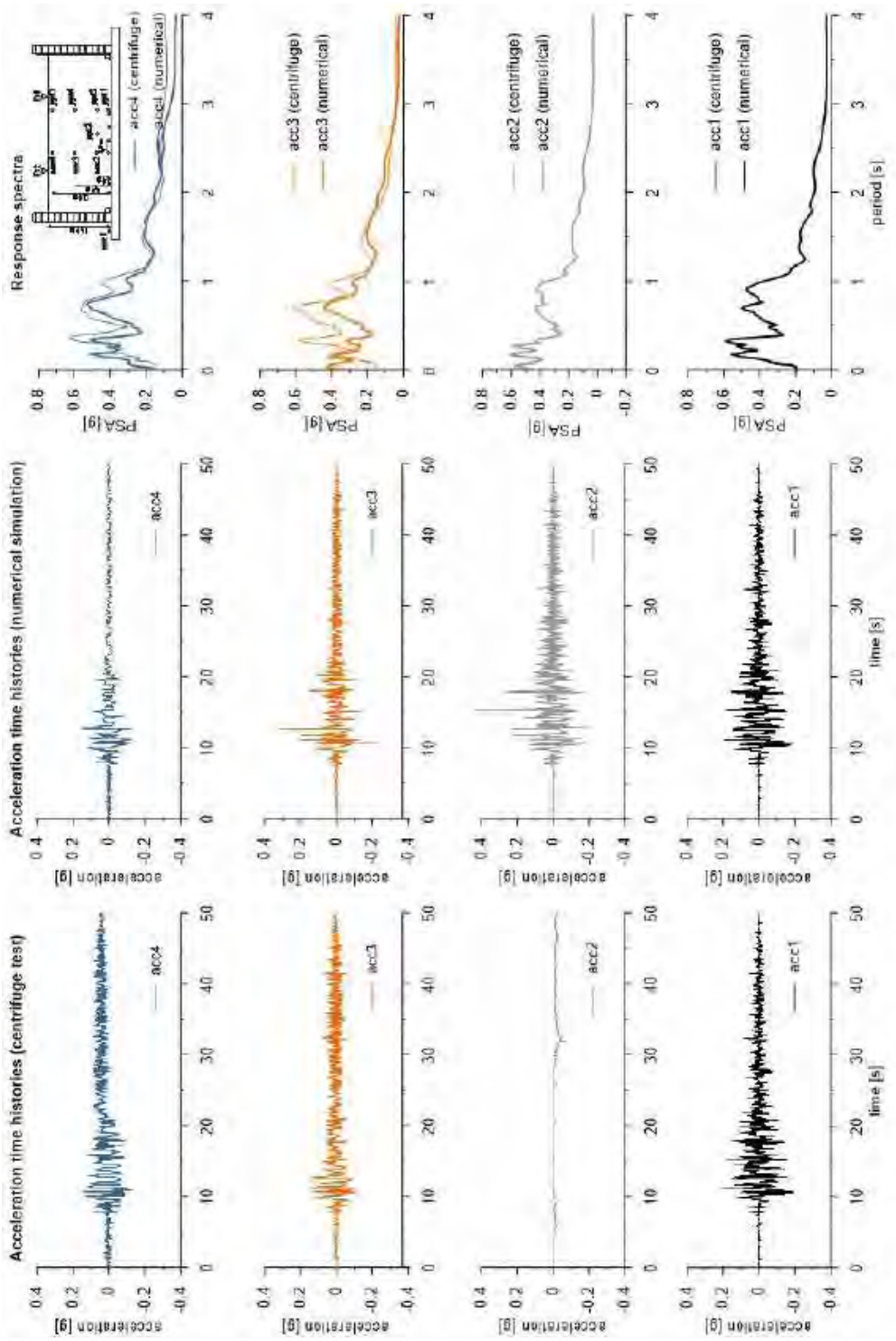

This project has received funding from the European Union's Horizon 2020 research and innovation programme under grant agreement No. 700748

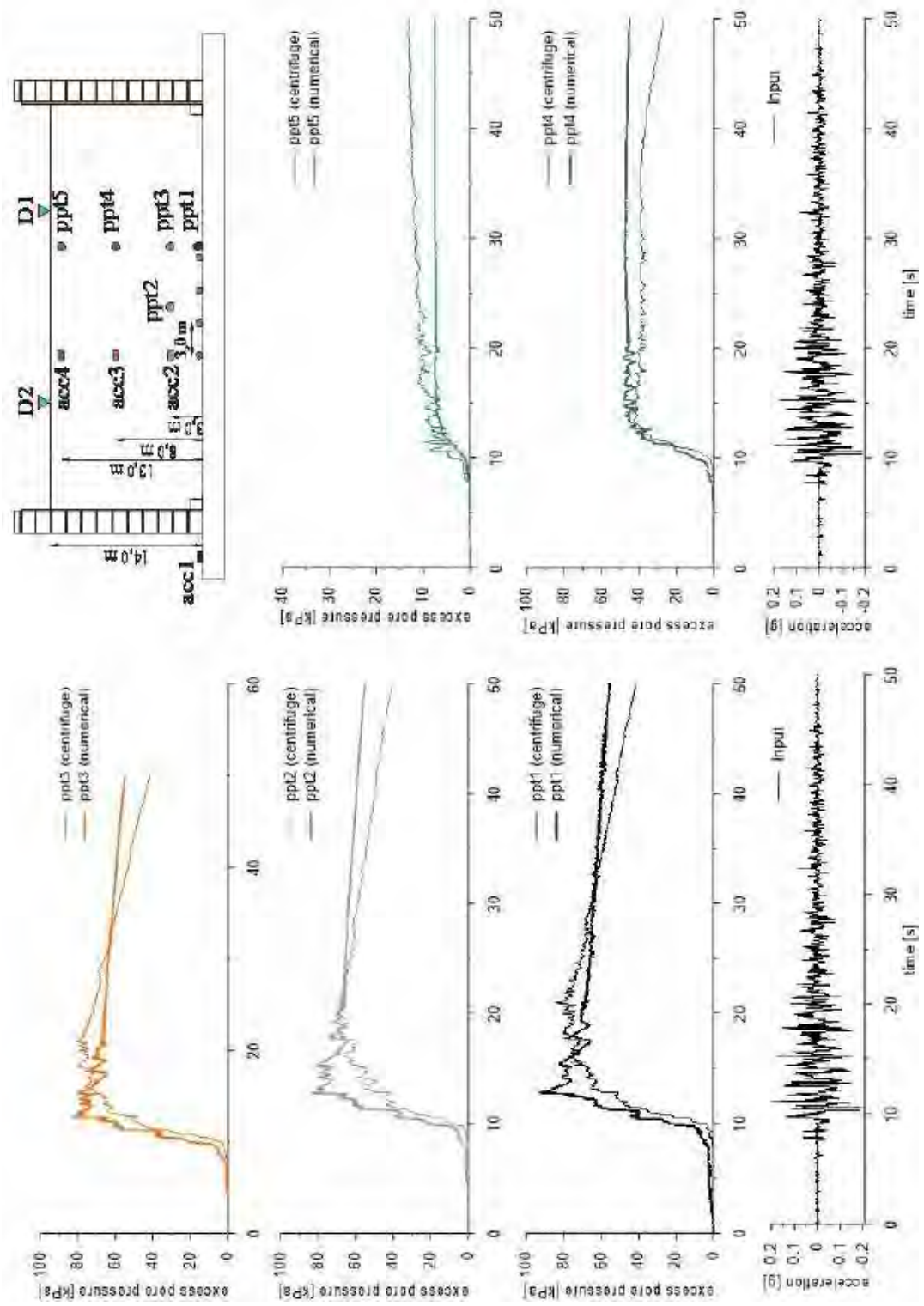

This project has received funding from the European Union's Horizon 2020 research and innovation programme under grant agreement No. 700748

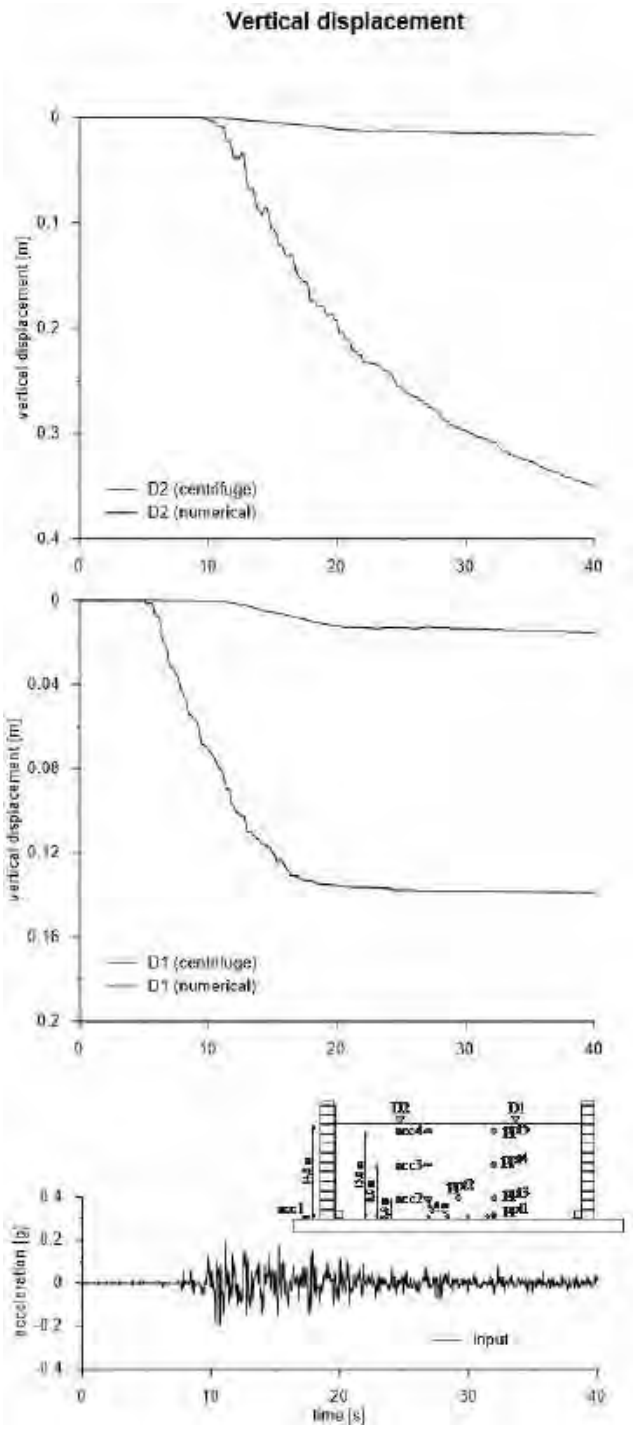

This project has received funding from the European Union's Horizon 2020 research and innovation programme under grant agreement No. 700748

5.5 FINAL REMARKS

In this section, the centrifuge tests carried out with the mitigation interventions (horizontal drains HD and induced partial saturation IPS) have been simulated with different models.

Similarly, to what was observed for the simulations with no mitigation interventions, the two constitutive models are able to catch the pore pressure build up along the soil profile caused by the imposed ground motion.

On the contrary, the simulations are generally speaking unable to get realistically the vertical displacements measured at ground level, again similarly to what has been found for the simulations reported in §4. (see §4.5).

In all cases, the adoption of HD or IPS has a beneficial effect in terms of pore pressure increments, confirming the suitability of these technologies for the mitigation of liquefaction risk. As physically expected, because of the lower pore pressures in the models with HD or IPS, the accelerations calculated close to ground level are higher than in the case of no mitigation action.

Interestingly, PM4Sand is able to take into account simply the change of degree of saturation (see §3.3.1.2), calculating the effective stresses with the Bishop notation. The results are physically consistent, as previously shown.

This project has received funding from the European Union's Horizon 2020 research and innovation programme under grant agreement No. 700748

6 PARAMETRIC STUDY TO EVALUATE THE PERFORMANCE OF MITIGATION TECHNIQUES AGAINST SOIL LIQUEFACTION

6.1 HORIZONTAL DRAINS (HD)

The analyses reported in this section have been carried out with two different goals: the ones from §6.1.1.1 to §6.1.1.9 have been carried out on geometrical schemes identical or similar to the ones tested in the centrifuge using a unique value of the initial void ratio, input motion and ground water table depth (because in the centrifuge these quantities were slightly different from test to test); in such a way, a reference set of results has been obtained. In this sequence of analyses, the reference physical scheme is the centrifuge free field one. This means that the set of parameters used refers to this physical test (ID SF_xx_TC_PM4_31). The other simulations with the geometrical configurations similar or identical to the ones in the centrifuge allow to compare the effect of different input motions or relative densities on the effectiveness of the use of horizontal drains.

The second set of analyses has been carried out on a geometrical indefinite scheme (indicated in the ID with the label HDU) to check the influence of different spacing and depths from the water table (sections from §6.1.1.10 to §6.1.1.44).

In all the analyses reported in this section, the permeability of the drains has been considered infinite, while in the back analyses of the centrifuge tests reported in §5 a finite value was adopted. From a numerical point of view, the condition of infinite permeability was simulated by imposing a hydrostatic pressure on the drains boundary.

6.1.1 FEM SIMULATIONS WITH PLAXIS2D

6.1.1.1 ID: SF_HD_H05_s05 & ID: SF_HD_H05_s10

The model consists of a homogenous soil profile of Ticino sand. The ground motion applied was the number 31.

ID: SF_HD_H05_s05
ID: SF_HD_H05_s10

This project has received funding from the European Union's Horizon 2020 research and innovation programme under grant agreement No. 700748

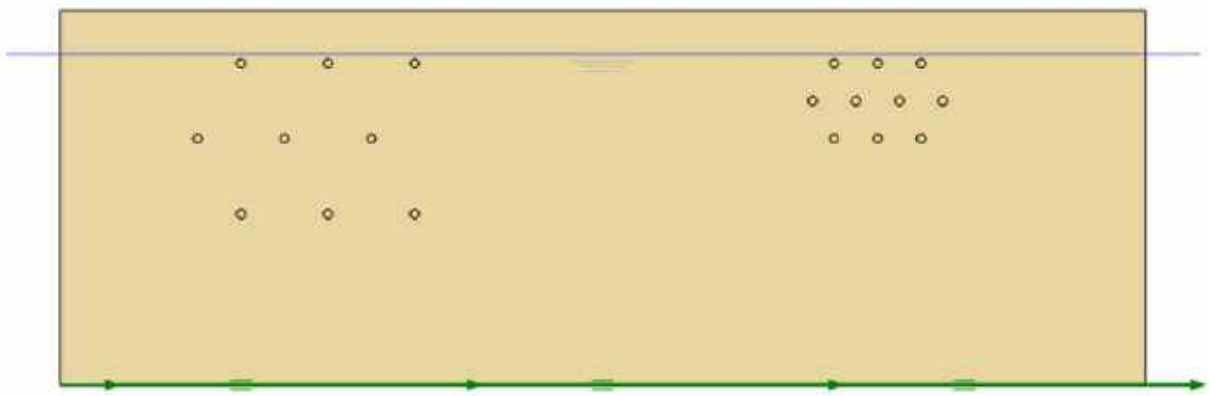

Layouts of the model reproduced in Plaxis 2D

This project has received funding from the European Union's Horizon 2020 research and innovation programme under grant agreement No. 700748

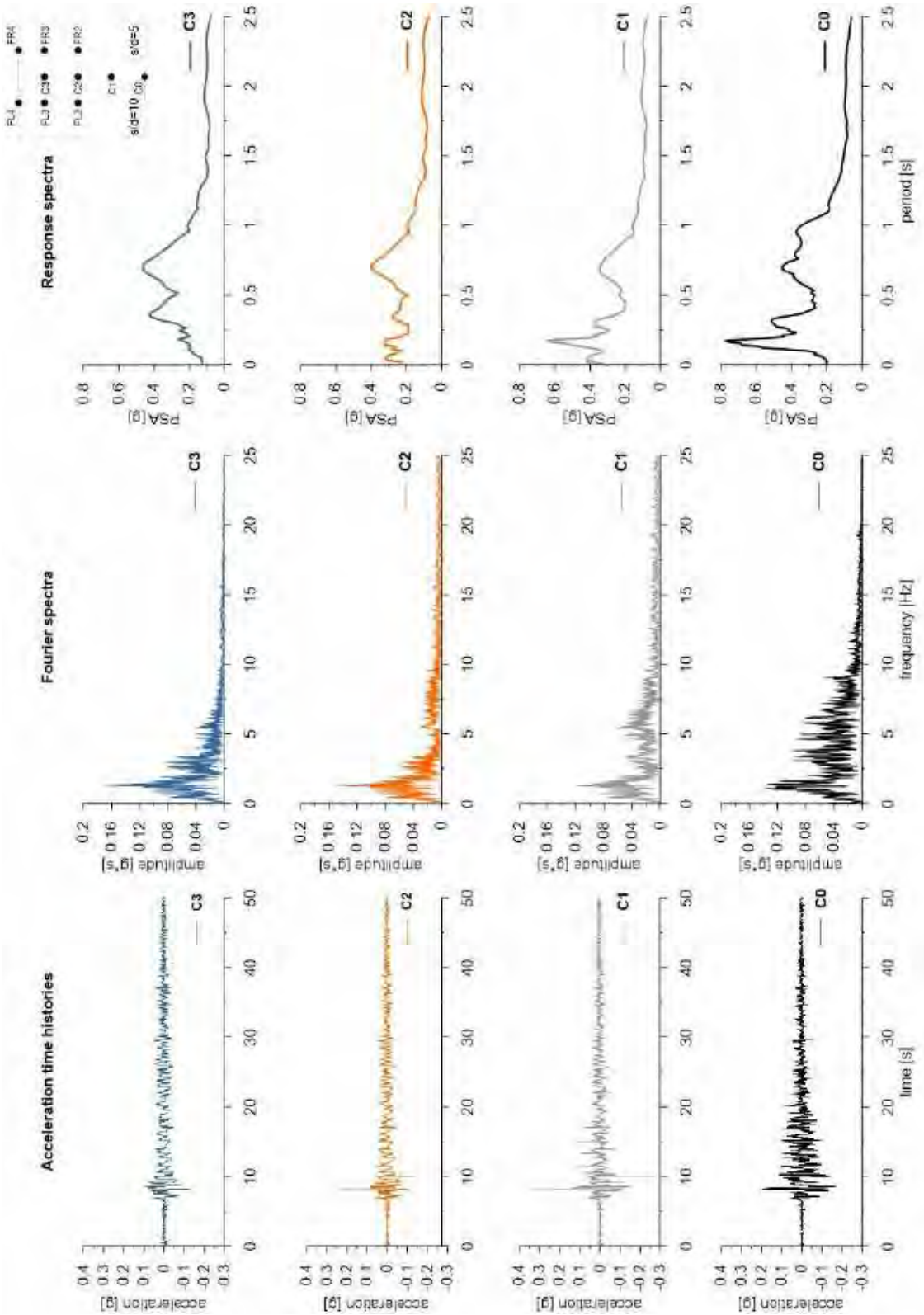

This project has received funding from the European Union's Horizon 2020 research and innovation programme under grant agreement No. 700748

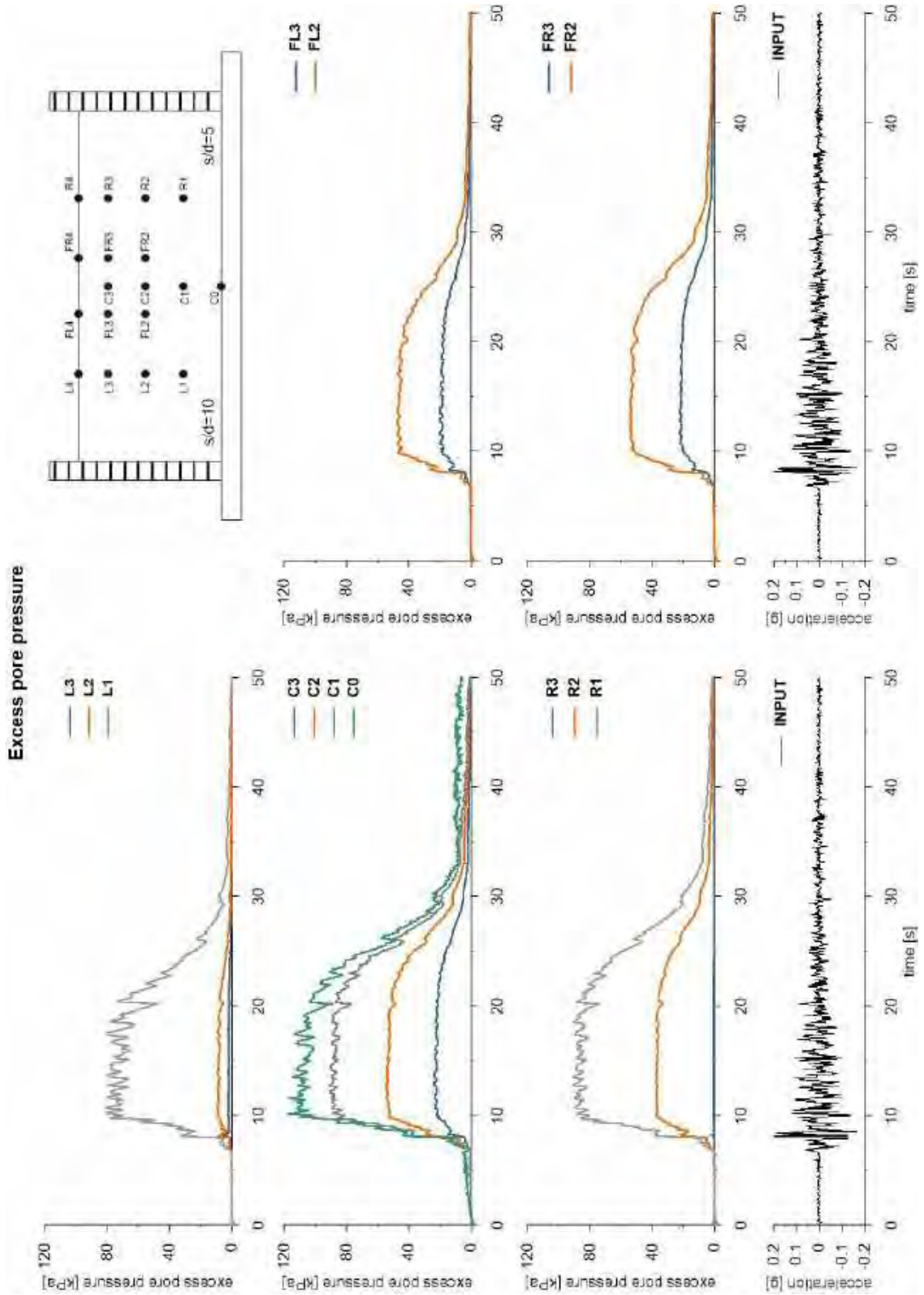

This project has received funding from the European Union's Horizon 2020 research and innovation programme under grant agreement No. 700748

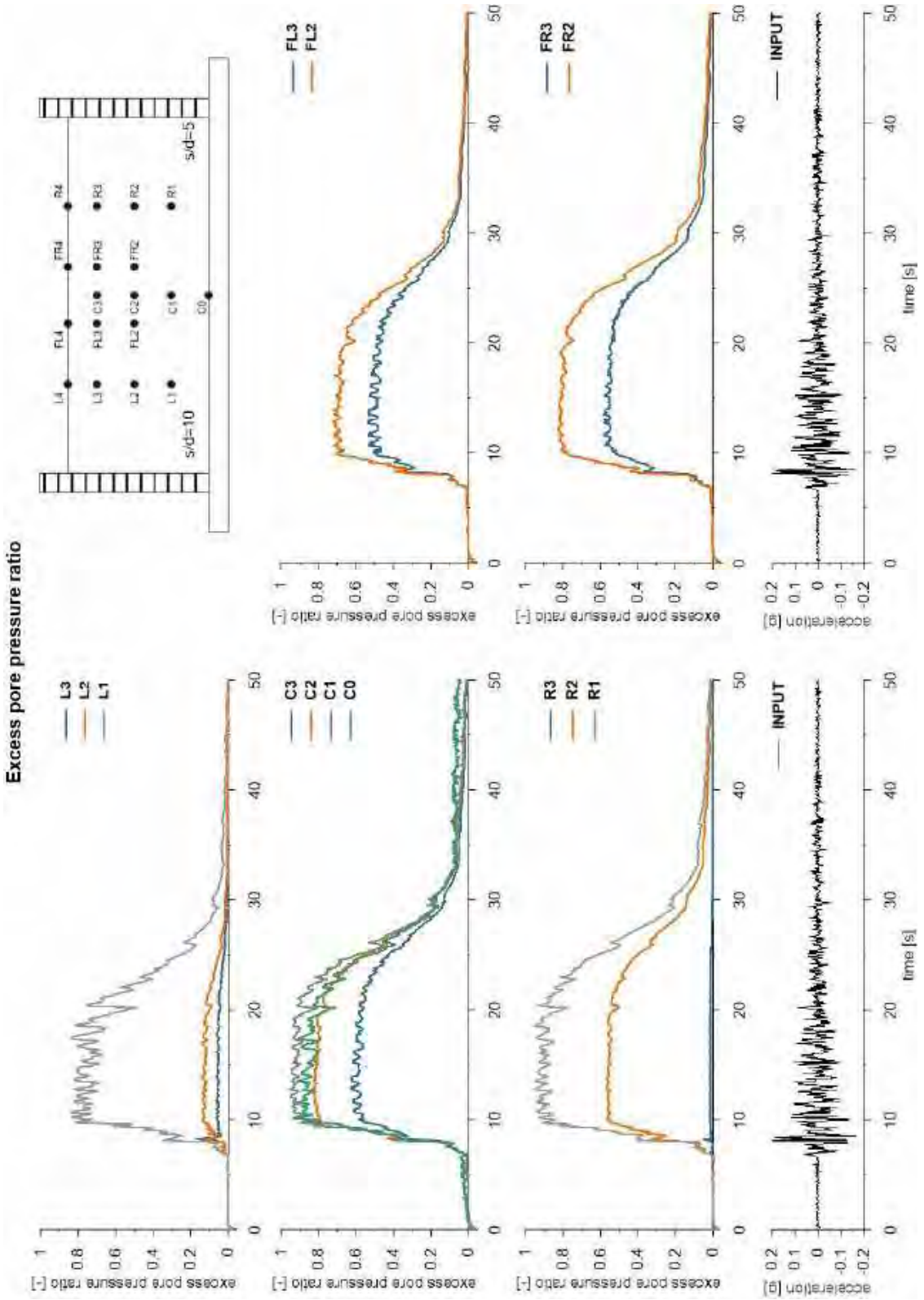

This project has received funding from the European Union's Horizon 2020 research and innovation programme under grant agreement No. 700748

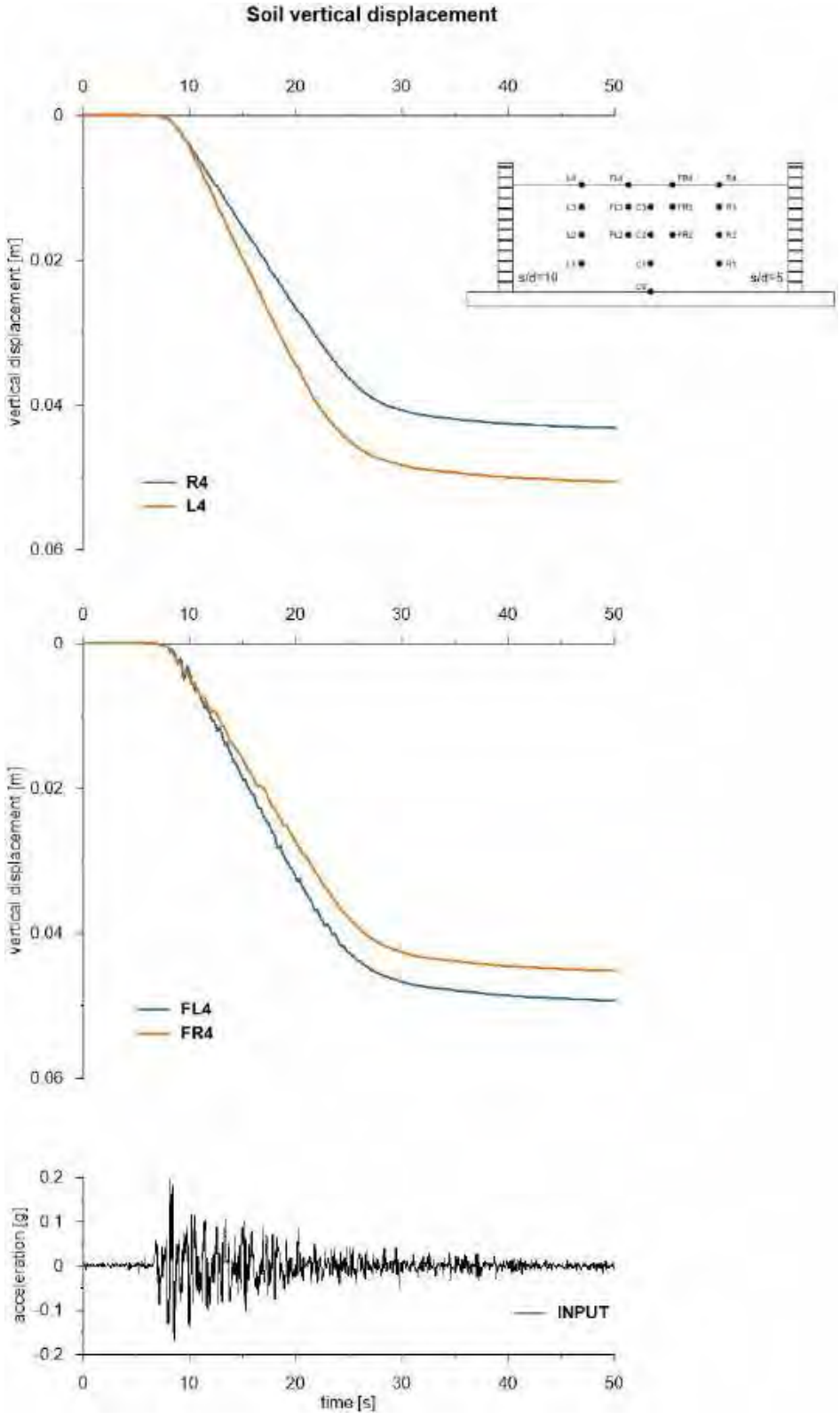

This project has received funding from the European Union's Horizon 2020 research and innovation programme under grant agreement No. 700748

6.1.1.2 ID: SS_xx_xx_xx

The model consists of a homogenous soil profile of Ticino sand. The ground motion applied was the number 31.

ID: SS_xx_xx_xx

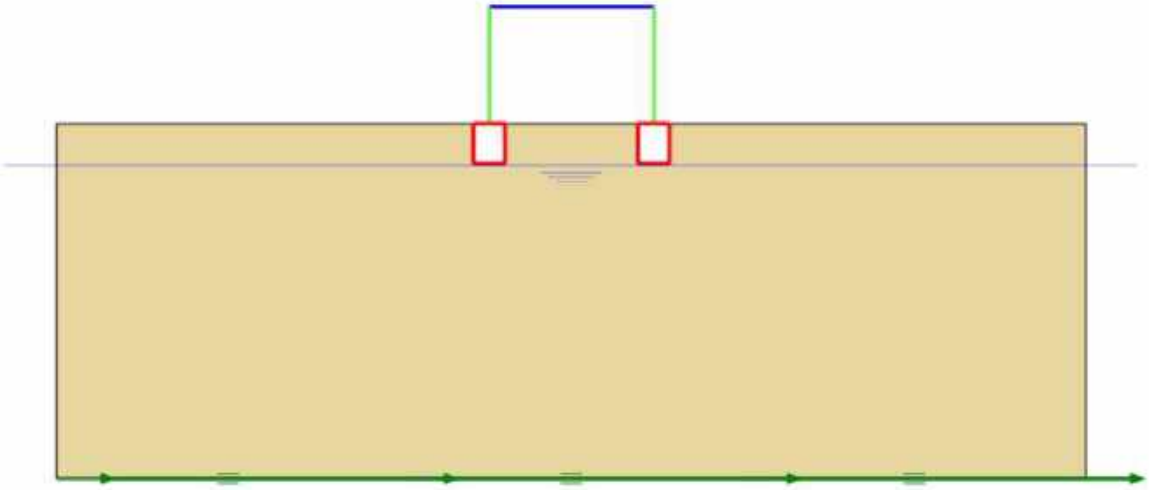

Layouts of the model reproduced in Plaxis 2D

This project has received funding from the European Union's Horizon 2020 research and innovation programme under grant agreement No. 700748

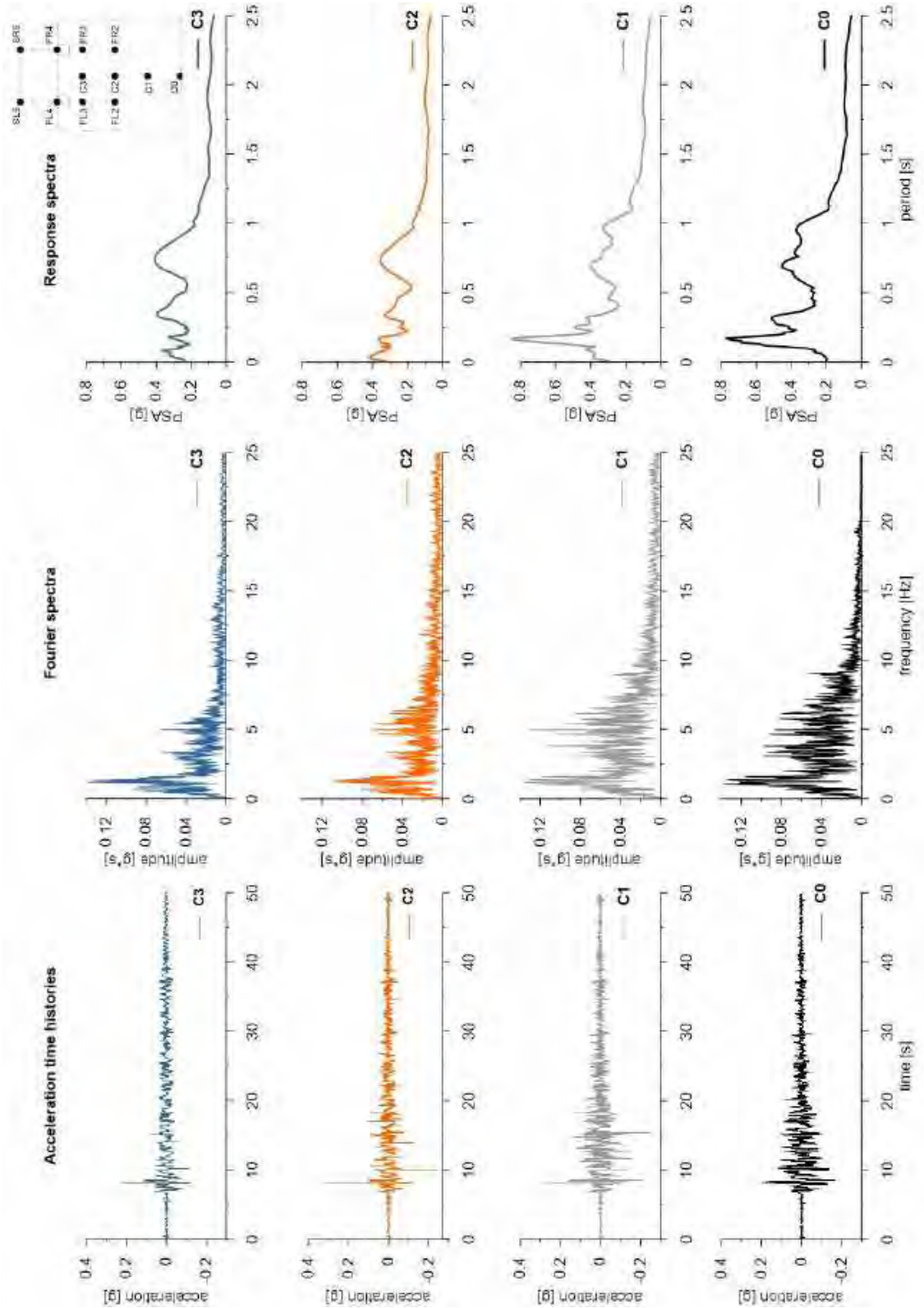

This project has received funding from the European Union's Horizon 2020 research and innovation programme under grant agreement No. 700748

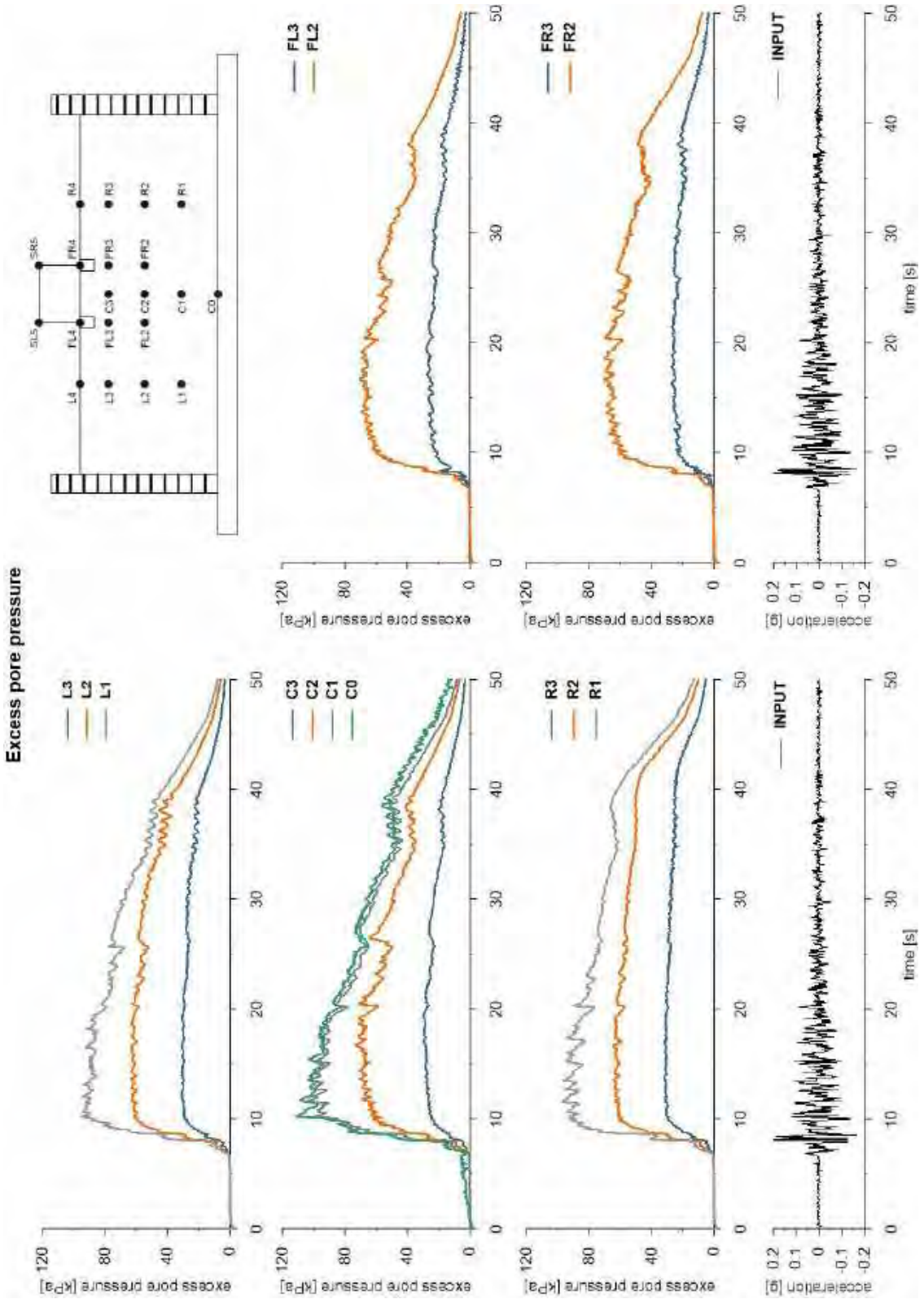

This project has received funding from the European Union's Horizon 2020 research and innovation programme under grant agreement No. 700748

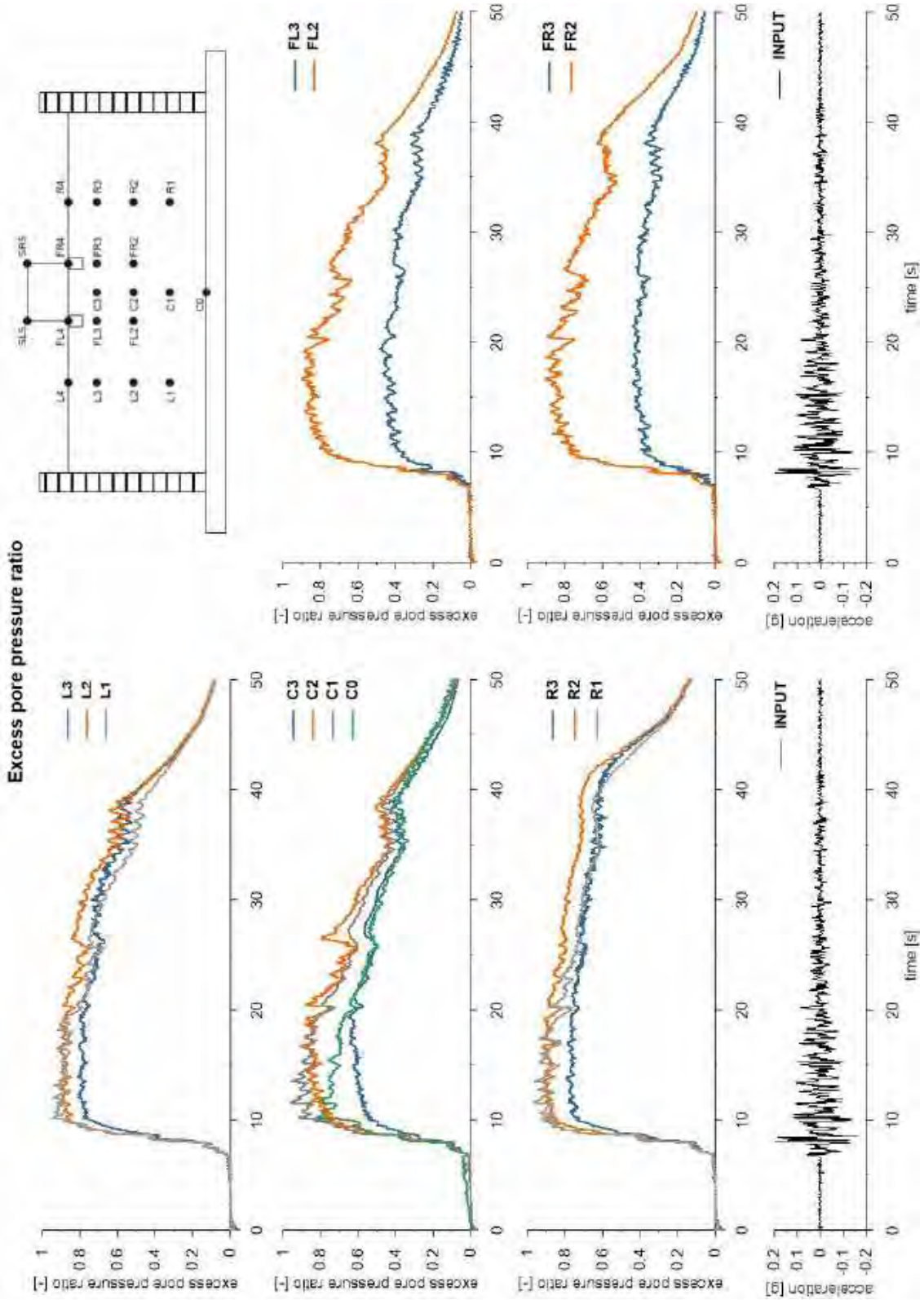

This project has received funding from the European Union's Horizon 2020 research and innovation programme under grant agreement No. 700748

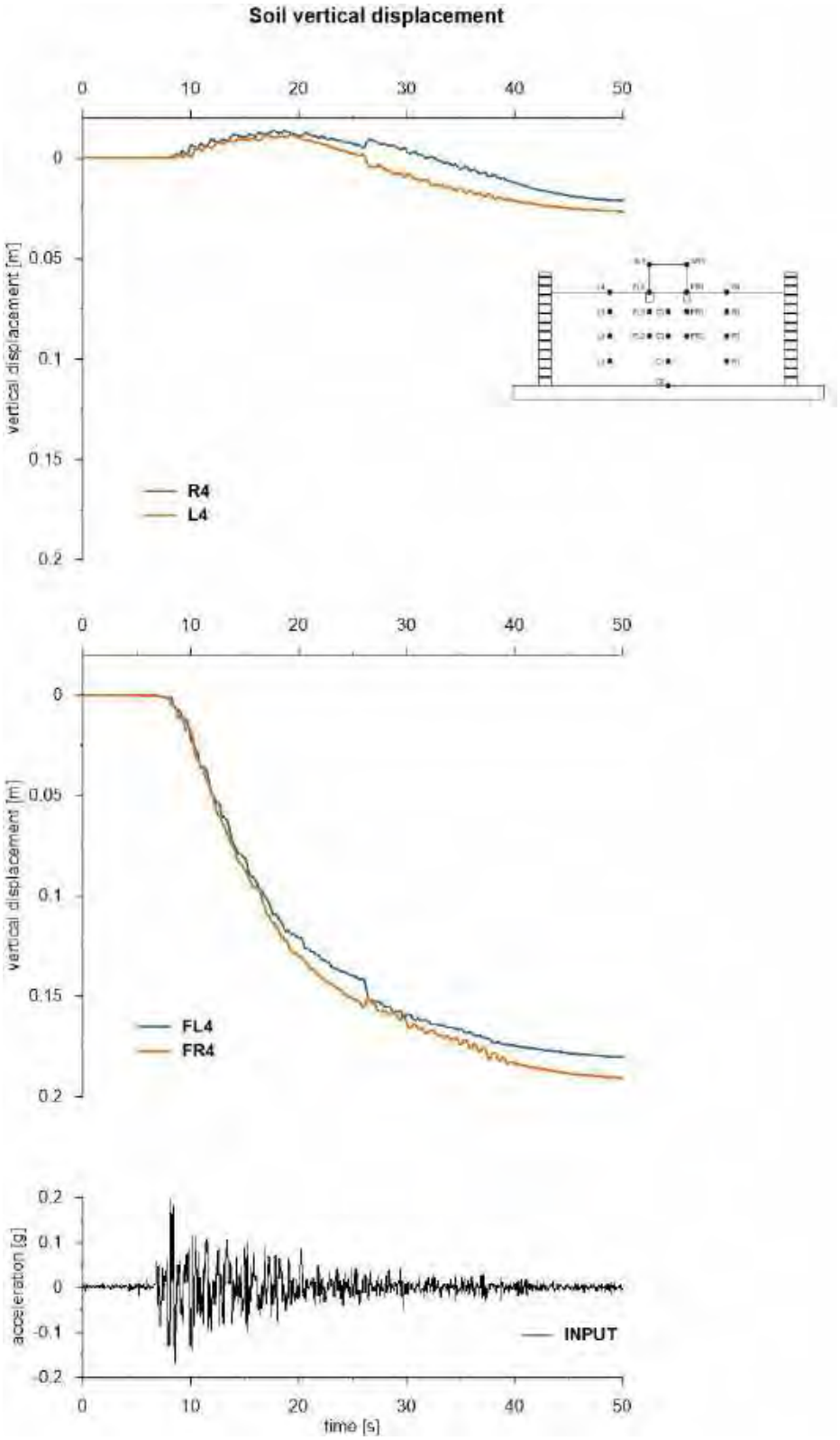

This project has received funding from the European Union's Horizon 2020 research and innovation programme under grant agreement No. 700748

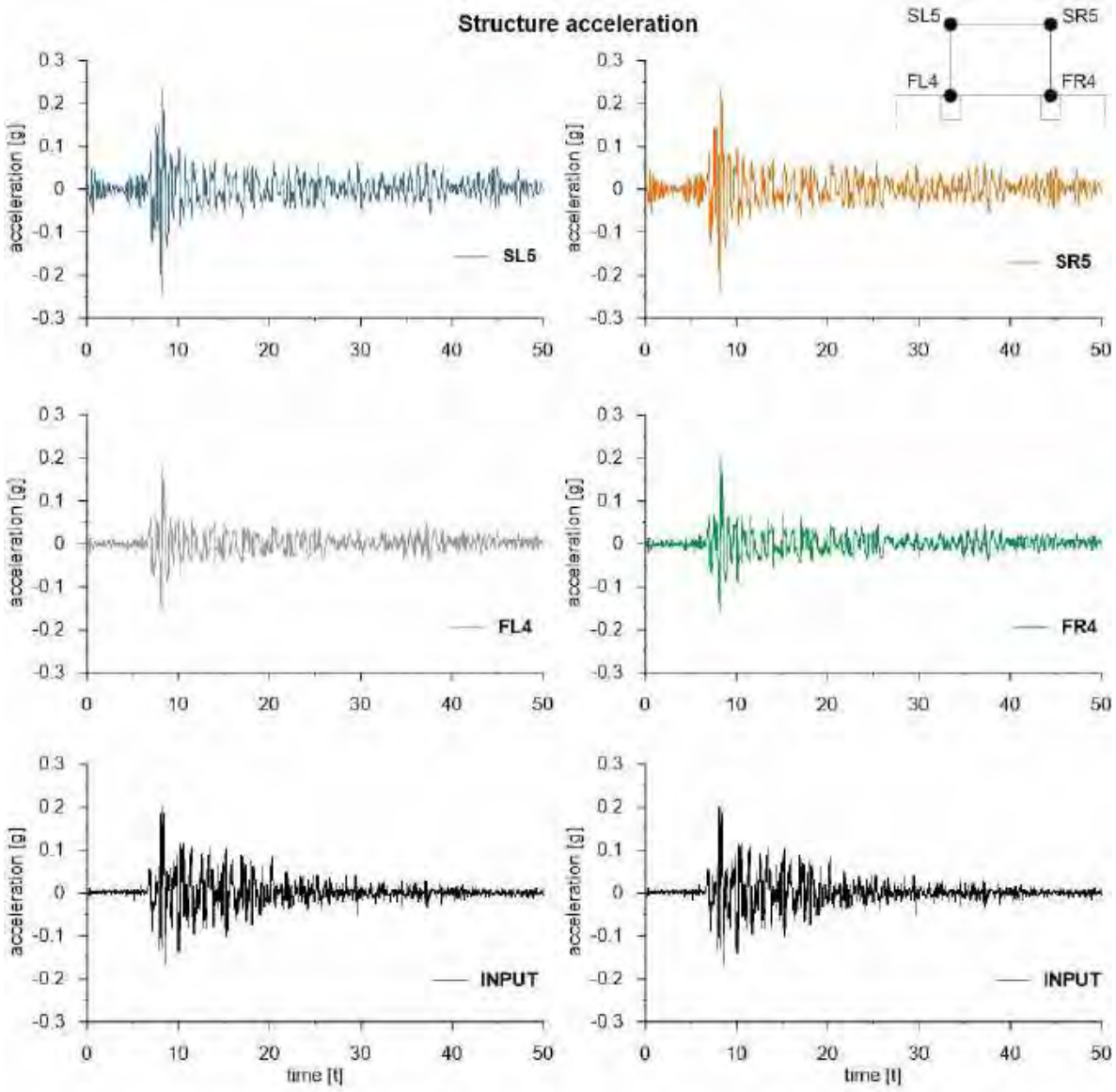

This project has received funding from the European Union's Horizon 2020 research and innovation programme under grant agreement No. 700748

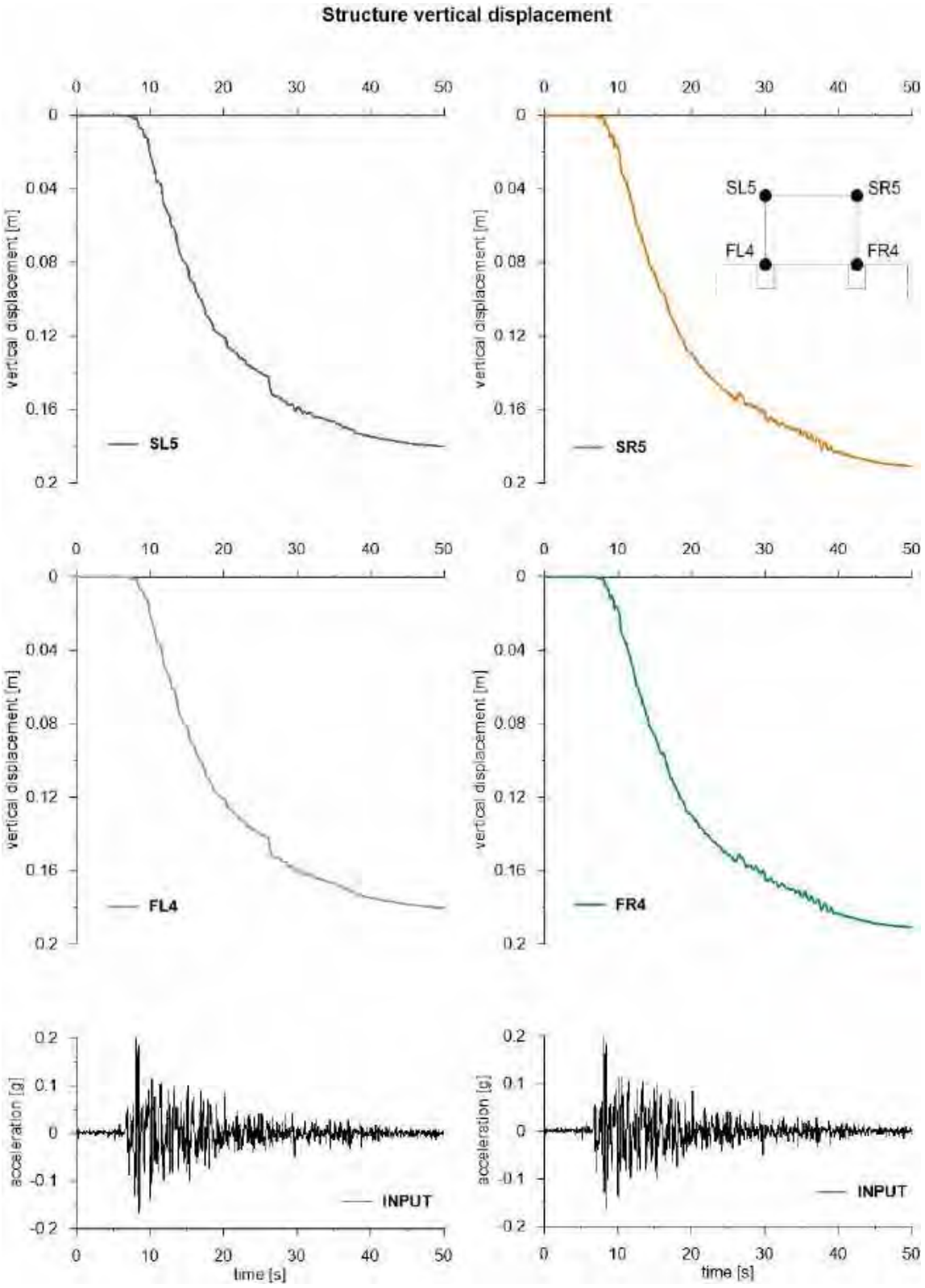

This project has received funding from the European Union's Horizon 2020 research and innovation programme under grant agreement No. 700748

6.1.1.3 ID: SS_HD_H05_s10

The model consists of a homogenous soil profile of Ticino sand. The ground motion applied was the number 31.

ID: SS_HD_H05_s10

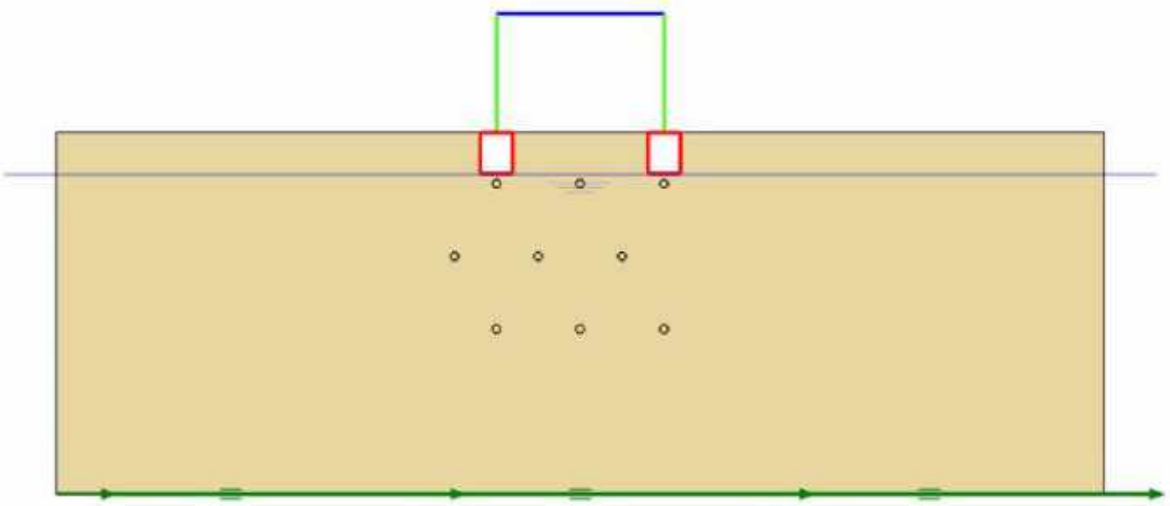

Layouts of the model reproduced in Plaxis 2D

This project has received funding from the European Union's Horizon 2020 research and innovation programme under grant agreement No. 700748

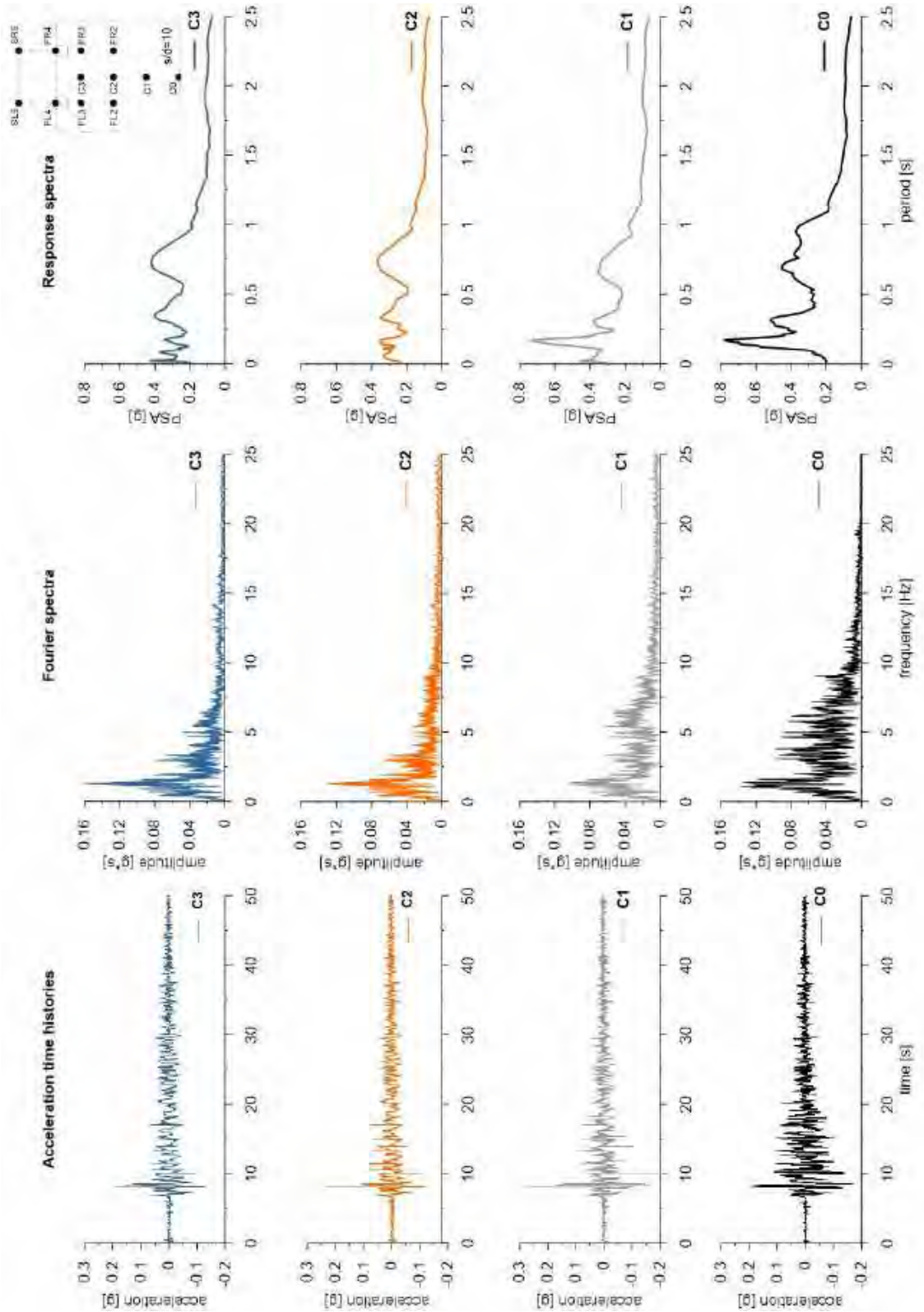

This project has received funding from the European Union's Horizon 2020 research and innovation programme under grant agreement No. 700748

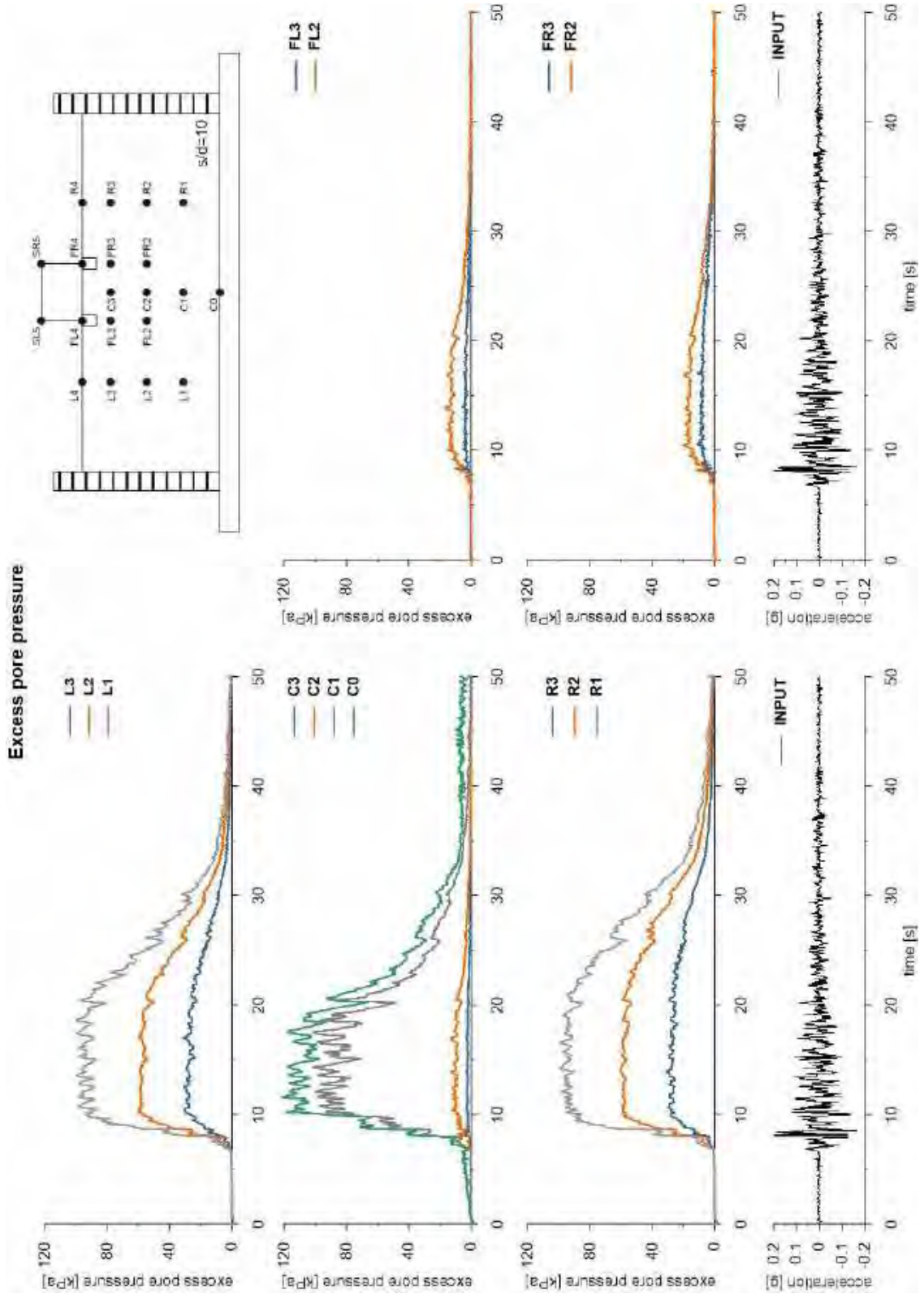

This project has received funding from the European Union's Horizon 2020 research and innovation programme under grant agreement No. 700748

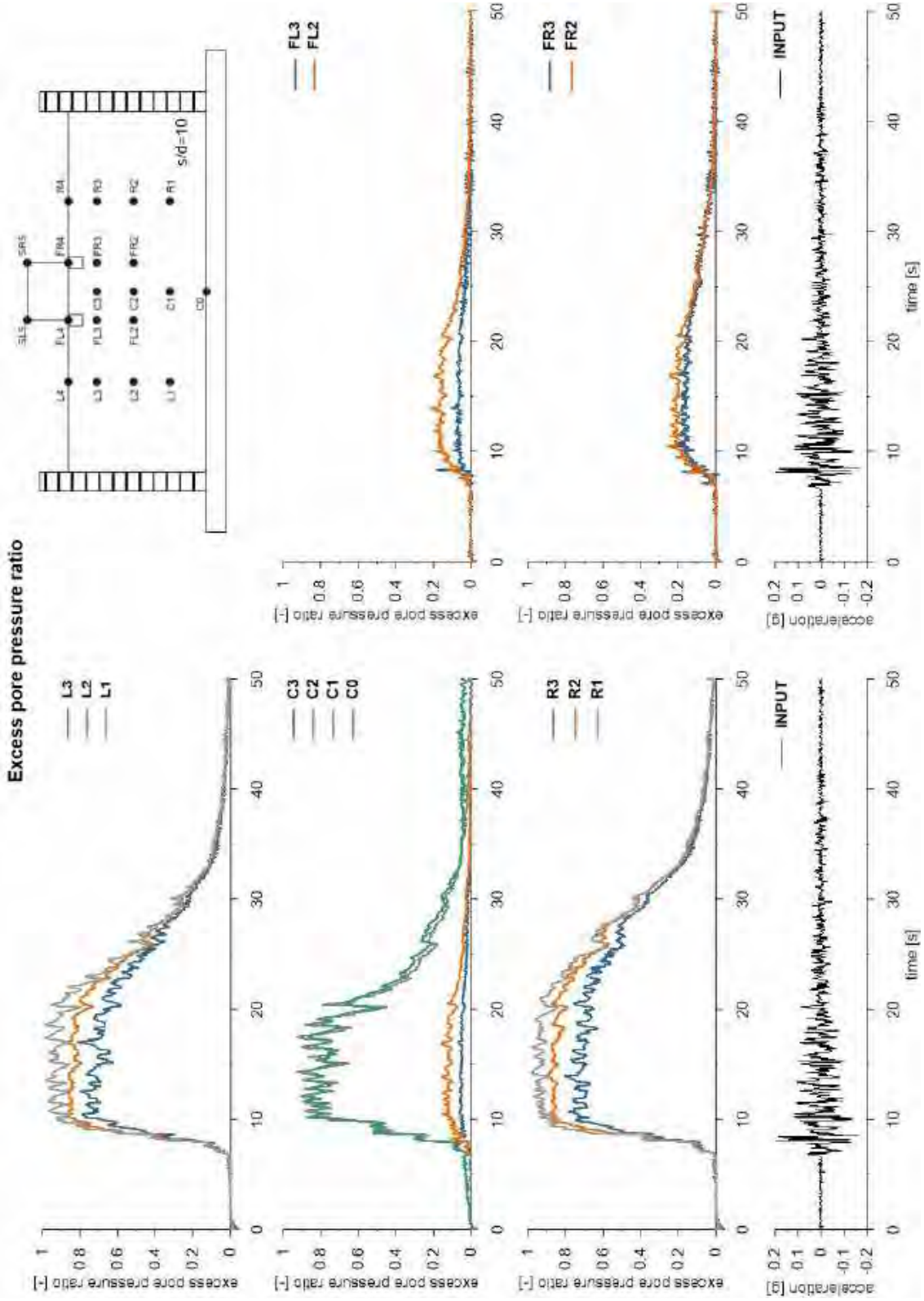

This project has received funding from the European Union's Horizon 2020 research and innovation programme under grant agreement No. 700748

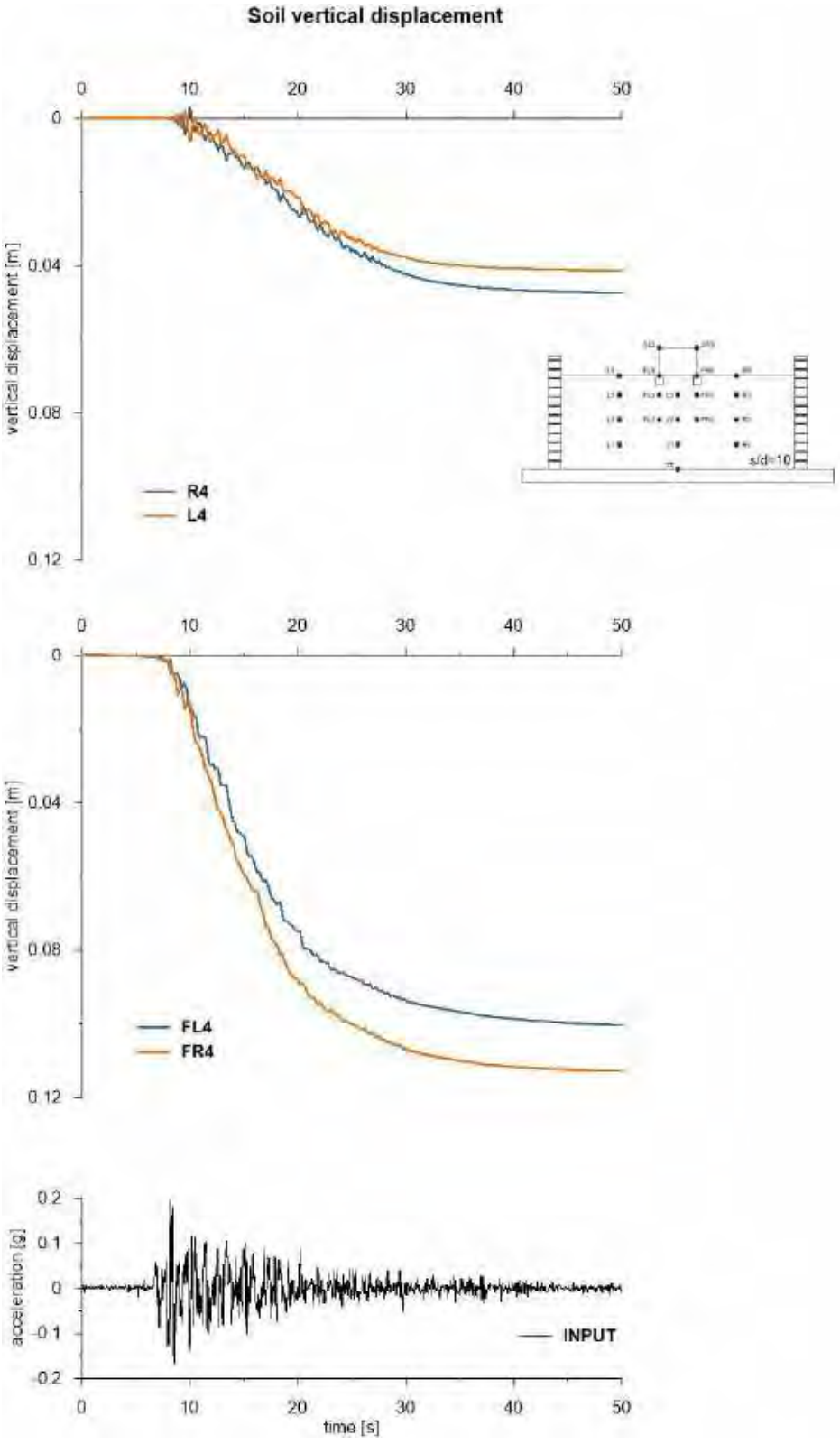

This project has received funding from the European Union's Horizon 2020 research and innovation programme under grant agreement No. 700748

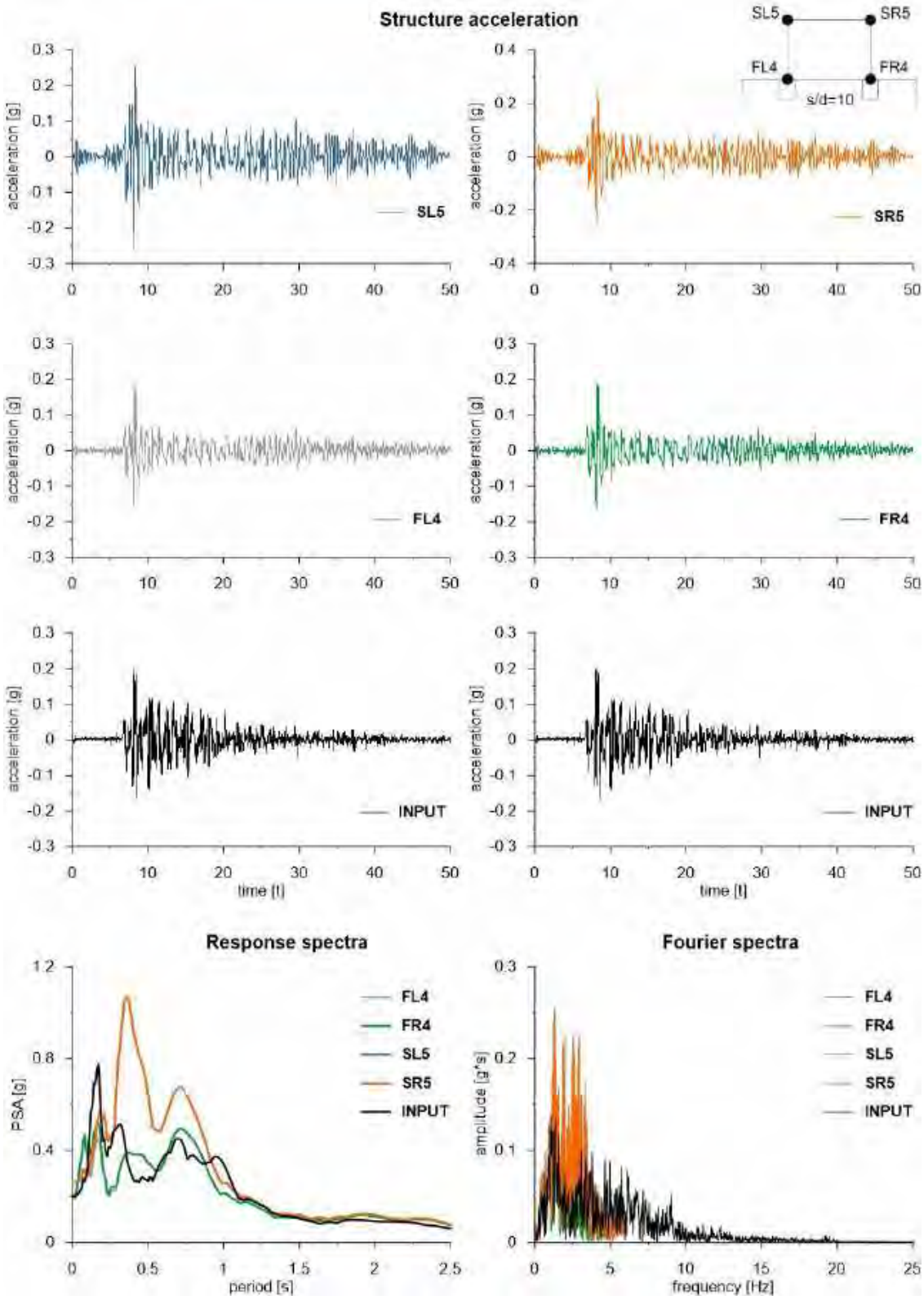

This project has received funding from the European Union's Horizon 2020 research and innovation programme under grant agreement No. 700748

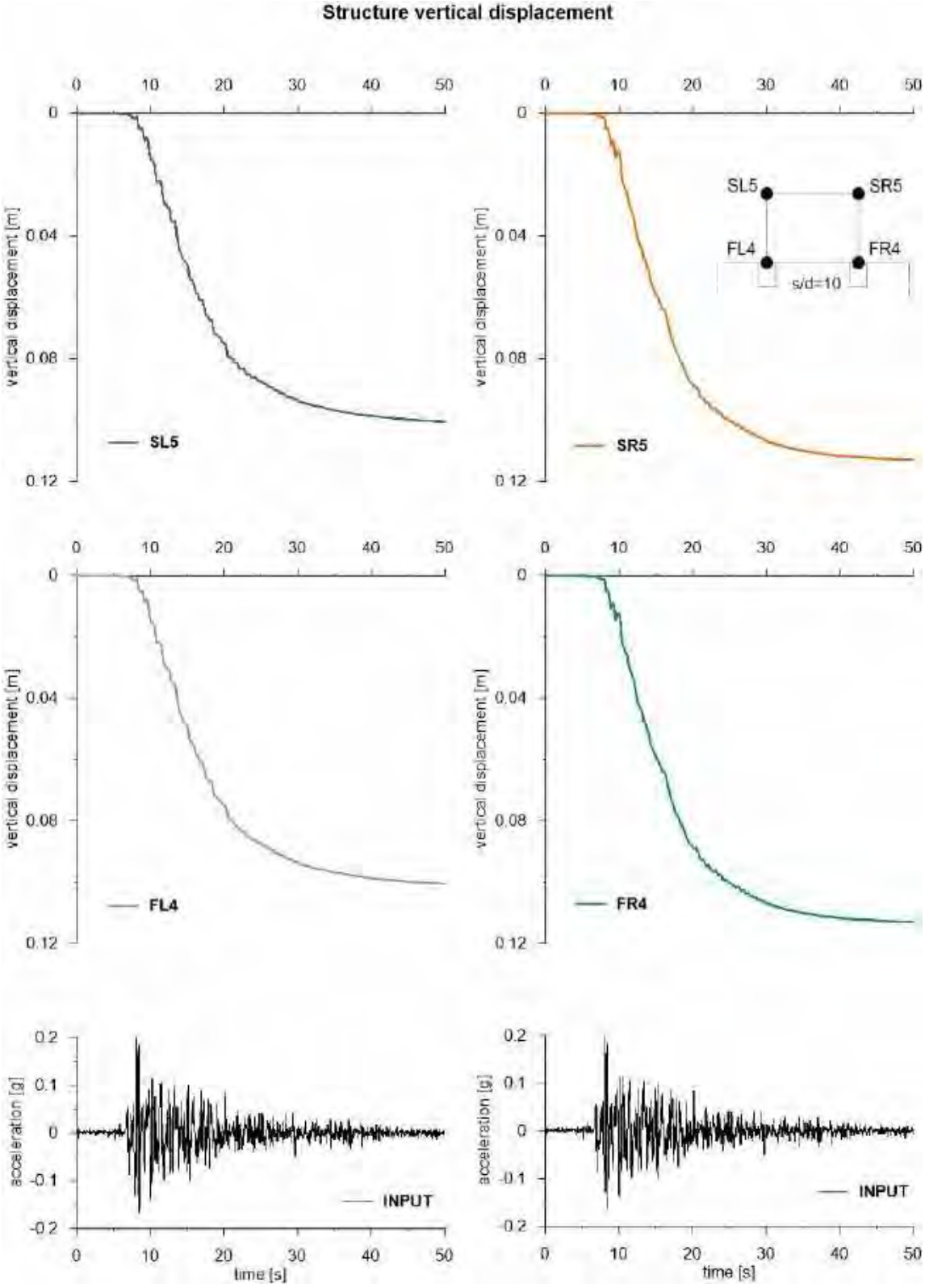

This project has received funding from the European Union's Horizon 2020 research and innovation programme under grant agreement No. 700748

6.1.1.4 ID: SS_HD_H05_s05

The model consists of a homogenous soil profile of Ticino sand. The ground motion applied was the number 31.

ID: SS_HD_H05_s05

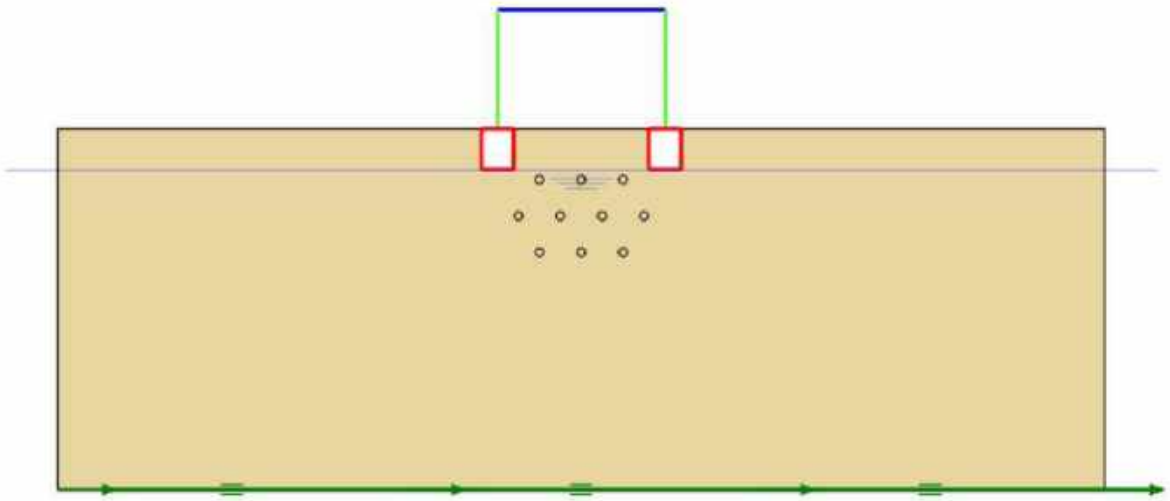

Layouts of the model reproduced in Plaxis 2D

This project has received funding from the European Union's Horizon 2020 research and innovation programme under grant agreement No. 700748

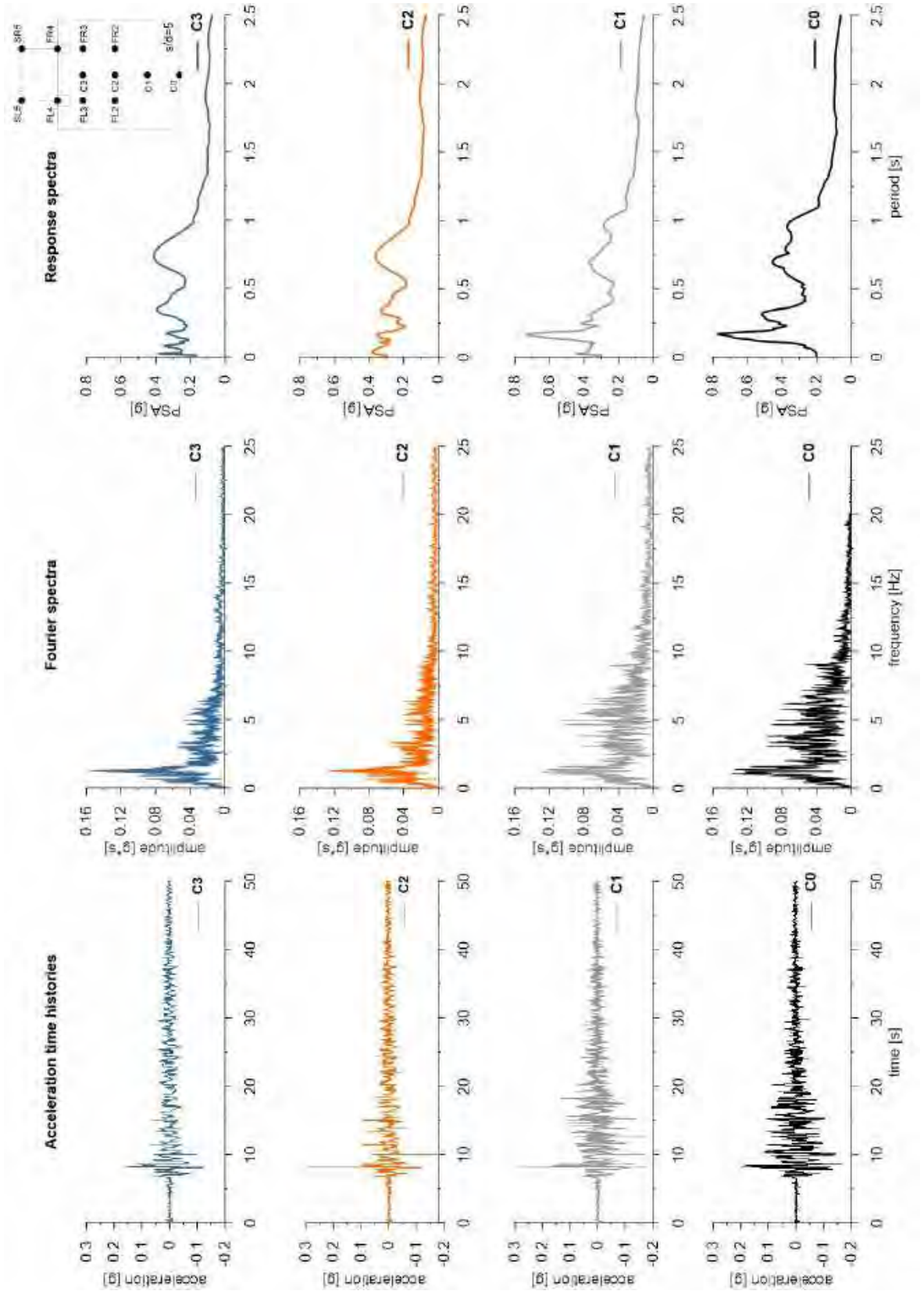

This project has received funding from the European Union's Horizon 2020 research and innovation programme under grant agreement No. 700748

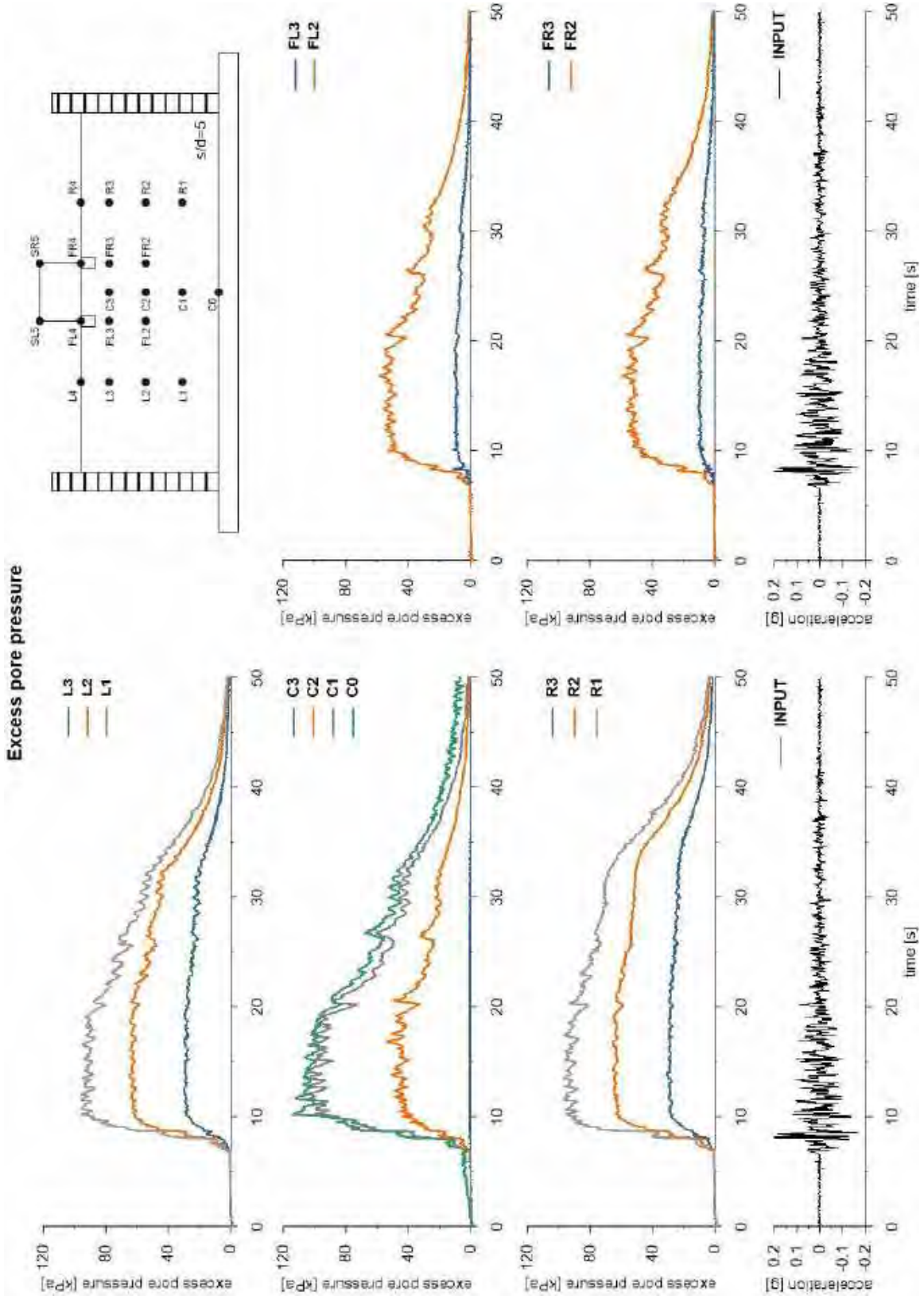

This project has received funding from the European Union's Horizon 2020 research and innovation programme under grant agreement No. 700748

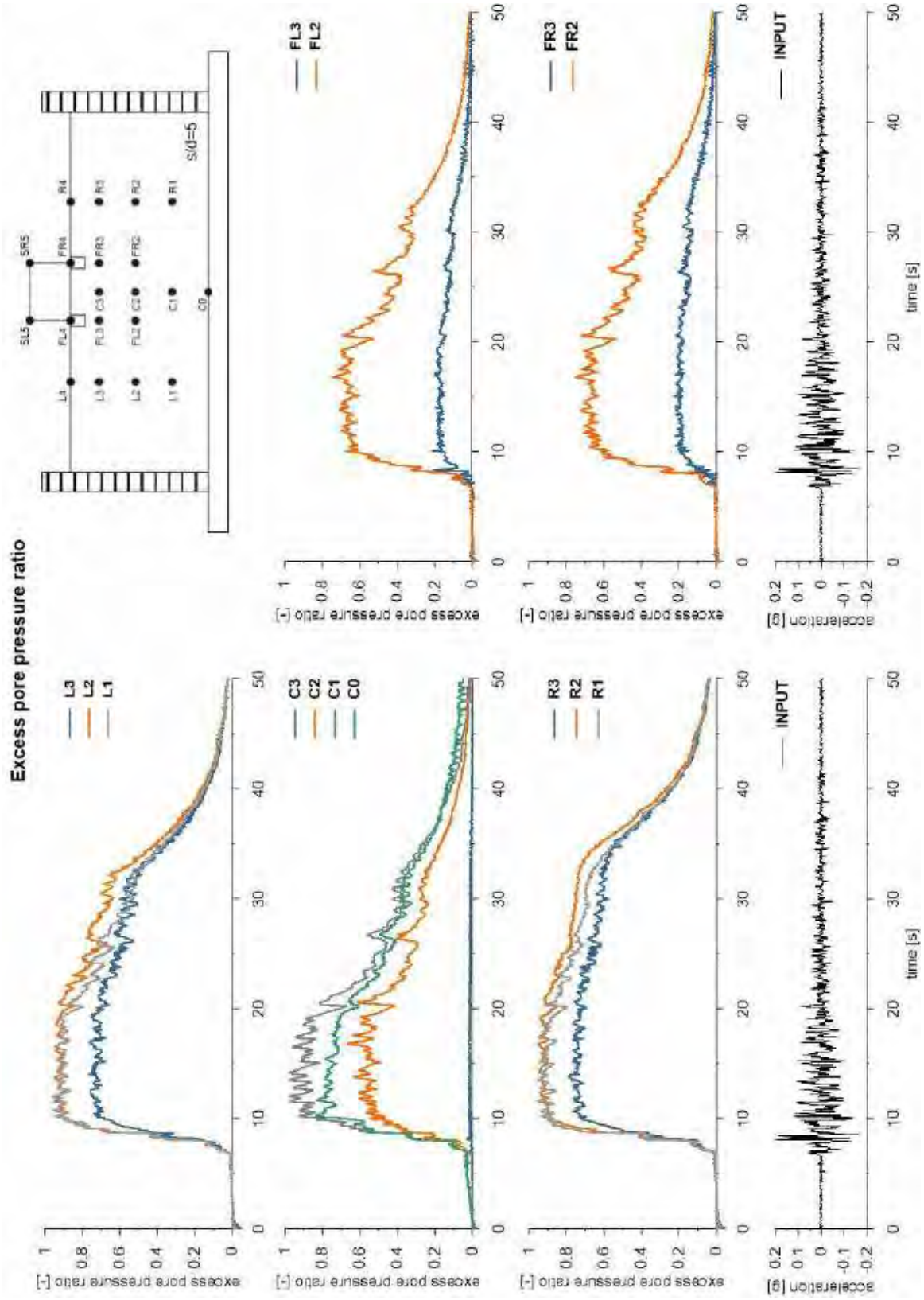

This project has received funding from the European Union's Horizon 2020 research and innovation programme under grant agreement No. 700748

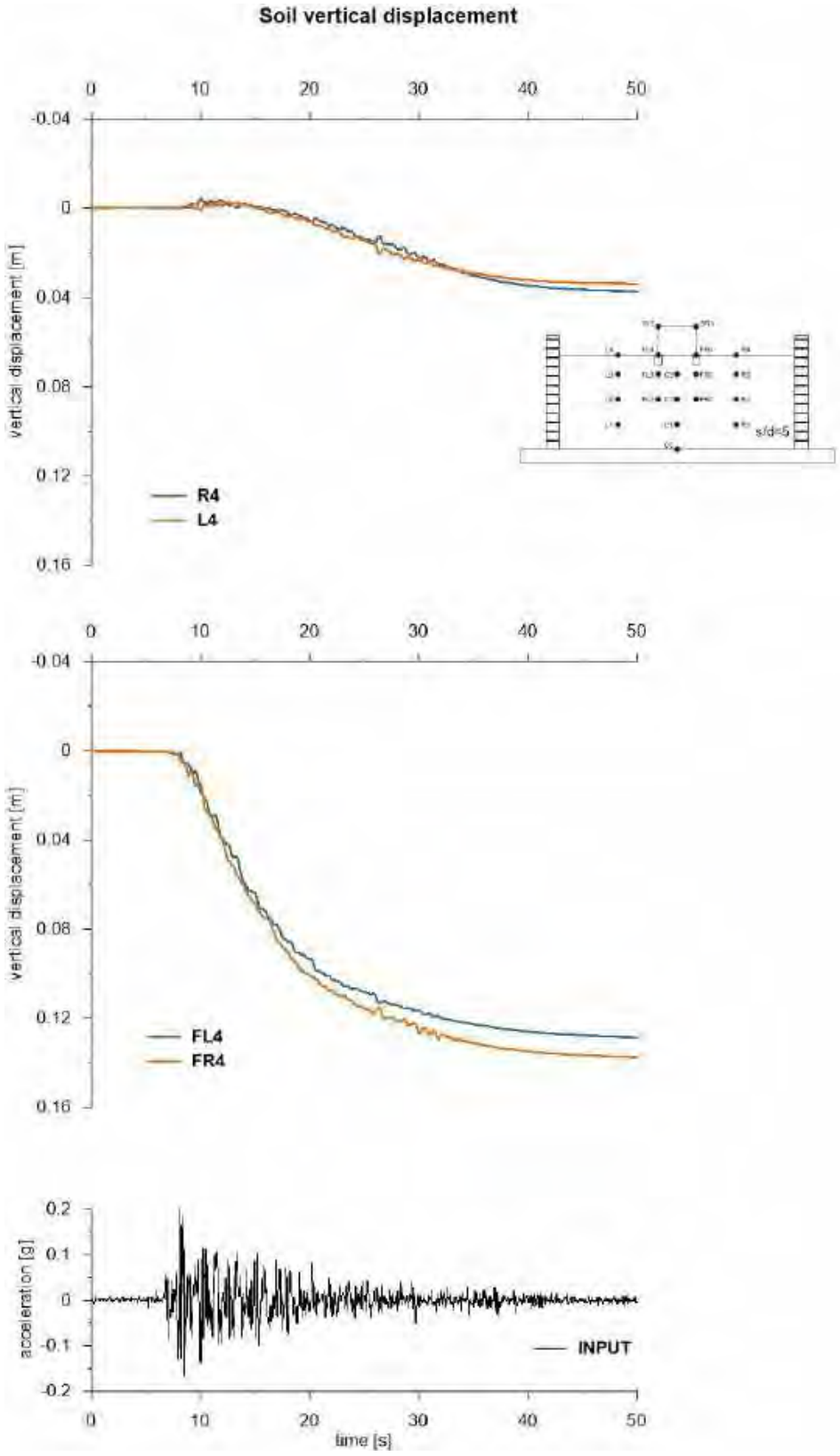

This project has received funding from the European Union's Horizon 2020 research and innovation programme under grant agreement No. 700748

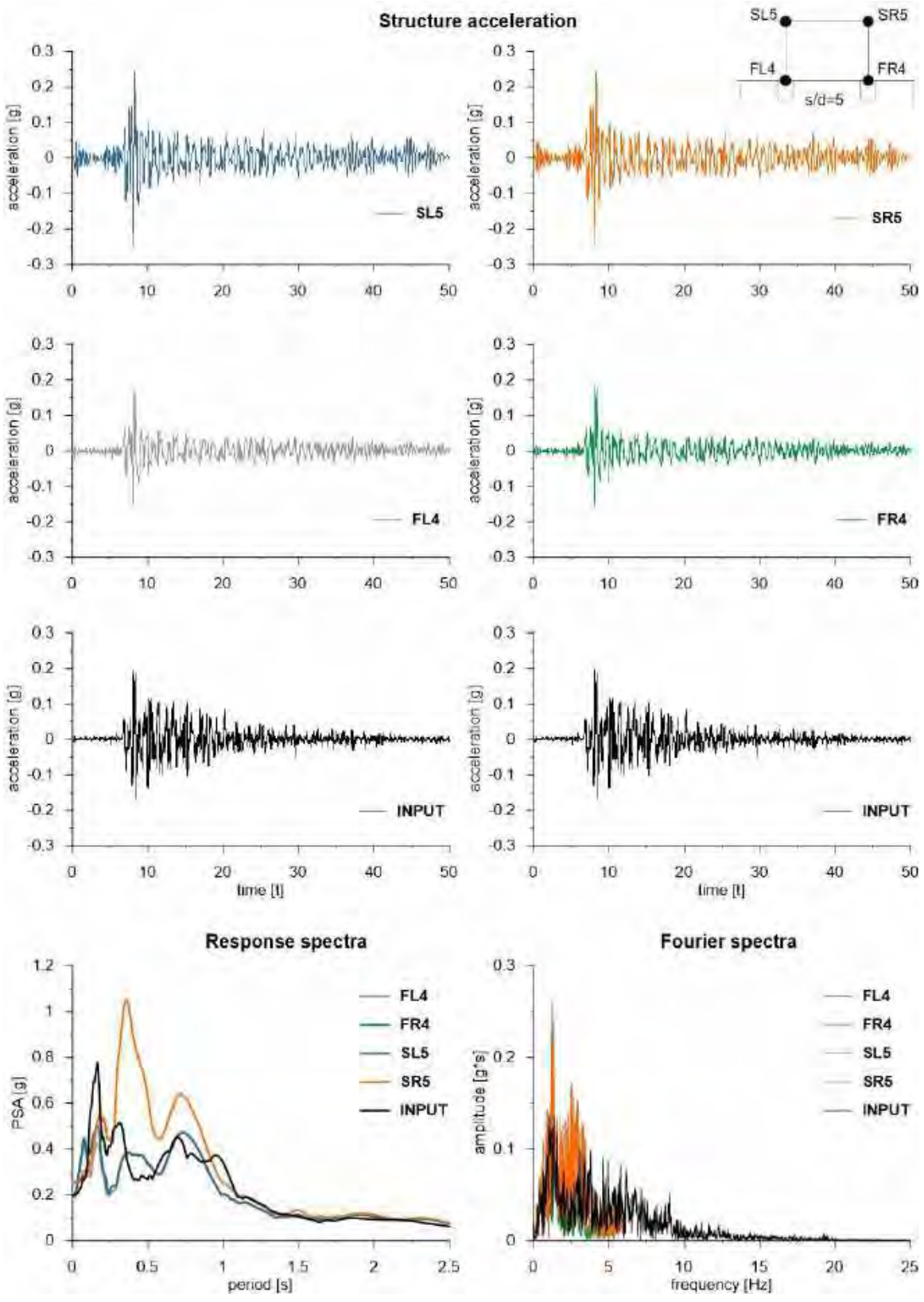

This project has received funding from the European Union's Horizon 2020 research and innovation programme under grant agreement No. 700748

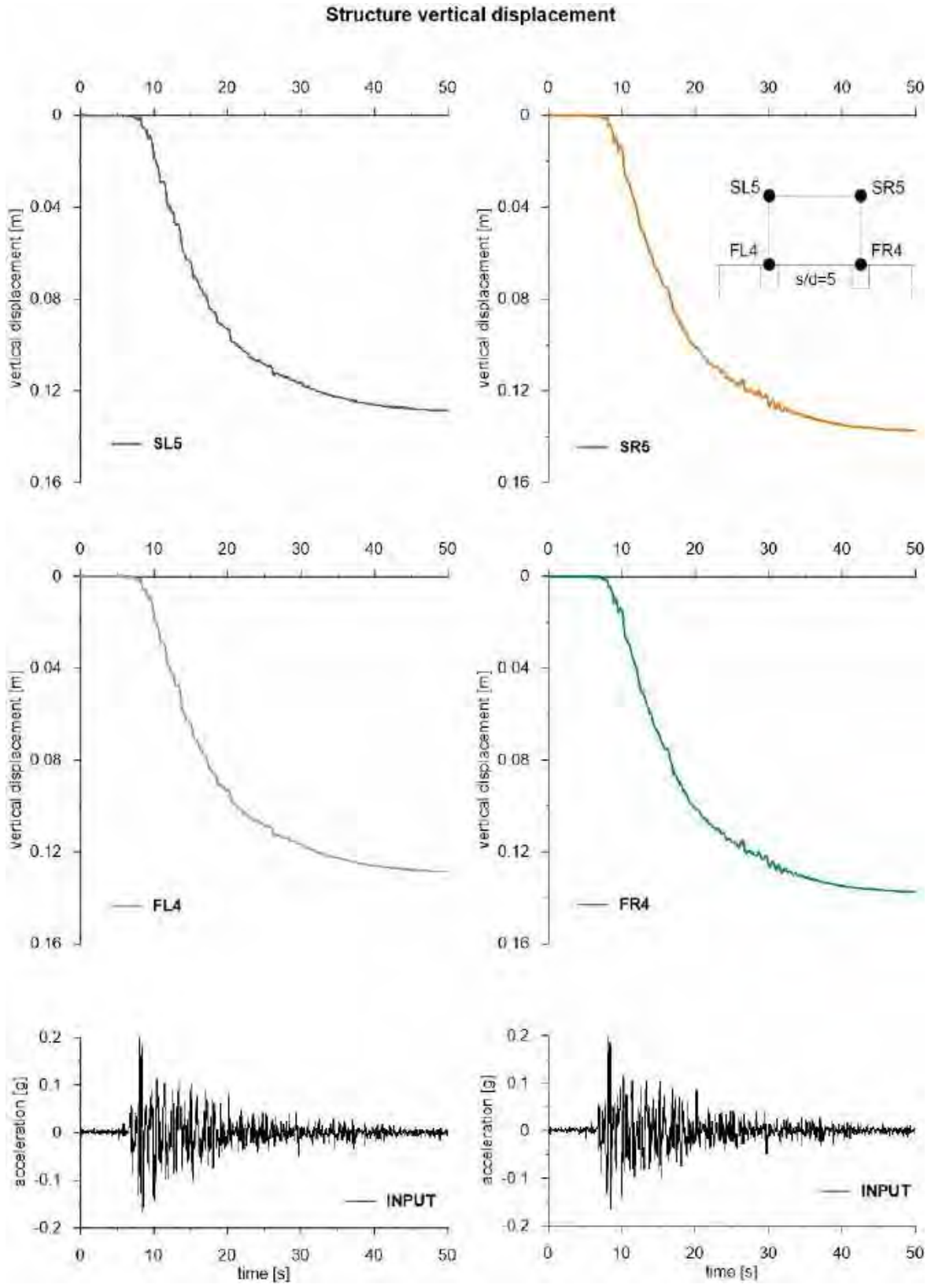

This project has received funding from the European Union's Horizon 2020 research and innovation programme under grant agreement No. 700748

6.1.1.5 ID: DF_HD_H05_s05 & ID: DF_HD_H05_s10

The model consists of a double soil profile of clay and Ticino sand. The ground motion applied was the number 31.

ID: DF_HD_H05_s05
ID: DF_HD_H05_s10

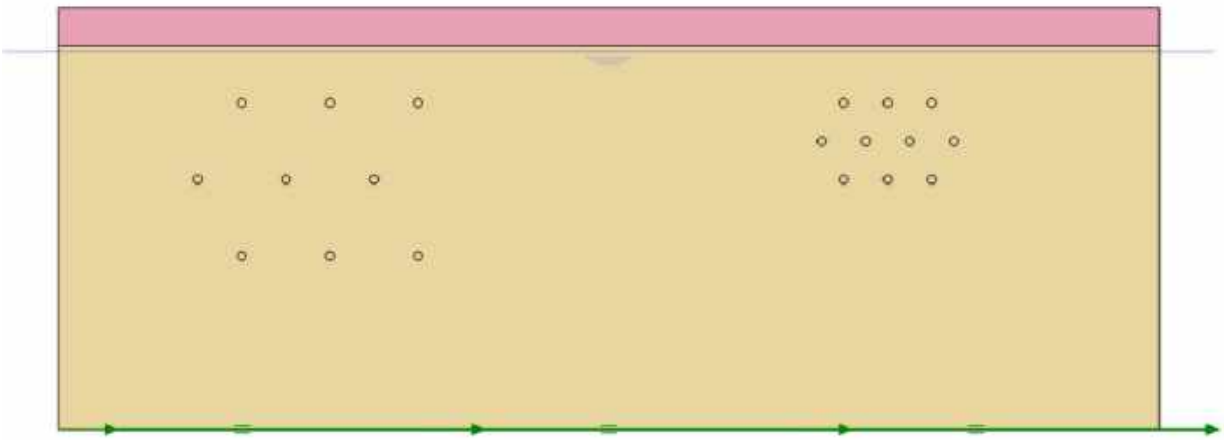

Layouts of the model reproduced in Plaxis 2D

This project has received funding from the European Union's Horizon 2020 research and innovation programme under grant agreement No. 700748

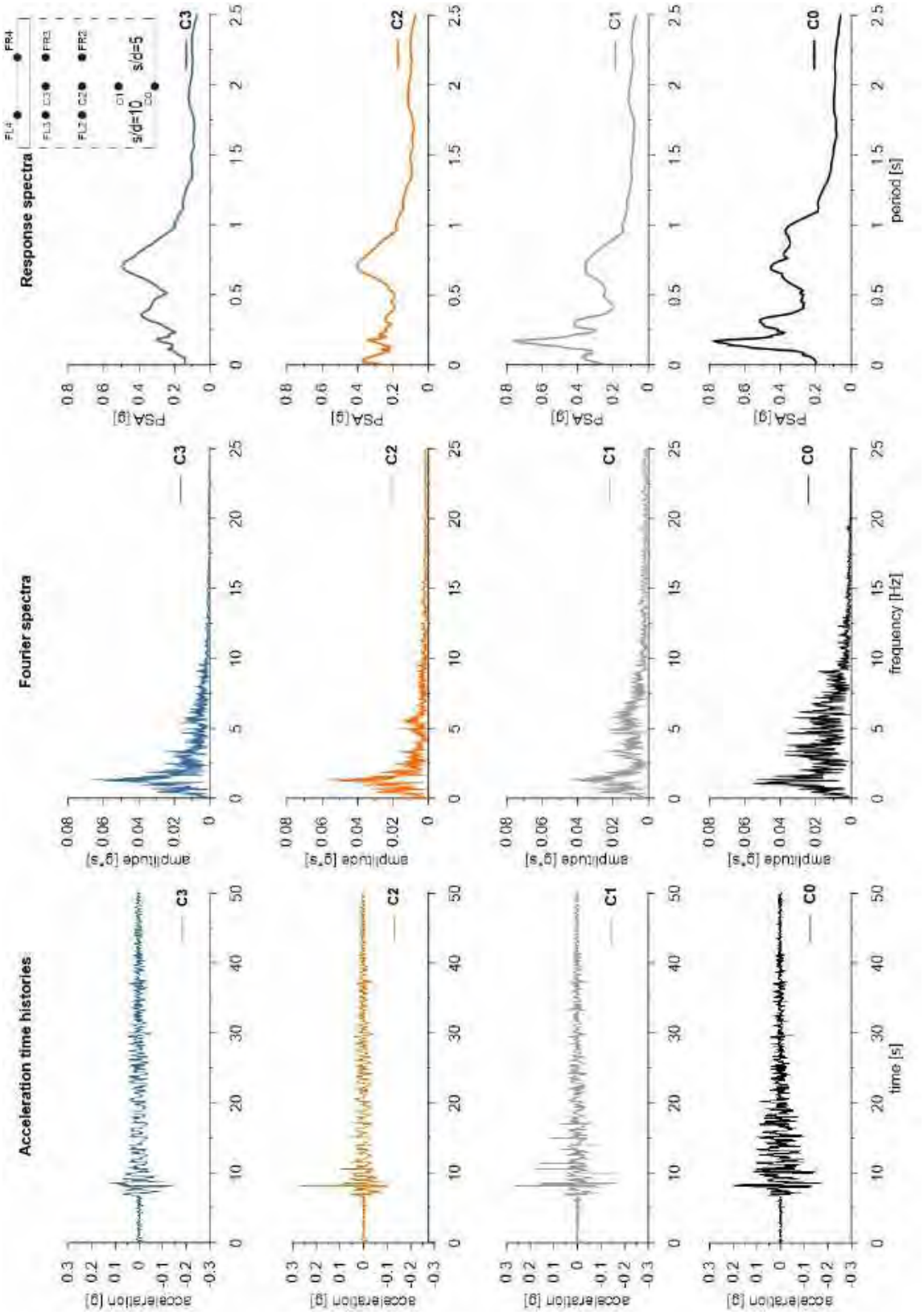

This project has received funding from the European Union's Horizon 2020 research and innovation programme under grant agreement No. 700748

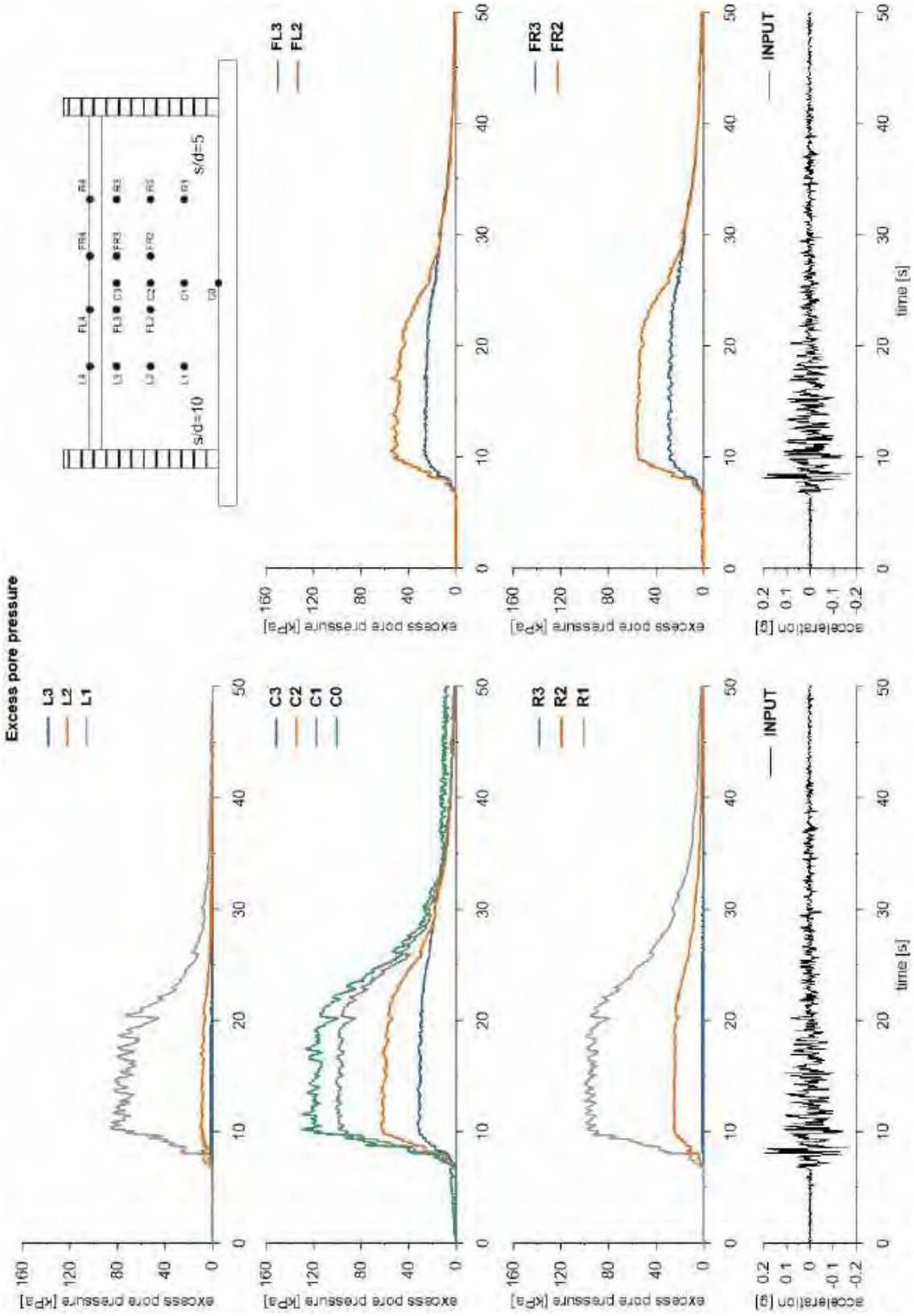

This project has received funding from the European Union's Horizon 2020 research and innovation programme under grant agreement No. 700748

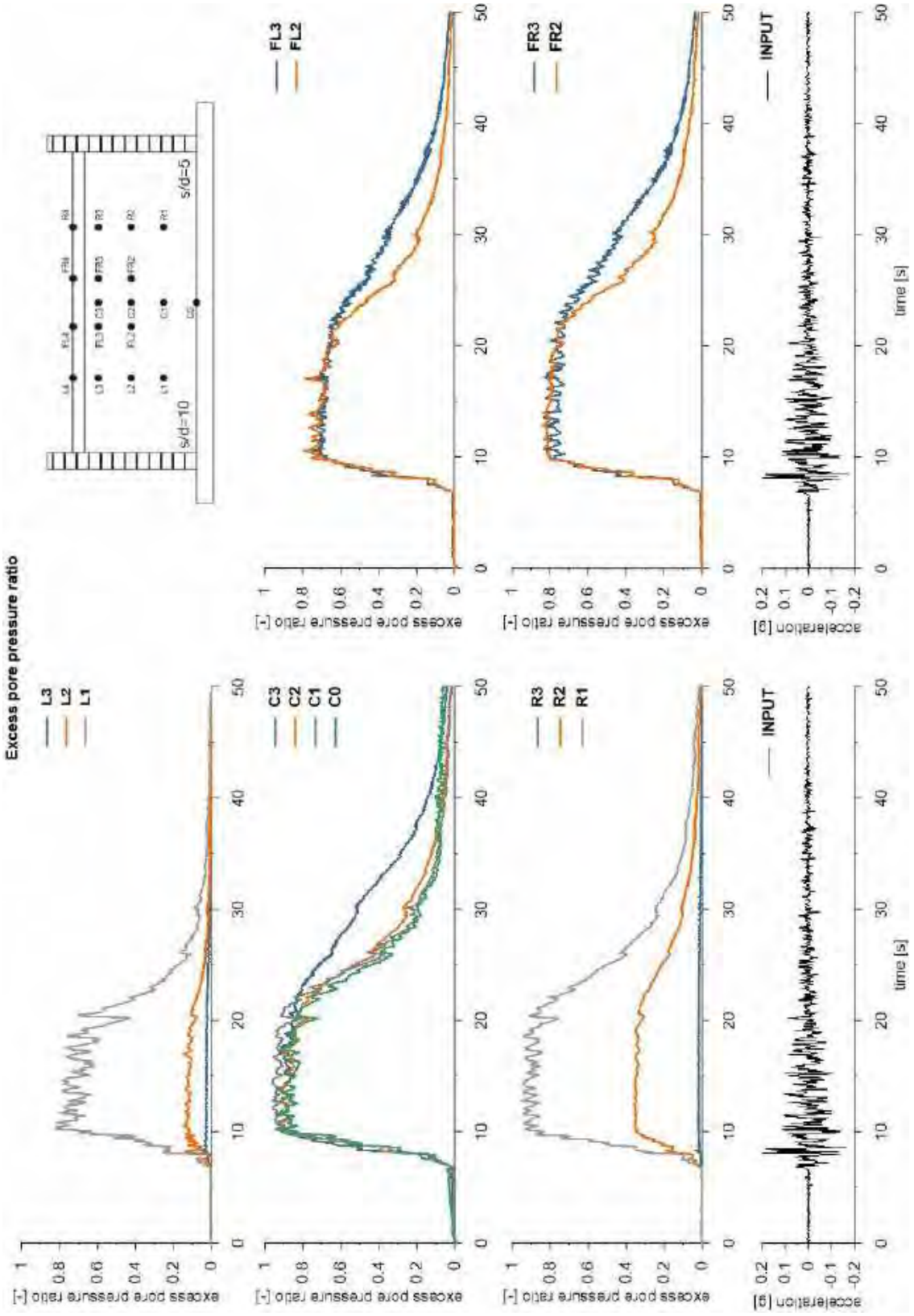

This project has received funding from the European Union's Horizon 2020 research and innovation programme under grant agreement No. 700748

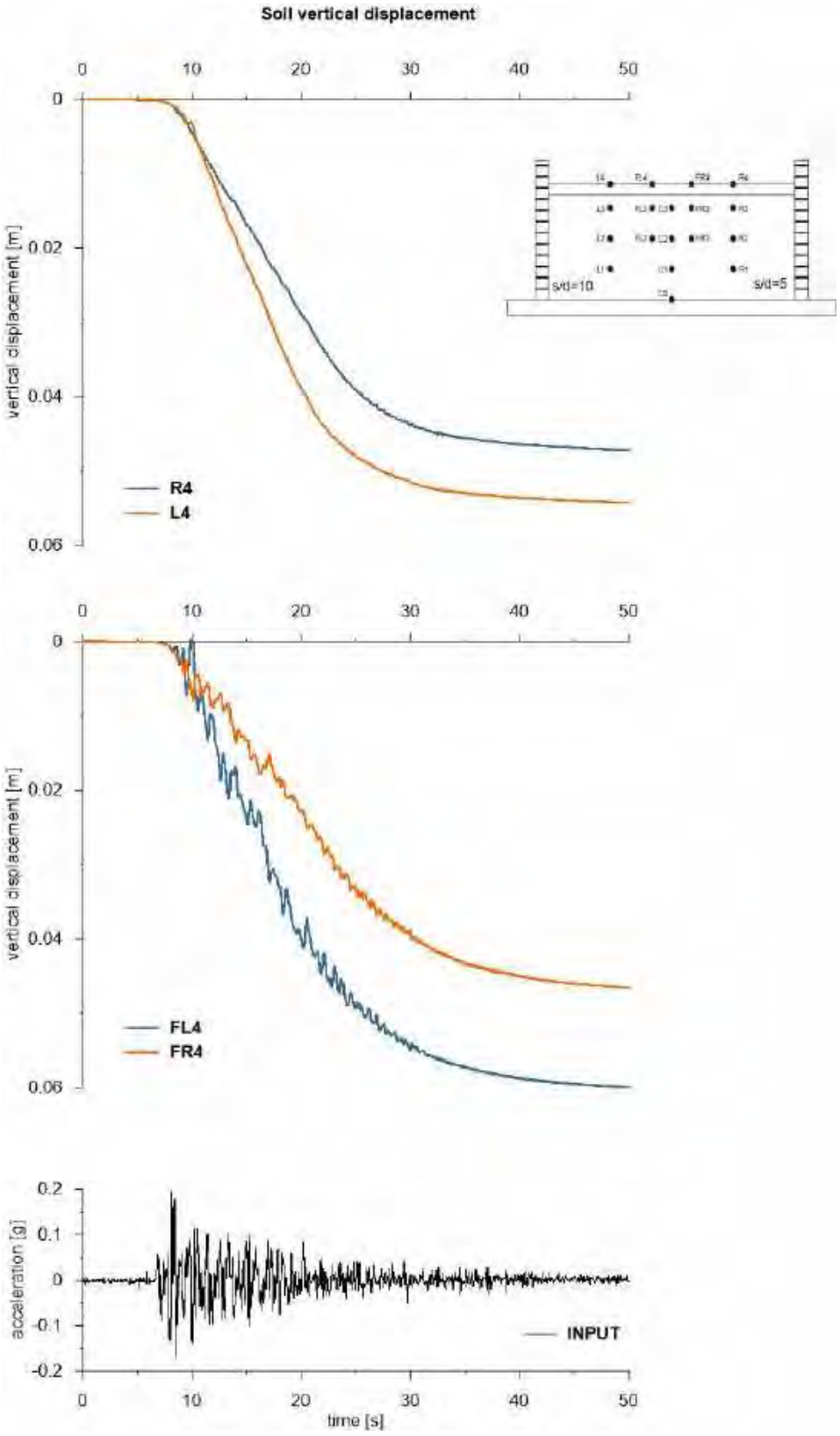

This project has received funding from the European Union's Horizon 2020 research and innovation programme under grant agreement No. 700748

6.1.1.6 ID: DS_xx_xx_xx

The model consists of a double soil profile of clay and Ticino sand. The ground motion applied was the number 31.

ID: DS_xx_xx_xx

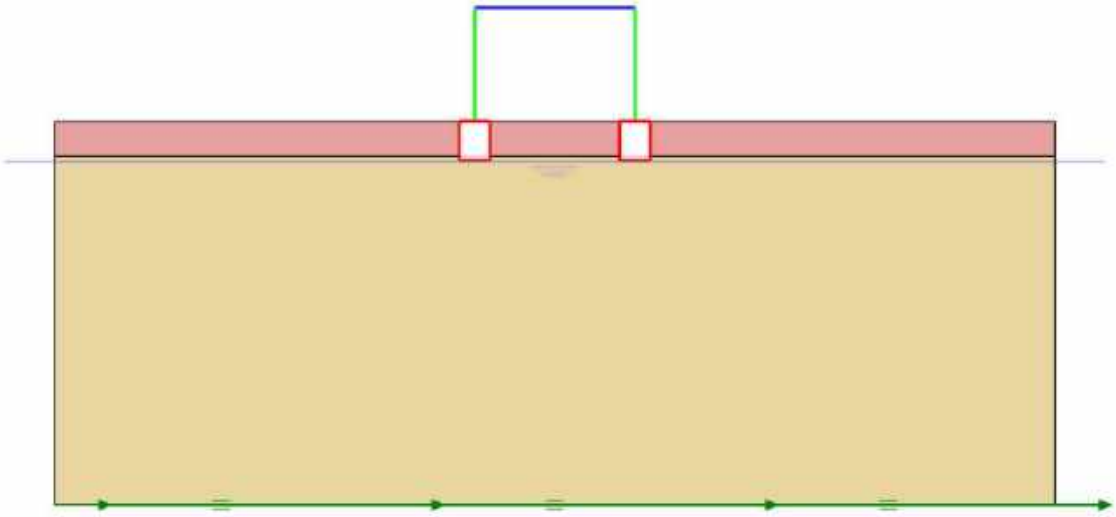

Layouts of the model reproduced in Plaxis 2D

This project has received funding from the European Union's Horizon 2020 research and innovation programme under grant agreement No. 700748

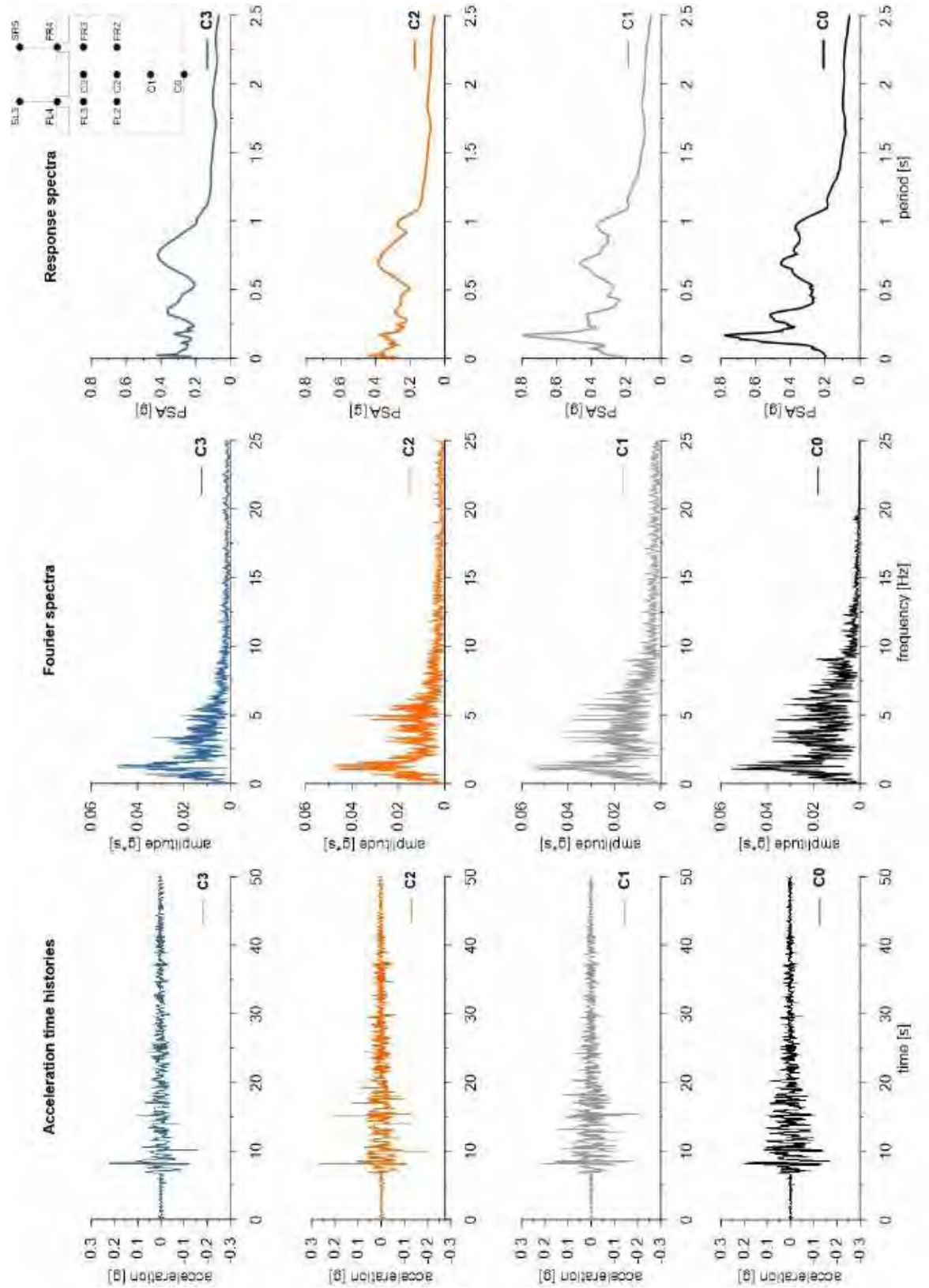

This project has received funding from the European Union's Horizon 2020 research and innovation programme under grant agreement No. 700748

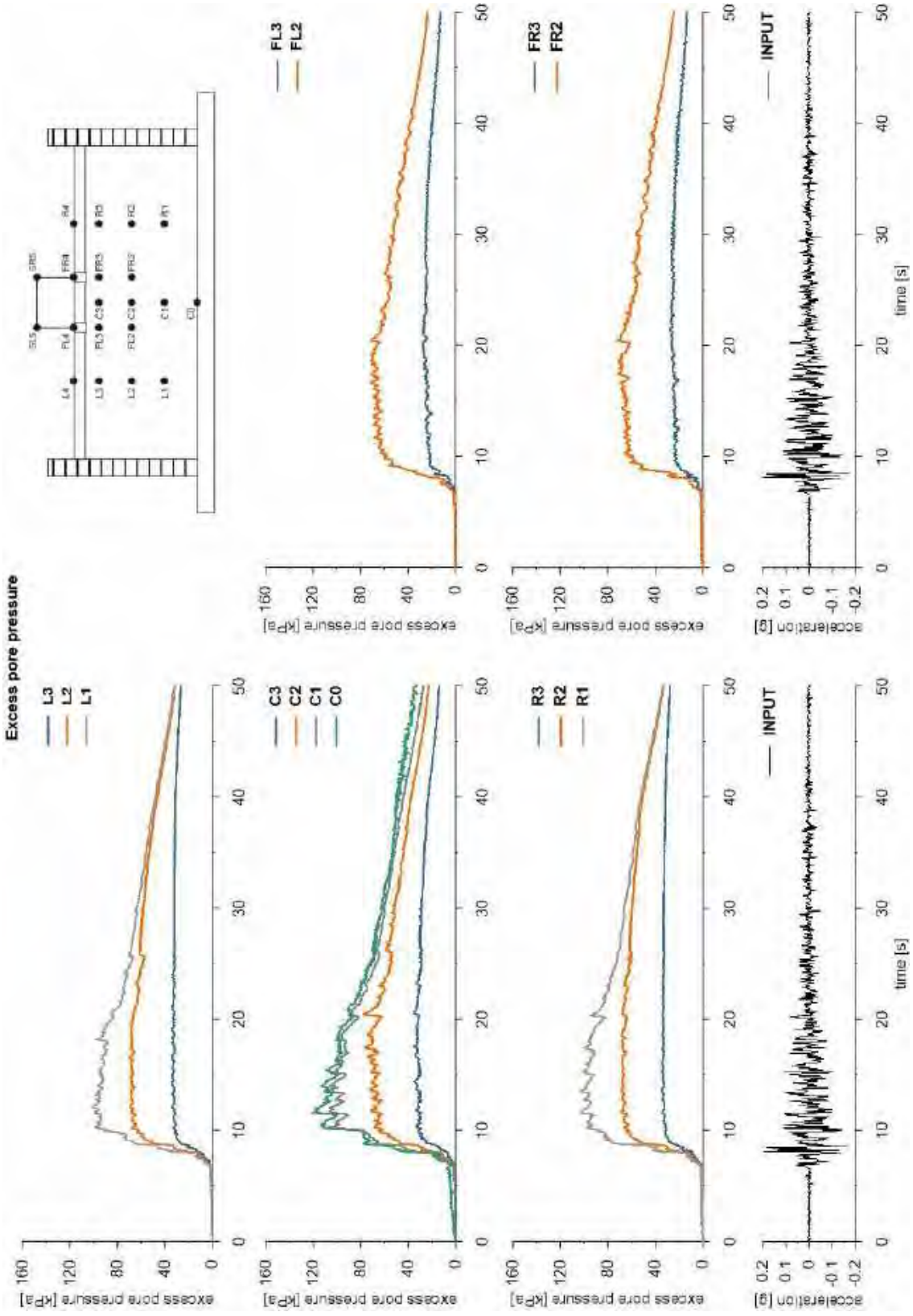

This project has received funding from the European Union's Horizon 2020 research and innovation programme under grant agreement No. 700748

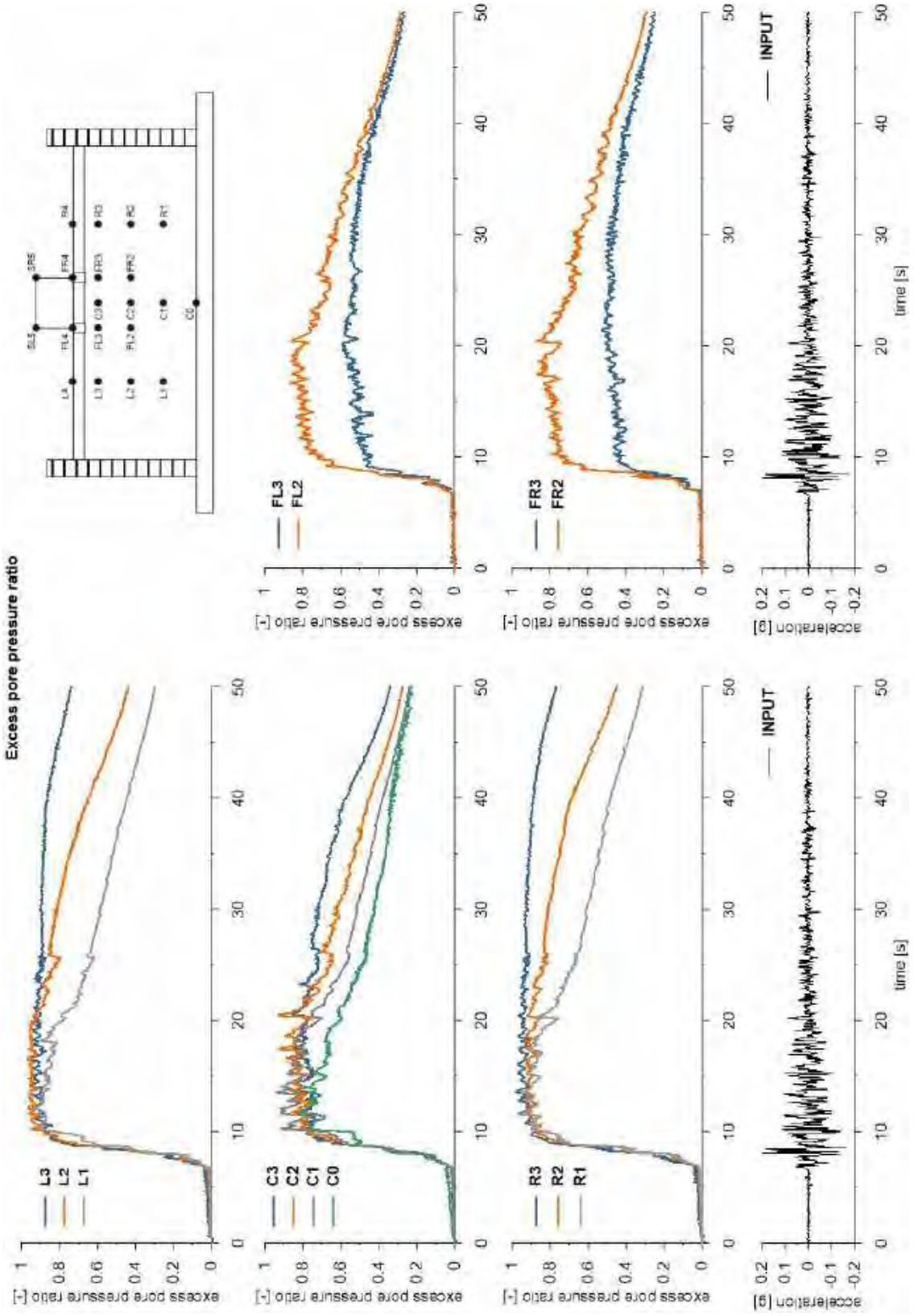

This project has received funding from the European Union's Horizon 2020 research and innovation programme under grant agreement No. 700748

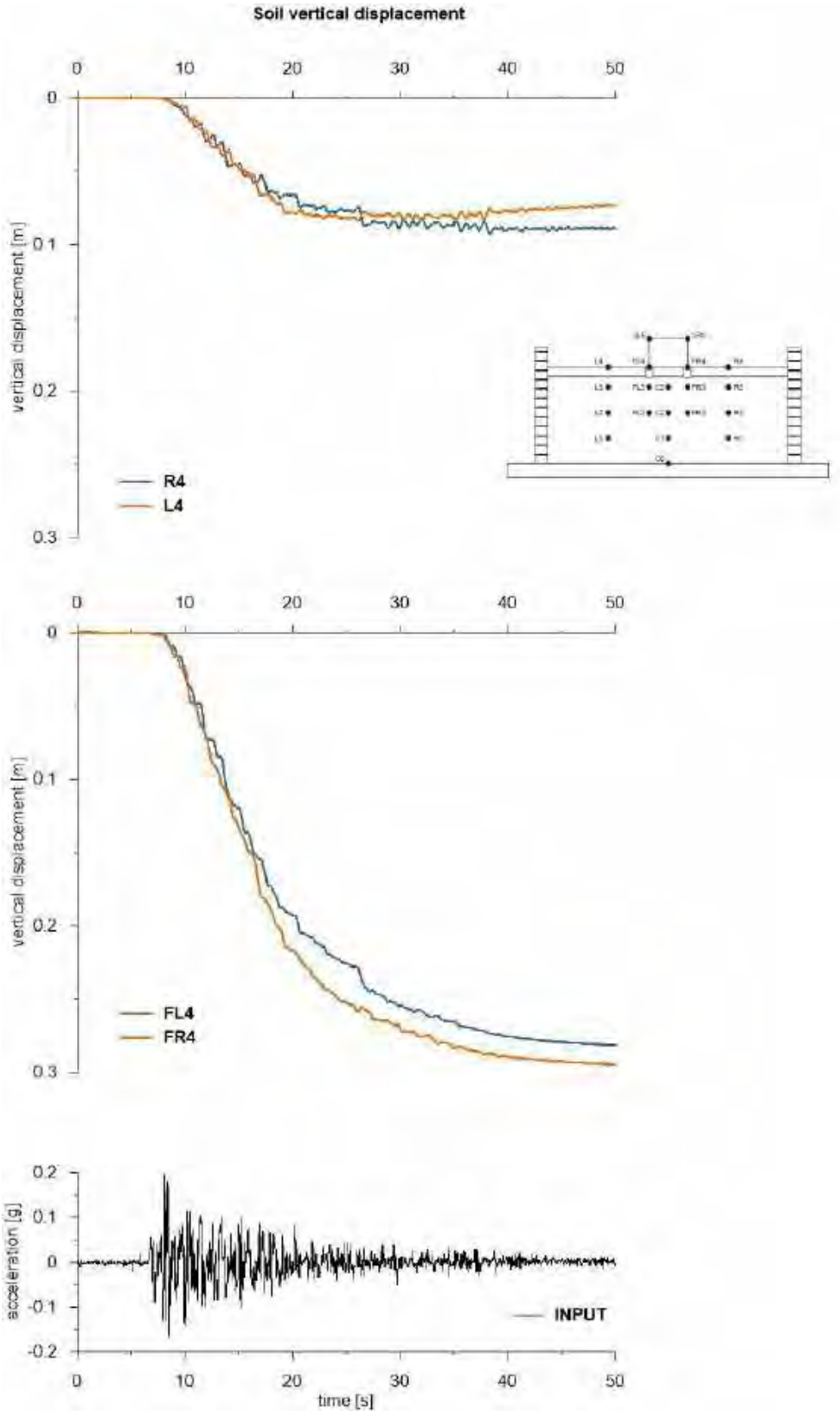

This project has received funding from the European Union's Horizon 2020 research and innovation programme under grant agreement No. 700748

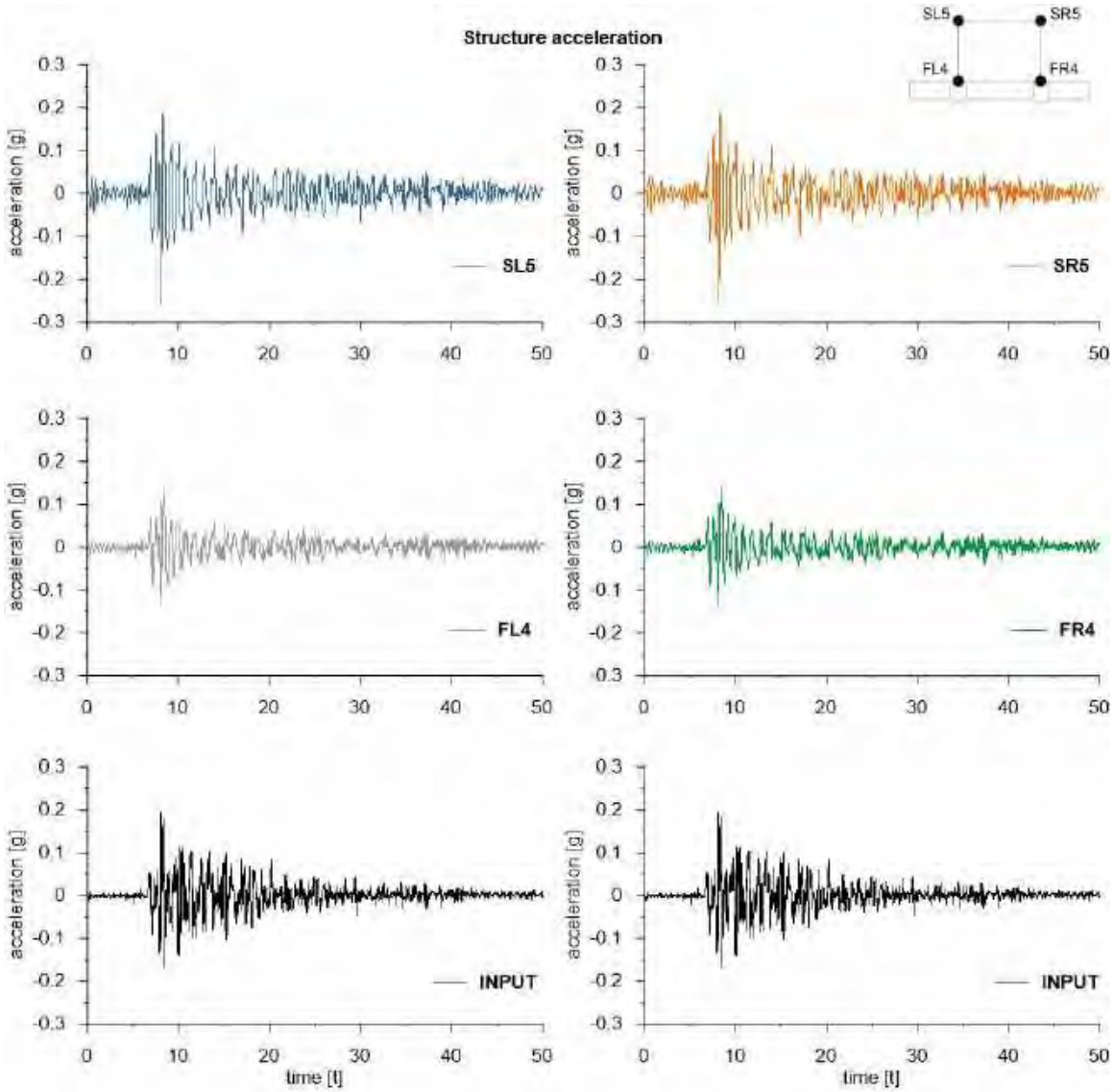

This project has received funding from the European Union's Horizon 2020 research and innovation programme under grant agreement No. 700748

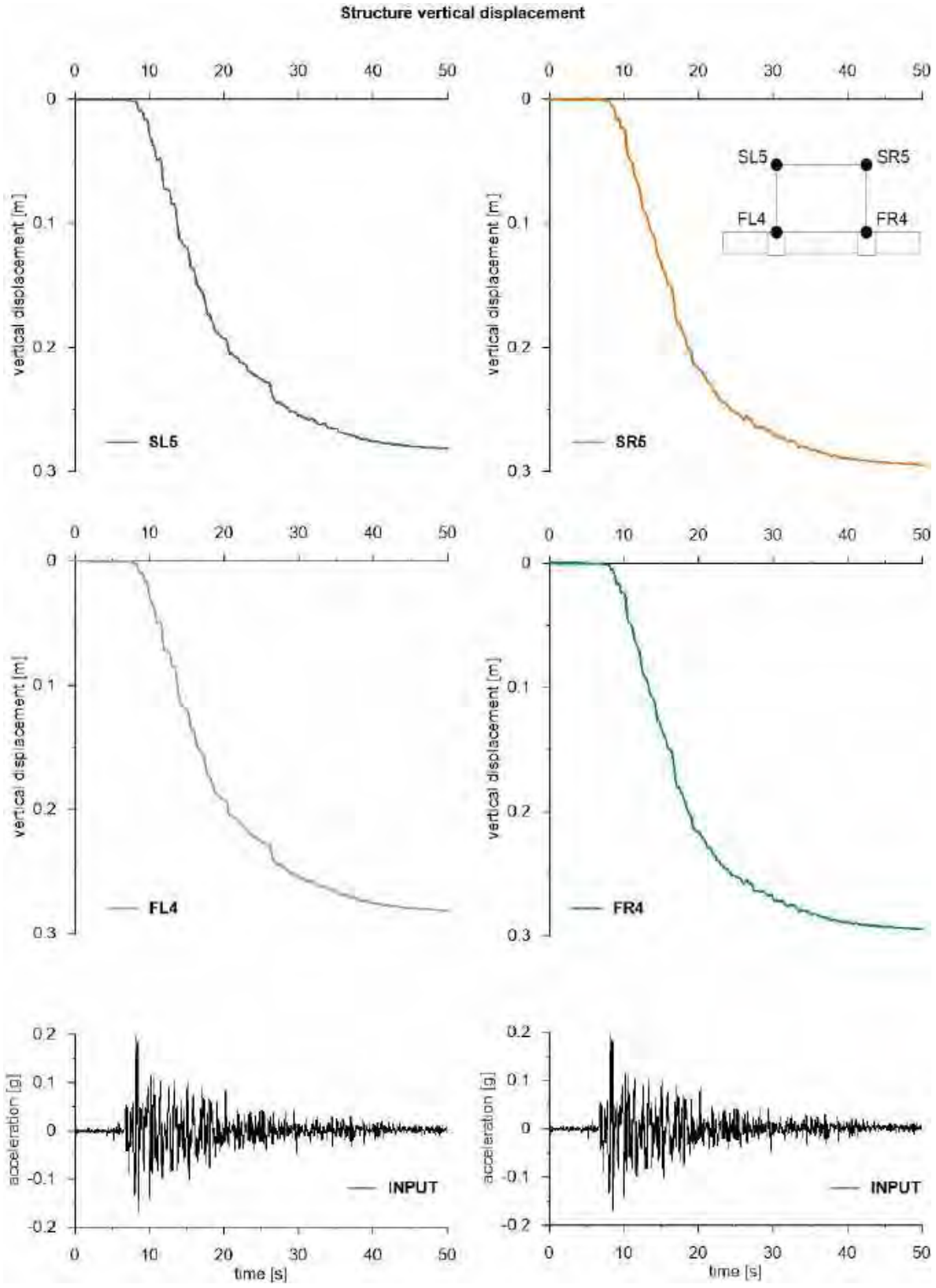

This project has received funding from the European Union's Horizon 2020 research and innovation programme under grant agreement No. 700748

6.1.1.7 ID: DS_HD_H05_s10

The model consists of a double soil profile of clay and Ticino sand. The ground motion applied was the number 31.

ID: DS_HD_H05_s10

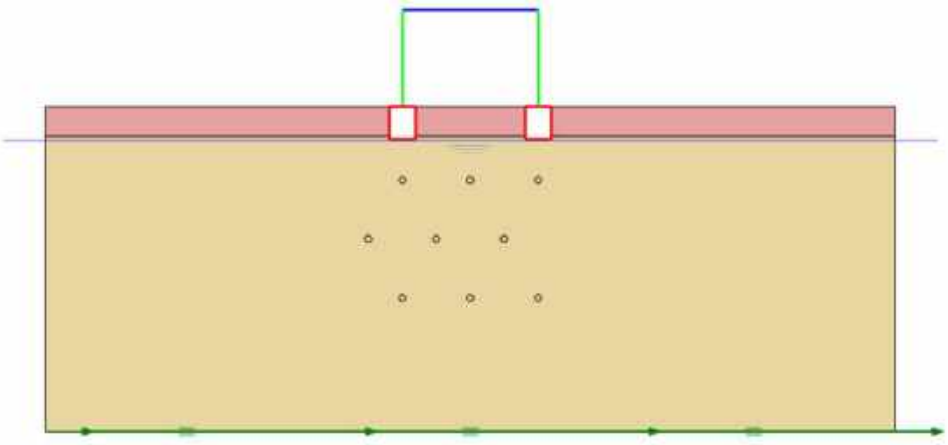

Layouts of the model reproduced in Plaxis 2D

This project has received funding from the European Union's Horizon 2020 research and innovation programme under grant agreement No. 700748

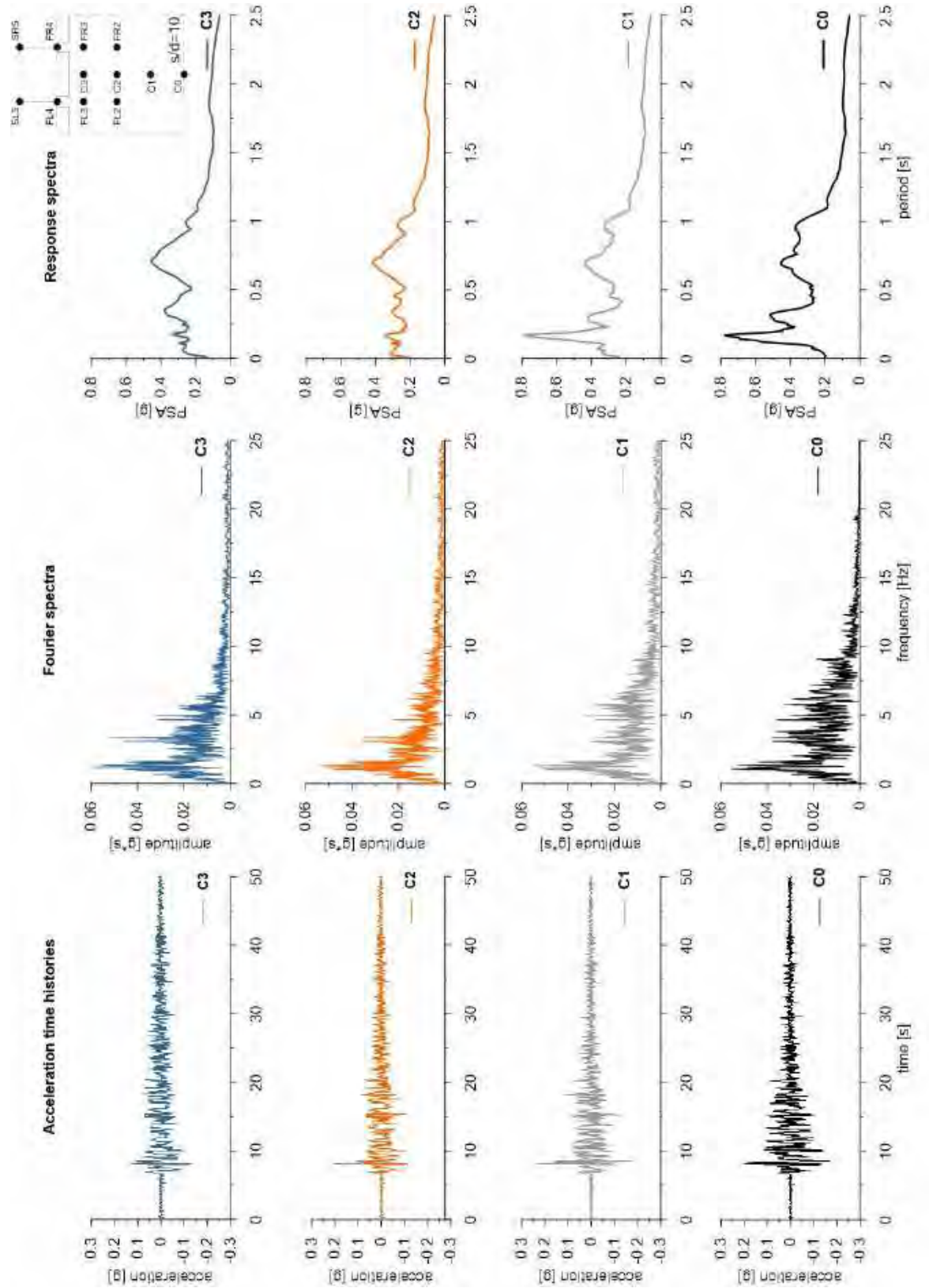

This project has received funding from the European Union's Horizon 2020 research and innovation programme under grant agreement No. 700748

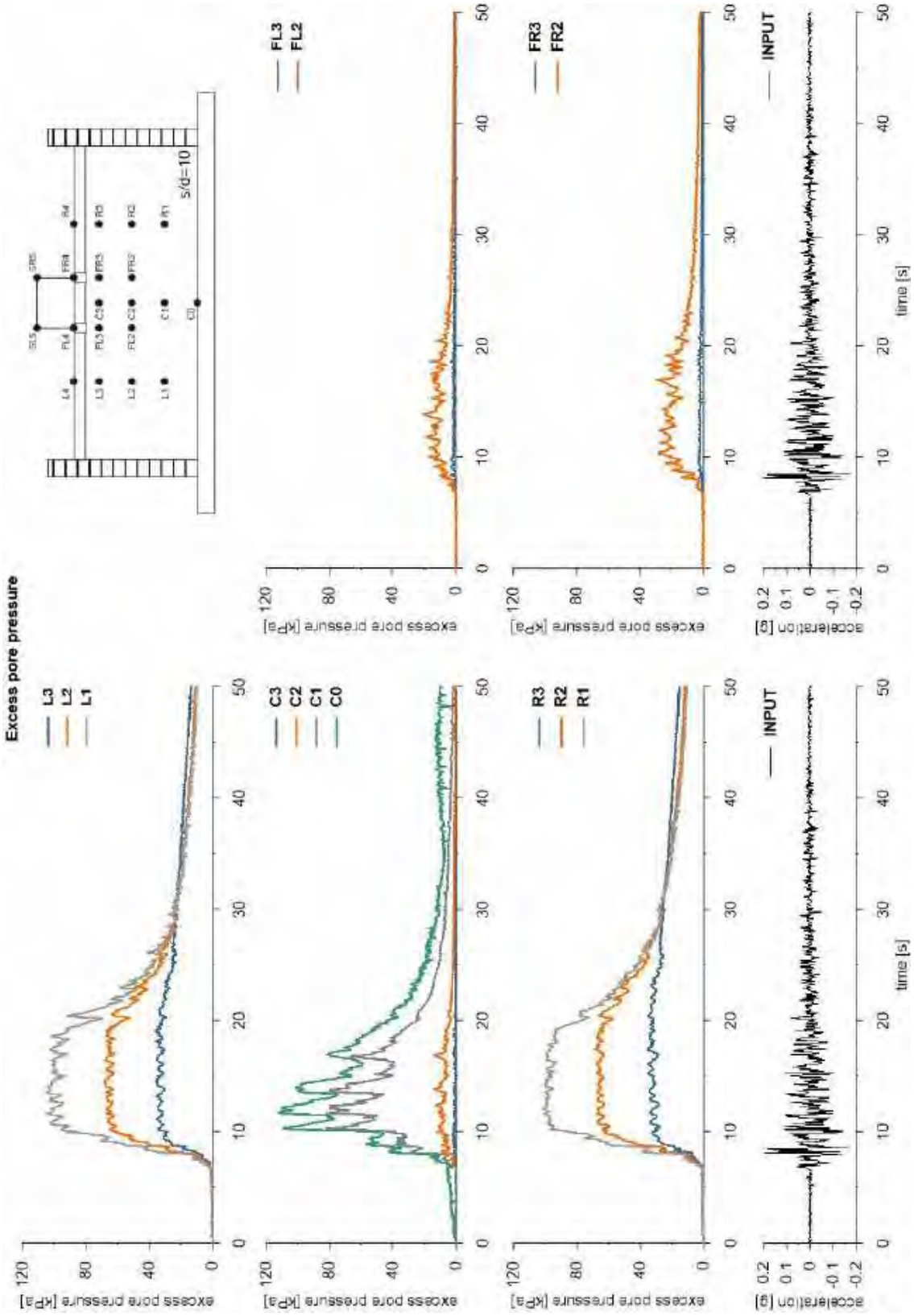

This project has received funding from the European Union's Horizon 2020 research and innovation programme under grant agreement No. 700748

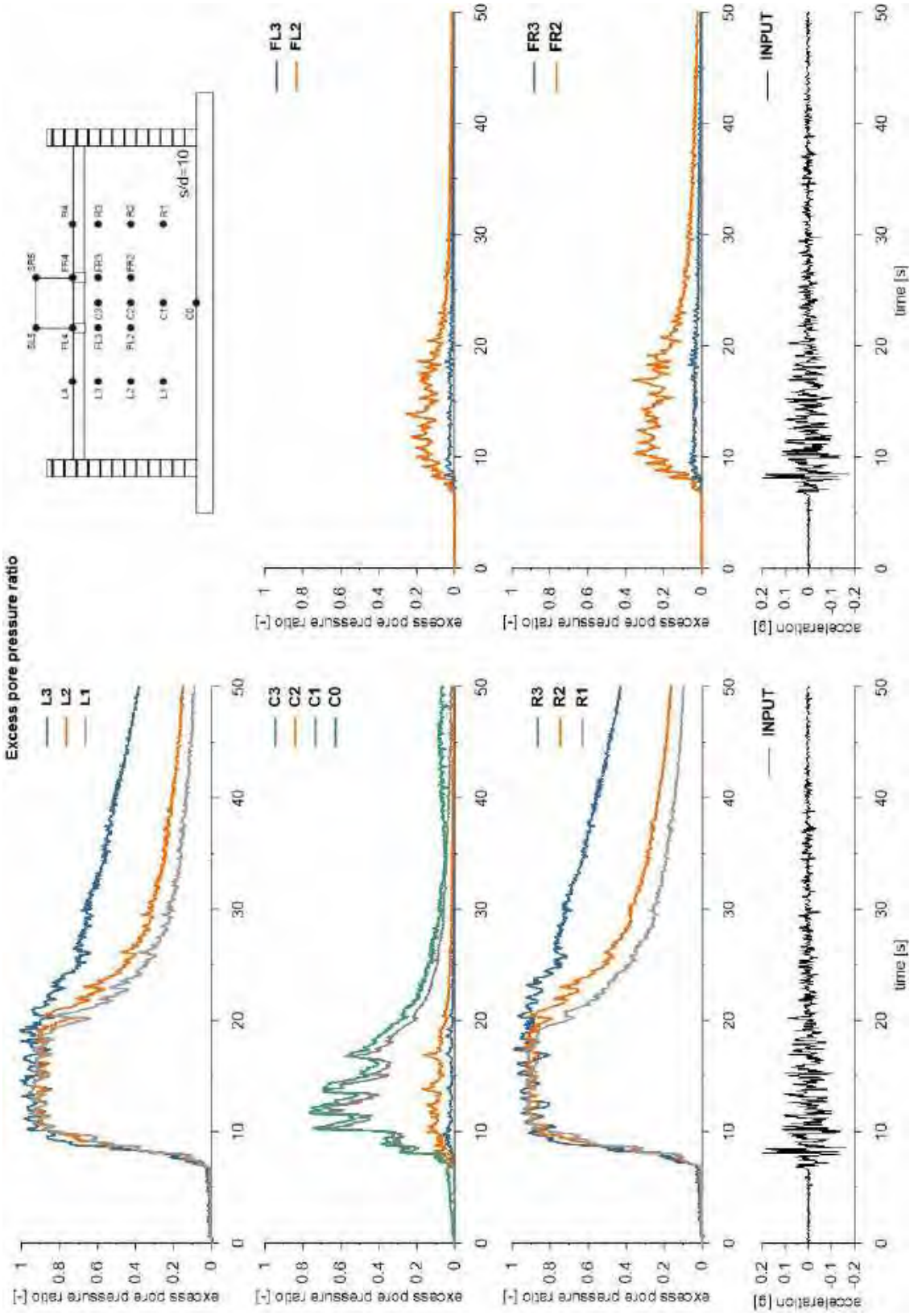

This project has received funding from the European Union's Horizon 2020 research and innovation programme under grant agreement No. 700748

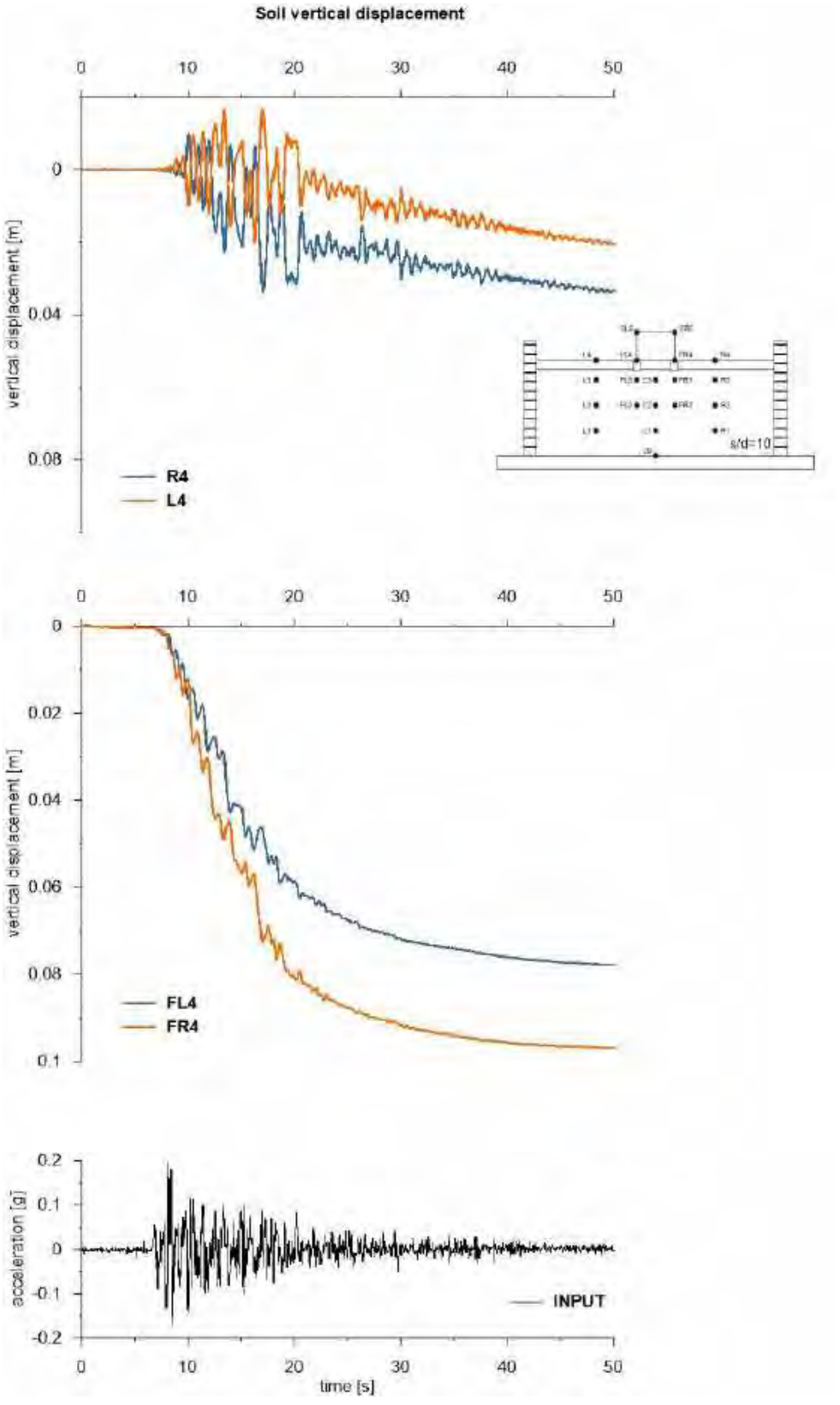

This project has received funding from the European Union's Horizon 2020 research and innovation programme under grant agreement No. 700748

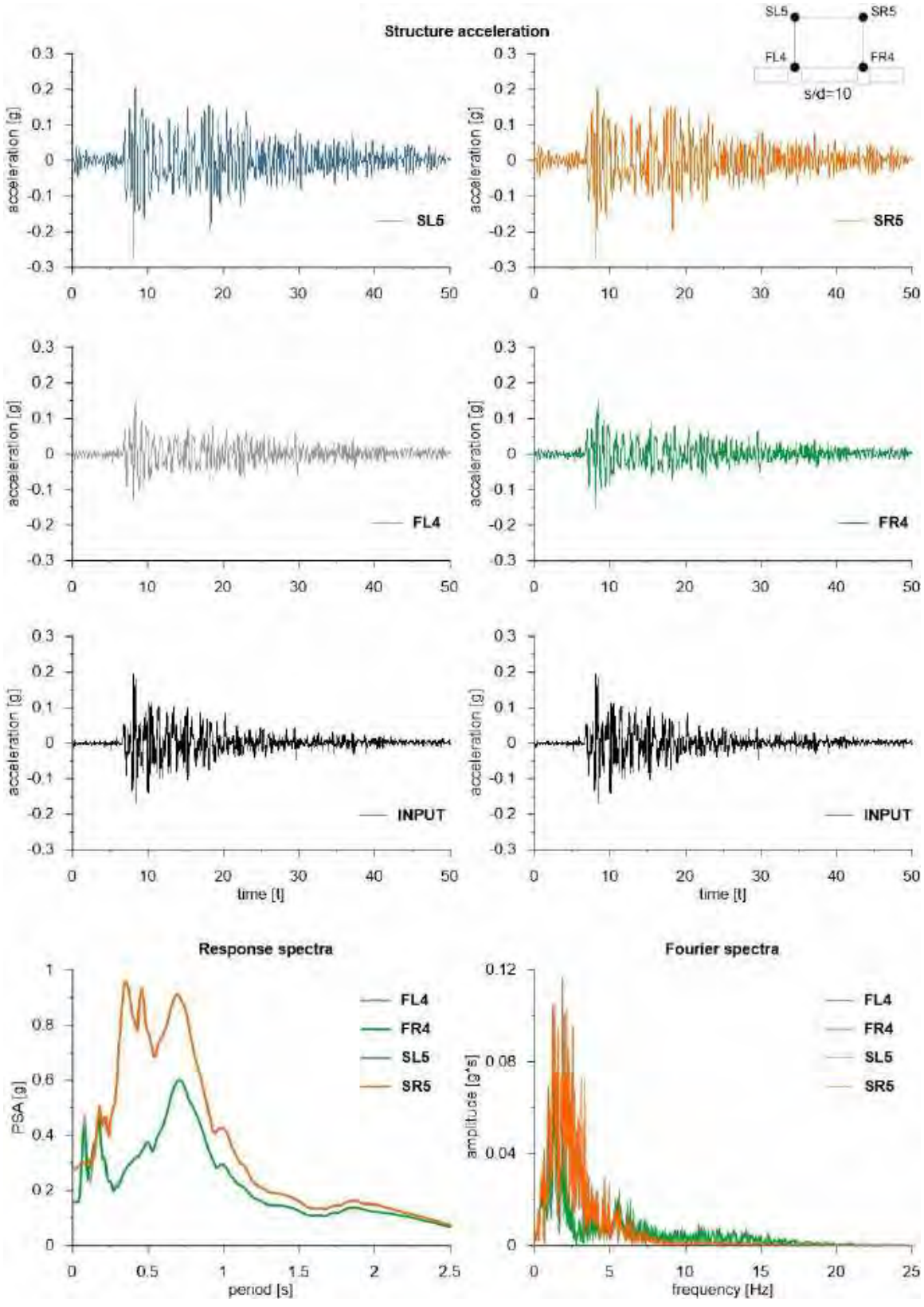

This project has received funding from the European Union's Horizon 2020 research and innovation programme under grant agreement No. 700748

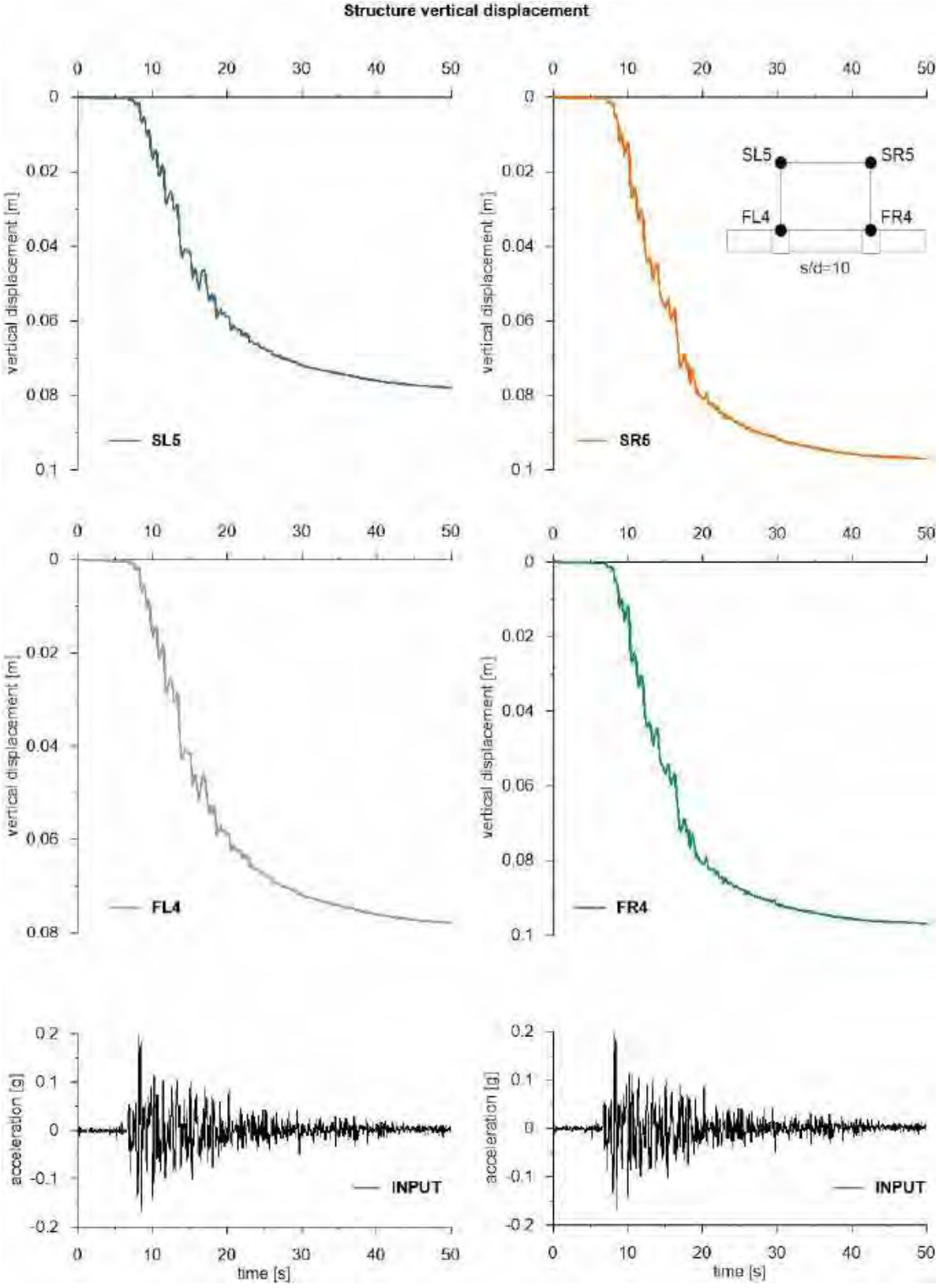

This project has received funding from the European Union's Horizon 2020 research and innovation programme under grant agreement No. 700748

6.1.1.8 ID: DS_HD_H05_s05

The model consists of a double soil profile of clay and Ticino sand. The ground motion applied was the number 31.

ID: DS_HD_H05_s05

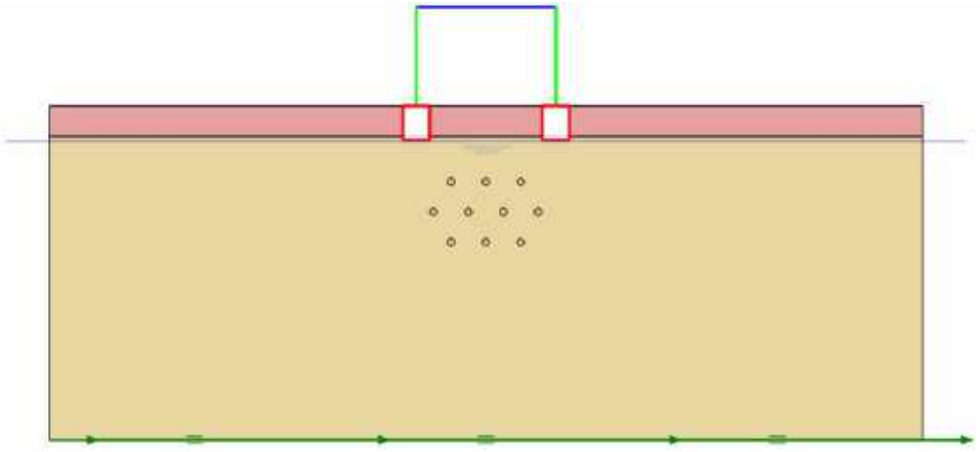

Layouts of the model reproduced in Plaxis 2D

This project has received funding from the European Union's Horizon 2020 research and innovation programme under grant agreement No. 700748

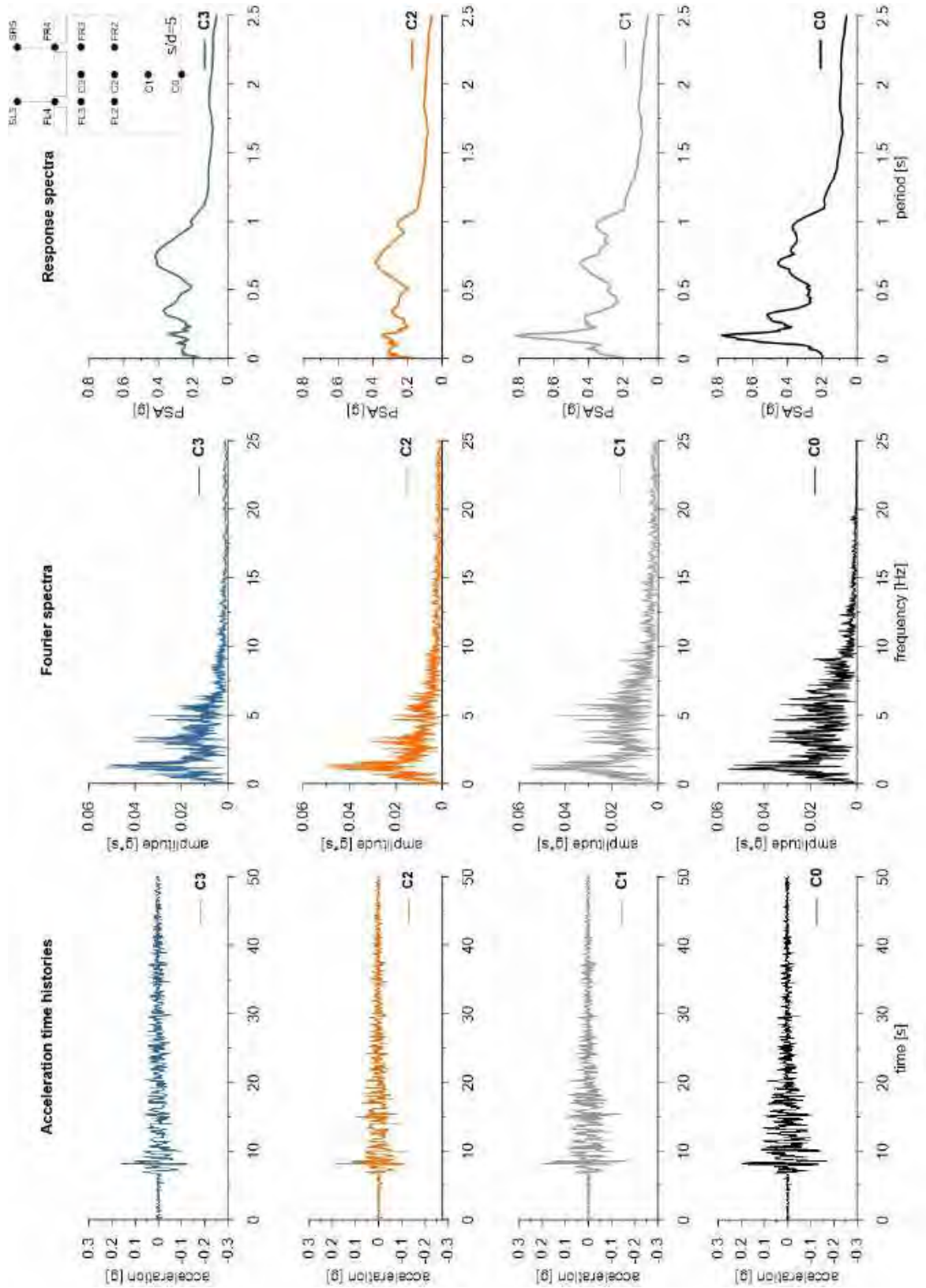

This project has received funding from the European Union's Horizon 2020 research and innovation programme under grant agreement No. 700748

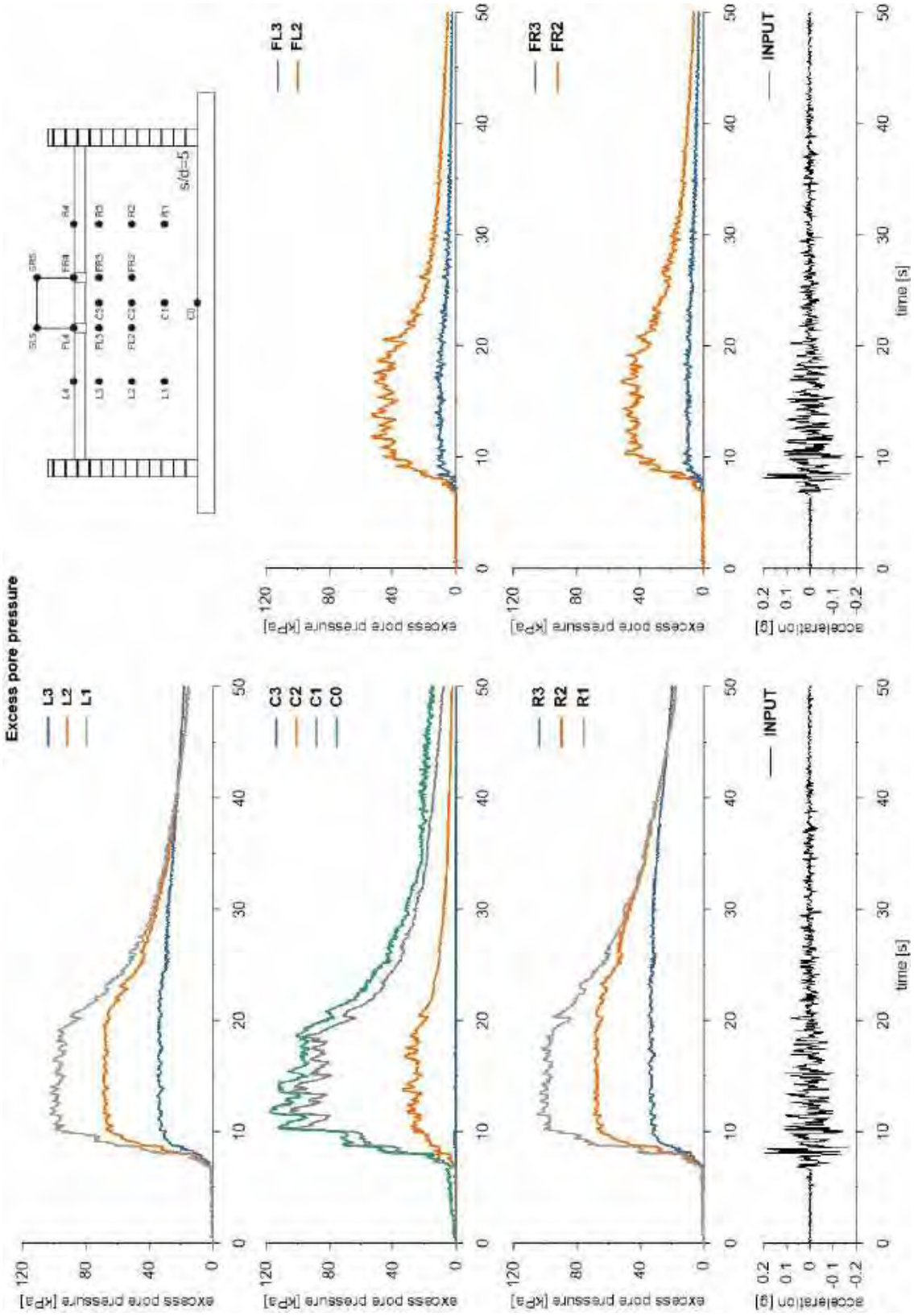

This project has received funding from the European Union's Horizon 2020 research and innovation programme under grant agreement No. 700748

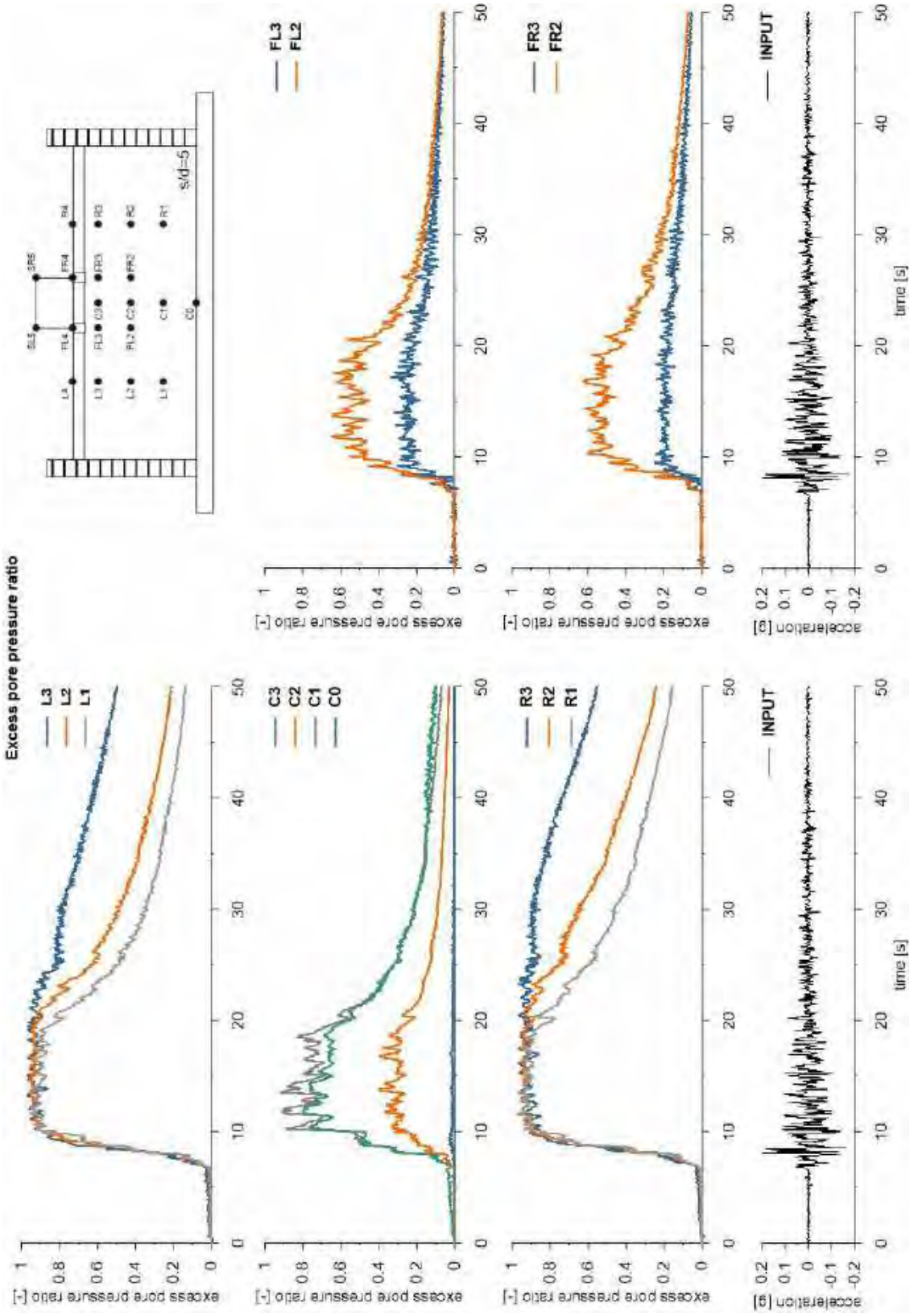

This project has received funding from the European Union's Horizon 2020 research and innovation programme under grant agreement No. 700748

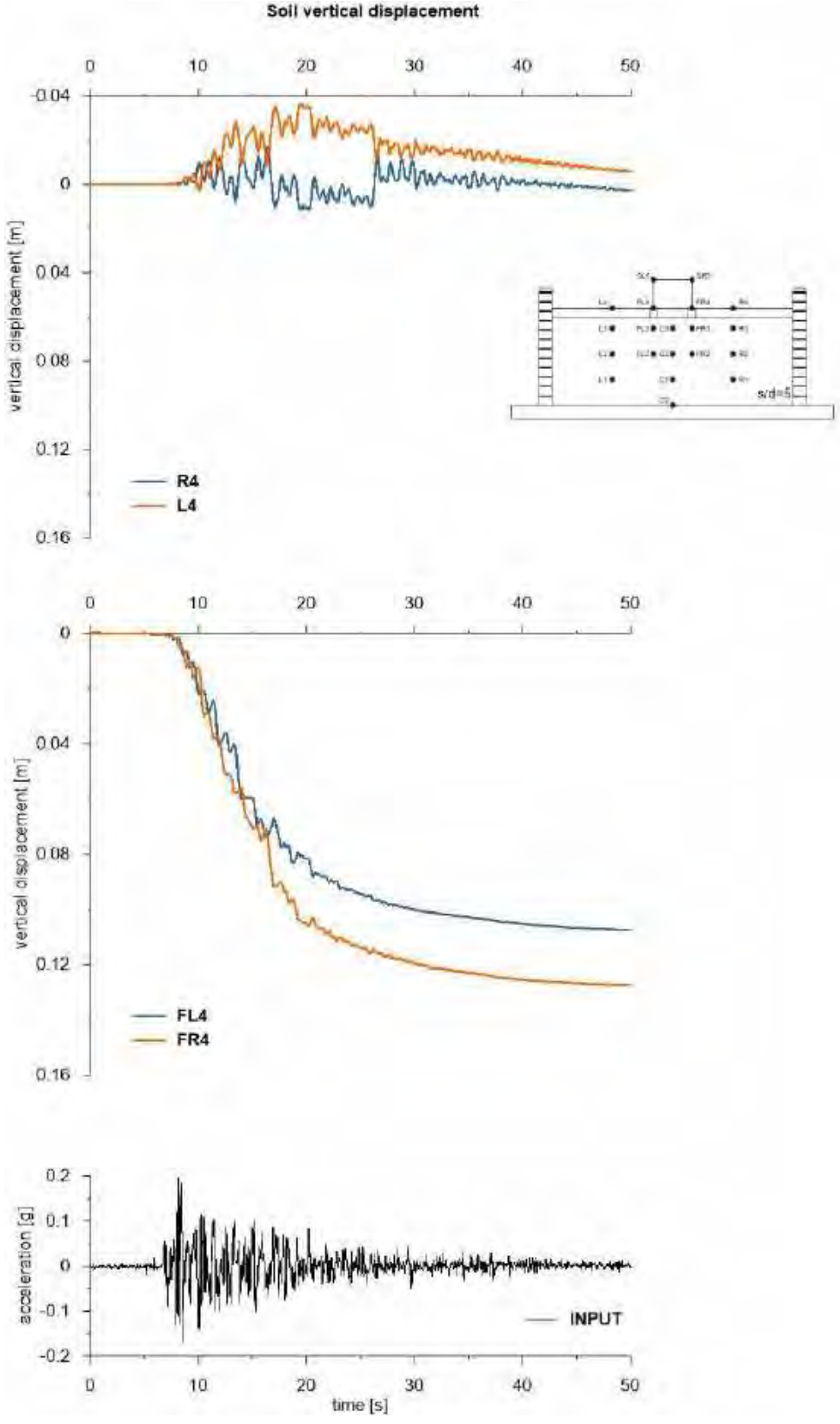

This project has received funding from the European Union's Horizon 2020 research and innovation programme under grant agreement No. 700748

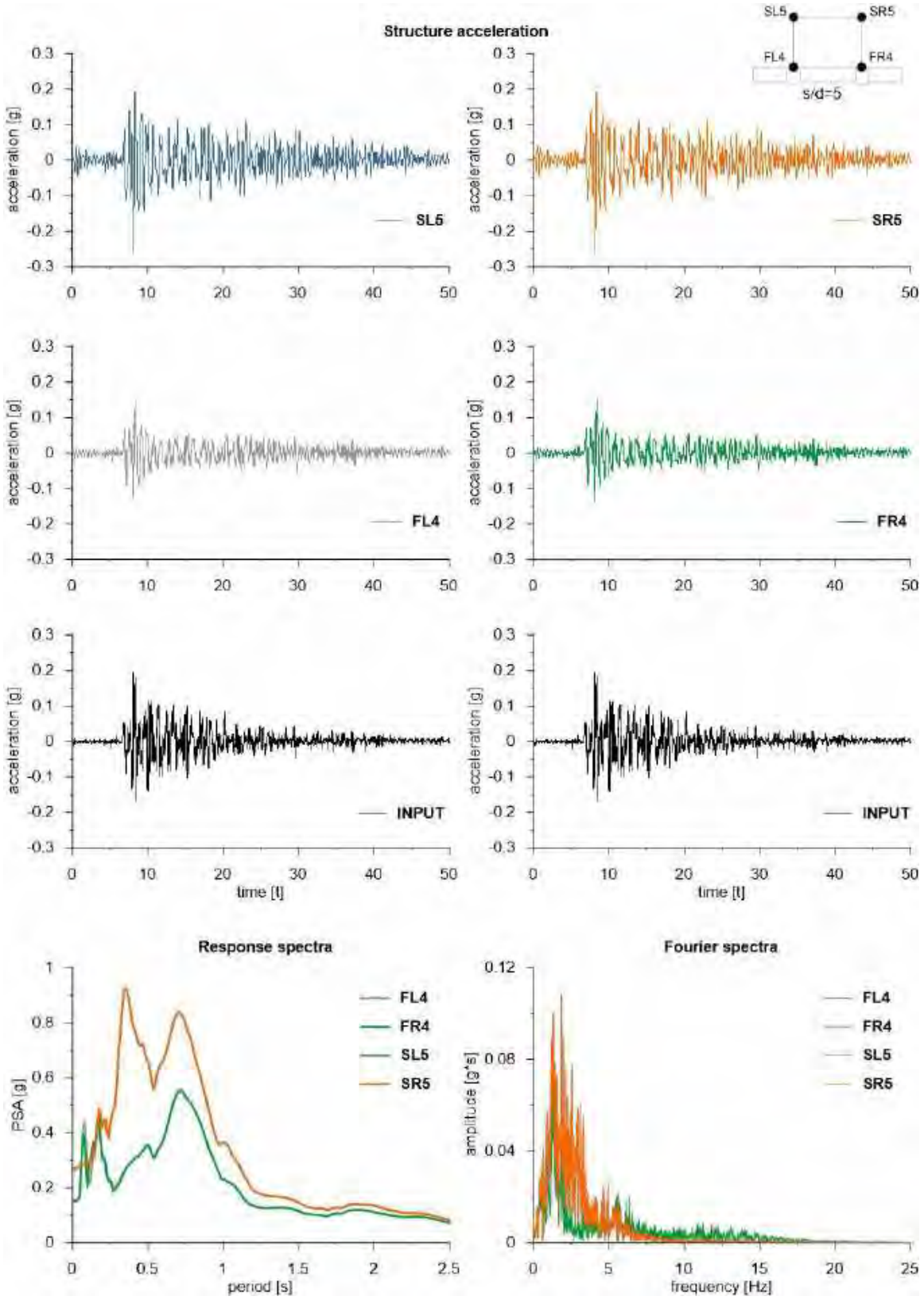

This project has received funding from the European Union's Horizon 2020 research and innovation programme under grant agreement No. 700748

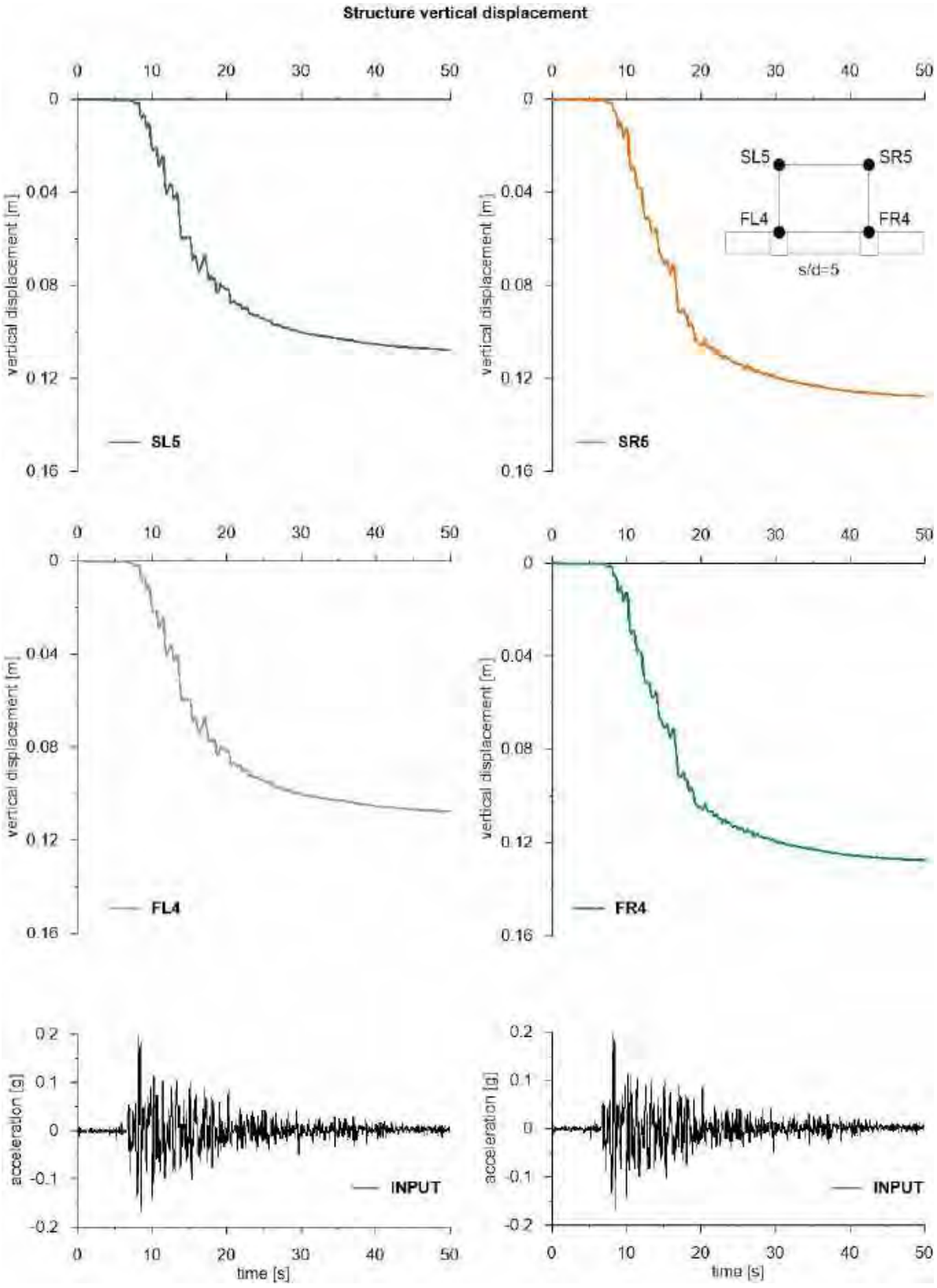

This project has received funding from the European Union's Horizon 2020 research and innovation programme under grant agreement No. 700748

6.1.1.9 ID: SF_HDU_H05_s05

The model consists of a homogenous soil profile of Ticino sand. The ground motion applied was the number 31.

ID: SF_HDU_H05_s05

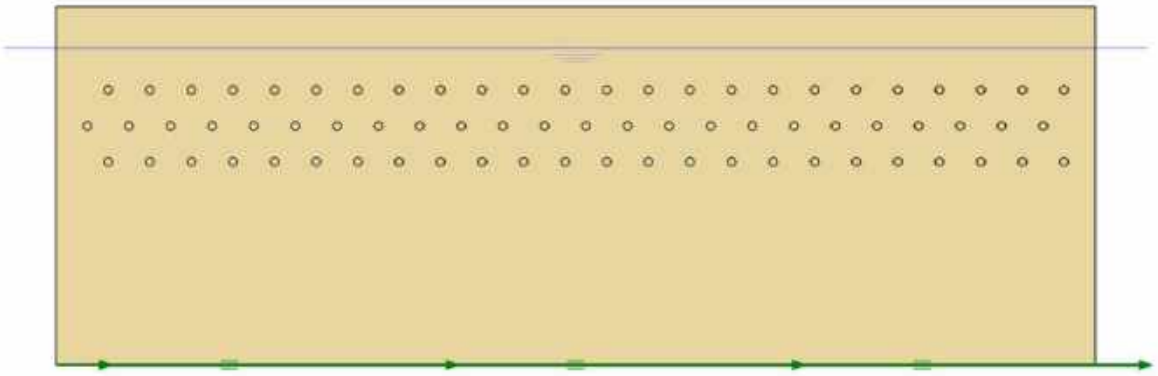

Layouts of the model reproduced in Plaxis 2D

This project has received funding from the European Union's Horizon 2020 research and innovation programme under grant agreement No. 700748

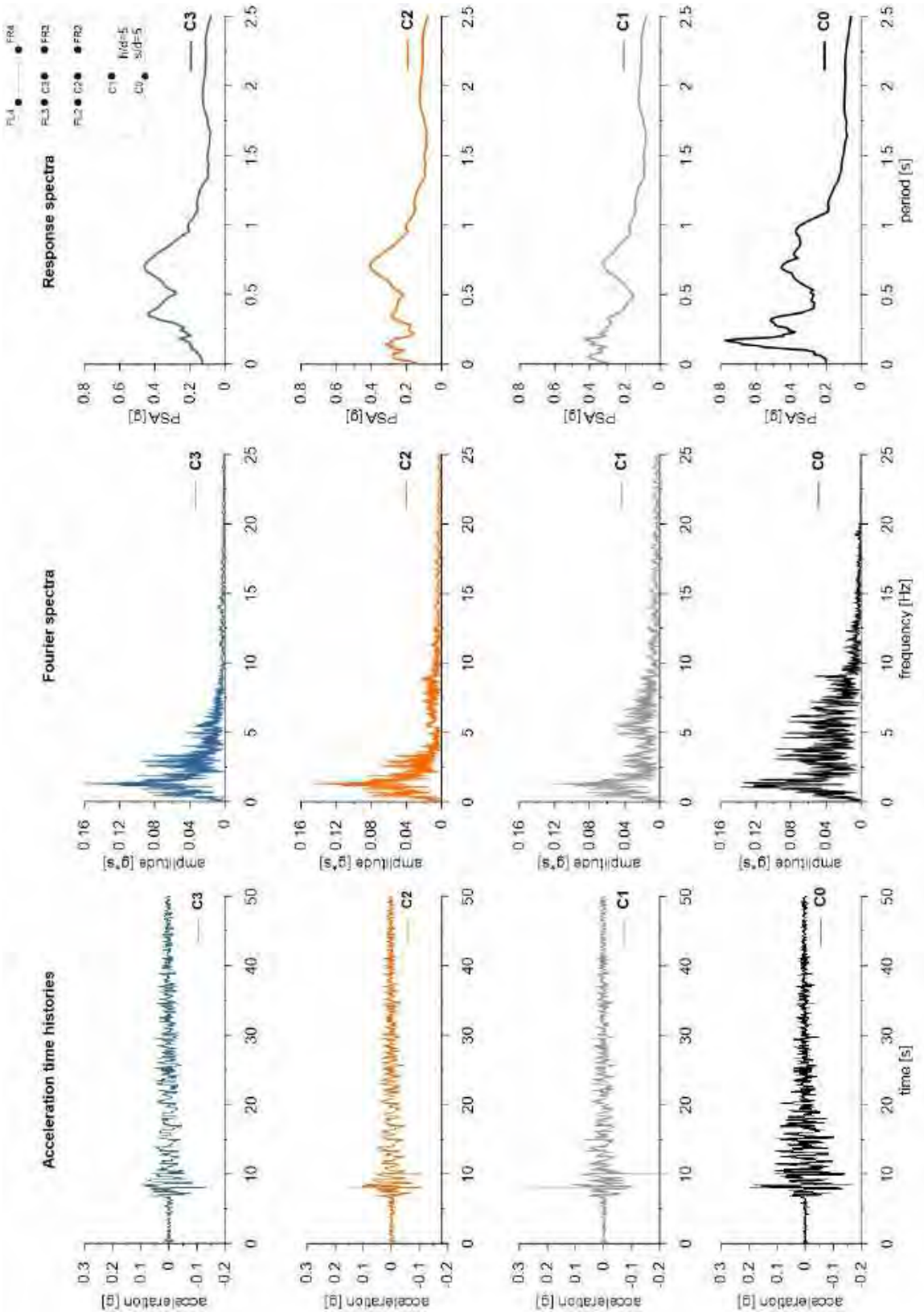

This project has received funding from the European Union's Horizon 2020 research and innovation programme under grant agreement No. 700748

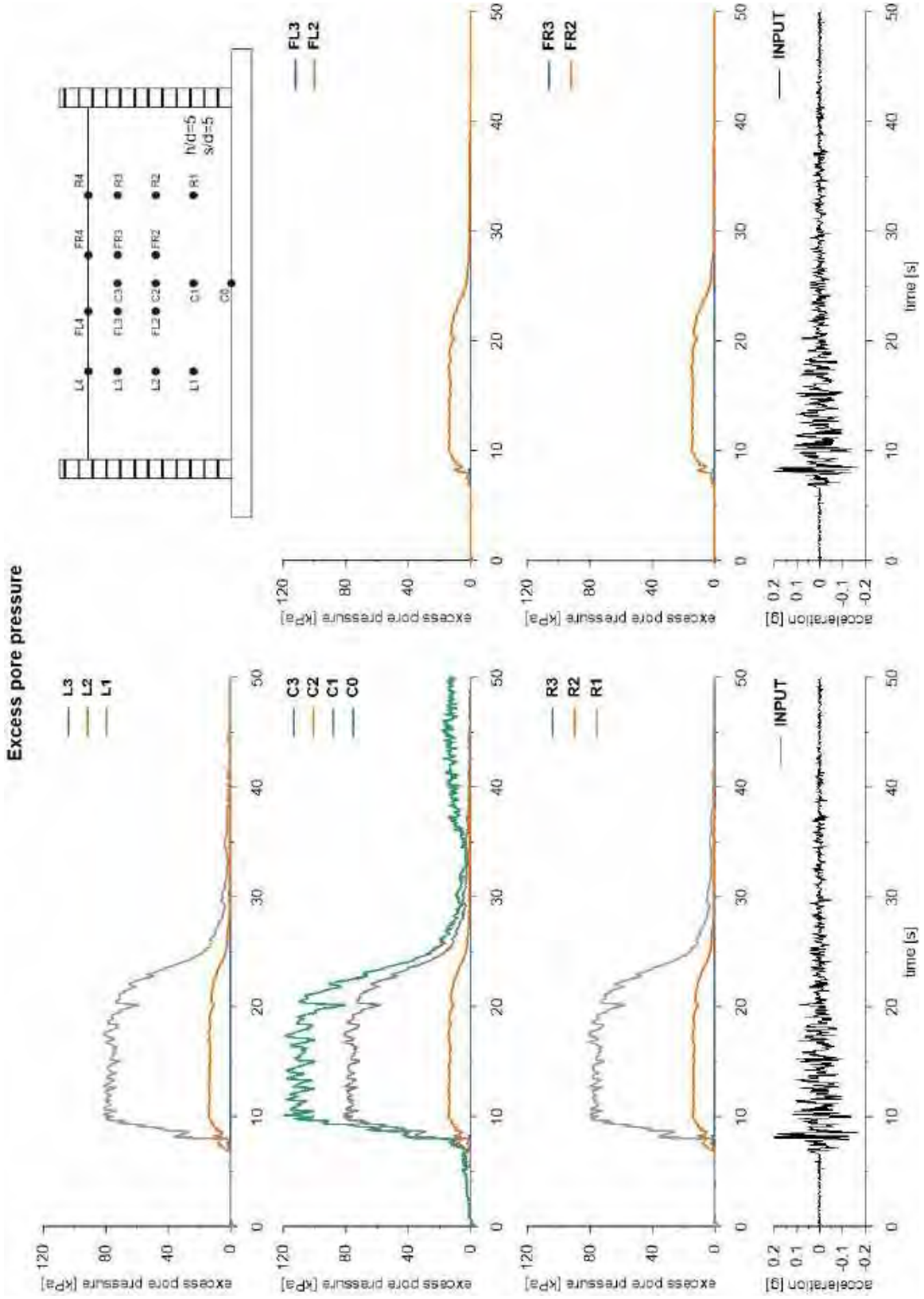

This project has received funding from the European Union's Horizon 2020 research and innovation programme under grant agreement No. 700748

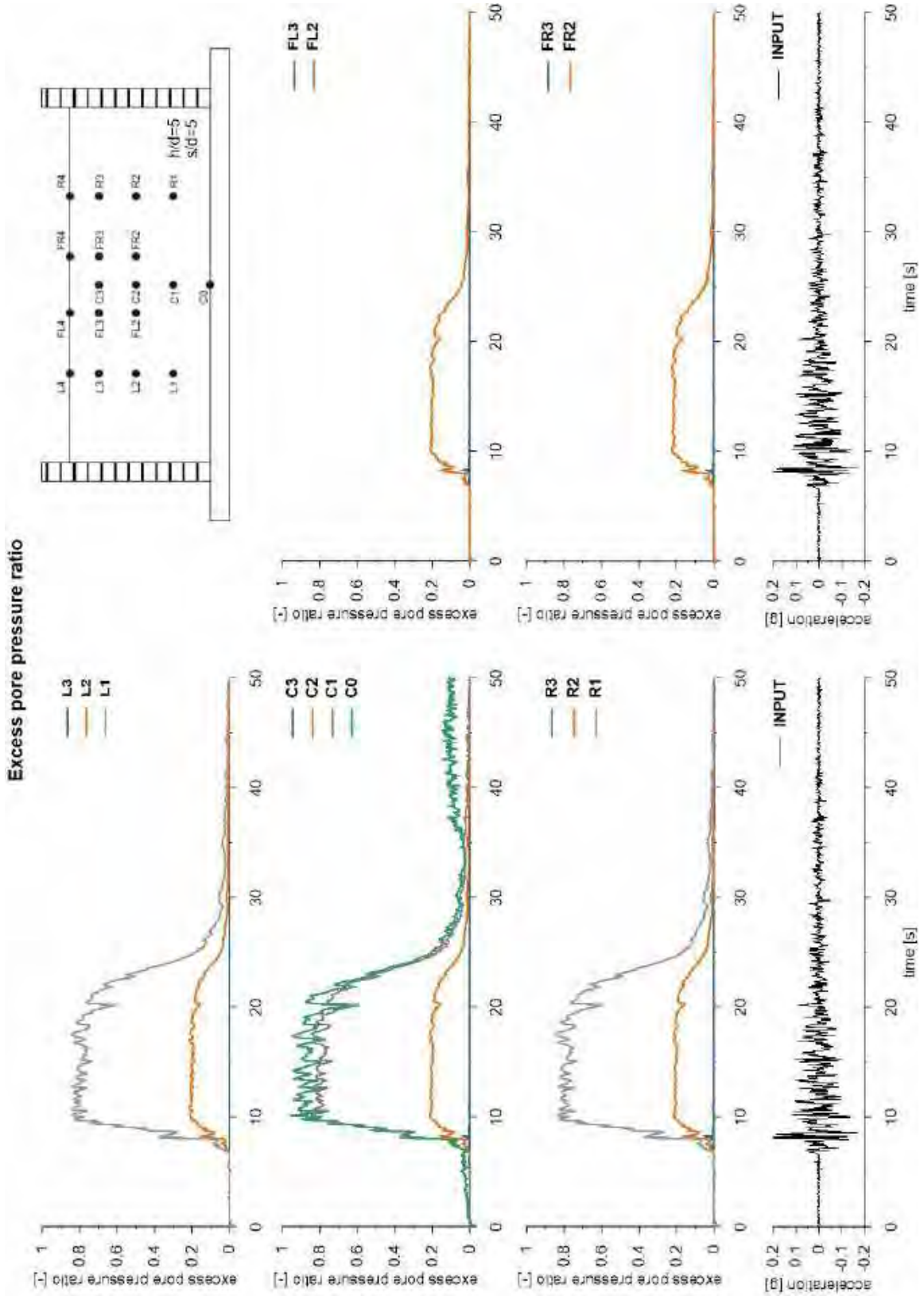

This project has received funding from the European Union's Horizon 2020 research and innovation programme under grant agreement No. 700748

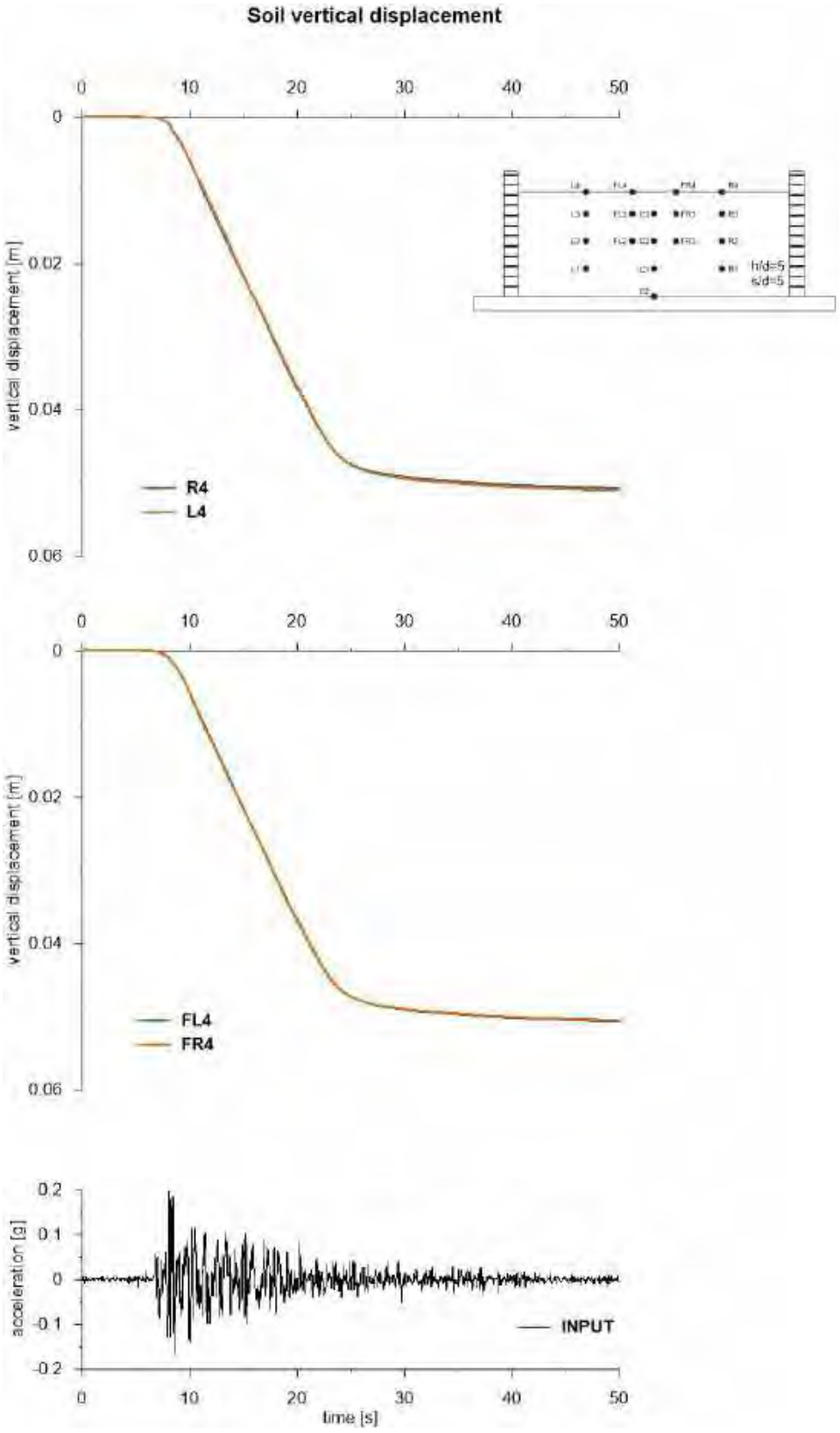

This project has received funding from the European Union's Horizon 2020 research and innovation programme under grant agreement No. 700748

6.1.1.10 ID: SF_HDU_H05_s10

The model consists of a homogenous soil profile of Ticino sand. The ground motion applied was the number 31.

ID: SF_HDU_H05_s10

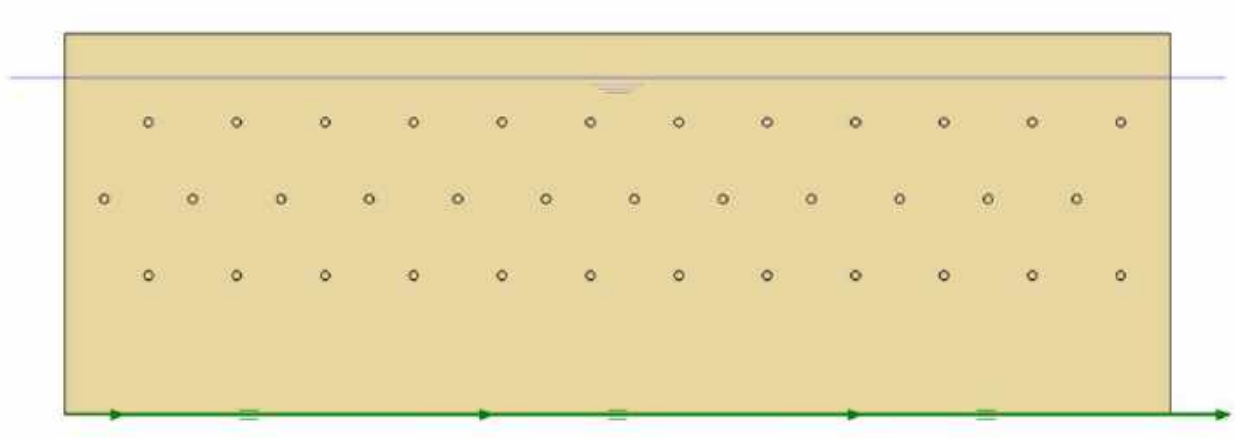

Layouts of the model reproduced in Plaxis 2D

This project has received funding from the European Union's Horizon 2020 research and innovation programme under grant agreement No. 700748

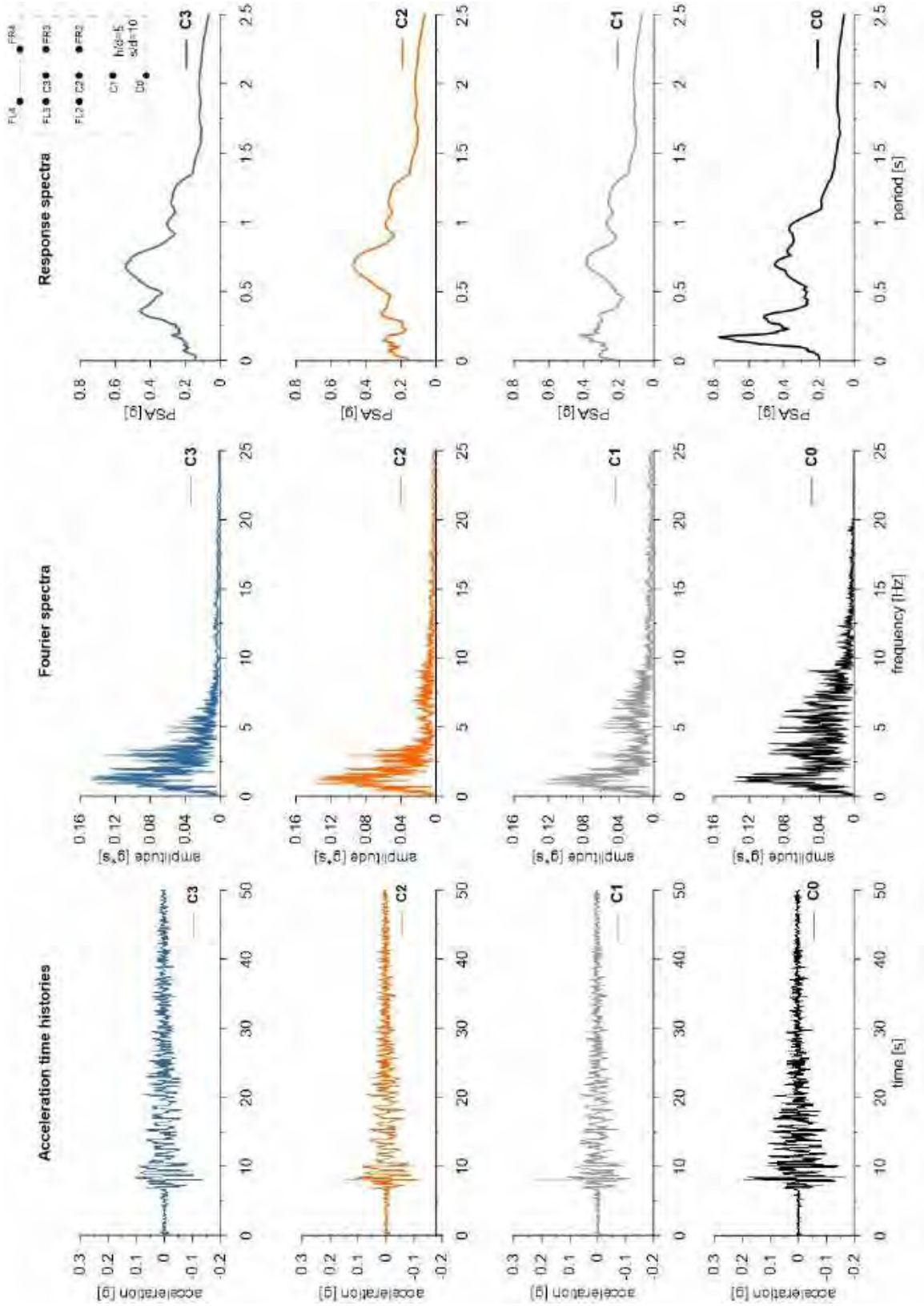

This project has received funding from the European Union's Horizon 2020 research and innovation programme under grant agreement No. 700748

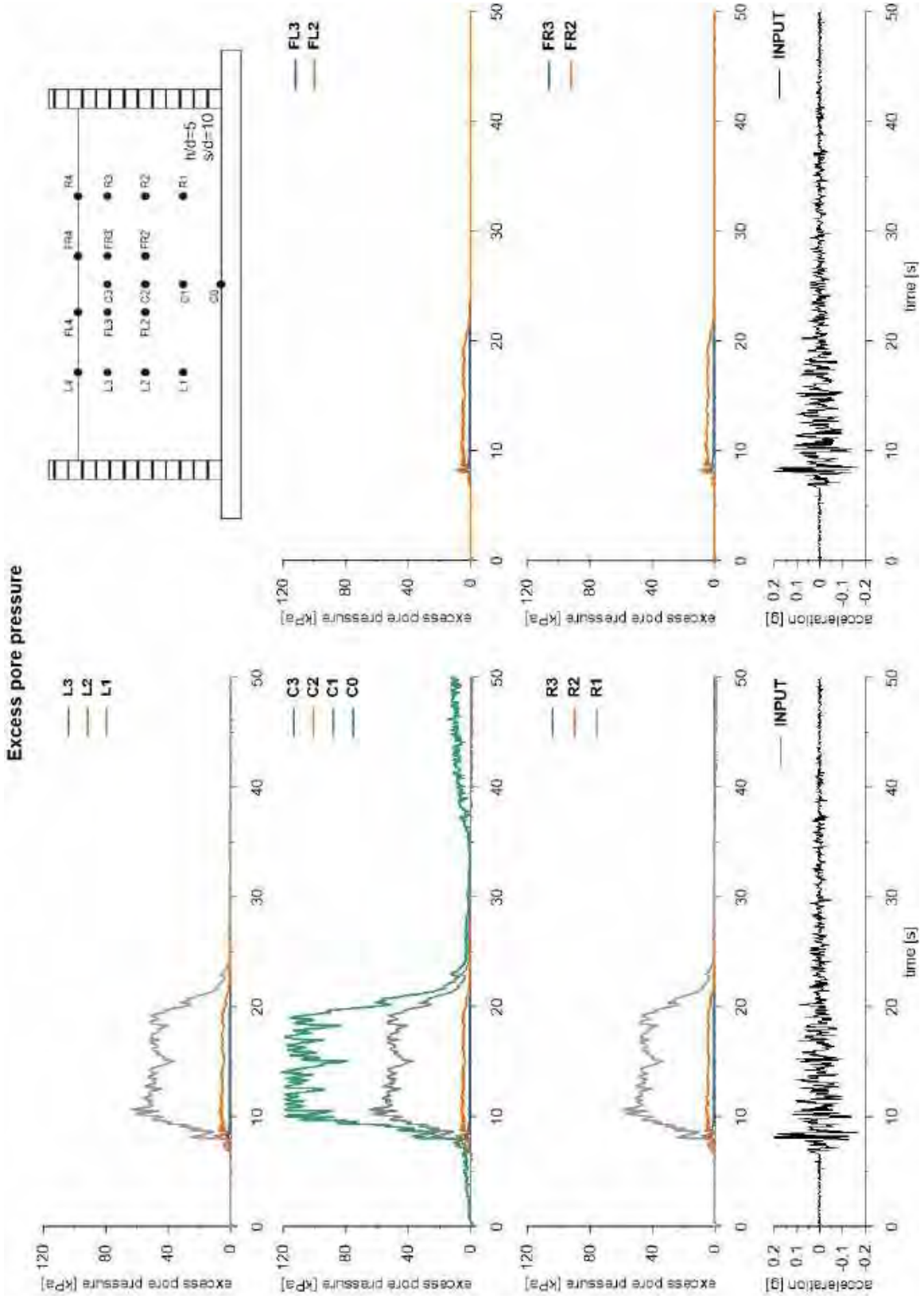

This project has received funding from the European Union's Horizon 2020 research and innovation programme under grant agreement No. 700748

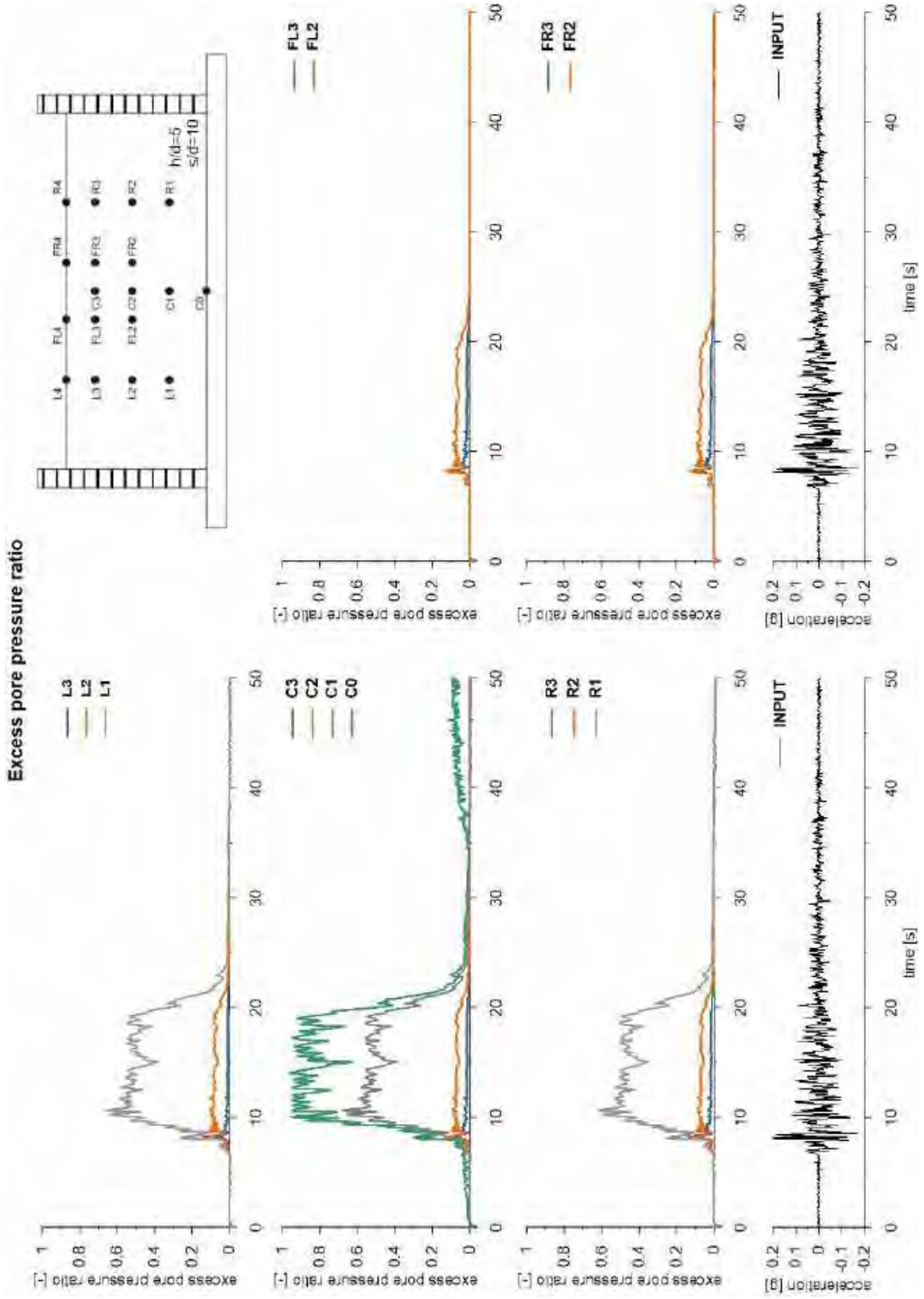

This project has received funding from the European Union's Horizon 2020 research and innovation programme under grant agreement No. 700748

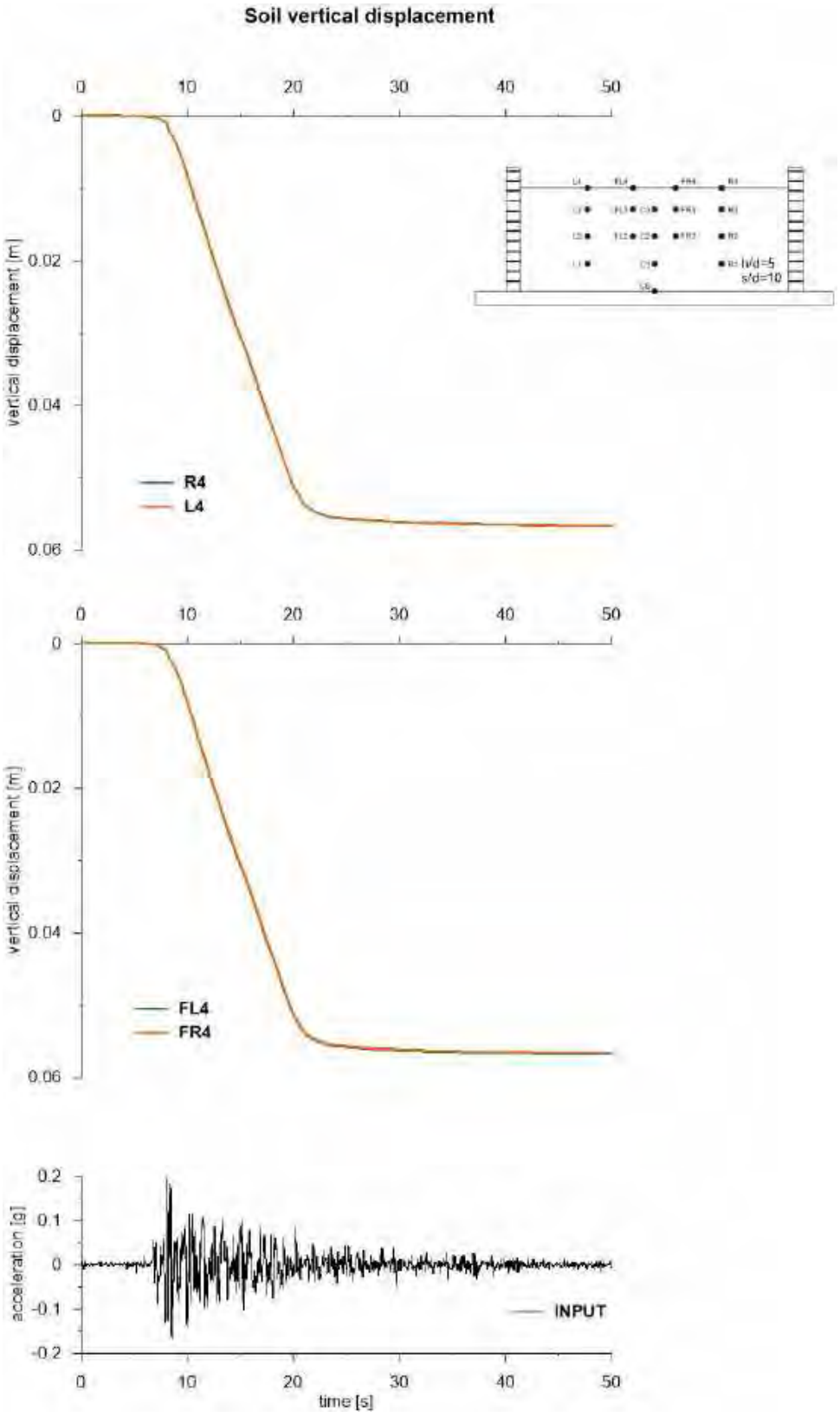

This project has received funding from the European Union's Horizon 2020 research and innovation programme under grant agreement No. 700748

6.1.1.11 ID: SF_HDU_H05_s15

The model consists of a homogenous soil profile of Ticino sand. The ground motion applied was the number 31.

ID: SF_HDU_H05_s15

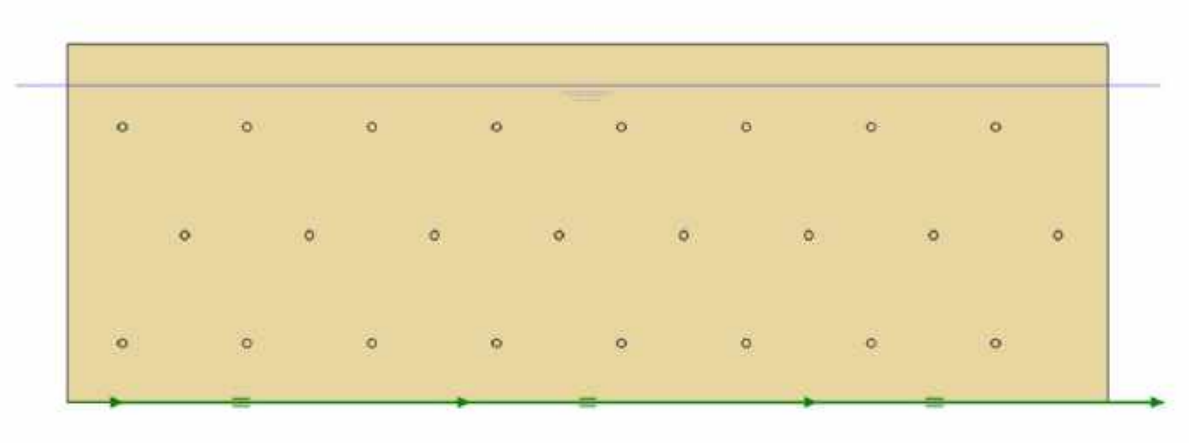

Layouts of the model reproduced in Plaxis 2D

This project has received funding from the European Union's Horizon 2020 research and innovation programme under grant agreement No. 700748

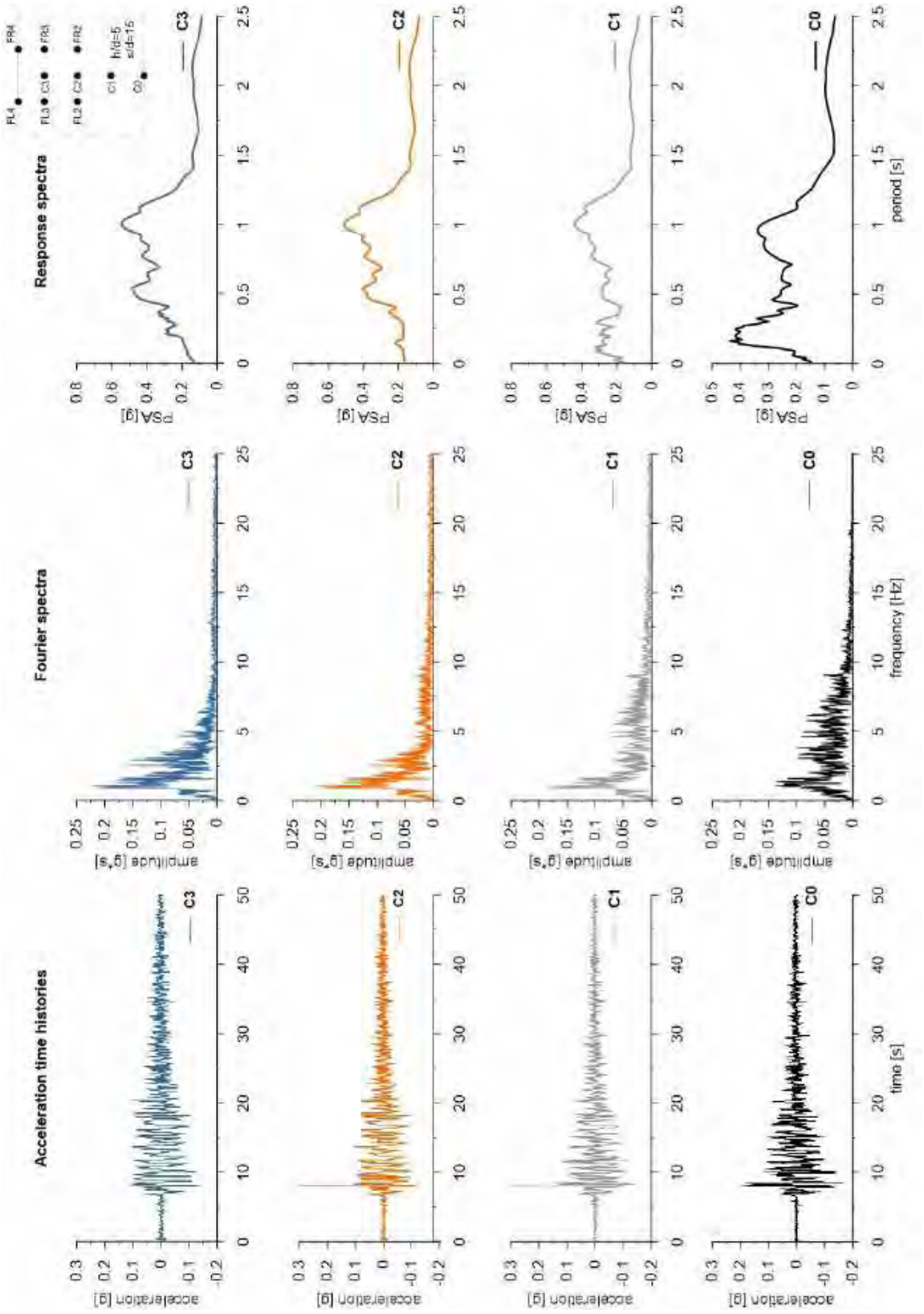

This project has received funding from the European Union's Horizon 2020 research and innovation programme under grant agreement No. 700748

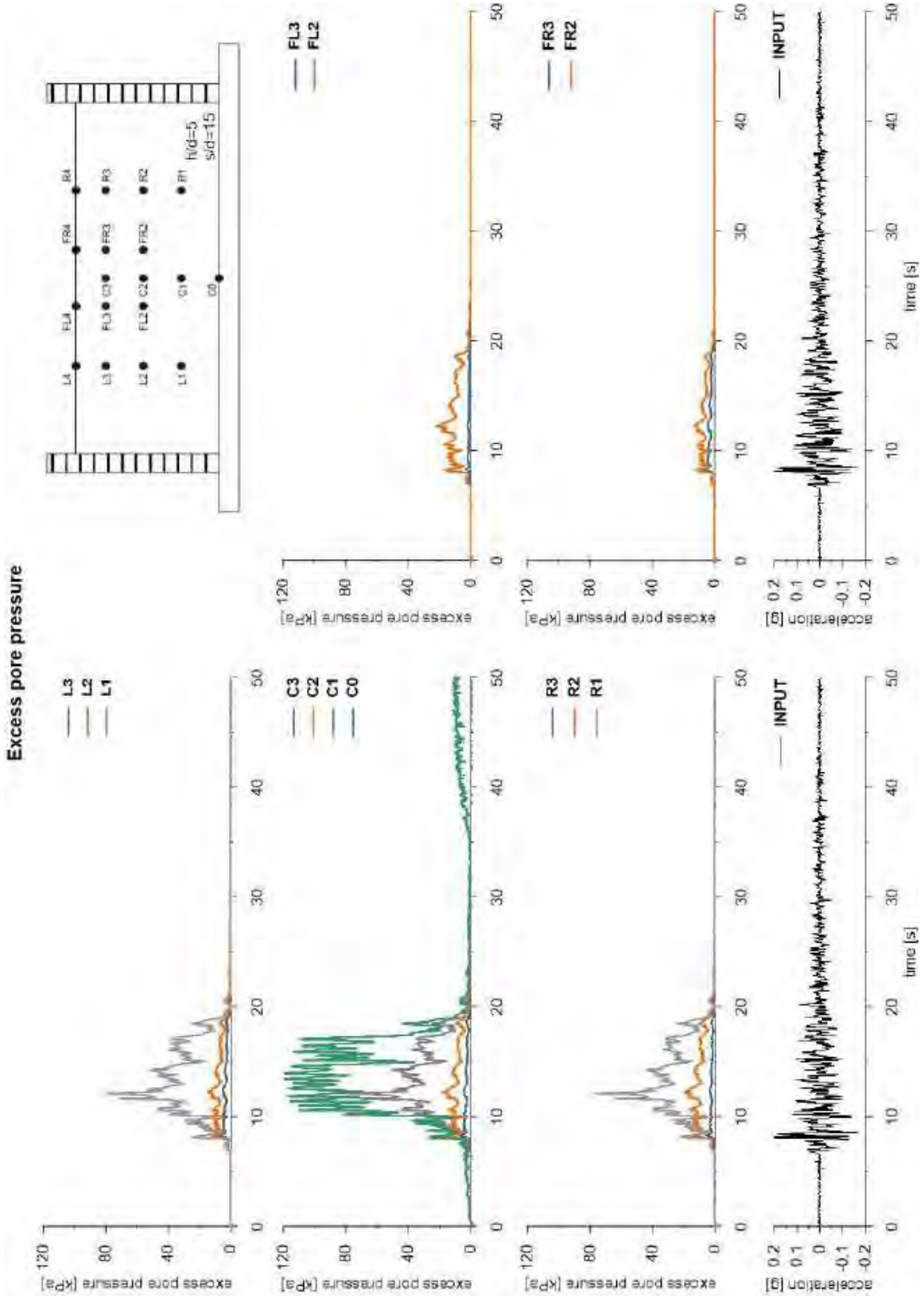

This project has received funding from the European Union's Horizon 2020 research and innovation programme under grant agreement No. 700748

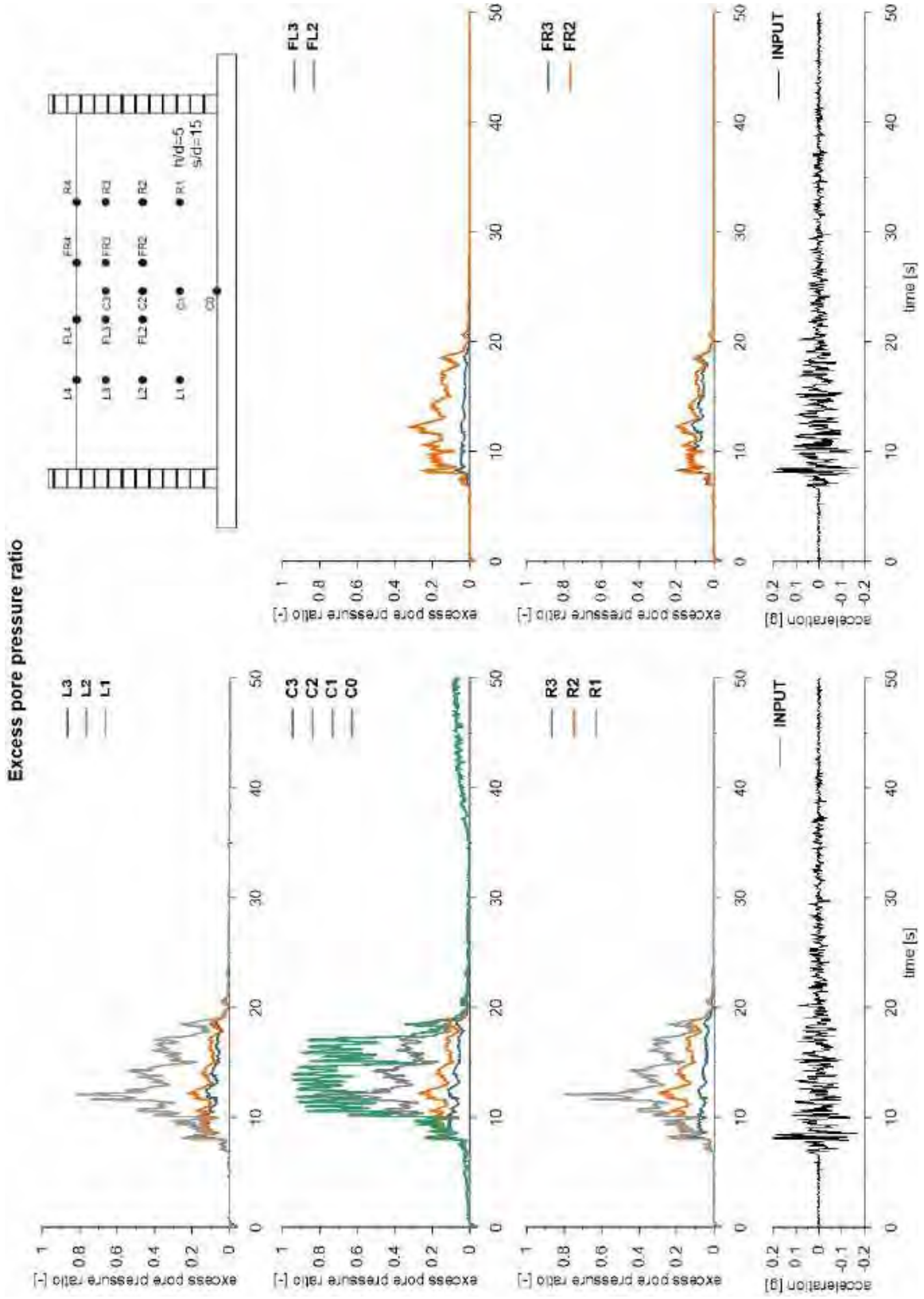

This project has received funding from the European Union's Horizon 2020 research and innovation programme under grant agreement No. 700748

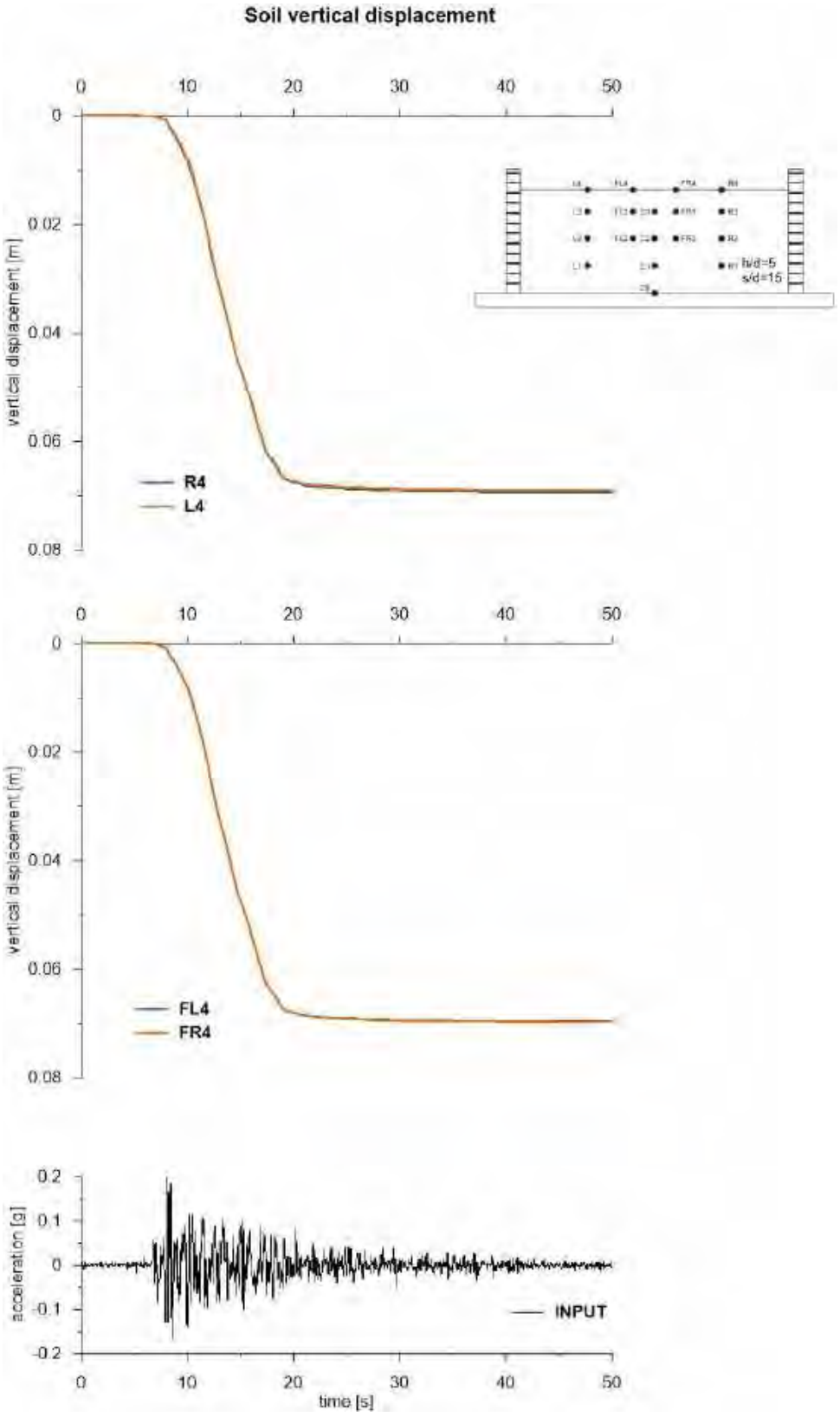

This project has received funding from the European Union's Horizon 2020 research and innovation programme under grant agreement No. 700748

6.1.1.12 ID: SF_HDU_H10_s05

The model consists of a homogenous soil profile of Ticino sand. The ground motion applied was the number 31.

ID: SF_HDU_H10_s05

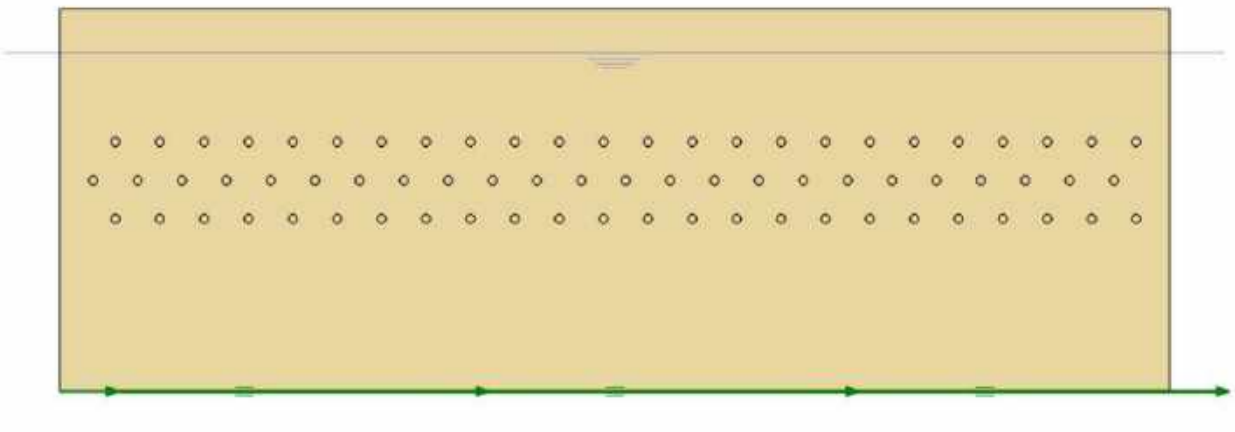

Layouts of the model reproduced in Plaxis 2D

This project has received funding from the European Union's Horizon 2020 research and innovation programme under grant agreement No. 700748

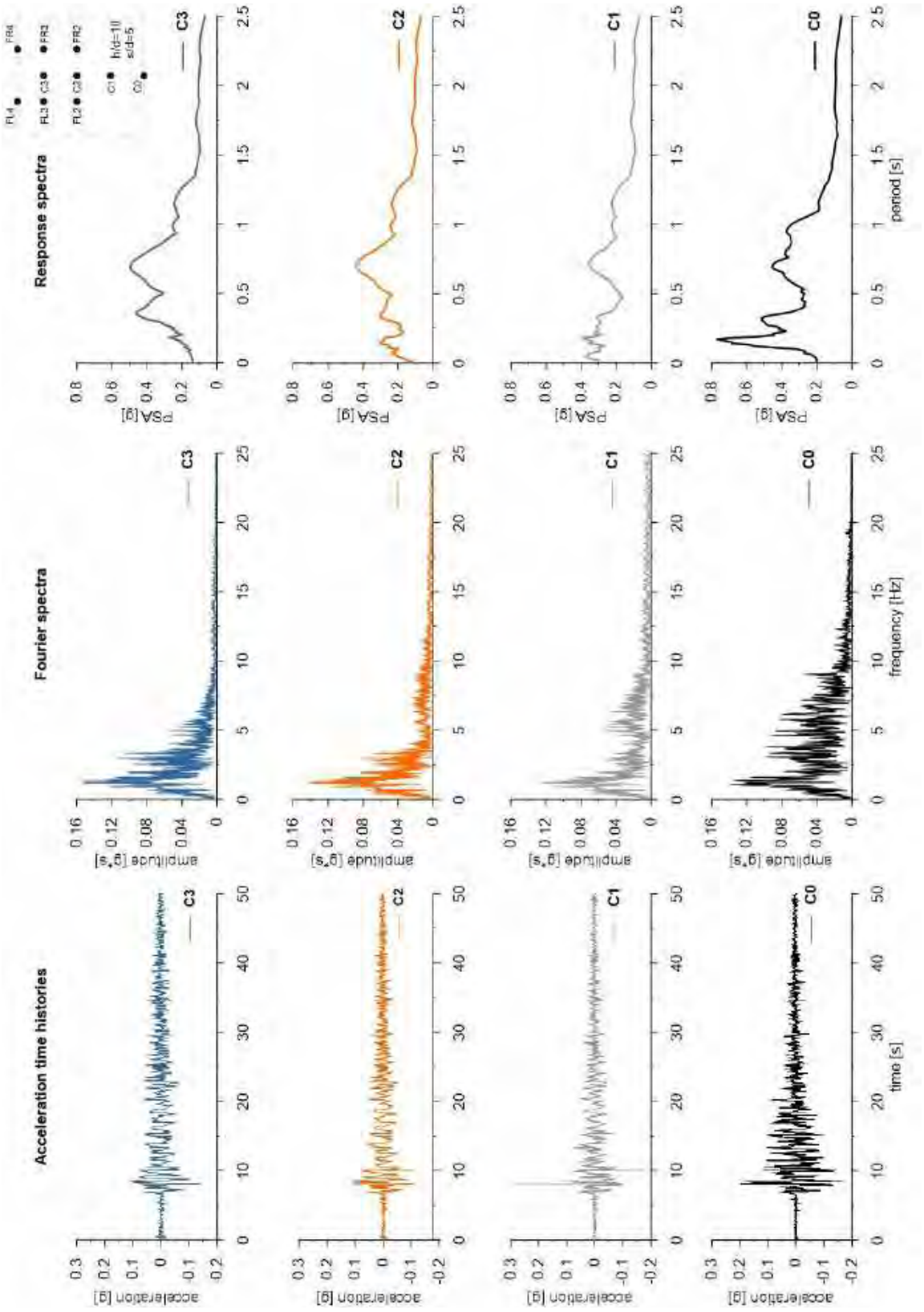

This project has received funding from the European Union's Horizon 2020 research and innovation programme under grant agreement No. 700748

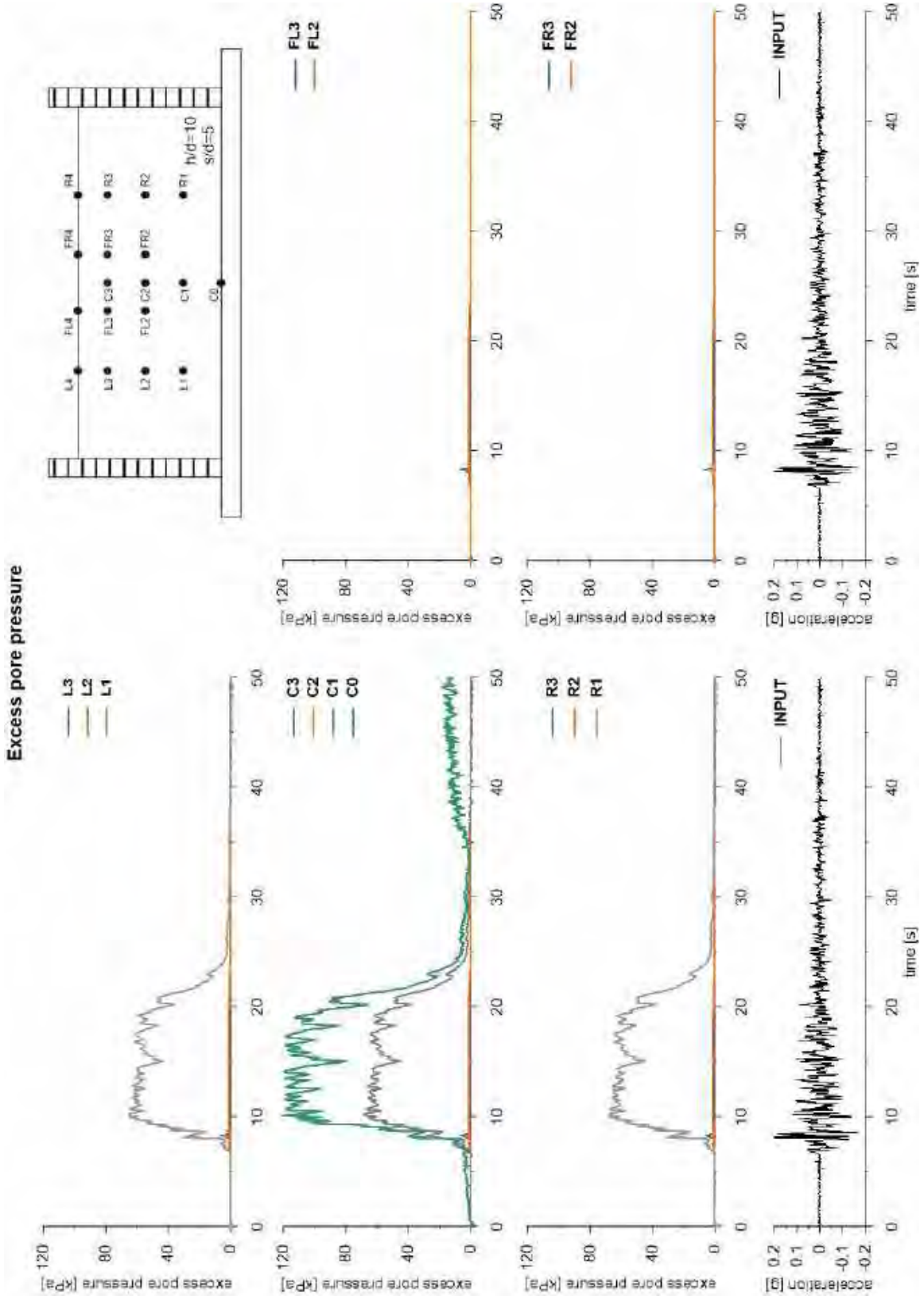

This project has received funding from the European Union's Horizon 2020 research and innovation programme under grant agreement No. 700748

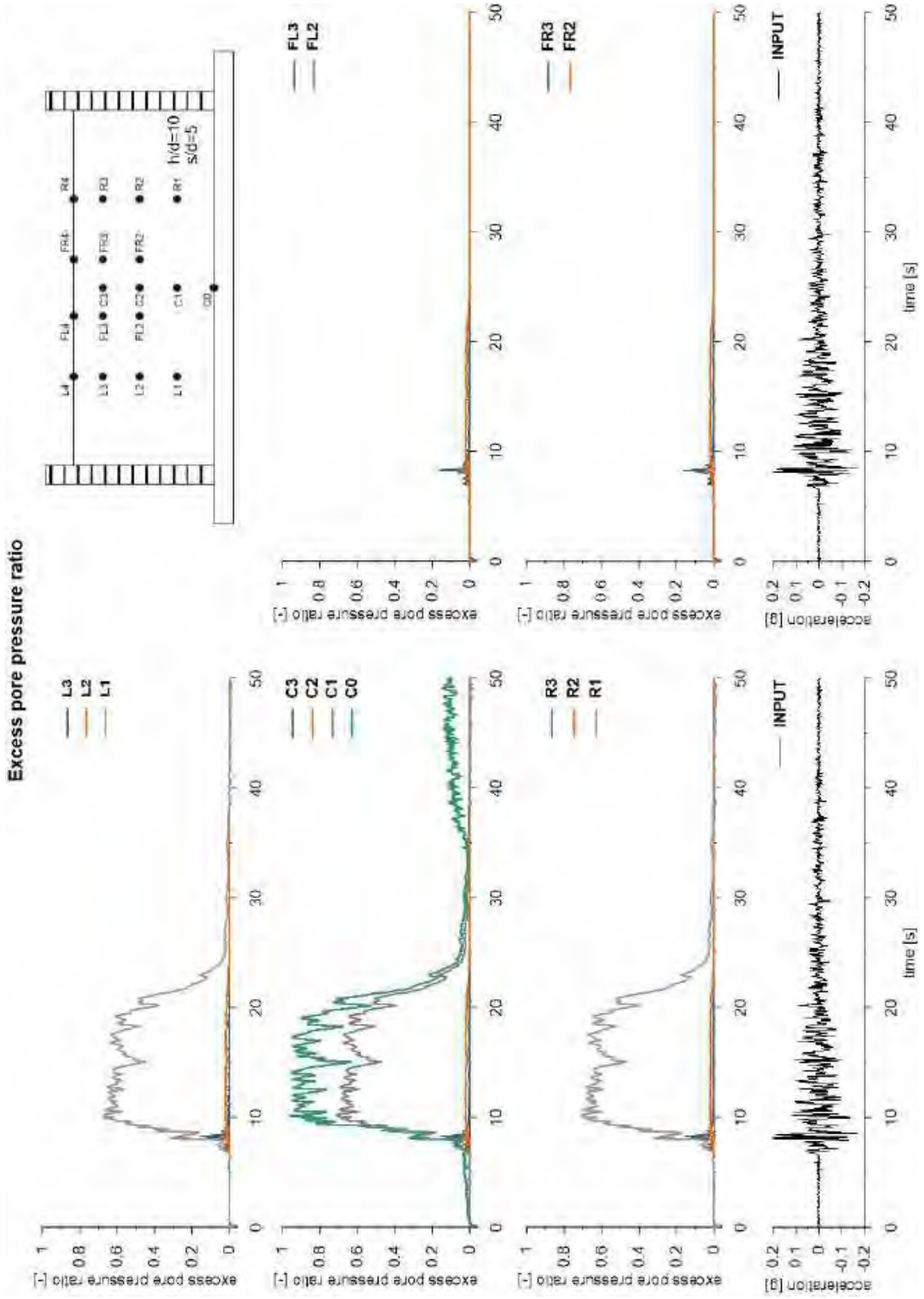

This project has received funding from the European Union's Horizon 2020 research and innovation programme under grant agreement No. 700748

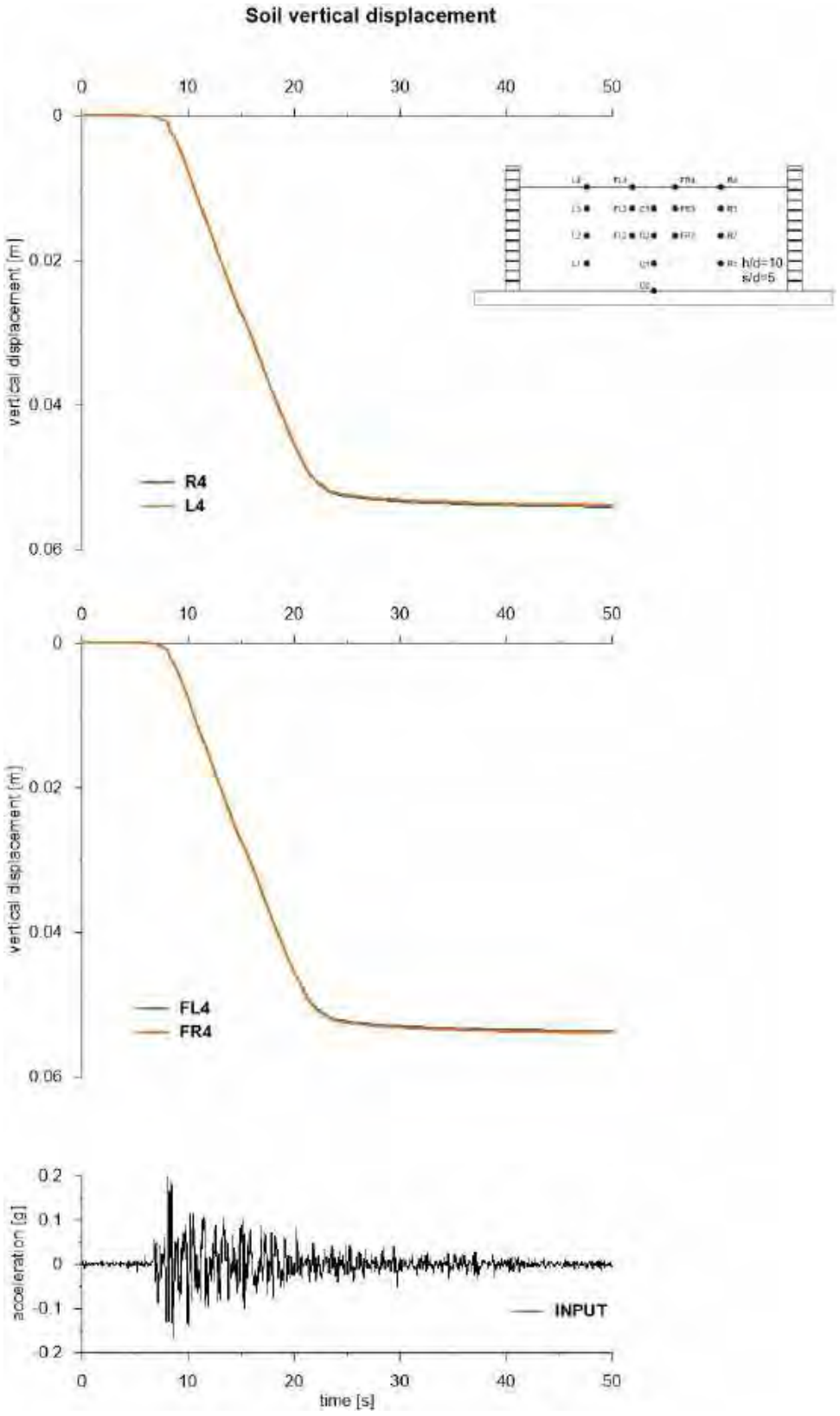

This project has received funding from the European Union's Horizon 2020 research and innovation programme under grant agreement No. 700748

6.1.1.13 ID: SF_HDU_H10_s10

The model consists of a homogenous soil profile of Ticino sand. The ground motion applied was the number 31.

ID: SF_HDU_H10_s10

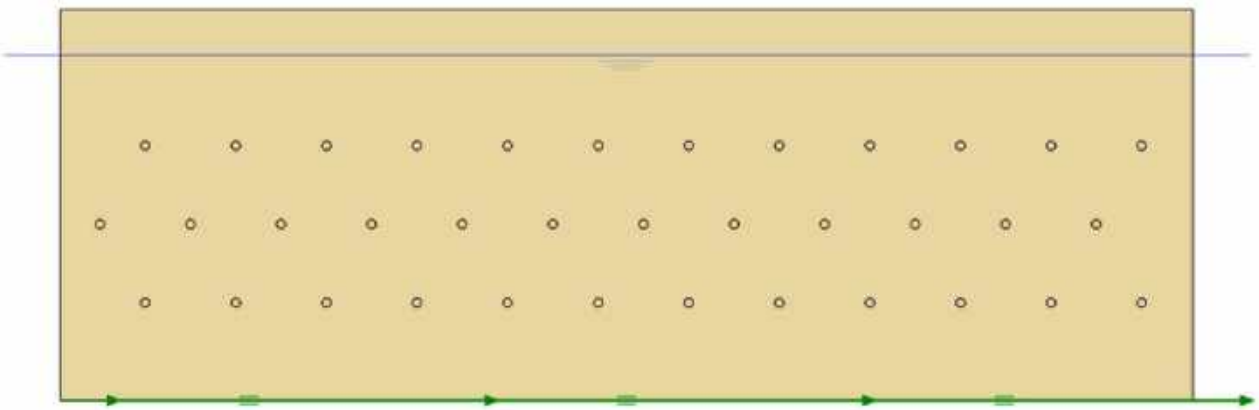

Layouts of the model reproduced in Plaxis 2D

This project has received funding from the European Union's Horizon 2020 research and innovation programme under grant agreement No. 700748

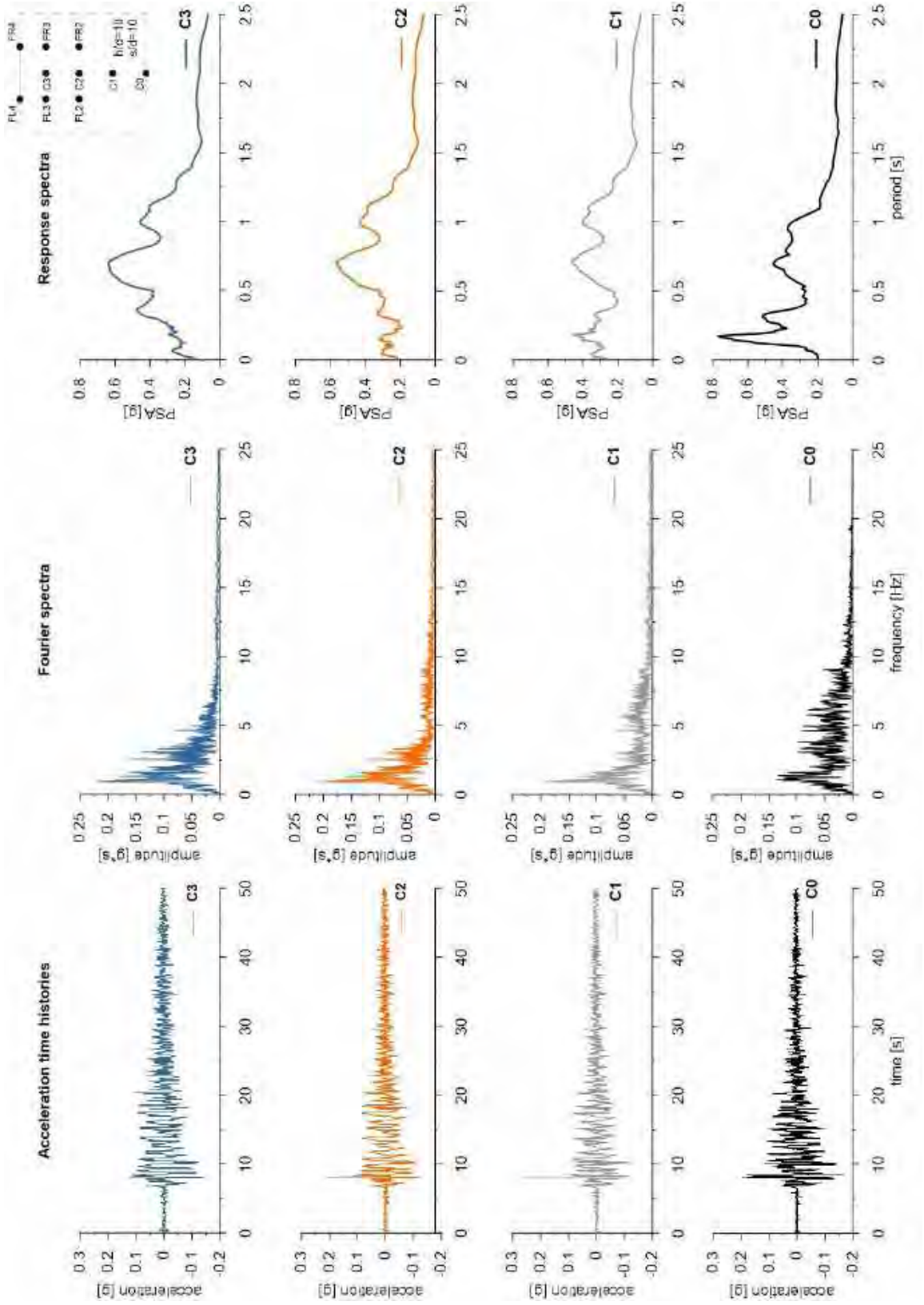

This project has received funding from the European Union's Horizon 2020 research and innovation programme under grant agreement No. 700748

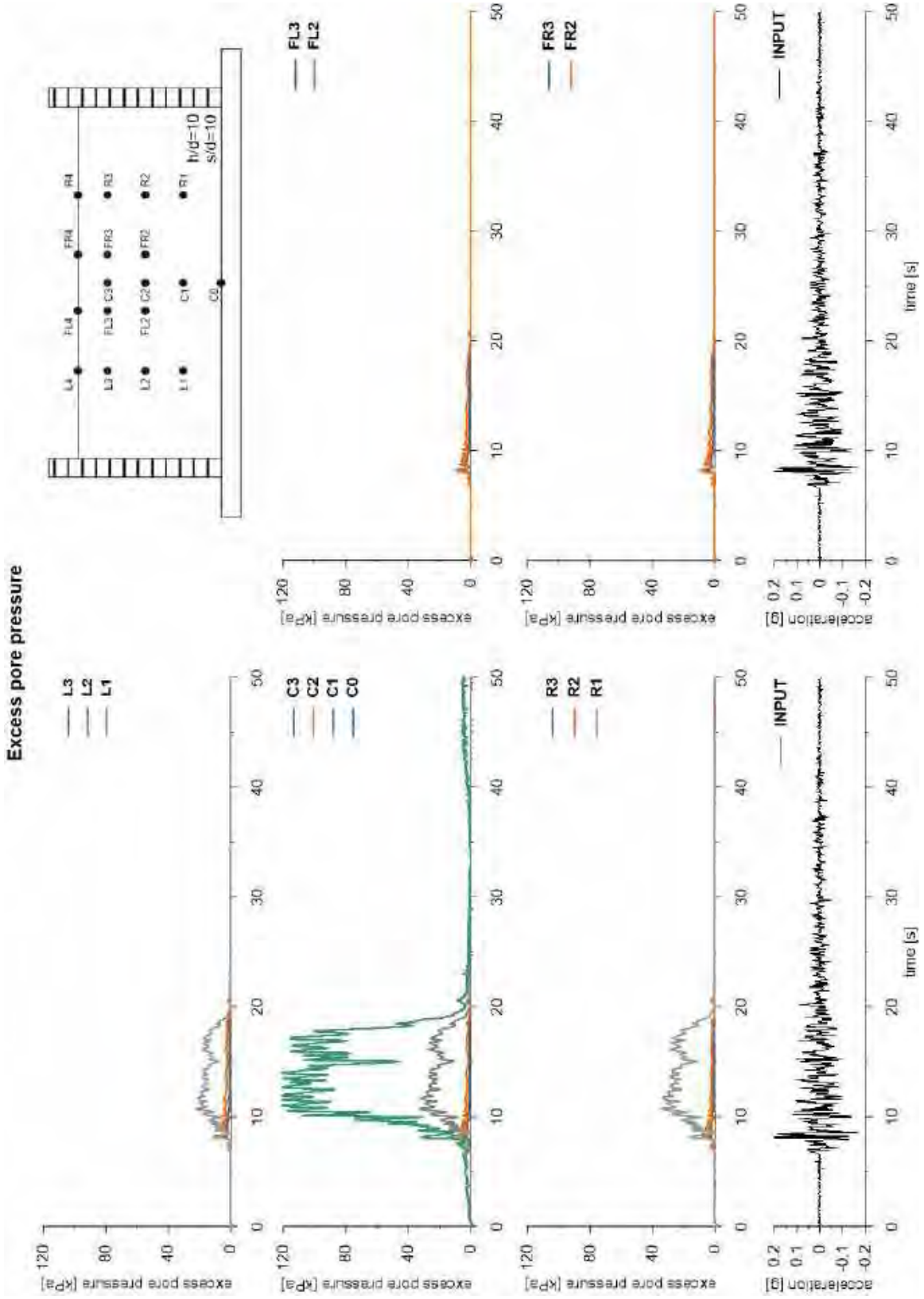

This project has received funding from the European Union's Horizon 2020 research and innovation programme under grant agreement No. 700748

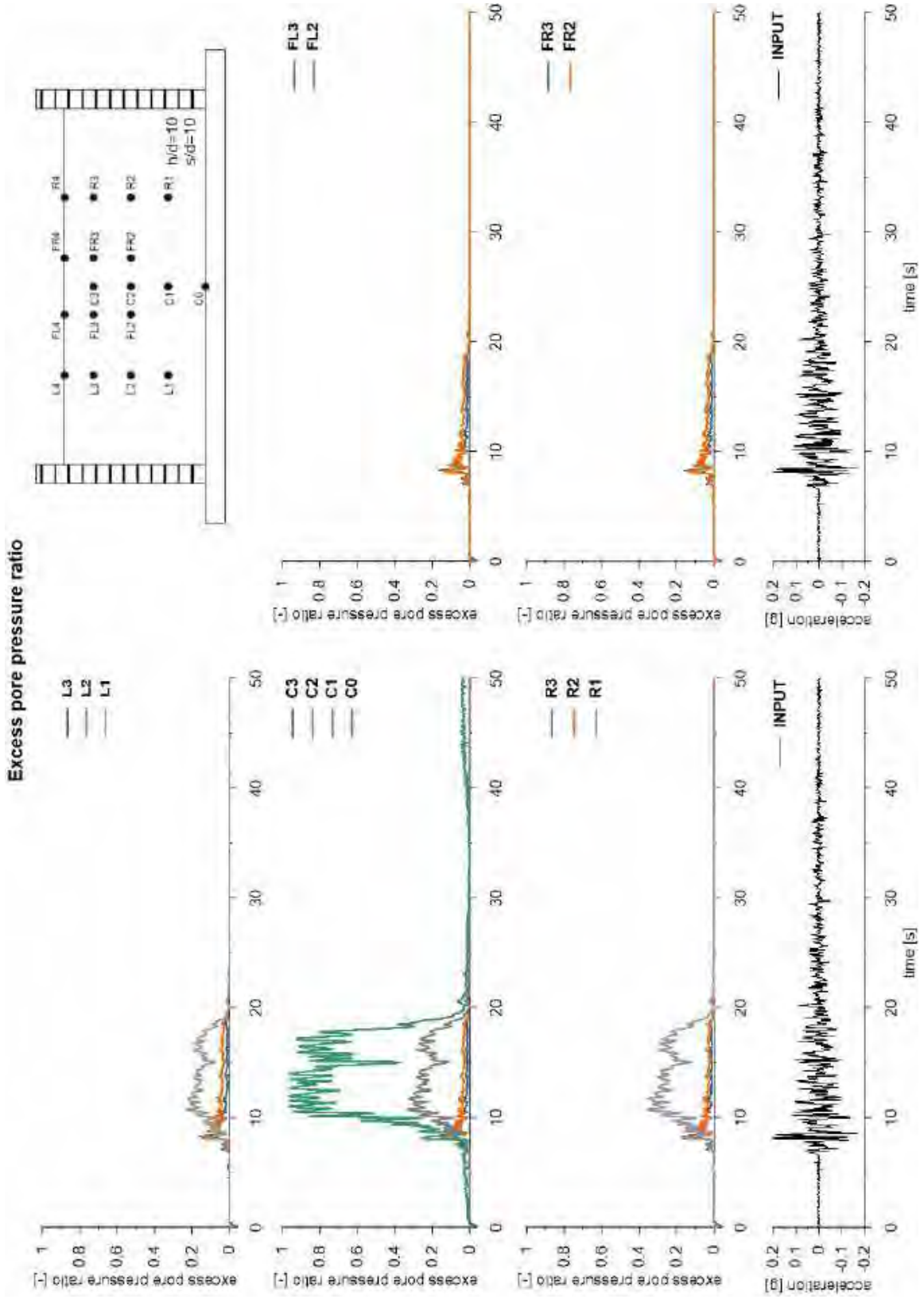

This project has received funding from the European Union's Horizon 2020 research and innovation programme under grant agreement No. 700748

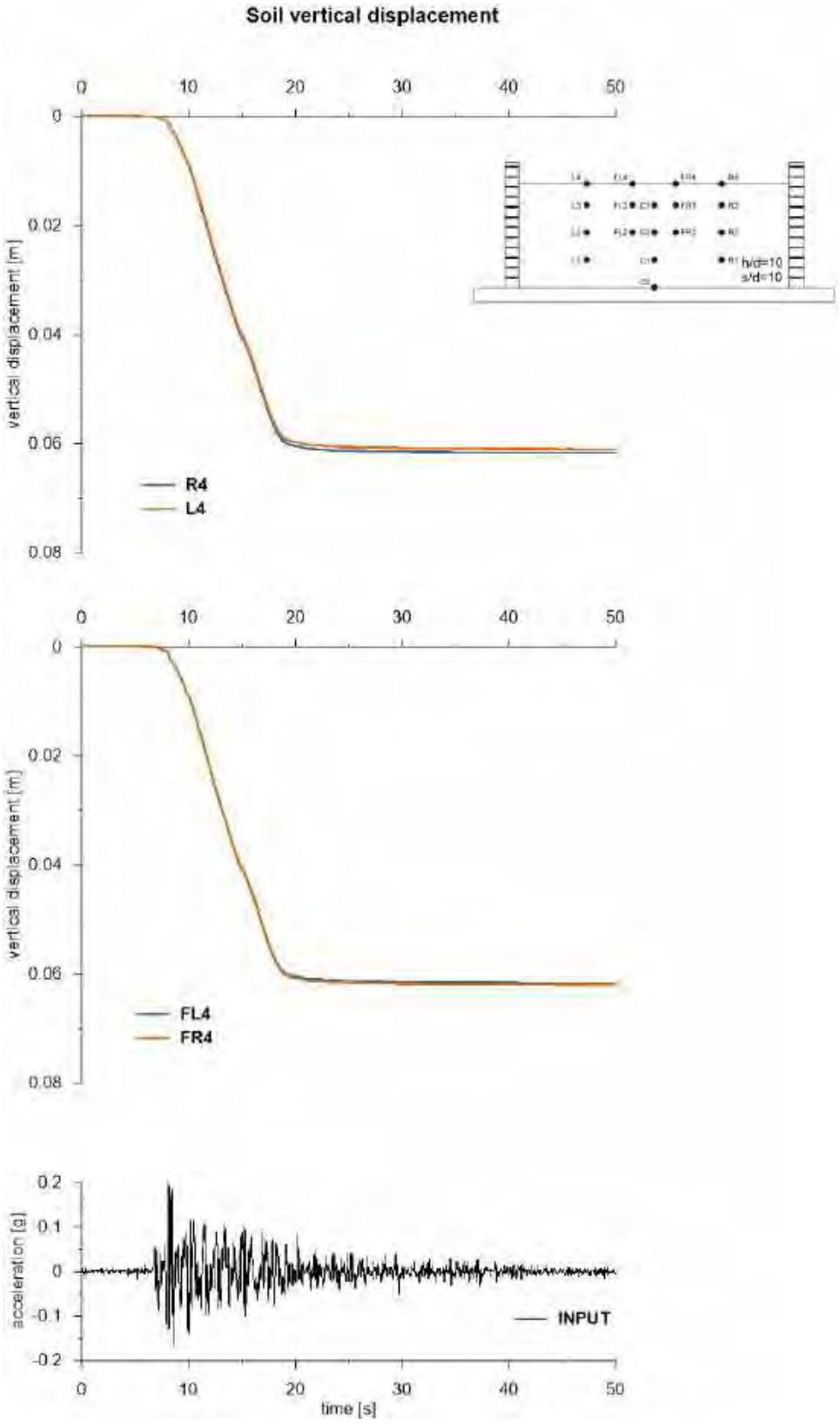

This project has received funding from the European Union's Horizon 2020 research and innovation programme under grant agreement No. 700748

6.1.1.14 ID: SF_HDU_H10_s15

The model consists of a homogenous soil profile of Ticino sand. The ground motion applied was the number 31.

ID: SF_HDU_H10_s15

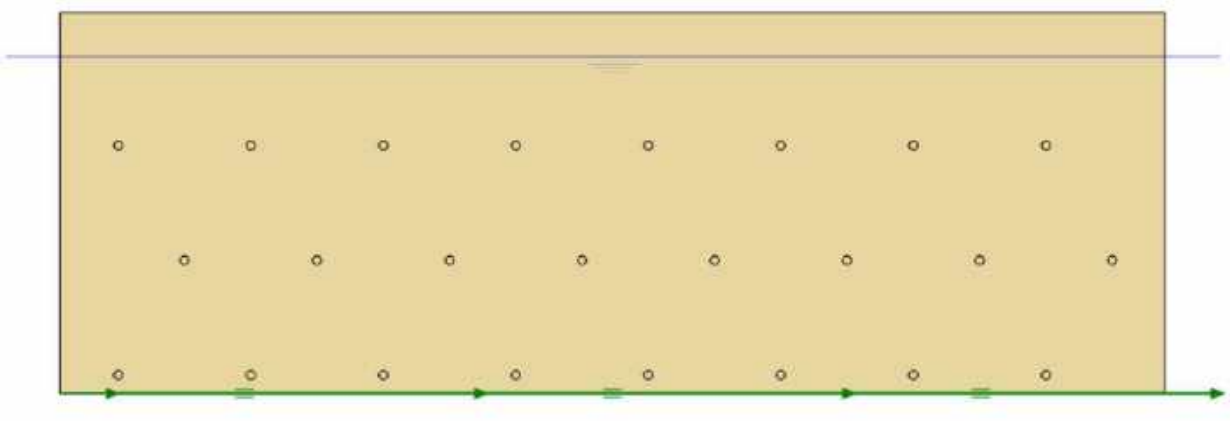

Layouts of the model reproduced in Plaxis 2D

This project has received funding from the European Union's Horizon 2020 research and innovation programme under grant agreement No. 700748

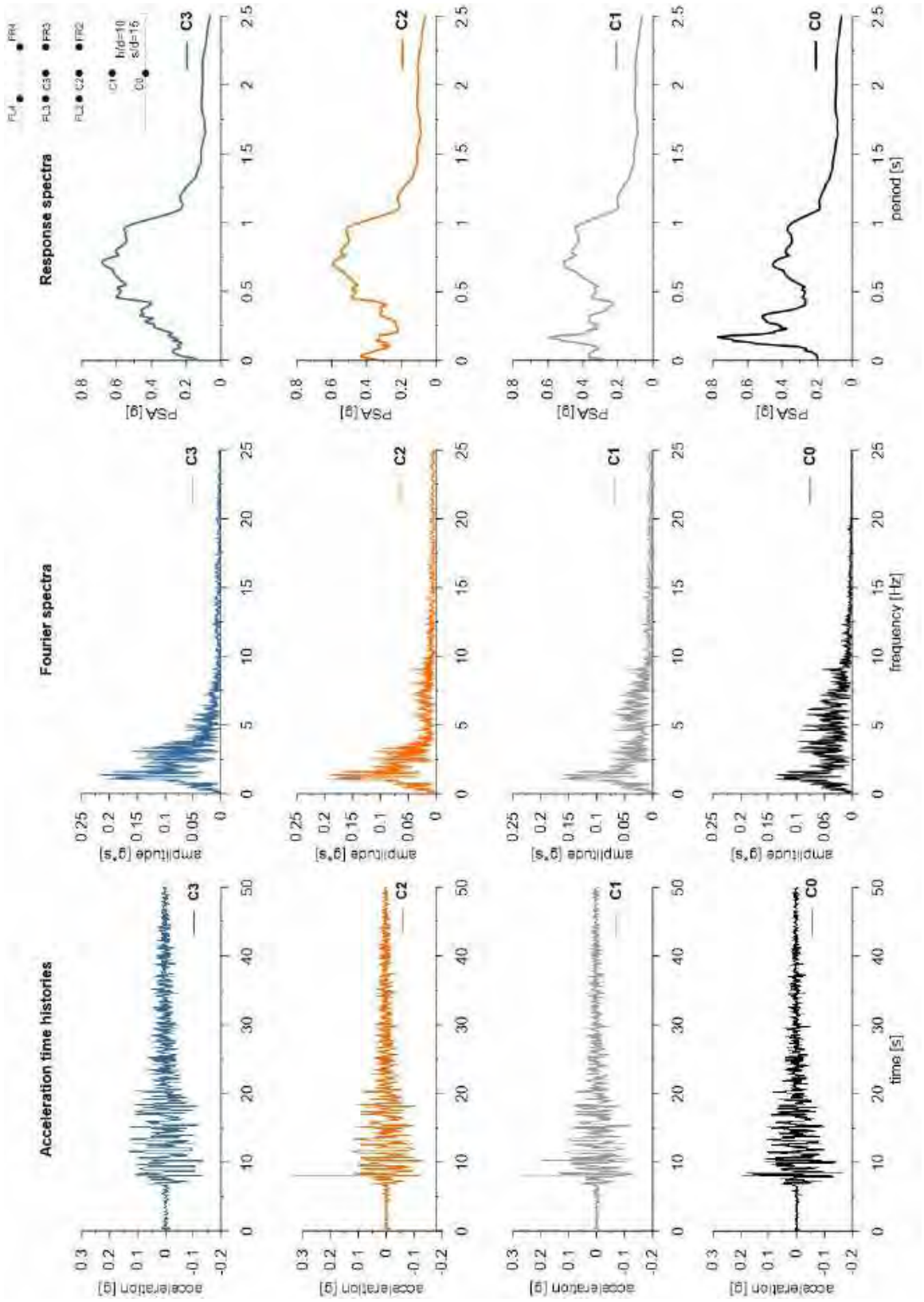

This project has received funding from the European Union's Horizon 2020 research and innovation programme under grant agreement No. 700748

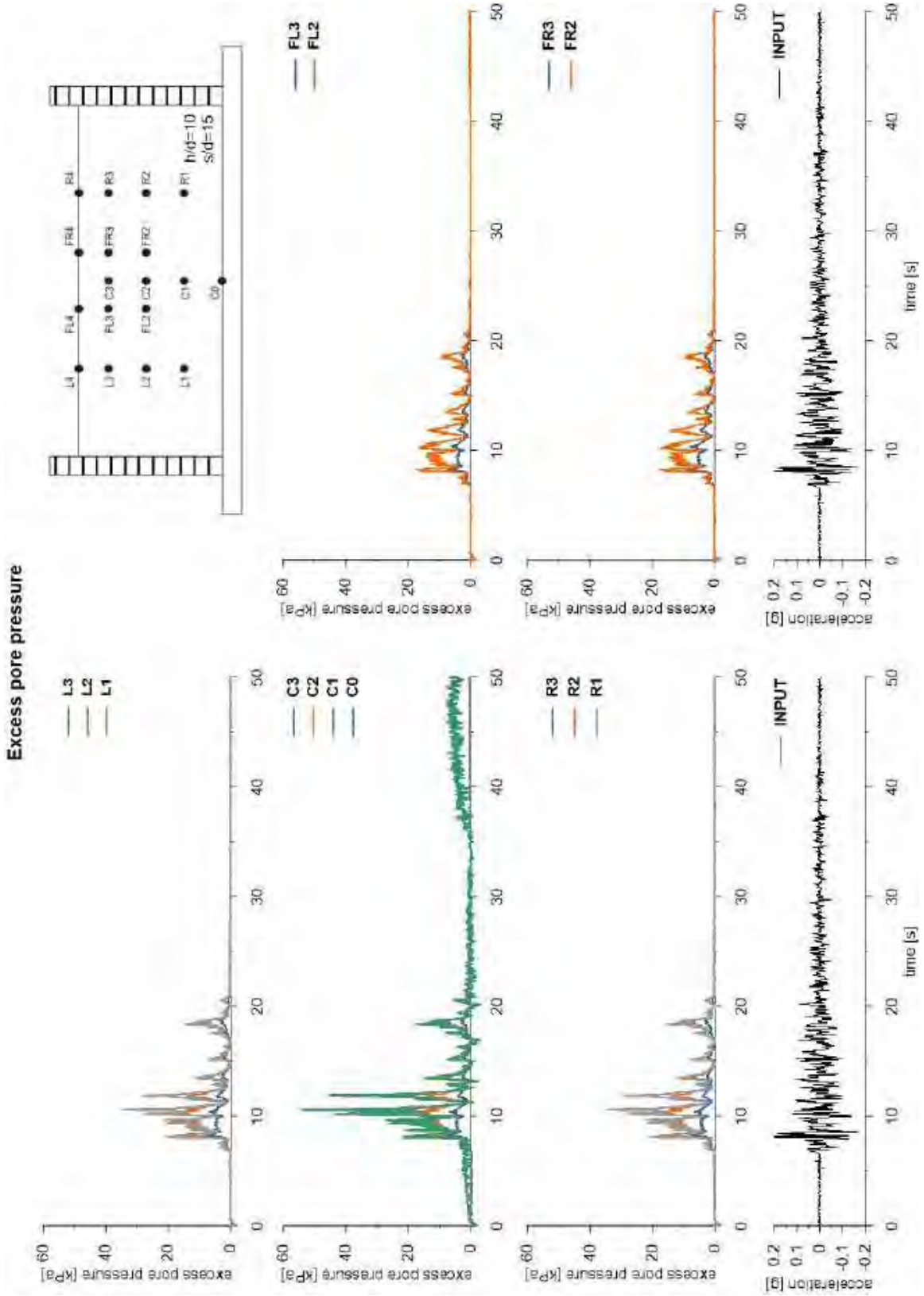

This project has received funding from the European Union's Horizon 2020 research and innovation programme under grant agreement No. 700748

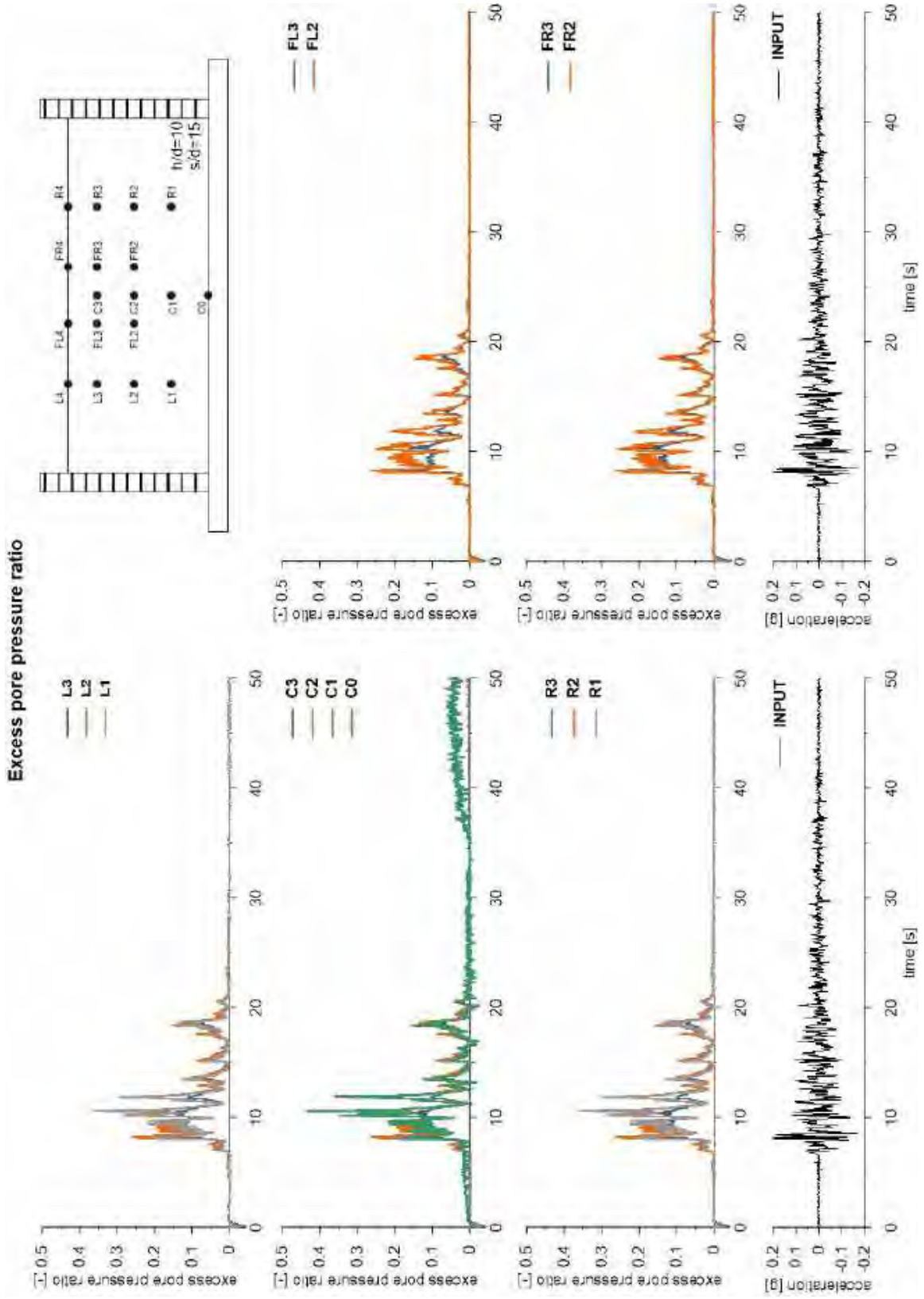

This project has received funding from the European Union's Horizon 2020 research and innovation programme under grant agreement No. 700748

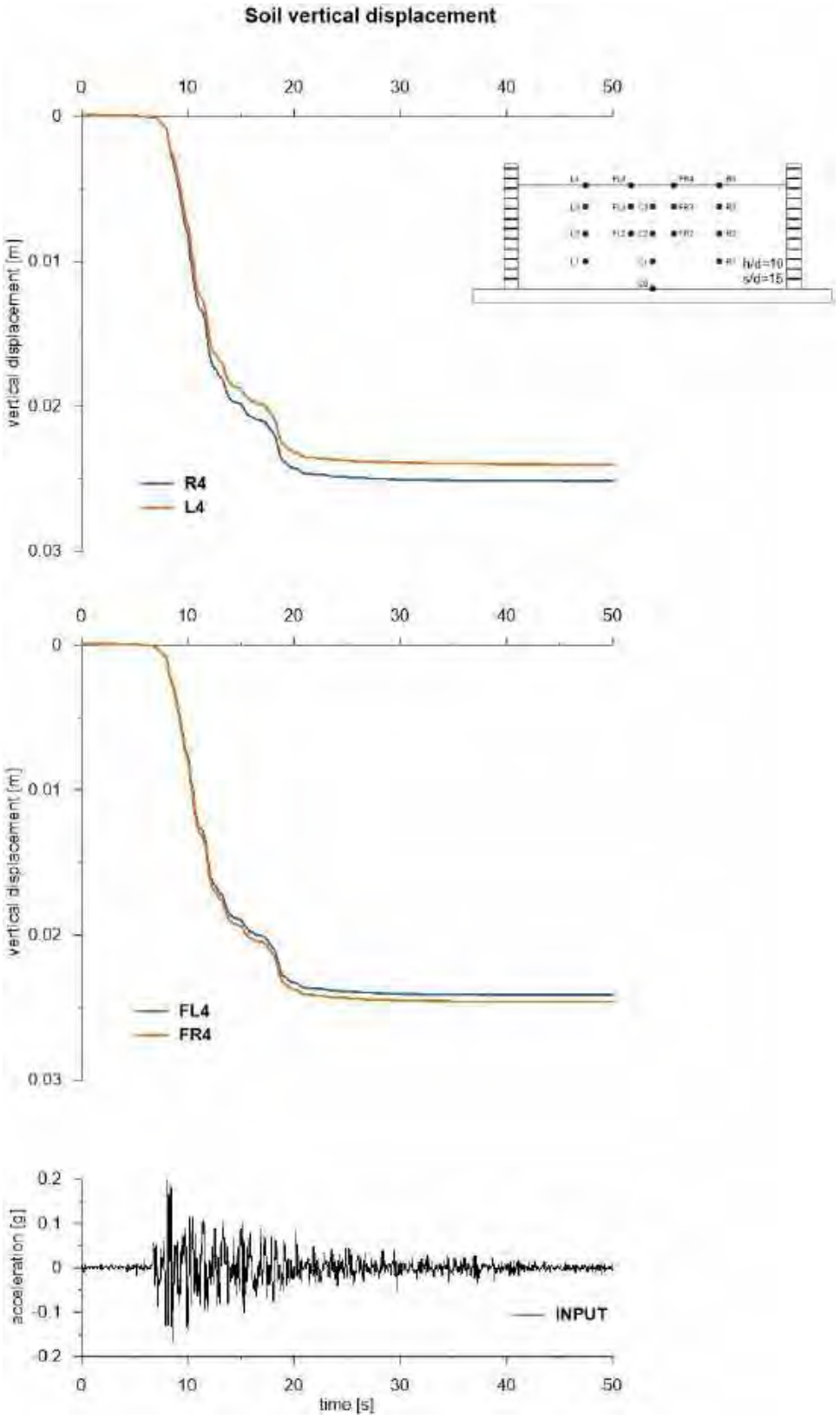

This project has received funding from the European Union's Horizon 2020 research and innovation programme under grant agreement No. 700748

6.1.1.15 ID: SF_HDU_H15_s05

The model consists of a homogenous soil profile of Ticino sand. The ground motion applied was the number 31.

ID: SF_HDU_H15_s05

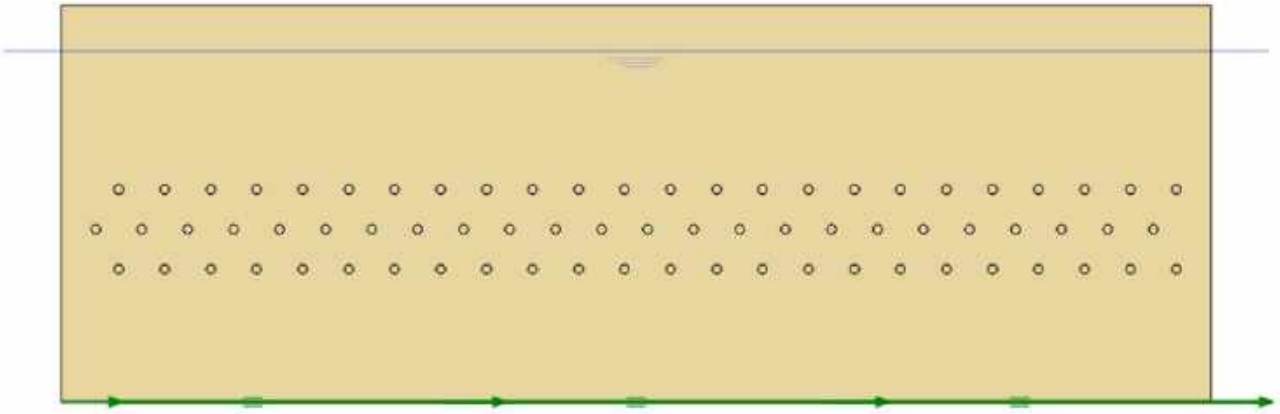

Layouts of the model reproduced in Plaxis 2D

This project has received funding from the European Union's Horizon 2020 research and innovation programme under grant agreement No. 700748

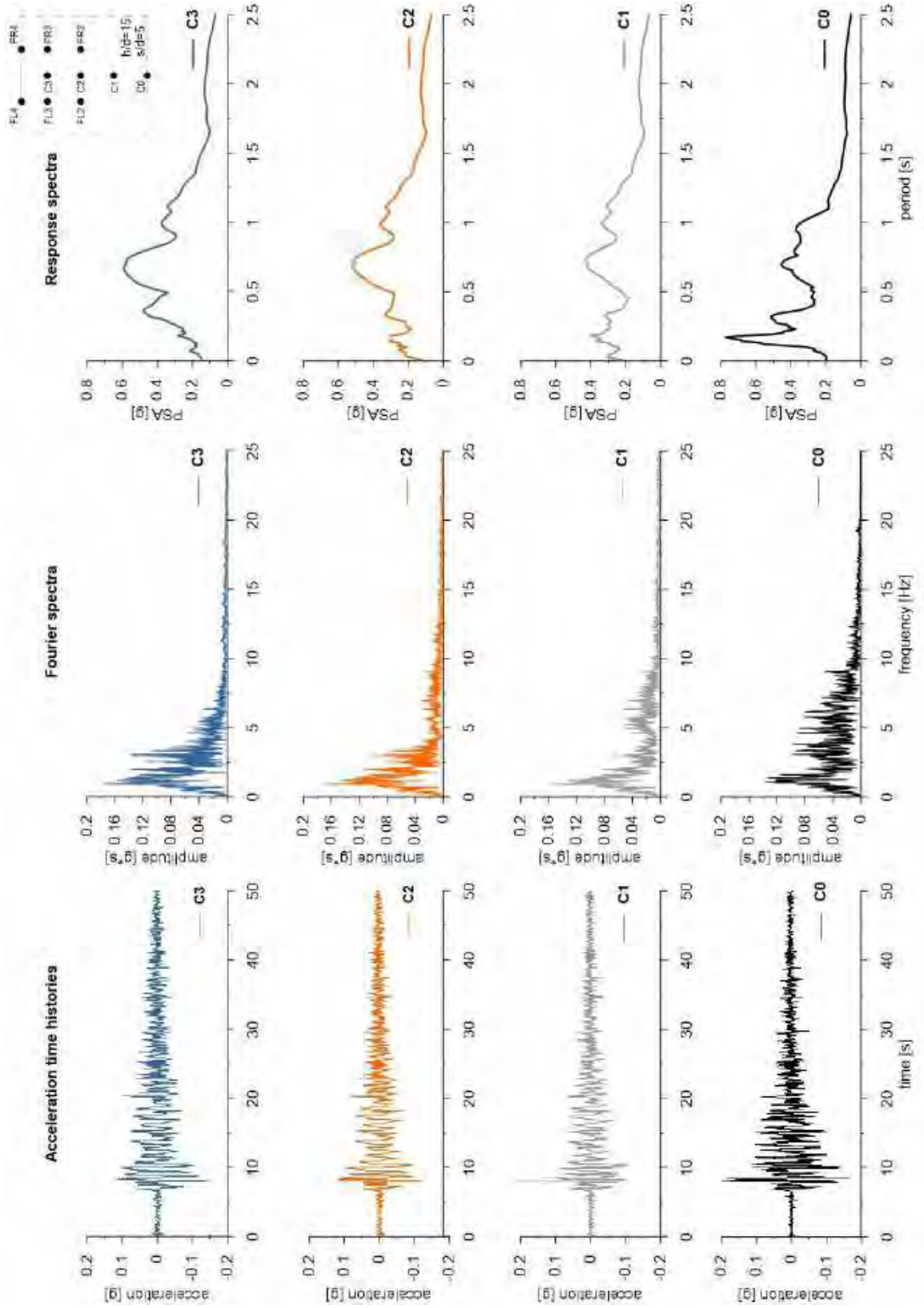

This project has received funding from the European Union's Horizon 2020 research and innovation programme under grant agreement No. 700748

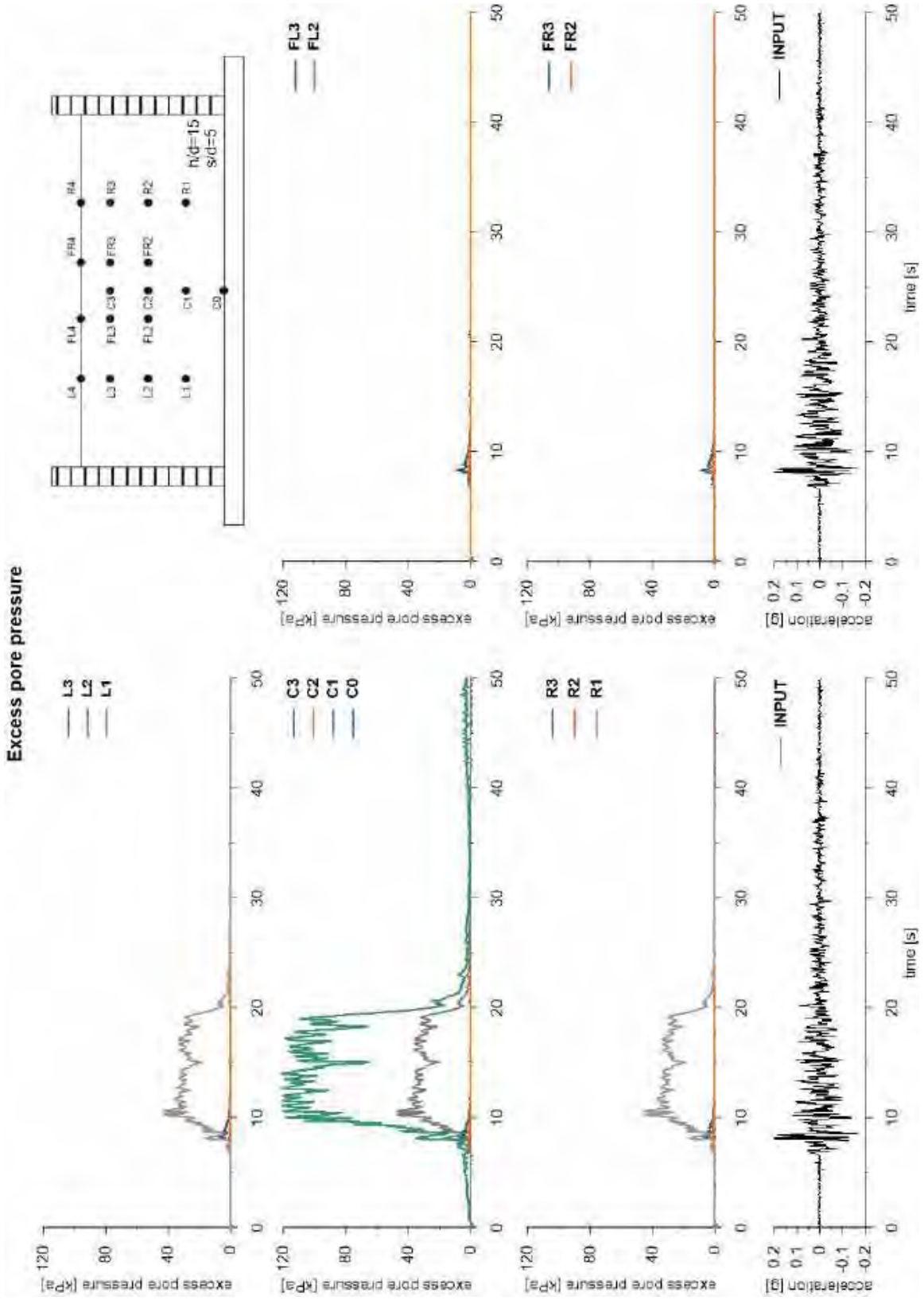

This project has received funding from the European Union's Horizon 2020 research and innovation programme under grant agreement No. 700748

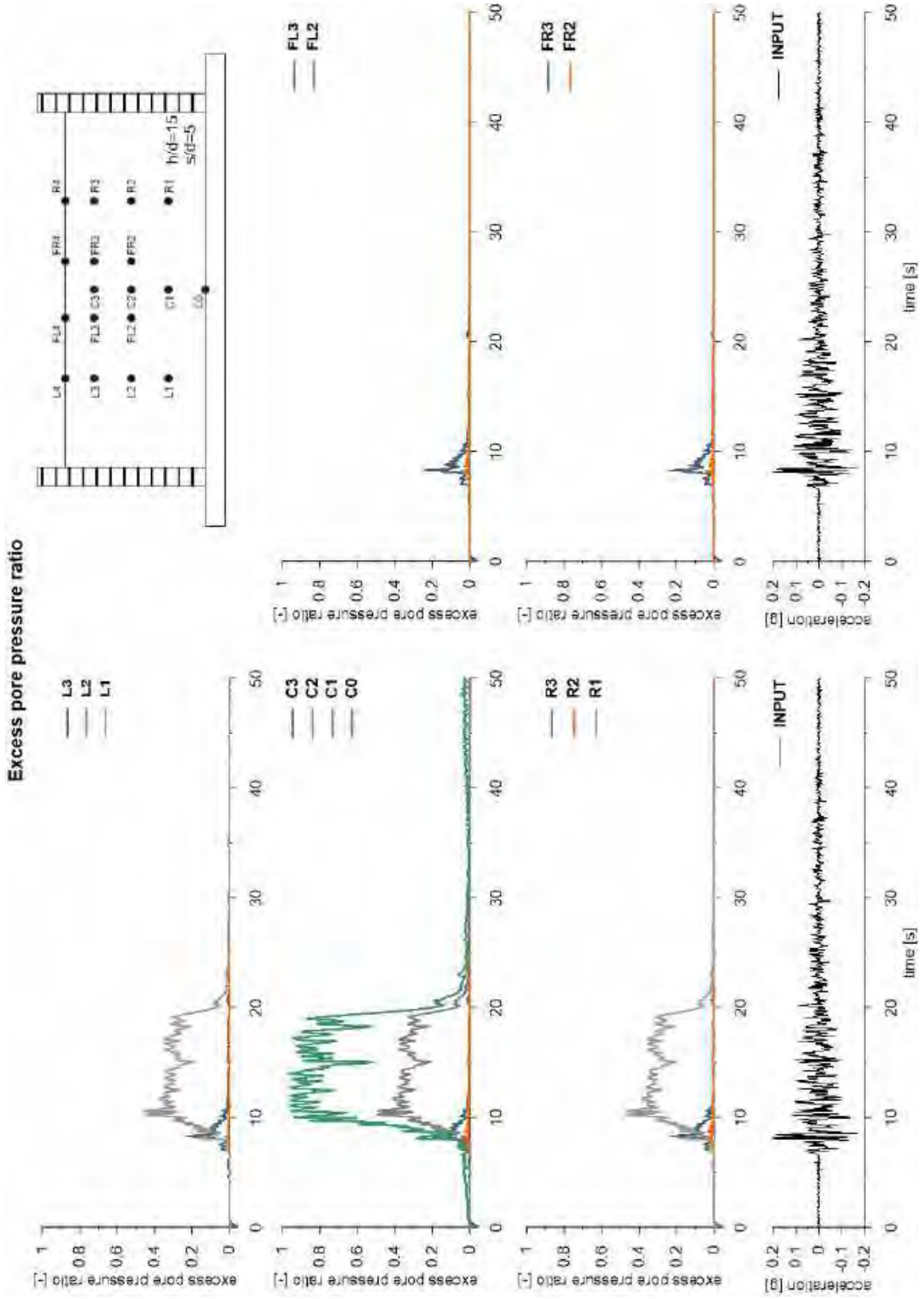

This project has received funding from the European Union's Horizon 2020 research and innovation programme under grant agreement No. 700748

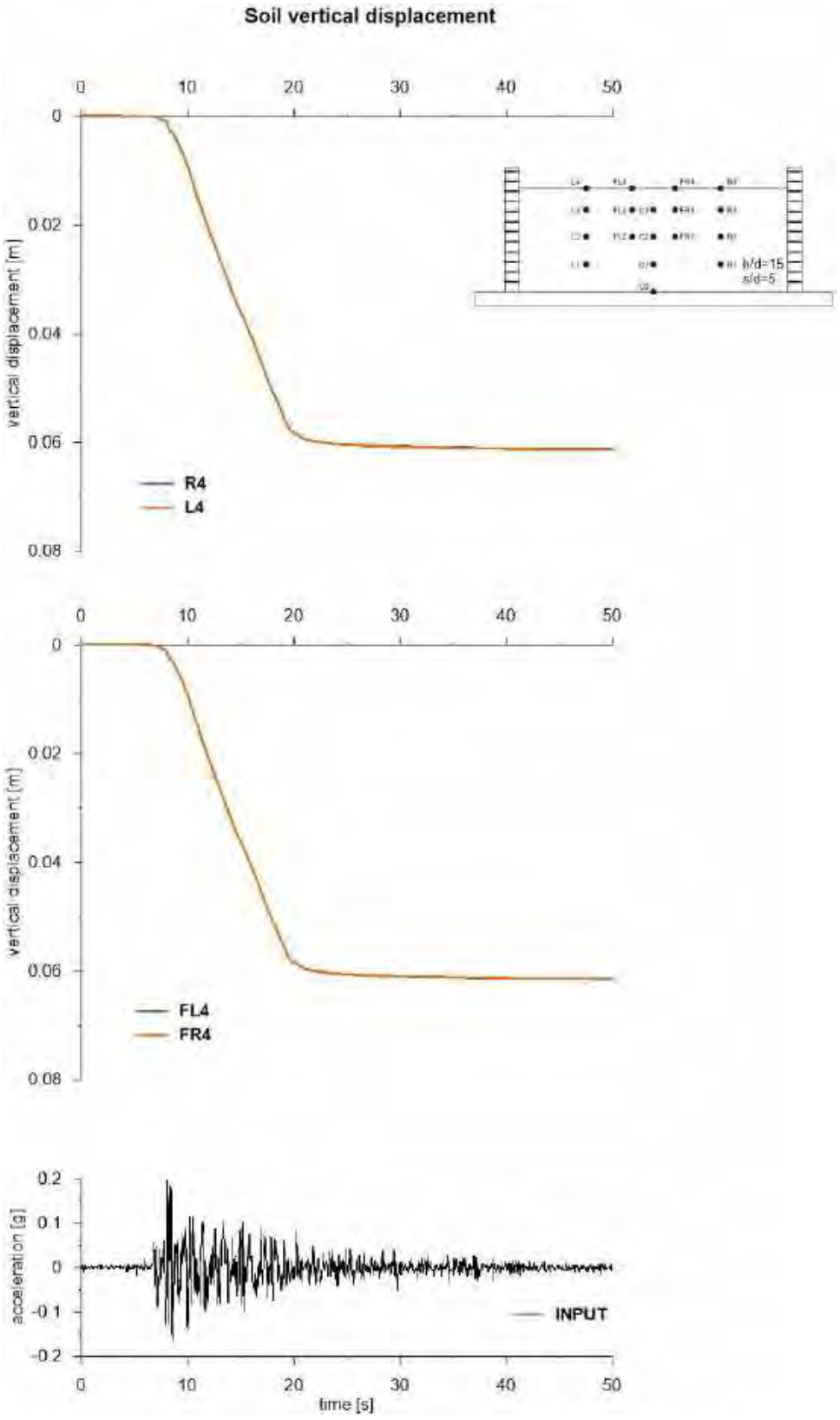

This project has received funding from the European Union's Horizon 2020 research and innovation programme under grant agreement No. 700748

6.1.1.16 ID: SF_HDU_H15_s10

The model consists of a homogenous soil profile of Ticino sand. The ground motion applied was the number 31.

ID: SF_HDU_H15_s10

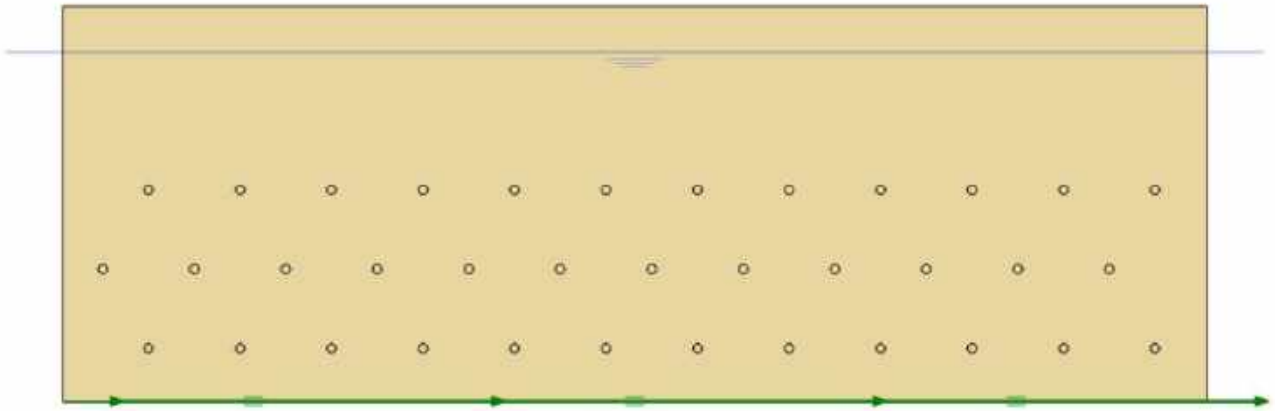

Layouts of the model reproduced in Plaxis 2D

This project has received funding from the European Union's Horizon 2020 research and innovation programme under grant agreement No. 700748

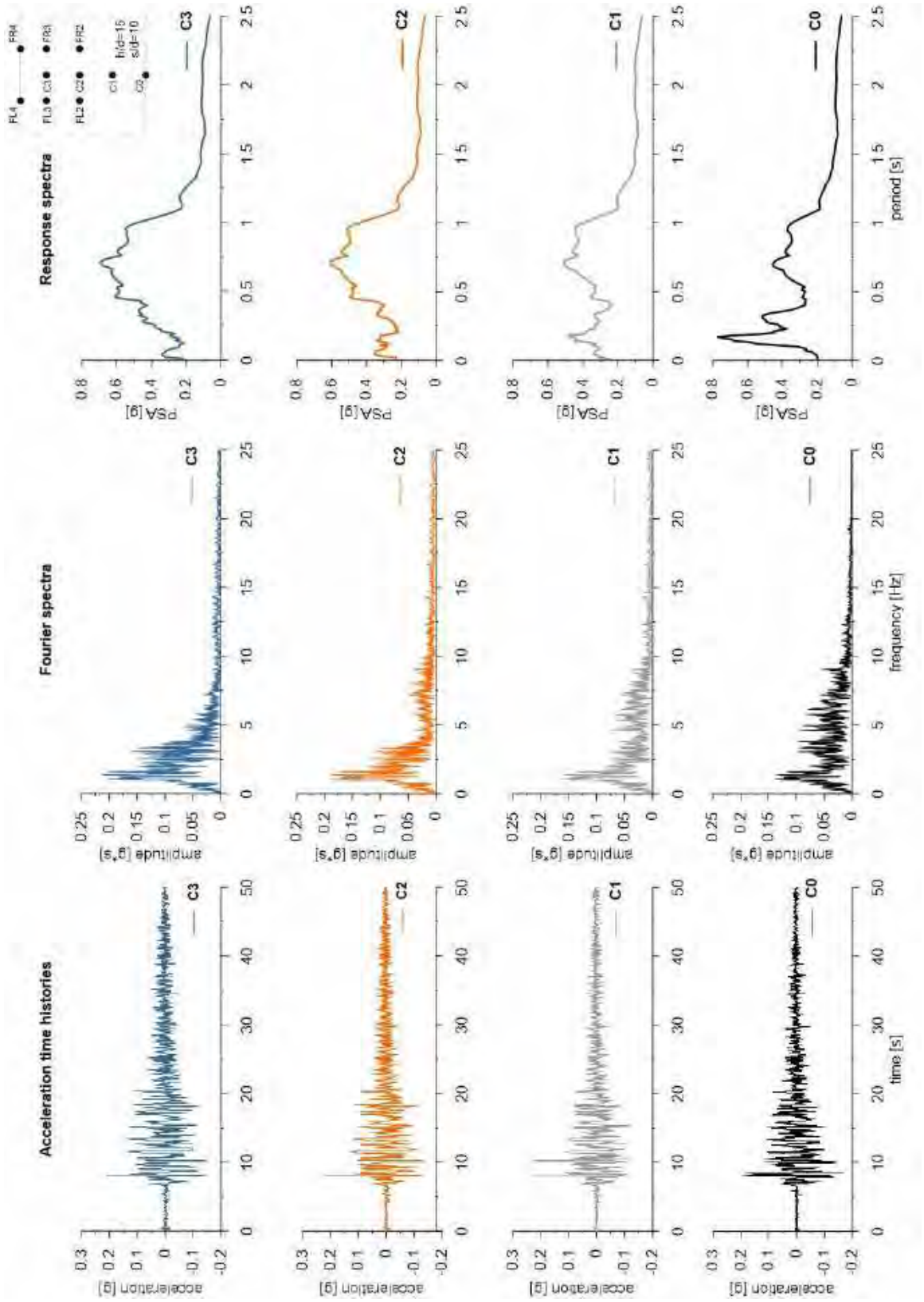

This project has received funding from the European Union's Horizon 2020 research and innovation programme under grant agreement No. 700748

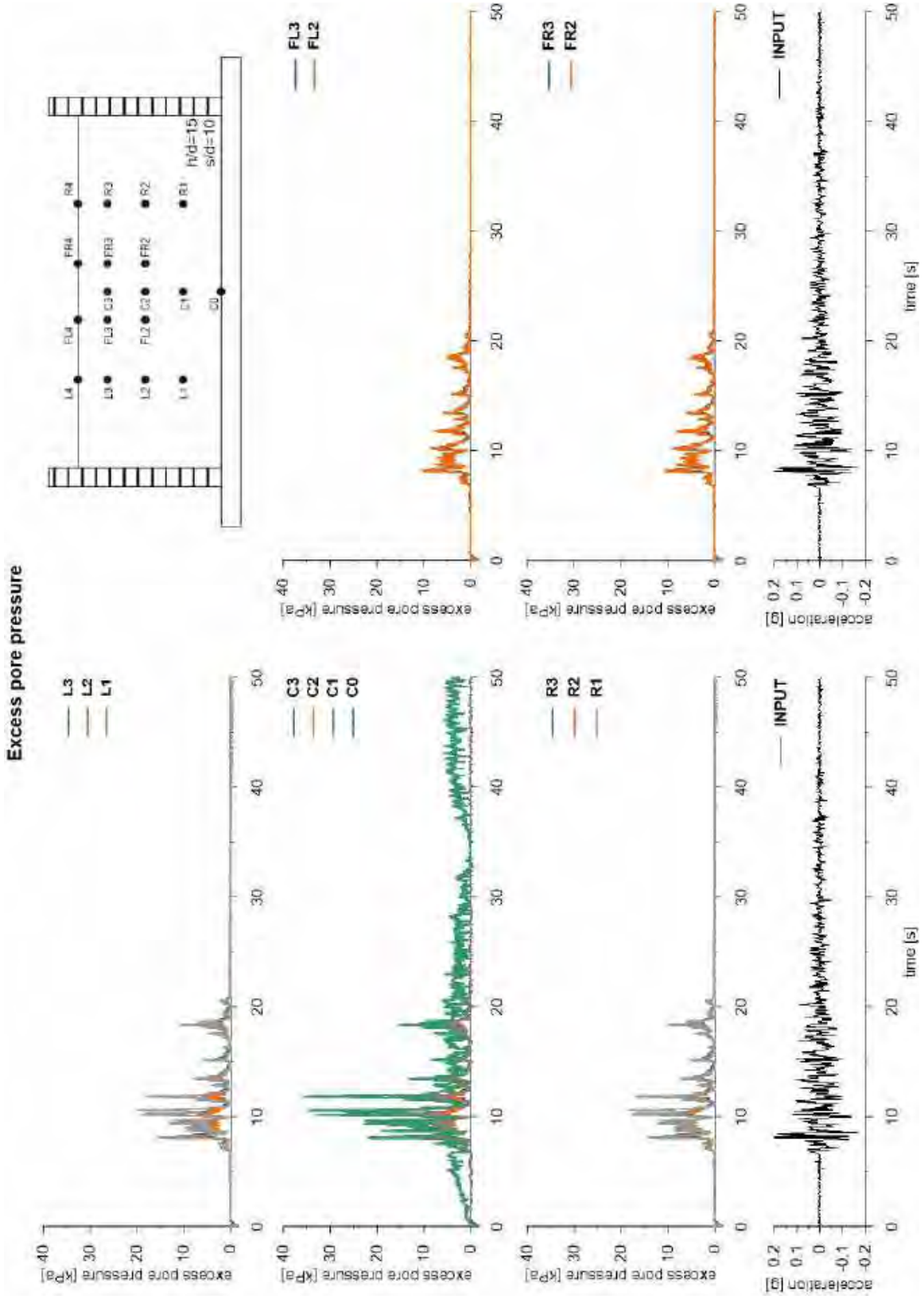

This project has received funding from the European Union's Horizon 2020 research and innovation programme under grant agreement No. 700748

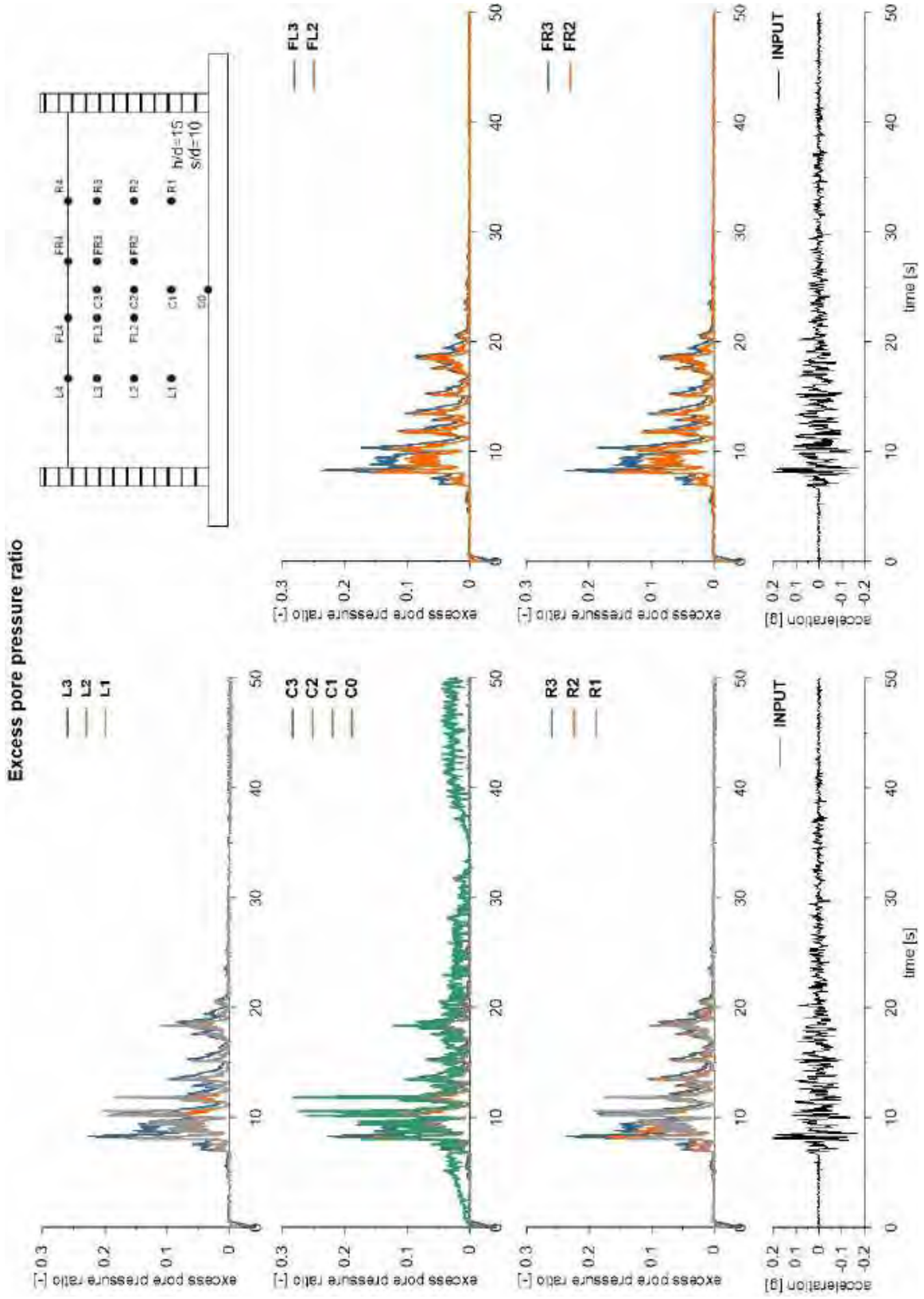

This project has received funding from the European Union's Horizon 2020 research and innovation programme under grant agreement No. 700748

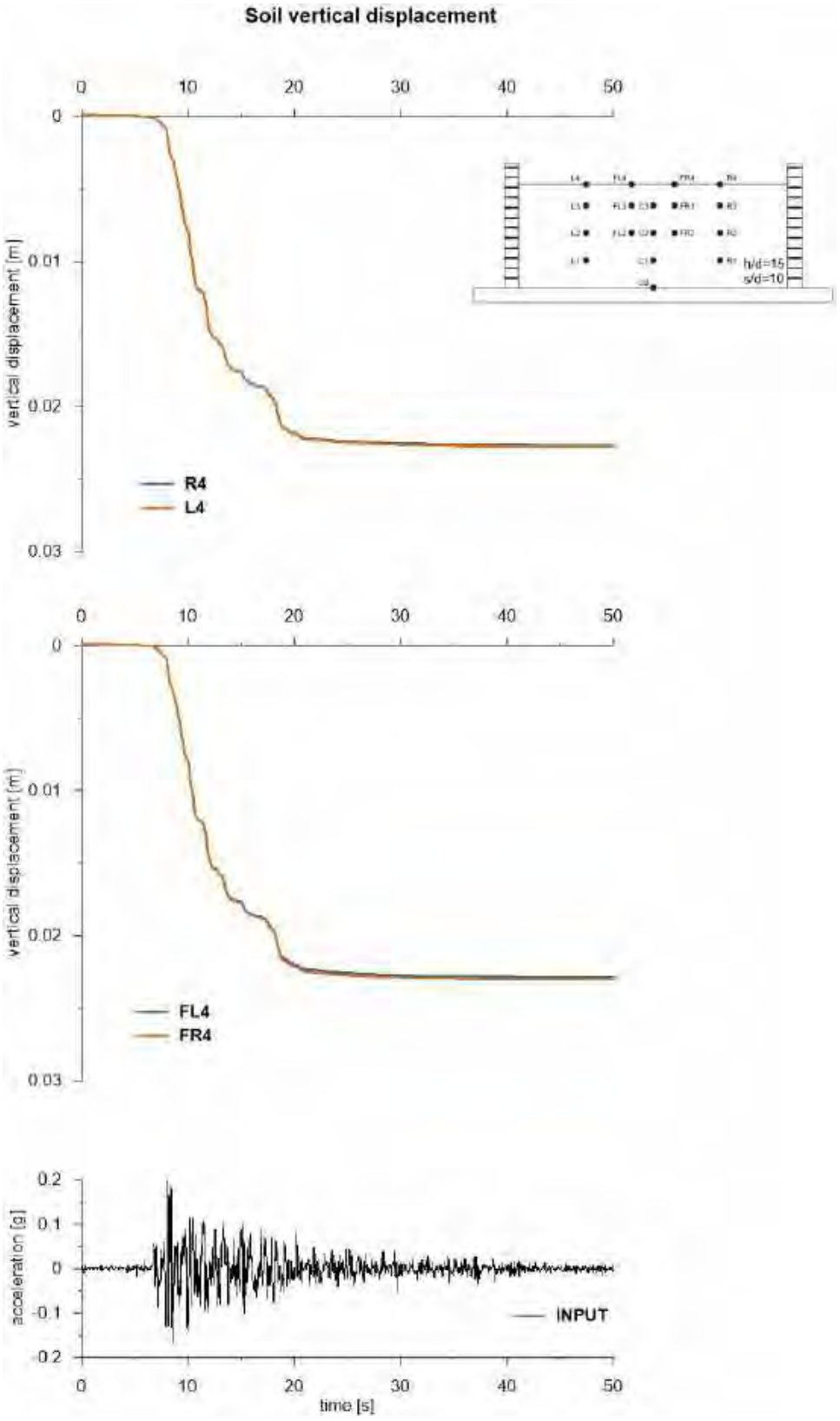

This project has received funding from the European Union's Horizon 2020 research and innovation programme under grant agreement No. 700748

6.1.1.17 ID: SF_HDU_H15_s15

The model consists of a homogenous soil profile of Ticino sand. The ground motion applied was the number 31.

ID: SF_HDU_H15_s15

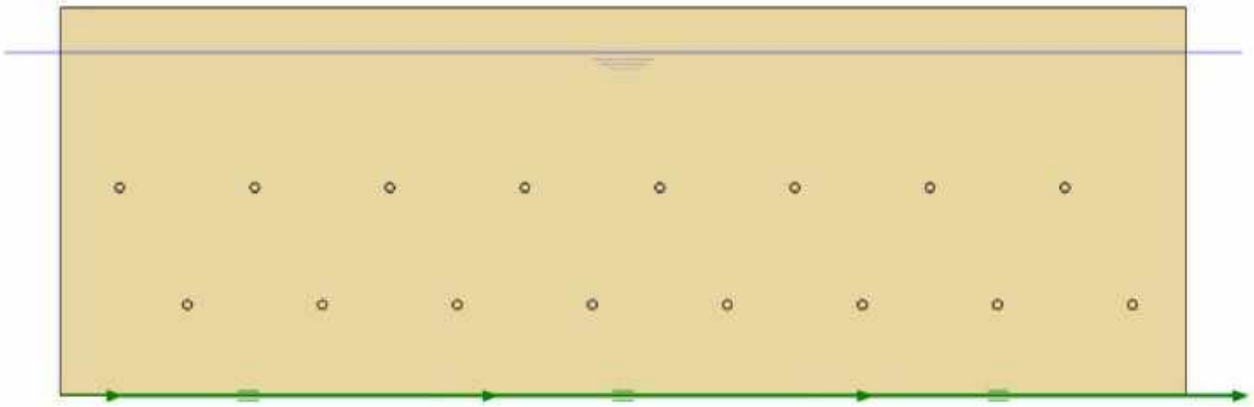

Layouts of the model reproduced in Plaxis 2D

This project has received funding from the European Union's Horizon 2020 research and innovation programme under grant agreement No. 700748

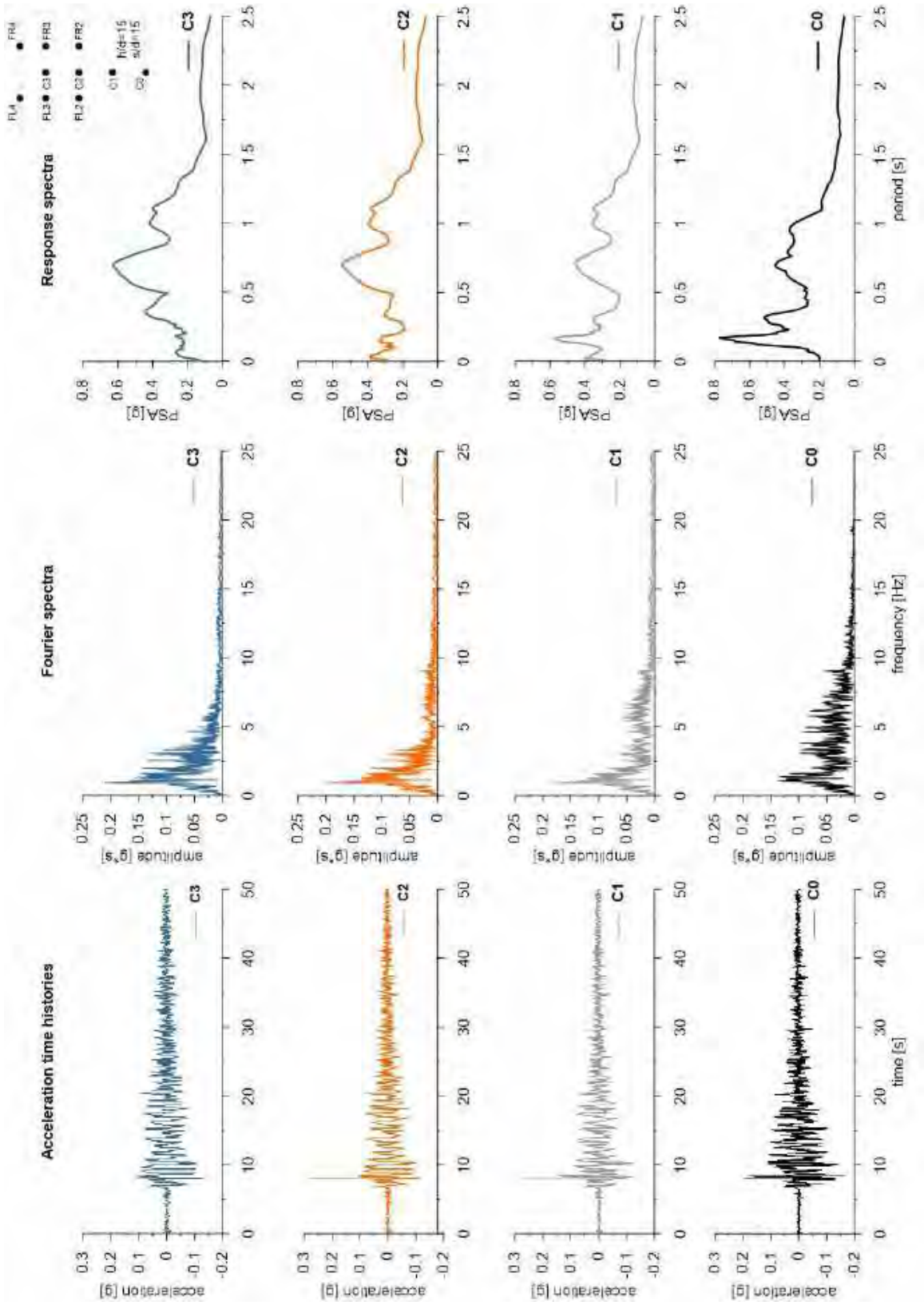

This project has received funding from the European Union's Horizon 2020 research and innovation programme under grant agreement No. 700748

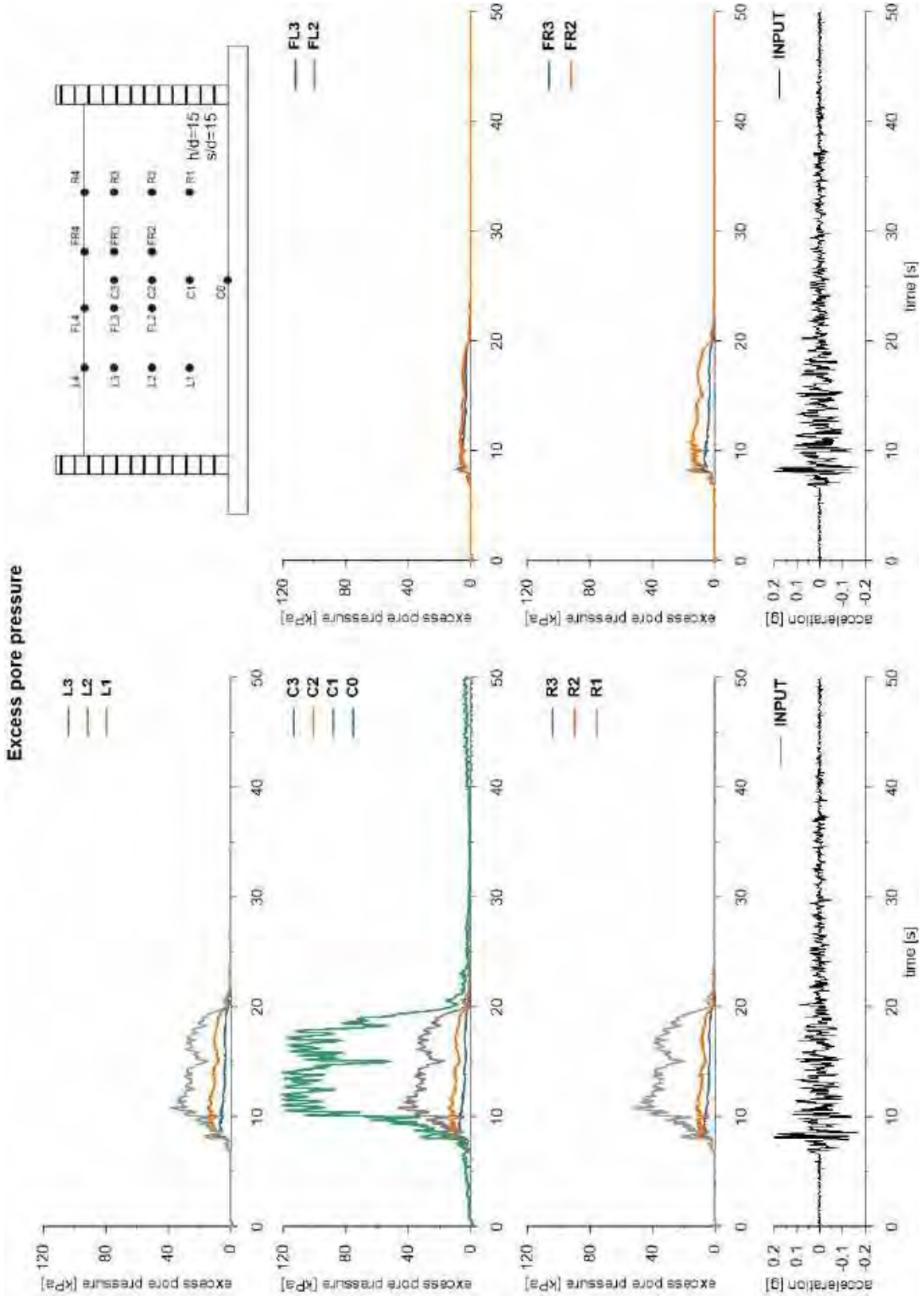

This project has received funding from the European Union's Horizon 2020 research and innovation programme under grant agreement No. 700748

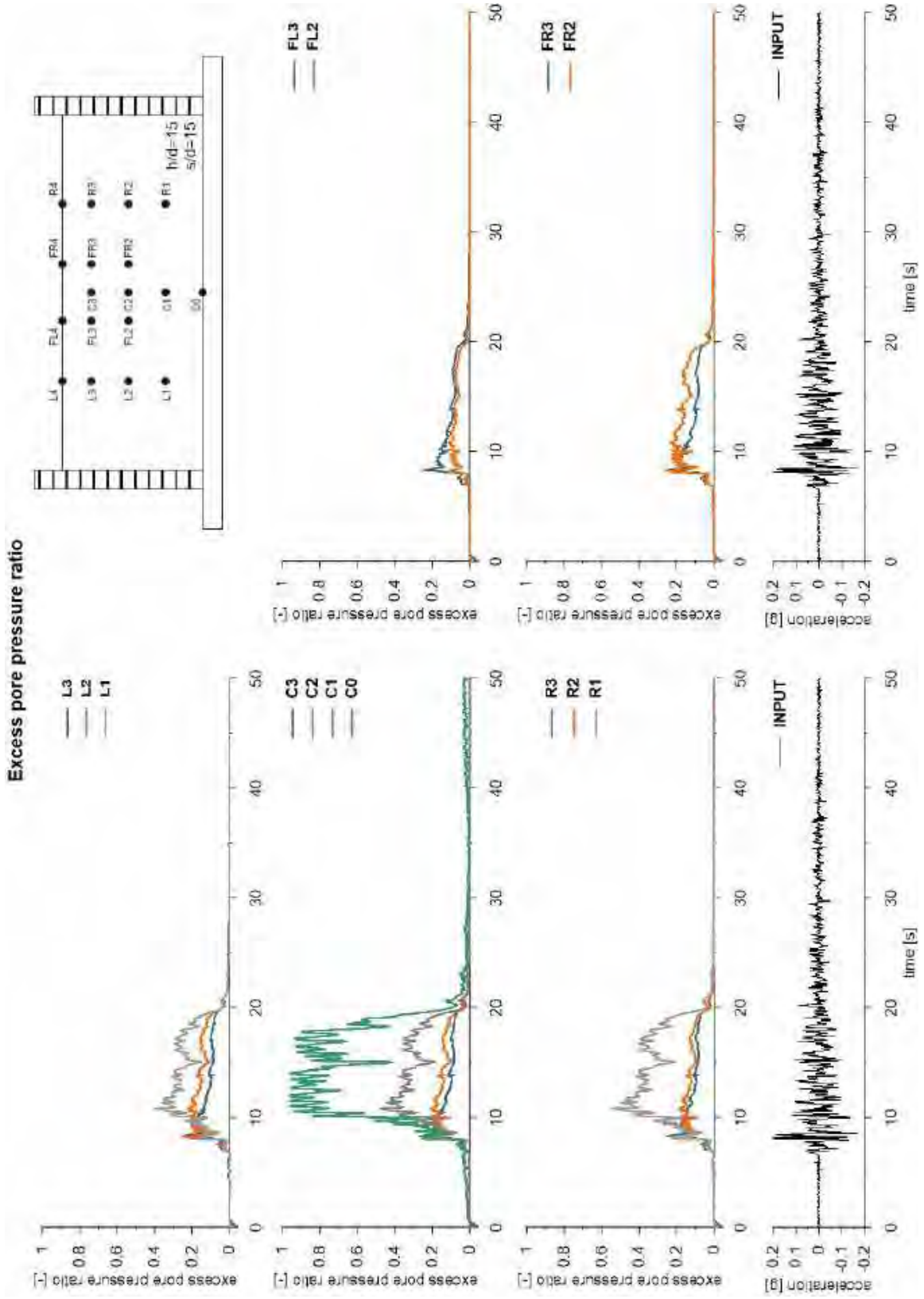

This project has received funding from the European Union's Horizon 2020 research and innovation programme under grant agreement No. 700748

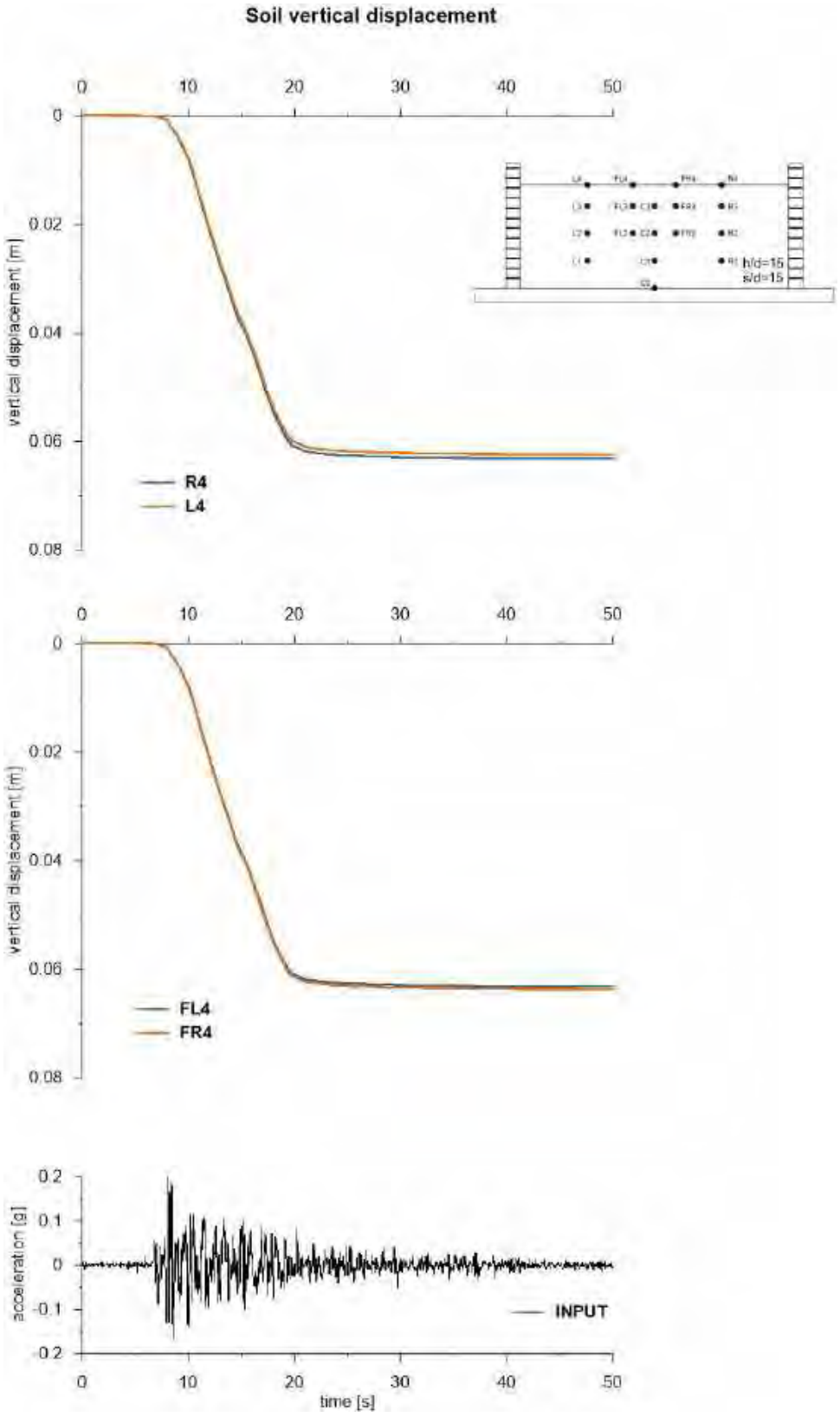

This project has received funding from the European Union's Horizon 2020 research and innovation programme under grant agreement No. 700748

6.1.1.18 ID: DF_HDU_H05_s05

The model consists of a double soil profile of clay and Ticino sand. The ground motion applied was the number 31.

ID: DF_HDU_H05_s05

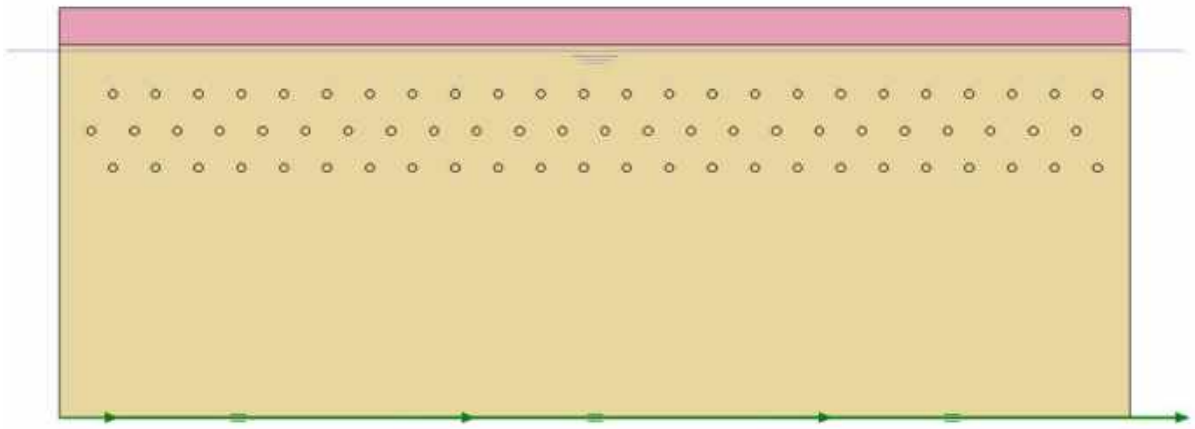

Layouts of the model reproduced in Plaxis 2D

This project has received funding from the European Union's Horizon 2020 research and innovation programme under grant agreement No. 700748

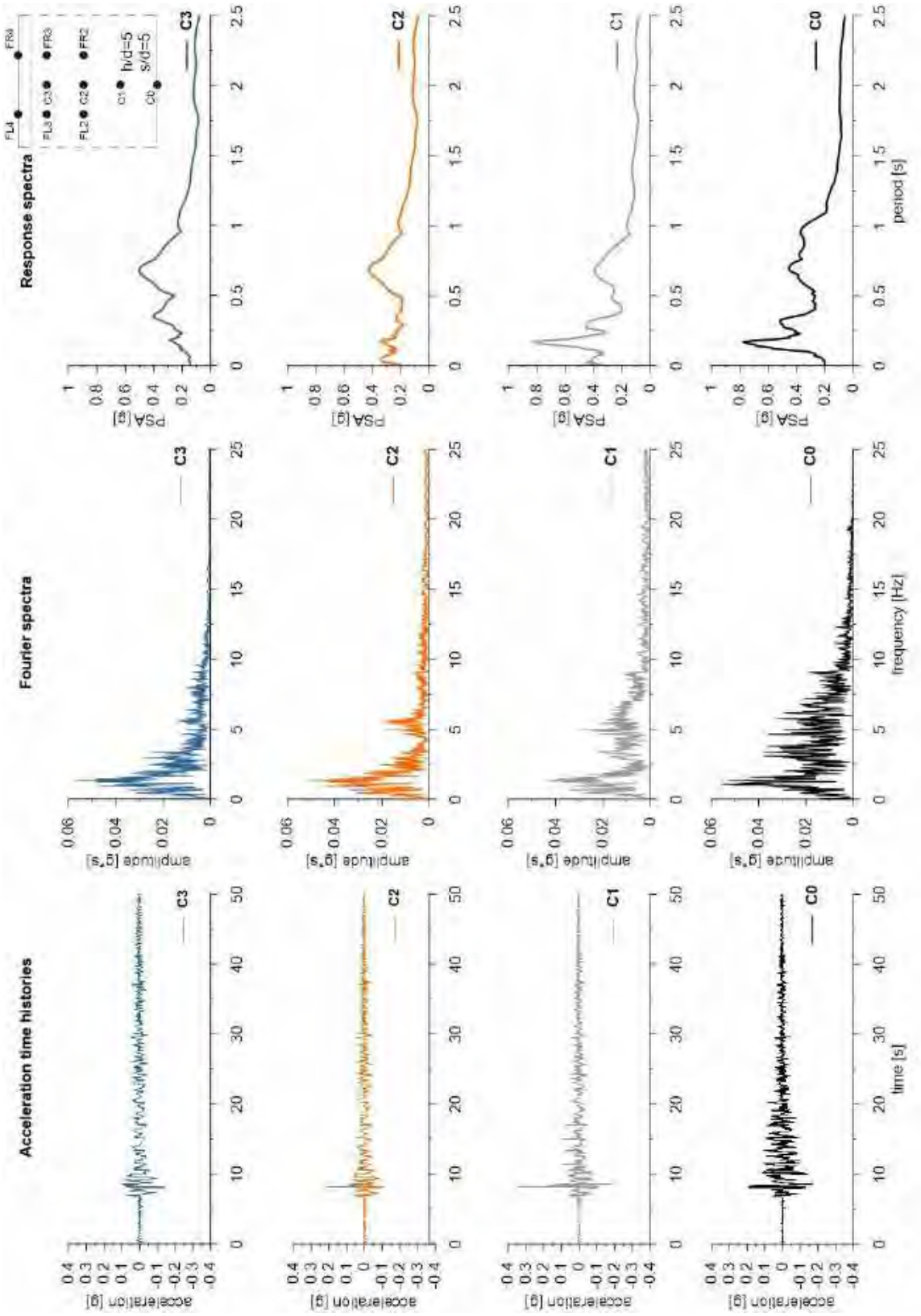

This project has received funding from the European Union's Horizon 2020 research and innovation programme under grant agreement No. 700748

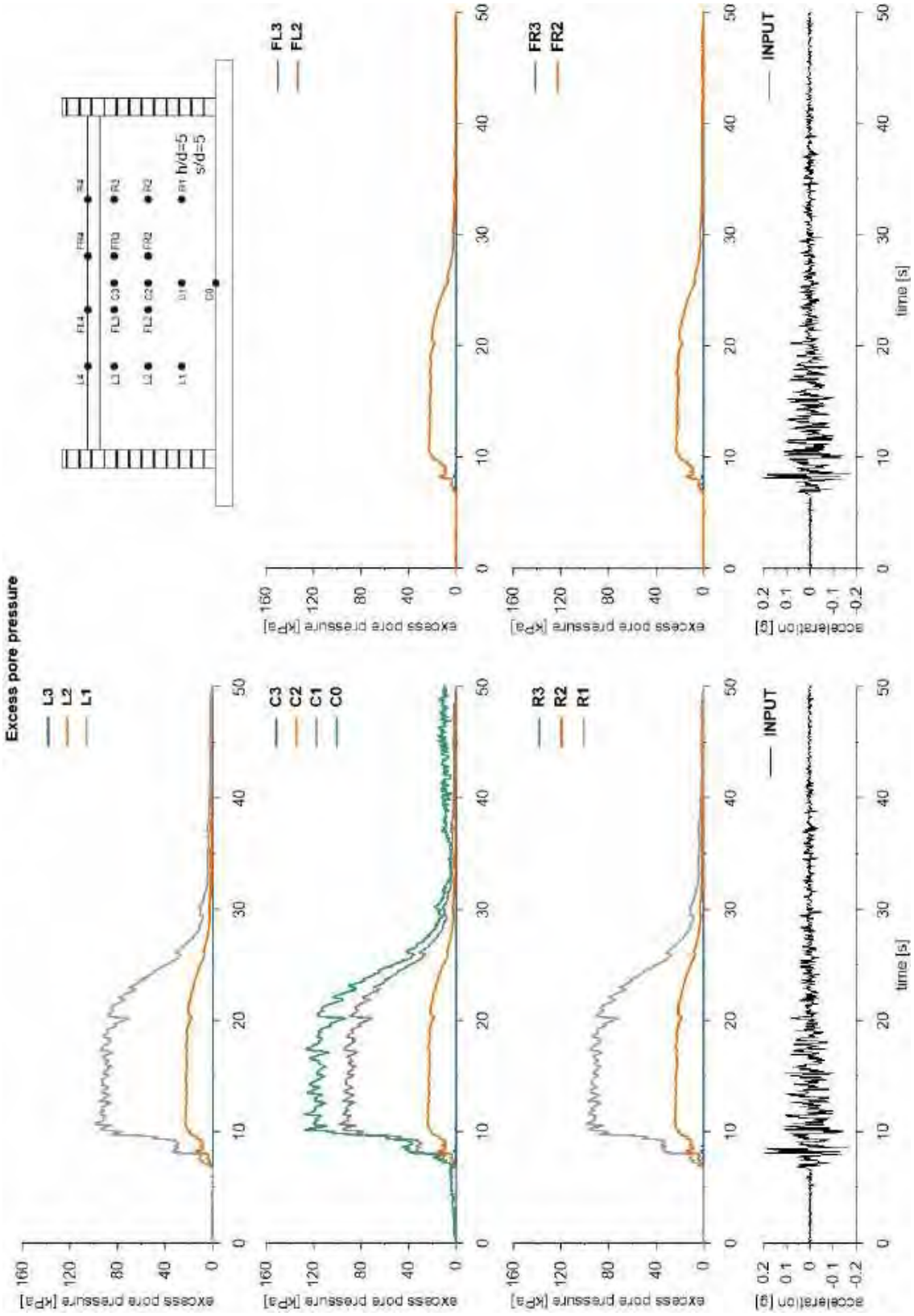

This project has received funding from the European Union's Horizon 2020 research and innovation programme under grant agreement No. 700748

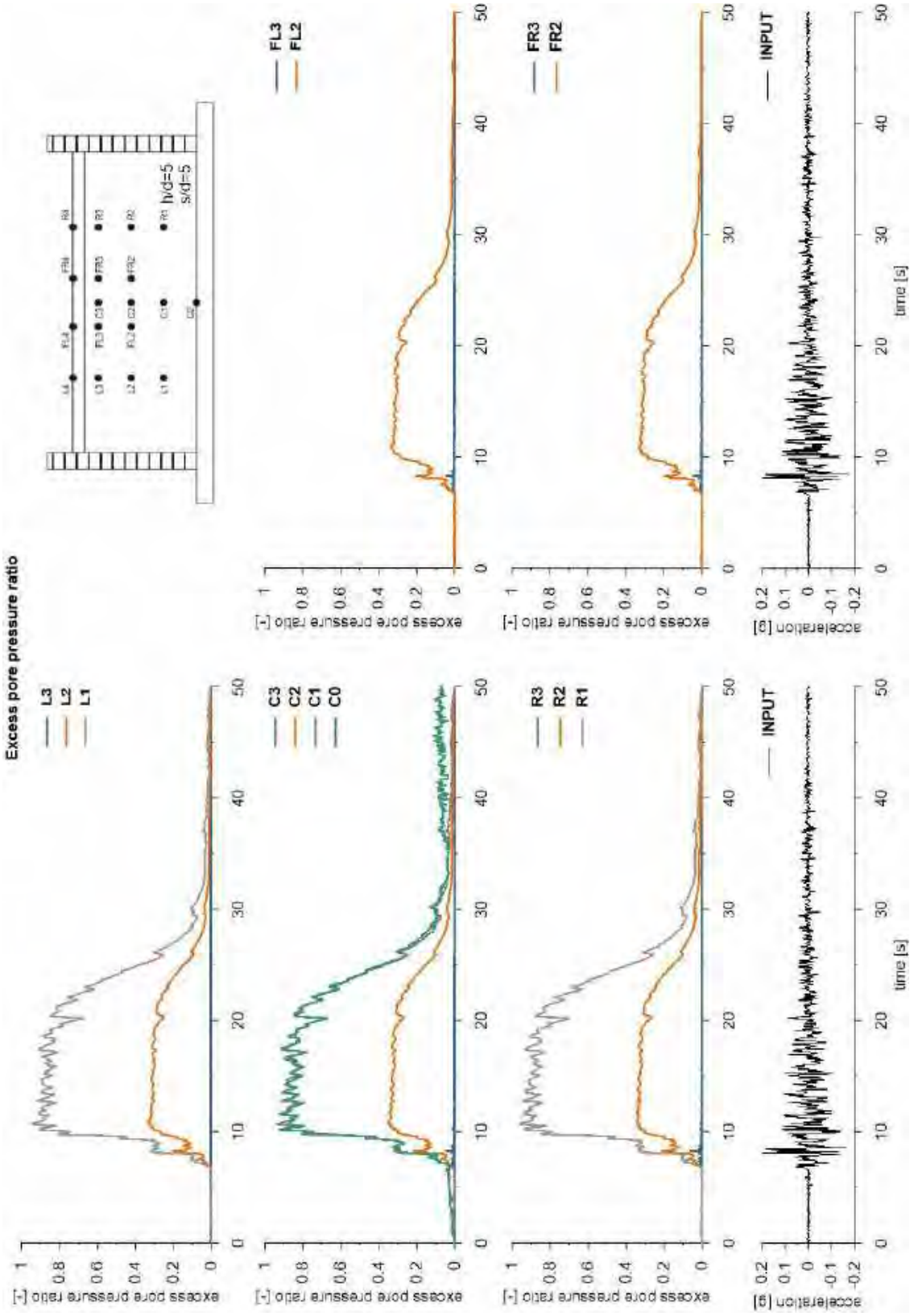

This project has received funding from the European Union's Horizon 2020 research and innovation programme under grant agreement No. 700748

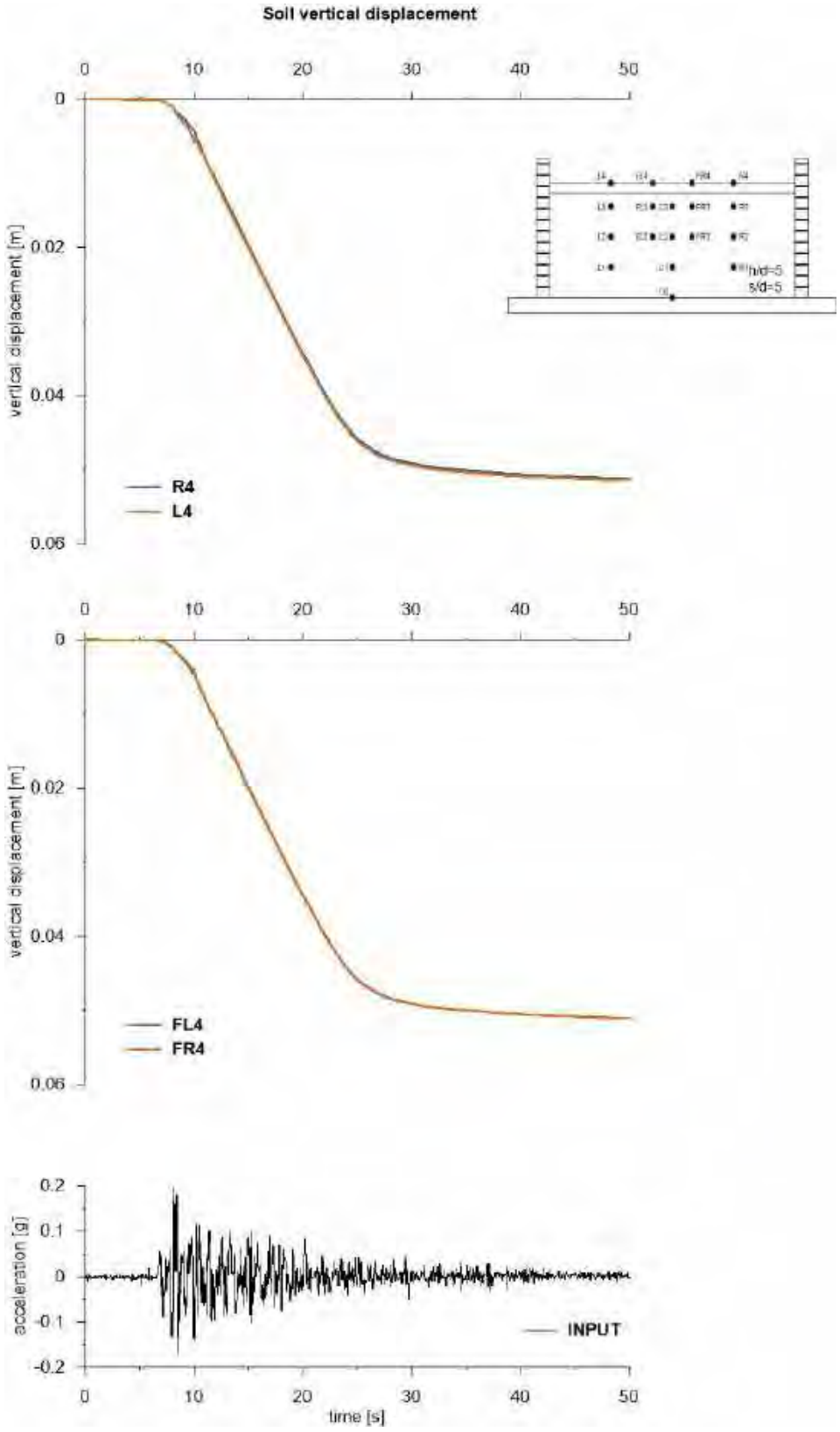

This project has received funding from the European Union's Horizon 2020 research and innovation programme under grant agreement No. 700748

6.1.1.19 ID: DF_HDU_H05_s10

The model consists of a double soil profile of clay and Ticino sand. The ground motion applied was the number 31.

ID: DF_HDU_H05_s10

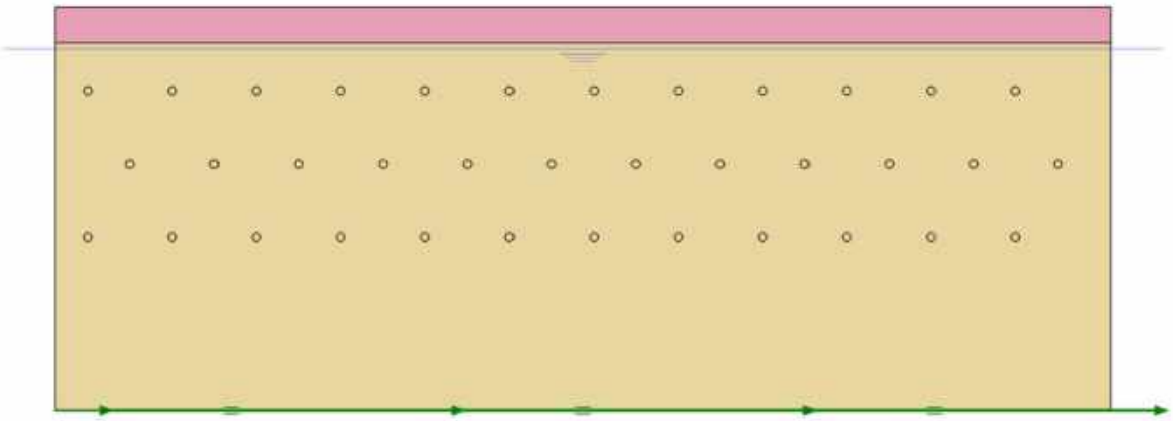

Layouts of the model reproduced in Plaxis 2D

This project has received funding from the European Union's Horizon 2020 research and innovation programme under grant agreement No. 700748

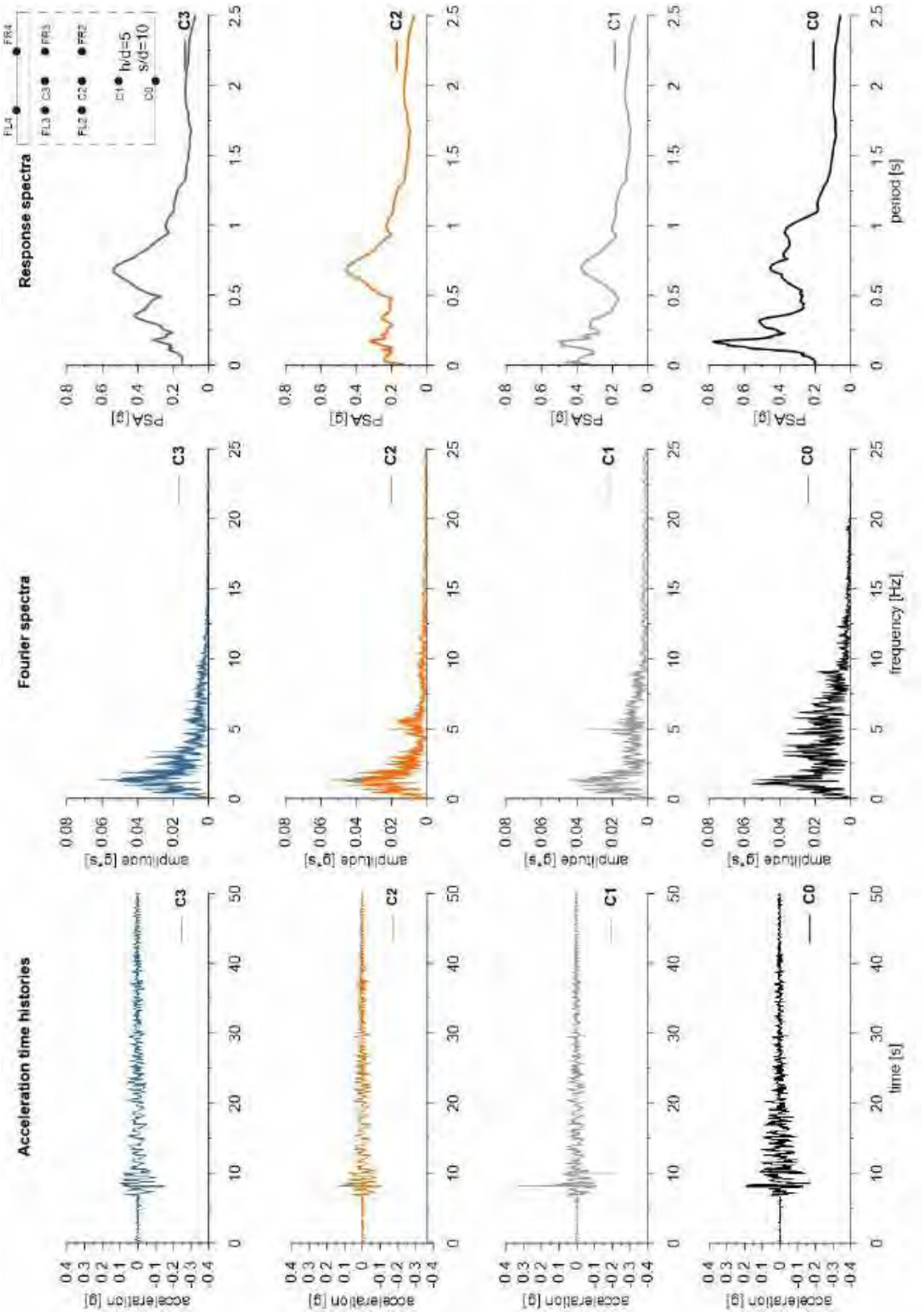

This project has received funding from the European Union's Horizon 2020 research and innovation programme under grant agreement No. 700748

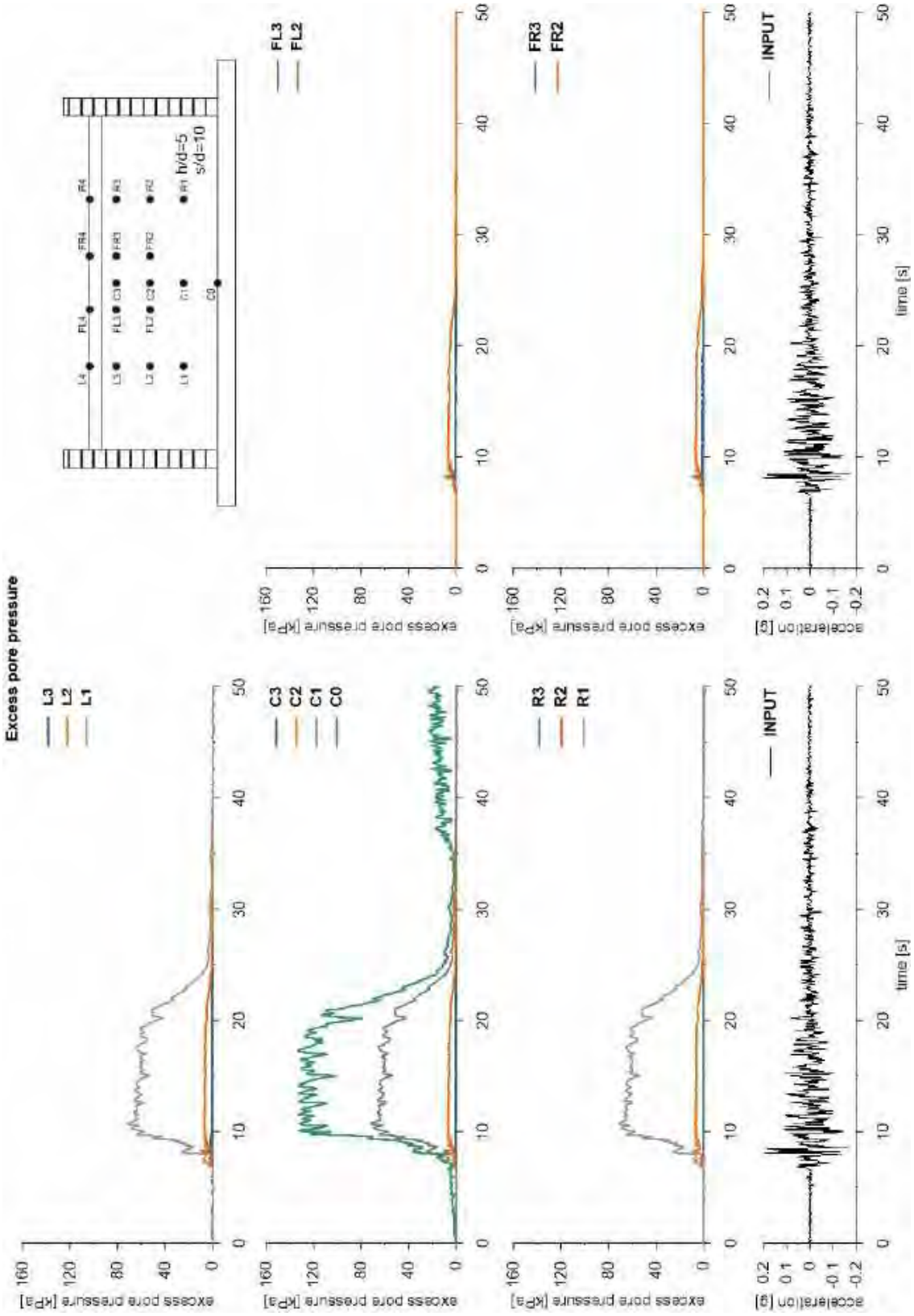

This project has received funding from the European Union's Horizon 2020 research and innovation programme under grant agreement No. 700748

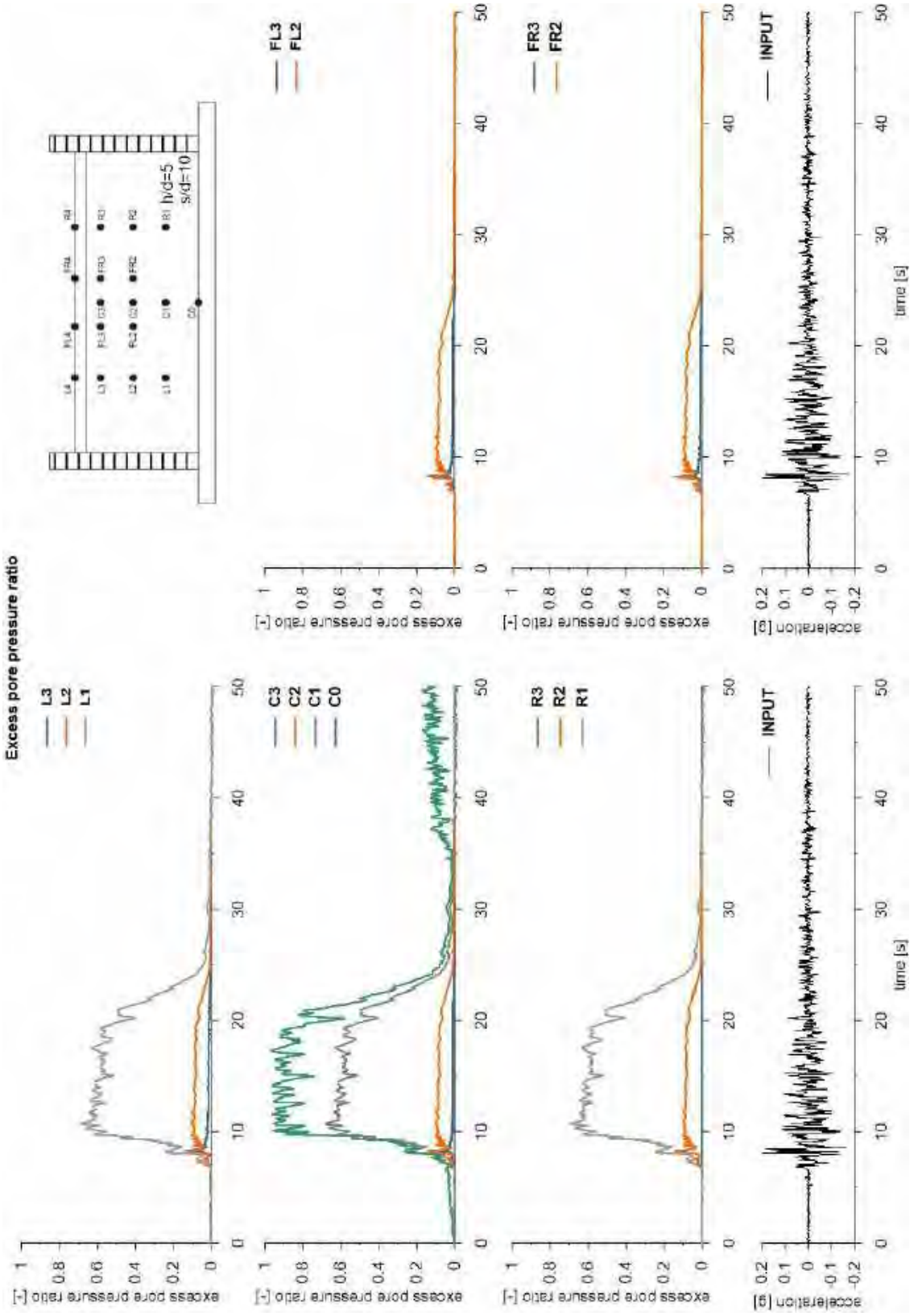

This project has received funding from the European Union's Horizon 2020 research and innovation programme under grant agreement No. 700748

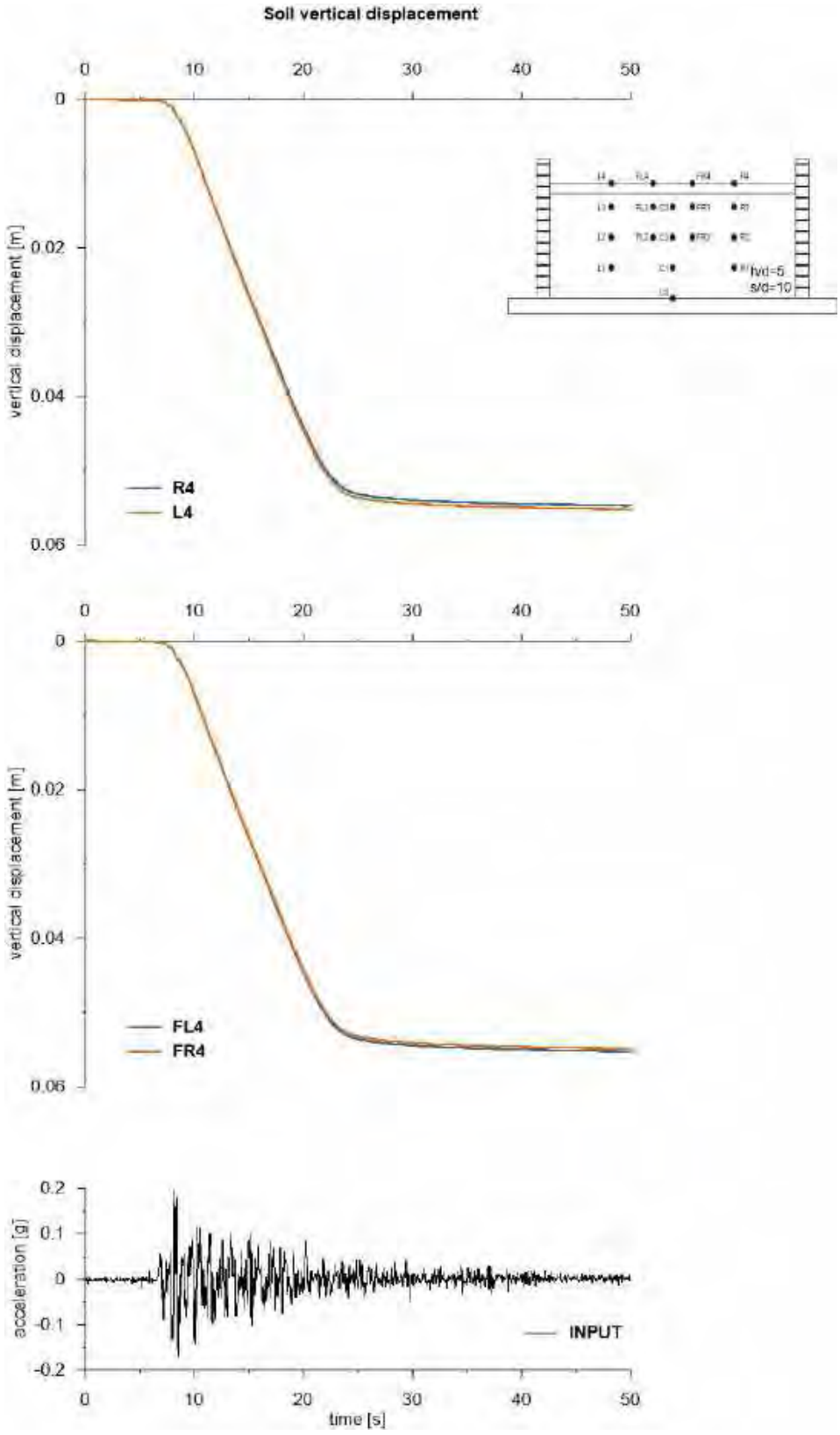

This project has received funding from the European Union's Horizon 2020 research and innovation programme under grant agreement No. 700748

6.1.1.20 ID: DF_HDU_H05_s15

The model consists of a double soil profile of clay and Ticino sand. The ground motion applied was the number 31.

ID: DF_HDU_H05_s15

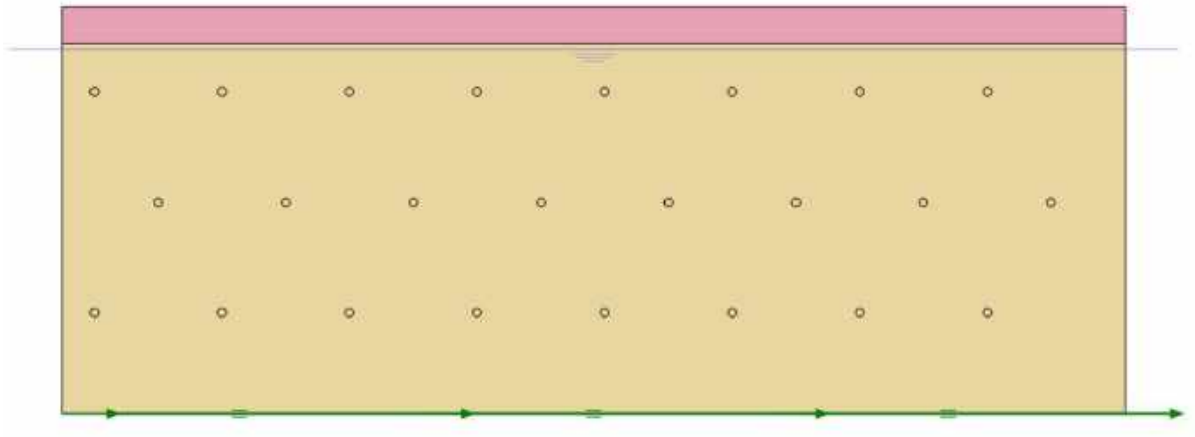

Layouts of the model reproduced in Plaxis 2D

This project has received funding from the European Union's Horizon 2020 research and innovation programme under grant agreement No. 700748

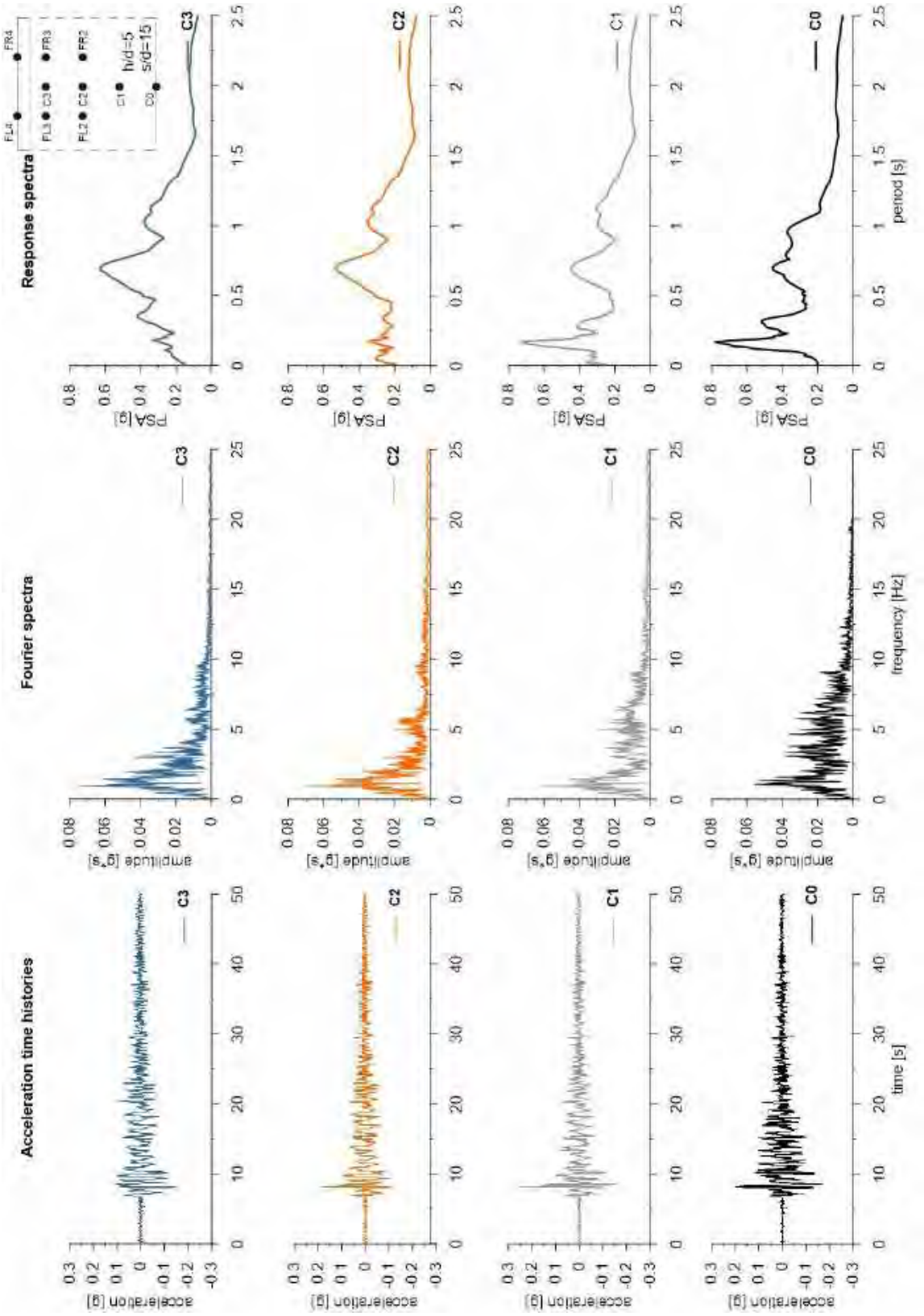

This project has received funding from the European Union's Horizon 2020 research and innovation programme under grant agreement No. 700748

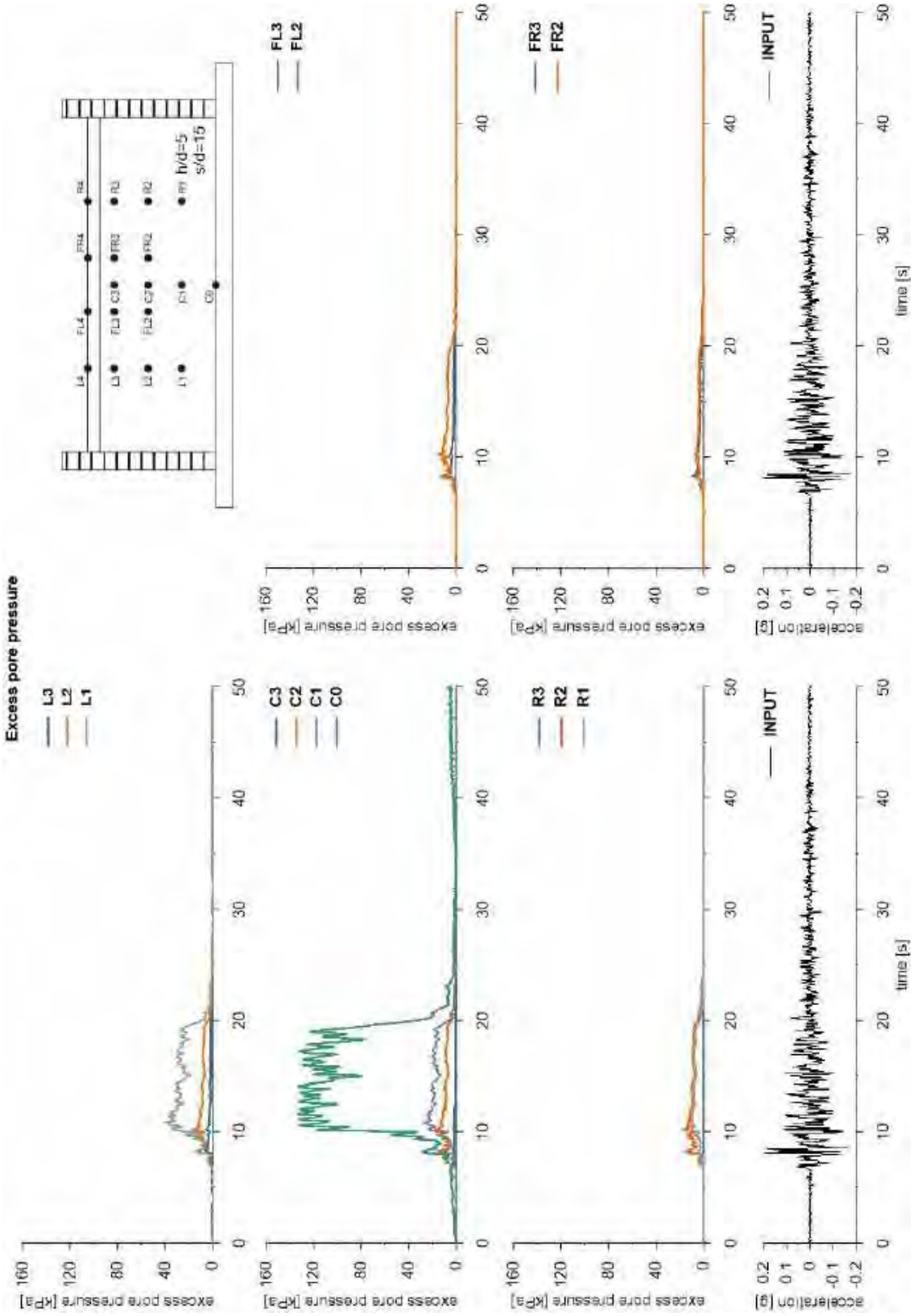

This project has received funding from the European Union's Horizon 2020 research and innovation programme under grant agreement No. 700748

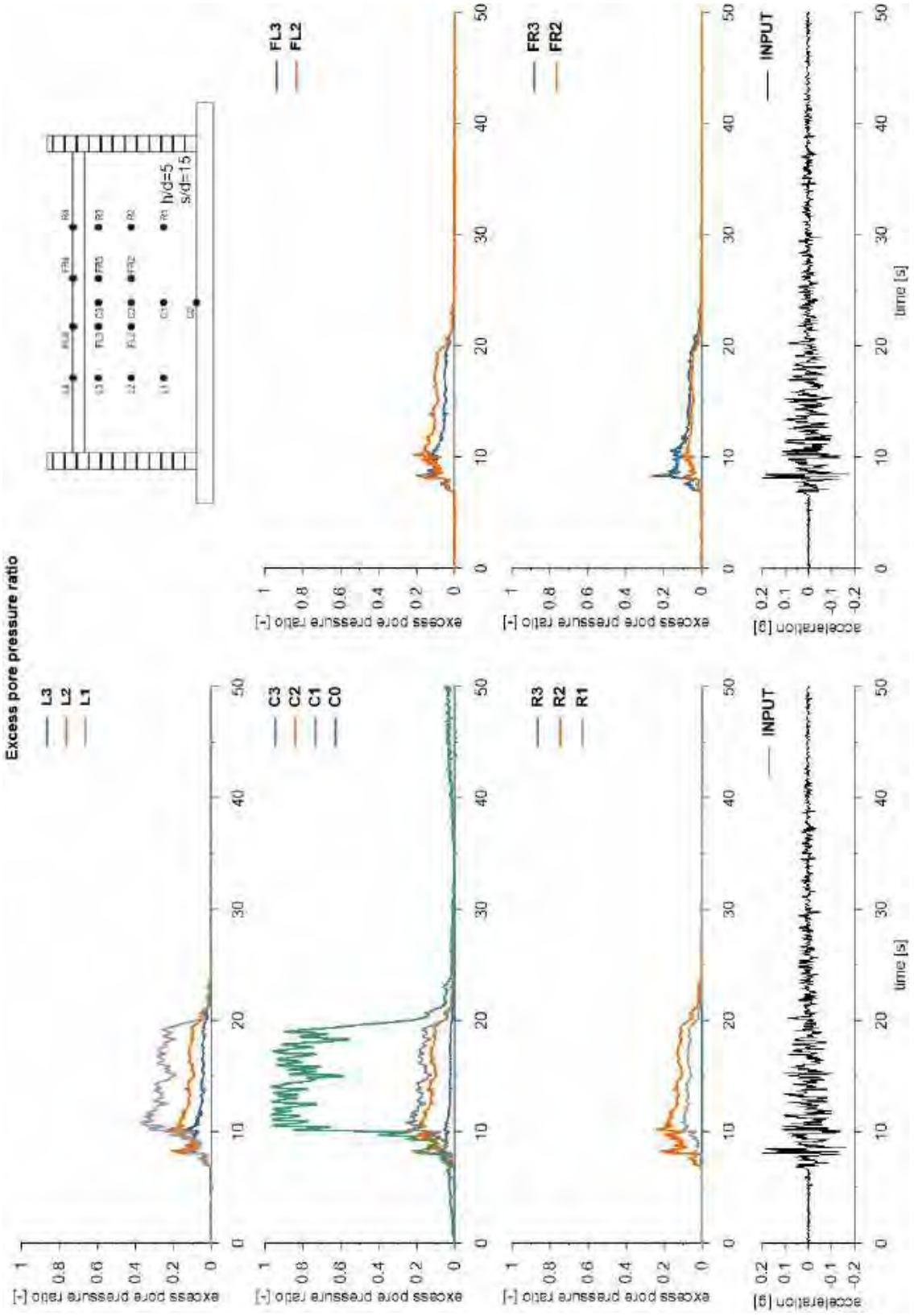

This project has received funding from the European Union's Horizon 2020 research and innovation programme under grant agreement No. 700748

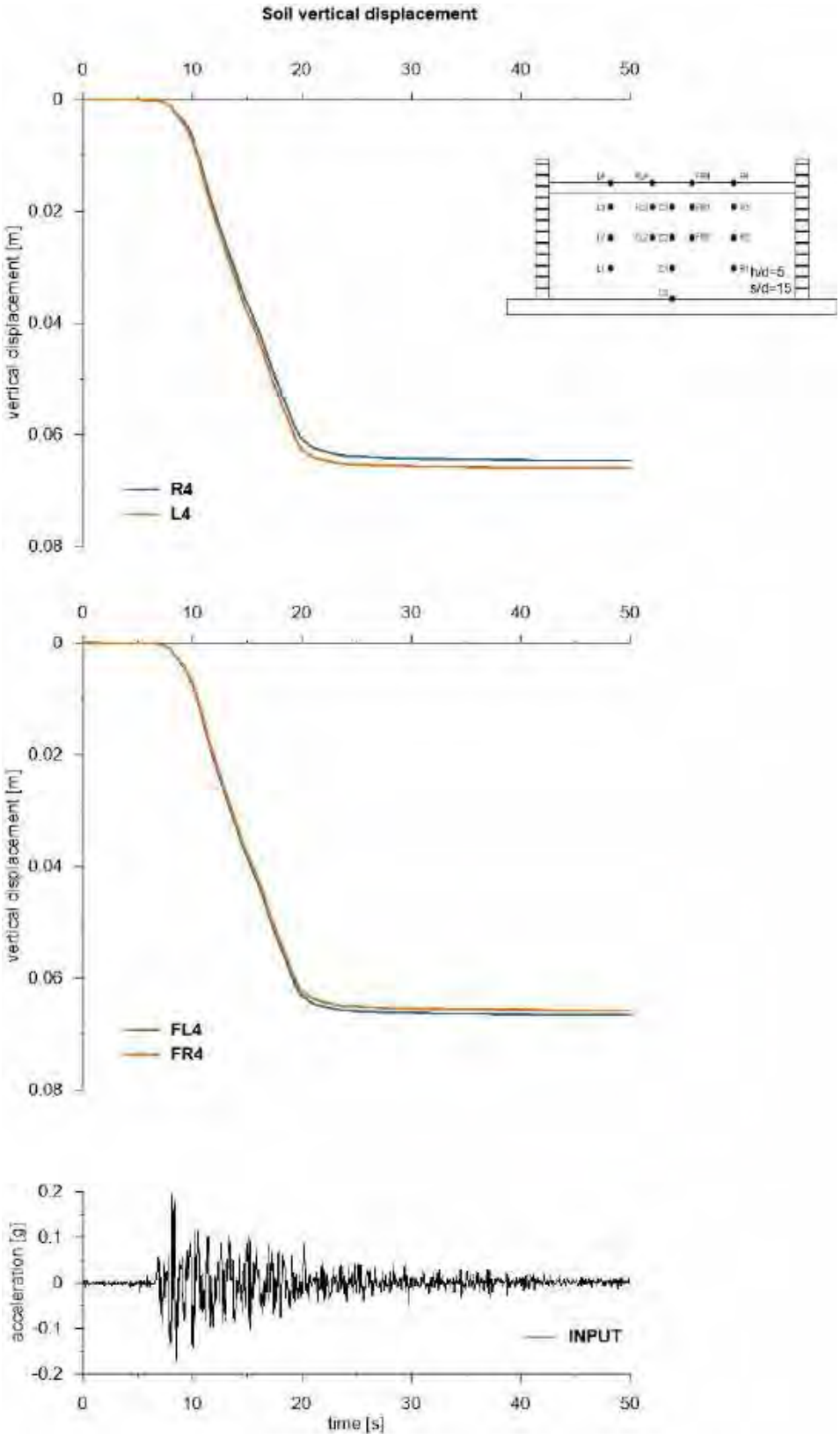

This project has received funding from the European Union's Horizon 2020 research and innovation programme under grant agreement No. 700748

6.1.1.21 ID: DF_HDU_H10_s05

The model consists of a double soil profile of clay and Ticino sand. The ground motion applied was the number 31.

ID: DF_HDU_H10_s05

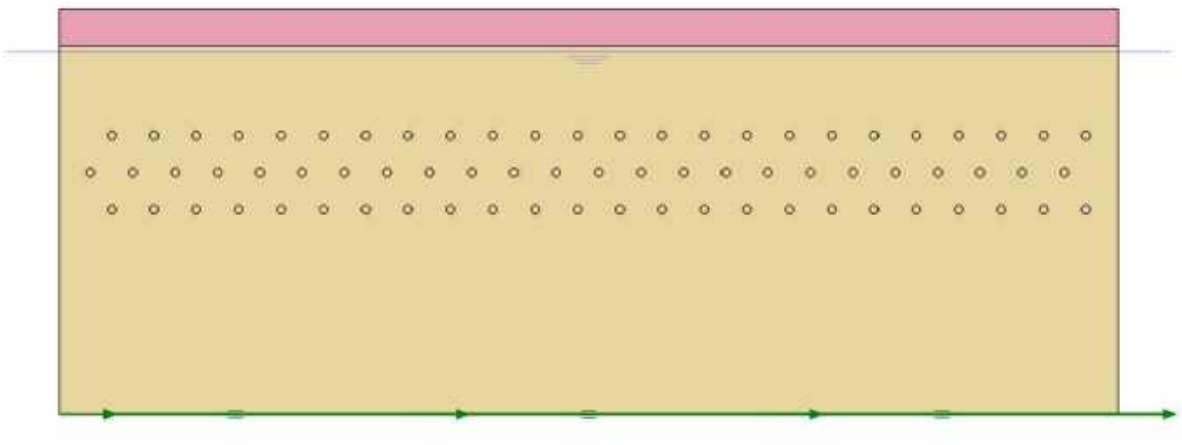

Layouts of the model reproduced in Plaxis 2D

This project has received funding from the European Union's Horizon 2020 research and innovation programme under grant agreement No. 700748

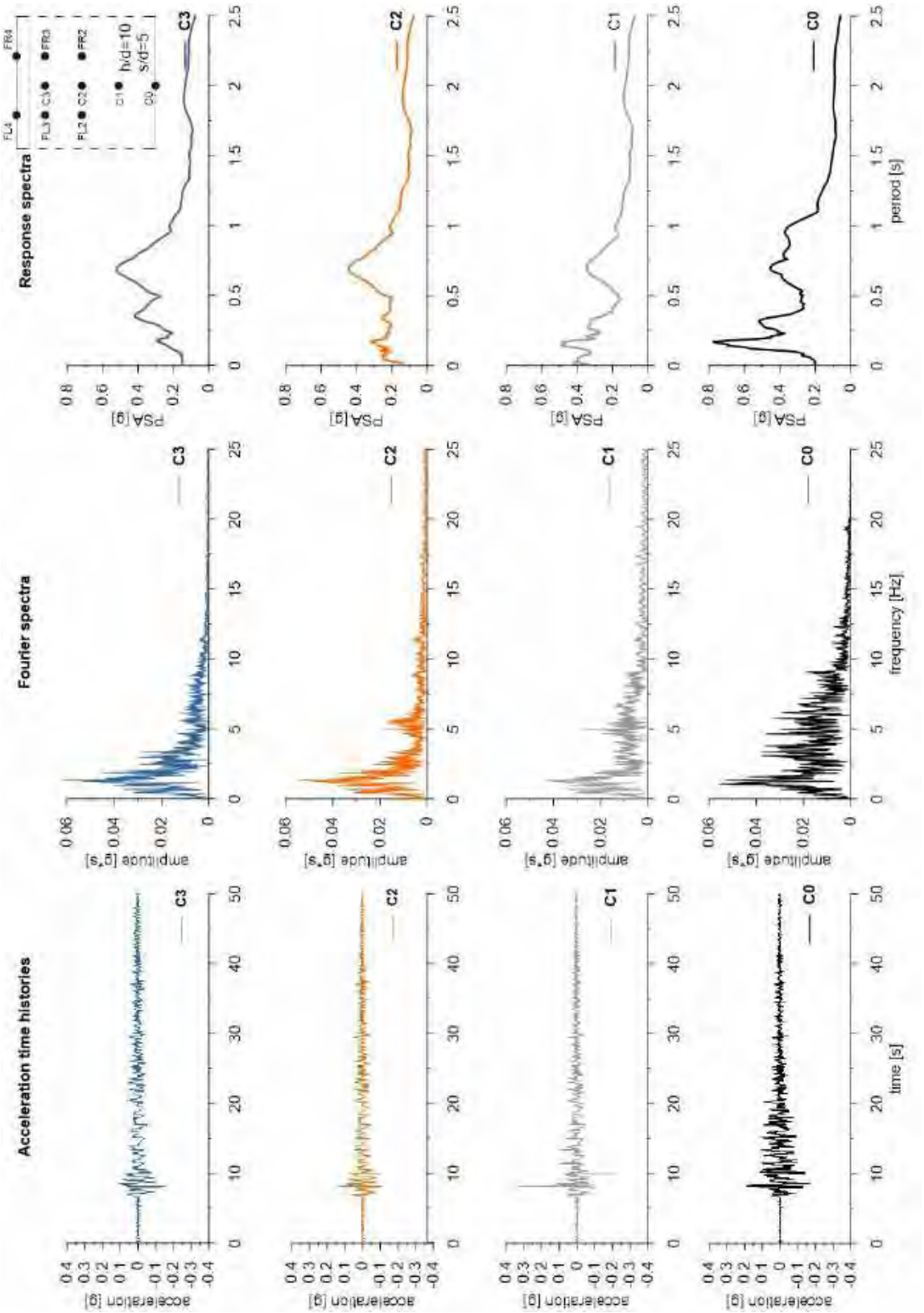

This project has received funding from the European Union's Horizon 2020 research and innovation programme under grant agreement No. 700748

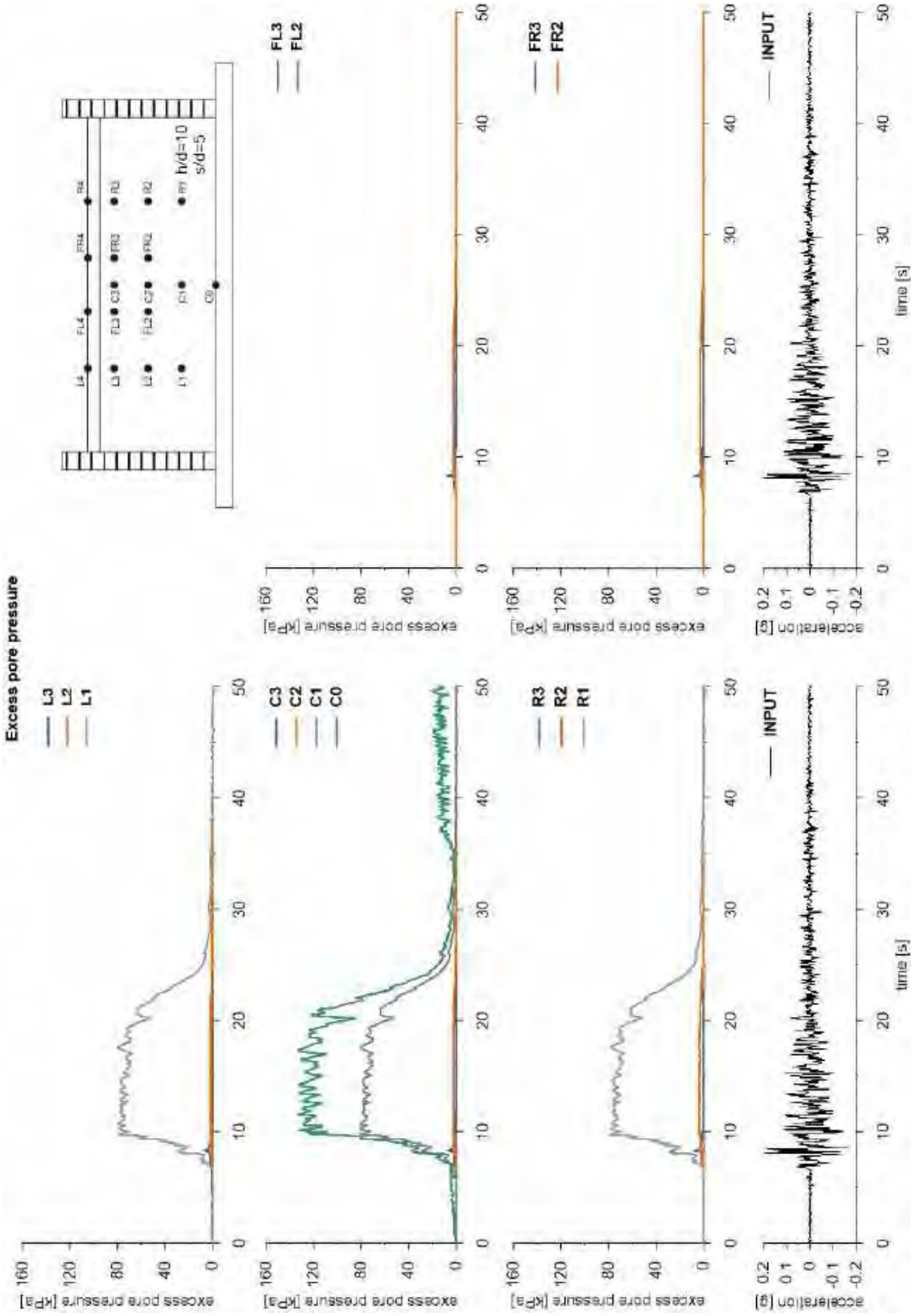

This project has received funding from the European Union's Horizon 2020 research and innovation programme under grant agreement No. 700748

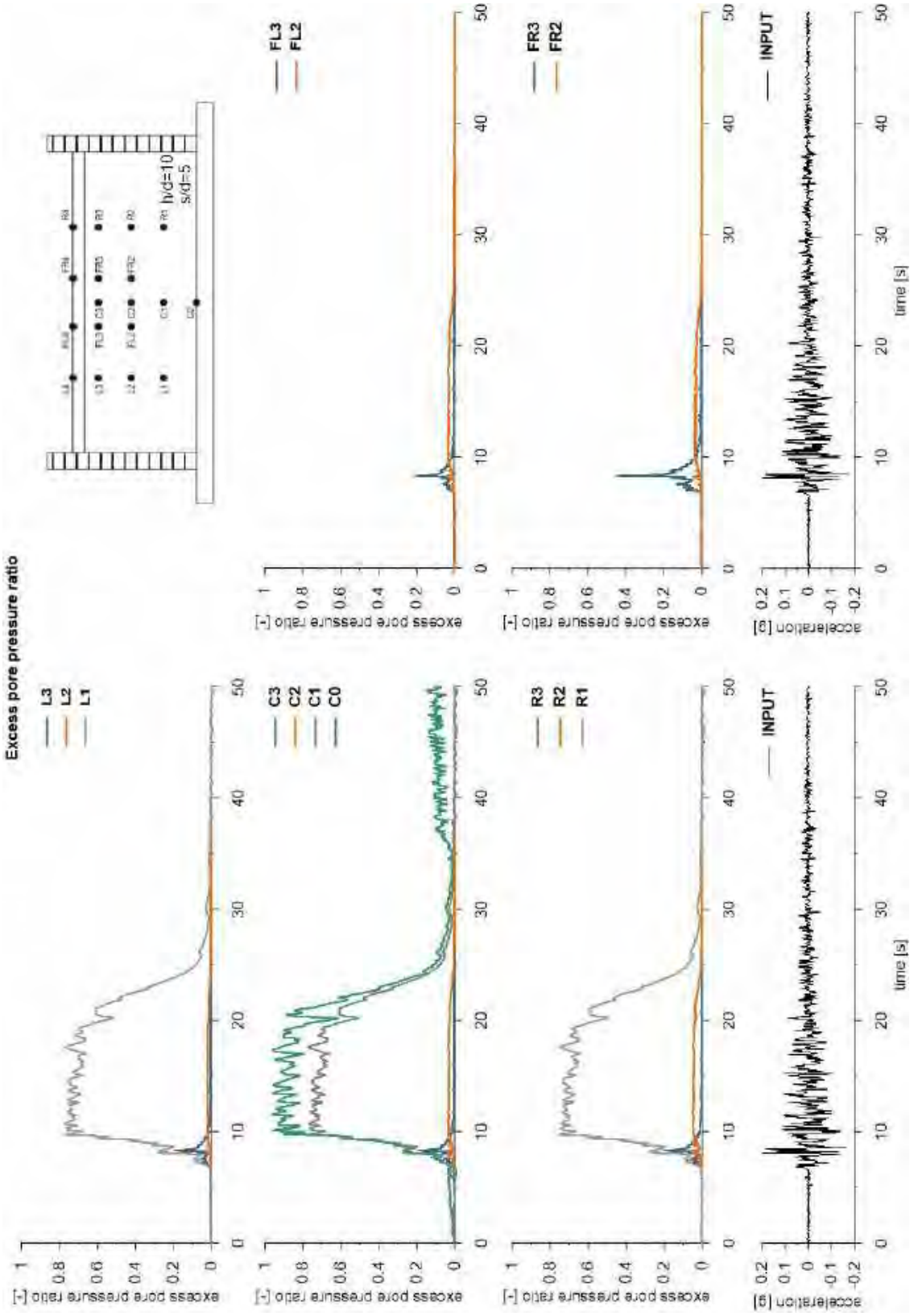

This project has received funding from the European Union's Horizon 2020 research and innovation programme under grant agreement No. 700748

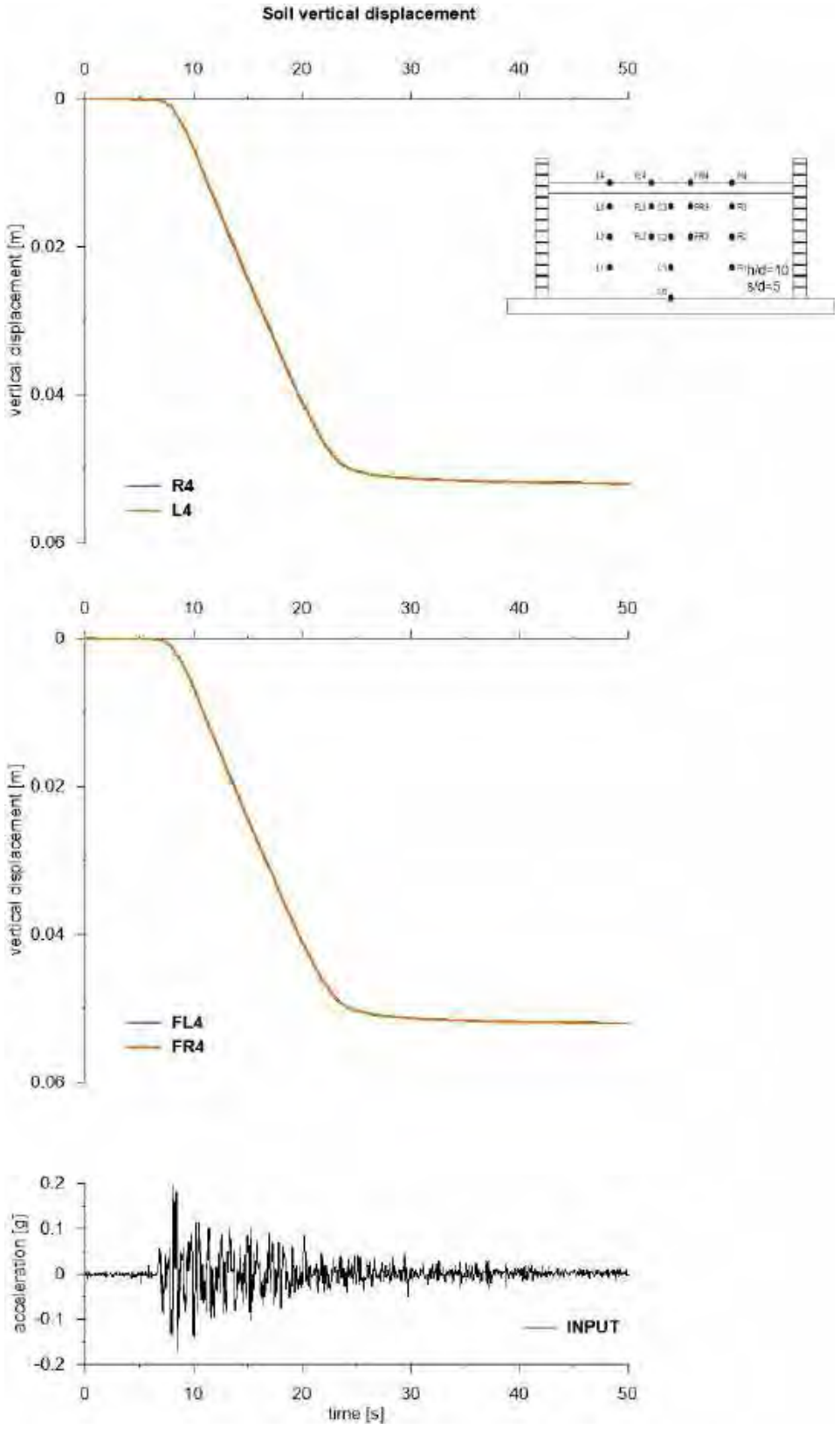

This project has received funding from the European Union's Horizon 2020 research and innovation programme under grant agreement No. 700748

6.1.1.22 ID: DF_HDU_H10_s10

The model consists of a double soil profile of clay and Ticino sand. The ground motion applied was the number 31.

ID: DF_HDU_H10_s10

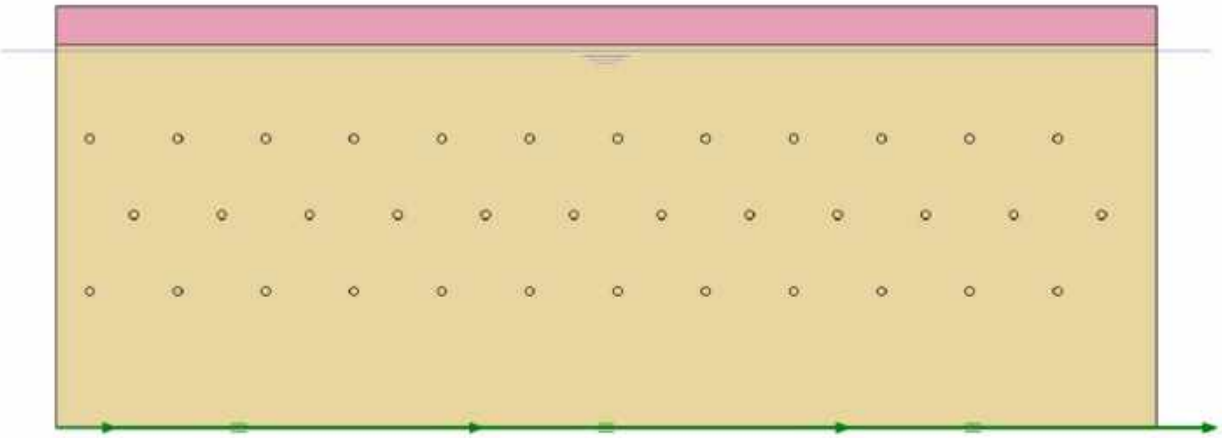

Layouts of the model reproduced in Plaxis 2D

This project has received funding from the European Union's Horizon 2020 research and innovation programme under grant agreement No. 700748

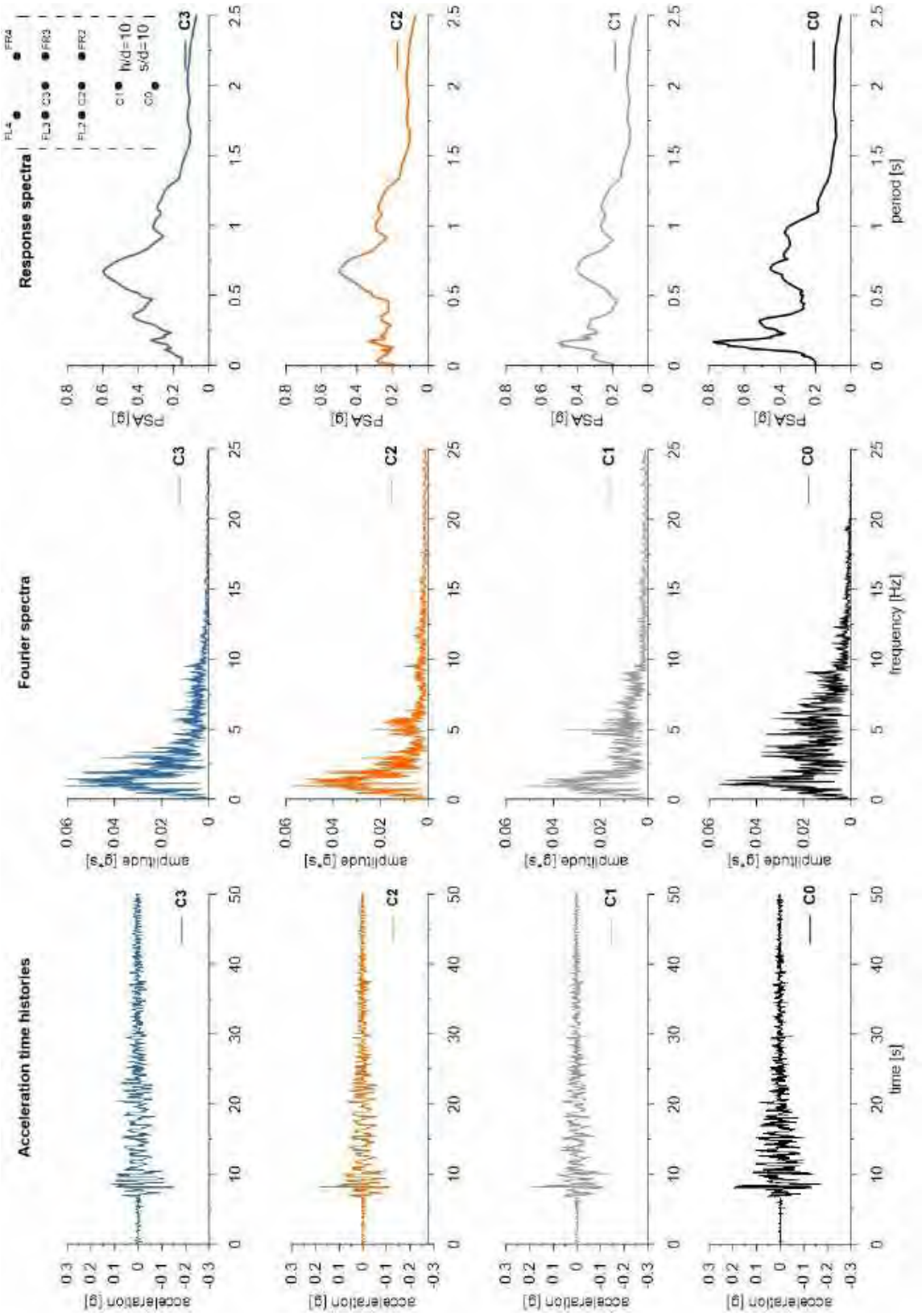

This project has received funding from the European Union's Horizon 2020 research and innovation programme under grant agreement No. 700748

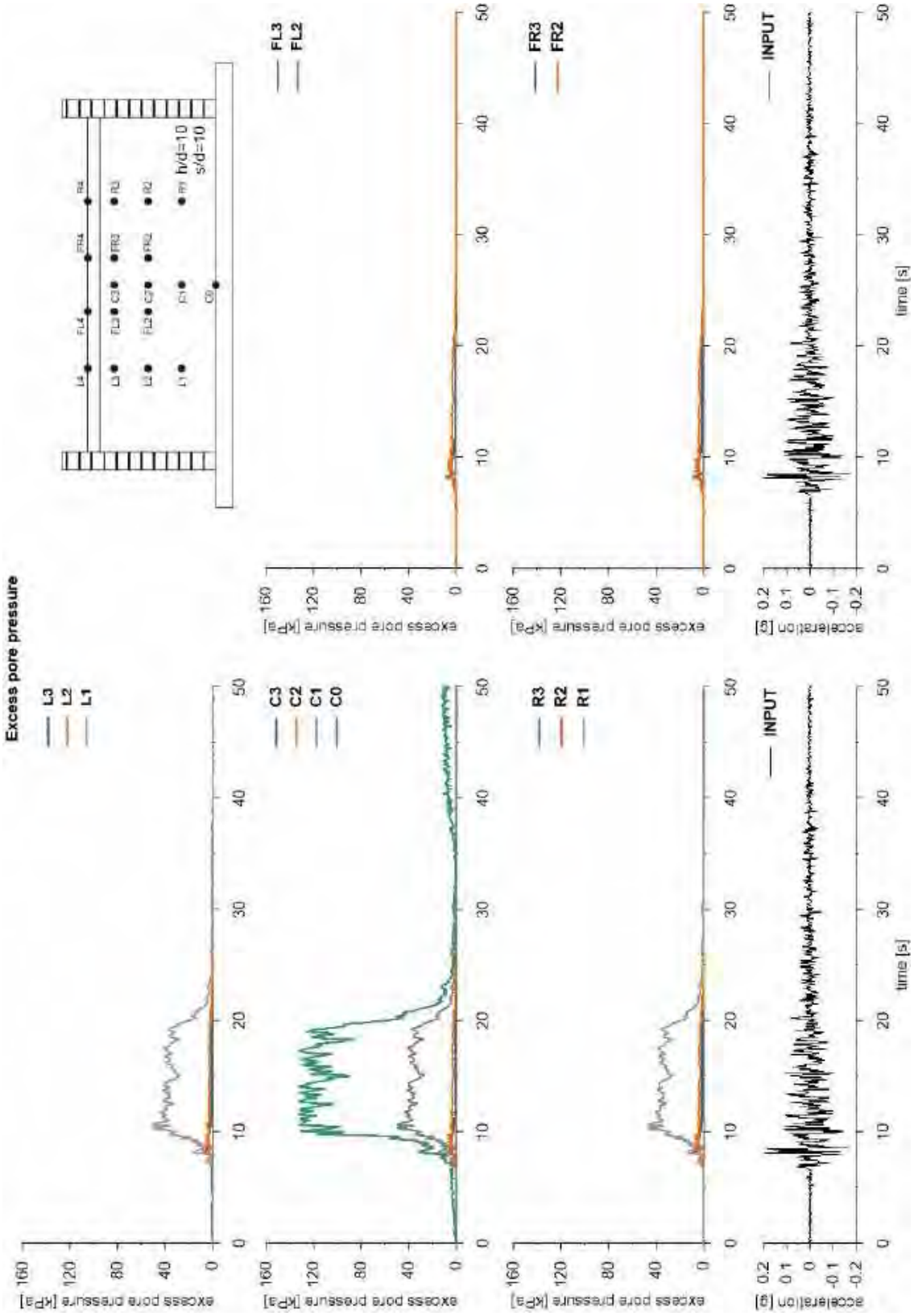

This project has received funding from the European Union's Horizon 2020 research and innovation programme under grant agreement No. 700748

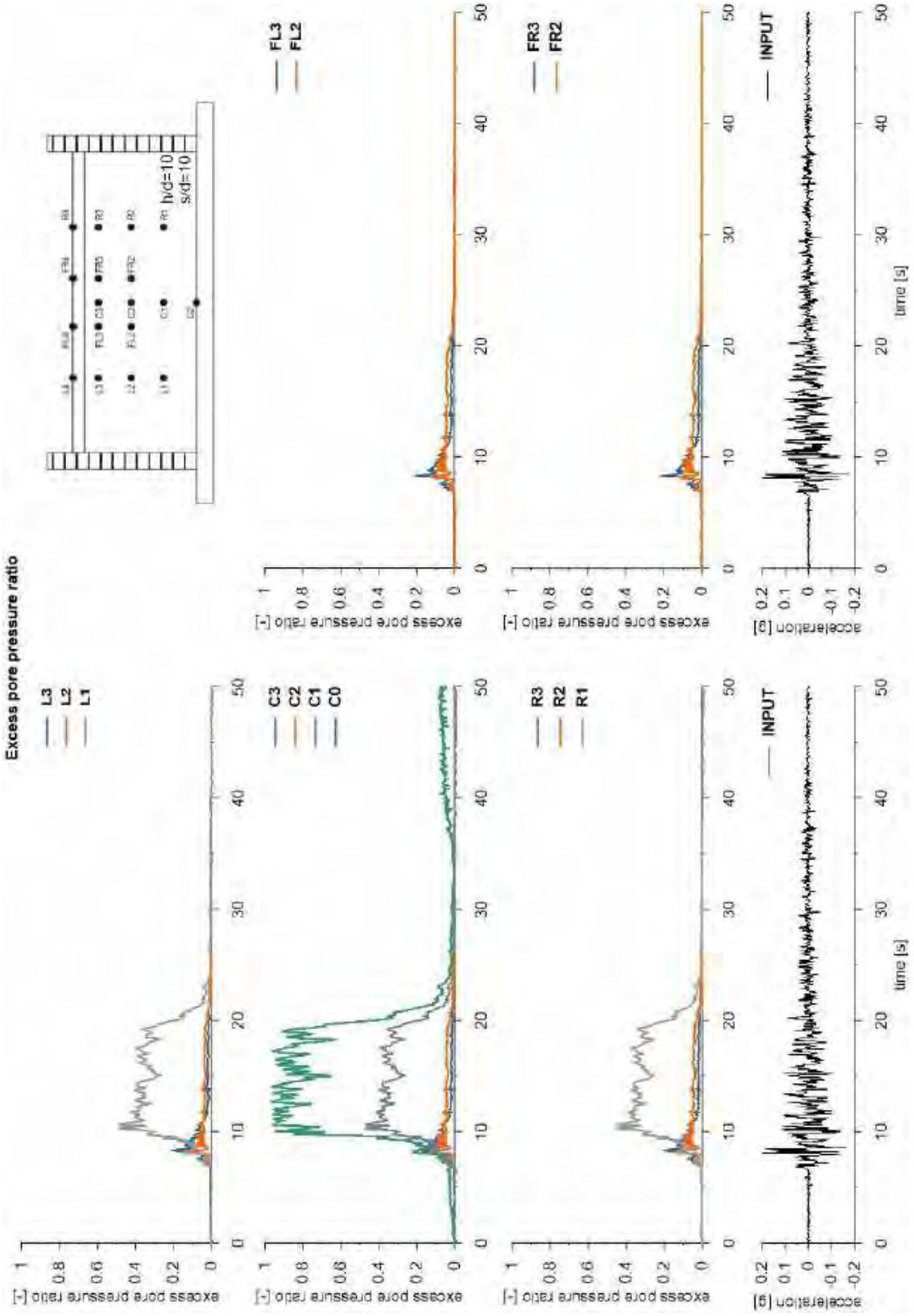

This project has received funding from the European Union's Horizon 2020 research and innovation programme under grant agreement No. 700748

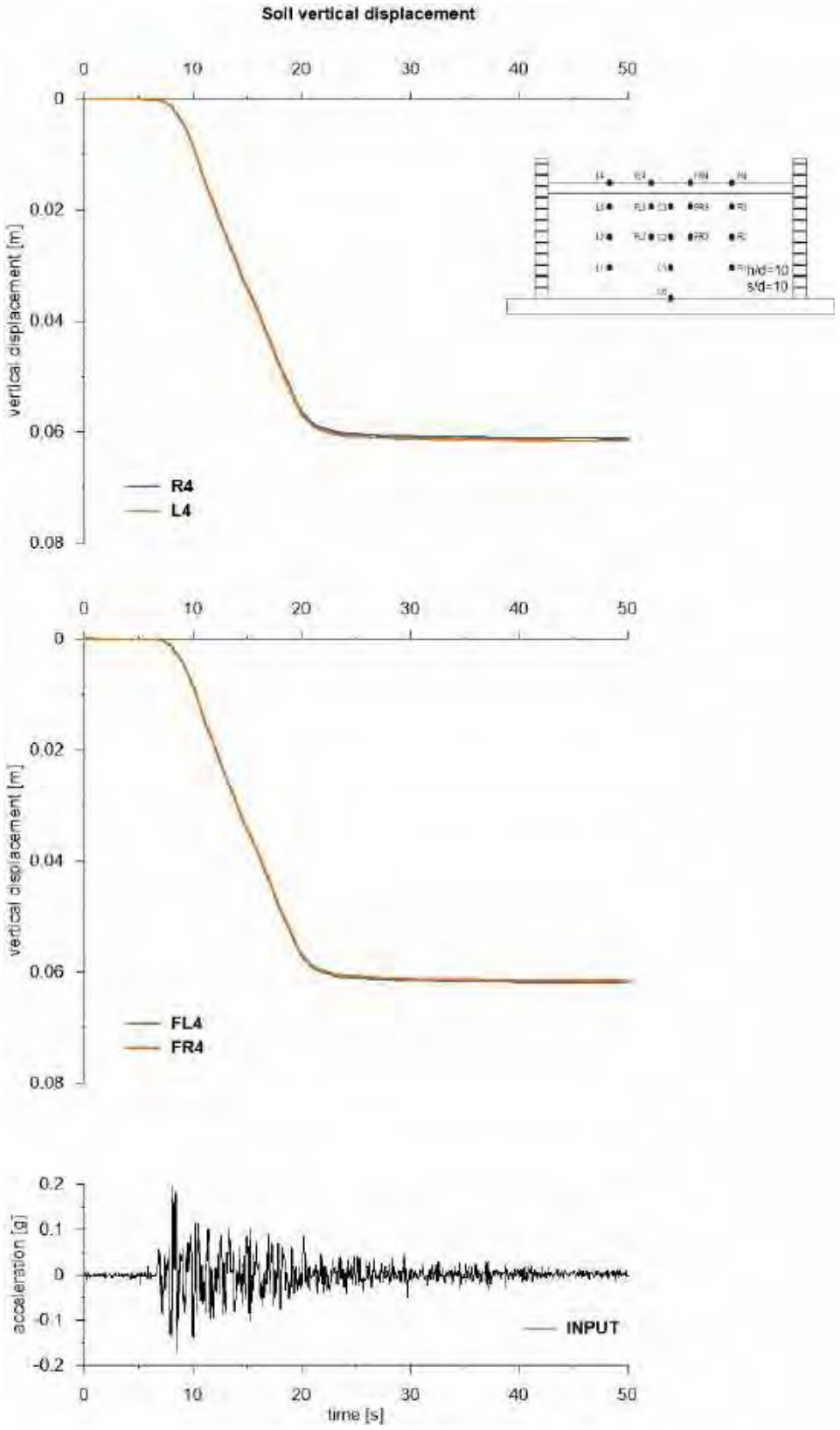

This project has received funding from the European Union's Horizon 2020 research and innovation programme under grant agreement No. 700748

6.1.1.23 ID: DF_HDU_H10_s15

The model consists of a double soil profile of clay and Ticino sand. The ground motion applied was the number 31.

ID: DF_HDU_H10_s15

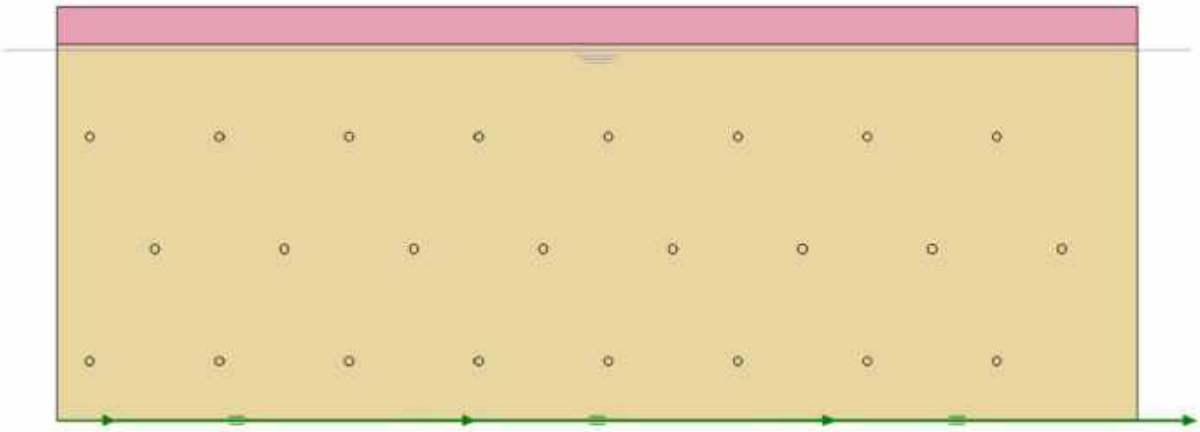

Layouts of the model reproduced in Plaxis 2D

This project has received funding from the European Union's Horizon 2020 research and innovation programme under grant agreement No. 700748

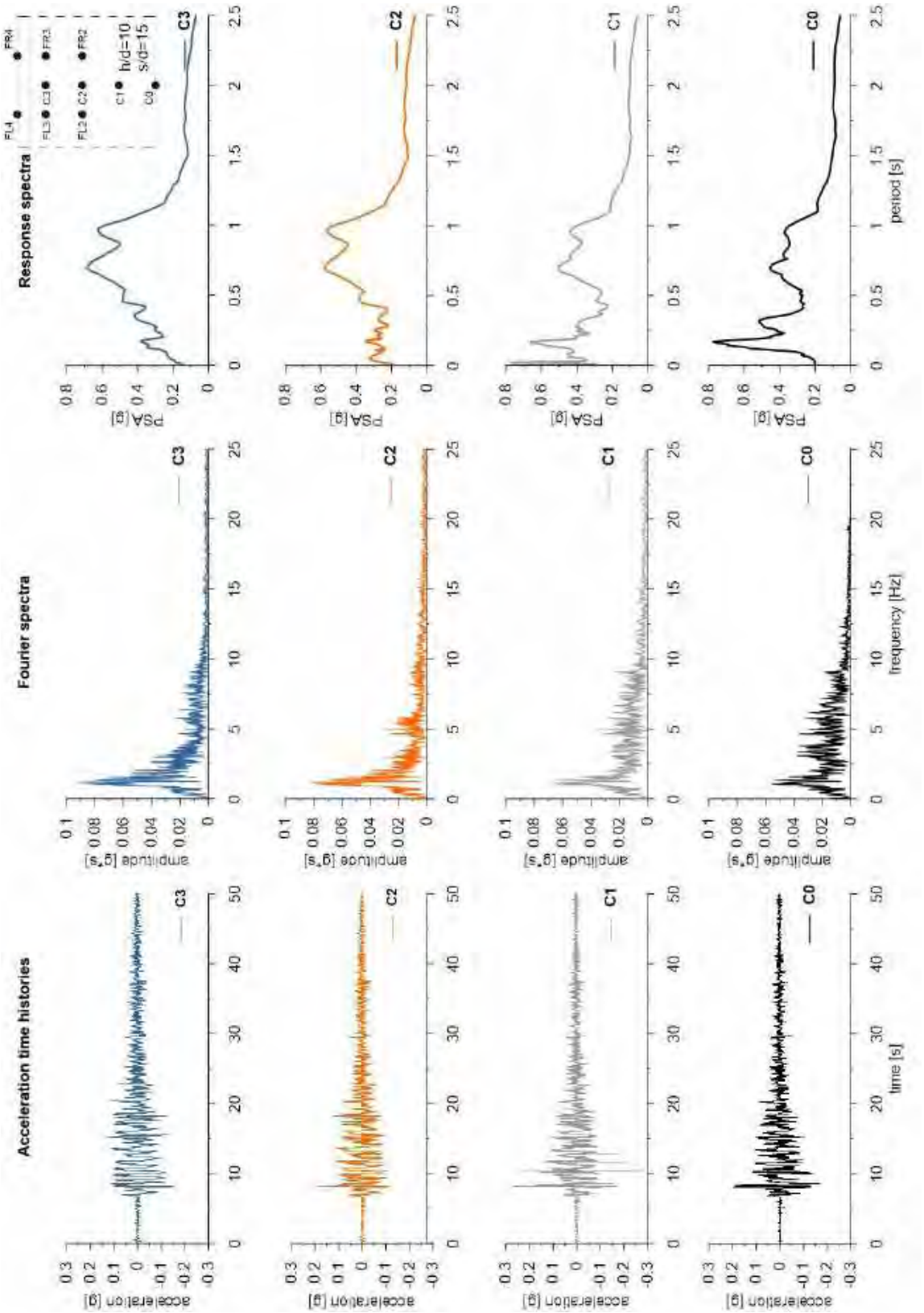

This project has received funding from the European Union's Horizon 2020 research and innovation programme under grant agreement No. 700748

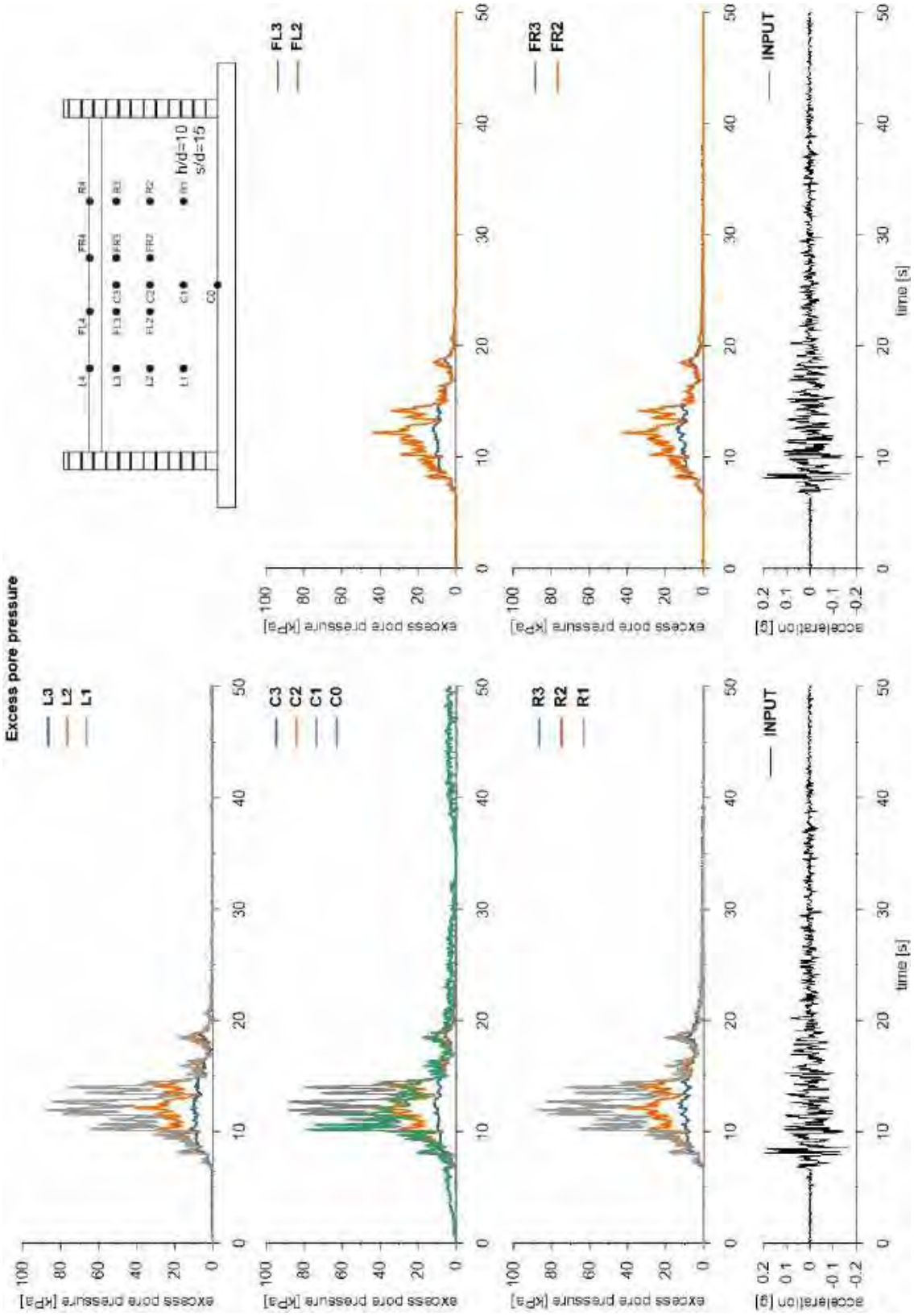

This project has received funding from the European Union's Horizon 2020 research and innovation programme under grant agreement No. 700748

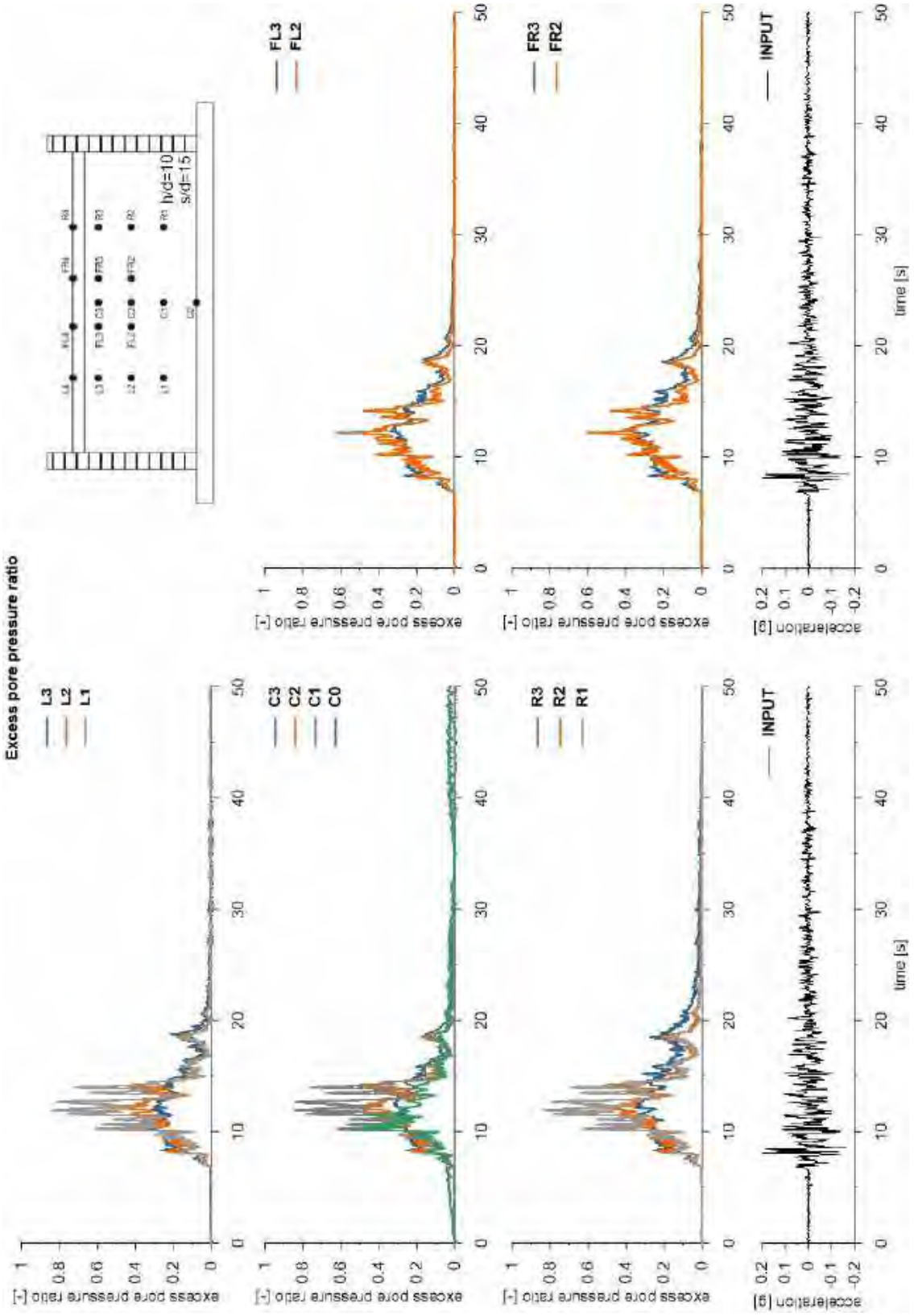

This project has received funding from the European Union's Horizon 2020 research and innovation programme under grant agreement No. 700748

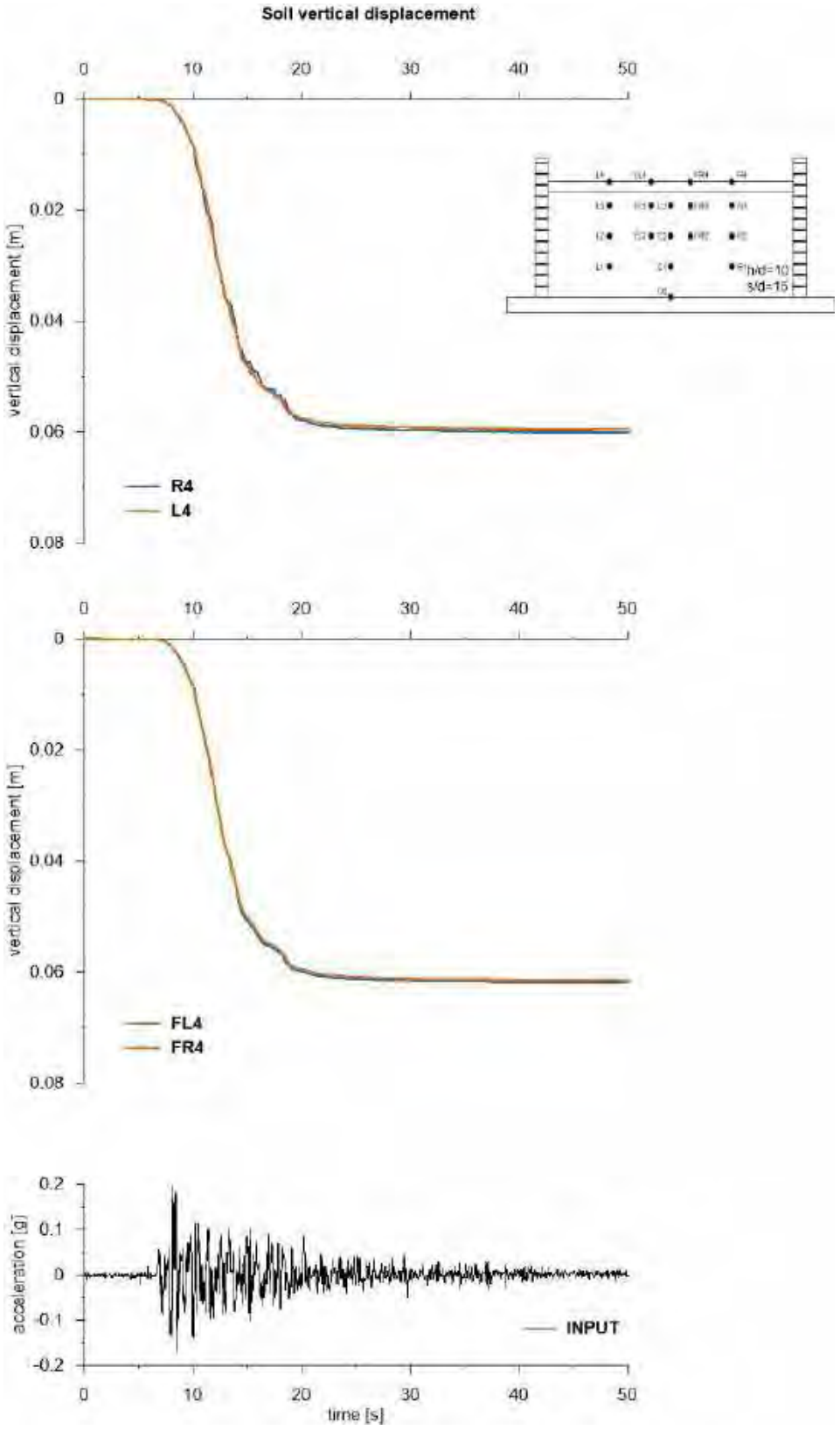

This project has received funding from the European Union's Horizon 2020 research and innovation programme under grant agreement No. 700748

6.1.1.24 ID: DF_HDU_H15_s05

The model consists of a double soil profile of clay and Ticino sand. The ground motion applied was the number 31.

ID: DF_HDU_H15_s05

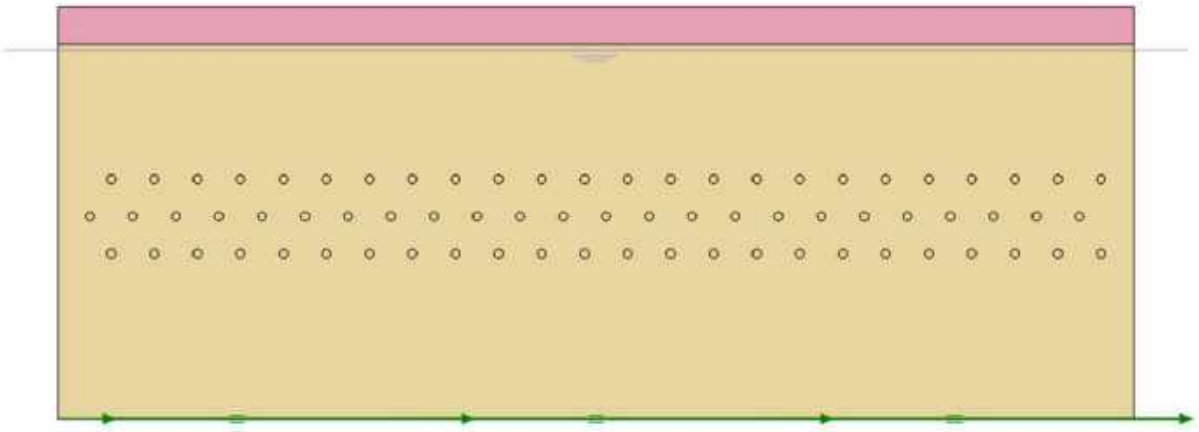

Layouts of the model reproduced in Plaxis 2D

This project has received funding from the European Union's Horizon 2020 research and innovation programme under grant agreement No. 700748

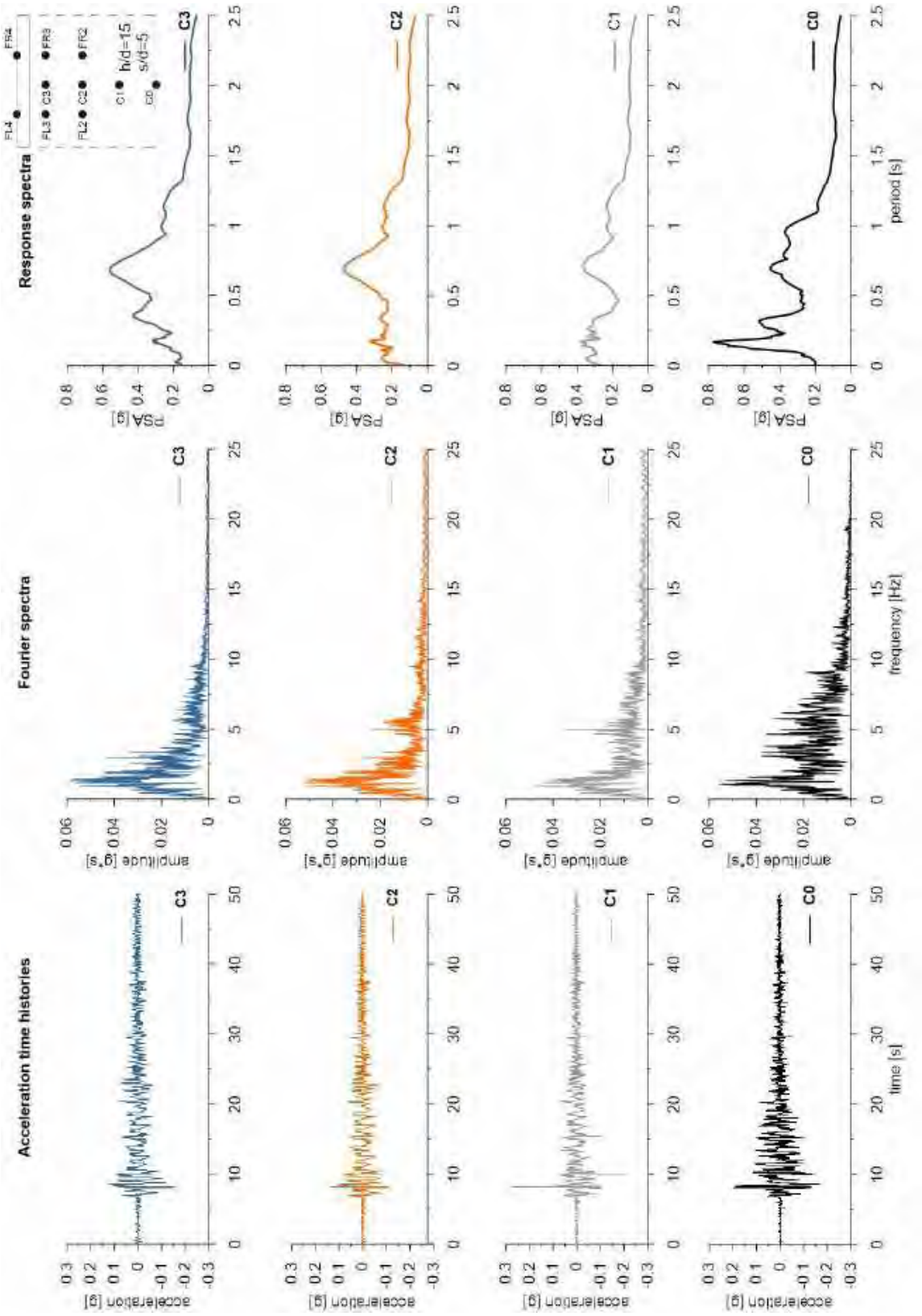

This project has received funding from the European Union's Horizon 2020 research and innovation programme under grant agreement No. 700748

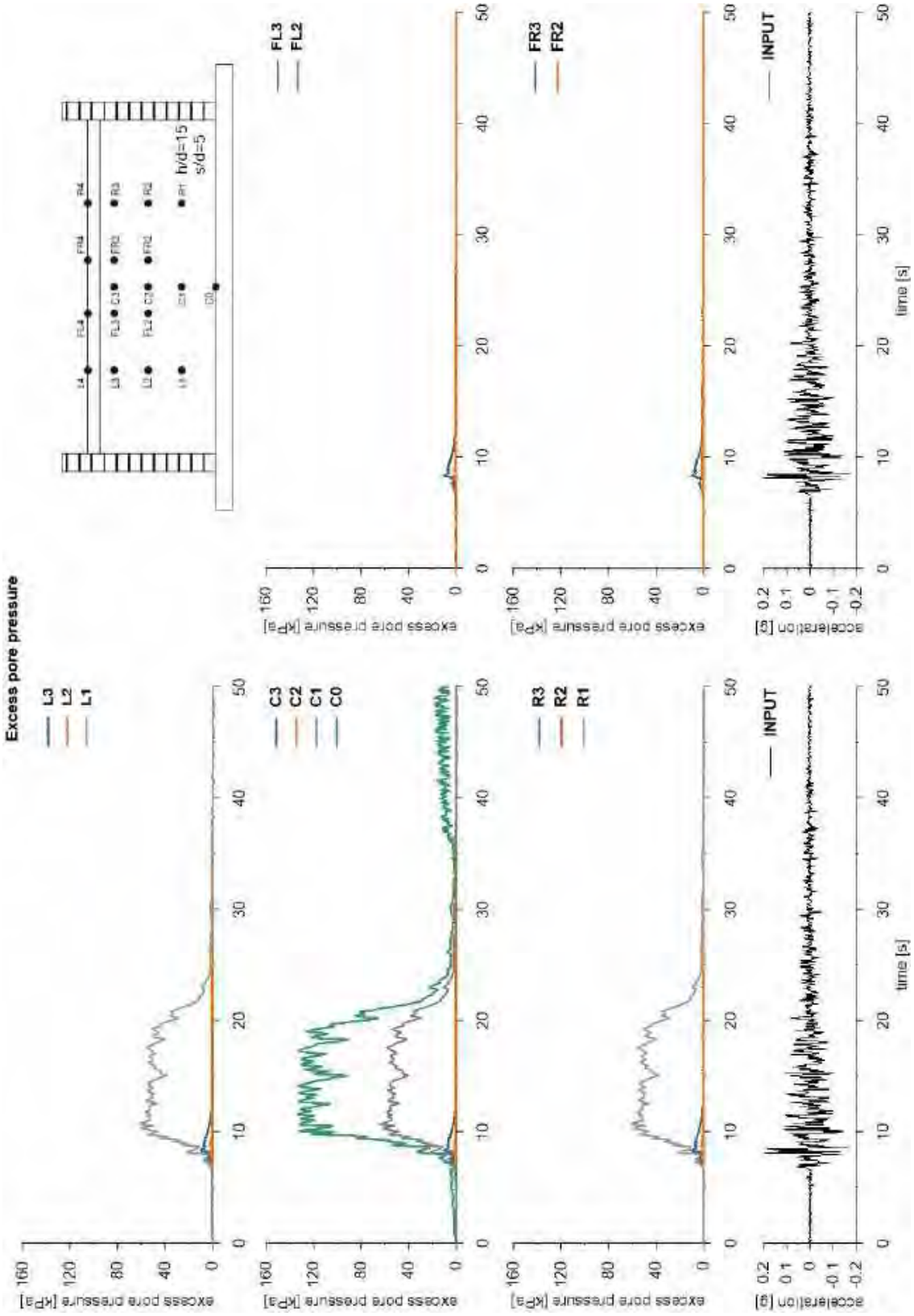

This project has received funding from the European Union's Horizon 2020 research and innovation programme under grant agreement No. 700748

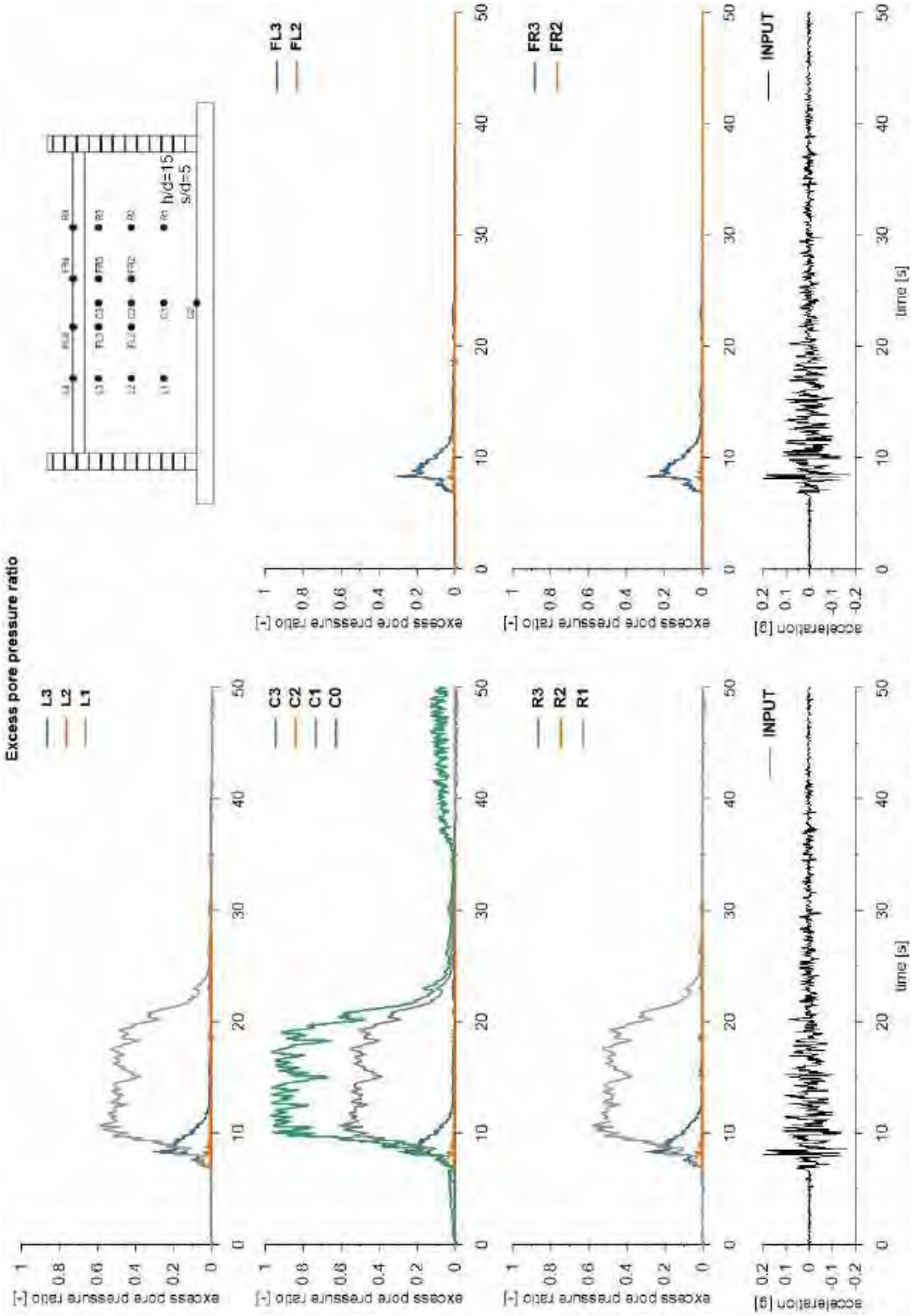

This project has received funding from the European Union's Horizon 2020 research and innovation programme under grant agreement No. 700748

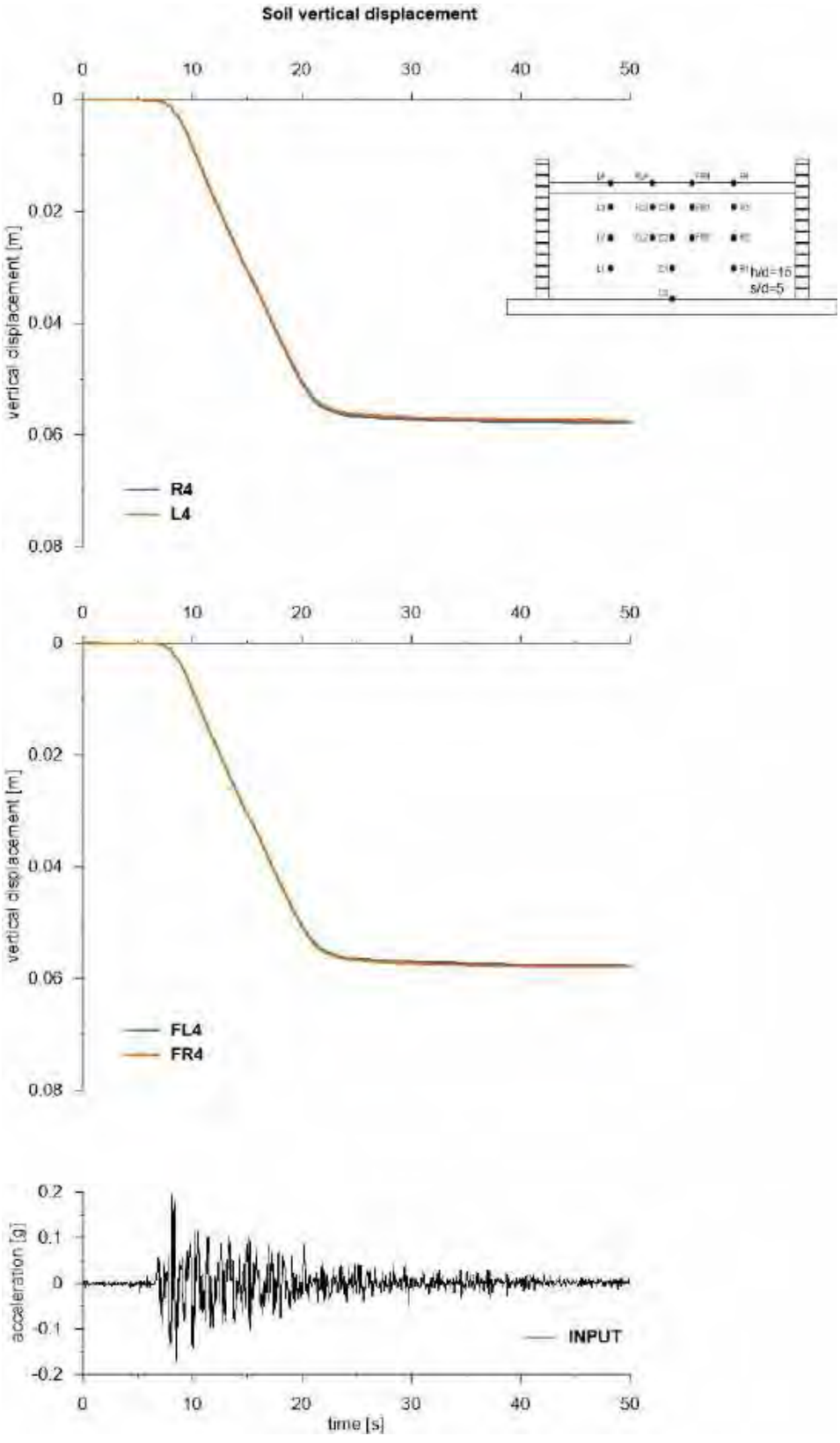

This project has received funding from the European Union's Horizon 2020 research and innovation programme under grant agreement No. 700748

6.1.1.25 ID: DF_HDU_H15_s10

The model consists of a double soil profile of clay and Ticino sand. The ground motion applied was the number 31.

ID: DF_HDU_H15_s10

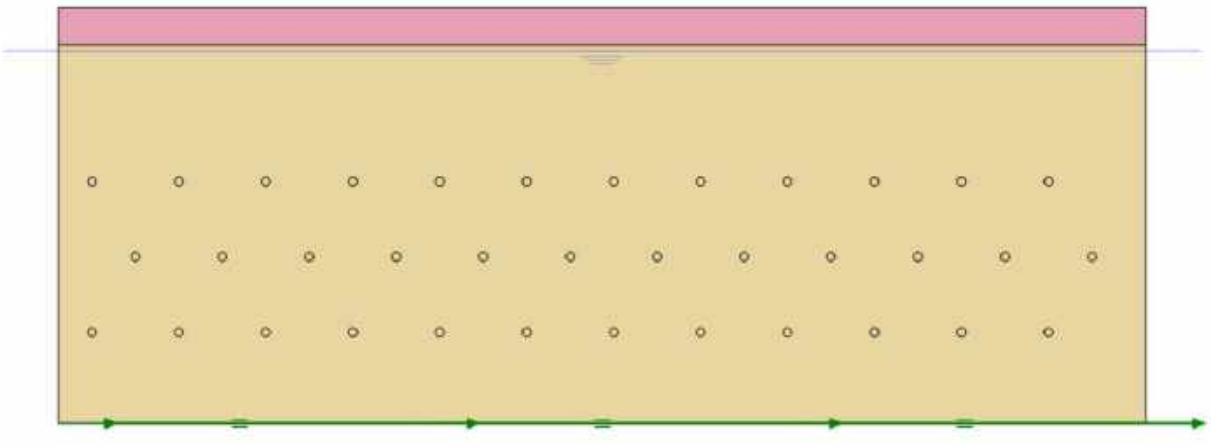

Layouts of the model reproduced in Plaxis 2D

This project has received funding from the European Union's Horizon 2020 research and innovation programme under grant agreement No. 700748

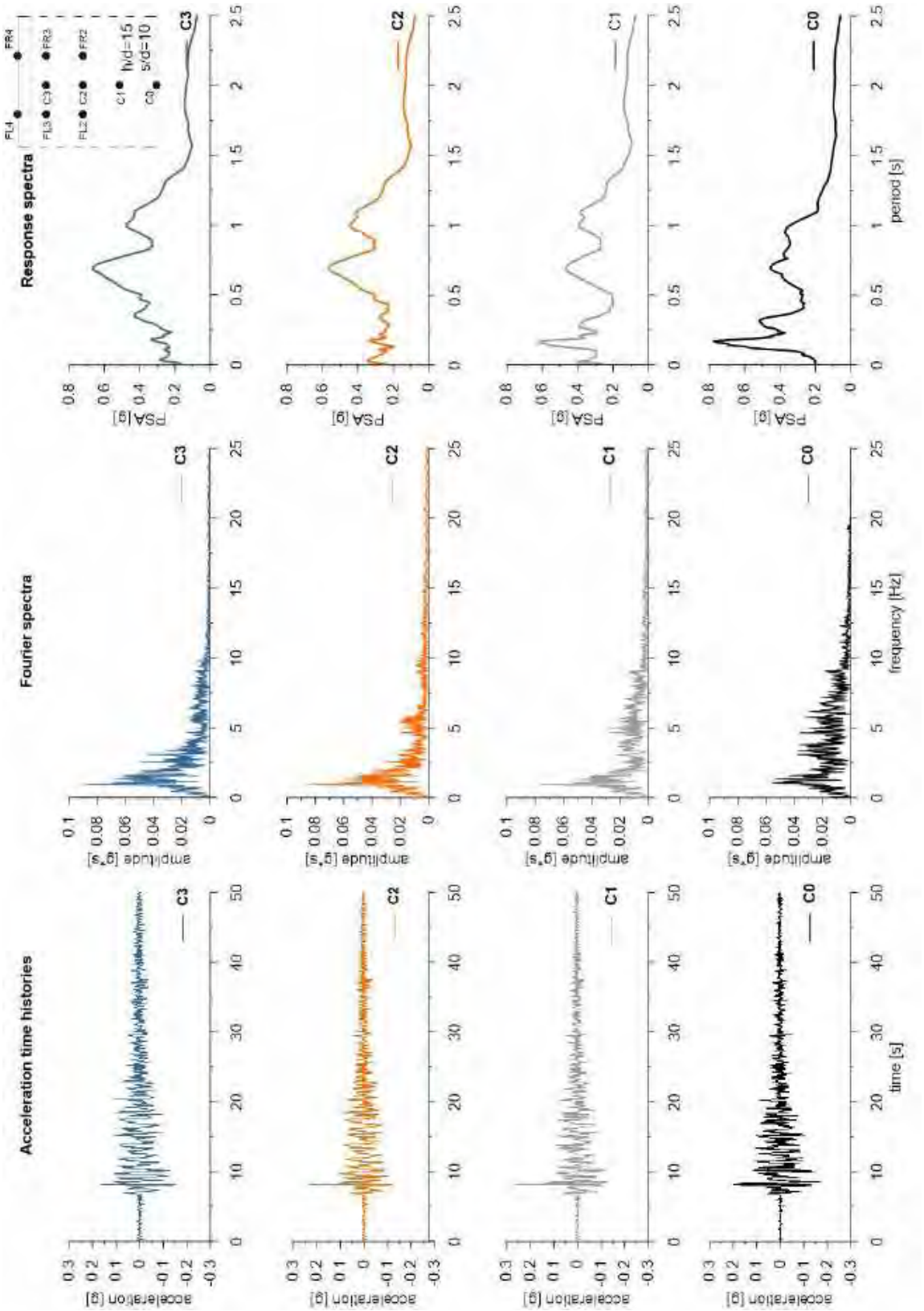

This project has received funding from the European Union's Horizon 2020 research and innovation programme under grant agreement No. 700748

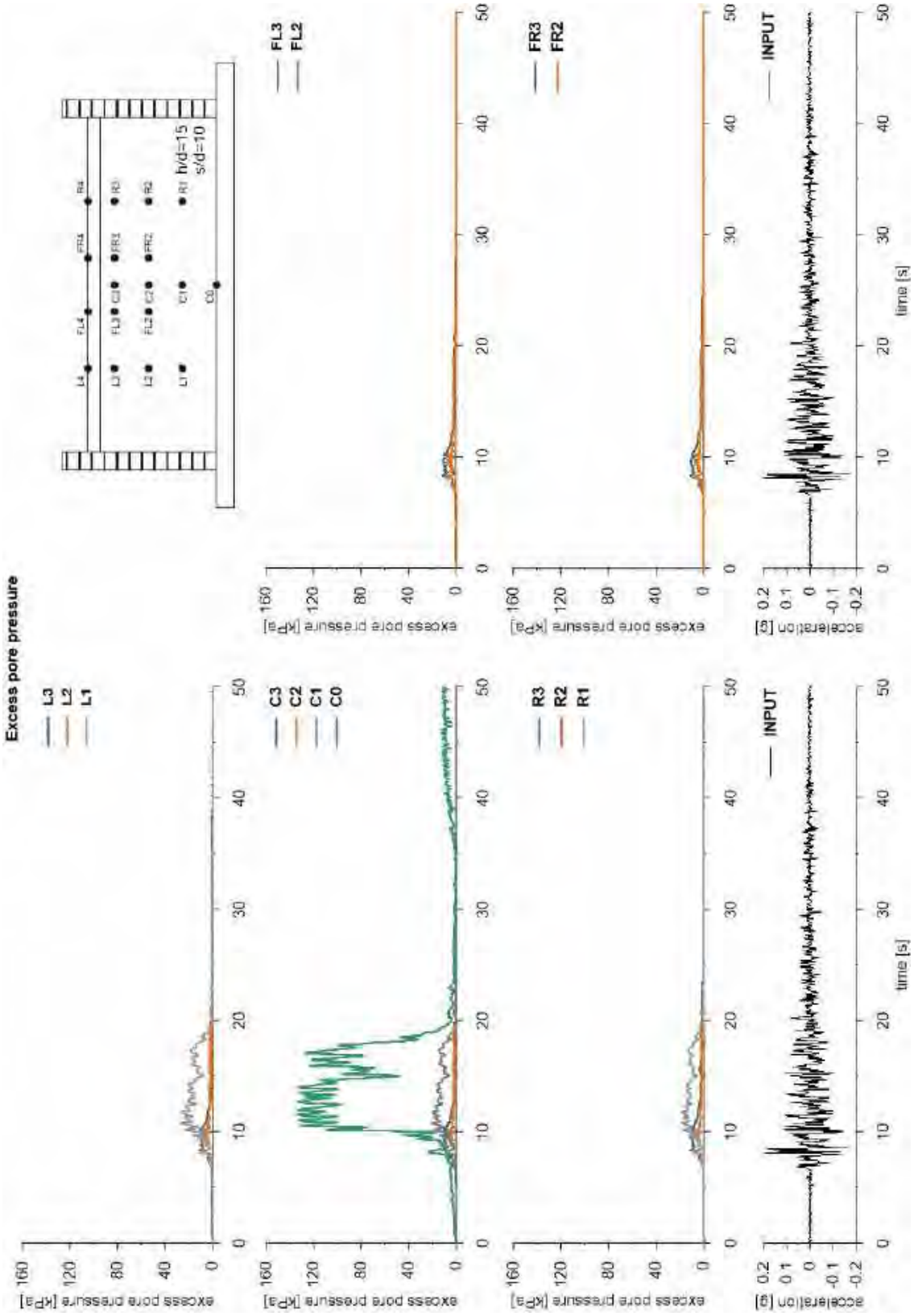

This project has received funding from the European Union's Horizon 2020 research and innovation programme under grant agreement No. 700748

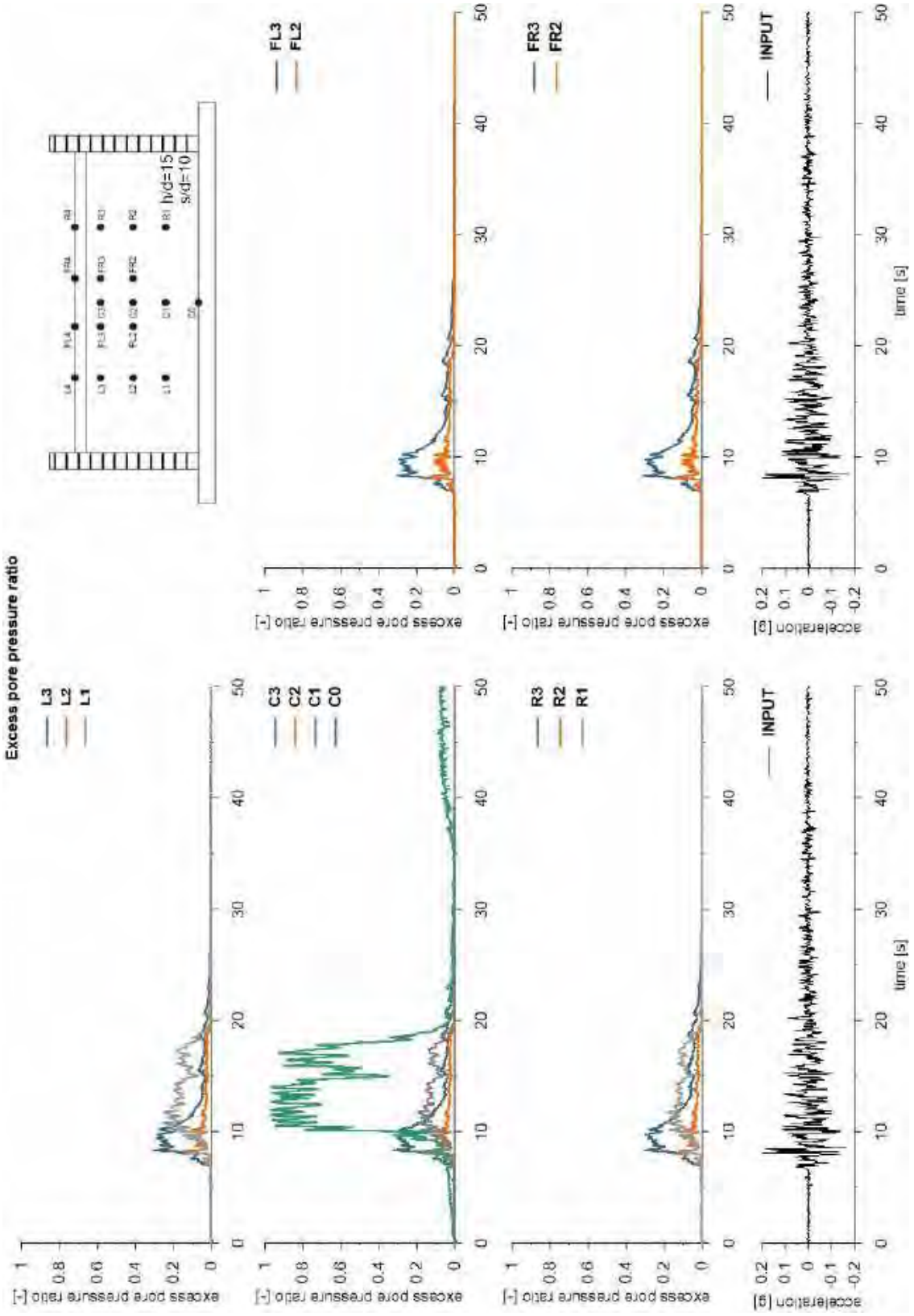

This project has received funding from the European Union's Horizon 2020 research and innovation programme under grant agreement No. 700748

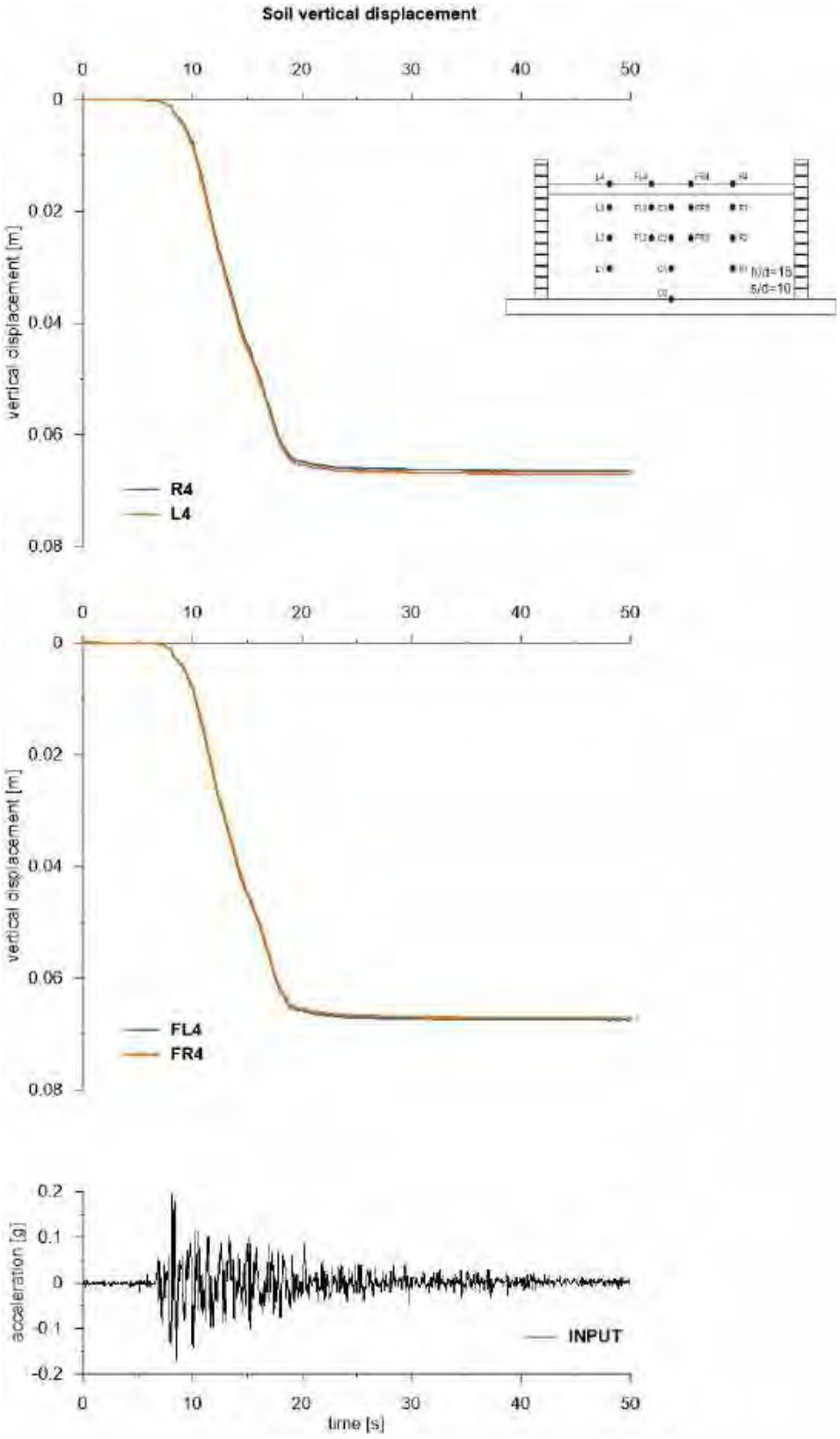

This project has received funding from the European Union's Horizon 2020 research and innovation programme under grant agreement No. 700748

6.1.1.26 ID: DF_HDU_H15_s15

The model consists of a double soil profile of clay and Ticino sand. The ground motion applied was the number 31.

ID: DF_HDU_H15_s15

Layouts of the model reproduced in Plaxis 2D

This project has received funding from the European Union's Horizon 2020 research and innovation programme under grant agreement No. 700748

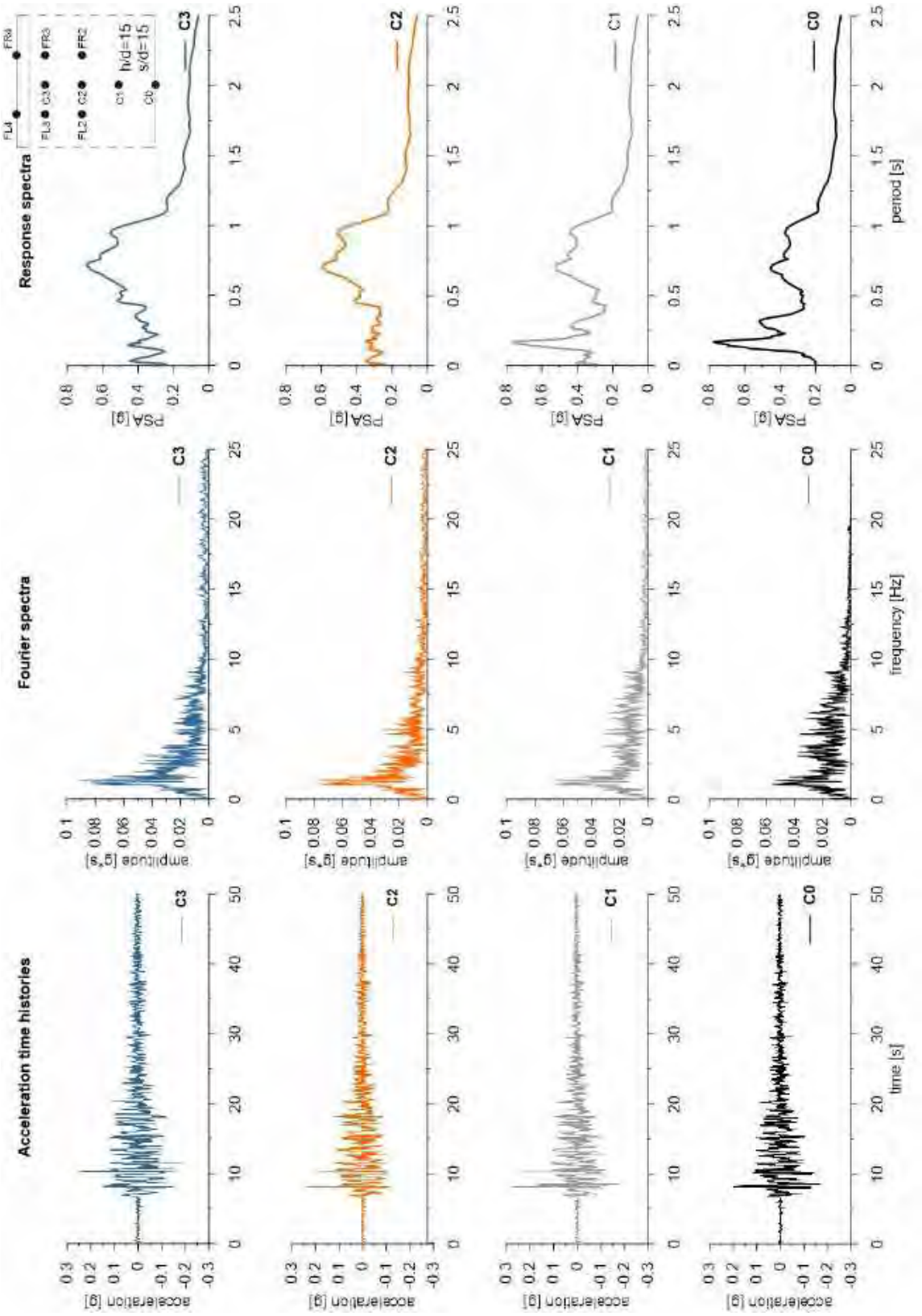

This project has received funding from the European Union's Horizon 2020 research and innovation programme under grant agreement No. 700748

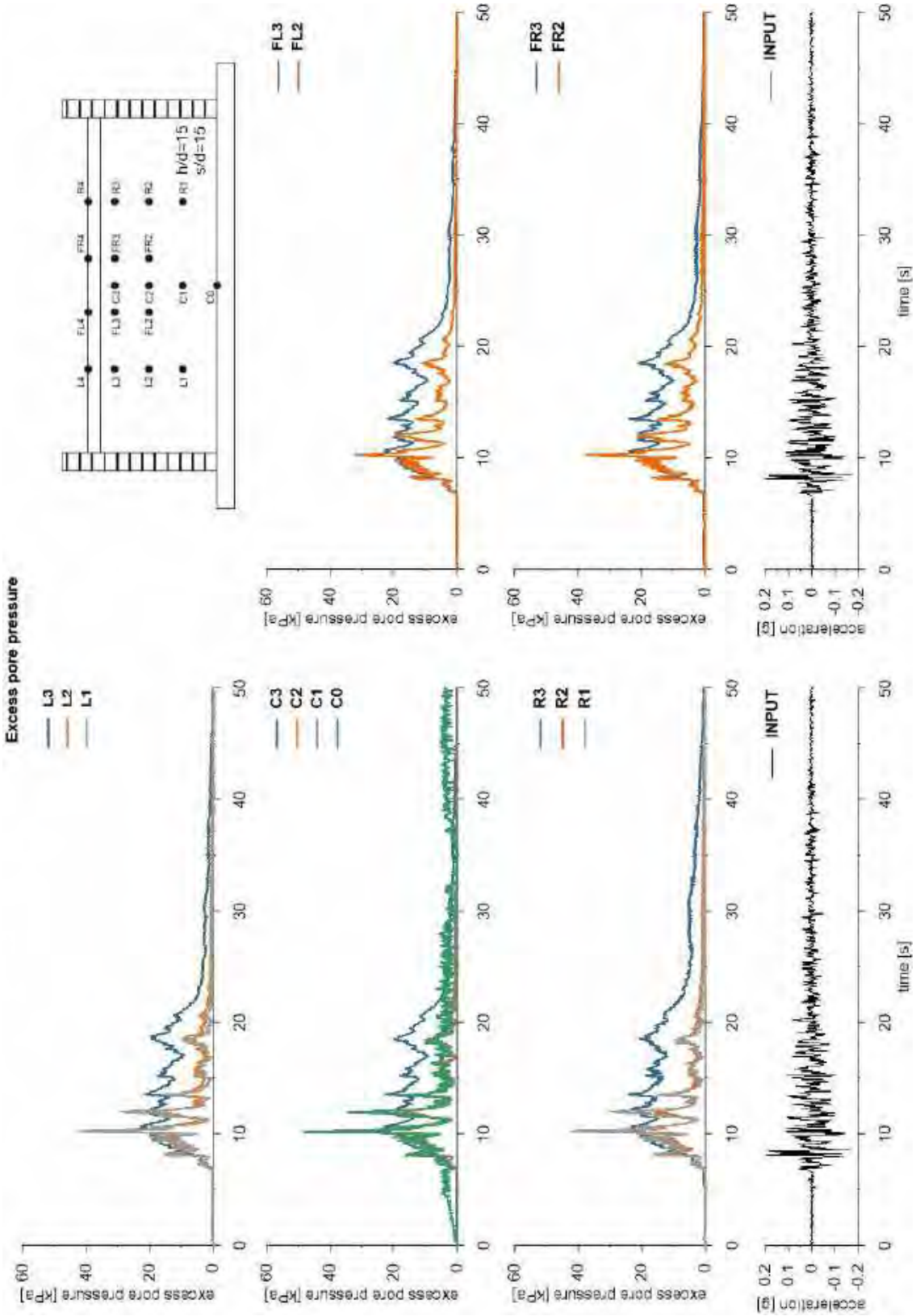

This project has received funding from the European Union's Horizon 2020 research and innovation programme under grant agreement No. 700748

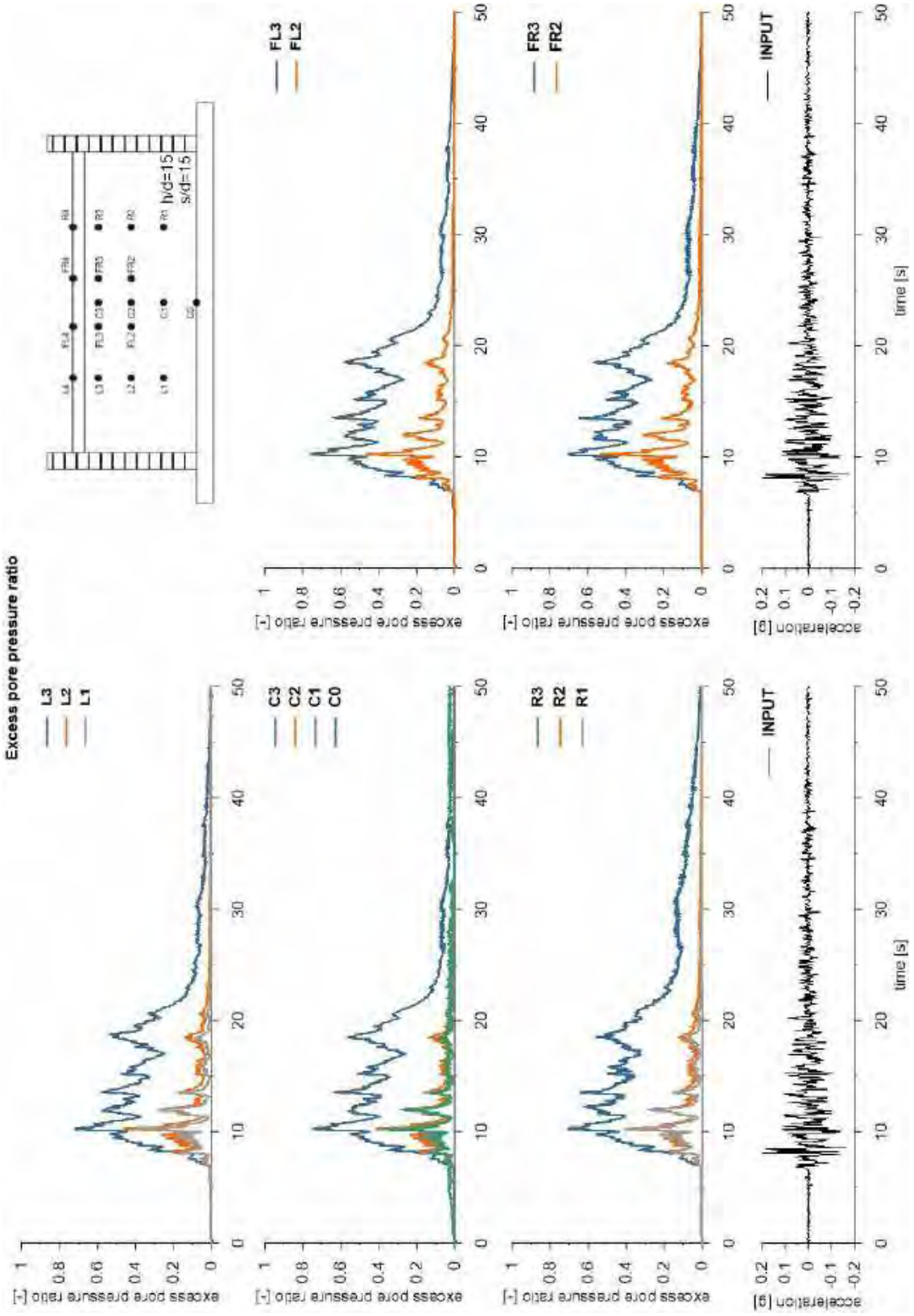

This project has received funding from the European Union's Horizon 2020 research and innovation programme under grant agreement No. 700748

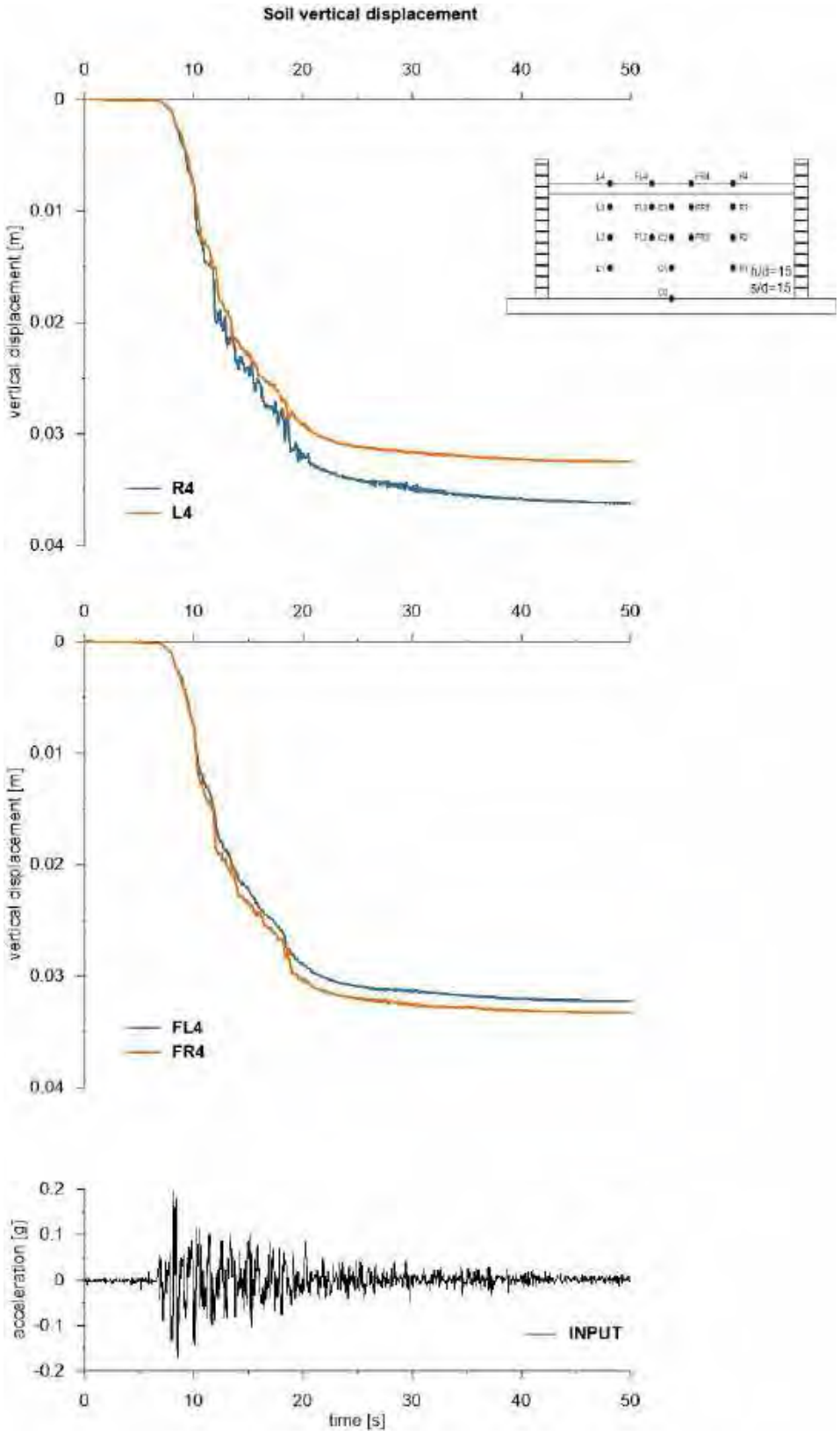

This project has received funding from the European Union's Horizon 2020 research and innovation programme under grant agreement No. 700748

6.1.1.27 ID: SS_HDU_H05_s05

The model consists of a homogenous soil profile of Ticino sand. The ground motion applied was the number 31.

ID: SS_HDU_H05_s05

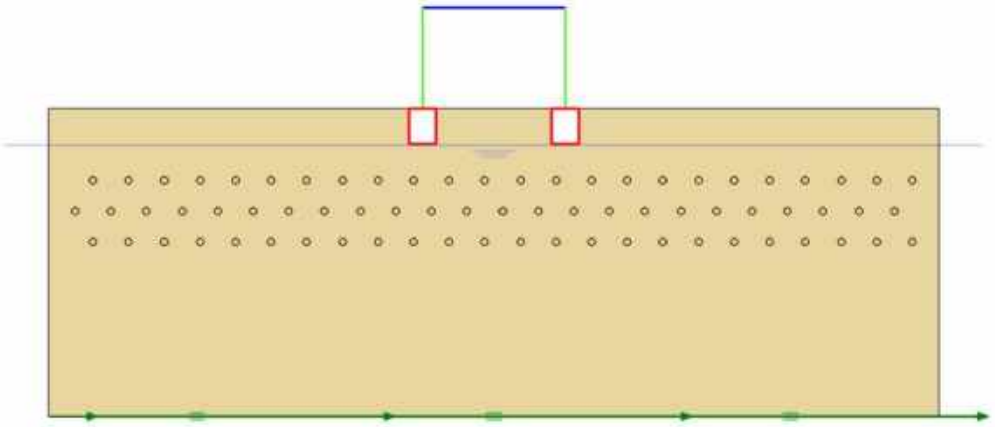

Layouts of the model reproduced in Plaxis 2D

This project has received funding from the European Union's Horizon 2020 research and innovation programme under grant agreement No. 700748

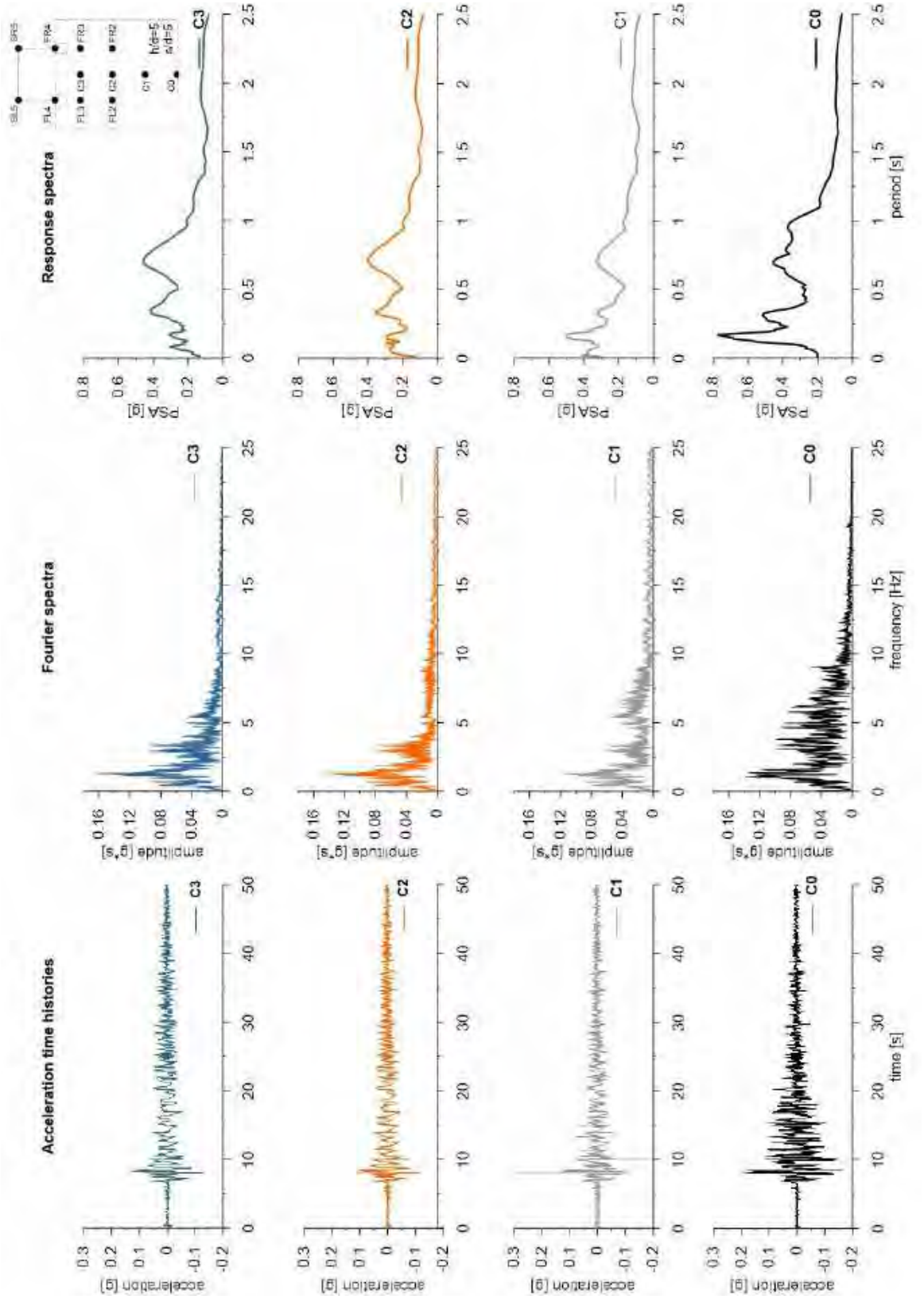

This project has received funding from the European Union's Horizon 2020 research and innovation programme under grant agreement No. 700748

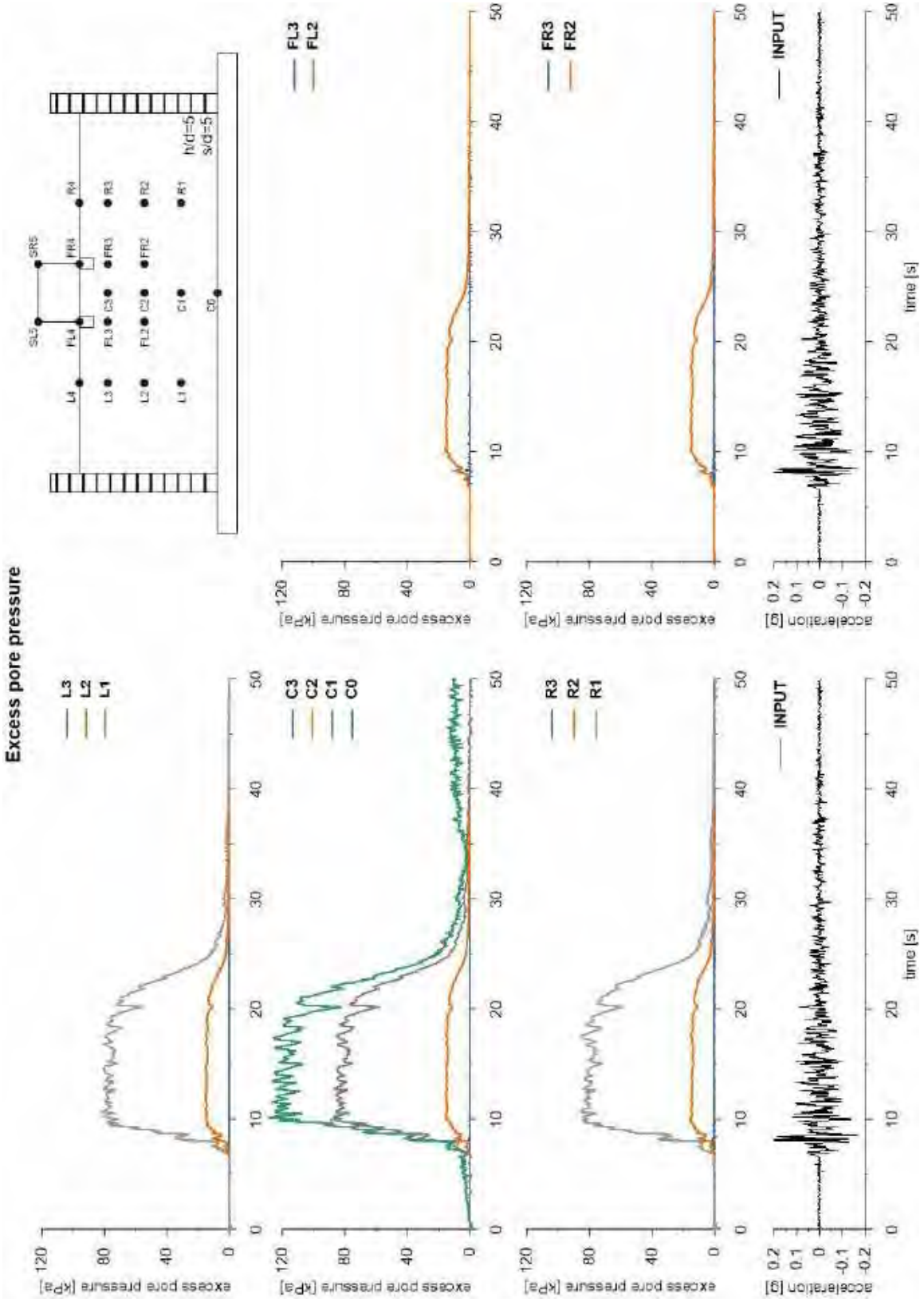

This project has received funding from the European Union's Horizon 2020 research and innovation programme under grant agreement No. 700748

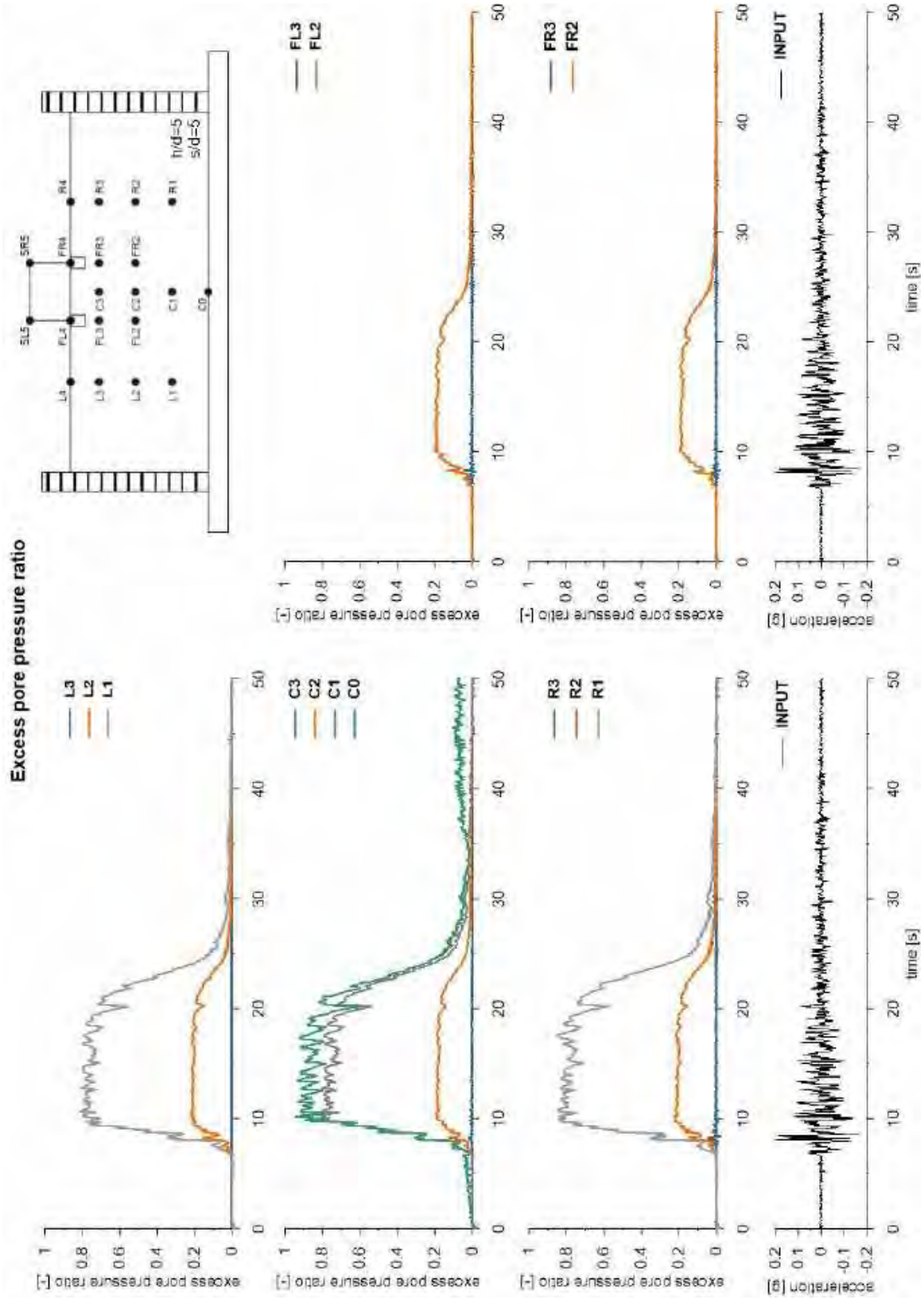

This project has received funding from the European Union's Horizon 2020 research and innovation programme under grant agreement No. 700748

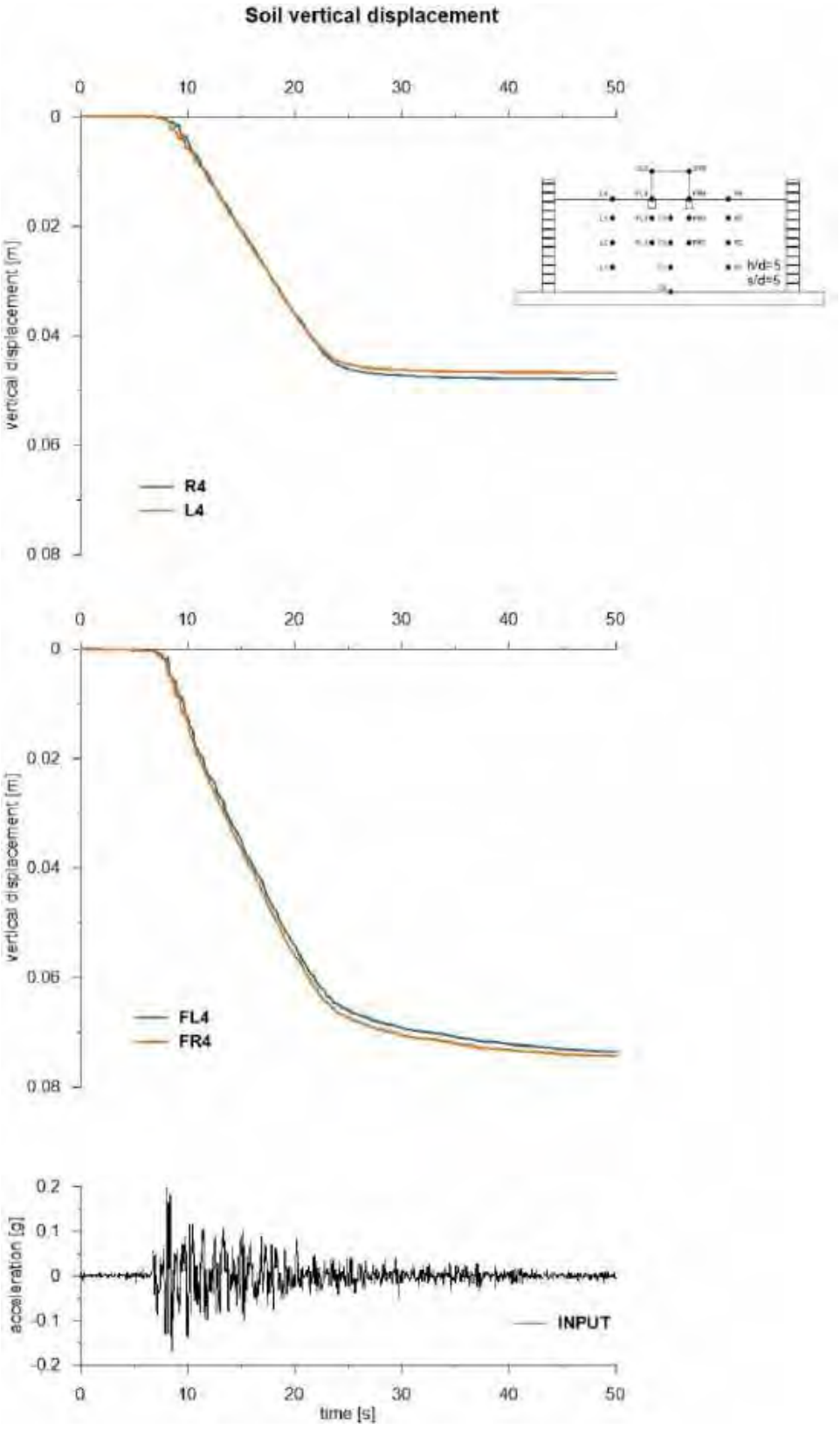

This project has received funding from the European Union's Horizon 2020 research and innovation programme under grant agreement No. 700748

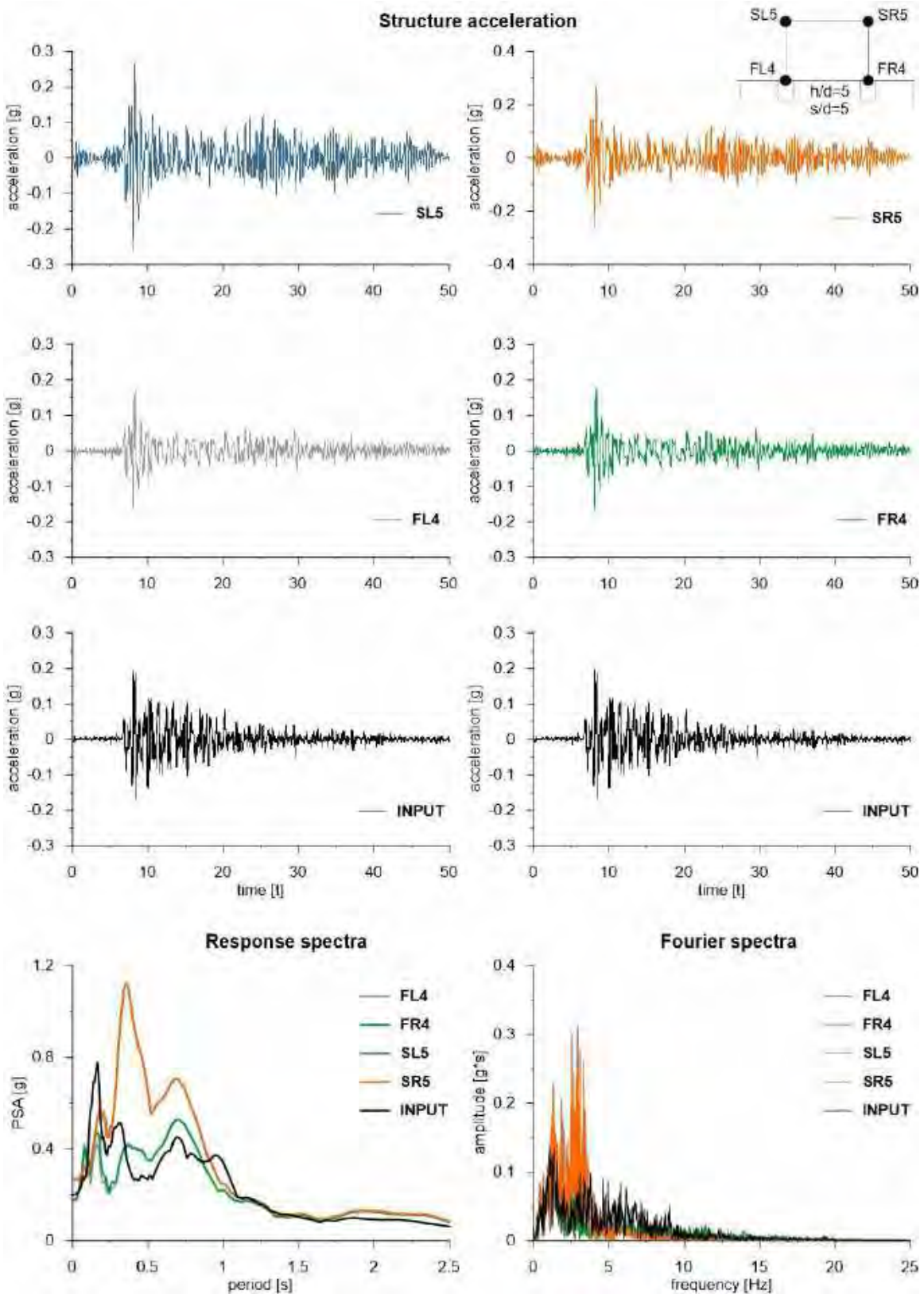

This project has received funding from the European Union's Horizon 2020 research and innovation programme under grant agreement No. 700748

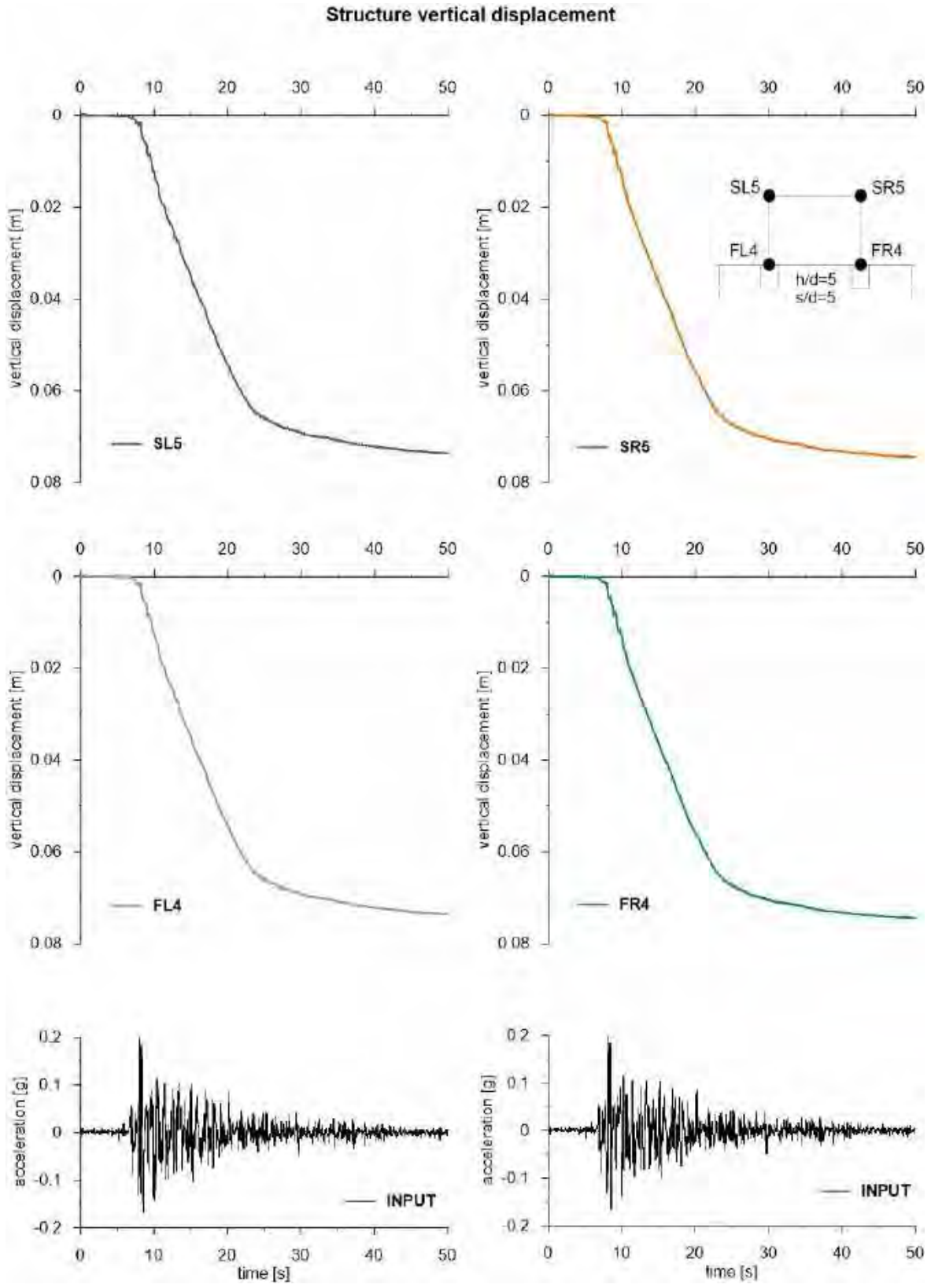

This project has received funding from the European Union's Horizon 2020 research and innovation programme under grant agreement No. 700748

6.1.1.28 ID: SS_HDU_H05_s10

The model consists of a homogenous soil profile of Ticino sand. The ground motion applied was the number 31.

ID: SS_HDU_H05_s10

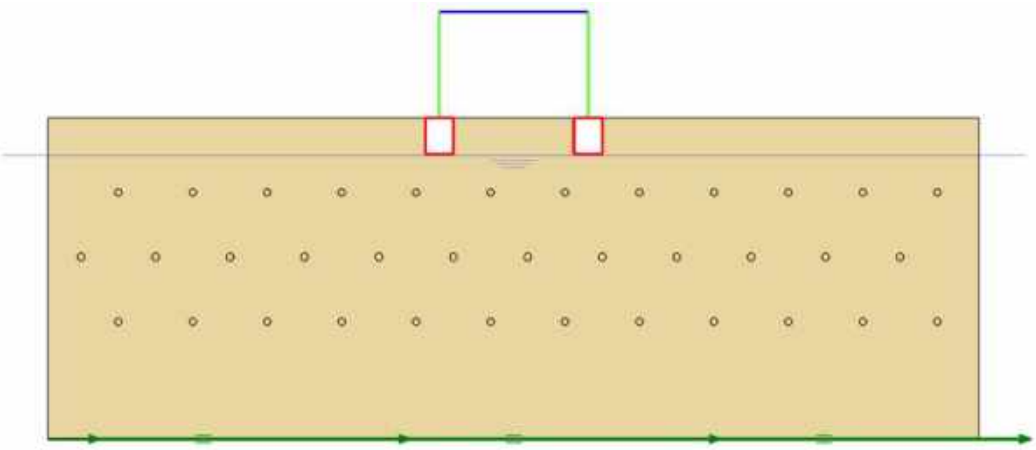

Layouts of the model reproduced in Plaxis 2D

This project has received funding from the European Union's Horizon 2020 research and innovation programme under grant agreement No. 700748

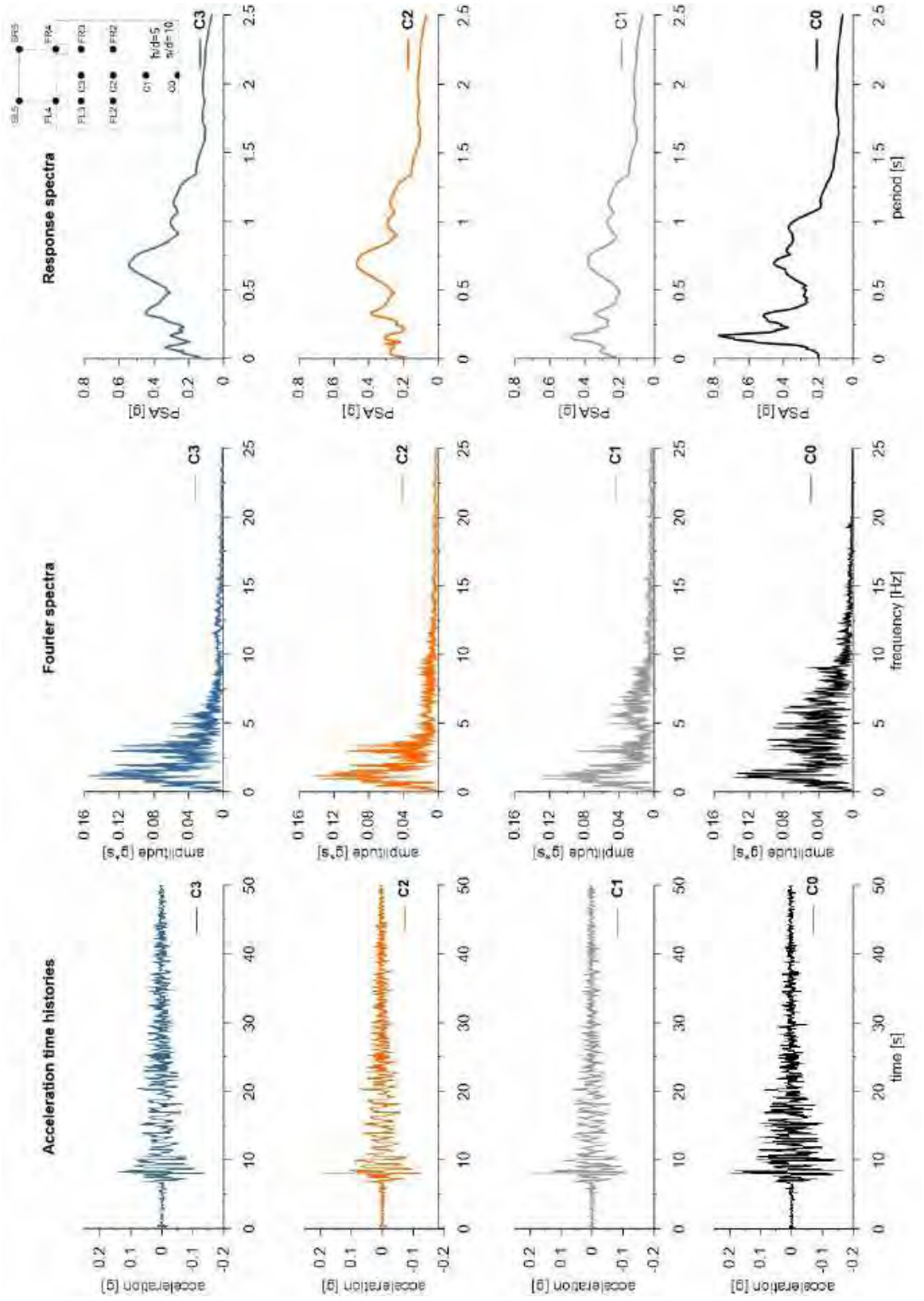

This project has received funding from the European Union's Horizon 2020 research and innovation programme under grant agreement No. 700748

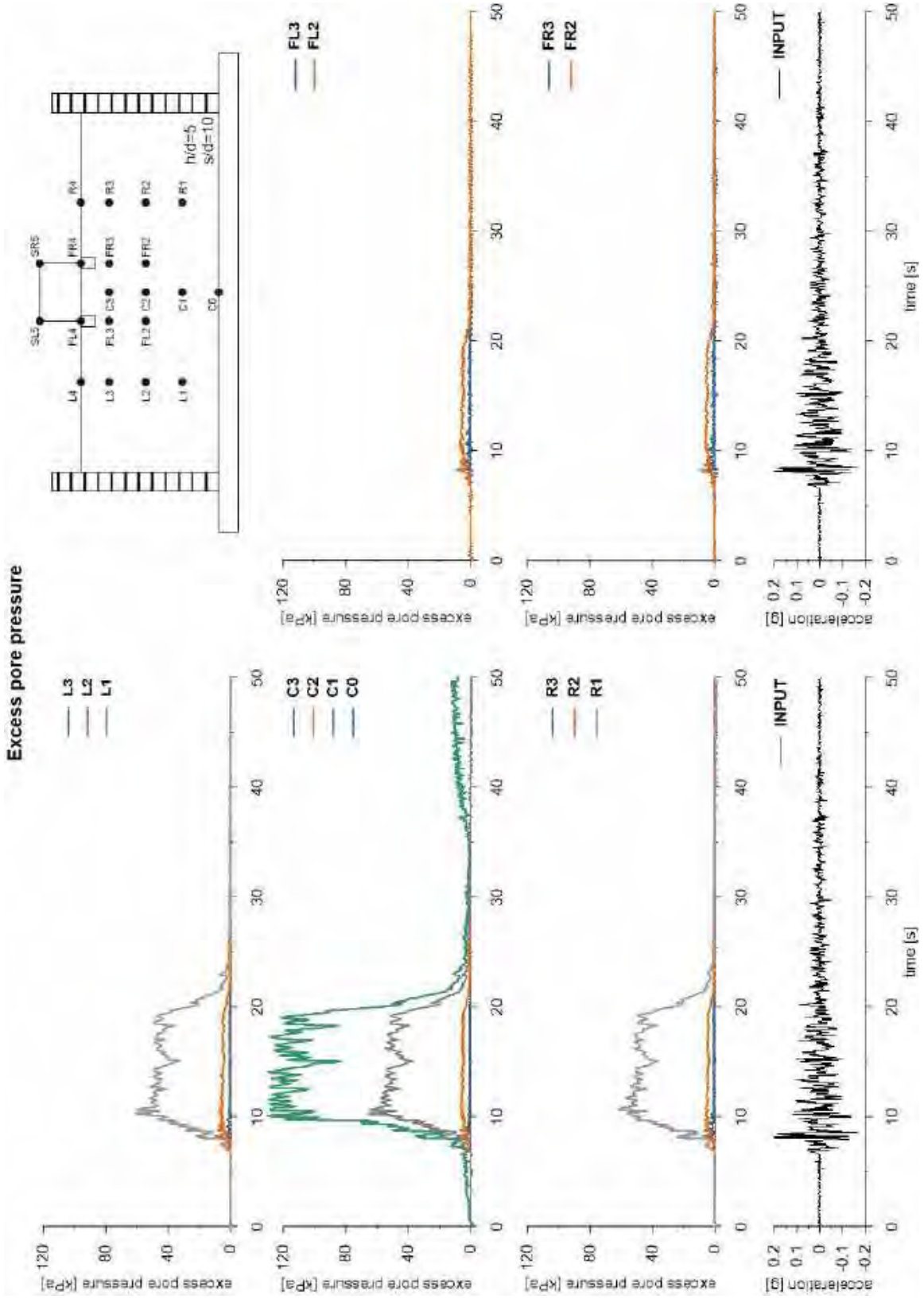

This project has received funding from the European Union's Horizon 2020 research and innovation programme under grant agreement No. 700748

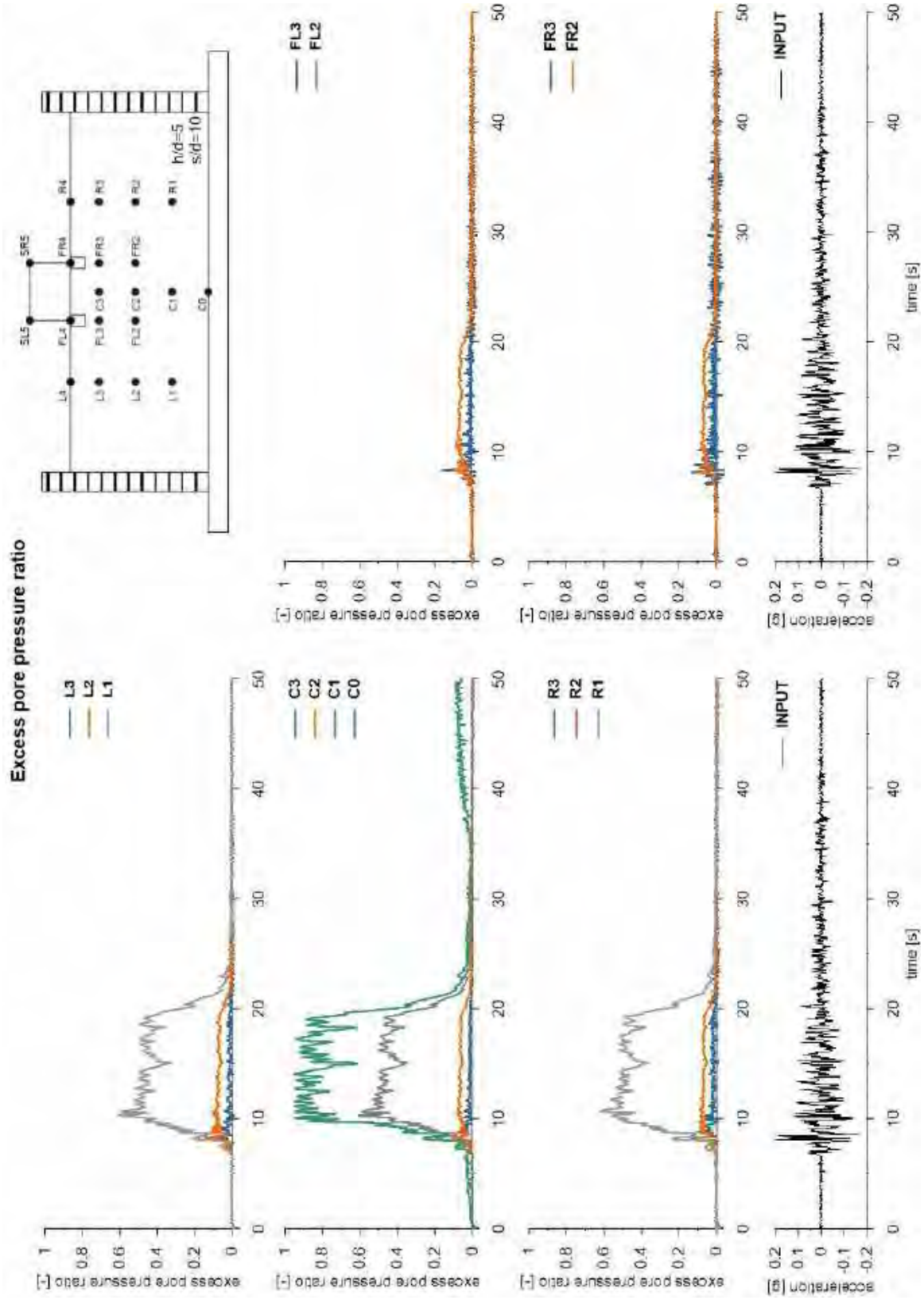

This project has received funding from the European Union's Horizon 2020 research and innovation programme under grant agreement No. 700748

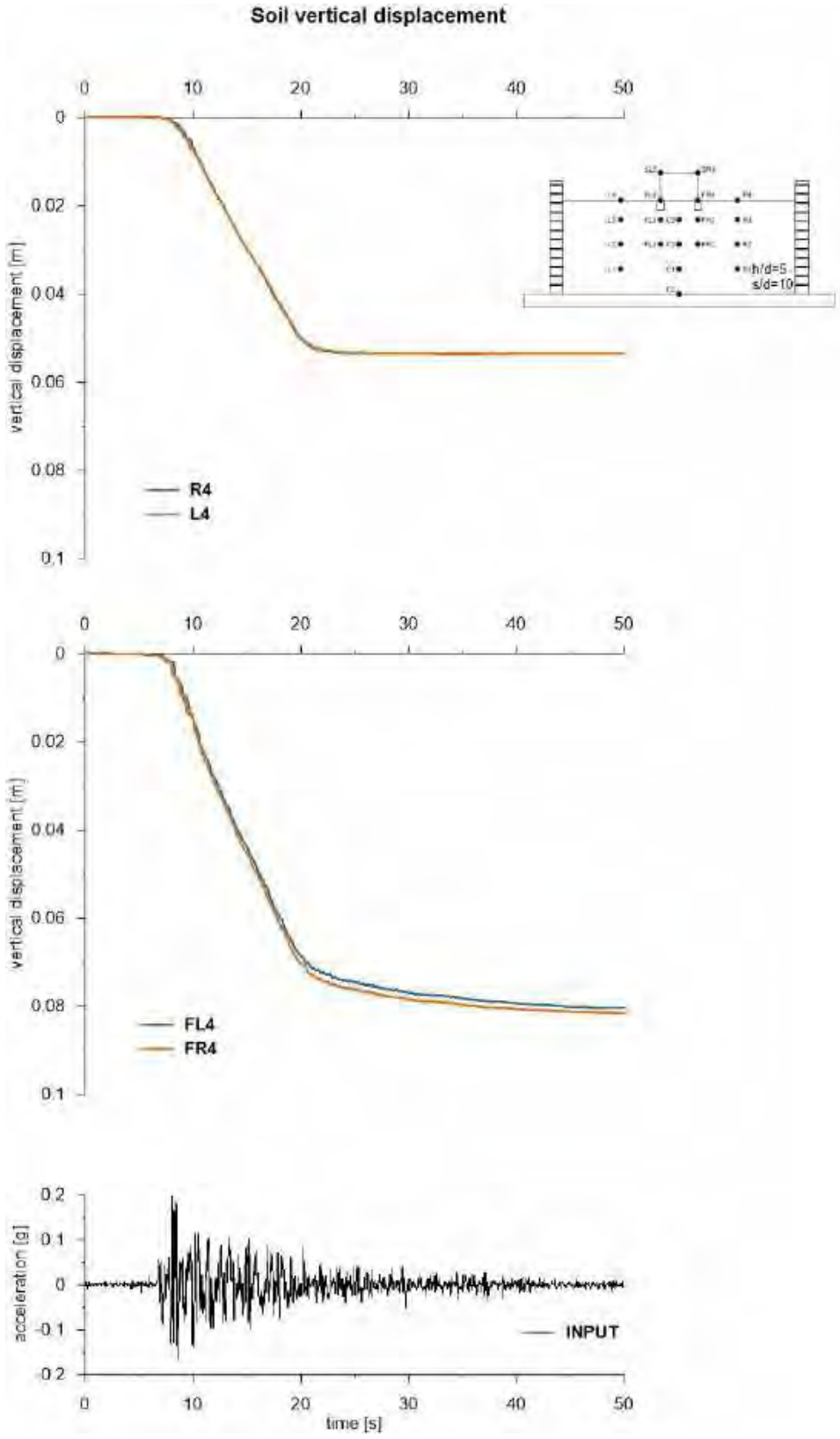

This project has received funding from the European Union's Horizon 2020 research and innovation programme under grant agreement No. 700748

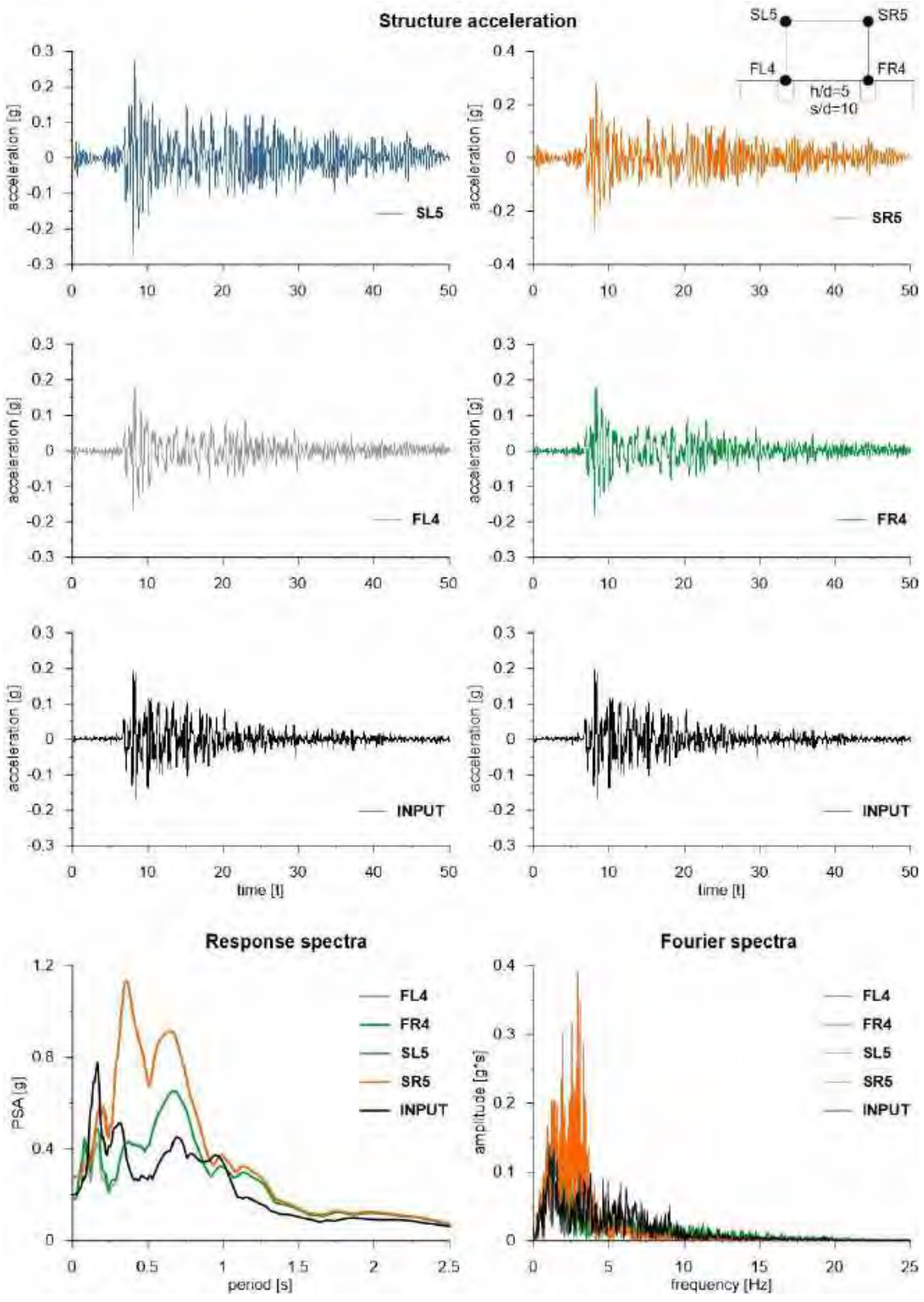

This project has received funding from the European Union's Horizon 2020 research and innovation programme under grant agreement No. 700748

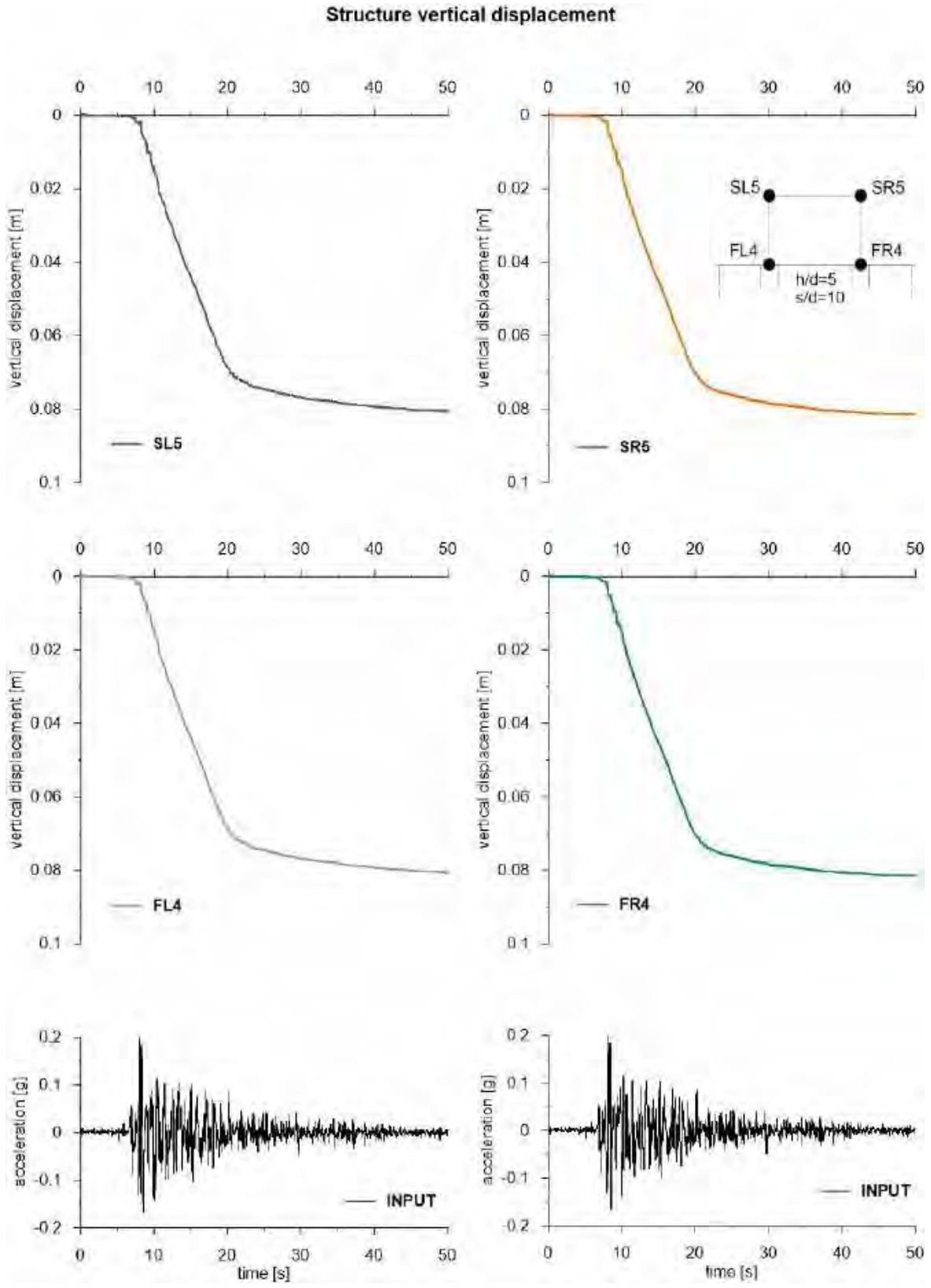

This project has received funding from the European Union's Horizon 2020 research and innovation programme under grant agreement No. 700748

6.1.1.29 ID: SS_HDU_H05_s15

The model consists of a homogenous soil profile of Ticino sand. The ground motion applied was the number 31.

ID: SS_HDU_H05_s15

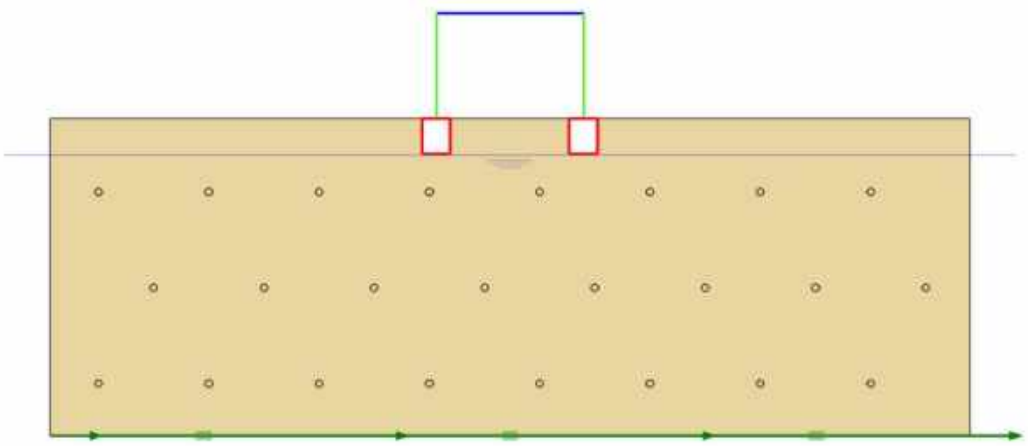

Layouts of the model reproduced in Plaxis 2D

This project has received funding from the European Union's Horizon 2020 research and innovation programme under grant agreement No. 700748

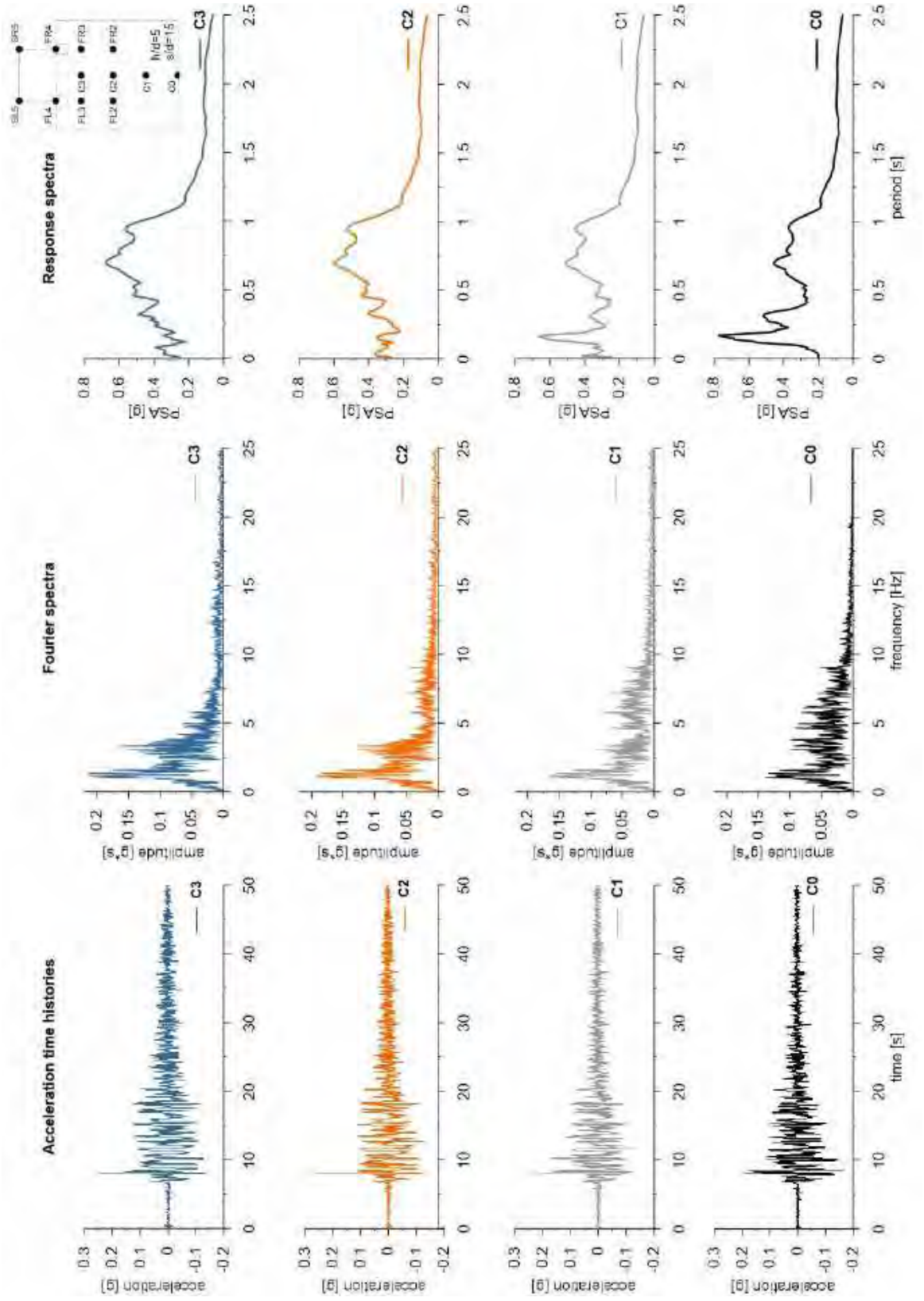

This project has received funding from the European Union's Horizon 2020 research and innovation programme under grant agreement No. 700748

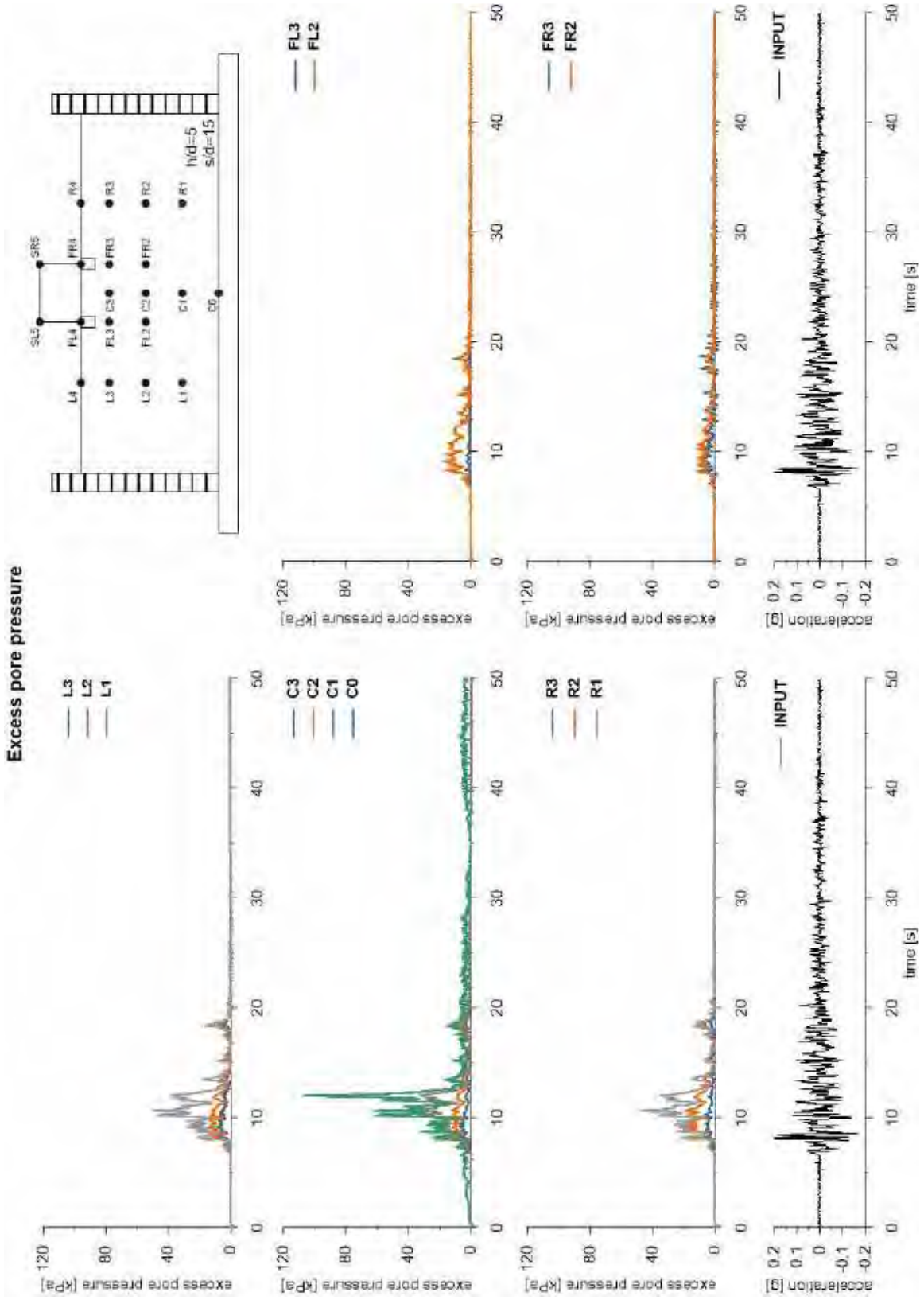

This project has received funding from the European Union's Horizon 2020 research and innovation programme under grant agreement No. 700748

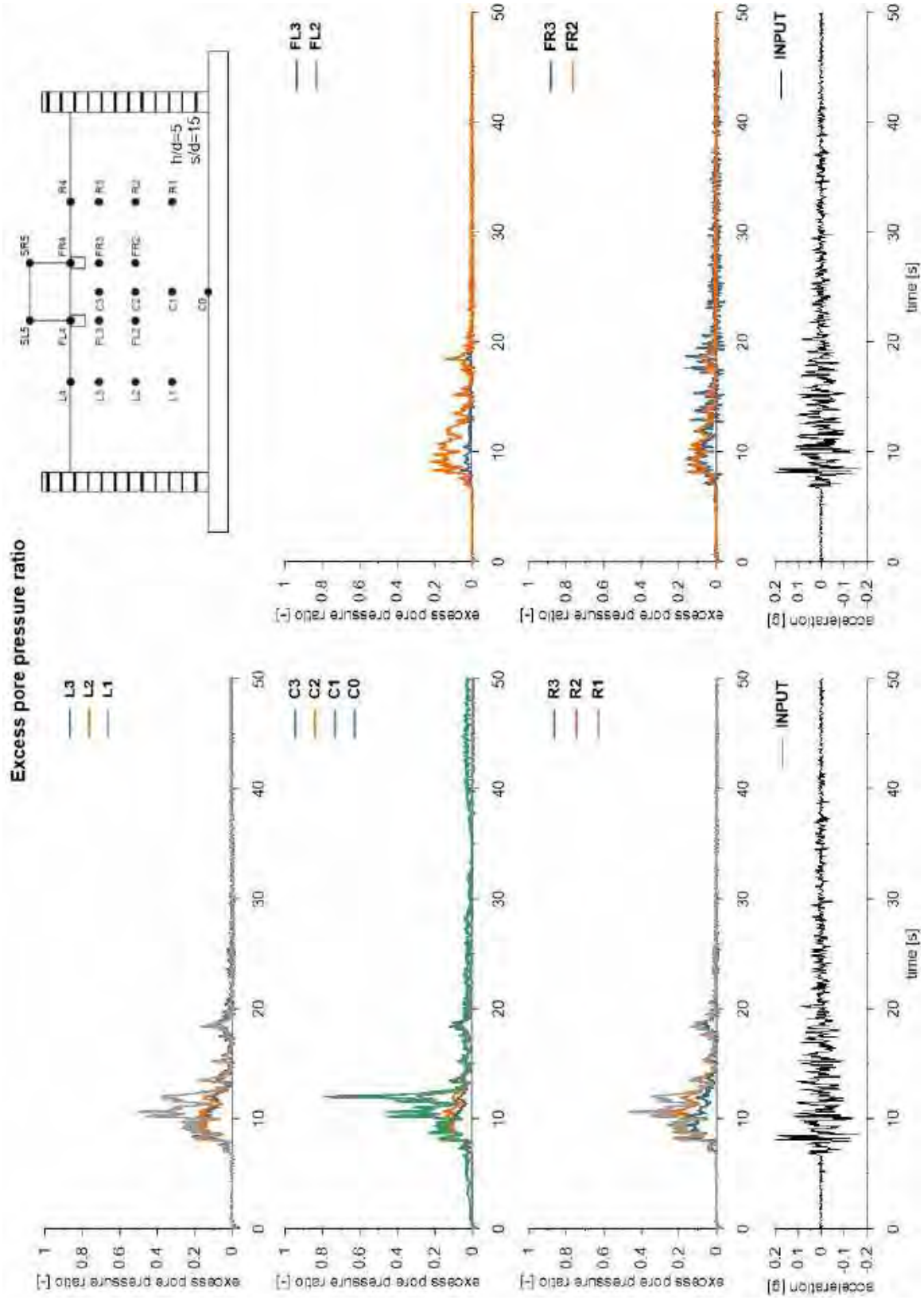

This project has received funding from the European Union's Horizon 2020 research and innovation programme under grant agreement No. 700748

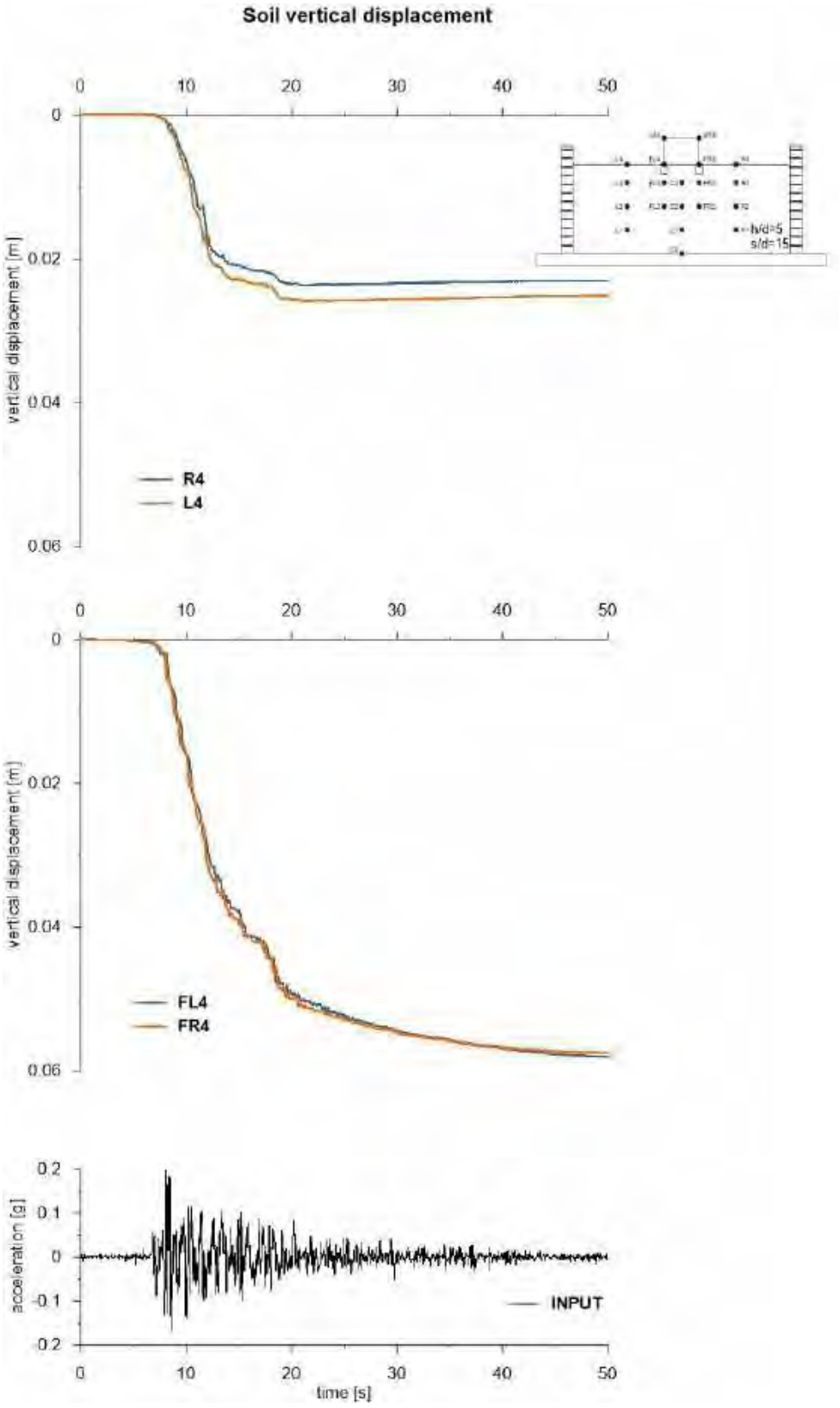

This project has received funding from the European Union's Horizon 2020 research and innovation programme under grant agreement No. 700748

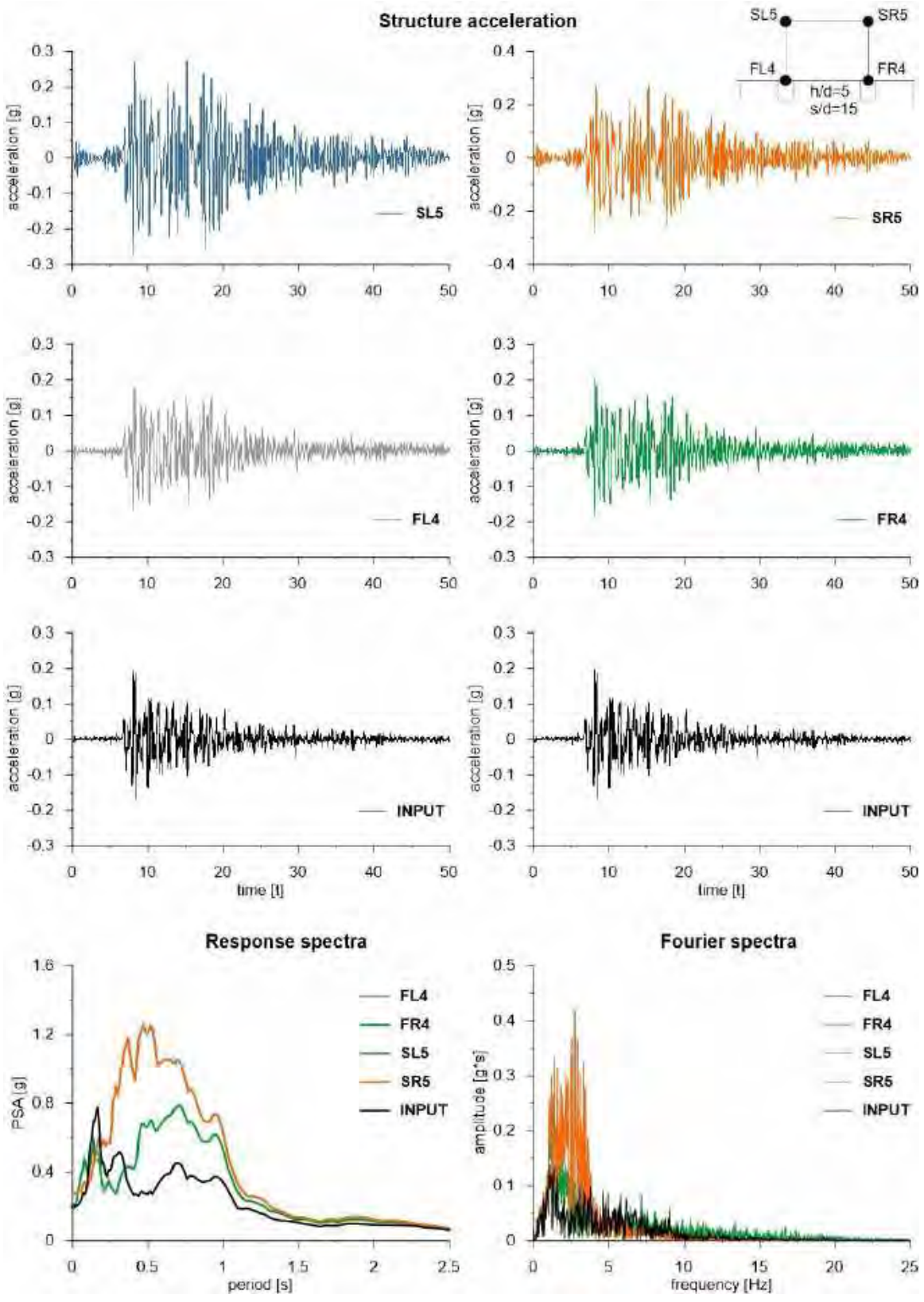

This project has received funding from the European Union's Horizon 2020 research and innovation programme under grant agreement No. 700748

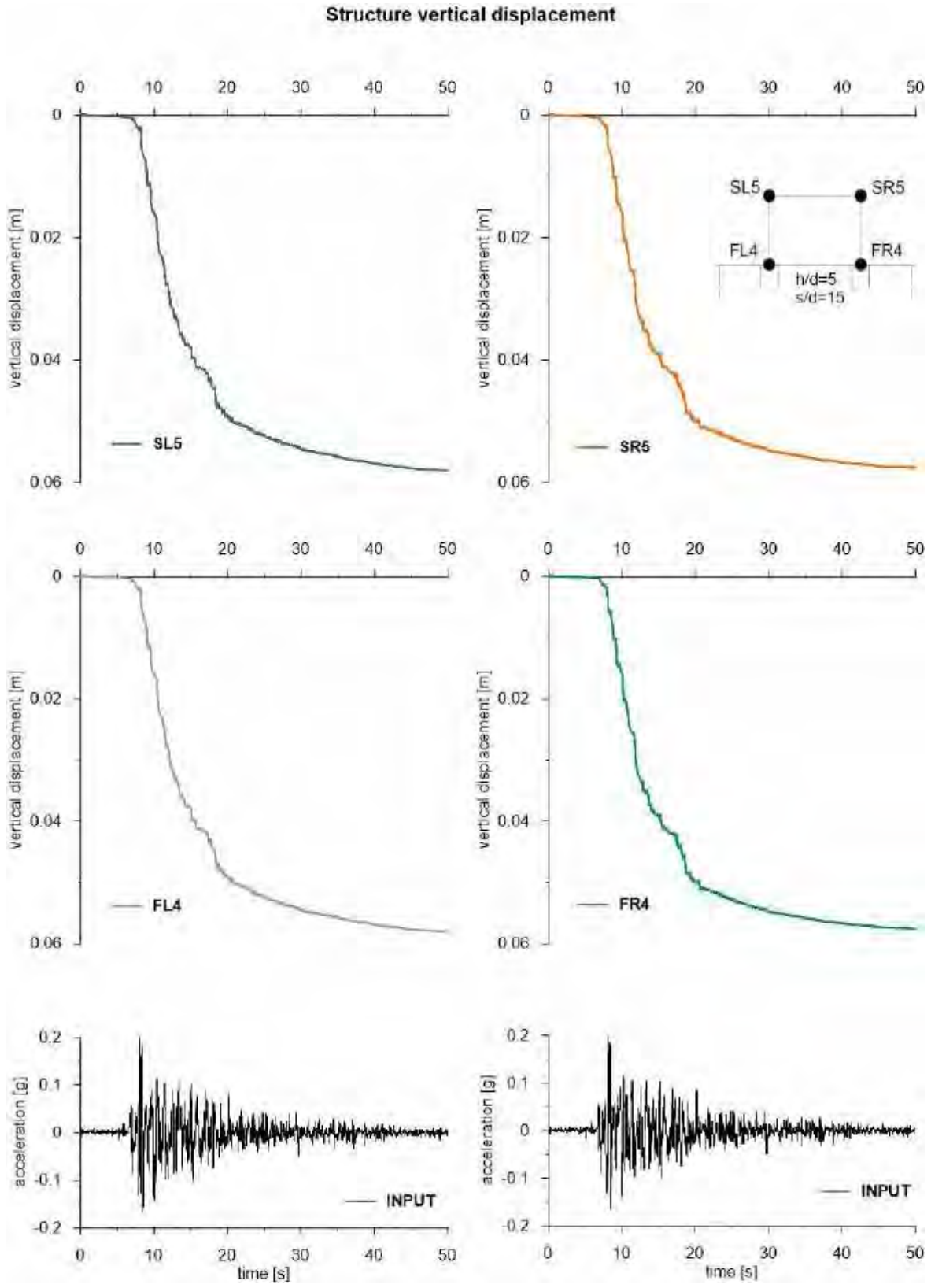

This project has received funding from the European Union's Horizon 2020 research and innovation programme under grant agreement No. 700748

6.1.1.30 ID: SS_HDU_H10_s05

The model consists of a homogenous soil profile of Ticino sand. The ground motion applied was the number 31.

ID: SS_HDU_H10_s05

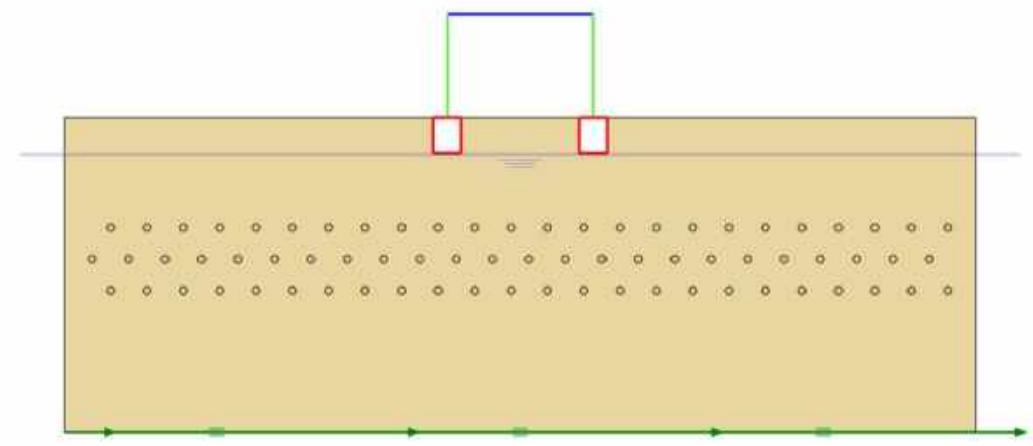

Layouts of the model reproduced in Plaxis 2D

This project has received funding from the European Union's Horizon 2020 research and innovation programme under grant agreement No. 700748

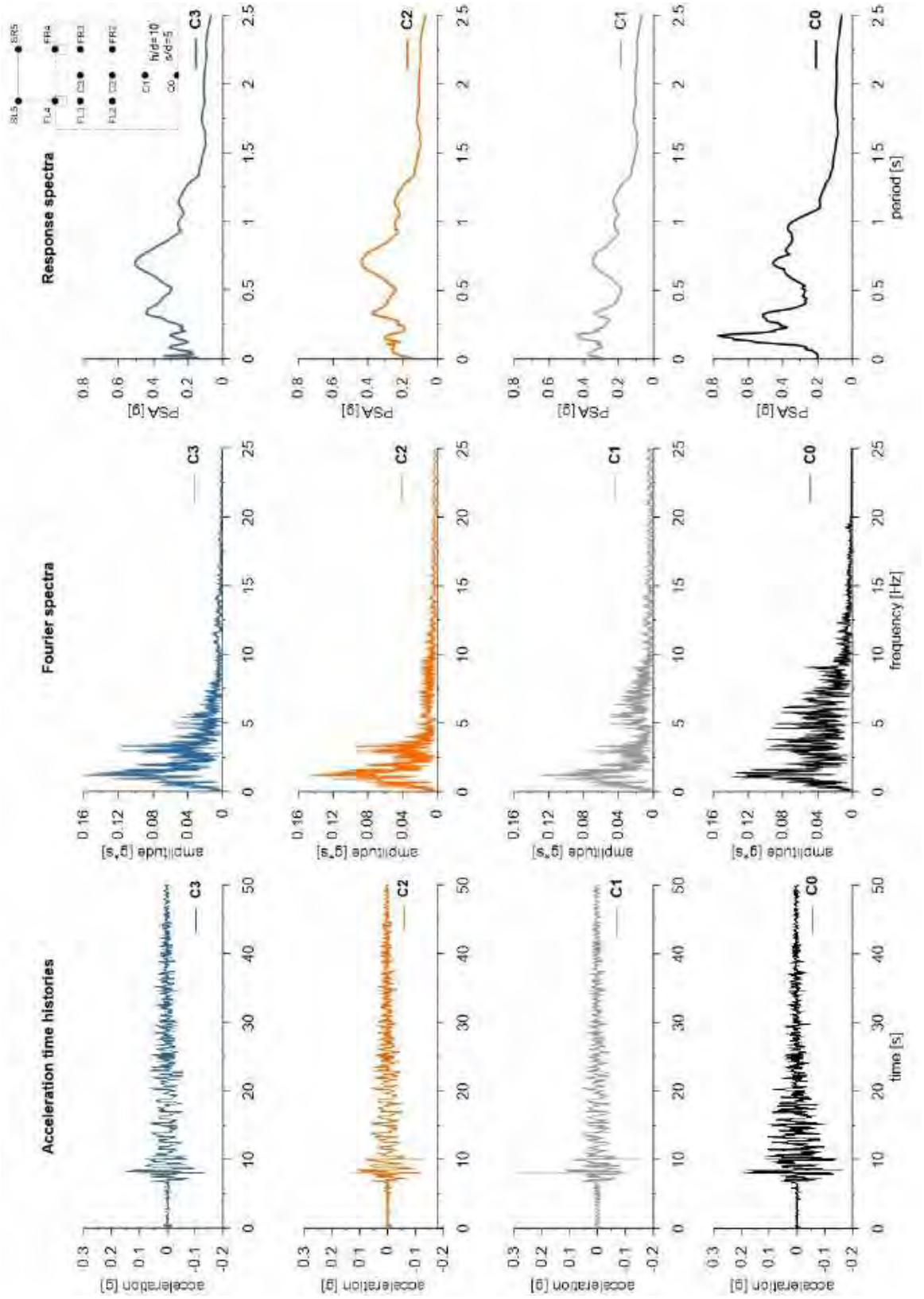

This project has received funding from the European Union's Horizon 2020 research and innovation programme under grant agreement No. 700748

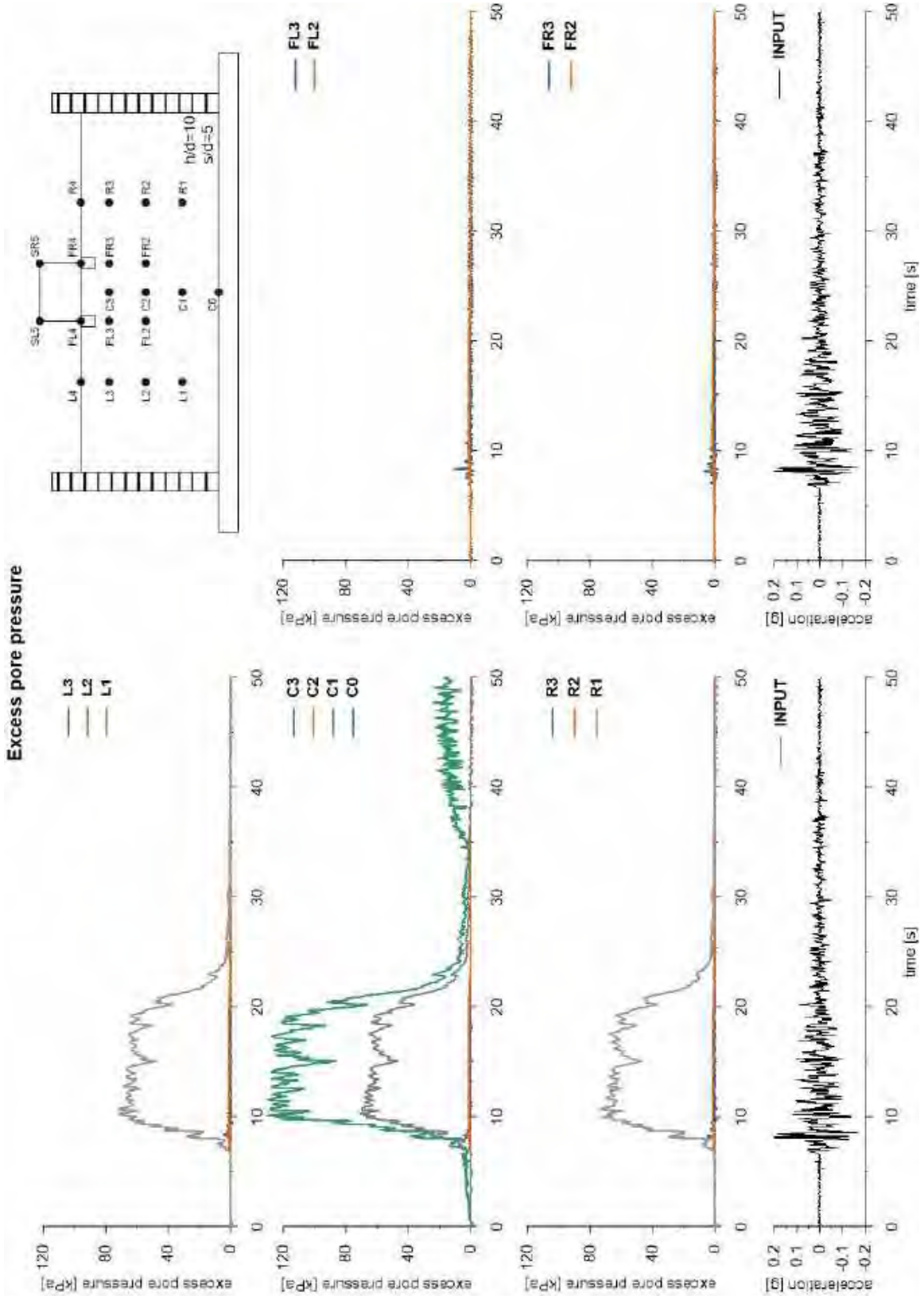

This project has received funding from the European Union's Horizon 2020 research and innovation programme under grant agreement No. 700748

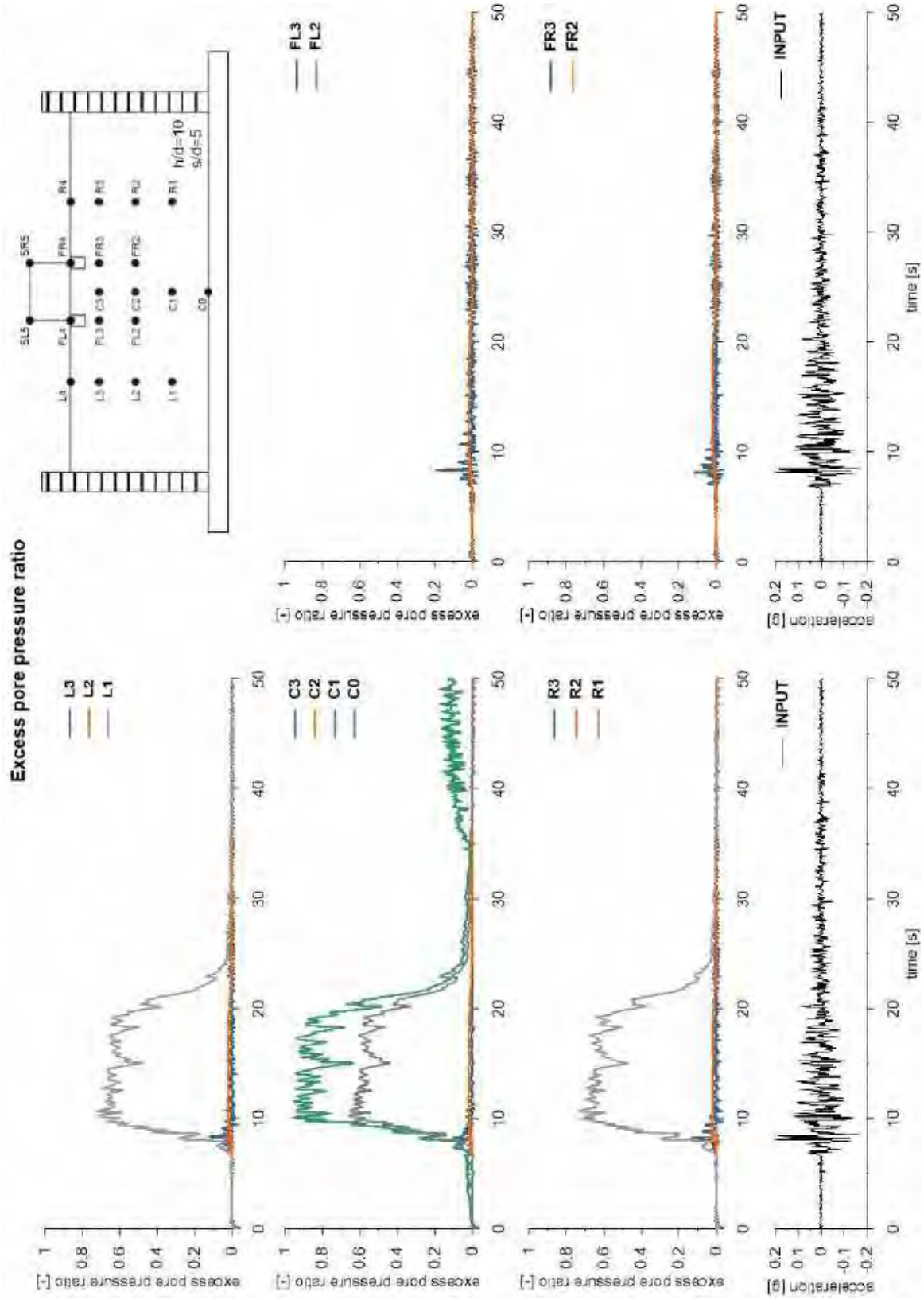

This project has received funding from the European Union's Horizon 2020 research and innovation programme under grant agreement No. 700748

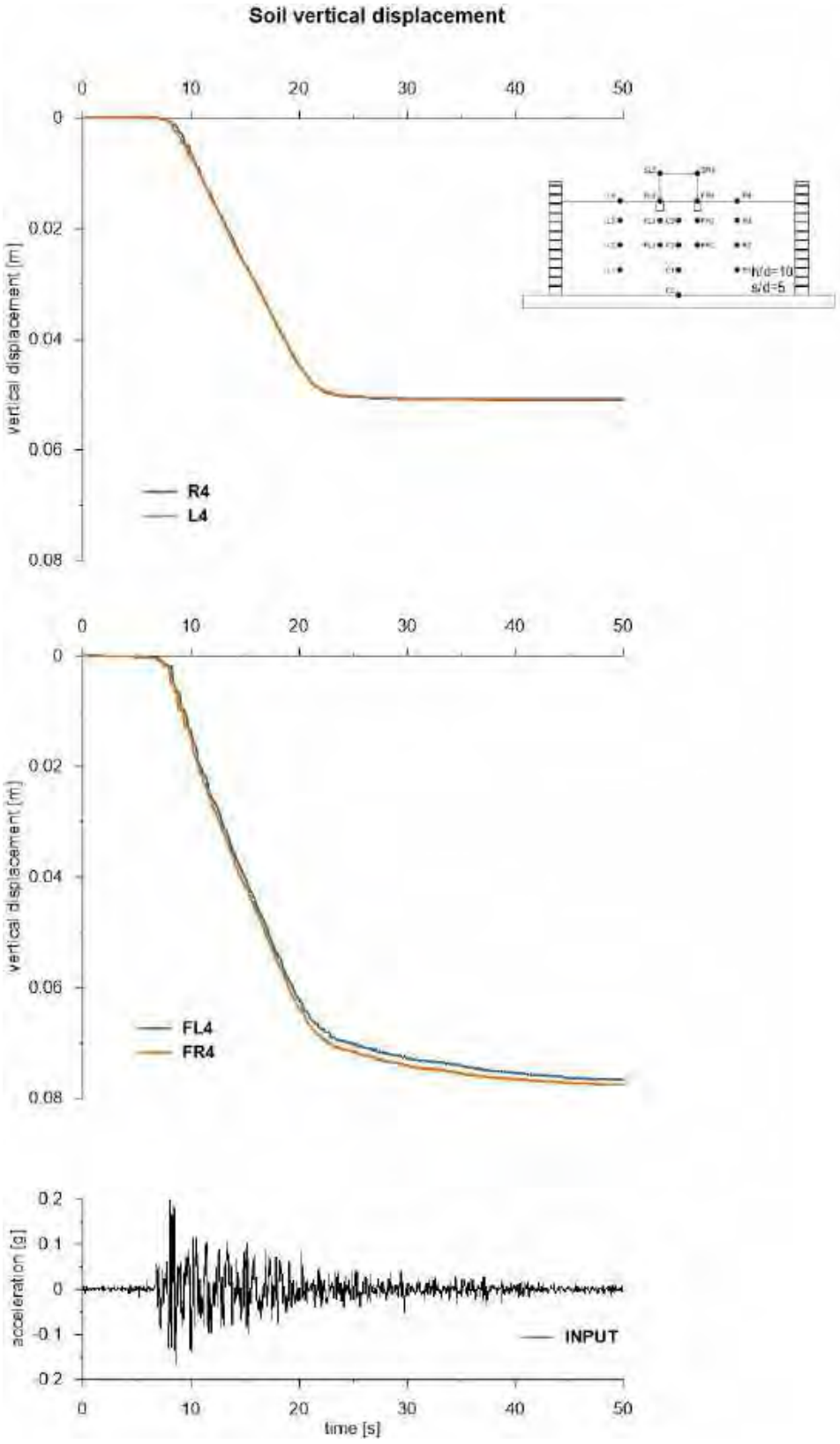

This project has received funding from the European Union's Horizon 2020 research and innovation programme under grant agreement No. 700748

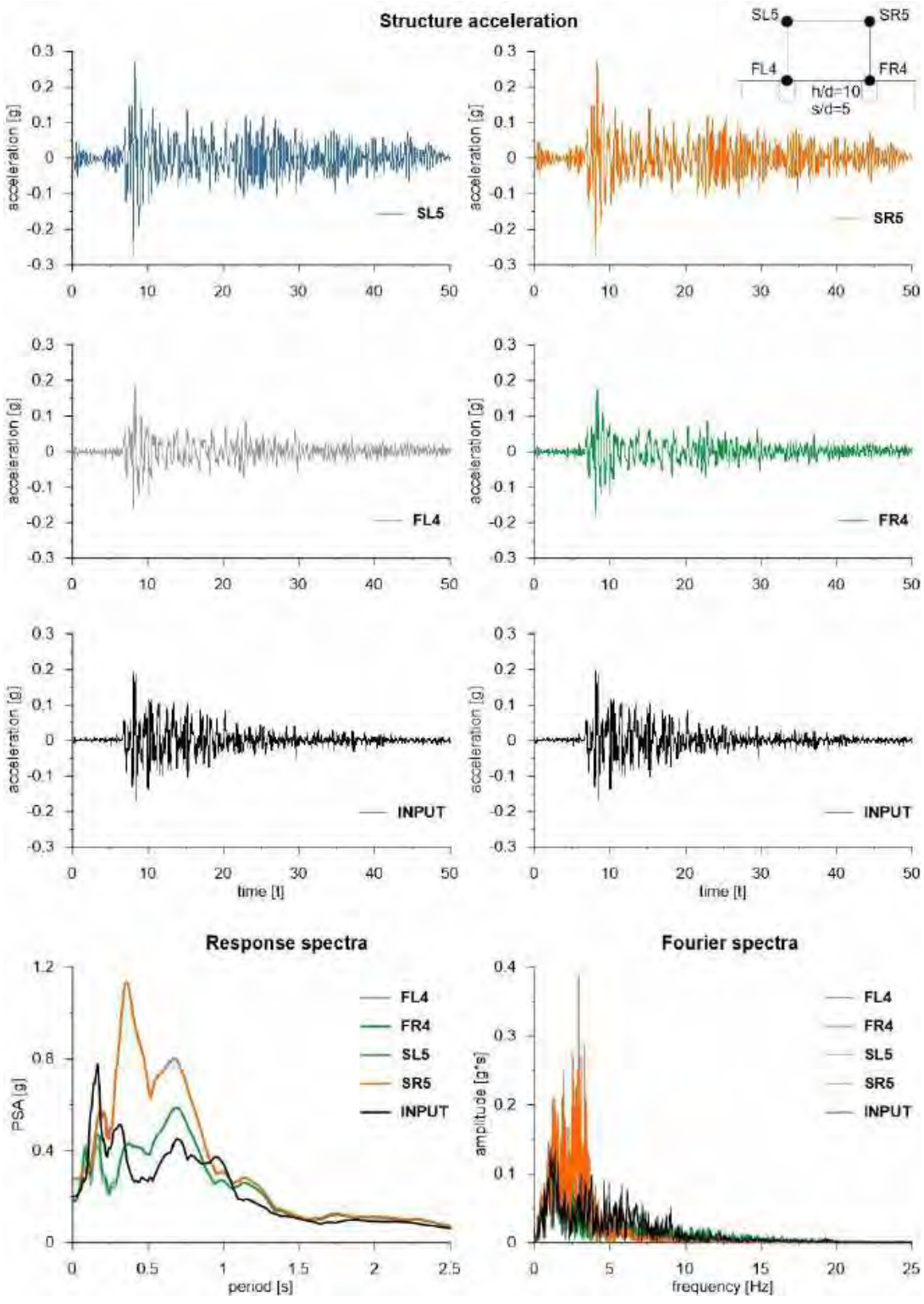

This project has received funding from the European Union's Horizon 2020 research and innovation programme under grant agreement No. 700748

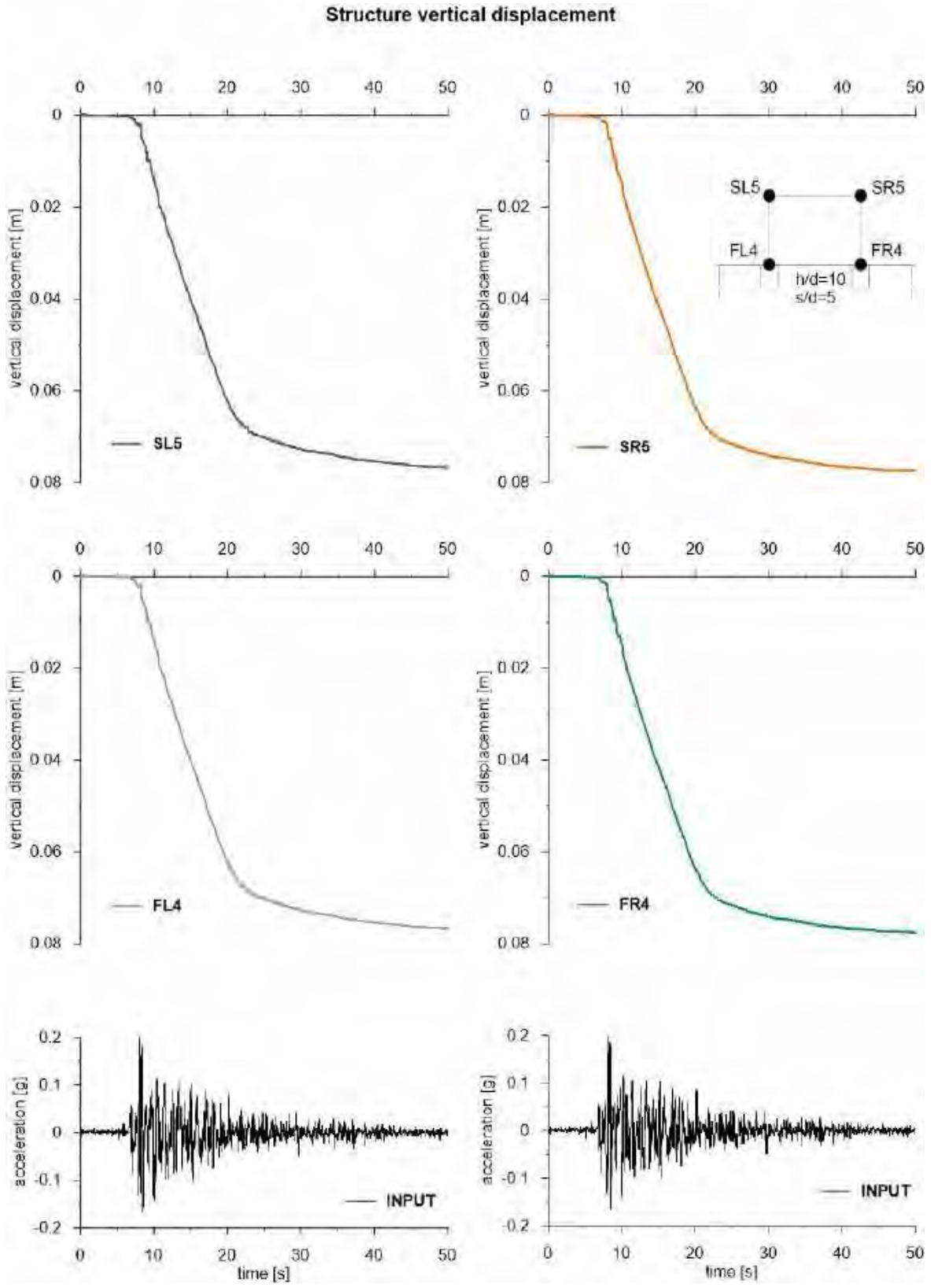

This project has received funding from the European Union's Horizon 2020 research and innovation programme under grant agreement No. 700748

6.1.1.31 ID: SS_HDU_H10_s10

The model consists of a homogenous soil profile of Ticino sand. The ground motion applied was the number 31.

ID: SS_HDU_H10_s10

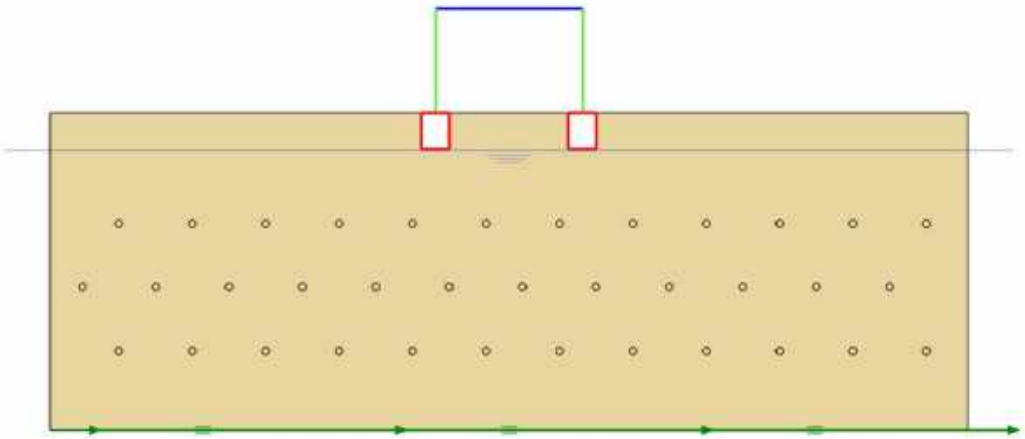

Layouts of the model reproduced in Plaxis 2D

This project has received funding from the European Union's Horizon 2020 research and innovation programme under grant agreement No. 700748

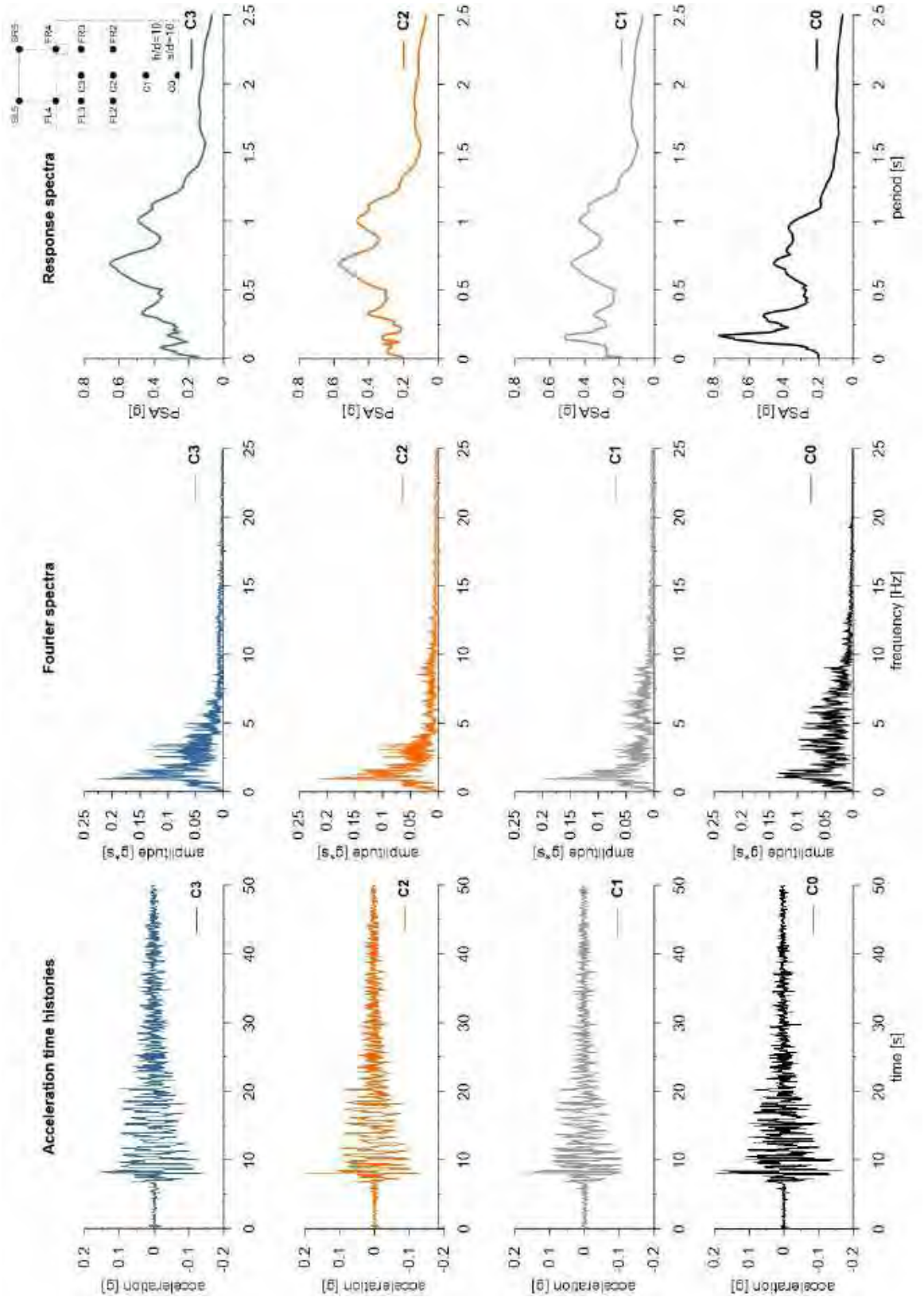

This project has received funding from the European Union's Horizon 2020 research and innovation programme under grant agreement No. 700748

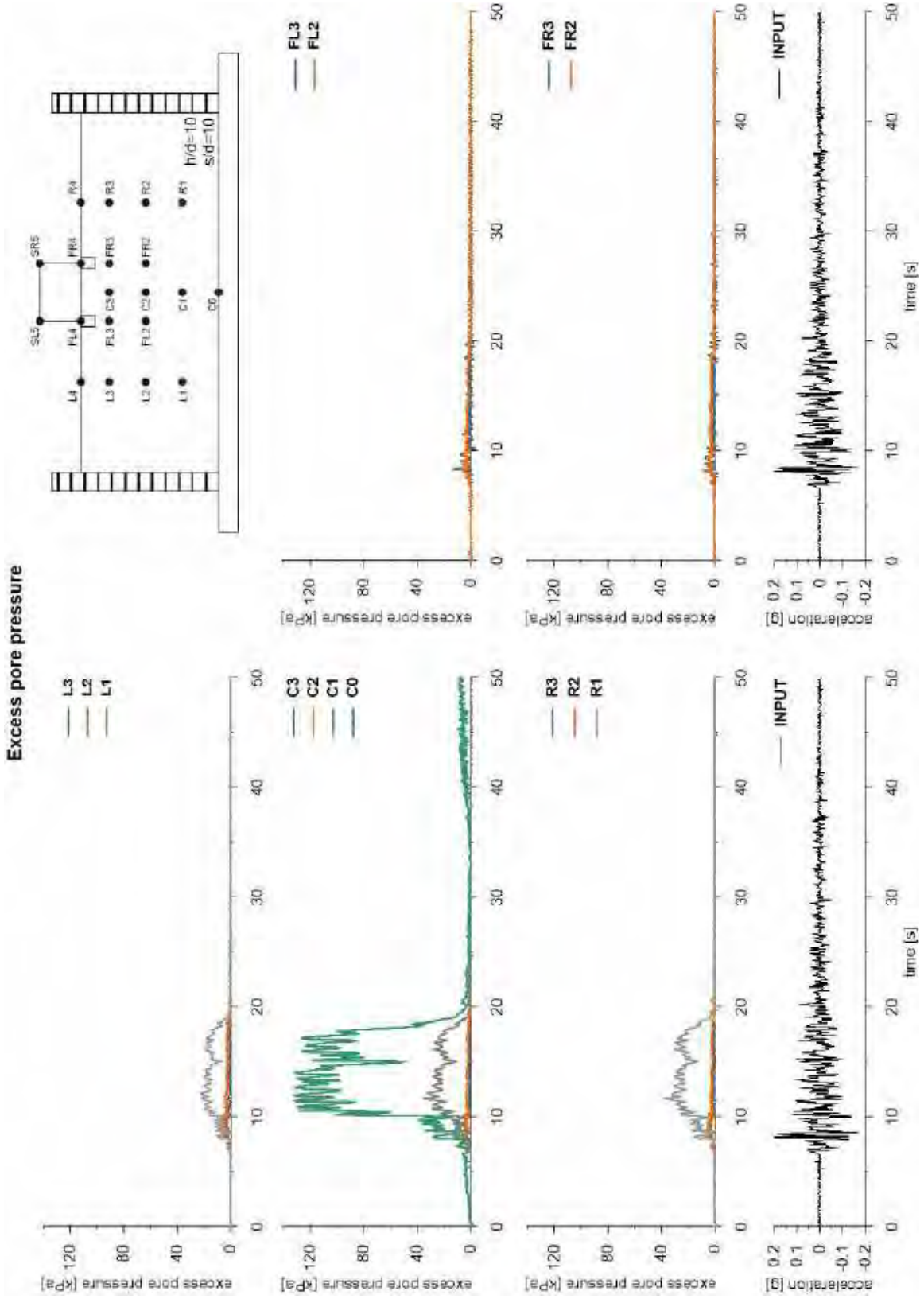

This project has received funding from the European Union's Horizon 2020 research and innovation programme under grant agreement No. 700748

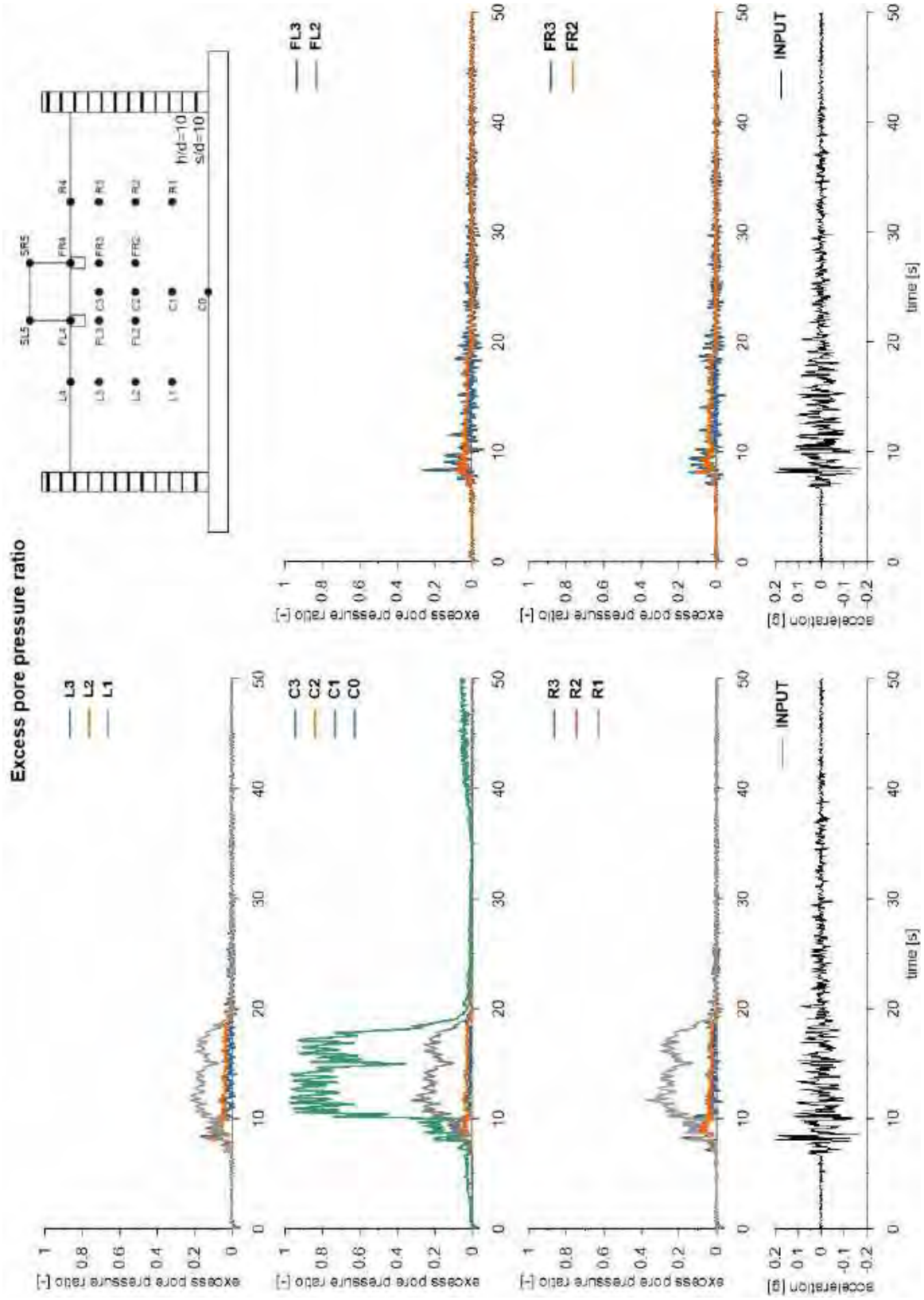

This project has received funding from the European Union's Horizon 2020 research and innovation programme under grant agreement No. 700748

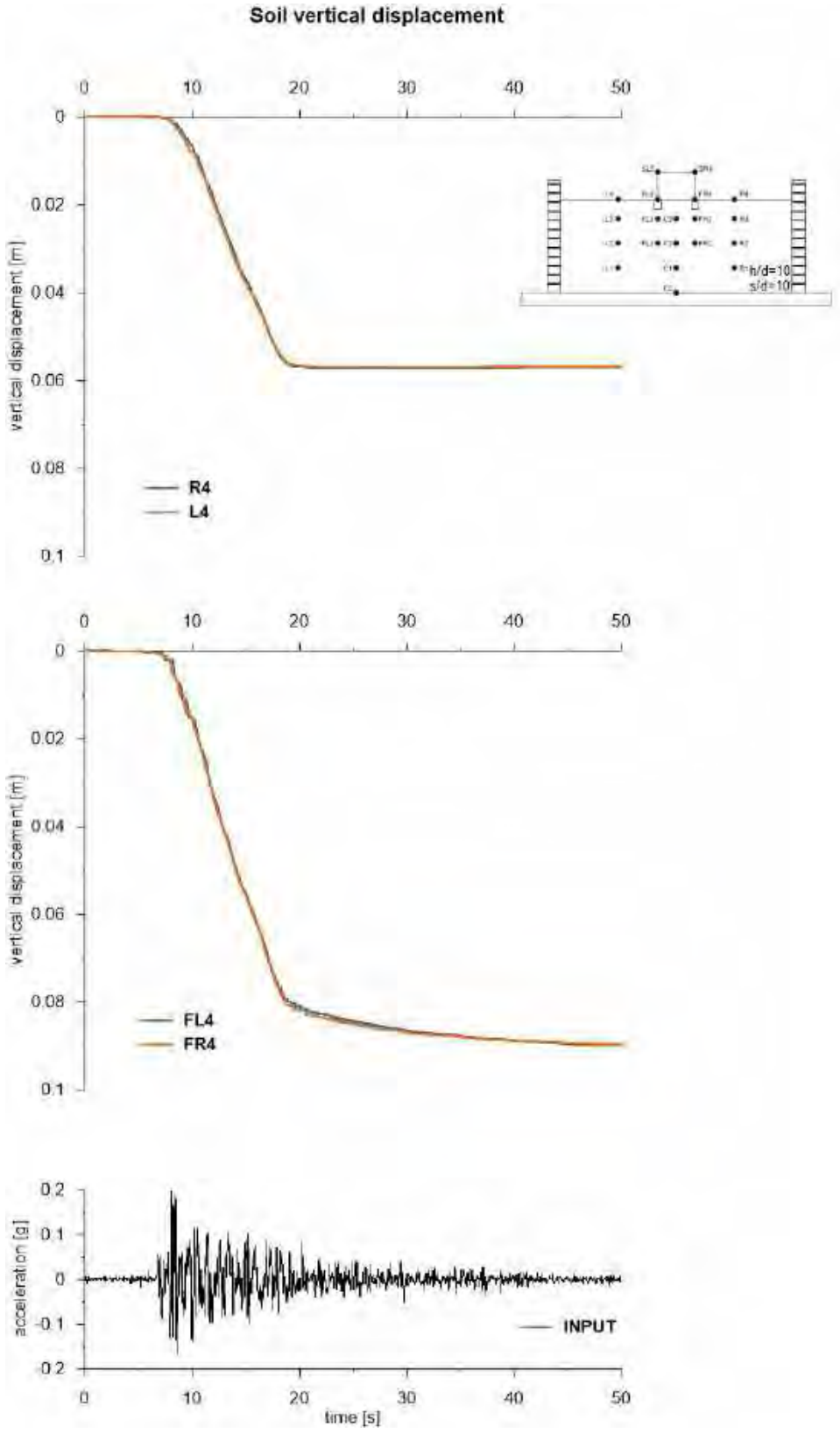

This project has received funding from the European Union's Horizon 2020 research and innovation programme under grant agreement No. 700748

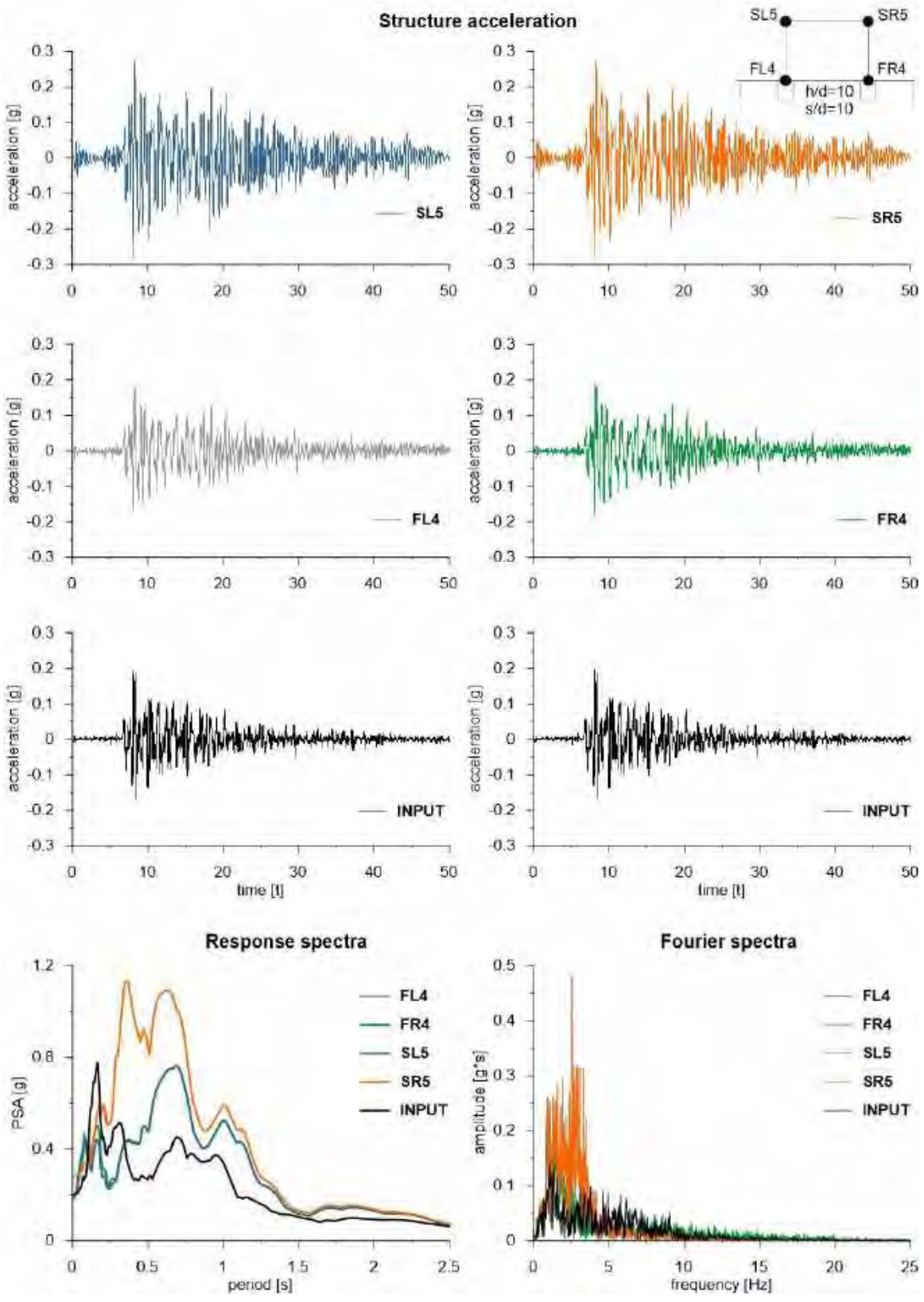

This project has received funding from the European Union's Horizon 2020 research and innovation programme under grant agreement No. 700748

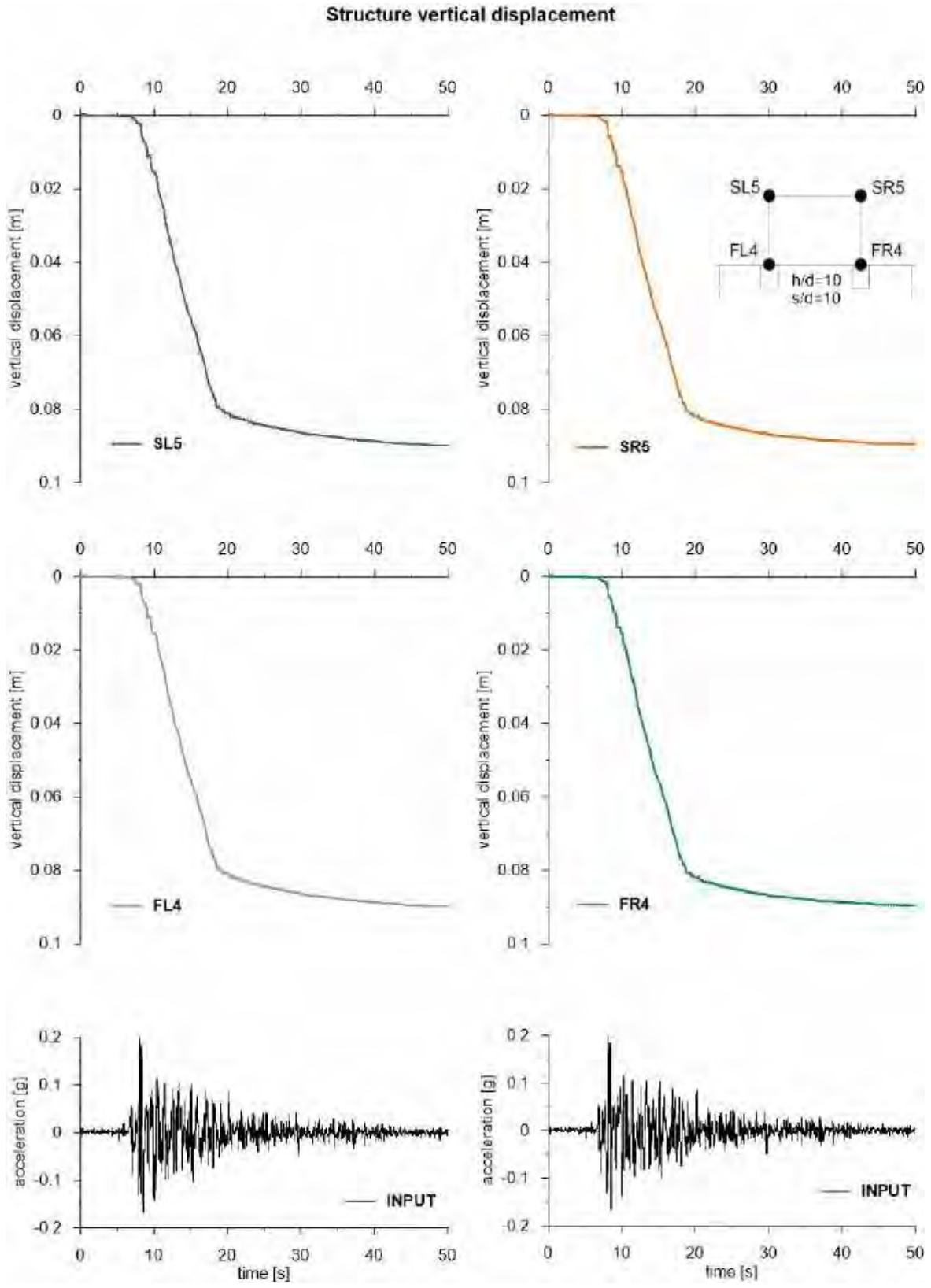

This project has received funding from the European Union's Horizon 2020 research and innovation programme under grant agreement No. 700748

6.1.1.32 ID: SS_HDU_H10_s15

The model consists of a homogenous soil profile of Ticino sand. The ground motion applied was the number 31.

ID: SS_HDU_H10_s15

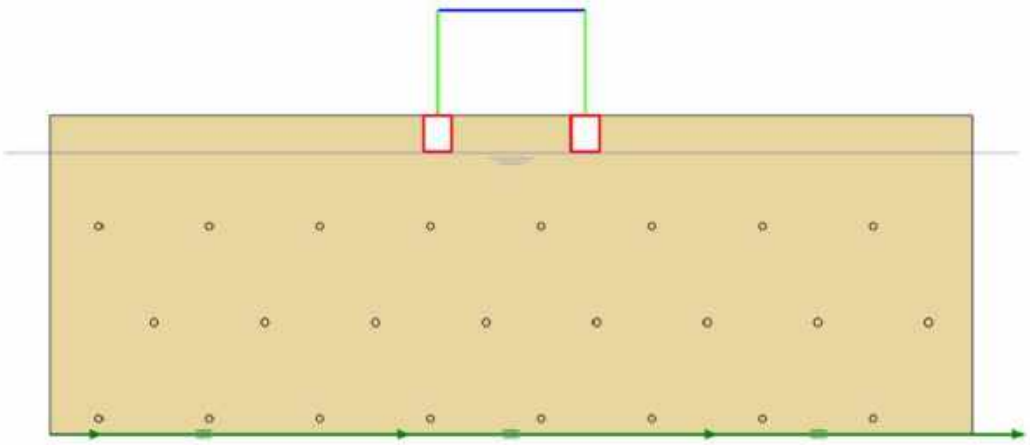

Layouts of the model reproduced in Plaxis 2D

This project has received funding from the European Union's Horizon 2020 research and innovation programme under grant agreement No. 700748

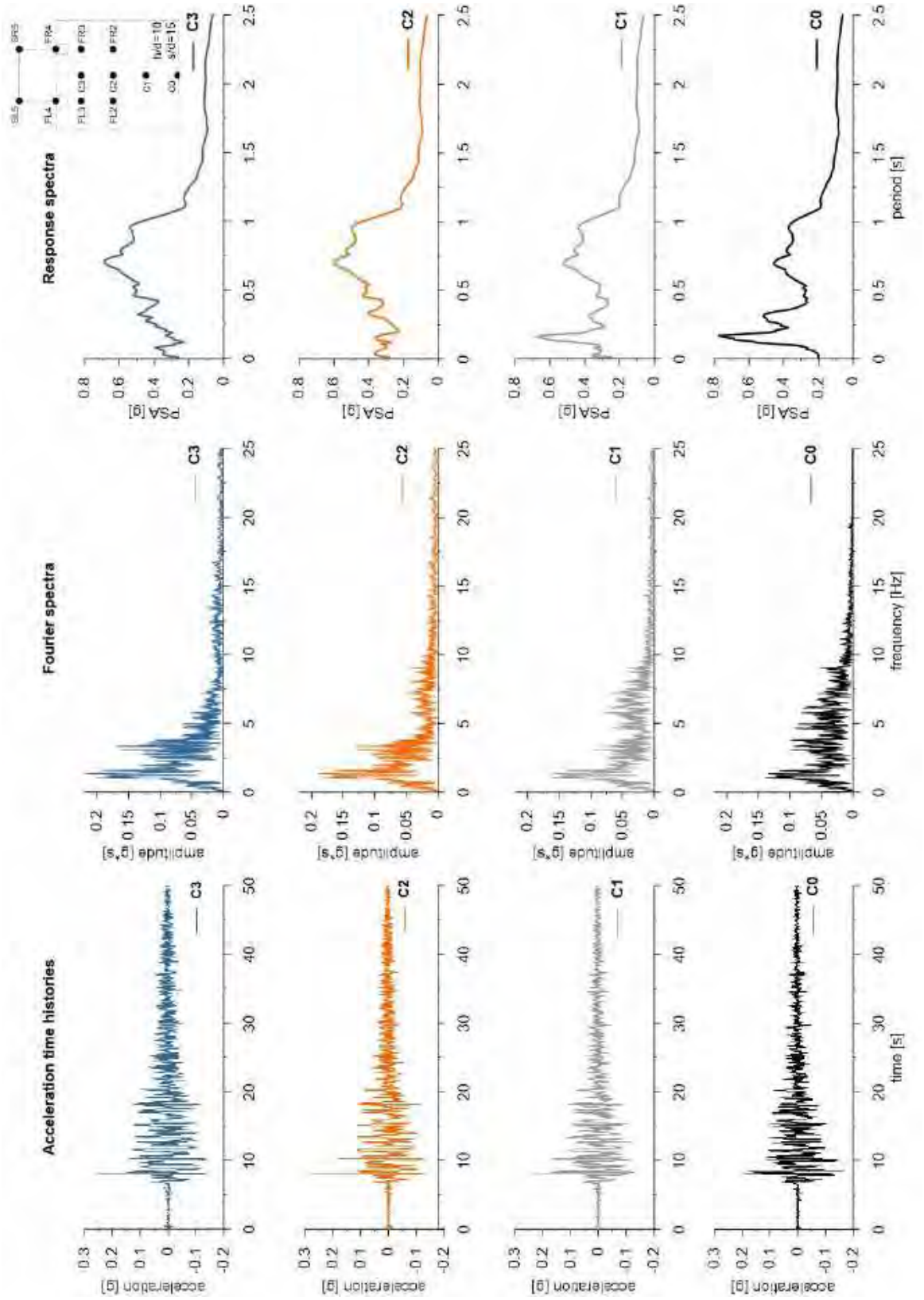

This project has received funding from the European Union's Horizon 2020 research and innovation programme under grant agreement No. 700748

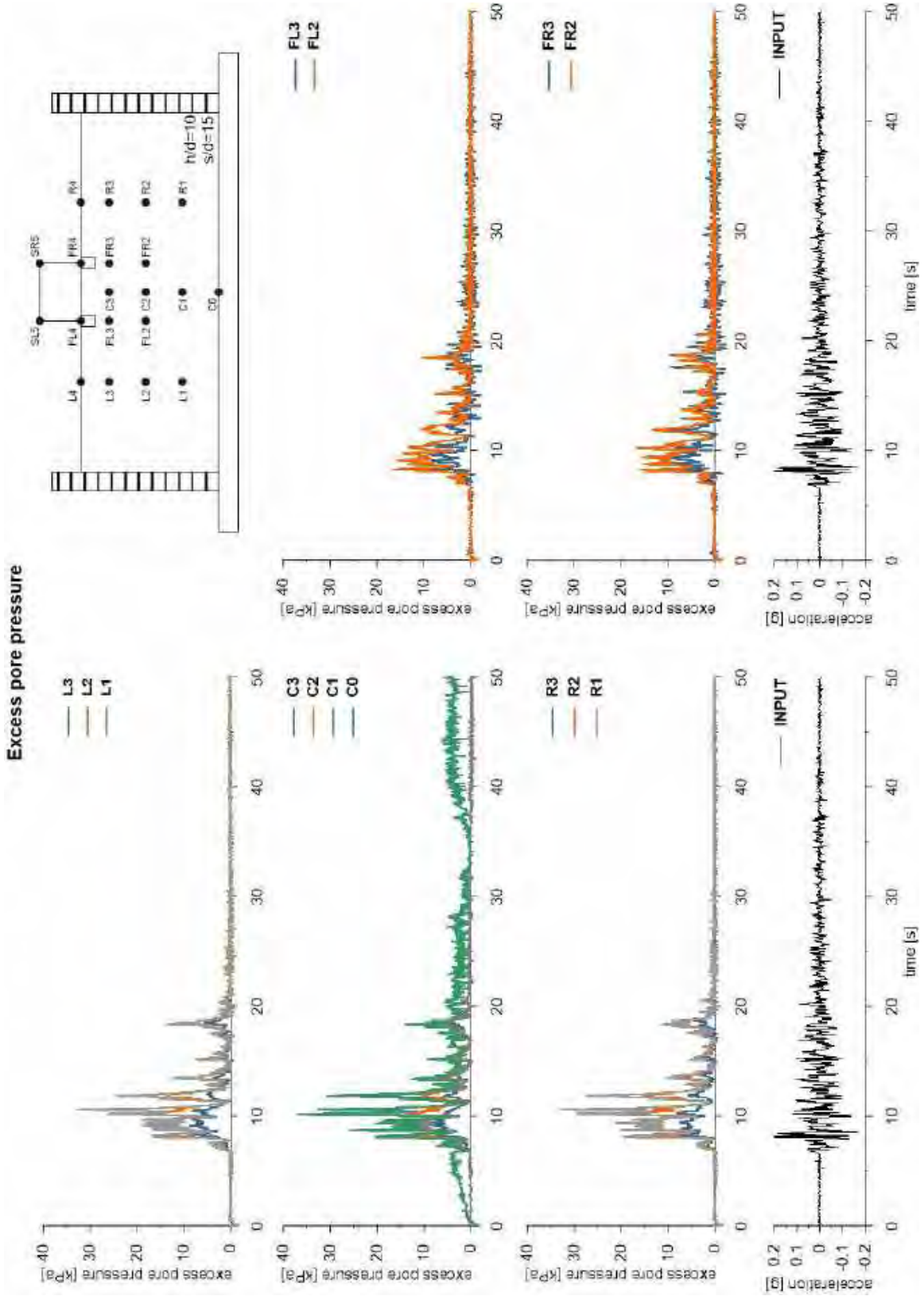

This project has received funding from the European Union's Horizon 2020 research and innovation programme under grant agreement No. 700748

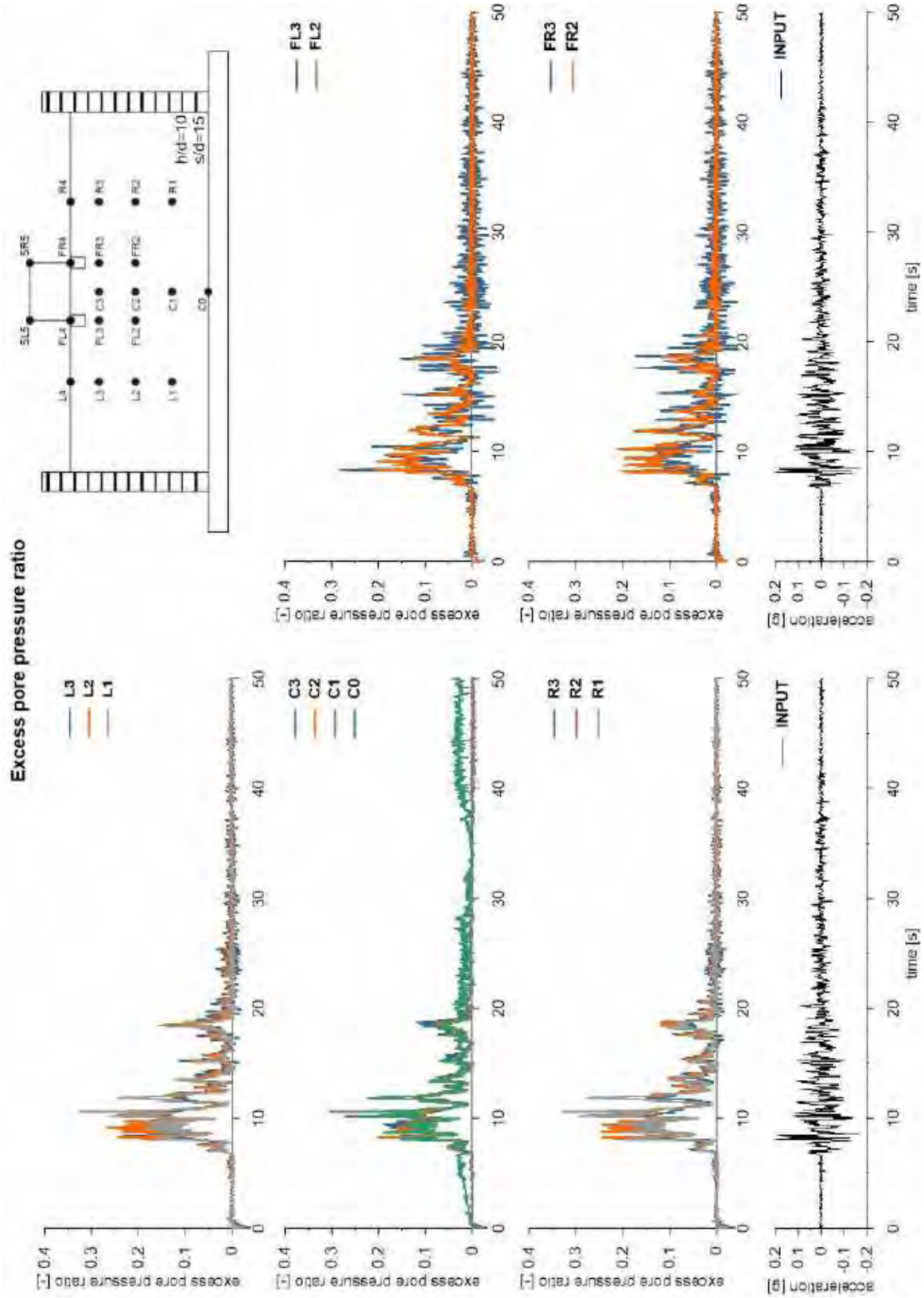

This project has received funding from the European Union's Horizon 2020 research and innovation programme under grant agreement No. 700748

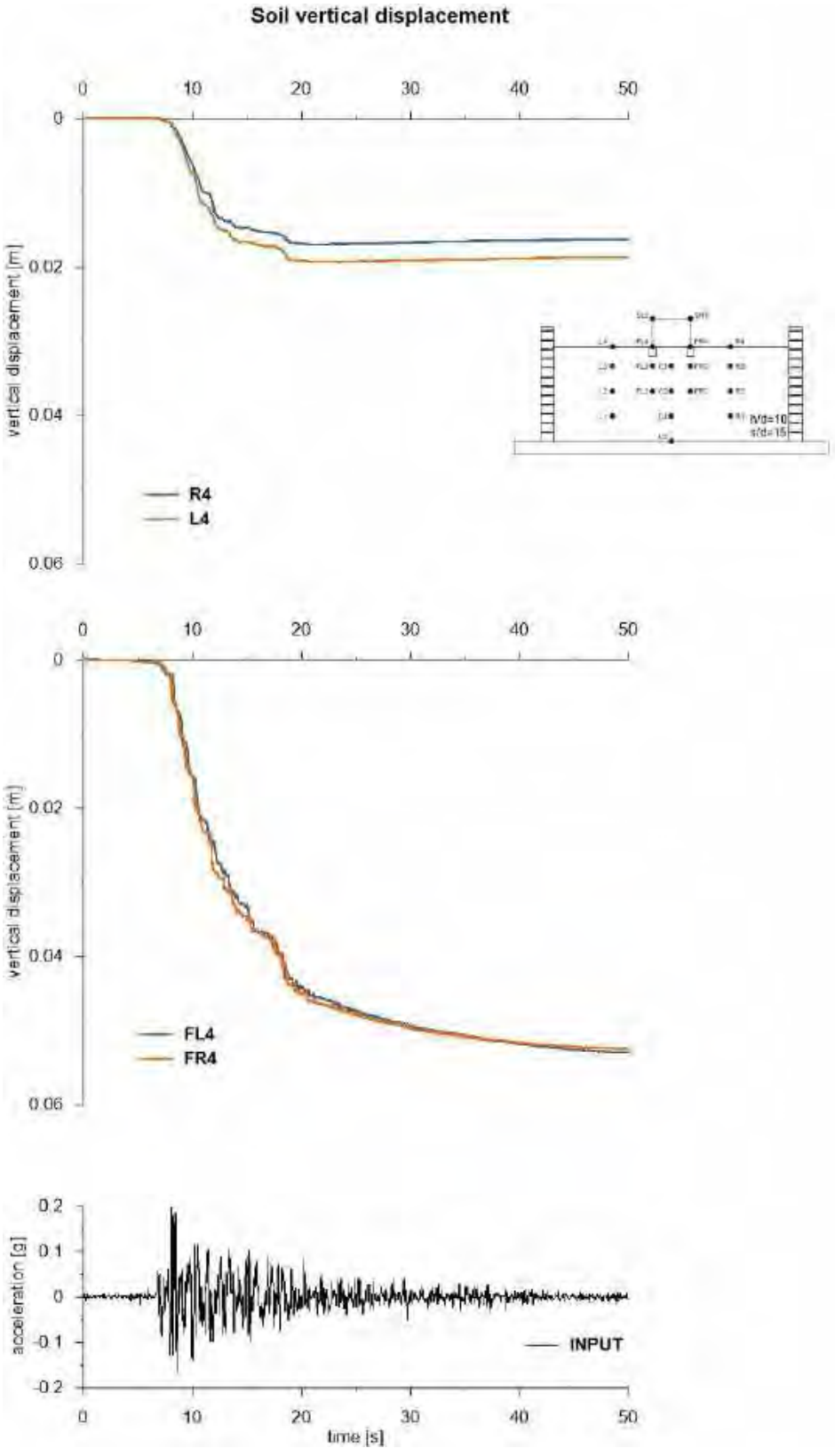

This project has received funding from the European Union's Horizon 2020 research and innovation programme under grant agreement No. 700748

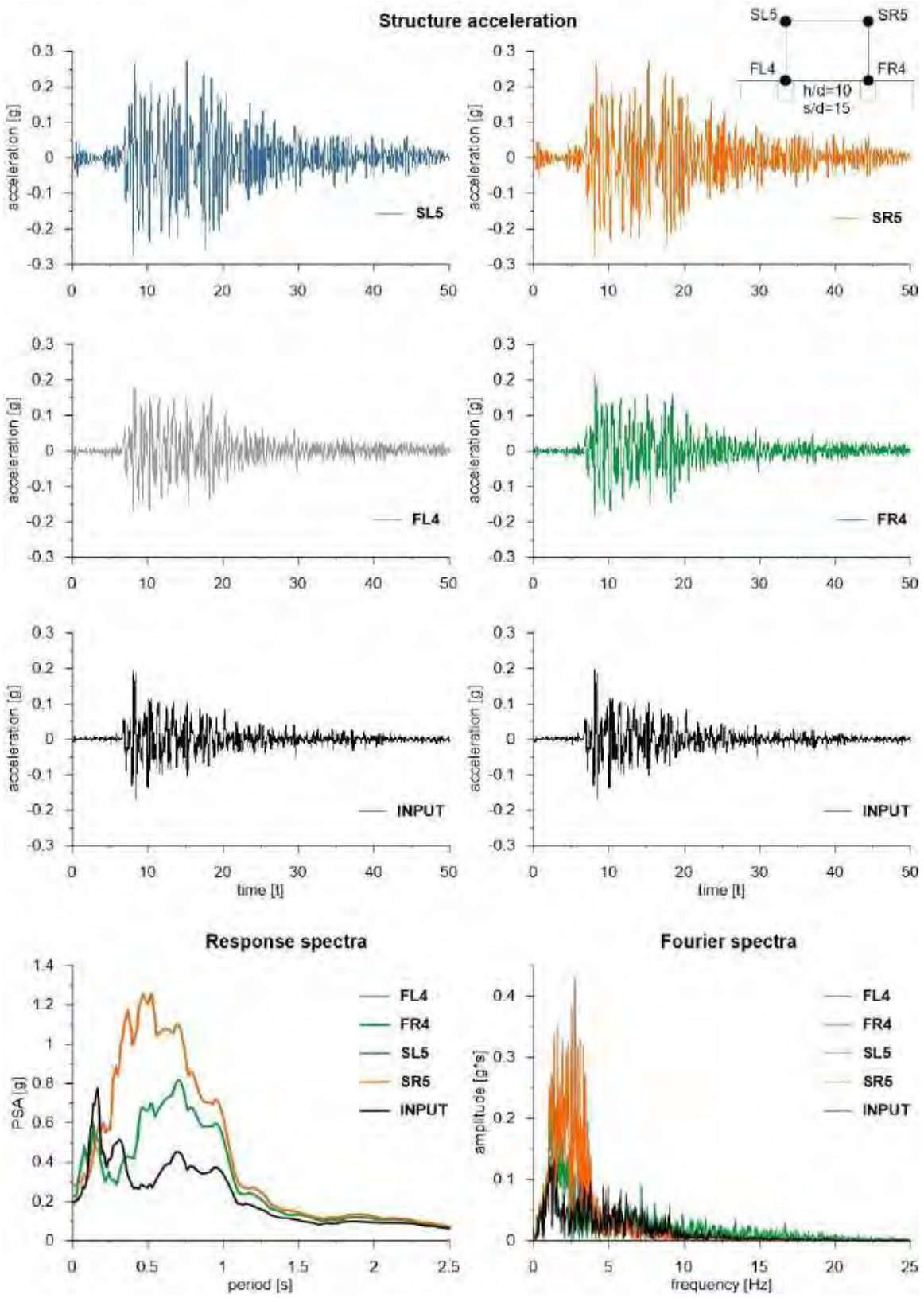

This project has received funding from the European Union's Horizon 2020 research and innovation programme under grant agreement No. 700748

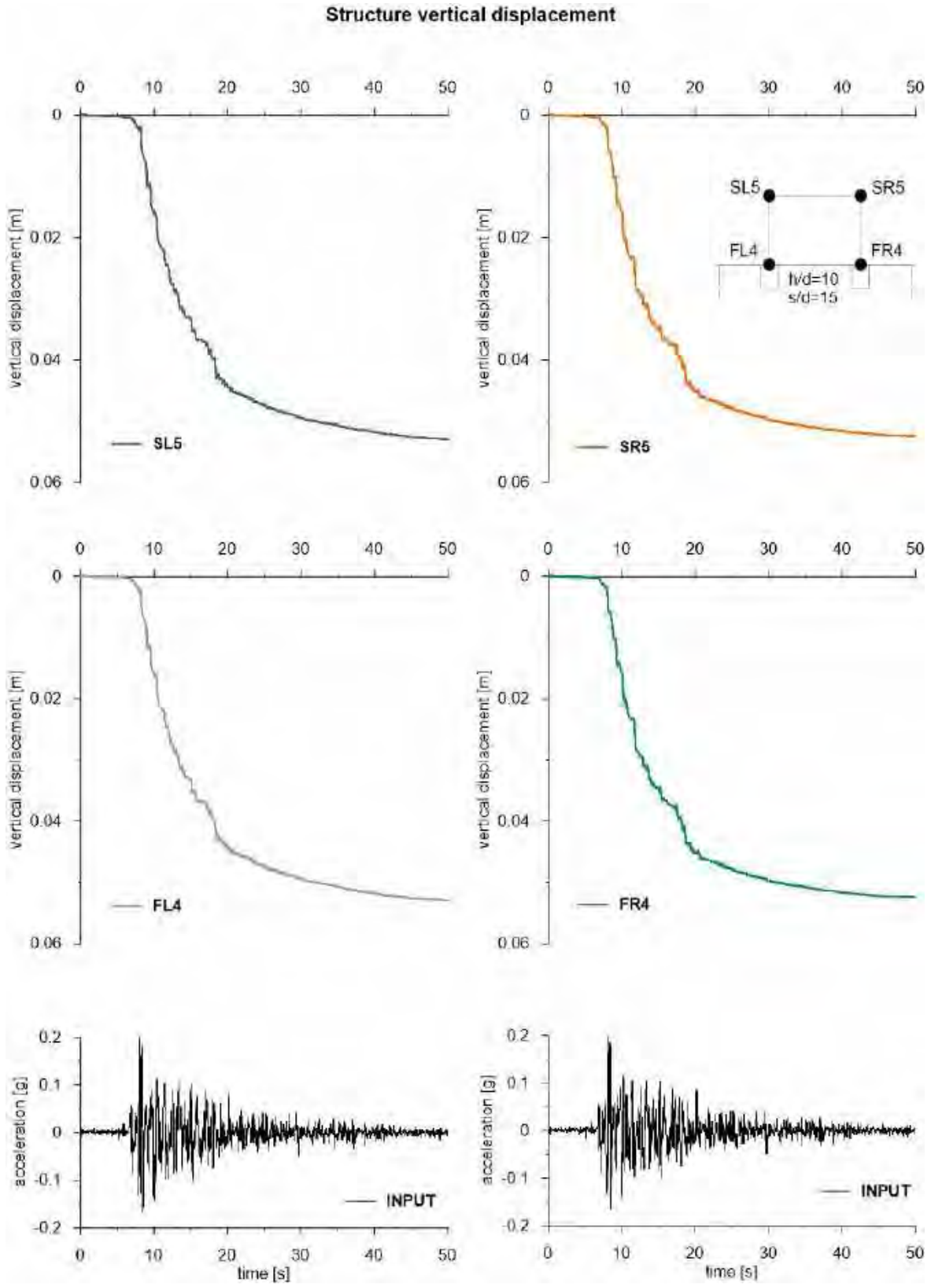

This project has received funding from the European Union's Horizon 2020 research and innovation programme under grant agreement No. 700748

6.1.1.33 ID: SS_HDU_H15_s05

The model consists of a homogenous soil profile of Ticino sand. The ground motion applied was the number 31.

ID: SS_HDU_H15_s05

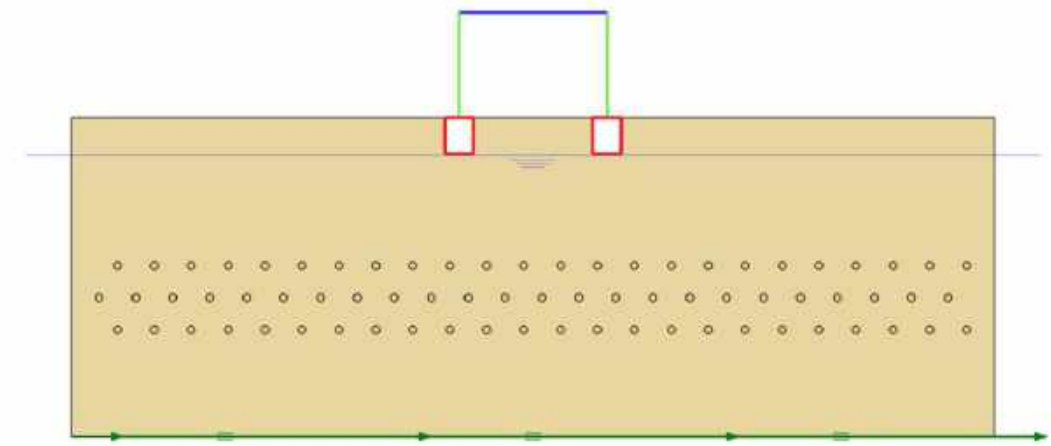

Layouts of the model reproduced in Plaxis 2D

This project has received funding from the European Union's Horizon 2020 research and innovation programme under grant agreement No. 700748

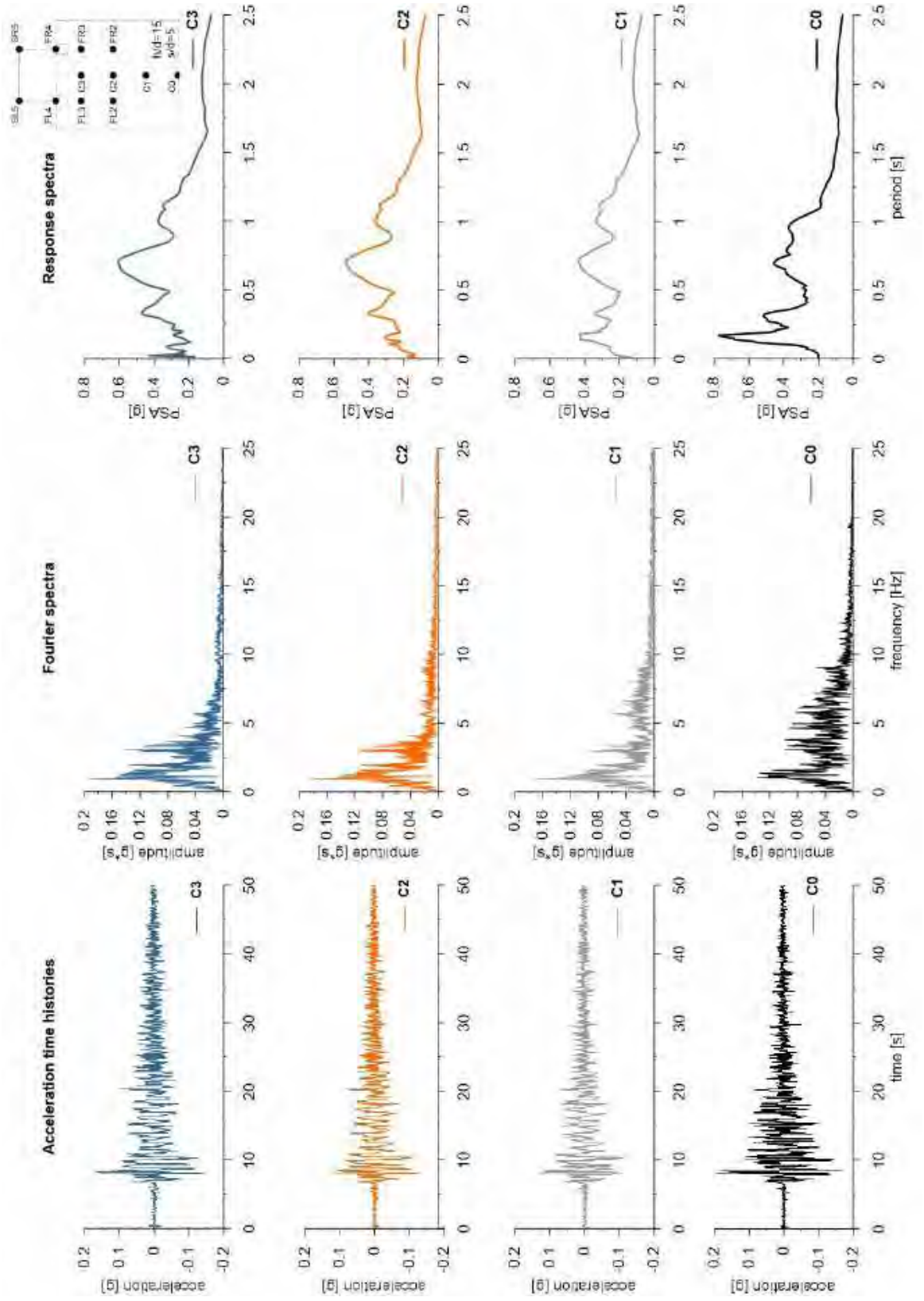

This project has received funding from the European Union's Horizon 2020 research and innovation programme under grant agreement No. 700748

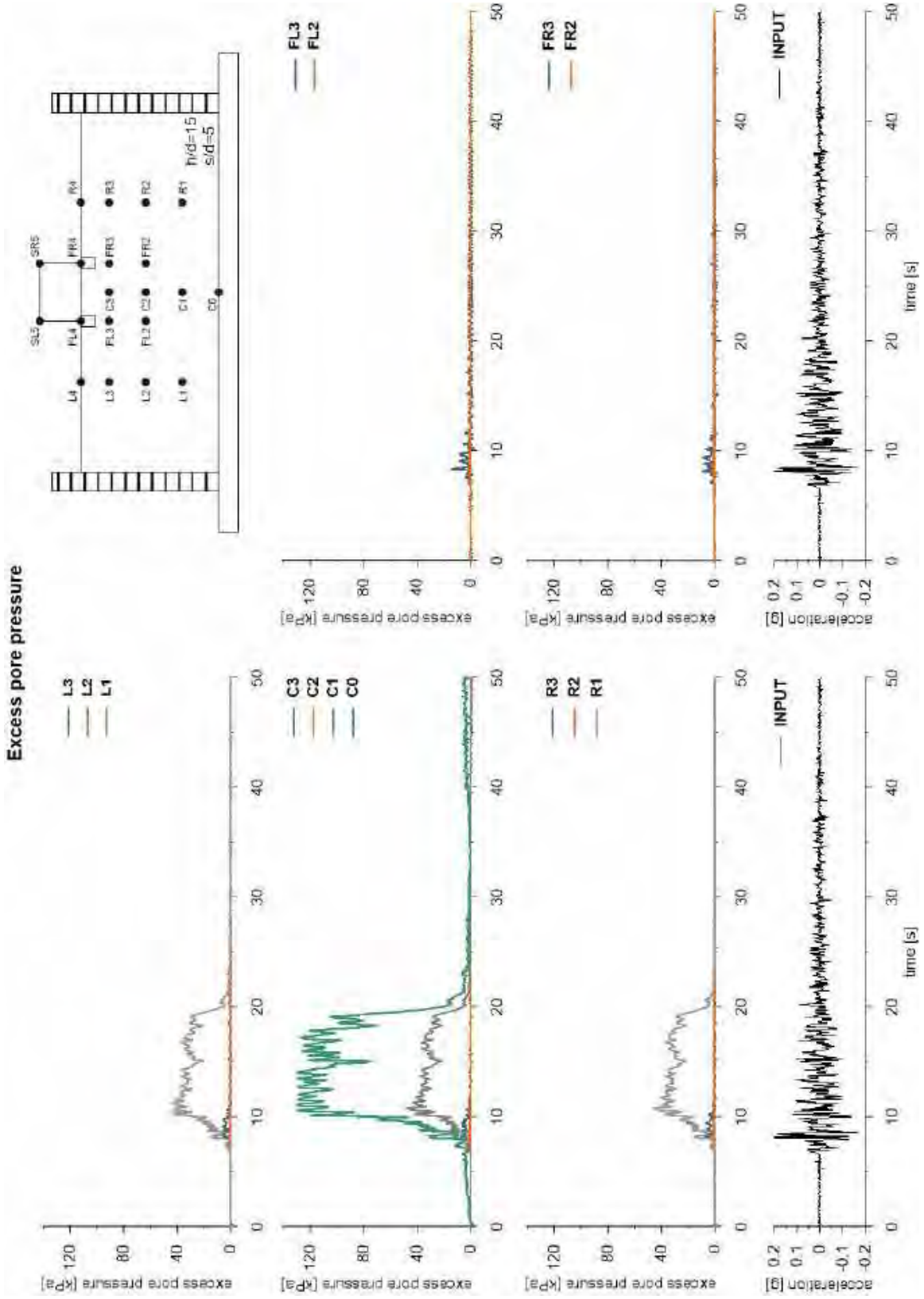

This project has received funding from the European Union's Horizon 2020 research and innovation programme under grant agreement No. 700748

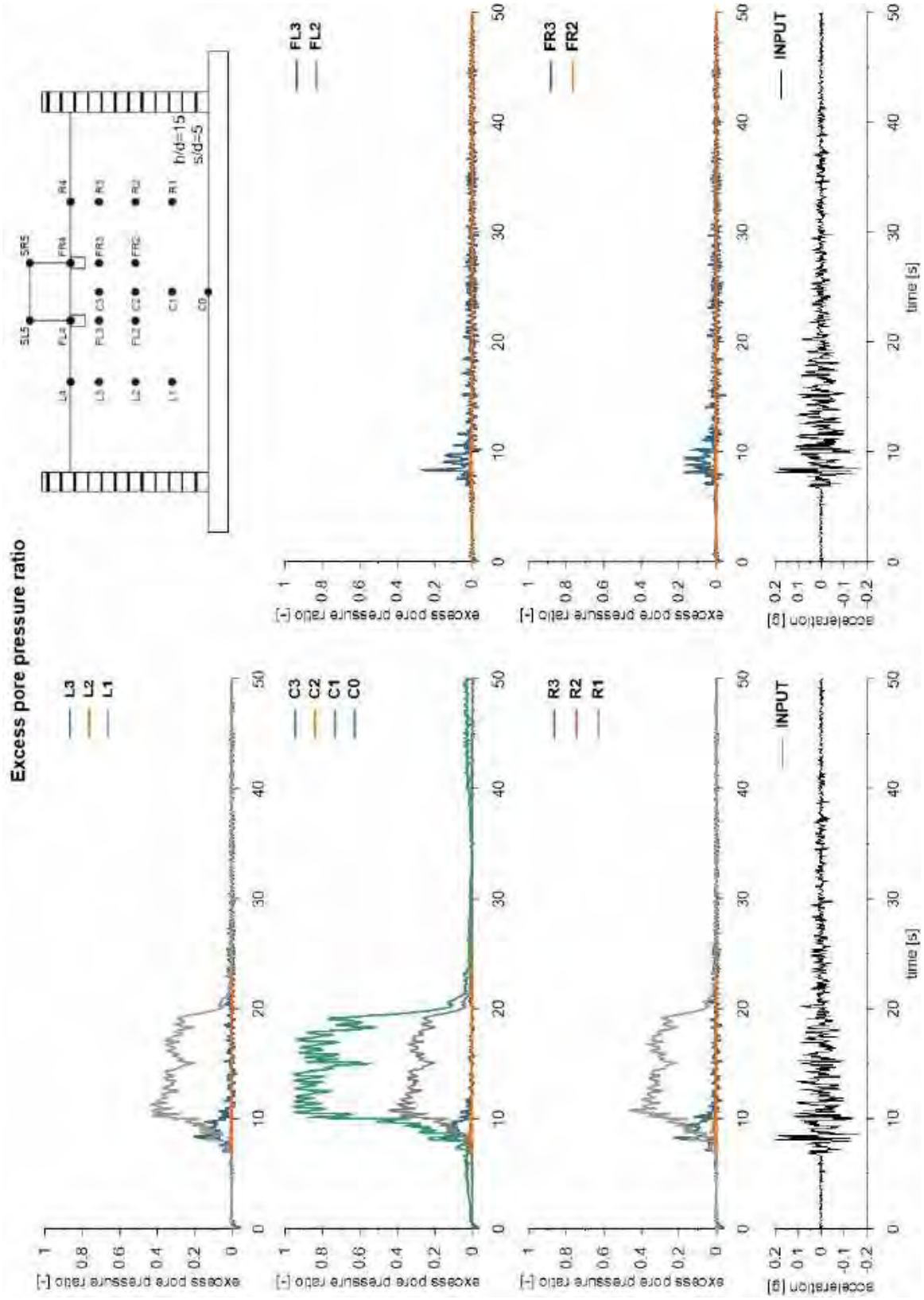

This project has received funding from the European Union's Horizon 2020 research and innovation programme under grant agreement No. 700748

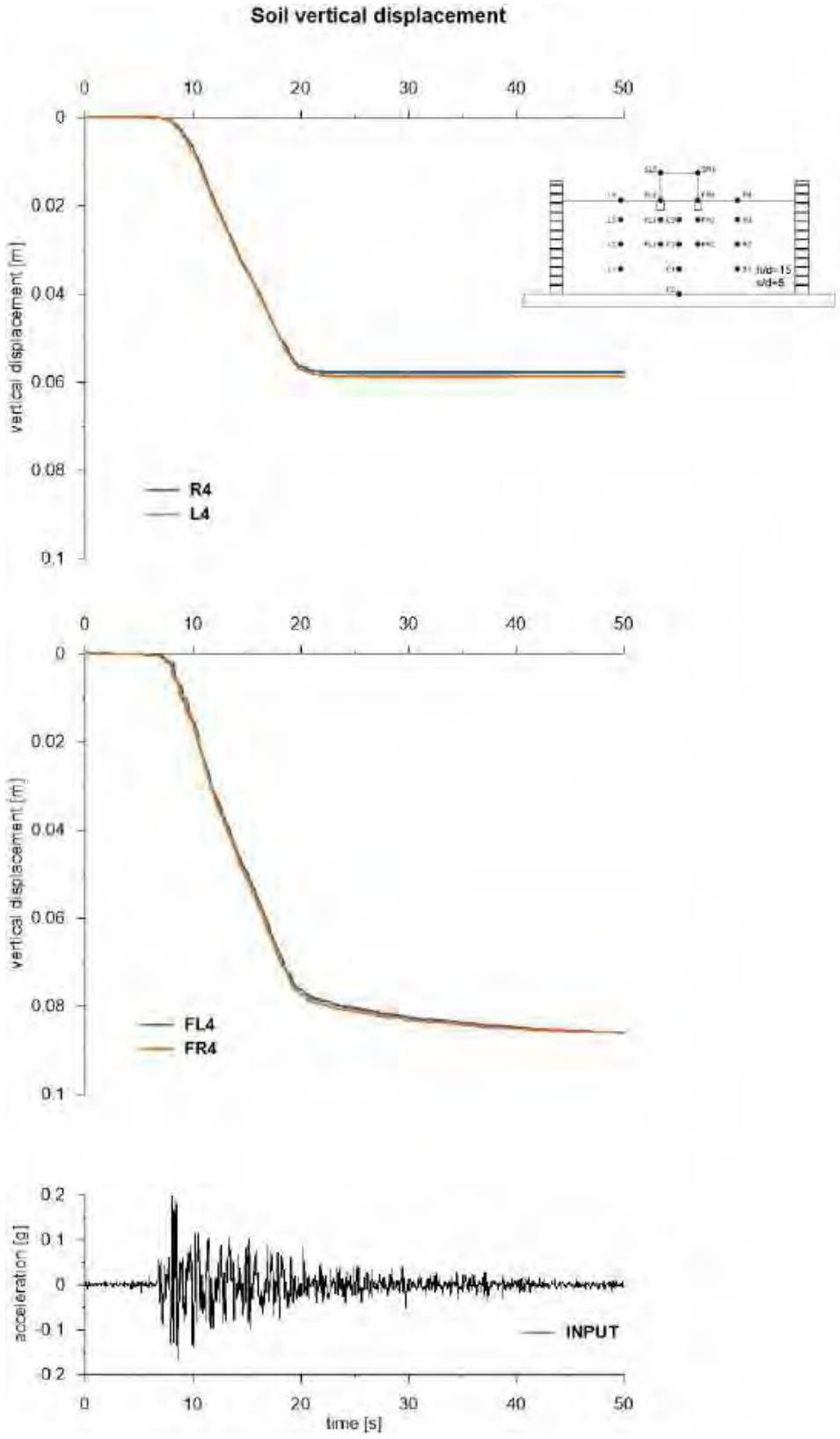

This project has received funding from the European Union's Horizon 2020 research and innovation programme under grant agreement No. 700748

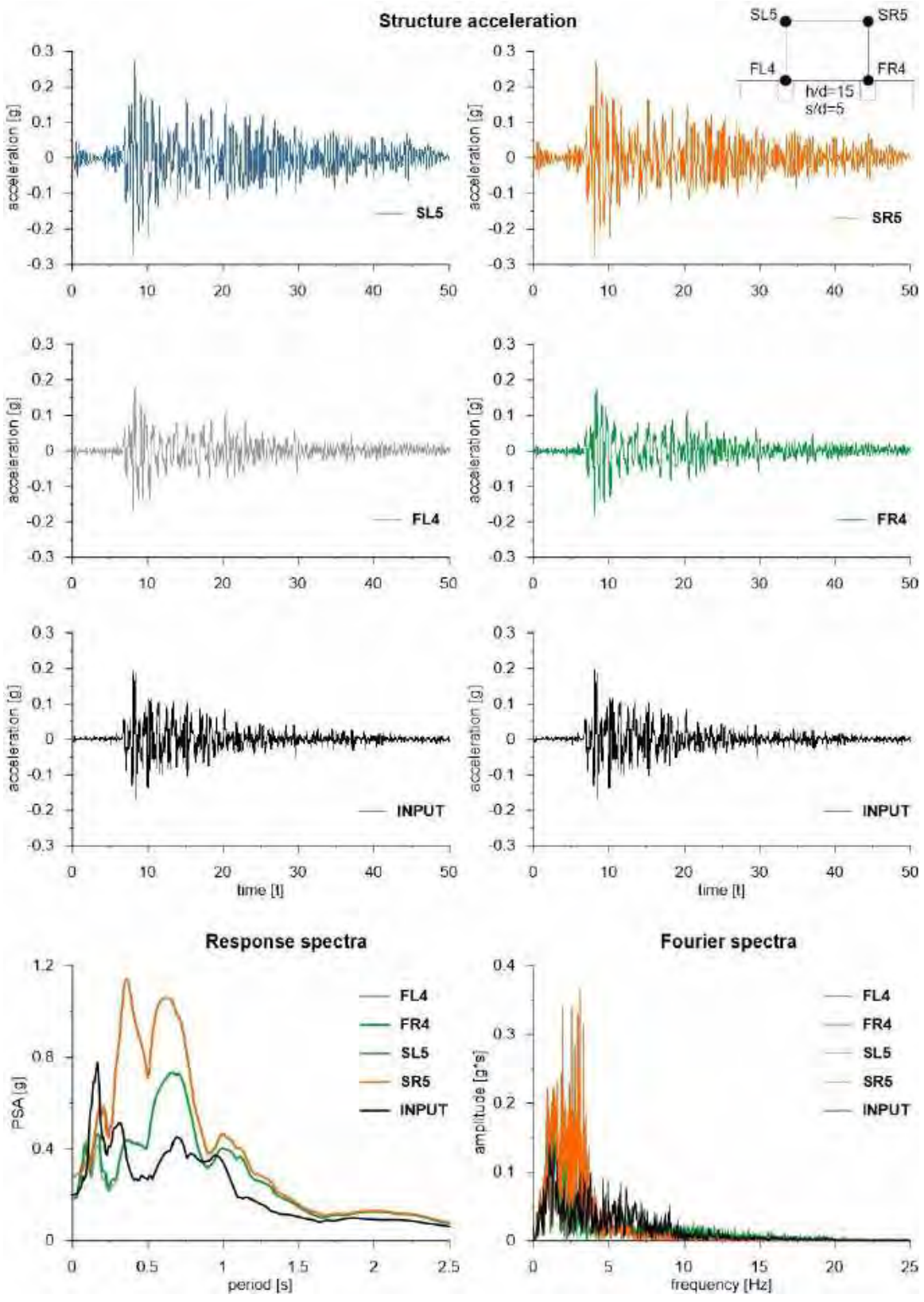

This project has received funding from the European Union's Horizon 2020 research and innovation programme under grant agreement No. 700748

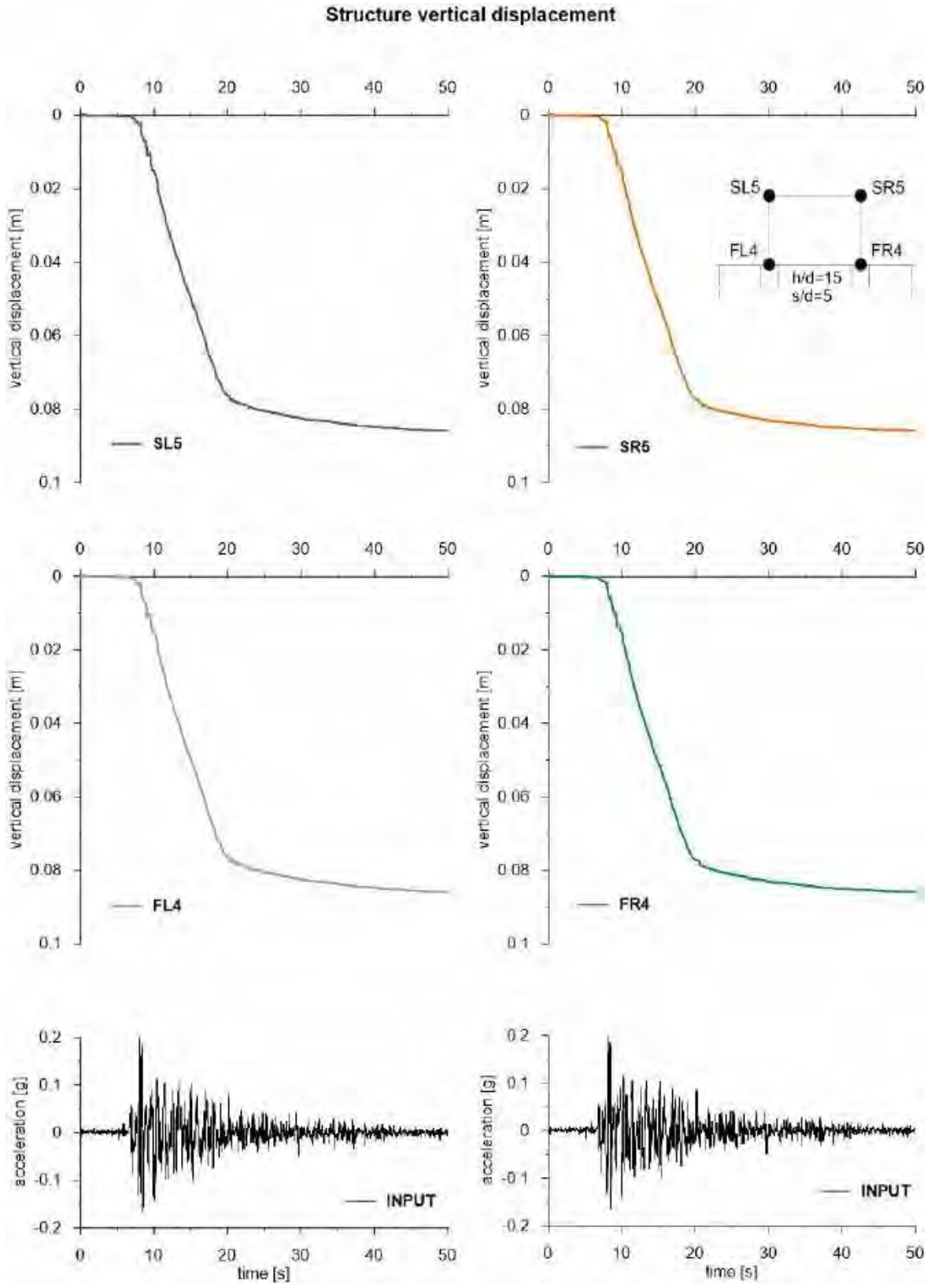

This project has received funding from the European Union's Horizon 2020 research and innovation programme under grant agreement No. 700748

6.1.1.34 ID: SS_HDU_H15_s10

The model consists of a homogenous soil profile of Ticino sand. The ground motion applied was the number 31.

ID: SS_HDU_H15_s10

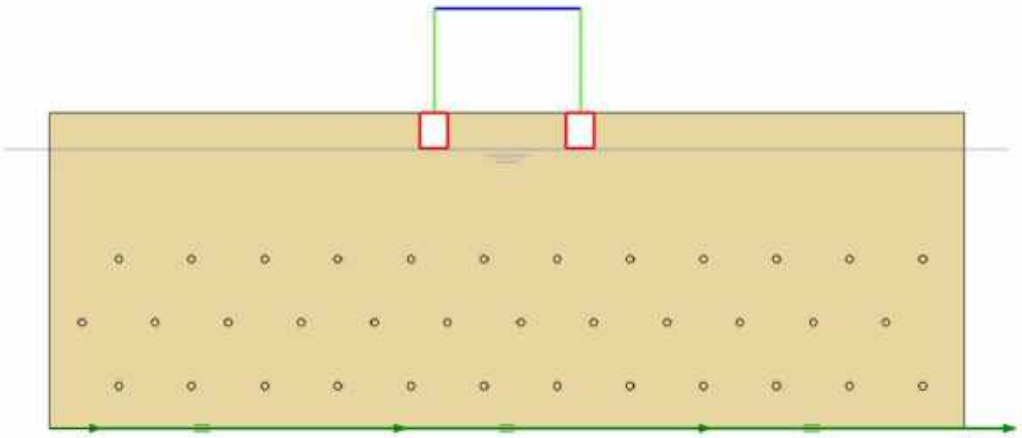

Layouts of the model reproduced in Plaxis 2D

This project has received funding from the European Union's Horizon 2020 research and innovation programme under grant agreement No. 700748

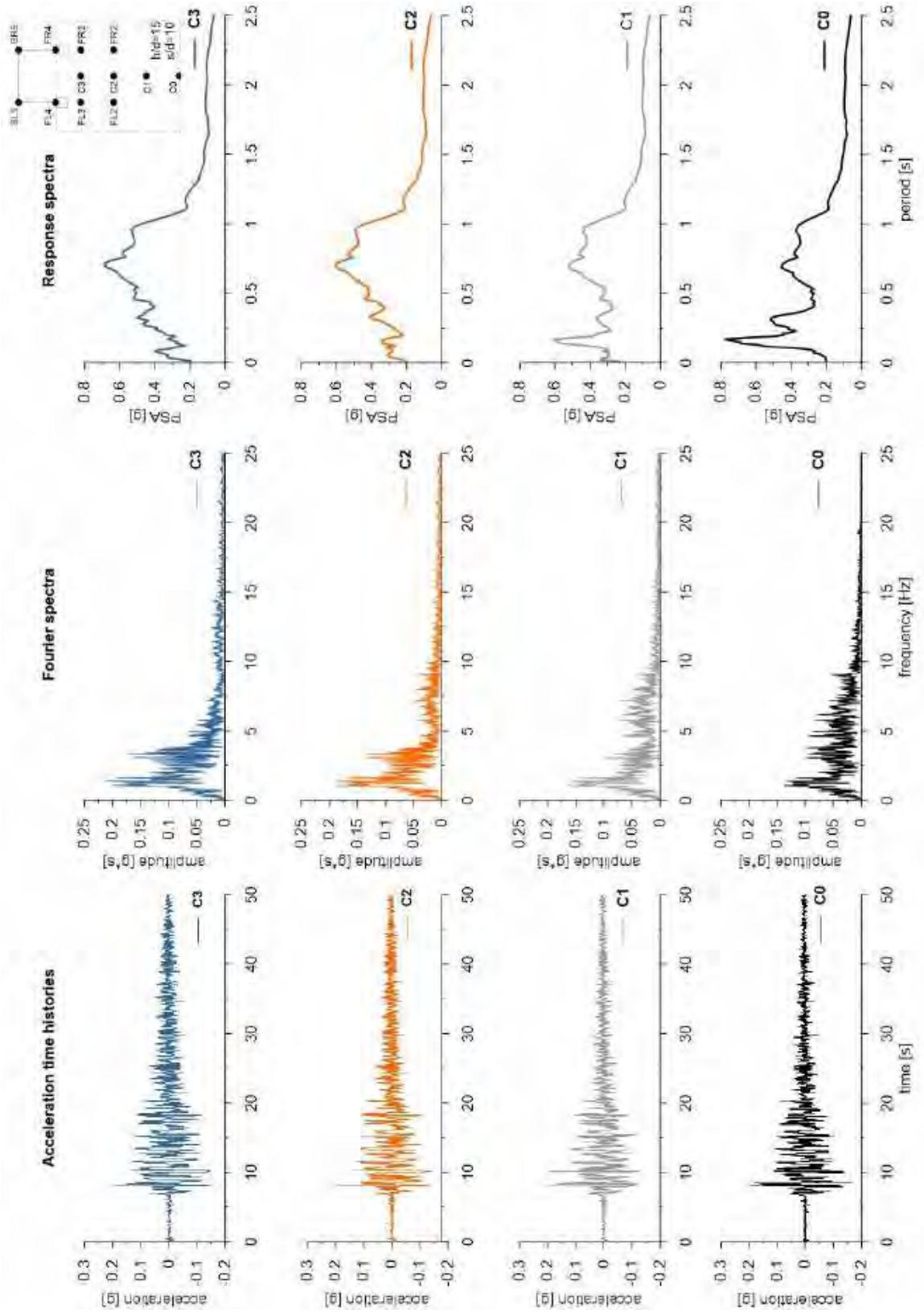

This project has received funding from the European Union's Horizon 2020 research and innovation programme under grant agreement No. 700748

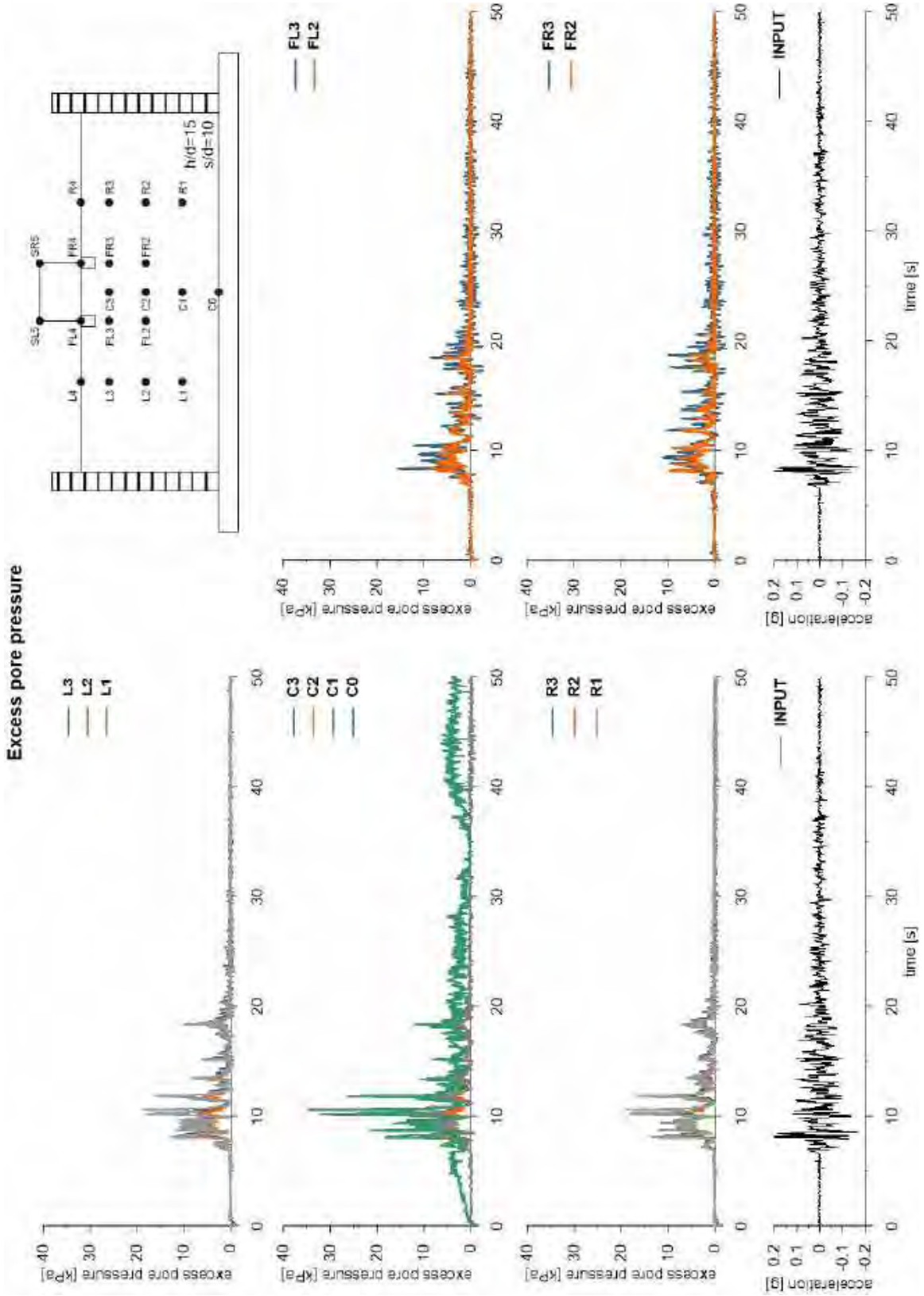

This project has received funding from the European Union's Horizon 2020 research and innovation programme under grant agreement No. 700748

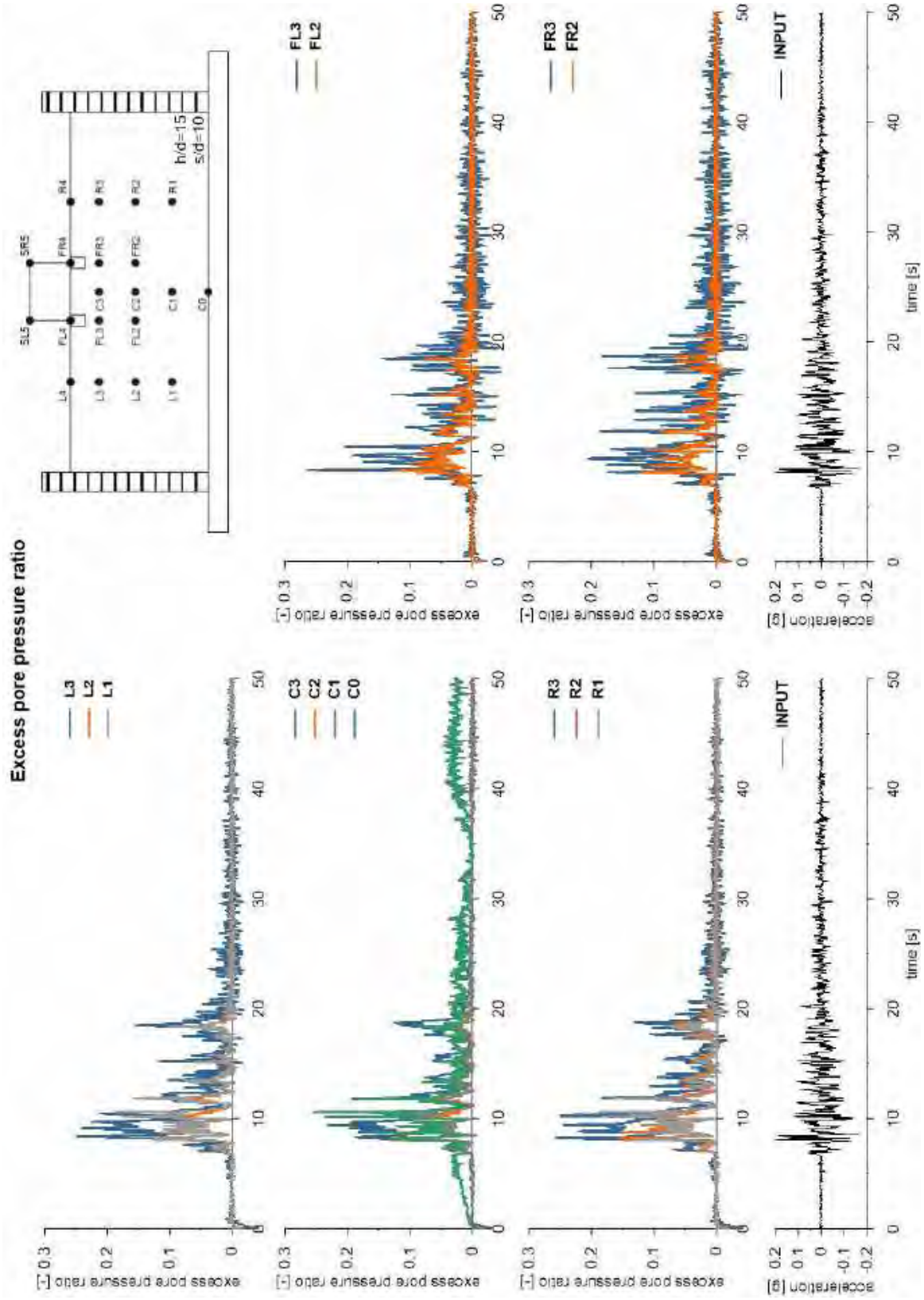

This project has received funding from the European Union's Horizon 2020 research and innovation programme under grant agreement No. 700748

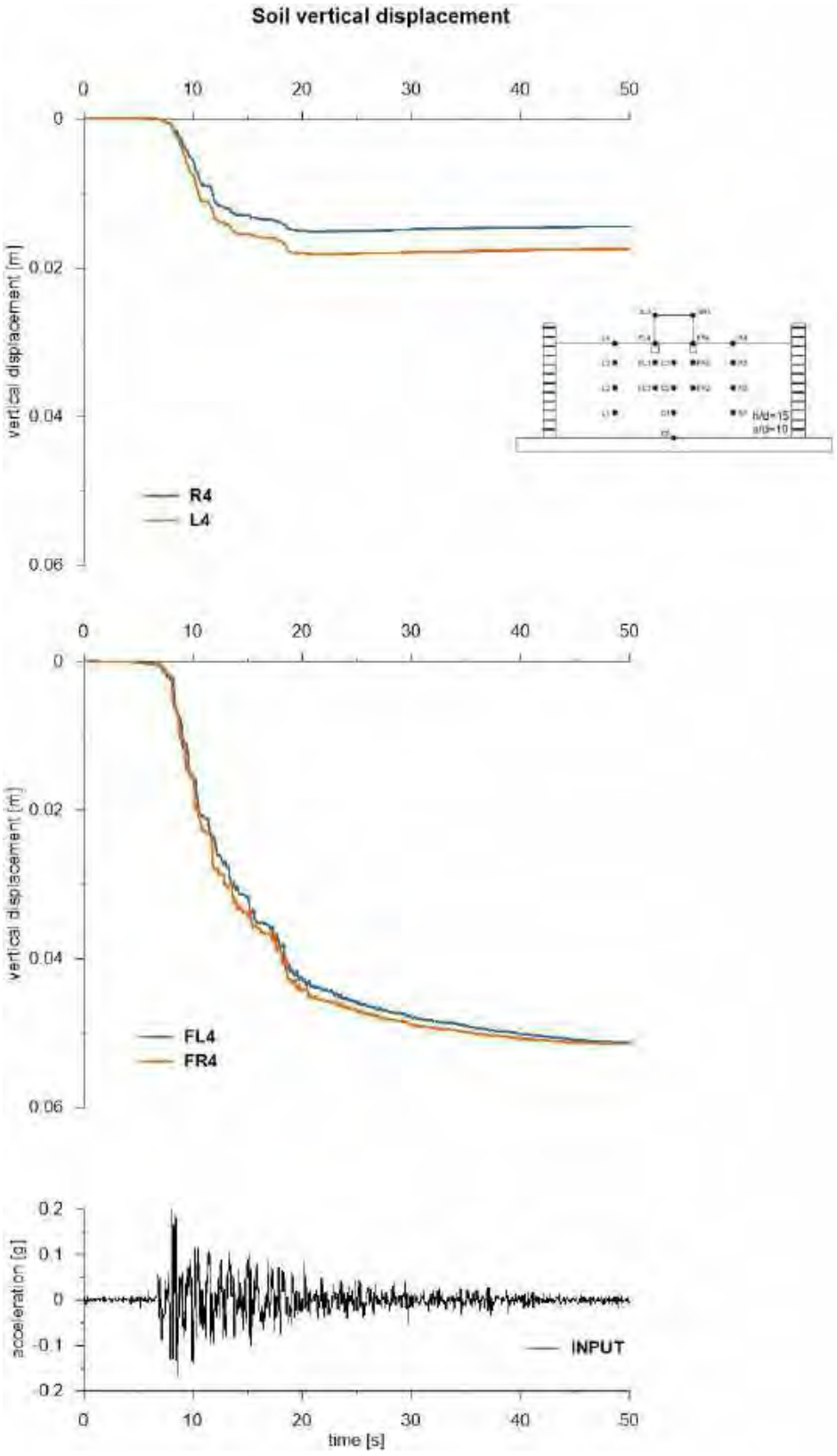

This project has received funding from the European Union's Horizon 2020 research and innovation programme under grant agreement No. 700748

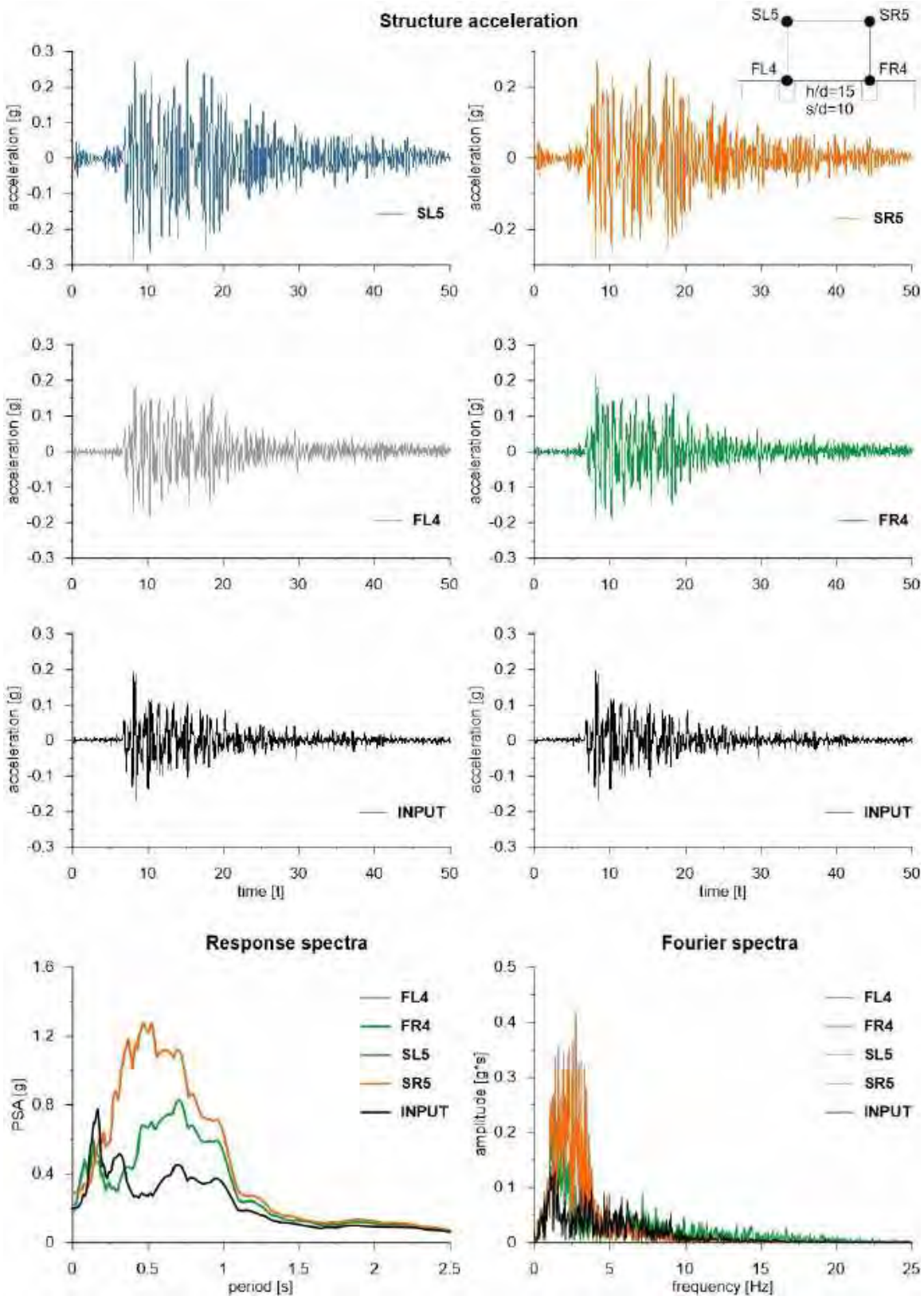

This project has received funding from the European Union's Horizon 2020 research and innovation programme under grant agreement No. 700748

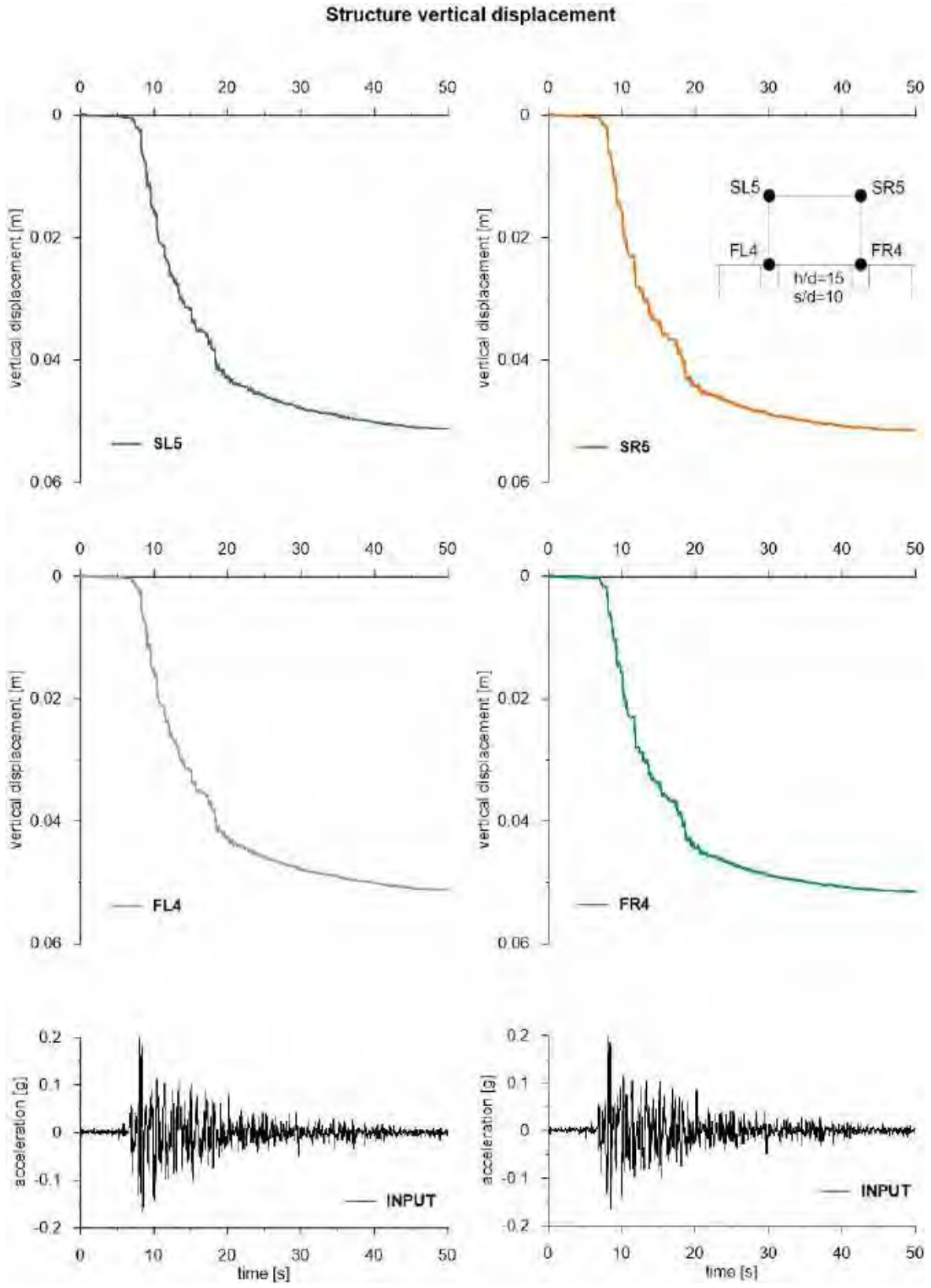

This project has received funding from the European Union's Horizon 2020 research and innovation programme under grant agreement No. 700748

6.1.1.35 ID: SS_HDU_H15_s15

The model consists of a homogenous soil profile of Ticino sand. The ground motion applied was the number 31.

ID: SS_HDU_H15_s15

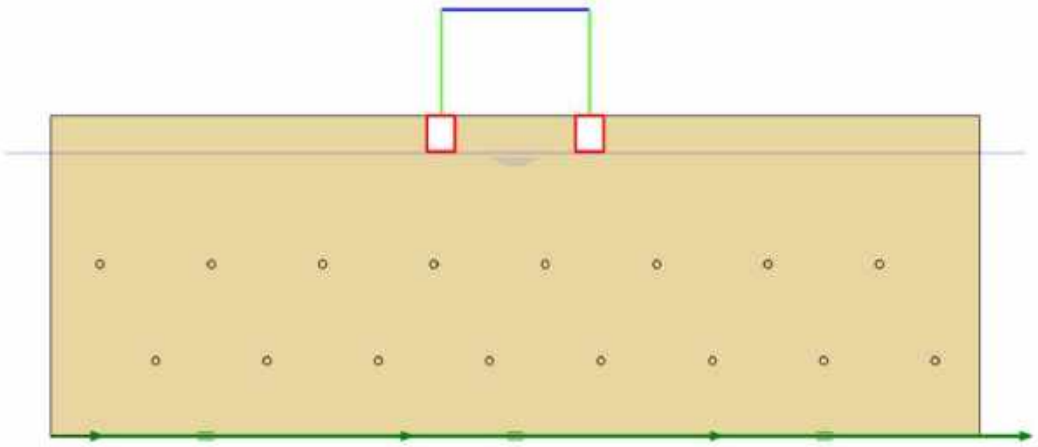

Layouts of the model reproduced in Plaxis 2D

This project has received funding from the European Union's Horizon 2020 research and innovation programme under grant agreement No. 700748

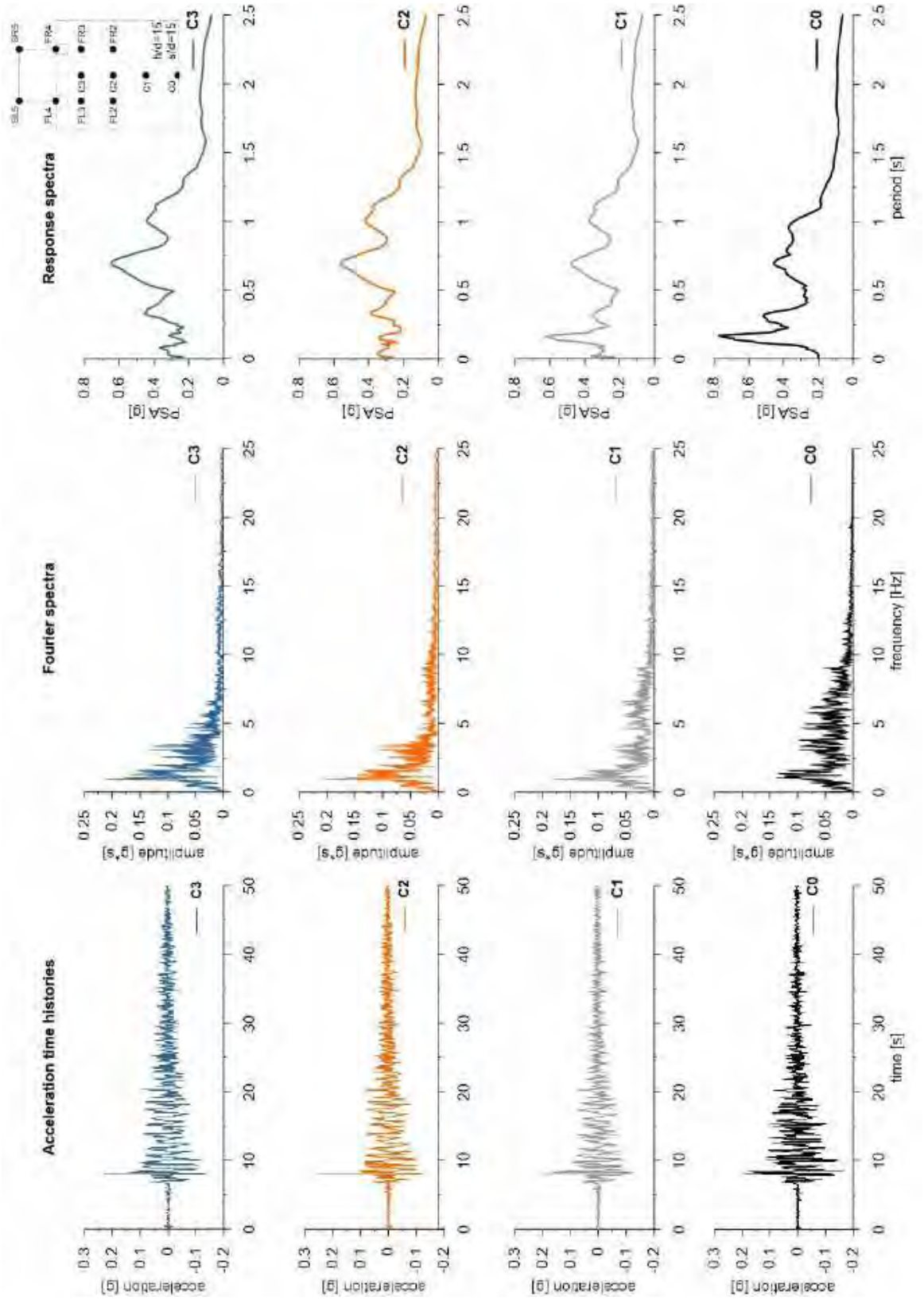

This project has received funding from the European Union's Horizon 2020 research and innovation programme under grant agreement No. 700748

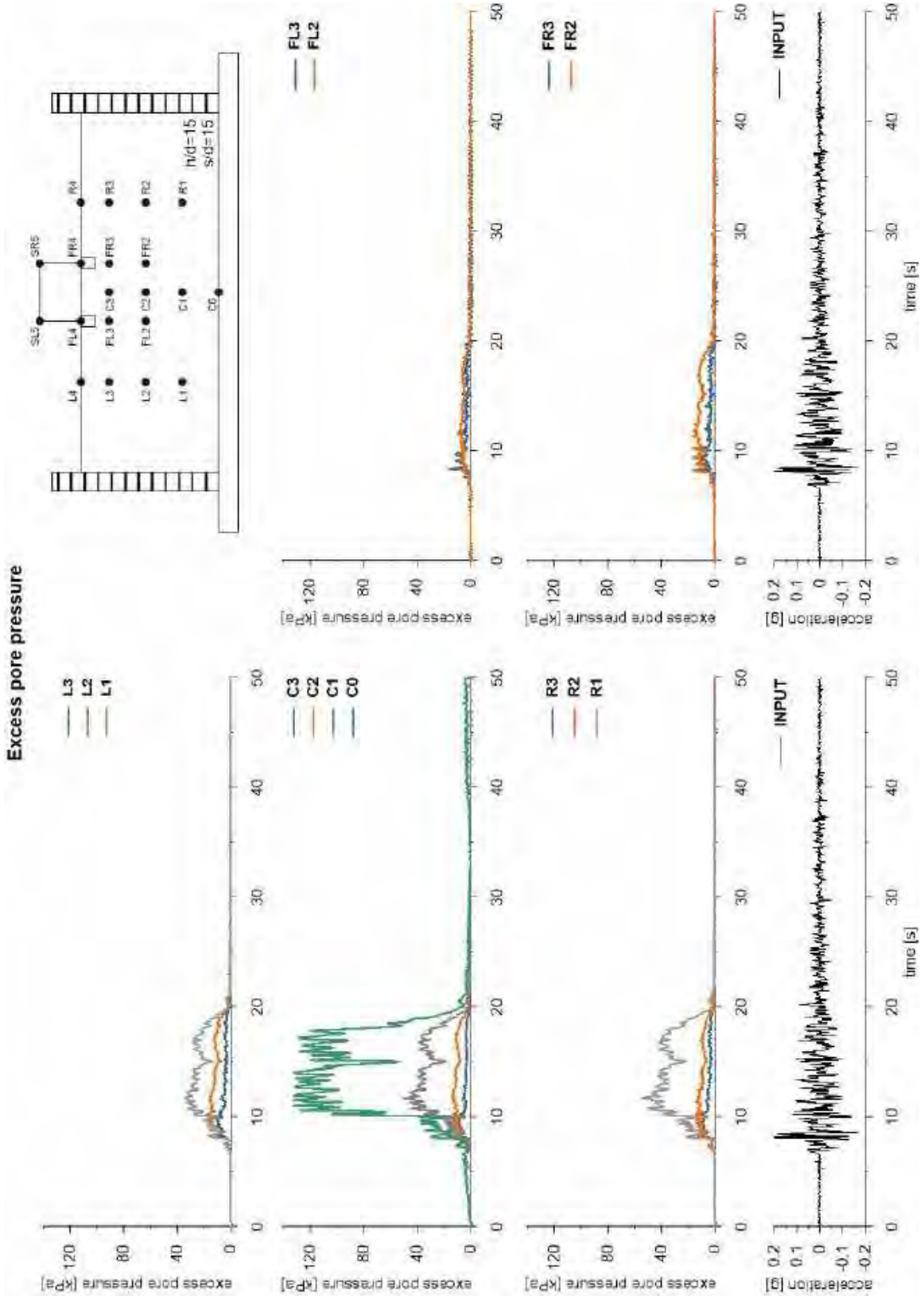

This project has received funding from the European Union's Horizon 2020 research and innovation programme under grant agreement No. 700748

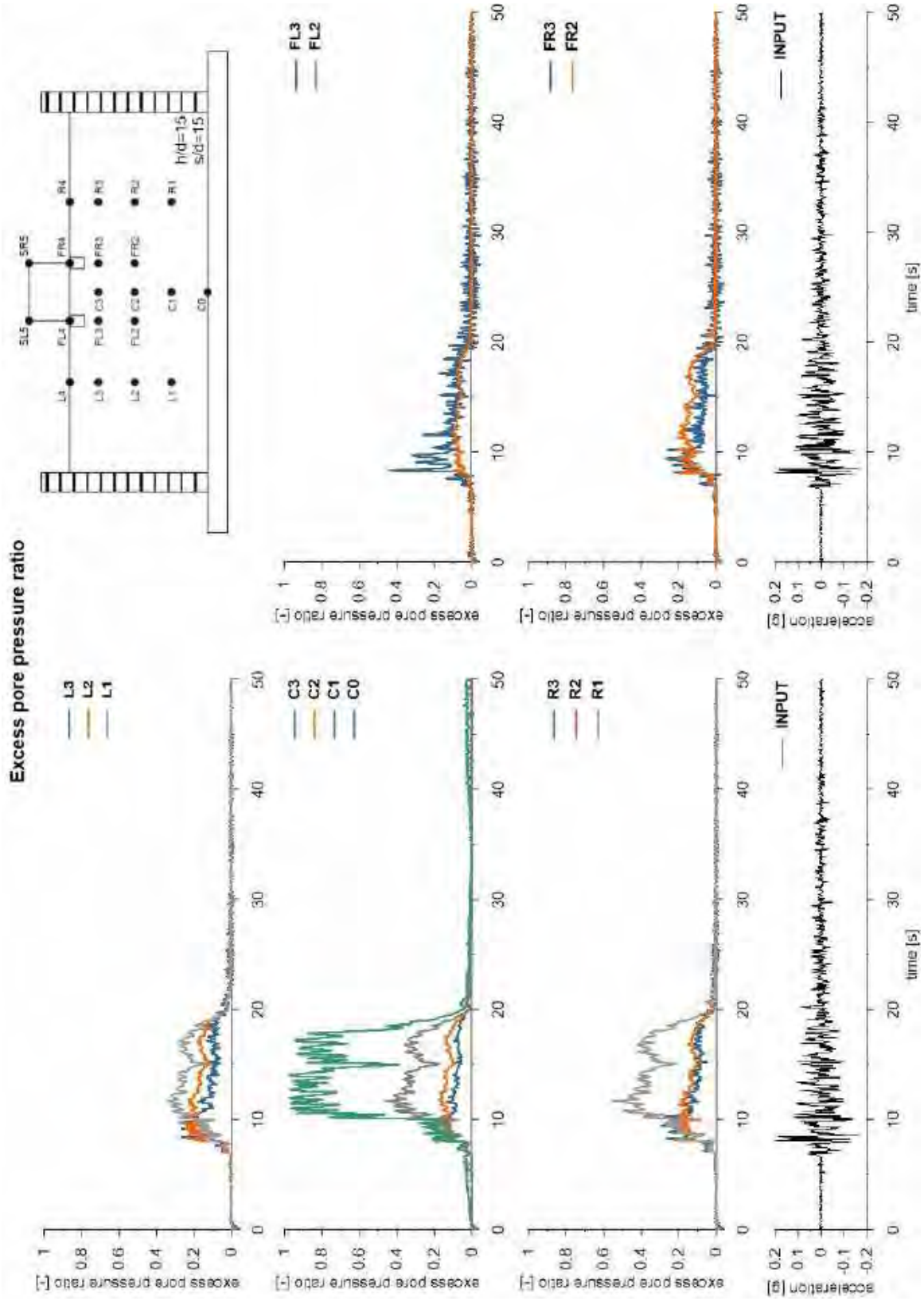

This project has received funding from the European Union's Horizon 2020 research and innovation programme under grant agreement No. 700748

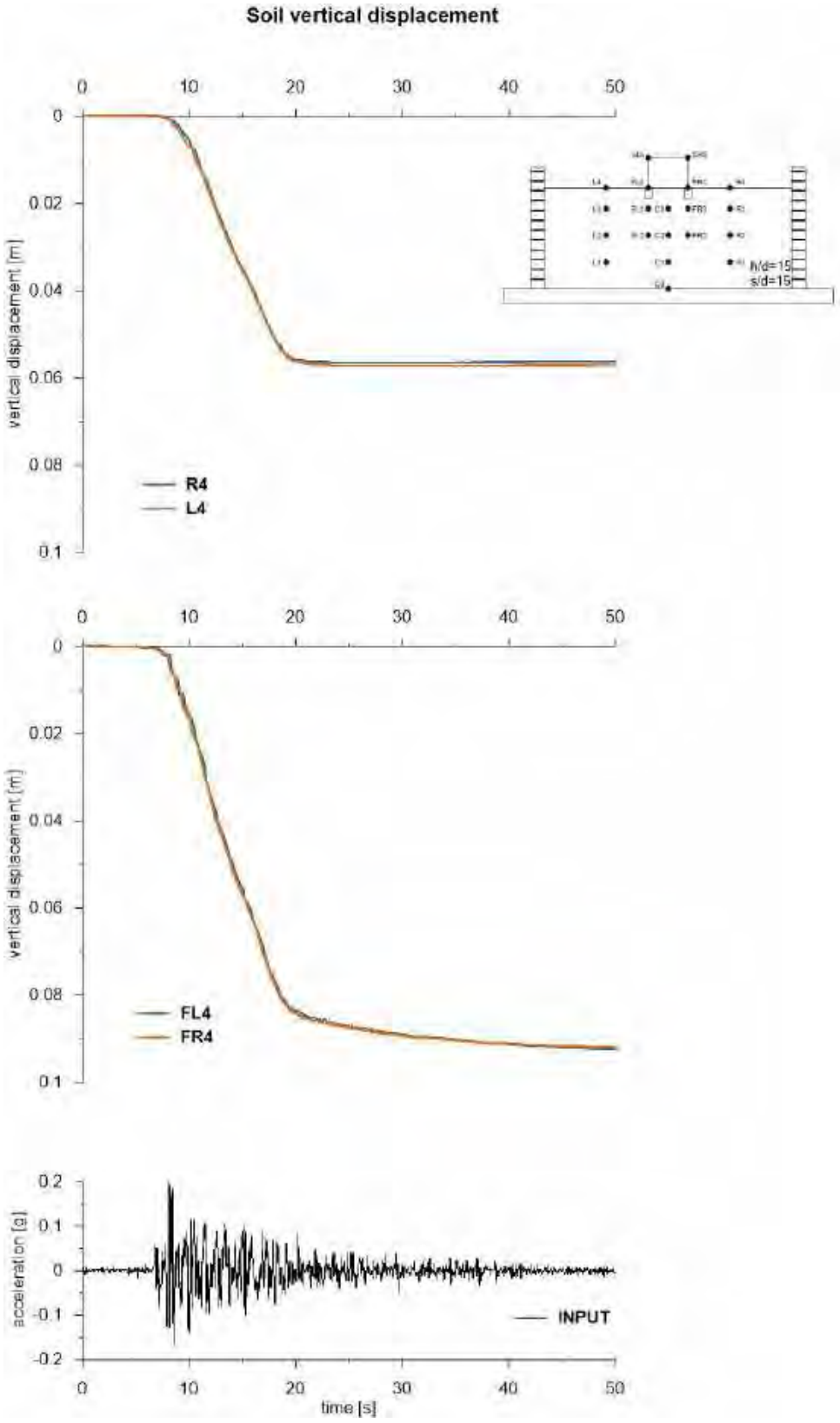

This project has received funding from the European Union's Horizon 2020 research and innovation programme under grant agreement No. 700748

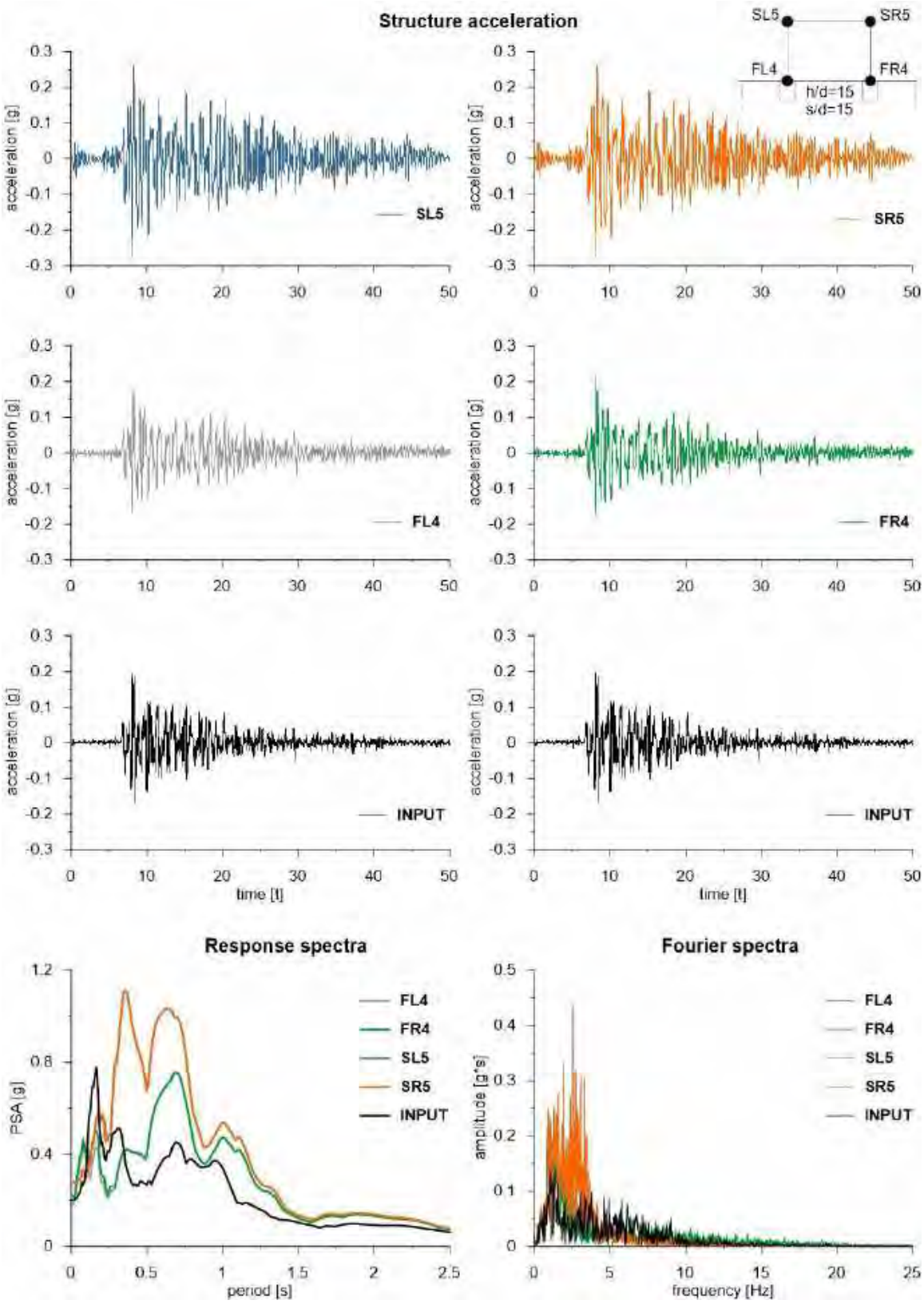

This project has received funding from the European Union's Horizon 2020 research and innovation programme under grant agreement No. 700748

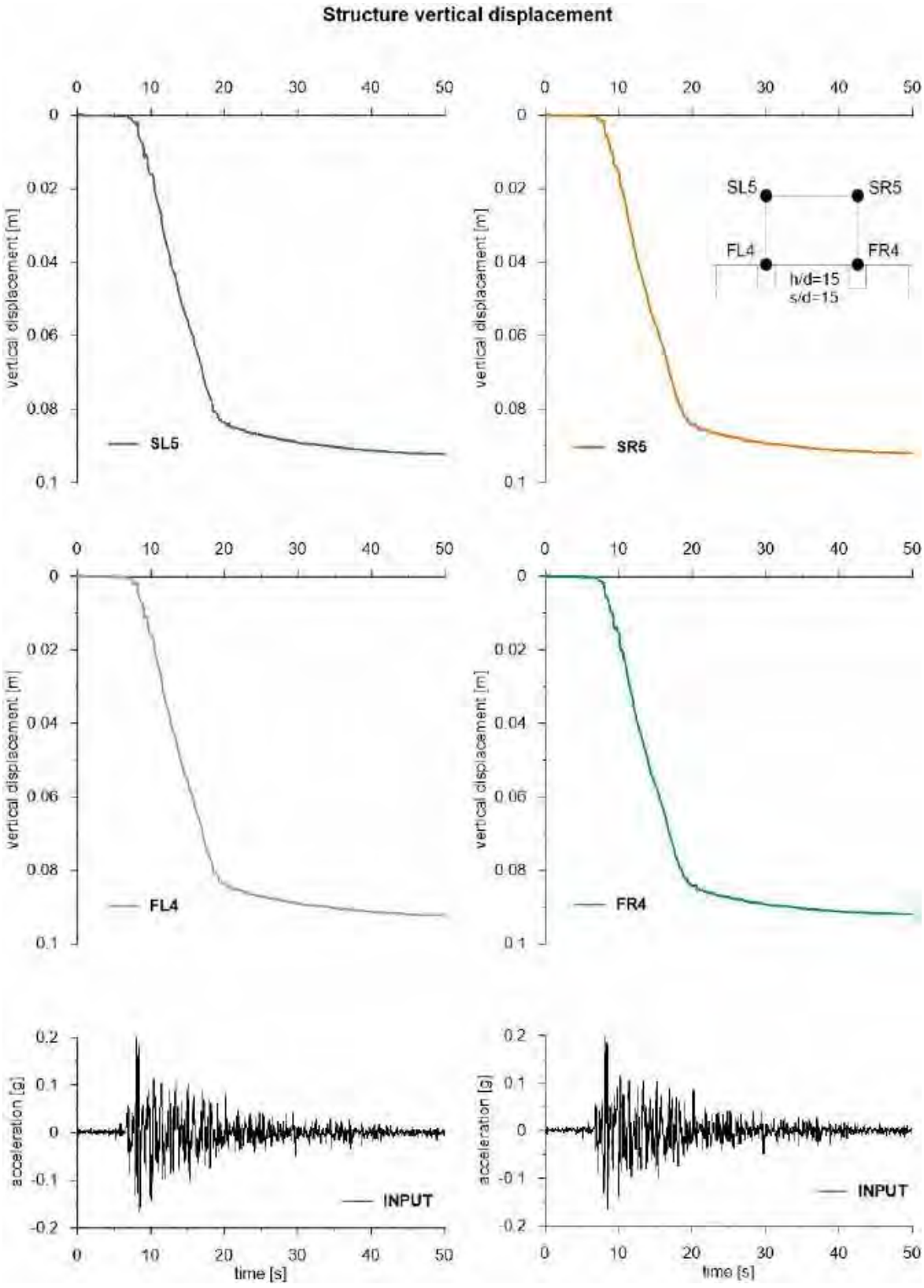

This project has received funding from the European Union's Horizon 2020 research and innovation programme under grant agreement No. 700748

6.1.1.36 ID: SS_HDU_H05_s05

The model consists of a double soil profile of clay and Ticino sand. The ground motion applied was the number 31.

ID: SS_HDU_H05_s05

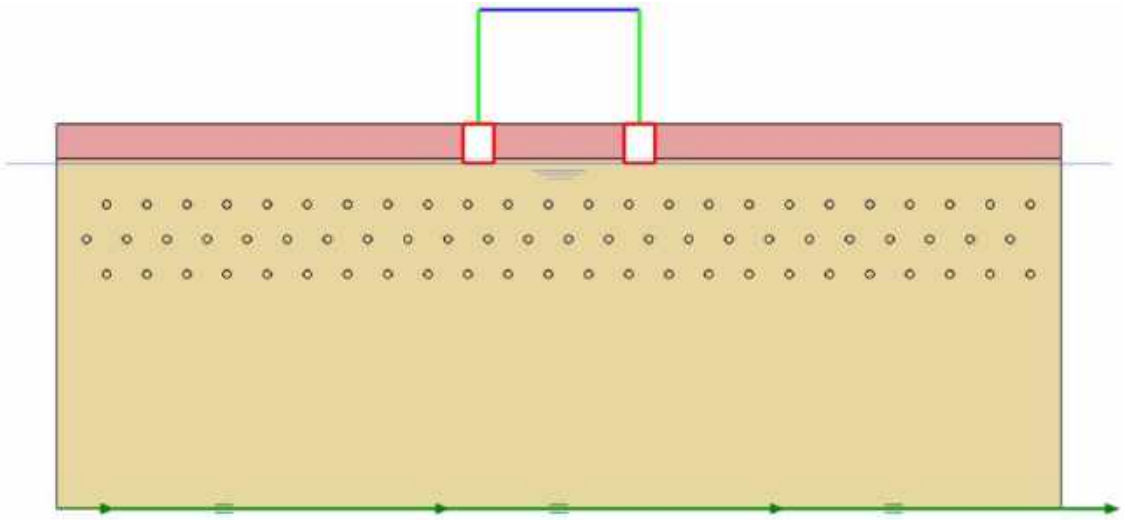

Layouts of the model reproduced in Plaxis 2D

This project has received funding from the European Union's Horizon 2020 research and innovation programme under grant agreement No. 700748

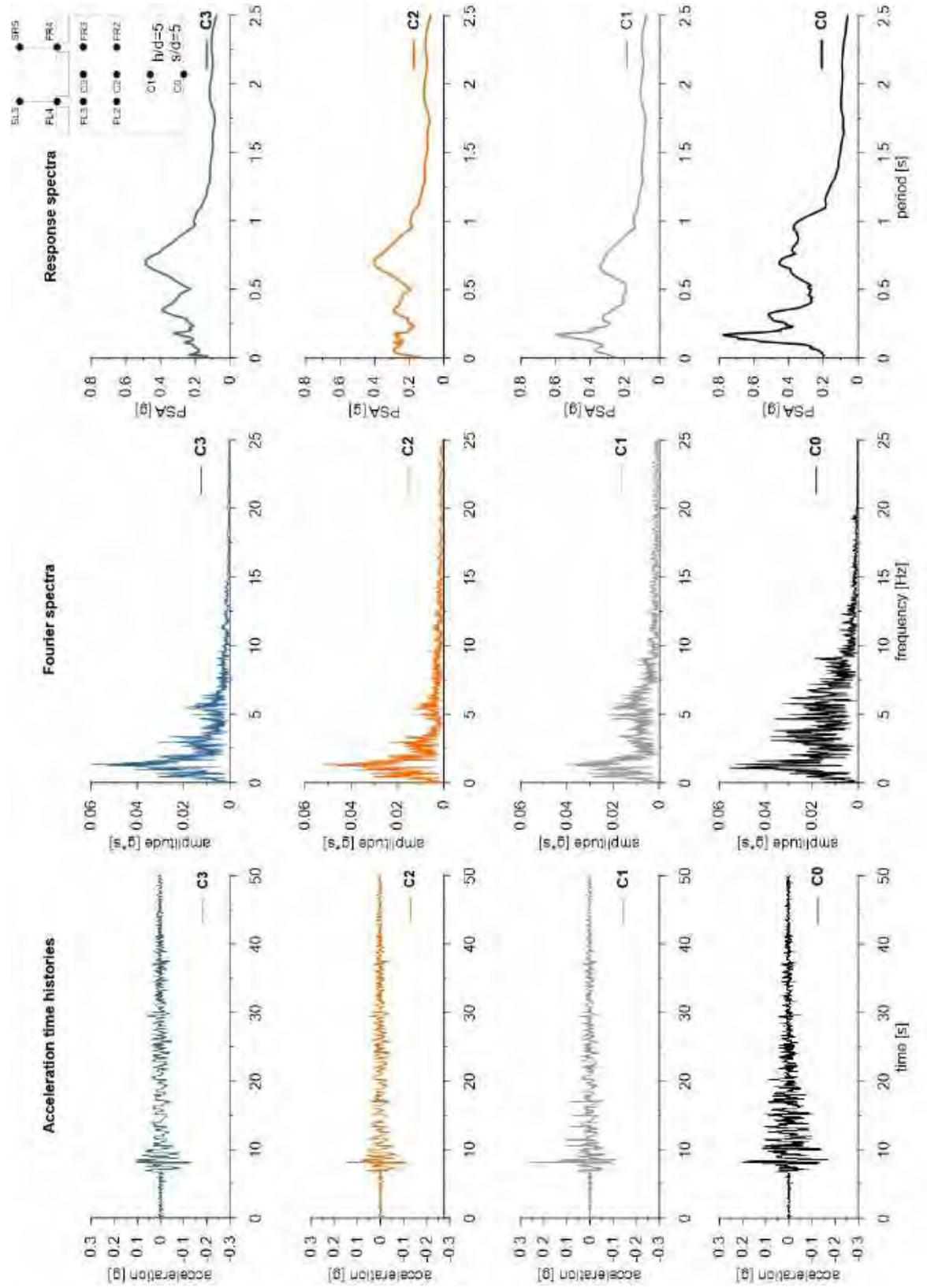

This project has received funding from the European Union's Horizon 2020 research and innovation programme under grant agreement No. 700748

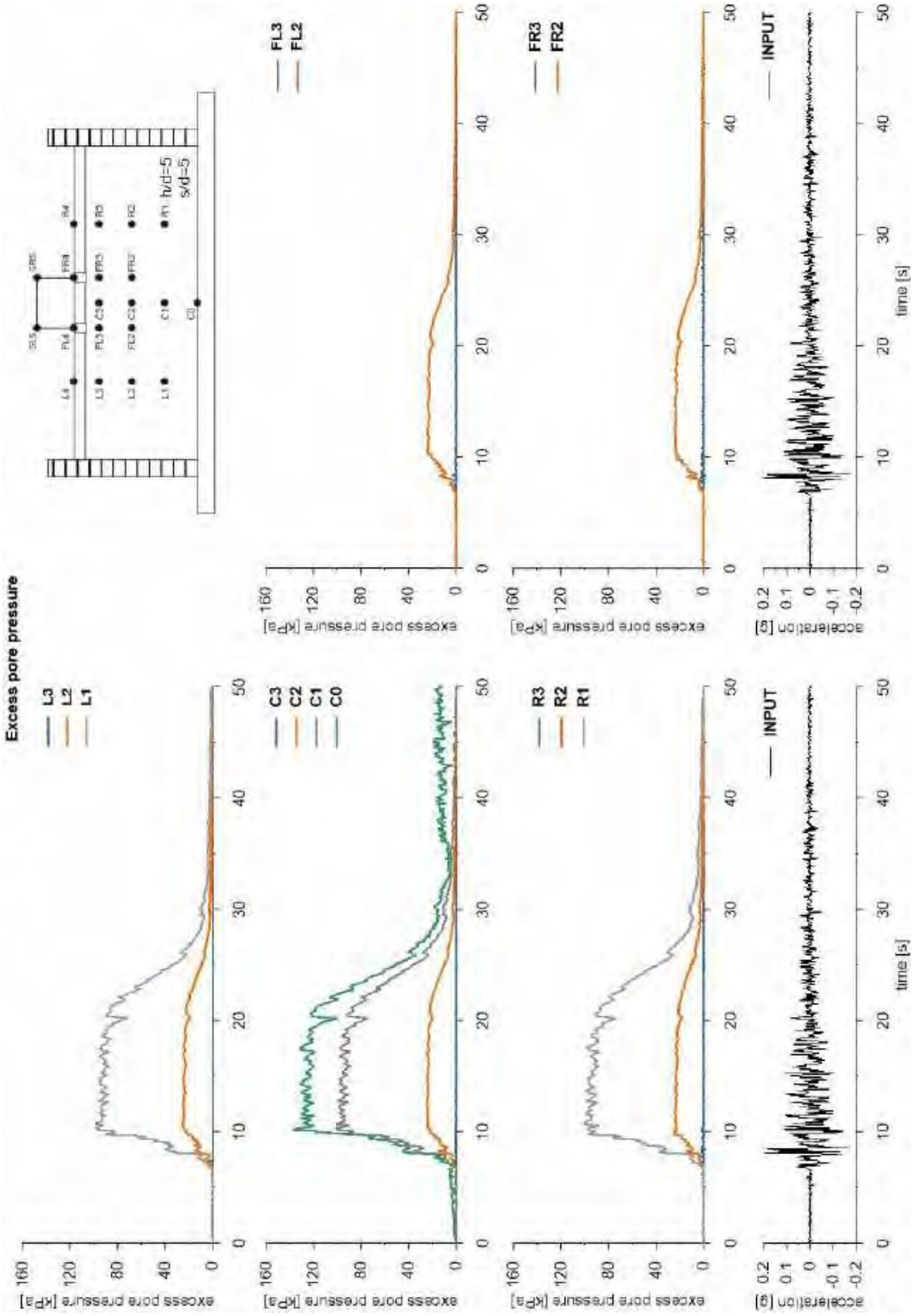

This project has received funding from the European Union's Horizon 2020 research and innovation programme under grant agreement No. 700748

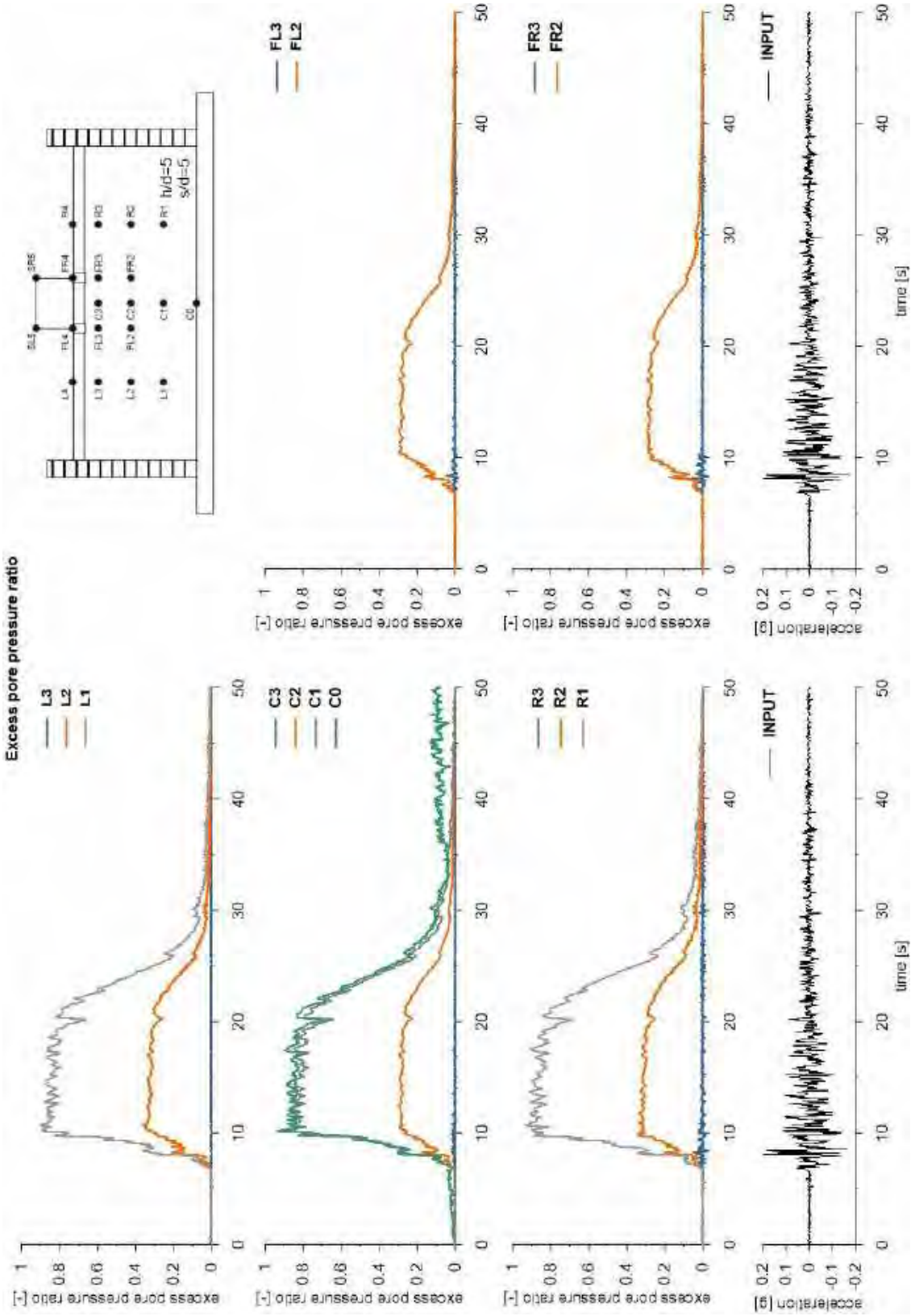

This project has received funding from the European Union's Horizon 2020 research and innovation programme under grant agreement No. 700748

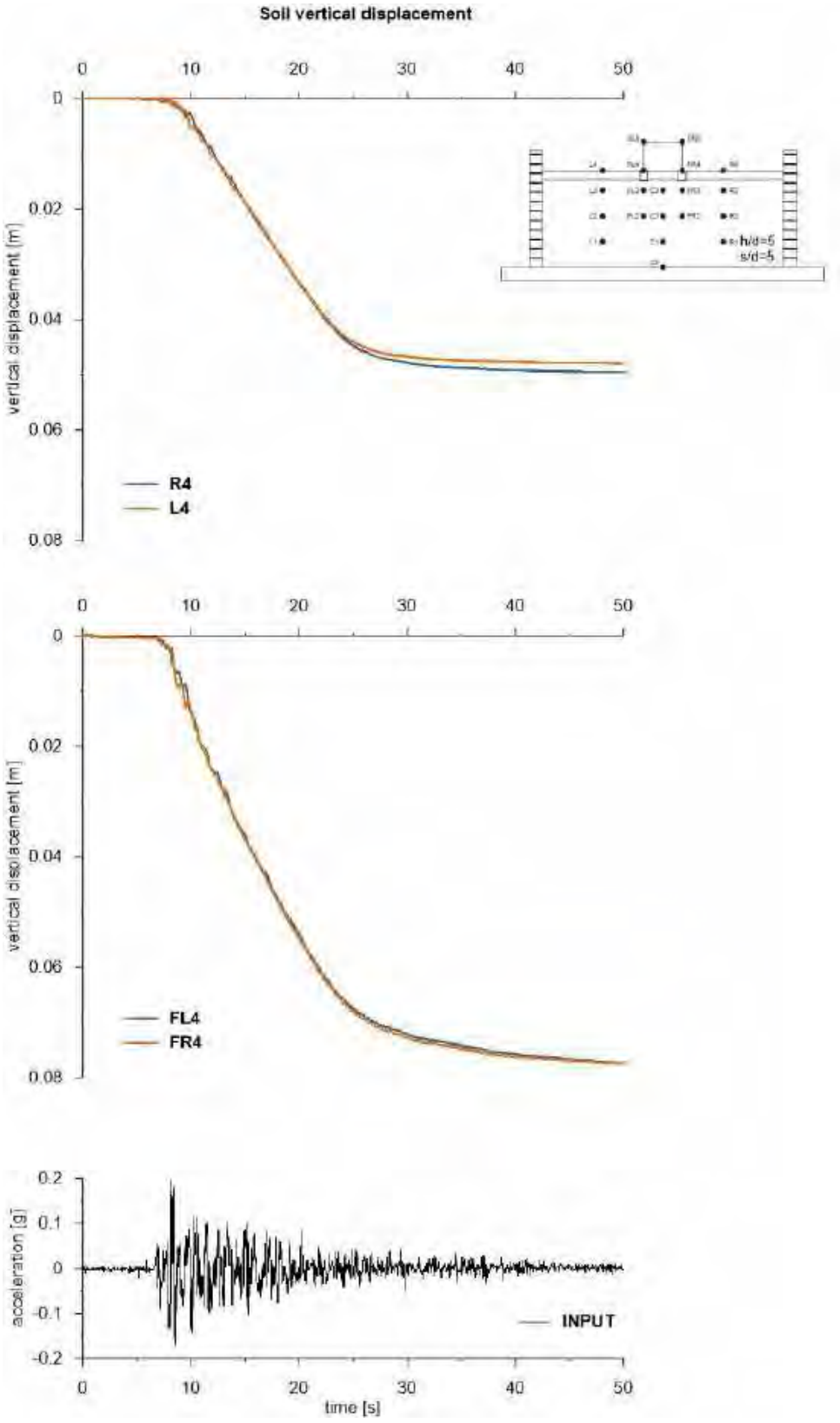

This project has received funding from the European Union's Horizon 2020 research and innovation programme under grant agreement No. 700748

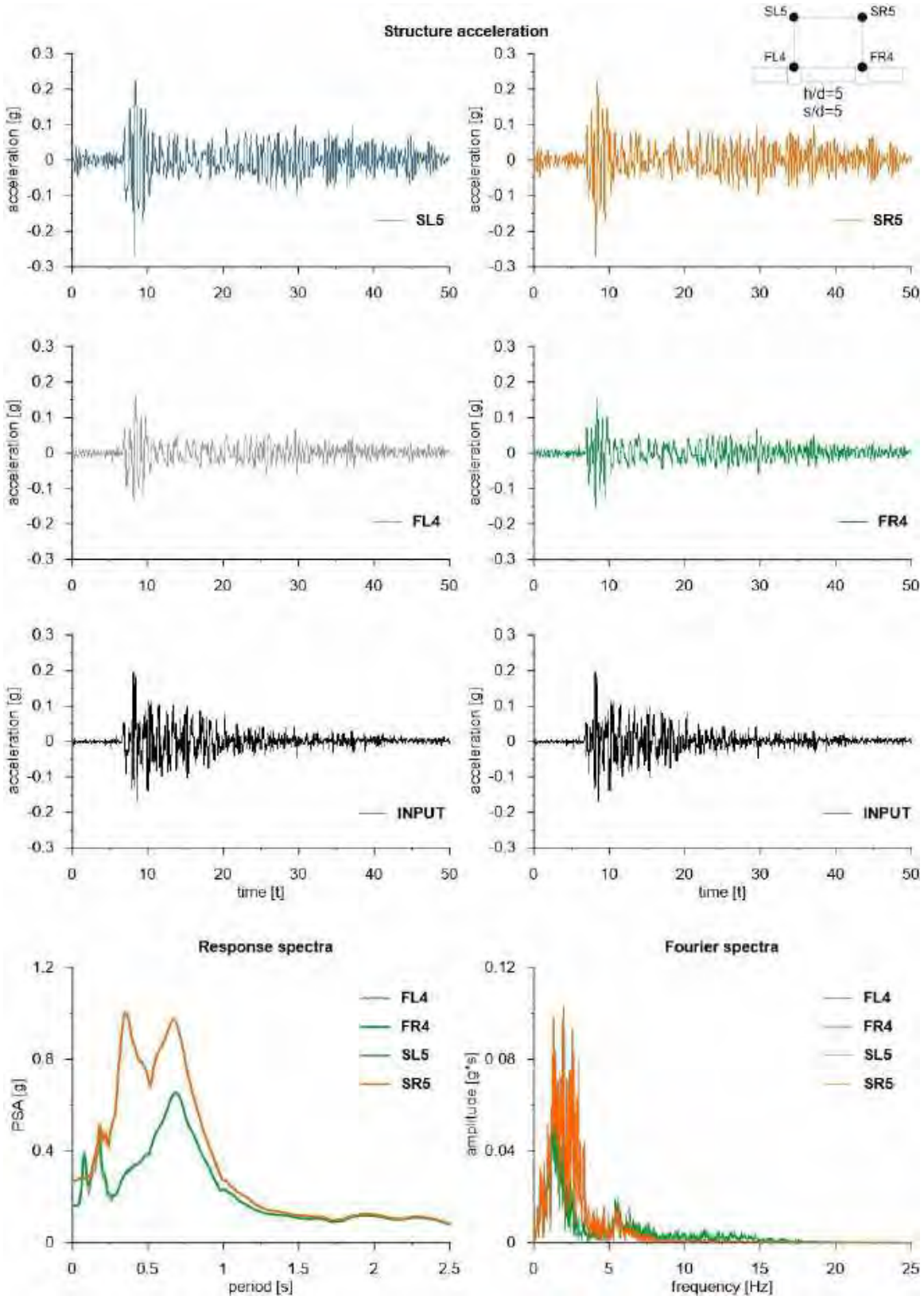

This project has received funding from the European Union's Horizon 2020 research and innovation programme under grant agreement No. 700748

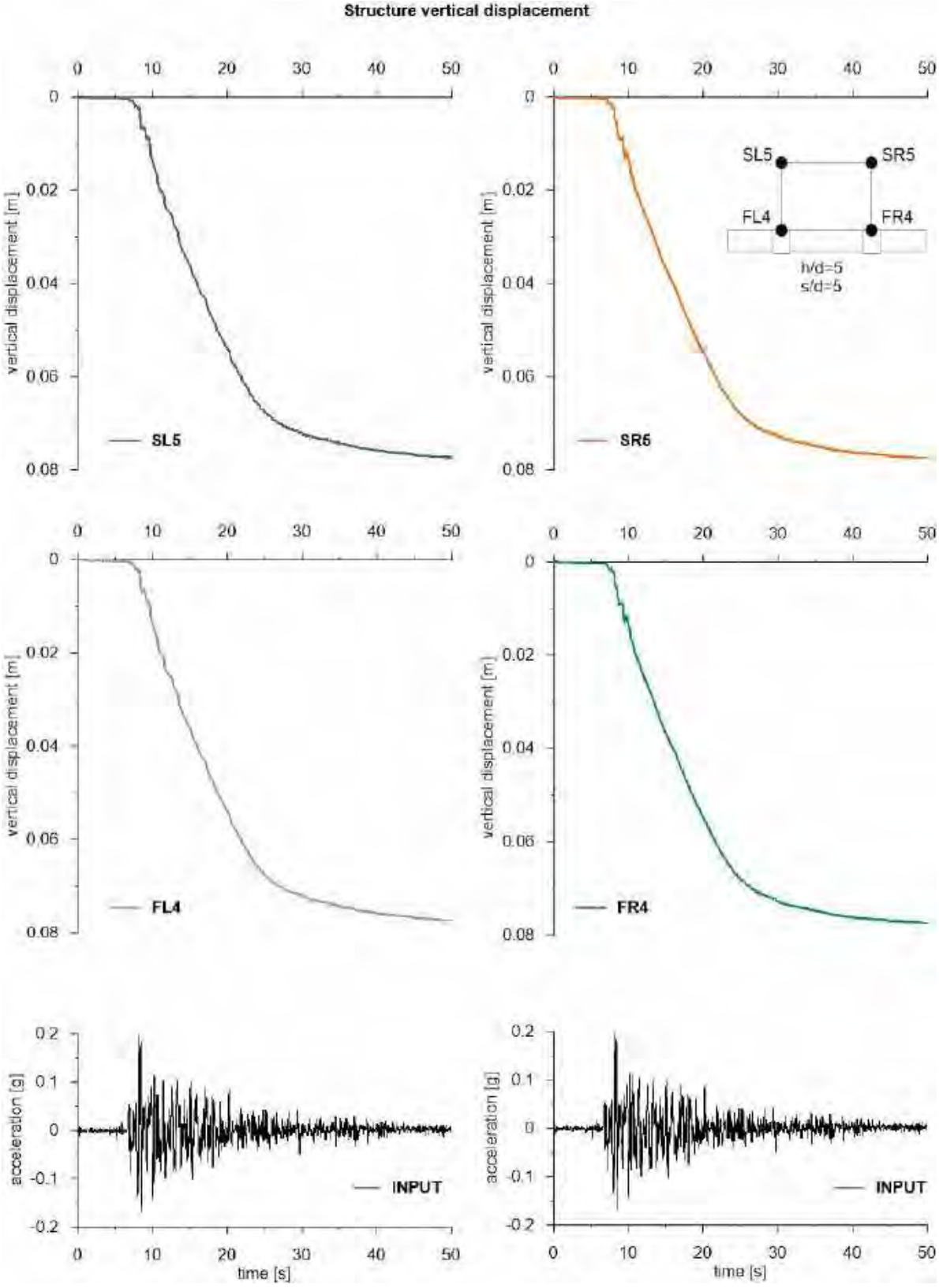

This project has received funding from the European Union's Horizon 2020 research and innovation programme under grant agreement No. 700748

6.1.1.37 ID: SS_HDU_H05_s10

The model consists of a double soil profile of clay and Ticino sand. The ground motion applied was the number 31.

ID: SS_HDU_H05_s10

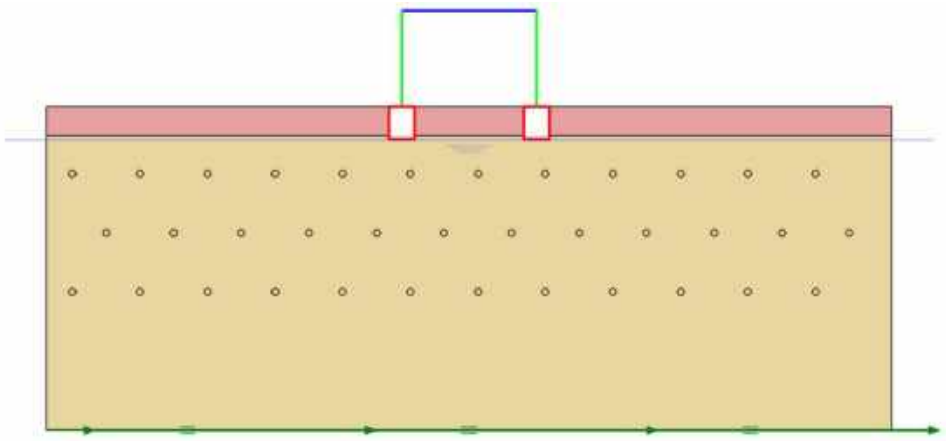

Layouts of the model reproduced in Plaxis 2D

This project has received funding from the European Union's Horizon 2020 research and innovation programme under grant agreement No. 700748

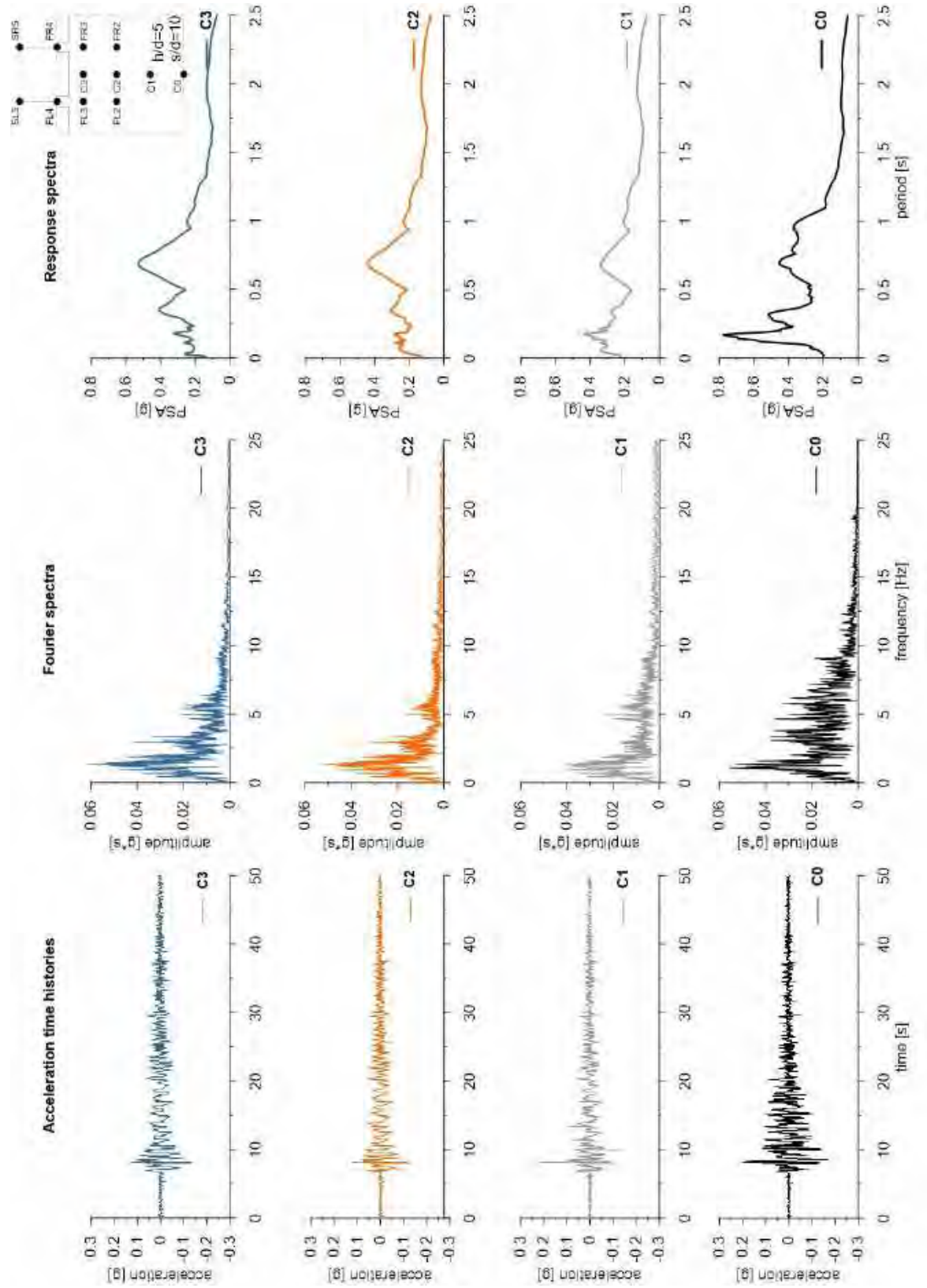

This project has received funding from the European Union's Horizon 2020 research and innovation programme under grant agreement No. 700748

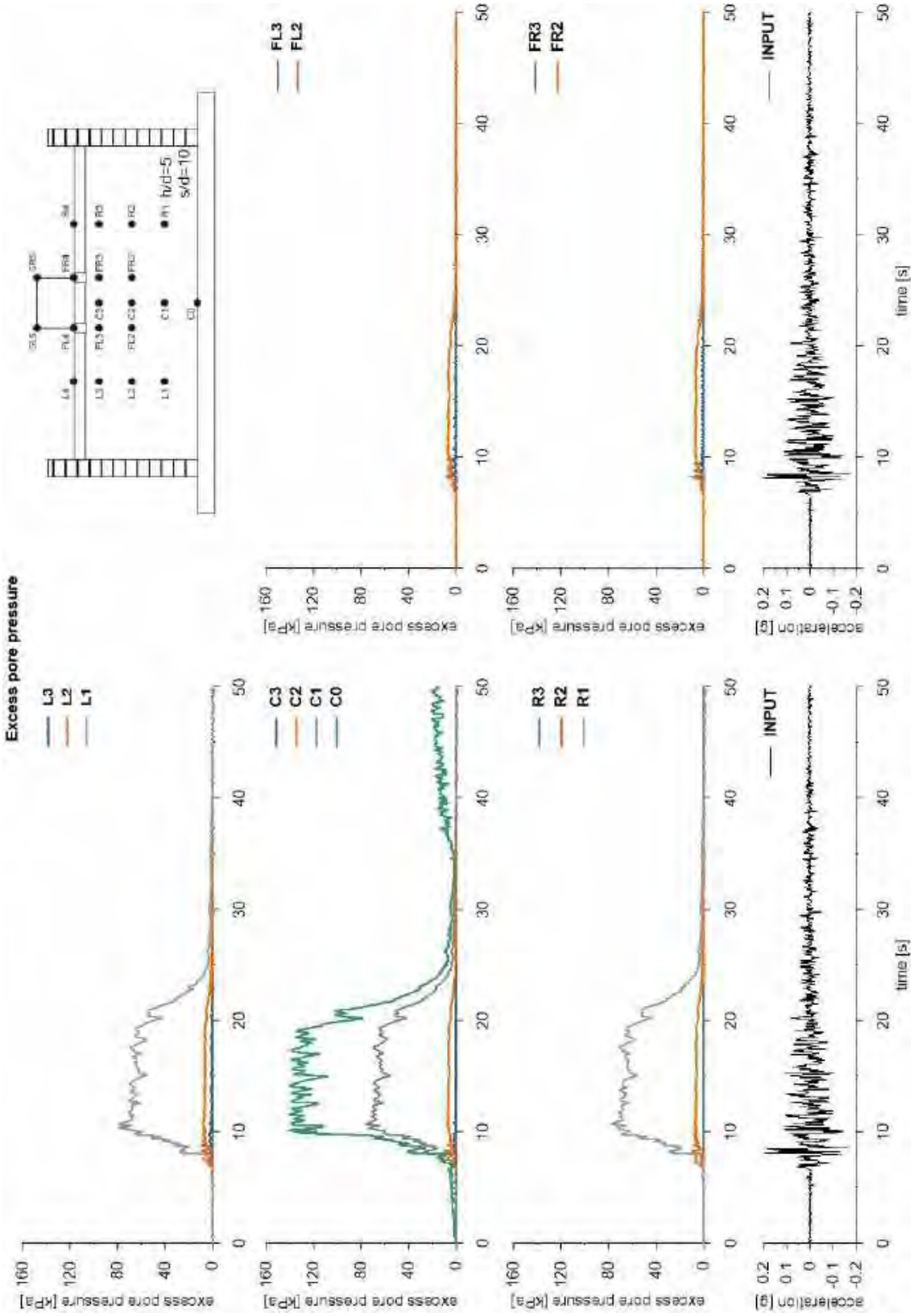

This project has received funding from the European Union's Horizon 2020 research and innovation programme under grant agreement No. 700748

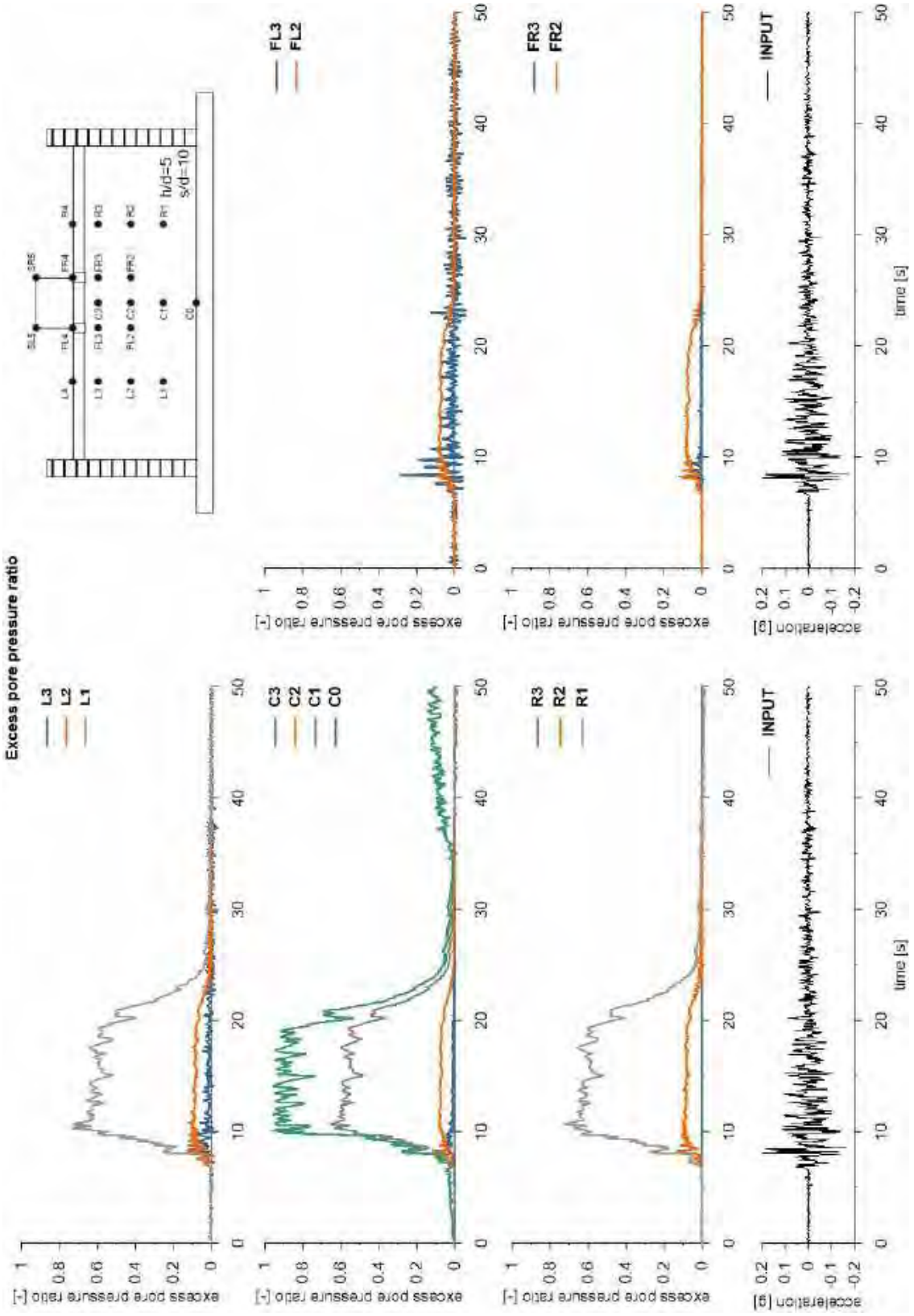

This project has received funding from the European Union's Horizon 2020 research and innovation programme under grant agreement No. 700748

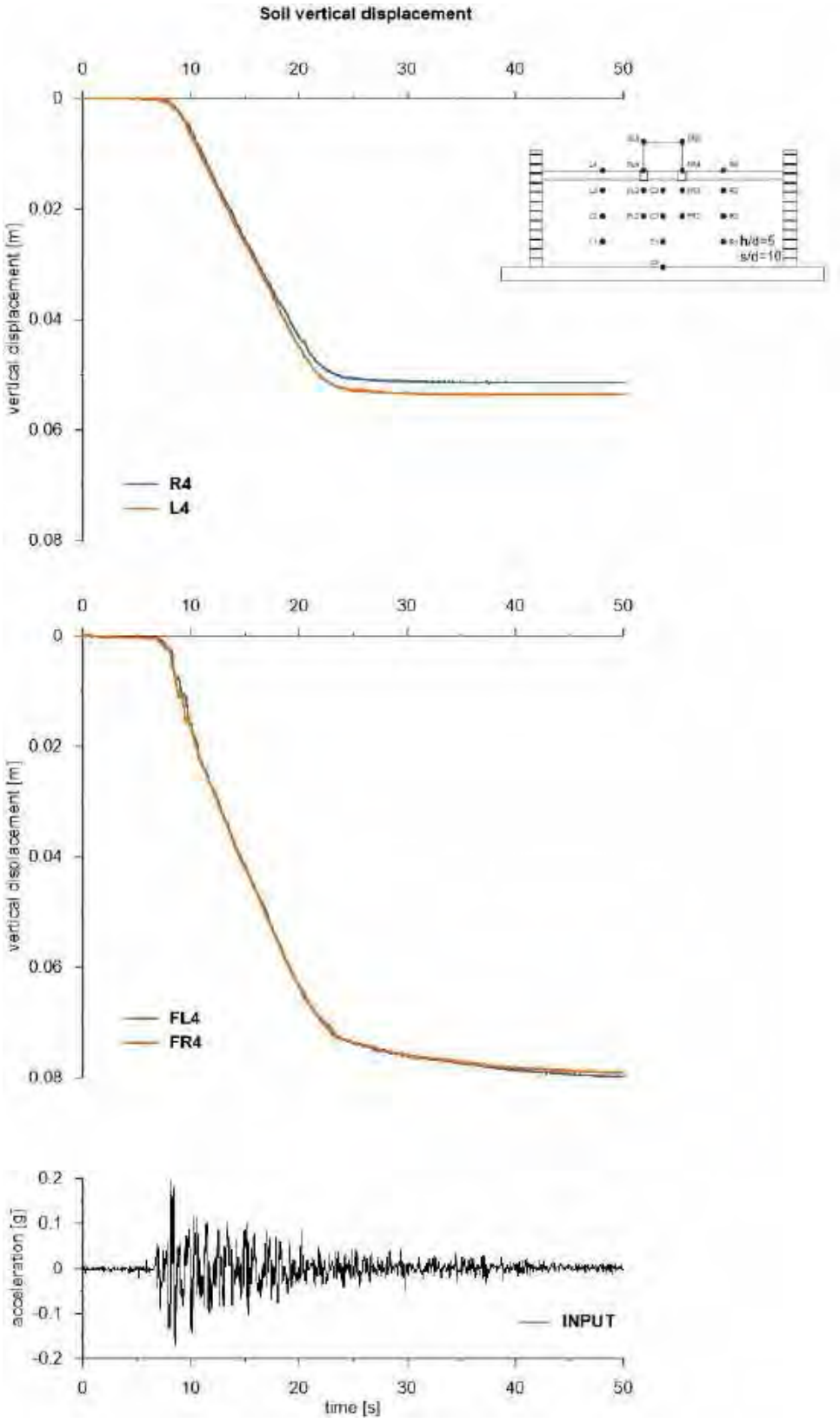

This project has received funding from the European Union's Horizon 2020 research and innovation programme under grant agreement No. 700748

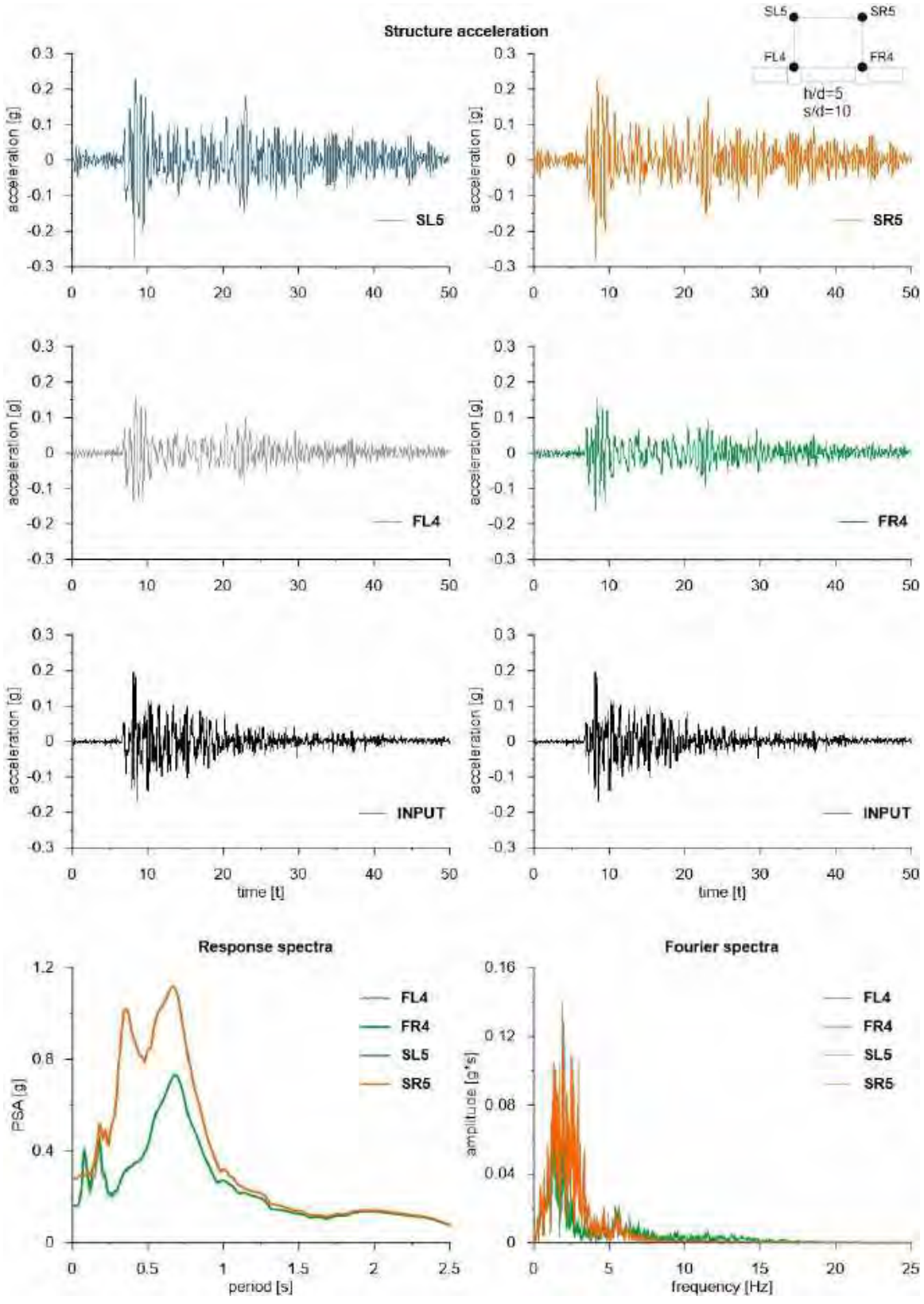

This project has received funding from the European Union's Horizon 2020 research and innovation programme under grant agreement No. 700748

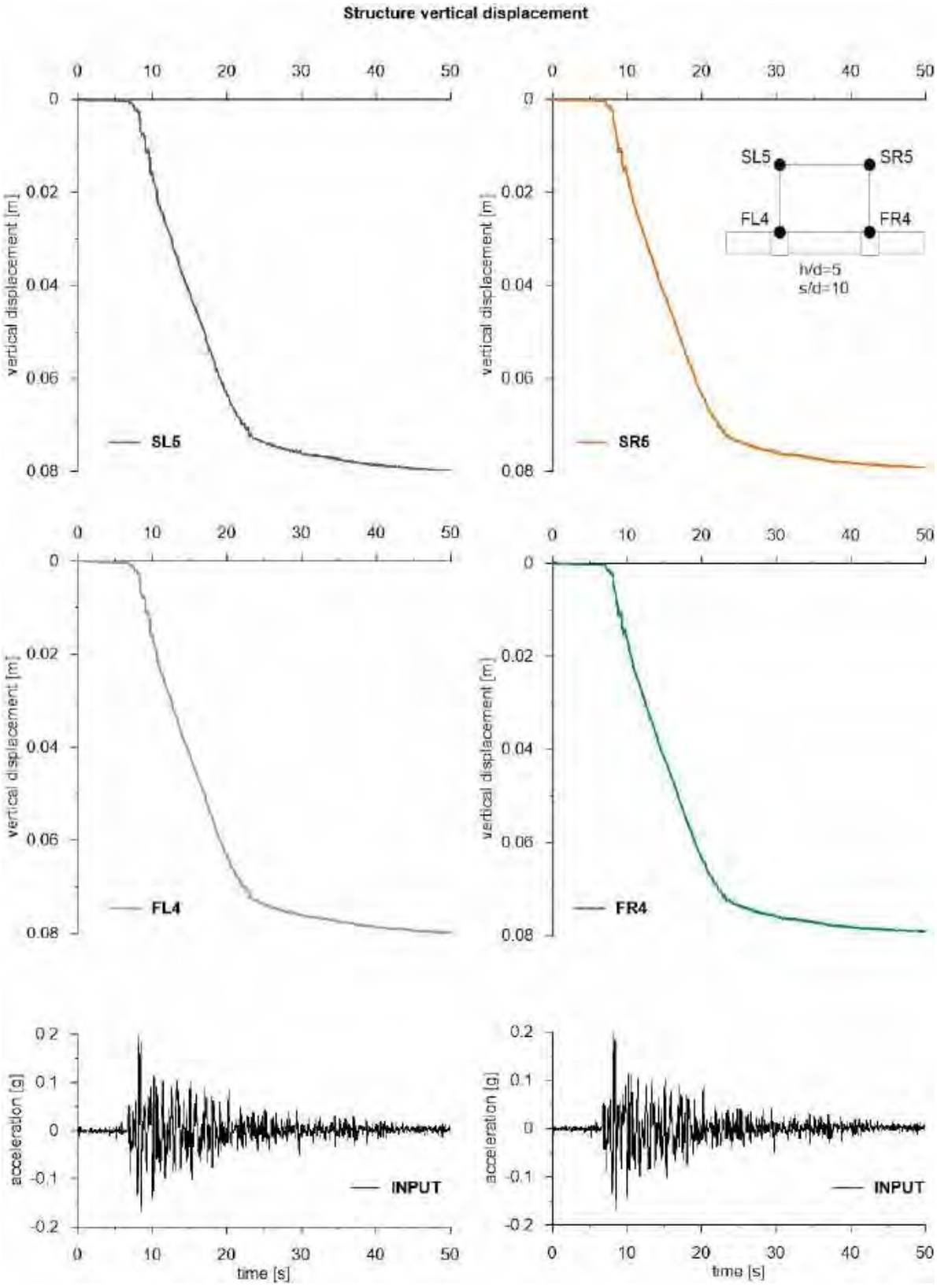

This project has received funding from the European Union's Horizon 2020 research and innovation programme under grant agreement No. 700748

6.1.1.38 ID: SS_HDU_H05_s15

The model consists of a double soil profile of clay and Ticino sand. The ground motion applied was the number 31.

ID: SS_HDU_H05_s15

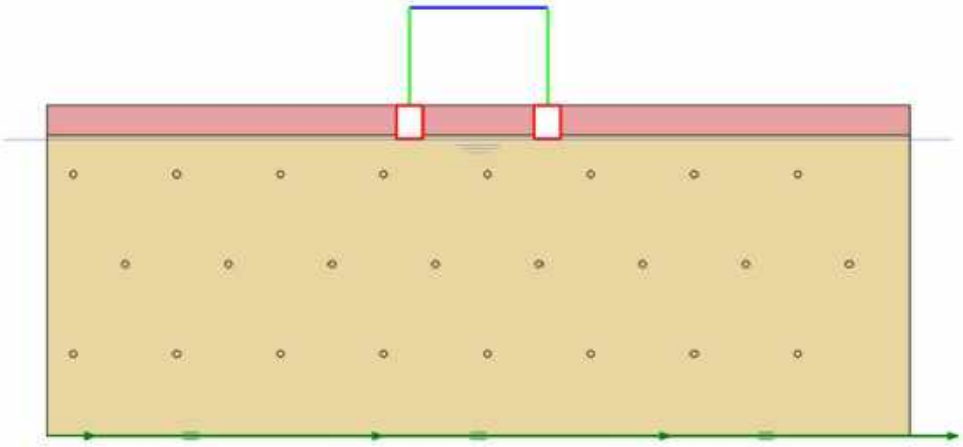

Layouts of the model reproduced in Plaxis 2D

This project has received funding from the European Union's Horizon 2020 research and innovation programme under grant agreement No. 700748

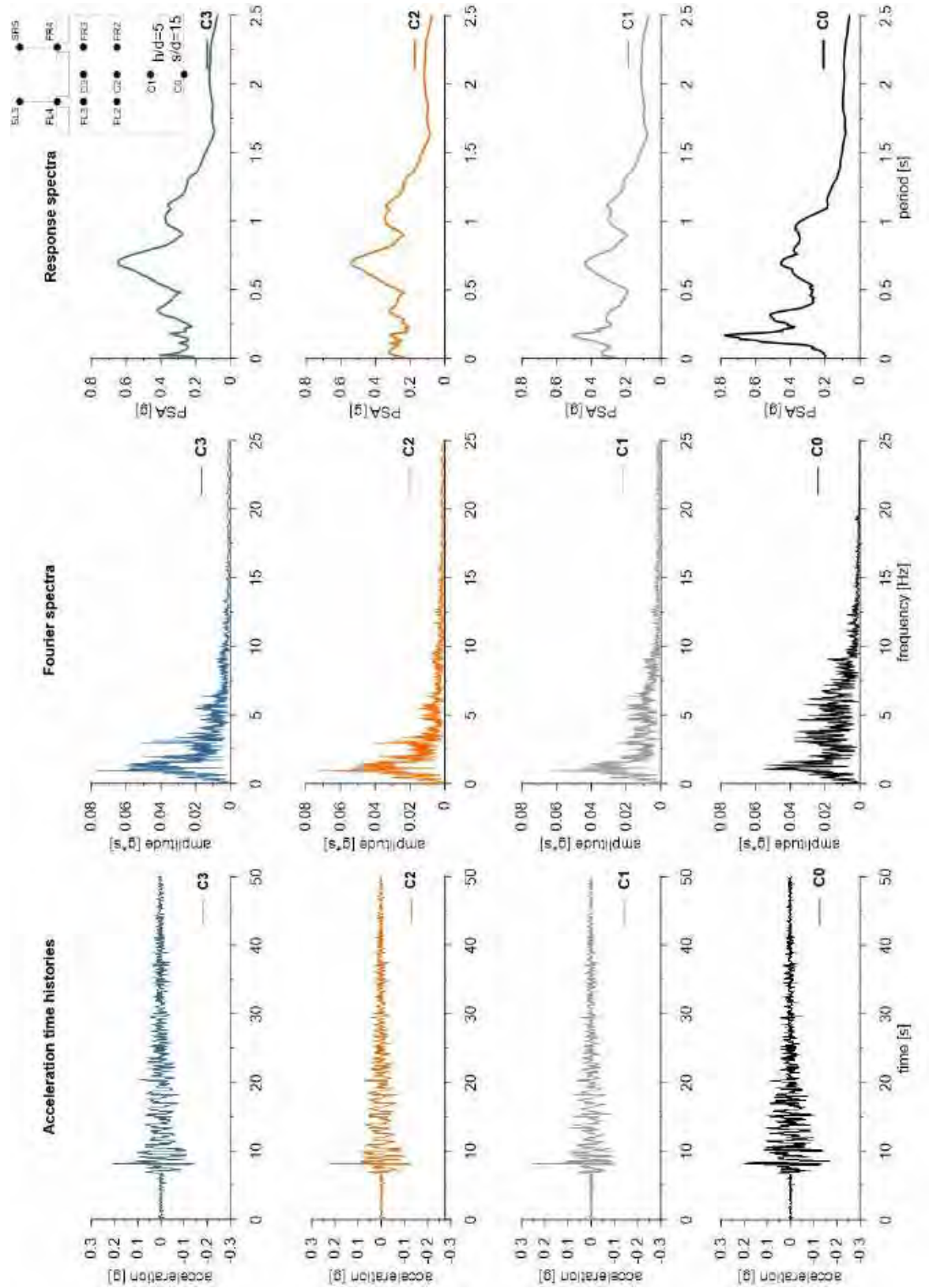

This project has received funding from the European Union's Horizon 2020 research and innovation programme under grant agreement No. 700748

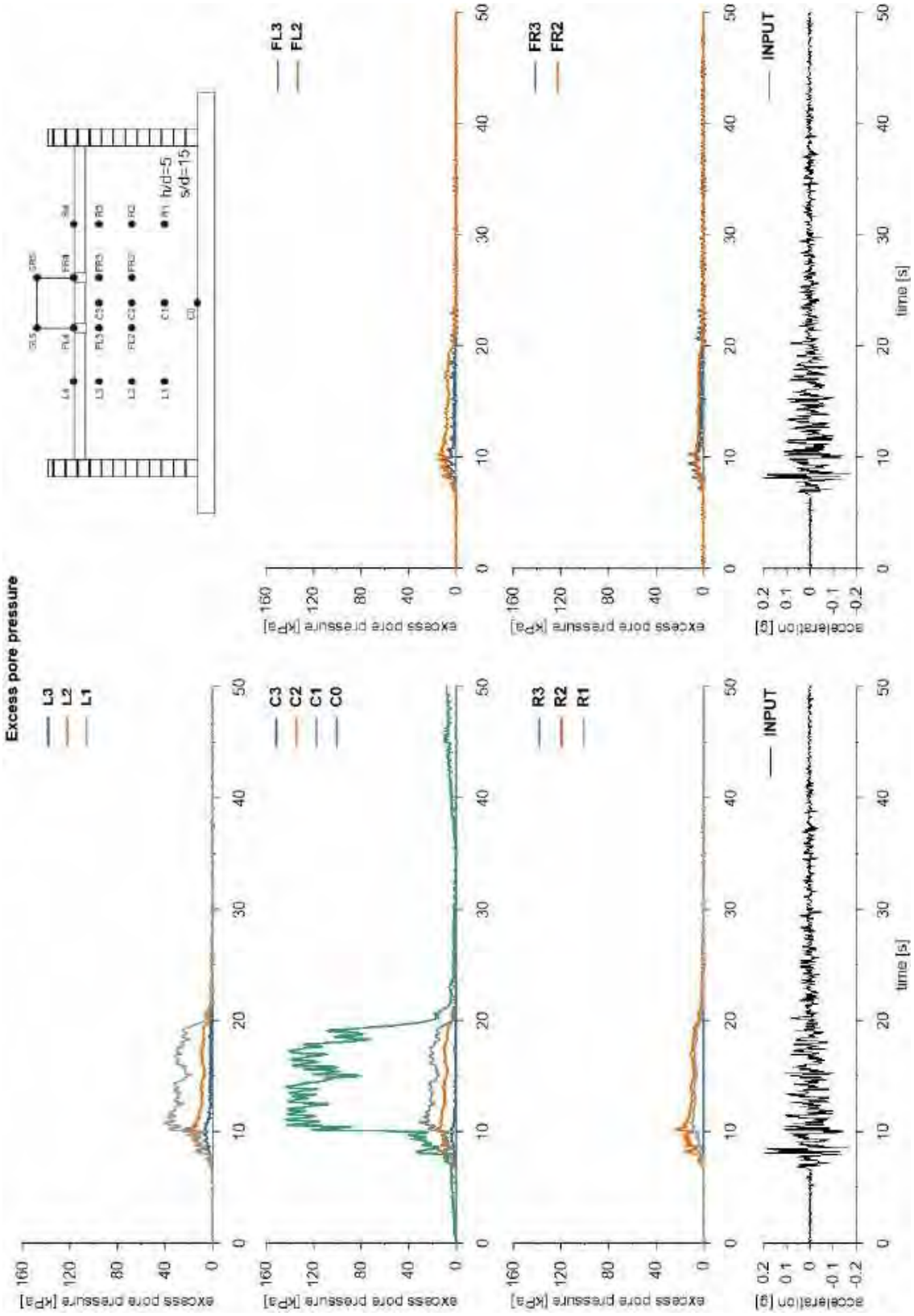

This project has received funding from the European Union's Horizon 2020 research and innovation programme under grant agreement No. 700748

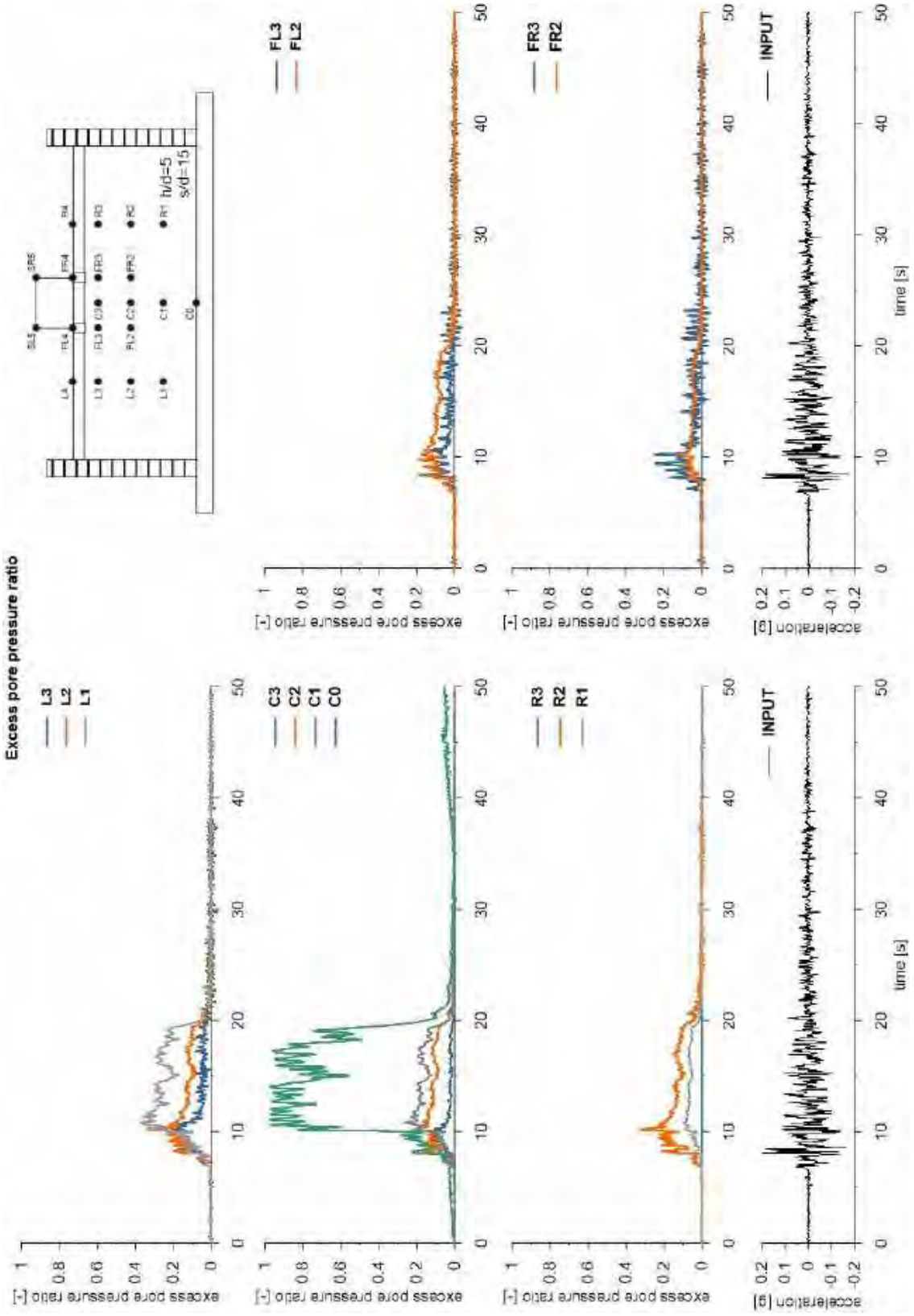

This project has received funding from the European Union's Horizon 2020 research and innovation programme under grant agreement No. 700748

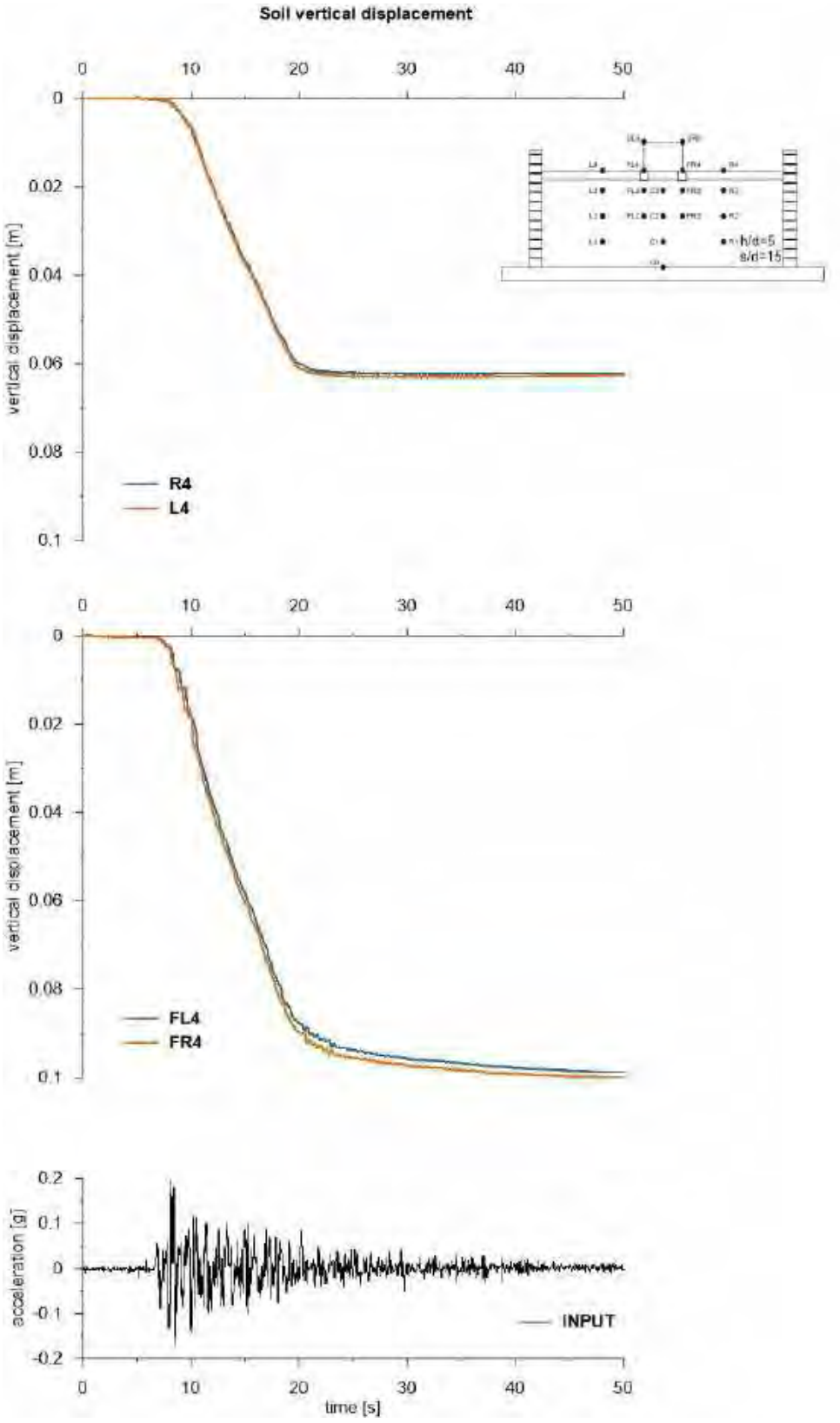

This project has received funding from the European Union's Horizon 2020 research and innovation programme under grant agreement No. 700748

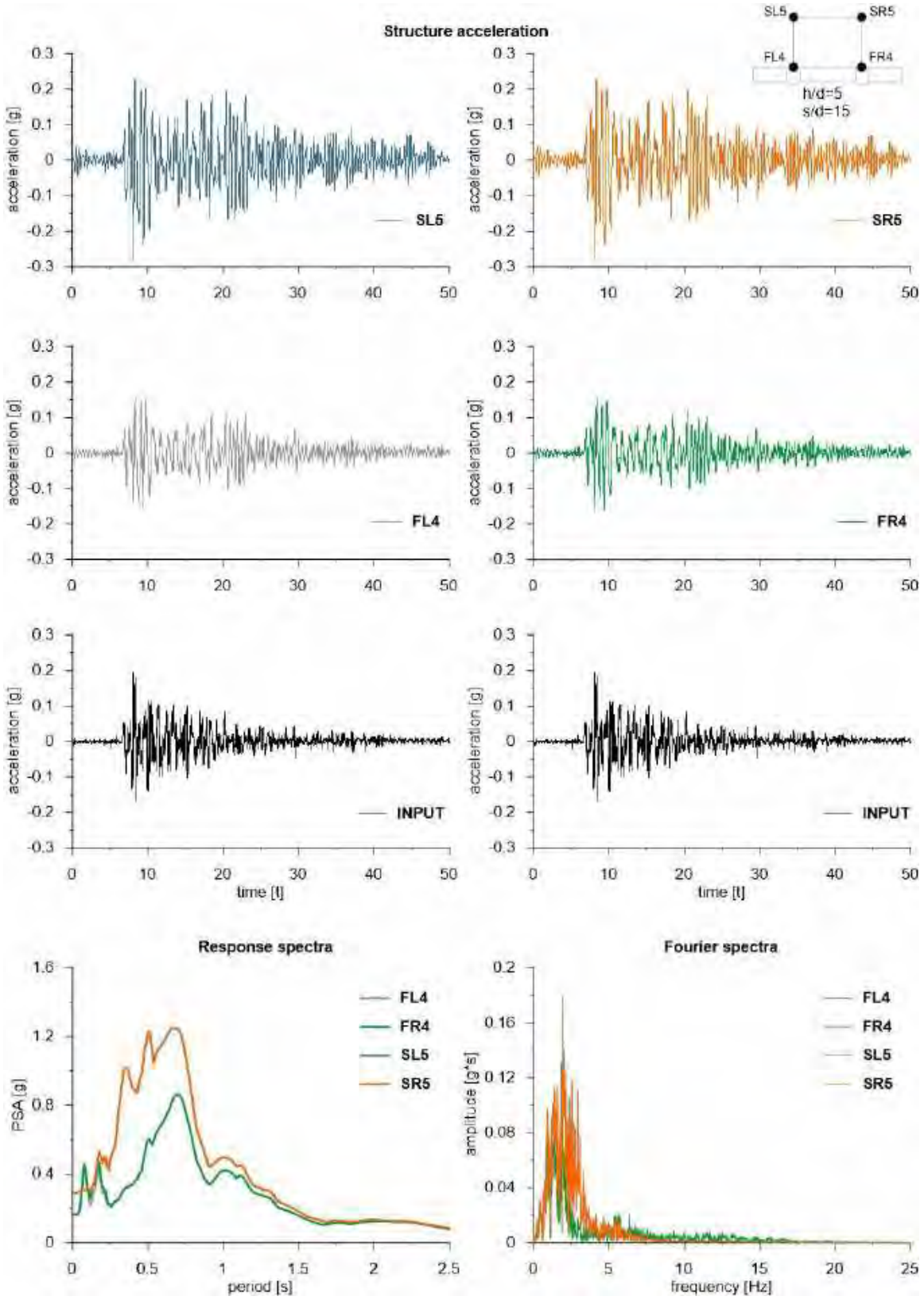

This project has received funding from the European Union's Horizon 2020 research and innovation programme under grant agreement No. 700748

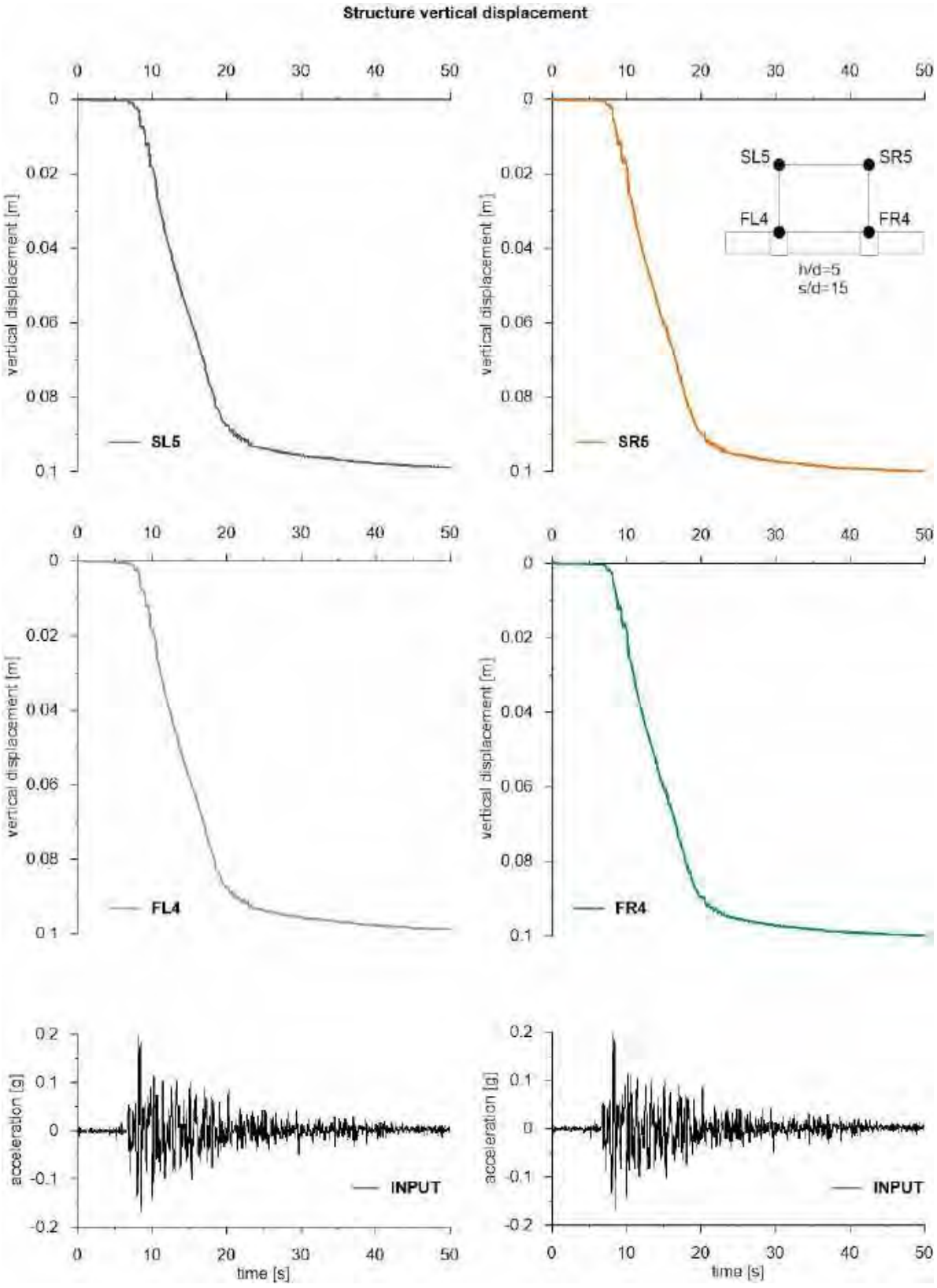

This project has received funding from the European Union's Horizon 2020 research and innovation programme under grant agreement No. 700748

6.1.1.39 ID: SS_HDU_H10_s05

The model consists of a double soil profile of clay and Ticino sand. The ground motion applied was the number 31.

ID: SS_HDU_H10_s05

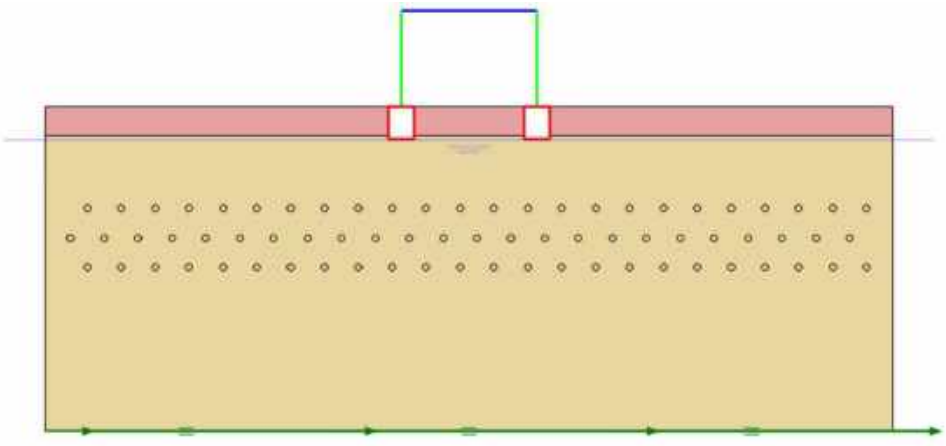

Layouts of the model reproduced in Plaxis 2D

This project has received funding from the European Union's Horizon 2020 research and innovation programme under grant agreement No. 700748

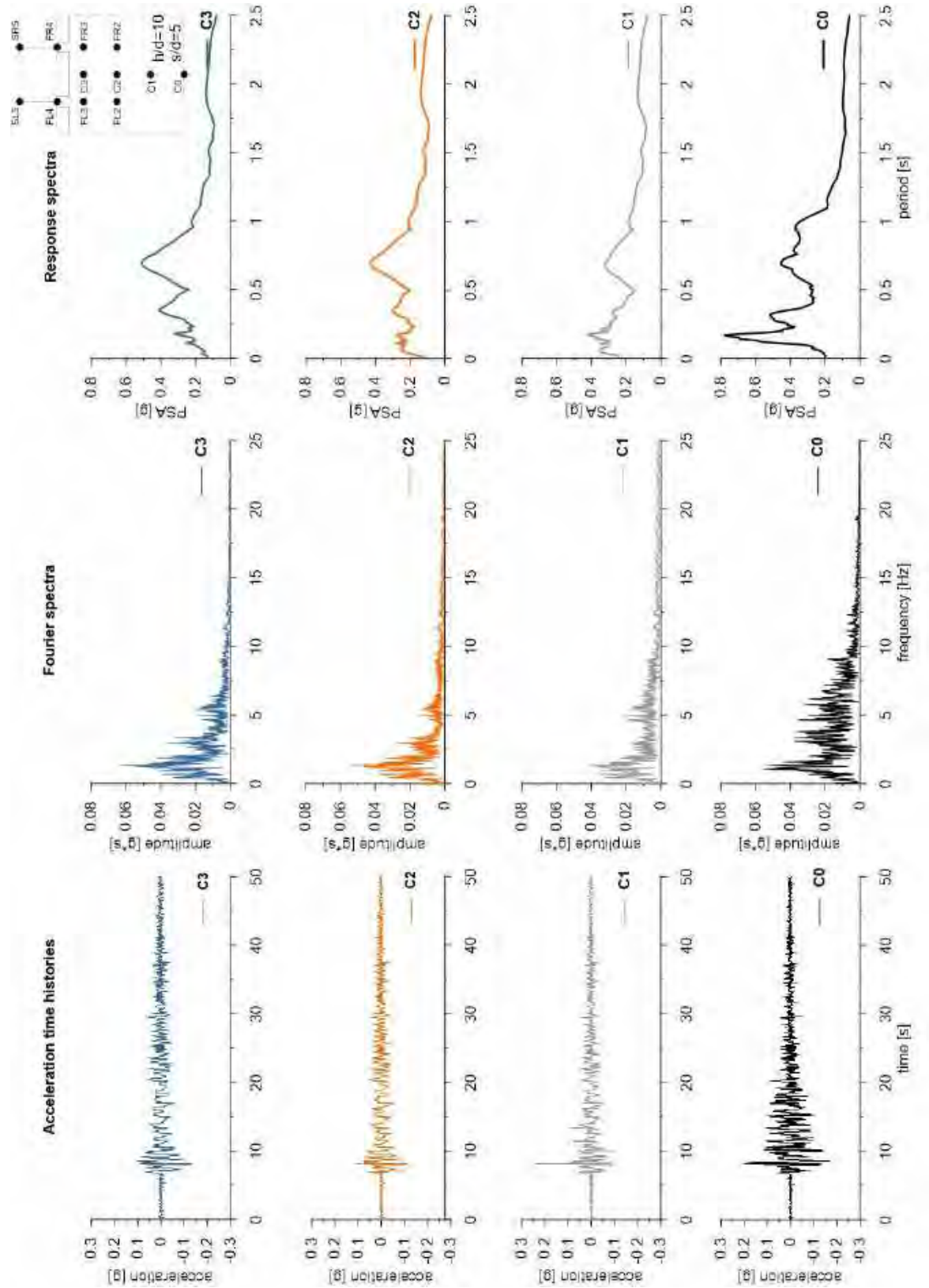

This project has received funding from the European Union's Horizon 2020 research and innovation programme under grant agreement No. 700748

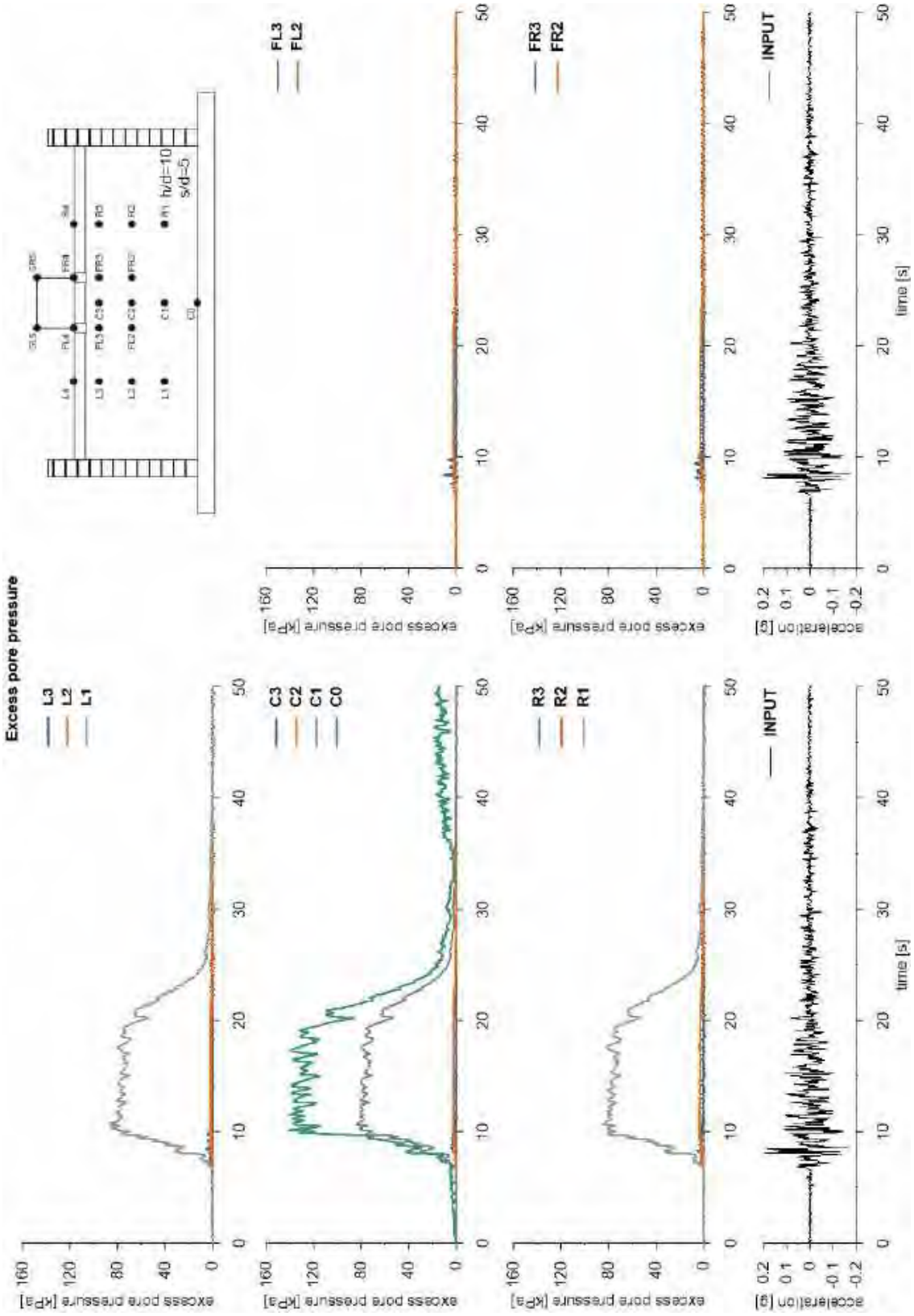

This project has received funding from the European Union's Horizon 2020 research and innovation programme under grant agreement No. 700748

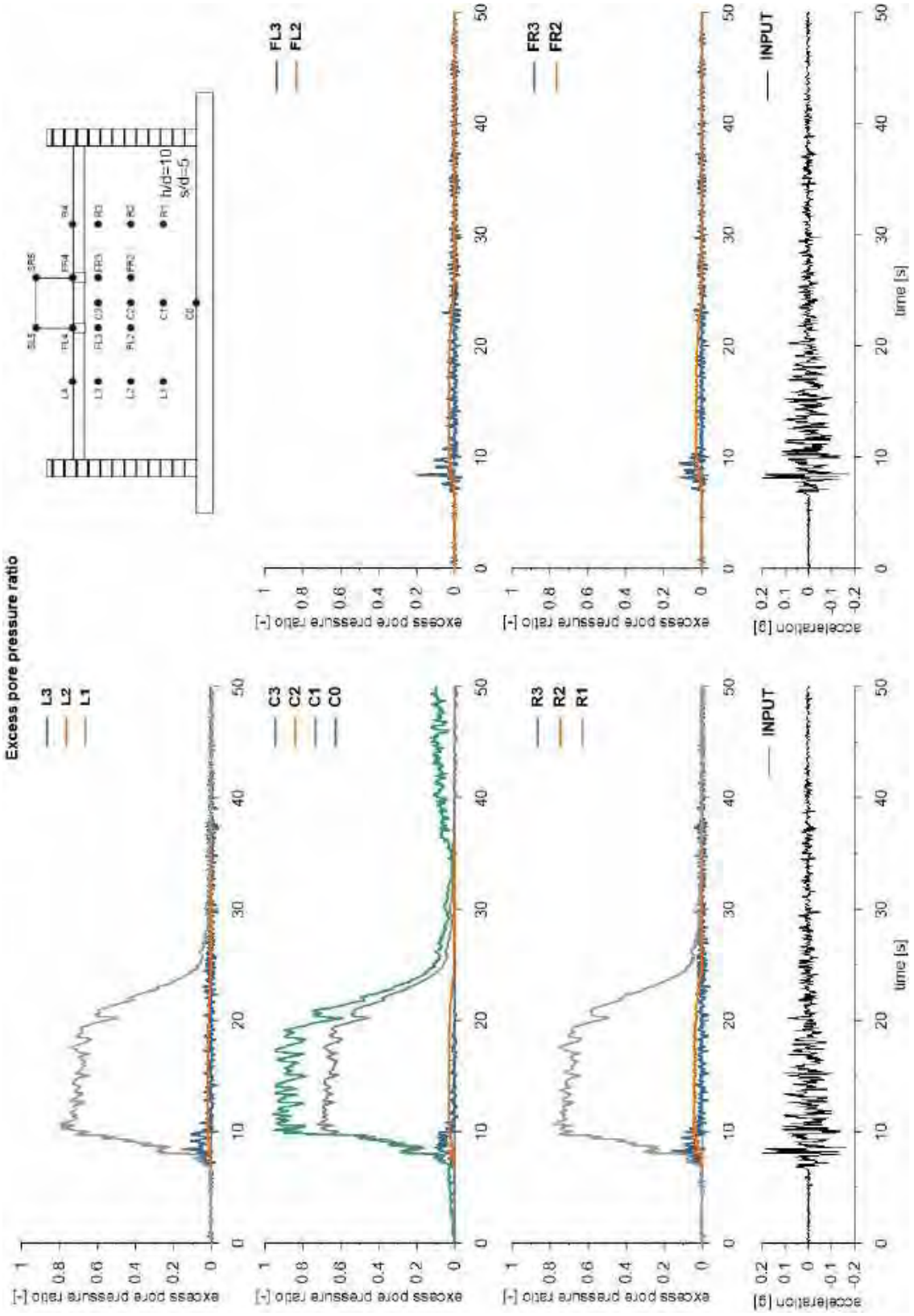

This project has received funding from the European Union's Horizon 2020 research and innovation programme under grant agreement No. 700748

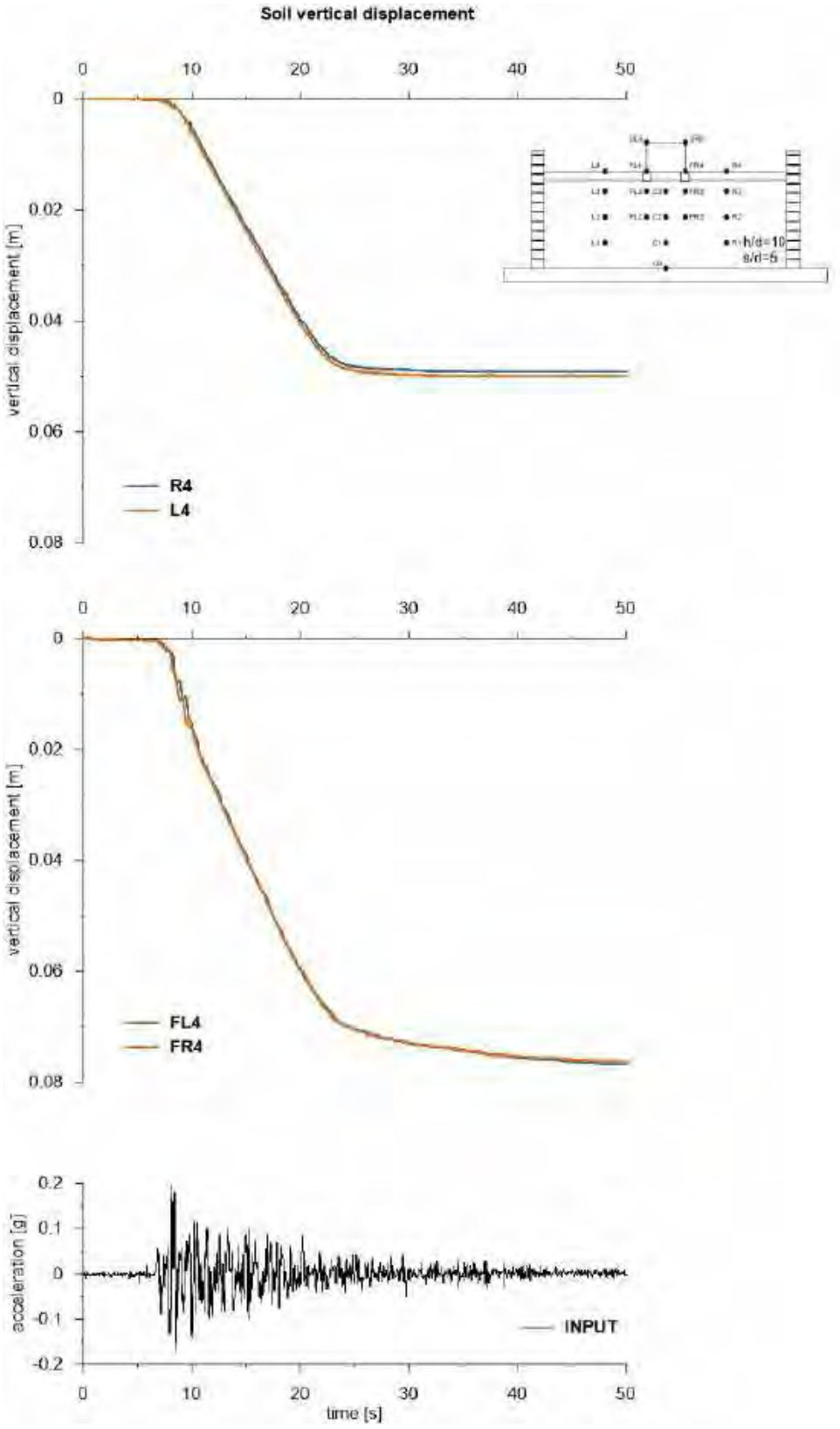

This project has received funding from the European Union's Horizon 2020 research and innovation programme under grant agreement No. 700748

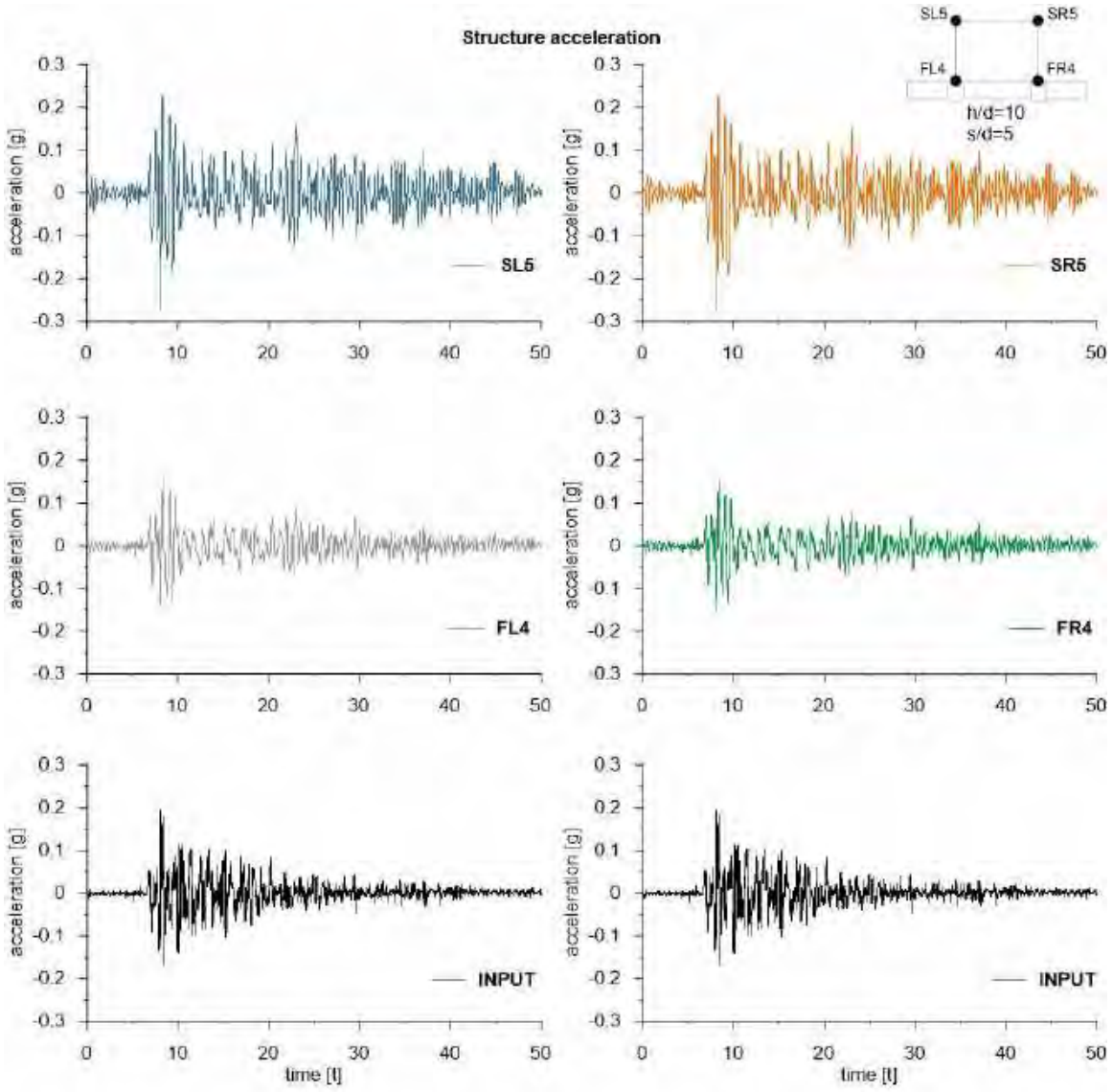

This project has received funding from the European Union's Horizon 2020 research and innovation programme under grant agreement No. 700748

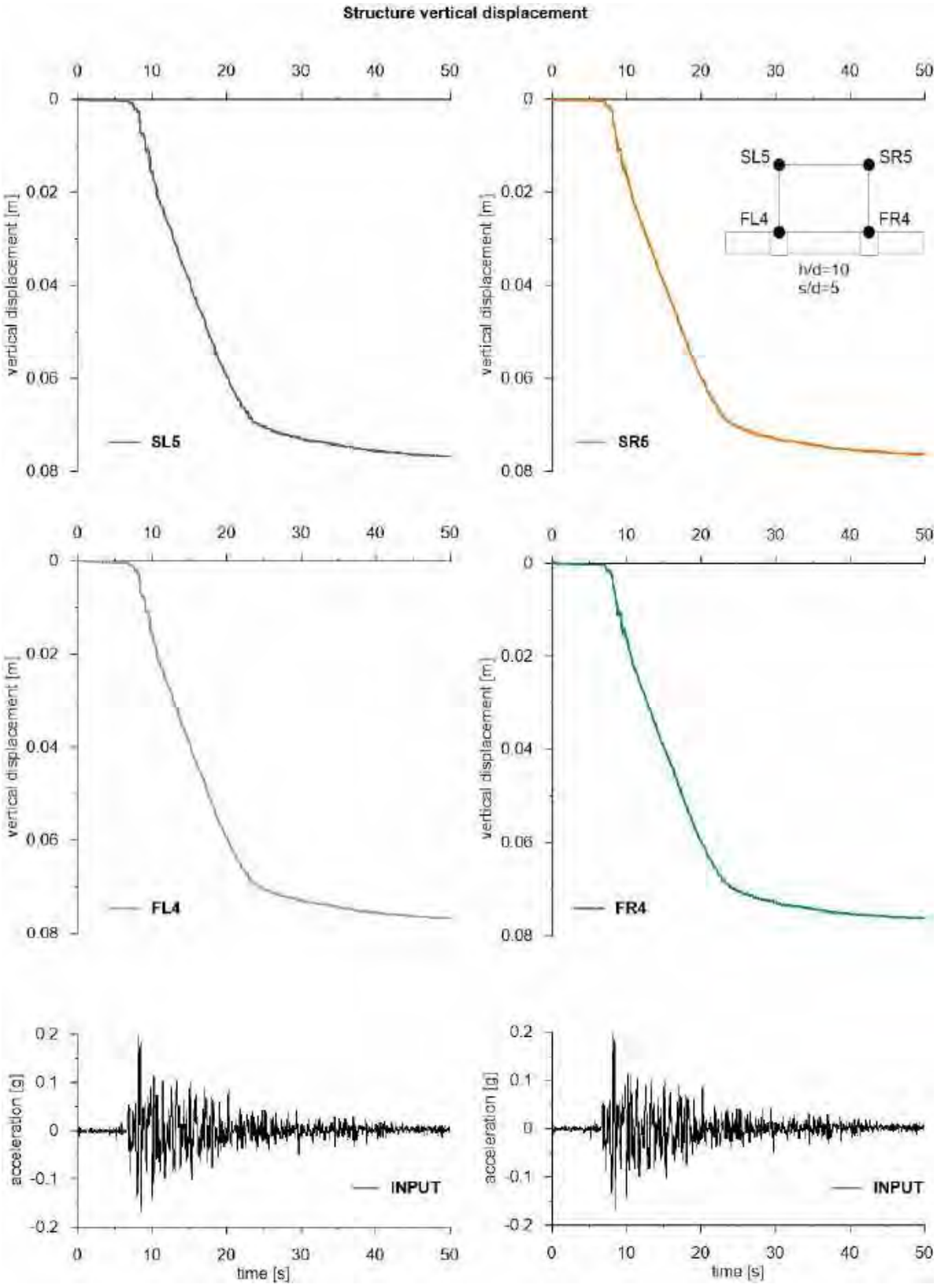

This project has received funding from the European Union's Horizon 2020 research and innovation programme under grant agreement No. 700748

6.1.1.40 ID: SS_HDU_H10_s10

The model consists of a double soil profile of clay and Ticino sand. The ground motion applied was the number 31.

ID: SS_HDU_H10_s10

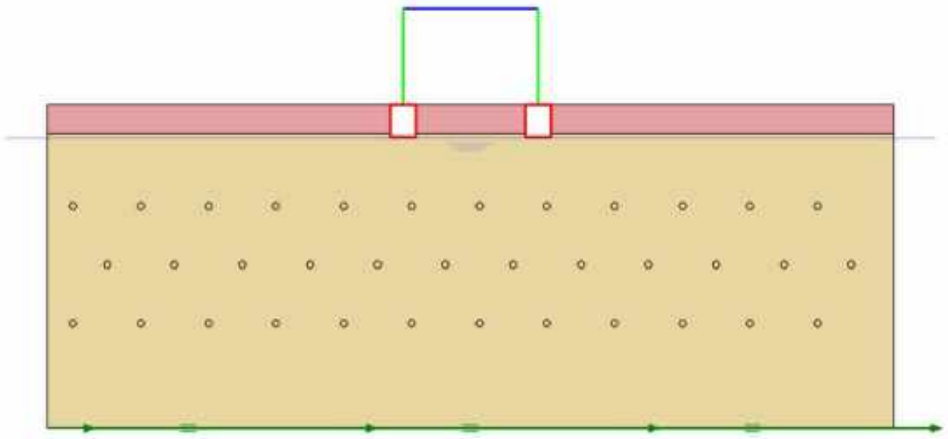

Layouts of the model reproduced in Plaxis 2D

This project has received funding from the European Union's Horizon 2020 research and innovation programme under grant agreement No. 700748

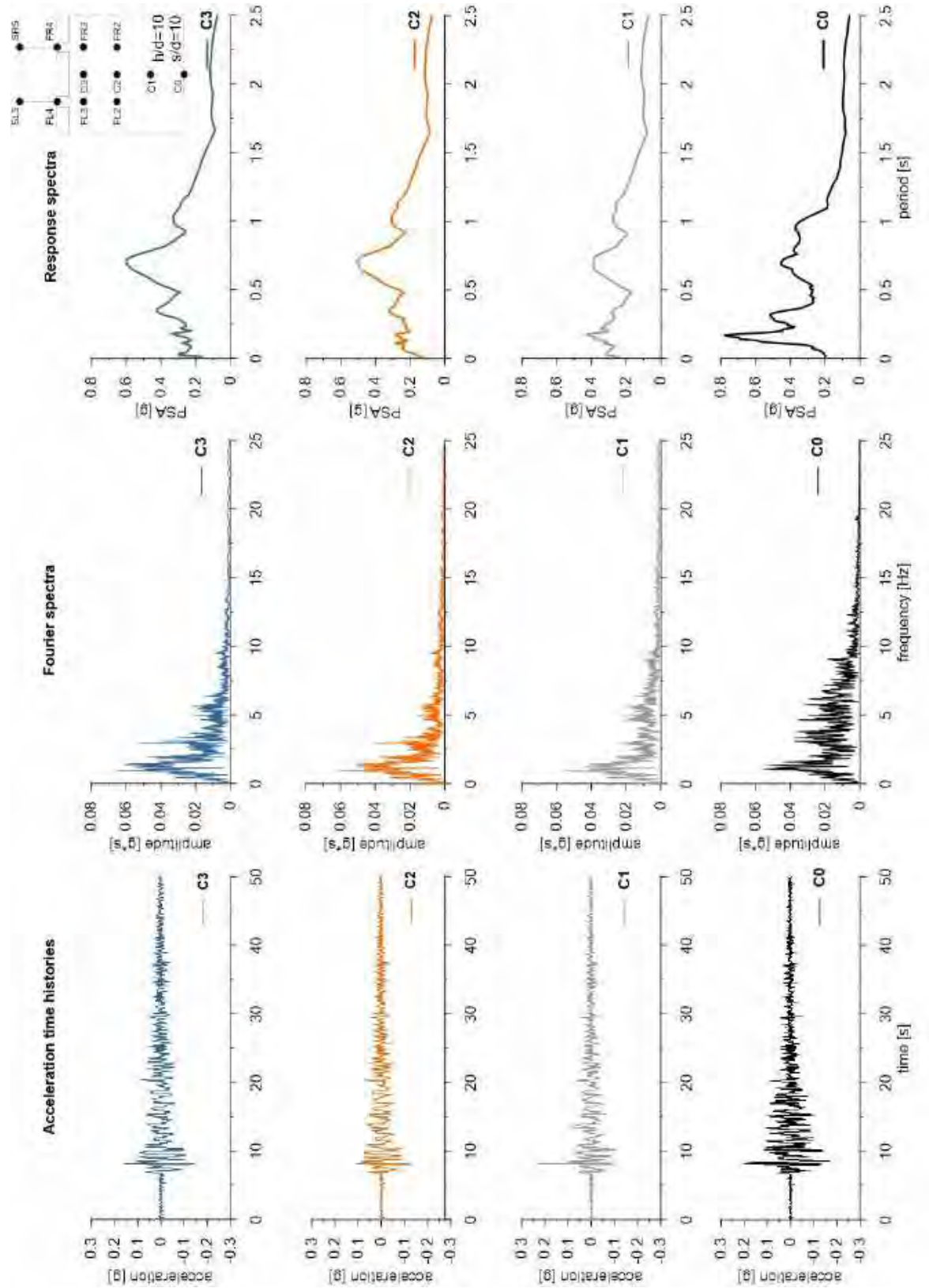

This project has received funding from the European Union's Horizon 2020 research and innovation programme under grant agreement No. 700748

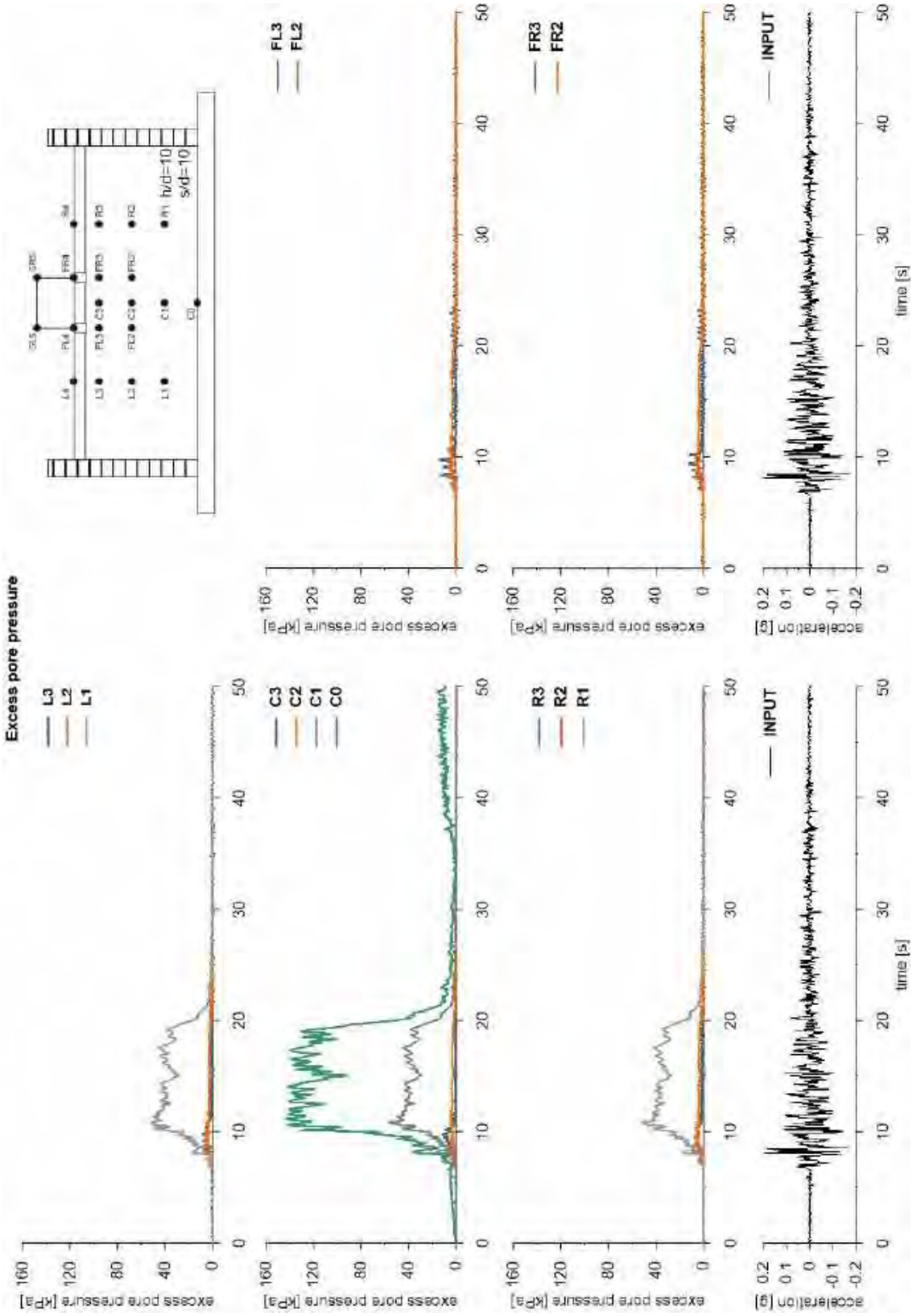

This project has received funding from the European Union's Horizon 2020 research and innovation programme under grant agreement No. 700748

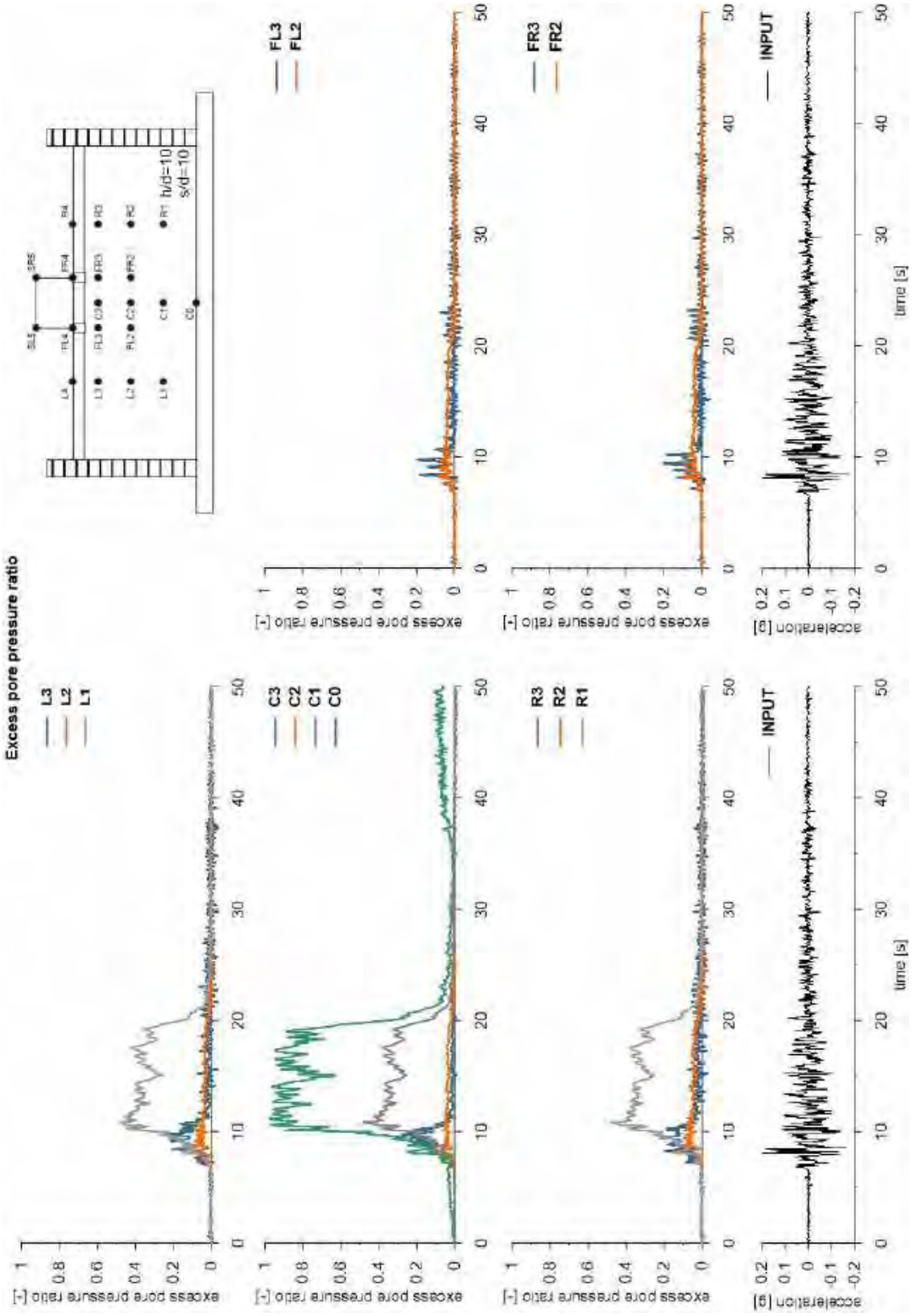

This project has received funding from the European Union's Horizon 2020 research and innovation programme under grant agreement No. 700748

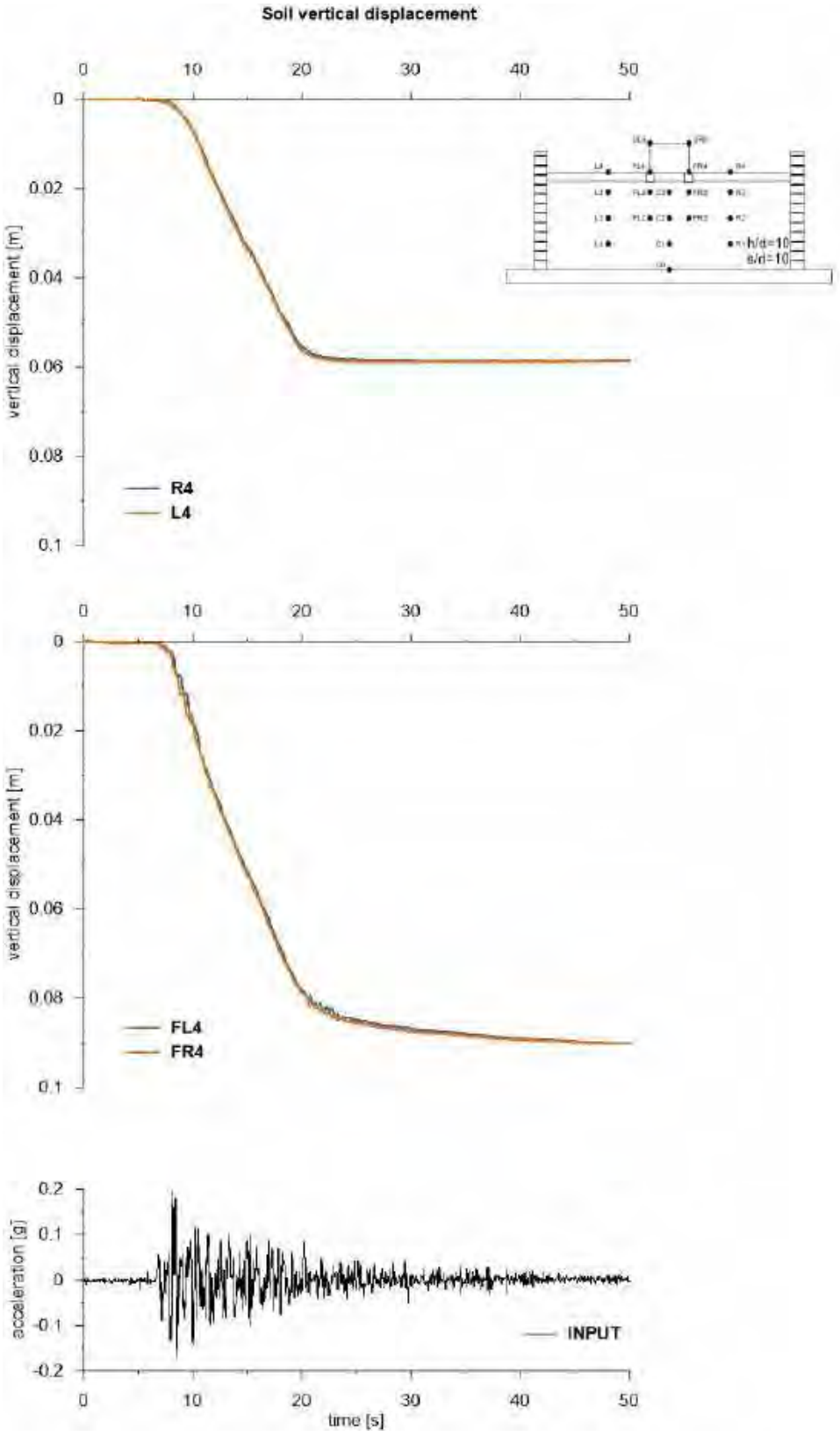

This project has received funding from the European Union's Horizon 2020 research and innovation programme under grant agreement No. 700748

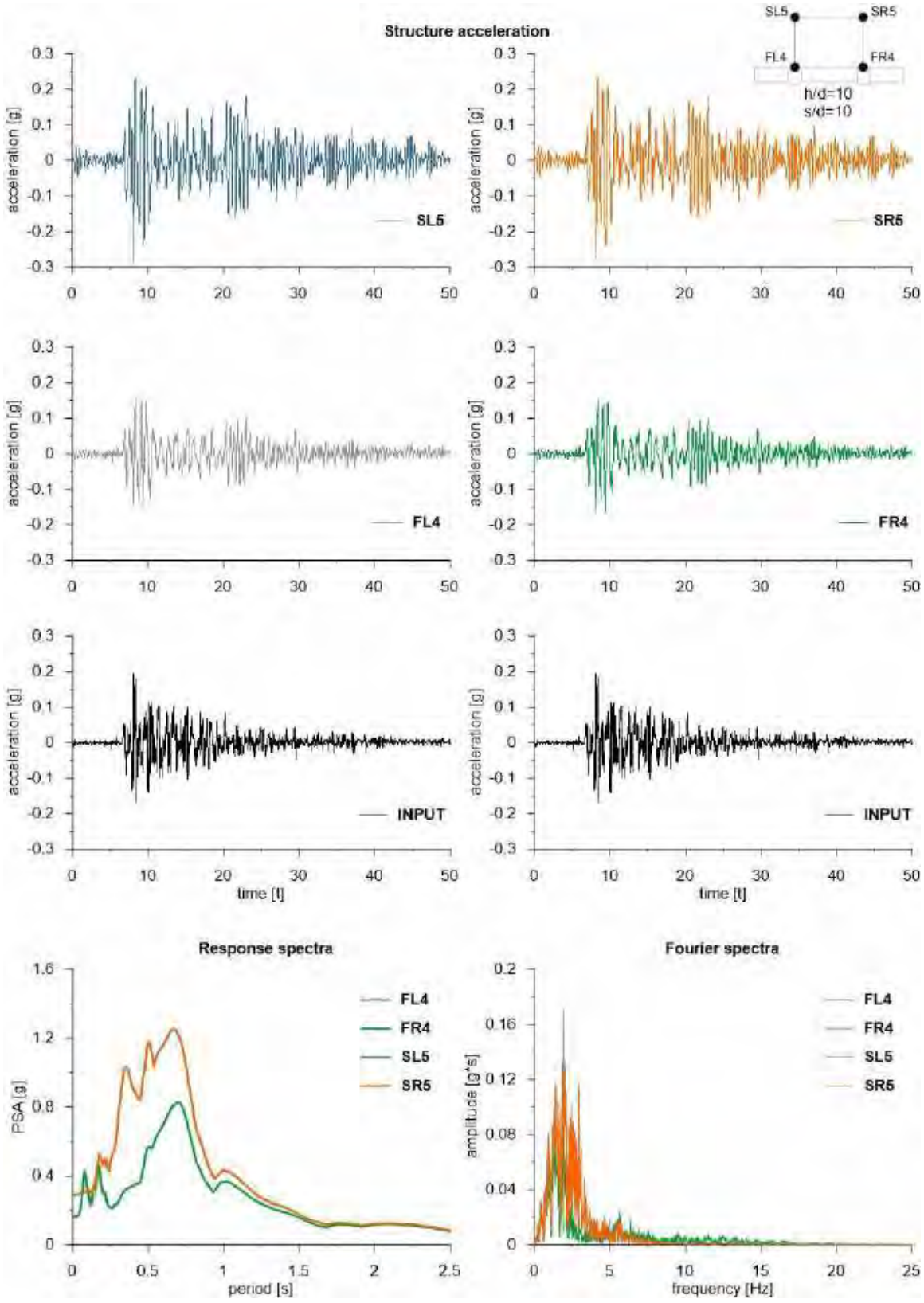

This project has received funding from the European Union's Horizon 2020 research and innovation programme under grant agreement No. 700748

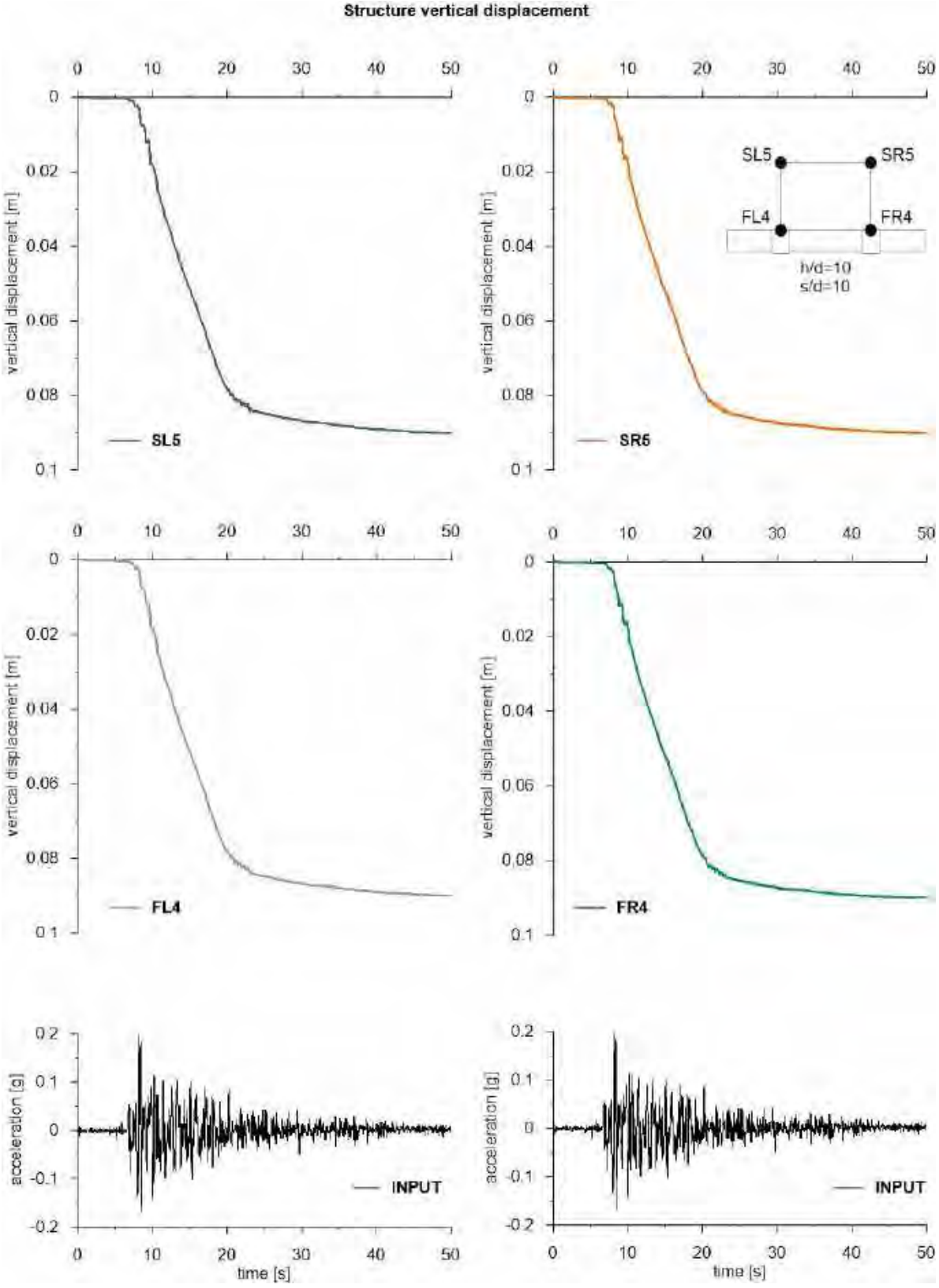

This project has received funding from the European Union's Horizon 2020 research and innovation programme under grant agreement No. 700748

6.1.1.41 ID: SS_HDU_H10_s15

The model consists of a double soil profile of clay and Ticino sand. The ground motion applied was the number 31.

ID: SS_HDU_H10_s15

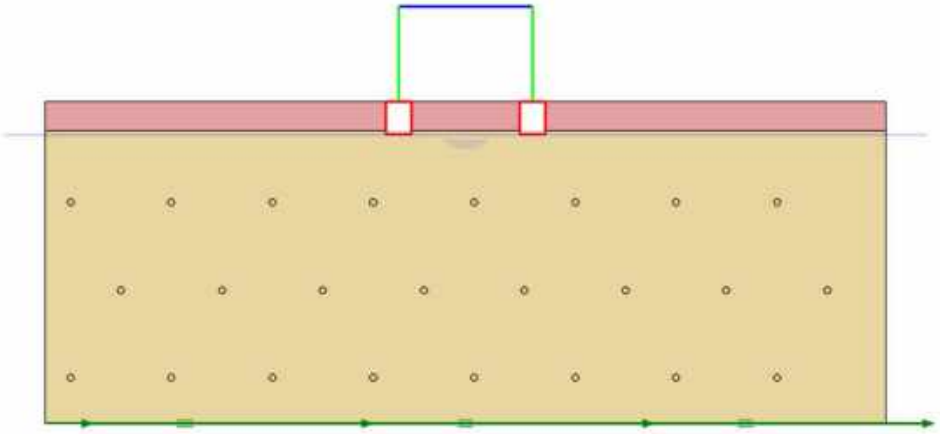

Layouts of the model reproduced in Plaxis 2D

This project has received funding from the European Union's Horizon 2020 research and innovation programme under grant agreement No. 700748

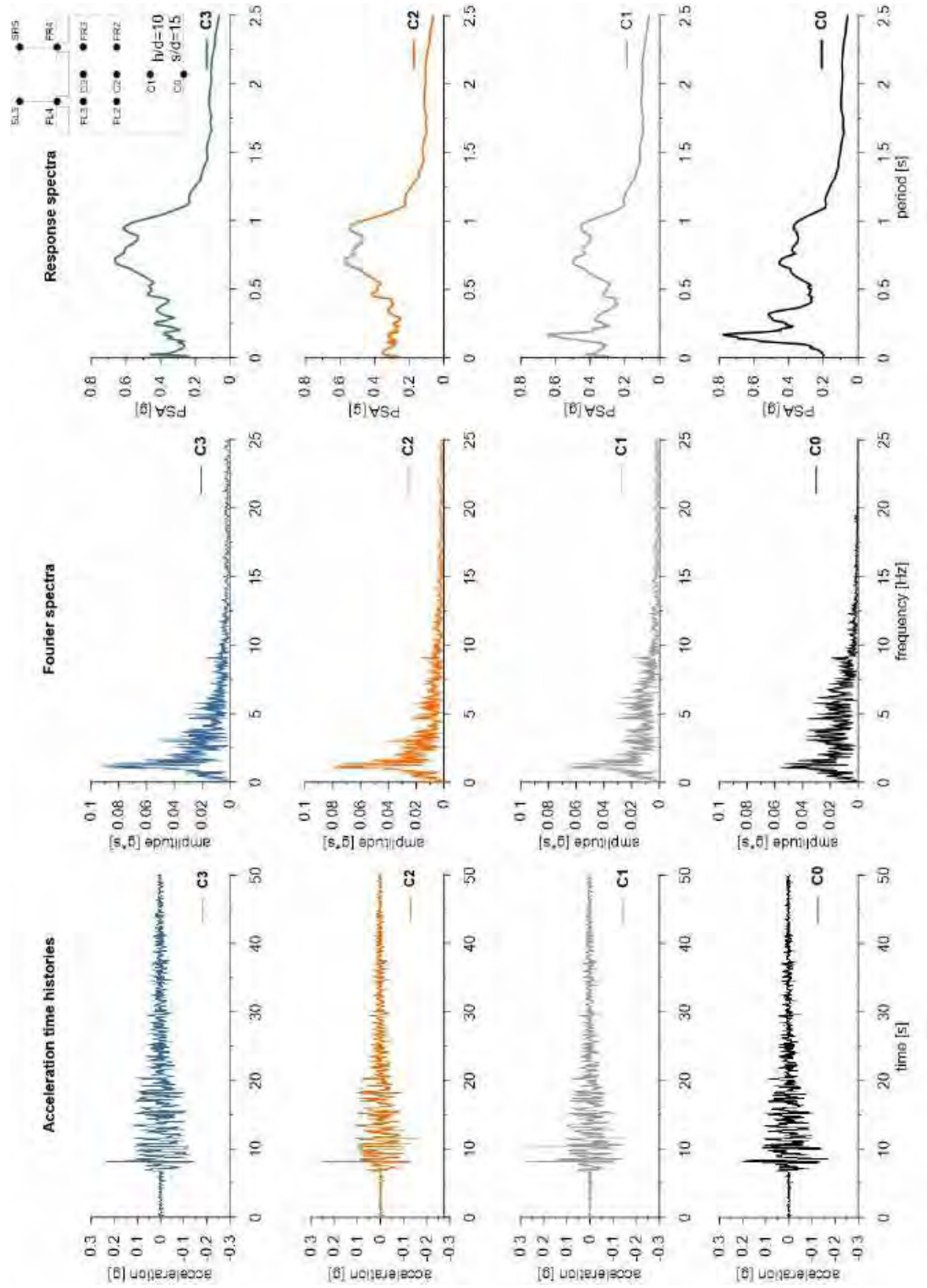

This project has received funding from the European Union's Horizon 2020 research and innovation programme under grant agreement No. 700748

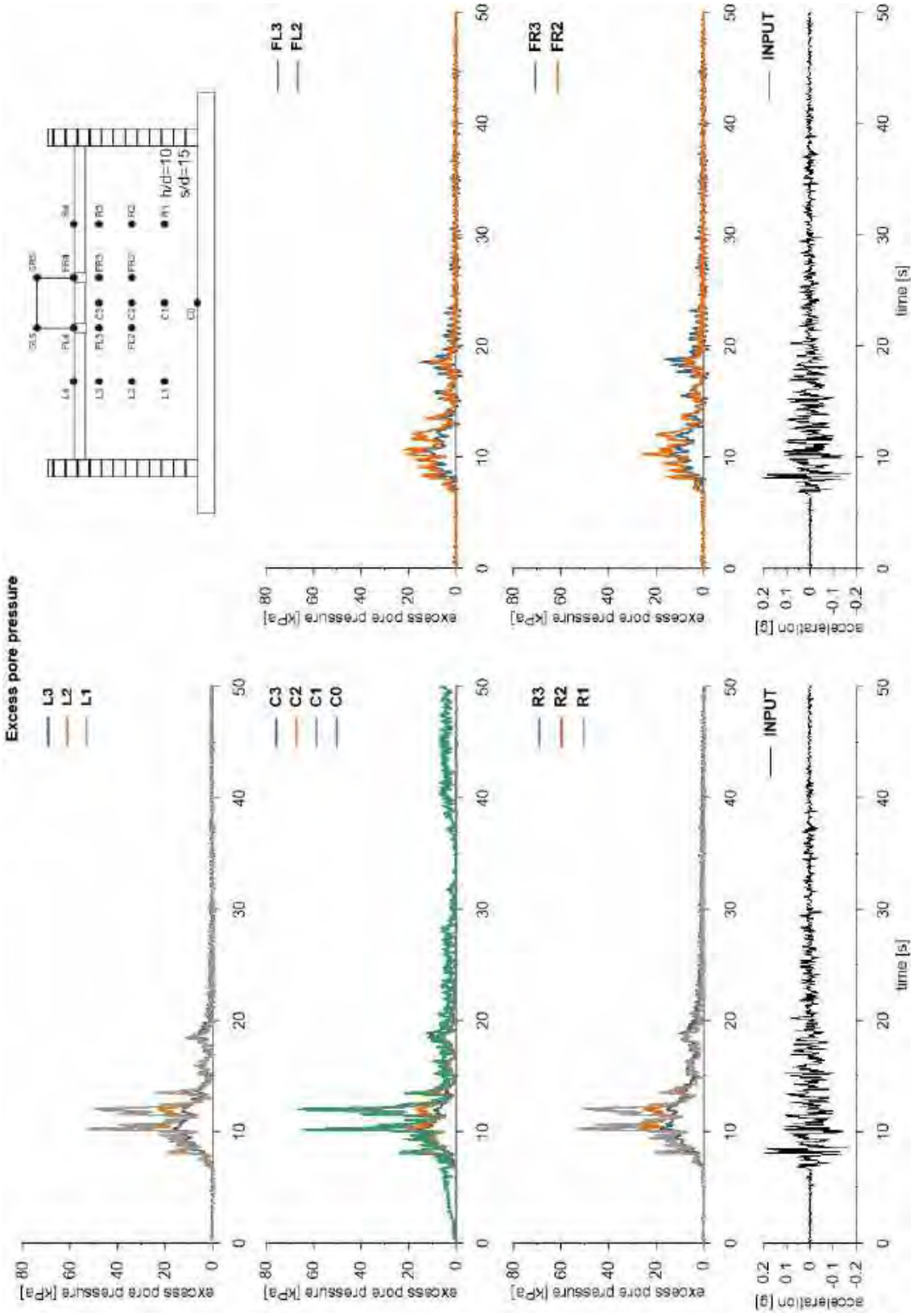

This project has received funding from the European Union's Horizon 2020 research and innovation programme under grant agreement No. 700748

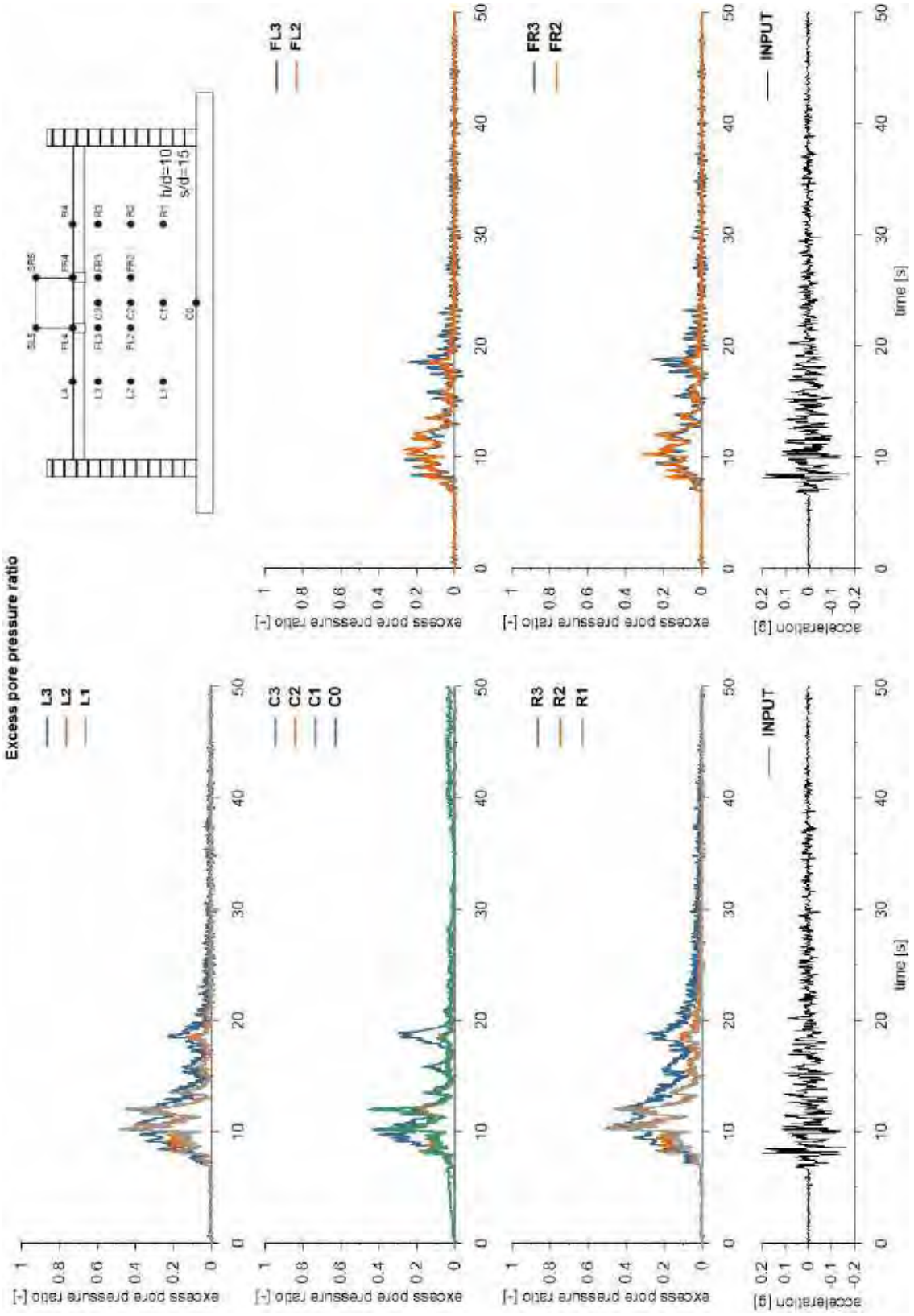

This project has received funding from the European Union's Horizon 2020 research and innovation programme under grant agreement No. 700748

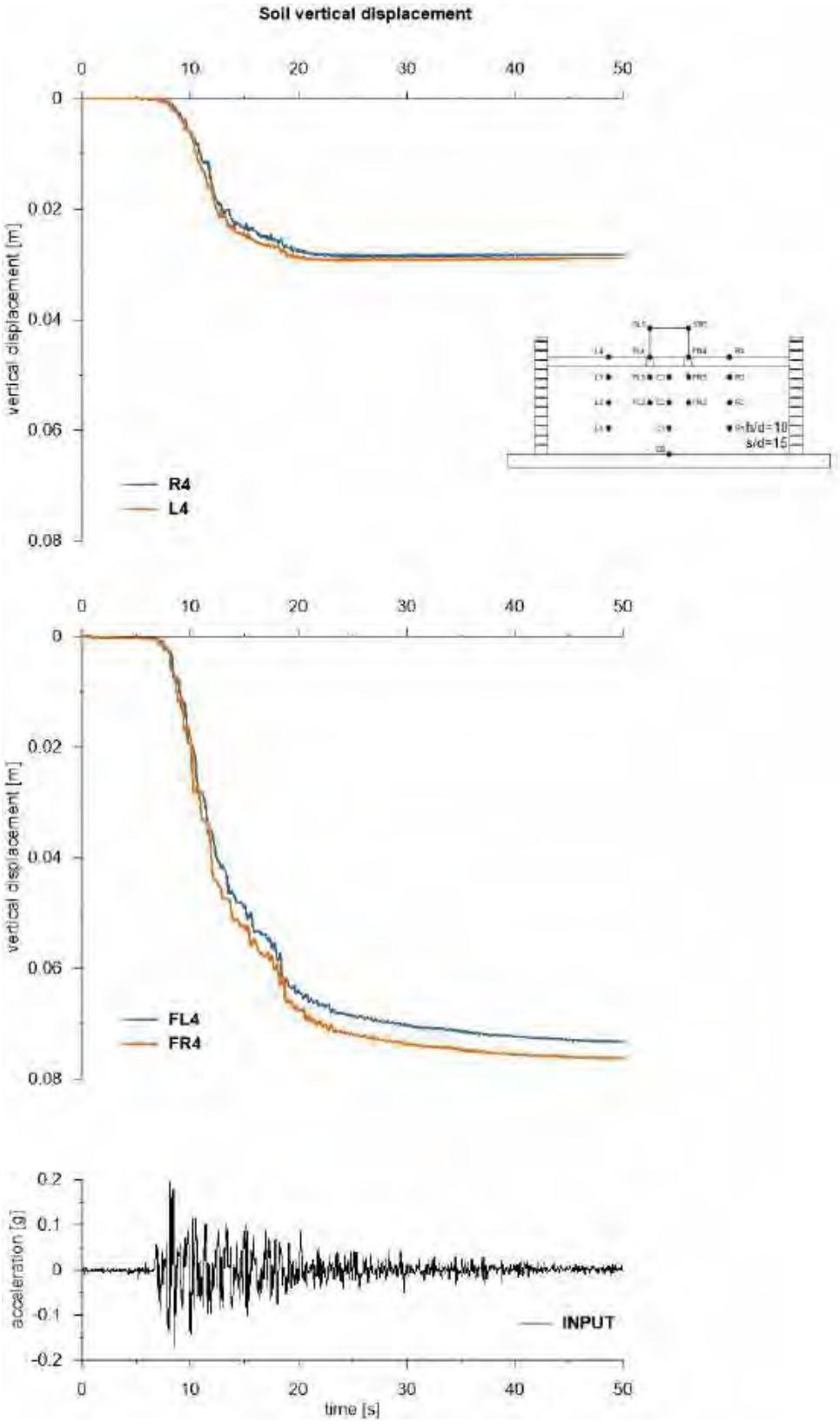

This project has received funding from the European Union's Horizon 2020 research and innovation programme under grant agreement No. 700748

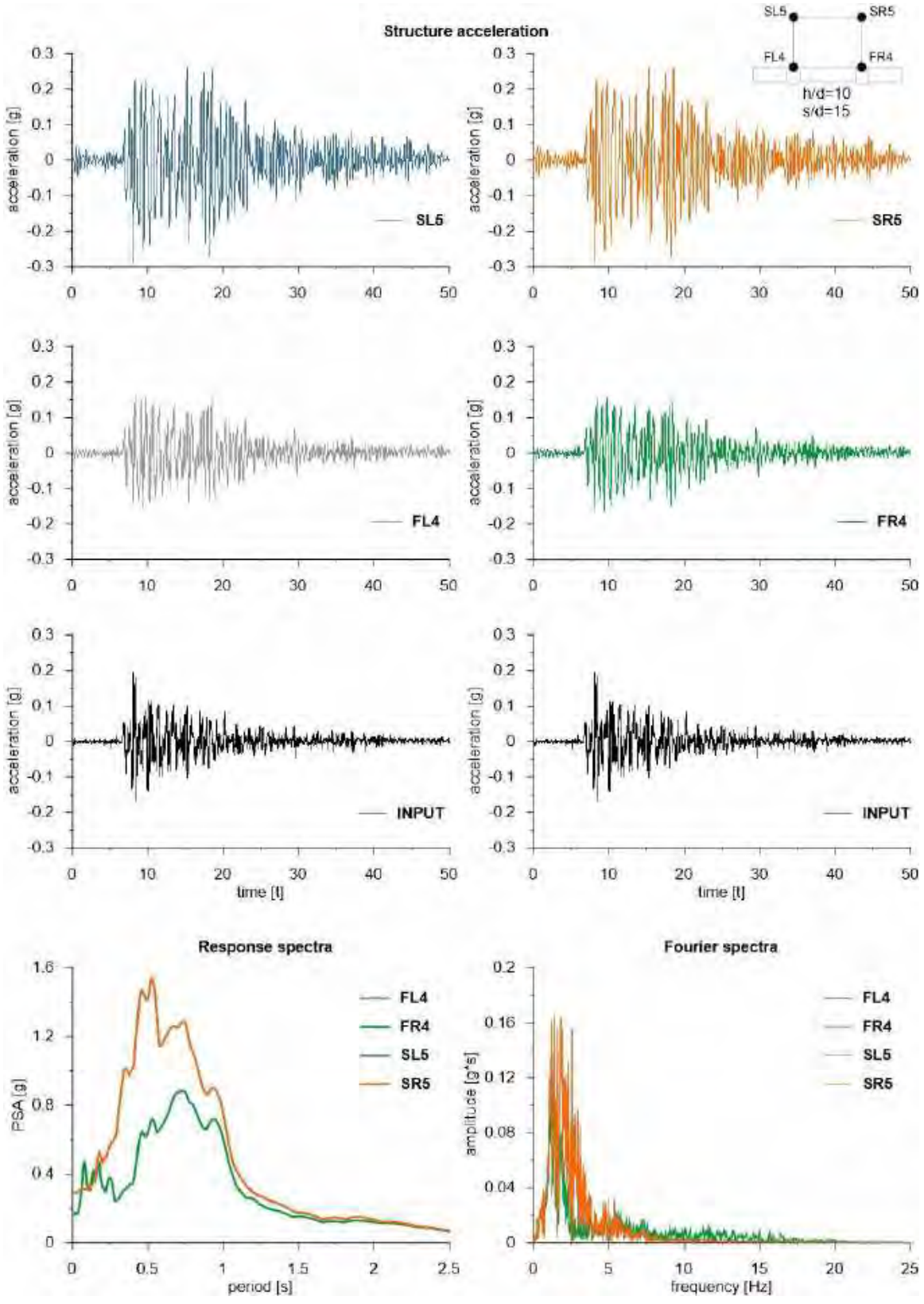

This project has received funding from the European Union's Horizon 2020 research and innovation programme under grant agreement No. 700748

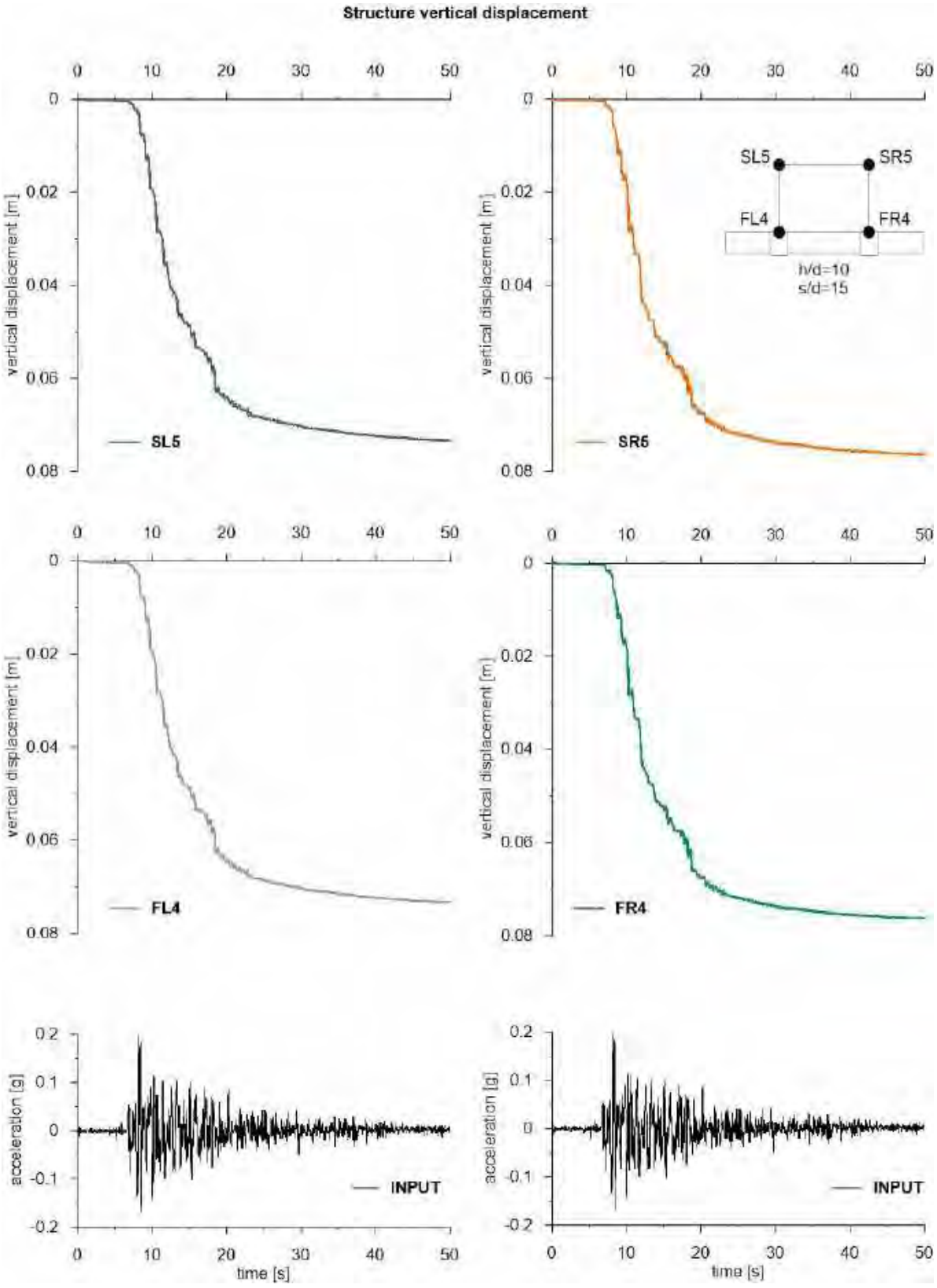

This project has received funding from the European Union's Horizon 2020 research and innovation programme under grant agreement No. 700748

6.1.1.42 ID: SS_HDU_H15_s05

The model consists of a double soil profile of clay and Ticino sand. The ground motion applied was the number 31.

ID: SS_HDU_H15_s05

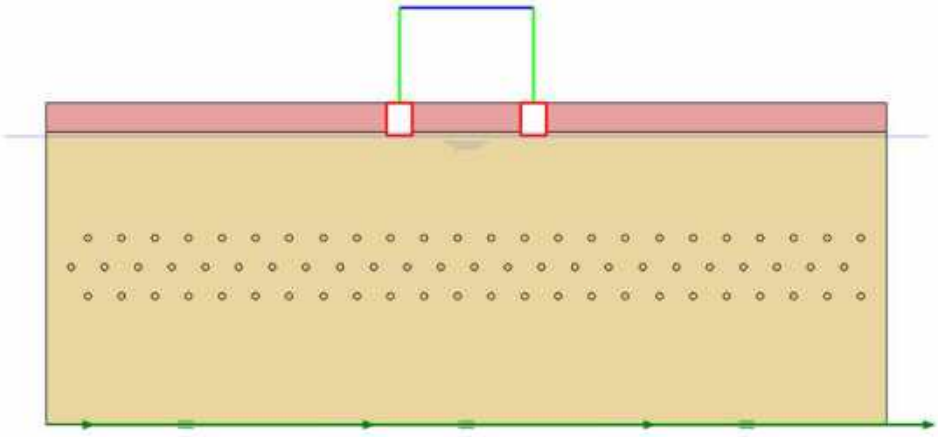

Layouts of the model reproduced in Plaxis 2D

This project has received funding from the European Union's Horizon 2020 research and innovation programme under grant agreement No. 700748

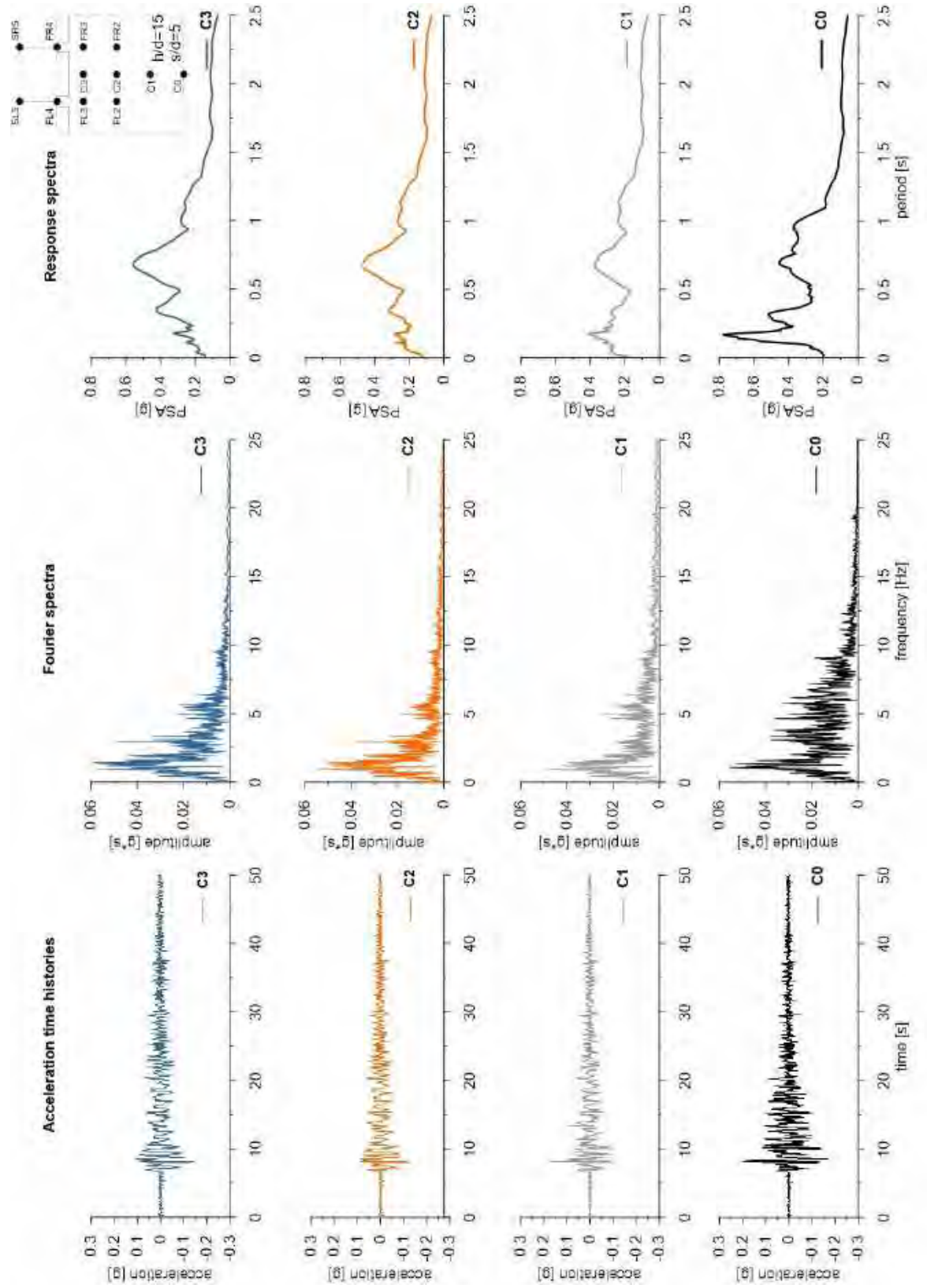

This project has received funding from the European Union's Horizon 2020 research and innovation programme under grant agreement No. 700748

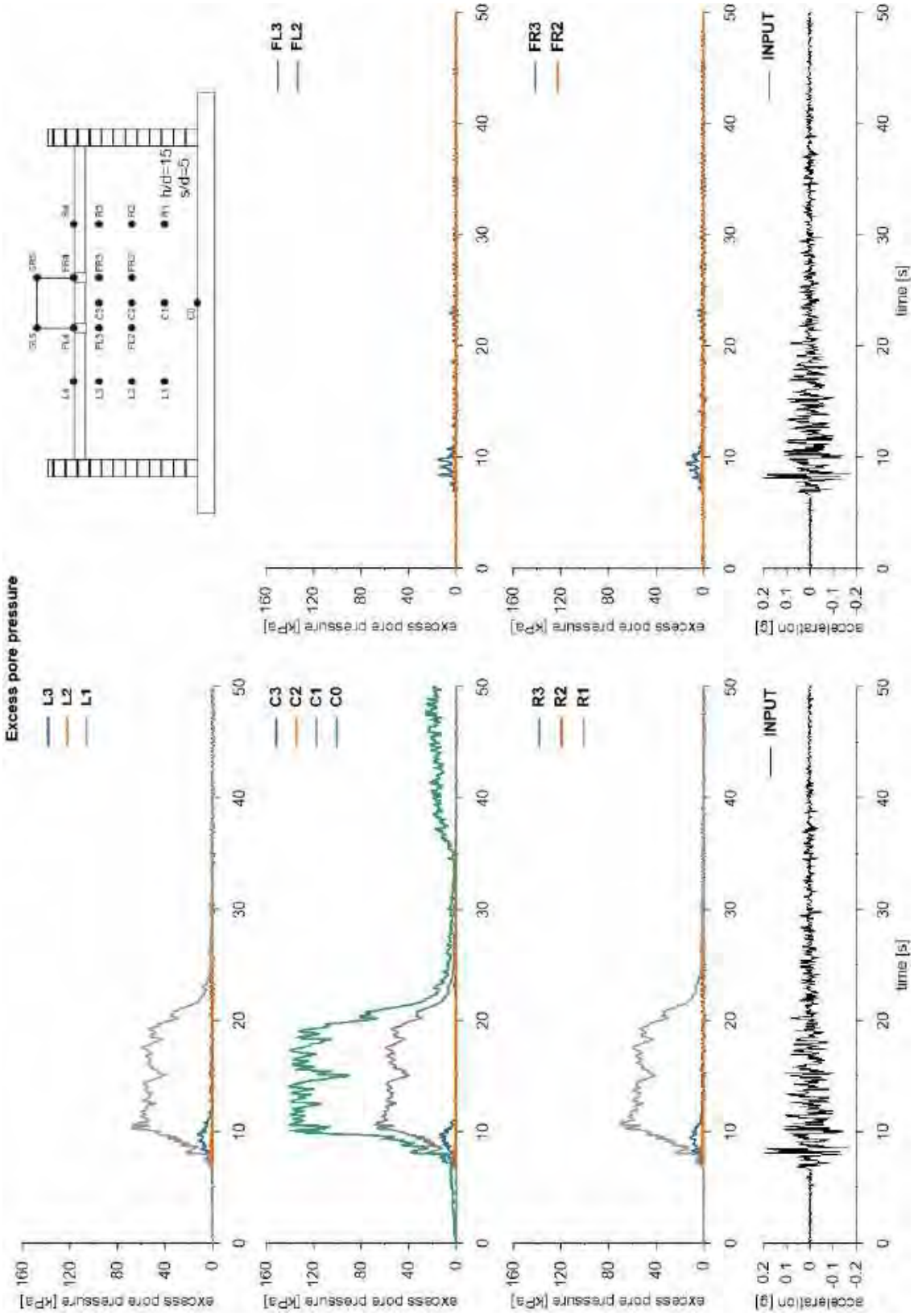

This project has received funding from the European Union's Horizon 2020 research and innovation programme under grant agreement No. 700748

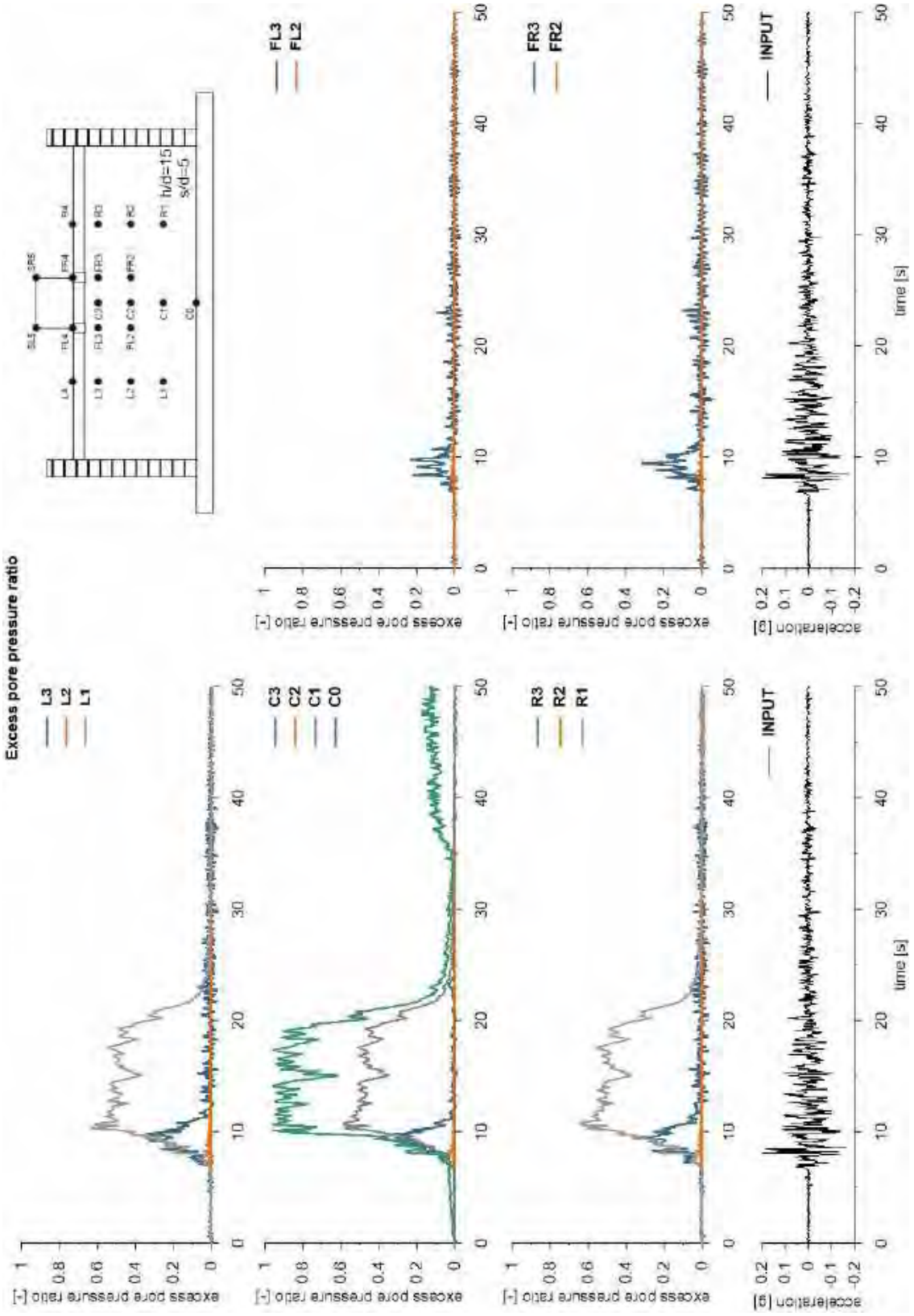

This project has received funding from the European Union's Horizon 2020 research and innovation programme under grant agreement No. 700748

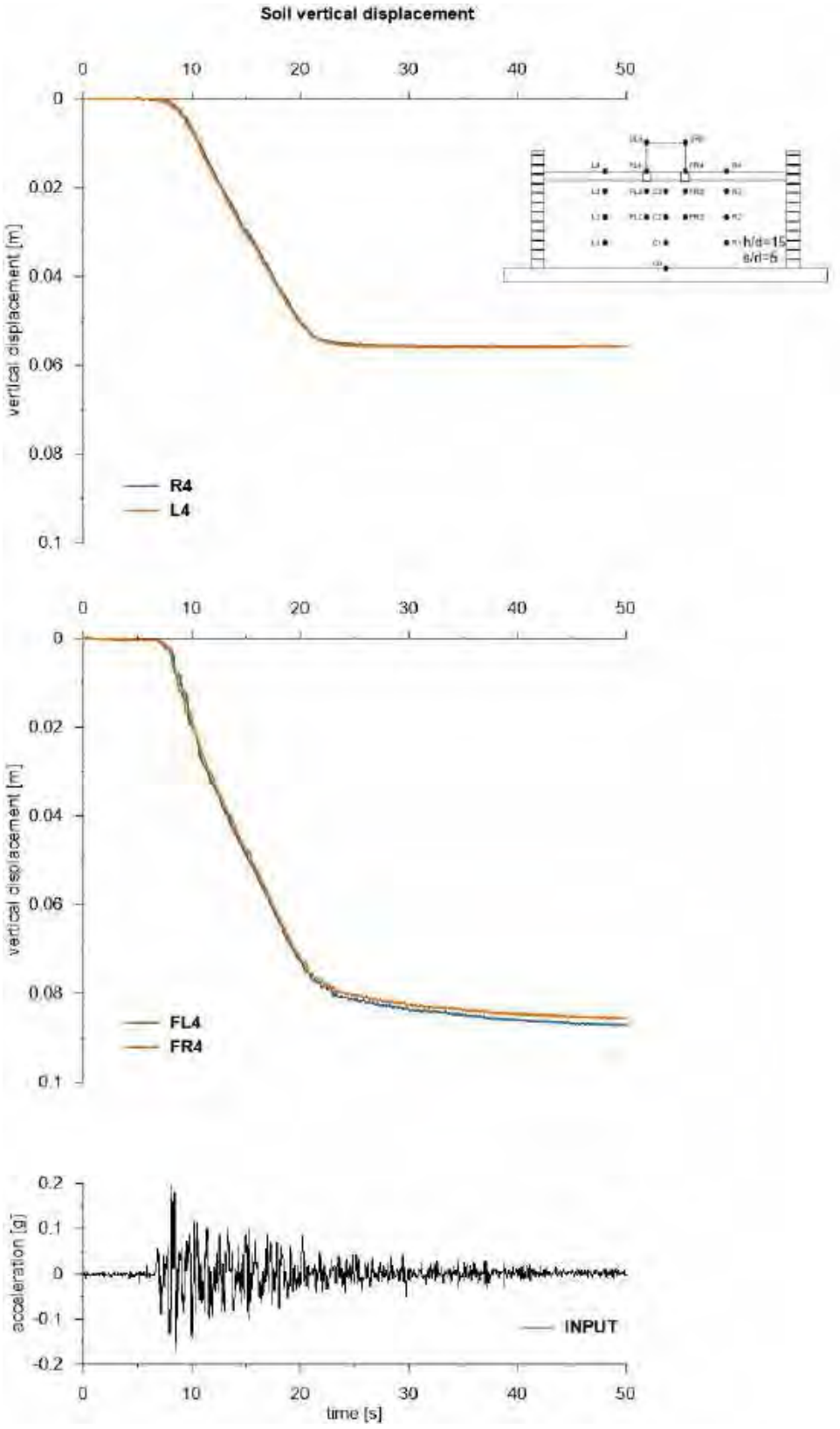

This project has received funding from the European Union's Horizon 2020 research and innovation programme under grant agreement No. 700748

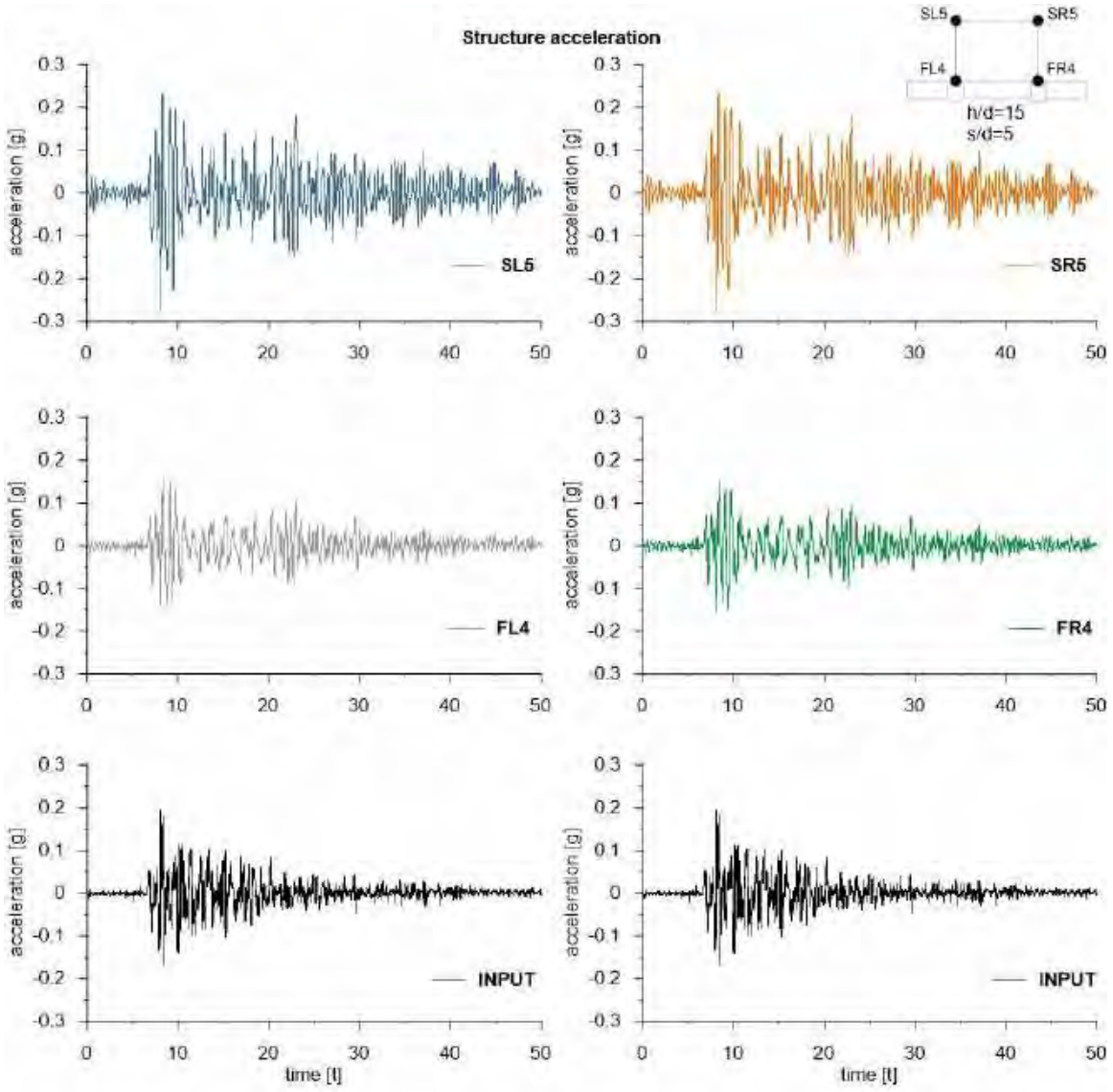

This project has received funding from the European Union's Horizon 2020 research and innovation programme under grant agreement No. 700748

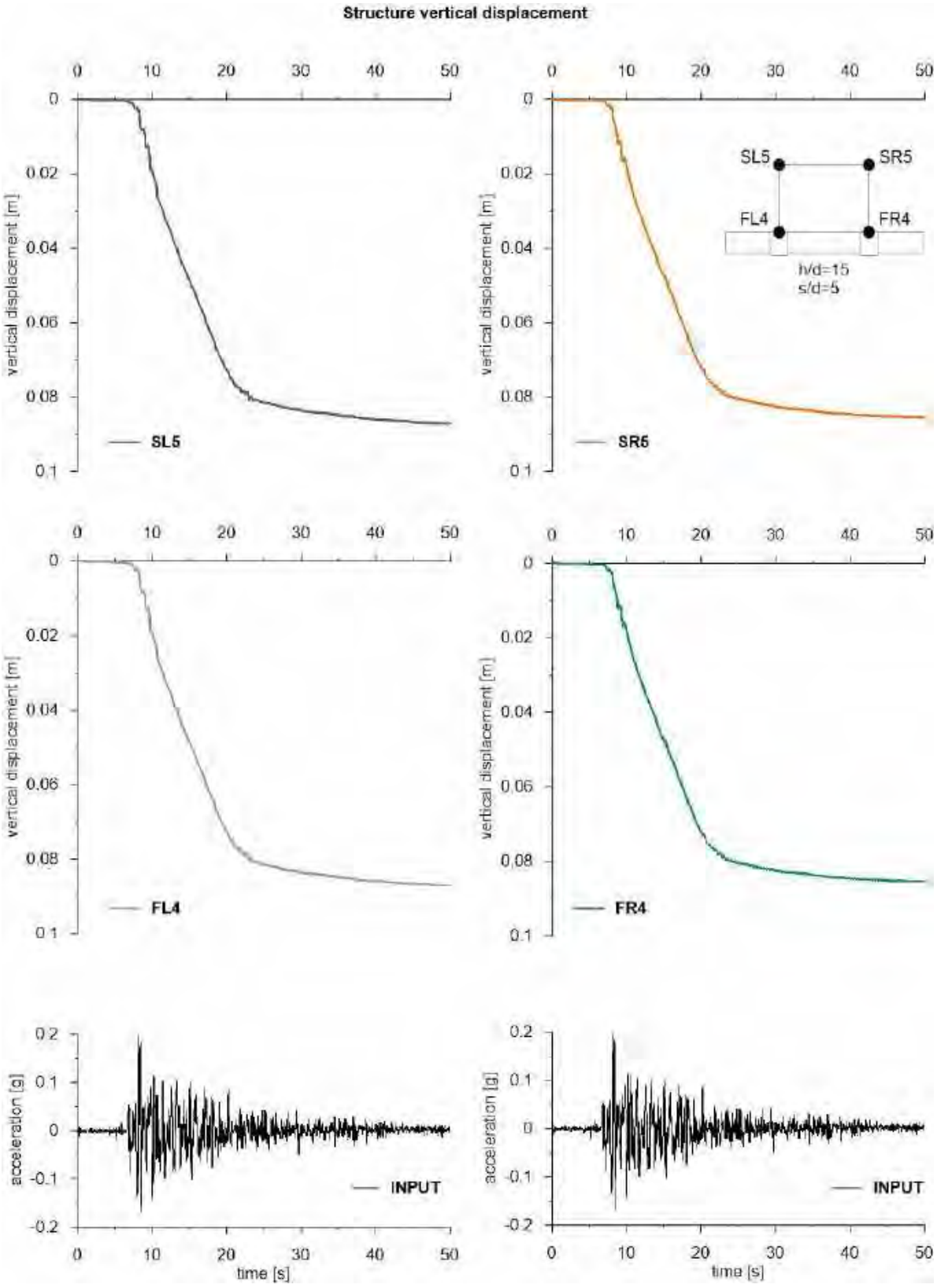

This project has received funding from the European Union's Horizon 2020 research and innovation programme under grant agreement No. 700748

6.1.1.43 ID: SS_HDU_H15_s10

The model consists of a double soil profile of clay and Ticino sand. The ground motion applied was the number 31.

ID: SS_HDU_H15_s10

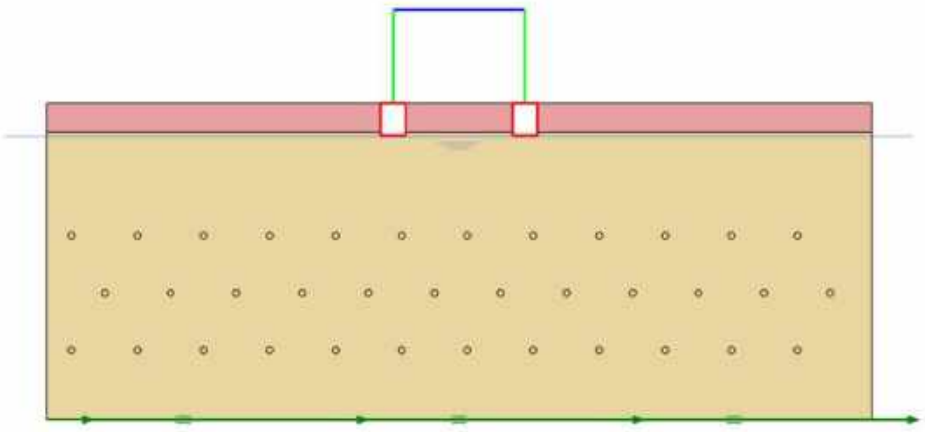

Layouts of the model reproduced in Plaxis 2D

This project has received funding from the European Union's Horizon 2020 research and innovation programme under grant agreement No. 700748

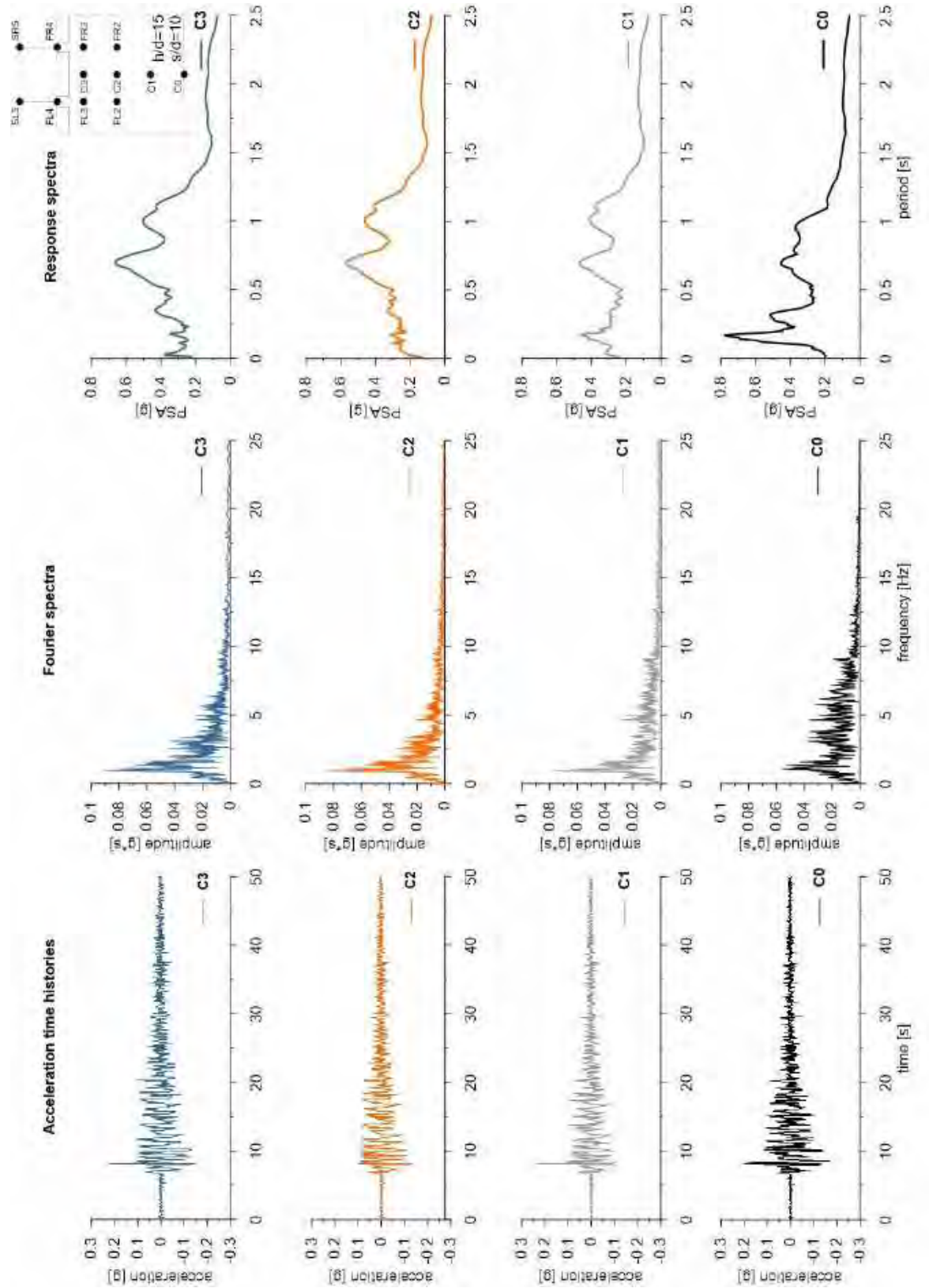

This project has received funding from the European Union's Horizon 2020 research and innovation programme under grant agreement No. 700748

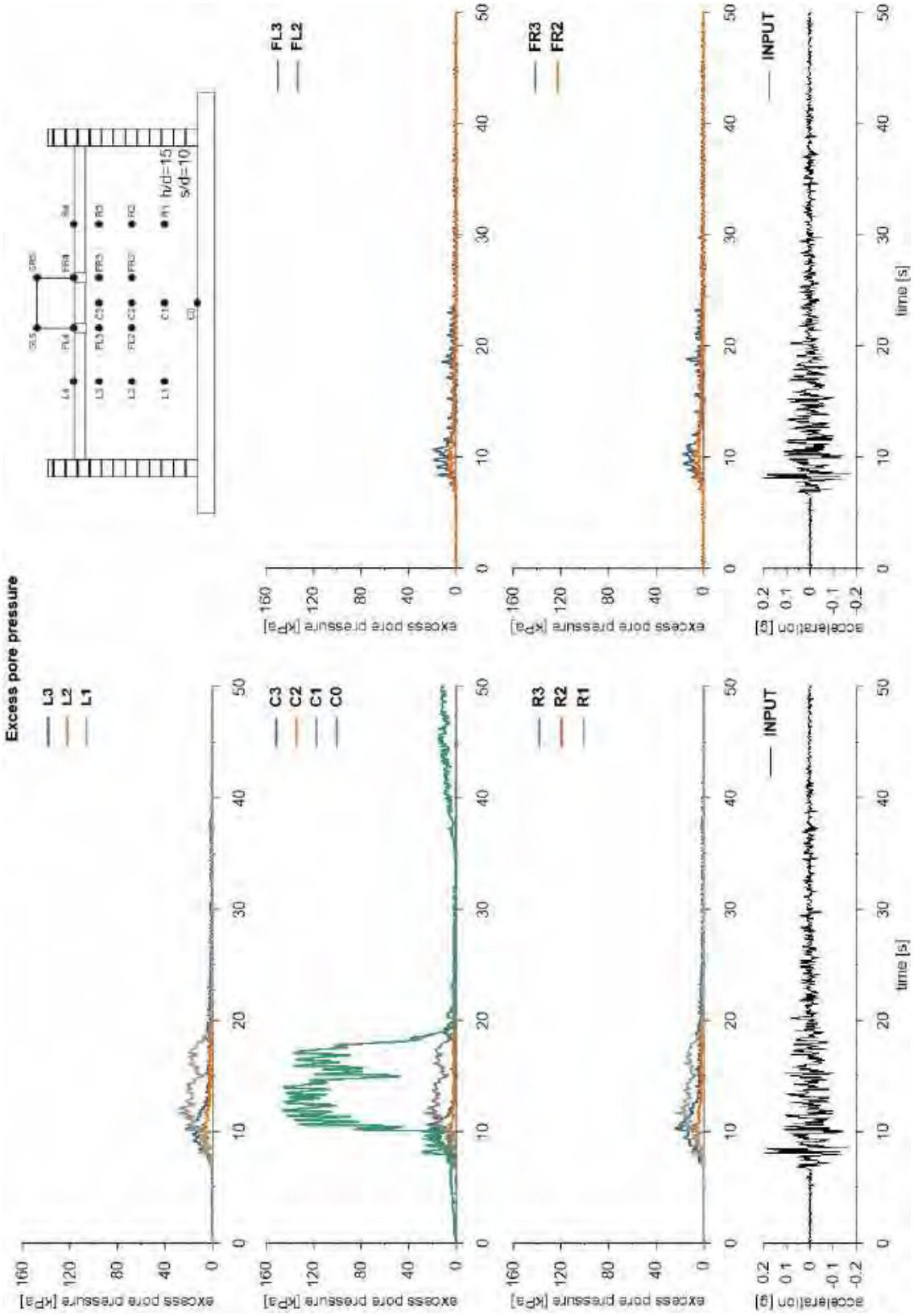

This project has received funding from the European Union's Horizon 2020 research and innovation programme under grant agreement No. 700748

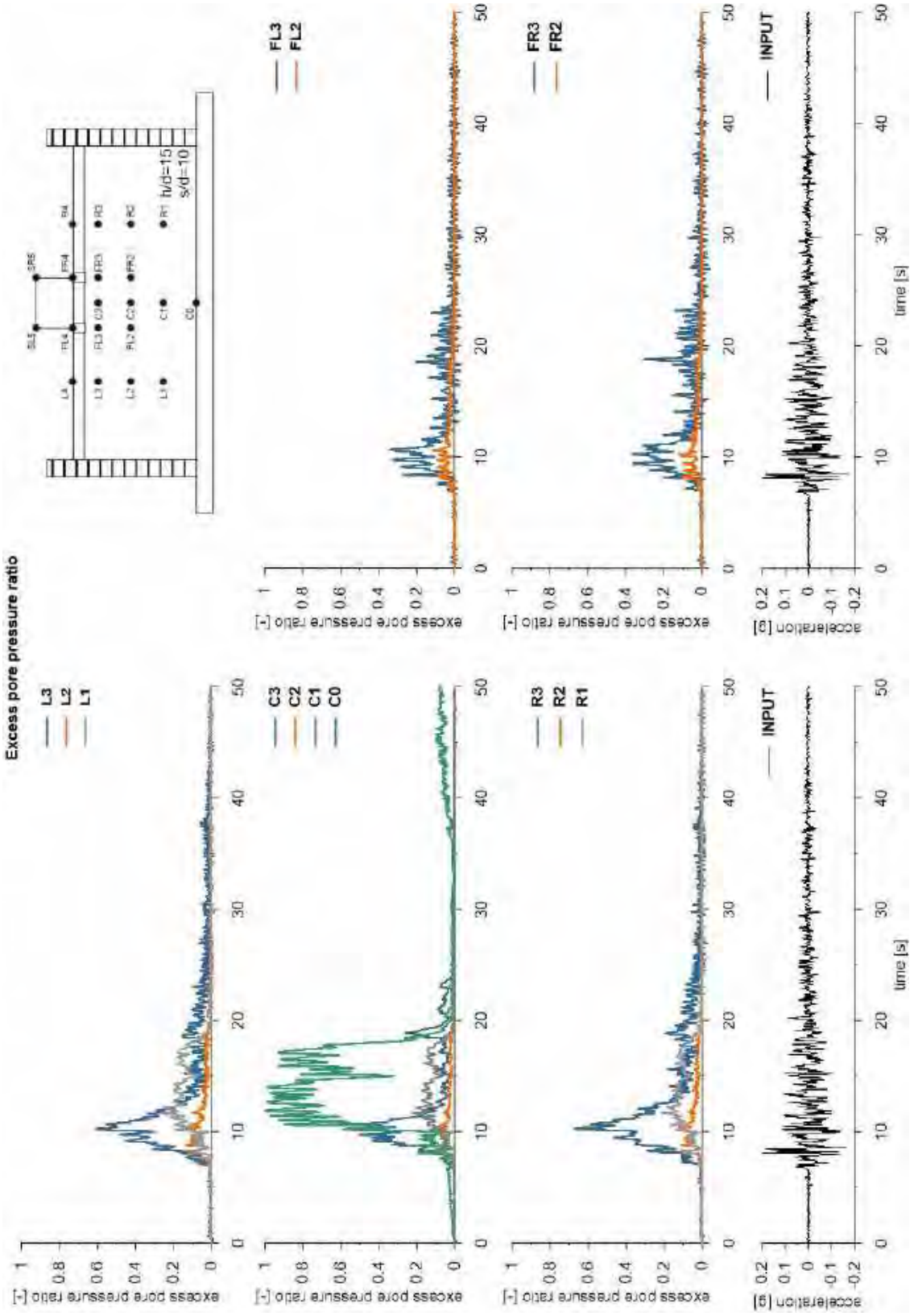

This project has received funding from the European Union's Horizon 2020 research and innovation programme under grant agreement No. 700748

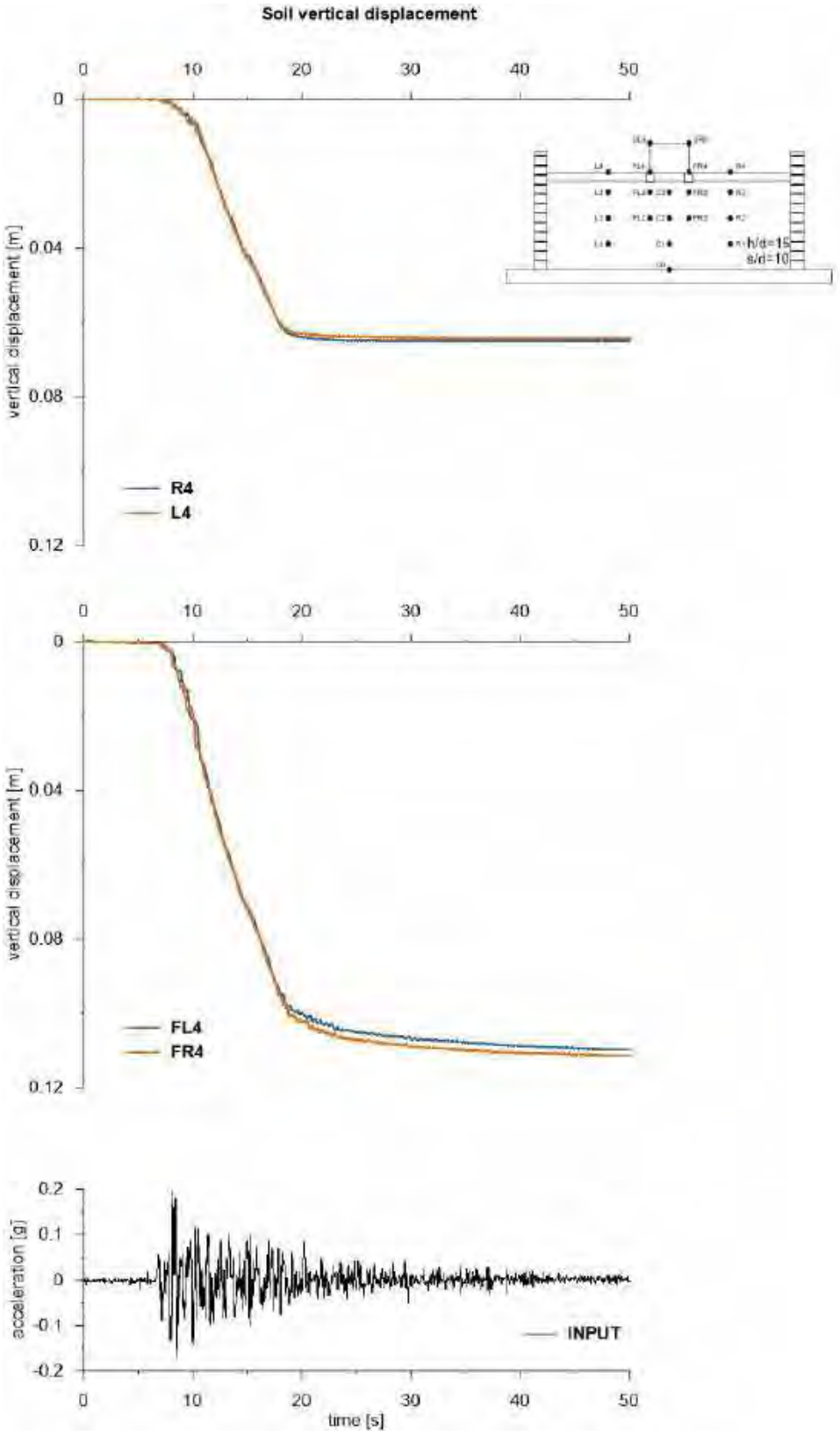

This project has received funding from the European Union's Horizon 2020 research and innovation programme under grant agreement No. 700748

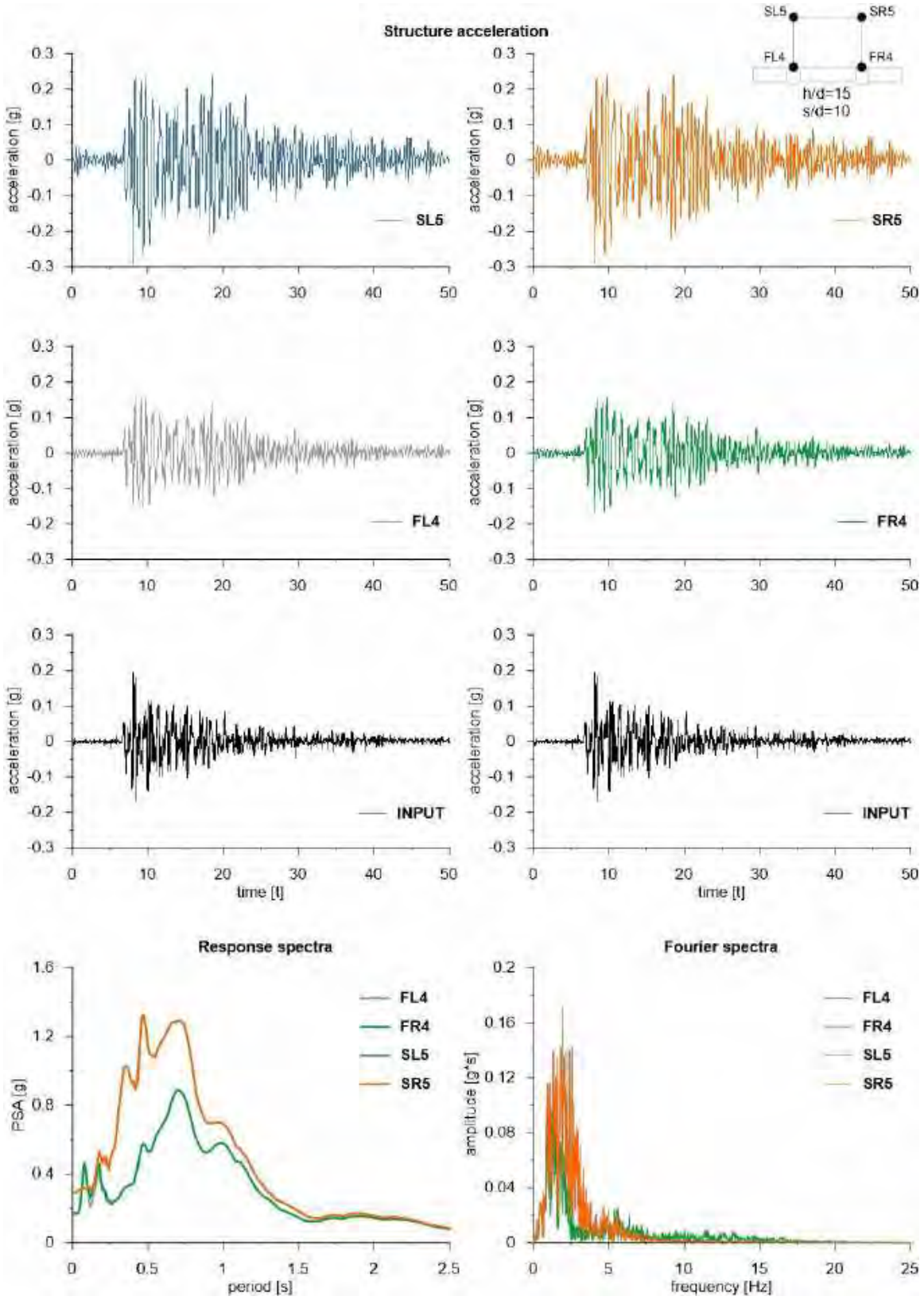

This project has received funding from the European Union's Horizon 2020 research and innovation programme under grant agreement No. 700748

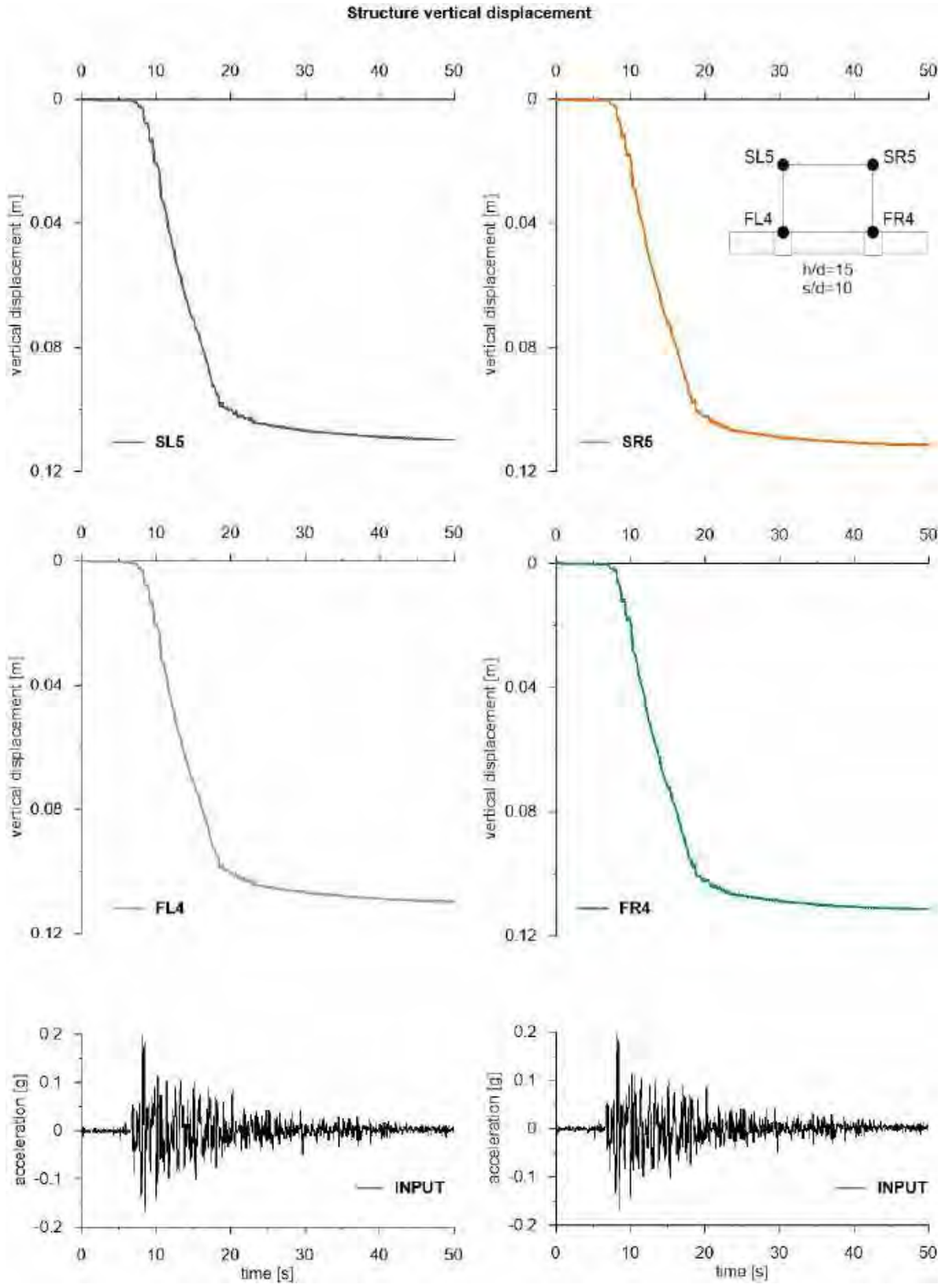

This project has received funding from the European Union's Horizon 2020 research and innovation programme under grant agreement No. 700748

6.1.1.44 ID: SS_HDU_H15_s15

The model consists of a double soil profile of clay and Ticino sand. The ground motion applied was the number 31.

ID: SS_HDU_H15_s15

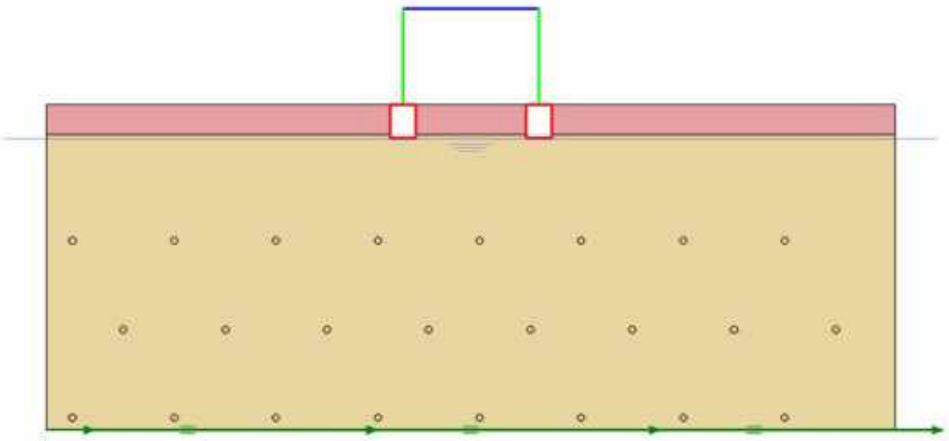

Layouts of the model reproduced in Plaxis 2D

This project has received funding from the European Union's Horizon 2020 research and innovation programme under grant agreement No. 700748

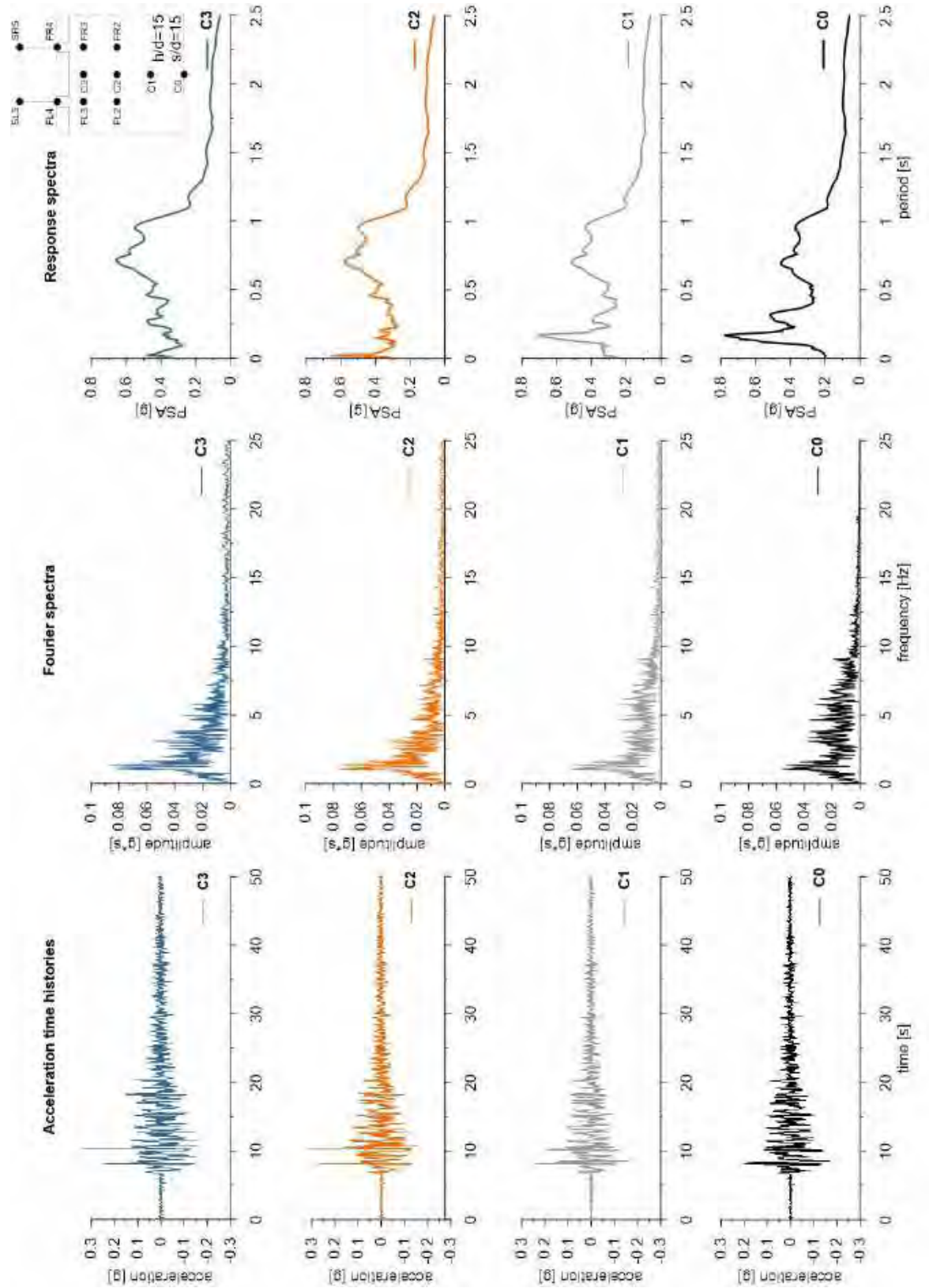

This project has received funding from the European Union's Horizon 2020 research and innovation programme under grant agreement No. 700748

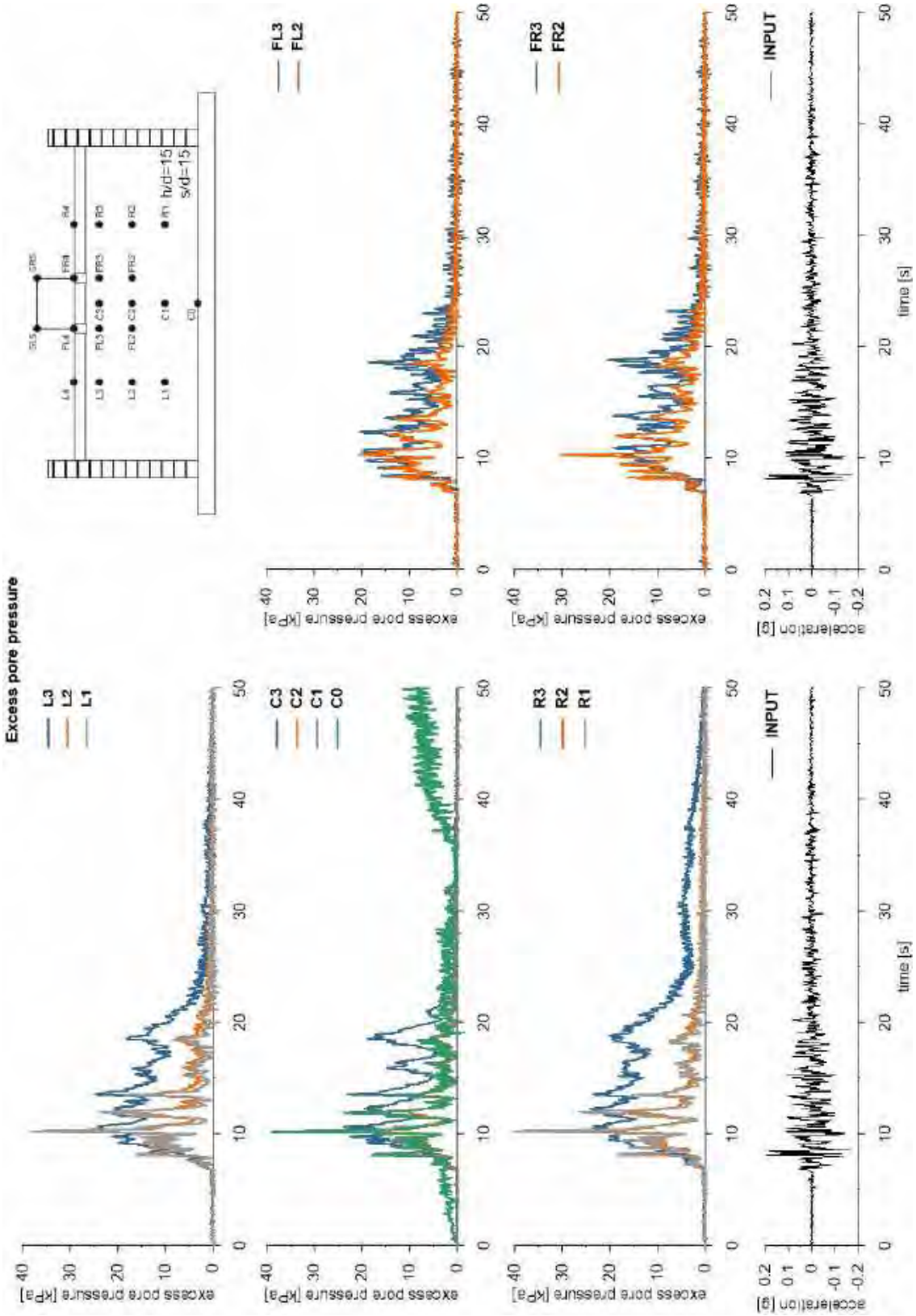

This project has received funding from the European Union's Horizon 2020 research and innovation programme under grant agreement No. 700748

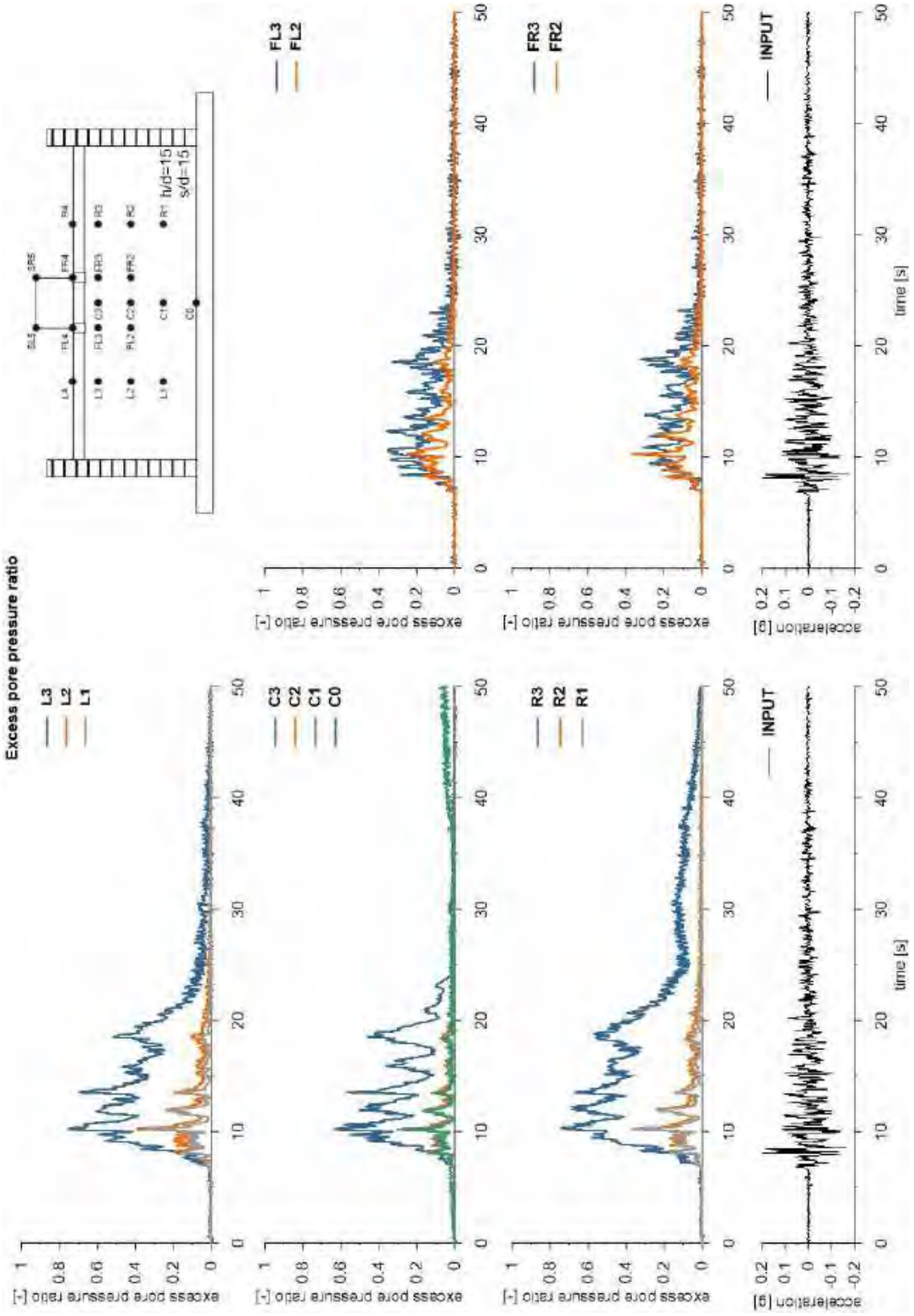

This project has received funding from the European Union's Horizon 2020 research and innovation programme under grant agreement No. 700748

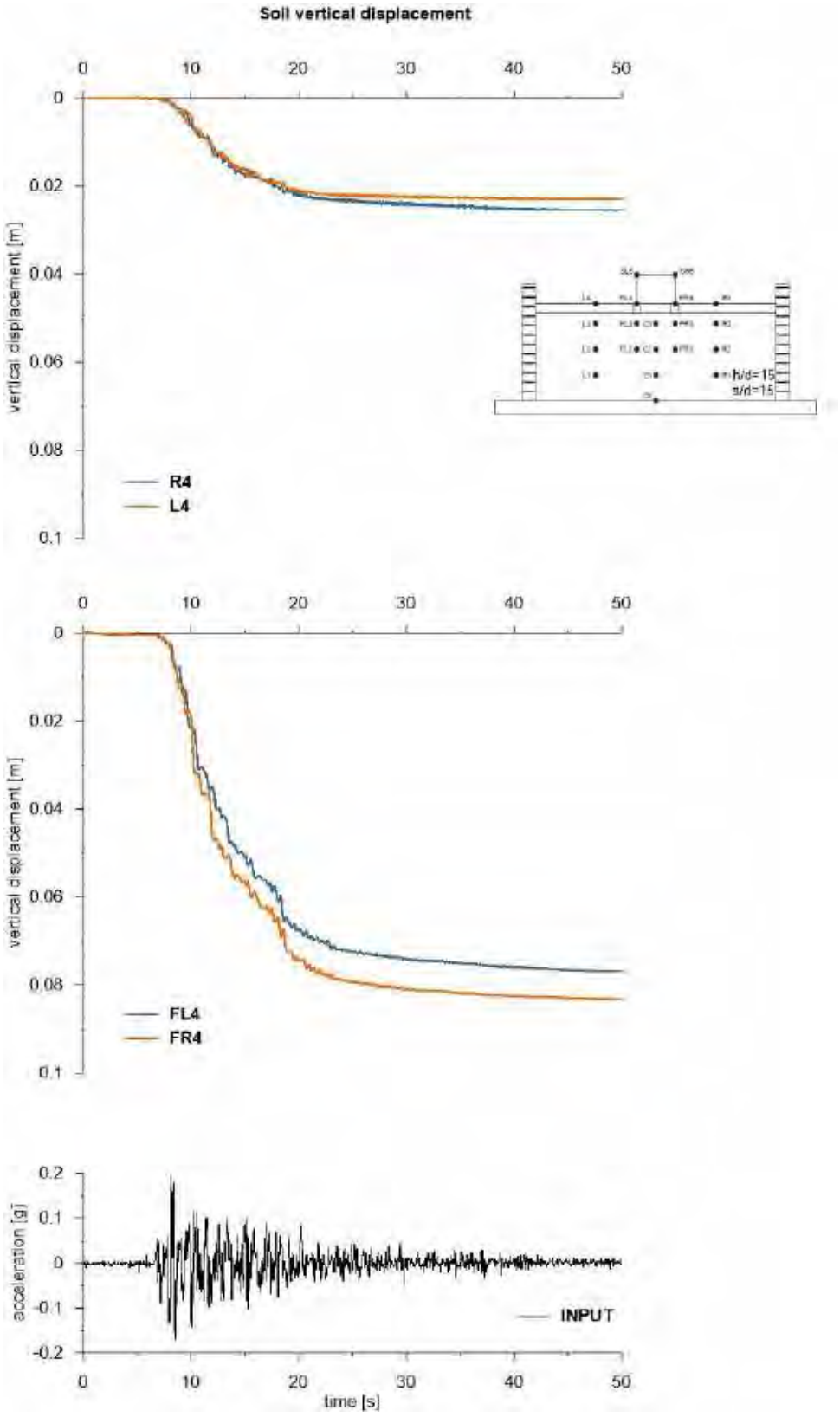

This project has received funding from the European Union's Horizon 2020 research and innovation programme under grant agreement No. 700748

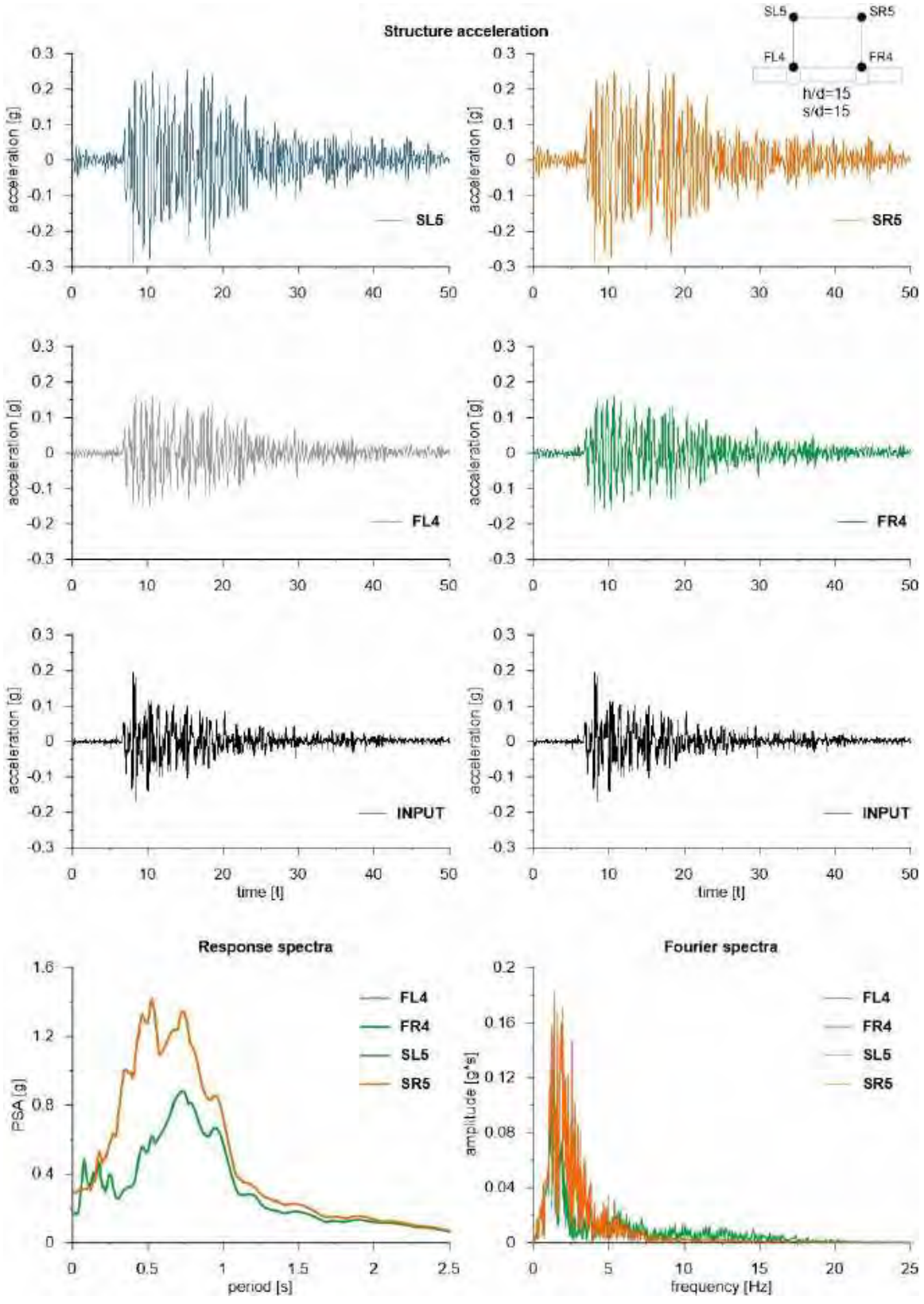

This project has received funding from the European Union's Horizon 2020 research and innovation programme under grant agreement No. 700748

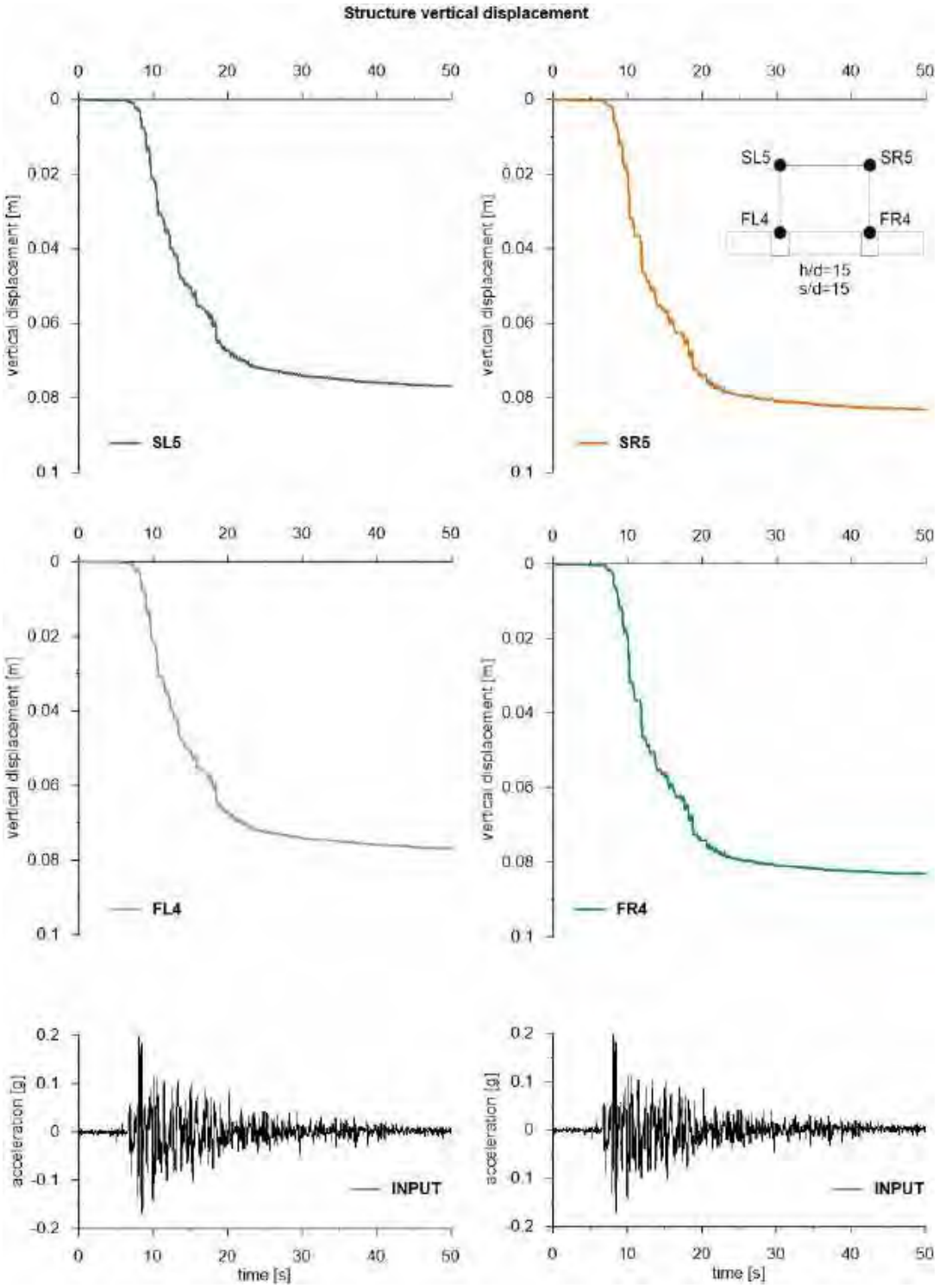

This project has received funding from the European Union's Horizon 2020 research and innovation programme under grant agreement No. 700748

6.2 FINAL REMARKS

The analyses were carried out to check the relevance of the depth and spacing of a uniform set of horizontal drains.

The first series of analyses was conducted on the scheme with a single layer of liquefiable sand (Figure 6.1).

Table 6.1 reports the results in terms of maximum R_u in some specific positions of the subsoil (see Figure 6.1). The second set of analyses was carried out considering a double layer subsoil (Figure 6.2 and Table 6.2).

Since these control points have a constant depth and a fixed abscissa, their position relative to the drains changes with the spacing among them. Because of this, the results reported in the table give an indication of the maximum pore pressure increment in these points, that cannot be always considered as a maximum value at their depth. In order to have a general idea of the effect of the drains, therefore, the contours of pore pressure increments have been plotted and reported in Appendix B.

The analyses show that in the investigated range of spacings, the most relevant parameter ruling the effectiveness of drainage is the depth H (see Figure 6.1 and Figure 6.2). Deeper positions of the drains lead to a larger drained portion of the ground.

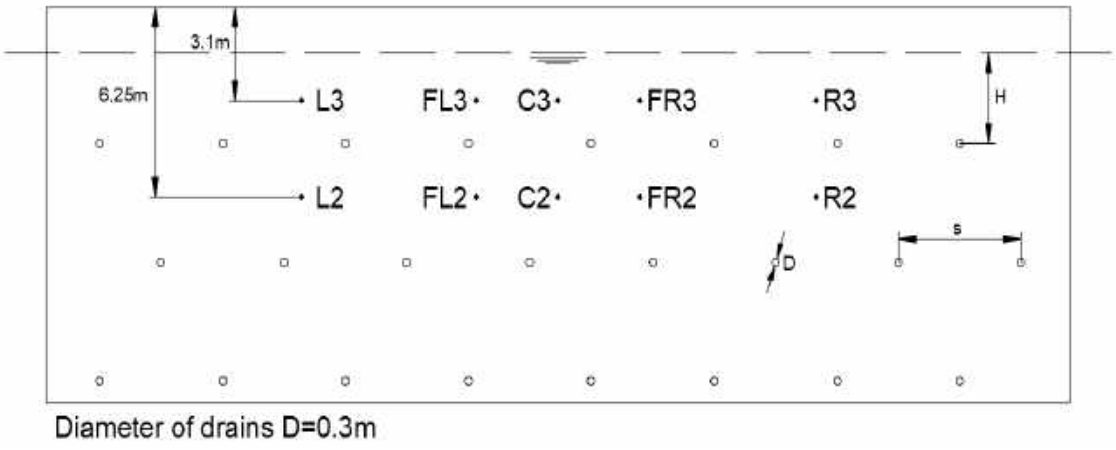

Figure 6.1. single layer of liquefiable sand.

Table 6.1. Series of analyses was conducted on the scheme with a single layer.

ID	Structure	s/D	H/D	Depth (m)	Position for $R_{u,max}$	$R_{u,max}$
SF_HDU_H05_s05	No	5	5	3,1	R3	0,05
				6,25	FR2	0,23
SF_HDU_H05_s10	No	10	5	3,1	R3	0,14
				6,25	L2	0,15

This project has received funding from the European Union's Horizon 2020 research and innovation programme under grant agreement No. 700748

SF_HDU_H05_s15	No	15	5	3,1	L3	0,21
				6,25	FL2	0,33
SF_HDU_H10_s05	No	5	10	3,1	FR3	0,16
				6,25	L2	0,05
SF_HDU_H10_s10	No	10	10	3,1	R3	0,17
				6,25	L2	0,15
SF_HDU_H10_s15	No	15	10	3,1	FR3	0,24
				6,25	C2	0,26
SF_HDU_H15_s05	No	5	15	3,1	FL3	0,24
				6,25	R2	0,06
SF_HDU_H15_s10	No	10	15	3,1	FR3/R3	0,24
				6,25	R2	0,17
SF_HDU_H15_s15	No	15	15	3,1	C3	0,26
				6,25	FR2	0,25

ID	Structure	s/D	H/D	Depth (m)	Position for $R_{u,max}$	$R_{u,max}$
SS_HDU_H05_s05	Yes	5	5	3,1	FL3	0,04
				6,25	R2	0,23
SS_HDU_H05_s10	Yes	10	5	3,1	FL3	0,16
				6,25	L2	0,14
SS_HDU_H05_s15	Yes	15	5	3,1	L3	0,21
				6,25	R2	0,27
SS_HDU_H10_s05	Yes	5	10	3,1	FL3	0,19
				6,25	L2	0,04
SS_HDU_H10_s10	Yes	10	10	3,1	FL3	0,26
				6,25	L2	0,15
SS_HDU_H10_s15	Yes	15	10	3,1	FL3	0,28
				6,25	R2	0,28
SS_HDU_H15_s05	Yes	5	15	3,1	FL3	0,26
				6,25	R2	0,05
SS_HDU_H15_s10	Yes	10	15	3,1	FL3	0,26
				6,25	R2	0,16
SS_HDU_H15_s15	Yes	15	15	3,1	FL3	0,44
				6,25	L2	0,27

ID	Structure	s/D	H/D	Depth (m)	Position for $R_{u,max}$	$R_{u,max}$

This project has received funding from the European Union's Horizon 2020 research and innovation programme under grant agreement No. 700748

SS_xx_xx_xx	Yes	-	-	3,1	L3	0,81
				6,25	R2	0,92
SF_xx_xx_xx	No	-	-	3,1	FL3	0,85
				6,25	L2	0,94

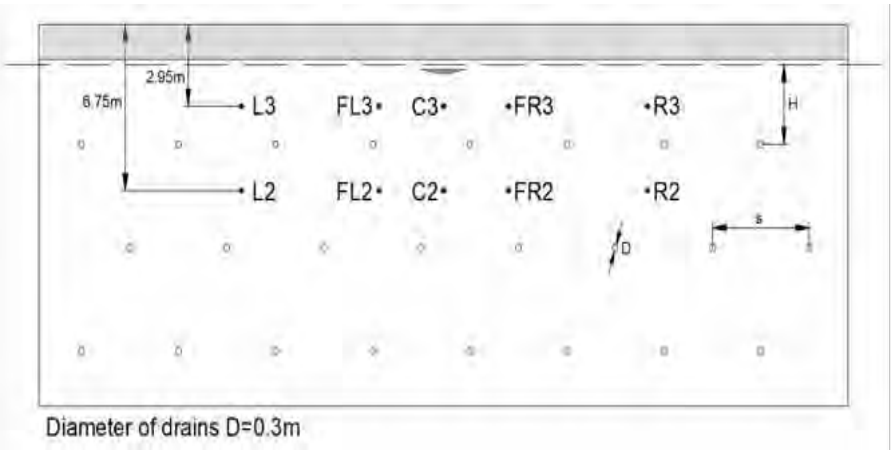

Figure 6.2. Double layer with liquefiable sand and upper clay.

Table 6.2. Series of analyses was conducted on the scheme with a double layer.

ID	Structure	s/D	H/D	Depth (m)	Position for $R_{u,max}$	$R_{u,max}$
DF_HDU_H05_s05	No	5	5	2,95	R3	0,062
				6,75	C2	0,35
DF_HDU_H05_s10	No	10	5	2,95	L3	0,135
				6,75	FL2, FR2	0,141
DF_HDU_H05_s15	No	15	5	2,95	FR3	0,258
				6,75	C2	0,244
DF_HDU_H10_s05	No	5	10	2,95	FR3	0,447
				6,75	R2	0,054
DF_HDU_H10_s10	No	10	10	2,95	L3, FR3	0,211
				6,75	R3	0,134
DF_HDU_H10_s15	No	15	10	2,95	FR3	0,379
				6,75	C2	0,641
DF_HDU_H15_s05	No	5	15	2,95	FL3	0,302
				6,75	L2	0,042
DF_HDU_H15_s10	No	10	15	2,95	C3	0,319
				6,75	L2	0,138
DF_HDU_H15_s15	No	15	15	2,95	FL3	0,759

This project has received funding from the European Union's Horizon 2020 research and innovation programme under grant agreement No. 700748

				6,75	FR2	0,534
ID	**Structure**	**s/D**	**H/D**	**Depth (m)**	**Position for $R_{u,max}$**	**$R_{u,max}$**
DS_HDU_H05_s05	Yes	5	5	2,95	FR3	0,052
				6,75	L2	0,357
DS_HDU_H05_s10	Yes	10	5	2,95	FL3	0,286
				6,75	R2	0,134
DS_HDU_H05_s15	Yes	15	5	2,95	FR3	0,251
				6,75	L2	0,327
DS_HDU_H10_s05	Yes	5	10	2,95	FL3	0,193
				6,75	R2	0,047
DS_HDU_H10_s10	Yes	10	10	2,95	C3	0,278
				6,75	R2	0,127
DS_HDU_H10_s15	Yes	15	10	2,95	R3	0,504
				6,75	R2	0,468
DS_HDU_H15_s05	Yes	5	15	2,95	L3	0,343
				6,75	L2	0,039
DS_HDU_H15_s10	Yes	10	15	2,95	R3	0,668
				6,75	L2	0,181
DS_HDU_H15_s15	Yes	15	15	2,95	L3	0,75
				6,75	L2	0,39

ID	**Structure**	**s/D**	**H/D**	**Depth (m)**	**Position for $R_{u,max}$**	**$R_{u,max}$**
DF_xx_xx_xx	No	-	-	2,95	R3	0,952
				6,75	R2	0,971
DS_xx_xx_xx	Yes	-	-	2,95	R3	0,978
				6,75	L2	0,969

This project has received funding from the European Union's Horizon 2020 research and innovation programme under grant agreement No. 700748

7 NUMERICAL ANALYSES OF FIELD TRIALS

7.1 DESCRIPTION OF THE FIELD TRIALS

7.1.1 SITE CHARACTERIZATION

The field trial is located in the Pieve di Cento municipality (Emilia Romagna Region, Italy), were the 2012 Emilia earthquake (M_w =6.1) produced significant and widespread liquefaction effects (Figure 7.1). The field trial is located along the paleochannel of Reno river. Two mitigation techniques against liquefaction have been tested in the field trial: horizontal drainage system (HD) with two different configurations and induced partial saturation (IPS). The in-situ geotechnical investigation campaign is located around the areas where the two mitigation techniques were designed and executed.

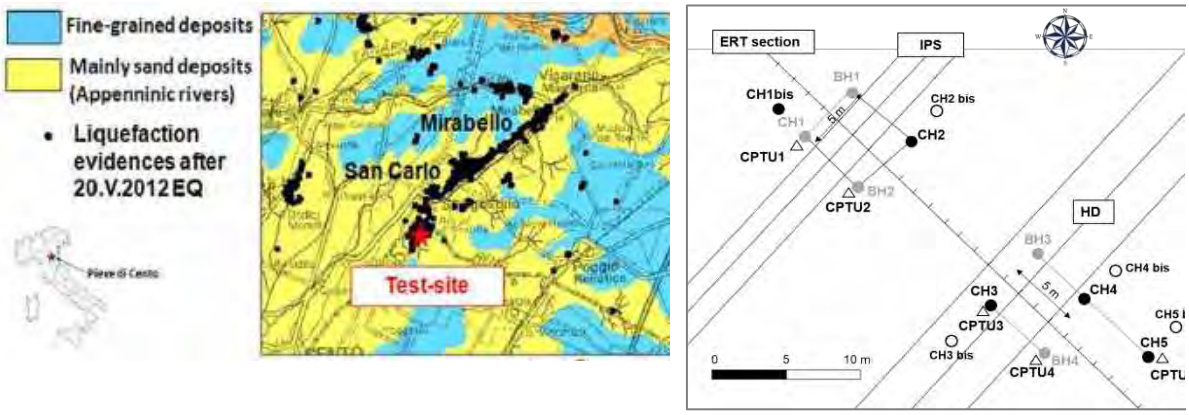

(a) (b)

Figure 7.1. (a) Location (a) and plan view (b) of the test site.

Ground investigation was carried out aiming to define the soil stratigraphic sequence and to obtain information on the geotechnical properties of soil layers. It consisted of:

- 5 boreholes reaching 10 m below the ground surface (CH1bis, CH2, CH3, CH4, CH5);
- 4 additional boreholes (CH2bis, CH3bis, CH4bis, CH5bis) performed only for retrieving undisturbed samples (with Osterberg and Gel Push samplers);
- 5 boreholes (BH1, CH1, BH2, BH3, BH4) up to 10 m from ground level used for seismic investigations (cross-holes tomographies).
- 5 penetration tests with piezocone (CPTU1, CPTU2, CPTU3, CPTU4 and CPTU5) up to a depth of 11 m from ground level;
- an Electrical Resistivity Tomography (ERT) performed at the surface along the longitudinal section covering both areas (HD and IPS).

This project has received funding from the European Union's Horizon 2020 research and innovation programme under grant agreement No. 700748

Field investigation was also integrated with many laboratory tests (grain size analyses, Atterberg's limit tests, drained triaxial, eodometric, cyclic triaxial, cyclic simple shear and cyclic torsional shear tests) carried out on both undisturbed and reconstituted soil specimens with the goal to contribute to the definition of a geotechnical model.

The soil column consists of an upper crust 1 m thick of silty sand overlying a sandy silt layer, which has a thickness ranging between 1 and 2 m. A grey silty sand deposit (GSS) is located between 2.8 and 6 m with a thin clayey layer identified at a depth between 4.4 and 4.7 m. This thin layer belongs to the same formation of silty clay located beyond 6 m depth from the ground surface (Figure 7.2).

Regarding the physical properties, the sandy silt layer is constituted by heterogeneous soils (well-graded and with variable fine content between 60 – 85% and low-plasticity fine), while the grey silty sand (GSS) is quite homogeneous with a fine content ranging from 5 ÷ 12 %. The clayey layer has a plasticity index of 0.55 and it can be assumed as an impermeable layer. The depth of the ground water table is located at 1.8 m below the ground level, as revealed by the in-situ investigations.

The grey silty sand (GSS) it is supposed to be the liquefiable layer: it is a saturated sand deposit (Vs≈120m/s) quite superficial with a low value of relative density (Dr ≈ 40%) and a soil behaviour type index, Ic, less than 2.0. With reference to the upper sandy silt, it is characterized by Ic values ranging between 2.0 and 3, approximately, which highlight the alternation of liquefiable and non-liquefiable material (Figure 7.3).

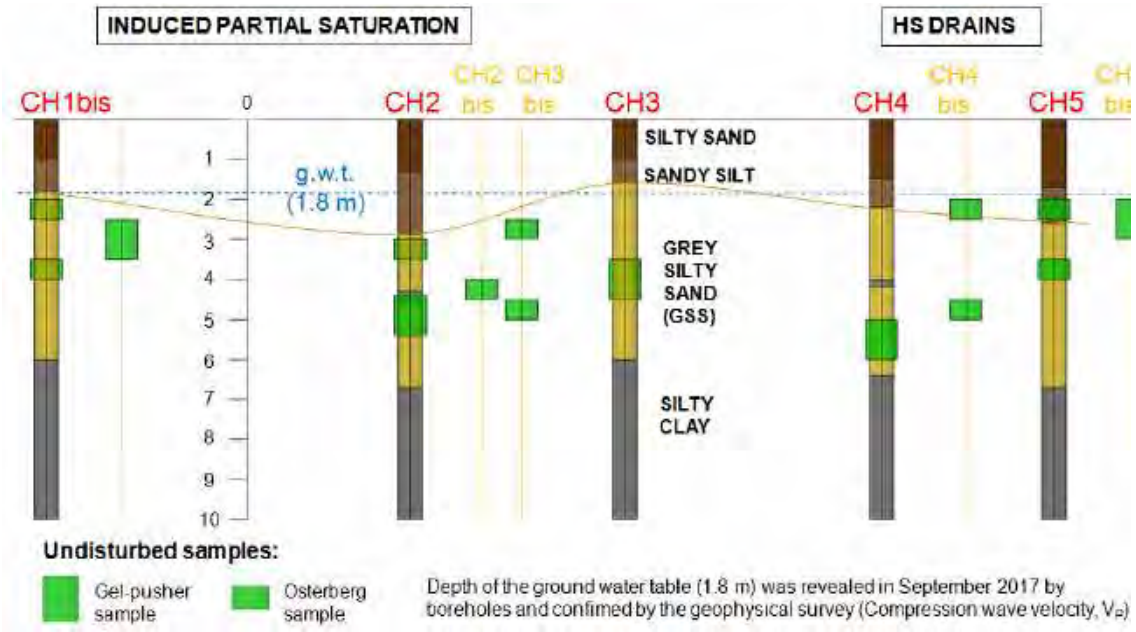

(a)

Figure 7.2. Representative soil profile and location of soil sampling

This project has received funding from the European Union's Horizon 2020 research and innovation programme under grant agreement No. 700748

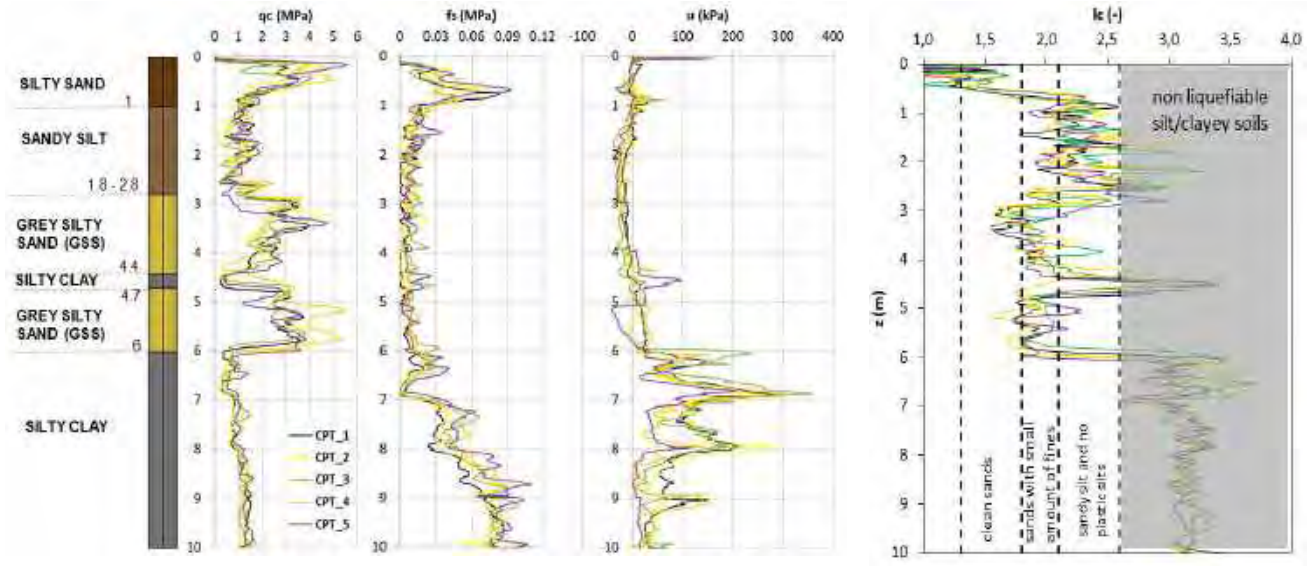

(a) (b)

Figure 7.3. Representative soil profile and CPTU results (a), soil behaviour type index Ic *(b)*

7.1.2 MITIGATION TECHNIQUES

The two mitigation techniques (HD and IPS) have been installed in the upper part of the silty sand layer (GSS), at a depth ranging between 2.8 and 4.4 m from the ground surface. For the HD, two different geometrical configurations were tested in site (Figure 7.5):

- "line configuration": three draining pipes located at a depth of 3.5 m from the ground surface with a spacing of 1.8 m;
- "rhombus configuration": four draining pipes located at a depth ranging from 2.8 m (the shallowest one) and 4.2 m (the deepest one), with a spacing of 1.0 m.

For the IPS technique, the partial saturation was obtained by injecting pressurized air from two horizontal pipes installed at a depth of 4.0 m from the ground surface with a spacing of 2 m. Some preliminary in situ injection tests have been performed in July 2018 in order to correctly compute the necessary air volume to be injected for inducing a low desaturation.

7.1.3 EXPERIMENTAL TESTING PROGRAM

The goal of the field tests carried out in Pieve di Cento was to initially evaluate the liquefaction potential of the in-situ untreated soil, and then to repeat the liquefaction tests in the areas where the two selected mitigation techniques were installed. A shear-wave vibrator (M13S/609 S-Wave, Figure 7.4) was used as a dynamic loading source at the ground surface. A preliminary excavation of 1 m of depth has been realized in order to place the dynamic loading source closest to the liquefiable sandy layer. In each test, the static vertical loading of

This project has received funding from the European Union's Horizon 2020 research and innovation programme under grant agreement No. 700748

the machine was firstly applied and, after verifying that the consolidation process was completed, a dynamic loading at 10 Hz was applied for a duration of 100 s or 200 s, in the first and in the second phase of shaking, respectively.

Type	*M13S/609 S-WAVE*
Maker	Mertz Inc
Hold Down Weight	178 kN
Reaction mass	3175 kg
Base plate (2)	0.6 x 1.6 m
Peak horizontal force	138 kN
Frequency range	3 – 80 Hz

(a) (b)

Figure 7.4. Pictures of the S-wave vibrator and vibrating base plate (a) and main specifications of the machine.

Pore pressure transducers and geophones were installed below the loading area to monitor the response at specific horizons and distances under the vibration source (Figure 7.5). A detailed topographic and photogrammetric survey has been carried out in order to measure the soil settlement after the application of the dynamic loading.

Figure 7.5 shows the four areas were the liquefaction tests were carried out. In the Area 1 (without mitigation techniques) some tests were performed to analyze the response of the untreated soil to the shaking. In the Area 2 and 3, other tests were performed to verify the effectiveness of horizontal drainage systems ("rhombus configuration" in Area 2 and "line configuration" in Area 3) as liquefaction mitigation techniques. In the Area 4, the liquefaction tests were carried out to analyze the response of the soil treated with IPS technique.

This project has received funding from the European Union's Horizon 2020 research and innovation programme under grant agreement No. 700748

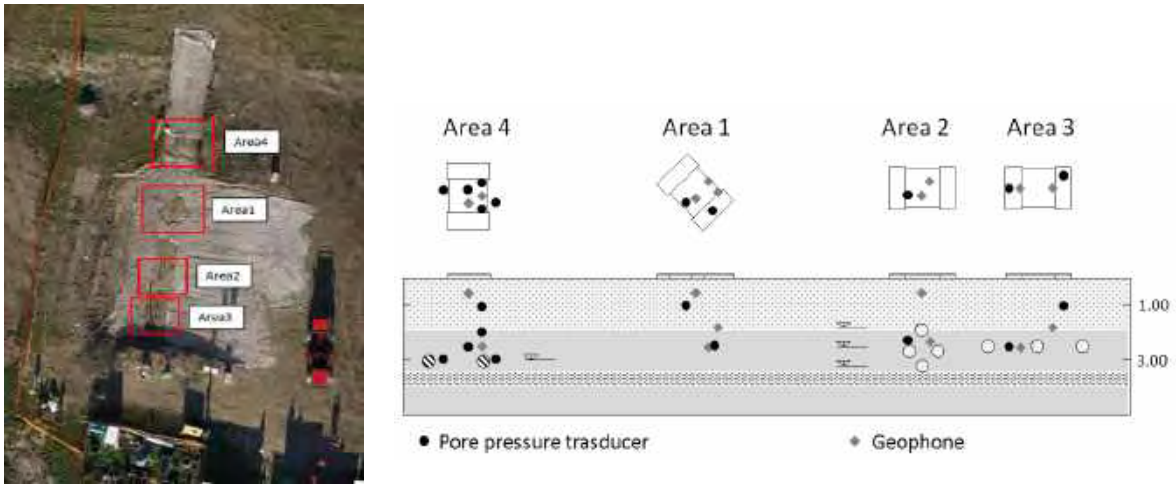

(a) (b)

Figure 7.5. Photogrammetric survey of the testing areas (a) and cross section (b).

7.2 3D NUMERICAL MODEL

The field trials have been simulated with 3D numerical analyses carried out through the finite difference code FLAC 3D (Itasca 2013). The problem configuration and the mesh used is presented in Figure 7.6. The analysis domain was defined after a sensitivity study, considering an elastic and an elasto-plastic behaviour of the soils. The stratigraphical sequence of the model is the same described in §7.1. Each material was divided in sublayers and the maximum allowable element thickness was determined at each depth based on the V_s profile and the maximum frequency content, f_{max}, of the dynamic loading, set equal to 25 Hz. The minimum wavelength ($\lambda_{min} = V_S/f_{max}$) was divided by 8 at each depth to obtain the maximum allowable thickness ($h_{max} = \lambda_{min}/8$) required by Kuhlemeyer and Lysmer (1973) criterion. The minimum wavelength was further divided by a factor of 2 in the liquefiable layer, in order to consider soil softening (i.e., reduction in V_S) during simulation, as suggested by Ramirez et al. (2018). The other two sizes of each single element were defined in order to have a shape ratio lower than 5.

Viscous quiet boundaries in normal and tangent direction were applied at the four edges and at the bottom of the analysis domain to avoid wave reflection at the borders. Moreover, since coupled analysis with generation and dissipation of excess pore water pressure were performed, hydrostatic pore pressure distribution was fixed at the four borders of the domain in order to simulate permeable boundaries and to allow drainage of excess pore water pressure in the horizontal directions.

The response of the non-liquefiable soils was simulated with the Mohr-Coulomb elasto-plastic constitutive model, assuming undrained strength parameters. A hysteretic damping has been also introduced according the sigmoidal model with four parameters (Itasca 2016).

This project has received funding from the European Union's Horizon 2020 research and innovation programme under grant agreement No. 700748

The response of the liquefiable layer was simulated adopting two different constitutive models: Finn-Byrne model, already described in §3.1.1, with the use of Mohr-Coulomb yield surface and the bounding surface plasticity model SANISAND, described in§3.1.3. Details about the calibration process are provided in the following §7.3.

In order to take into account the dissipative behaviour of soils at small-strains, a viscous damping was added in the model according to the Rayleigh formulation with a single frequency control.

Hydraulic and mechanical soil properties were defined on the results of in-situ and laboratory investigation.

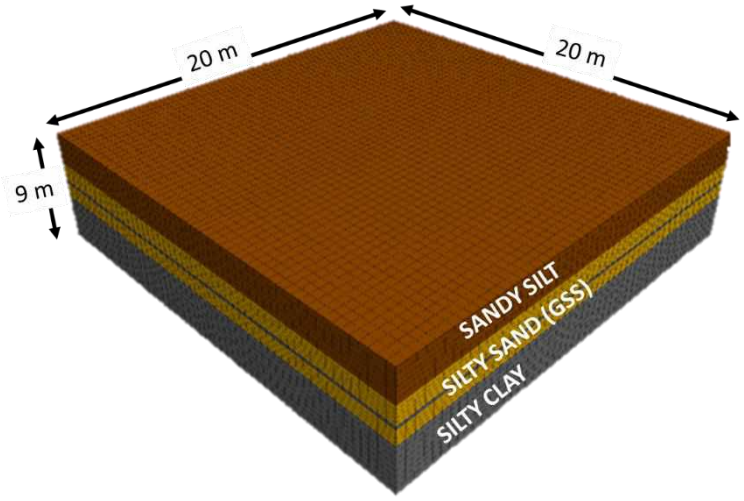

Figure 7.6. Numerical model used for simulation of the field trials.

The soil properties adopted in the 3D analyses are reported in Table 7.1.

Table 7.1. Soil properties adopted in the 3D numerical model.

Soil layer	H [m]	Model	γ [kN/m^3]	V_S [m/s]	D_0 [%]	cu [kPa]	φ_p [°]	c' (kPa)	Dr (%)	k [m/s]
sandy silt	0.8	Mohr -Coulomb	18.1	126	1.7	-	34	0	30	$1*10^{-07}$
grey silty sand	2.6	Finn/SANISAND	19.3	130	1.6	-	35	0	38	$1.84*10^{-05}$
silty clay	0.3	Mohr -Coulomb	18.3	117	2.41	30	27.5	15	-	$1*10^{-10}$
grey silty sand	1.3	Finn/SANISAND	19.3	138	1.6	-	35	0	38	$1.84*10^{-05}$

This project has received funding from the European Union's Horizon 2020 research and innovation programme under grant agreement No. 700748

silty clay	1	Mohr -Coulomb	18.3	145	2.41	60	27.5	15	-	$1*10^{-10}$
silty clay	1	Mohr -Coulomb	18.3	154	2.41	60	27.5	15	-	$1*10^{-10}$
silty clay	1	Mohr -Coulomb	18.3	163	2.41	60	27.5	15	-	$1*10^{-10}$
silty clay	1	Mohr -Coulomb	18.3	163	2.41	60	27.5	15	-	$1*10^{-10}$

Finally, all the analyses were performed in three steps:

- Static phase allows to reproduce the initial stress state (Figure 7.7);
- Static phase in which the shaker load was applied (Figure 7.8). The two baseplates of the S-vibrator (1.6 x 0.6 m) were considered rigid and modelled by constraining the nodes of the baseplate to have the same displacements. The baseplates were not directly modelled as structural elements in order to avoid time-consuming analyses.
- Dynamic phase in which the acceleration time history recorded on the baseplate was applied as surface dynamic loading (Figure 7.9).

Simulation results of the field trails on untreated a treated soil with IPS are reported in the following §7.3 and §7.4, respectively.

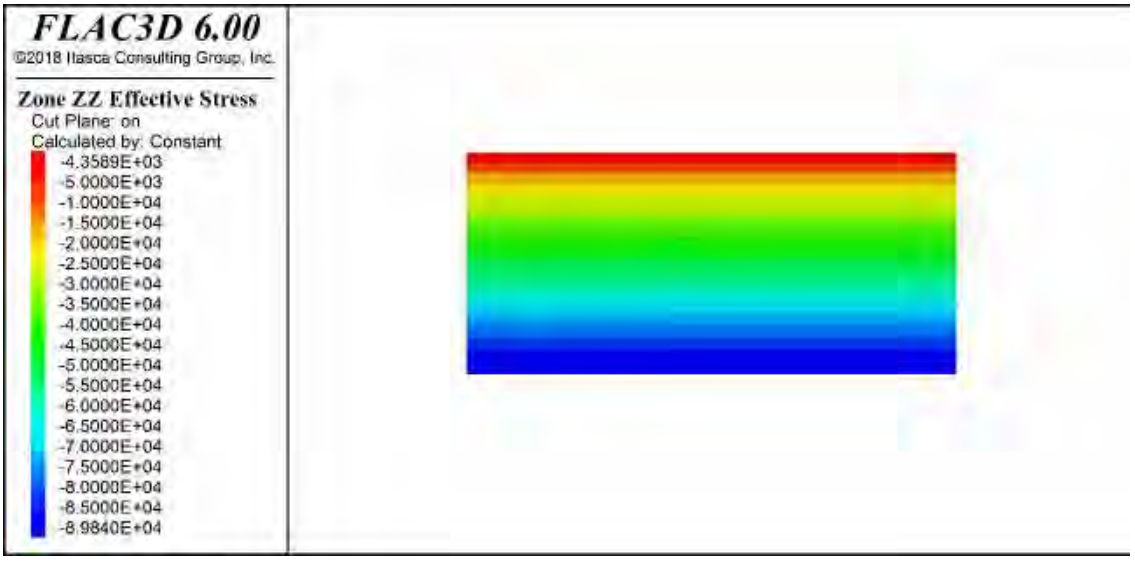

(a)

This project has received funding from the European Union's Horizon 2020 research and innovation programme under grant agreement No. 700748

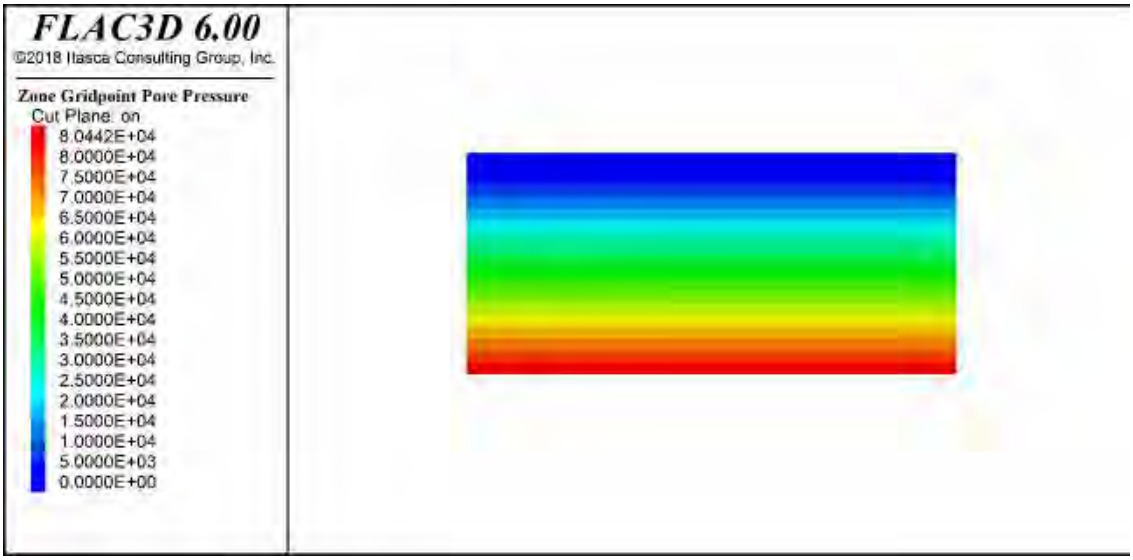

(b)

Figure 7.7. Initial effective vertical stress (in Pa) (a) and pore pressure (in Pa) (b) distribution.

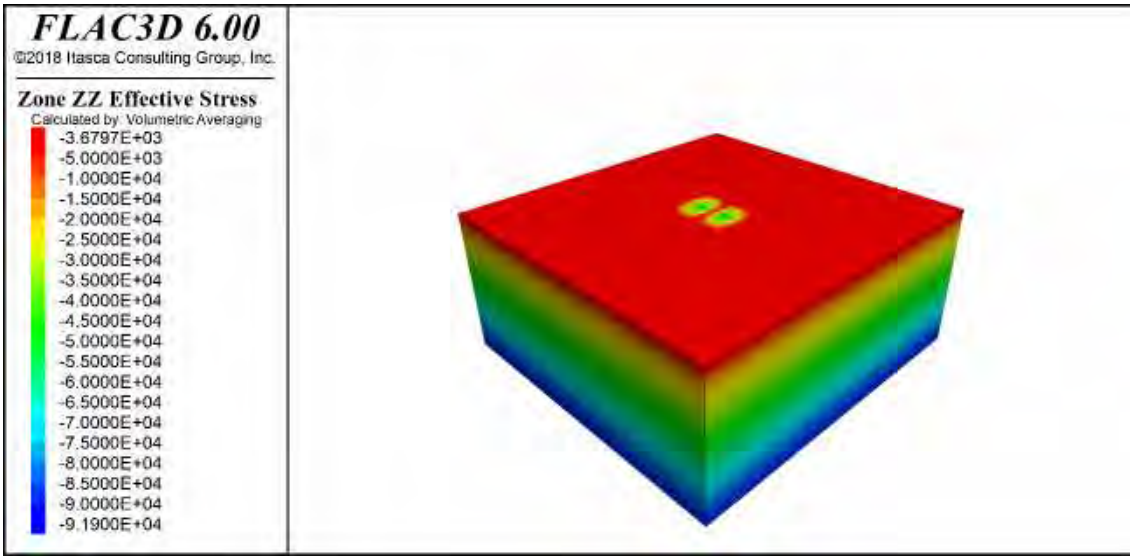

(a)

This project has received funding from the European Union's Horizon 2020 research and innovation programme under grant agreement No. 700748

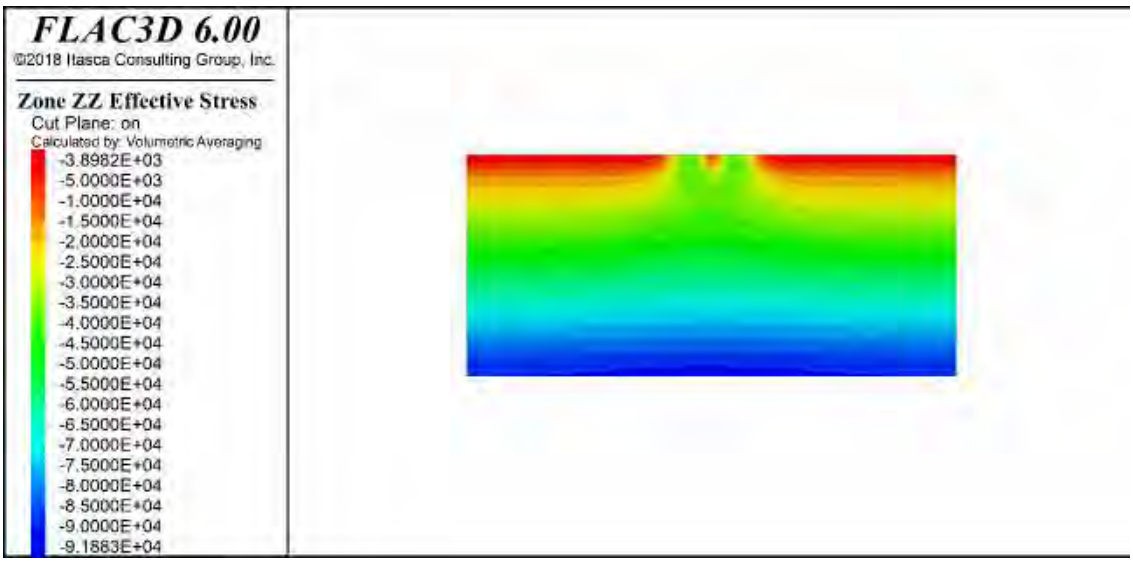

(b
)

Figure 7.8. Effective vertical stress state induced by the S-vibrator before the shaking in 3D view (a) and along the cross section cutting the baseplate (b).

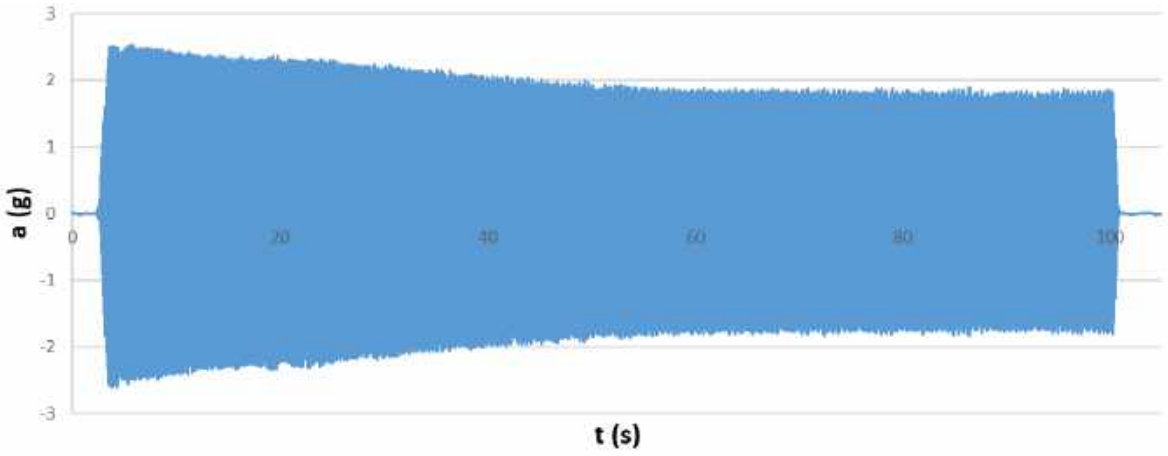

Figure 7.9 Recorded acceleration time history recorded at the baseplate and applied as input at the surface of the model.

This project has received funding from the European Union's Horizon 2020 research and innovation programme under grant agreement No. 700748

7.3 NUMERICAL SIMULATIONS ON VIRGIN SOIL

7.3.1 ANALYSES USING THE FINN MODEL (VS_FIN)

The model consists of the 3D layering soil profile already described in section §7.2, where the dynamic response of the liquefiable soil deposit is reproduced with the Finn model (model calibration described in §3.3).

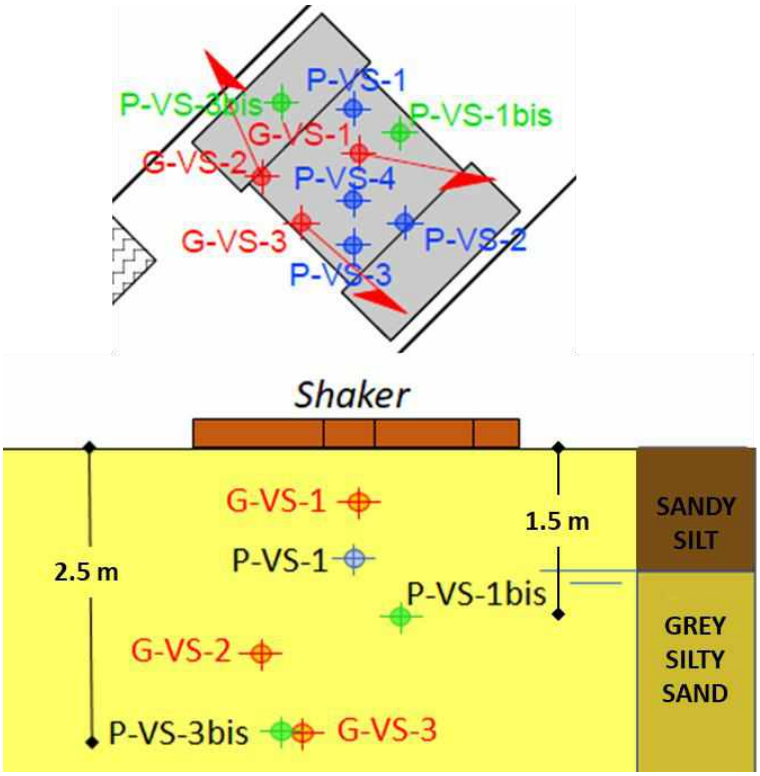

The results of the analysis are reported in terms of the vertical profile of maximum acceleration and excess pore water pressure along the cental axis of the soil model. The maximum values of acceleration and excess pore water pressure measured by the different sensors during the experiment are also reported.

The time histories of velocity at the depth where geophones were located during the experiment (0.5, 1.8 and 2.5 m) are compared to the experimental time histories.

The time histories of excess pore pressure at the depth where pore pressure traducers were located during the experiment are compared to the experimental ones. Finally, the time history of vertical displacement under the baseplate are compared with the final vertical settlement measured at the end of the test.

This project has received funding from the European Union's Horizon 2020 research and innovation programme under grant agreement No. 700748

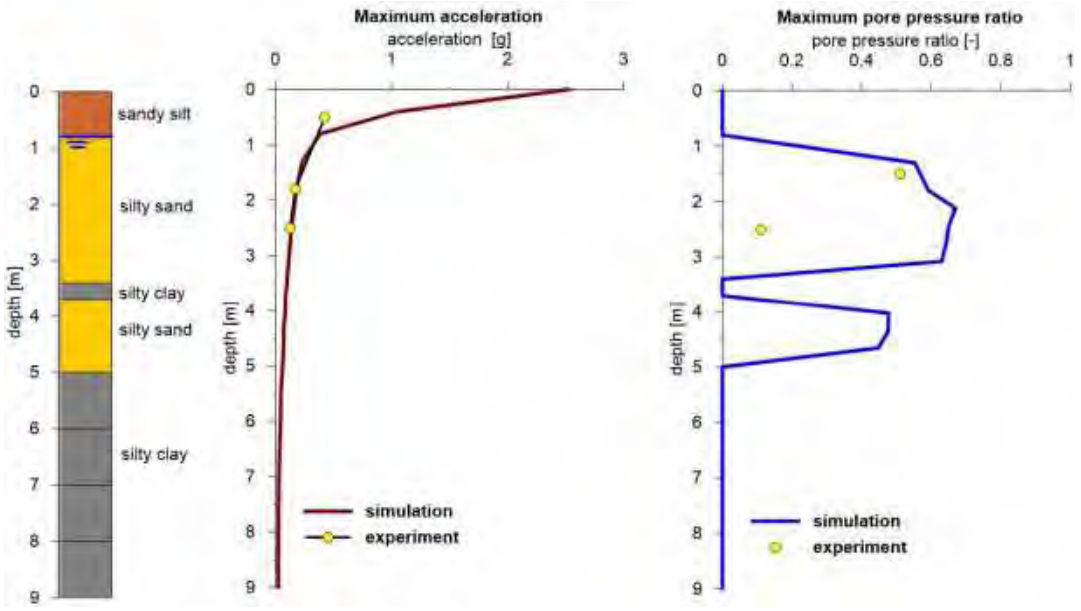

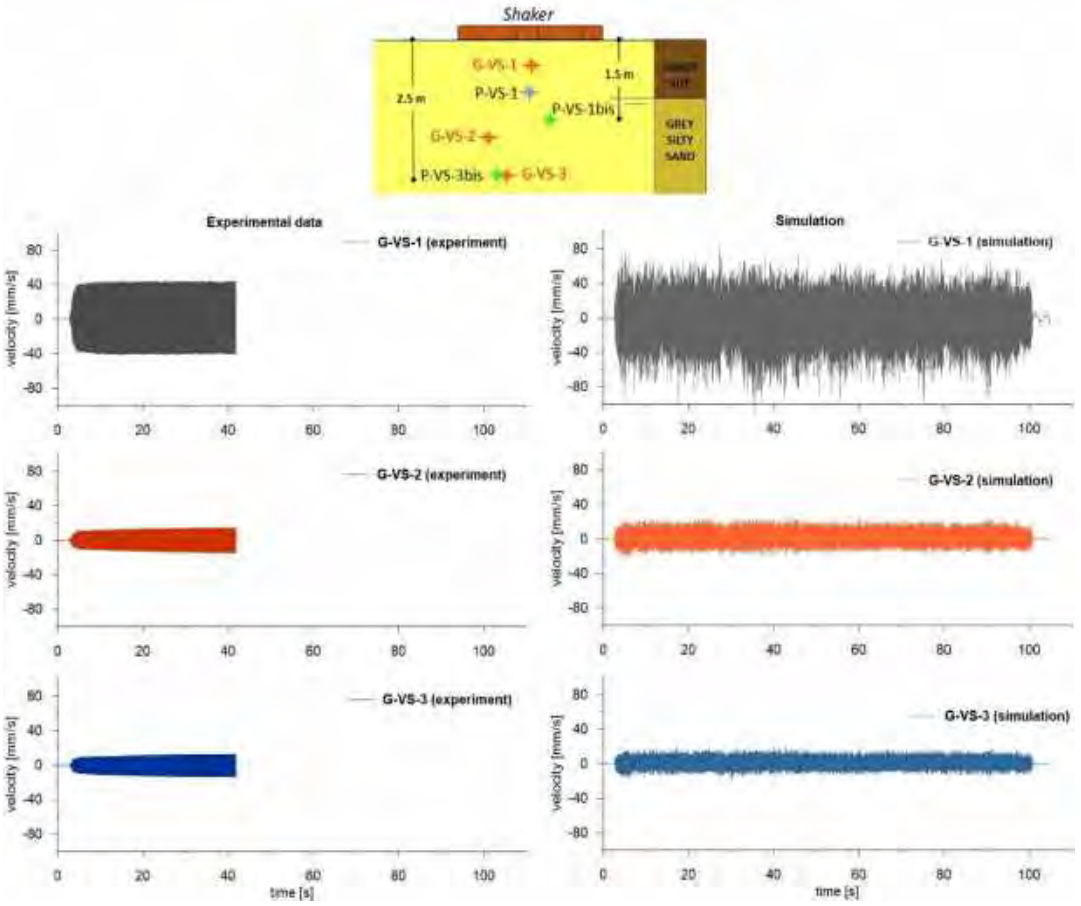

This project has received funding from the European Union's Horizon 2020 research and innovation programme under grant agreement No. 700748

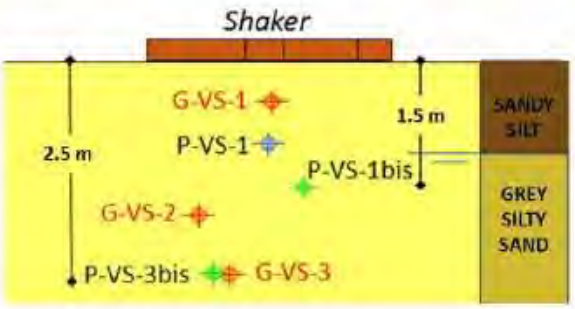

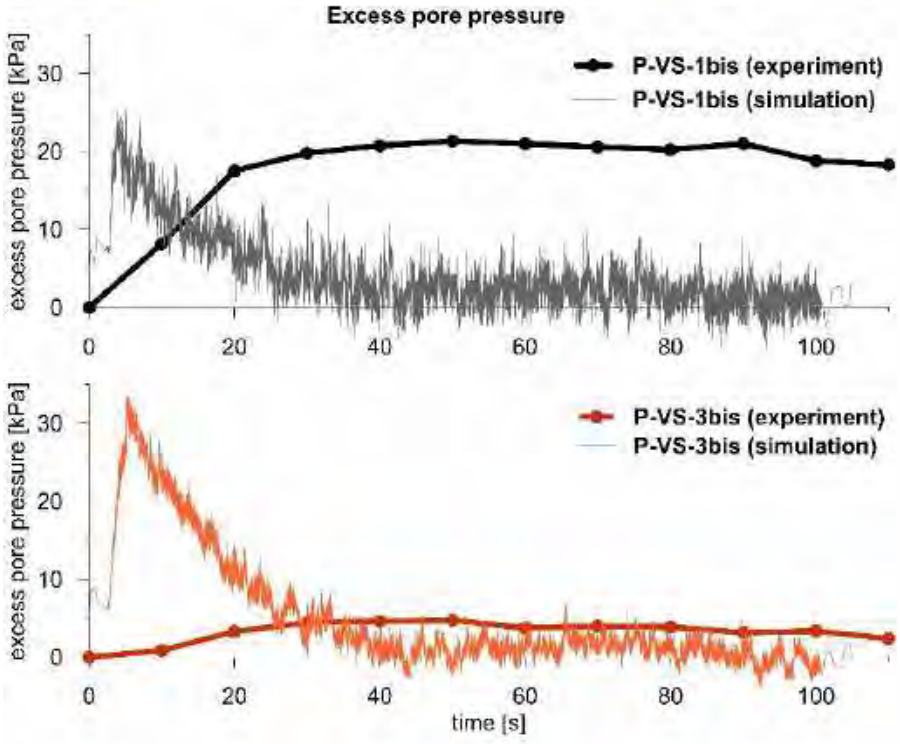

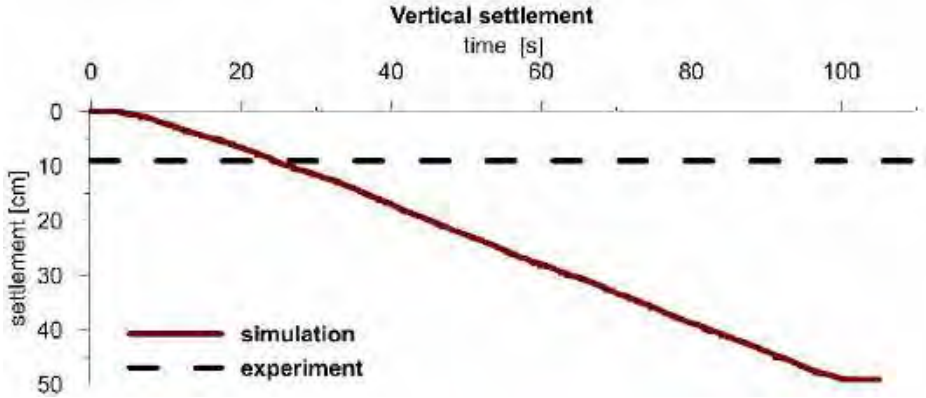

This project has received funding from the European Union's Horizon 2020 research and innovation programme under grant agreement No. 700748

7.3.2 ANALYSES USING THE SANISAND MODEL (VS_SAN)

The model consists of the 3D layering soil profile, already described in section §7.2, were the dynamic response of the liquefiable soil deposit is reproduced with the SANISAND model (model calibration described in §3.3).

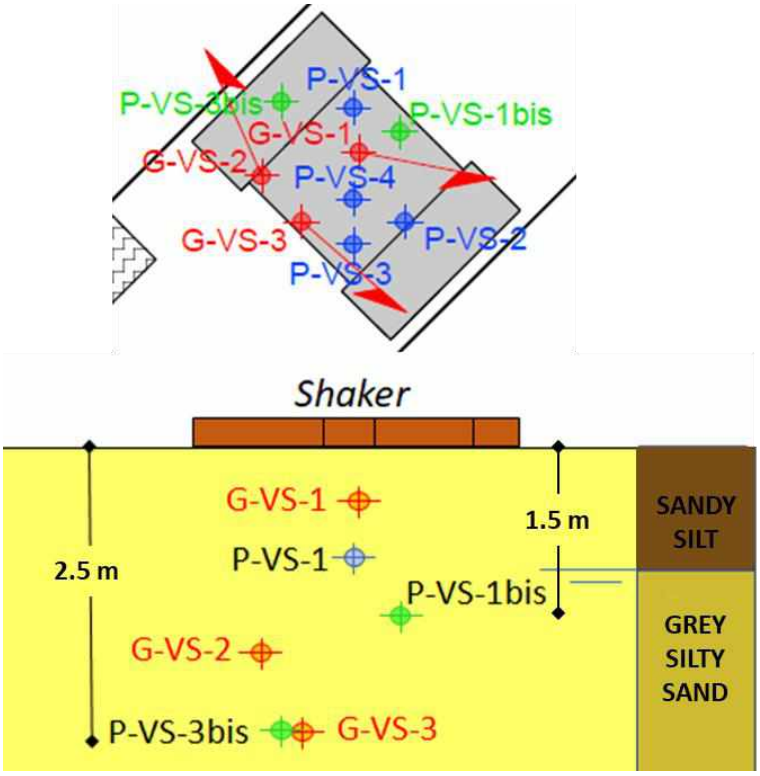

The results of the analysis are reported in terms of vertical profile of maximum acceleration and excess pore water pressure along the baricentric axis of the soil model. The maximum acceleration and excess pore water pressure measured by the different sensors during the experiment are also reported.

The time histories of velocity at the depth where geophones were located during the experiment (0.5, 1.8 and 2.5 m) are compared to the experimental time histories.

The time histories of excess pore pressure at the depth where pore pressure traducers were located during the experiment are compared to the experimental ones. Finally, the time history of vertical displacement under the baseplate are compared with the final vertical settlement measured at the end of the test.

This project has received funding from the European Union's Horizon 2020 research and innovation programme under grant agreement No. 700748

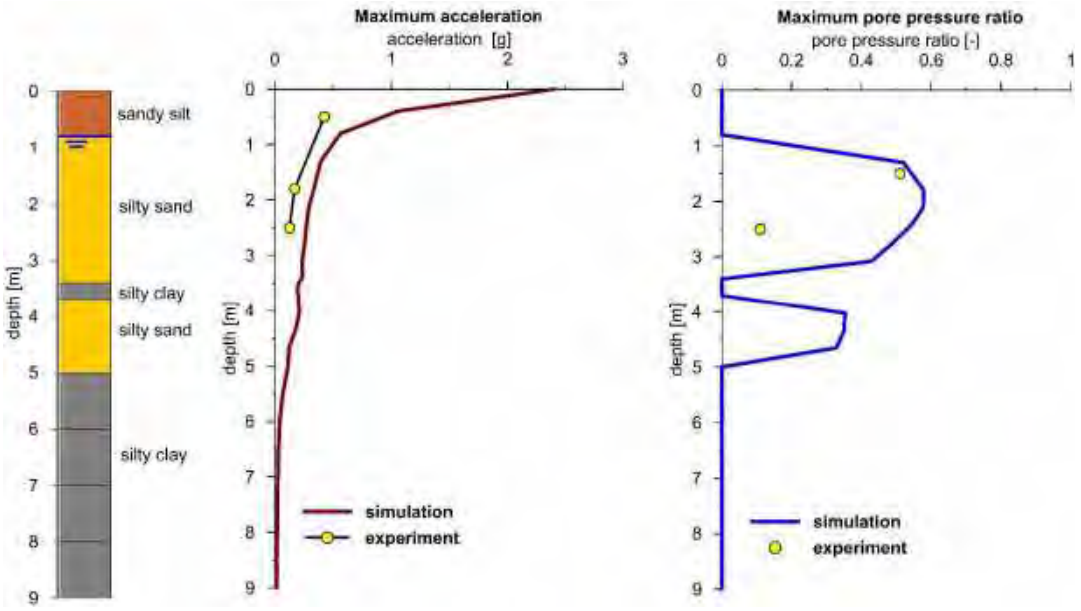

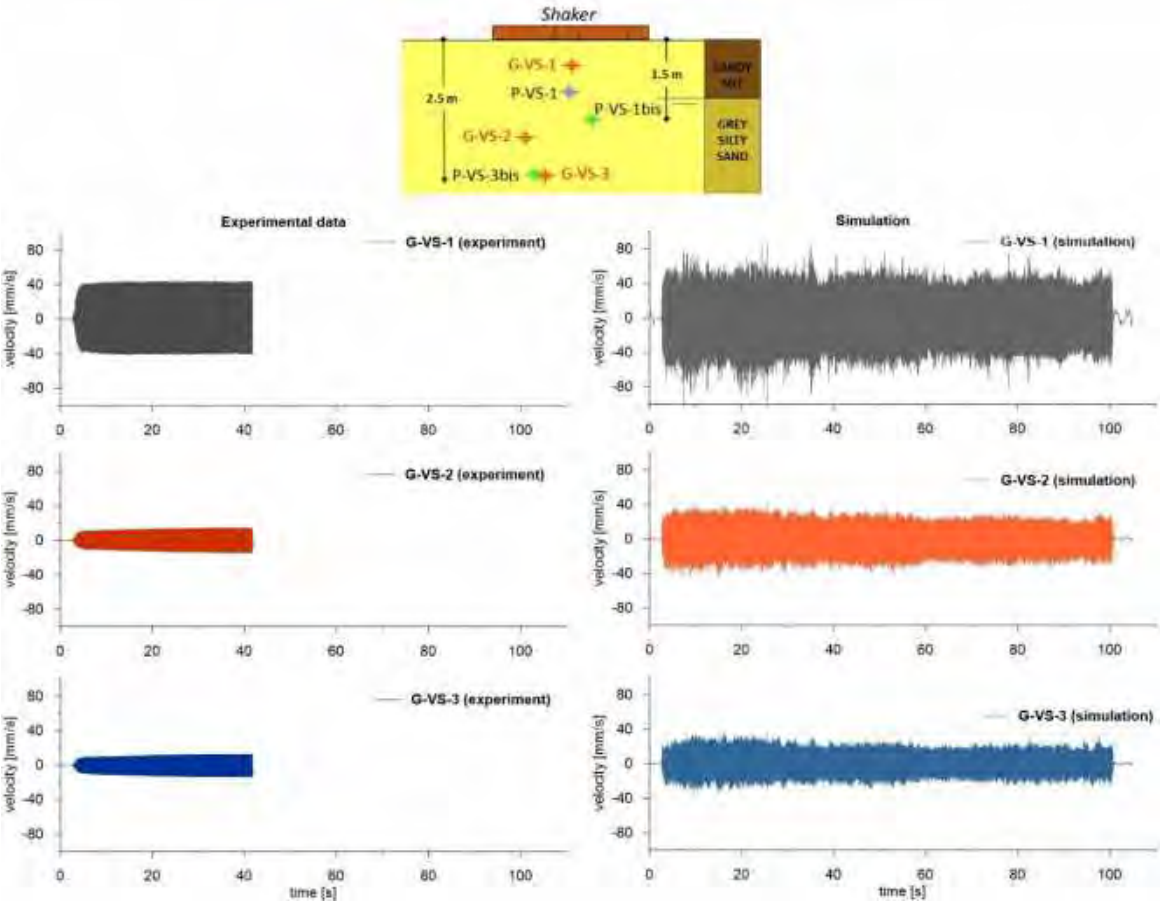

This project has received funding from the European Union's Horizon 2020 research and innovation programme under grant agreement No. 700748

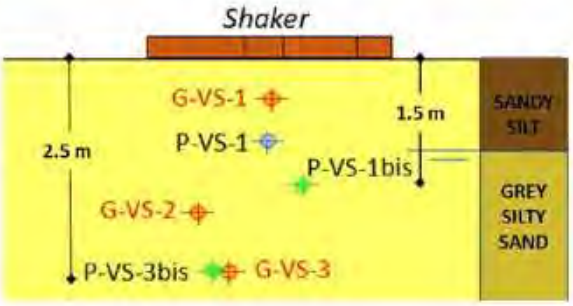

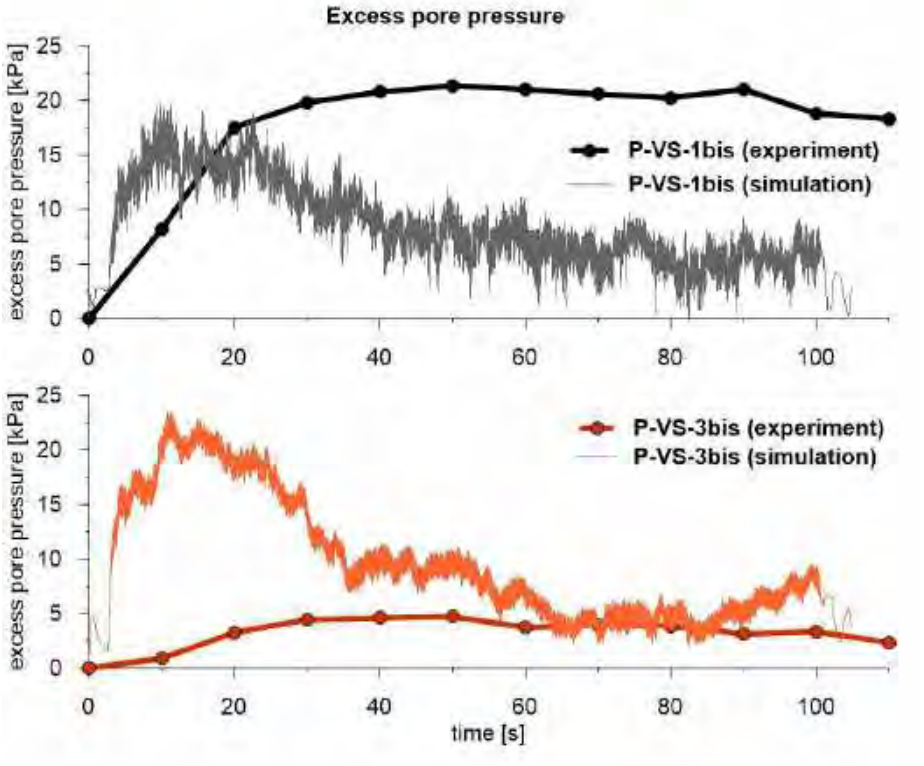

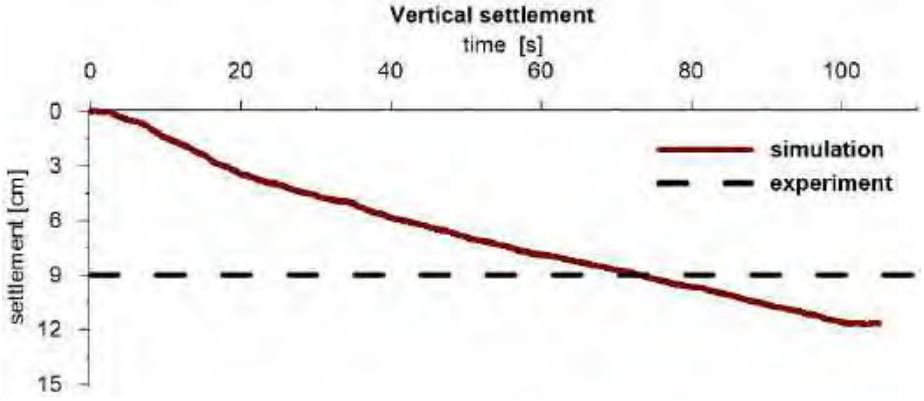

This project has received funding from the European Union's Horizon 2020 research and innovation programme under grant agreement No. 700748

7.4 NUMERICAL SIMULATIONS ON SOIL WITH INDUCED PARTIAL SATURATION (IPS_FIN)

The model consists of the 3D layering soil profile, already described in section §7.2, were the dynamic response of the liquefiable soil deposit is reproduced with the Finn model (model calibration described in §3.3). The induced partial saturation has been modelled in the simulation by reducing the water bulk modulus from $2*10^6$ kPa (Sr = 1) to $2*10^3$ kPa (Sr = 95%) in the treated soil (0.8 ÷ 3.4 m under the surface). Figure 7.10 shows the configuration of the field trial on treated soil with IPS and Table 7.2 lists the sensors and their depth from the ground level.

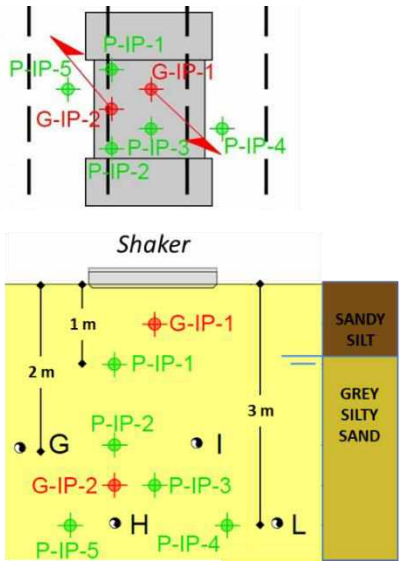

Figure 7.10. Plan (a) and cross section (b) of the field trial on treated soil with IPS.

Table 7.2 Depth of the sensors from the ground level.

Sensor	Depth [m]
G-IP-1	0.5
G-IP-2	2.5
P-IP-1	1.0
P-IP-2	2.0
P-IP-3	2.5
P-IP-4	3.0
P-IP-5	3.0

This project has received funding from the European Union's Horizon 2020 research and innovation programme under grant agreement No. 700748

The results of the analysis are reported in terms of vertical profile of maximum acceleration and excess pore water pressure along the central axis of the soil model (Figure 7.11). Maximum acceleration and excess pore water pressure measured by the different sensors during the experiment are also reported.

The time histories of velocity at the depth where geophones were located during the experiment (0.5 and 2.5 m) are compared to the experimental time histories (Figure 7.12).

The time histories of excess pore pressure at the depth where pore pressure traducers were located during the experiment are compared to the experimental ones (Figure 7.13). Finally, the time history of vertical displacement under the baseplate are compared with the final vertical settlement measured at the end of the test (Figure 7.14).

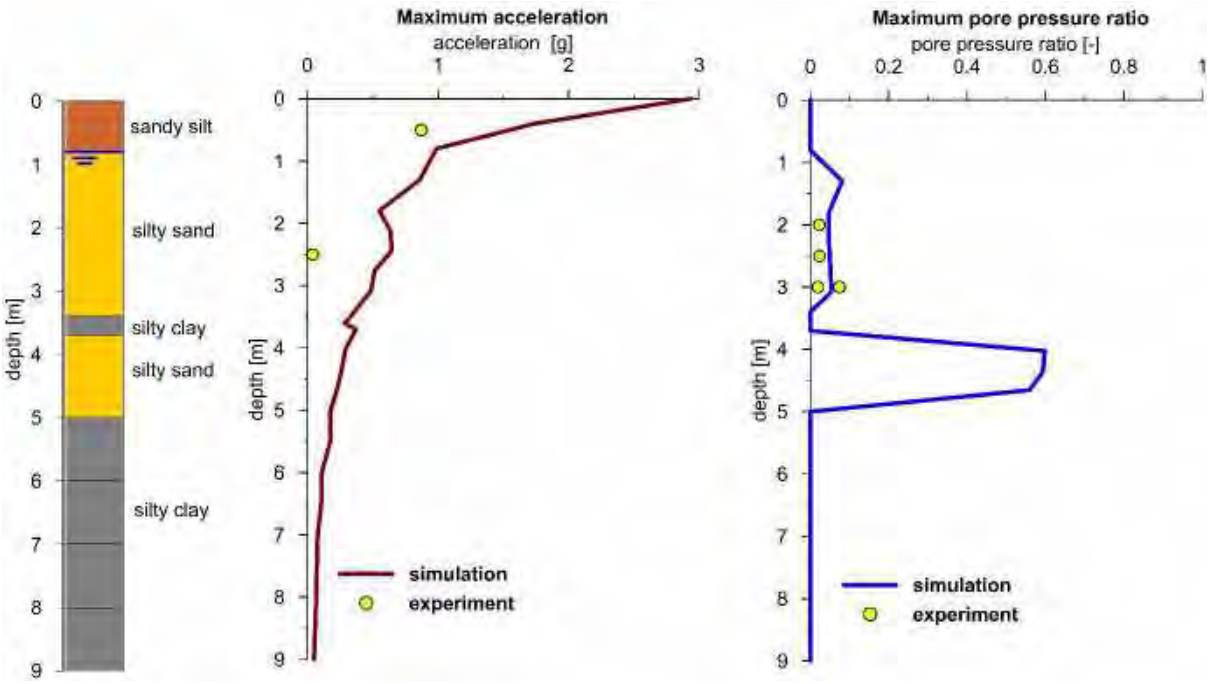

Figure 7.11. Vertical profiles of maximum acceleration and pore pressure ratio along the baricentric axis of the soil model.

This project has received funding from the European Union's Horizon 2020 research and innovation programme under grant agreement No. 700748

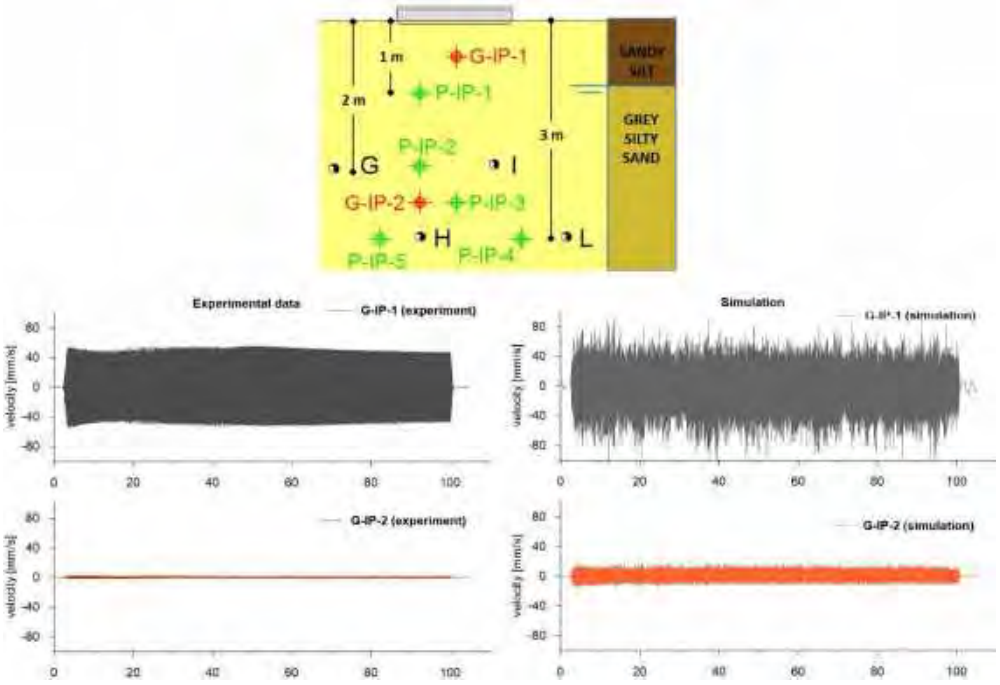

Figure 7.12 Time histories of velocity recorded during the field-trial compared with the simulated ones.

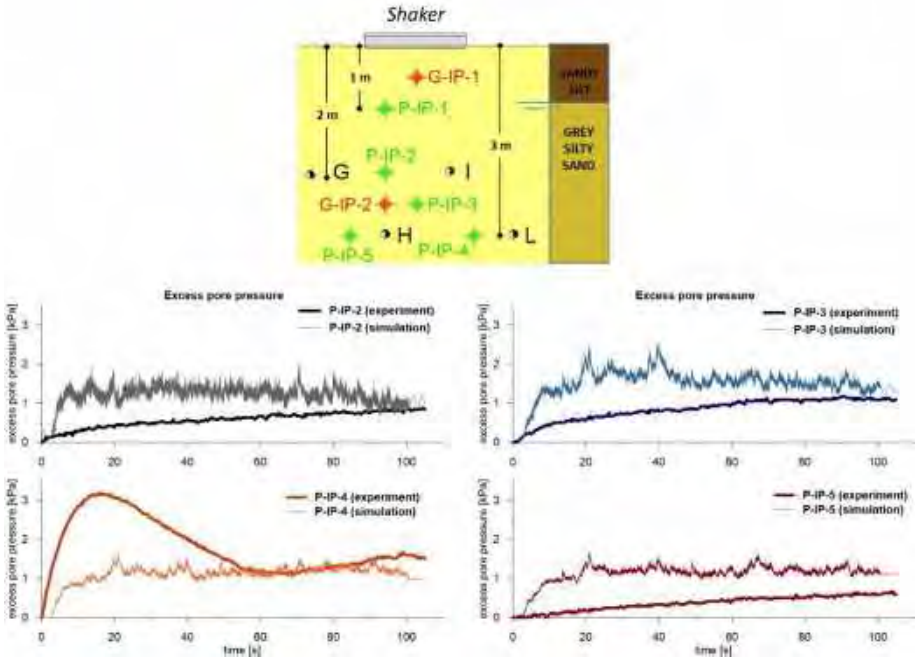

Figure 7.13. Time histories of pore water pressure recorded during the field-trials compared with the simulated ones

This project has received funding from the European Union's Horizon 2020 research and innovation programme under grant agreement No. 700748

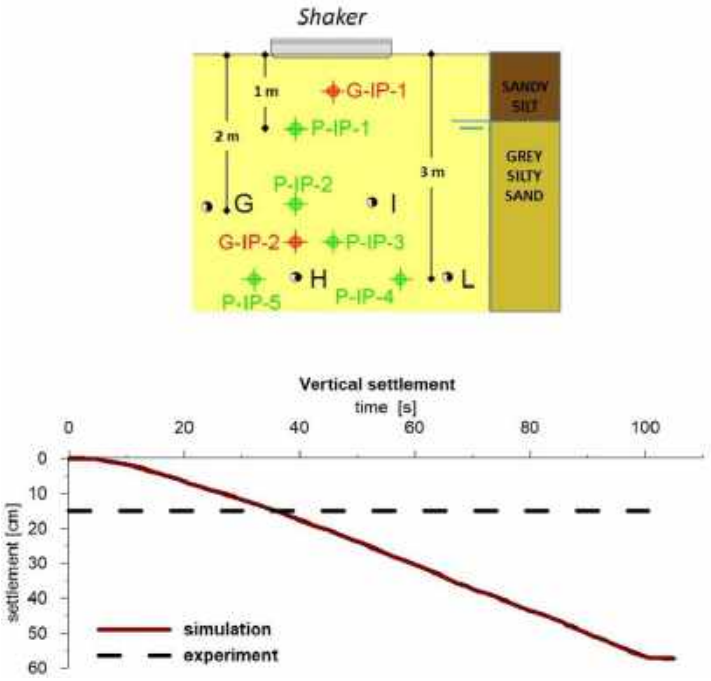

Figure 7.14. Simulated time history of vertical displacement under the baseplate compared with the experimental settlement measured after the end of the shaking on site.

This project has received funding from the European Union's Horizon 2020 research and innovation programme under grant agreement No. 700748

8 PARAMETRIC STUDY TO EVALUATE STRUCTURAL PERFORMANCE AT THE TEST SITE

8.1 1D NONLINEAR EFFECTIVE-STRESS ANALYSIS OF THE GROUND CONDITIONS

8.1.1 GENERALITIES

A nonlinear dynamic effective stress analysis of the ground conditions of Pieve di Cento was performed using the commercial software FLAC 8.0 (Itasca, 2016). One-dimensional elastic and elasto-plastic analyses were run to assess changes in the free-field soil profile response. This computer platform uses the finite difference method to solve the equation of motion and uses an explicit Lagrangian solution scheme, which allows large deformations problems to be solved.

This chapter outlines the key aspects of the 1-D FLAC model and various validation and verification steps that were taken in the development of this model.

8.1.2 KEY MODEL ASPECTS

The soil profile was defined and modelled as three uniform horizontal layers. The earthquake shaking was simulated as a horizontal shear force applied at the base of the model. The model was assumed to be infinite in the vertical dimension and was therefore used quiet-boundaries in the base. The groundwater level was varied from 1 m, 1.5 m and 2 m to reflect seasonal changes

8.1.3 GROUND MOTIONS

The ground motions were taken as the upward propagating motions from a site response analysis at 20m depth (base of the FLAC model). 21 ground motions were selected to represent the seismic hazard for three different return periods (475, 975, and 2475 years), seven motions for each return period.

8.1.4 GEOMETRICAL MODEL

The considered soil profile has three distinguishable layers with a total model thickness of 20 m and width of 2 m. The first layer (surface) is 1.9 m thick. The second layer (middle) is 4.1 m thick. The third layer (bottom) is 14.0 m thick.

The finite difference mesh was set to have aspect ratio of its zone dimensions near unity for greatest accuracy. The considered finite difference mesh is shown in Figure 8.1.

This project has received funding from the European Union's Horizon 2020 research and innovation programme under grant agreement No. 700748

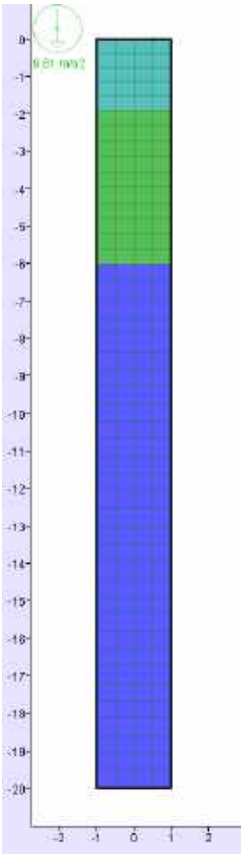

Figure 8.1. 1-D numerical model in FLAC.

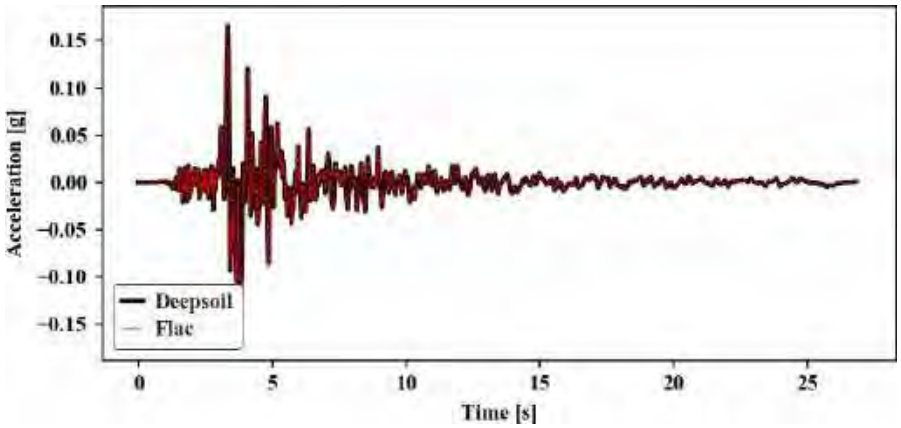

Figure 8.2. Calibration of (v_s-τ) factor.

This project has received funding from the European Union's Horizon 2020 research and innovation programme under grant agreement No. 700748

8.1.5 BOUNDARY CONDITIONS

The lateral nodes at each depth were attached so they moved together and the base used a compliant (also referred to as absorbing) boundary (Mejia and Dawson, 2006). The ground motion that was input into the base of the model was the upward propagating shear wave at 20m depth from an equivalent linear analysis that modelled the ground motion propagation from the bedrock. Since a compliant boundary was used, the upward propagating motion was input as a shear stress by converting the velocity time series as:

$$\sigma_S = -factor \cdot \rho \cdot C_s \cdot v_s \qquad (8.1)$$

Where σs is the applied shear stress, ρ is the mass density of the bottom layer, Cs is the speed of Shear wave propagation velocity and vs is the input shear particle velocity.

Note that the f actor in Eq. (8.1) accounts for the input energy dividing into downward and upward propagating waves. The factor required calibration so that the input stress wave would produce the appropriate velocities at the bottom of the model that corresponds to the input velocity (Itasca, 2016). In the calibration procedure followed (Mejia and Dawson, 2006), an elastic analysis was conducted in DeepSoil (Hashash et al., 2016) and in FLAC, where the surface accelerations were compared to ensure that they matched. In DeepSoil, the ground motion was applied as an acceleration time-history signal, and in FLAC, the motion was input as a shear stress time-history corresponding to the same acceleration.

The computed acceleration time series at top of the column is shown in Figure 8.2. To obtain the same record in the surface, the factor was set to 1.2.

8.1.6 MATERIAL MODELS

All the layers are composed of sandy material. The soil was modelled with only two constitutive models, one for a liquefiable sand and another for non-liquefiable sands.

8.1.7 STATIC PROPERTIES OF THE SOILS

Before applying the ground motion, a Mohr-Coulomb constitutive model was used in the three layers to calculate the initial stresses in the soil profile. Table 8.1 gives the list of input parameters to the static phases.

This project has received funding from the European Union's Horizon 2020 research and innovation programme under grant agreement No. 700748

Table 8.1 Input parameters of the Mohr-Coulomb model

Parameter	Unit	Layer 1	Layer 2	Layer 3
Height (H)	m	1.9	4.1	14.0
Density (ρ_{dry})	kg/m^3	1633	1544	1369
Shear modulus (G)	MPa	2.76x10^4	4.72x10^4	3.56x10^4
Bulk modulus (K)	MPa	5.94x10^4	1.02x10^5	1.07x10^5
Angle of shear resistance (φ')	°	*35.0*	*31.0*	*27.5*
Effective cohesion (c')	kPa	0.0	0.0	15.0
Dilation (ψ)	—	0.0	0.0	0.0
Tensile strength (σ^t)	kPa	0.0	0.0	0.0
Porosity (η)	—	0.384	0.417	0.493
Permeability (k_H)	m/s	8.69x10^{-5}	8.69x10^{-5}	1.0x10^{-12}

8.1.8 PERMEABILITY

The permeability of any material should be set by the mobility coefficient (coefficient of the pore pressure term in Darcy's law) required by FLAC and designated by k (m2/Pa.sec) (Itasca, 2016).·This mobility coefficient could be related to hydraulic conductivity, designated by kH (m/s), usually termed as "coefficient of permeability", by means of k=kH/(g·ρw) where g is the gravitational acceleration and ρ_w is the water density.

8.1.9 DYNAMIC PROPERTIES OF THE SOILS

8.1.9.1 LIQUEFIABLE SAND

The PM4Sand constitutive model was adopted to simulate the constitutive behaviour of the second layer in the dynamic phase. The model is coded as a user defined material in a dynamic link library (DLL) (Itasca, 2011). PM4Sand is a sand plasticity model for geotechnical earthquake engineering applications. This model follows the basic framework of the stress-ratio controlled, critical state compatible, bounding surface plasticity model for sand presented by Dafalias and Manzari (2004). Modifications to the model were developed and implemented by Boulanger (2010) (version 1), Boulanger and Ziotopoulou (2012) (version 2), and further by Boulanger and Ziotopoulou (2015) (version 3) to improve its ability to

This project has received funding from the European Union's Horizon 2020 research and innovation programme under grant agreement No. 700748

approximate the stress-strain responses important to geotechnical earthquake engineering applications.

The constitutive model parameters are grouped into two categories; a primary set of six parameters (three properties, two flags, and atmospheric pressure) that are most important for model calibration, and a secondary set of parameters that may be modified from their default values in special circumstances (Boulanger and Ziotopoulou, 2015). The primary model input properties of soil are:

- D_r - an apparent relative density which affects the peak drained and undrained strengths and the rate of strain accumulation during cyclic loading
- G_o - the shear modulus coefficient related with the shear modulus (G, this one corresponding G_{max} = Vs2) which should be calibrated to the estimated or measured in-situ shear wave velocity.
- h_{po} - the contraction rate parameter which is used to calibrate to the estimated in-situ cyclic resistance ratio (CRR) after all other properties have been set.

Table 8.2gives the list of input primary properties to the layer 2.

The PM4Sand constitutive model provides hysteretic damping. An additional 2.0% Rayleigh damping is used centered at an average frequency between the natural frequency of the soil and the mean frequency of the input motion (See Section 1.5.3). A detailed description about the constitutive model characteristics can be found in Boulanger and Ziotopoulou (2015).

Table 8.2 Input parameters of the PM4Sand model.

Parameter	Unit	Layer 2
Relative density (D_R)	%	38
Shear modulus coefficient (Go)	—	655
Contraction rate parameter (h_{po})	—	0.9

8.1.9.2 NON LIQUEFIABLE SANDS

During the dynamic load, the crust and base of the non-liquefiable sand layers were modelled with the Mohr-Coulomb model and the hysteretic damping option. The models were combined to provide suitable modelling of the site-response and bearing capacity. The site-response is sensitive to the shear stiffness and strain-based degradation of stiffness, and therefore was captured using the hysteretic damping option. The bearing capacity is sensitive to the soil strength capacity and therefore the Mohr-Coloumb constitutive (MC) model was used to achieve this. By using the MC model, additional benefit came out when the yield criterion is met, which is the hysteretic damping becoming inactive in those zones (page 1-83 Dynamic Analysis FLAC Manual).

This project has received funding from the European Union's Horizon 2020 research and innovation programme under grant agreement No. 700748

The model was fitted to the Sigmoidal model (sig4) functional form in FLAC. Sigmoidal curves are monotonic within the defined range and have the appropriate asymptotic behaviour. Thus the functions are well-suited to the purpose of representing modulus degradation curves. The sig4 model is defined as:

$$M_S = y_0 + \frac{a}{1 + \exp\left(-\frac{(L - x_0)}{b}\right)} \qquad (8.2)$$

where Ms is the strain-dependent normalized secant modulus and L is the logarithmic strain. For this model, the 4 symbols, a, b, x0 and y0, are entered. Table 8.3 gives the list of input parameters to layers 1 and 3.

Table 8.3. Input parameters of the hysteretic damping model

Parameter	Layer 1	Layer 3
a	0.95098	1.00023
b	-0.35966	-0.39049
x_0	-1.53922	-0.89651
y_0	0.04902	-0.00023

The model was initialised with the Mohr-Coulomb model with no hysteretic damping applied. This allowed for a quick convergence and it meant that the static stresses from the foundation do not affect the non-linearity from the hysteretic damping, (page 1-83 Dynamic Analysis - FLAC MANUAL).

8.1.9.3 RAYLEIGH DAMPING PARAMETERS

A small amount of Rayleigh damping was used in the numerical model to provide stability and simulate energy loss at small strain, consistent with other uses of the PM4Sand model (e.g. Luque (2017)). The parameters for the Rayleigh damping were input by setting the damping as both stiffness and mass proportional and then defining the ξ_{min} and f_{min} parameter using Equations (8.3) and (8.4), which correspond to the minimum point in the damping versus frequency relationship. f_1 and f_2 correspond to the lowest and highest frequencies of interest in the model, and $\xi_{1,2}$ is the ratio of critical damping set at those frequencies.

$$\varepsilon_{min} = \sqrt{\alpha \cdot \beta} \qquad (8.3)$$

This project has received funding from the European Union's Horizon 2020 research and innovation programme under grant agreement No. 700748

$$f_{min} = \frac{2 \cdot f_1 \cdot f_2}{\sqrt{4 \cdot f_1 \cdot f_2}} \quad (8.4)$$

$$\alpha = \frac{2 \cdot w_1 \cdot w_2}{w_2^2 - w_1^2}(w_2 \varepsilon_{12} - w_1 \varepsilon_{12}) \quad (8.5)$$

$$\beta = \frac{2}{w_2^2 - w_1^2}(w_2 \varepsilon_{12} - w_1 \varepsilon_{12}) \quad (8.6)$$

The lowest frequency of interest (f1) is typically governed by the lowest natural frequency of the soil deposit or the lowest frequency of soil-structure system. The lowest frequency of the soil deposit corresponds to the first mode of the liquefied site, which was estimated by performing an elastic site response analysis f1 = 0.62 [Hz] using the software DeepSoil (Hashash et al., 2016) with a reduction in stiffness in the liquefied layer to 10% of the original stiffness. The highest frequency of interest was governed by the 2nd mode frequency of the soil-structure system f2= 5 [Hz].

8.1.10 RESULTS

This section contains the results from the 1-D FLAC analysis whit a groundwater level at a depth of 1.5 m. However, some comparisons with the results using groundwater level of 1.0 m and 2.0 m will be discussed.

The liquefaction potential can be expressed by means of the excess pore pressure ratio (r_u), which represents the ratio of the excess pore pressure and the initial effective vertical stress at that depth. When the excess pore pressure ratio (r_u) is equal to 1.0 it means a completely liquefied state.

Figure 8.3 shows that the second layer did not liquefy when was reached by the ground motion RP475-3 (3), otherwise when a stronger ground motion (RP2475-1 (15)) was applied, this layer liquefies (Figure 8.4).

This project has received funding from the European Union's Horizon 2020 research and innovation programme under grant agreement No. 700748

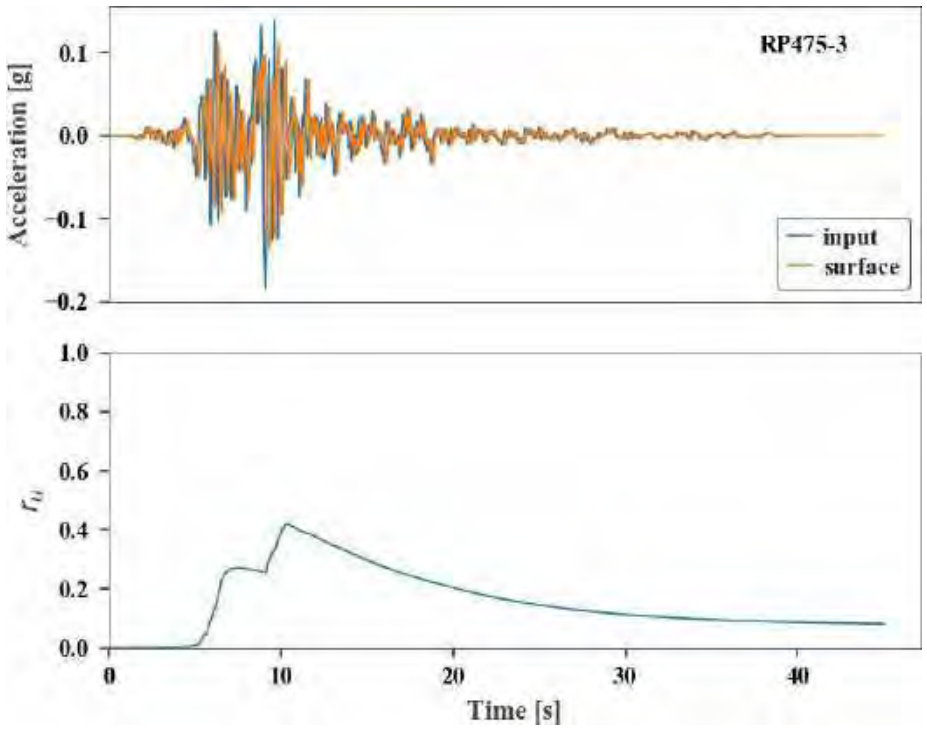

Figure 8.3. Excess pore pressure ratio in the center of the second layer, motion 3.

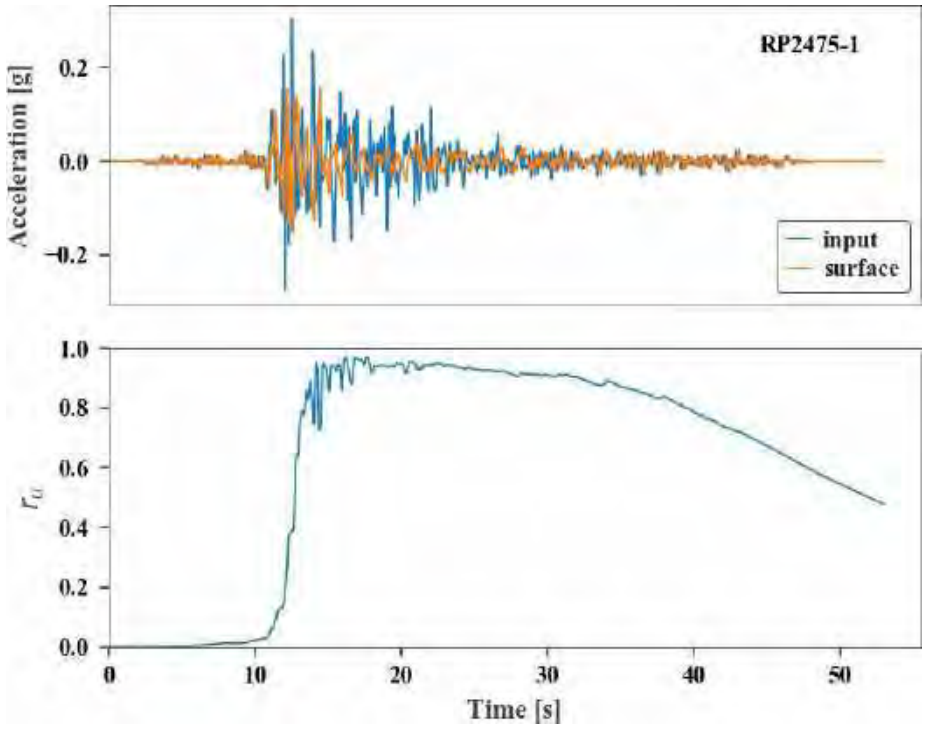

Figure 8.4. Excess pore pressure ratio in the centre of the second layer, motion 15

This project has received funding from the European Union's Horizon 2020 research and innovation programme under grant agreement No. 700748

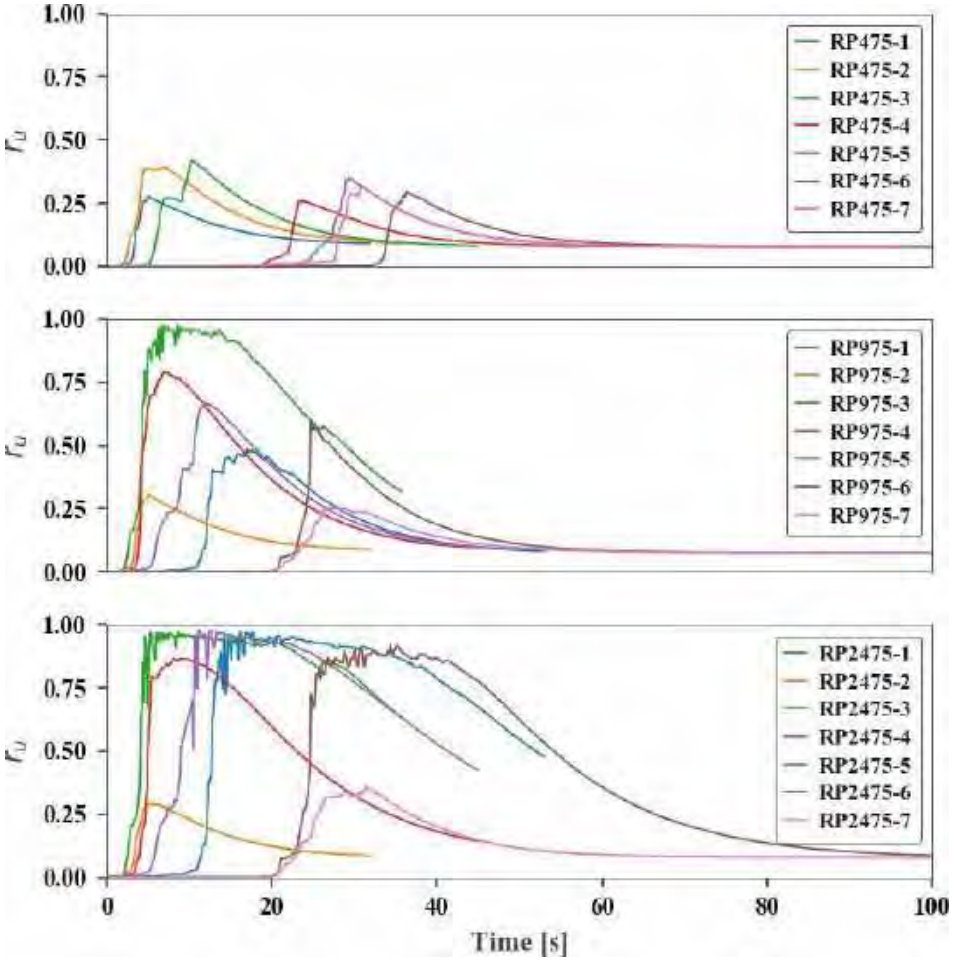

Figure 8.5. Excess pore pressure ratio

Figure 8.5 shows the excess pore pressure ratio (ru) for all the motions for the three different return periods. The motions with the smaller return period did not generate liquefaction in the sandy layer.

Figure 8.6 shows the excess pore pressure ratio at the top (L2T), centre (L2C) and at the bottom (L2B) of the second layer for one ground motion in each return period, using the three different ground water table levels (wtl) considered. When the groundwater level is deeper, small excess pore pressure is generated in the top of the layer. Whereas, in the others two layers the change in water level sometimes resulted in increased pore pressure ratio and sometimes a decrease. In the middle and in the bottom of the layer, the stronger ground motion generates similar excess pore pressure, even using the different groundwater levels. The appendix A contains all the surface acceleration, excess pore pressure ratio and strains figures for all the ground motions.

This project has received funding from the European Union's Horizon 2020 research and innovation programme under grant agreement No. 700748

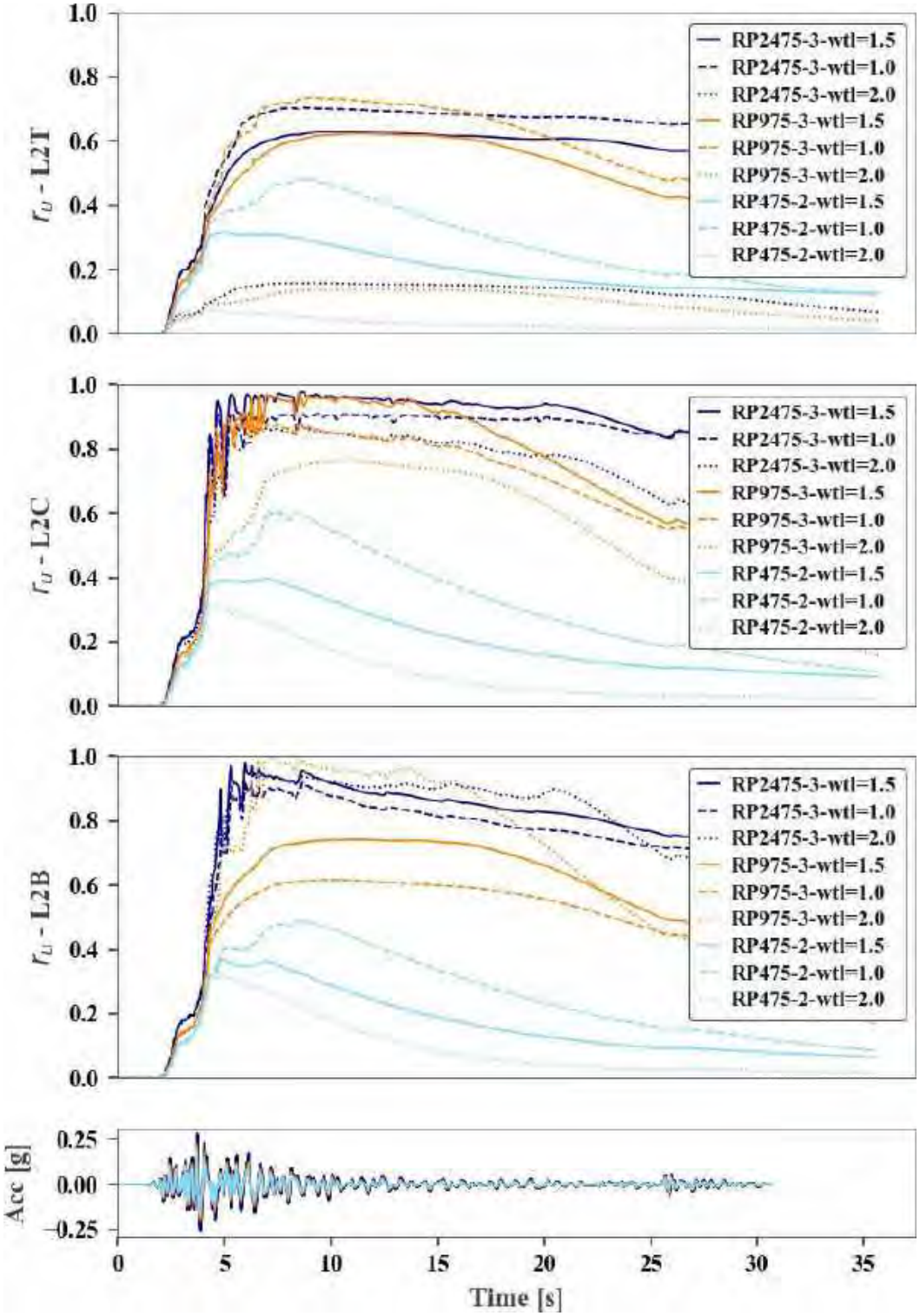

Figure 8.6. Excess pore pressure ratio in the second layer at the top (L2T), centre (L2C) and at the bottom (L2B), using different groundwater level, motions 2, 10 and 17

This project has received funding from the European Union's Horizon 2020 research and innovation programme under grant agreement No. 700748

The response spectra of surface motion for all the motions for the three different return period is shown in Figure 8.7. It can be seen that the high frequency content of the motions are damped out on the surface motion, especially for the stronger motions. For the same input ground motion at different scale factors produce almost the same response acceleration for low periods (less than 0.7s).

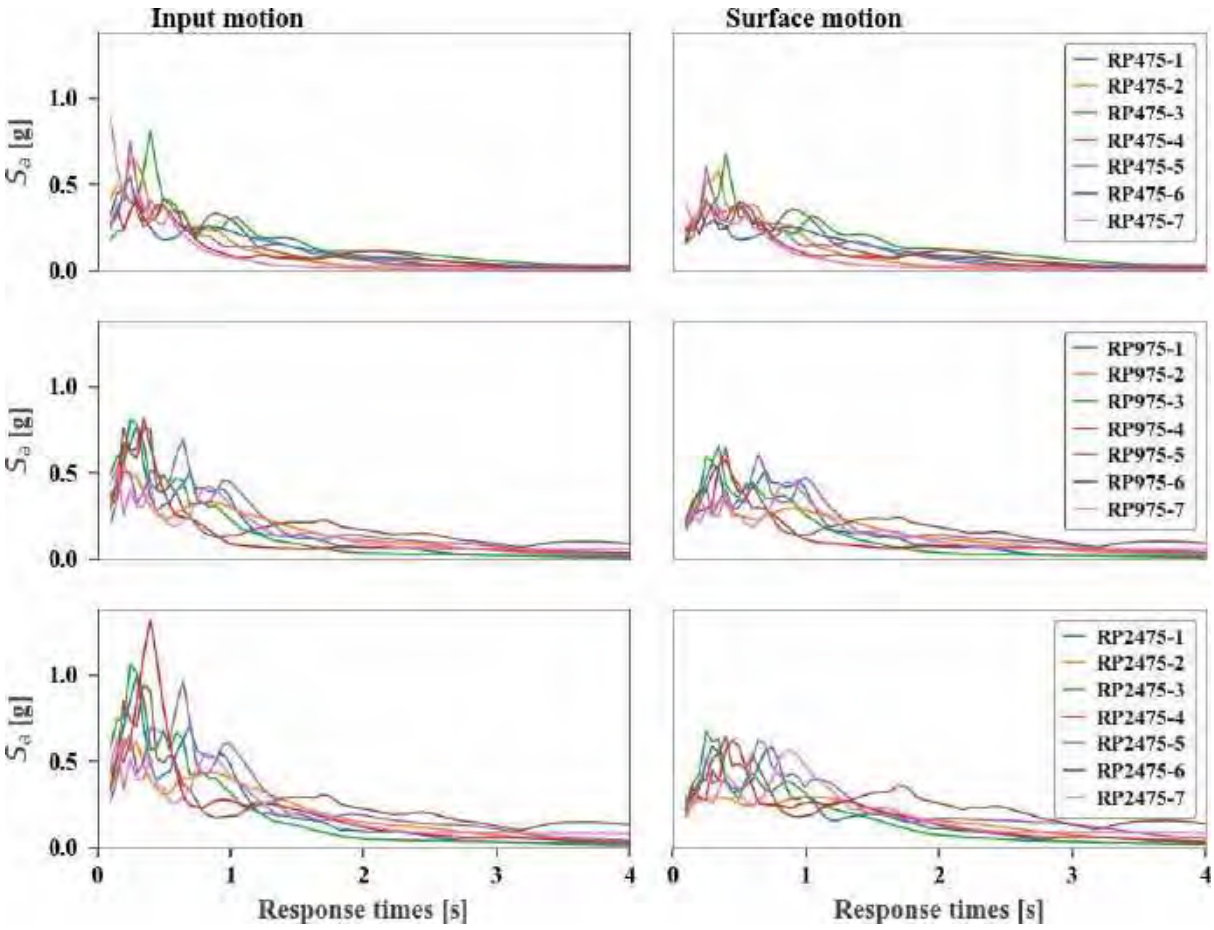

Figure 8.7. Response spectra of the base and surface

This project has received funding from the European Union's Horizon 2020 research and innovation programme under grant agreement No. 700748

This point is further emphasised in Figure 8.7, where response spectra of the upward propagating motion and surface motion for the same motion in each return period are shown in Figure 8.8 a) and b) respectively. The three motions produce almost the same response in the surface.

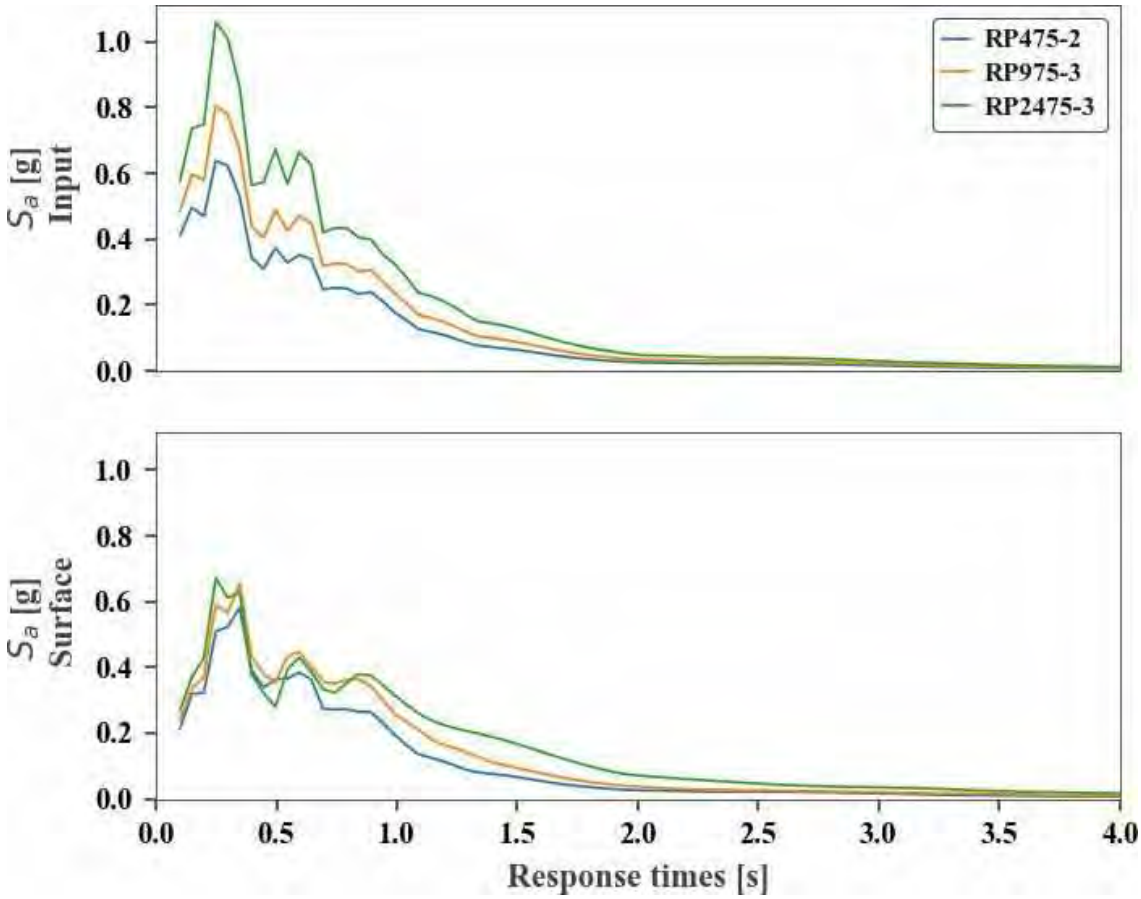

Figure 8.8. Response spectra, motion 475-2 (2), 975-3 (10) and 2475-3 (17)

This project has received funding from the European Union's Horizon 2020 research and innovation programme under grant agreement No. 700748

Additionally, Figure 8.9 shows those response spectra of surface when the groundwater level is varied. Again, the response spectra of surface is almost the same regardless of the return period and the groundwater level.

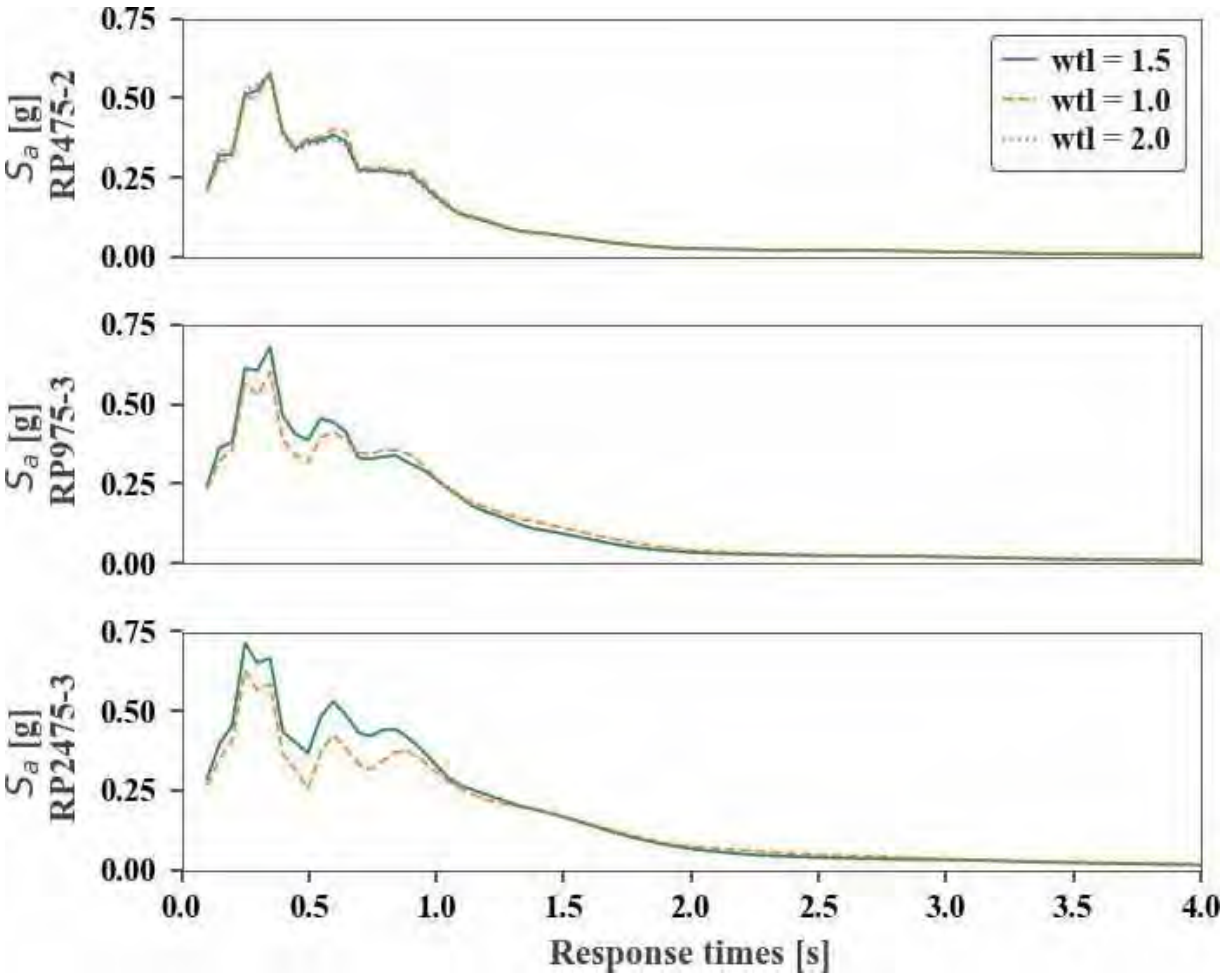

Figure 8.9. Response spectra using three different groundwater level

The Fourier spectra of the surface motion for all the motions for the three different return periods are shown in Figure 8.10. On the left column the Fourier spectra of the input motions and on the right column the Fourier spectra of the surface ground motions.

The amplification of different frequency content can be seen in Figure 8.11 for all the motions for the three different return periods. In general, the high frequency content was de-amplified, and the de-amplification was more pronounced for larger motions where more nonlinear deformation occurred in the soil. Some frequency was amplified at high frequencies due to numerical noise when liquefaction occurred, consistent with Tsiapas and Bouckovalas (2018).

This project has received funding from the European Union's Horizon 2020 research and innovation programme under grant agreement No. 700748

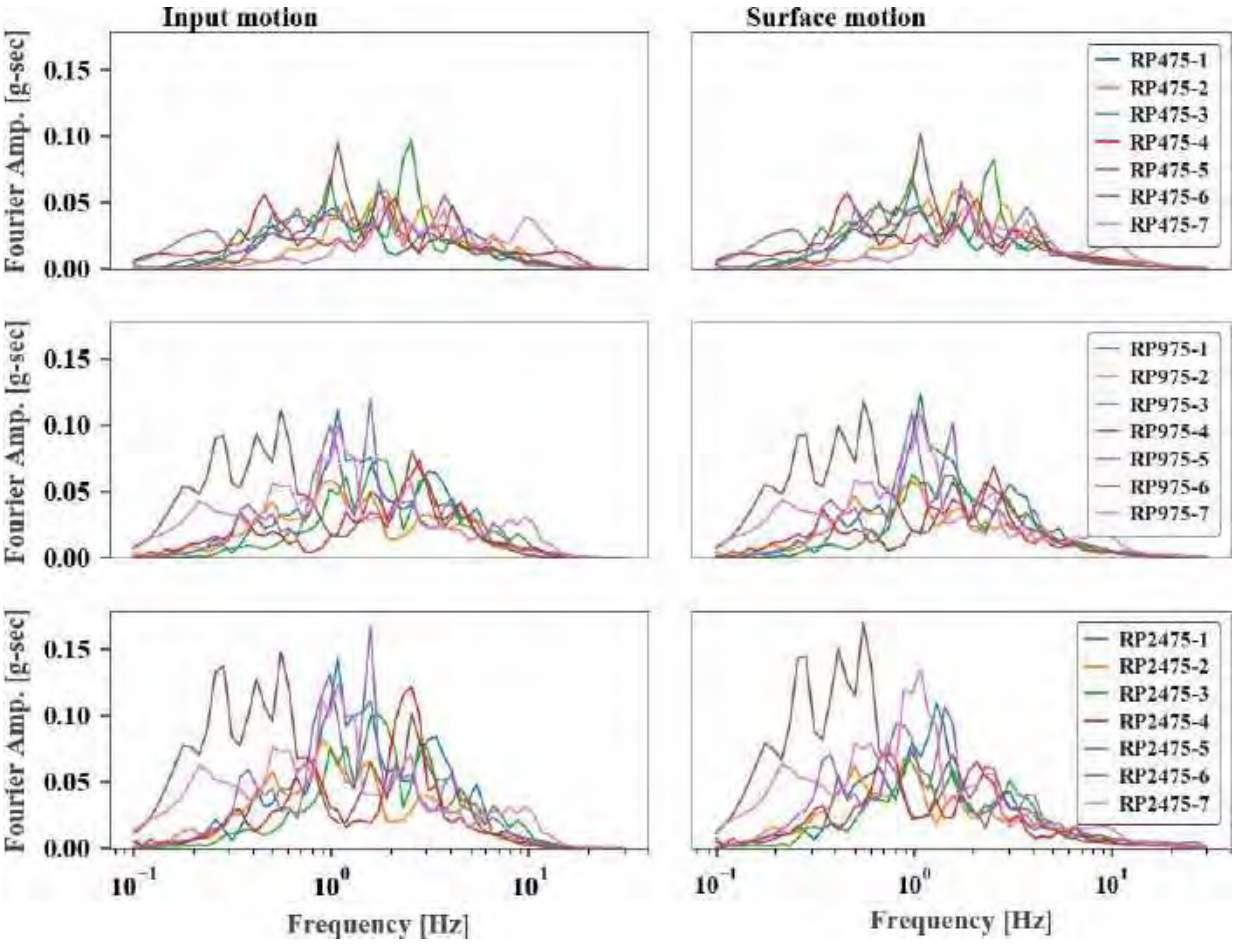

Figure 8.10. Fourier spectra.

This project has received funding from the European Union's Horizon 2020 research and innovation programme under grant agreement No. 700748

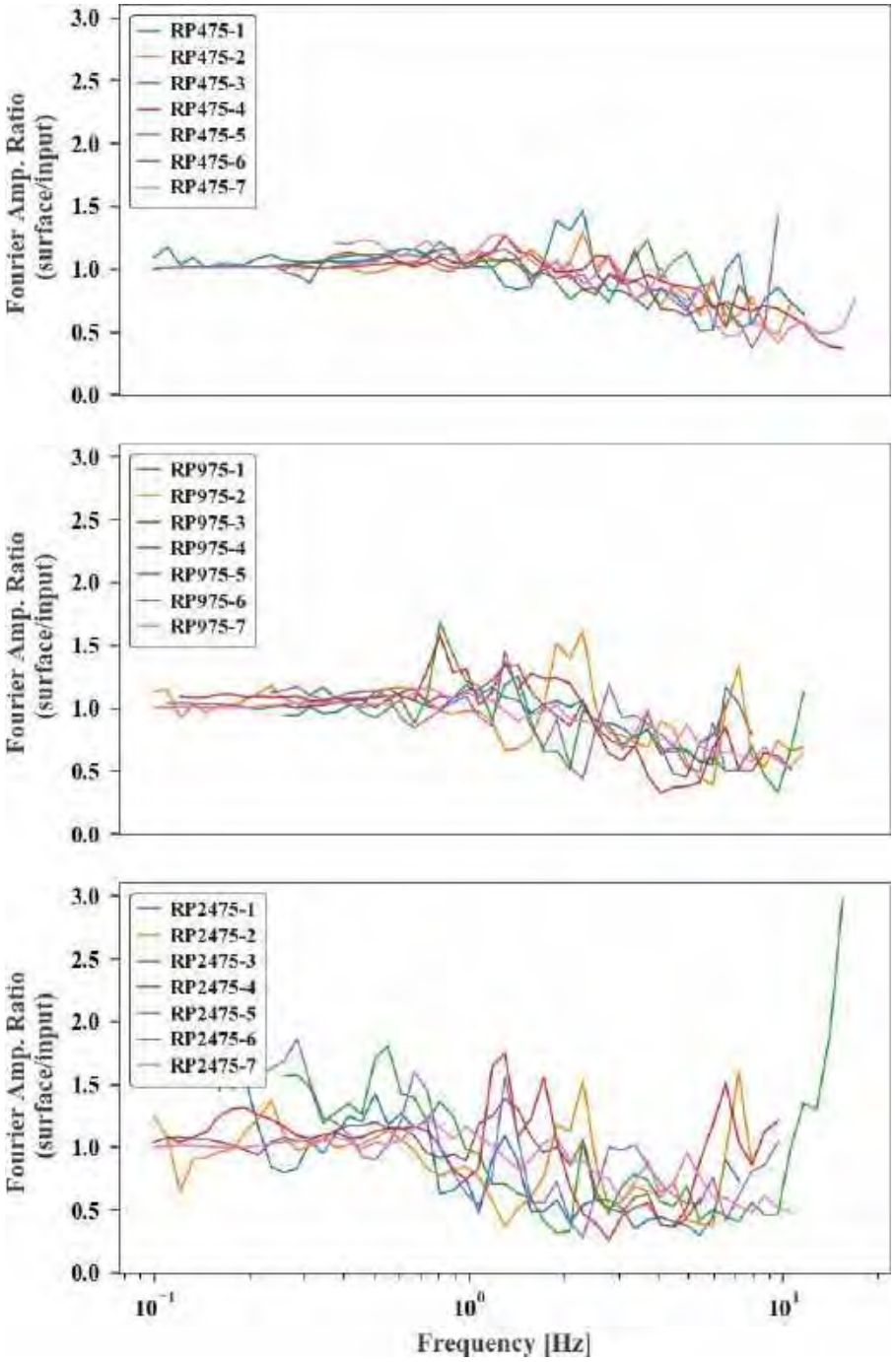

Figure 8.11 Fourier amplitude ratio for all motions.

This project has received funding from the European Union's Horizon 2020 research and innovation programme under grant agreement No. 700748

8.2 2D NONLINEAR EFFECTIVE-STRESS ANALYSIS OF THE GROUND CONDITIONS

8.2.1 GENERALITIES

Two-dimensional analyses were used to assess the performance of a building on top of the soil profile in Pieve di Cento. This chapter outlines the key aspects of the FLAC 2D model and the results of the analyses.

8.2.2 KEY MODEL FEATURES

For this analysis the same soil properties, boundary conditions, ground motions and damping properties were used.

The finite difference mesh (Figure 8.12) was refined in the region closer to the building and gradually coarsened towards the left and right boundaries to provide a better discretisation in the area of interest.

The water table was set at 1.5 metres.

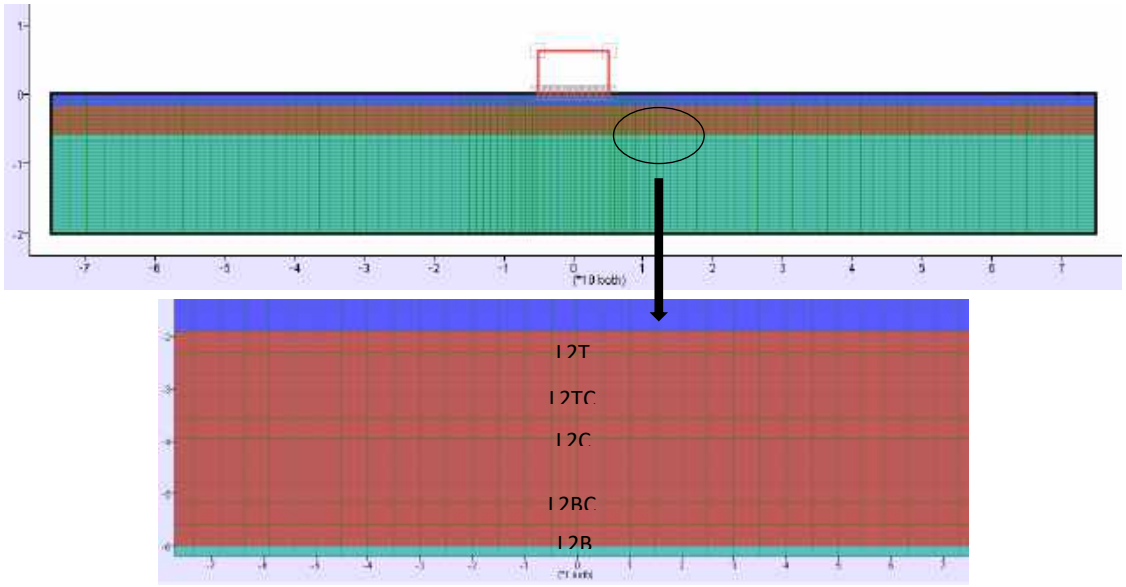

Figure 8.12. Numerical model with building in FLAC.

This project has received funding from the European Union's Horizon 2020 research and innovation programme under grant agreement No. 700748

8.2.3 BUILDING

The building elements were modelled as beam elements into the FLAC software. The width and height of the beams were 1.0 m. The building bearing pressure was set to 45 kPa, distributed in four elements, the foundation (20%), two columns (10%) and the top element (70%). The height of the structure was 6.0 metres, its width was 10 metres and its period was 0.4 seconds.

To consider a period of 0.4 seconds it was necessary to adjust the Young's modulus (E) of the two columns elements using Equations (8.7) and (8.8).

$$E = \frac{K \cdot L^3}{2 \cdot 12 \cdot I} \tag{8.7}$$

$$K = \frac{4 \cdot \pi^2 \cdot m}{T^2} \tag{8.8}$$

where L is the length of the columns (6 metres), I is the moment of inertia, m is the mass and T is the period of the structure and K is the stiffness of a portal frame deforming only in shear.

8.2.4 RESULTS

First, the results of the low amplitude motion (motion RP475-3) are shown in Figure 2.2, where it can be seen that liquefaction was not reached in the free field or under the building. The free field conditions were captured sufficiently faraway from the foundation (three foundation widths from the edge of the foundation and four foundation widths from the boundary).

Note that the pore pressure ratio under the building was calculated using the Equation 1.8, where $\sigma'_{v,0}$ was the initial vertical effective stress, including the building pressure ($\Delta\sigma'_{v,0}$). The "Boston approximation" (Equation 2.3) was used to calculate the building pressure in a specific depth.

$$\Delta\sigma_{V0} = \frac{q \cdot B}{B + y} \tag{8.9}$$

where q is the building pressure at the surface, B is the building width and y is the depth.

This project has received funding from the European Union's Horizon 2020 research and innovation programme under grant agreement No. 700748

Figure 8.13 also shows the pore pressure ratio under the building in different vertical points of the second layer. In the top of the layer (L2T and L2TC) was generate less excess pore pressure and in the bottom (L2BC and L2B) was reached a greater excess pore pressure ratio. The excess pore pressure ratio in the free field conditions was compared with the 1-D analysis results noting similarity in the response.

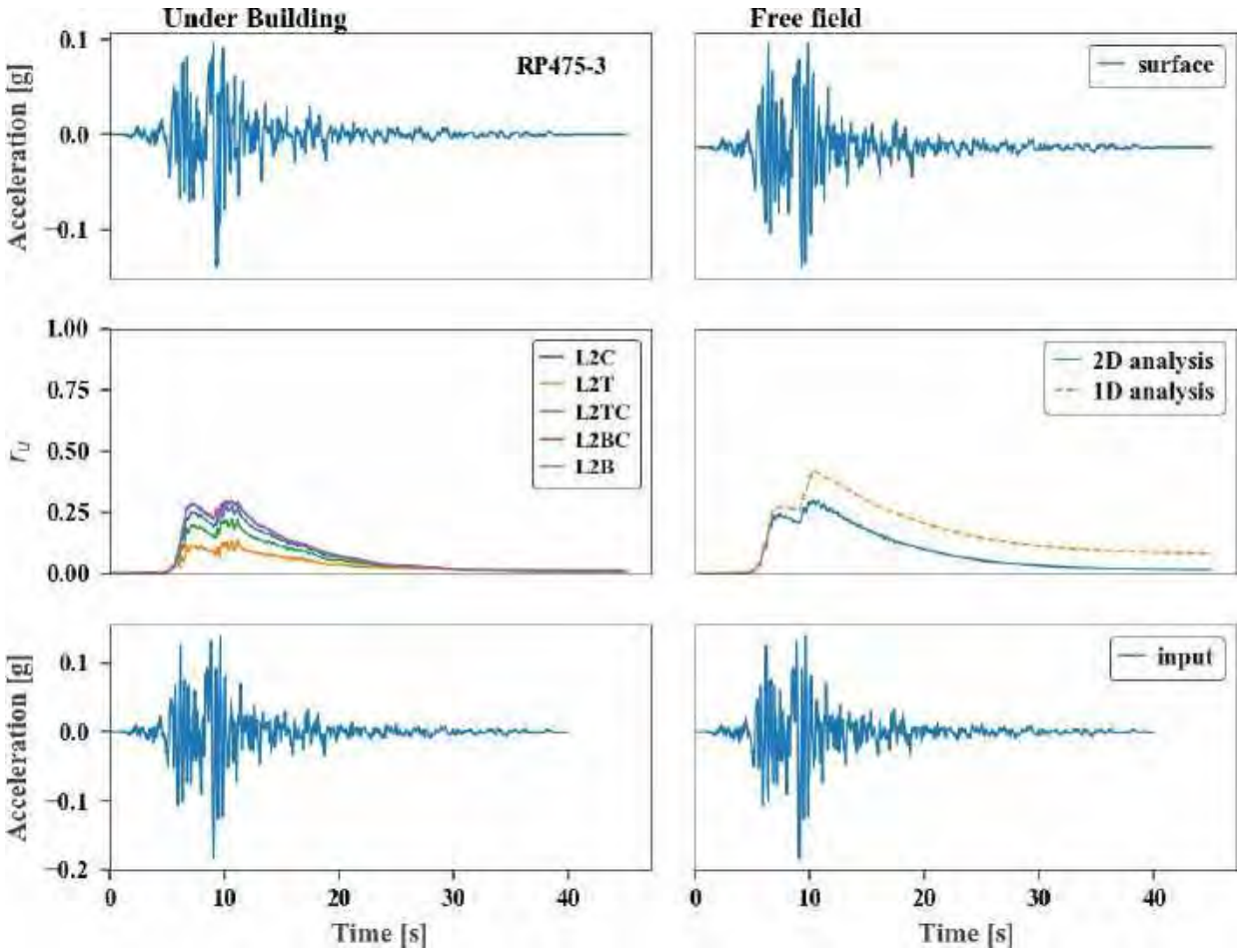

Figure 8.13. Excess pore pressure ratio under the building and in free field, motion 3.

This project has received funding from the European Union's Horizon 2020 research and innovation programme under grant agreement No. 700748

Figure 8.14 shows that under the stronger RP2475-1 (15) motion, liquefaction was reached in the free field. Under the building, the pore pressure starts to increase but then decreases almost to the hydro-static pressure.

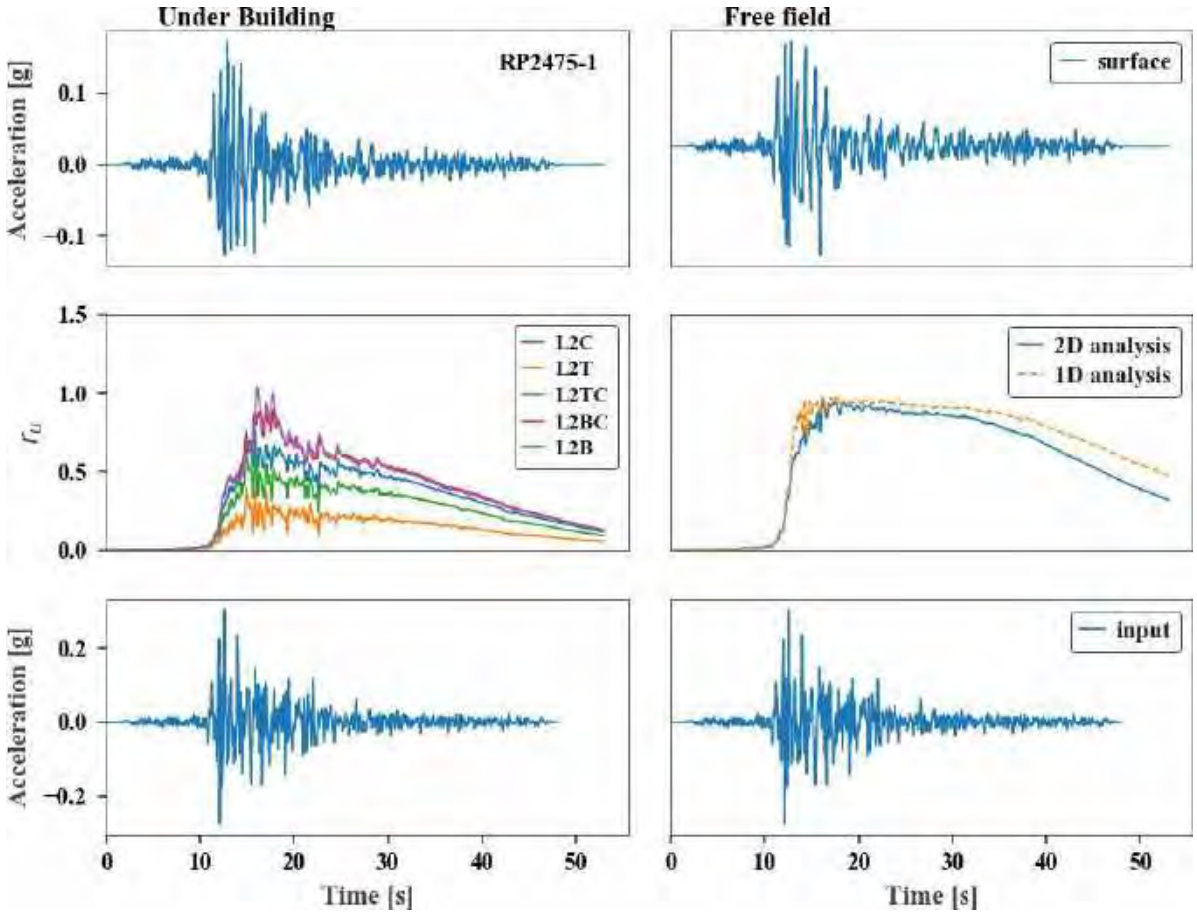

Figure 8.14. Excess pore pressure ratio under the building and in free field, motion 15.

This project has received funding from the European Union's Horizon 2020 research and innovation programme under grant agreement No. 700748

Figure 8.15 shows the excess pore pressure ratio (ru) in the centre of the second layer (L2C) for all the motions for the three different return periods. For all the ground motions under the building the pore pressure starts to increase but due to the water flows to the lateral sides, later the pore pressure decreases and starts to increase in the free field zones causing or not liquefaction depending on the ground motion properties. The motions with the smaller return period did not generate liquefaction in the sandy layers. The appendix B contains all the surface acceleration and excess pore pressure ratio for all the ground motions.

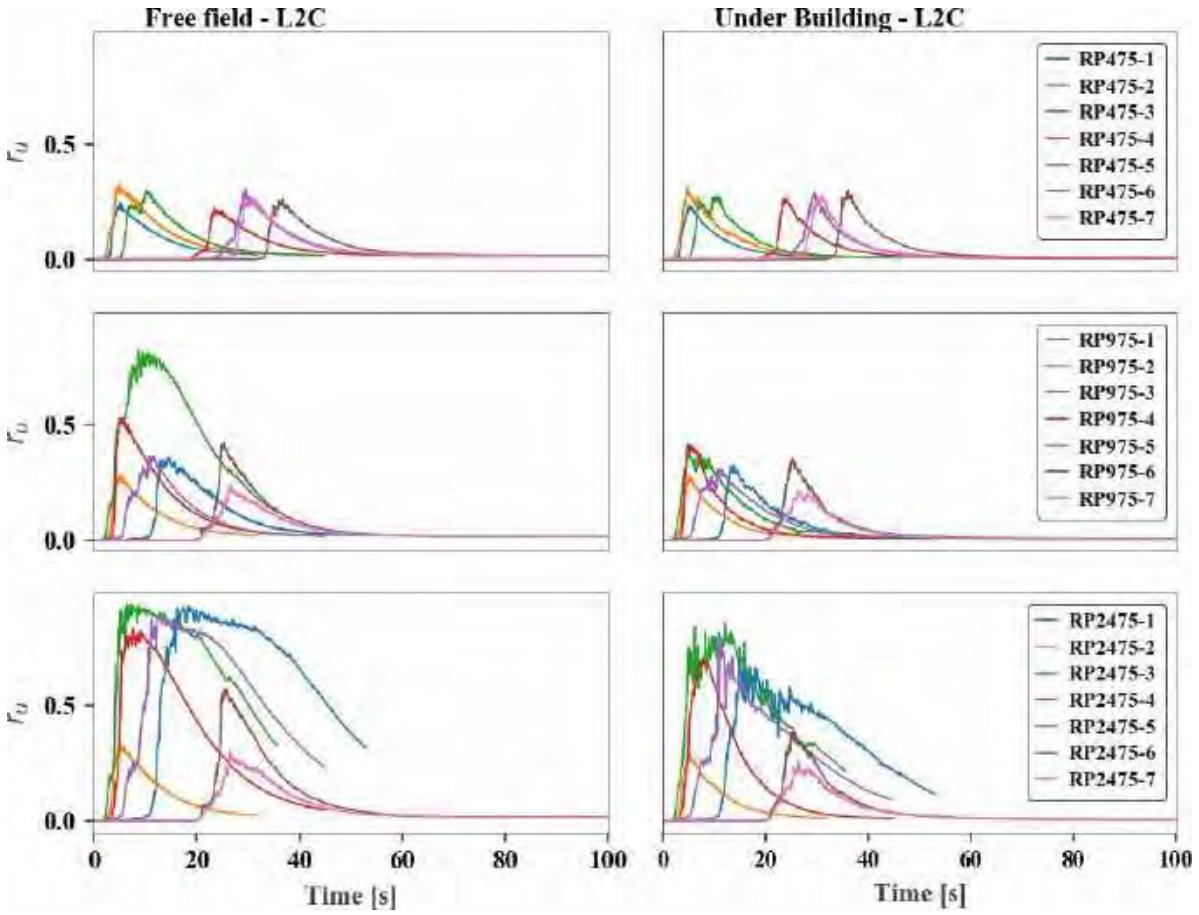

Figure 8.15. Excess pore pressure ratio

This project has received funding from the European Union's Horizon 2020 research and innovation programme under grant agreement No. 700748

The response spectra of input and surface motion (under the building and in free field) for all the motions for the three different return periods is shown in Figure 8.16.

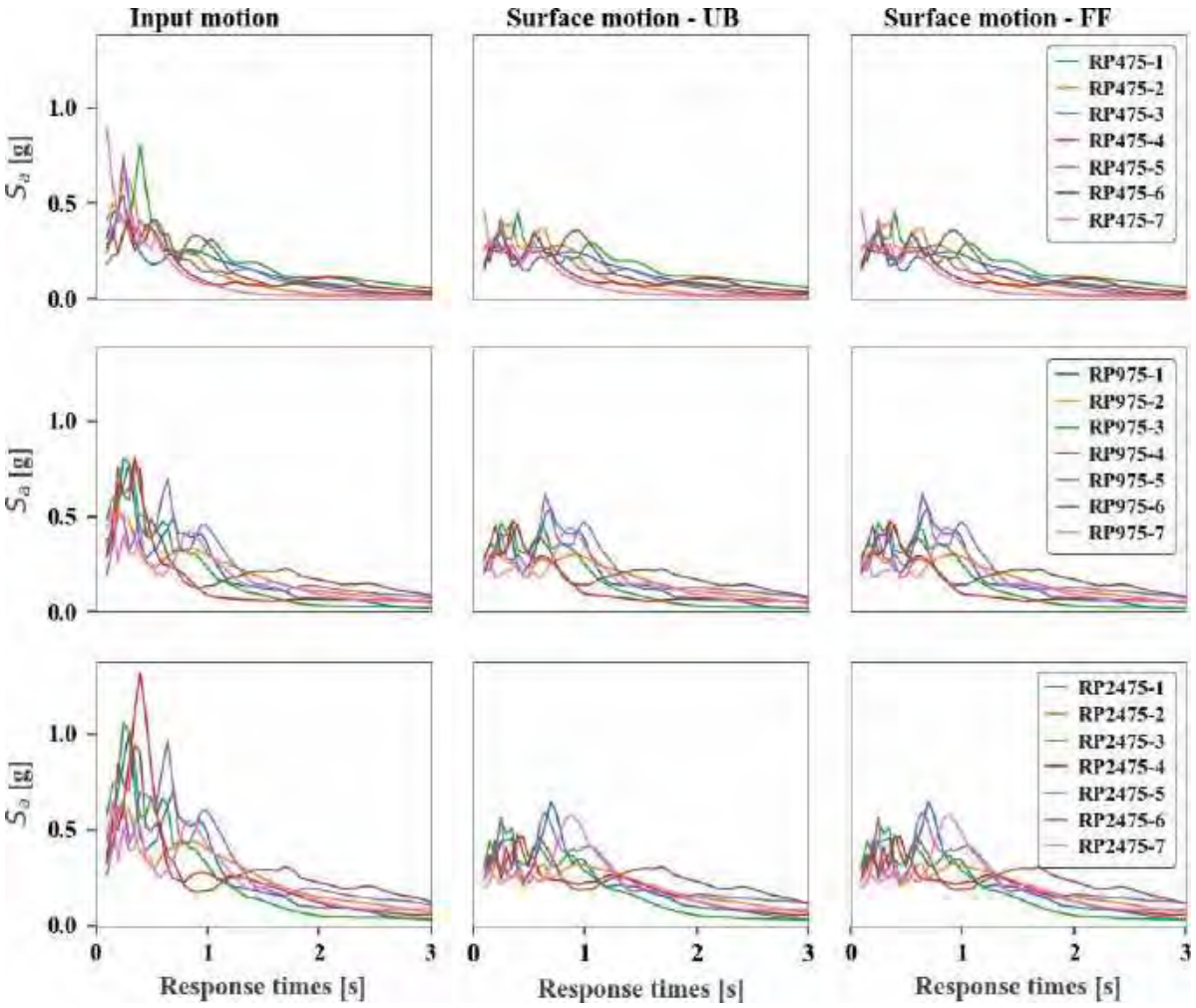

Figure 8.16. Response spectra under the structure (UB: under the building; and, FF: free field))

This project has received funding from the European Union's Horizon 2020 research and innovation programme under grant agreement No. 700748

The response spectra of the upward propagating motion, surface motion under the structure and surface motion in free field conditions for the same ground motion (RP475-2) in each return period is shown in Figure 8.17 a), b) and c) respectively. It can be seen that the high frequency contents of the motions are damped out on the surface motion and for low periods (less than 0.7s) produce almost the same response acceleration regardless of the return period. Additionally, the response spectra in the free field was compared with the response spectre from the 1-D analysis, noting similarity in the response.

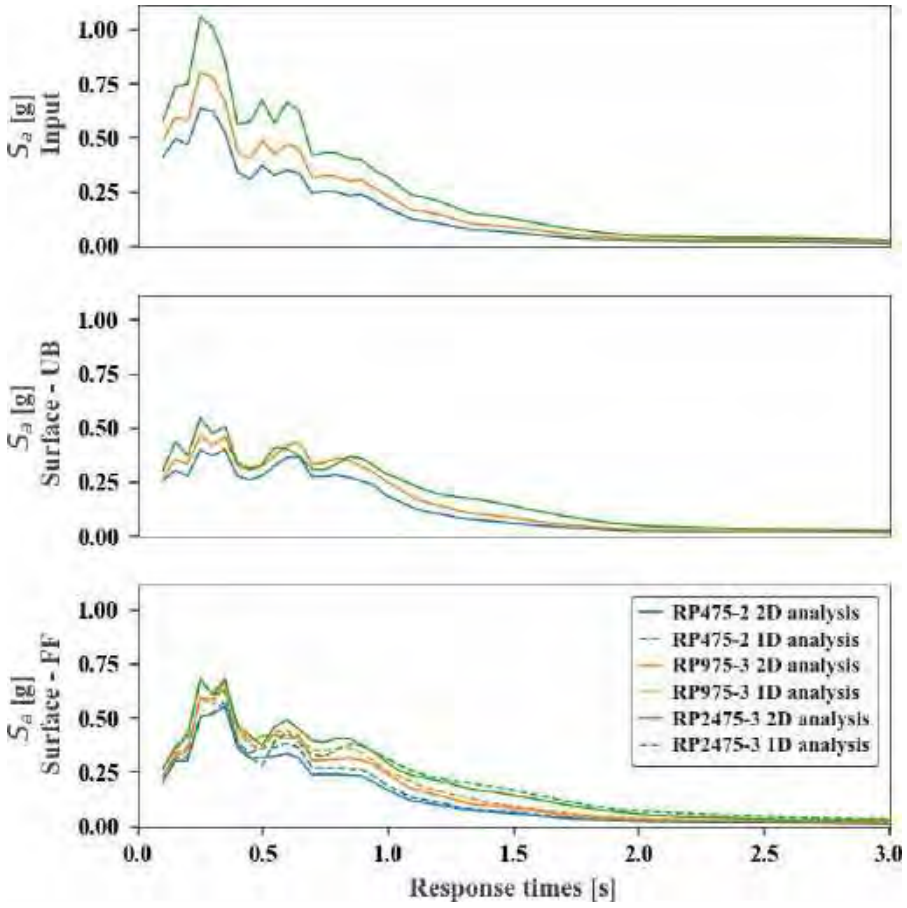

Figure 8.17. Response spectra, motion 475-2, 975-3 and 2475-3

The Fourier spectra of the surface motion under the building for all the motions for the three different return period is shown in Figure 8.18. On the left column the Fourier spectra of the input motions and on the right column the Fourier spectra of the surface ground motions under the building. The Figure 8.19 shows the Fourier spectra of the surface motions in free field conditions.

This project has received funding from the European Union's Horizon 2020 research and innovation programme under grant agreement No. 700748

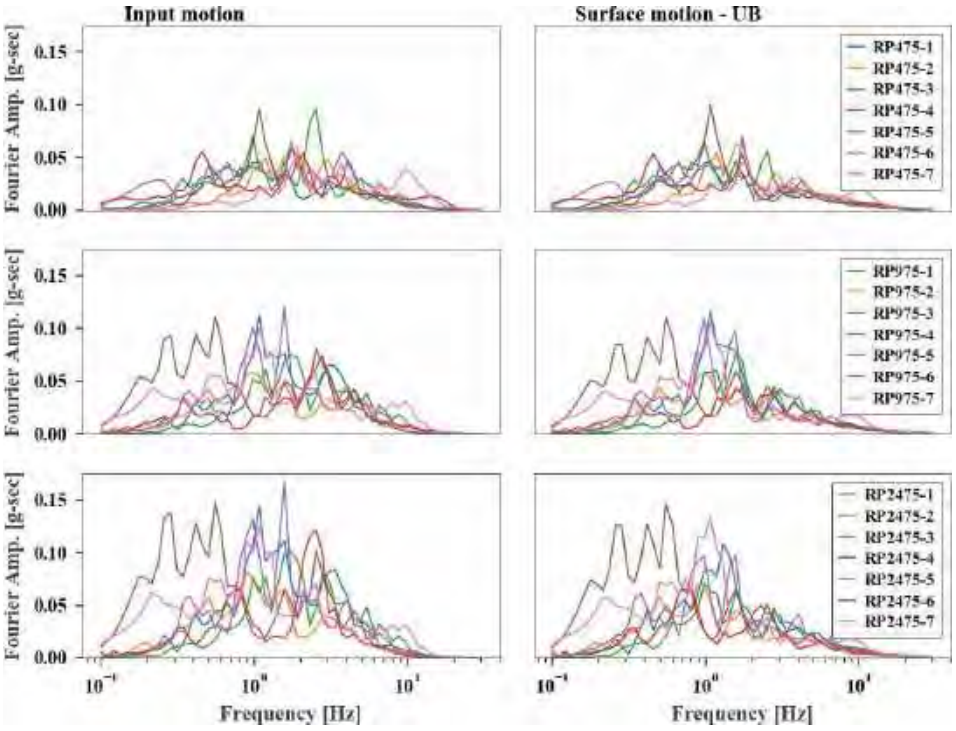

Figure 8.18. Fourier spectra under the structure.

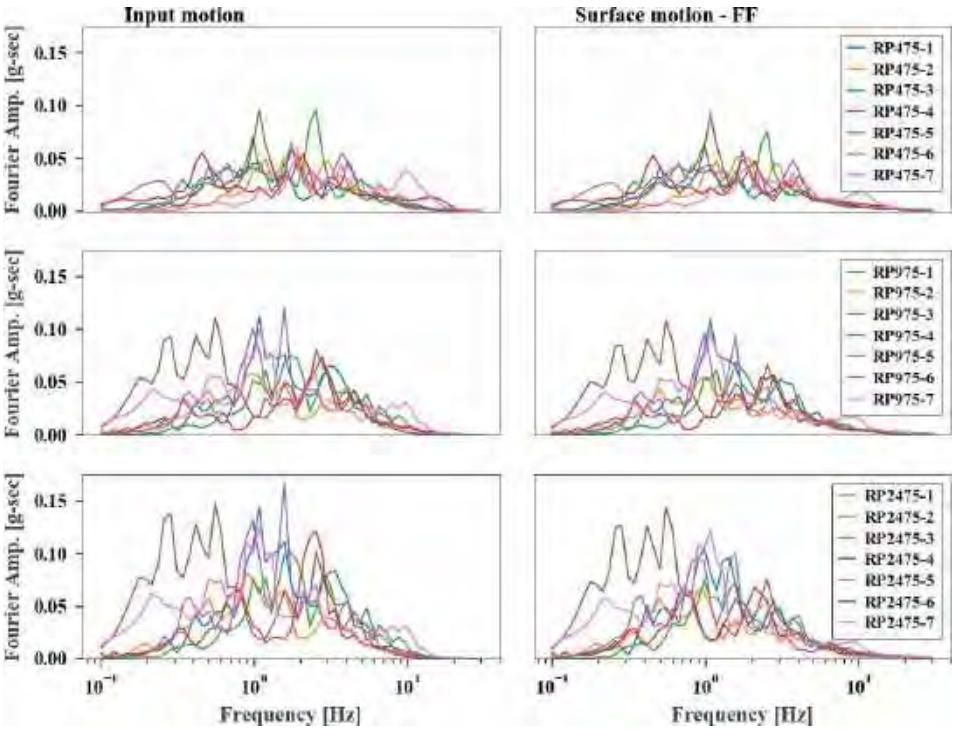

Figure 8.19. Fourier spectra in free field conditions.

This project has received funding from the European Union's Horizon 2020 research and innovation programme under grant agreement No. 700748

The amplification ratio for all the motions for the three different return period under the structure and in free field conditions is shown in Figure 8.20. High frequency amplification occurred in some records due to numerical noise, consistent with Tsiapas and Bouckovalas (2018). Then, for dynamic structural analysis, the records should be filtered to remove the high frequency content above 10 Hz.

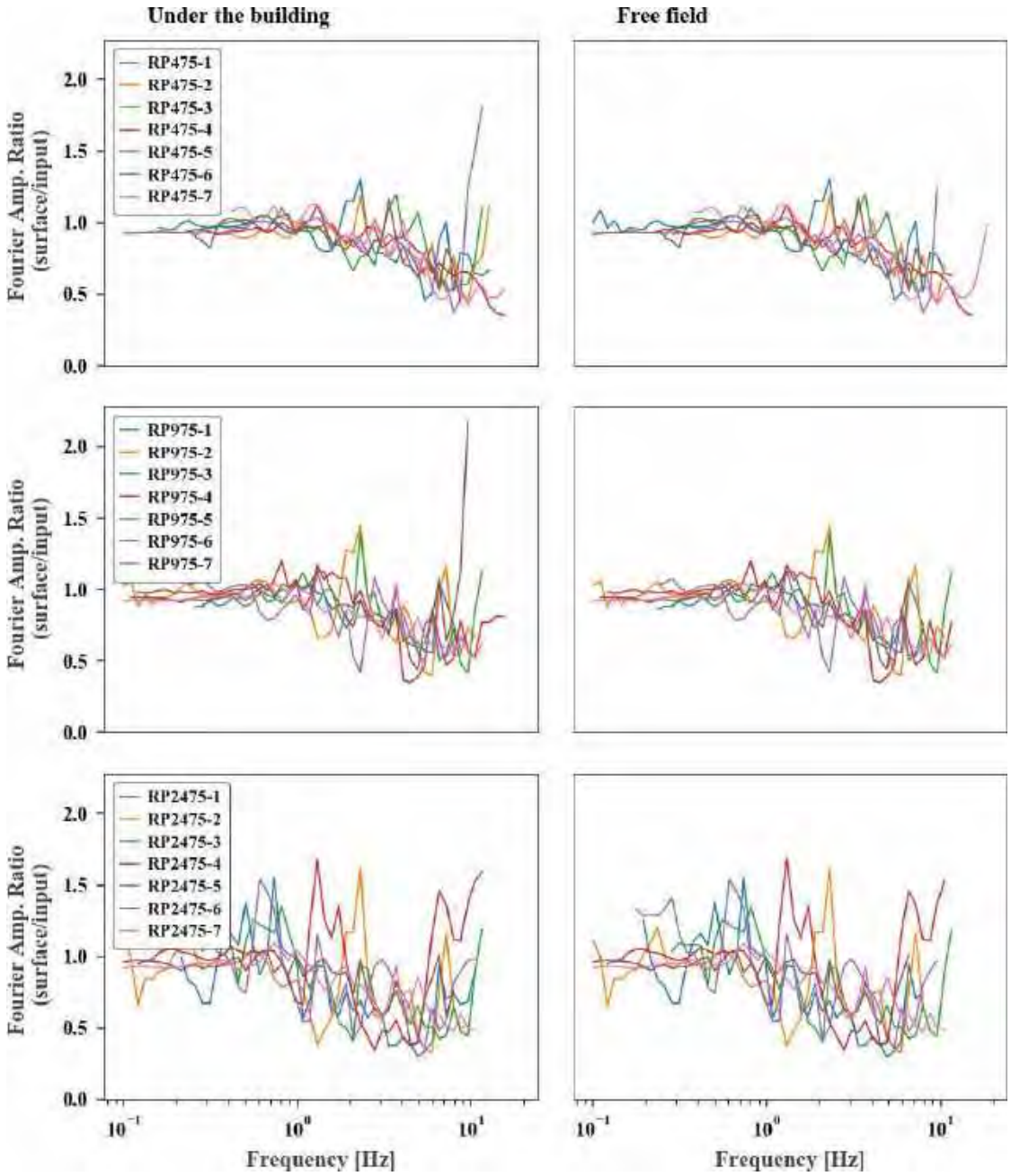

Figure 8.20. Transfer function

This project has received funding from the European Union's Horizon 2020 research and innovation programme under grant agreement No. 700748

Figure 8.21 shows the settlements in the centre of the building. As expected, the settlements using the stronger motions were greater. The dots in the figure represent the settlements calculated from the simplified settlement estimation method from Karamitros (2013). Some discrepancies can be observed, but in general, this approach provided reasonably consistent estimates of settlement compared to the results from FLAC, especially for the stronger ground motions.

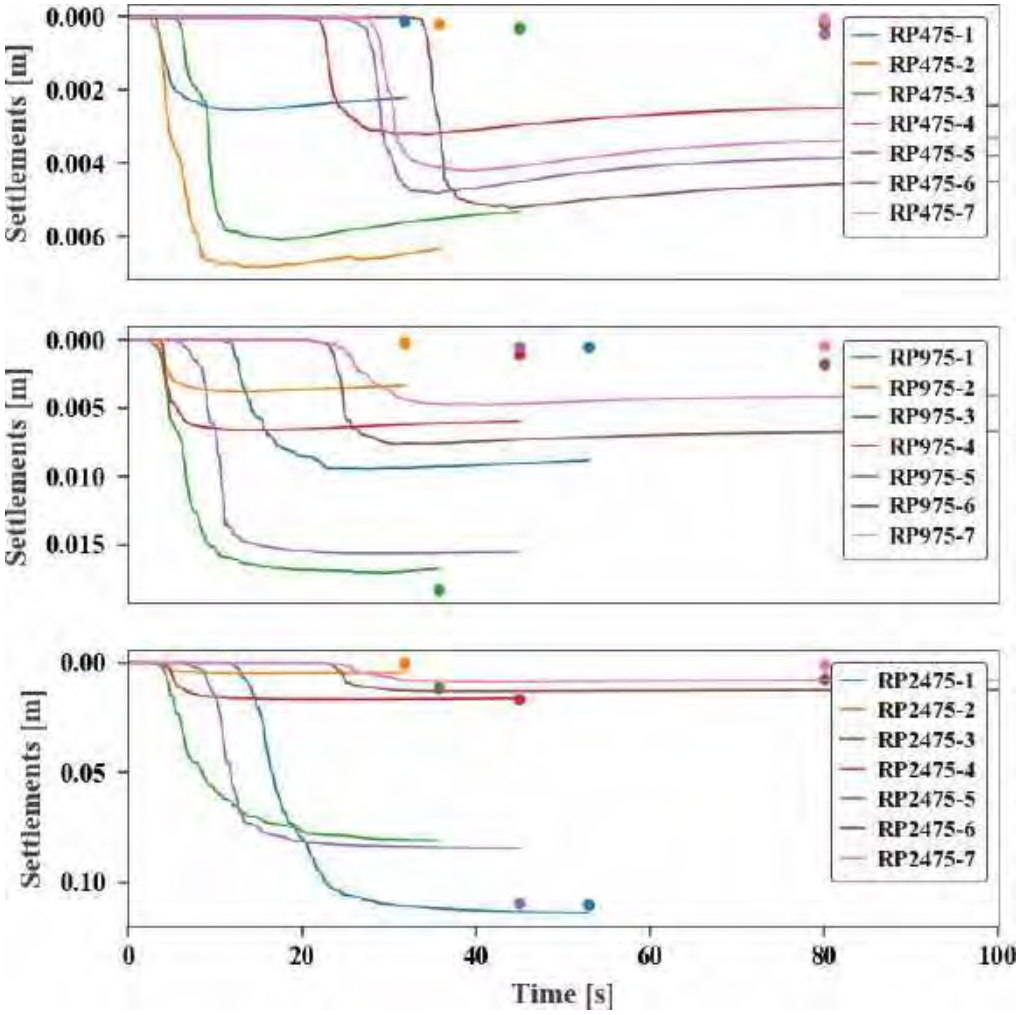

Figure 8.21. Settlements in the middle of the structure (lines from FLAC analyses and dots calculated from Karamitros simplified settlement estimation method)

8.3 FINAL CONSIDERATIONS ON 1D AND 2D ANALYSES

One-dimensional analyses were performed to assess changes in the free-field soil profile response. Seven ground motions caused large excess pore pressure build up close to or causing liquefaction for a ground water level of 1.5m. When the groundwater level was varied from 1.5 m to 1.0 m and 2 m to the surface response acceleration did not change considerably. On the other hand, the excess pore pressure generated in the second layer is similar in the middle and in the bottom of the layer. The excess pore pressure generated in the top of the layer when the groundwater level is deeper was negligible.

Two-dimensional analyses were used to assess the performance of a building on top of the soil profile. Five ground motions caused liquefaction in the free field with the effects of the building in the ground. Comparisons were performed between the response in the free field and the 1-D analysis showing similarity in the results, with slightly lower pore pressure in the 2D analyses. The settlements of the foundation were greater with the larger motions (higher return period).

8.4 STRUCTURAL ANALYSIS: MODEL DESCRIPTION

8.4.1 GENERALITIES

A large number of nonlinear dynamic analyses were performed on a set of reference structural models located in Pieve di Cento (Italy), using the open source software OpenSEES (Mazzoni et al., 2006). This software framework uses the finite element method for simulating the response of structural and geotechnical systems subjected to earthquakes.

This chapter outlines the key aspects of the OpenSEES model and various validation and verification steps that were taken in the development of the model.

8.4.2 KEY FEATURES OF THE PHYSICAL MODEL

Five reinforced concrete (RC) frames (with or without masonry infills) were considered as reference structures for analysis, each with three distinct configurations of the soil-foundation-structure interface. The three-storey three-bay structures have same geometric properties, as reported in Figure 8.22 and Table 8.4.

The structures have been designed based on gravity-only loading actions, neglecting the dynamic features of the structure, in order to reproduce a non-seismic RC building. The simulated design was performed by running a static gravity analysis in OpenSEES using a gravity load for a design combination of actions uniformly distributed on the beams, and a fixed base structure. The output of this gravity analysis was passed to a specific Matlab code, which designed the beam and column reinforcement, and the footing dimensions accordingly. All columns have been designed with the same reinforcement; while a specific reinforcement was designed for central and end sections of each beam.

This project has received funding from the European Union's Horizon 2020 research and innovation programme under grant agreement No. 700748

A second gravity analysis was then performed using a uniform load associated to a seismic combination of actions and additional weight of the infills, in order to calculate the footing loads and nodal masses for the subsequent calculation of settlement and dynamic analysis. In order to save computational time, in the dynamic analysis the dynamic effects of masses of the superstructure were only considered in the horizontal direction (the direction of the applied ground motion), while, in the foundation model described in the subsequent sections, the corresponding nodal masses act in the three degrees of freedom. This is a common assumption in 2D models with horizontal-only applied motion. The masses were calculated according to the axial load levels at the top of each column, by subtracting the total axial load of the above floors to the axial load at the lower storey.

Since the masses were only considered in the horizontal direction, the uniform gravity load for seismic combination of actions was statically applied in the subsequent dynamic analysis, in order to model the vertical static load, prior and during the dynamic application of the horizontal ground motion.

The five RC frames have been designed by randomly assigning the material properties (concrete and steel stiffness and strength), and the values of the uniformly distributed gravitational loads in design and seismic combinations of actions. The distributions and truncation values used are reported in Table 8.5, and the corresponding generated parameters for the five buildings are reported in Table 8.6.

Table 8.4: Geometric parameters for the reference model

Parameter	Measure
Number of storeys	3
Number of bays	3
Bay length	4.35 m
Height of ground floor	3.20 m
Height of upper floors	2.90 m
Beam height	45 cm
Beam width	25 cm
Column depth	30 cm
Column width	25 cm

This project has received funding from the European Union's Horizon 2020 research and innovation programme under grant agreement No. 700748

Table 8.5: Random parameters for the reference model

Parameter	Type of distribution	Mean value (μ)	Std. deviation (σ)	Trunc. (min)	Trunc. (max)	Notes
Strength of concrete (MPa)	Gamma distr	24		12	70	Shape=6 Scale=4
Yield strength of steel (class s1) (MPa)	Normal distr.	344	68.8	230	500	
Yield strength of steel (class s2) (MPa)	Normal distr.	495	22	400	550	
Yield strength of steel (class s3) (MPa)	Normal distr.	589	30	500	670	
Steel class	Triangular distr.	2		1	3	s1=25% s2=50% s3=25%
Gravity load for design combination of actions (kN/m)	Triangular distr.	50		35	65	
Ratio of gravity loads in seismic/design combination of actions	Triangular distr.	0.30		0.25	0.35	

Table 8.6: Random parameters generated for the five models

Parameter	BD1	BD2	BD3	BD4	BD5
Strength of concrete (MPa)	14.7	15.8	21.8	15.0	16.0
Steel class	1	1	2	3	2
Yield strength of steel (MPa)	305	425	496	607	504
Gravity load for design combination of actions (kN/m)	49.6	52.5	47.0	51.5	48.2
Gravity load for seismic combination of actions (kN/m)	15.5	13.7	12.4	17.6	13.8

This project has received funding from the European Union's Horizon 2020 research and innovation programme under grant agreement No. 700748

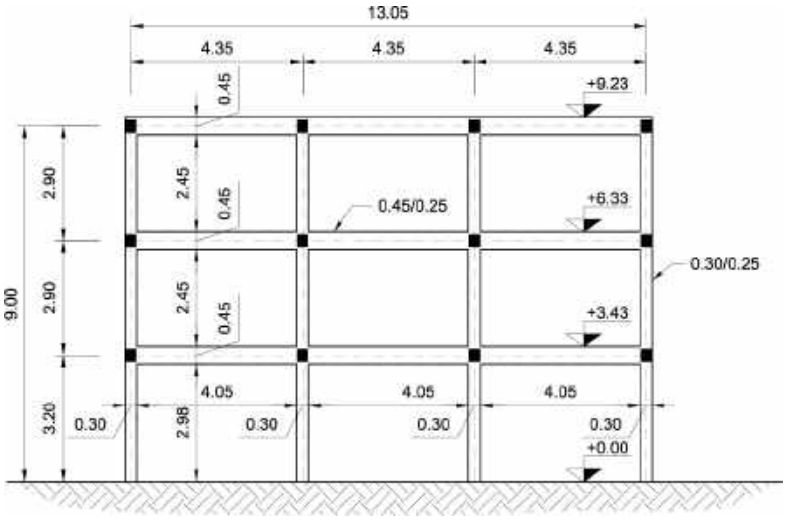

Figure 8.22: Physical model of the reference structure

Each benchmark structure has been studied in three different foundation-soil configurations, as shown in Figure 8.23. In case a, the building foundations laid on a very stiff layer (bedrock), which prevented any displacement/rotation of the foundation. In such conditions, the bedrock ground motions do not undergo any amplification or modification in frequency content and intersect the soil surface unaltered.

In case b, the soil beneath the foundation level corresponded to the soil model developed for Pieve di Cento site. The foundation was a very stiff continuous shallow foundation, which prevented differential settlements and/or base tilt.

Case c presents the same soil layers of case b. The foundation system was composed of shallow isolated footings, which were prone to differential settlements/rotations.

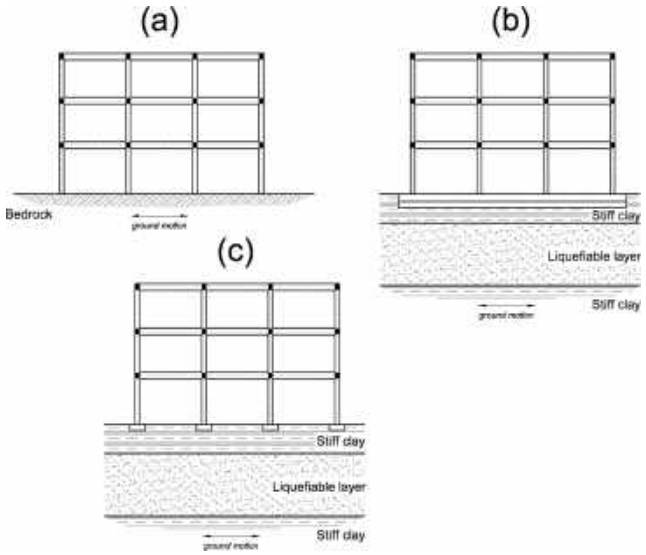

Figure 8.23: Foundation-soil systems: (a) rigid foundation on bedrock; (b) rigid foundation on

This project has received funding from the European Union's Horizon 2020 research and innovation programme under grant agreement No. 700748

compressible soil; (c) isolated footings on compressible soil

8.4.3 GROUND MOTIONS

The ground motions at the bedrock were taken as the upward propagating motions from a site response analysis at 20m depth (see section on FLAC analysis). The seismic hazard was represented by a set of ground motions referred to three different return periods equal to 475, 975, and 2475 years, according to Italian Standard (NTC, 2018). Seven motions were considered for each return period, for a total of 21 ground motions. For soil- structure configuration a, the bed rock ground motions were directly applied to the base nodes of the structure in the dynamic analysis. For configurations b and c, the input motions were the surface motions from the 2D effective stress FLAC site response analysis, as described in the previous section (§8.1). The surface motions obtained from this analysis were filtered using a 4^{th} order Butterworth lowpass filter at 15Hz, because the numerical noise was produced in the FLAC analyses and was especially prominent above this frequency (See Chapter FLAC Analysis). The filtered surface motions were applied at the base of the structural model, as shown in the next section.

8.4.4 STRUCTURAL MODEL

The general modelling strategy adopted for the frame elements involved an association of nonlinear springs and elastic elements in series combined with a nonlinear moment-rotation joint model, following the main assumptions and strategies proposed in Ibarra et al., 2005; Lignos and Krawinkler, 2011; Haselton et al. 2016; Jeon et al. 2015; Baradaran Shoraka and Elwood, 2013; Elwood, 2004.

8.4.4.1 BEAMS AND COLUMNS

The structure in elevation for cases a and b was modelled in OpenSees with a 2D model (Figure 8.24) (the same configuration used in the design phase). The RC frame was represented using 21 elastic beam-column elements (linear elastic), 9 for the beams and 12 for the columns (referred to as elasticBeamColumn elements in OpenSees).

A simple leaning column model accounted for P-Δ effects (in grey in Figure 8.24). The leaning column has a very high axial stiffness, a very low bending stiffness and it was linked to the structure by axially rigid truss elements, in order to not transfer the relevant horizontal displacements to the frame structure. A concentrated vertical load was applied to the leaning column at the level of each floor of the structure, equal to the weight of that floor.

8.4.4.2 BEAM-COLUMNS JOINTS

The linear elements were connected by nonlinear beam-column joints (Joint2D elements), connecting the end sections of beams and columns. The two-dimensional beam-column joints were modelled as parallelogram-shaped shear panels (rotational springs) with adjacent

This project has received funding from the European Union's Horizon 2020 research and innovation programme under grant agreement No. 700748

elements connected to their mid-points (detail in Figure 8.24). Each beam or column was connected to the shear panel through a shear and a rotational spring (ZeroLength elements). The system composed by the shear panel and the four spring elements at the external nodes was able to reproduce the nonlinear response of the structure under monotonic and cyclic strain, thanks to the specific properties of the materials associated to each component.

The central rotational spring was modelled with a hysteretic material (uniaxialMaterial Hysteretic), with pinching of force and deformation, damage due to ductility and energy, and degraded unloading stiffness based on ductility. The external rotational springs were modelled with a material (ModIMKPeakOriented) that simulates the modified Ibarra-Medina-Krawinkler deterioration model with peak-oriented hysteretic response (Lignos and Krawinkler, 2012). The strength and stiffness associated to these materials was a function of the physical characteristics of the sections of the corresponding elements (beams or columns), that were determined in the design phase, where the reinforcement of the structural elements was calculated.

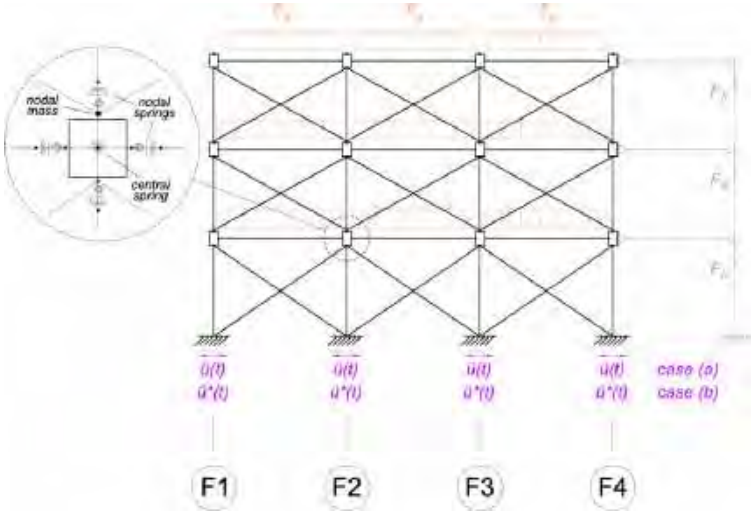

Figure 8.24: Numerical model for cases (a) and (b) and detail of the beam-column joints configuration.

8.4.4.3 MASONRY INFILLS

Masonry infills were modelled with the equivalent strut approach, which is one of the commonly used principles when developing nonlinear mathematical models of infilled frames for earthquake analysis (Zarnic and Gostic, 1998).

The elements used were nonlinear truss elements that were assigned a nonlinear stress-strain material model simulating the infill behaviour. Two diagonal struts (as shown in Figure 8.24) were used to simulate one infill and were connected to the beam-column joints at the column level. The equivalent area of each strut was established based on the maximum lateral force of the infill (Zarnic and Gostic, 1997), transformed to the direction of the diagonal, and on the masonry compressive stress f_m. Maximum strength was assumed to be reached at an inter-

storey drift of 0.2% (Dolsek and Fajfar, 2008). The lateral displacement of each infill was transformed into the diagonal displacement for the subsequent definition of the strain of the strut.

The parameters obtained, i.e. the maximum stress and strain, were used to define the masonry material with zero tensile strength simulated by the Concrete01 material (Noh et al., 2017). The peak compression strength f_m was equal to 3.1 MPa and all infills had a thickness of 0.1 m. Additionally, a residual strength equal to 10% of the peak strength was considered for numerical stability, which was reached at an inter-storey drift five times the peak inter-storey drift. A unit weight of 6.87 kN/m^3 was considered for the infills (Hak et al., 2012).

The infills were included in the structural model to involve realistic values of stiffness and mass. Nevertheless, the damage of the infills during the application of the seismic load was not considered in the subsequent assessment of the performance of the structure, where only the response of beams and columns elements were considered.

8.4.5 FOUNDATION MODEL

8.4.5.1 INTRODUCTION

For cases a and b, foundations were modelled as "rigid base" (Figure 8.24). Thus, the rock ground motions (a) and the surface ground motions (b) were applied directly at the base nodes as acceleration time series ($\ddot{u}(t)$ and $\ddot{u}^*(t)$, respectively).

In case c, the more complex behaviour of the isolated foundations required the model shown in Figure 8.25 whose foundation system was composed of squared isolated pads whose dimensions were determined for each building in the design phase. The footings were designed to be all equal, by considering the most loaded column and applying Meyerhof (1963) method to design a square section. In the numerical model, the base node of each column of the ground floor was connected to the constrained node by means of a nonlinear spring-damper system acting along the three degrees of freedom. The surface motions $\ddot{u}^*(t)$ were applied at the fixed nodes.

The spring system was composed of a vertical, a horizontal, and a rotational component. The damping (dashpot) system (not shown in Figure 8.25) acted in parallel with the spring system, and it was composed of three components as the spring system. The system was modelled in OpenSees by two ZeroLength elements, one for the spring and one for the dashpot element. The materials used for modelling the behaviour of these elements in each of the three components are described in the following section.

This project has received funding from the European Union's Horizon 2020 research and innovation programme under grant agreement No. 700748

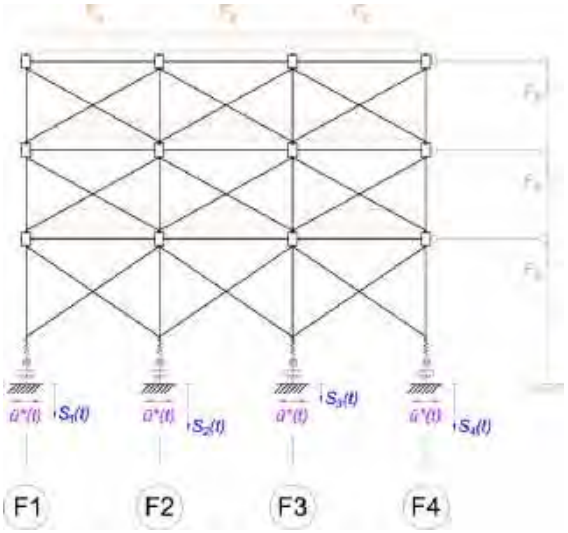

Figure 8.25: Numerical model for structure with isolated footings.

8.4.5.2 MATERIAL MODELS FOR SPRING AND DASHPOT ELEMENTS

The behaviour of the materials used to model the spring-dashpot system was not linear and depended on the time series r_u calculated in FLAC analysis , as described in the previous section (8.1).

8.4.5.2.1 HORIZONTAL SPRING ELEMENT

The spring element was composed of three components, each of which was associated to a specific material. The horizontal spring was modelled with a linear elastic material (denominated as Elastic in OpenSees). The only parameter required to define this material was the stiffness modulus K_h, which was constant. The formulation proposed by Gazetas (1991) for a rectangular foundation was adopted:

$$K_h = \frac{2Gl}{1-\nu}(2 + 2.50\chi^{0.85})k_y \qquad (8.10)$$

where:

- $\chi = \frac{A_b}{4L^2}$
- $A_b = 4bl$ is the area of the foundation-soil contact surface
- $b = 2B$ and $l = 2L$ are the foundation semi-width and semi-length, respectively

k_y is a dynamic coefficient, which depends on the frequency-dependent term a_0:

This project has received funding from the European Union's Horizon 2020 research and innovation programme under grant agreement No. 700748

$$a_0 = \frac{\omega b}{V_s} \qquad (8.11)$$

where $\omega = 2\pi f$ is the circular frequency of the applied force (from the structure to the foundation soil), and V_s is the shear wave velocity of the foundation soil. The relation between the dynamic coefficient and a_0 was graphically provided by the author. For the soil studied, imposing a period $T = \frac{1}{f}$ of 1s it was $k_y = 1$:

8.4.5.2.2 VERTICAL SPRING ELEMENT

The vertical elastic component depended on the characteristics of the soil, which in turn varied with the mean effective stress. The springs had zero vertical tensile capacity. The material adopted was an elastic no-tension material (ENT material), characterized by a stiffness modulus K_v, dependent on the mean effective stress p'. In order to directly link the mean effective stress to r_u time series, a normalized form of the first was considered:

$$p'_{norm} = \frac{p'}{p'_i} \qquad (8.12)$$

where p'_i was the mean effective stress before the application of the ground motion. Adopting this definition, p'_{norm} depended on r_u through the following:

$$p'_{norm} = 1 - r_u \qquad (8.13)$$

At the beginning of the analysis it was r_u = 0 and p'_{norm} = 1. When the pore pressure increased as an effect of the applied dynamic load, r_u increased, p'_{norm} decreased, and the soil tended towards liquefaction for r_u = 1 and p'_{norm} = 0.

Vertical stiffness modulus assumed an initial value $K_{v,i}$ corresponding to p'_{norm} = 1 and decreased linearly up to a residual value $K_{v,res} = rK_{v,i}$ for p'_{norm} = 0, where r was a ratio of the initial over residual stiffness. The linear relation was:

$$K_v = K_{v,i} \cdot [1 - (1 - p'_{norm})(1 - r)] \qquad (8.14)$$

If p'_{norm} was outside the interval [0,1] (e.g. when the soil manifested dilatant behaviour), the stiffness modulus did not exceed the interval between the initial and the residual value, as shown in Figure 8.26.

This project has received funding from the European Union's Horizon 2020 research and innovation programme under grant agreement No. 700748

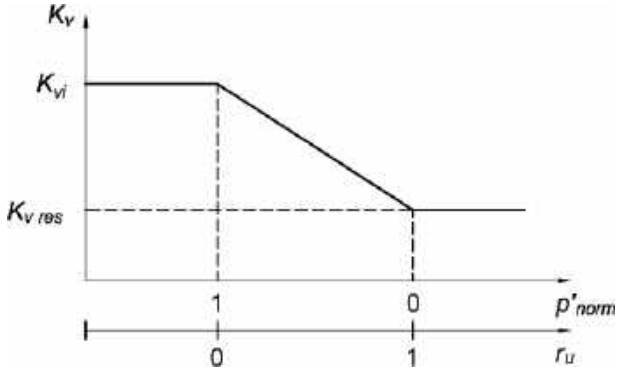

Figure 8.26: Model for vertical stiffness degradation.

For the initial vertical stiffness, Gazetas (1991) formulation was adopted:

$$K_{v,i} = \frac{2Gl}{2-\nu}(0.73 + 1.54\chi^{0.75})k_z \qquad (8.15)$$

with the same meaning of the variables of equation **Errore. L'origine riferimento non è stata trovata.**). The dynamic coefficient was $k_z = 1$.

The parameter r was calculated using the research by Karadzia et al. (2017). Karadzia et al. (2017) presented the results for the dimensionless static stiffness ratio $\frac{\tilde{K}_{ij}}{K_{ij}}$ of a multilayer configuration with a shallow non-liquefiable layer (crust) and a second liquefiable layer (similarly to the configuration shown in Figure 8.23 b and c). The stiffness ratio was presented as a function of the crust and liquefiable layer heights, foundation width, and ratio of shear wave velocity measured in the crust and in the second layer in liquefied conditions. Term $\tilde{K}_{ij}$ indicates the post-liquefied dynamic stiffness, while K_{ij} indicates the pre-liquefied stiffness. This ratio was adopted in the present case as parameter r to be introduced in expression (8.14).

In the OpenSees implementation, p'_{norm} was introduced as a time series and it was calculated from the r_u time series, which was imported from the analysis results performed in FLAC as described in the previous section (§8.1). Hence, the value of K_v was calculated at each analysis step through expression (8.14), and the corresponding updated value was input in the analysis.

8.4.5.2.3 ROCKING SPRING ELEMENT

Rotational springs were modelled in OpenSees using material PyLiq1. This is an elastic hardening-plastic material with ultimate capacity that incorporates liquefaction effects. It was described in Boulanger et al. (1999). The constitutive response of PyLiq1 (in terms of ultimate capacity and stiffness) was scaled in proportion to the mean effective stress time series. Both stiffness and ultimate capacity reduction were modelled with the same linear interpolation

This project has received funding from the European Union's Horizon 2020 research and innovation programme under grant agreement No. 700748

of Figure 8.26. Nevertheless, the material definition prescribes a nil value for the residual stiffness. Initial stiffness was calculated according to Gazetas (1991) proposal:

$$K_{r,i} = \frac{G}{2-\nu} I_{bx}^{0.75} \left(\frac{l}{b}\right)^{0.25} \left(2.4 + 0.5\frac{b}{l}\right) k_{rx} \qquad (8.16)$$

where I_{bx} is the area moment of inertia of the foundation-soil contact surface around an axis parallel to the direction of the foundation length:

$$I_{bx} = \frac{1}{12}(2l)(2b)^3 = \frac{1}{12}LB^3 \qquad (8.17)$$

The dynamic coefficient was $k_{rx} = 1$, and the remaining terms are reported in equation **Errore. L'origine riferimento non è stata trovata.**). When p'_{norm} = 0, the ultimate rotational c apacity was considered to be coincident with:

$$M_{cap,i} = N\frac{B}{2}\left(1 - \frac{N}{N_{cap}}\right) \qquad (8.18)$$

where $N_{cap} = B \cdot L \cdot q_{ult}$ is the foundation bearing capacity in static conditions, calculated with Meyerhof (1963); and N is the vertical load due to the self-weight of the tributary area of each footing, calculated in static conditions.

As aforementioned, ultimate capacity decreased linearly with p'_{norm}, from $M_{cap,i}$ to $M_{cap,res}$, following qualitatively the scheme of Figure 8.26. The ratio of the capacities was calculated following Karatzia et al. (2017) formulation, although this was developed for stiffness reduction computation.

PyLiq1 material incorporates a component for viscous damping. Thus, for the rotational component, only one element was necessary in the model, as the material accounts for both stiffness and dashpot components. The properties of the viscous damping are detailed in the next section.

It is worth noting that material PyLiq1 is a symmetric material (behaving equally in tension and compression) which was designed to best behave in symmetric cyclic conditions (cycles around 0 shear stress). For these reasons, it is not suitable to be used for modelling vertical springs behaviour, which presented an initial compressive stress due to the static vertical loads.

8.4.5.2.4 DASHPOT ELEMENTS

The dashpots were modelled in OpenSees with a ZeroLength element acting in the horizontal and vertical components. As referred to in the previous section, the rocking viscous component was coupled with the elastic element of the same component, due to the particular material used. The rocking viscous component of PyLiq1 material requires the

definition of the damping coefficient. The materials associated to the ZeroLength elements were two Viscous type materials, which require the definition of a damping coefficient and a power factor (which was set equal to 1). The damping coefficients for the horizontal, vertical, and rocking components were calculated according to Gazetas (1991):

$$C_h = \rho V_s A_b c_y \quad (8.19)$$

$$C_v = \rho V_{La} A_b c_z \quad (8.20)$$

$$C_r = \rho V_{La} I_{bx} c_{rz} \quad (8.21)$$

where:

- A_b is the area of the footing
- $V_s = \sqrt{\frac{G}{\rho}}$ is the shear wave velocity of the upper soil layer
- $V_{La} = \frac{3.4}{(\pi(1-\nu))V_s}$ is Lysmer's analog wave velocity of the upper soil layer
- ρ is the density of the upper soil layer

Coefficient $c_y(a_0)$, $c_z(a_0)$, and $c_{rx}(a_0)$ are the dynamic coefficients, which depend on the frequency-dependent term a_0. For the particular soil studied (imposing a period of 1s) it was:

$$c_y = 1; c_z = 1; c_{rx} = 0.1 \quad (8.22)$$

8.4.5.3 PROCEDURE OF ANALYSIS

As referred, a design phase was carried out for each building before the dynamic analysis, in order to calculate the design properties of the structural elements, and to calculate the equivalent lumped masses. The lumped masses for dynamic response calculated in the design phase were located in the nodes above the shear panels, as shown in Figure 8.24.

For infilled structures, the extra masses and gravity loads due to the infills were added to the previously calculated nodal masses and distributed gravity load.

This project has received funding from the European Union's Horizon 2020 research and innovation programme under grant agreement No. 700748

For the structures supported by the non-linear spring-damper system at the footings (Figure 8.25), a nodal mass corresponding to a half the vertical distributed load acting on the tributary span of the ground floor was placed in correspondence of each footing at the node between the spring-damper system and the column. The remaining 50% of the load was assumed to be directly transmitted to the ground between the footings and was not accounted in the structural analysis.

During the dynamic analyses, the gravitational loads for the seismic combination of actions was imposed as a uniform distributed load on each of the beam elements, and a horizontal ground motion was applied at the foundation level. For the structures with isolated footings, an imposed settlement time series $S(t)$ was applied at the base of each vertical spring, in order to take into account the liquefaction induced settlements calculated in the FLAC analysis as described in the previous section (§8.1). In order to include the effects of soil inhomogeneity, at each footing the settlement time series was multiplied by a constant coefficient. A specific coefficient c_i was assigned at each footing, selected from a uniform distribution included in the interval [0.7-1.2]:

$$S_i(t) = c_i S(t) \qquad (8.23)$$

with i = 1...4. The four randomly generated coefficients c_i are [1.107, 1.153, 0.763, 1.157], for footings from F1 to F4 (as in Figure 8.25), respectively. These values were used in all the analyses performed on structures supported by the spring-damper systems.

Each dynamic analysis had a total duration equal to the duration of the applied ground motion increased by 5 seconds. This additional time is estimated as being sufficient to let the free vibration of the structure after the end of the shaking stabilise and provide an adequate estimate of residual strain.

8.5 STRUCTURAL ANALYSIS: MODEL PERFORMANCE

8.5.1 NONLINEAR PUSHOVER ANALYSIS

A static nonlinear pushover analysis has been performed on each of the five RC frames in order to perform a preliminary assessment of the capacity of each benchmark structure. These analyses are intended to be complementary simplified analyses, useful to validate the dynamic analyses presented in the next section. The pushover analyses were performed using displacement-controlled loading. A horizontal displacement was imposed at the top storey of the building, and the corresponding horizontal reaction from the structure was computed. Atriangular distribution of force was imposed at the lower floors, as shown in Figure 8.27.,A pushover analysis was performed for each frame with and without masonry infills, and in the conditions of fixed-end base and spring-damper system. Therefore, 20 analyses were performed.

This project has received funding from the European Union's Horizon 2020 research and innovation programme under grant agreement No. 700748

A conventional pushover curve describes the relationship between base shear (V_b) and top displacement ($\Delta_{MDOF(top)}$) of a multi-degree of freedom (MDOF) structure when an increasing lateral force is applied in accordance with a certain predefined pattern. With the increase in the magnitude of the loading, weak links and failure modes of the structure are found (Habibullah and Pyle, 1998). Krawinkler and Seneviratna (1998) stated that such approach is a valuable tool in vulnerability assessment due to its simplicity, ease of use and reduced running time, despite its inability to reproduce certain phenomena such as viscous damping, strength deterioration or pinching effect. In the present analysis, the structure performance was assessed by imposing an increasing triangular-shaped lateral load at the level of each floor of the structure, as shown in Figure 8.27. The load was zero at the ground floor and maximum at the top floor. For each analysis, the load was imposed in static conditions. The base shear is the sum of all the horizontal reactions at the fixed nodes of the structure and coincides with the sum of all the applied lateral loads at a given step. This is plotted in a graph against the correspondent lateral displacement of the structure.

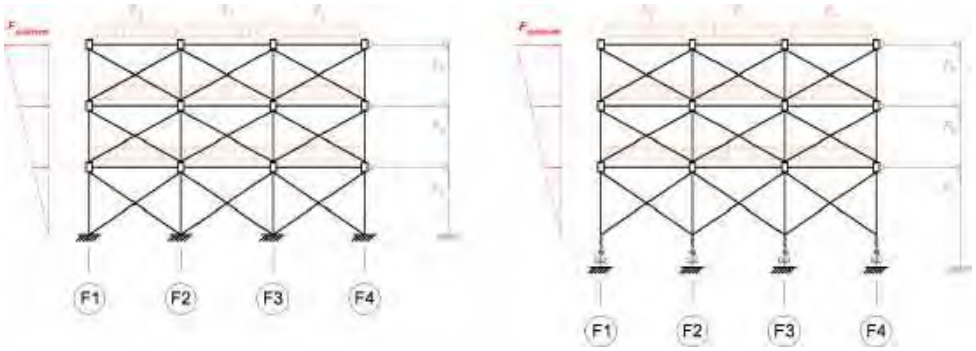

Figure 8.27: Load applied in pushover analysis on fixed base and spring-damper system

The acceleration-displacement response spectrum (ADRS) method prescribes that the real MDOF system response shall be transformed in the capacity curve of an equivalent single degree of freedom (SDOF) structure. The capacity curve shall be plotted on the same graph along with the demand spectrum of a given ground motion in order to assess the performance of the structure when submitted to that motion.

The demand spectrum of a ground motion is a plot of the acceleration response spectrum of the motion against its displacement response spectrum. Response spectra are curves relating the maximum response of a SDOF system with a range of different vibration periods subjected to specified earthquake ground motion. A (acceleration or displacement) response spectrum can be interpreted as the locus of maximum response (in acceleration or displacement) of a SDOF system for given damping ratio. Response spectra thus help in obtaining the peak structural responses under the linear range, which can be used for obtaining lateral forces developed in a structure due to an earthquake, thus facilitates in earthquake-resistant design of structures. In a ADRS spectrum, the acceleration and displacement response spectra are plotted against each other (instead of being plotted against period or frequency).

This project has received funding from the European Union's Horizon 2020 research and innovation programme under grant agreement No. 700748

In order determine the properties of the equivalent SDOF structure, Priestley et al.(2007) equations shall be applied:

$$m_e = \frac{\sum_{i=1}^{n}(m_i \Delta_i)}{\Delta_{sys}} \quad (8.24)$$

$$\Delta_{sys} = \frac{\sum_{i=1}^{n}(m_i \Delta_i^2)}{\sum_{i=1}^{n}(m_i \Delta_i)} \quad (8.25)$$

$$h_e = \frac{\sum_{i=1}^{n}(m_i \Delta_i h_i)}{\sum_{i=1}^{n}(m_i \Delta_i)} \quad (8.26)$$

where:

- Δ_i is the displacement of the i-th floor of the MDOF structure
- m_i is the mass of the i-th floor
- h_i is the height of the i-th floor
- m_e is the equivalent mass of the SDOF structure
- h_e is the equivalent height

These equations can be approximated to obtain a simplified solution, which leads to the following:

$$h_e \approx h_{MDOF(2f)} \quad (8.27)$$

$$m_e \approx 0.8 \sum_{i=1}^{n} m_i \quad (8.28)$$

The effective equivalent height is approximately the height of the second floor of the MDOF structure and the effective mass is 0.8 times the total mass of the MDOF structure. Hence, the top displacement of the equivalent SDOF structure (Δ_e) is approximated by the lateral displacement of the second floor of the MDOF structure:

$$\Delta_e \approx \Delta_{MDOF(2f)} \quad (8.29)$$

This project has received funding from the European Union's Horizon 2020 research and innovation programme under grant agreement No. 700748

The base shear shall be normalized by a mass, in order to be consistent in units with the spectral acceleration of the demand curve. The base shear was normalized by the effective mass of the structure, i.e. the mass correspondent to an equivalent SDOF structure:

$$\frac{V_b}{m_e} \approx \frac{V_b}{0.8\sum_{i=1}^{n} m_i} \qquad (8.30)$$

In this way, the capacity curve of the equivalent SDOF structure can be superimposed with the demand spectrum of a given ground motion. The performance for a given set of values is defined by the intersection of the capacity curve and the single demand spectrum curve. This has been done for the five buildings (with and without infills), for the three foundation-soil configurations presented in Figure 8.23. For the case of rigid foundation on bedrock (i.e. fixed base structure and input ground motions), the capacity curves of the five buildings were superimposed with the demand spectra of the 21 input ground motions. For rigid foundation on compressible soil (fixed base structure and surface motions), the structural models are the same as in the precedent case, thus the same capacity curves are used in this case. The demand spectra are referred to the 21 surface ground motion obtained from FLAC analysis. The same spectra are used for the case of isolated footings on compressible soil (spring-damper model and surface motions), and the capacity curves are referred on the building with spring-damper soil-structure interface.

The results are shown in Figure 8.28. For each graph, the five capacity curves were superimposed with the 21 demand spectra. The analyses relative to the input ground motions and fixed base structure with and without infills are shown in graphs a and b, respectively. The comparison between the two figures shows that the masonry infills give the structures an increased peak resistance at small strain levels, which is rapidly lost as the strain increases. The infilled structures tend to the same normalized base shear of the corresponding structures without infills, although a minor increase in response is observed even at large strain, as an effect of the residual strength of the strut elements. For the infilled structure, the majority of the demand spectra intersect the capacity curves in the linear elastic domain. Thus, it is not expected that these ground motions cause major damage in the structures. The capacity curves relative to the structures without infills present a change in slope in a range of displacements between 20 and 40 mm. Many ground motion spectra intersect these curves in the same range of displacement. Thus, damage in some structural element is expected in this case.

This project has received funding from the European Union's Horizon 2020 research and innovation programme under grant agreement No. 700748

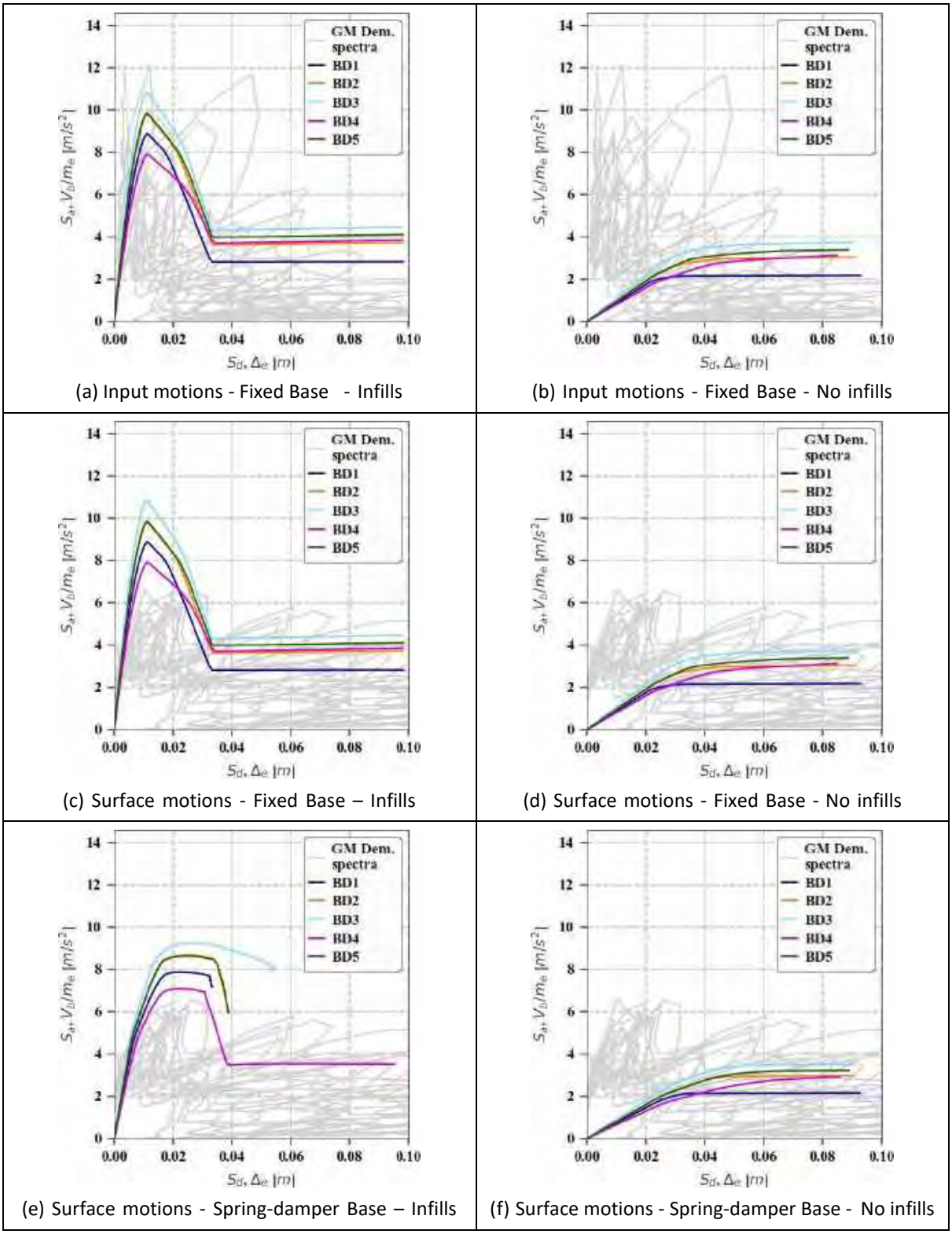

(a) Input motions - Fixed Base - Infills

(b) Input motions - Fixed Base - No infills

(c) Surface motions - Fixed Base – Infills

(d) Surface motions - Fixed Base - No infills

(e) Surface motions - Spring-damper Base – Infills

(f) Surface motions - Spring-damper Base - No infills

Figure 8.28: Results of pushover analysis.

This project has received funding from the European Union's Horizon 2020 research and innovation programme under grant agreement No. 700748

Graphs c and d show the same capacity curves against the demand spectra referred to the surface motions. The demand spectra of the surface motions show a clear loss in high frequency content (the spectral acceleration in the top left of the figure), and a minor amplification in the low frequency response with respect to the corresponding input motions. In this case the intersection points between the demand spectra and the capacity curves of the infilled structures are all in the linear elastic domain. Thus, no shaking damage is expected to be observed in the dynamic performance of the infilled structures. In the non-infilled structures, the situation is similar to the prior case. A minor increase in damage is expected in this case as an effect of the small increase in the low frequency content, which affects more the non-infilled structures, as their fundamental natural vibration periods (ranging from 0.6 to 0.8 s) are higher than the corresponding periods of the infilled frames (ranging from 0.15 to 0.18 s).

The capacity graphs for the structures modelled with nonlinear soil-structure interaction are reported in graphs e and f of Figure 8.28. As expected, the capacity curves (of infilled and non-infilled frames) present a lower initial stiffness than that of the corresponding fixed-base structures. The infilled structures show failure for a relatively small displacement. This is due to the moment generated by the resultant of the applied forces and the base reactions, which causes uplift of one or more footings (typically F1 and possibly F2). Since the vertical springs associated to these footings cannot provide a tensile reaction, this causes non-convergence of the analysis. The demand spectra of these graphs are the same of graphs c and d. As in the precedent case, no major damage is expected in the infilled frames and a similar level of damage as in the prior case is foreseen for the non-infilled frames.

8.5.2 RESULTS

8.5.2.1 INTER-STOREY DRIFT

Due to the great number of analysis performed (5 buildings in 3 different soil-structure interface configurations, with and without infills, 21 ground motion cases each, for a total of 630 dynamic analyses performed), the results are presented in a synthetic form, with simple parameters able to represent the performance of the structures, and a parameter to measure the intensity of the applied motions.

The performance of the structure is assessed through peak and residual inter-storey drifts of the superstructure. For the i-th storey, inter-storey drift $\theta_{ss,i}$ is defined as the following time series:

$$\theta_{ss,i}(t) = \frac{\Delta_i(t) - \Delta_{i-1}(t)}{h_i} \qquad (8.31)$$

with the same meaning of the symbols of equations (8.24) (8.26).

An example of the evolution of the inter-storey drift during an analysis is reported in Figure 8.29.

This project has received funding from the European Union's Horizon 2020 research and innovation programme under grant agreement No. 700748

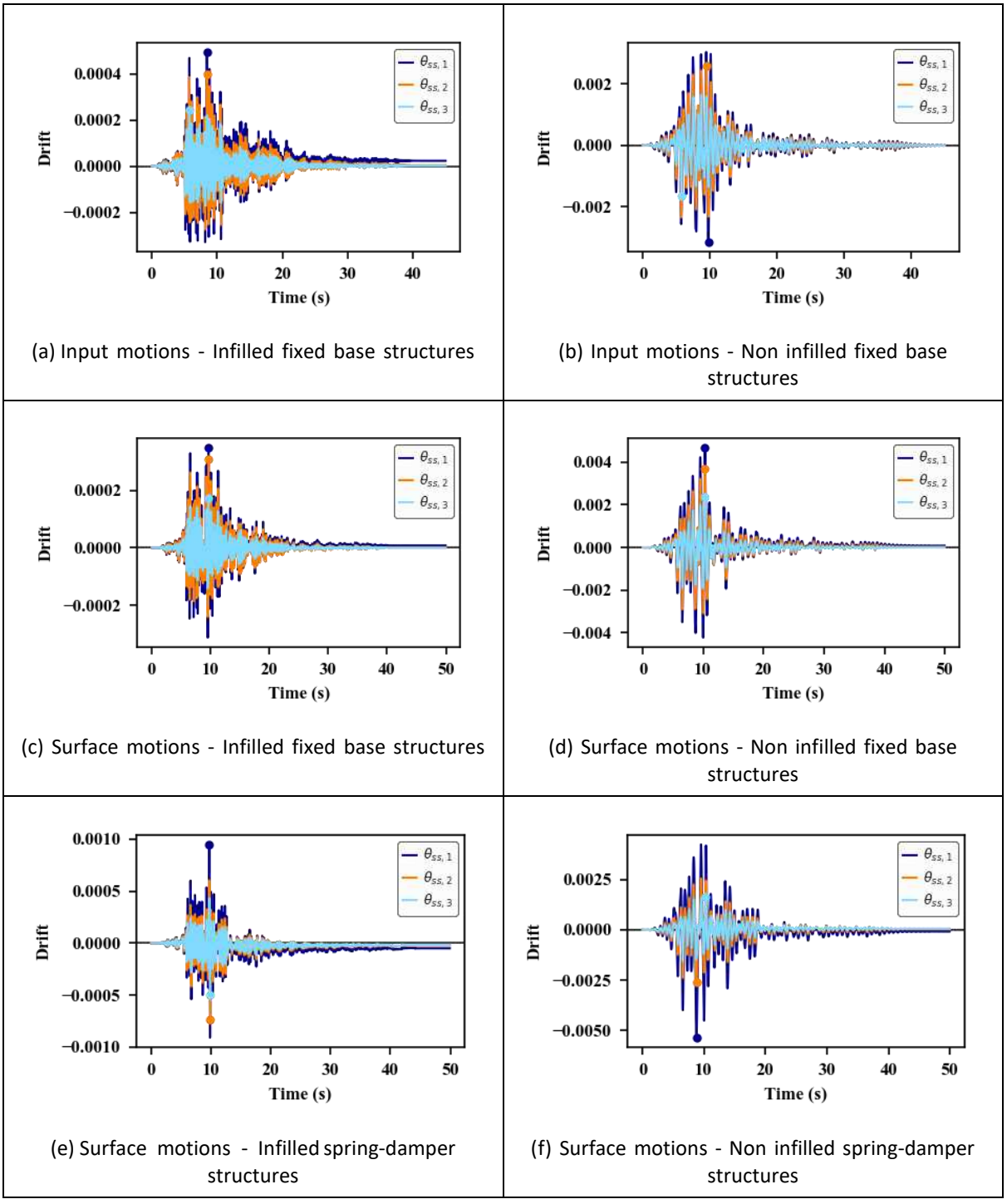

(a) Input motions - Infilled fixed base structures

(b) Input motions - Non infilled fixed base structures

(c) Surface motions - Infilled fixed base structures

(d) Surface motions - Non infilled fixed base structures

(e) Surface motions - Infilled spring-damper structures

(f) Surface motions - Non infilled spring-damper structures

Figure 8.29: Example of inter-storey drift for motion m3 with return period of 475 years

The peak inter-storey drift of the i-th storey is the maximum in absolute value of this time series (marked with a point in Figure 8.29):

This project has received funding from the European Union's Horizon 2020 research and innovation programme under grant agreement No. 700748

$$\theta_{ss,i,p} = \max_t |\theta_{ss,i}(t)| \quad (8.32)$$

Peak inter-storey drift of the superstructure is defined as the maximum inter-storey drift of each floor:

$$\theta_{ss,p} = \max_i (\theta_{ss,i,p}) \quad (8.33)$$

Residual inter-storey drift of the i-th storey is the absolute value of the inter-storey drift of that storey at the end of the analysis:

$$\theta_{ss,i,r} = \max_t |\theta_{ss,i}(t = t_{analysis})| \quad (8.34)$$

The residual inter-storey drift of the superstructure is the maximum value of the residual inter-storey drifts of each storey:

$$\theta_{ss,r} = \max_i (\theta_{ss,i,r}) \quad (8.35)$$

Peak and residual inter-storey drifts were plotted for each analysis in a graph against a parameter representative of the intensity of the ground motion applied in that analysis. The selected parameter is the spectral acceleration of the motion at a period T of 1s ($S_{A,T=1s}$).

In Figure 8.30, the results relative to the maximum inter-storey drift of all the analyses are presented. The results are presented in 6 separate graphs, following the same layout used to present the results relative to the pushover analyses. Each graph is referred to one of the three configurations presented in Figure 8.23, and to infilled or non infilled structures. As expected, the maximum drifts observed in the infilled structures (graphs a, c, and e) are very low (<0.5%) do not lead to damage in the structural components. The larger peak values are observed in the response of infilled structures submitted to the action of the input motions (graph a), which have the largest high frequency content, while the peak response of the surface motions is smaller, consistently with the cut off in the high frequency content.

This project has received funding from the European Union's Horizon 2020 research and innovation programme under grant agreement No. 700748

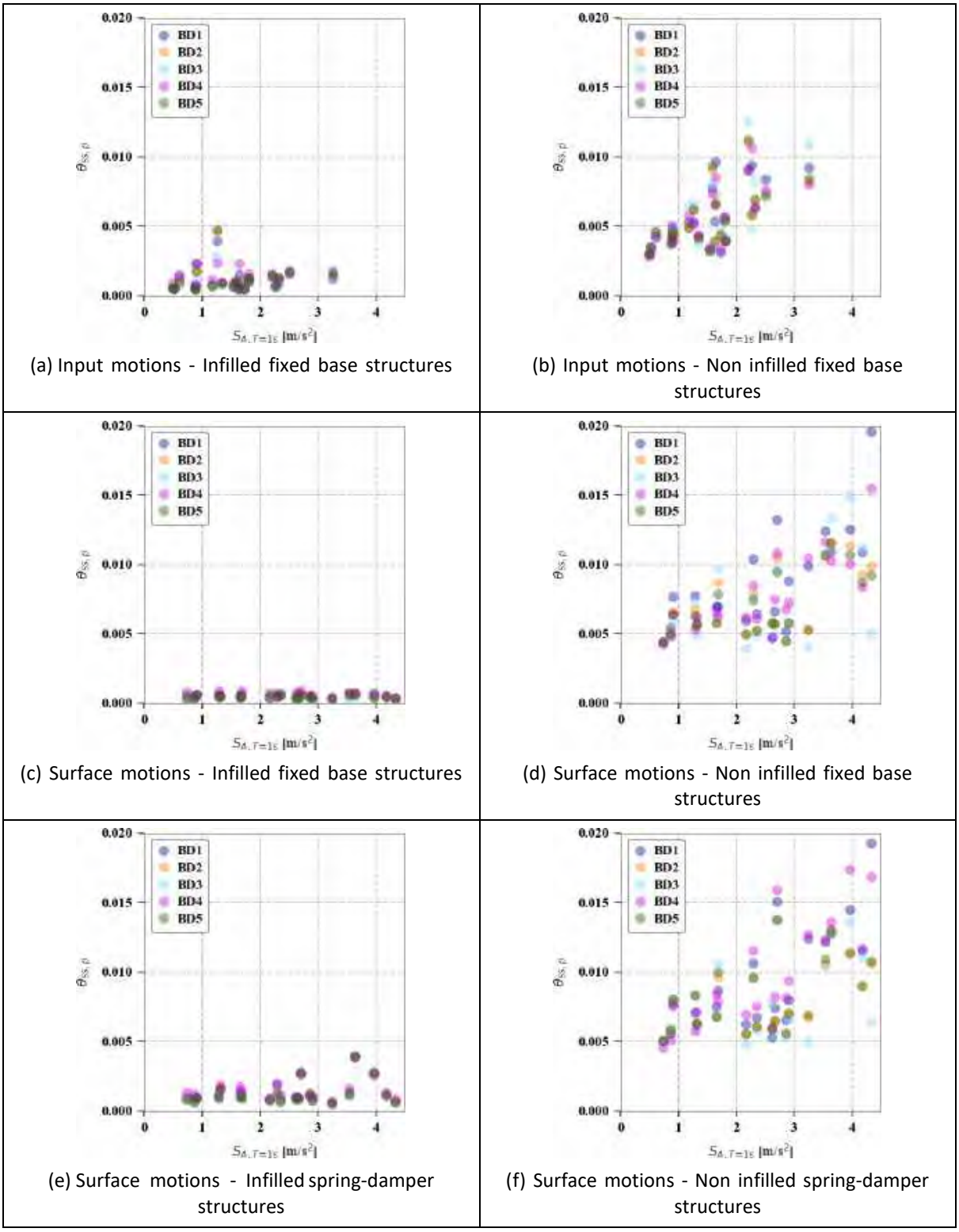

(a) Input motions - Infilled fixed base structures

(b) Input motions - Non infilled fixed base structures

(c) Surface motions - Infilled fixed base structures

(d) Surface motions - Non infilled fixed base structures

(e) Surface motions - Infilled spring-damper structures

(f) Surface motions - Non infilled spring-damper structures

Figure 8.30. Peak inter-storey drift.

Non infilled structures present higher peak inter storey drifts (graphs b, d, and f of Figure 8.30). Graph b shows a rather good correlation between the drift of the fixed-base structures and the spectral acceleration at 1s of the input ground motions. The maximum drift is slightly higher than 1%. Graphs d and f confirm the direct trend between the two selected parameters for the structures and the motions. The surface motions are shifted towards higher values of $S_{A,T=1s}$. Consistently, the peak drifts are higher and reach 2%.

The residual drifts shown in Figure 8.31 confirm that the structures did not suffer significant inelastic deformation. The infilled structures present negligible values of residual inter-storey drift (graphs a, c, and e). Only six analyses in the case with flexible foundations show a relevant residual drift. Nevertheless, they are all under 0.4%, which is typically a level of drift economically acceptable for repair. Non infilled structures present moderate values of residual drift with a higher scatter with respect to infilled structures. In a few number of analyses, the residual drift is higher than 0.4%, reaching values higher than 0.7%. In such cases the economical sustainability of repairing the structure should be carefully assessed.

8.5.2.2 FOUNDATION SETTLEMENT

The structures modelled with the nonlinear spring-damper system at each footing are subjected to an imposed settlement time series, as reported in section 8.4.5.1. An example of result is reported in Figure 8.32 a and b, for an infilled and non infilled frame, respectively. The settlement time series $S(t)$ calculated in FLAC analysis as described in the previous section (§8.1). is represented in the figure as a black continuous line. The four settlements obtained by multiplying this time series by the four random parameters expressed in equation (8.35) are reported as dashed lines. For each footing, a continuous line of the same colour of the dashed line shows the effective settlement of the foundation (which includes the spring deformation), corresponding to the base node of the respective column. In both figures it can be observed that footings F2 and F4 detach from the soil in the early stages of shaking. As the vertical springs do not react to tensile loads, these footings cease to bear vertical load from the instant they detach from the soil until the end of shaking. Thus, the vertical load initially distributed on four footings is concentrated on footings F1 and F3, which are the only footings able to transfer load to the surrounding soil. It is worth noting that F1 and F3 are the nodes associated to the smaller values of the random factors. The remaining footings detach from the soil because the stiffness of the superstructure prevents the occurrence of large distortional strains and allows the structure to be supported by two footings. This is seen in both the infilled and the non infilled structures, the only difference being an increase in the differential settlements between footing F3 and the remaining footings in the latter case.

The detachment of the footing from the surrounding soil is a limitation of the model, due to the fact that the settlement time series is calculated in the hypothesis of constant vertical load. Such simplification does not take into account the load redistribution from the nodes with a higher rate of settlement with time to the nodes with a lower rate of settlement, which in turn tends to homogenize the rates of settlement of the different footings. However, it

This project has received funding from the European Union's Horizon 2020 research and innovation programme under grant agreement No. 700748

highlights that modelling differential settlement by imposing displacements directly to the footing is unrealistic except for the most flexible buildings. It should also be noted that these analyses did not capture settlement and tilt related to sand ejecta and consolidation.

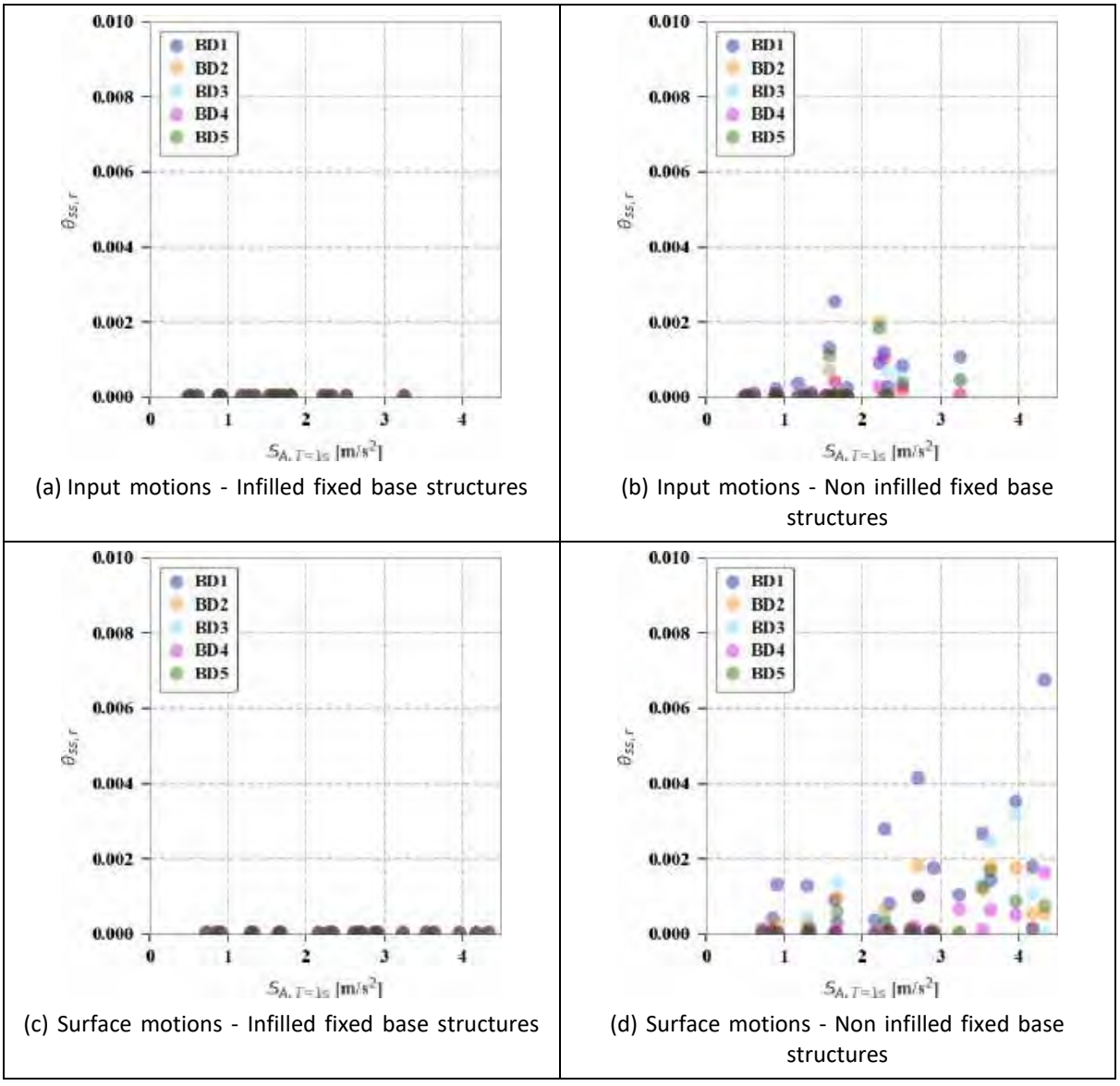

(a) Input motions - Infilled fixed base structures

(b) Input motions - Non infilled fixed base structures

(c) Surface motions - Infilled fixed base structures

(d) Surface motions - Non infilled fixed base structures

This project has received funding from the European Union's Horizon 2020 research and innovation programme under grant agreement No. 700748

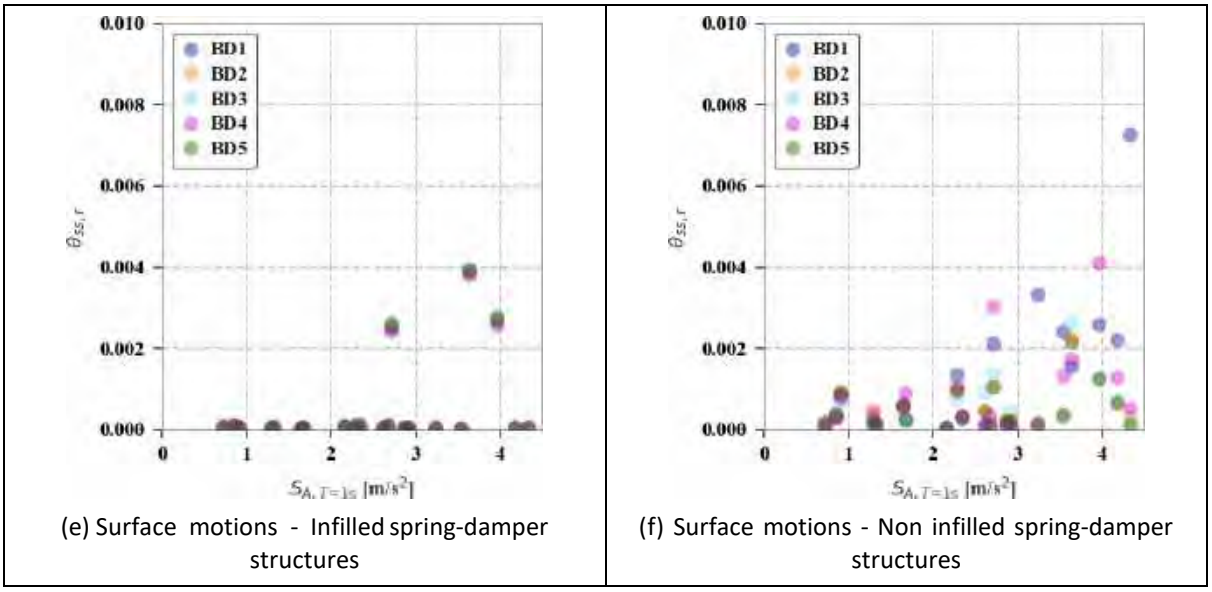

(e) Surface motions - Infilled spring-damper structures

(f) Surface motions - Non infilled spring-damper structures

Figure 8.31. Residual inter-storey drift.

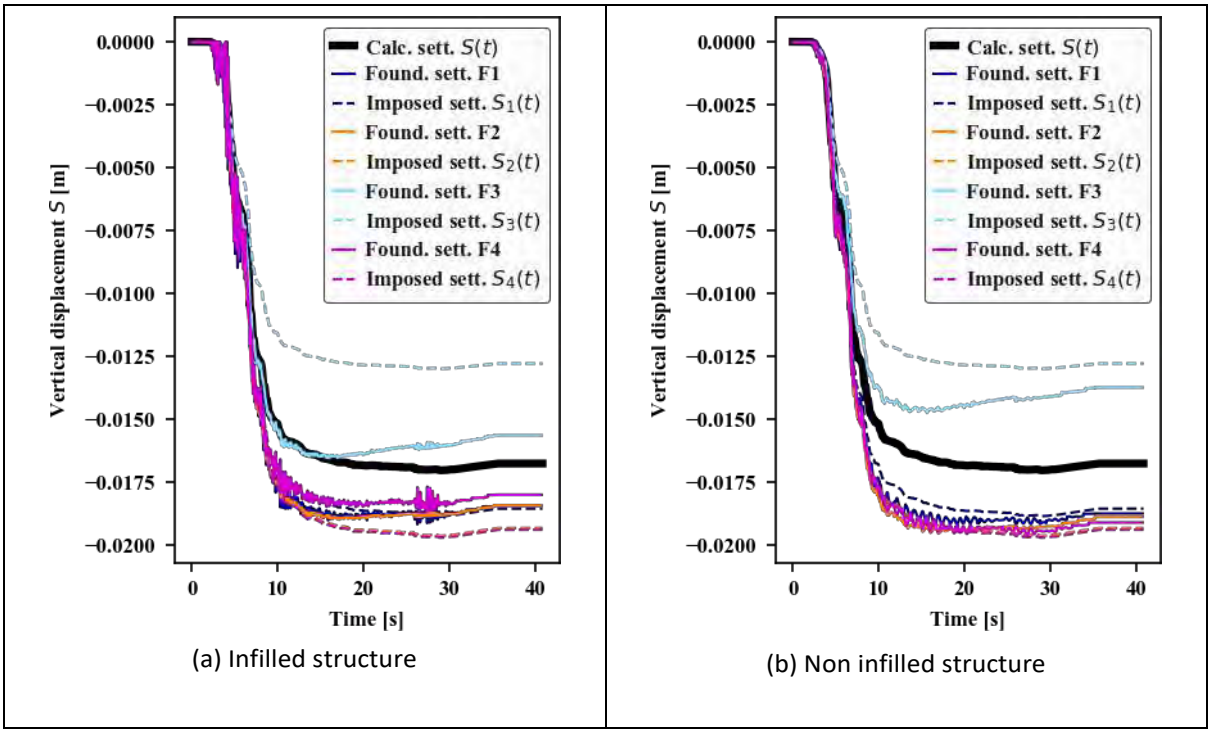

(a) Infilled structure

(b) Non infilled structure

Figure 8.32. Foundation settlements of building 1 submitted to surface motion 975-m3.

This project has received funding from the European Union's Horizon 2020 research and innovation programme under grant agreement No. 700748

8.5.3 DISCUSSION

The performance of the fixed base structures submitted to the input motions (graphs a and b of Figure 8.30 and Figure 8.31) was compared with the performance of the same structures when submitted to the surface motions (graphs c and d of the same figures). The results in terms of peak and residual inter-storey drifts are shown in Figure 8.33.

Figure 8.33.a shows that, for the infilled structures, higher peak drifts are observed when input ground motions are applied. As referred in the former section, this is due to the different frequency content of the input and surface motions, where the dominant frequency of the input motions are closer to the natural vibration period the infilled structures. On the other hand, slightly higher peak drifts are observed when surface motions are applied to non infilled structures, in comparison with the application of input motions to the same structures (Figure 8.33.b). The longer period of the former motions is more similar to the natural period of the non infilled structures. The residual drifts confirm the trend for non infilled structures (Figure 8.33.d), while for infilled structures the values are not significant in both cases (Figure 8.33.c).

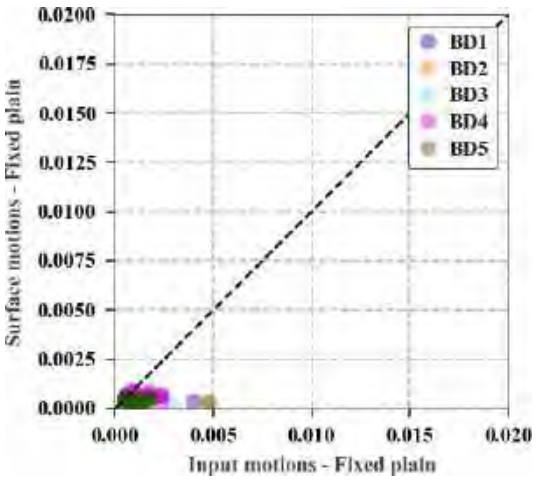

(a) Peak inter-storey drift - Infilled structures

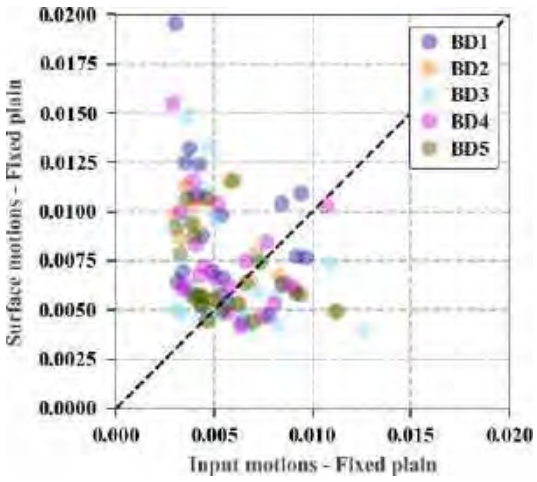

(b) Peak inter-storey drift - Non infilled structures

This project has received funding from the European Union's Horizon 2020 research and innovation programme under grant agreement No. 700748

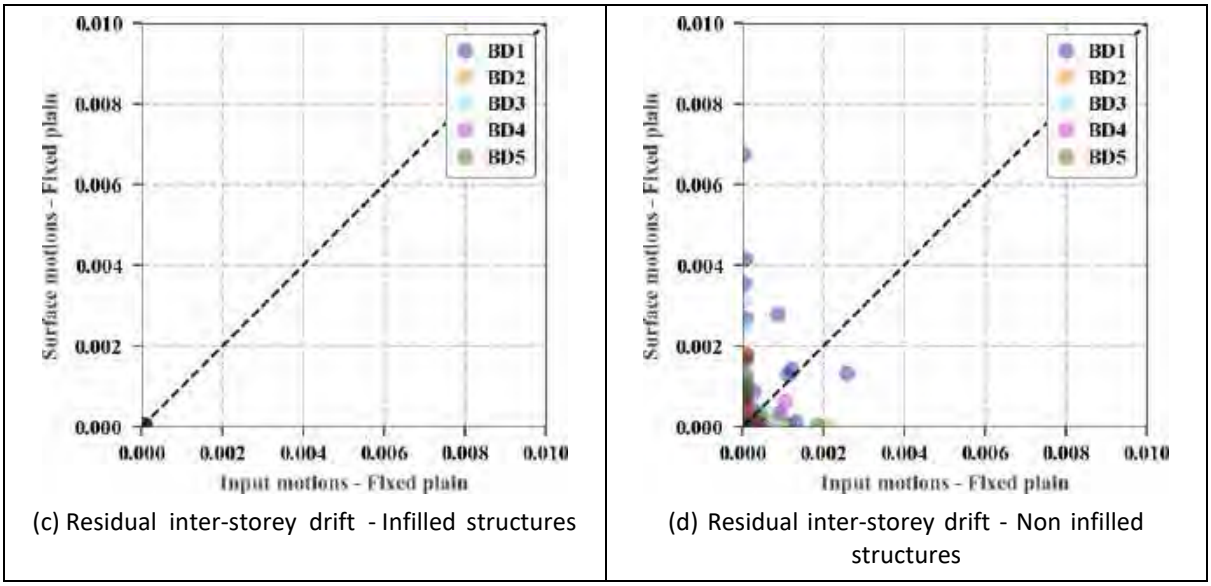

(c) Residual inter-storey drift - Infilled structures

(d) Residual inter-storey drift - Non infilled structures

Figure 8.33: Comparison between inter-storey drifts of fixed base structures. Response to input motions against surface motions.

The response of the fixed base structures submitted to surface motions was compared with the response of the structure supported by spring-damper systems at the footings (graphs e and f of Figure 8.30 and Figure 8.31). The results of the comparison are shown in Figure 8.34. The infilled structures exhibit an increase in peak and residual inter-storey drifts for the nonlinear soil-spring interaction model with respect to the same structures with a fixed base (graphs a and b). This is an expectable result, given the increase in flexibility of the system due to the soil-foundation interaction (it is worth noting that the inter-storey drift takes into account the distortion of the structural elements and the tilt of the foundation plane). In the same way, such result is observed for non infilled structures in the peak inter- story drifts (graph b). The same results for residual values (graph d) shows a dispersed set of points without a clear tendency. This can be interpreted as the fact that the contribution of the spring-damper systems does not affect considerably the permanent deformation of these structures.

This project has received funding from the European Union's Horizon 2020 research and innovation programme under grant agreement No. 700748

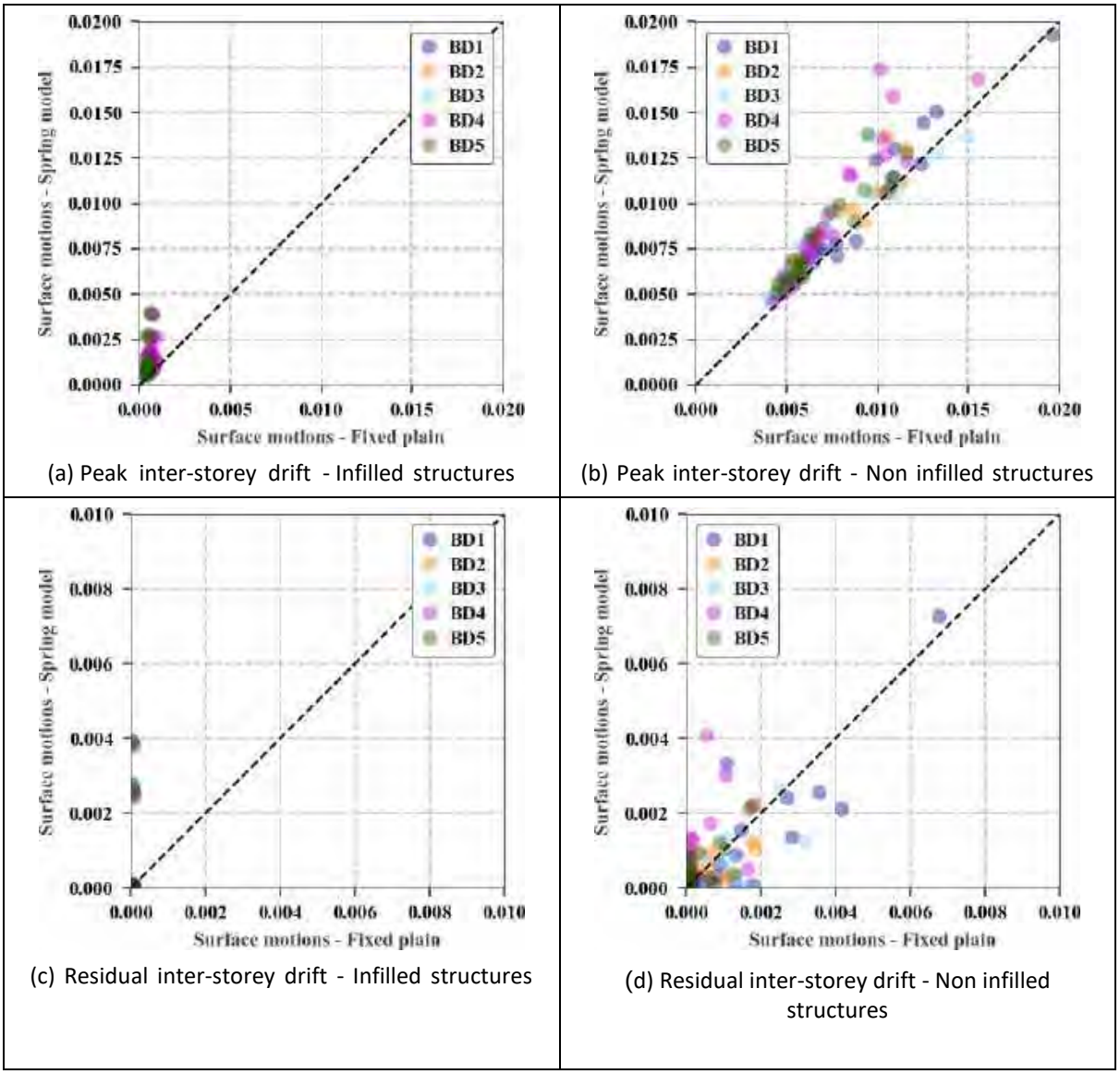

(a) Peak inter-storey drift - Infilled structures

(b) Peak inter-storey drift - Non infilled structures

(c) Residual inter-storey drift - Infilled structures

(d) Residual inter-storey drift - Non infilled structures

Figure 8.34: Comparison between inter-storey drifts of structures subjected to surface motions. Response of fixed base structures against spring-damper structures.

This project has received funding from the European Union's Horizon 2020 research and innovation programme under grant agreement No. 700748

8.6 FINAL CONSIDERATIONS ON BUILDINGS PERFORMANCE

A comprehensive set of nonlinear dynamic analyses was performed on five reference buildings, infilled and non infilled, fixed at the base or considering a soil-structure interaction model. The geometric characteristics and material properties of each structure were modelled through a simulated design involving only gravity loads, to obtain non-seismically designed structures. The configuration of the soil underneath the structures was modelled referring to the site of Pieve Di Cento (Italy). For the analyses reported in this section, the geotechnical model of this site includes three soil layers: an upper non-liquefiable fine grained crust, a second layer of liquefiable sandy material, and a deeper stiff clay layer. The properties of the soils of these layers were inferred from the interpretation of in situ tests (particularly CPTu and V_s surveys) and laboratory tests over undisturbed samples (details in the previous section (§8.1).

In each analysis, a single horizontal ground motion was applied, in the form of an acceleration time series. Seven motions were analysed, referred to three standard return periods, for a total of 21 motions. The motions are applied in separate analyses in the original form (input motions), and in a modified form (surface motions), in order to take into account the site response related to the three-layered soil configuration specified.

Three specific combinations of structure, soil-structure interface and applied motion were selected, yielding the following cases:

- a set of fixed base structures submitted to input ground motions
- a set of fixed base structures submitted to surface ground motions
- a set of structures supported by a nonlinear spring-damper soil-structure interface and submitted to surface ground motions

For each of the three cases, five structures were considered, with and without infills, and 21 motions were applied at the fixed nodes, for a total of 210 analyses. Hence, the total number of analyses performed was 630. All the analyses were performed imposing a static gravity load, followed by the application of the ground motion as an acceleration time series. An imposed settlement time series was applied to the structures of the third case, to simulate the liquefaction-related effects. The settlement was calculated for each motion in a specific FLAC analysis (as described in the previous section (8.1) and applied to each footing by applying a specific random multiplying factor, in order to model soil inhomogeneity.

A static pushover analysis was performed for each structure considered in the subsequent dynamic analysis, in order to validate the results obtained.

The results show small to moderate values of peak and residual inter-storey drifts. No significant damage is foreseen in all the infilled structures, with peak drifts below 0.5% and negligible residual drifts.

This project has received funding from the European Union's Horizon 2020 research and innovation programme under grant agreement No. 700748

Non-infilled structures are prone to higher peak drifts, especially when surface motions (characterised by low frequency content) are applied. Peak drifts up to 2% were observed in such cases. Residual drifts were small but not negligible, and in certain cases the economic sustainability of repairing should be assessed.

The settlement history of the footings in the case of flexible foundations shows that, due to the stiffness of the structures studied, the bottom sections of the ground floor columns do not always follow the imposed settlement at the base node of the spring-damper system.

In all the analyses, two footings detach from the soil and do not provide vertical reaction, while the remaining two provide the entire vertical reaction to the applied loads. This is a limitation of the model due to the fact that the settlement time series is calculated in static conditions, prior to the application of the horizontal motion. While the springs account for the majority of the effects of load redistribution on the performance of the building, the perceived settlement of the soil (spring) is not realistic.

A comparison was made between the response of structures submitted to input and surface motions. The comparison of the inter-storey drifts observed in the two cases showed that the input motions have a higher impact on the infilled structures, while the surface motions affect more the non-infilled structures. This is consistent with the different frequency content of the two ground motion groups, related to the different natural vibration period of the two types of frames.

A second analysis compared the drifts observed in fixed base structures with the drifts observed in structures supported by flexible footings. An increased level of drift is observed in the second case, as expected, due to the increased flexibility of the structures caused by the soil-foundation-structure interaction model, confirming the necessity to take into account soil-structure interaction in the evaluation of liquefaction induced damages to buildings.

This project has received funding from the European Union's Horizon 2020 research and innovation programme under grant agreement No. 700748

REFERENCES

Airoldi S, Fioravante V, Giretti D, Moglie J (2018). Deliverable D4.2-Report on validation of retrofitting techniques from small scale models, LiquefACT Project Report, v1.1.

Baradaran Shoraka, M. and Elwood, K. J. (2013). Mechanical Model for Non Ductile Reinforced Concrete Columns. Journal of Earthquake Engineering, 17:7, 937-957.

Beaty, M. H., and Byrne, P. M. (2011). UBCSAND CONSTITUTIVE MODEL Version 904aR. Itasca UDM Web Site.

Belotti R, Jamiolkowski M, Lo Presti DCF, O'Neill DA (1996). Anisotropy of small strain stiffness in Ticino sand. Géotechnique 46(1): 115-131.

Bindi D, Pacor F, Luzi L, Puglia R, Massa M, Ameri G, et al. (2011). Ground motion prediction equations derived from the Italian strong motion database. Bull Earthq Eng. 9(6):1899-1920..

Boulanger, R.W. (2003). "Relating Kα to Relative State Parameter Index." Journal of Geotechnical and Geoenvironmental Engineering, 129(8), 770–773.

Boulanger, R.W. (2010). A sand plasticity model for earthquake engineering applications, Report No. UCD/CGM-10-01. Technical report, Center for Geotechnical Modeling, Department of Civil and Environmental Engineering, University of California.

Boulanger, R.W., Curras, C. J., Kutter, B. L., Wilson, D. W., and Abghari, A. (1999). Seismic soil-pile-structure interaction experiments and analyses. Journal of Geotechnical and Geoenvironmental Engineering, 125(9):750–759.

Boulanger, R.W. and Z. Ziotopoulou (2012). PM4Sand (Version 2): A sand plasticity model for earthquake engineering applications, Report No. UCD/CGM-12/01. Technical report, Center for Geotechnical Modeling, Department of Civil and Environmental Engineering College of Engineering, University of California at Davis.

Boulanger, R.W. and Z. Ziotopoulou (2015). PM4Sand (Version 3): A sand plasticity model for earthquake engineering applications, Report No. UCD/CGM-15/01. Technical report, Center for Geotechnical Modeling, Department of Civil and Environmental Engineering College of Engineering, University of California at Davis.

Bryne P (1991). A cyclic shear-volume coupling and pore-pressure model for sand. In: Second International Conference on Recent Advances in Geotechnical Earthquake Engineering and Soil Dynamics, 11-15 March, St. Louis, Missouri (USA).

Chiaradonna A, Tropeano G, d'Onofrio, Silvestri F (2017). Development of a simplified model for pore water pressure build-up induced by cyclic loading. Bulletin of Earthquake Engineering (submitted).

Chiaradonna A, Andreotti G., Lai CG, Bilotta E, Flora A (2018a). Previsione della risposta dinamica di un sottosuolo liquefacibile ad una sollecitazione ciclica applicata in superficie. Proceedings of the IARG2018. Genova, Italy, July, 2018.

Chiaradonna, A., Ozcebe, A.G., Bozzoni, F., Fama, A., Zuccolo, E., Lai, C.G., Flora, A., Cosentini,

R.M., d'Onofrio, A., Bilotta, E., Silvestri, F. (2018b). "Numerical simulation of soil liquefaction during the 20 May 2012 M6.1 Emilia Earthquake in Northern Italy: the case study of Pieve di Cento". Proceedings, 16th European Conference on Earthquake Engineering, 16ECEE, Thessaloniki, Greece,18-21, June, 2018.

Corigliano M, Lai CG, Rota M, Strobbia CL (2012). ASCONA: automated selection of compatible natural accelerograms. Earthquake Spectra 28(3): 965-987.

Cubrinovski, M. (1993). A constitutive model for sandy soils based on a stress-dependent density parameter. Dr. Eng. thesis, University of Tokyo, Japan.

Cubrinovski, M. and Ishihara, K. (1998a). Modelling of sand behaviour based on state concept. Soils and Foundations, Vol. 38, No. 3, pp. 115-127.

Cubrinovski, M. and Ishihara, K. (1998b). State concept and modified elastoplasticity for sand modelling. Soils and Foundations; Vol. 38, No. 4, pp. 213-225.

Dafalias, Y. F., and Manzari, M. T. (2004). "Simple Plasticity Sand Model Accounting for Fabric Change Effects." ASCE, Journal of Geotechnical Engineering Division, 130(6), 622–634.

Darendeli M.B. (2001). Development of a new family of normalized modulus reduction and material damping curves. Ph.D. Dissertation. The University of Texas, Austin (USA).

Dafalias, Y. and M. Manzari (2004). Simple plasticity sand model accounting for fabric change effects. Journal of Engineering Mechanics (130(6)), 622–634.

Dolsek, M. and Fajfar, P. (2008). The effect of masonry infills on the seismic response of a four-storey reinforced concrete frame—a deterministic assessment. Engineering Structures, 30(7):1991–2001.

Elwood, K. J. (2004). Modelling failures in existing reinforced concrete columns. Canadian Journal of Civil Engineering, 31(5), 846–859.

Fioravante V (2018). Session discussions, OSLO Partner Meeting, LIQUEFACT Project.

Fioravante V, Giretti D (2016). Unidirectional cyclic resistance of Ticino and Toyoura sands from centrifuge cone penetration tests. Acta Geotechnica 11: 953-968.

Gazetas, G. (1991). Foundation vibrations. In Foundation engineering handbook, pages 553–593. Springer.

Habibullah, A. and Pyle, S. (1998). Practical three dimensional nonlinear static pushover analysis. Structure magazine, Winter.

Hak, S., Morandi, P., Magenes, G., and Sullivan, T. J. (2012). Damage control for clay masonry infills in the design of RC frame structures. Journal of Earthquake Engineering, 16(sup1):1–35.

Haselton, CB., Liel A B., Taylor Lange, S., and Deierlein, G.G. (2016). Calibration of Reinforced Concrete Beam-Columns for Simulating Seismic Response to Collapse. ACI Structural Journal, 113(6): 1141-1152.

Hashash, Y.,M. Musgrove, J. Harmon, D. Groholski, C. Phillips, and D. Park (2016). DEEPSOIL 6.1, User Manual.

This project has received funding from the European Union's Horizon 2020 research and innovation programme under grant agreement No. 700748

Idriss, I. M., and Boulanger, R. W. (2008). Soil liquefaction during earthquakes. Earthquake Engineering Research Institute.

Itasca Consulting Group (2015). FLAC 3D– Fast Lagrangian Analysis of Continua – Computer Program and the User's Manual. Minneapolis.

Itasca (2016b). FLAC, Fast Lagrangian Analysis of Continua, version 6.0 Computer Program and the User's Guide, Itasca Consulting Group Inc., Thrasher Square East.

Itasca (2016b). FLAC, Fast Lagrangian Analysis of Continua, version 7.0 Computer Program and the User's Guide, Itasca Consulting Group Inc., Thrasher Square East.

Itasca (2016b). FLAC, Fast Lagrangian Analysis of Continua, version 8.0 Computer Program and the User's Guide, Itasca Consulting Group Inc., Thrasher Square East.

Karamitros, D. K. Bouckovalas, G. D. C. Y. K. (2013). Seismic settlements of shallow foundations on liquefiable soil with a clay crust. Soil Dynamics and Earthquake Engineering (46), 64–76.

Ibarra, L.F., Medina, R., and Krawinkler, H. (2005). Hysteretic Models that Incorporate Strength and Stiffness Deterioration. Earthquake Engineering & Structural Dynamics, 34. 1489 - 1511. 10.1002/eqe.495.

Jeon, J.S., Lowes, L.N., DesRoches, R., and Brilakis, I. (2015). Fragility curves for non-ductile reinforced concrete frames that exhibit different component response mechanisms. Engineering Structures, 85: 127-143.

Karamitros, D. K., Bouckovalas, G. D., and Chaloulos, Y. K. (2013). Seismic settlements of shallow foundations on liquefiable soil with a clay crust. Soil Dynamics and Earthquake Engineering, 46, 64-76.

Karatzia, X., Mylonakis, G., and Bouckovalas, G. (2017). Equivalent-linear dynamic stiffness of surface footings on liquefiable soil. In COMPDYN 2017 - Proceedings of the 6th International Conference on Computational Methods in Structural Dynamics and Earthquake Engineering, pages 1388–1402. National Technical University of Athens.

Krawinkler, H. and Seneviratna, G. (1998). Pros and cons of a pushover analysis of seismic performance evaluation. Engineering structures, 20(4-6):452–464.

Kuhlemeyer RL, Lysmer J (1973). Finite Element Method Accuracy for Wave Propagation Problems. J Soil Mech Found Div 99(SM5):421–427.

Kulhawy FH, Mayne PW (1990). Manual on estimating soil properties for foundation design. Report EL-6800, Electric Power Research Institute, Palo Alto, 306 p. www.epri.com.

Lignos D, Krawinkler H (2011). Deterioration Modeling of Steel Components in Support of Collapse Prediction of Steel Moment Frames under Earthquake Loading. Journal of Structural Engineering, 137(11): 1291-1302.

Lignos, D. G. and Krawinkler, H. (2012). Development and utilization of structural component databases for performance-based earthquake engineering. Journal of Structural Engineering, 139(8):1382–1394.

This project has received funding from the European Union's Horizon 2020 research and innovation programme under grant agreement No. 700748

Luque, R. (2017, August). Numerical Analyses of Liquefaction-Induced Building Settlement . Ph. D. thesis.

Manzari, M. T., and Dafalias, Y. F. (1997). "A critical state two-surface plasticity model for sands." Géotechnique, 47(2), 255–272.

Martelli L, Romani M (2013). Microzonazione sismica e analisi della condizione limite per l'emergenza delle aree epicentrali dei terremoti della pianura emiliana di maggio-giugno 2012 (Ordinanza del commissario delegato n. 70/2012), Relazione Illustrativa (in Italian); http://ambiente.regione.emilia-romagna.it

Mazzoni, S., McKenna, F., Scott, M. H., and Fenves, G. L. (2006). OpenSees command language manual. Pacific Earthquake Engineering Research (PEER) Center, 264.

Meyerhof, G. G. (1963). Some recent research on the bearing capacity of foundations. Canadian Geotechnical Journal, 1(1):16–26.

McKenna F, Fenves GL, and Scott MH (2000). Open system for earthquake engineering simulation. University of California, Berkeley, CA.

Mejia, L. and E. Dawson (2006). Earthquake deconvolution for flac. 4th International FLAC Symposium on Numerical Modeling in Geomechanics (04-10), 1–9.

Minarelli L, Amoroso S, Tarabusi G, Stefani M, Pulelli G (2016). Down-hole geophysical characterization of middle-upper Quaternary sequences in the Apennine Foredeep, Mirabello, Italy. Annals of Geophysics, 59(5), doi: 10.4401/ag-7114.

Naesgaard, E. (2011). "A hybrid effective stress–total stress procedure for analyzing soil embankments subjected to potential liquefaction and flow." University of British Columbia.

National Academies of Sciences, Engineering and Medicine (2016). State of the art and practice in the assessment of earthquake-induced soil liquefaction and its consequences (Editors: Kavazanjian E (Jr), et al.). The National Academies Press, ISBN: 978-0-309-44027-1, 350 pages.

Noh, N. M., Liberatore, L., Mollaioli, F., and Tesfamariam, S. (2017). Modelling of masonry infilled RC frames subjected to cyclic loads: State of the art review and modelling with OpenSees. Engineering Structures, 150: 599–621.

NTC (2018). Norme tecniche per le costruzioni (NTC 2018). Standard, Ministero Infrastrutture e Trasporti, Rome, IT.

Paolucci E, Albarello D, D'Amico S, Lunidei E, Martelli L, Mucciarelli M, Pileggi D (2015). A large scale ambient vibration survey in the area damaged by May-June 2012 seismic sequence in Emilia Romagna, Italy. Bulletin of Earthquake Engineering, 13(11):3187-3206.

PEER (2010a). Technical report for the PEER ground motion database web application-Beta Version-October 1, 2010.

PEER (2010b). User's Manual for the PEER ground motion database web application-Beta Version-October 1, 2010.

Petalas, A. (2012). PLAXIS LIQUEFACTION MODEL UBC3D-PLM.

Prevost JH (1985). A simple plasticity theory for frictional cohesionless soil. Soil Dynamics and Earthquake Engineering 4(1):9-17.

Priestley, M., Calvi, G., and Kowalsky, M. (2007). Direct displacement-based seismic design. In 2005 NZSEE Conference, pages 33–43.

Puebla, H., Byrne, P. M., and Phillips, R. (1997). "Analysis of CANLEX liquefaction embankments: prototype and centrifuge models." Canadian Geotechnical Journal, 34(5), 641–657.

Ramirez J, Barrero AR, Chen L, Dashti S, Ghofrani A, Taiebat M, Arduino P (2018). Site Response in a Layered Liquefiable Deposit: Evaluation of Different Numerical Tools and Methodologies with Centrifuge Experimental Results. J Geotech Geoenv Eng 04018073-1 https://doi.org/10.1061/(ASCE)GT.1943-5606.0001947.

Revil A, Cathles LM III (1999). Permeability of shaly sands. Water Resources Research 35(3): 651-662.

Rowe, P. W. (1962). "The Stress-Dilatancy Relation for Static Equilibrium of an Assembly of Particles in Contact." Proceedings of the Royal Society A: Mathematical, Physical and Engineering Sciences, 269(1339), 500–527.

Tonni L. Gottardi G, Amoroso S, Bardotti R, Bonzi L, Chiaradonna A, d'Onofrio A, Fioravante V, Ghinelli A, Giretti D, Lanzo G, Madiai C, Marchi M, Martelli L, Monaco P, Porcino D, Razzano R, Rosselli S, Severi P, Silvestri F, Simeoni L, Vannucchi G, and Aversa S (2015). Interpreting the deformation phenomena triggered by the 2012 Emilia seismic sequence on the Canale Diversivo di Burana banks. Italian Geotechnical Journal, 2: 28 - 58 (in Italian).

Tropeano G, Chiaradonna A, d'Onofrio A, Silvestri F (2016). An innovative computer code for 1D seismic response analysis including shear strength of soils. Géotechnique, 66(2): 95–105.

Tsegaye, A. (2010). "Plaxis liquefaction model." external report. PLAXIS knowledge base: www. plaxis. nl.

Tsiapas, Y. Z. and G. D. Bouckovalas (2018). Numerical noise effects and filtering in liquefiable site response analyses. In Numerical Methods in Geo Eng IX, pp. 1–8.

Wood, D. M., and Liu, D. M. (1994). "Strain softening and state parameter for sand modelling." Géotechnique, 44(2), 335–339.

Nuques Luque, R.X. (2017). "Numerical Analyses of Liquefaction-Induced Building Settlement." University of California, Berkeley.

Yang Z, Elgamal A, Parra E (2003). Computational model for cyclic mobility and associated shear deformation. Journal of Geotechnical and Geoenvironmental Enginering 129(12): 1119-1127.

Zarnic, R. and Gostic, S. (1997). Masonry infilled frames as an effective structural sub-

This project has received funding from the European Union's Horizon 2020 research and innovation programme under grant agreement No. 700748

assemblage. In Proceedings of the international workshop on seismic design methodologies for the next generation of codes.

Zarnic, R. and Gostic, S. (1998). Non-linear modelling of masonry infilled frames. In 11th ECEE, Paris, France. A.A. Balkema, Rotterdam.

This project has received funding from the European Union's Horizon 2020 research and innovation programme under grant agreement No. 700748

APPENDIX A: VERIFICATION OF PIEVE DI CENTO SITE DURING M6.1 MAY, 20 2012 EVENT (§2)

A.1. INTRODUCTION

This appendix illustrates the work presented in 16th European Conference on Earthquake Engineering (16ECEE) at Thessaloniki, fully described in Chiaradonna et al. (2018b). The scope of the work is to back-assess the observed liquefaction at target site of Pieve di Cento during M6.1 May, 20 2012 event and use 21 ground motions that are defined in Section 2new in estimating the future likelihood of the same phenomenon. Due to these reasons, two different type of ground motions are provided:

1. Deterministic ground motion: Deconvolving the registered motion at MRN station (east-west component) to bedrock level, then carrying it to Pieve di Cento position through multiplying with a factor assigned according to Bindi et al. (2011). Finally, deconvolved and scaled MRN-EW motion is propagated up to 15 meters.
2. Probabilistic ground motion sets.

Analysis are carried out by SCOSSA (Tropeano et al., 2016) and Finn-Bryne model in FLAC for the deterministic ground motion case. Instead for systematic evaluations of soil liquefaction as a result of probabilistic ground motion sets, only SCOSSA is used.

In Figure A.2, comparisons of two coupled site response analyses are provided in terms of maximum horizontal acceleration (left) and peak excess pore water ratio profiles. It could be observed both codes may consistently predict the soil liquefaction at around 4 and 5.5 meters.

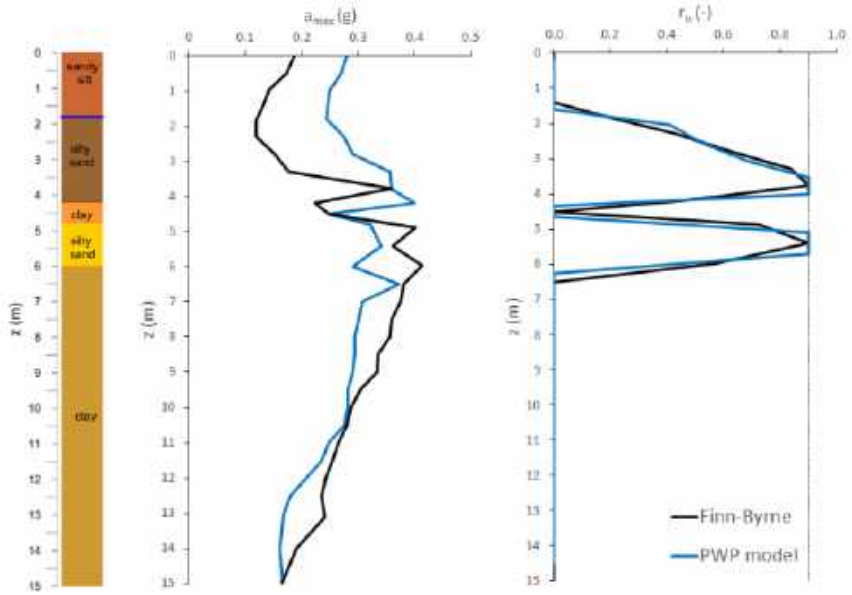

Figure A.1 Shear wave velocity profiles. (a) up to 230 meters, (b) up to 1 meters (from Chiaradonna et al., 2018b).

This project has received funding from the European Union's Horizon 2020 research and innovation programme under grant agreement No. 700748

A.2. RESULTS CONSIDERING THE SHAKE TABLE MOTIONS AT 15 METERS

Given the fact that two codes were benchmarked on the response due to deconvolved motion, analyses of liquefaction through shake table motions are applied through only SCOSSA. In Figure A.1, all the results are expressed as maximum excess pore water pressure ratio profiles as shown in Figure A.2. It is observed that liquefaction is attained in the great majority of the cases, only in the return period of 475 dataset, liquefaction is not reached by the mean profile.

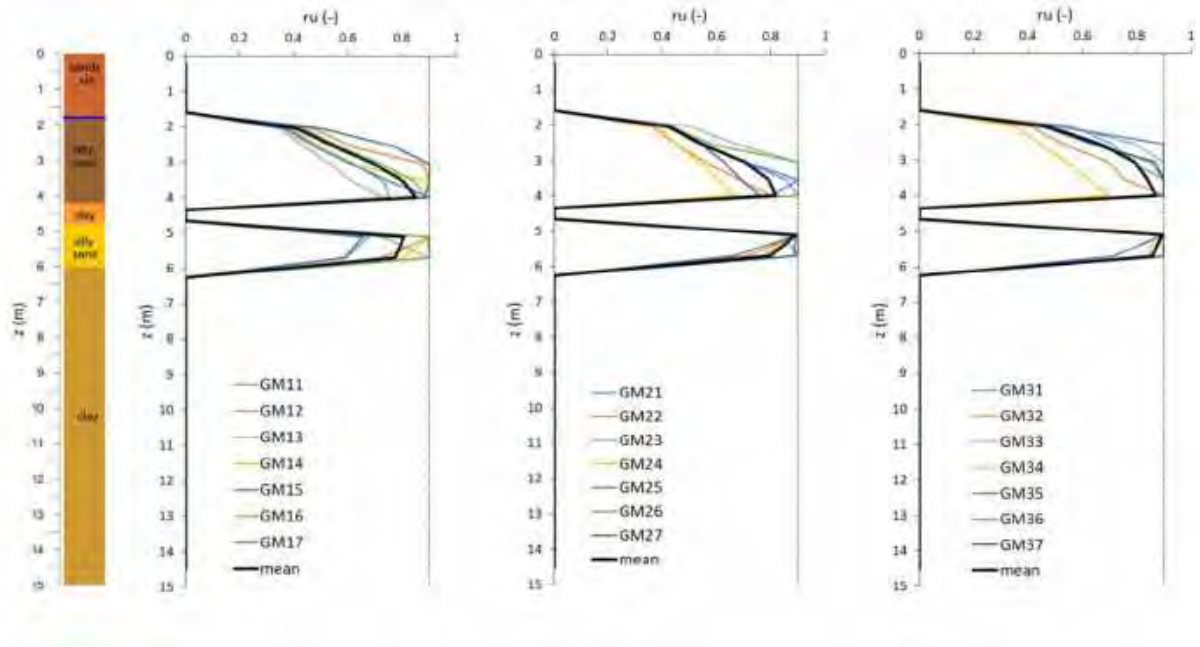

Figure A.2. Results of excess pore water ratio profiles (from left to right: for 475, 975, and 2475 years).

This project has received funding from the European Union's Horizon 2020 research and innovation programme under grant agreement No. 700748

APPENDIX B: CONTOUR PLOTS OF ΔU FROM THE PARAMETRIC ANALYSES (§6.1)

B.1. FREE FIELD SINGLE LAYER

ID: SF_xx_xx_xx

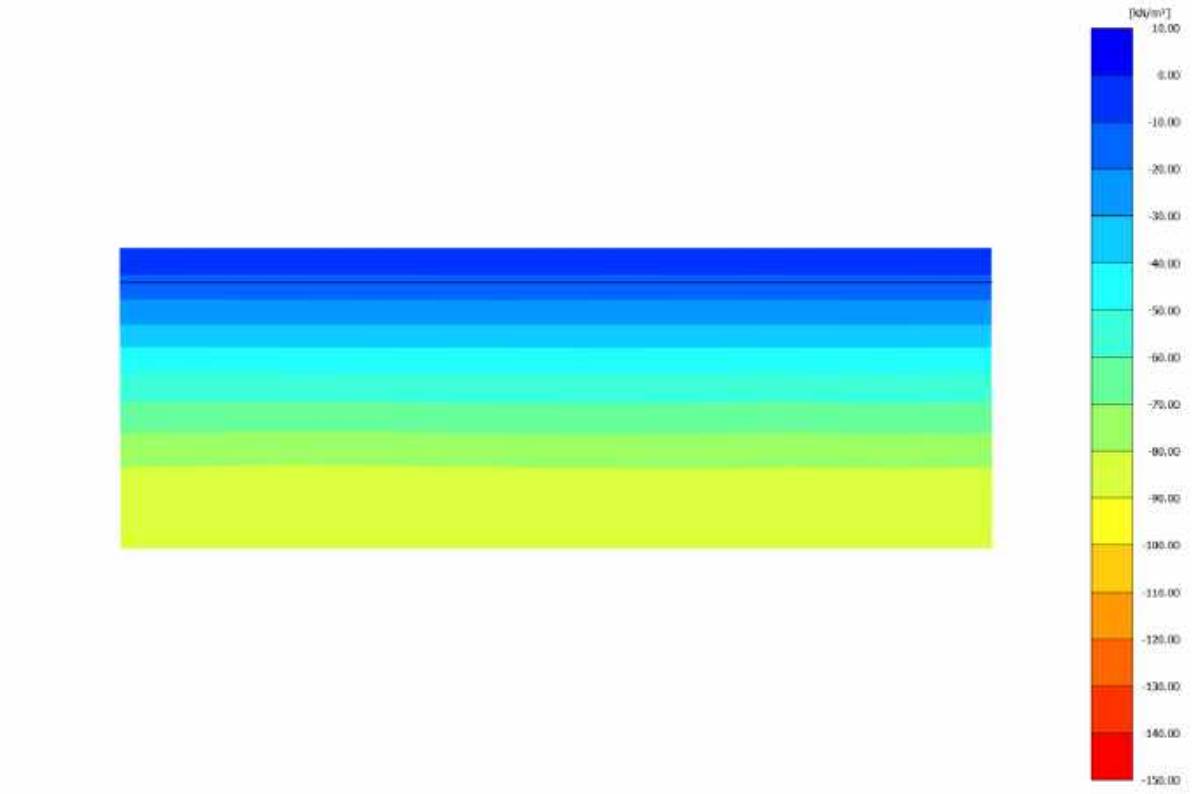

This project has received funding from the European Union's Horizon 2020 research and innovation programme under grant agreement No. 700748

ID: SF_HDU_H05_s05

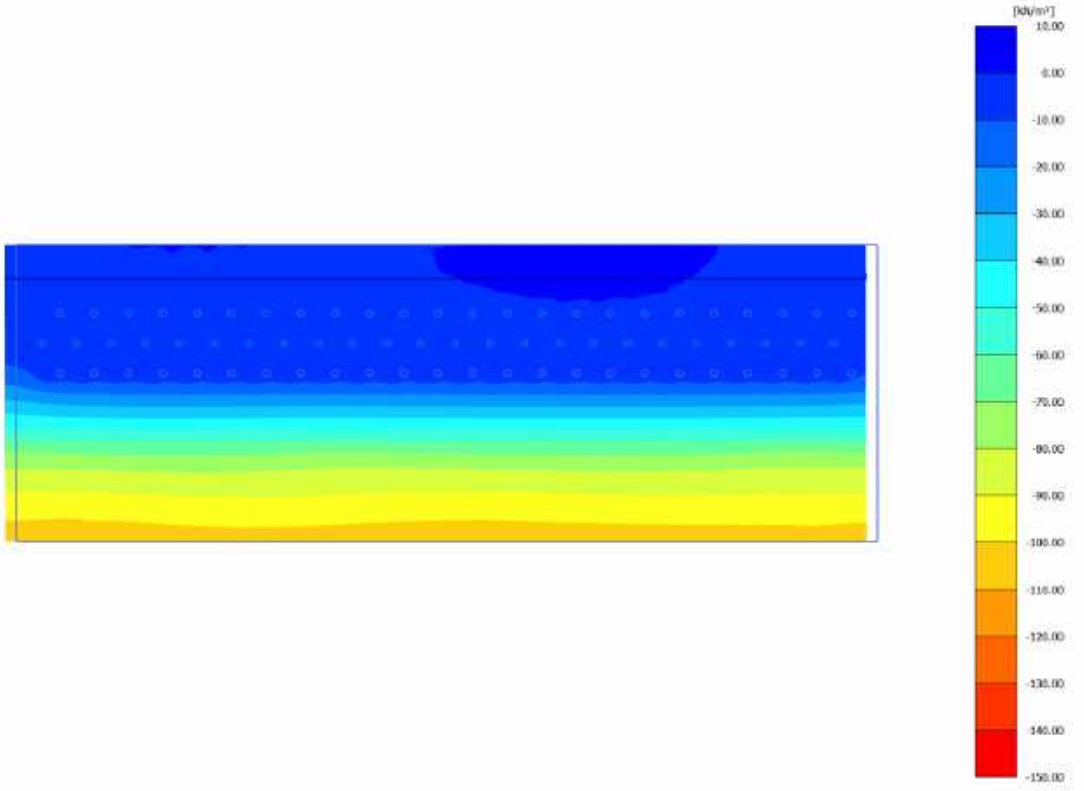

This project has received funding from the European Union's Horizon 2020 research and innovation programme under grant agreement No. 700748

ID: SF_HDU_H05_s10

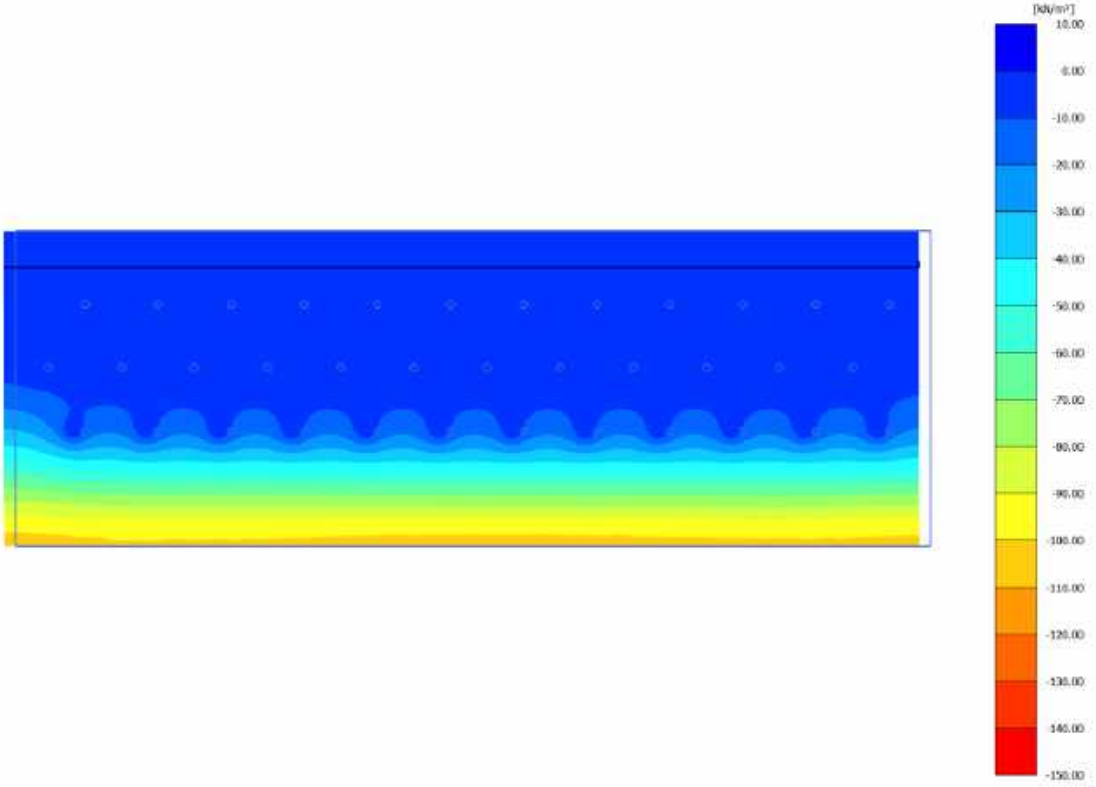

This project has received funding from the European Union's Horizon 2020 research and innovation programme under grant agreement No. 700748

ID: SF_HDU_H05_s15

This project has received funding from the European Union's Horizon 2020 research and innovation programme under grant agreement No. 700748

ID: SF_HDU_H10_s05

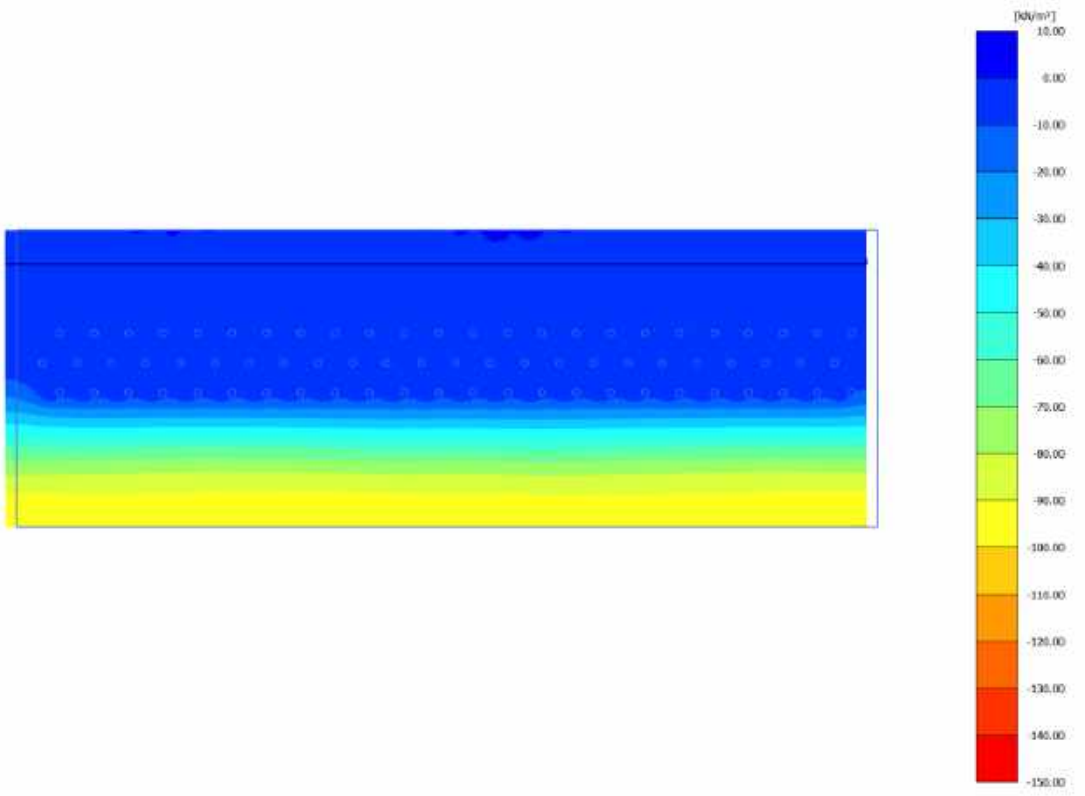

This project has received funding from the European Union's Horizon 2020 research and innovation programme under grant agreement No. 700748

ID: SF_HDU_H10_s10

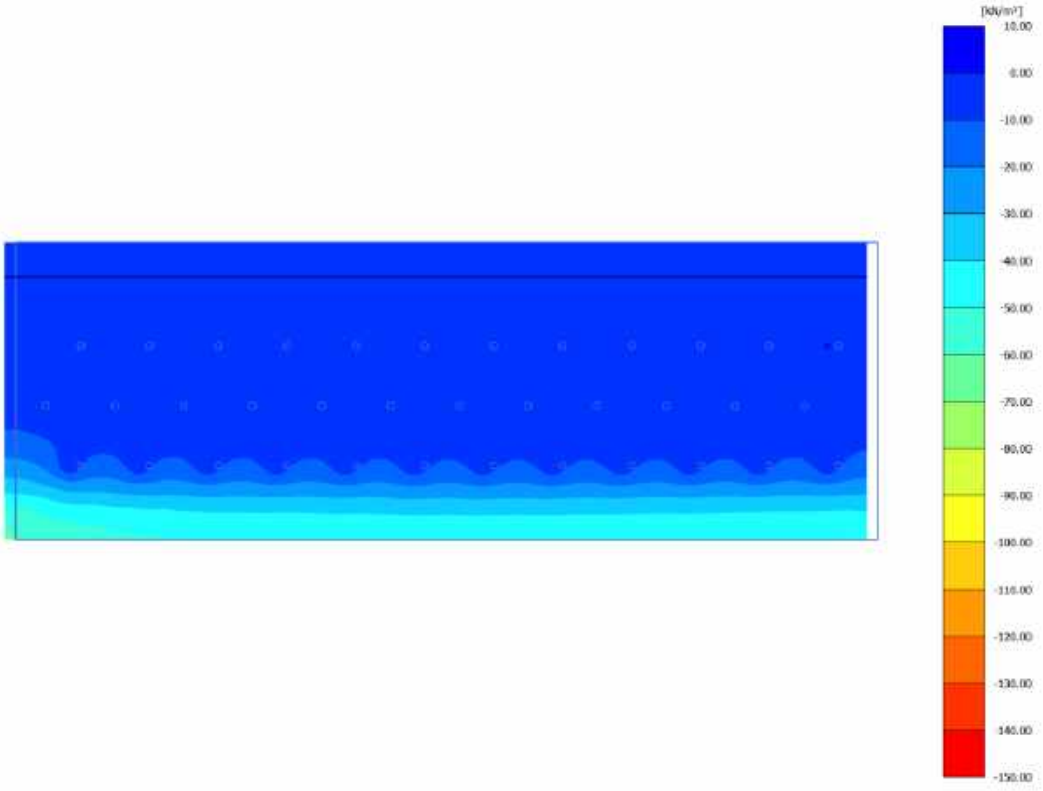

This project has received funding from the European Union's Horizon 2020 research and innovation programme under grant agreement No. 700748

ID: SF_HDU_H10_s15

This project has received funding from the European Union's Horizon 2020 research and innovation programme under grant agreement No. 700748

ID: SF_HDU_H15_s05

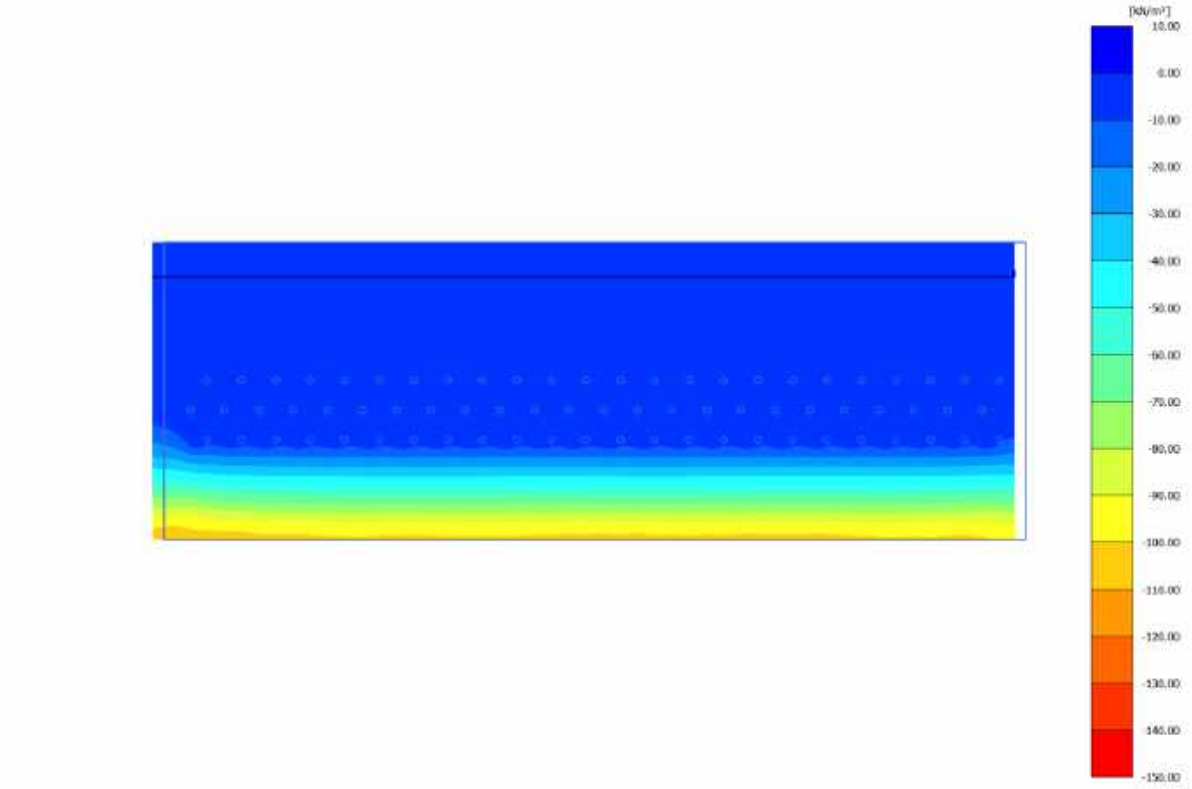

This project has received funding from the European Union's Horizon 2020 research and innovation programme under grant agreement No. 700748

ID: SF_HDU_H15_s10

This project has received funding from the European Union's Horizon 2020 research and innovation programme under grant agreement No. 700748

ID: SF_HDU_H15_s15

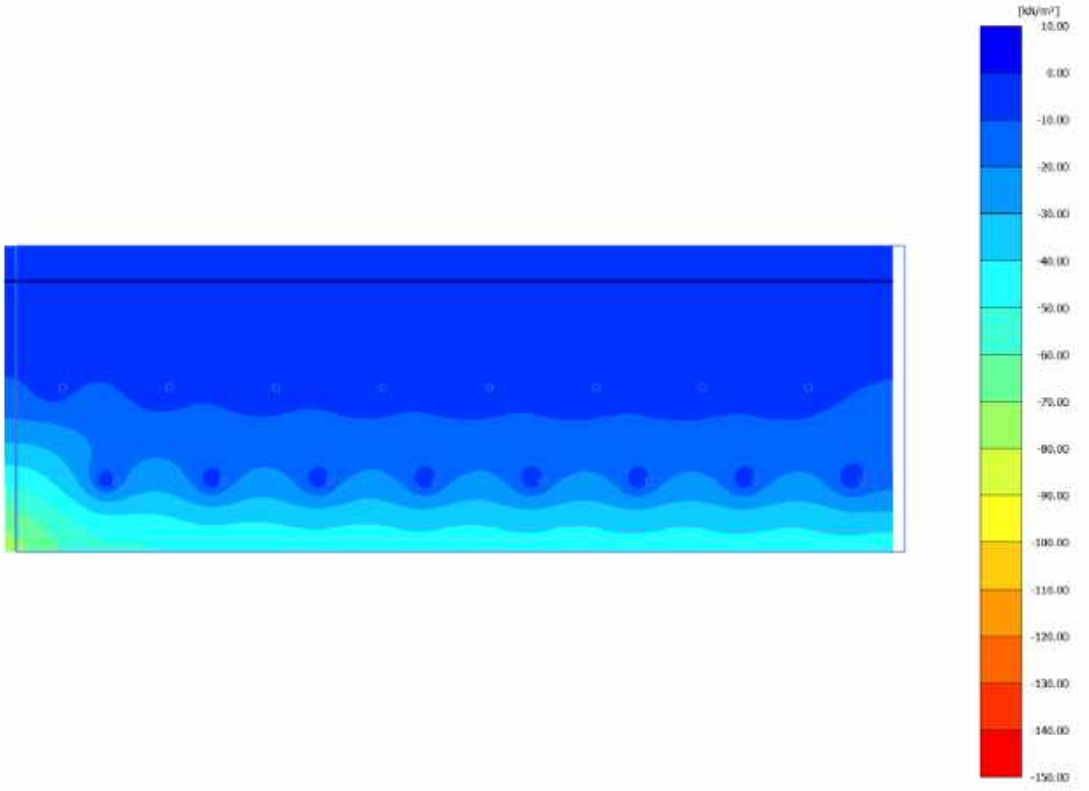

This project has received funding from the European Union's Horizon 2020 research and innovation programme under grant agreement No. 700748

B.2. SINGLE LAYER WITH STRUCTURE

ID: SS_xx_xx_xx

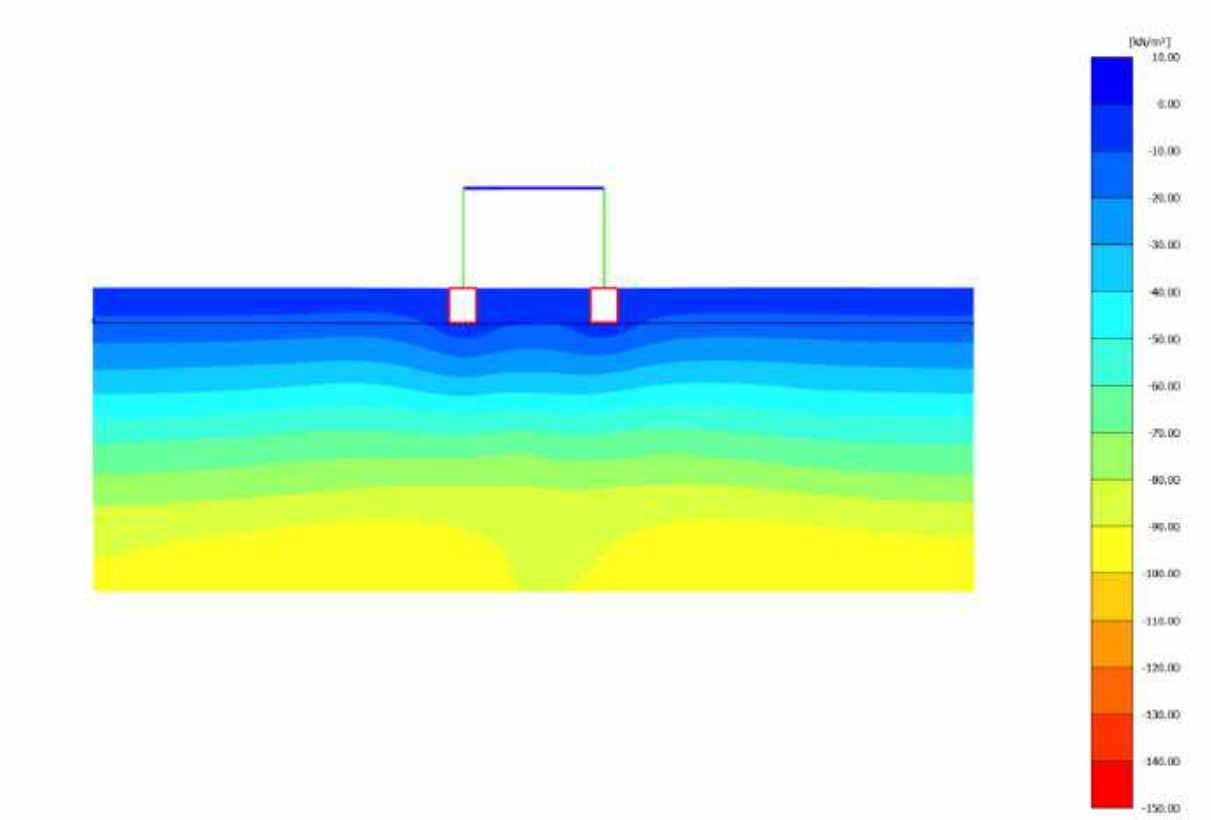

This project has received funding from the European Union's Horizon 2020 research and innovation programme under grant agreement No. 700748

ID: SS_HDU_H05_s05

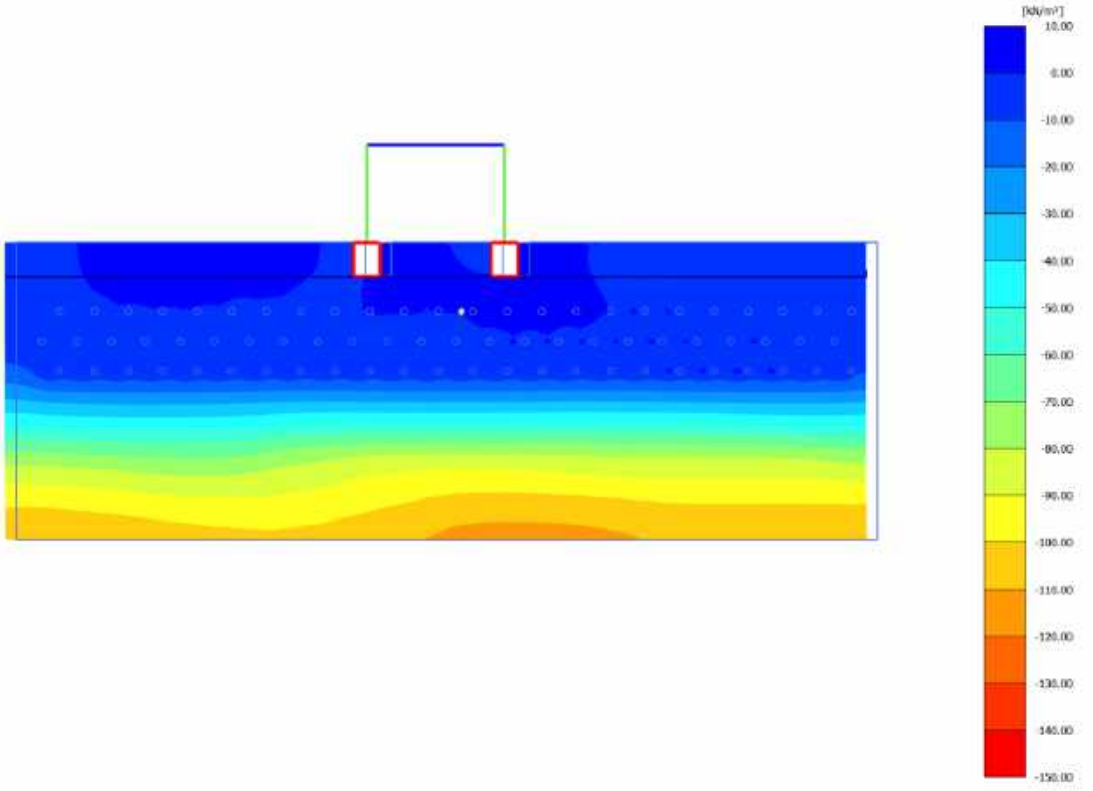

This project has received funding from the European Union's Horizon 2020 research and innovation programme under grant agreement No. 700748

ID: SS_HDU_H05_s10

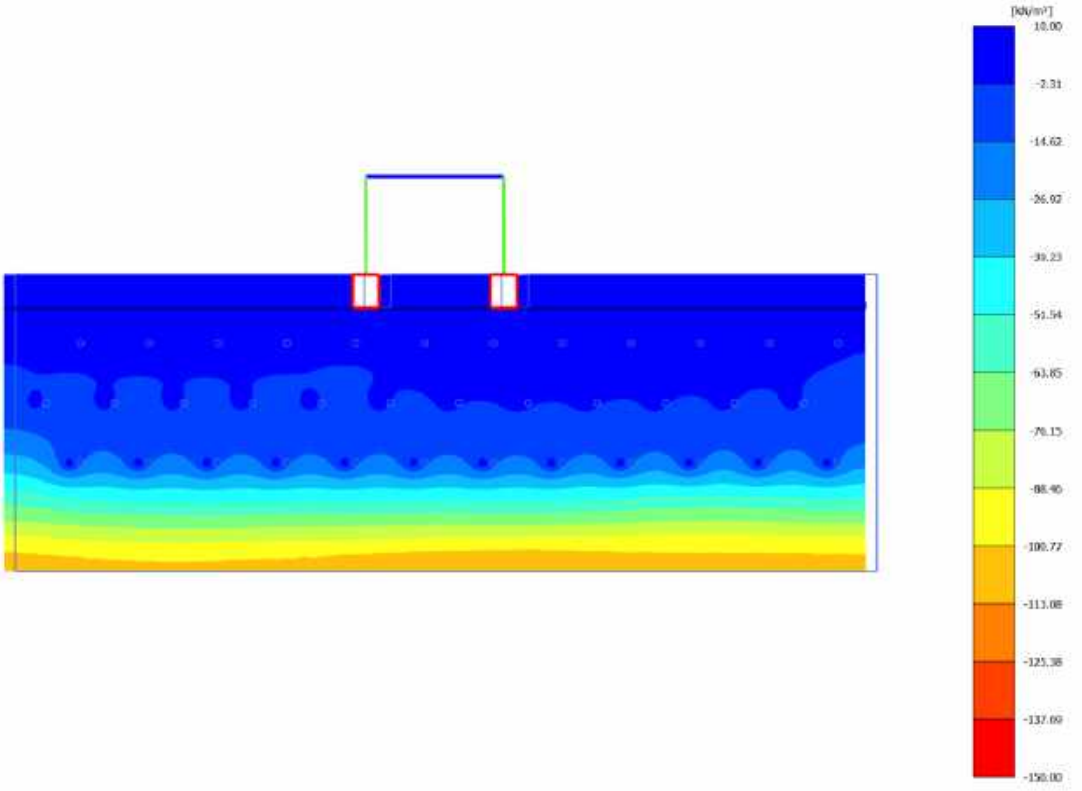

This project has received funding from the European Union's Horizon 2020 research and innovation programme under grant agreement No. 700748

ID: SS_HDU_H05_s15

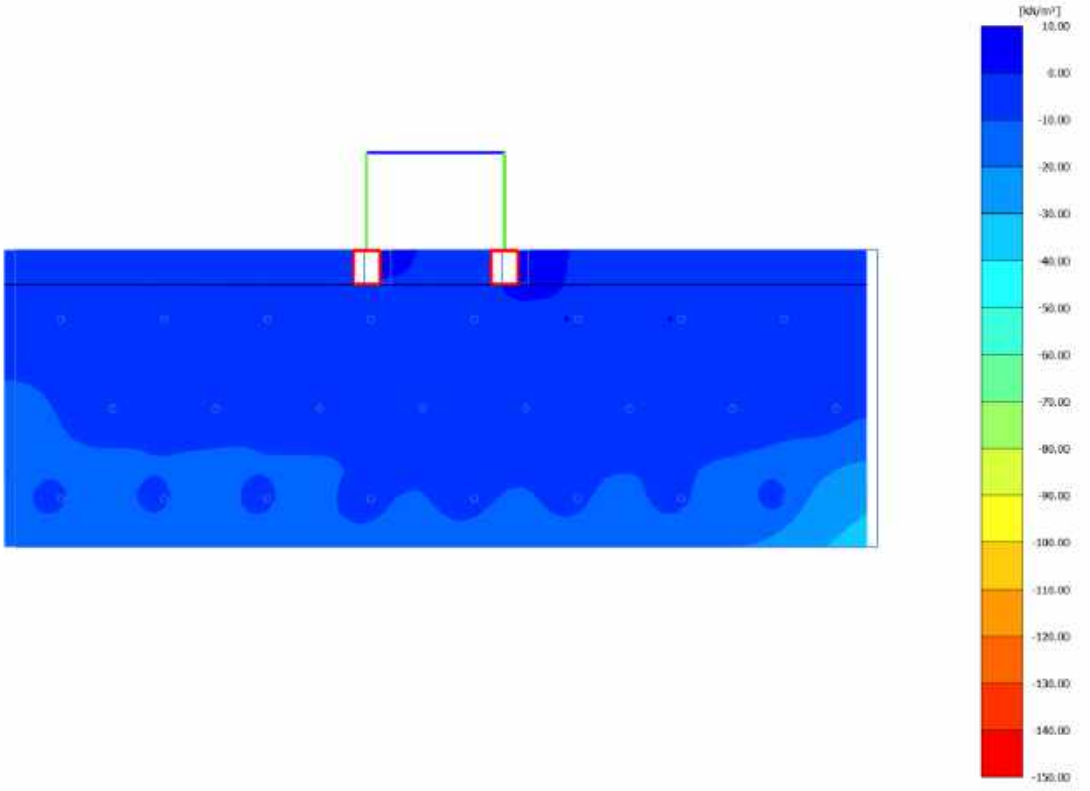

This project has received funding from the European Union's Horizon 2020 research and innovation programme under grant agreement No. 700748

ID: SS_HDU_H10_s05

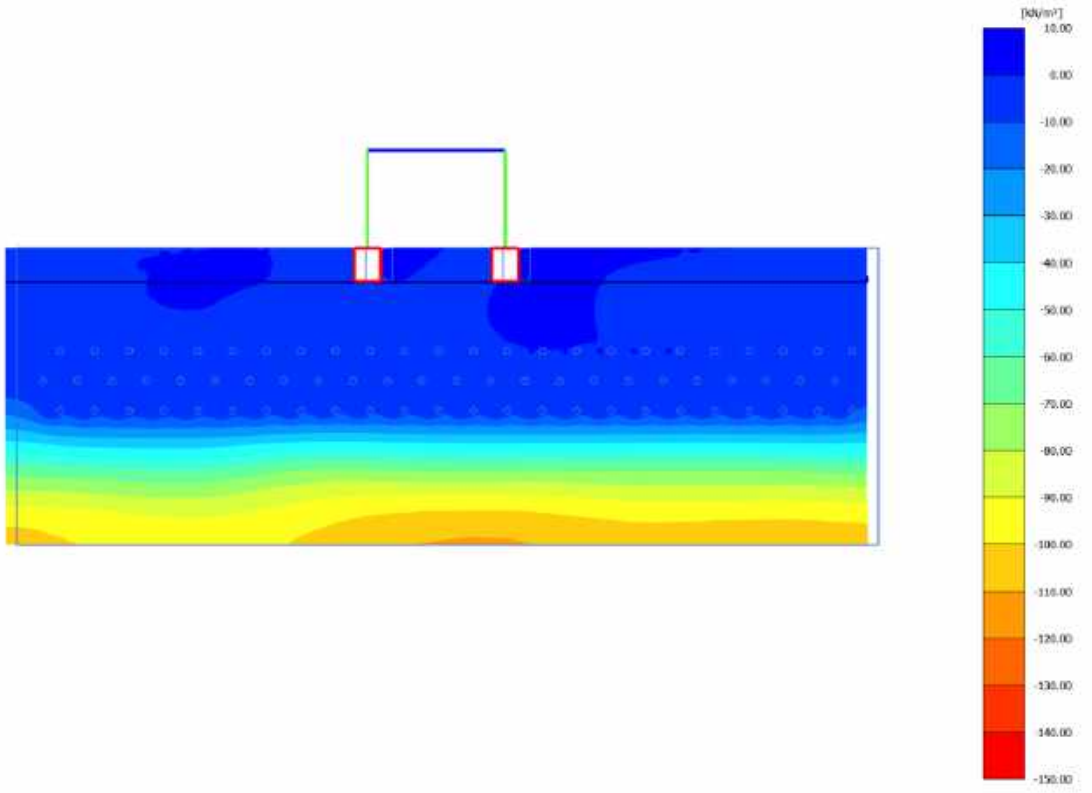

This project has received funding from the European Union's Horizon 2020 research and innovation programme under grant agreement No. 700748

ID: SS_HDU_H10_s10

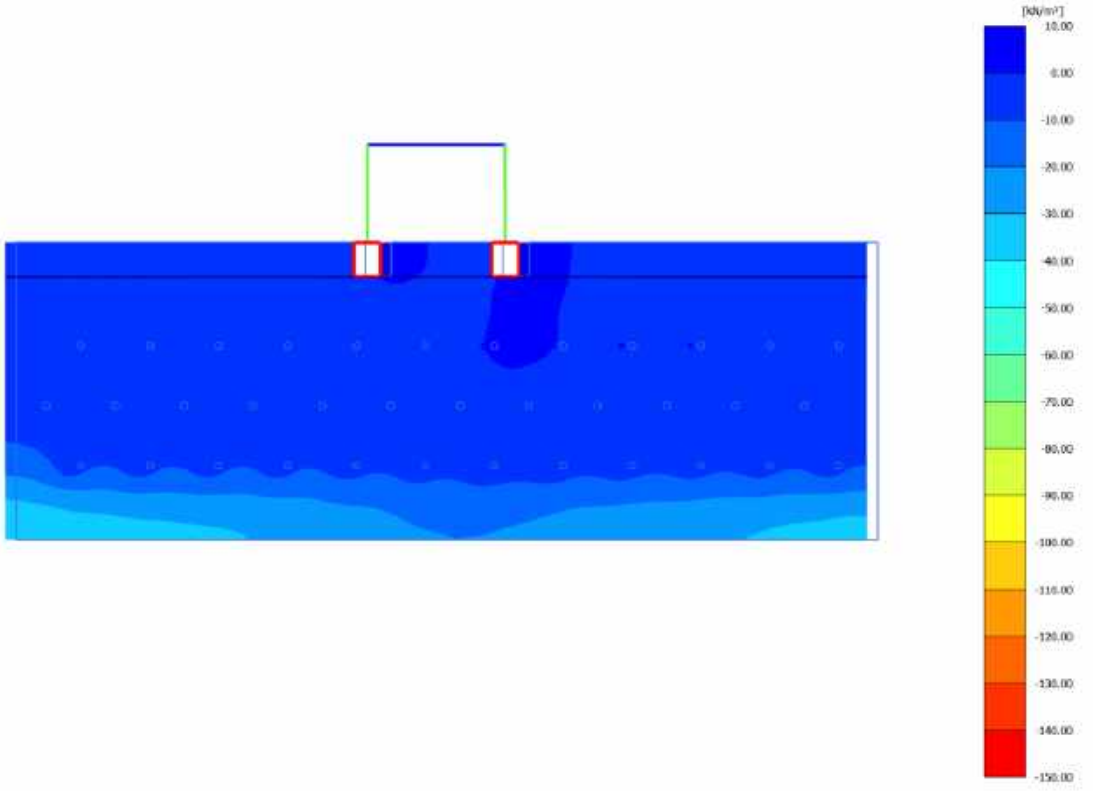

This project has received funding from the European Union's Horizon 2020 research and innovation programme under grant agreement No. 700748

ID: SS_HDU_H10_s15

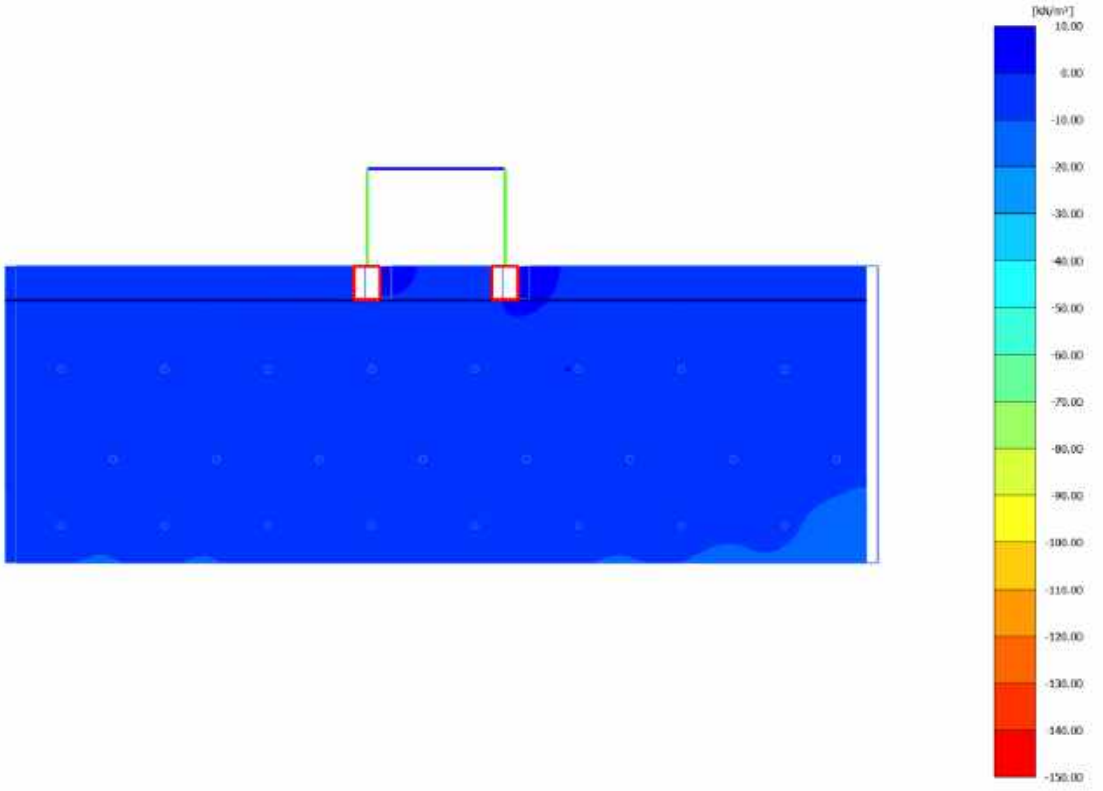

This project has received funding from the European Union's Horizon 2020 research and innovation programme under grant agreement No. 700748

ID: SS_HDU_H15_s05

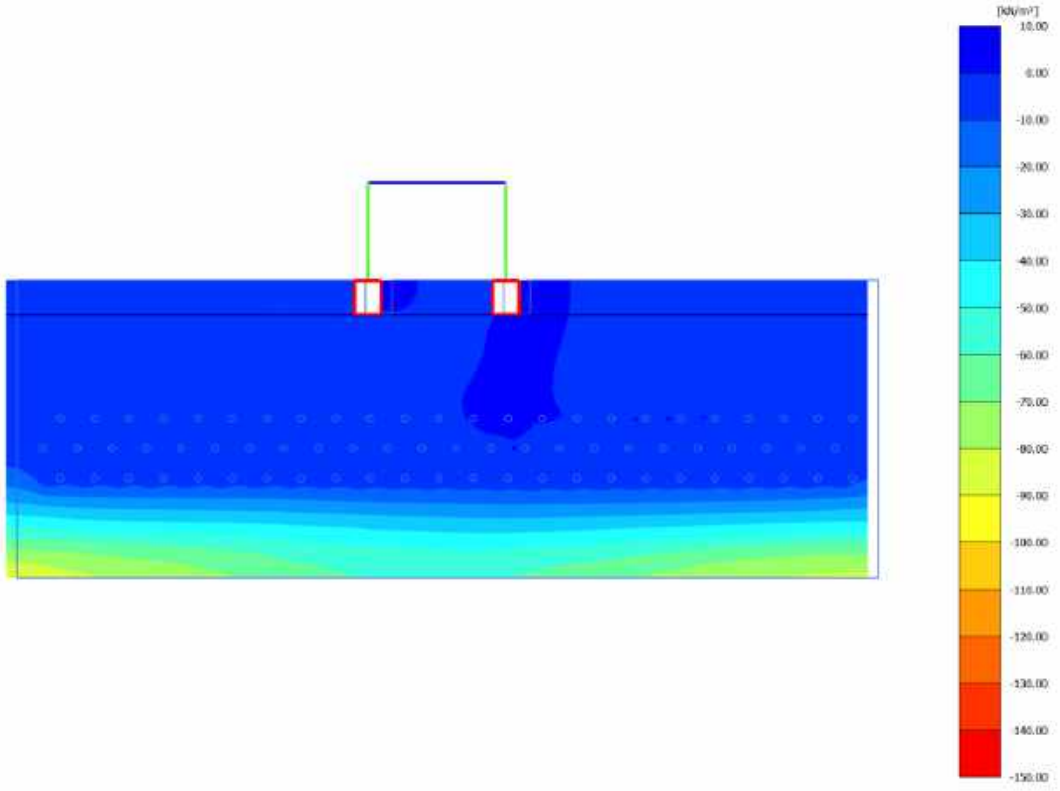

This project has received funding from the European Union's Horizon 2020 research and innovation programme under grant agreement No. 700748

ID: SS_HDU_H15_s10

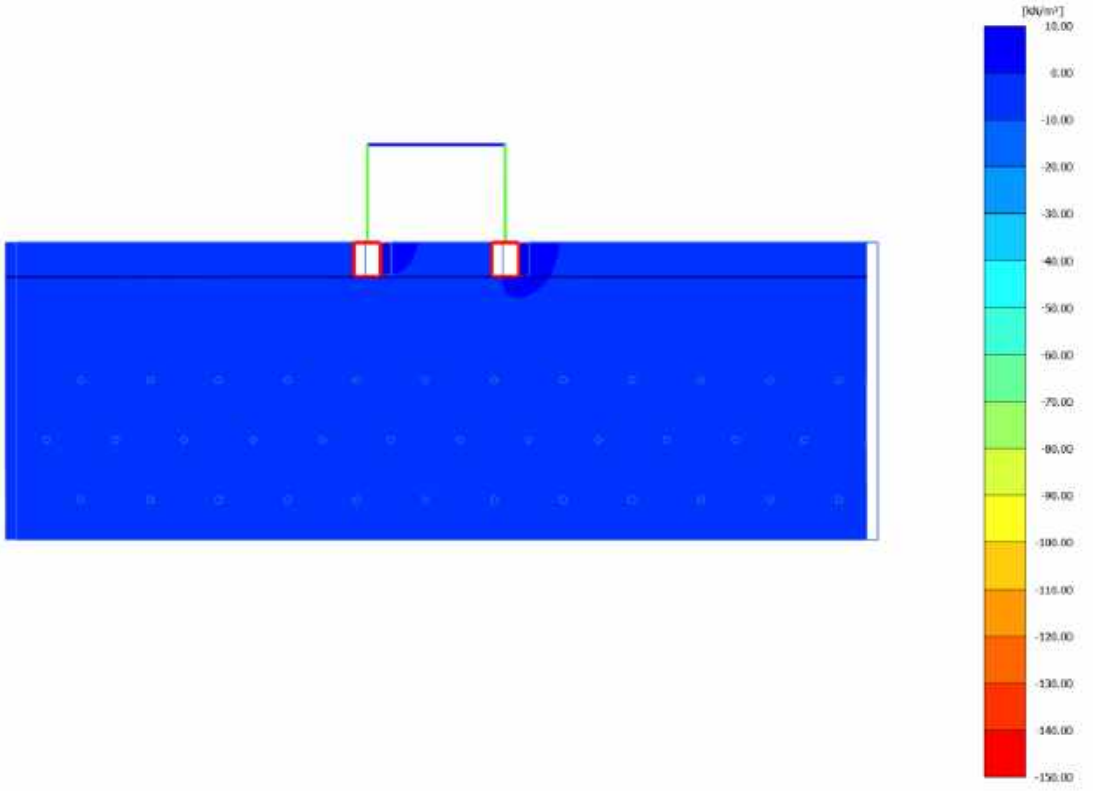

This project has received funding from the European Union's Horizon 2020 research and innovation programme under grant agreement No. 700748

ID: SS_HDU_H15_s15

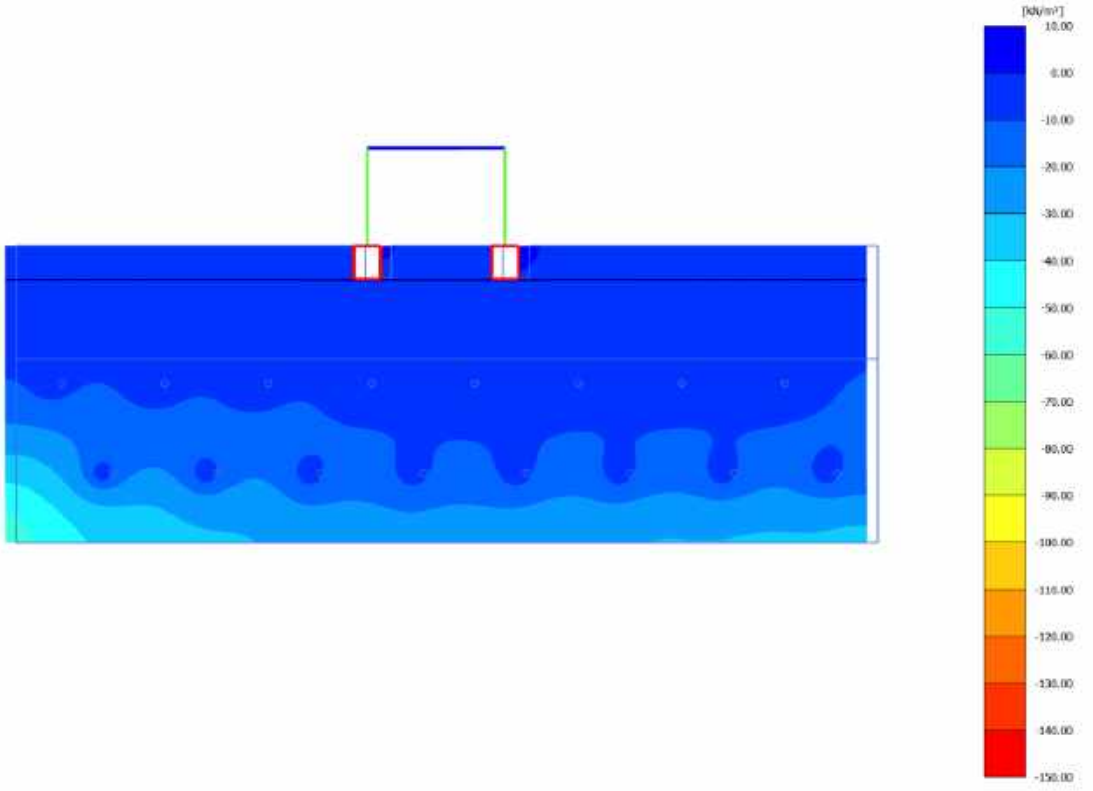

This project has received funding from the European Union's Horizon 2020 research and innovation programme under grant agreement No. 700748

B.3. FREE FIELD TWO LAYERS

ID: DF_xx_xx_xx

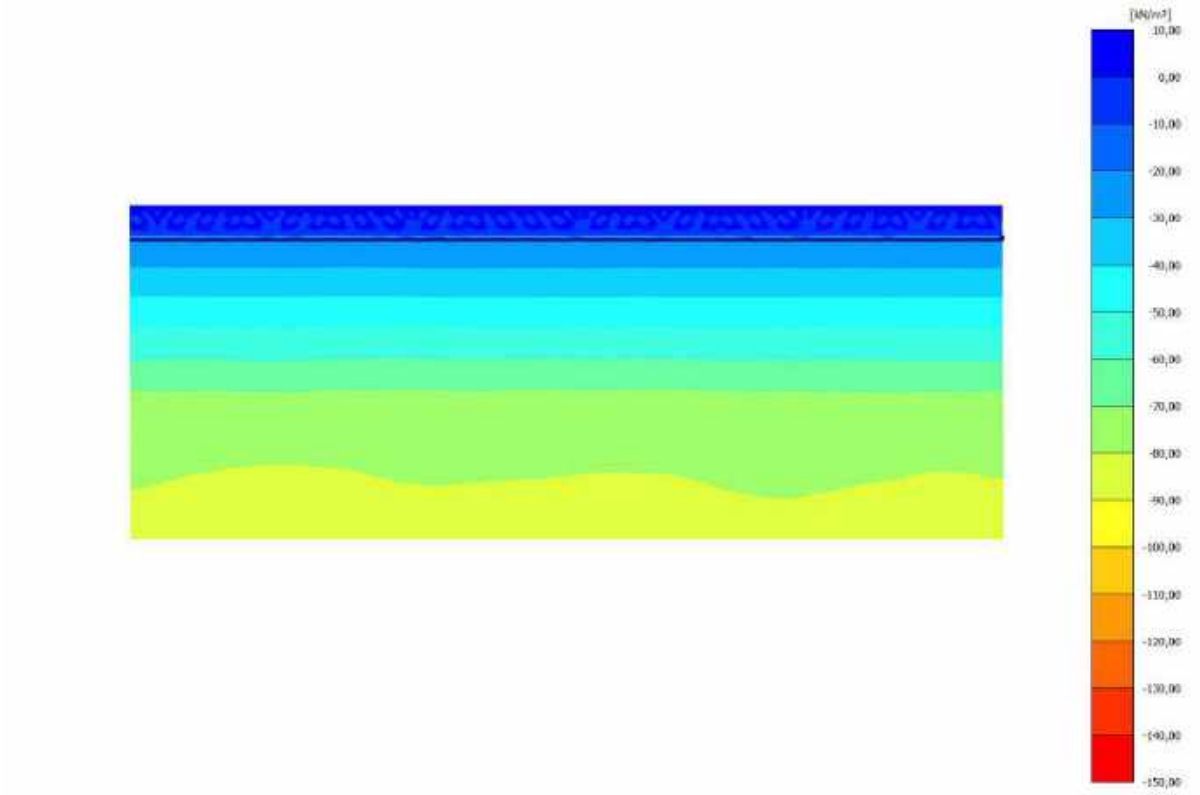

This project has received funding from the European Union's Horizon 2020 research and innovation programme under grant agreement No. 700748

ID: DF_HDU_H05_s05

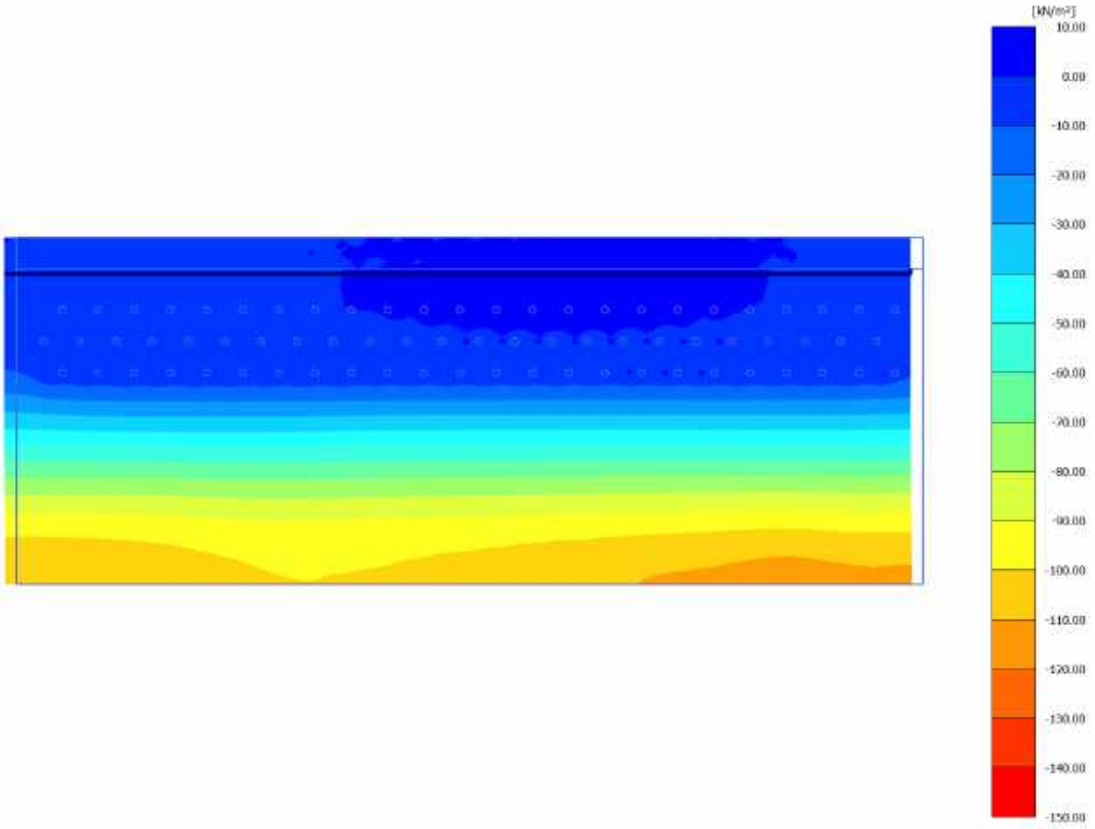

ID: DF_HDU_H05_s10

This project has received funding from the European Union's Horizon 2020 research and innovation programme under grant agreement No. 700748

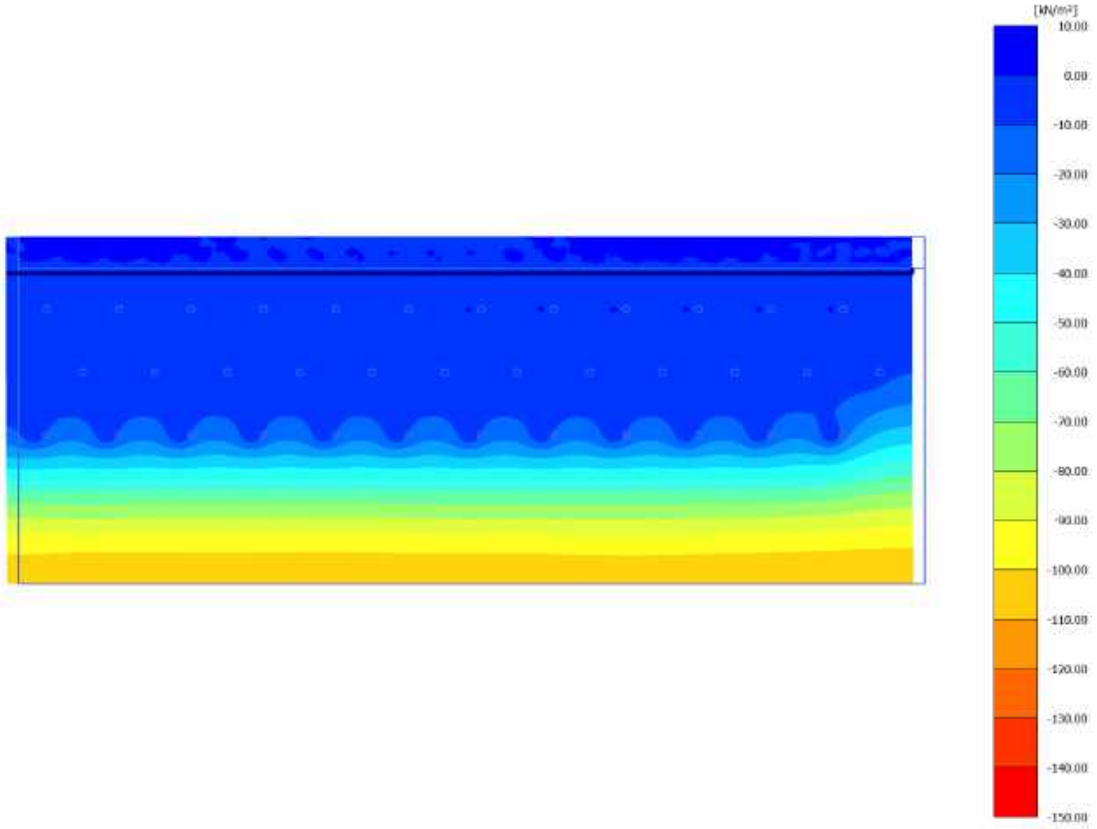

DF_HDU_H05_s15

This project has received funding from the European Union's Horizon 2020 research and innovation programme under grant agreement No. 700748

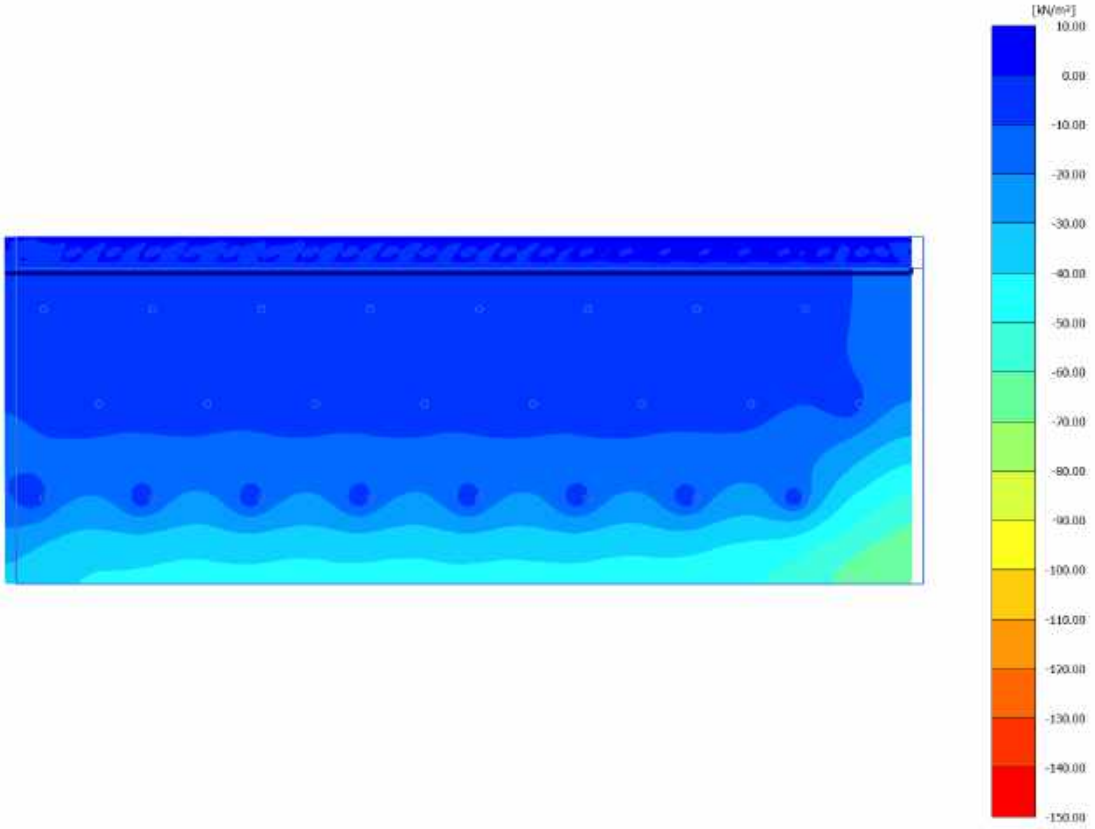

DF_HDU_H10_s05

This project has received funding from the European Union's Horizon 2020 research and innovation programme under grant agreement No. 700748

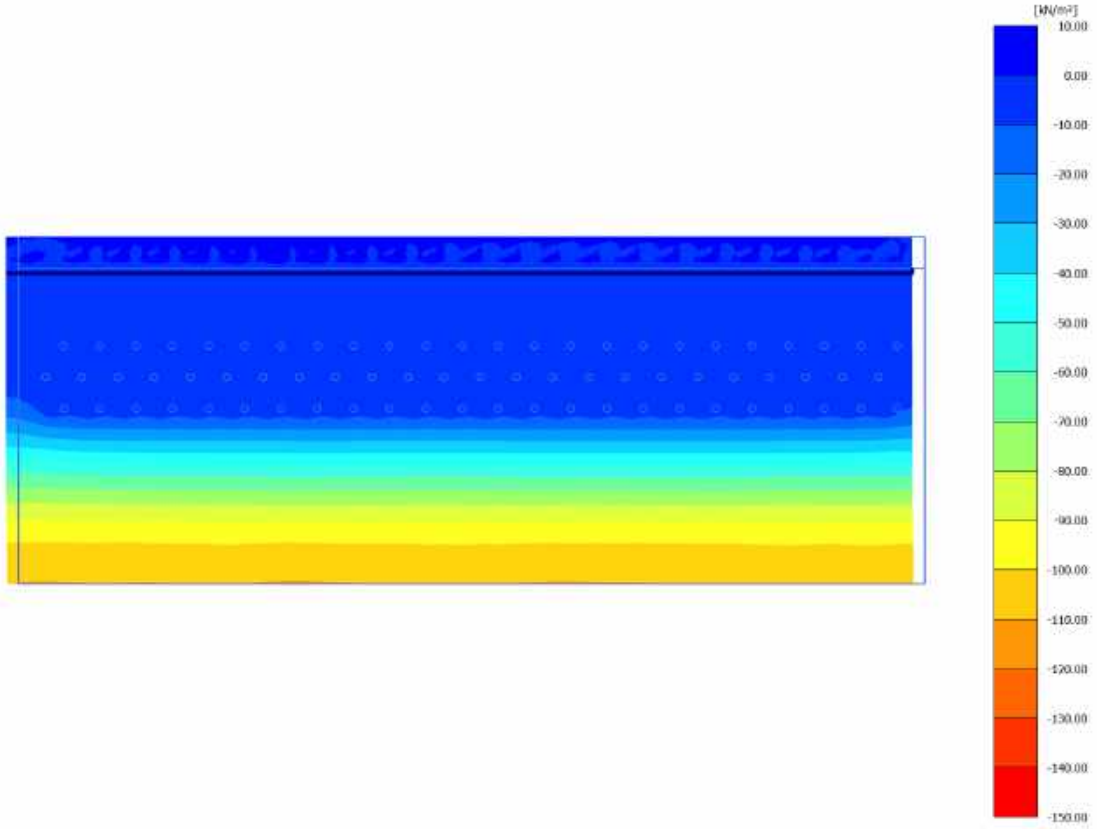

DF_HDU_H10_s10

This project has received funding from the European Union's Horizon 2020 research and innovation programme under grant agreement No. 700748

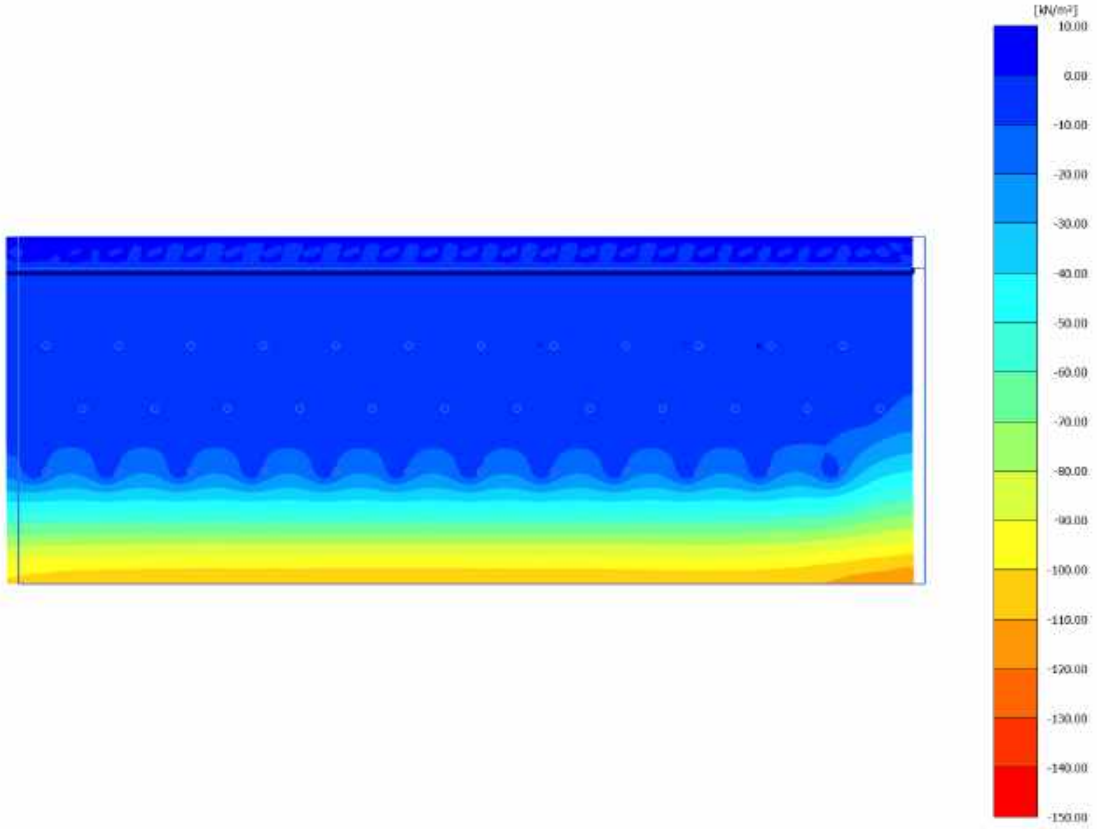

DF_HDU_H10_s15

This project has received funding from the European Union's Horizon 2020 research and innovation programme under grant agreement No. 700748

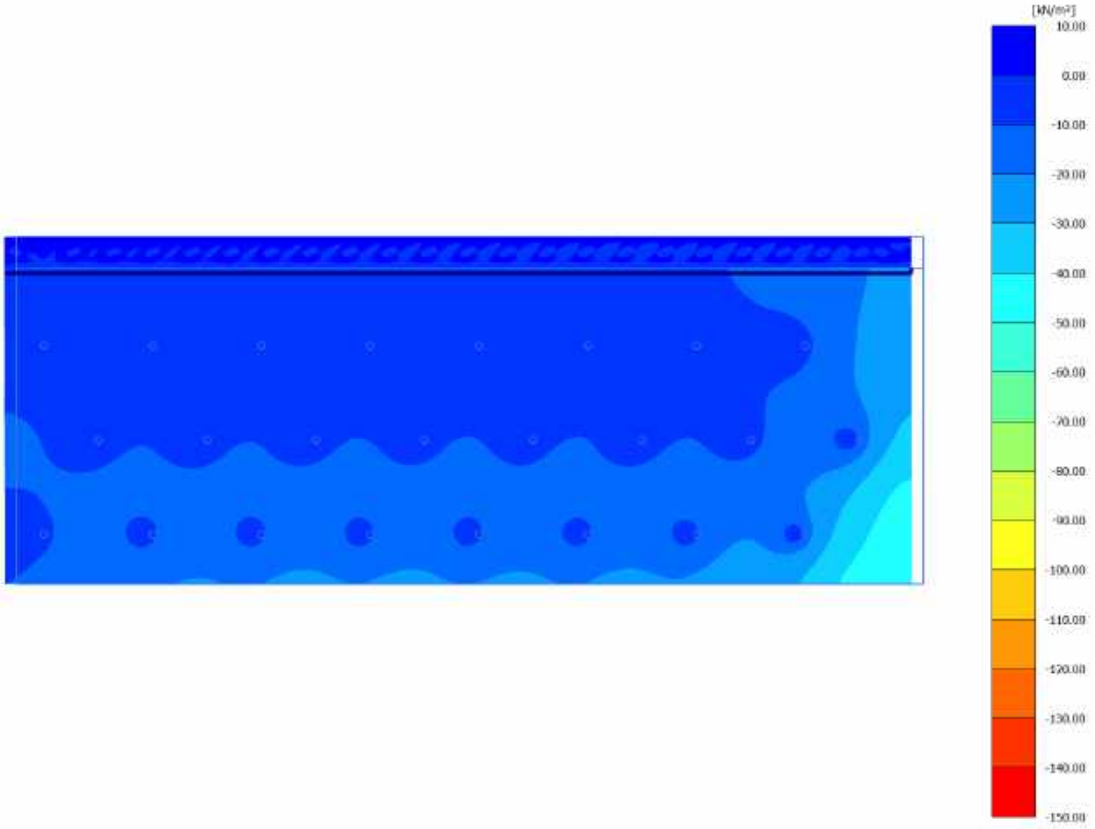

DF_HDU_H15_s05

This project has received funding from the European Union's Horizon 2020 research and innovation programme under grant agreement No. 700748

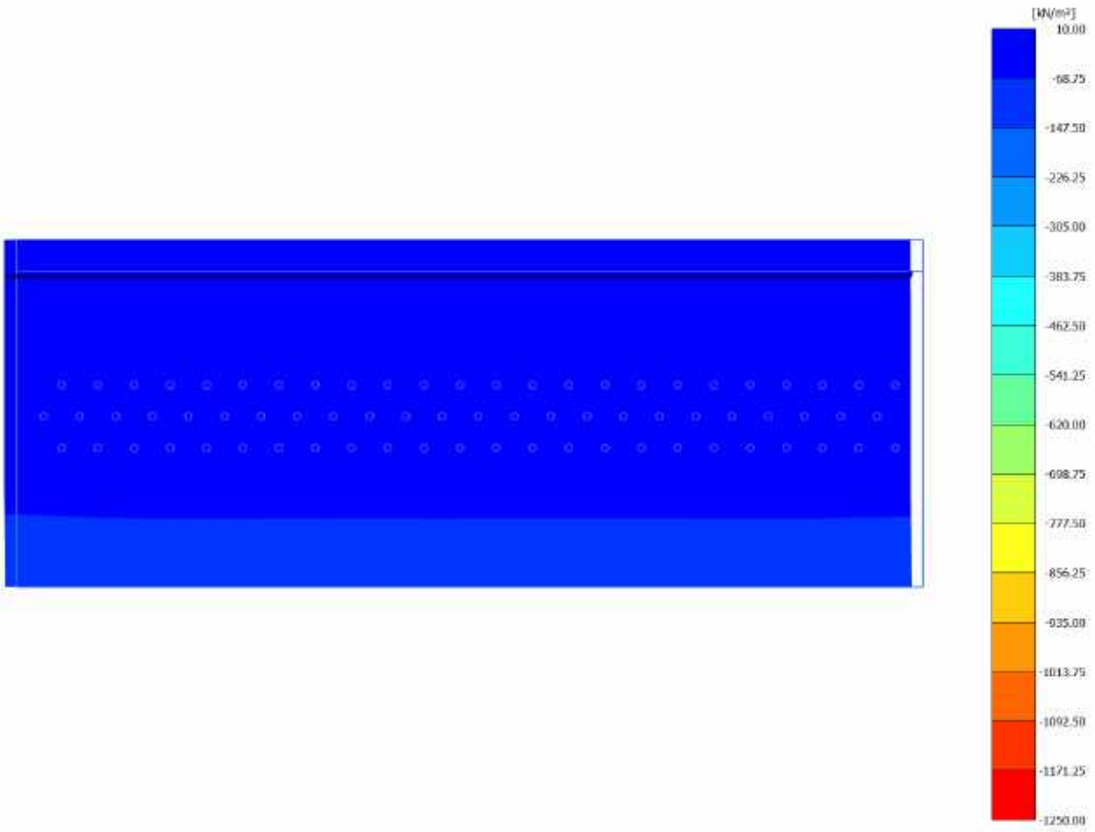

DF_HDU_H15_s10

This project has received funding from the European Union's Horizon 2020 research and innovation programme under grant agreement No. 700748

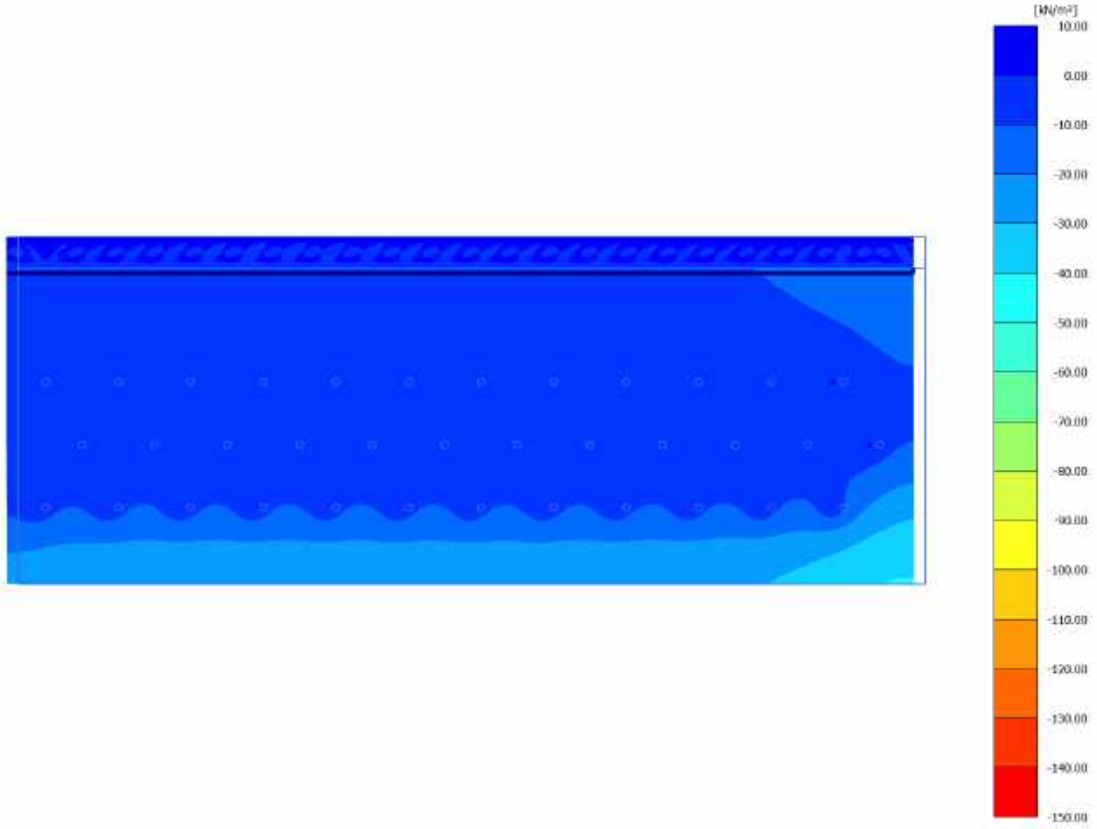

DF_HDU_H15_s15

This project has received funding from the European Union's Horizon 2020 research and innovation programme under grant agreement No. 700748

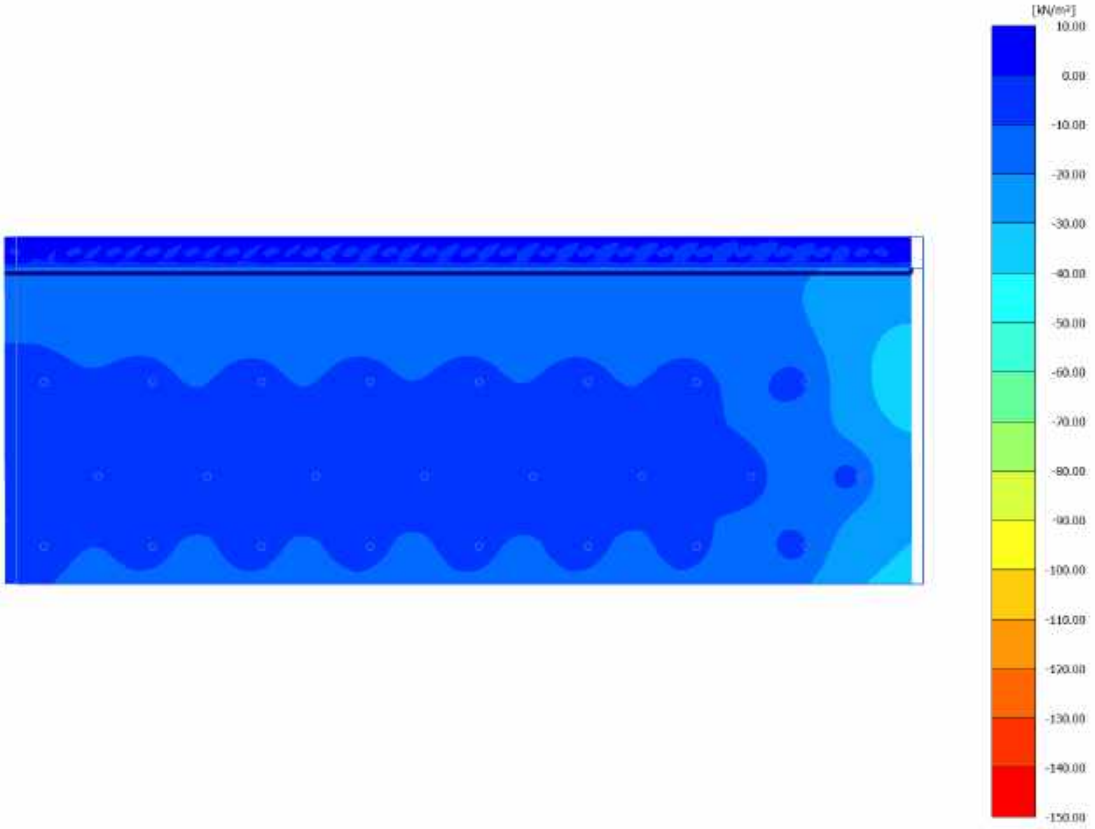

B.4. TWO LAYERS WITH STRUCTURE

ID: DS_xx_xx_xx

This project has received funding from the European Union's Horizon 2020 research and innovation programme under grant agreement No. 700748

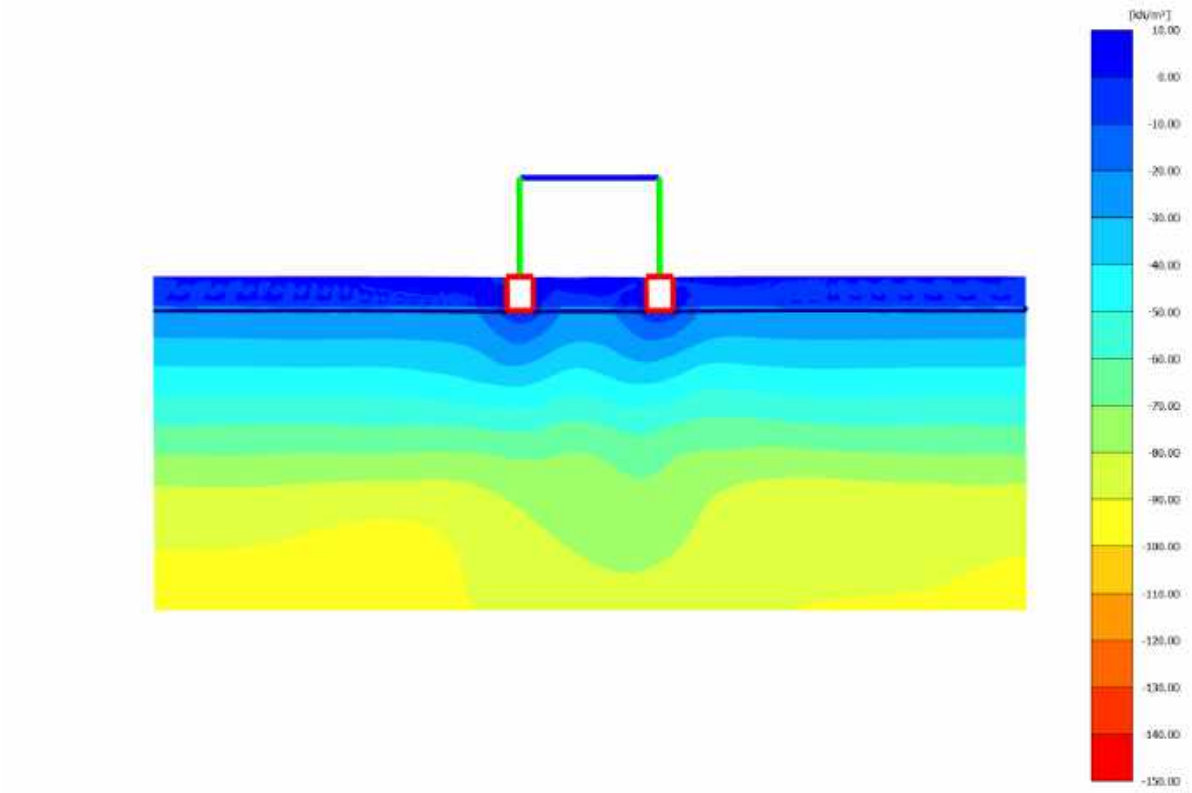

This project has received funding from the European Union's Horizon 2020 research and innovation programme under grant agreement No. 700748

DS_HDU_H05_s05

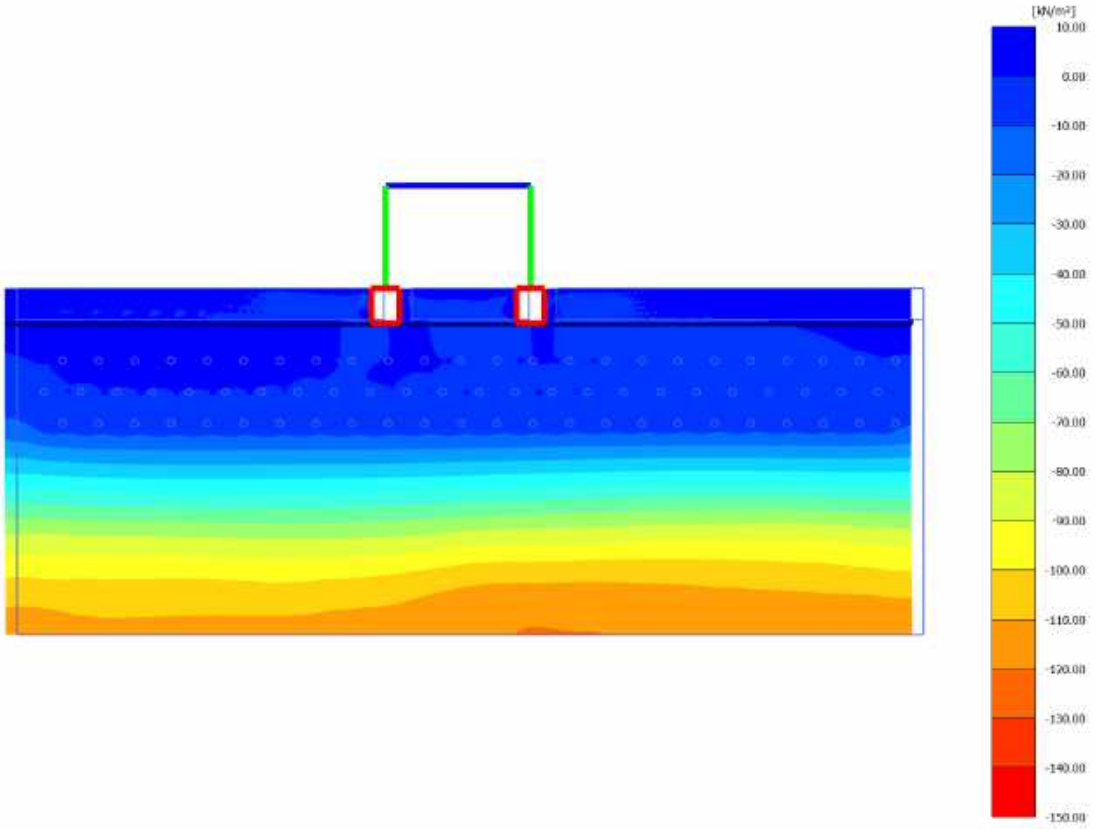

DS_HDU_H05_s10

This project has received funding from the European Union's Horizon 2020 research and innovation programme under grant agreement No. 700748

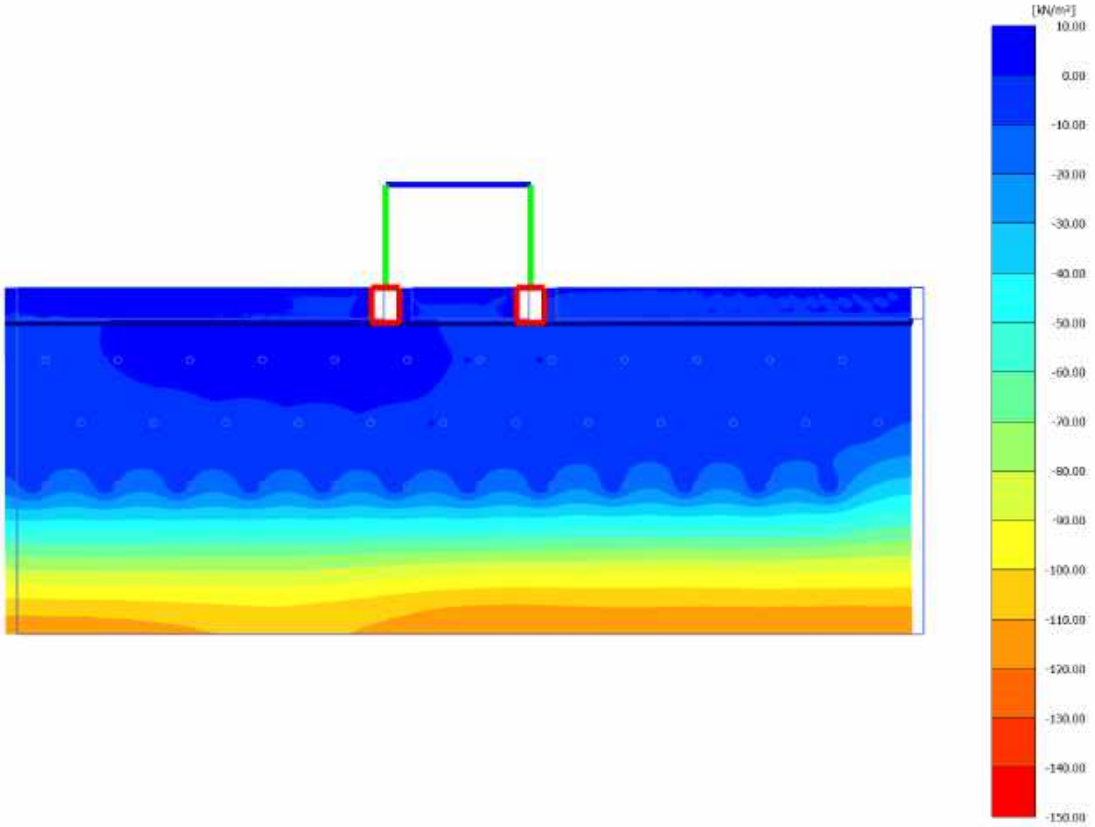

DS_HDU_H05_s15

This project has received funding from the European Union's Horizon 2020 research and innovation programme under grant agreement No. 700748

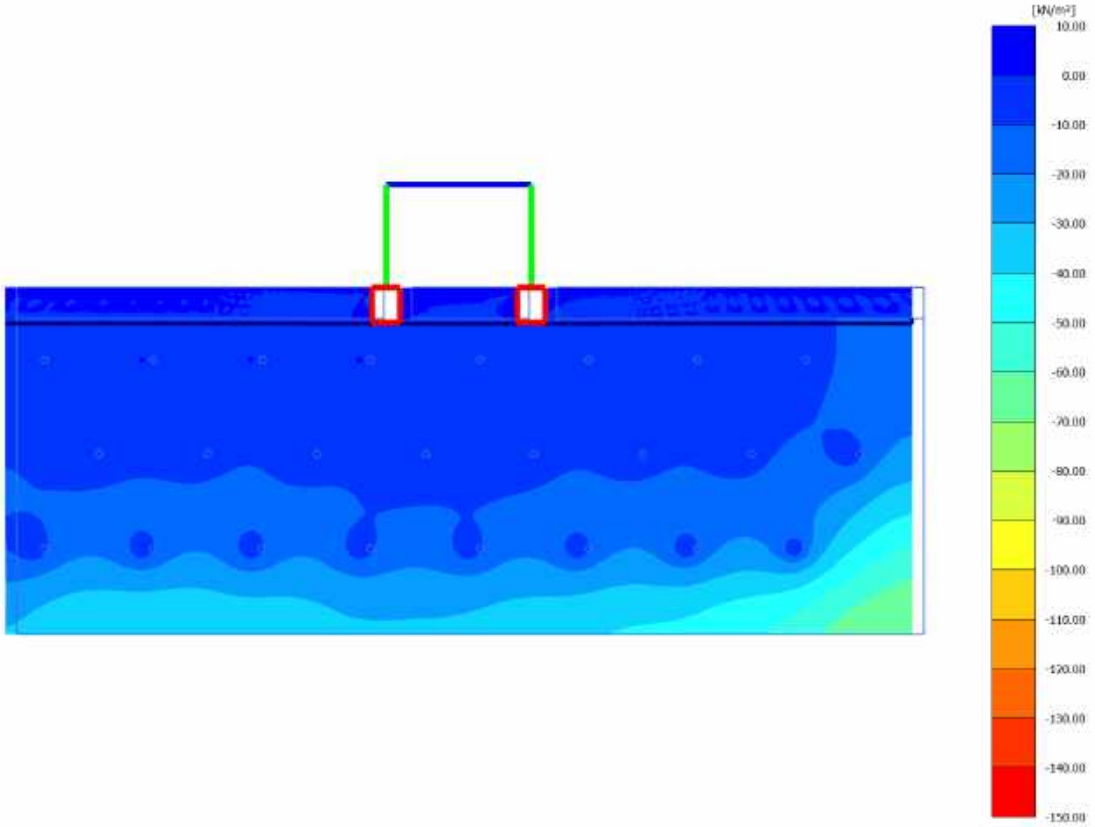

DS_HDU_H10_s05

This project has received funding from the European Union's Horizon 2020 research and innovation programme under grant agreement No. 700748

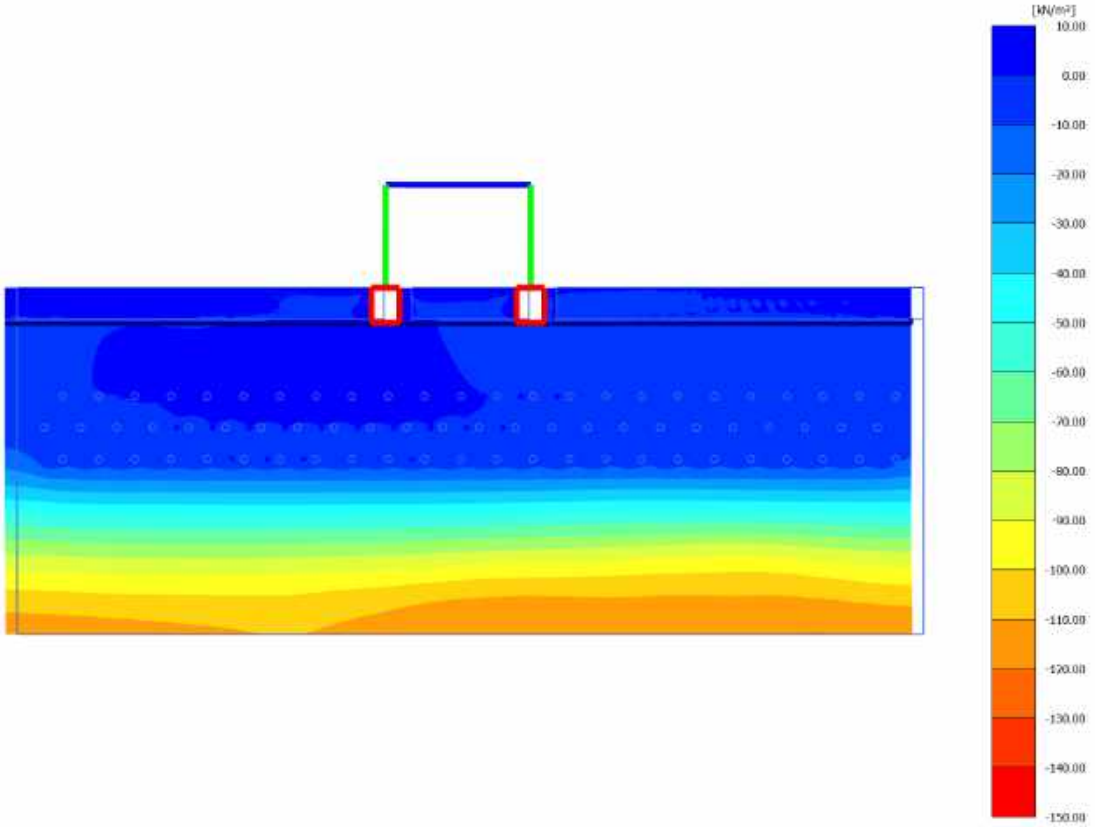

DS_HDU_H10_s10

This project has received funding from the European Union's Horizon 2020 research and innovation programme under grant agreement No. 700748

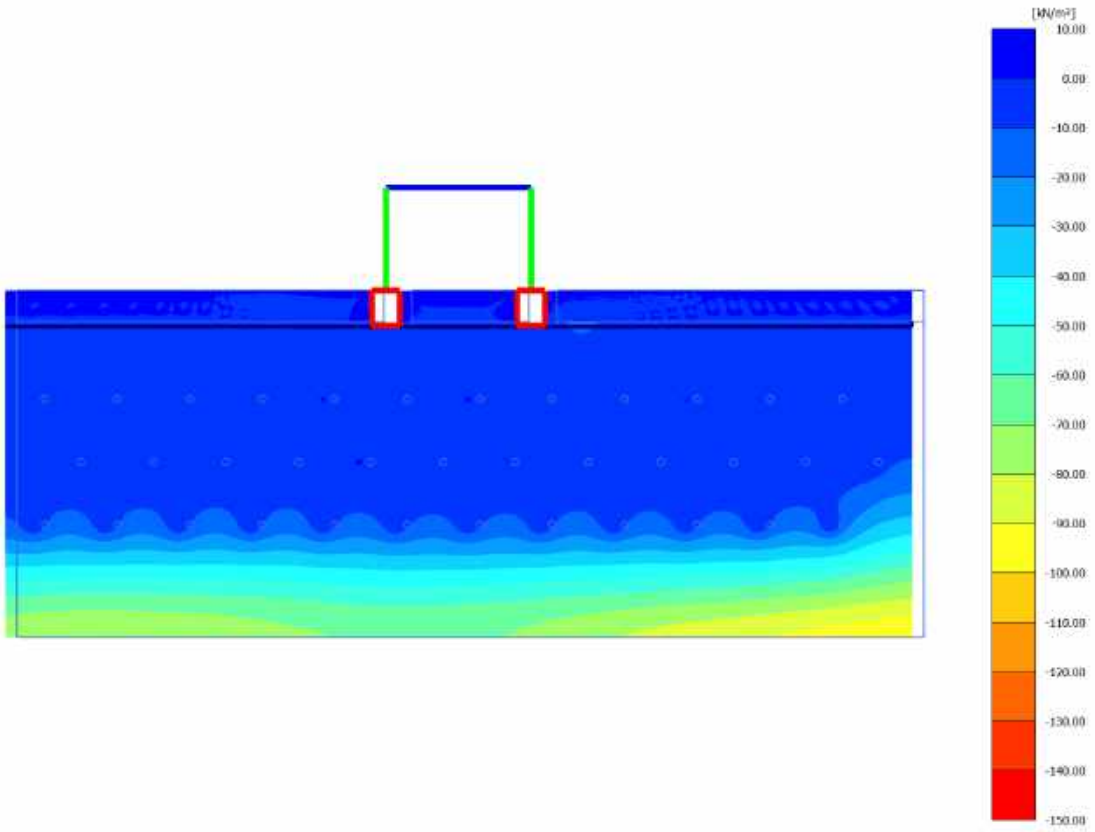

DS_HDU_H10_s15

This project has received funding from the European Union's Horizon 2020 research and innovation programme under grant agreement No. 700748

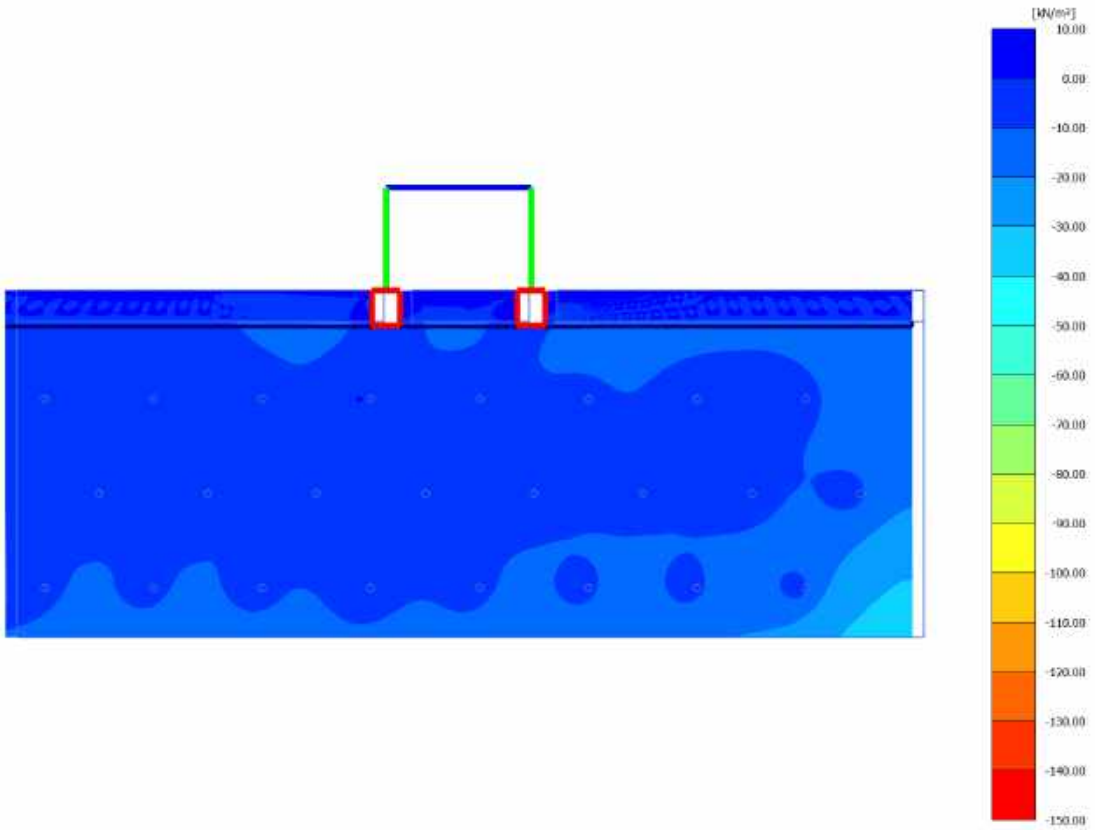

DS_HDU_H15_s05

This project has received funding from the European Union's Horizon 2020 research and innovation programme under grant agreement No. 700748

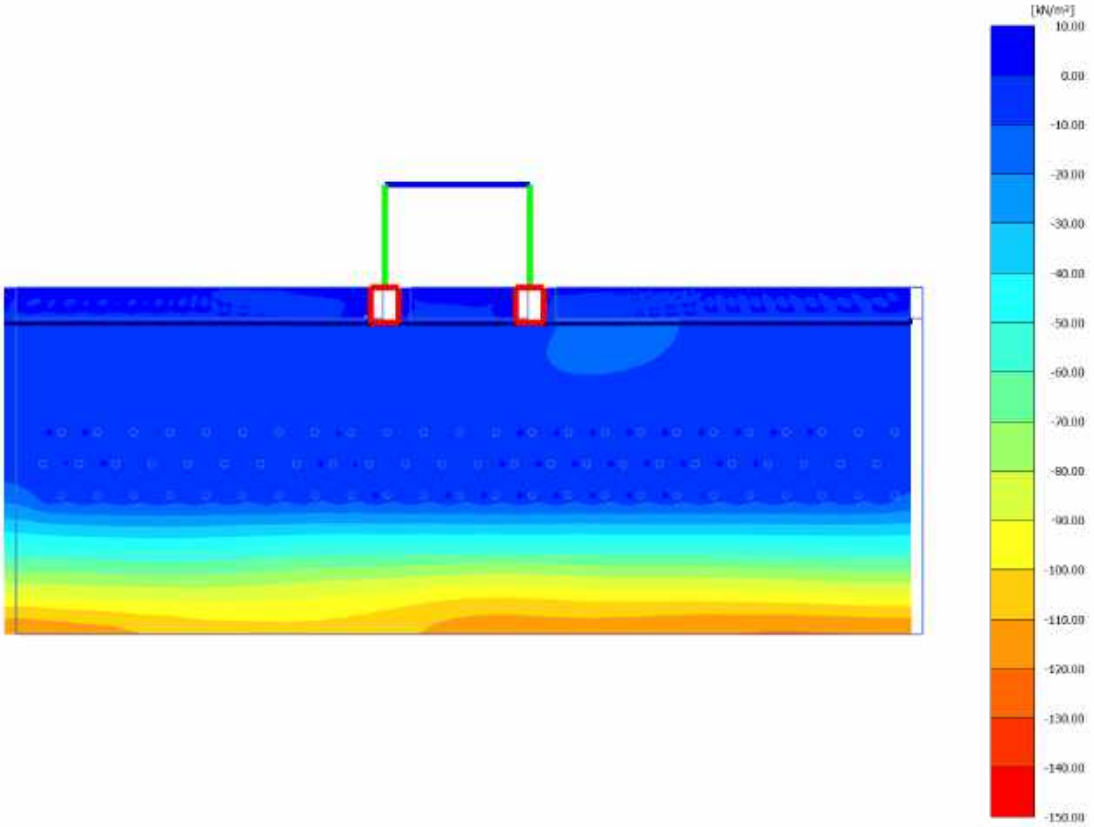

DS_HDU_H15_s10

This project has received funding from the European Union's Horizon 2020 research and innovation programme under grant agreement No. 700748

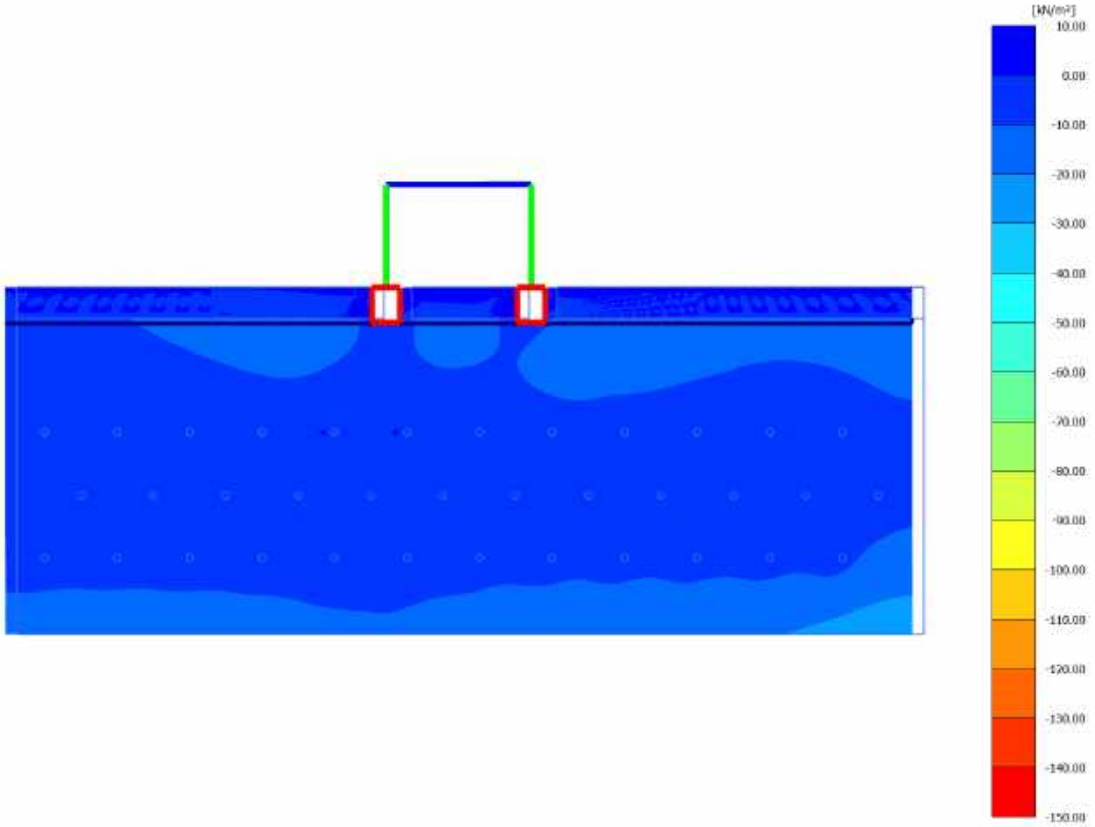

DS_HDU_H15_s15

This project has received funding from the European Union's Horizon 2020 research and innovation programme under grant agreement No. 700748

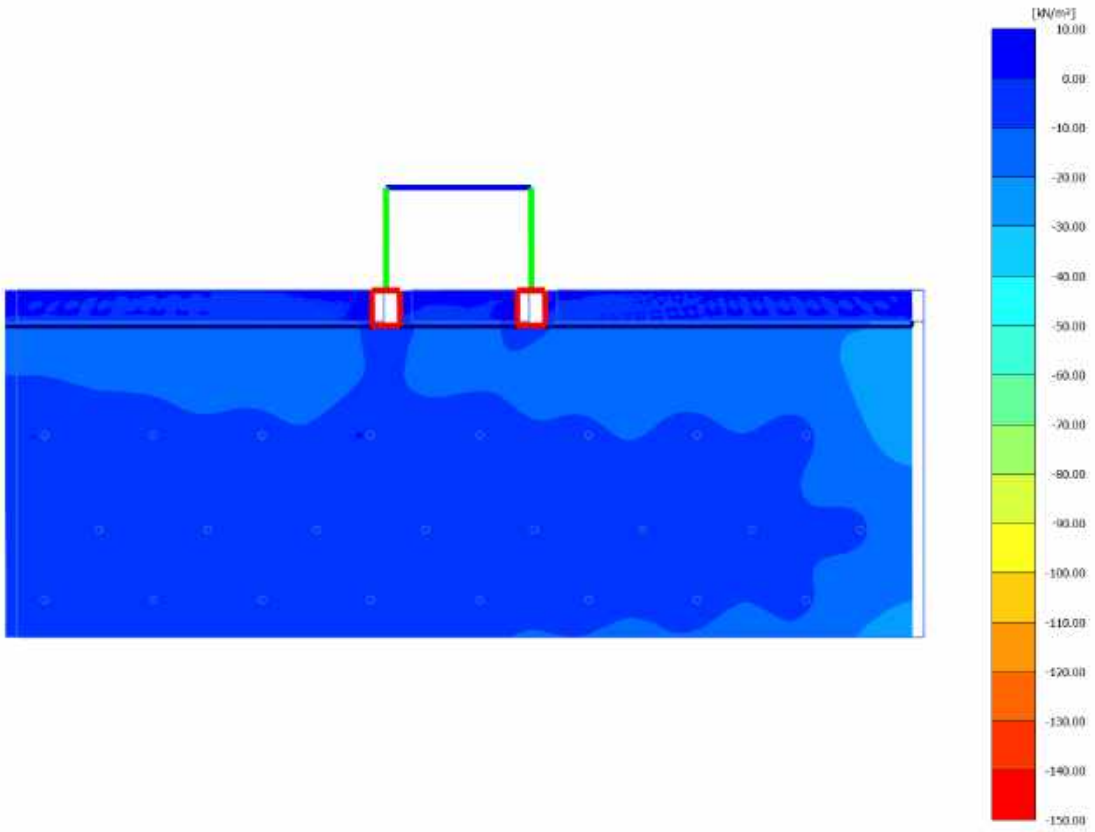

This project has received funding from the European Union's Horizon 2020 research and innovation programme under grant agreement No. 700748

APPENDIX C: 1-D model results (§8.1)

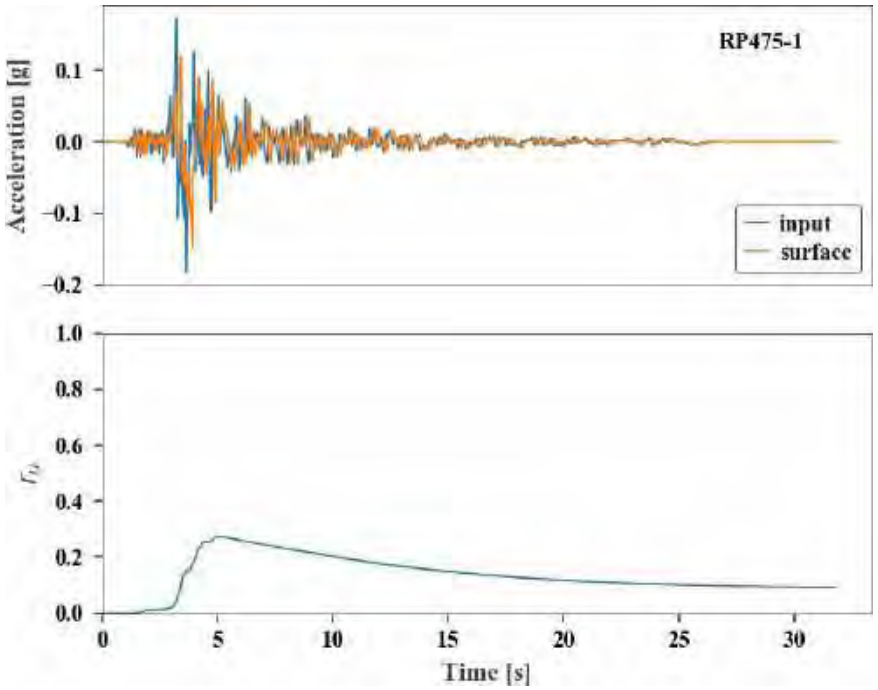

Figure B.1 Acceleration at base and bottom of the model, motion 1, 475-1

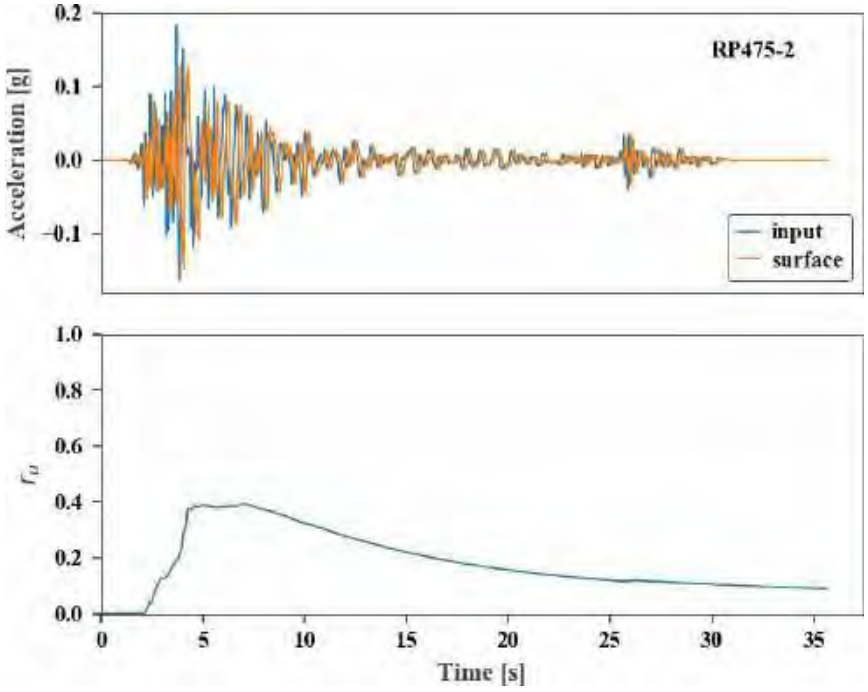

Figure B.2. Acceleration at base and bottom of the model, motion 2, 475-2.

This project has received funding from the European Union's Horizon 2020 research and innovation programme under grant agreement No. 700748

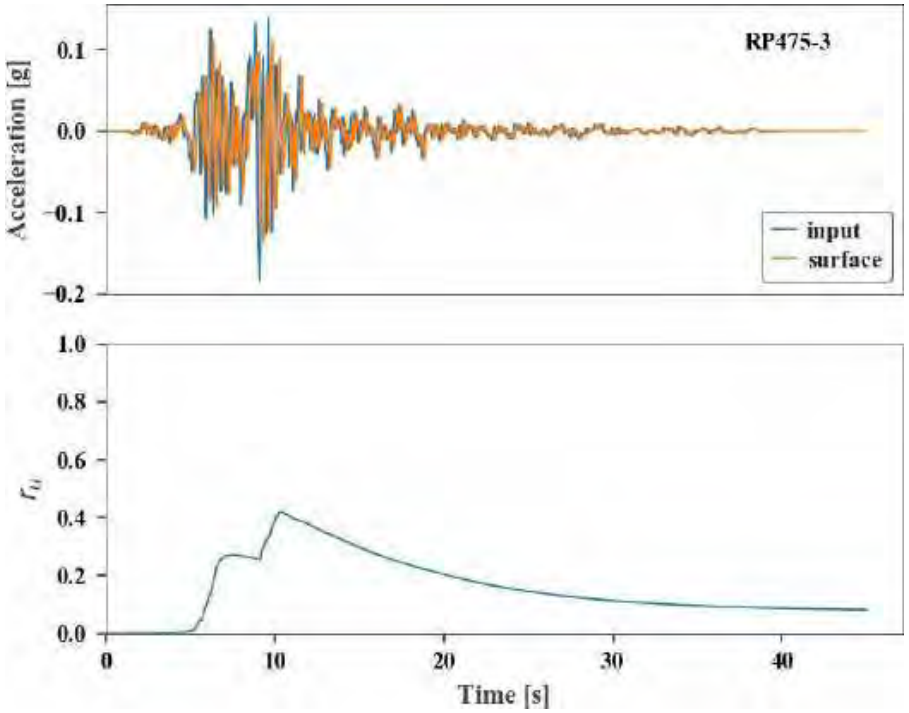

Figure B.3. Acceleration at base and bottom of the model, motion 3, 475-3.

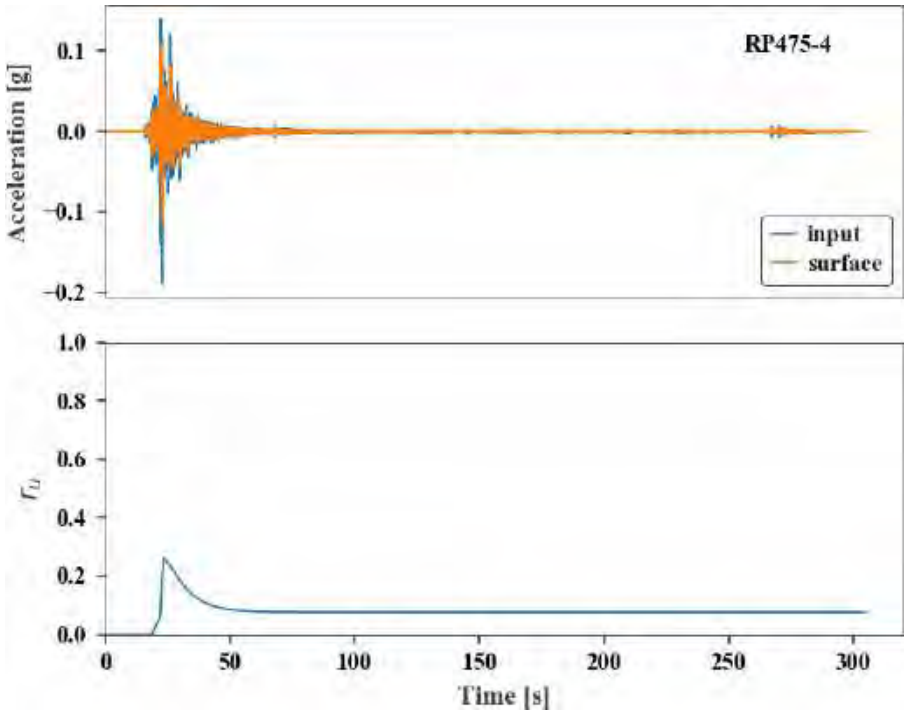

Figure B.4. Acceleration at base and bottom of the model, motion 4, 475-4.

This project has received funding from the European Union's Horizon 2020 research and innovation programme under grant agreement No. 700748

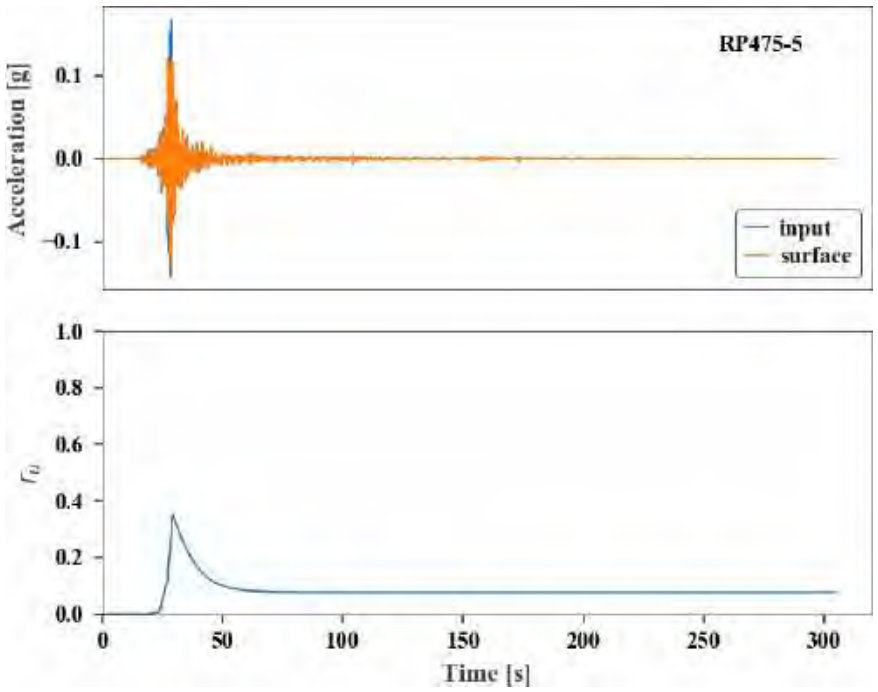

Figure B.5. Acceleration at base and bottom of the model, motion 5, 475-5.

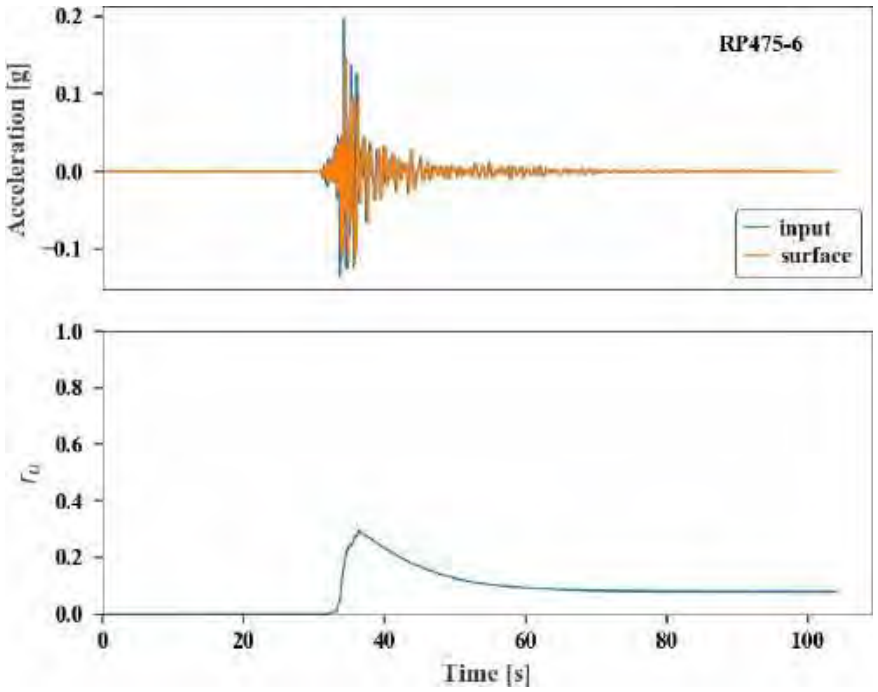

Figure B.6. Acceleration at base and bottom of the model, motion 6, 475-6.

This project has received funding from the European Union's Horizon 2020 research and innovation programme under grant agreement No. 700748

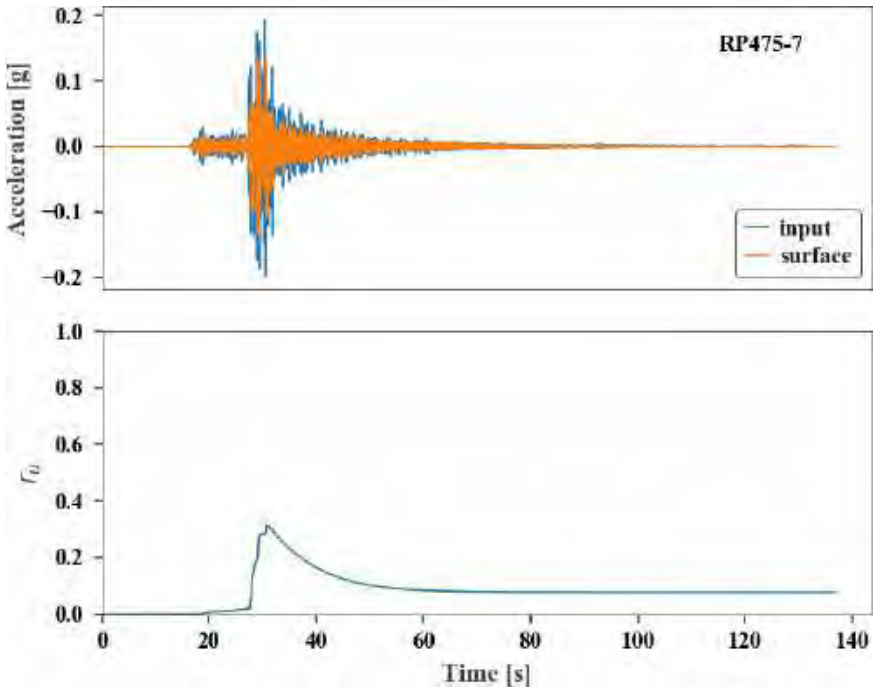

Figure B.7. Acceleration at base and bottom of the model, motion 7, 475-7.

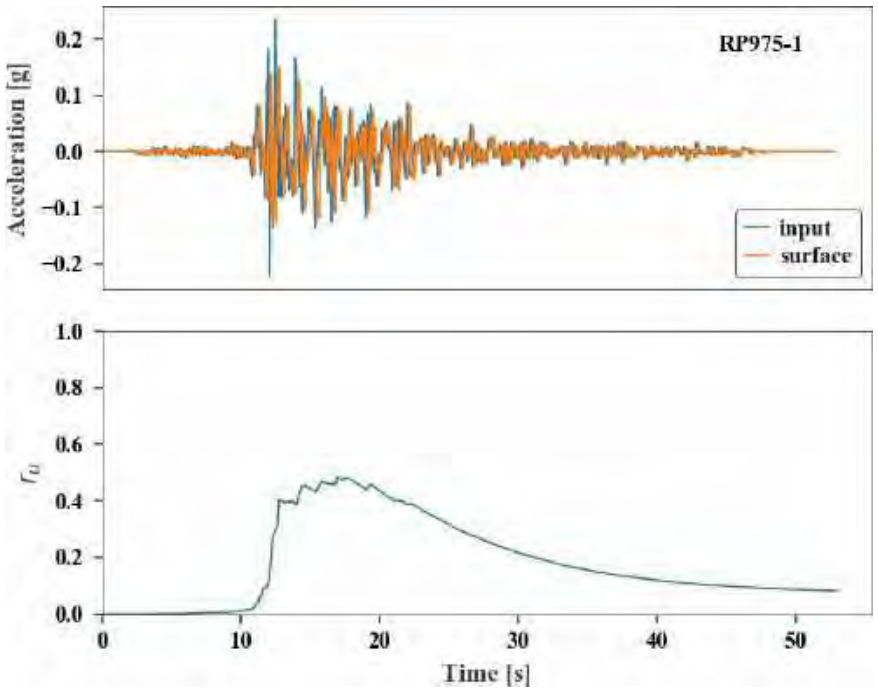

Figure B.8. Acceleration at base and bottom of the model, motion 8, 975-1.

This project has received funding from the European Union's Horizon 2020 research and innovation programme under grant agreement No. 700748

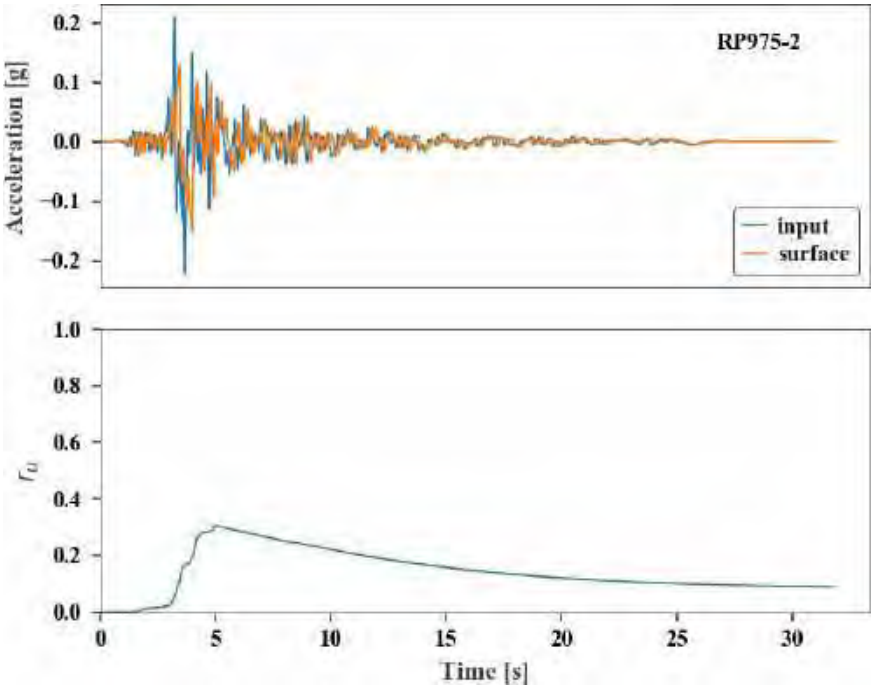

Figure B.9. Acceleration at base and bottom of the model, motion 9, 975-2.

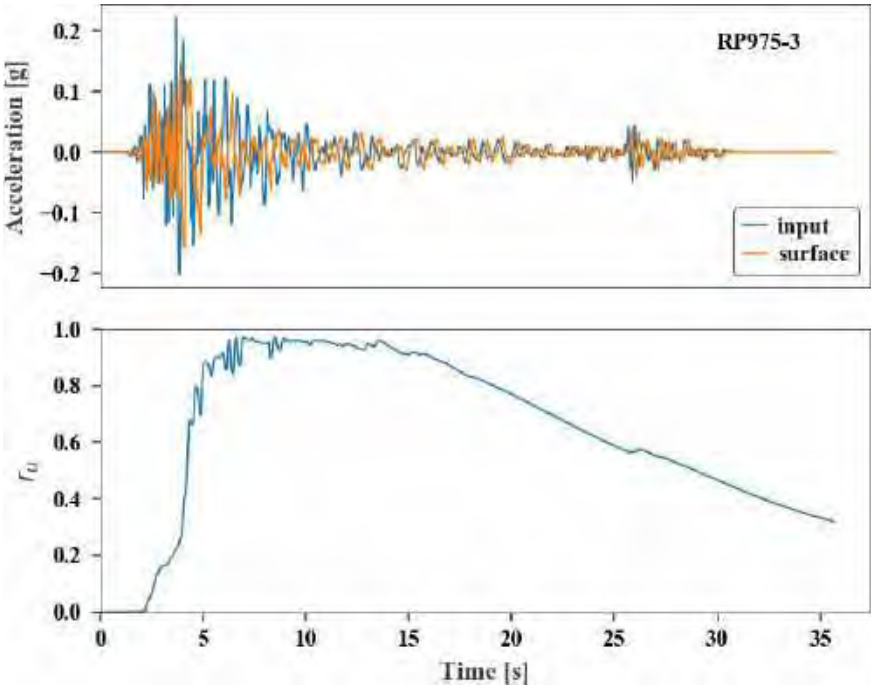

Figure B.10. Acceleration at base and bottom of the model, motion 10, 975-3.

This project has received funding from the European Union's Horizon 2020 research and innovation programme under grant agreement No. 700748

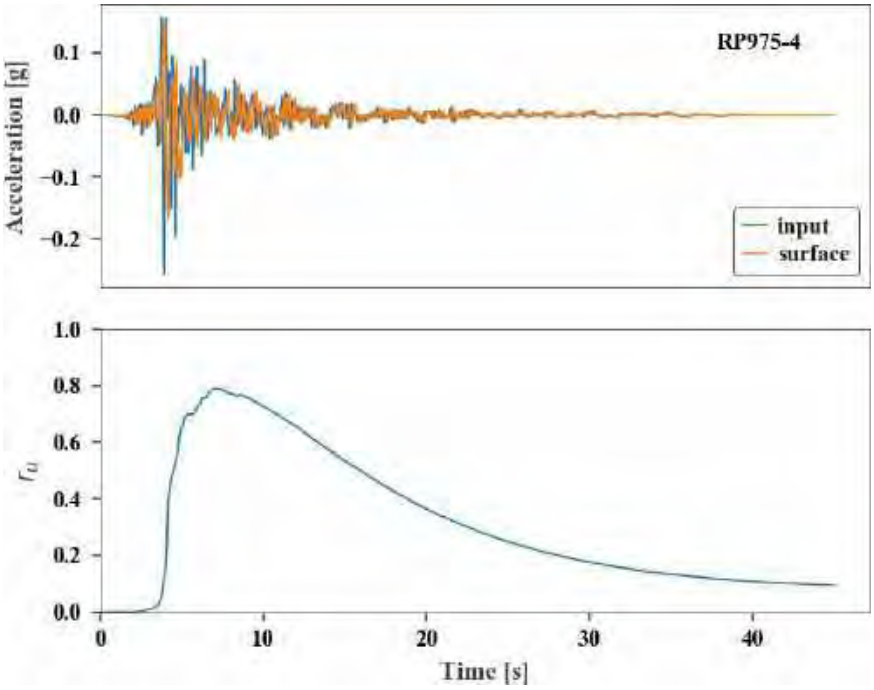

Figure B.11. Acceleration at base and bottom of the model, motion 11, 975-4.

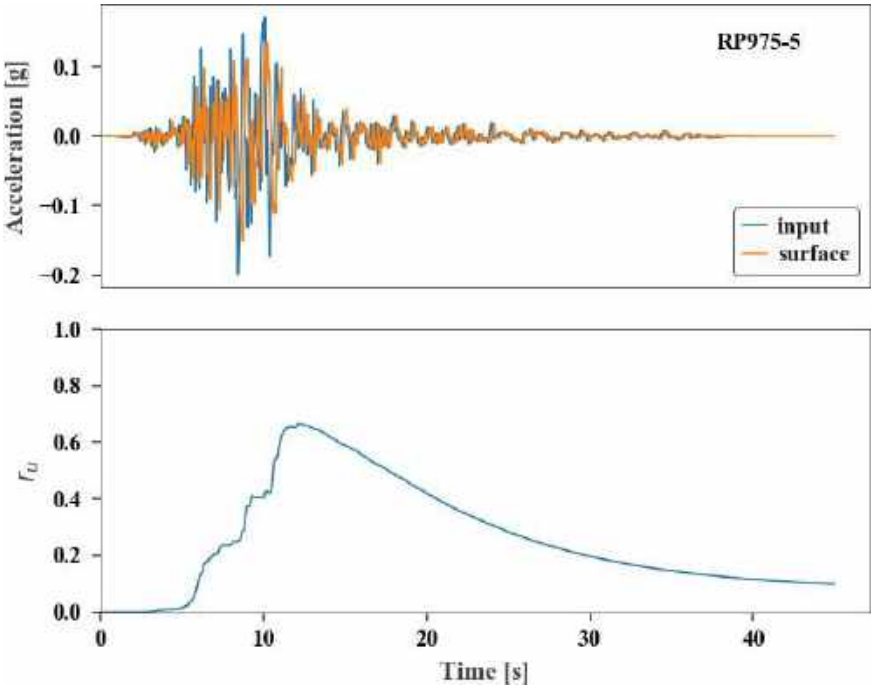

Figure B.12. Acceleration at base and bottom of the model, motion 12, 975-5.

This project has received funding from the European Union's Horizon 2020 research and innovation programme under grant agreement No. 700748

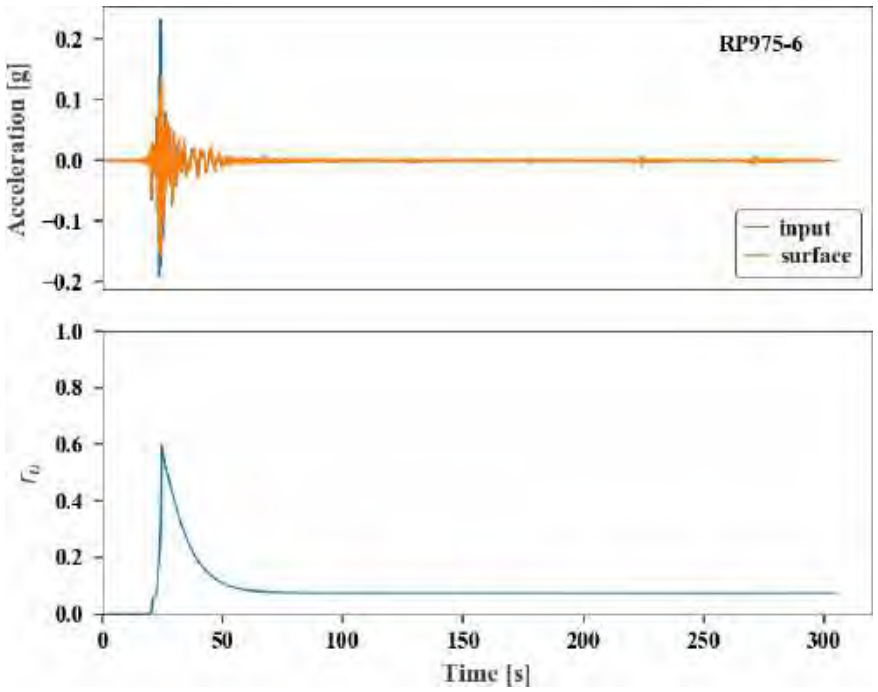

Figure B.13. Acceleration at base and bottom of the model, motion 13, 975-6.

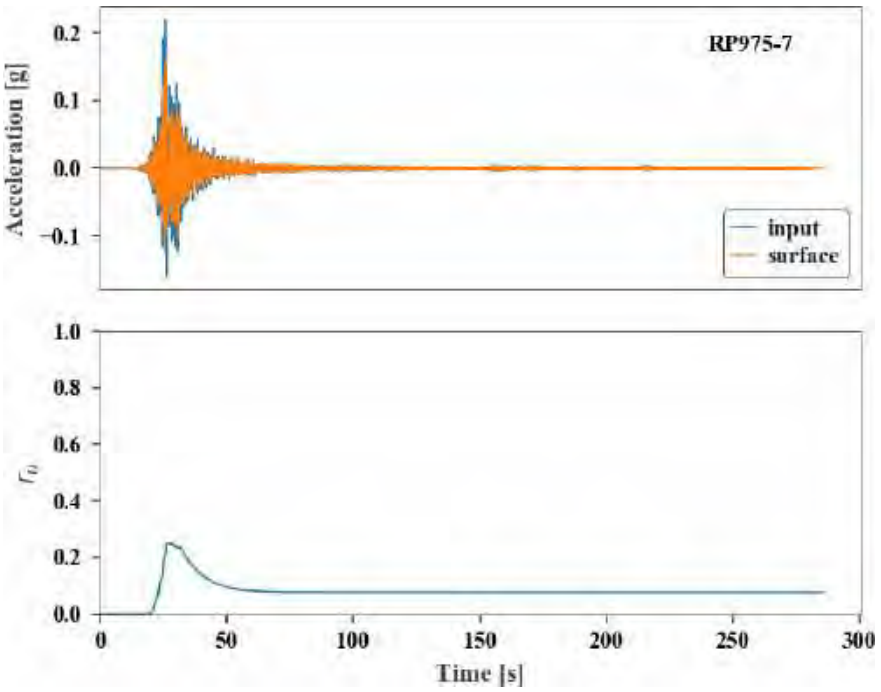

Figure B.14. Acceleration at base and bottom of the model, motion 14, 975-7.

This project has received funding from the European Union's Horizon 2020 research and innovation programme under grant agreement No. 700748

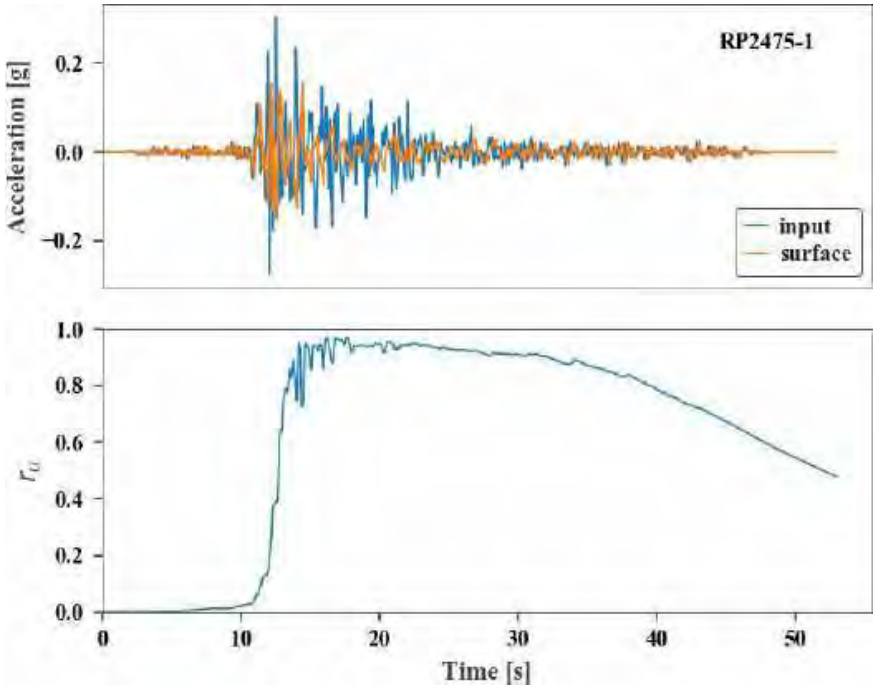

Figure B. 15. Acceleration at base and bottom of the model, motion 15, 2475-1.

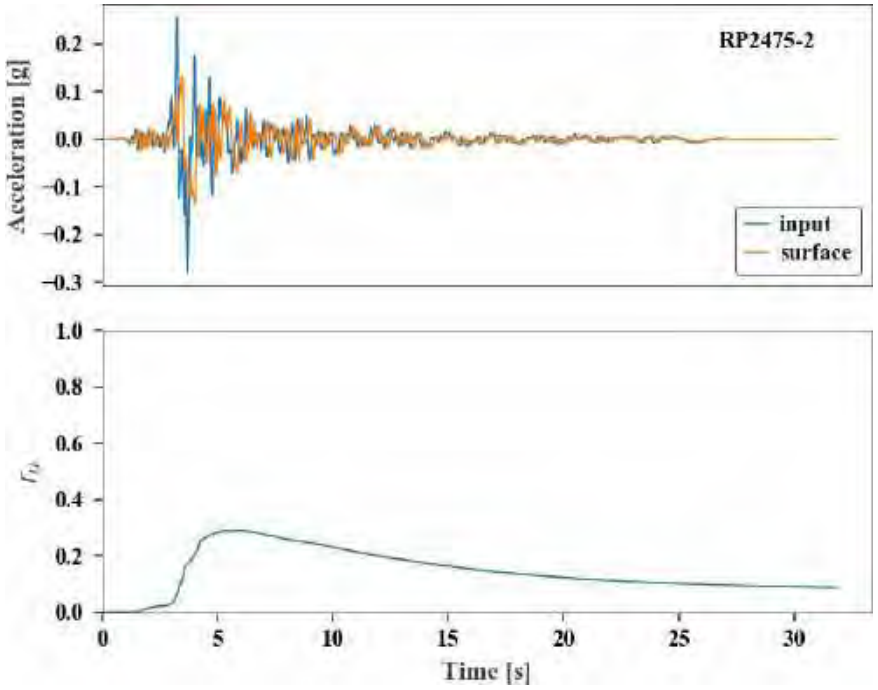

Figure B.16. Acceleration at base and bottom of the model, motion 16, 2475-2.

This project has received funding from the European Union's Horizon 2020 research and innovation programme under grant agreement No. 700748

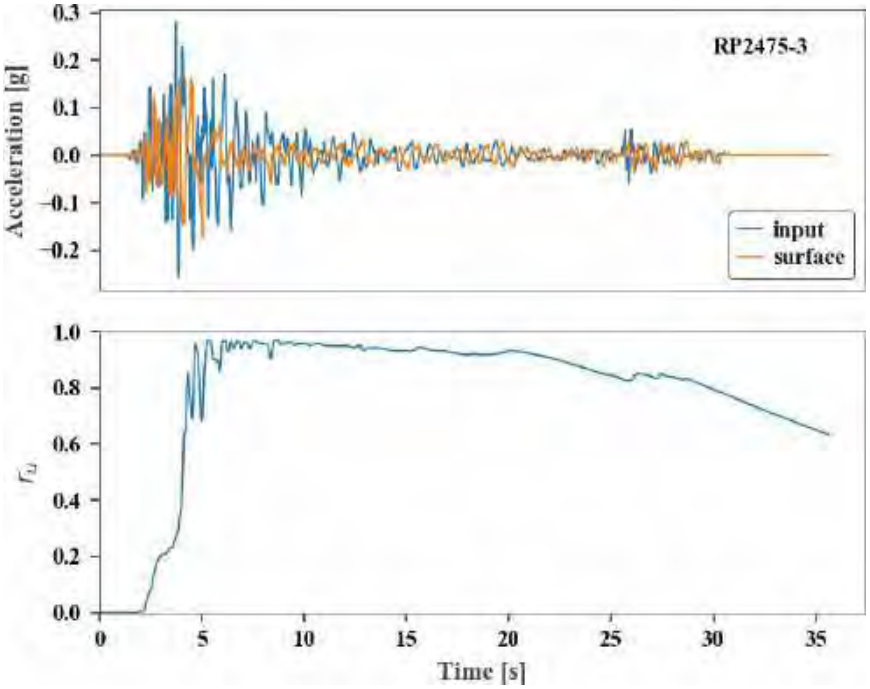

Figure B.17. Acceleration at base and bottom of the model, motion 17, 2475-3.

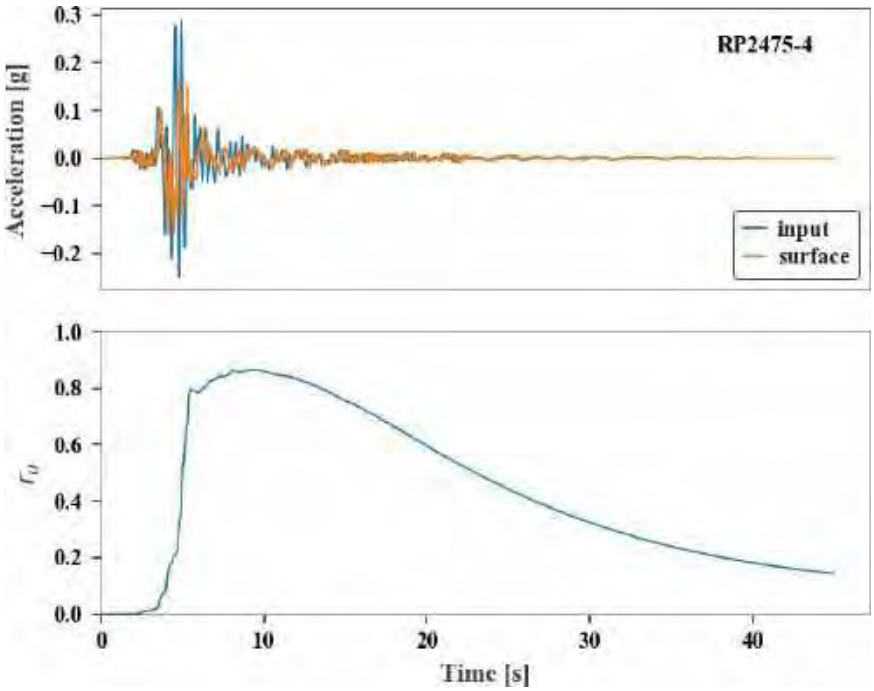

Figure B.18. Acceleration at base and bottom of the model, motion 18, 2475-4.

This project has received funding from the European Union's Horizon 2020 research and innovation programme under grant agreement No. 700748

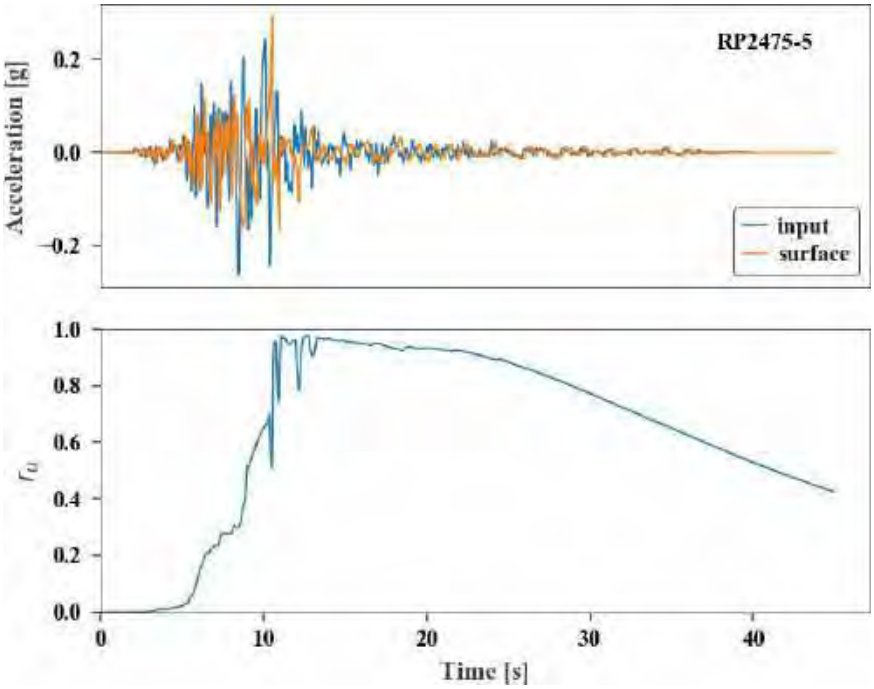

Figure B.19. Acceleration at base and bottom of the model, motion 19, 2475-5.

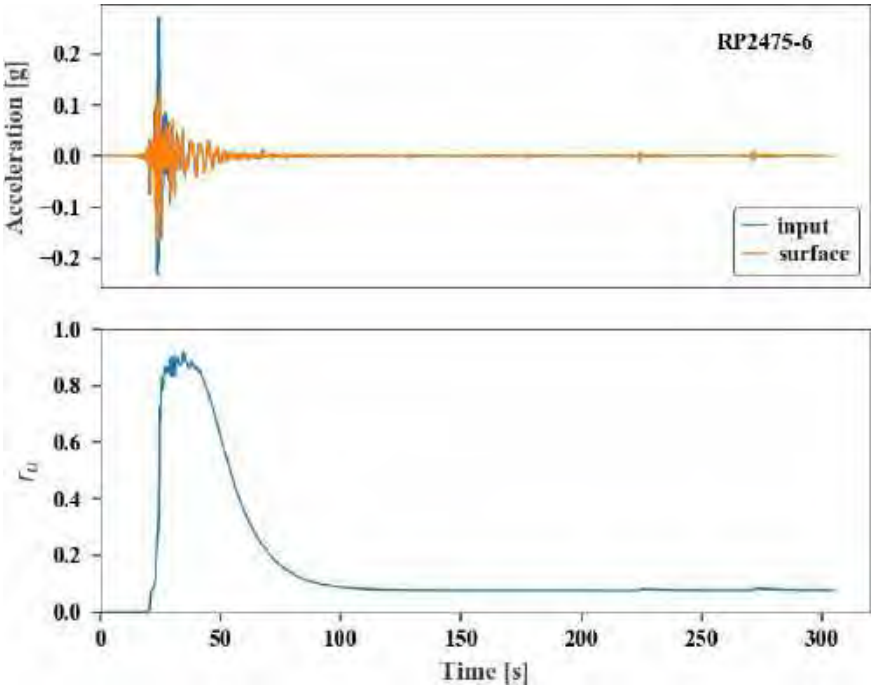

Figure B.20. Acceleration at base and bottom of the model, motion 20, 2475-6.

This project has received funding from the European Union's Horizon 2020 research and innovation programme under grant agreement No. 700748

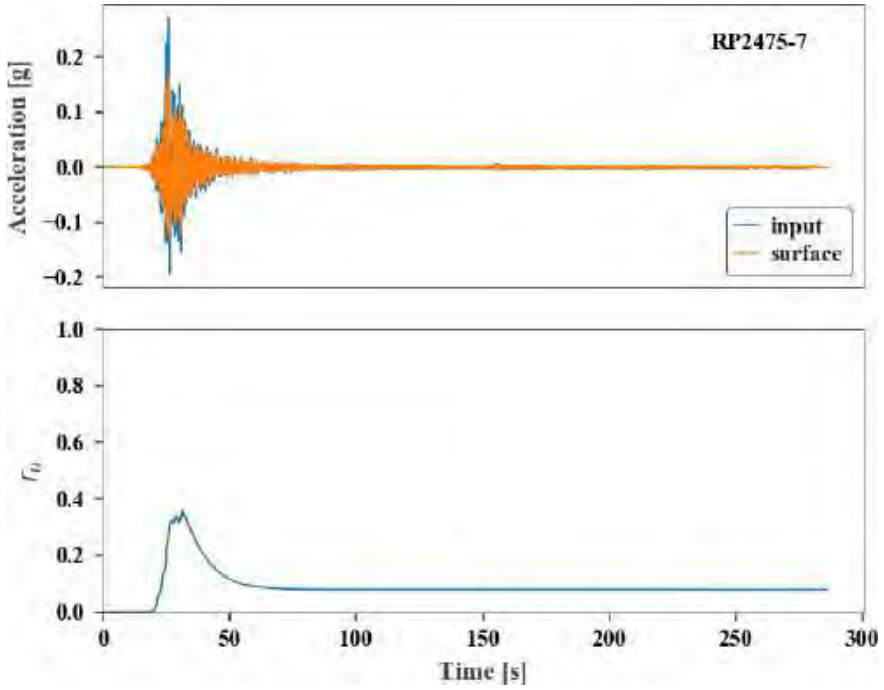

Figure B.21. Acceleration at base and bottom of the model, motion 21, 2475-7.

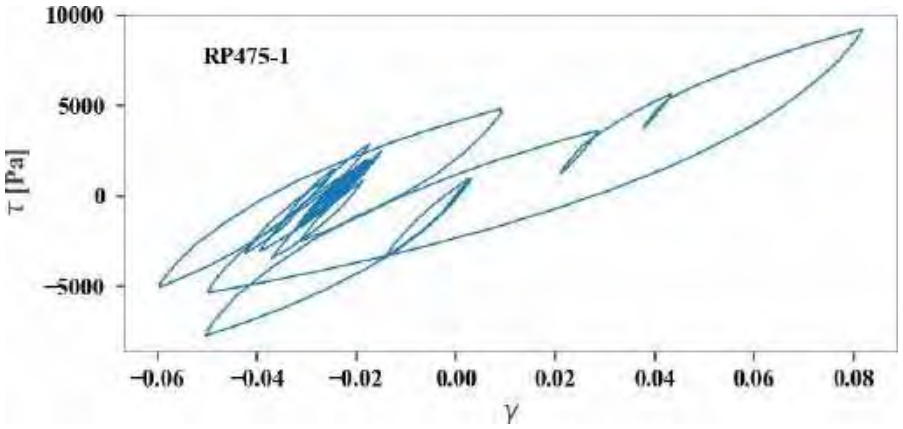

Figure B.22. Shear stress vs shear strain, motion 1, 475-1.

This project has received funding from the European Union's Horizon 2020 research and innovation programme under grant agreement No. 700748

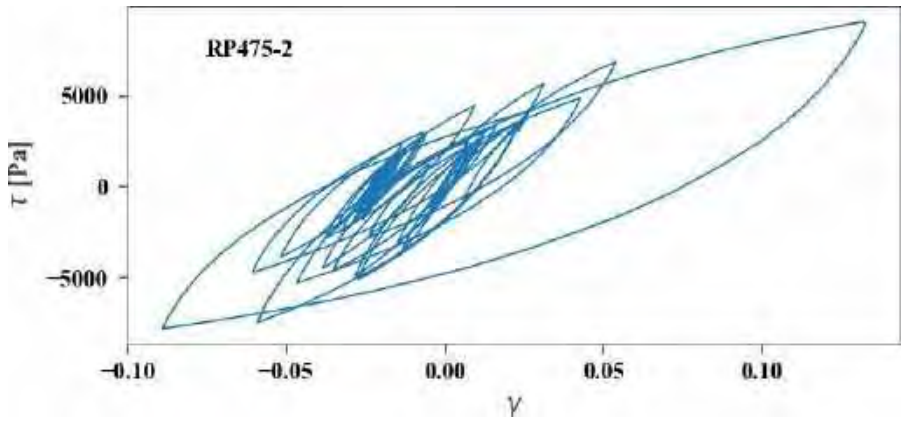

Figure B.23. Shear stress vs shear strain, motion 2, 475-2.

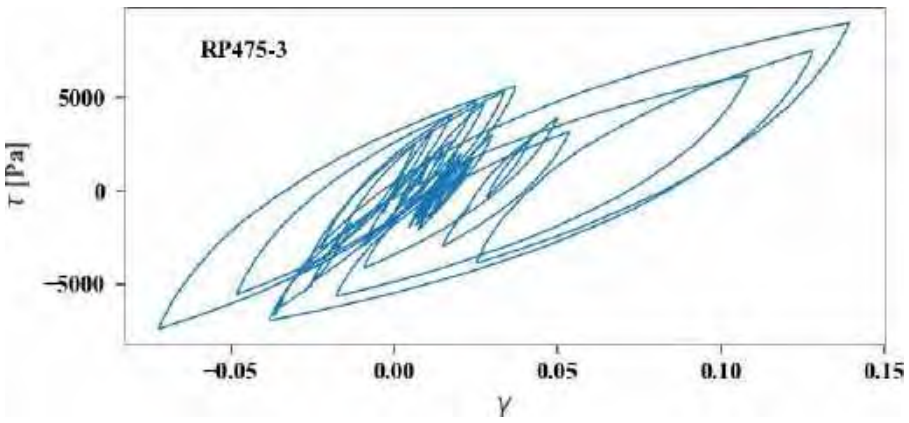

Figure B.24. Shear stress vs shear strain, motion 3, 475-3.

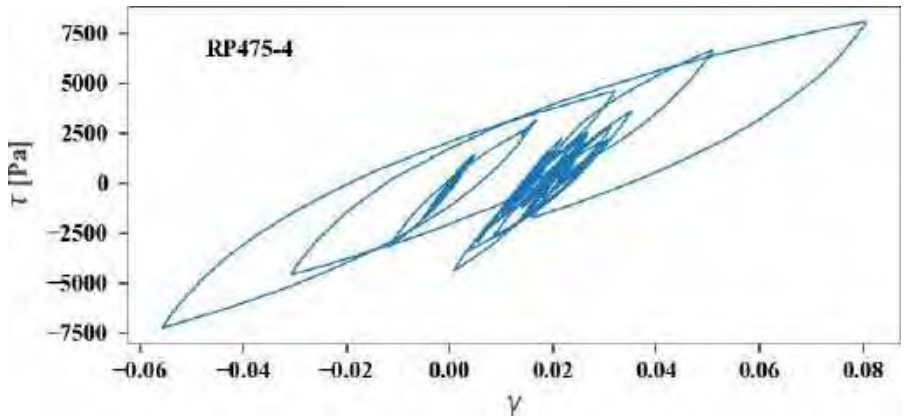

Figure B.25. Shear stress vs shear strain, motion 4, 475-4.

This project has received funding from the European Union's Horizon 2020 research and innovation programme under grant agreement No. 700748

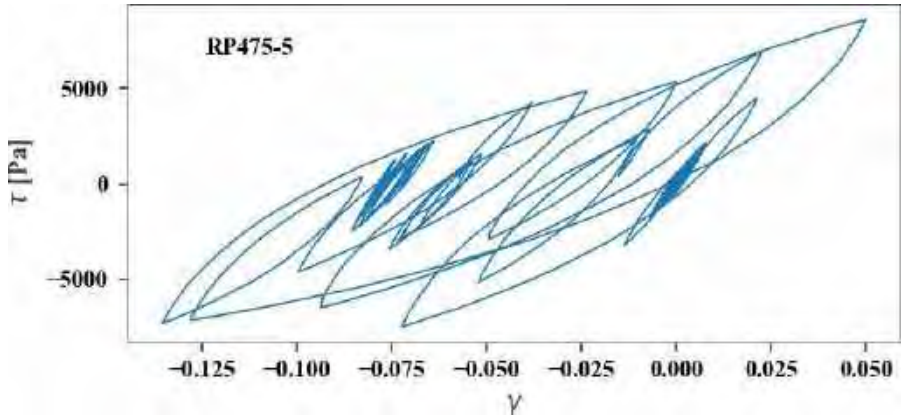

Figure B.26. Shear stress vs shear strain, motion 5, 475-5.

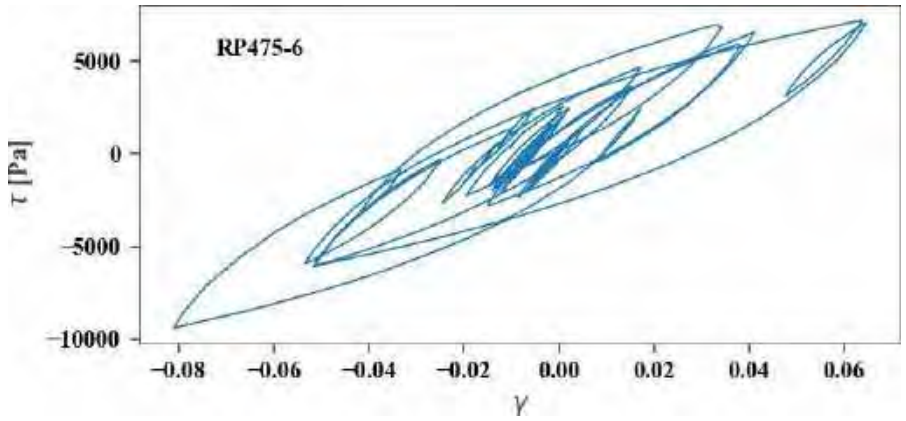

Figure B.27. Shear stress vs shear strain, motion 6, 475-6.

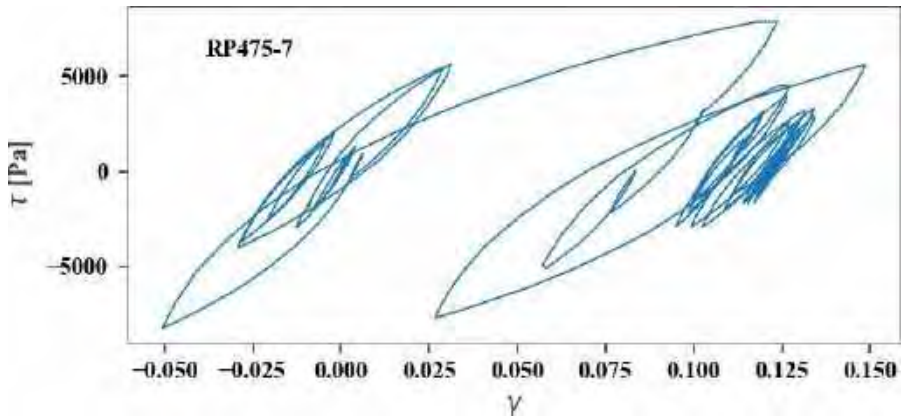

Figure B.28. Shear stress vs shear strain, motion 7, 475-7.

This project has received funding from the European Union's Horizon 2020 research and innovation programme under grant agreement No. 700748

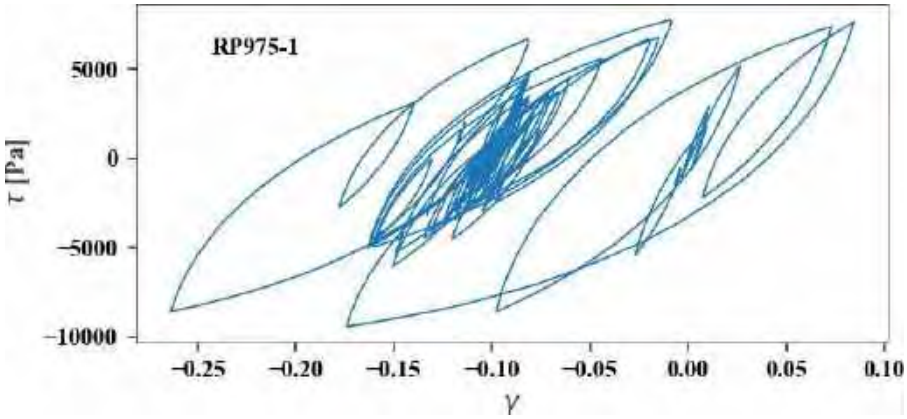

Figure B.29. Shear stress vs shear strain, motion 8, 975-1.

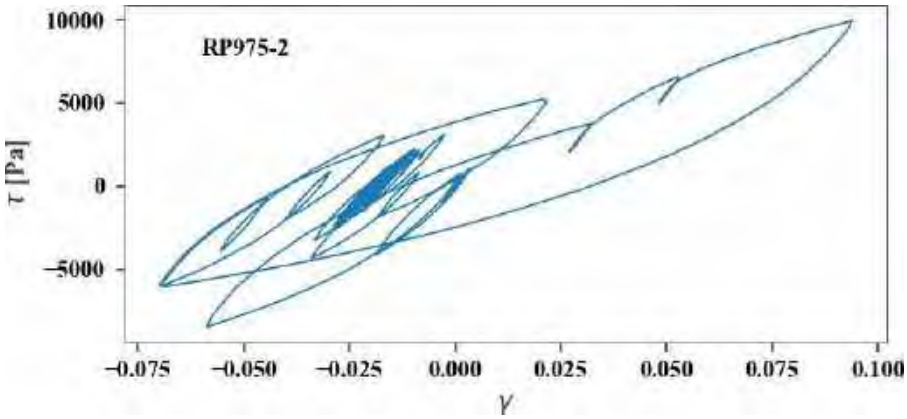

Figure B.30. Shear stress vs shear strain, motion 9, 975-2.

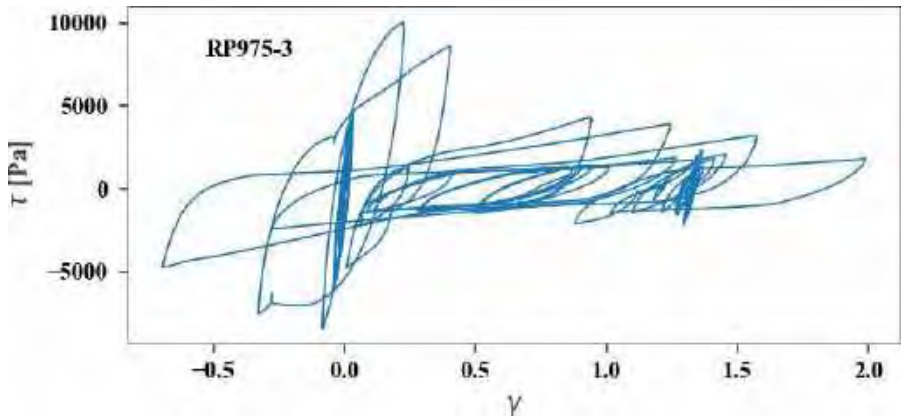

Figure B.31. Shear stress vs shear strain, motion 10, 975-3.

This project has received funding from the European Union's Horizon 2020 research and innovation programme under grant agreement No. 700748

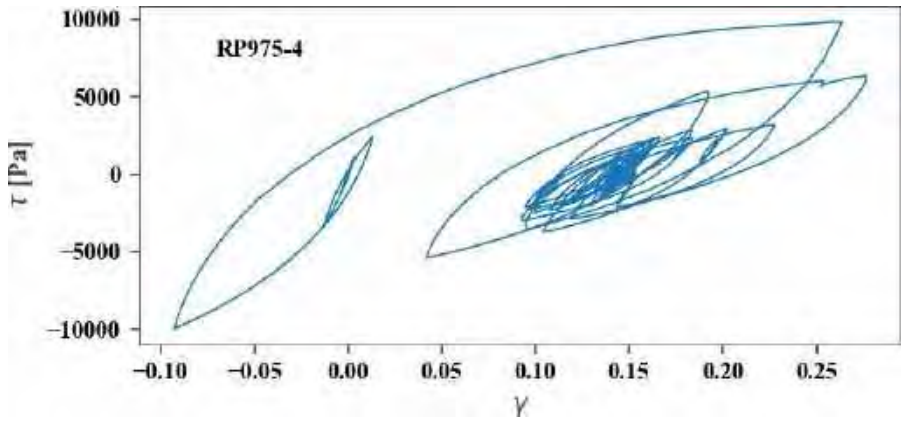

Figure B.32. Shear stress vs shear strain, motion 11, 975-4.

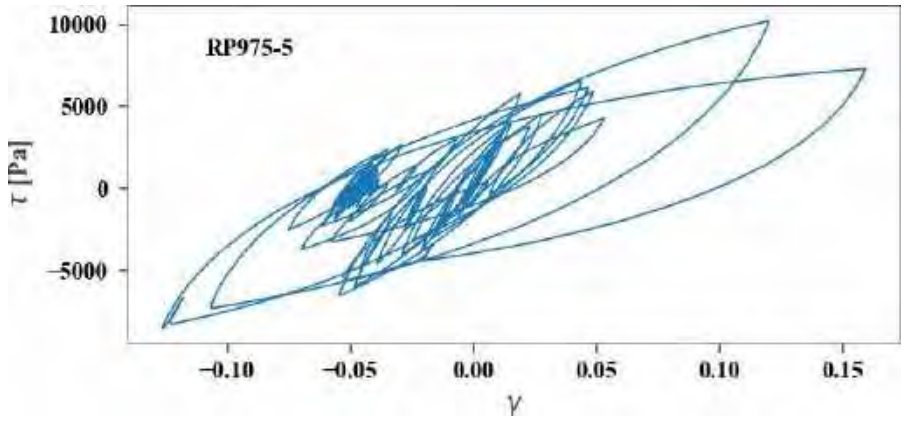

Figure B. 33. Shear stress vs shear strain, motion 12, 975-5.

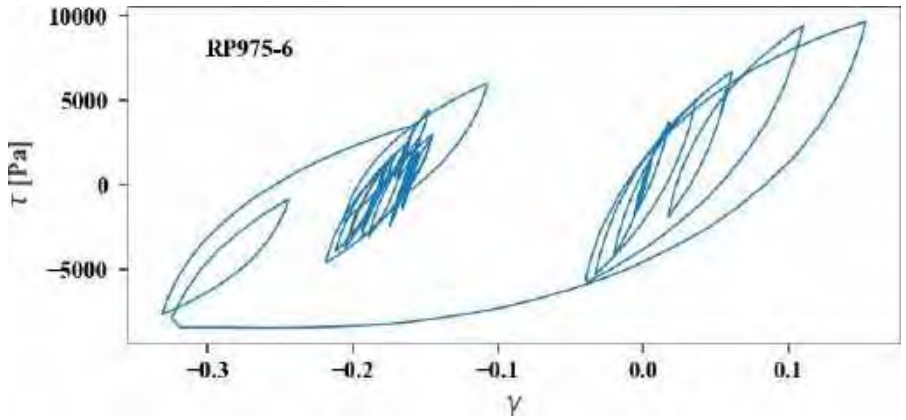

Figure B.34. Shear stress vs shear strain, motion 13, 975-6.

This project has received funding from the European Union's Horizon 2020 research and innovation programme under grant agreement No. 700748

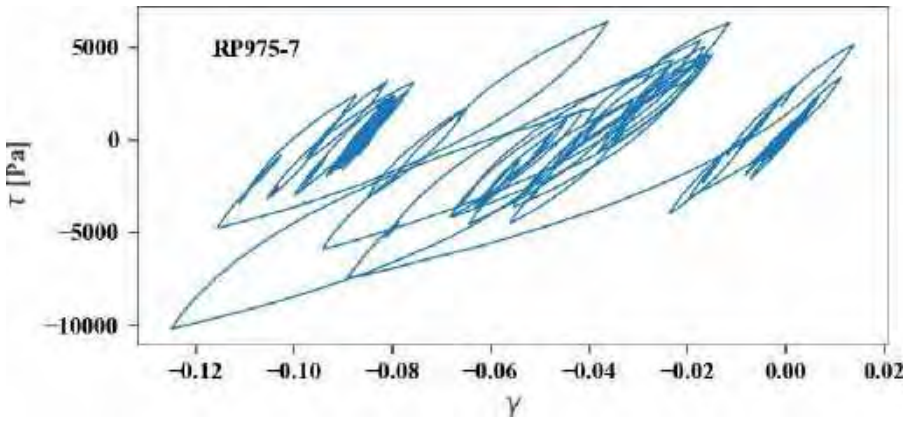

Figure B.35. Shear stress vs shear strain, motion 14, 975-7.

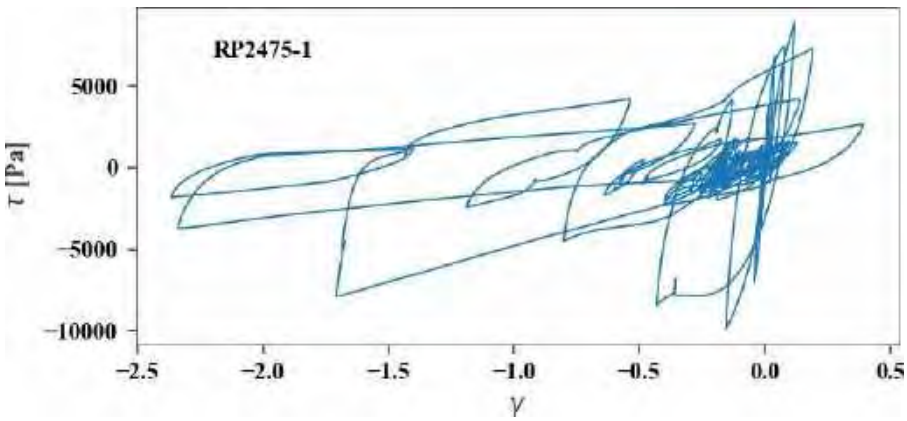

Figure B.36. Shear stress vs shear strain, motion 15, 2475-1.

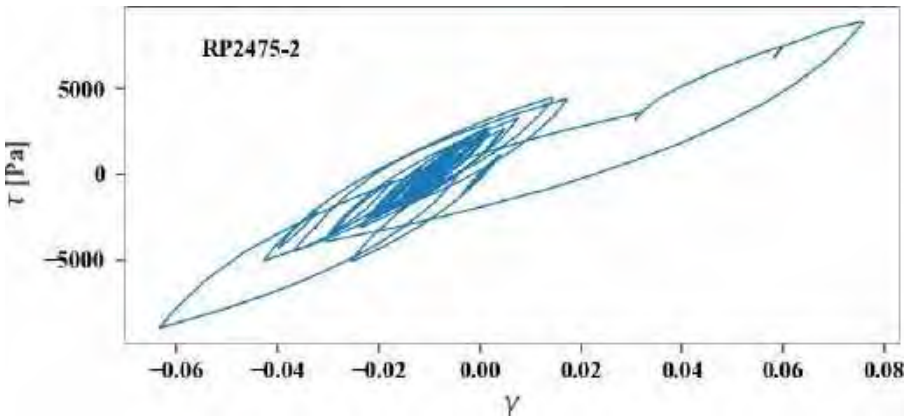

Figure B.37. Shear stress vs shear strain, motion 16, 2475-2.

This project has received funding from the European Union's Horizon 2020 research and innovation programme under grant agreement No. 700748

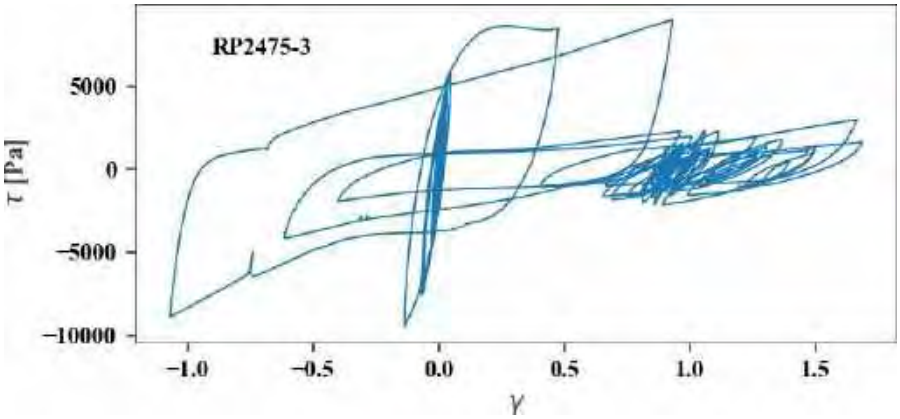

Figure B.38. Shear stress vs shear strain, motion 17, 2475-3.

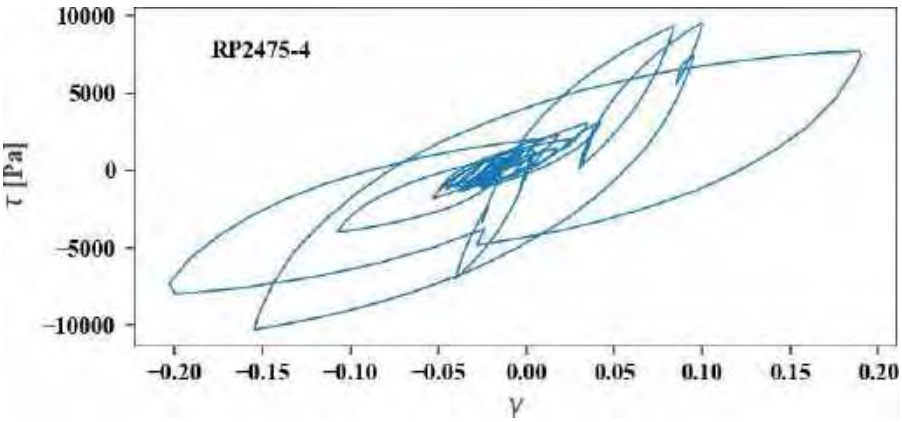

Figure B.39. Shear stress vs shear strain, motion 18, 2475-4.

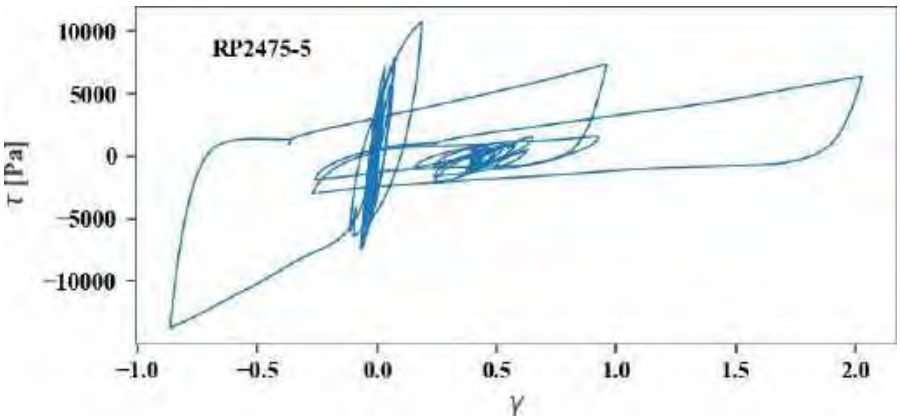

Figure B.40. Shear stress vs shear strain, motion 19, 2475-5.

This project has received funding from the European Union's Horizon 2020 research and innovation programme under grant agreement No. 700748

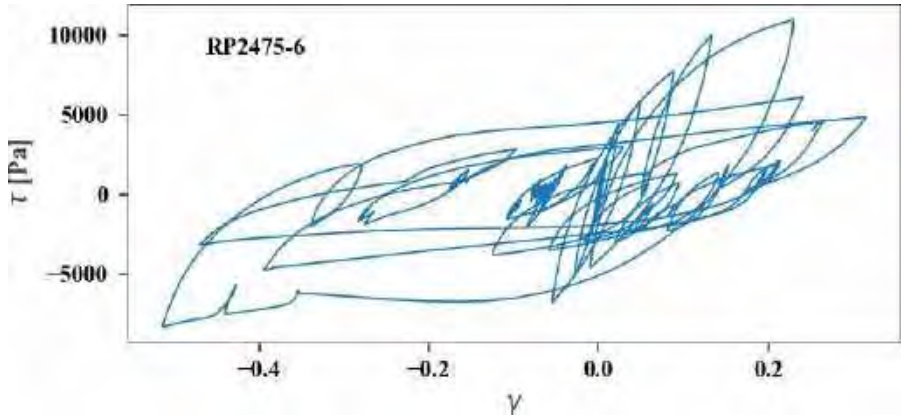

Figure B.41. Shear stress vs shear strain, motion 20, 2475-6.

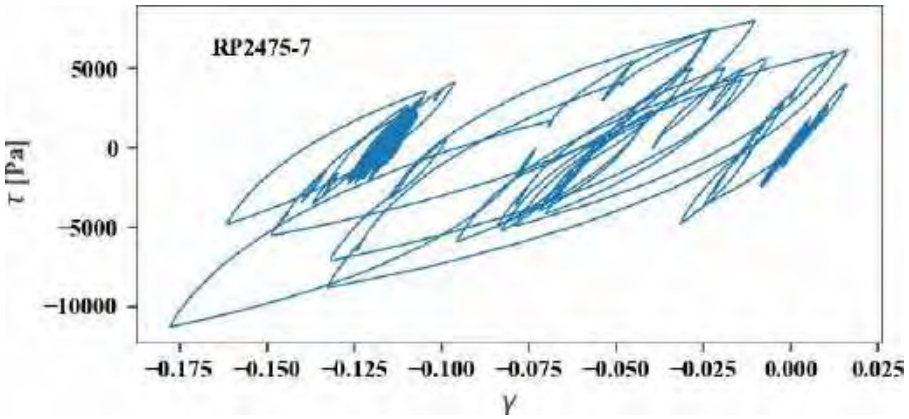

Figure B.42. Shear stress vs shear strain, motion 21, 2475-7.

This project has received funding from the European Union's Horizon 2020 research and innovation programme under grant agreement No. 700748

APPENDIX D: 2-D model results (§8.2)

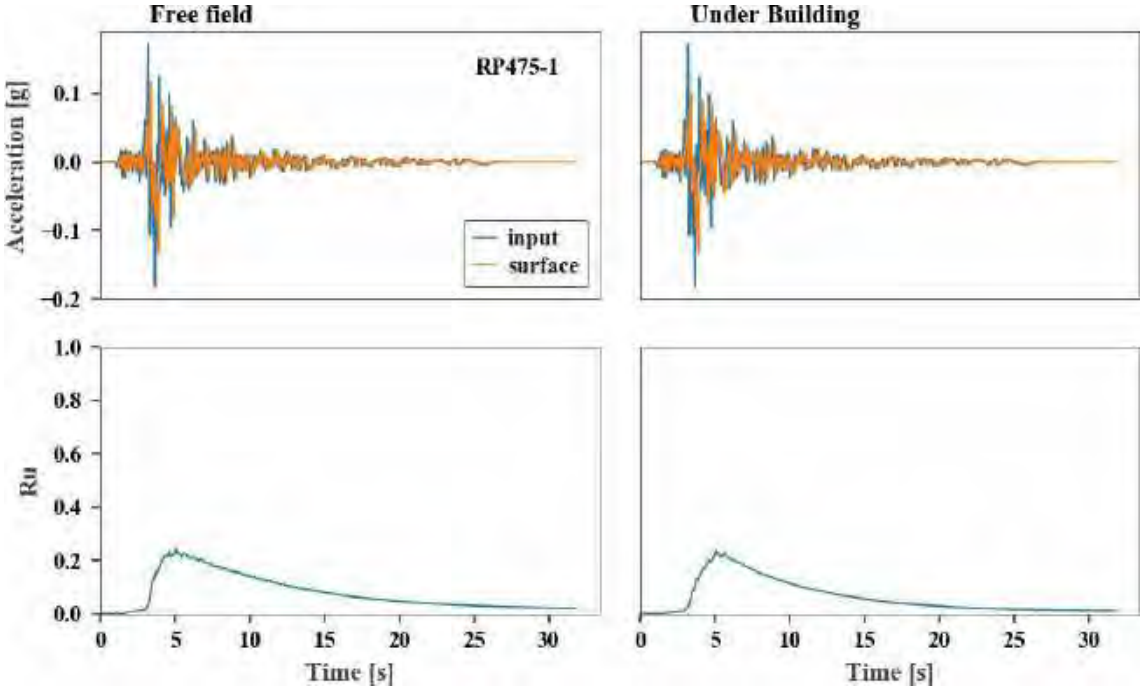

Figure C.1. Acceleration at base and bottom of the model, motion 1, 475-1.

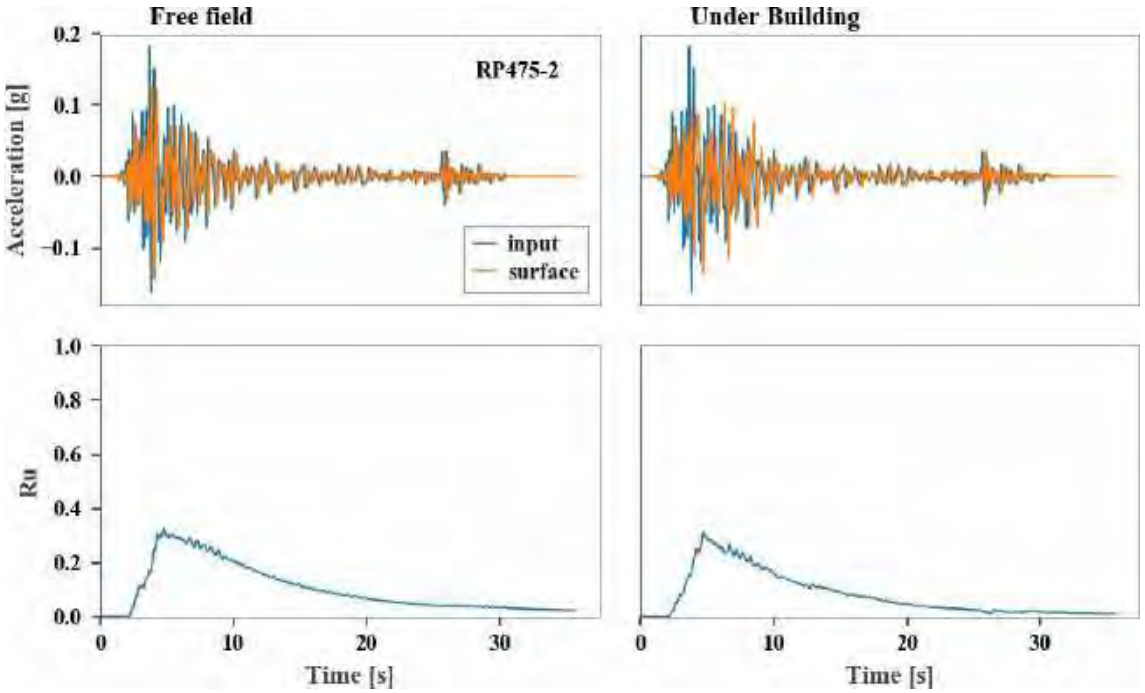

Figure C.2. Acceleration at base and bottom of the model, motion 2, 475-2.

This project has received funding from the European Union's Horizon 2020 research and innovation programme under grant agreement No. 700748

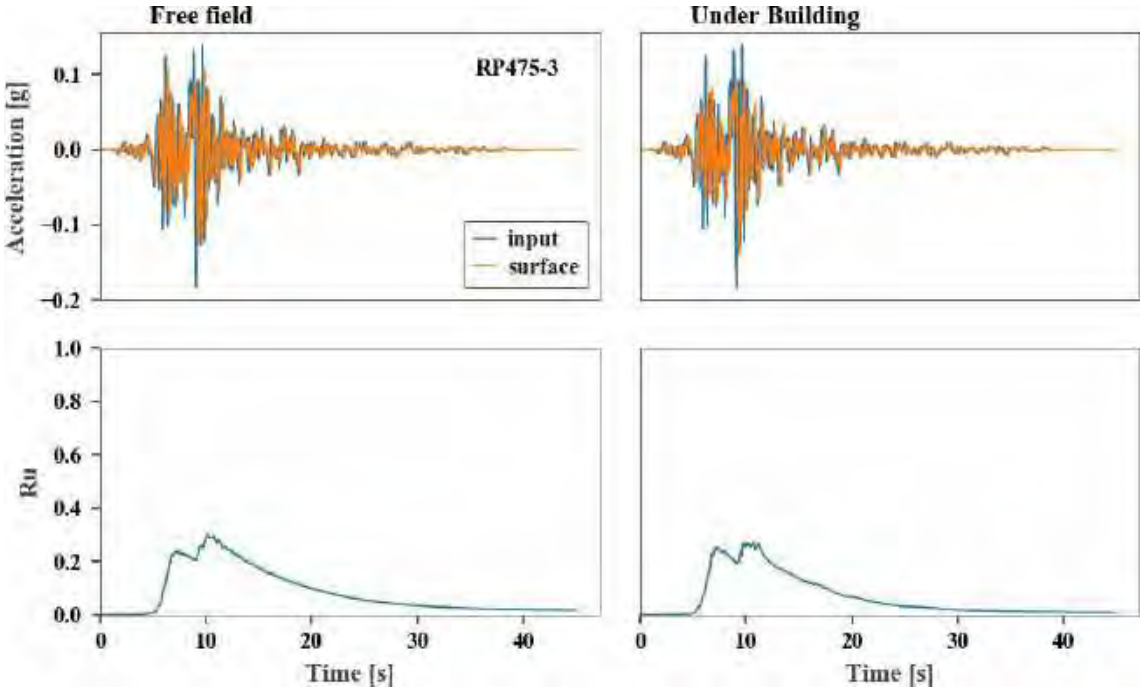

Figure C.3. Acceleration at base and bottom of the model, motion 3, 475-3.

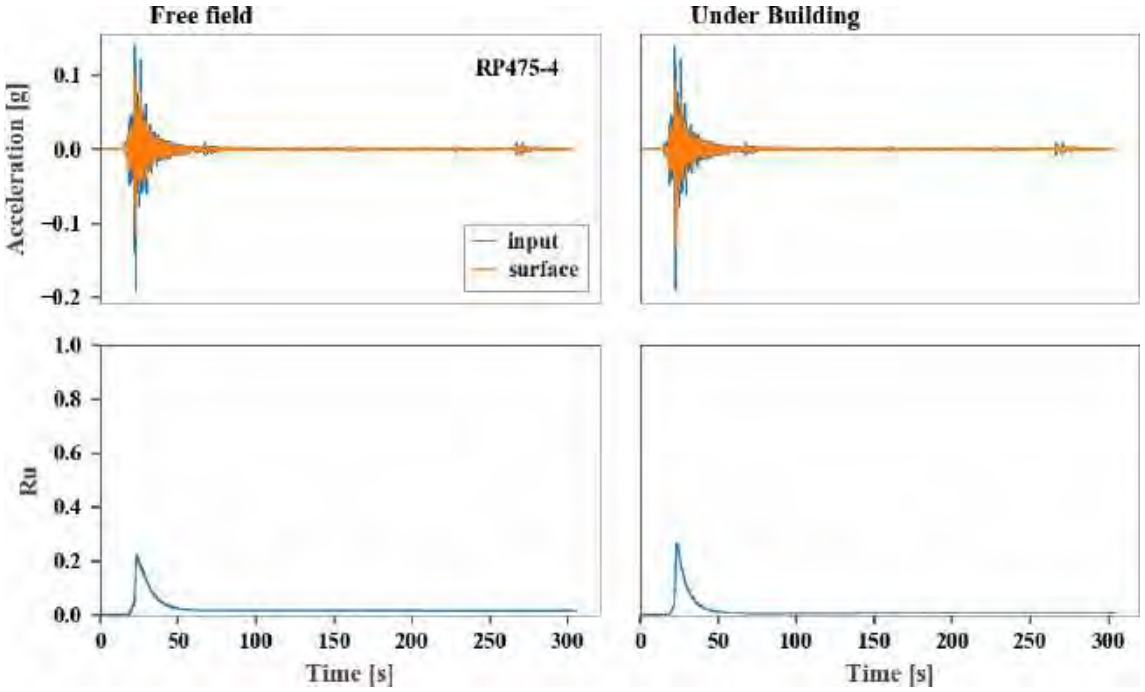

Figure C.4. Acceleration at base and bottom of the model, motion 4, 475-4.

This project has received funding from the European Union's Horizon 2020 research and innovation programme under grant agreement No. 700748

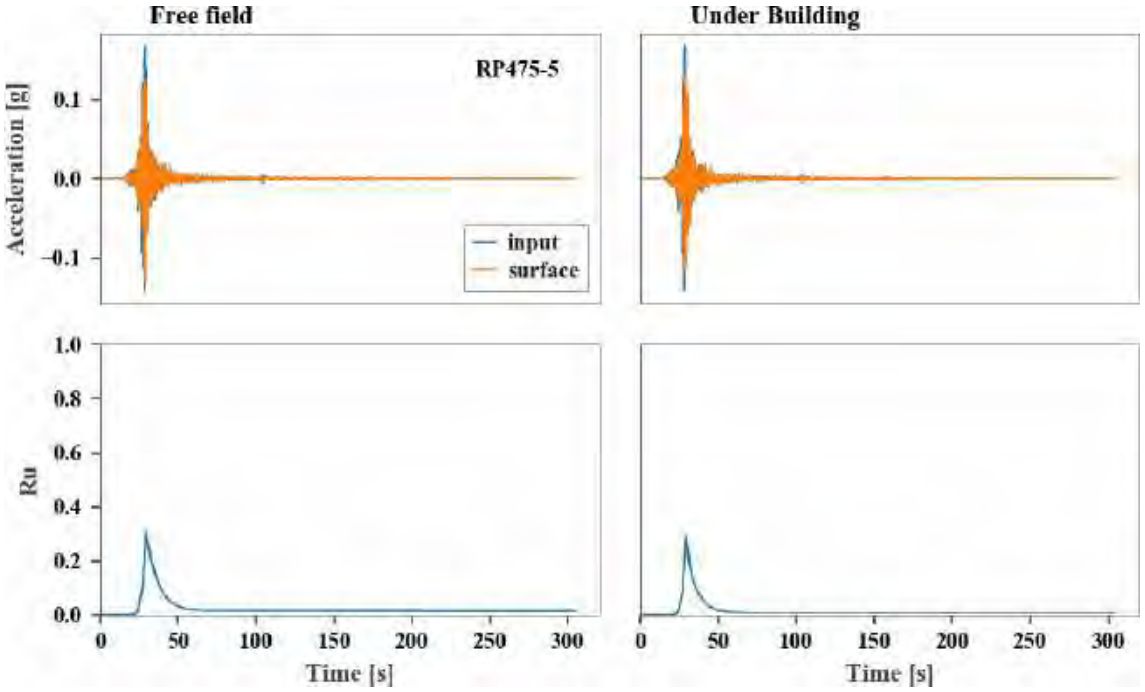

Figure C.5. Acceleration at base and bottom of the model, motion 5, 475-5.

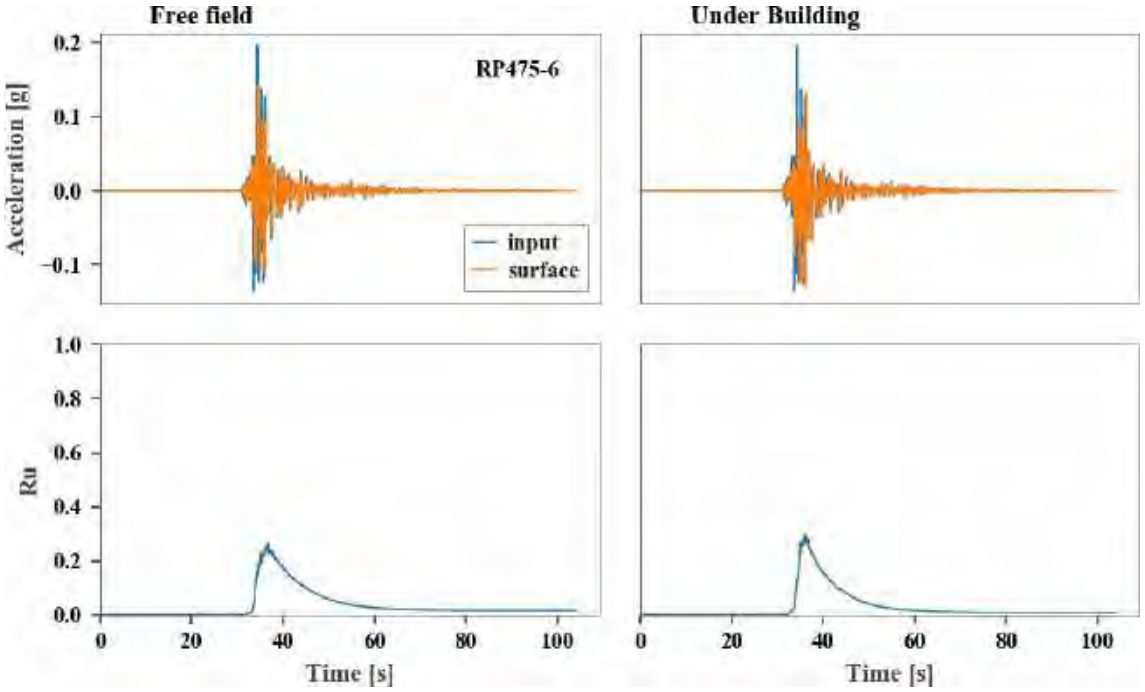

Figure C.6. Acceleration at base and bottom of the model, motion 6, 475-6.

This project has received funding from the European Union's Horizon 2020 research and innovation programme under grant agreement No. 700748

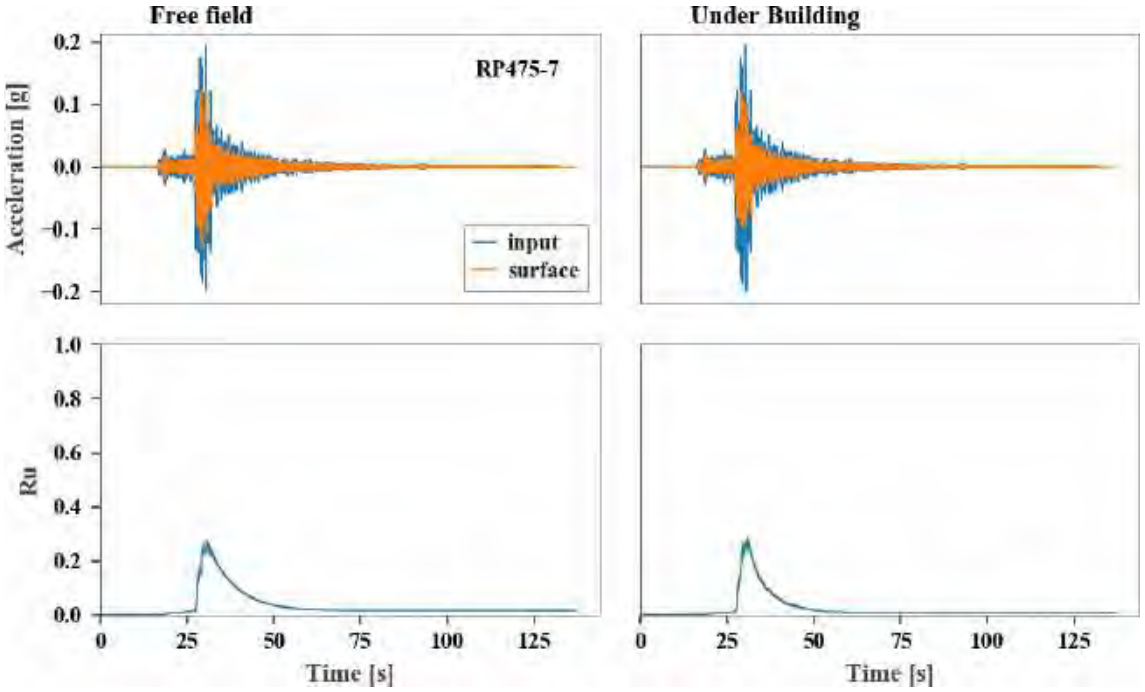

Figure C.7. Acceleration at base and bottom of the model, motion 7, 475-7.

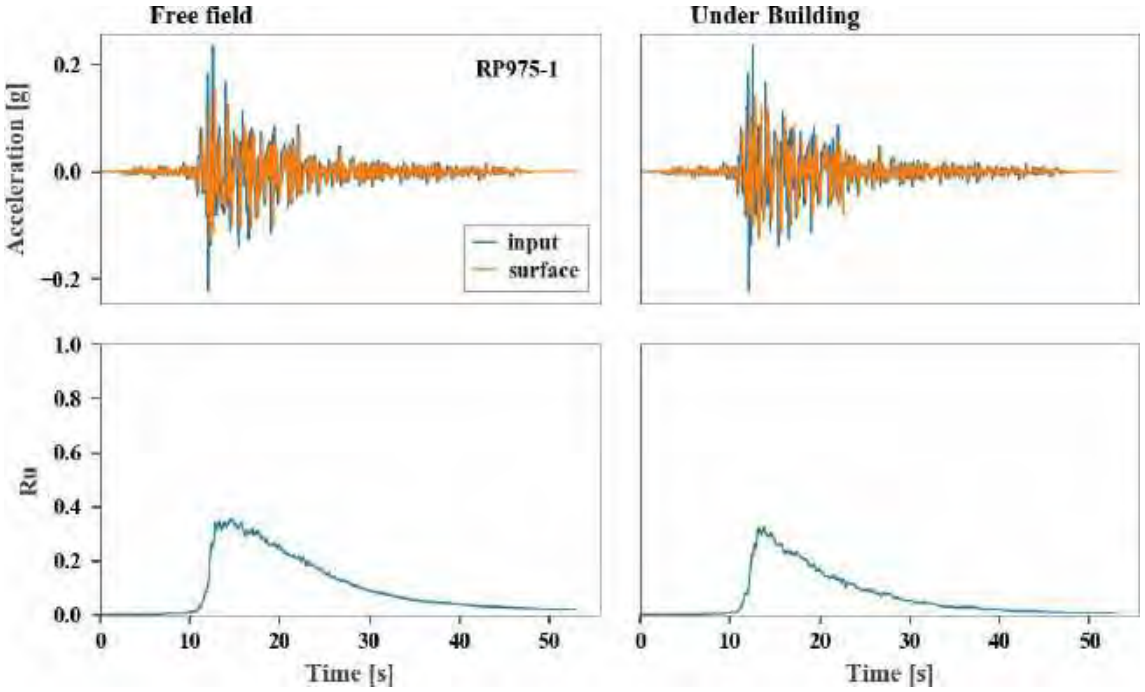

Figure C.8. Acceleration at base and bottom of the model, motion 8, 975-1.

This project has received funding from the European Union's Horizon 2020 research and innovation programme under grant agreement No. 700748

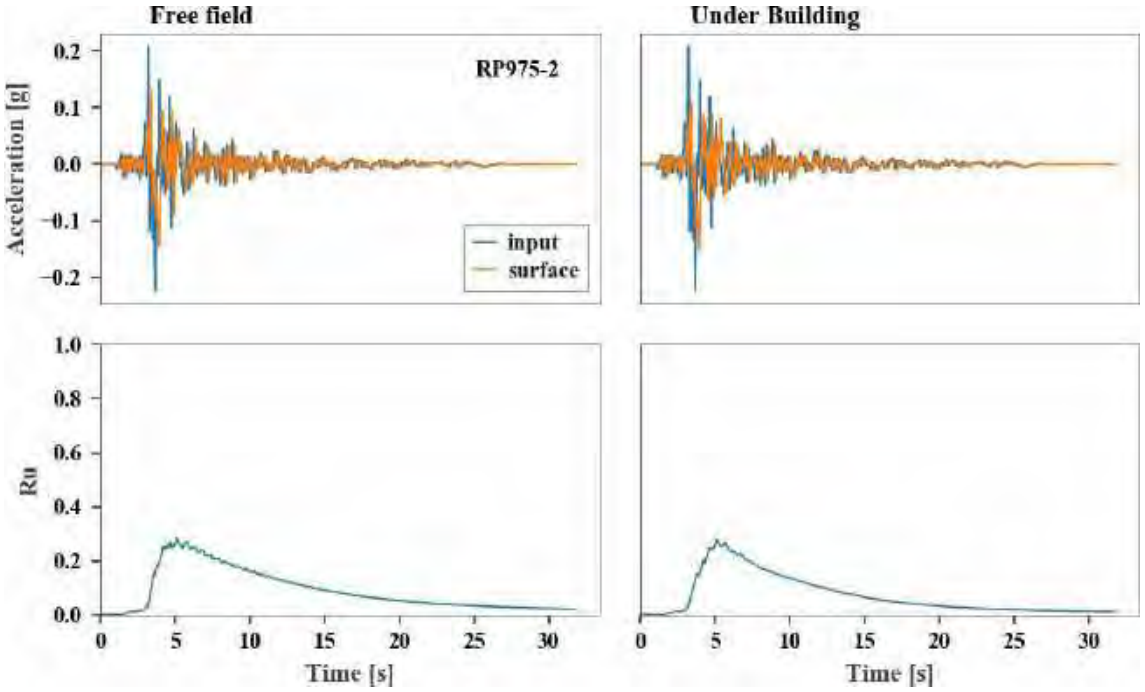

Figure C.9 Acceleration at base and bottom of the model, motion 9, 975-2.

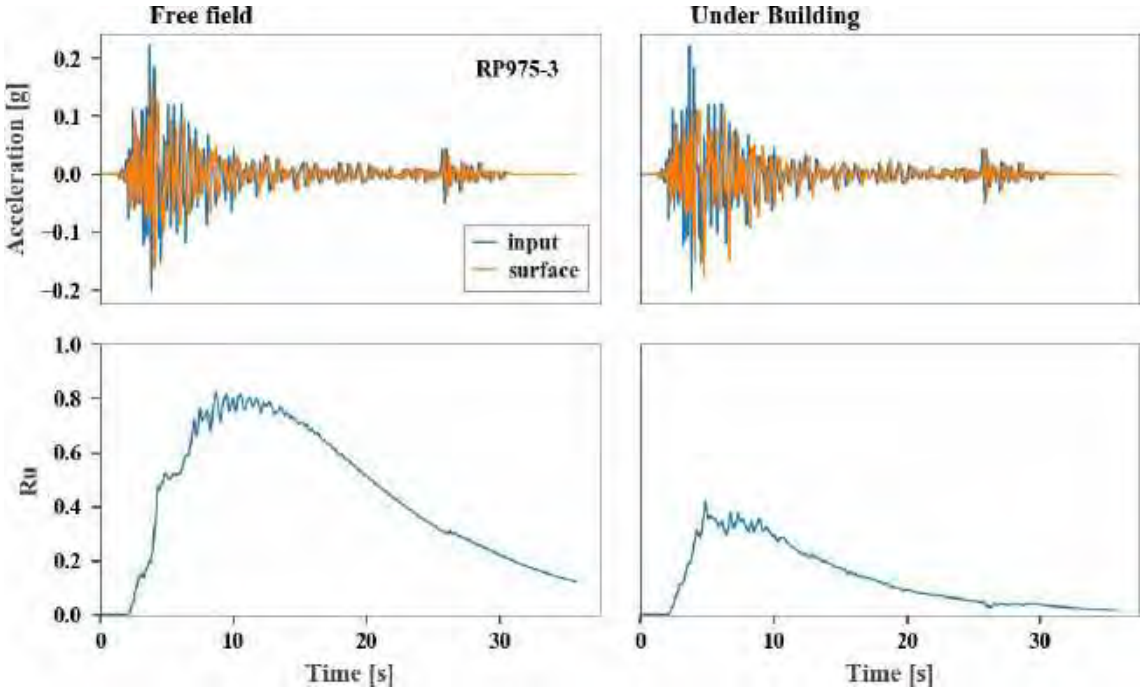

Figure C.10. Acceleration at base and bottom of the model, motion 10, 975-3.

This project has received funding from the European Union's Horizon 2020 research and innovation programme under grant agreement No. 700748

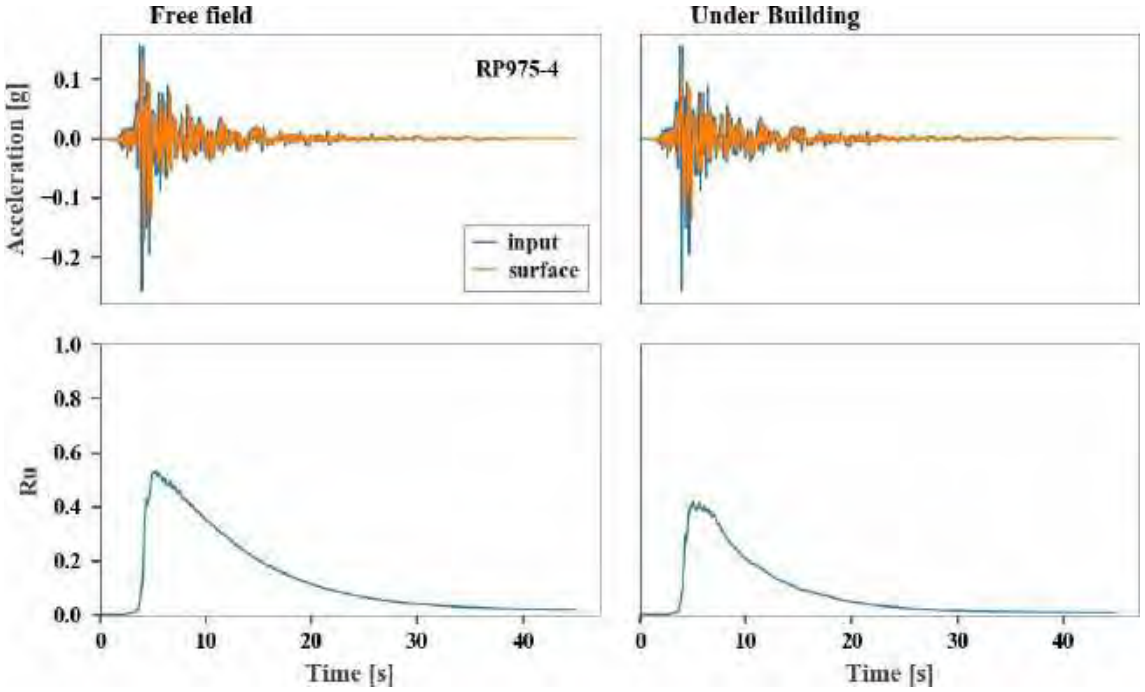

Figure C.11. Acceleration at base and bottom of the model, motion 11, 975-4.

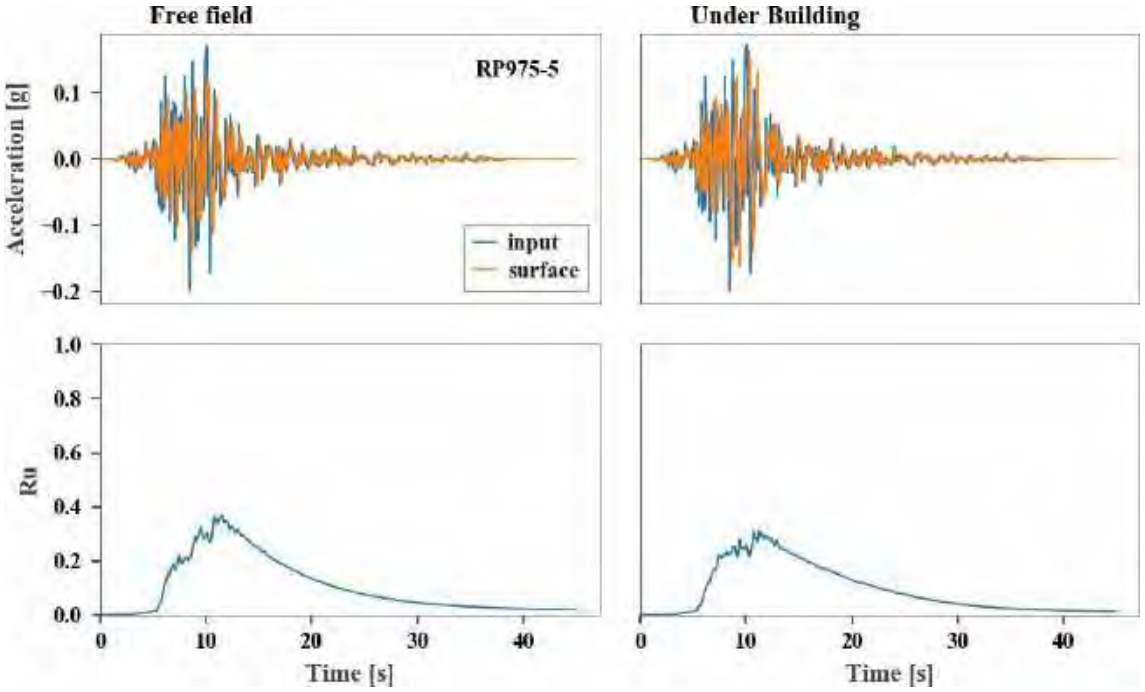

Figure C.12. Acceleration at base and bottom of the model, motion 12, 975-5.

This project has received funding from the European Union's Horizon 2020 research and innovation programme under grant agreement No. 700748

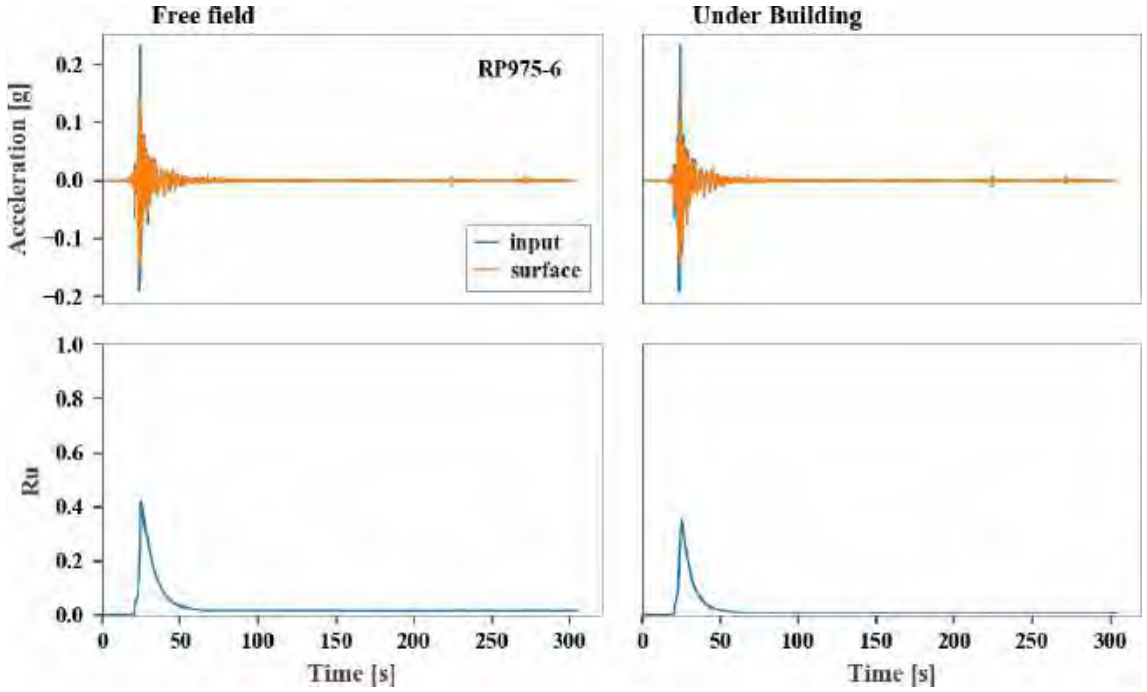

Figure C.13. Acceleration at base and bottom of the model, motion 13, 975-6.

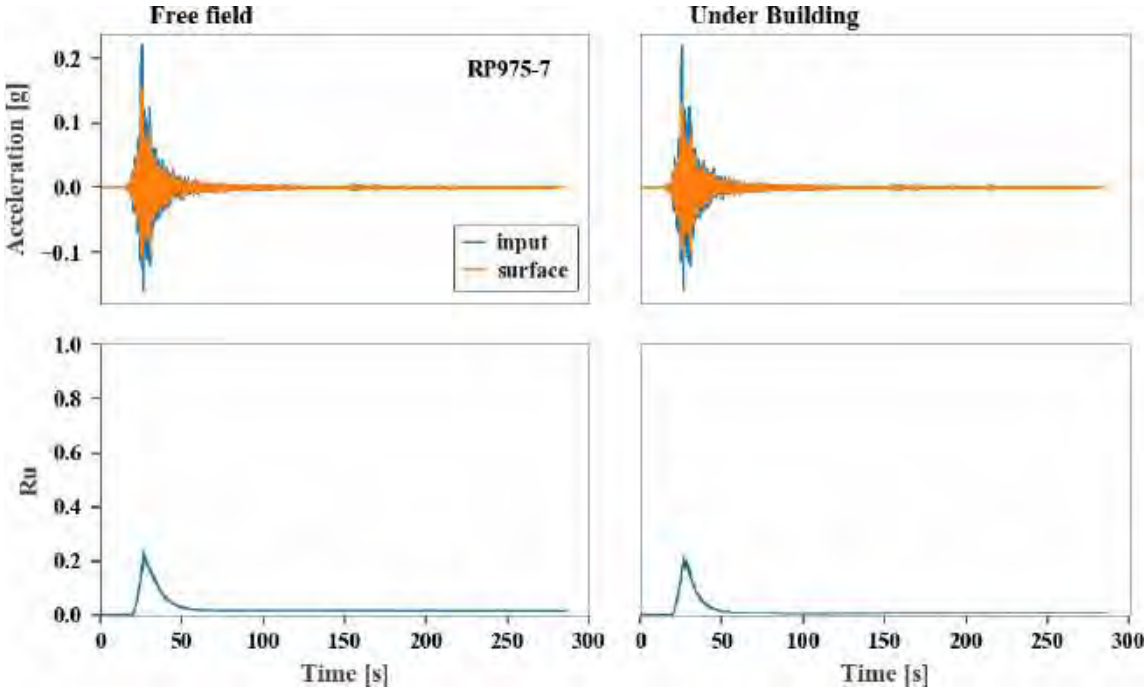

Figure C.14. Acceleration at base and bottom of the model, motion 14, 975-7.

This project has received funding from the European Union's Horizon 2020 research and innovation programme under grant agreement No. 700748

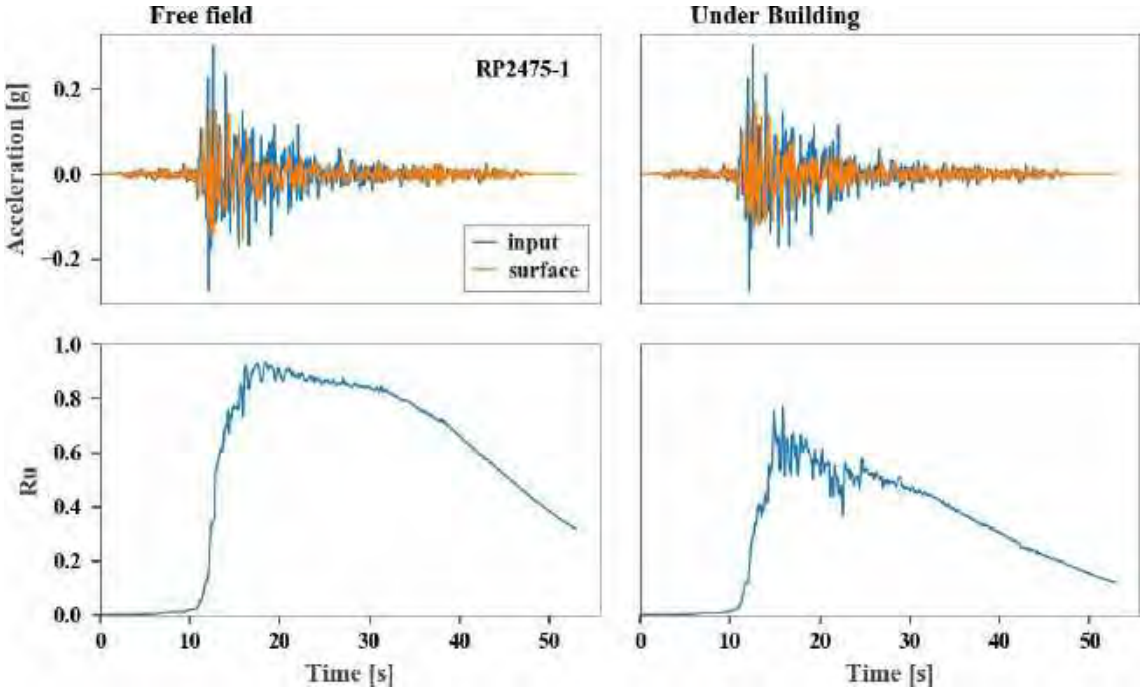

Figure C.15. Acceleration at base and bottom of the model, motion 15, 2475-1.

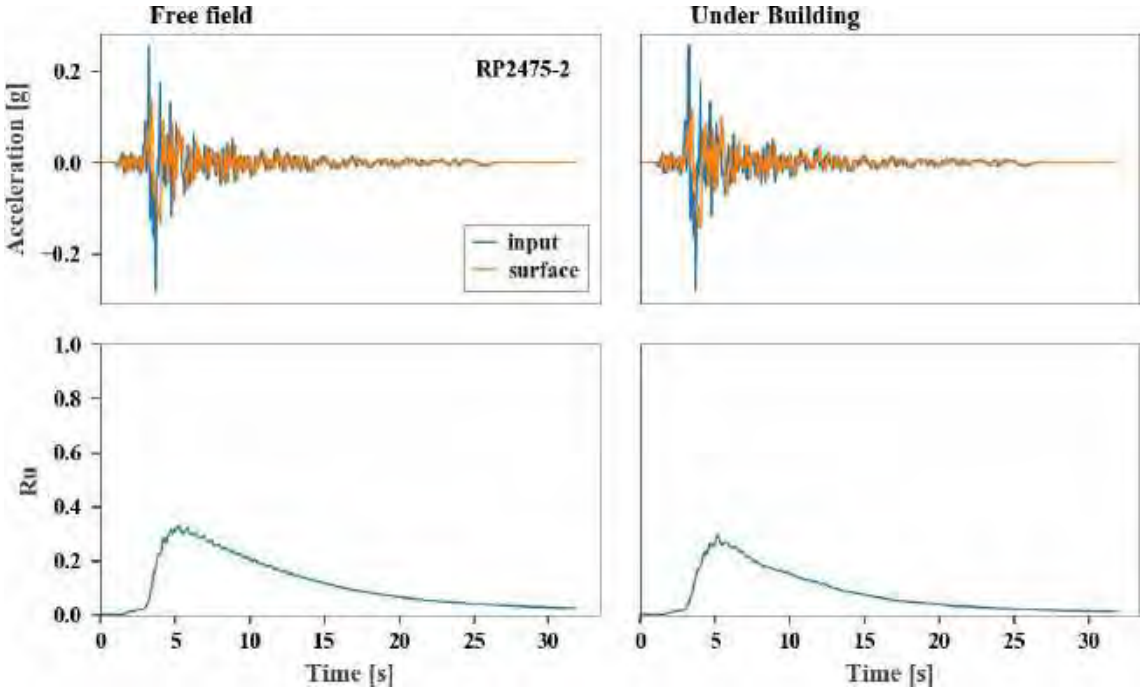

Figure C.16. Acceleration at base and bottom of the model, motion 16, 2475-2.

This project has received funding from the European Union's Horizon 2020 research and innovation programme under grant agreement No. 700748

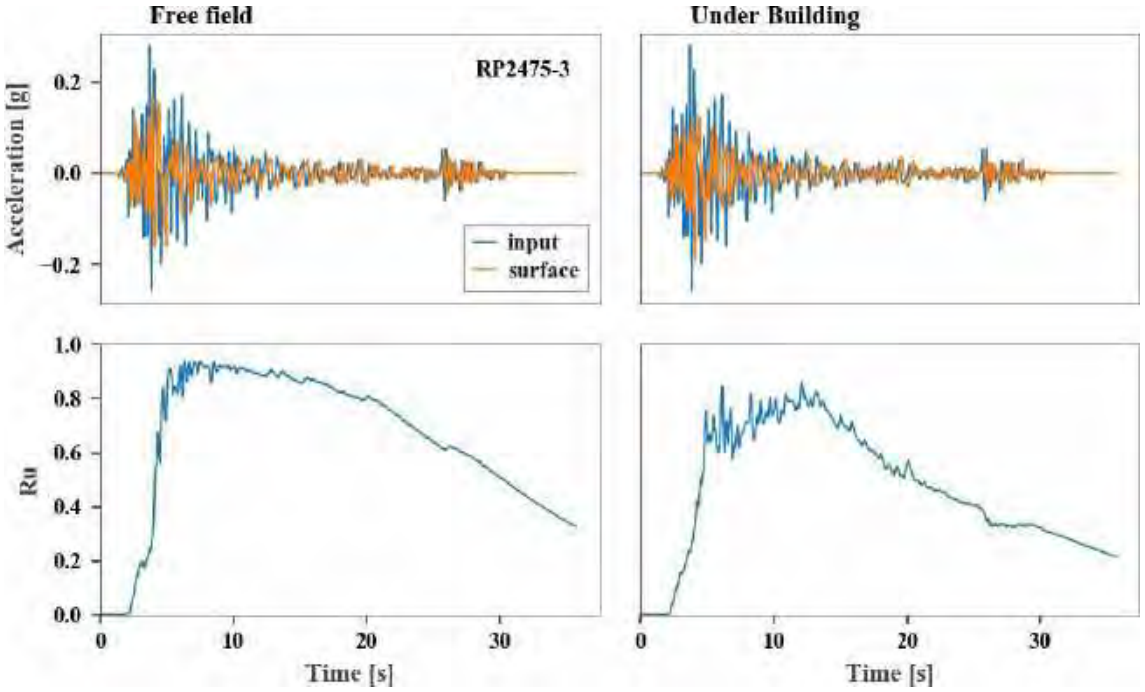

Figure C.17. Acceleration at base and bottom of the model, motion 17, 2475-3.

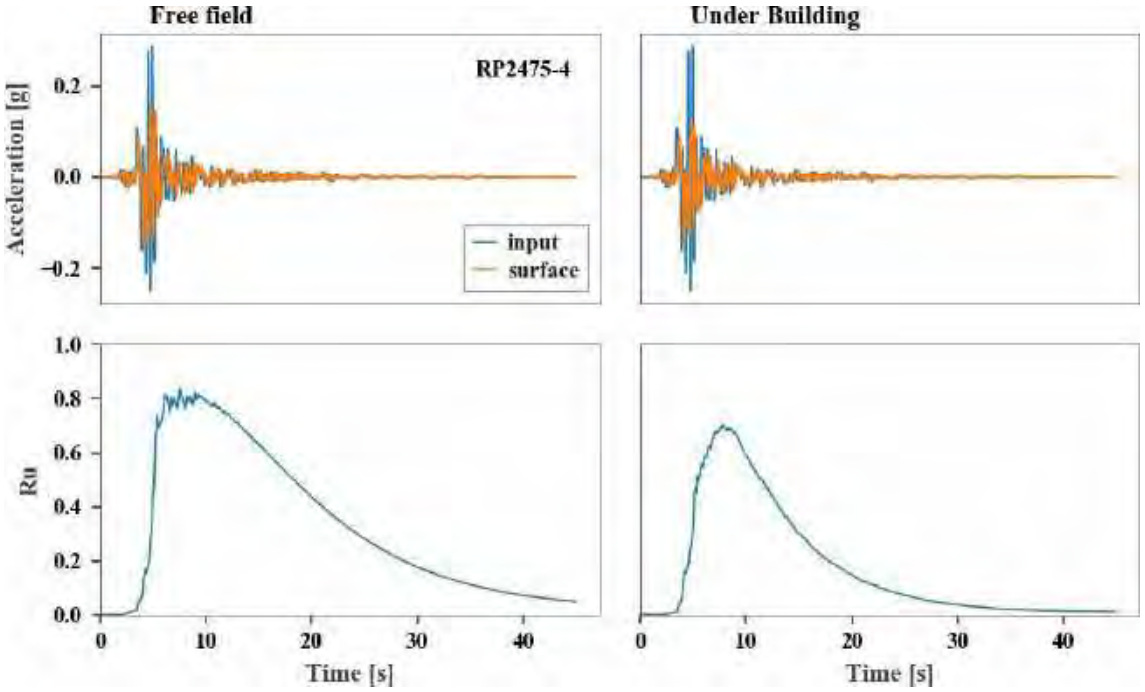

Figure C.18. Acceleration at base and bottom of the model, motion 18, 2475-4.

This project has received funding from the European Union's Horizon 2020 research and innovation programme under grant agreement No. 700748

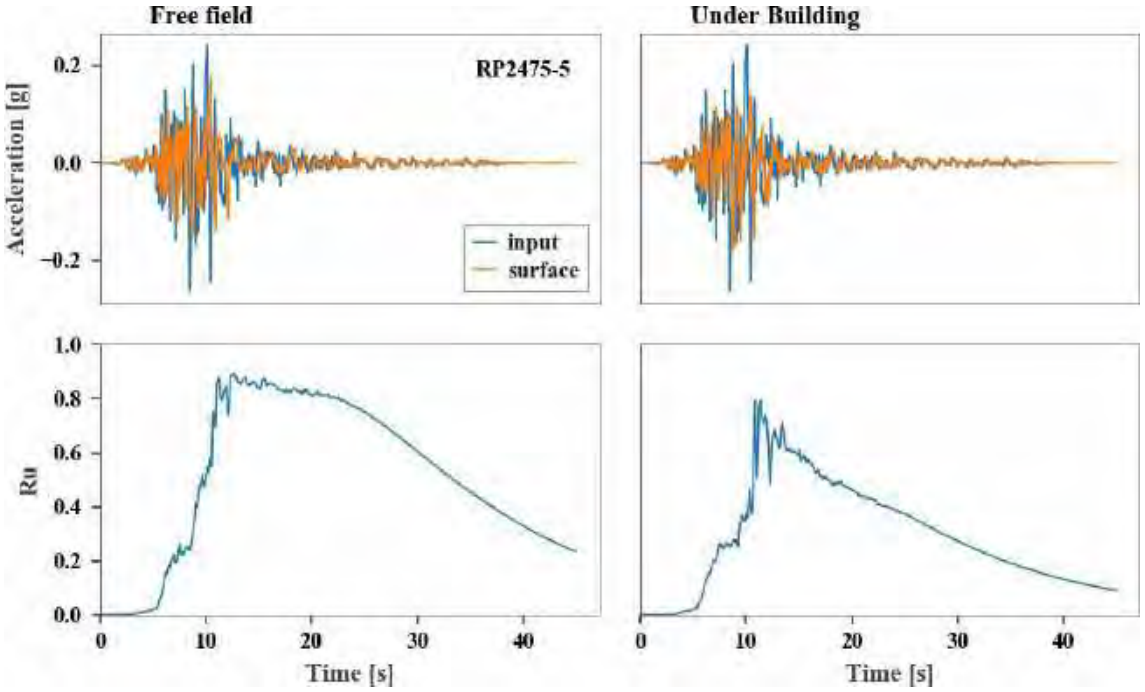

Figure C.19. Acceleration at base and bottom of the model, motion 19, 2475-5.

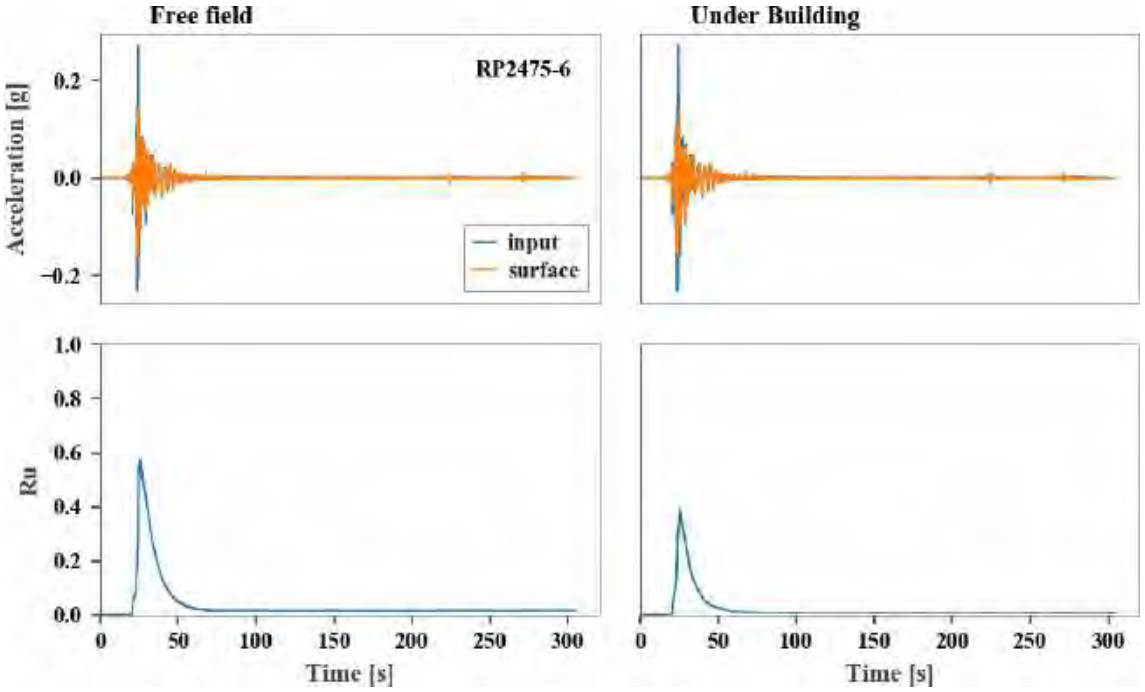

Figure C.20. Acceleration at base and bottom of the model, motion 20, 2475-6.

This project has received funding from the European Union's Horizon 2020 research and innovation programme under grant agreement No. 700748

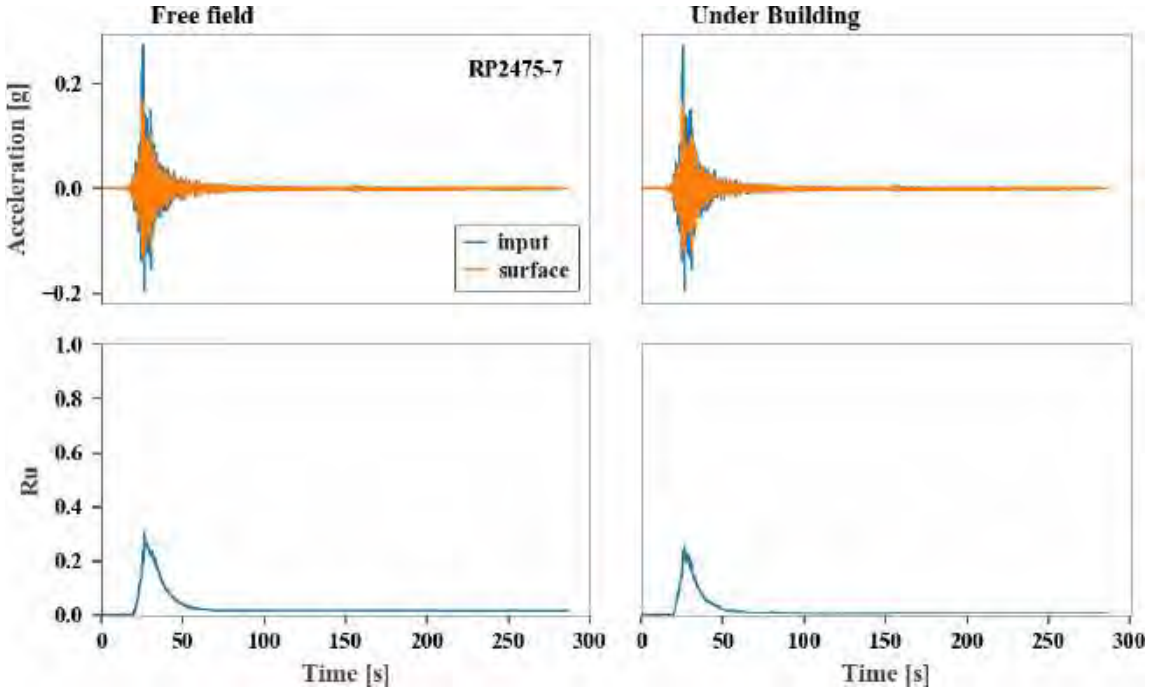

Figure C.21. Acceleration at base and bottom of the model, motion 21, 2475-7.